

Passive Microwave Remote Sensing of the Earth

Physical Foundations

Springer

Berlin

Heidelberg

New York

Hong Kong

London

Milan

Paris

Tokyo

Eugene A. Sharkov

Passive Microwave Remote Sensing of the Earth

Physical Foundations



Springer

Published in association with
Praxis Publishing
Chichester, UK



Professor Eugene A. Sharkov
Space Research Institute
Russian Academy of Sciences
Moscow
Russia

SPRINGER-PRAXIS BOOKS IN GEOPHYSICAL SCIENCES
SUBJECT ADVISORY EDITOR: Dr Philippe Blondel, C.Geol., F.G.S., Ph.D., M.Sc., Senior Scientist,
Department of Physics, University of Bath, Bath, UK

ISBN 3-540-43946-3 Springer-Verlag Berlin Heidelberg New York

Springer-Verlag is a part of Springer Science+Business Media (springeronline.com)
Bibliographic information published by Die Deutsche Bibliothek

Die Deutsche Bibliothek lists this publication in the Deutsche Nationalbibliografie;
detailed bibliographic data are available from the Internet at <http://dnb.ddb.de>

Library of Congress Cataloging-in-Publication Data
■ details to come ■

Apart from any fair dealing for the purposes of research or private study, or criticism or review, as permitted under the Copyright, Designs and Patents Act 1988, this publication may only be reproduced, stored or transmitted, in any form or by any means, with the prior permission in writing of the publishers, or in the case of reprographic reproduction in accordance with the terms of licences issued by the Copyright Licensing Agency. Enquiries concerning reproduction outside those terms should be sent to the publishers.

© Praxis Publishing Ltd, Chichester, UK, 2003
Printed in Germany

The use of general descriptive names, registered names, trademarks, etc. in this publication does not imply, even in the absence of a specific statement, that such names are exempt from the relevant protective laws and regulations and therefore free for general use.

Cover design: Jim Wilkie
Project Management: Originator Publishing Services, Gt Yarmouth, Norfolk, UK

Printed on acid-free paper

Contents

Preface	xiii
List of figures	xvii
List of tables	xxv
List of colour plates.	xxvii
1 Scientific and applied rationales of remote sensing study	1
1.1 What is meant by remote sensing?	1
1.2 The wave nature and spectrum of electromagnetic radiation.	2
1.3 Passive and active sensing.	9
1.4 Thermal radiation: the role and sources	11
1.5 Recognition and understanding of microwave signatures	16
1.6 Basic statements of wave electromagnetic theory	20
2 Random signals and fields	35
2.1 Determinate and stochastic description of natural processes	35
2.2 Basic characteristics of random processes	37
2.2.1 Ensembles of realizations	40
2.2.2 Probability densities of random processes	40
2.2.3 Moment functions of random processes.	44
2.2.4 Stationary random processes	45
2.2.5 Ergodic property.	46
2.3 Fundamentals of the correlation theory of random processes	47
2.3.1 Basic properties of the correlation function	48
2.3.2 The correlation coefficient.	48
2.3.3 The statistical spectrum	49

2.4	Quasi-ergodic processes	53
2.5	Types of spectra	55
2.5.1	Rectangular low-frequency spectrum	56
2.5.2	Gaussian spectrum	57
2.5.3	The Lorentzian spectrum	57
2.5.4	Band noise	58
2.5.5	Harmonic signal	58
2.5.6	White noise	59
2.5.7	Coloured noise	59
2.6	Linear and nonlinear systems and media	62
2.6.1	Low-pass filter (LPF).	67
2.7	Nonlinear transformations of random processes	69
2.8	Measurement of noise signal intensity	75
3	Microwave radiometers: functions, design concepts, characteristics	79
3.1	Basic types of passive microwave devices	79
3.2	Basic components of a passive microwave radiometer and their functions	84
3.3	The language of equivalent circuits: the antenna, radiobrightness and noise temperatures	87
3.4	Compensatory scheme of noise signal measurement	89
3.5	The fluctuation threshold sensitivity of radiometric systems	93
3.6	The modulation method of noise signal measurement	97
3.6.1	Modulation radiometer block-diagram	98
3.6.2	Temporal and spectral cyclograms	100
3.6.3	Synchronous detector	102
3.6.4	Modulation reception peculiarities	103
3.6.5	Threshold sensitivity	105
3.6.6	Null-balancing type	108
3.7	Experimental methods of threshold sensitivity measurement	111
3.8	Measurement of the frequency responses of radiometric systems by Fourier spectroscopy methods	114
3.9	Basic concepts of amplifying devices	121
3.9.1	Detector receivers	122
3.9.2	Direct amplification receivers	122
3.9.3	Superheterodyne-type receivers	122
3.10	Limiting sensitivities of radiometric systems	123
4	Thermal fluctuations and their fundamental laws	127
4.1	Thermal radiation and thermal fluctuations: a historical review	127
4.2	The fluctuation–dissipation theorem: a qualitative approach	131
4.3	Thermal fluctuations in the electrodynamics	135
4.4	Local thermal equilibrium	140

5 Emission fields and antenna systems	143
5.1 Basic characteristics of the emission field	143
5.1.1 Spectral intensity	144
5.1.2 Spectral radiation flux	145
5.1.3 Spectral radiant energy density	147
5.2 Microwave antennas and their characteristics	148
5.2.1 Emission of radiowaves	149
5.2.2 Antenna directional pattern (ADP)	149
5.2.3 The effective surface	153
5.2.4 Antenna directivity	154
5.2.5 Antenna gain	154
5.3 Antennas and brightness temperatures	155
5.3.1 Extended source	158
5.3.2 Discrete source	158
5.4 The scattering coefficient of antennas	160
5.5 Antenna temperature of antenna with resistance loss	164
5.6 Spatial-temporal dynamics in passive remote sensing	166
5.7 The equation of antenna smoothing	169
5.8 Outdoor calibration of radiometer instruments: the method of contrasting half-spaces	179
5.8.1 MCH procedure	190
5.8.2 Estimation of the main lobe width	192
5.8.3 Geometry of position of beams of multifrequency instruments	193
5.9 Antenna parameters of airborne microwave instruments	193
5.10 Antenna parameters of satellite microwave instruments	197
6 Black-body radiation	203
6.1 The ideal black-body model: historical aspects	203
6.1.1 Definition of a black body	204
6.1.2 Properties of a black body	204
6.1.3 Historical aspects	206
6.2 Black-body radiation laws	209
6.2.1 The Planck law (formula)	209
6.2.2 The Wien radiation law	213
6.2.3 The Rayleigh–Jeans radiation law	213
6.2.4 The Wien displacement law	214
6.2.5 The Stefan–Boltzmann law	214
6.2.6 Correlation properties of black-body radiation	215
6.3 The Kirchhoff law	217
6.3.1 Emissive ability	217
6.3.2 Absorbing ability	218
6.3.3 The Kirchhoff law forms	219

7 Grey-body radio-emission	223
7.1 Surface reflectivity	223
7.1.1 Reflection distribution function	224
7.1.2 Directional-hemispherical reflectivity	225
7.1.3 Hemispherical reflectivity	226
7.1.4 Diffuse and specular reflection	226
7.2 Effective radiation of reflecting surface	227
7.3 Reflection and transmission of plane waves at the plane interface boundary	233
7.4 Polarization features of radiation of a grey half-space with a smooth boundary	237
7.4.1 Nadir measurements	240
7.4.2 Angular measurements	241
7.5 Features of emission of a two-layer structure in the monochromatic approximation	245
7.6 Properties of quasi-coherence in thermal emission and the limits of its applicability	253
7.7 Thermal emission of multi-layered non-isothermal media	258
7.7.1 Physical substance of the problem	259
7.7.2 Thermal emission of non-isothermal media with arbitrary parameters	261
7.7.3 Limiting cases of general theory	264
7.7.4 Conditions for the method's feasibility	267
7.7.5 Spectral characteristics of thermal emission for some stratified media	268
8 Dielectric and emissive properties of terrestrial surfaces	277
8.1 Frequency dispersion of the electromagnetic properties of dielectrics	277
8.1.1 Dispersive properties	278
8.1.2 The Kronig–Kramers relations	281
8.2 Physical mechanisms of the polarization of dielectrics	282
8.3 Relaxation polarization models	288
8.3.1 The Debye model	289
8.3.2 Models of multiplicity of relaxation times	293
8.3.3 The Cole–Cole model	296
8.3.4 The Davidson–Cole model	297
8.3.5 The Havriliak–Negami model	297
8.4 Dielectric properties of freshwater	298
8.4.1 The structure of water	299
8.4.2 The experimental data processing technique	302
8.4.3 Empirical models	307
8.4.4 The analysis of the $\varepsilon_0(t)$ and $\lambda_S(t)$ parameters	310
8.4.5 Analysis of parameter $\varepsilon_\infty(t)$	311

8.5	Dielectric properties of salt water	314
8.5.1	Electrolyte structure	315
8.5.2	The experimental data processing technique	318
8.5.3	Spectral dependences of strong electrolytes.	319
8.5.4	The C-C diagrams for strong electrolytes.	323
8.5.5	The C-C model parameters for strong electrolytes	325
8.5.6	Dielectric properties of polyelectrolytes	328
8.6	Spectral and temperature characteristics of the emissive properties of water basins	329
8.6.1	Requirements for SSS observations.	335
8.7	Emissive properties of ice surfaces	336
8.8	Radiation properties of the terrestrial surfaces.	341
8.8.1	Primitive models.	341
8.8.2	Rocks.	343
8.8.3	Soils.	344
8.8.4	Tilled soil	353
8.8.5	Vegetation.	354
9	Foundations of radiative transfer theory	357
9.1	Radiative transfer theory phenomenology.	357
9.1.1	RTT applicability conditions.	359
9.2	Energy transformation by a volume element.	360
9.2.1	The act of absorption	360
9.2.2	The act of emission.	361
9.2.3	The act of scattering	362
9.3	The radiative transfer equation.	365
9.4	Special cases of the radiative transfer equation	367
9.4.1	A purely scattering medium	367
9.4.2	The absorbing and emitting medium.	368
9.4.3	Transparent medium	369
9.4.4	The ‘cold’ layer approximation	369
9.5	Equation of radiative transfer for the plane layer case	370
9.6	Boundary conditions	375
9.6.1	The transparent boundaries.	375
9.6.2	The black boundaries	375
9.6.3	Mirror-reflecting and black boundaries	376
9.7	Radiative transfer in the emitting and absorbing medium	376
9.8	Features of radiation of a half-space with the semi-transparent atmosphere.	378
9.8.1	Brightness contrast	379
9.8.2	Angular measurements.	380
9.8.3	The oblique section method	381
9.9	Radiative transfer in the emitting, absorbing and scattering medium.	383
9.10	Radiation of the inhomogeneous and non-isothermal half-space .	385

x **Contents**

9.11 Approximate methods for solution of the complete transfer equation	388
9.11.1 The spherical harmonics method	389
9.11.2 The Gaussian quadratures method	391
9.11.3 Approximate formulas	394
10 Electromagnetic properties of disperse media	397
10.1 Electromagnetic properties of secluded particles	397
10.1.1 The scattering cross-section and the scattering amplitude	398
10.1.2 The absorption cross-section	400
10.1.3 The extinction cross-section	401
10.1.4 The single scattering albedo	401
10.1.5 The scattering indicatrix	401
10.1.6 The optical theorem	402
10.1.7 Integral presentations of scattering amplitude and absorption cross-section	403
10.2 Basic concepts of Mie theory	404
10.2.1 Parameters of the Mie theory	405
10.3 Rayleigh scattering features	409
10.3.1 Metal particles	412
10.3.2 Soft particles	412
10.3.3 Water particles	413
10.4 Features of scattering properties of aqueous particles	414
10.5 Electromagnetic properties of polydisperse media	416
10.5.1 The density function	418
10.5.2 The volume density of particles	418
10.5.3 The integral distribution function	419
10.5.4 The relative density function	419
10.5.5 The density sampling probability	419
10.5.6 The total mass and the relative volume concentration of water	420
10.5.7 Radar reflectivity	421
10.5.8 Rainfall rates	421
10.5.9 Natural polydisperse media	422
10.5.10 Analytical forms of the density function	423
10.5.11 Parameters of attenuation and scattering of a polydisperse medium	425
10.6 Features of radiative transfer in dense media	428
10.6.1 Disperse medium and its characteristics	430
10.6.2 Experimental technique	433
10.6.3 Average values of electrodynamical characteristics	433
10.6.4 Fluctuation mode of extinction	435
11 Selective radiation	443
11.1 Mechanisms of selective radiation	443

11.2	The detailed equilibrium principle	446
11.3	The photon model and the transfer equation for quantum systems	448
11.4	Mechanisms of broadening of spectral lines	450
11.5	Radiation transmission through a gas layer	462
11.6	Microwave radiative transfer in the terrestrial atmosphere	467
11.6.1	Atmospheric models	468
11.6.2	Stratified atmosphere radiation	468
11.6.3	Molecular oxygen	470
11.6.4	Atmospheric water vapour	474
11.6.5	Absorption of microwaves in the terrestrial atmosphere	476
12	Radiative properties of the terrestrial ‘surface – atmosphere’ system	479
12.1	Radiation of the homogeneous ocean–atmosphere system	479
12.1.1	The basis model	479
12.1.2	Integral parameters	484
12.1.3	Temperature profiles	486
12.2	Microwave remote sensing of cloud fields	488
12.2.1	Cloud classification schemes – the contribution of microwave radiometry	488
12.2.2	Microwave remote sensing of rainfalls	492
12.3	Microwave remote sensing of surface oceanic heat flux fields	495
12.3.1	Radiothermal spectroscopy of the ocean–atmosphere transition layer	498
12.4	Microwave remote sensing of the oceanic surface	501
12.4.1	Rough sea surface	502
12.4.2	Sea wave breaking fields	507
12.5	Microwave remote sensing of catastrophic oil spills on the sea surface	511
12.5.1	Investigation techniques and processing of the results	512
12.5.2	Analysis of radar mapping data	516
12.5.3	Radiothermal measurement data analysis	517
12.5.4	Joint analysis of radar and radiothermal images	521
12.5.5	Radio-spectroscopic observations	522
13	Inversion problems for passive microwave measurements	525
13.1	Features of microwave measurements	525
13.2	Basic categories of inversion procedures for microwave sensing	526
13.2.1	Statistical techniques	527
13.2.2	Forward model inversion	527
13.2.3	Explicit inverse	529
13.2.4	Other techniques	530
14	Passive microwave space missions	531
14.1	Elements of microwave radiometry history	531
14.2	Ongoing missions and tendencies of their development	536

14.2.1	DMSP mission	536
14.2.2	TRMM.	538
14.2.3	Aqua mission.	539
14.2.4	ADEOS-II mission	542
14.3	Future passive microwave space missions	544
14.3.1	MTVZA-OK mission.	544
14.3.2	CLOUDS mission.	546
14.3.3	MEGHA-TROPIQUES mission.	548
14.3.4	NPOESS program.	552
14.3.5	OSIRIS concept	554
Conclusion	557
Appendix A – The International System of Units (SI units)	559
Appendix B – Fundamental theorems and correlations of Fourier spectrum analysis	565
References and bibliography	569
Index	611

Preface

The inclusion of the methods and means of microwave diagnostics into space observations in the 1970s was, undoubtedly, a significant landmark in the development of remote sensing of the Earth as a whole. When compared with the use of just the optical and infrared spectral ranges, the study and understanding of the microwave patterns in the Earth's surface–atmosphere system brings the essentially different physical information capacity of microwave sensing to the study of terrestrial objects. It is this circumstance that has drastically changed both the configuration of potential satellite systems, designed for sensing the Earth, and the character and information saturation of remote sensing as a whole. At present, none of the planned large satellite missions for investigating the Earth (or, which is interesting, those for detailed investigation of the planets) manages without applying either passive or active radiophysical devices in some configuration. In addition, the other advantages of microwave diagnostics – such as the possibility of obtaining information at any time of the day, the wide weather range, the independence of solar illumination – have attracted the attention of a great swathe of researchers. And, in many cases, it has been these circumstances that have played a key part in the early stages of introducing radiophysical methods into remote-sensing tasks. However, the subsequent development of these methods has shown that the basic importance of introducing them into remote sensing is on a quite different plane, that is in the diffraction nature of the interaction of microwave electromagnetic waves with rough objects of the Earth's surface and with meteostructures in the Earth's atmosphere, and, on the other hand – with the features of quantum radiation of physical objects in the microwave range.

An obviously high physical information capacity of microwave methods has impelled a lot of experts in various disciplines – meteorologists, geophysicists, oceanologists, geologists, soil scientists – to actively participate in mastering remotely sensed microwave information. However, not possessing special knowledge in radio-physics, interested researchers sometimes interpret wrongly the radiopatterns of the

physical objects they are studying because they are using geometrical optics methodology for the optical range, which is natural for a human being. The author has had many opportunities to discover this fact through his personal experience in collaborating with experts in various disciplines during his 25-year period of work in the area of microwave remote sensing of the Earth.

In the field of the application of microwave observation data, a book was needed which would give a systematic and unified presentation of the fundamental statements and basic principles of the theory of natural radiation of physical objects, as well as of the various instrumental and methodological issues of microwave measurements. In addition, it seemed useful to present a unified and systematic description of recent achievements in microwave sensing, which would be easily accessible to advanced undergraduate and postgraduate students, to researchers and to instrument engineers. For this reason, unlike the well-known microwave sensing monographs, the present book was conceived, on the one hand, as a manual for a course of lectures on radiophysical methods in the remote sensing of the Earth and, on the other hand, as a text giving a systematized idea of the possibilities and modern achievements of the microwave diagnostics method, intended for a wide range of specialists and other interested readers.

The present book was prepared on the basis of lecture courses delivered by the author for many years (1975–2002) to senior students at the Moscow Physical and Technical Institute (Dolgoprudny town) and at the Moscow State University of Geodesy and Cartography (Moscow). This approach has substantially conditioned both the structure of the book and the character of the educational material. The presentation is configured in such a manner that the reader can acquire the necessary fundamental knowledge of the quantum mechanism of thermal radiation, and the most complete ideas on the modern level of development of microwave diagnostics. The content of this book is much broader than the requirements usually claimed for a manual for students. Many parts of the book contain detailed information and can be used as a work of reference on some special issues of microwave remote diagnostics.

Chapter 1 deals with the science and application aspects of remote sensing of the Earth, the role and place of radiophysical methods, the basic statements of electromagnetic theory, the physical features of thermal radiation, and the possibilities of passive and active microwave diagnostics methods. Chapter 2, devoted to basic statements of the representation and transformation of random signals and fields, has a reference character to some extent. Nevertheless, the information given in this chapter will be very necessary for further mastering of the material. The basic methods and schemes of noise signal measurement are considered in Chapter 3.

The fundamental law of nature, which relates the quantum fluctuation radiation of an object of any physical nature with its dissipation macro-properties and is named the fluctuation–dissipation theorem (FDT), is the subject considered in Chapter 4. In addition, this chapter analyses the quasi-stationary FDT approximation, known as the Nyquist formula, and the geometric-optical approximation – the Kirchhoff law – which are very important for applications. Chapter 5 chiefly pays

attention to the basic characteristics of radiation fields and to the physical aspects of forming the radiation fields of microwave antennas. This chapter also considers the basic methods of measuring the parameters of ground and onboard antenna systems, introduces the equation for antenna smoothing and analyses the procedures of reconstruction (restoration) of radio-emissive microwave images.

The absolutely black-body model, which is paramount in thermal radiation theory and practice, and the fundamental laws of radiation of such a system are subjects of consideration in Chapter 6. Here the concepts of the emissivity of physical bodies of grey-body radiation character are introduced, and the experimental data on natural media emissivities are presented. The more detailed analysis of features of grey-body radiation and the elementary (but, nevertheless, widely used in observational practice) physical models for calculating the media of grey-body radiation character are considered in Chapter 7. Chapter 8 presents the rich set of experimental observational data on emissive characteristics and dielectric properties of substances distributed both on the Earth and on terrestrial planets.

Chapters 9 to 11 present the phenomenological basis and also give the analysis of basic equations and fundamental statements, which are necessary for studying radiation transfer in absorbing, radiating and dissipating media. The formal and approximate solutions of the equation of radiation transfer, presented in Chapter 9, are widely used in later chapters for consideration of the radiation transfer in disperse media (hydrometeors and aerosols in the atmosphere). Here an important component of the analysis is the consideration of diffraction scattering (Mie scattering) of electromagnetic waves on the individual particles (Chapter 10) which form the disperse mixtures. A principally new (namely, quantum-mechanical) methodology is offered in Chapter 11 to describe the radiation transfer in gaseous media with subsequent derivation of the transfer equation for the photon gas. The features of selective types of gas systems' radiation, principal among which are the physical mechanisms of line broadening and the modern shapes of lines, are outlined in detail here.

On the basis of the data obtained in previous sections, the spectral patterns of microwave radiation are formed in Chapter 12 for the ocean–atmosphere and land–atmosphere systems for observations from satellites and aircraft. The main focus is on the latest experimental results from studies of the thermal radiation of disturbed sea surface, cloudy atmosphere with various types of hydrometeors and moist soil surfaces with various types of vegetation. This chapter can be considered, to some extent, as a brief review of the modern state of microwave sensing.

In Chapter 13 the reader will find the detailed analysis of inversion problems in microwave sensing. This chapter includes consideration of empirical, semi-empirical, and physical algorithms for advanced inversion procedures.

Chapter 14 is devoted to the detailed historical analysis of time evolution of microwave airborne and spaceborne missions beginning with the first successful launches of Russian ‘Kosmos-243’ and ‘Kosmos-384’ satellites carrying microwave, multifrequency instruments. The original Russian microwave systems and then more modern ones are outlined in detail. The contemporary situation in the

equipment part of planned microwave missions, the ways observation techniques and methods developed, the antenna systems, and the mastering of new frequency ranges are also considered in detail in this chapter.

The book's detailed Bibliography will certainly be useful, for both students and postgraduates in the relevant disciplines, and for researchers and engineers. These references cannot be considered exhaustive in certain more specialist areas.

Some of the experimental and natural results used in preparing this book were obtained by the author during his work in the Department of Microwave Remote Sensing of the Earth of the Institute for Space Research (Russian Academy of Sciences). The Department was headed at that time by the untimely deceased Professor V. S. Etkin (1931–1995). The natural experiments, carried out in the period of 1973–1982 with microwave equipment of heightened sensitivity, as well as the unique results obtained with these instruments, have determined in many respects the configuration of future aero-satellite microwave remote-sensing systems. The author is grateful to colleagues in the Department, whose support was indispensable for performing the unique full-scale (location) experiments, and, especially, to I. V. Pokrovskaya, M. D. Raev, M. G. Bulatov, V. M. Veselov, V. G. Mirovsky, I. V. Cherny, and V. Yu. Raizer. The author greatly regrets that we have already lost such active participants in the first stage of the experimental work as E. A. Bespalova and Yu. A. Militsky, who made so significant a contribution to its organization and implementation.

The author is grateful to Mr Yu. Preobrazhenskii for his constructive approach in translating the manuscript into English. The typing of the intricate draft by Mrs Nataly Komarova is appreciated. I also wish to express my thanks for the support and encouragement received from Clive Horwood, Chairman of Praxis Publishing.

The author has taken advantage of the advice and recommendations of his colleagues throughout the time the manuscript has been in preparation.

Acknowledging the complexity of the subject matter of this publication and desiring to perfect his presentation of it, the author will be glad to receive constructive comments and suggestions from interested readers (email: esharkov@iki.rssi.ru).

List of figures

1.1	The spectrum of electromagnetic radiation	5
1.2	Schematic presentation of the influence on a human of the surrounding electromagnetic radiation	8
1.3	The qualitative picture of the correlation between the main sources of radiation and features of the Earth's atmosphere	13
1.4	Simplified model to demonstrate the possibilities of emitted and backscattering signals in vegetation	18
2.1	Air survey experimental results of the disturbed sea surface	38
2.2	Simplified scheme to generate the statistical ensemble for the random process	41
2.3	Typical example of amplitude nonlinear characteristic for the radiotechnic amplifier	64
2.4	Schematic presentation of the functioning of a low-pass filter	67
2.5	Schematic presentation of the functioning of a nonlinear square-law electrical circuit	71
2.6	Transformation of a narrowband spectrum by a square-law circuit	74
2.7	The scheme to measure the intensity of a random signal	76
3.1	The qualitative picture (in temperature units) of the spectrum of electromagnetic emissions and artificial radiations	80
3.2	Microwave radiometers for spectral line observations	83
3.3	Schematic presentation of the transmission of information data from a natural object	85
3.4	The output signal record of a radiometer	91
3.5	Functional scheme of a compensative radiometer	92
3.6	The output signal record (Gaussian random process) of a compensative radiometer	94
3.7	The correlation between output spectra of a compensative radiometer	96
3.8	Functional scheme (block-diagram) of a switched radiometer	99
3.9	Temporal and spectral cyclograms of working for a switched radiometer	101

3.10	Physical presentation of the work of a synchronous detector	102
3.11	Detailed temporal cyclogram for outputs of a square-law detector	104
3.12	Block-diagram of a null-balancing radiometer	110
3.13	Experimental registrogram of an output fluctuation Gaussian signal for calculating the radiometer threshold sensitivity using a ‘step input’ signal.	113
3.14	Block-diagram of the measurement scheme and the switched radiometer	118
3.15	Experimental results by Fourier spectroscopy processing.	120
5.1	System of axes for the determination of spectral intensity	144
5.2	System of axes for resulting emission flow	146
5.3	Schematic presentation of an antenna directional pattern (ADP) formation .	152
5.4	Schematic presentation of receiving procedure for the antenna temperature determination	156
5.5	The relationship of antenna temperature value to a solid angular value of source	159
5.6	Schematic presentation of the antenna temperature components	161
5.7	The signal registration at the moment (t_0) of the flight over a thermal ‘cold’ object.	169
5.8	Schematic presentation of smoothing procedure for a complicated one-dimensional source	171
5.9	The smoothing procedure for two identical plane objects	172
5.10	Examples of the relationship between antenna directional pattern (ADP) and special spectrum	174
5.11	The restoration of a stepped signal model from the convolution of this model with the ideal ADP	176
5.12	Qualitative picture of the restoration of a signal in the presence of noise components	178
5.13	Fragments of the output radiometer signal of airborne instruments when crossing a water–land transition	181
5.14	Fragments of the output signal of airborne radiometer R-18 when crossing a land–water transition of various heights	185
5.15	Fragments of the output signal of airborne radiometer R-18 when crossing a water–land and a land–water transition	186
5.16	Fragment of the output signal of airborne radiometer R-2 when crossing a land–water transition at various heights	187
5.17	Schematic presentation of a water–land transition airborne experiment	188
5.18	Schematic presentation of geometry for main axes and values of ADP main lobes of radiometric instruments	194
5.19	Fragments of synchronous output signals of airborne radiometers R8, R2 and R0.8 when crossing a land–sea transition.	195
5.20	Scheme of satellite experiment geometry (longitudinal section in orbit plane) .	196
5.21	Fragment of radiometer ($\lambda = 3.4$ cm) output signal of satellite ‘Kosmos-243’ instruments.	198
5.22	Fragment of radiometer ($\lambda = 8.5$ cm) output signal of satellite ‘Kosmos-243’ instruments.	199
5.23	Fragment of radiometer ($\lambda = 3.4$ cm) output signal of satellite ‘Kosmos-384’ instruments.	201
5.24	Fragment of radiometer ($\lambda = 1.55$ cm) output signal of satellite ‘Nimbus-5’ instruments.	201

6.1	Classic experimental model of black-body source	207
6.2	Hemispherical spectral radiation flux of black bodies for some values of temperatures versus wavelengths.	211
6.3	Hemispherical of black-body spectral radiation flux distribution versus generalized coordinates	213
6.4	Correlation coefficient of spectral black-body radiant energy density versus generalized lag	216
7.1	Schematic beam representation of the incident and reflected radiations for the determination of the bidirectional reflectivity	224
7.2	Schematic beam representation of the emitted, incident and reflected radiations for the determination of effective emission	228
7.3	Schematic beam presentation of remote sensing measuring procedure	230
7.4	Remote microwave results of the specialized nadir–zenithal airborne (Russian IL-14) instruments.	232
7.5	Schematic presentation of the remote sensing polarization procedure	238
7.6	Emissivity of dielectric medium with smooth surface as a function of real relative dielectric constant (ϵ_1)	240
7.7	Polarization properties of emissivities of water surface and dielectric media	242
7.8	Schematic presentation of airborne remote sensing measuring procedure for the incline of a smooth surface with θ angle slope	244
7.9	Reflections and transmissions of plane waves at the smooth boundaries of a two-layered structure	247
7.10	Relationships of emissivity of two-layered structures as a function of the ice depth	248
7.11	Polarization properties at 0.8 cm of oil sheet–water structure.	250
7.12	Polarization properties of air–ice–water structure	250
7.13	Spectral characteristics of the emission of an isothermal three-layered structure with nadir observation.	252
7.14	Spectral characteristics of the emission of air–water–ice structure with nadir observation.	253
7.15	Relationships of two-layered medium (ice–water) emissivity averaged over the amplitude-frequency characteristic (AFC) versus ice depth with nadir observation.	257
7.16	The ratio $T(h)/T(\infty)$ versus a layer depth for sand–metal plate structure with nadir observation	258
7.17	Spectral characteristics of the natural radiation of a three-layered non-isothermal medium	269
7.18	Spectral characteristics of the natural radiation of a three-layered medium (model B) with a sharp ‘pulse-like’ temperature anomaly	270
7.19	Spectral characteristics of the natural radiation of a three-layered medium with a ‘pulse-like’ anomaly of dielectric losses (model C)	272
7.20	Spectral characteristics of the natural radiation of a three-layered medium with an anomalous value of the dielectric losses	272
7.21	Spectral characteristics of the natural radiation as a function of the number of subdivisions, N , of the layer in the medium	273
		274

xx List of figures

8.1	Schematic presentation of the effect on polarization properties in the case of the resonance mechanism	284
8.2	Schematic presentation of the effect on polarization properties in the case of the relaxation mechanism	285
8.3	The semi-quantitative presentation of a complex index of a refraction for liquid water	286
8.4	The semi-quantitative presentation of a complex index of reflection for ice samples	287
8.5	Frequency properties of $\varepsilon_1(\omega)$ and $\varepsilon_2(\omega)$ for Debye-type dielectric media	290
8.6	Relationship of the imaginary part of complex permittivity as a function of the real part (Cole–Cole diagram) for dielectric medium with various polarization mechanisms	292
8.7	Electronic and structural peculiarities of the water molecule	300
8.8	Experimental diagrams for $\varepsilon_1(\lambda)$ as function $\varepsilon_2(\lambda)/\lambda$ and for $\varepsilon_1(\lambda)$ as function $\varepsilon_2(\lambda) \cdot \lambda$	303
8.9	Temperature-dependence of static constant of liquid water	305
8.10	Temperature-dependence of relaxation wavelength	306
8.11	Frequency dependence of the real part for the complex permittivity at temperatures from -4.1°C to 80°C	307
8.12	Temperature-dependent optic constant in the Debye model	309
8.13	Schematic presentation of a hydro-rotation atmosphere of an ion in water solution	316
8.14	Spectra of the real part of the permittivity of water solution NaCl in the range 0.4 – 3.5 cm at 250°C	320
8.15	Experimental and calculated spectra of imaginary full ε_2 and corrected ε_{2c} parts of the permittivity of water solution NaCl	321
8.16	Cole–Cole diagrams for the water solution NaCl	324
8.17	Relation of C–C and D model parameters to salinity of water solution NaCl	326
8.18	Spectra of smooth water surface emissivity at temperatures 0 , 20 and 30°C for fresh and salt water	331
8.19	Spectra of radiobrightness temperature of a smooth water surface at temperatures 0 , 20 and 30°C for fresh and salt water	332
8.20	Temperature-dependent radiobrightness of a smooth water surface	332
8.21	Salinity-dependent radiobrightness of a smooth water surface	333
8.22	Nadir emissivity spectra of natural media	339
8.23	Emissivity curves for vertical incidence and for different permittivities of various terrestrial media	342
8.24	Nadir field moisture-dependent emissivity of bare soils	347
8.25	Field moisture-dependent polarization coefficient of bare clay (a) and sand (b) soils at various wavelengths	349
8.26	Polarization features of radio-emission for clay soil surface with moisture 10%	350
9.1	Schematic presentation of the geometry of the radiative transfer procedure by a volume element	361
9.2	Schematic presentation of the radiative transfer passing through the absorbing and emitting one-dimensional layer	369
9.3	The coordinate system for the plane-parallel case	371

9.4	The coordinate system for the formal solution of the radiative transfer equation for the plane-parallel case	371
9.5	The mirror-reflecting, emissive and black boundary conditions for the radiative transfer equation solution	371
9.6	The measurement scheme for recording the outgoing radiation by the aircarrier (A) (aircraft) inside the atmosphere and by a satellite (S) outside the atmosphere	377
9.7	Emissivity of the atmosphere–surface system as a function of the atmospheric optical thickness	380
9.8	Polarization dependences of the atmosphere–surface system (solid lines) and of the surface (dashed lines)	381
9.9	Measured atmospheric opacity at 19 (squares) and 35 GHz (circles) under clear weather conditions	383
10.1	Schematic presentation of the geometry in scattering studies in particles.	399
10.2	The geometrical positions of the point within the particle (r') and the observation point (R) studies of scattering amplitude	403
10.3	The backscattering efficiency factor of a metal sphere as a function of the size parameter (at microwave bands).	409
10.4	The efficiency factors of scattering (Q_s), absorption (Q_A) and extinction (Q_E) for small spheres	413
10.5	The efficiency factors of scattering (Q_s), backscattering (Q_{BS}) and extinction (Q_E) for aqueous spheres	415
10.6	Single-scattering albedo of aqueous spheres as a function of size parameter (normalized radius) at 4, 6, 9, 15, 34.8 and 100 GHz.	416
10.7	The extinction factor of spherical raindrops as a function of frequency	417
10.8	Particle-size distributions (the density functions) for natural disperse media	422
10.9	Frequency characteristics of rain attenuation at rain temperature of 20°C, for Laws–Parsons (solid curves) and Marshall–Palmer (dashed curves) drop-size distributions	427
10.10	Frequency characteristics of attenuation for natural disperse media: rain (solid curves) and fog (dashed curves)	428
10.11	The photographs of disperse water drop medium with relative volume concentrations.	431
10.12	The experimental histograms of droplet radii for medium N_1 (a) and for medium N_2 (b)	432
10.13	The extinction coefficient (γ), radiobrightness temperature (T_B) and backscattering cross-section (σ_{BS}) of disperse water drop media as functions of the volume concentration (C) and the number density (N)	434
10.14	The photographic regisograms of a signal (at intermediate frequency)	436
10.15	The statistical characteristics of radiation intensity of a signal transmitted through a water drop medium	437
10.16	The structure function of intensity fluctuations for a signal transmitted through a water drop medium with three volume concentrations	438
10.17	Normalized Doppler spectra of backscattering signal from a disperse medium with three volume concentrations	439
11.1	Schematic sketch of single spectral line shape.	451

11.2	Schematic presentation of an electrical field amplitude in the form of oscillation intervals, emitted by a single atom	457
11.3	A line shape for Doppler and Lorentzian broadenings	459
11.4	Schematic sketches of spectral intensity transfer by way of a gas layer	465
11.5	Schematic presentation of a total profile for the compound emission line of a non-homogeneous structure	467
11.6	Frequency characteristics of the one-way attenuation in terrestrial oxygen in the 5-millimetre range	472
11.7	Frequency characteristics of the brightness temperature with zenithal observation in the 5-millimetre range at sea level condition	473
11.8	The effect of vertical humidity profile on water vapour emission line shape at 22.2 GHz frequency	476
11.9	One-way attenuation in the terrestrial atmosphere over the frequency range from 0 to 350 GHz	477
12.1	Qualitative microwave spectra of the brightness temperature for the ocean-atmosphere system in sensing at the nadir with a satellite	480
12.2	Spectra of the brightness temperature for the ocean-atmosphere system in sensing at the nadir with a satellite at frequency range 115–125 GHz	481
12.3	Normalized weighting functions in sensing at the nadir with a satellite at frequency range 115–118.5 GHz	481
12.4	Theoretical spectra of the brightness temperature for the ocean-atmosphere system at microwave frequency range	482
12.5	Theoretical spectra of partial derivatives of the brightness temperature of a clouded atmosphere	483
12.6	Schematic diagram of the microwave index f versus cloud top temperature for cloud classification	491
12.7	Backscattering and thermal radiation signals of a tropical convective cloud system	494
12.8	Theoretical microwave spectra of relative variations of the brightness temperature for water surfaces with a non-isothermal skin-layer	499
12.9	Polarization characteristics of relative variations of the brightness temperature for water surfaces with a non-isothermal skin-layer	500
12.10	Diagram for recovering profile parameters	501
12.11	The experimental result of flight investigations that made possible the detection of the azimuthal anisotropy effect in sea surface microwave emission	504
12.12	The experimental results of flight investigations (10 October 1978, the Sea of Japan) in the azimuthal anisotropy study of sea surface microwave emission	505
12.13	The experimental results of flight investigations (20 October 1978, the Sea of Japan) in the azimuthal anisotropy study of sea surface microwave emission and backscattering	506
12.14	Fragment of the output signal of airborne (Russia airplane-laboratory IL-18) high-performance radiometer R2 (wavelength 2 cm) versus the flight distance	509
12.15	Backscattering images of a rough sea surface obtained by side-looking radar ‘Toros’ (Russian research airplane AN-24)	513
12.16	The spatial-temporal evolution of catastrophic oil spills presented by a temporal series of schematic maps of the backscattering images	514
12.17	Radio-emission isothermal maps of the sea surface studied at wavelength 8 mm (26 November 1976)	515

12.18	Fragments of synchronous output signals of airborne radiometers R2 and R0.8 when crossing an area under study	518
12.19	Fragments of synchronous output signals of airborne radiometers R2 and R0.8 when crossing an area under study	519
12.20	Experimental spectra of radiobrightness temperature variations against the pure (non-pollution) sea emission signal at three frequency channels (wavelengths 0.8, 2 and 3 cm).	520
12.21	SLR schematic map combines with fragments of the radio-emission isothermal map	521
12.22	The spatial distribution of averaged oil film thickness	522
12.23	Schematic superposition of observing data from four types of sensing of oil pollution areas	523

List of tables

5.1	The main characteristics of radiotelescopes (the Crimea, Pushchino)	160
5.2	Antenna characteristics of microwave instruments onboard airplane-laboratory IL-18 (1975–1976)	191
5.3	Measured antenna characteristics of microwave instruments by the MCH method.	193
5.4	Antenna parameters of satellite microwave instruments	200
7.1	Maximum errors in T_{br} , K	273
8.1	Parameters of the D relaxation model for freshwater from experimental evidence	304
8.2	Calculated values of A_i and B_i coefficients in approximations $\varepsilon_0(S, t)$; $\lambda_S(S, t)$ and $\alpha(S, t)$	328
8.3	Dielectric characteristics of mixed electrolyte solutions	330
8.4	Dielectric characteristics of strong electrolyte NaCl	334
8.5	Average emissivity of surface categories	340
14.1	History of microwave radiometry in space	534
14.2	SSM/I characteristics (DMSP mission)	537
14.3	TMI characteristics (TRMM)	539
14.4	AMSR-E characteristics (Aqua mission)	540
14.5	AMSR Characteristics (ADEOS-II Mission)	543
14.6	MTVZA-OK microwave frequency channel characteristics	545
14.7	Instrument features and expected performances of CIWSIR (CLOUDS mission)	549
14.8	Instrument features and expected performances of CLAPMIR (CLOUDS mission)	550
14.9	Microwave sensor comparison	554
14.10	Key baseline system characteristics of OSIRIS mission	555

A.1	Base units	557
A.2	Derived SI units	558
A.3	Prefixes used with the SI system	559
A.4	Frequently used constants in SI units	560
A.5	Length	561
A.6	Energy	561
A.7	Pressure	561
A.8	Concentration (by mass)	562

Colour plates (between pages III and III)

- 1 Non-resolvable sources (spaced quasars and galaxies) noise and receiver noise are presented as a spatial point radiomap at wavelength 1.2 mm taken with the best existing radiotelescope (the France IRAM telescope). The false-colour map (right) shows the region mapped with a multibeam millimetre radiometer (MAMBO), and the inset (lower left) shows the decrease in the noise intensities (black traces) in the 36 off-source radiometer elements as a function of time (net noise), while the on-source detector (red trace) shows the signal from the radio source in the centre of the field. This source was also detected with the VLA radio interferometer at wavelength 20 cm, and with an IR telescope at wavelength 2.2 μ m (upper left). The colour scale (right) shows power flux measurement in units of millijanskys (mJy) (see Appendix A, Tables A2 and A3).
- 2 The microwave remotely sensed sea surface salinity fields off Chesapeake Bay for (a) 14 September 1996 and (b) 20 September 1996.
- 3 False-colour polar projection map of 1.55-cm microwave radiometer data obtained on 16–18 December 1972 from the Nimbus 5 satellite in the vicinity of the South Pole. The white area enclosed in the upper right corner of Antarctica is open water in the Ross Sea between the Ross Ice Shelf and the sea ice pack.
- 4 Optical and radiothermal images of biological structures in the visual band (left) and at frequency 600 GHz (right): (a) the image of a birch leaf; (b) the image of an oak leaf. Radiothermal images are presented with false-colour maps. Images sizes are 40 \times 40 mm.

1

Scientific and applied rationales of remote sensing study

This chapter will outline the scientific and applied rationales of the remote sensing of the Earth, the role and value of radiophysical methods, the basic statements of electromagnetic theory, the physical features of thermal radiation, and the possibilities of passive and active methods of microwave diagnostics.

1.1 WHAT IS MEANT BY REMOTE SENSING?

A person acquires an overwhelming amount of information about the surrounding world by the remote sensing method, i.e. without direct contact with physical objects. This equally relates both to ordinary human life and to obtaining information for the purposes of scientific research and applications. Here we should mention, first of all, the aerospace investigations of our planet and surrounding space, which have been intensively developed in the last 40 years and have equipped mankind with new knowledge both of space, and of our home planet. Certainly, it is impossible, in principle, to obtain information on physical objects in deep space by any other method except remote sensing. The material carrier of information about physical objects in space is the long-range electromagnetic field. In the hundred years that have passed since the experimental discovery of the electromagnetic field, mankind has learned to fairly efficiently control this form of matter and to understand the information which can be conveyed ('encoded') in the values of electromagnetic field parameters. In dense media (such as the air and water environment) other material carriers of information exist – acoustic fields and temperature fields are efficient carriers of remote information in the World Ocean.

However, in the interaction between physical bodies there exists, along with the electromagnetic field, another more long-range field, namely, the gravitational field, which efficiently reveals itself under the conditions of outer space and the rather large masses of physical bodies. Although the most general regularities of the gravitational field are understood by researchers, they strongly diverge in their views on the

structure and basic characteristics of this field. Attempts to discover the wave structure of the gravitational field (gravitational waves) have not been successful yet. Therefore we cannot (at least at the present stage of knowledge) consider the gravitational field as a useful material carrier of remote information.

Thus, by remote sensing is meant the science of obtaining physical information about a physical object at some distance from it by means of the purposeful processing of a received electromagnetic field which, in its turn, has interacted with the object under study. Electromagnetic field energy can belong both to the thermal radiation of a physical body, and to be the energy reflected from a body from some extraneous source (the Sun, for instance). In actual observational practice these electromagnetic fields exist in the ‘mixed’ mode, and sometimes the fairly complicated problem of separating these radiations arises, since they ‘carry’ in themselves completely different physical information.

The remote sensing process is usually subdivided into various components (or units) (Sabins, 1987; Pease 1991; Megie and Readings, 2000; Kramer, 1996; Danson and Plummer, 1995).

- (1) The source of electromagnetic energy – the first requirement in remote sensing concerns the presence either of a source of energy, or of natural radiation, or of an external source with respect to the object under study.
- (2) The interaction with the object – during interaction with an object its physical and geometrical properties are represented (‘encoded’) in the values of electromagnetic field parameters.
- (3) The radiation and a medium – in the passage of the electromagnetic field from an object to the receiver of radiation it can be additionally distorted (for example, by the presence of the atmosphere) and weakened.
- (4) The reception of radiation is carried out by special onboard devices (sensors), which receive the electromagnetic field from empty space and then process it in order to obtain the steady characteristics.
- (5) The transmission, reception and processing – the received information is usually transformed by the onboard device into electronic form and then translated through special communication channels (by means of the electromagnetic waves of other ranges) to receiving stations where, in its turn, it undergoes primary processing and is then transmitted to archival carriers.
- (6) The interpretation and analysis – the received information undergoes thematic processing with the purpose of obtaining necessary physical parametres for thematic analysis and the solution of particular physical or administrative tasks.

In this book we shall deal with each of the aforementioned components of sensing as applied to passive microwave remote sensing.

1.2 THE WAVE NATURE AND SPECTRUM OF ELECTROMAGNETIC RADIATION

The emission, propagation and interaction of electromagnetic energy with physical bodies can be considered and described from two quite identical points

of view: classical electromagnetic wave theory and quantum mechanics. In accordance with classical electromagnetic Maxwell theory, the energy of radiation propagates as electromagnetic waves and, in accordance with the quantum-mechanical approach, as separate, discrete quanta. These approaches are both equally applied in remote sensing problems. So, electromagnetic theory results are widely applied in calculating the radiation properties of physical surfaces (water, land), such as the degree of blackness and reflectivity of media, as well as in designing and manufacturing the radiophysical instruments for remote sensing. The quantum theory results are used in the determination of radiation energy emitted by physical bodies in the given frequency range, depending on its physical temperature, as well as in studying the radiation properties of gases, which can be explained and calculated from the quantum mechanics position only. In studying natural systems, however (for example, the radiation of hydrometeors in the Earth's gas atmosphere), the fundamental results were obtained using mixed approaches. It is important to note that the strict quantum-mechanical analysis of radiation interaction with substance leads, in a number of important applications, to equations and results which are substantially similar to the classical approach. For this reason, in solving practical remote sensing tasks, researchers adhere to the wave theory, since the latter has undoubtedly advantages, both in the observational practice of remote sensing and in the development and utilization of remote sensing instruments.

Within the wave theory framework electromagnetic radiation is described by the laws determining the behaviour of transverse waves, in which the synchronous oscillations of electric and magnetic fields occur in directions perpendicular to each other and perpendicular to the wave propagation direction. The oscillations propagate in space at a finite velocity, which depends on the properties of the medium. The velocity of electromagnetic waves in a vacuum is equal to $c_0 = 2.9979 \times 10^8 \text{ m s}^{-1}$.

The types of electromagnetic radiation can be classified according to their wavelength in a vacuum or to their frequency of oscillation. These two characteristics of an electromagnetic field are especially important for understanding the physics of the interaction of radiation with the physical objects being studied. By the wavelength is meant the length of one cycle of oscillations, which is measured as a distance between two neighbouring crests of a wave (λ). The wavelength is measured in metres (m), or in corresponding fractions of a metre, such as nanometres (nm, 10^{-9} m), micrometres (μm 10^{-6} m) or centimetres (cm, 10^{-2} m). The frequency refers to the number of cycles of a wave passing a fixed point per unit of time. The frequency is normally measured in hertz (Hz), equivalent to one cycle per second, and various multiples of hertz.

The frequency (designated as ν or f) of oscillations of coupled electrical and magnetic fields is associated with the wavelength by the following important relation: $c_0 = \lambda\nu$.

The understanding of electromagnetic radiation characteristics in terms of their wavelength and frequency is crucial to understanding the information to be extracted from remote sensing and space research data. Below we shall consider in detail the

scale and ranges of electromagnetic waves, mainly in their application to remote sensing and space research problems.

Figure 1.1 presents the scale of electromagnetic waves (the electromagnetic spectrum) and its accepted subdivision into ranges, as well as the types of artificial and natural radiation and the physical mechanisms of electromagnetic radiation. It should be noted first of all that the separation of electromagnetic spectrum ranges has a long (and sometimes complicated) history and was determined not only by physical and astronomical laws (for example, by the presence of a medium-class star – the Sun – at a fairly short distance from the Earth and by the physical properties of the Earth's atmosphere), but also by the development of ways and methods of excitation, generation and recording of electromagnetic waves. There are no strict boundaries between the spectrum ranges separated and determined till now, and, apparently, it is impossible (and also inexpedient) to present these ranges in a strictly fixed form, taking into account the rapid progress in remote sensing and radio communication technology, as well as in wave reception technology in ultraviolet, X-ray and gamma astrophysics.

The spectrum of electromagnetic waves used in space and physical investigations is extremely extensive – from the very short wavelengths of the gamma and X-ray ranges up to the superlow-frequency range (tens and hundreds of kilometres). The ranges that are directly used for remote sensing are the visible, infrared (IR) and radio ranges. This is mainly due to the fact that various types of electromagnetic radiation are generated by quite different factors and interact in quite different ways with the Earth's atmosphere. So, whereas gamma radiation arises in nuclear processes, in radioactive decay and in the fission of nuclei, X-ray radiation arises in atomic processes – when a substance is bombarded by high-energy electrons. The electromagnetic radiation formed in the visible, IR and radio ranges has been called thermal radiation. It arises due to the internal energy of a substance caused by transitions between rotation-vibration levels of molecules in gases, as well as by the oscillations of molecules in liquid and solid bodies and by the vibrations of a lattice in solid bodies (Figure 1.1(a),(b)). Thus, whereas in the reception and processing of electromagnetic waves in the gamma and X-ray ranges it is possible to obtain information on nuclear and atomic processes occurring in the substance studied, the reception and processing of electromagnetic waves in the visible, IR and radio ranges provides principally new information – data about the macro-characteristics of a substance, such as its physical and chemical composition, and its thermal properties, as well as about the geometrical properties of an object (Figure 1.1(b)). Along with thermal radiation in the microwave and radio ranges, a number of electromagnetic radiations arise, which are formed in plasma and plasma-like media – the emissions from the corona of the Sun, from the Earth's magnetosphere and ionosphere, and from thunderstorm activity in the Earth's atmosphere (Figure 1.1(b)). The powerful artificial radiation sources in the radio range are also well known: broadcasting radio stations, television stations, radars and space communications systems (Figure 1.1(a)). The activity of these systems sometimes erects very serious obstacles to remote sensing of the Earth in these ranges.

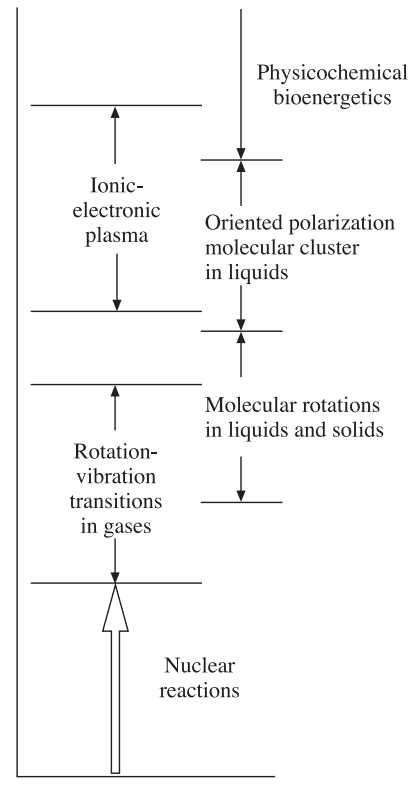
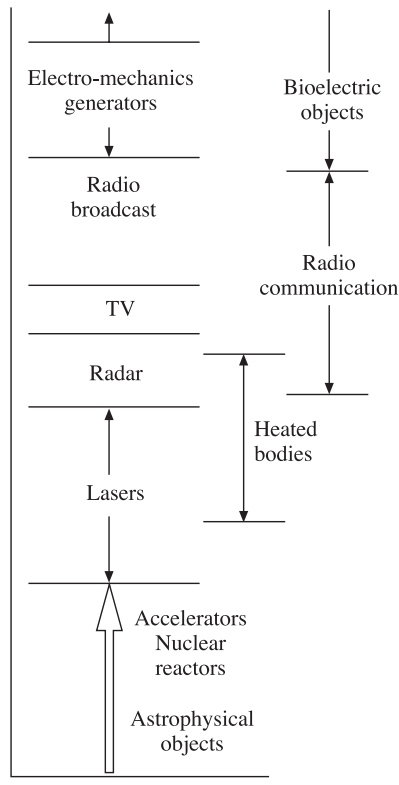
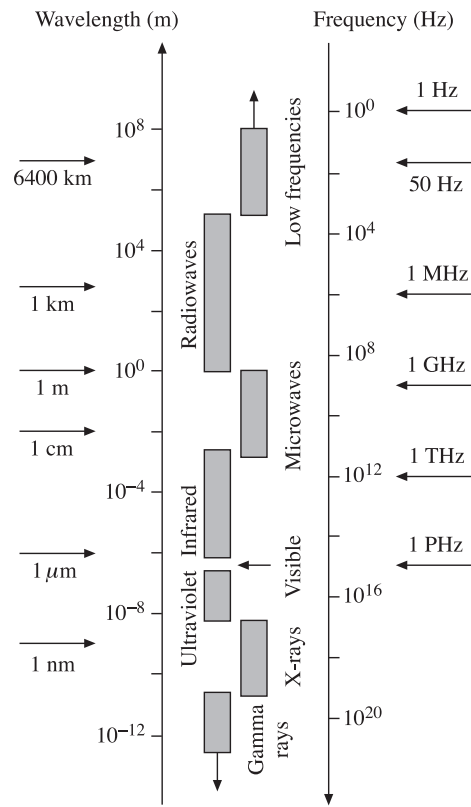


Figure 1.1. The spectrum of electromagnetic radiation. (a) The sources of radiation. (b) Physical mechanisms of electromagnetic radiation.

For direct human activity, the most important range of the electromagnetic spectrum (which was historically first in mankind's practical activity) is the visible range, covering the interval from approximately $0.4\text{ }\mu\text{m}$ to $0.7\text{ }\mu\text{m}$. Certainly, we should be aware of how amazingly small the visible part of a spectrum is in comparison with the whole range of electromagnetic radiation surrounding mankind which is not perceived at all by human organs of sense. The separation of six subranges within this range underlies the psycho-physiological concept of human colour vision (the concept of colours):

- Violet: $0.4\text{--}0.446\text{ }\mu\text{m}$
- Blue: $0.446\text{--}0.500\text{ }\mu\text{m}$
- Green: $0.500\text{--}0.578\text{ }\mu\text{m}$
- Yellow: $0.578\text{--}0.592\text{ }\mu\text{m}$
- Orange: $0.592\text{--}0.620\text{ }\mu\text{m}$
- Red: $0.620\text{--}0.7\text{ }\mu\text{m}$

Optical observations are formed on the basis of a complex combination of solar radiation scattered and re-scattered by physical bodies. This radiation is strongly transformed in intensity and spectral composition, which just generates a bright-colour picture of mankind's environment. For efficient remote investigation of various types of surfaces on the Earth (such as the water surface, mountain rocks, minerals, vegetation) specialists subdivide the total visible range into a number of subranges, which are determined by the physical properties of substances and do not correspond at all to the psychological perception of colours by humans. A vast specialist literature is devoted to studying these issues, and so they are not considered in this book.

The next portion of the electromagnetic spectrum, which is intensively used in remote sensing and in a number of important applied areas (such as rocket technology and nuclear power engineering), stretches from the red boundary of the visible spectrum to wavelengths of the order of $100\text{ }\mu\text{m}$. This range comprises the major part of thermal radiation energy (taking into account, certainly, those thermodynamic temperatures that can be achieved under Earth's conditions). This spectral range is called the infrared. From the viewpoint of technological applications this range is subdivided into the near-infrared region, which extends from the visible range to wavelengths of approximately $25\text{ }\mu\text{m}$, and the far-infrared region corresponding to longer waves, up to $1000\text{ }\mu\text{m}$ (0.1 cm). The remote sensing specialists, however, adhere to the other concept concerned with the physical features of remote observations in these ranges. So, the main IR range can be subdivided into two subranges in accordance with their radiation properties – reflected IR and emitted, or thermal, IR. Reflected IR covers wavelengths from approximately $0.7\text{ }\mu\text{m}$ to $3.0\text{ }\mu\text{m}$ and radiation in the reflected IR region is used for remote sensing purposes in ways very similar to solar radiation in the visible portion. It is important to note that the thermal IR region essentially differs from the visible and reflected IR regions, since the source of radiation in this range is the physical body itself that is subject to investigation. Thermal IR covers wavelengths from approximately $3.0\text{ }\mu\text{m}$ to $100\text{ }\mu\text{m}$. Inside the thermal range is the important subrange, whose value can hardly be exaggerated.

This range, extending from $8\text{ }\mu\text{m}$ up to $12\text{ }\mu\text{m}$ is characterized by the fact that the information obtained when using it strictly corresponds to the thermodynamic temperature of any physical object on the Earth. Actually, each modern operative and research satellite system carries remote sensing devices of this range in its structure. It should also be noted that the range from $100\text{ }\mu\text{m}$ to $1000\text{ }\mu\text{m}$ is intensively explored now from the viewpoint of using it in remote sensing tasks. Radiophysicists often call it the submillimetre range, and often include it in the ‘radiowaves’ notion.

The huge range of wavelengths, from 1×10^{-5} to 10^{10} m (and, accordingly, with frequencies from $3 \times 10^{12}\text{ Hz}$ to several Hz), is called radiowaves. After successful experiments by the Russian physicist A. S. Popov (1895–1899) and G. Marconi (1897–1901) on using electromagnetic waves in the range of $1\text{--}200\text{ m}$ for accomplishing a wireless communication at a distance, a wide practical application of electromagnetic waves in the metre and decametre ranges began. The experimental discovery by A. S. Popov in 1897 of the phenomenon of the reflection of electromagnetic waves from physical bodies (military ships) can be considered as the first example of using electromagnetic waves as a remote information carrier. The practical usage of radiowaves from various frequency subranges is dependent on the features of the propagation of radiowaves of various wavelengths and on the conditions of their generation and directional emission. Proceeding from these physical circumstances, the International Radio-Communication Regulation approved the division of radiowaves into ranges strictly corresponding to the wavelengths (millimetre, centimetre, decimetre, metre, kilometre etc.), as well as into some special subranges allocated for the operation of radio stations, television stations, communication systems, mobile communications, space communications. Low-frequency and hyperlow-frequency electromagnetic waves are widely used in industry (the alternating current of 50-Hz frequency with the wavelength of 6000 km is best-known in domestic conditions). Waves in these ranges are generated both in electronic circuits and by means of electromechanical generators. Figure 1.1 specially marks the wavelength corresponding to the length of radius of the Earth globe, as well as the wavelengths corresponding to the spatial dimensions actually encountered in ordinary human life (1 km , 1 m , 1 cm). In view of the saturation of the radio range with various kinds of radio communication, e.g. TV, broadcasting and radar, international organizations (URSI, in particular), have accepted rules that regulate (and sharply limit) the activity of any type of radiation by rigid frequency frames and, accordingly, new frequency classifiers are introduced. Similar frequency limitations have also been introduced for radio-physical remote sensing systems and for radio-astronomical investigations (Zuzek, 2000; Zuzek *et al.*, 2000; Wende, 2000; Rochard, 2000; Huneycutt and Zuzek, 2000). As problems related to exploration of the radio range increase, the boundaries of the frequency ranges undergo (and, undoubtedly, will continue to undergo) significant variations. So, in view of the active exploration of the millimetre and submillimetre ranges for studying the content of and variations in the small gas components (greenhouse gases) in the troposphere and stratosphere, a new frequency classification of these ranges has now been elaborated (Maeda *et al.*, 2000; Maier *et al.*, 2000; Konig *et al.*, 2000; Hartmann *et al.*, 1996; Greving, 2000).

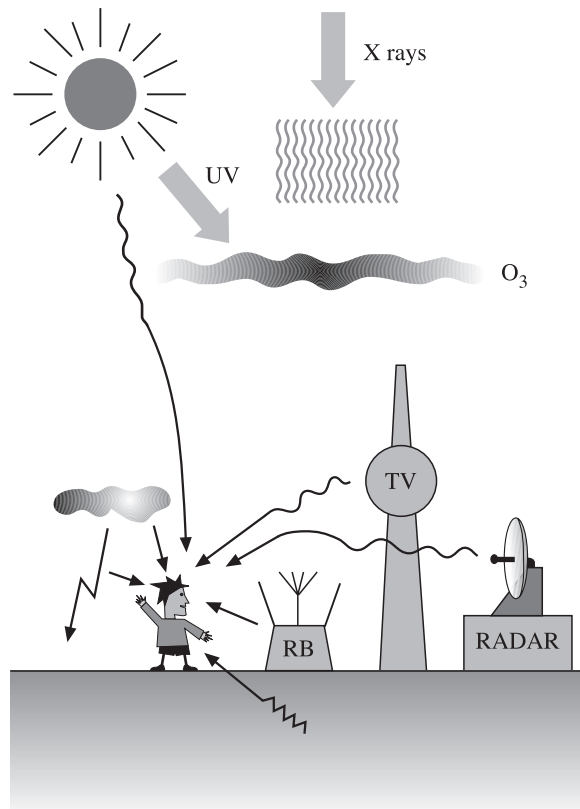


Figure 1.2. Schematic presentation of the influence on a human of the surrounding electromagnetic radiation fields. UV is ultraviolet waves; O₃ is ozone layer; RB is radio broadcasting transmitter.

For the purpose of simplifying the qualitative approach, remote sensing specialists have accepted the following separation of the radio range: microwaves, with wavelengths from 1 mm to 1 m; and radiowaves, with wavelengths from 1 m to 10 km. Until now, from the viewpoint of remote sensing activity, the ‘long’ millimetre and centimetre and ‘short’ decimetre ranges have been well explored. The advance into the metre and decametre ranges meets, however, some major difficulties, first of all the problems of insufficient spatial resolution and external ‘parasitic’ emissions. On the other hand, in exploring the submillimetre range, problems of insufficient power sensitivity of the equipment arise; but they have been successfully overcome.

Though the energy of electromagnetic radiations of quite different types and huge intensity permanently surrounds us (Figure 1.2), we, nevertheless, do not actually notice this, since our organs of sense are capable of detecting directly only a very small portion of this energy, first of all in the visible range and, to an essentially lower degree, in the IR thermal range. For detecting all the rest of the

electromagnetic spectrum, special instruments are required. Our eyes, being very sensitive and direct receivers of electromagnetic waves in the visible range, represent a perfect optical interferometer with a slightly fluctuating base (the distance between the pupils), which forms a signal for subsequent processing in our brain as a spatial-correlation function of the three-dimensional image (the hologram, in essence). Our brain possesses the unique property of processing and restoring (with a particular time constant of about 0.05 s) the received hologram into three-dimensional colour images. With the help of eyesight we receive (according to different estimations) from 80% to 95% of the information we need. On the other hand, because of the psycho-physiological mechanism of image interpretation, human eyesight and visual perception by the brain has many limitations, among which are both physical and physiological fatigue and optical illusions. The generalization of images in the human brain sometimes assumes fantastic forms, which have nothing in common with reality. For these reasons human eyesight is far from being a reliable physical tool in all cases.

Our skin is sensitive to electromagnetic waves of IR thermal range, but to an insufficient degree to be a source of serious remote information (which is well known from daily life). However, some biological organisms from the animal world (for example, the rattlesnake) orient themselves in space mainly using precisely this range of electromagnetic radiation.

We are not susceptible at all to emissions in the radio range, and this is a great boon for us, since the effective radiation from TV and radio stations and radars is many millions of times greater than the radiation we receive from the Sun. This human unreceptiveness to waves in the radio range is associated, first of all, with a very small value of the radiophoton quantum, which does not influence the physical-chemical links in the biological molecules of the human body. If this were not the case, the biological life of a man in the modern environment of super-power radio emission would be impossible.

It is the full absorption of these emissions by the upper layers of the atmosphere which saves a man (and the entire biological community on the Earth in general) from the X-ray and gamma radiation of powerful extraterrestrial sources, which are very dangerous to the biological life. The ultraviolet radiation of the Sun is essentially suppressed in the ozone layer of the stratosphere.

1.3 PASSIVE AND ACTIVE SENSING

In relation to the objects studied, remote sensing methods are subdivided into passive ones, i.e. providing only reception of the electromagnetic field, and active ones, which provide both emission of an electromagnetic field with given characteristics (its form, amplitude and phase – the coherent signal), and reception of a signal, reflected from the studied object, whose characteristics incorporate physical information about the object. In the first case, the physical information on a studied object is incorporated both in the intensity of a received fluctuation signal and in its spectral characteristics. In the second case it is incorporated both in the amplitude and form

of a reflected signal, and in its phase distortions. The data on the phase features of a reflected signal qualitatively change the information obtained about physical objects, thus making it possible to determine their kinematic properties, to measure the distance to an object and to implement essentially new signal processing modes (the so-called aperture synthesis modes). The latter methods increase the resolution of the entire system (certainly, after specialized processing) 100–1000 times with respect to the so-called Rayleigh diffraction limit.

Along with coherent signals, in the active modes there are also used the so-called incoherent (noise) sources, which do not allow the recording and the handling of the phases of oscillations because of the wide range frequencies used in these cases. A striking representative of this kind of source is the Sun – the star nearest to the Earth – which plays for remote sensing the part of a fairly ‘standard’ source of ‘illumination’ in the visible range for an illuminated part of the globe. Part of the electromagnetic energy of the Sun in the visible range is absorbed by the surface–atmosphere system, transfers into heat and only then is re-emitted, but now in quite other ranges of electromagnetic wavelengths – IR and microwave.

An obvious advantage of artificial active sources is the possibility of using them as required during the experiment, regardless of the time of day and the season. However, the operation of active systems under onboard conditions requires the presence of considerable sources of energy on the flying vehicle, for the generation of electromagnetic waves of appropriate range and power, corresponding to the orbital conditions of flight and the reflective properties of an object.

The passive methods are based on the reception of the so-called thermal radiation of physical objects due to the internal (thermal) energy of matter, which enables spontaneous transitions between rotation-vibration levels of molecules in gases, the oscillations of molecules in liquid and solid bodies and vibrations of a lattice in solid bodies. We shall devote the basic part of this book to studying this type of radiation. The instruments, which carry out the reception and processing of such radiation, are called radiometers (in the corresponding range of wavelengths).

The passive methods include: the radiothermal location of the Earth and planets, radio-astronomy, optical and IR astronomy, X-ray astronomy, and various modes of thermal IR survey of the Earth and planetary surface. The active methods include: scatterometry, radar survey in the modes with a real aperture and with a synthesized aperture, Doppler radar, and optical measurements with active illumination (the Sun, lidars). The important direction is now the study of the possibilities of radiothermal (passive) reception in the Michelson-type interferometre mode and in the aperture synthesis mode. The implementation of such modes of a typically coherent type for noise signals seems surprising at the first sight. However, as will be studied in Chapters 2 and 7, any narrowband noise signal possesses some kind of coherent-noise dualism, i.e. under some conditions the noise signal behaves as if coherent (for example, a sine wave).

It is emphasized once again that the principal distinction between passive and active remote sensing methods consists in the fact that the data obtained by passive systems (radiometers) comprise information on the thermal state of a studied object, whereas the data of active systems convey information on the kinematics and surface

roughness of an object. So, for instance, no information can be obtained (by active methods) about the state (physics and chemistry, pressure, temperature) of gases in the pure atmosphere, because the scattering of electromagnetic waves on gas molecules is extremely insignificant (as opposed to the scattering on hydrometeors and aerosols in the Earth's atmosphere). At the same time, thermal radiation, being a purely quantum effect, provides amazing (in its information capacity) data about the state of gas media on the Earth, on planets (their atmospheres) and in outer space (molecular clouds, stellar atmospheres). In addition, we mention one more important peculiarity: the information on dielectric, geometric and volumetric properties and on the state of surface (the degree of roughness) of a studied object is 'incorporated' in the passive and active sensing data with various degrees of information capacity. This is precisely the reason why these methods do not duplicate each other at all, despite their being treated as if they did in some manuals. On the contrary, these methods mutually supplement each other and enrich the information on a physical object. In recent years the curious tendency has arisen for simultaneous (complex) processing of the data obtained by active and passive radio-physical remote instruments, by using some specialized synergetic retrieval algorithms. New results, obtained by means of such processing, obviously provide evidence of the mutual supplementation of these two approaches in radiophysical sensing. Similar conclusions can be drawn with respect to sensing in other ranges too (laser active sensing in the visible and IR ranges supplement the traditional methods).

1.4 THERMAL RADIATION: THE ROLE AND SOURCES

One of the fundamental factors explaining the major importance of thermal radiation in remote sensing and astrophysical applications is its rather transparent physical linkage with the internal thermal structure of a physical object and with its physical and chemical features. The role of thermal radiation is also large in a number of industrial-technological applications, such as power engineering, rocket technology and metallurgy.

All physical objects, having physical temperatures that differ from the absolute zero, continuously emit the fluctuation electromagnetic field arising due to the internal energy, which enables spontaneous transitions between rotation-vibration levels of molecules in gases, oscillations of molecules in liquid and solid bodies and vibrations of a lattice in solid bodies with subsequent de-excitation of electromagnetic quanta. The radiation has a typically quantum character. The energy of radiation covers a very wide range of wavelengths and has (according to radiophysical terminology) a continuous spectrum of rather complex form, the position of maximum of which depends on the thermal temperature of the substance. As this temperature increases, the total energy of emitted thermal radiation grows, and the spectrum maximum shifts to the region of short wavelengths. Thermal radiation is emitted both by all physical bodies under Earth conditions (including our own planet) and by stars, galaxies, nebulae and molecular clouds situated in the deep space, and even by such exotic objects as black holes, one of which is situated at the centre of our

galaxy (the Milky Way). Certainly, along with thermal radiation, the whole spectrum of other electromagnetic emissions falls on the Earth from space. One much emission is the so-called maser radiation from peculiar huge areas near stars consisting of molecules and atoms of gases, which are permanently in the excited state due to the presence of external emissions. Physical ties between the intensity and the spectrum of maser radiation and a quantum structure of substances are rather complicated and cannot be described in frameworks of thermal radiation theory.

Thermal radiation arises under the detailed equilibrium conditions in a substance for all emissionless processes, i.e. for various types of collisions of particles in gases and plasma, and for the exchange of energies of electronic and oscillatory motions in liquids and solid bodies. At local thermodynamic equilibrium, where thermal radiation is characterized by the value of temperature at a given point, thermal radiation is not at thermodynamic equilibrium with the substance. And in this case the emission of radiation to external space with redistribution of a temperature regime within a body is possible. To maintain the stationary state, in which the gradient thermal field must be sustained, the loss of thermal energy must be replenished from extraneous sources. The radiation spectrum at full thermodynamic equilibrium (the equilibrium or black-body radiation) possesses striking properties – it does not depend on the nature of the substance and is determined by the fundamental law of nature: Planck's law of radiation.

For black and non-black bodies Kirchhoff's law of radiation (or, in a more general form, the fluctuation-dissipation theorem) is valid. This law relates the emissive and absorptive powers of these bodies with the emissive power of an absolutely black body. Applying the aforementioned radiation laws under the local thermodynamic equilibrium conditions to the emission and absorption of thermal radiation in physical bodies, we can study the radiation transfer processes within the framework of the so-called phenomenological theory of radiation transfer. The importance of this theory for remote sensing tasks and astrophysical applications is difficult to overestimate. In fact, all the fundamental results of remote sensing and astrophysics obtained till now, are based to an overwhelming degree on using the methodology and interpretation of outcomes of radiation transfer theory (rather than on Maxwell's wave theory of electromagnetism, however surprising this may be). In the appropriate chapters (Chapters 9–12) we shall study in detail the issues of the construction of radiation transfer theory and the application of its results for practical remote sensing tasks.

Concerning remote investigations under Earth conditions, we can indicate three basic sources of thermal fluctuation electromagnetic radiation:

- the star nearest to us – the Sun – which represents black-body radiation with a physical temperature of 6000 K;
- our planet Earth properly, which possesses radiation close to black-body radiation with a physical temperature of 287 K;
- the microwave background radiation of the universe, possessing black-body radiation with a high degree of spatial-angular isotropy and a temperature of 2.73 K.

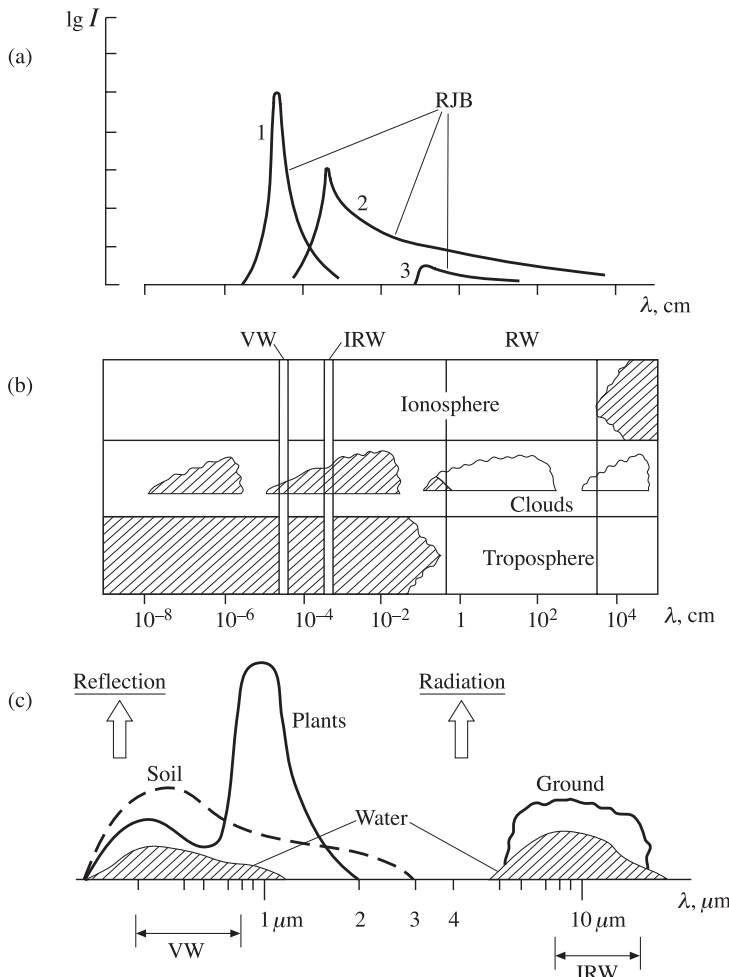


Figure 1.3. The qualitative picture of the correlation between the main sources of radiation and features of the Earth's atmosphere. (a) Large-scale spectra of Sun reflection radiation (1), the Earth's thermal emission (2), the background microwave radiation (3). RJB are Rayleigh–Jeans branches. (b) Simplified schematic presentation of the propagation of electromagnetic waves through the ionosphere, cloud systems and the troposphere. VW is the visible window; IRW is the infrared window; RW is the radio window. (c) Detailed (in wavelength range 0.3–14 μm) spectra (in arbitrary units) of Sun radiation reflected from soil, plants and water surface, and of thermal radiation emitted from ground and water surface and soil.

The qualitative picture of radiation spectra of all three sources of radiation is presented in Figure 1.3(a), where the solar spectrum is shown as radiation reflected from a conventional object with a reflection coefficient of about 0.05.

The discovery of the latter type of radiation (microwave background radiation) was the major experimental evidence in favour of the ideas of the hot universe model

and isotropy of its expansion and its homogeneity. The black-body character of background radiation was retained as a relic, as the ‘memory’ of the early period of evolution (after the Big Bang). The maximum of relict radiation intensity is reached at the wavelength of $1\text{ }\mu\text{m}$ and then (at higher frequencies) its intensity sharply drops (Figure 1.3(a)). Thus, the contribution of the relict background radiation to IR and the visible ranges is actually insignificant, whereas for fairly fine measurements in the radio range (mm, cm and dm) the relict background radiation must be taken into account without fail. Properly speaking, A. Penzias and R. Wilson (Nobel prize, 1978) discovered the relict background radiation in 1965 during experiments of a purely radiophysical type (the measurement of antenna system parametres) in the centimetre range.

The Sun – the star nearest to us – is a necessary component in the support of the biological life on our planet. The radiation, coming from the Sun to the external observer on the Earth, arises in the thin superficial layer – the photosphere – and represents thermal radiation (Planck radiation) with a temperature of 6000 K. More than 30 000 narrow lines of absorption (Fraunhofer lines) of atoms, situated in the Sun’s chromosphere and absorbing radiation of the photosphere, were discovered and identified in the continuous radiation spectrum. However, their presence has virtually no effect on the total power of photosphere emission in the optical range. Advancing into the far-IR and radio ranges, the situation drastically changes: the chromosphere and corona of the Sun, being transparent for the visible range, become opaque for radiowaves and, as the wavelength increases, the radiation comes from ever higher and hotter levels of the Sun’s atmosphere. So, in the centimetre range, the radiation intensity corresponds to the temperature of 10 000 K and monotonically increases up to 10^6 K in the range from 3 cm to 100 cm. The intensity of radio emission of the chromosphere and corona undergoes considerable changes, both slow and fast (up to millisecond scales). The latter are associated with non-thermal plasma processes in the solar corona and can cause bursts and noise storms with a radiation intensity in the metre range, corresponding to a temperature up to 10^9 – 10^{11} K. Such powerful emissions can be sources of serious interference for remote sensing in the ranges mentioned.

The third source, which perhaps is the most important for remote sensing tasks, is the thermal radiation of the planet Earth, which has a huge wavelength range, from thermal IR up to the metre radio range. The principal point here is the great distinction between the thermal radiation of a planet and that of a black body, in the radio range especially. It is this distinction which bears the most important remote information on the state and characteristics of the surface–atmosphere system. The formation of the distinction mentioned between the thermal radiation of the Earth and that of a black body is caused by the presence of some important physical properties of the Earth’s atmosphere and, primarily, of the transparency bands – the atmospheric windows (and, accordingly, the bands of opacity) for electromagnetic waves. The Earth’s atmosphere has three ground windows of transparency for electromagnetic radiation (Figure 1.3(b, c)):

- the visible and near-IR window (wavelengths from 0.3 to $1.0\text{ }\mu\text{m}$),

- the thermal IR window ($8\text{--}12\text{ }\mu\text{m}$),
- the radio window (2.5 mm to 20–50 m).

Actually, the Earth receives all its energy from the Sun in the form of electromagnetic radiation concentrated in the spectral range of $0.3\text{--}2\text{ }\mu\text{m}$. About 30% of this energy is reflected by the Earth's atmosphere system back into space. A considerable portion of energy (more than 51%) passes through the visible atmospheric window and is absorbed by the Earth's surface (land and ocean), while the remainder (19%) is absorbed in the atmospheric gases. This radiation is frequently called short-wave solar radiation. The absorbed part of short-wave energy transfers into heat and then is redistributed over the planet by means of dynamic and turbulent-convection processes and through the radiative transfer of the long-wave atmospheric radiation. It is this part of the energy that in the long run determines the whole variety of conditions of the atmosphere and surface below it. A certain part of long-wave radiation is de-excited back into space through the IR and atmospheric radio windows; however, the majority of it is absorbed by minor gas components of the atmosphere (H_2O , CO_2 , O_3 , N_2O , CO , CH_4). And, first of all, we should mention here the generation of greenhouse warming in the ocean–atmosphere system, which provides the mean temperature on the planetary surface of about 287 K ($t = +14^\circ\text{C}$) and, accordingly, the possibility of the existence of biological life and huge reservoirs of liquid water on the Earth.

The short-wave boundary of the radio-window is determined by absorption of water vapour and oxygen molecules, whereas the long-wave boundary is determined by absorption of ionosphere medium (the plasma processes). The radio-window possesses a remarkable feature: radiation with wavelengths greater than 1 cm virtually freely passes through the cloudy cover of the Earth's atmosphere. Taking into account the fact that clouds shield 55% of the Earth's surface on average, this window offers the only opportunity 'to glance' under the clouds and to observe the processes occurring between the cloud and the surface of the Earth. On the other hand, the possibility of measuring the thermal radiation of the atmosphere and observing the Earth's landscape in the microwave region may seem surprising at first sight, because the intensity of emission of long-wave radiation drops sharply as the square of frequency (the Rayleigh–Jeans formula), and at the transition from the $10\text{ }\mu\text{m}$ to the 10 cm wavelength the radiation intensity value decreases 10^8 times! Nevertheless, sensitive modern instruments for noise signals in the radio range (microwave radiometers), the measurement of such levels of electromagnetic emission (and their variations) does not present any difficulties (see Chapter 3).

Note one more important circumstance. Whereas in forming the thermal balance of a planet the role and meaning of a radio-window is, obviously, insignificant, for the information maintenance of remote sensing the principal role and meaning of a radio-window is beyond any doubt now. First of all, this is due to the fact that, unlike the IR range, the radiative properties of Earth's surface essentially differ from black-body emitters and, thus, the high recognizability of Earth's surface elements from radiation intensity variations is made possible. (This possibility, by the way, is completely absent in the IR thermal range.) In addition,

considerable frequency variations of radiation intensity are observed with advancement from millimetre to decimetre ranges, which makes it possible to use the spectral images of objects as reliable information attributes. The further advance into the metre range encounters serious difficulties related to powerful external emissions of artificial and natural origin (the emission of television stations, radio-transmitters, noise storms on the Sun, radio-emission of our galaxy).

Undoubtedly surprising (and also, by the way, a necessary condition for biological life on the Earth) is the fact that the maxima of spectra of basic sources (under Earth's conditions certainly) exactly correspond to the transparency windows of the Earth's gaseous atmosphere (Figure 1.3(a), (b)).

1.5 RECOGNITION AND UNDERSTANDING OF MICROWAVE SIGNATURES

In this section, for a specific example of considering the data of remote sensing of the Earth's surface with vegetation, we shall try to reveal the principal information possibilities provided by studying Earth objects with active and passive methods in the radio range.

By measuring the electromagnetic energy that is reflected (or emitted) by a physical object in various wavelength ranges, we can generate a spectral response for that object. Then, by comparing the space-time peculiarities of spectral responses received in various ranges, we can recognize and identify the objects, which sometimes cannot be done when you have the data at one frequency only. So, for example, water surfaces and vegetation can reflect solar radiation in a very similar manner in the visible range and, accordingly, they can actually be indistinguishable in optics, whereas they differ considerably in their recognition and identification in the radio range. A set of spectral responses and their spatial features are called signatures. The knowledge of signatures and understanding of the laws of their formation in various ranges are the principal conditions for generating geographical and geophysical bases of data about physical objects on the Earth's surface.

Before considering microwave signatures, we summarize the qualitative features which are revealed in observation of objects in various wavelength ranges attributed to atmospheric windows.

Optical observations are characterized by the reception of scattered and re-scattered solar radiation with its very strong transformation in spectral structure of the reflected radiation and in its intensity, which creates the colourful picture of the world surrounding us. The thickness of a layer forming the reflected electromagnetic energy of physical bodies (the skin-layer) is of the order of $1\text{ }\mu\text{m}$ which causes a very strong and non-unique dependence on the degree of roughness of the surface. In reflection from physical surfaces a rather complicated picture arises, which represents a mixture of mirror and diffusion components giving rise to strong spectral variations (spectral responses) within the visible range. The observed picture very heavily depends on the time of day and on the season, and on the state of cloudiness, and on the presence of various types of aerosols of natural

and artificial origin, and is characterized by rapid time variability. For certain unification of the results of satellite measurements, the ballistic parametres of a spacecraft are specifically chosen so that the crossing of the equator takes place on each orbit at a strictly defined local time (for example, at 9.30 a.m.). Such a type of orbit is called Sun-synchronous.

Observations in the thermal IR range are completely independent of the solar radiation (and, accordingly, of the time of day). The intensity of thermal radiation almost exactly corresponds to the thermodynamic temperature of an object (to an accuracy of 1–2%); it virtually does not depend on the dielectric properties of physical emitting bodies; the radiation is diffusive; it is very weakly dependent on the degree of roughness. The skin-layer of radiation of solid and liquid bodies (i.e. the thickness, on which the basic portion of radiation is formed) equals about 10 μm ; the skin-layer of cloudy systems equals about 50–200 m. The observed picture represents, in essence, the temperature field of the surface–atmosphere system and heavily depends on the presence of cloudiness which, in its turn, can be rather clearly recognized in the values of intensity (the temperature of the upper boundary of cloudy systems is essentially lower than the Earth's surface temperature). No specific choice of ballistic maintenance for satellite systems is required in this case (unless related to spatial resolution problems).

Observations in the radio range are completely independent of solar illumination (the time of day), and are virtually independent of the presence of cloudiness and aerosols. The intensity of radio emission of a physical object is strictly proportional to its thermal temperature and radiative properties (the corollary of the Rayleigh–Jeans approximation). And, as a consequence of this circumstance, the radio emission of physical bodies strongly depends on the dielectric properties of an object, on its physical and chemical structure, and on the internal geometrical and phase structure. It is important to note a significant depth of a skin-layer of radiation and scattering of radiowaves – for Sakhara sands the skin-layer equals 6–10 m; for glaciers of the Antarctic Continent and Greenland the skin-layer reaches 1–3 km! In view of the high sensitivity of radiowaves to diffraction interactions, a strong (sometimes non-unique) dependence on the structure of a surface roughness is observed in the radio range. (This fact, properly speaking, underlies quite efficient radio-methods of sounding the sea surface.) The active methods are quite sensitive to the kinematic characteristics of an object (Doppler radar). In addition, the coherency of the emitted signal (the knowledge of the signal phase) makes it possible to accomplish very important modes of observation called the aperture synthesis, which make it possible to sharply increase the spatial resolution of radars. At present, the possibility of using such modes for passive sensing is being actively studied.

No specific choice of ballistic maintenance for satellite systems with passive microwave equipment is required (unless related to spatial resolution problems). For spacecraft with active equipment the optimum ballistic maintenance of a vehicle plays a major part, since this is strictly associated both with the power of a transmitter (and, accordingly, with the power supply of the spacecraft) and with the sensitivity of receiving equipment and with the type of surfaces under study.

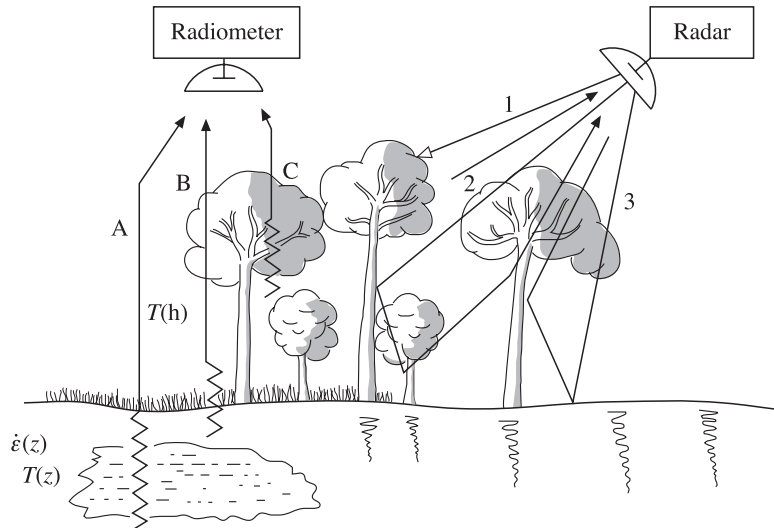


Figure 1.4. Simplified model to demonstrate the possibilities of emitted and backscattering signals in vegetation. 1: The generated signal is reflected on the canopy. 2: The signal is reflected by stems. 3: The signal is reflected from the soil and then the stem back to the antenna. A: Thermal signal is emitted from subsurface layers. B: Thermal signal is emitted by surface structures. C: The signal is emitted by the volume of the canopy. $T(z)$ and $\dot{\epsilon}(z)$ are temperature and dielectric profiles (in depth). $T(h)$ is temperature profile (above the ground).

Taking into account the above analysis, we shall return to the consideration of a qualitative picture of the formation and recognition of microwave signatures obtained while observing a conventional Earth surface with vegetation. A schematic (simplified) picture of signal formation is presented in Figure 1.4, where the left half of the drawing relates to the passive method of sensing and the right half to the active one.

The microwave instruments carried by satellites have the important potential to provide us with information on vegetation, agricultural crops and the soil in which they grow. As well as generating images when visible/IR sensors are unavailable because of cloud, the information from microwave instrumentation may not only be complementary to that from optical systems but may also carry new information. The reason for this is the difference in the processes and scale sizes of vegetation and agricultural features with which microwave and optical wavelengths interact. The response of a field of vegetation to optical radiation is determined by structures on micrometre scales and by processes of chemical absorption. Microwave radiation, by contrast, penetrates significant distances into a vegetation canopy and interacts most strongly with structures (leaves, stems etc.) on scales comparable with the radiation's wavelength (a few centimetres to a few tens of centimetres). Thus, microwave instruments may be thought of as probing, in a very direct manner, the structural components of a plant canopy.

Owing to its penetrative power, significant amounts of radar (active instrument) energy can, in certain circumstances, pass completely through a crop canopy to reach the soil below (Figure 1.4). When this happens, the radar image will be influenced by the reflective properties of the soil.

Passive microwave radio sets (radiometers) receive emission from soil and vegetation layers (Figure 1.4). As distinct from active regimes, thermal emission is rigidly bound up with thermal regimes in soil layers and vegetation volumes.

Thus, in very broad terms, imaging vegetation with radar and radiometers raises the possibility of exploiting differences both in plant structure and in soil properties for the purposes of differentiating vegetation and crop types, thermal and moisture conditions or agricultural management practices.

The properties of vegetation and the soil which influence the amount of microwave power scattered back towards the radar, and emitted towards the radiometer, fall under the principal headings of geometric structure and dielectric constant, and (for the passive regime) of thermal features.

In structure we include the major plant constituents on scales greater than a few millimetres (leaves, stems, flowers, fruits/seed heads). Their sizes, shapes and orientation determine the interaction of individual isolated components with the microwaves. A flattened leaf, for example, scatters microwaves in a different directional pattern to a vertical stem. Below the plant canopy, the soil surface does not act as a simple mirror; rather the scattering from it is influenced by its roughness properties, especially on scales comparable to the radar wavelength. The moisture of the soil influences, through local chemistry, its dielectric constant. For different soil types, there is a different relationship between moisture content and dielectric constant, determined by the soil constituents.

It is very important to note that the contributions of these components (headings) to passive and active measurements differ essentially. Hence the useful information embedded in the passive and active signatures is also very different.

Understanding the interactions with individual vegetation and plant components or the soil is not straightforward. Electromagnetic modelling has at its disposal a range of techniques and approximations to describe the scattering by at least the more simple shapes which may be encountered in vegetation and crop canopies and by a soil surface with a known roughness profile. The real situation, however, is rather more complex than just microwaves scattering off isolated structures or the soil. The relative positions and spatial densities of plant constituents determine how they respond as an ensemble to the radar, through multiple scattering events or coherent interactions. Similarly, the soil cannot always be considered separately from the crop above it. Rather, a radar wave may be scattered by a leaf before being reflected off the ground and back to the radar. Furthermore, the relative importance of different interactions, whether single or multiple (some involving reflecting off the ground and others not) is believed to change significantly as a crop develops during the growing season.

Developments in the modelling of microwave scattering for agriculture have taken advantage of the increasing availability of computing power, to create ever more realistic and explicit models for the structures with which the radiation

interacts. The models aim to explain or predict the brightness in radar and passive images of different crop types under changing environmental conditions or different stages of growth during a season. Early developments in the 1970–1980s were based around empirical or semi-empirical models for scattering at particular wavelengths. These did not attempt to represent crops as recognizable structures, but invoked tunable parametres and were limited in their applicability over the wide range of microwave and vegetation parametres which may be encountered (see Chapters 8 and 12).

Widespread recent work has placed greater emphasis on realistic descriptions of plant components, which can be related very directly to measurable parametres (the shapes of leaves, their thickness and moisture content, etc.). It is conceivable that significant improvements in the accuracy of predictions will entail even more explicit models of plants ‘grown’ in the computer, which include descriptions of the spatial interrelationships between leaves, stems and fruits.

One more factor should be pointed out. It is known that the scattered field carries the passive and active signatures of the target. Also, it is held that the microwave brightness and backscattering cross-section could be an effective discriminant for inverse target problems for non-fractal scatterers. However, any type of vegetation is a multifractal target (Mandelbrot, 1982). There is no doubt that the passive and scattered fields from vegetation carry the fractal signatures of targets, modelling experiments have confirmed these assumptions. The question is raised as to whether fractal characteristics may be experimentally determined from microwave signatures.

1.6 BASIC STATEMENTS OF WAVE ELECTROMAGNETIC THEORY

As we have already noted, the wave approach to electromagnetic phenomena plays a fundamental part in remote sensing. Below we shall outline the basic components and statements of Maxwell’s electromagnetic theory which shall be used throughout the presentation of the material in this book.

The features of electromagnetic waves, the laws of their excitation and propagation are described by Maxwell’s equations as being a fundamental law of nature and a direct consequence (from the viewpoint of modern geometry) of fundamental properties of space-time (Dubrovin *et al.*, 1986).

The equations were formulated by J. Maxwell in the 1860s on the basis of a generalization of the empirical laws of electric and magnetic phenomena and using phenomenological mechanistic concepts. The modern symmetric form of the equations was proposed by H. Hertz and O. Heaviside (Krug, 1936; Stratton, 1941; de Broglie, 1941; Alpert *et al.*, 1953).

Maxwell’s equations associate the quantities characterizing the electromagnetic field with its sources, i.e. with the spatial distribution of electrical charges and currents. In a vacuum the electromagnetic field is characterized by the electric field strength \mathbf{E} and the magnetic induction \mathbf{B} , vector quantities depending on spatial coordinates and time. These quantities determine the forces acting from the

field side on charges and currents, whose distribution in space is specified by the volume density of charge ρ and electric current density \mathbf{j} . To describe electromagnetic processes in a material medium the auxiliary vector quantities are introduced in addition to \mathbf{E} and \mathbf{B} . These quantities, which depend on the state and properties of a medium, are the electric displacement \mathbf{D} and the magnetic field strength \mathbf{H} . The second pair of vectors, \mathbf{D} and \mathbf{H} , are determined from the charges and currents in the field, as the lines of force originating from the charges and currents.

Maxwell's equations enable us to determine the basic characteristics of the field (\mathbf{E} , \mathbf{B} , \mathbf{D} and \mathbf{H}) at each point of space and at any time instant, if the sources of the field \mathbf{j} and ρ are known as functions of position and time.

If electric charges and currents exist in any region of space, then their variation in time results in emission and propagation of electromagnetic waves in space. The character of electromagnetic wave propagation is essentially influenced by the medium they propagate in. In real media the waves can undergo refraction and dispersion; near inhomogeneities the diffraction and interference of waves are observed, as well as total internal reflection and other phenomena inherent in waves of any nature.

Maxwell's equations can be written both in the integral and the differential form. In the integral form the equations determine not the vectors at separate points, but some integral quantities depending on the distribution of these characteristics of the field. In electromagnetic wave propagation and remote sensing tasks the differential Maxwell's equations are most frequently used, which characterize the fields at each point in space:

$$\text{rot } \bar{\mathbf{H}} = \mathbf{j} + \frac{\partial \bar{\mathbf{D}}}{\partial t}, \quad (1.1a)$$

$$\text{rot } \bar{\mathbf{E}} = -\frac{\partial \bar{\mathbf{B}}}{\partial t}, \quad (1.1b)$$

$$\text{div } \bar{\mathbf{B}} = 0, \quad (1.1c)$$

$$\text{div } \bar{\mathbf{D}} = \rho. \quad (1.1d)$$

The physical sense of the first equation consists in Maxwell's generalization of the Biot–Savart law of magnetic field excitation both by electric conductivity currents and displacement currents to the variable fields. The second equation represents the mathematical formulation of Faraday's electromagnetic induction law. The third equation reflects the experimental data on the absence of magnetic charges (the magnetic field is generated by electric currents only). And the fourth equation represents the generalization of the law of interaction of motionless electric currents – Coulomb's law.

However, in the form presented above, Maxwell's equations do not form a complete closed system allowing us to calculate the electromagnetic processes in the presence of material medium. They must be supplemented by the equations of

state, or the constitutive equations of the medium, which determine the relationship between the properties of a medium and its state, namely:

$$\mathbf{D} = \mathbf{D}(\mathbf{E}), \mathbf{B} = \mathbf{B}(\mathbf{H}), \mathbf{j} = \mathbf{j}(\mathbf{E}). \quad (1.2)$$

The set of the equations of field (1.1) and the equations of state (1.2) just form the complete system of Maxwell's equations.

The constitutive equations of the medium are very complicated in the general case, because the fields \mathbf{D} , \mathbf{B} and \mathbf{j} at a given point and at a given time instant may depend on the fields \mathbf{E} and \mathbf{H} at all points of a medium and at all previous time instants (the after-effect). However, for the majority of natural isotropic media that the remote sensing activity deals with, the constitutive equations of the medium have a simple linear form (which is proved by direct experiments):

$$\mathbf{D} = \varepsilon(x, y, z)\varepsilon_0\mathbf{E}, \mathbf{B} = \mu(x, y, z)\mu_0\mathbf{H}, \mathbf{j} = \sigma\mathbf{E}. \quad (1.3)$$

Here $\varepsilon(x, y, z)$ and $\mu(x, y, z)$ are the relative (and dimensionless) permittivity and relative permeability of a material medium, and $\sigma(x, y, z)$ is called the electrical conductivity of a medium. The latter relation in (1.3) represents the well-known Ohm's law for a conducting medium. In materials not obeying Ohm's law the relation between the field and current is more complicated.

Note one principal point now: in relations (1.3) ε_0 and μ_0 are dimensional constants, which depend on the chosen system of units and are called permittivity and permeability constants. Unlike the relative permittivity, which depends on the type of substance, on its physical and chemical composition, on the geometrical volume properties, on temperature, pressure and other parameters, the permittivity constant depends on the choice of a system of units only. A similar conclusion can also be drawn for the relation between the relative permeability and the permeability constant. In this case it should be noted, however, that the majority of natural media possess a relative permeability value equal to unity. For empty space the values of relative permittivity and permeability are equal to unity, which is a proven experimental fact. In the International System of Units (SI) we shall adhere to (see Appendix A), the values of permittivity and permeability constants are equal to:

$$\varepsilon_0 = (\mu_0 c_0^2)^{-1} = \frac{10^7}{4\pi c_0^2} \text{ F m}^{-1}, \quad (1.4)$$

$$\mu_0 = 4\pi \times 10^{-7} \text{ H m}^{-1}. \quad (1.5)$$

In the symmetric Gaussian system of units $\varepsilon_0 = \mu_0 = 1$ (this system of units is mainly used in theoretical works).

In the original phenomenological Maxwell's theory the macroscopic characteristics of the electromagnetic properties of a medium ε , μ , and σ should be found by the experimental method or calculated proceeding from particular concepts of the structure of substance. These concepts can be either purely phenomenological, or must be obtained from the Lorentz–Maxwell equations formulated for microscopic fields with subsequent averaging of microfields over space–time intervals and finding the particular form of the constitutive equations of the medium. For remote sensing

activity the set of aforementioned procedures is very important, because their application closely relates to the problems of interpretation of the physical-chemical composition and geometrical volume properties of physical bodies, based on the data of measurement of their thermal radiation or, in other words, on the solution of reverse remote sensing problems (see Chapters 7, 8 and 13).

Maxwell's equations are valid at any point of space, where the fields do not undergo discontinuity. On the surface of discontinuities (two adjacent media) the fields can undergo discontinuities (jumps). In this case the basic equations (1.1) are supplemented by the boundary conditions, which are obtained as limiting transitions of the basic equations to the surface element:

$$[\mathbf{n} \cdot \mathbf{H}]_2 - [\mathbf{n} \cdot \mathbf{H}]_1 = \mathbf{j}_s, \quad (1.6a)$$

$$[\mathbf{n} \cdot \mathbf{E}]_2 - [\mathbf{n} \cdot \mathbf{E}]_1 = 0, \quad (1.6b)$$

$$[\mathbf{n} \cdot \mathbf{D}]_2 - [\mathbf{n} \cdot \mathbf{D}]_1 = \rho_s, \quad (1.6c)$$

$$[\mathbf{n} \cdot \mathbf{B}]_2 - [\mathbf{n} \cdot \mathbf{B}]_1 = 0. \quad (1.6d)$$

Here \mathbf{j} and ρ_s are surface current and charge densities; the square and round brackets correspond to vector and scalar products of vectors, \mathbf{n} is the unit vector of a normal to the interface surface and of the direction from the first medium to the second one ($1 \rightarrow 2$); the subscripts relate to different sides of the interface boundary. The physical sense of these conditions is as follows: the tangential component of the electric field (1.6b) and the normal component of the magnetic induction vector (1.6d) are continuous on the interface; the tangential component of the magnetic field (1.6a) and the normal component of the electric induction (1.6c) undergo discontinuity in the presence of currents and charges on the surface.

The spatial distribution of electromagnetic fields (the time-dependencies of electric and magnetic fields) which determine the type of wave (planar, spherical, cylindrical etc.), the type of polarization and other features of electromagnetic waves are specified, on the one hand, by the character of radiation source, and, on the other, by the properties of the medium in which the waves propagate. In the case of homogeneous and isotropic medium, far from the charges and currents, which generate the electromagnetic field properly (in the case of $\mathbf{j} = \rho = 0$), Maxwell's equations give rise to the familiar wave equations:

$$\Delta \mathbf{E} - \varepsilon_0 \varepsilon_0 \mu_0 \mu \frac{\partial^2 \mathbf{E}}{\partial t^2} = 0, \quad (1.7a)$$

$$\Delta \mathbf{H} - \varepsilon_0 \varepsilon_0 \mu_0 \mu \frac{\partial^2 \mathbf{H}}{\partial t^2} = 0. \quad (1.7b)$$

where Δ is the Laplace operator:

$$\frac{\partial^2}{\partial x^2} + \frac{\partial^2}{\partial y^2} + \frac{\partial^2}{\partial z^2}.$$

Equations (1.7) express the fact that electromagnetic waves propagate in a medium, characterized by constants ε and μ , at velocity $c = c_0/\sqrt{\varepsilon\mu}$ and, in particular, at the speed of light in vacuum. This result represents one of the first major achievements of electromagnetic field theory. The general solution of this equation (which is presented here, for better physical clarity, for one component of the electric field E_x propagating in the direction z) has the form:

$$E_x = f\left(z - \frac{t}{c}\right) + g\left(z + \frac{t}{c}\right)$$

where f and g are arbitrary differentiable functions which describe the wave propagation in the positive and negative directions respectively of axis z . To determine the phase velocity of the wave we place the observer in the coordinate system, which moves together with the wave; then the value of the argument in the function will be fixed (constant). Taking the time derivative from the argument, we obtain the propagation velocity value presented above.

In linear media satisfying relations (1.3) and, in particular, in a vacuum, Maxwell's equations are linear, so that the wave superposition principle is valid for these media. And, in this sense, it is convenient to consider primarily the electromagnetic processes as being harmonic in time, namely, in the complex designation $e^{j\omega t}$. For harmonic (in time) processes equations (1.7) assume the form:

$$\Delta \mathbf{E} + \omega^2 \varepsilon_0 \varepsilon \mu_0 \mu \mathbf{E} = 0, \quad (1.8a)$$

$$\Delta \mathbf{H} + \omega^2 \varepsilon_0 \varepsilon \mu_0 \mu \mathbf{H} = 0. \quad (1.8b)$$

In this case the very important class of partial solutions of Maxwell's equations is found – the planar monochromatic waves, which are determined by the following relations:

$$E = E_0 \cos(\mathbf{k} \cdot \mathbf{r} - \omega t + \varphi), \quad (1.9a)$$

$$H = H_0 \cos(\mathbf{k} \cdot \mathbf{r} - \omega t + \varphi). \quad (1.9b)$$

Here E_0 and H_0 are the amplitudes of vectors of electric and magnetic fields, $\omega = 2\pi\nu$ is the circular frequency of oscillations, \mathbf{r} is the radius-vector of the observation point, φ is the arbitrary phase shift and \mathbf{k} is the wave vector, whose direction coincides with the direction of propagation of a running electromagnetic wave. The wave vector magnitude, the wave number, is associated with the circular frequency ω , phase velocity of wave v_p and its spatial period (wavelength λ) by the relation:

$$|\mathbf{k}| = \frac{2\pi}{\lambda} = \frac{\omega}{v_p}.$$

Note, that in optics and spectroscopy the wave number often designates the quantity reversal to the wavelength, $k = 1/\lambda$. Besides, it should be noted that the wave energy flux is directed along vector \mathbf{k} , generally speaking, in isotropic media only (for example, in a vacuum).

To determine the structure of electromagnetic waves it is necessary to address Maxwell's equations (with $\rho = 0$). It follows from relations (1.1c,d), that vectors \mathbf{k} , \mathbf{E} and \mathbf{H} are associated by the following relations:

$$(\mathbf{k} \cdot \mathbf{E}) = 0, (\mathbf{k} \cdot \mathbf{H}) = 0, \quad (1.10)$$

The first two equations of (1.1a,b) for vectors \mathbf{E} and \mathbf{H} of a running planar wave form the following relation:

$$\mathbf{E} = -\frac{1}{|\mathbf{k}|} \sqrt{\frac{\mu_0 \mu}{\epsilon_0 \epsilon}} [\mathbf{k} \cdot \mathbf{H}]. \quad (1.11)$$

This implies, that the vector fields \mathbf{E} and \mathbf{H} are strictly transversal, i.e. both vectors are perpendicular to the propagation direction and, besides, both are perpendicular to each other and form the right orthogonal triplet of vectors. In a vacuum the values of fields themselves are equal between each other in magnitude, if they are expressed by means of the chosen system of units. In empty space the indicated mode of electromagnetic waves is the only one.

The relation between the amplitudes of electric and magnetic fields in a planar wave plays an important part when the wave propagation in various media is considered, and for these reasons this parameter was specifically called the intrinsic impedance of a medium (or the wave resistance of a medium) Z_0 :

$$Z_0 = \frac{E_0}{H_0} = \sqrt{\frac{\mu \mu_0}{\epsilon \epsilon_0}}. \quad (1.12)$$

It follows from this relation, that the characteristic impedance depends only on the properties of a medium where the electromagnetic energy propagation takes place. For a vacuum ($\epsilon = \mu = 1$) this is a universal constant, which in the SI system of units is equal to:

$$Z_0 = \sqrt{\frac{\mu_0}{\epsilon_0}} = 120\pi = 376.6 \text{ ohms}. \quad (1.13)$$

This circumstance is one of the entire spectrum of serious reasons, which result in important analogies between the wave propagation of electromagnetic energy and its propagation in transmission lines and, in particular, with the impedance approach (the method of impedances) (Krug, 1936; Stratton, 1941; Slater, 1942). Many problems of wave propagation of electromagnetic energy (and, in particular, the refraction of waves at media interfaces, and wave propagation in stratified media and in waveguides, as well as the emission of stratified media) can be successfully solved within the framework of the method of impedances. We shall repeatedly use this approach in various sections of this book.

Since the waves of any form can be presented as a sum of harmonic components, then for linear media, for which the wave superposition principle is valid, all emission, propagation and absorption problems are reduced to the solution of problems for harmonic electromagnetic waves. Certainly, this fully relates to remote sensing activity.

Now we consider the important question of energy transfer by the electromagnetic field, based on the ideas of the Russian physicist N. A. Umov. He introduced for the first time (1874) the general notion of energy flux in the continuous medium, as well as the notion of a physical field's energy flux vector, which is numerically equal to the energy transferred per unit time through the unit area perpendicular to the energy flux direction at a given point. The energy conservation law can be written in the following differential form (Stratton, 1941; Vinogradova *et al.*, 1979):

$$\frac{\partial W}{\partial t} + \operatorname{div} \mathbf{S} = 0, \quad (1.14)$$

where W is the volume density of energy and \mathbf{S} is the energy flux vector.

The physical sense of this expression consists in the fact, that the change of energy in some volume per unit time equals the energy flux through the surface confining this volume. To find the explicit form of quantities W and \mathbf{S} for the electromagnetic field, we take advantage of the system of Maxwell's equations for the isotropic medium, in which $\sigma = 0$. Multiplying the first equation of (1.6a) by \mathbf{E} and the second one by \mathbf{H} and subtracting one from another, we obtain the following expression:

$$\frac{\partial}{\partial t} \frac{1}{2} (\mathbf{E} \cdot \mathbf{D} + \mathbf{H} \cdot \mathbf{B}) + \operatorname{div} [\mathbf{E} \cdot \mathbf{H}] = 0. \quad (1.15)$$

Comparing (1.15) with (1.14), we can interpret the vector

$$\mathbf{S} = [\mathbf{E} \cdot \mathbf{H}], \quad (1.16)$$

which is known as Poynting's vector, as the flux of the electromagnetic field energy, and the scalar quantity

$$W = \frac{1}{2} (\mathbf{E} \cdot \mathbf{D} + \mathbf{H} \cdot \mathbf{B}) \quad (1.17)$$

as the density of volume energy of the electromagnetic field. Since in the isotropic medium vectors \mathbf{E} , \mathbf{H} and \mathbf{k} form a right-handed screw system, \mathbf{S} coincides with the direction of propagation of electromagnetic waves. In anisotropic media (and also near conducting surfaces) \mathbf{S} may not coincide with the wave propagation direction. Besides, as seen from (1.16–1.17), the electromagnetic field always possesses the energy, and the energy flux differs from zero only in the case where both electric and magnetic fields exist simultaneously, their vectors being not parallel to each other.

Since the vector fields are often used in the complex form, after rather simple transformations and with account taken of the fact that the mean value of a square of sine and cosine are equal to 1/2, we obtain the mean value of Poynting's vector $\bar{\mathbf{S}}$ over the period in the following form (Slater, 1942):

$$\bar{\mathbf{S}} = \frac{1}{2} \operatorname{Re} [\mathbf{E} \cdot \mathbf{H}^*]. \quad (1.18)$$

Of interest also is the vector relation between the mean value of the flux density in a planar electromagnetic wave and the volume density of energy. Using relations (1.11), (1.17) and (1.18), we obtain, after some transformations,

$$\bar{\mathbf{S}} = \frac{1}{2} \operatorname{Re} [\mathbf{E}[\mathbf{k} \cdot \mathbf{E}^*]] \sqrt{\frac{\epsilon\epsilon_0}{\mu\mu_0}} \frac{1}{|\mathbf{k}|} = \mathbf{c} \cdot \mathbf{W}, \quad (1.19)$$

where $|\mathbf{c}| = c_0/\sqrt{\epsilon\mu}$, and the direction of transfer velocity coincides with the wave propagation direction (vector \mathbf{k}). Also, remembering the expression for the impedance of a medium (1.12), we obtain the following expression for the mean value of Poynting's vector:

$$\bar{\mathbf{S}} = \frac{1}{2} \operatorname{Re} \frac{|\mathbf{E}|^2}{Z_0}. \quad (1.20)$$

Thus, Poynting's vector becomes a complete analogue of the current-by-voltage product (i.e. the power) in transmission lines and in circuits with concentrated elements (resistors, capacitors, inductors). And, hence, we arrive once again at the possibility of using (certainly, within a limited framework) the impedance approach to wave problems. So, for example, on an ideal conductor's surface the tangential component of the electric field is zero (see the boundary conditions) and, accordingly, the impedance at this point of the surface is also zero, which is equivalent to a shorted electrical circuit. On the ideal magnetic surface the tangential component of the magnetic field is zero and, accordingly, the impedance is equal to infinity, which is equivalent to a disconnected electrical circuit.

Now we consider one more aspect that is revealed in electromagnetic wave propagation in material media, that is, dispersion effects – the change in a medium's properties when an electromagnetic field of different frequencies is imposed on the medium. These effects play a primary part in microwave remote sensing problems, providing the possibility of obtaining information on physical and chemical volume properties of physical bodies based on their thermal radio emission data (see Chapters 7 and 8). (This, by the way, cannot be done based on the direct data from optical and IR ranges.)

The physical essence of these effects is as follows. As we have noted, the properties of a medium in Maxwell's electrodynamics should be taken into account in the constitutive equations of the medium, which for static ($\lambda \rightarrow \infty$) and slowly varying fields can be written in the linear form (1.3). In this case the values of \mathbf{D} , \mathbf{B} and \mathbf{j} at some point of a medium and at some time instant are determined by the values of \mathbf{E} and \mathbf{H} at the same point and at the same time instant. However, if the external electromagnetic field varies more rapidly, then, owing to the inertia of internal motions and the particular spatial structure of a physical body (the medium), the values of \mathbf{D} , \mathbf{B} and \mathbf{j} at the point of the medium under study will depend on the fields at other points of the medium and at other (previous) time instants. Although for gaseous, liquid and solid media the specific physical mechanisms, causing dispersion effects in media, very strongly differ from each other (some of them will be discussed

in Chapter 8), nevertheless, the dispersion properties of media can be described in a unified and convenient manner using the notion of a complex relative permittivity (remember, that the relative permeability of the majority of natural media is equal to unity). For this purpose fields are considered which depend on time according to a sine law (the Fourier presentation), and complex quantities are used for describing these fields.

If only the frequency dispersion in a medium is taken into account, the constitutive equations of the medium (1.3) have the following form:

$$\mathbf{D}(\omega, r) = \varepsilon(\omega)\mathbf{E}(\omega, r); \mathbf{j}(\omega, r) = \sigma(\omega)\mathbf{E}(\omega, r). \quad (1.21)$$

Whereas in the non-dispersed medium the relative permittivity is a purely reactive parameter and the conductivity is purely active one, in the medium with dispersion this distinction is lost (see, for example, Alpert *et al.*, 1953). As the frequency of the external field approaches some natural frequencies in a medium, the distinction between the properties of dielectrics and conductors completely disappears (for fresh water this wavelength equals about 1 cm). So, the presence of an imaginary part of the relative permittivity in a medium is indistinguishable, from the macroscopic point of view, from the existence of conductivity – both of them cause release of the heat. Thus, for high-frequency monochromatic fields it is convenient to introduce, instead of relative permittivity and conductivity, the complex relative permittivity, which combines both these notions. The same characteristic includes the so-called dielectric losses, which are determined by that part of the external variable electric field that is transformed into heat at re-polarization of a dielectric. All motions of particles in a substance are related to dissipation of the part of energy imparted to particles by the electric field. Finally, this part of energy transfers into heat. If the small displacements of electrons and ions play a basic part in the polarization of a dielectric, then they can be considered as a set of harmonic oscillators, which undergo forced oscillations in the variable field. The losses of energy in such oscillations are maximal when the frequency of external effects is close to the frequency of the natural oscillations of the oscillators (the resonance). At exit from the resonance region the amplitudes of oscillations and the velocities of particles sharply decrease, and the dielectric (relaxation) losses become small. For the electronic polarization mechanism the maximum of losses falls on optical frequencies (about 10^{15} Hz). For polarization caused by displacement of ions, the maximum of dielectric losses displaces into the IR range (10^{12} – 10^{13} Hz). The lower frequencies (in the radio range) correspond to the maximum of losses with orientation-type polarization of individual molecules (fresh water) or of clusters of molecules (salted water). In electrically non-homogeneous media, intersurface polarization can be observed. It is caused by the motion of free carriers of charges accumulating near interface boundaries between the regions with heightened specific resistance (intercrystal layers, microcracks, fluctuations of physical-chemical composition, etc.) The maxima of dielectric losses for such media are situated in a wide range of frequencies (10^3 – 10^9 Hz). Remarkable natural examples of such media are various modifications of sea ice and freshwater ice, the moist soil with combined water electrolytes inside the ground

volume, as well as the water–ice system and the snow cover at the phase transition instant.

To introduce the complex relative permittivity we consider the propagation of a planar electromagnetic wave in the isotropic homogeneous medium with a finite value of conductivity in the z direction of a right-handed-screw coordinate system (x, y, z) . The electric field is directed along axis x and the magnetic field along axis y . Then Maxwell's equations will assume the following form of a wave equation for E_x :

$$\frac{\partial^2 E_x}{\partial z^2} - \varepsilon_0 \varepsilon \mu_0 \mu \frac{\partial^2 E_x}{\partial t^2} - \mu_0 \mu \sigma \frac{\partial E_x}{\partial t} = 0. \quad (1.22)$$

A similar equation can also be obtained for the magnetic field component H_y . The solution of equation (1.22) with respect to E_x can be written in the following compact complex form:

$$E_x = E_{x0} \exp(j\omega t + j\dot{\psi}), \quad (1.23)$$

where $\dot{\psi}$ is the total complex phase, \dot{n} is the complex refractive index for the conducting medium:

$$\dot{\psi} = \frac{\omega}{c_0} \dot{n} z, \dot{n} = n + j\chi. \quad (1.24)$$

Now we introduce the complex relative permittivity of a medium as:

$$\dot{\varepsilon} = \varepsilon_1 + j\varepsilon_2 = (\dot{n})^2. \quad (1.25)$$

From this definition we can easily obtain the direct relation:

$$\operatorname{Re} \dot{\varepsilon} = \varepsilon_1 = n^2 - \chi^2, \operatorname{Im} \dot{\varepsilon} = \varepsilon_2 = 2n\chi, \quad (1.26)$$

and the opposite one:

$$n^2 = \frac{\varepsilon_1}{2} \left(1 + \sqrt{1 + \operatorname{tg}^2 \delta} \right), \quad (1.27)$$

$$\chi^2 = \frac{\varepsilon_1}{2} \left(\sqrt{1 + \operatorname{tg}^2 \delta} - 1 \right). \quad (1.28)$$

Here the quantity $\operatorname{tg} \delta = \varepsilon_2 / \varepsilon_1$ was called the tangent of the angle of losses in a medium.

In the presence of complicated relaxation mechanisms of polarization in a medium the introduced complex relative permittivity (and, accordingly, the complex refractive index) can be a rather complicated function of frequency (or of the wavelength). So far we have considered the simplest version of a non-dispersed (in dielectric properties) medium with a finite conductivity.

Substituting (1.23) into (1.22), we obtain the required solution in the form of two exponents, the first of which describes the total attenuation in a medium, and the argument in the second exponent determines the time delay of a signal, when it

passes distance z in a medium:

$$\dot{E}_x = E_{x0} \exp\left(-\frac{\omega}{c_0}\chi z\right) \exp\left(j\omega\left(t - \frac{n}{c_0}z\right)\right), \quad (1.29a)$$

$$\dot{H}_y = \frac{E_{x0}}{\dot{Z}_c} \exp\left(-\frac{\omega}{c_0}\chi z\right) \exp\left(j\omega\left(t - \frac{n}{c_0}z\right)\right). \quad (1.29b)$$

The wave resistance of a medium in the case under consideration (of finite conductivity) is a complex quantity:

$$\dot{Z}_c = \sqrt{\frac{\mu\mu_0}{\dot{\varepsilon}\varepsilon_0}} = \sqrt{\frac{\mu\mu_0}{\varepsilon_0\varepsilon_1(1 + jt g\delta)}} = |\dot{Z}_c| \exp(j\varphi), \quad (1.30)$$

where

$$|\dot{Z}_c| = \sqrt{\frac{\mu_0\mu \cos \delta}{\varepsilon_0\varepsilon}}, \varphi = \frac{\delta}{2}.$$

The presence of losses in a medium leads to a decrease in the magnitude of wave resistance of a medium, i.e. to an increase in the magnetic field value for a given electric field value. In addition, the phase shift appears between vectors \mathbf{E} and \mathbf{H} , the magnetic field vector being delayed in phase with respect to vector \mathbf{E} by the angle equal to a half of the angle of losses ($\delta/2$). The phase velocity of a planar wave is $v_p = c_0/n(\sigma)$, and the wavelength in a medium $\lambda = \lambda_0/n(\sigma)$ is less than its values in a loss-free medium with the same dielectric parameters, and at a given frequency they decrease with increasing conductivity (see (1.27)). Complex Poynting's vector contains both the real and imaginary part, which implies that there exist both active (transfer) and reactive heating fluxes of energy.

Proceeding from the solution obtained, important propagation parameters are introduced, namely, the coefficient of attenuation in a medium per unit length along the field $\gamma_\varepsilon = (\omega/c_0)\chi$ (neper/m), and the time delay of a signal $\Delta t = (n/c_0)z$. These propagation parameters play an important part in practical observation, since they can be measured experimentally to a high accuracy.

Taking into account relation (1.28), we obtain the important relationship between the value of specific coefficient of attenuation in a medium with its dielectric characteristics:

$$\gamma_E = \frac{2\pi}{\lambda_0} \sqrt{\frac{\varepsilon_1}{2}} \sqrt{\sqrt{1 + \operatorname{tg}^2 \delta} - 1}. \quad (1.31)$$

For semi-transparent media with a small value of the tangent of the angle of losses, $\operatorname{tg}\delta \ll 1$, relation (1.31) is transformed into the well-known expression, which is often used for experimental estimations in various ranges of wavelengths (from optical to radiowaves):

$$\gamma_E = \frac{\pi}{\lambda_0} \sqrt{\varepsilon_1} \operatorname{tg}\delta. \quad (1.32)$$

Note here one important circumstance: the specific coefficient of attenuation in a medium depends both on the real part of the relative permittivity, and on the imaginary part.

Since the energy flux through the surface unit, transferred by the electromagnetic wave (Poynting's vector) is proportional to the square of the amplitude of the electric field strength (1.20) and, in other words, to the radiation intensity, then, on the basis of (1.20) and (1.29), the specific attenuation in a medium for the radiation intensity is equal: $\gamma_p = 2\gamma_E$.

In experimental practice, for convenient coordination of the total attenuation in a medium, expressed in terms of the first component in relation (1.29), with specific coefficient of attenuation in a medium, an approach is used that determines the characteristics of attenuation in a medium in the logarithmic scale. The physical sense of this approach is fairly obvious. The expression for intensity of radiation, past the distance z in a medium, can be presented as

$$|S(z)| = |S(0)| \exp(-\gamma_p z).$$

Taking the logarithm from both parts of the equality, we obtain the expression in the logarithmic form for the total attenuation in a medium occurring at the distance z . This expression, expressed in decibels (dB), is as follows:

$$\gamma(\text{dB}) = 10 \lg |S(0)|/|S(z)| = 20 \lg |E(0)|/|E(z)| = 4.3\gamma_p z, \quad (1.33)$$

and the expression for the total attenuation in a medium per unit length is written as:

$$\gamma(\text{dB/m}) = 4.3\gamma_p (\text{neper/m}) = 8.69\gamma_E (\text{neper/m}). \quad (1.34)$$

It can easily be seen from (1.33) that the total attenuation in a medium of 1 dB corresponds to a 1.26-fold change of radiation intensity (a 1.12-fold change of the field), 3 dB corresponds to a 2-fold change of intensity (a 1.41-fold change of the field), 10 dB corresponds to a 10-fold change of intensity (a 3.16-fold change of the field), and 20 dB corresponds to a 100-fold change of intensity (a 10-fold change of the field), etc. When the radiation passes through various media with different attenuations, its total attenuation is the sum of individual attenuations expressed in the logarithmic scale. This circumstance is very often used, both in observational experiments and in technological applications.

Consider now another important characteristic whose value for various natural media will be fairly frequently used in remote sensing data analysis. We mean the distance (depth), passing which the electromagnetic field weakens e times in a medium and, accordingly, the information on the physical properties of a substance can be obtained from this layer based on the thermal radiation data. This characteristic is called the depth of field penetration into the medium (the skin-layer), and it is determined as a quantity the reciprocal of the coefficient of attenuation:

$$L_S = \frac{1}{\gamma_E} = \frac{\lambda_0}{2\pi} \left[\frac{\varepsilon_1}{2} \left(\sqrt{1 + \tan^2 \delta} - 1 \right) \right]^{-1/2}. \quad (1.35)$$

So, as we have noted, Maxwell's wave equations describe an extensive area of physical phenomena. These equations underlie electrical engineering and radio engineering and play a fundamental part in the development of such topical directions of modern physics and geophysics as remote sensing of the Earth, planets and interplanetary space, plasma physics, magnetic hydrodynamics, nonlinear optics, astrophysics and other disciplines. Maxwell's equations are directly inapplicable only at high frequencies (in the X-ray and gamma ranges), where purely quantum effects become essential. However, in a number of problems, quantum effects can also be essential in lower-frequency bands – optical and IR – and even in the microwave band (the thermal emission of gases). The solution of such problems necessitate the use of quantum concepts, such as the flux of quasi-particles – photons (see Chapter 11).

The complete solution of Maxwell's equations is fairly labour-intensive and cannot be obtained in the general form. However, depending on the relation between the wavelength (λ) of the electromagnetic field used in science experiments or in technological applications, and the geometric size of physical objects (L), a number of important approximations can be obtained. So, for $\lambda \gg L$ the quasi-stationary approximation is used. It is characterized by the fact that electromagnetic processes can be concentrated at separate components (resistors, capacitors, inductors) and that the method of complex impedance (or, in other words, complex Kirchhoff's rules for branched electrical circuits (Krug, 1936)) is used in calculations. This approach has been successfully used in both electrical engineering and radio engineering applications, as well as in physical experiments and in radio communication and TV broadcasting practice. For the reverse relation $\lambda \ll L$ the approximation approach is called the geometrical optics approximation; it uses beam concepts for electromagnetic radiation propagation, including such features as the rectilinearity of light beams, geometrical shadow and the reflection and refraction of light. All these features are well known from daily life. Owing to the achievements of calculus, the methods for the calculation of electromagnetic processes in the geometrical optics approximation have reached high perfection. For the relation $\lambda \leq L$ the approximation approach is called the theory of long lines, which is characterized by the use of the ideology of dispersed (distributed in a line) capacitive and inductive parameters and the use of the impedance approach in calculations. The most complicated case is the area, where the relation is $\lambda \approx L$, and, thus, the use of complete diffraction approaches and complete solutions of Maxwell's equations is necessary. Till now a great diversity of modifications of the approaches mentioned has been obtained, so that it is actually impossible (and, apparently, inexpedient) to give any completed form of approaches with their frequency – spatial differentiation. There exist a lot of interdependent approaches; so, the geometrical and wave approaches are formally combined in the geometrical diffraction theory, in which, along with rectilinear beams, the existence of various types of diffracted (curved) beams is postulated. At present, the solution of virtually any physical problem of the interaction of electromagnetic radiation with physical bodies can be obtained in various approximations (or in combinations of approximations), and the major problem

in interpreting the solutions is understanding the adequacy of the accepted approximation to the given physical problem.

As far as the electromagnetic field of thermal radiation is concerned, we have already paid attention to the fact that this wave process has a random (chaotic) character, both during its development in time and during its propagation in space. For these reasons, the determination and measurement of the energy flux (in essence, the intensity of the flux) in such random processes and the separation of determinate components from data obtained (which just bear the information content in remote investigations) represent a special problem which will be considered in detail in Chapters 2 and 3 – and results of solving this problem will be used throughout the book.

2

Random signals and fields

The purpose of this chapter is to offer the reader a brief review of modern methods for the analysis of random signals and fields as applied, first of all, to studying the physical principles of thermal radiation formation, then to considering the methods and techniques of fluctuation signal reception and also to the analysis and interpretation of remote microwave sensing data. The chapter has a reference character to some extent and does not require special knowledge on the part of the reader, except for an acquaintance with the basic principles of the classic spectral analysis of deterministic signals. However, the information given in this chapter will be indispensable for further exploration of the material.

2.1 DETERMINISTIC AND STOCHASTIC DESCRIPTION OF NATURAL PROCESSES

Even the ancient philosophers advanced ideas on the possibility of forecasting the future behaviour of natural processes, which seem to be purely random phenomena to an external observer. However, all these procedures have been accomplished at a purely emotional level. The subsequent mathematical formulation of the laws of nature and the great successes in studying the problems of the motion of planets (space research, in modern terms) gave rise to the well-known deterministic Laplacian picture of the world. However, the other – probabilistic – approach had been developed almost simultaneously, supported by thermodynamics and statistical physics and, later, by quantum mechanics. This approach dealt with systems with a very great number of interacting components and, accordingly, with a great number of degrees of freedom in a physical system. The use of such approaches resulted in introducing the time irreversibility (or the ‘time arrow’) principle into the natural sciences, and the predictability of such (stochastic) systems could be formulated only in probabilistic language. Up to the middle of the 1960s the subdivision of natural objects (and processes) into two similar large classes seemed to be quite natural and

lawful. The former class – deterministic processes with a small number of degrees of freedom – is described within the framework of dynamic systems, where the future is unambiguously determined by the past, and behaviour is fully predictable. The second class includes stochastic processes with a great number of degrees of freedom or with a great number of possible reviews of the system's parameters, where the future does not depend on the past, and the behaviour of processes can be described in probabilistic language. The classical (and rather banal at first sight) example is the repeated tossing of a bone or coin. This procedure was called the Bernoulli scheme (Bernoulli trials); it consisted in performing repeated independent trials with two probable results: ‘success’ and ‘failure’ (Feller, 1971; Rytov, 1966; Mandel and Wolf, 1995). More complicated mechanical probabilistic models (modifications and generalizations of the Bernoulli trial scheme) resulted in the appearance of a wide spectrum of probabilistic distributions which have been widely used in statistical physics (for example, the Bose–Einstein statistics for photons and the Fermi–Dirac statistics for electrons, neutrons and protons). The classical probability theory (on Kolmogorov’s axiomatic basis) investigates probabilistic processes ‘in statics’, considering them as a fixed result of the experiments performed (the random quantities theory). However, the physical observational practice (including remote sensing) gives us no less remarkable examples, which reflect the evolution of random phenomena of nature both in space and in time. They include the thermal emission of physical objects, the turbulent motions in the atmosphere, the relic background of the universe, the rough surface of the Earth and the dynamic disturbance of seas. The methods of the classical theory of probabilities of random quantities are insufficient in any given case. Similar problems are studied by a special branch of mathematics known as the theory of random processes. A brief description of this theory will be presented below.

In multiple observations of the sequence of tests of a random process (the Bernoulli scheme, for instance) or in studying the spatial-temporal image of a stochastic phenomenon within the wide range of spatial-temporal scales, some regularities can be revealed which are called statistical characteristics. These regularities can provide, in a sense, some possibility of controlling random phenomena and forecasting their future behaviour (certainly, within limited boundaries).

Till the 1970s these two fundamental classes, intended for describing natural processes, were supposed to have no interrelations between themselves. In the last 20 years one more important class of natural phenomena was found; it is described as the so-called deterministic chaos system. It was shown also, that there is no distinct boundary between deterministic and stochastic processes (Nicolis and Prigogine, 1977; Haken, 1978; Schuster, 1984; Glass and Mackey, 1988; Kadanov, 1993; Chen and Dong, 1996; Kravtsov, 1997; Blanter and Shnirman, 1997; Dubois, 1998). Moreover, the simplest physical deterministic systems (of the mechanical pendulum type) can exhibit (under particular conditions) obvious stochastic behaviour. And, similarly, in predominantly stochastic systems quite definite determinate (and long-lived) structures arise. So, under certain conditions spirals and concentric circles are born (develop and dissipate) in chemically intermixed solutions (the Belousov–Zhabotinsky reaction). At the same time, under turbulent

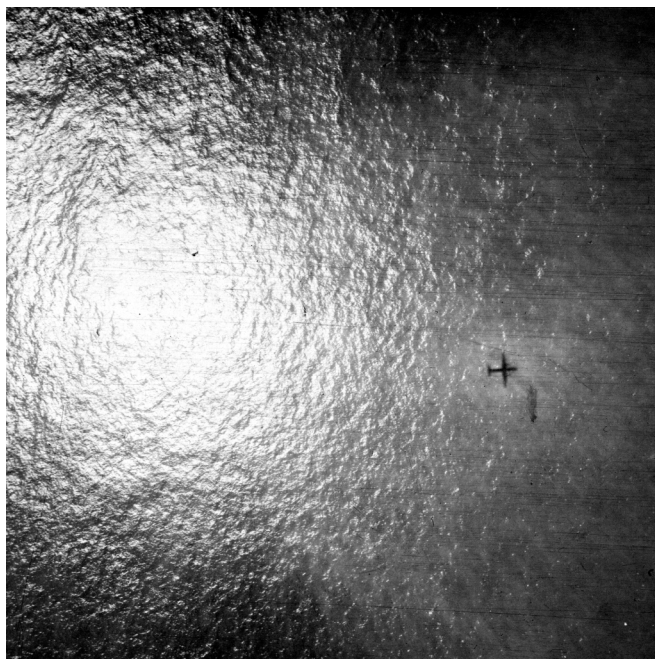
conditions of tropical atmosphere and in the presence of virtually gradientless atmospheric pressure fields, powerful spiral-type long-living vortices arise – the tropical cyclones – with a complicated topological and hierarchic structure of wind flows. Similar systems and phenomena were found in hydrodynamics, the physics of lasers, chemical kinetics, astrophysics, geophysics, ecology and biophysics and, what is most interesting, in social-economic systems of human society (banking, business, stockmarkets, the evolution of population, transport service systems and governmental management systems). In any of these fields of knowledge, of considerable interest is the arising of such a stable large-scale structure from some ‘primary’ chaos (this phenomenon is sometimes called a self-organization process). And very great attention is given to revealing particular physical self-organization mechanisms in particular physical, geophysical, social-economic or social-political systems (see, for example, Seidov, 1989; Rodrigues-Iturbe and Rinaldo, 1997; Schweitzer, 1997; Allen, 1997; Beniston, 1998; Kohonen, 1989; Lam, 1998; Milne, 1988; Dubois, 1998; Astafyeva *et al.*, 1994a,b; Astafyeva and Sharkov, 1998; Saperstein, 1999; Sornette, 2000). The methods of studying such processes can, certainly, be neither purely determinate, nor purely probabilistic. Some special analytical methods have been developed for these investigations, which allow us to analyse the state of a system within a very wide range of spatial-temporal scales simultaneously with finding all possible inter-scale interactions. Below we shall briefly discuss some of them. And for now we shall return to the problem of the probabilistic description of random processes.

2.2 BASIC CHARACTERISTICS OF RANDOM PROCESSES

By the random process $\xi(t)$ we shall mean some continuous function, which at any time instant t assumes random (i.e. unpredictable) values. If the set of times in a trial is discrete and finite, then the process is said to be a random sequence of events. Certainly, this definition has heuristic implications and is not a strict mathematical definition. The treatment of randomness as unpredictability is only one of the possible approaches to the concept of randomness. The theoretic-mathematical approach, which constitutes the basis of modern probability theory, associates randomness with the existence of a probabilistic measure (probabilistic distributions), while considering any quantities, processes and fields which possess a probabilistic measure as random ones (Kolmogorov’s axiomatics) (Feller, 1971; Rytov, 1966; Monin and Yaglom, 1971; Rytov *et al.*, 1978; Frisch, 1995; Mandel and Wolf, 1995; Kravtsov, 1997). In experimental physics and geophysics randomness is most frequently associated with the loss of linkage (correlation) in a system. These approaches are fairly closely interrelated; however, some fine distinctions also exist. So, the process with complicated internal links can be attributed to determinate ones from the point of view of one approach (for example, the approach which identifies the randomness with unpredictability), and to probabilistic ones within the framework of the other (correlation) approach (Kravtsov, 1997). Below we shall adhere to the correlation approach as most adequately reflecting the concept of randomness (stochasticity) in studying remote sensing data.



(a)



(b)



(c)

Figure 2.1. Air survey experimental results of the disturbed sea surface (Pacific, Japan Sea). (a) the height of air survey is 500 m; (b), (c) the height of air survey is 3000 m. The spatial distance between (b) and (c) frames is 20 km.

If we consider the processes progressing both in space and in time, $\xi(x, y, t)$, then in this case we imply the random (or stochastic) fields. A remarkable example of a spatial-temporal random field is the well-known sea disturbance (Figure 2.1(a)), which represents a continuously changing field of elevations over the average level. A lot of serious experiments have shown that sea disturbance (at various stages of its development) represents a virtually ideal random process (of Gaussian type), when it is considered both in space (the random three-dimensional field) and in time, for example, at the same measurement point (the random time signal or the time series).

When the source of illumination – the Sun – changes its position with respect to a recording device on the aircraft, the situation drastically changes. The quasi-reflecting stochastic surface converts the image of an almost point-like source (remember that the angular dimension of the Sun equals 30 minutes of arc) into the fluctuating field of patches of sunlight, which is just recorded by the remote sensing device at some particular time instant (Figure 2.1(b)). In surveying another time instant the field of patches of sunlight will be, certainly, different, i.e. another (and independent) ensemble of the field of patches of sunlight will take place. However, in this case some specific large-scale characteristics of the field of patches of sunlight (the elliptical pattern, its characteristic dimensions – the axes of

an ellipse) will be strictly conserved. The characteristic dimensions (angular or spatial) of a random field of patches of sunlight are closely associated with statistical characteristics of the field of elevations of the sea surface (and, more specifically, of the field of slopes) and, accordingly, with characteristics of the disturbance (the sea force, the near-surface wind velocity).

In the context of optical survey, performed from a low-altitude (500 m) aircraft (Figure 2.1(a)), a large sea wave breaking in the form of a crest foam package is observed. As we shall see below (Chapter 12), the field of breaking gravitational waves also represents the ideal random process to some extent, but of a quite different, Poisson point-like, type.

2.2.1 Ensembles of realizations

Dealing with the deterministic signals, we can map them in the form of functional time dependence, where one particular process has a *single realization*. In the case of random processes the situation is much more complicated. Fixing instantaneous values of a random signal on a particular time interval, we obtain *one of the possible realizations* of this random process. The distinction from determinate signals is paramount here. The fact is, that in its complete form the random process is expressed via the infinite combination of such realizations, which form *a statistical ensemble*. Such an ensemble can represent a system of noise signals $\{\xi_1(t), \xi_2(t), \dots, \xi_k(t), \dots\}$, which can be observed simultaneously at outputs of completely identical amplifiers (without a determinate input signal). The intrinsic (and non-removable in any circumstances) noises of radio equipment are called Nyquist noise. A schematized version of such a model experiment is shown in Figure 2.2(a). There is no problem in carrying out such an experiment at the modern technological level of manufacturing radio-engineering systems. The example of experimental noise signal recording at an output of a solitary radio instrument is presented in Fig 2.2(b).

Another example is the set of data on measuring sea roughness heights obtained from *in situ* height measurement instruments spaced at very large distances from each other. Such measurements no longer have a model character; they actually yield serious results. From a purely external point of view, sea roughness height recordings obtained at one measurement point look like just as shown in Figure 2.2(b). The noise type of a signal, received from radio instruments and from sea roughness measurements, is (surprising as it may seem) the same – the Gaussian process (see below).

Examples of realizations of the three-dimensional field of slopes of the sea surface, obtained at the fixed time instant but under various illumination conditions, are presented in Figure 2.1(a), (b).

2.2.2 Probability densities of random processes

Let $\xi(t)$ be the random process specified by an ensemble of realizations, and t_1 be some arbitrary time instant. Fixing the values of random processes at this instant

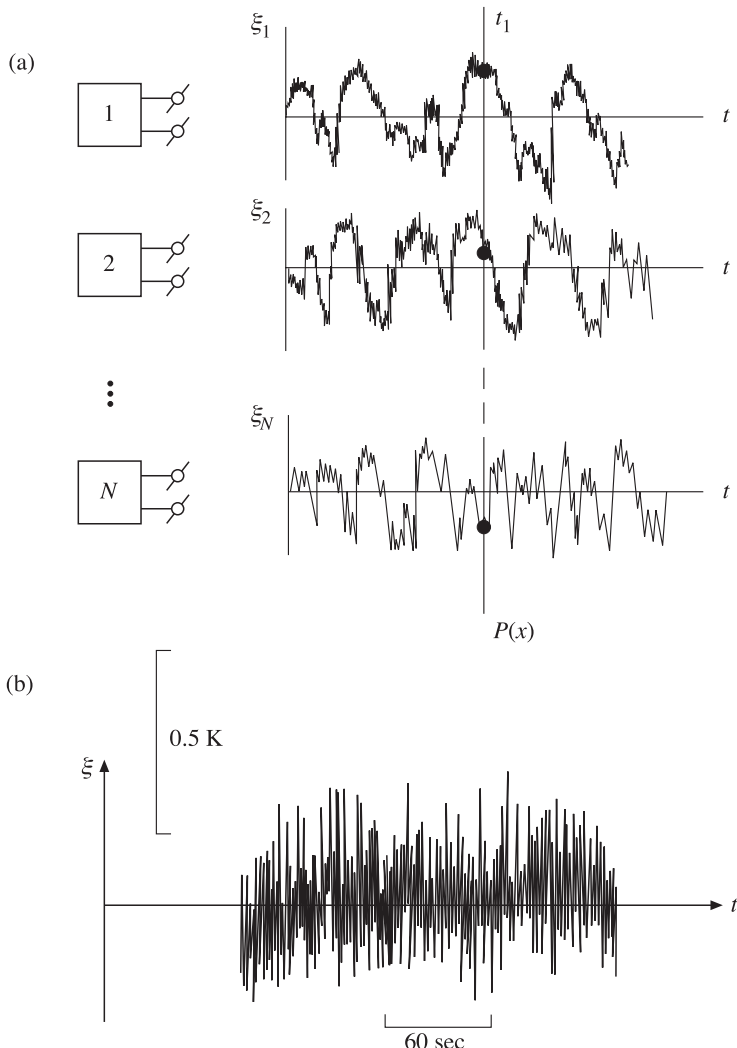


Figure 2.2. Simplified scheme to generate the statistical ensemble for the random process (electrical noise example). (a) The set of identical amplifiers with noise output signals (the qualitative presentation). (b) Experimental time series of output noise normal signal for the individual high-sensitive microwave radiometer. Time and intensity scales (in kelvins) are shown on abscissa and on ordinate.

for the whole ensemble $\{\xi_1(t_1), \xi_2(t_1), \dots, \xi_k(t_1), \dots\}$ simultaneously, we obtain the one-dimensional cross-section of the given random process $\xi(t_1)$. Here the important characteristic is introduced, $p(\xi, t_1)$, which is called the one-dimensional probability density function, or the density function $\xi(t)$ at time instant t_1 . The physical significance of this important characteristic is as follows: quantity

$P(\xi < \xi(t_1) \leq \xi + d\xi) = p(\xi, t_1) d\xi$ is the probability of the fact, that the realizations of a random process at time instant t_1 will assume the values lying in the range $(\xi, \xi + d\xi)$. An integral analogue for the probability density is the distribution function of a random quantity, which is equal to the probability that the random values $\xi(t_1)$ will assume values equal to, or smaller than, some particular ξ :

$$F(\xi, t_1) = P\{\xi(t_1) \leq \xi\}. \quad (2.1)$$

And, accordingly, the density function is determined as the derivative of the distribution function:

$$p(\xi, t_1) = dF(\xi, t_1)/d\xi. \quad (2.2)$$

The probability density possesses the following basic properties:

- (1) The probability density is non-negative (the positive definiteness condition), i.e. $p_1(\xi) \geq 0$.
- (2) The probability of a random quantity falling in the range of (ξ_1, ξ_2) is equal to the integral of the probability density within these limits:

$$P = \{\xi_1 \leq \xi < \xi_2\} = \int_{\xi_1}^{\xi_2} p_1(\xi) d\xi = F(\xi_2) - F(\xi_1). \quad (2.3)$$

- (3) The integral within the infinite limits of function $p_1(\xi)$ is equal to unity (the normalization condition):

$$\int_{-\infty}^{\infty} p_1(\xi) d\xi = 1. \quad (2.4)$$

In the theory and practice of random processes (including remote sensing tasks), of fundamental importance is the Gaussian (normal) one-dimensional probability density:

$$p_1(\xi) = \frac{1}{\sqrt{2\pi}\sigma} \exp\left[-\frac{(\xi-m)^2}{2\sigma^2}\right], \quad (2.5)$$

which is determined by two numerical parameters m and σ . The corresponding plot represents the well-known symmetrical bell-shaped curve with a single maximum at point m and exponentially falling tails of distributions. When parameter σ decreases, the density function tends to be localized in the vicinity of point m . The physical significance of parameters is obvious enough: parameter m is the mean value of a random quantity, and parameter σ^2 , called a variance, characterizes the degree of ‘dispersion’ of random values of the process under study around the mean value. In the normal distribution the probability of a random quantity falling in the given interval (α, β) is:

$$P(\alpha \leq \xi \leq \beta) = \Phi[(\beta-m)/\sigma] - \Phi[(\alpha-m)/\sigma], \quad (2.6)$$

where

$$\Phi(z) = \frac{1}{\sqrt{2}} \int_{-\infty}^{\infty} \exp\left(-\frac{x^2}{2}\right) dx; \Phi(-z) = 1 - \Phi(z), \quad (2.7)$$

is the tabulated probability integral. It follows directly from this condition, that the probability of the fact that the signal falls in the interval between the values of $m - \sigma$ and $m + \sigma$, equals 0.683. And, on the other hand, the Gaussian signal almost always (with a probability of 0.9973) lies within the interval between $m - 3\sigma$ and $m + 3\sigma$ (the so-called ‘three sigma rule’). This circumstance has often (and successfully) been used in experimental practice, as we shall see below (Chapter 3). You should not, however, think, that the normal distribution possesses some unique intrinsic universality. There are a lot of distributions which appear in quite diverse problems, including those of a geophysical, hydrodynamic and radio-physical type, and possess not lower universality than the normal distribution, such as Poisson’s distribution, Rayleigh’s distribution and the binomial distribution (Feller, 1971; Rytov, 1966; Zolotarev, 1983; Mandel and Wolf, 1995). A remarkable example in this respect is the turbulence phenomenon in various physical media, in the atmosphere, in the ocean and in plasma media. In spite of the fact, that some turbulence properties are close to Gaussian ones, in general turbulence represents an essentially non-Gaussian process, because otherwise the internal flow (Richardson–Kolmogorov’s cascade) of energy over various scales would be absent. It is the functioning of such an energy cascade in a fairly complicated, alternating regime which provides the existence of turbulence as a widespread physical phenomenon (see, for instance, Monin and Yaglom, 1971; Frisch, 1995; Anselmet *et al.*, 2001). Another interesting example can be the studies of statistical properties of the time sequence of the intensity of a global tropical cyclogenesis, namely, the discovery of the Poisson character of some its properties in the limited time scale. In general, however, the global cyclogenesis process principally differs from the Poisson-type process in the existence of complicated internal hierachic correlation links, since in the opposite case (i.e. in a purely Poisson regime) the definite stability and cyclic character of temporal functioning of this process would not be provided (Sharkov, 2000).

The physical significance of one-dimensional probability density is rather transparent: this is the distribution of instantaneous amplitudes of the process, obtained by mapping the whole statistical ensemble at a fixed time instant. Thus, this characteristic, while providing information on amplitude features of the process, is mainly insufficient for obtaining information on the character of process development in time (or in space).

New information about the internal temporal (or spatial) relationships of the process can be obtained by making two cross-sections of a random process at non-coinciding time instants t_1 and t_2 . The two-dimensional random quantity arising in such a mental experiment which is extracted from the ensemble of realizations, $\{\xi(t_1), \xi(t_2)\}$, is represented by the two-dimensional probability density $p(\xi_1, \xi_2, t_1, t_2)$. This characteristic allows us to calculate the probability of the event involving the fact that the realization of a random process at t_1 takes place in the vicinity of point $\xi = \xi_1$, and at $t = t_2$ in the vicinity of point $\xi = \xi_2$. This results in the principal distinction of this two-dimensional characteristic from the one-dimensional probability density, namely, the two-dimensional probability density contains information on the internal correlation links of a process.

The evident further generalization is the n -dimensional cross-section of a random process ($n > 2$) leading to the n -dimensional probability density $p_n(\xi_1, \xi_2, \dots, \xi_n; t_1, t_2, \dots, t_n)$. The physical significance of this characteristic is rather complicated now: here we deal with the n -dimensional correlation internal links in the process. The multidimensional probability density should satisfy the conventional conditions imposed on one-dimensional densities, as well as the condition of symmetry. This means that the density should not change at any re-arrangement of their arguments. And, moreover, the multidimensional probability density should satisfy the condition of coherence, which means that, knowing the n -dimensional density, it is always possible to find the m -dimensional density, for $m < n$, by integrating over the ‘superfluous’ coordinates.

The multidimensional probability densities of comparatively high dimension make it possible to describe the properties of random processes in a great detail. So, the multidimensional process $\xi(t)$, which depends on a single real parameter t (time), is considered to be completely defined over the interval $(0, T)$, if for arbitrary number n and for any time instants t_1, t_2, \dots, t_n the n -dimensional probability distribution density $p_n(\xi_1, \xi_2, \dots, \xi_n; t_1, t_2, \dots, t_n)$ is known over this interval. However, the experimental determination and studying of multidimensional (except for one-dimensional) densities is a fairly complicated (and often insolvable) problem.

2.2.3 Moment functions of random processes

In some cases, for the solution of experimental and practical problems related to studying random processes it is sufficient to consider simpler characteristics of integral type, called the moments of those random quantities, which are observed at cross-sections of these processes. Since in the general case these moments may depend on time arguments, they are called moment functions. As in the case of densities of distributions, it is possible to generate the n -dimensional moment function. However, being within the framework of the so-called spectral-correlation approach, we shall consider only three moment functions of lower orders which, nevertheless, will ensure (as we shall see below) significant progress in the understanding and quantitative description of energy characteristics of a random process.

The one-dimensional initial moment function of the first order,

$$M\{\varepsilon(t)\} = m_1(t) = \int_{-\infty}^{\infty} \xi p_1(\xi; t) d\xi = \overline{\xi(t)}, \quad (2.8)$$

is called the mathematical expectation (the mean value or the ensemble average) of a random process at the current time instant t . Note that the averaging is performed here over the whole ensemble of realizations, and this value is, generally speaking, different for different time instants.

The one-dimensional central moment function of the second order is defined as

$$\sigma^2(t) = M\{[\xi(t) - m_1(t)]^2\} = \int_{-\infty}^{\infty} [\xi(t) - m_1(t)]^2 p_1(\xi, t) d\xi, \quad (2.9)$$

and called the variance of a process – the parameter determining the degree of

scattering of instantaneous values that the separate realizations of the process assume at the fixed cross-section. Disclosing the square at the right-hand side and taking the integral, we obtain the important relationship we shall use many times hereafter:

$$\sigma^2(t) = M\{\xi^2(t)\} - m_1^2(t) = \overline{\xi^2(t)} - [\overline{\xi(t)}]^2. \quad (2.10)$$

The two-dimensional initial moment function of the second order,

$$M\{\xi(t_1), \xi(t_2)\} = \int_{-\infty}^{\infty} \int_{-\infty}^{\infty} \xi_1 \xi_2 p_2(\xi_1, \xi_2; t_1, t_2) d\xi_1 d\xi_2 = B(t_1, t_2), \quad (2.11)$$

is called the correlation function of a random process $\xi(t)$.

This function characterizes the degree of statistical coupling of those random quantities, which are observed at $t = t_1$ and $t = t_2$. In other words, the integral is taken over two separate realizations of a random process at non-coinciding time instants. The physical significance of a correlation function can hardly be overestimated – it contains the whole information on the intensity of the process, which is required for an overwhelming majority of investigations. The consideration based on the use of a correlation function is called the spectral-correlation approach (see, for example, Davenport and Root, 1958; Kharkevich, 1962; Rytov, 1966; Bendat and Piersol, 1966; Cressie, 1993). Certainly, this approach does not cover all the finer features of random process functioning. So, for example, such an approach fails to reveal the spatial-temporal hierarchy of interactions in complicated natural processes, such as the global climate, the El Niño phenomenon and the global tropical cyclogenesis (IPCC, 2001; Beniston, 1998; Diaz and Margraf, 1993; Tziperman *et al.*, 1997; Navarra, 1998; Sharkov, 2000). But, nevertheless, the spectral-correlation approach has been successfully used for the description of the general energy characteristics of a process. Such a consideration is quite sufficient for a number of problems in radio physics and remote sensing, as we shall see below.

2.2.4 Stationary random processes

An important class of random processes is represented by the stationary random processes, i.e. those random processes whose statistical characteristics are invariable in time. The random process $\xi(t)$ is called stationary, in a narrow sense, if all its probability distribution densities $p_n(\xi_1, \xi_2, \dots, \xi_n; t_1, t_2, \dots, t_n)$ of arbitrary order n do not change, when all points t_1, t_2, \dots, t_n are simultaneously shifted along the time axis for any time shift τ . Stationary, in a broad sense, is such a random process, $\xi(t)$, whose mathematical expectation $M\{\xi(t)\}$ and variance do not depend on the current time, and whose correlation function $B(t_1, t_2)$ depends only on the difference (lag) $\tau = |t_1 - t_2|$ between time instants under consideration, i.e. $B(t_1, t_2) = B(\tau)$. It is clear that the stability in a broad sense follows from the stability in a narrow sense, but not the opposite. Both these notions of stability coincide for the Gaussian process, since the stationary Gaussian process is completely determined by the mathematical expectation and correlation function of the process. In other words, the mathematical expectation and correlation function allow us to calculate

any multidimensional probability density of the stationary Gaussian random process. The one-dimensional density is given by formula (2.5), and two-dimensional density is determined by the following relation:

$$\begin{aligned} p_2(\xi_1, \xi_2) &= \frac{1}{2\pi\sigma^2\sqrt{1-R^2(\tau)}} \\ &\times \exp \left\{ \frac{1}{2\pi\sigma^2\sqrt{1-R^2(\tau)}} \right. \\ &\quad \left. \times [(\xi_1 - m)^2 - 2R(\tau)(\xi_1 - m)(\xi_2 - m) + (\xi_2 - m)^2] \right\}, \end{aligned} \quad (2.12)$$

where σ^2 is the variance of the process, and $R(\tau) = [B(\tau) - m^2]/\sigma^2$.

Pay attention once again to the fact, that, unlike the one-dimensional distribution density, the two-dimensional density contains mainly new information about the correlation (spatial or temporal) properties of the process. Thus, processes with completely different internal correlation properties can have Gaussian one-dimensional distribution (in magnitude).

2.2.5 Ergodic property

The stationary random process is called ergodic if, in finding any statistical characteristics, the averaging over a statistical ensemble with the probability of unity is equal to a time-averaged characteristic, taken over any single realization of the process. In this case the averaging operation is performed over a single realization of the process whose length, T , tends to infinity. Designating time-averaged values by an overbar, we can write the ergodicity condition as follows:

$$M\{\xi(t)\} = \overline{\xi(t)} = \lim_{T \rightarrow \infty} (1/T) \int_0^T \xi(t) dt, \quad (2.13)$$

$$B(\tau) = M[\xi(t)\xi(t-\tau)] = \overline{\xi(t)\xi(t-\tau)} = \lim_{T \rightarrow \infty} (1/T) \int_0^T \xi(t)\xi(t-\tau) dt. \quad (2.14)$$

Note at once, that

$$B(0) = M[\xi^2(t)] = \overline{\xi^2(t)} = \lim_{T \rightarrow \infty} (1/T) \int_0^T \xi^2(t) dt. \quad (2.15)$$

Thus, the variance of the ergodic stationary process is equal to

$$D(\xi) = \sigma^2 = M(\xi^2) - M^2(\xi) = \overline{\xi^2(t)} - [\overline{\xi(t)}]^2 = B(0) - M^2(\xi) \quad (2.16)$$

The relation obtained for ergodic processes absolutely corresponds to the similar equality obtained for characteristics of random processes in their averaging over the statistical ensemble (2.10).

In order that the random process be ergodic, it should, first of all, be stationary in a broad sense (the necessary condition). The sufficient condition of ergodicity is

the tending to zero of the correlation function (with subtraction of a constant component) with the unlimited growth of time lag:

$$\lim_{\tau \rightarrow \infty} \{B(\tau) - m^2\} = 0 \quad (2.17)$$

Detailed mathematical analysis has shown that these requirements can be essentially ‘softened’, and the class of ergodic processes can be expanded (see, for instance, Rytov, 1966; Monin and Yaglom, 1971; Frisch, 1995).

The concept of ergodicity can be transferred from time to space and to performing any determinate operation with a random process (Monin and Yaglom, 1971; Rytov *et al.*, 1978; Frisch, 1995). So, the stationary field $\zeta(t, x, y, z) = \zeta(t, \mathbf{r})$, as a function of time and three coordinates, is ergodic if we suppose that for an arbitrary determinate function the following equality is almost certainly valid:

$$\langle f[\zeta(t, \mathbf{r})] \rangle = \lim_{T \rightarrow \infty} (1/T) \int_0^T f[\zeta(t, \mathbf{r})] dt,$$

where the angle brackets imply averaging over the statistical ensemble with the density function, which will correspond to the determinate transformation (see section 2.5 below), and the time T of averaging over the temporal realization should essentially exceed the characteristic correlation times of the process (see section 2.3).

Along with ergodicity in time, we can introduce the notion of spatial and spatial-temporal ergodicity. So, for homogeneous, spatially ergodic fields the ensemble-averaged values in a sense of convergence in probability are equal to spatial-averaged values. This actually means that for the arbitrary determinate function f the following equality can be considered to be valid:

$$\langle f[\zeta(t, \mathbf{r})] \rangle = \lim_{V \rightarrow \infty} (1/V) \int_0^V f[\zeta(t, \mathbf{r})] d^3 r,$$

where V is the spatial domain, over which the spatial averaging is carried out. The limiting transition $V \rightarrow \infty$ can be stopped on spatial domains whose size is great as compared to characteristic correlation features of the statistical field (see section 2.3).

The concept of the spatial-temporal ergodicity of stationary and homogeneous fields is applied in cases where the convergence over the ensemble takes place both for $T \rightarrow \infty$, and for $V \rightarrow \infty$, i.e. when the aforementioned equalities are fulfilled simultaneously.

2.3 FUNDAMENTALS OF THE CORRELATION THEORY OF RANDOM PROCESSES

Along with a complete description of random process properties by means of multi-dimensional probability densities, another approach is also possible, where the random processes are characterized by their moment functions. The theory of random processes, based on using the moment functions of the second order and

lower, was called the *correlation theory* (or the spectral-correlation approach). As we have noted above, the undoubted advantages of such an approach consist, first, in a fairly complete description of the energy characteristics of a stochastic process, which is quite sufficient for the solution of basic problems in many applications. And, second, such an approach provides a reliable experimental methodology and instrumental basis for measurement procedures using random processes. A similar conclusion cannot be drawn (at least for today) for the approach that uses multi-dimensional densities of statistical ensembles.

2.3.1 Basic properties of the correlation function

The correlation functions of stationary ergodic processes possess some important properties which are widely used in experimental and observational practice:

- (1) As follows from the definition of a stationary random process, function $B(\tau)$ is even: $B(\tau) = B(-\tau)$.
- (2) The absolute magnitude of the correlation function of a stationary random process for any τ cannot exceed its values for $\tau = 0$:

$$|B(\tau)| \leq B(0) = D(\xi) + [\overline{\xi(t)}]^2.$$

- (3) As τ increases without limit, function $[B(\tau) - m^2]$ tends to zero (the sufficient condition of ergodicity), i.e. $\lim_{\tau \rightarrow \infty} [B(\tau) - m^2] = 0$.

It is very important to understand the physical significance of the correlation function of a random process. For this purpose, let us imagine that the random process $\xi(t)$ under consideration is some fluctuating voltage supplied to the active resistance with numerical value of one ohm. According to the Joule–Lenz law, the time-averaged value of the square of the voltage is equal to the amount of heat which is released in such a conductor per unit time (one second). Thus, in the physical sense, $B(0) = [\xi^2(t)]$ is the total power of the fluctuation process, and $[\overline{\xi(t)}]^2$ is the power of a constant component of the process. Remembering relation (2.16), we can easily grasp that the variance of a random process characterizes the power of the fluctuation component of a process. We shall repeatedly return to such a convenient physical treatment of the correlation function, since it allows us to understand the physical peculiarities of phenomena in many complicated situations.

2.3.2 The correlation coefficient

To eliminate the amplitude characteristics of the process and to reveal its purely correlation properties, we introduce the notion of a normalized correlation coefficient $R(\tau)$:

$$R(\tau) = [B(\tau) - B(\infty)]/[B(0) - B(\infty)] = [B(\tau) - (\bar{\xi})^2]/\sigma^2. \quad (2.18)$$

In accordance with the properties of the correlation function listed above, the correlation coefficient has a form of either monotonously decreasing function or attenuating oscillating functions, and for $\tau = 0$ the correlation coefficient of any

random process is always equal to unity. Note that it is of great importance, on the one hand, to determine the character of decreasing of the coefficient for large values of shift and, on the other hand, to find the specific shape of the ‘nose’ of a correlation coefficient for $\tau \rightarrow 0$. The latter feature determines the small-scale (pixel) structure of the process, whereas the large-scale structures of the process are characterized by the form of the correlation coefficient for large shifts. Since the correlation coefficient is even, its values are considered for positive shifts (lags) only. The degree of correlation of a random process can be characterized by the following numerical parameter, the interval (or time) of correlation τ_k , which is determined as follows:

$$\tau_k = \int_0^\infty |R(\tau)| d\tau. \quad (2.19)$$

Geometrically, the correlation interval is equal to the base of a rectangle with a height equal to unity, whose area is equal to the area included between the $|R(\tau)|$ curve for $\tau > 0$ and the abscissa axis. In some cases, the correlation time means the value of τ for which the first intersection of zero takes place.

The value of τ_k gives a rough idea of over which time interval, on average, the correlation between the random process values takes place. Slightly simplifying the situation, we can say that the probabilistic forecasting of the behaviour of any realization of a random process is possible over time spans smaller or of the order of time τ_k , if the information on its behaviour ‘in the past’ is known. However, any attempt to accomplish forecasting for the time essentially exceeding the correlation interval will be abortive: the instantaneous values, in time spans essentially greater than the value τ_k , are virtually uncorrelated; in other words, the mean value of the product $\xi(t)\xi(t + \tau)$ is close to zero.

2.3.3 The statistical spectrum

The spectral theory of deterministic signals is well known. However, the probabilistic character of separate realizations of a random process makes it impossible to transfer the methods of spectral analysis of determinate signals directly (straightforwardly) into the theory and practice of random processes. If we calculate the spectral density of a random process $\xi(t)$ by the standard formula of the Fourier integral.

$$\dot{S}(\omega) = \int_{-\infty}^{\infty} \xi(t) \exp(-j\omega t) dt, \quad (2.20)$$

then the complex function obtained, $\dot{S}(\omega)$, will be a random function and, moreover, it could not exist at all, generally speaking. We shall obtain here the result, which can be called a spectrum of one of possible realizations of the random process. Under conditions of real observation of some random process proceeding during time T , we can really obtain the *current spectrum* of the given realization, i.e. the complex function $\dot{S}_T(\omega)$:

$$\dot{S}_T(\omega) = \int_0^T \xi(t) \exp(-j\omega t) dt. \quad (2.21)$$

However, if we consider various realizations of the random process $\xi(t)$ of finite duration T , then for them the complex function $\hat{S}_T(\omega)$ will vary in a random manner from one realization to another, not tending to any finite limit at $T \rightarrow \infty$, in the general case.

Thus, it is desirable to introduce such spectral concepts, which would lead to non-random (deterministic) functions, and then to use the procedures that are methodologically close to the Fourier spectral procedures. In developing the spectral methodology suitable for analyzing random processes, of principal significance is the mathematical theorem proved by the well-known mathematicians, A. Ya. Khintchin and N. Wiener, which is known now as the Wiener–Khintchin theorem. According to this theorem, the correlation function $B(\tau)$ can be presented as

$$B(\tau) = \int_{-\infty}^{\infty} \exp(j\omega\tau) dF(\omega), \quad (2.22)$$

where $F(\omega)$ is a non-decreasing limited function. If function $F(\omega)$ is differentiable, designating

$$[dF(\omega)/d\omega] = \frac{1}{2}G(\omega),$$

we obtain, instead of (2.22),

$$B(\tau) = \frac{1}{2} \int_{-\infty}^{\infty} G(\omega) \exp(j\omega\tau) d\omega. \quad (2.23)$$

Thus, the nearly introduced function $G(\omega)$ is nothing other than the usual Fourier transformation for the correlation function:

$$G(\omega) = \frac{1}{\pi} \int_{-\infty}^{\infty} B(\tau) \exp(j\omega\tau) d\tau. \quad (2.24)$$

Function $G(\omega)$ is just what is called the statistical spectrum of a random process (Wiener's spectrum), and formula (2.24) is the main definition of this function. It should be noted, that both $B(\tau)$, and $G(\omega)$ are even functions of their arguments. As a result, relations (2.23) and (2.24) can be written in the real form of two Fourier cosine-transformations:

$$B(\tau) = \int_0^{\infty} G(\omega) \cos(\omega\tau) d\omega, \quad (2.25)$$

$$G(\omega) = \frac{2}{\pi} \int_0^{\infty} B(\tau) \cos(\omega\tau) d\tau. \quad (2.26)$$

The physical significance of functions $\xi(t)$ and $G(\omega)$ can easily be clarified by letting $\tau = 0$ in (2.25). Using this procedure, we obtain

$$B(0) = P = \int_0^{\infty} G(\omega) d\omega. \quad (2.27)$$

Remembering the physical significance of the correlation function for $\tau = 0$ as a total power of process P , it can easily be understood that function $G(\omega)$ expresses the

power of process $\xi(t)$ falling on the frequency band $d\omega$ in the vicinity of selected frequency ω . In other words, function $G(\omega)$ represents the spectral density of power. On this basis $G(\omega)$ is called the power spectrum (or Wiener's spectrum) of process $\xi(t)$. By its physical significance the power spectrum is real and nonnegative, $G(\omega) \geq 0$. This property, however, imposes rather strict limitations on the form of admissible correlation functions: so it follows from relation (2.25), that the correlation function of a stationary process should satisfy the additional (to the three aforementioned ones) condition

$$\int_0^\infty B(\tau) \cos(\omega\tau) d\tau \geq 0. \quad (2.28)$$

So, principally inadmissible is the approximation presentation of a correlation function in the form of rectangle, i.e.

$$B(\tau) = \begin{cases} B_0 & |\tau| < \tau_0 \\ 0 & |\tau| > \tau_0 \end{cases},$$

since in this case the corresponding power spectrum will have negative values, and condition (2.28) is not satisfied either. It is interesting to note that functions of the type $\exp\{\alpha\tau^n\}$ are also unsuitable for approximations of $B(\tau)$, except for the Gaussian curve and exponent ($n = 1, 2$). We shall encounter these circumstances below in analysing particular forms of spectra.

As to the power spectrum dimension, it completely depends on the physical character of a random process. So, if the random process is the electrical voltage, then its power spectrum, according to relation (2.25), has dimension [$V^2 \text{ sec/rad}$]. If, however, the stochastic behaviour of sea disturbance is investigated, then the power spectrum of fluctuating altitudes has dimension [$m^2 \text{ sec/rad}$]. We shall not forget here that the circular frequency ω has dimension [rad/sec] and is associated with frequency (f), measured in hertz, by the relation $\omega = 2\pi f$.

In applications the necessity often arises to consider the behaviour of a random process and, in particular, its energy characteristics within the limited frequency band (ω_1, ω_2) . In this case the power of the process P_{12} , concluded within the finite band between ω_1 and ω_2 , can be determined by integrating $G(\omega)$ within corresponding limits (for $\omega > 0$):

$$P_{12} = \int_{\omega_1}^{\omega_2} G(\omega) d\omega. \quad (2.29)$$

In addition, it is necessary to have in mind that the experimentally measured power spectrum is taken over positive frequencies only. Thus, in experimental practice the notion of one-sided power spectrum is introduced. This spectrum $G_S(f)$ represents the mean power of the process fallen per unit frequency band of width 1 Hz:

$$G_S(f) = \begin{cases} 2\pi G(2\pi f) & \text{for } f \geq 0 \\ 0 & \text{for } f < 0 \end{cases}.$$

The one-sided power spectrum has dimension which differs from the dimension of a total power spectrum. So, for the process associated with the electric voltage, the

dimension of the spectrum will be [V^2/Hz], and for the spectrum of sea wave heights it will be [m^2/Hz].

Thus, the total power of the process can be written as

$$B(0) = \int_0^\infty G(\omega) d\omega = \int_0^\infty G_S(f) df.$$

For further analysis it is important to find the relationship between the statistical spectrum and the current spectrum of any realization. We take advantage of the following energy considerations: the total energy of the process, released for time T , will be equal to the following value:

$$E_T = \int_0^T \xi^2(t) dt = \frac{1}{\pi} \int_0^\infty |\dot{S}_T(\omega)|^2 d\omega.$$

This relation expresses the Parseval identity for the finite time interval T (see Appendix B). The average power of the process P_T for time T is obtained by dividing the value of energy for interval T by its value:

$$P_T = \frac{E_T}{T} = \frac{1}{\pi T} \int_0^\infty |\dot{S}_T(\omega)|^2 d\omega. \quad (2.30)$$

This quantity depends, generally speaking, on the value of interval T , but for a stationary and ergodic process it tends, with increasing T , to the constant limit, which just expresses the power of the process:

$$P = \lim_{T \rightarrow \infty} P_T = \frac{1}{\pi} \lim_{T \rightarrow \infty} (1/T) \int_0^\infty |\dot{S}_T(\omega)|^2 d\omega. \quad (2.31)$$

Exchanging the places of integral and limiting procedures and comparing (2.31) with (2.27), we see that the statistical spectrum is related to the current spectrum by the important equation

$$G(\omega) = \frac{1}{\pi} \lim_{T \rightarrow \infty} (1/T) |\dot{S}_T(\omega)|^2. \quad (2.32)$$

The analysis of this relation allows us to draw the following important conclusion. The power spectrum of a stationary random process, being always real, does not bear any information on phase relations between separate spectral components. This makes it impossible to restore any individual realization of a random process from the power spectrum. In other words, the well-known theorem of uniqueness of the spectral analysis of determinate signals ('one spectrum: one realization') has no place in the analysis of stochastic signals. So, it is possible to find a set of various random functions (for example, by transforming the phase spectrum) having the same spectral density and correlation function. Of course, the opposite situation also arises, i.e. the infinite diversity of time sequences of random processes may correspond, generally speaking, to a single power spectrum.

In a number of applications the necessity arises of separating the mean (constant) value from a random process, or, in other words, of performing the

procedure of centring the initial process $\xi_0(t) = \xi(t) - m$. In such a case the correlation function of a centred stationary process $B_0(\tau)$ will be equal to:

$$B_0(\tau) = B(\tau) - m^2, \quad (2.33)$$

and the spectral density $G_0(\omega)$ of a centred process will be as follows:

$$G_0(\omega) = G(\omega) - m^2 \delta(\omega - 0), \quad (2.34)$$

where by symbol $\delta(\omega)$ is meant the delta-function with its well-known formal presentation

$$\delta(\omega - \omega_0) = \frac{1}{\pi} \int_{-\infty}^{\infty} \exp[j(\omega - \omega_0)t] dt. \quad (2.35)$$

In such an approach (which is often used in practice) the constant component of the process is treated as a spectral component with the wavelength equal to infinity (or with the frequency equal to zero). For $m = 0$ both spectral density presentations coincide; therefore, hereafter the distinctions in these characteristics will be noticed in the case of necessity only.

In physical experiments the situation fairly often arises where the random signal is functioning together with a purely determinate one; so, the windy sea disturbance as a random field is often developed against the background of almost harmonic swell. Whereas it is quite difficult to separate directly each component on time realizations of the total process, this procedure can be fairly easily performed (i.e. the random process can be centred against the harmonic component background) by using the spectral-correlation approach. Thus, it is necessary to construct the correlation function and the power spectrum for the process $\xi_{0H}(t) = \xi(t) - A \cos \omega_0 t$. Using the ergodicity properties (2.14), we obtain the expression for the sought correlation function $B_{0H}(\tau)$ as

$$B_{0H}(\tau) = B(\tau) - A^2 \cos \omega_0 \tau \quad (2.36)$$

and, accordingly, the spectral density $G_{0H}(\omega)$ of the process, centred on the harmonic component, is equal, taking into account (2.35), to

$$G_{0H}(\omega) = G(\omega) - A^2 \delta(\omega - \omega_0). \quad (2.37)$$

The continuation of the procedure consists in the band filtering (and in the elimination, if necessary) of the spectral component found.

2.4 QUASI-ERGODIC PROCESSES

In actual physical practice, the overwhelming majority of processes proceed in regimes that cannot be called purely ergodic. This is due to the fact that any chaotized processes subject to investigation are limited physically both in time and in space. But it is this spatial-temporal limitation, inside which it is necessary, as a rule, to study the behaviour (or evolution) of the system by determining the variation of characteristics of the process, such as its mean value or the change of the noise intensity level in a system (i.e. the value of variance). Situations are often also

possible where the spatial-temporal field is ergodic only for a part of spatial arguments, for example, only on the plane (x, y) or in a part of physical three-dimensional space. The latter situation often arises in studying the dynamical and radiation properties of the Earth's atmosphere, as well as the dynamical state of the ocean surface. Furthermore, if the spatial field is periodic in spatial variables (coordinates), then the mean value over the spatial periodicity cell will give a poor approximation to the mean value over an ensemble, if the period is not too great compared to the correlation scale. There are also such physical processes that ergodic concepts cannot be applied to straightforwardly. So, it is important to note, that there is no accurate ergodic theorem for groups of rotations in a space (for example, for spiral vortices in the atmosphere), since the rotation can be accomplished by finite angles only (Frisch, 1995).

Therefore, in physical experiments it is important in many cases to use the concept of the quasi-ergodic field, which is in the same relation to ergodic fields as the quasi-homogeneous fields are to homogeneous ones (Rytov *et al.*, 1978).

The physical significance of such an approach consists in the fact that such fields (or temporal one-dimensional processes) are ergodic only in small volumes as compared to characteristic scales L of variation of the field's statistical characteristics (the mean value, variance etc.). It should be noted that it is these variations of a field's parameters which bear the physical load in the study of the physical state and evolution of the field as a physical object. Thus, the region of spatial (or temporal) averaging for quasi-ergodic processes should be compulsorily limited from above by the scale L , but in this case the characteristic size of the averaging region should exceed the characteristic correlation dimensions (spatial or temporal) of the process. Therefore, we can say that the field is quasi-ergodic only in the case where such an averaging volume V can be introduced that satisfies the two-sided inequality

$$L \gg V^{1/3} \gg l_C, \quad (2.38)$$

where l_C is the spatial correlation radius. In other words, the averaging volume should be sufficiently large for the field to experience many spatial fluctuations within V and the accumulation could be accomplished. On the other hand, this volume should be small enough, so that within its limits the studied fields are fairly homogeneous and the process macro-characteristics do not vary. Similar reasoning can be applied to temporary processes, but in this case the spatial correlation radius should be replaced by the correlation interval. In phenomenological physics, by V is usually meant a 'physically infinitely small volume', which performs, in essence, the same functions as the averaging volume considered above (Rytov *et al.*, 1978).

However, attention should be paid to the fact that, despite a seemingly simple form of inequality (2.38), the comprehension of its physical sense meets some difficulties in each particular physical experiment. So, in processing experimental natural data the correct understanding and fulfilment of this inequality requires considerable efforts. The inadvertent merging of scales, presented in inequality (2.38), can involve serious artefacts in the final scientific interpretation of results. All nuances of this

complicated situation are especially visible in analysing studies on the spatial-temporal characteristics of complicated, natural, chaotized processes, such as atmospheric turbulence (Levich and Tzvetkov, 1985; Hussain, 1986; Tsinober, 1994; Frisch, 1995), fields of global and regional precipitations (Lovejoy and Schertzer, 1985; Arkin and Xie, 1994; Davis *et al.*, 1996; Olsson, 1996; Sevruk and Niemczynowicz, 1996; Chang and Chiu, 1997; Jameson *et al.*, 1998; Smith *et al.*, 1998; Lucero, 1998; Andrade *et al.*, 1998; Sorooshian *et al.*, 2000; Simpson *et al.*, 2000), the evolution and stochastic behaviour of the global climate (IPCC, 2001; Ghil *et al.*, 1985; Glantz *et al.*, 1991; Beniston, 1998; Monin and Shishkov, 2000), or the stochasticity of global tropical cyclogenesis (Sharkov, 2000).

We shall touch on the quasi-ergodicity issue in different sections of the book as required.

2.5 TYPES OF SPECTRA

The spectral patterns of stochastic natural objects and processes are fairly diverse. Nevertheless, there are some typical features of power spectra (the shape of spectra, the characteristic band of a spectrum, the spectral density moments), which make it possible to classify fairly rapidly and reliably the received experimental data and to obtain the initial model physical ideas about the processes under study.

It is the effective spectrum width that is most frequently used as a basic quantitative characteristic, namely,

$$\Delta f(\text{Hz}) = \frac{\Delta\omega}{2\pi} = \frac{1}{G_{S0}} \int_0^\infty G_S(f) df = \frac{1}{G_0} \int_{-\infty}^\infty G(\omega) d\omega / 2\pi, \quad (2.39)$$

where subscript 0 denotes the extremal spectral density values. This numerical characteristic is frequently used in experimental practice and engineering calculations, thus making it possible to easily find the variance (power) of a random signal: $\sigma^2 = G_{S0} \Delta f = 2G_0 \Delta\omega$.

Generally speaking, the effective width of a spectrum of the random process can also be determined by different methods, for example, from the condition of power spectrum decreasing at the boundary of this frequency range down to the level of $0.1G_{S0}$. In any case, between the correlation interval τ_k and the effective width, some ‘uncertainty’ principle should take place (this term is borrowed from quantum mechanics), namely,

$$\Delta f \tau_k = \text{const} = O(1) \quad (2.40)$$

that follows from the basic properties of the Fourier transformation. Having determined the effective band and correlation interval proceeding from definitions (2.19) and (2.39) presented above, we can obtain for symmetrical spectra relative to zero the value of the constant as $\frac{1}{4}$. Thus, the broader the power spectrum of noise, the more chaotic the time variations of its temporal realizations and the smaller the correlation interval value. However, the knowledge of only these parameters of a random process is, in a number of important cases, not sufficient for determining the

physical features and intrinsic dynamics of the phenomena. Here we can refer to problems mentioned above of studying the internal structure of turbulence, climate stochasticity and global tropical cyclogenesis. Much more insight into the processes is achieved by studying the power spectrum form for the phenomenon under investigation within a wide frequency range. In such a case it is important to know not only the central and maximum parts of a spectrum (or, as is sometimes said, the energy-carrying part of the spectrum), but also the distant (from the extremal value) down-falling tails of a spectrum, which, in their turn, can consist of several branches coupled in a particular succession. It is the parameters of these branches and the succession of their coupling which determine the most important processes of energy transformation in a system, the external energy input to a system and output from it (the dissipation processes, such as transfer into heat). And here again we can point out, as an example, the important features of spectra of velocity fluctuations in the turbulent atmosphere (Kolmogorov and anti-Kolmogorov branches), which determine quite different physical processes: the direct (decay) and reverse (self-organization) cascades of energy transfer in a system over spatial scales.

Below we shall consider some of the most frequently used approximations of spectral densities and their corresponding correlation functions.

2.5.1 Rectangular low-frequency spectrum

The rectangular low-frequency spectrum represents a spectrum located very close to a zero frequency

$$G(\omega) = \begin{cases} G_0 & |\omega| \leq \Delta\omega \\ 0 & |\omega| > \Delta\omega \end{cases}.$$

The total power of such a model random process will be $\sigma^2 = 2G_0 \Delta\omega = G_{0S} \Delta f$. Using formula (2.23), we find the correlation function and then we pass to the expression for the correlation coefficient:

$$R(\tau) = \sin \Delta\omega\tau / \Delta\omega\tau. \quad (2.41)$$

It is important to note that the correlation function of the given random process is sign-alternating, and the change of a sign takes place for time shift τ that is a multiple of the quantity $\pi/\Delta\omega$. This means that, as τ increases, the positive correlation between two values of a signal, spaced at τ , rapidly drops, passes through zero (the absence of any correlation), and then becomes significant again, but with the other sign – negative in this case. Such a property of the correlation function indicates the quasi-periodicity of any realization of the given random process, which is certainly understood in the probabilistic, rather than in the absolute, sense. It is interesting to note that for the other forms of spectra, which are seemingly close to the form under consideration (see below), such a quasi-periodicity in correlation properties is not observed.

When the argument tends to zero, the value of the correlation coefficient tends to unity, since the limiting value of function $\{\sin x/x\}$ for $x \rightarrow 0$ equals unity (Gradshteyn and Ryzhik, 2000). By the correlation interval in this case is meant

the first value of the argument, for which $R(\tau_k) = 0$. It can easily be seen from (2.41), that $\tau_k = \frac{1}{4}(\Delta f)^{-1}$.

Since the spectral band value is of the order of the central frequency value (we consider the positive frequencies here), such processes are called broadband random processes. Owing to its relative simplicity, the type of a random signal spectrum considered is fairly often used for the first model approximation.

Remember, however, that the opposite situation – the rectangular approximation of a correlation function – does not take place and is prohibited by the rules of transition between Fourier transforms.

2.5.2 Gaussian spectrum

Suppose the power spectrum of a random signal to be described by the Gaussian function (the quadratic exponent)

$$G(\omega) = G_0 \exp(-\beta\omega^2).$$

To find the correlation function we shall use formula (2.25) and the well-known determinate integral (Gradshteyn and Ryzhik, 2000)

$$R(\tau) = \exp(-\tau^2/4\beta). \quad (2.42)$$

The total power of the process will be $\sigma^2 = G_0\sqrt{\pi}/2\sqrt{\beta}$, the effective band of the process (2.39) will be $\Delta f = \frac{1}{4}\sqrt{\pi\beta}$, and the correlation interval is $\tau_k = \sqrt{\pi\beta}$. In this case the uncertainty relation will be, as would be expected, the value of $\frac{1}{4}$. So, the Gaussian character (Gaussian shape) of a power spectrum results in the correlation function of Gaussian type as well, and any quasi-periodicity in correlation properties is absent in this case.

2.5.3 The Lorentzian spectrum

As we shall see later, natural processes often involve random signals which have a correlation coefficient decreasing according to the exponential law

$$R(\tau) = \exp(-\alpha|\tau|) \quad (2.43)$$

with some real and positive parameter α . Based on (2.26) and using the well-known determinate integrals (Gradshteyn and Ryzhik, 2000), its power spectrum will have the following expression:

$$G(\omega) = \frac{2\sigma^2}{\pi} \int_0^\infty \exp(\alpha\tau) \cos \omega\tau d\tau = \frac{2\sigma^2}{\pi} [\alpha/(\alpha^2 + \omega^2)]. \quad (2.44)$$

It follows from this expression that the power spectrum of the process under consideration has a prominent low-frequency character: the spectral density maximum is observed at zero frequency. In addition, the shape of the spectrum has a peculiar appearance, which is called the Lorentzian spectrum (or the Lorentzian shape). Note also an important feature of the Lorentzian spectrum: as the frequency increases, the drop (the tail) of a spectrum has the typical power-law

form $1/\omega^2$. The value of the effective band of the spectral density of the given process will be $\Delta f = \alpha/4$, and the correlation interval will be $\tau_k = 1/\alpha$.

2.5.4 Band noise

The necessity fairly often arises to approximate a rather narrow spectrum around some central frequency, f_0 , i.e. provided that the effective band of a noise signal is essentially lower than some central frequency ($\Delta f/f_0 \ll 1$). Depending on physical processes under study, the value of this parameter (the so-called relative frequency band) can be encompassed within very wide limits – from 10^{-2} to 10^{-8} and lower. Processes of such a type are called narrowband random processes (band noise). The simplest approximation of such a process can be represented as a rectangular spectrum around the central frequency:

$$G(\omega) = \begin{cases} G_0 & \omega_0 - \Delta\omega \leq |\omega| \leq \omega_0 + \Delta\omega \\ 0 & \omega_0 - \Delta\omega > |\omega| > \omega_0 + \Delta\omega \end{cases}. \quad (2.45)$$

This directly leads to the following value of the total power of the process: $\sigma^2 = 4G_0 \Delta\omega$, since the total band of frequencies around frequency ω_0 equals $2\Delta\omega$. However, the form of the correlation function is considerably more complicated in this case. Using formula (2.25) and well-known trigonometric relations, we obtain the following expression for the correlation coefficient:

$$R(\tau) = \{\sin(\Delta\omega\tau)/\Delta\omega\} \cos\omega_0\tau. \quad (2.46)$$

Unlike the form of the correlation coefficient for a broadband signal, the narrowband signal possesses internal cosine typing, which reflects the fact that the noise signal is as though concentrated around the central frequency and not only can be characterized as a random process, but also can possess quasi-determinate properties. As in the case of broadband signal, the correlation properties can be numerically determined from the first zero value of the correlation coefficient's envelope. In this case $\tau_k = \frac{1}{4}(\Delta f)^{-1}$, where by Δf is meant the magnitude of the noise band of a system. This is an important circumstance, since the central frequency value does not effect the correlation properties of a noise process.

However, as the frequency band narrows, quasi-deterministic properties should be emphasized in more and more detail. To elucidate the physical essence of such a kind of dualism of random processes, we shall consider below two limiting cases: first, when the noise spectral band tends to zero and, second, when the band will grow to infinity, and the process will possess a smooth spectrum.

2.5.5 Harmonic signal

To obtain such an approximation, we shall tend the spectrum width in expression (2.46) to zero and perform a limiting transition. In such a case we arrive at the model of a random harmonic signal with the correlation coefficient

$$R(\tau) = \cos\omega_0\tau. \quad (2.47)$$

The spectrum corresponds to such a function after the limiting transition in (2.45):

$$G(\omega) = G_0 \delta(\omega - \omega_0), \quad (2.48)$$

and the process itself is described by the harmonic function

$$\xi(t) = a \cos(\omega_0 t + \varphi) \quad (2.49)$$

with the constant (and non-random) amplitude and the phase randomly distributed in the range of 0 – 2π . It should be noted, that such a process is essentially non-Gaussian.

2.5.6 White noise

Let us imagine, that the noise band will occupy the entire frequency band: from $-\infty$ to $+\infty$ with the constant value of G_0 . In this case, using relation (2.35), we obtain the expression for the correlation function

$$B(\tau) = G_0 \pi \delta(\tau - 0);$$

and, accordingly, $R(\tau) = 1$ for $\tau = 0$ and $R(\tau) = 0$ for $\tau \neq 0$.

The name of this model of a noise signal is logically contradictory (as is known, the ‘white’ light in optical observations does not possess a smooth, constant spectrum), and the process itself is physically unrealizable, since for it

$$B(0) = \overline{\xi^2(t)} = \int_0^\infty G(\omega) d\omega \rightarrow \infty.$$

Nevertheless, this convenient mathematical model has been widely applied both in theoretical works and in experimental practice. For example, this model can successfully be used when the passband of a circuit (or device) under study, which is affected by the external random signal, turns out to be essentially narrower than some effective width of its spectrum. Such a process is frequently also called the ‘delta-correlated’ noise.

2.5.7 Coloured noise

As we have mentioned above, in determining the intrinsic dynamics and hierarchic structure of natural stochastic processes and systems, of principal significance are the situations where the power spectrum obeys the power law

$$G(\omega) = C|\omega|^{-n}, C > 0. \quad (2.50)$$

The physical significance of spectra with certain particular values of the exponent was found to be so great that the spectra of such a type acquired not only a generalized name, the ‘coloured’ spectra, but also, for particular values of n , their intrinsic names, since they reflect various physical processes controlling the energy transformation in a system. The spectrum with the value of $n = 5/3$ was called Kolmogorov’s spectrum (Monin and Yaglom, 1971; Frisch, 1995), and for $n = 1, 2$ the corresponding random signal was called the ‘red’ noise and ‘brown’ noise. As we have mentioned above, by white noise is meant a signal with the spectrum

for $n = 0$. In recent times such broadband noise, which arises in physical and geophysical systems under the effect of external conditions, began to be called, less poetically, ‘crackling’ noise (Sethna *et al.*, 2001; Burroughs and Tebbens, 2001).

However, the direct use of spectral-correlation means for studying random processes with such types of spectra does not yield meaningful results. We can easily be convinced of it by taking the integral from the total energy of a process (2.25). Substituting (2.50) into (2.27) we shall see that the integral diverges and, thus, the total power of the process becomes infinite, which is contradictory from the physical viewpoint. The divergence takes place either at high frequencies (in theoretical works this effect is called the ultraviolet* divergence or infrared catastrophe) for $n < 1$, or at low frequencies (the infrared* divergence or ultraviolet catastrophe) for $n > 1$, or at both limits for $n = 1$. This means that the stationary random function with a finite variance and power spectrum cannot exist (Frisch, 1995), and, accordingly, the direct use of spectral-correlation means, considered above, for such processes has fairly strict limitations.

The physical reason for such an unusual situation became clear only recently. The natural phenomena having power spectra really exist and possess surprising geometrical properties, namely, non-integer geometrical dimension and non-differentiability at each point of the process, though the continuity of the process conserves in general and at each point. However, both differentiability and continuity conserves for ‘usual’ smooth objects. For these reasons the use of probabilistic moments (the mean values, variances, etc.) and spectral moments is impossible, because they (moments) could not have finite values at all, and operations with such quantities are impossible as well.

It is a striking fact that it is these natural objects and processes (which have been called self-affine fractals) with peculiar geometrical properties (sometimes called scaling properties), which turn out to be deeply involved in the problems of time forecasting of systems’ behaviour and in the problems of transformation of structural properties of systems, such as the transformation of a chaotized system into a more organized structure (the generation of organized vortices in the small-scale turbulence), and, vice versa, the transformation of determinate systems into chaotized ones (the conversion of pendulum-type, near harmonic oscillations into chaotic shivering motions). Multi-year, laboratory, full-scale and theoretical investigations have shown that there exists a large class of natural objects and processes which belong to the ‘deterministic’ chaos, i.e. to some kind of boundary objects between purely determinate systems and ‘pure’ noise processes. It is the objects and processes of such a type which possess surprising geometrical and physical properties (Mandelbrot, 1977, 1982, 1989; Schuster, 1984; Zeldovich and Sokolov, 1985; Glass and Mackey, 1988; Takayasu, 1984, 1988; Kadanov, 1993; Chen and Dong, 1996; Dubois, 1998; Havlin, 1999; Holdom, 1998). In remote sensing problems, such objects include: the rough surface of soils, the geometrical shape of mountain arrays, cloud systems, the geometrical shape of vegetation, fields

* These names are purely conventional and, of course, have no relation to the electromagnetic spectrum ranges we have considered in Chapter 1.

of atmospheric precipitations, spatial fields of humidity of soils and landscapes, spatial fields of gravity waves breaking on the sea surface, and the spatial–hierarchic system of river beds (Lovejoy and Schertzer, 1985; Lovejoy and Mandelbrot, 1985; Zaslavskii and Sharkov, 1987; Voss, 1989; Cahalan, 1989; Vasil'ev and Tyuflin 1992; Vicsek, 1992; Shepard *et al.*, 1995; Davis *et al.*, 1994, 1996; Sharnov, 1996a,b; Gaspard, 1997; Rodrigues-Iturbe and Rinaldo, 1997; Arrault *et al.*, 1997; Hergarten and Neugebauer, 1998; Kothari and Islam, 1999; Dubois, 1998). In radio-physical problems fractal ideology is used in studying the propagation and scattering of electromagnetic waves from rough fractal surfaces (Franceschetti *et al.*, 1996, 1999a,b). Of interest is the fact, that the fractal construction and, accordingly, alternated time behaviour is also characteristic for the systems and objects of biological nature, including the peculiarities of human body architecture, the dynamics of behaviour and even the results of creative activities of a man (Ivanitskii *et al.*, 1998; Havlin, 1999; Ivanov *et al.*, 1999; Taylor *et al.*, 1999). In recent times, however, the problem of the prevalence of fractals in natural phenomena and processes has become the subject of rather strong polemics (Mandelbrot, 1998; Kirchner and Weil, 1998).

Slightly simplifying the situation, we can say that the secret of the behaviour of fractals lies in the exponential laws of the behaviour of basic characteristics of systems, such as the dependence of a system's substance mass on its radius, or the dependence of a number of unit elements of a system on the linear scale, or the power spectrum of fluctuations in a system (of type (2.50)). It can easily be seen that the exponential law

$$y = Ax^a \quad (2.51)$$

is equivalent to the following expression:

$$y(\lambda x) = \lambda^a y(x) \quad (2.52)$$

for all $\lambda > 0$. Mathematically, any function $y(x)$ that satisfies Equation (2.52) is called a homogeneous function. A homogeneous function is scale-invariant, i.e. if we change the scale of measuring x , so that $x \rightarrow x' (= \lambda x)$, then the new function $y'(x') [= y(x)]$ will still have the same form as the old one $y(x)$. This fact is guaranteed, since $y(x) = \lambda^{-a} y(x')$ according to equation (2.52), and, hence, $y'(x') \sim y(x')$.

The scale-invariance implies that a part of a system is magnified to the size of the initial system and this magnified part and the initial system will look similar to each other. In other words, there is no intrinsic scale in the initial system. A scale-invariant system must be self-similar and vice versa. Thus, we see that self-similarity, spatial power laws and scale-invariance are three equivalent ways of expressing the fact that the system lacks the characteristic length scale. It is important to note that the absence of the characteristic time scale in the system leads to temporal power laws (e.g. $1/f$ noise, the ubiquitous phenomenon in nature). To explain the widespread existence of fractals and scale-free behaviours in nonequilibrium systems, the hypothesis of self-organized criticality has been proposed (Bak *et al.*, 1987), which is supposed to be applicable to many natural and social systems (Larraza *et al.*, 1985;

Leung *et al.*, 1998; Kohonen, 1989; Sornette, 2000; Schweitzer, 1997; Tziperman *et al.*, 1997; Rodrigues-Iturbe and Rinaldo, 1997; Hergarten and Neugebauer, 1998; Henley, 1993). In the overwhelming majority of cases the natural objects are not, certainly, purely homogeneous fractals, but they are multi-fractals, i.e. they possess various fractal properties in various scales, or they represent rather complicated conglomerates of purely determinate systems and multi-fractals. In some cases such systems can be represented as so-called non-stationary multi-fractals (Marshak *et al.*, 1994, 1997). Of course, as we have noted above, the direct application of a standard spectral-correlation approach to studying such complicated systems cannot yield meaningful results. To perform such studies, special analytical methods have been developed, which make it possible to analyse the state of a system simultaneously in a very wide range of spatial-temporal scales and to reveal possible inter-scale (and, we should note, nonlinear) interactions. First of all, we should mention here the wavelet-transform methods which have been proposed fairly recently and which are now being developed quite intensively (Chui, 1992; Astafyeva, 1996; Basu and Levy, 1997; Bouman and Newell, 1998). Unlike classical Fourier analysis, the wavelet-transform has a ‘mobile’ time-frequency window that provides information on the evolution of the relative contribution of components at various scales, as the process under investigation develops in time. Thus, the wavelet-transform of a one-dimensional signal results in a two-dimensional field which demonstrates both the frequency-local properties of a basic signal, and their position in the time evolution of a process. This gives rise to the most important feature of the wavelet-transform: the possibility of analysing the temporal dynamics of power transmission at various scales. At present, the wavelet methods are widely used for analysing complicated physical processes where the use of classical Fourier analysis cannot yield satisfactory results. In this respect, we should first of all mention the studies of complicated atmospheric turbulence regimes, which include both Kolmogorov’s cascade processes and the formation and existence of coherent structures (Kaspersen and Krogstad, 2001; Terradellas *et al.*, 2001), of convective cloud systems (Yano *et al.*, 2001a,b), the stochastic regime of a global tropical cyclogenesis (Sharkov, 2000), and multi-scale analysis in structure recognition problems on IR and optical images (Frick *et al.*, 2001; Carvalho *et al.*, 2001; Michielsen and De Raedt, 2001). The wavelet-transform can be most efficiently used in analysing nonlinear systems where complicated frequency transformations take place, including the generation of new frequencies in a system (Ghanem and Romeo, 2001). More detailed information on the possibilities and techniques of application of the wavelet-transform and similar integral-geometrical methods can be found in papers by Farge *et al.* (1996), Astafyeva (1996), Bouman and Newell (1998), Frick *et al.* (2001), and Michielsen and De Raedt (2001).

2.6 LINEAR AND NONLINEAR SYSTEMS AND MEDIA

The natural media through which electromagnetic energy propagates, and the devices used for processing, transforming and transmitting the signals, can be

extremely diverse both in the principles of their intrinsic design and physical properties, and from the viewpoint of their external characteristics. In order to have the possibility of comparing and classifying such media and devices, the concepts are usually formulated using a block-diagram of the ‘black box’ type. The phenomenology of such a type is fairly wide spread in analysing the radiophysical and radio-technological type of system, as well as the various digital systems in computer systems engineering. The physical significance of such an approach is as follows. No matter how different various radio-technological and digital systems and devices are, we can always distinguish in their structure the *input*, designed for supplying initial signals, and the *output*, from which the transformed signals are delivered for further thematic usage. In the simplest case, both the input signal, $u_i(t)$, and output signal, $u_0(t)$, which is frequently called the response of a system, represent solitary functions of time. A more complicated case (for example, in computer systems engineering) might be the representation of an input signal in the form of an m -dimensional vector

$$\mathbf{U}_i(t) = [u_{i1}(t), u_{i2}(t), \dots, u_{im}(t)] \quad (2.53)$$

and of an output signal, the form of the n -dimensional vector:

$$\mathbf{U}_0(t) = [u_{01}(t), u_{02}(t), \dots, u_{0n}(t)]. \quad (2.54)$$

We should bear in mind that in experimental practice the situation frequently arises, where $n \neq m$.

The law of coupling between signals $\mathbf{U}_i(t)$ and $\mathbf{U}_0(t)$ is specified by means of the *system operator*, \mathbf{T} , whose effect on $\mathbf{U}_i(t)$ results in signal $\mathbf{U}_0(t)$:

$$\mathbf{U}_0(t) = \mathbf{T}\{\mathbf{U}_i(t)t\}. \quad (2.55)$$

The system operator can be contained inside both arithmetical transformations, and differentiation/integration operations, depending on the system’s properties. For definiteness of the problem, it is necessary to specify also the regions of admissible input effects (as well as the regions of output signals) in which the system retains its properties. In the simplest case, the question under consideration is the character of input signals (continuous or discrete, determinate or random) and their dynamic range.

The major principle of classification of systems (or natural media) is based on the fact that various systems, generally speaking, behave in various manners when a sum of several signals is delivered at the system’s input. If the operator of a system is such that the following equalities are valid:

$$\begin{aligned} \mathbf{T}\{\mathbf{U}_{i1} + \mathbf{U}_{i2}\} &= \mathbf{T}\{\mathbf{U}_{i1}\} + \mathbf{T}\{\mathbf{U}_{i2}\} \\ \mathbf{T}\{\alpha\mathbf{U}_{i1}(t)\} &= \alpha\mathbf{T}\{\mathbf{U}_{i1}(t)\}, \end{aligned} \quad (2.56)$$

where α is an arbitrary number, then the given system is called *linear*. The conditions (2.56) express the fundamental superposition principle.

The systems (or media) not obeying the superposition principle are called *nonlinear*. Strictly speaking, all physical systems and media are nonlinear to some extent. It can easily be understood that nonlinearity, as a physical property, is much

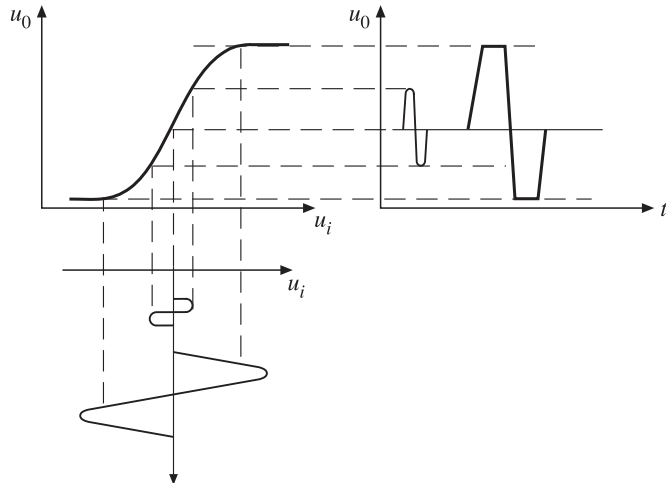


Figure 2.3. Typical example of amplitude nonlinear characteristic for the radiotechnic amplifier. u_i is the input signal; u_o is the output signal.

more general than linearity. However, there exists a great class of systems and media where the linear models that are used for their description yield quite reliable results. As the numerous investigations in this area have shown, linear systems are remarkable due to the fact that for them it is possible to obtain, at least theoretically, the solution of any problem related to the transformation of any input signal. Certainly, the same physical system can operate both as a linear system, and as a nonlinear one, depending on the input signal value. As an example, we may consider the signal of various intensities delivered to an amplifier, for which the response function (the system operator) has nonlinear character (Figure 2.3). We can easily see in Figure 2.3 that the signal with small amplitude is amplified in a linear manner. At the same time, in the case of the high intensity signal, its form (and its spectral composition) is highly distorted at the system's output.

We can also consider a simple (but, as we shall see later, a fundamental) purely nonlinear transformation $y = ax^2$. At the input of such a device a purely harmonic signal $x = \cos \omega_0 t$ with a single spectral component $\omega_0 = 2\pi f_0$ is delivered. Using well-known trigonometric formulas, we shall have at a nonlinear system's output the following signal: $y = \frac{1}{2} + \frac{1}{2}\cos 2\omega_0 t$, or, in other words, the constant component (zero frequency) and the harmonic signal, but with a doubled frequency. It follows from this fact that at the system's output the initial signal has been distorted: we now have the spectral composition, which was completely absent in the initial signal. In other words, the nonlinear system enriches the spectral composition of a signal with new components.

The violation of the superposition principle and the distortion of the spectral composition for nonlinear systems is, certainly, not the single principal distinction between linear and nonlinear systems. A lot of nonlinear systems are extremely sensitive to small variations of system parameters and initial conditions. Their

small variation can result in major ('disastrous') consequences: the system can acquire a significantly different time behaviour. An extensive literature is dedicated to elucidating these issues (see, for instance, Lam (1998)). It is the spectral aspect of this problem for systems stable against the change of parameters which will be important for us hereafter.

Now we consider the question of the relation between Fourier spectra and characteristics of a system. Suppose that some linear system is specified, which is described by the ordinary differential equation of the n th order with constant coefficients:

$$a_n \frac{d^n y}{dt^n} + a_{n-1} \frac{d^{n-1} y}{dt^{n-1}} + \cdots + a_1 \frac{dy}{dt} + a_0 y = x(t). \quad (2.57)$$

We apply the Fourier transformation to both sides of the equation

$$\int_{-\infty}^{\infty} f(t) \exp(-j\omega t) dt. \quad (2.58)$$

On the right-hand side we shall have the spectrum of the function of an input signal $x(t)$, and for integration of the left-hand side we apply one of basic formulas of spectral analysis (see Appendix B). Then we have

$$\left[\sum_{k=0}^n a_k (j\omega)^k \right] \dot{S}_y = \dot{S}_x. \quad (2.59)$$

Here \dot{S}_x and \dot{S}_y are spectra of functions $x(t)$ and $y(t)$, respectively. For a polynomial in square brackets we introduce the short designation as $\dot{Z}(j\omega)$. Thus, the spectrum of an output signal can be written as

$$\dot{S}_y(j\omega) = \frac{\dot{S}_x(j\omega)}{\dot{Z}(j\omega)}, \quad (2.60)$$

and, accordingly, we can write the expression for an output signal:

$$y(t) = \frac{1}{2\pi} \int_{-\infty}^{\infty} \frac{\dot{S}_x(j\omega)}{\dot{Z}(j\omega)} \exp(-j\omega t) d\omega. \quad (2.61)$$

This formula gives the complete solution of equation (2.57) by the Fourier integral method. In so doing, one more designation is introduced as:

$$\dot{K}(j\omega) = \frac{1}{\dot{Z}(j\omega)}. \quad (2.62)$$

This quantity, which expresses the ratio of complex amplitudes at a system's output and input in the harmonic mode, is called the complex frequency characteristic (or the complex transmission coefficient) of a system. Formula (2.60) can be written as:

$$\dot{S}_y(j\omega) = \dot{K}(j\omega) \dot{S}_x(j\omega). \quad (2.63)$$

It is important to note here that, for practical purposes, the transmission coefficient can be fairly simply obtained, in the majority of cases, by means of complex Ohm's law and Kirchhoff's rules for branched circuits.

Using the theorem on the product of spectra (Appendix B), we can find the output signal value in the form of convolution integral (the Duhamel integral)

$$y(t) = \int_{-\infty}^{\infty} x(\tau)h(t - \tau) d\tau, \quad (2.64)$$

where $h(t)$ is the Fourier transform of the frequency characteristic of a system that is called the pulse characteristic (pulse response) of a system, or, in other words, the system's response to an input signal in the form of delta-pulse. A great advantage of the Duhamel integral-based analytical technique is the fact that, when the pulse response of a system has been determined, the further stages of solution are reduced to completely formalized procedures.

Above we have outlined the methods that enable us to solve any problem related to determinate signals propagation through linear systems. Below we shall consider the methods of transferring these methods into the statistical area for stochastic signals. At the first stage we shall be interested in purely energetic relations only. In this case, remembering the relation for the Wiener spectrum and the current Fourier spectrum (2.32), we can immediately obtain the complete solution of the stated problem within the correlation approach framework. That is to say, the power spectrum of an output random signal is related to a similar spectrum of a signal at an input by means of the following equation:

$$G_0(\omega) = |\dot{K}(j\omega)|^2 G_i(\omega), \quad (2.65)$$

and the correlation function at the system's output, according to relation (2.23), will be equal to

$$B_y(\tau) = \frac{1}{2} \int_{-\infty}^{\infty} G_x(\omega) |\dot{K}(j\omega)|^2 \exp(j\omega\tau) d\omega. \quad (2.66)$$

Remembering relation (2.27), we can find the expression for a variance (or for the energy of a fluctuation part) of an output signal as:

$$\sigma_y^2 = B_y(0) = \int_0^{\infty} G_x(\omega) |\dot{K}(j\omega)|^2 d\omega. \quad (2.67)$$

As to the distribution densities, the normal processes possess the remarkable property of 'stability' with respect to linear (but not to nonlinear) transformations. Moreover, linear systems possess the surprising property of normality of an output random signal, which arises when an input non-normal (non-Gaussian) process has passed through the linear device under the natural condition that the time of correlation of an input process is essentially smaller than the time constant of a linear inertial circuit.

Below we shall consider an important example of an inertial integrating linear system, which is frequently used in applications, in particular, in separating a small constant value of a signal against the background of powerful noise.

2.6.1 Low-pass filter (LPF)

Experimentally the LPF is constructed as a circuit of a resistor and a capacitor (Figure 2.4(a)). With allowance for the complex Ohm's law we can obtain the expression for the complex transmission coefficient of the circuit:

$$\dot{K}(j\omega) = \frac{u_0(t)}{u_i(t)} = \frac{1}{1 + j\omega CR}, \quad (2.68)$$

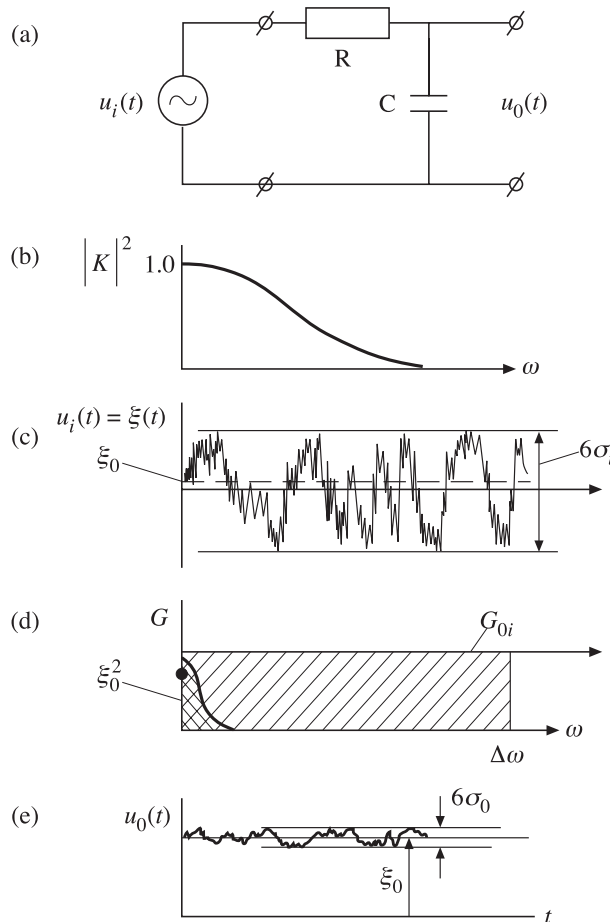


Figure 2.4. Schematic presentation of the functioning of a low-pass filter (signal integration electric circuit). (a) Wiring scheme of a low-pass filter. (b) Power transmission coefficient. (c) Time series of input signal; ξ_0 is statistical average; σ_i is statistical root-mean-square variation (RMS) of input signal. (d) Spectral densities of the input and output signals. (e) Time series of the output signal. σ_o is RMS of the output signal.

and, accordingly, the power transmission coefficient is

$$|\dot{K}(j\omega)|^2 = \frac{1}{1 + \omega^2\tau^2}, \quad (2.69)$$

where $\tau = RC$ is the circuit constant expressed in seconds. In this case it can easily be seen that the transmission coefficient maximum, which is equal to unity, will be located on a direct current (at zero frequency), and then, as the frequency grows, the transmission coefficient rapidly drops and accordingly suppresses initial high-frequency components (Figure 2.4(b)). This is the reason that the given circuit was called in such a manner. Let us imagine that at the circuit's input there is a strong fluctuation noise ($\xi(t)$) with a small constant level (ξ_0) of a signal, which just has to be separated and then recorded (Figure 2.4(c)). The spectral characteristics of an input signal can be written in the following slightly simplified form:

$$G_i(\omega) = \delta(\omega - 0)\xi_0^2 + G_{0i} \quad (2.70)$$

and, accordingly, the total power at the circuit's input will consist of a constant component's power and a fluctuation component's power:

$$B_i(0) = \xi_0^2 + \sigma_i^2 = \xi_0^2 + G_{0i}\Delta\omega. \quad (2.71)$$

Since a circuit's transmission coefficient on a direct current is equal to unity, the constant component of an input signal remains unchanged. The fluctuation component, however, will undergo qualitative changes. If we have at an input a broadband noise component with the correlation coefficient of type (2.41) and correlation time $\tau_k = \frac{1}{4}(\Delta f)^{-1}$, then at an output of the linear inertial system the spectral characteristics of a signal can be described, as can easily be seen, by the Lorentz-type spectrum (2.44) and correlation properties determined by expression (2.43), i.e. by the descending exponential curve, and with the correlation time equal to the integration constant of a circuit $\tau_k = RC$, which is just what should be expected, generally speaking. The value of an output signal variance can be found by using relation (2.67), substituting into it the values of the transmission coefficient on power (2.69). So, using the value of the known integral, we have:

$$\sigma_y^2 = G_{0i} \int_0^\infty \frac{d\omega}{1 + \omega^2\tau^2} = \frac{G_{0i}}{\tau} \frac{\pi}{2} = G_{0i}\Delta\Omega, \quad (2.72)$$

where by $\Delta\Omega$ is meant the effective LPF passband which, accordingly, can be rewritten as $\Delta f = 1/(4RC) = 1/(4\tau)$. As should be expected, the variance of a noise component of an output signal has sharply decreased, since in this case the band of frequencies, efficiently passed by a circuit, has shortened (Figure 2.4(e)). The efficiency of separating a constant component of the LPF can be naturally estimated as a ratio of variances of noise components at the circuit's output and input; or, more frequently, the ratio of root mean square (RMS) deviations is used:

$$\frac{\sigma_0}{\sigma_i} = \sqrt{\frac{\Delta\Omega}{\Delta\omega}} = \frac{1}{2\sqrt{\Delta f\tau}}. \quad (2.73)$$

This can be clearly seen graphically from the comparison of noise ‘tracks’ of a signal at a system’s input (Figure 2.4(c)) and output (Figure 2.4(e)) according to the ‘three sigma’ rule. Thus, the efficiency of separating a constant component is determined by the ratio of noise bands of input and output signals or by the signal accumulation time. Depending on physical features of observation, the accumulation time can vary within very wide limits, from some tenths of a second up to days. As we shall see soon, the aforementioned filter is an indispensable component of noise signal processing in microwave radiation reception systems.

At present, the operation considered above is usually performed directly by means of computer procedures.

2.7 NONLINEAR TRANSFORMATIONS OF RANDOM PROCESSES

Nonlinear transformations and, first of all, the quadratic transformation, play a fundamental part in the process of measuring the intensity of a random signal. The fact is that the procedure of measuring the spectral power of a noise signal cannot be constructed as any conceivable combinations of linear systems and circuits (this issue will be considered in more detail below in Section 2.8). The quadratic transformation of a noise signal occurs everywhere where it is necessary to measure the power of a fluctuation signal. This conclusion equally relates to the receivers of electromagnetic fluctuation radiation in the optical, IR and radio-frequency ranges, for example, the retina of the human eye, photographic devices, IR and microwave radiometers.

In analysing the transformation of random processes by nonlinear systems the problem is formulated as follows: supposing the parameters of a system and statistical characteristics of an input process $\xi(t)$ to be known, it is necessary to find the statistical characteristics of a transformed process at an output $\eta(t)$. As we have already noted, the nonlinear transformation changes both the external time appearance of the initial signal and its spectral composition; and, therefore, both density functions and the correlation function and spectral density of the initial signal also change. In general, the problem of transformation of random signals by nonlinear systems is very complicated; nevertheless, some particular results can be obtained within the framework of a spectral-correlation approach.

Suppose η to be the random quantity related with ξ by a single-valued functional dependence of form $y = f(x)$. Since the random quantities are interrelated by a single-valued determinate dependence, it can be supposed that from the fact that ξ lies within a fairly small interval $[\xi_0, \xi_0 + d\xi]$, it certainly follows that quantity η will lie within the interval $[\eta_0, \eta_0 + d\eta]$, where $\eta_0 = f(\xi_0)$. It follows from this fact that the probabilities of these two events are equal to each other (the property of invariance of the probability differential): $p(\xi) d\xi = p(\eta) |d\eta|$ (the modulus has appeared in the expression because the

probability density cannot be a negative quantity). Thus, the probability density of a transformed signal will be equal to:

$$p_1(\eta) = p_1(\xi) \left| \frac{d\xi}{d\eta} \right| = p_1\{g(\eta)\} \left| \frac{dg}{d\eta} \right|, \quad (2.74)$$

where $g(y) = x$ is the function reverse to $f(x) = y$.

If the functional relationship between quantities y and x is multi-valued, so that there are several reverse functions (as, for example, in the case of the transformation $y = ax^2$), then expression (2.74) is generalized as follows:

$$p_1(\eta) = \sum_{i=1}^N p_1(\xi_i) \left| \frac{d\xi_i}{d\eta} \right|, \quad (2.75)$$

where N is the number of reverse branches.

Using similar probabilistic constructions (namely, the property of invariance of a probability differential), we can obtain the following expression for the two-dimensional probability density $p_2(\xi_1, \xi_2)$:

$$p_2(\eta_1, \eta_2) = p_2\{g_1(\eta_1, \eta_2); g_2(\eta_1, \eta_2)\} |D_2|, \quad (2.76)$$

where D_2 is the Jacobian of transformation from random quantities ξ_1, ξ_2 to random quantities η_1, η_2 :

$$D_2 = \frac{\partial(\xi_1, \xi_2)}{\partial(\eta_1, \eta_2)} = \begin{vmatrix} \frac{\partial \xi_1}{\partial \eta_1} & \frac{\partial \xi_1}{\partial \eta_2} \\ \frac{\partial \xi_2}{\partial \eta_1} & \frac{\partial \xi_2}{\partial \eta_2} \end{vmatrix}. \quad (2.77)$$

If we consider the simple case of inertialess (without internal time delays) transformation, where the cross-relations between ξ_1 and η_2 and ξ_2 and η_1 are absent, then the Jacobian breaks up into the product of derivatives.

And, finally, from the basic definitions of the probability theory we shall have the following expressions for the mathematical expectation and for the second mixed moment (the correlation function) of the transformed process:

$$M_1(\eta) = \int_{-\infty}^{\infty} \eta p_1(\eta) d\eta = \int_{-\infty}^{\infty} f(\xi) p_1(\xi) d\xi \quad (2.78)$$

$$\begin{aligned} M_2(\eta_1, \eta_2) &= B(\eta_1, \eta_2) = \int_{-\infty}^{\infty} \int_{-\infty}^{\infty} \eta_1 \eta_2 p_2(\eta_1, \eta_2) d\eta_1 d\eta_2 = \\ &= \int_{-\infty}^{\infty} \int_{-\infty}^{\infty} f(\xi_1) f(\xi_2) p_2(\xi_1, \xi_2) d\xi_1 d\xi_2. \end{aligned} \quad (2.79)$$

Further, making use of the basic relation (2.24), we can transfer to spectral characteristics of a transformed signal.

Now we consider the important example of the inertialess quadratic transformation $y = ax^2$ ($a = 1$), where the normal stationary noise signal with a zero mean

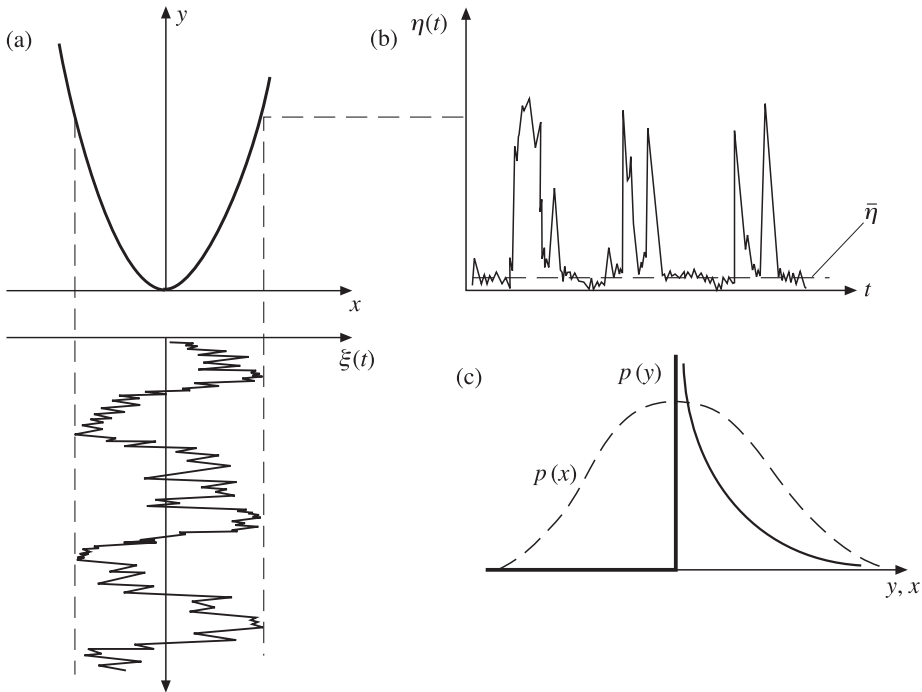


Figure 2.5. Schematic presentation of the functioning of a nonlinear square-law electrical circuit. (a) Square-law function and time series of the input signal. (b) Time series of the output signal. (c) The density function of the output signal.

value (ξ_0) acts on the input of a circuit. Schematically, the whole process of transformation of temporary and probabilistic characteristics is presented in Figure 2.5. Since the function for the transformation under study is double-valued, then, taking advantage of relation (2.75), we shall have for the density of a transformed signal the following general expression:

$$p_1(\eta) = \begin{cases} \frac{p_1(\sqrt{\eta}) + p_1(-\sqrt{\eta})}{2\sqrt{\eta}} & \eta > 0 \\ 0 & \eta \leq 0, \end{cases} \quad (2.80)$$

and for $\xi_0 = 0$ we obtain:

$$p_1(\eta) = \begin{cases} \frac{1}{\sqrt{2\pi\sigma^2}\eta} \exp\left(-\frac{y}{2\sigma^2}\right) & \eta \geq 0 \\ 0 & \eta < 0. \end{cases} \quad (2.81)$$

From consideration of (2.81) and Figure 2.5(b),(c) it can be seen that the time character of the transformed signal has radically changed: the values of a signal are only positive. The amplitude dependencies with respect to the initial signal

have also sharply distorted: the values of a signal with small amplitudes are considerably suppressed, and the values of a signal with large amplitudes have acquired the shape of sharp spikes. And, what is most important, in the quadratic transformation of a noise signal the constant component has appeared, which just bears the basic information on the power of an initial noise signal. All the above considerations are contained in the amplitude dependence of the density function of a transformed signal (Figure 2.5(c)). Note that the normalization in (2.81), which is necessary for distribution densities, is provided here; i.e., using the known determinate integrals (Gradshteyn and Ryzhik, 2000) we have:

$$\frac{1}{\sqrt{2\pi\sigma^2}} \int_0^\infty \frac{\exp\left(-\frac{y}{2\sigma^2}\right)}{\sqrt{y}} dy = 1. \quad (2.82)$$

For the mean value of an output signal, using (2.78) and known determinate integrals (Gradshteyn and Ryzhik, 2000), we obtain the important result

$$M_1(\eta) = \bar{\eta} = \int_{-\infty}^\infty x^2 \frac{1}{\sqrt{2_x\pi\sigma^2}} \exp\left(-\frac{x^2}{2\sigma_x^2}\right) dx = \sigma_\xi^2, \quad (2.83)$$

namely, the mean value (at zero frequency) of the transformed signal is exactly equal to the total power of an input noise signal.

However, for many applications it is necessary to know, along with purely amplitude characteristics, the detailed spectral properties of the transformed signal as well. For this purpose it is necessary to correct the spectral character of an initial signal. We shall suppose that the input signal represents a narrowband normal process with spectral-correlation properties presented by relations (2.45) and (2.46), and the two-dimensional density function is determined as (2.12). In this case the correlation function of the transformed output signal will be written as the following integral:

$$B(\tau)_\eta = \frac{1}{2\pi\sigma^2\sqrt{1-R^2(\tau)}} \int_{-\infty}^\infty \int_{-\infty}^\infty x_1^2 x_2^2 \times \exp\left\{-\frac{x_1^2 + x_2^2 - 2Rx_1x_2}{2\sigma^2(1-R^2)}\right\} dx_1 dx_2. \quad (2.84)$$

This integral is rather complicated. However, there exists a rather elegant (and nontrivial) substitution that allows us to transform the integral fairly rapidly to a convenient form. Substituting $R(\tau) = \cos\alpha$ (since $-1 < R(\tau) < 1$, then $0 < \alpha < \pi$) and also making the following substitution:

$$\begin{aligned} x_1 &= \sigma \cdot r \cos\left(\frac{\alpha}{2} + \varphi\right) \\ x_2 &= \sigma \cdot r \cos\left(\frac{\alpha}{2} - \varphi\right), \end{aligned} \quad (2.85)$$

we shall have with the help of the Jacobian the transformations of coordinates

$$\begin{aligned} dx_1 dx_2 &= D_2 dr d\varphi = \sigma \sin\alpha r dr d\varphi, \\ \frac{x_1^2 + x_2^2 - 2Rx_1x_2}{\sigma^2(1-R^2)} &= r^2. \end{aligned} \quad (2.86)$$

In this case the variables of integration are separated, and we have the following form of an initial integral:

$$B_\eta(\tau) = \frac{\sigma^4}{\pi} \int_0^\infty r^5 \exp\left(-\frac{r^2}{2}\right) dr \int_0^\pi \cos^2\left(\frac{\alpha}{2} + \varphi\right) \cos^2\left(\frac{\alpha}{2} + \varphi\right) d\varphi \quad (2.87)$$

and, in the final form, the expression for the correlation function of a transformed process assumes the following elegant form:

$$B_\eta(\tau) = \sigma^2(1 + 2R^2(\tau)). \quad (2.88)$$

This expression gives rise to some important conclusions. Substituting the value $\tau = 0$ into (2.88), we obtain the expression for the total power of a transformed signal

$$B_\eta(0) = 3\sigma^4 = 3(\bar{\eta})^2, \quad (2.89)$$

and in this case the power of a fluctuation component (the variance of a transformed signal) is equal to

$$\sigma_\eta^2 = B_\eta(0)B_\eta(\infty) = 2\sigma^4 = 2(\bar{\eta})^2. \quad (2.90)$$

It is interesting to note also, that if the initial signal possesses correlation properties in the form of a symmetric function, i.e. $R(\tau) = A(\tau) \cos \omega_0 \tau$, then the correlation function of a transformed signal (2.88) will be as follows:

$$B_\eta(\tau) = \sigma^4[1 + A^2(\tau) + A^2(\tau) \cos 2\omega_0 \tau]. \quad (2.91)$$

This indicates that, along with a constant component, there are two bands – the low-frequency band, assigned to a direct current (a zero frequency), and the high-frequency band, assigned to frequency of $2\omega_0$. It is interesting to note that from (2.91) it directly follows that the intensities of noise bands and the value of a constant component of the transformed signal are equal. This follows from the symmetry of the initial problem. However, the complete picture of the spectral density distribution can be obtained only after performing the corresponding Fourier transformation of (2.24) and (2.26).

Remembering the expression for the correlation function of a narrowband input noise signal (2.46) and using expressions for determinate integrals (Gradshteyn and Ryzhik, 2000) and for the delta-function (see equation (B.11) in Appendix B), we obtain after some transformations the expression for the spectral density of a

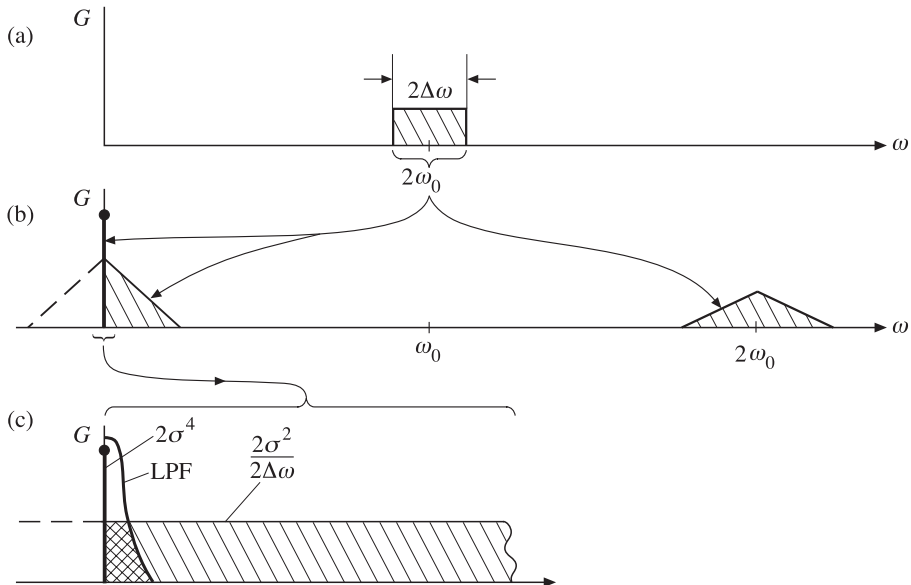


Figure 2.6. Transformation of a narrowband spectrum by a square-law circuit. (a) Spectrum of input signal. (b) Spectrum of transformed signal. (c) Spectrum of output signal by low-pass filter (LPF). See explanations in the text.

noise-transformed signal

$$G_\eta(\omega) = \sigma^4 \left\{ \delta(\omega - 0) + \frac{2}{(2\Delta\omega)^2} (2\Delta\omega - \omega) \right. \\ \left. + \frac{1}{(2\Delta\omega)^2} [(2\Delta\omega - 2\omega_0 + \omega) + (2\Delta\omega - 2\omega_0 - \omega)] \right\}. \quad (2.92)$$

Note, at first, that by $\Delta\omega$, as in (2.46), is meant a half of the total band of an input noise signal. Second, the different terms of expression (2.92) have different fields of existence: the second term is valid for $2\Delta\omega > \omega > 0$, the third term for $2\omega_0 - 2\Delta\omega < \omega < 2\omega_0$, and the fourth term for $2\omega_0 < \omega < 2\omega_0 + 2\Delta\omega$. The result obtained (presented graphically in Figure 2.6) is principally important. The physical significance of quadratic transformation of a band noise consists in the fact that, instead of a single band assigned to frequency ω_0 , the spectral density of an output signal consists of three components: the component at a zero frequency, which is equal to the intensity of an initial noise process; the spectrum of triangular type assigned to a zero frequency; and the spectrum in the form of an equilateral triangle assigned to frequency $2\omega_0$. It is important to note that the spectral components assigned to frequency ω_0 are completely absent in this case. Whereas the component at a zero frequency bears useful information (namely, the data on the value of noise intensity of an input signal), two other components are ‘parasitic’ in

some sense and are responsible for the intensity of noise of an output signal and, we emphasize, they are of obviously non-Gaussian in type (see (2.81)). All these features play an important part in the process of measuring the intensity of an initial noise signal.

2.8 MEASUREMENT OF NOISE SIGNAL INTENSITY

Now we consider the most important problem of the experimental technique of measuring the power of a noise signal. For argument's sake, we shall suppose the initial signal to be of electromagnetic nature (for example, noise voltage) – though this is, of course, absolutely not obligatory: the signal can be of any physical nature. The methodology considered below remains the same. The initial signal is supposed to be stationary and ergodic. In this connection we can take advantage of the important relation for stationary, ergodic processes, which determines the power within a restricted frequency band, by making use of the combination of relations (2.15) and (2.27):

$$\int_{\omega_1}^{\omega_2} G(\omega) d\omega = \lim_{T \rightarrow \infty} \frac{1}{T} \int_0^T \xi^2(t) dt. \quad (2.93)$$

Applying the well-known theorem on the mean value for the integral in the left-hand side of the equality, we shall have the expression for the estimate of a spectral density value $\hat{G}(\omega_i)$ inside the frequency band $\Delta\omega = \omega_2 - \omega_1$ at frequency ω_i and for the limited observation time T :

$$\hat{G}(\omega_i) = \frac{1}{\Delta\omega} \left[\frac{1}{T} \int_0^T \xi^2(t) dt \right]. \quad (2.94)$$

It follows from this expression, that the experimental estimate of the spectral density of a noise signal of any physical nature will consist of three most important elements:

- a linear filtration, whose parameters are specified by physical features of the problem under study;
- the nonlinear quadratic transformation of a signal;
- the time averaging (or accumulation of a signal) intended for separating a constant component of a transformed signal, whose value is proportional to the power of an initial analysed signal.

Figure 2.7 shows a schematized representation of an electrical analogue of the aforementioned procedure without (Figure 2.7(a)) and with (Figure 2.7(b)) accumulating a signal. The noise signal (noise voltage), received, for example, by some antenna system, is delivered to the input of a system. Then, because the signal most often happens to be rather 'weak' for further processing, it undergoes considerable amplification and frequency filtering in accordance with the physical problem stated. After this the amplified and filtered signal is delivered to the quadratic device, which is frequently called the quadratic detector. This device possesses a remarkable property: the current at the device's output is proportional

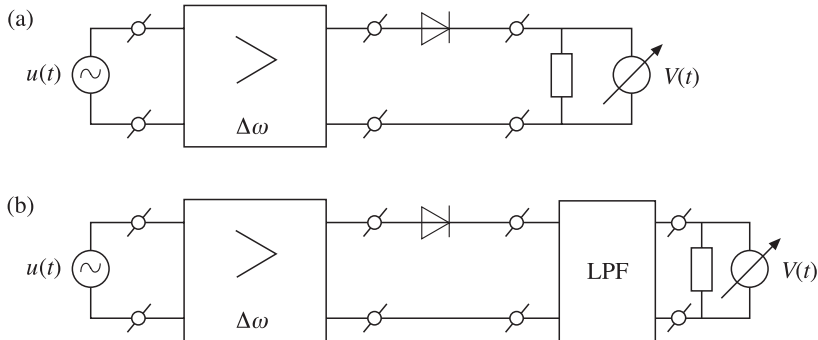


Figure 2.7. The scheme to measure the intensity of a random signal. (a) The scheme without low-pass filter (LPF). (b) The scheme with low-pass filter.

to the square of the voltage at its input (Figure 2.7(a)). Thus, at the output (or, as it is sometimes called, the loading) resistance the voltage (also, remember, of fluctuation type in itself) will be developed proportional to the square of the initial noise voltage, i.e. $V(t) = \beta U^2(t)$, where constant β will include all linear elements of transformation, amplification and filtration. As we have already noted, the output signal will consist of three components: the constant component and two ‘noise’ bands. The mean value of a signal at the system’s output is equal to $\bar{V}(t) = \beta U^2(t)$; in this case the variance (i.e. the power of a noise component) of a signal will be equal to $\sigma_V^2 = V^2 - (\bar{V})^2 = 2(\bar{V})^2 = 2\beta[U^2(t)]^2$. Since the probabilistic characteristics of a signal do not correspond to the normal distribution, the ‘three sigma’ rule is not suitable for this distribution. Some qualitative idea about the relationship between the mean value of a signal and noise components can be drawn from Figure 2.5(b). The analysis of this figure indicates, that for such a relationship between the variance and mean value, i.e. $\sigma_V^2/(\bar{V})^2 = 2$, we can hardly say anything about efficient separation and recording of the mean value. Certainly, for its satisfactory instrumental recording, this quantity should essentially be lower than unity. The most efficient method for satisfying this condition is the accumulation of a signal or, which is the same, the maximum removal of noise components of a transformed process by means of low-frequency filtering (see Section 2.6). Figure 2.6(c) gives a schematic representation of this procedure. Note here one important circumstance: no matter what the values of a filtering device’s parameters, the noise remainder of a low-frequency component of the transformed signal cannot be entirely eliminated, though it can be made as small as is desired by increasing the time of accumulation of an initial signal. The total power at the output of a linear low-pass filter (LPF) can be presented as

$$B_F(0) = \overline{V_F^2} = (\bar{V}_F)^2 + \sigma_F^2 = \int_0^\infty G_\eta(\omega) |\dot{K}(j\omega)|^2 d\omega. \quad (2.95)$$

Taking into account (2.92), the value of a low-frequency component at a direct current (2.92) and the effective passband of the filter (2.72), we obtain the expression

for a constant component and variance of residual noise at the output of the LPF filter as:

$$\overline{V_F^2} = \beta^2 \sigma^4 + 2\beta^2 \frac{\sigma^4}{(2\Delta\omega)} \Delta\Omega. \quad (2.96)$$

The efficiency of such a scheme of spectral intensity measurement can be estimated as a noise-to-signal (N/S) ratio, determined as the square root from the ratio of the value of residual noises to a useful signal – the constant component:

$$\frac{N}{S} = \sqrt{\frac{\sigma_F^2}{(\bar{V}_F)^2}} = \sqrt{2} \sqrt{\frac{\Delta\Omega}{2\Delta\omega}} = \sqrt{2} \sqrt{\frac{\Delta F}{2\Delta f}}. \quad (2.97)$$

Of principal significance here is the fact that the efficiency of the scheme is determined only by the ratio of frequency bands of the initial signal and of the output filter. It should also be noted that, by virtue of the considerable difference in the values of frequency bands, a sharp ‘normalization’ of an output process takes place, so that it represents, virtually, a purely Gaussian process. The experimental time series of such a process, normalized after passage through the low-pass filter, was presented earlier in Figure 2.2(b). Note also that, using rather simple methods and means, we manage to obtain a considerable gain in the signal-to-noise ratio in measuring the spectral density. So, in a series of microwave observations the characteristic values of frequency bands are as follows: $\Delta F = 0.1\text{--}1\text{ Hz}$, $2\Delta f = 10^8\text{--}10^9\text{ Hz}$. Hence the gain in the signal-to-noise ratio can achieve four to five orders of magnitude, whereas without low-pass filtering this ratio would be only $1/\sqrt{2}$.

The scheme of measurement of the spectral density of a random signal, considered above, is extremely widely used both for measuring the fluctuation electromagnetic radiation, and for studying stochastic processes of other physical natures. A rich literature is devoted to various aspects of such a kind of exploratory procedure, in the radiophysical area especially. We shall apply the materials presented in the present chapter first of all, to studying the physical principles of the formation of thermal radiation and, then, to considering the methods and techniques of fluctuation signal reception (Chapters 3–6). These materials will also be used in the analysis and interpretation of remote microwave sensing data (Chapters 11–13).

3

Microwave radiometers: functions, design concepts, characteristics

The purpose of this chapter is to consider the basic techniques and concepts of measuring thermal electromagnetic fluctuation radiation. Further, using the method of equivalent schemes, the basic notions of brightness and noise temperature are introduced, which have been widely used in the theory and practice of passive microwave remote observations. The functions and characteristics of components of passive remote sensing devices are considered in detail; and also the basic concepts of designing microwave radiometers and the methodology of measuring their basic frequency and power characteristics are discussed. The latter include: the fluctuation threshold sensitivity; the form of amplitude–frequency responses; and the radiometric and energy passbands of receiving systems. The question of the limiting sensitivity of a microwave radiometer is also considered.

3.1 BASIC TYPES OF PASSIVE MICROWAVE DEVICES

As we have already noted, the procedure of experimentally measuring the spectral density of a random signal of any physical nature, including a fluctuating electromagnetic field, will consist of three basic components:

- linear frequency filtering, whose parameters are specified by the physical features of the problem under study;
- nonlinear quadratic transformation of a signal;
- temporal accumulation of a signal intended for separating the constant component of a transformed signal, whose value is proportional to the power of an initial analysed signal.

Let us consider, first of all, the first element of a measurement procedure. The fact is that the physical space around us possesses a huge diversity of forms of thermal radiation spectra, beginning from almost ‘white’ noise up to quite

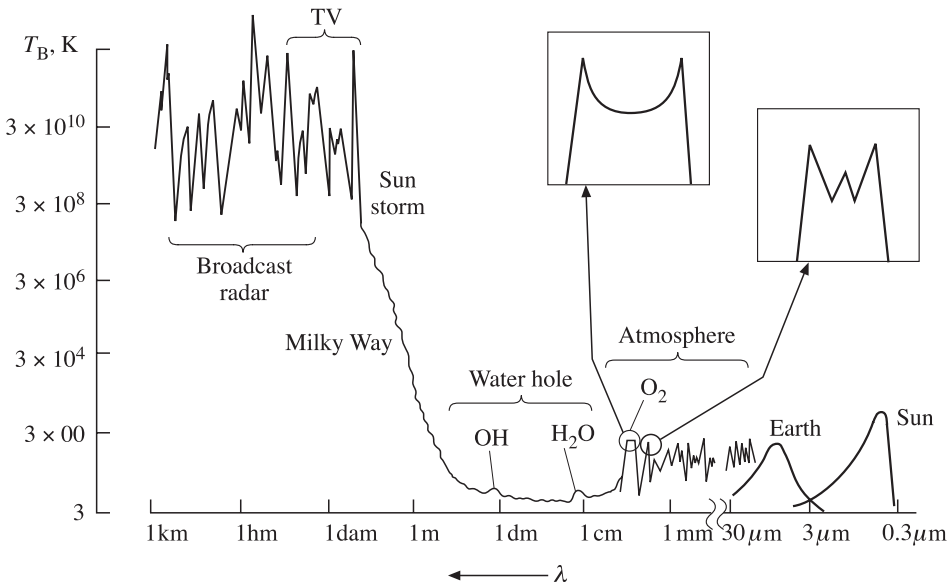


Figure 3.1. The qualitative picture (in temperature units) of the spectrum of electromagnetic emissions and artificial radiations.

complicated forms of spectra of radiation of gas media. Here, not only the intensity of a noise signal but also, most frequently, the form of a spectrum (or, as is sometimes said, the form of a line) bears useful physical information. To imagine a qualitative picture of natural thermal radiation, as well as the artificial electromagnetic radiations surrounding us (Figure 1.2), we shall turn to Figure 3.1, where electromagnetic radiation spectra are shown in the temperature brightness scale (see below) for a wide range of wavelengths, from the optical up to the kilometre band. If we move from optical frequencies into longer-wave regions, then here we should mention, first of all, the black-body radiation of the star nearest to the Earth, the Sun, whose radiation just ensures biological life on our planet. Then follows the nearly black-body radiation of our native planet, the Earth. And, further, almost the whole range of IR radiation up to the wavelength of 1 cm is ‘occupied’ by thermal radiation of the gases of the Earth’s atmosphere in the form of a huge number of sharp line spectra (in essence, some paling of lines). The form of these lines is determined by the quantum character of electromagnetic energy absorption in gases and also depends on the ratio of contributions of vertical profiles of temperature and density of the corresponding gas to the radiation intensity. In this connection, the form of a particular line can be quite peculiar. So, the insertions in Figure 3.1 indicate the forms of strong absorption lines of atmospheric oxygen (they amount to about 100 individual lines in the range 55–65 GHz), which have merged into a powerful single line of ‘two-finger’ shape. The form of an oxygen line in the range of 118 GHz resembles the form of a tower of the Moscow Kremlin. All

fine features of the forms of such lines play an important part in restoring the physical parameters of a gas medium and, consequently, they should not be ‘lost’ in the process of reception and processing of the original signal.

In cm and dm wavelength bands there exists some peculiar minimum of total radiation called the ‘water hole’ by radio-astronomers, because this band covers fairly weak (but very important in science) lines of absorption of water vapour (wavelength, 1.35 cm) and hydroxyl (OH) (wavelength, 18 cm). It is this band in which the ground radio-astronomical investigations have been carried out for a long time.

Beginning with the range of long decimetre wavelengths, the electromagnetic noise background sharply increases owing to the strong radio emission of the Sun and emission from our galaxy (the Milky Way). This emission has a strong spatial anisotropy and strong diurnal variations and, thus, highly impedes radiothermal investigations of the Earth’s surface.

As we have noted above, the metre, decametre and longer-wave bands are saturated with a huge quantity of artificial emissions, which in the overwhelming majority of cases can be considered as quasi-chaotic with very complicated laws of distribution of amplitude fluctuations. Of course, the statistical methods considered in Chapter 2 can also be applied to these emissions: for example, the intensity of quasi-chaotic emission can be estimated. Estimations that have been carried out demonstrate striking results: the intensity of artificial sources of electromagnetic radiation is millions of times stronger (in comparable units) than solar radiation in the optical range. Artificial emissions are characterized by strong spatial-temporal variability, and it is virtually impossible to obtain a complete spectral picture of these emissions.

This qualitative review allows us to easily understand the principal importance of the procedure of primary filtering of the original signal for remote sensing tasks. In virtue of the huge diversity of the frequency forms of thermal emissions, the whole spectrum of natural electromagnetic emissions is usually subdivided into two large classes of emissions: the broadened continuum part of the continuous spectrum and the many-line absorption spectrum. Accordingly, radiometric receiving devices are subdivided from this point of view into two large classes: radiometric receiving devices with a fairly broad reception band (these devices are called continuous spectrum radiometers) and multichannel radiometer-spectrometers, designed for studying narrowband emissions (the lines of emissions). Certainly, this subdivision is fairly conventional, generally speaking. In recent times, radiometric systems of a combined type appeared which serve to study both the large-scale frequency features of a continuous spectrum and the emission lines ‘built-in’ in the continuous spectrum basement. An indicative example of such a system is the MTVZA radiometric complex intended for operation on the Russian ‘Meteor-3M’ spacecraft (see Chapter 14). On the other hand, multi-frequency continuous spectrum radiometers undoubtedly acquire the features typical for spectral devices. An example of such a system can serve the radiothermal instruments, the Advanced Microwave Scanning Radiometre (AMSR) installed for space flight aboard NASDA’s ADEOS-2 and NASA’s Aqua spacecraft in 2002 (see Chapter 14).

In accordance with the spectral-correlation approach, the concept of a radiometric receiving complex can be implemented in two forms: (a) as an analogue multichannel filter system (a filter analyser), and (b) as an autocorrelation receiver, which provides the formation of an autocorrelation function of a measured process with subsequent Fourier transformation into its frequency spectrum (Figure 3.2(a), (b)). The principal diagram of an analogue filter amplifying system and the position of filtering narrowband channels are presented in Figure 3.2(a), (c). Since in the overwhelming majority of cases in measurement practice the original external signal happens to be too weak to be subject to specialized processing, the signal required for solving a physical problem in the appropriate (working) frequency band undergoes considerable amplification by means of specialized broadband amplifiers. Further, multichannel narrowband filtering is performed in the working frequency band by means of a particular number of narrowband filters (Figure 3.2(c)). Their quantity and position in the working frequency band is determined both by the features of the physical problem, and by the tactical-technological requirements of the onboard measurement system. Whereas for restoring the atmospheric parameters in the troposphere, space radiothermal systems usually have from three to ten narrowband channels, for radio-astronomical ground-based systems the number of channels reaches 1024 and more. Then the quadratic transformation and low-pass filtering are performed in each channel. Further accumulation, recording, storage and representation of the final information are usually accomplished in specialized digital units on a computerized basis. In optics, similar types of multi-channel devices have been called polychromators.

Autocorrelation reception is based on the decomposition of a time sequence of the basic signal according to the multichannel scheme. The growing time delay is introduced into each channel with subsequent multiplication of two signals, basic and delayed ones (Figure 3.2(b)) and accumulation of a signal (the time-averaging). The recording device forms the discrete values (corresponding to the number of channels) of the autocorrelation function and then transforms them into the spectral density of an original signal using the Fourier transformation. Further, the procedure of statistical evaluation of confidence intervals of the spectral density obtained is performed.

Both these approaches are equivalent, from the principal point of view. However, in remote sensing instrumentation for the microwave range, filter analysers of various types have prevailed for a long time for certain technological reasons. In recent times the scientific problems of modern radio-astronomy put on the agenda the production of broadband spectrum analysers with a high spectral resolution operating in real time. The manufacture of hybrid optical-digital processors, composed of optical-acoustic analysers and digital devices, promoted the solution of these problems. Owing to optimal distribution of processing functions between optical and digital parts, the optical-digital processor makes it possible to essentially increase the speed of processing and resolution capability. In such a type of hybrid processor, optical devices provide a high speed of integral transformations over the data set, and digital devices provide reliable and long-term storage and the required accuracy and flexibility of algorithms for subsequent data processing. The

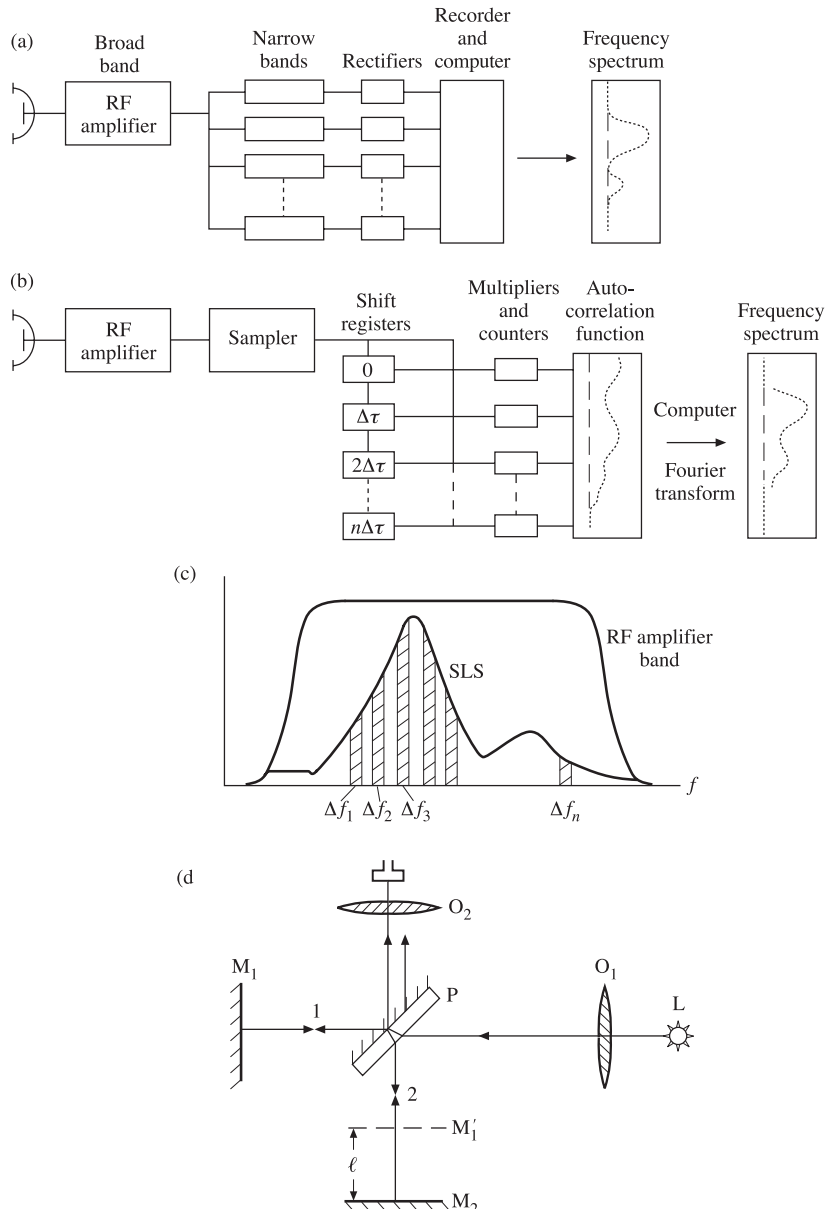


Figure 3.2. Microwave radiometers for spectral line observations: (a) an analogue filter bank RF-radio-frequencies system; (b) an autocorrelation spectrometer producing an autocorrelation function that can be Fourier-transformed to a frequency spectrum; (c) a schematic correlation between a spectral line shape (SLS) under study and narrowband filters; (d) the scheme of Michelson's interferometer. 1 and 2 are two coherent waves; L is a light source; O_1 and O_2 are convex lenses; P is a semitransparent plate; M_1 and M_2 are plane mirrors; M'_1 is the imaginary reflection of M_1 mirror; $2l$ is a difference in optical path (correlation lag).

physical basis of the optical-acoustic Fourier processor rests upon the method of spatial separation of wavelengths by means of a dispersing element (the diffraction lattice or prism, for example), which is well known in optics. The multicomponent linear matrix photo-receiver is installed at the output plane of an optical processor. It performs the functions of a polychromator, an accumulator of a useful signal and a high-speed commutator. Some of the largest radio-telescopes are equipped now with optical-digital radiospectrometers, which have ensured considerable progress in the spectral measurement of radio-emission from both remote objects (galaxies) with large signal accumulation time, and the nearest star, the Sun, with a millisecond accumulation time (Esepkina *et al.*, 1997, 2000; Sorai *et al.*, 1998).

On the other hand, in the long-wavelength part of the submillimetre band receivers of the Fourier spectrometre type have been efficiently developed and utilized. These devices accomplish continuous coding of wavelengths with the help of interference modulation arising in the two-beam interferometer by changing of the optical difference of path (the simplest scheme of Michelson's interferometer is presented in Figure 3.2(d)). The receiver of the emission at the interferometer output provides the signal in time – the interferogram (or, in other words, the continuous autocorrelation function of the external process under investigation), which is subject to Fourier transformation on a computer or on a special processor for obtaining the required spectrum (Bell, 1972; Prochorov, 1984; Mandel and Wolf, 1995; Persky, 1995). Fourier spectrometers are most efficient for studying the spectra of rather weak sources (the Earth's atmosphere, the planets) in the IR and submillimetre ranges, as well as for the solution of super-high-resolution problems. The active advancement of Fourier spectroscopy methods into the longer-wave region indicates that in the very near future correlation receivers of the Fourier spectrometer type in the microwave range will actively compete with filter analysers.

It should be noted that, in the historical respect, early remote microwave systems were almost completely based on the use of a radio-astronomical practice, and have only gradually been developed in this independent direction.

3.2 BASIC COMPONENTS OF A PASSIVE MICROWAVE RADIOMETER AND THEIR FUNCTIONS

In the most general form, the scheme of studying physical objects by the use of passive radiothermal techniques can be presented as shown in Figure 3.3(a). The radiothermal complex represents a functionally combined antenna system, a microwave radiothermal receiver, recording and storage devices and a radio-engineering system for the transmission of obtained data to the information processing points. The radiothermal complex should possess the following properties:

- receive electromagnetic radiation in the particular frequency band from a particular spatial direction and at a particular body angle;

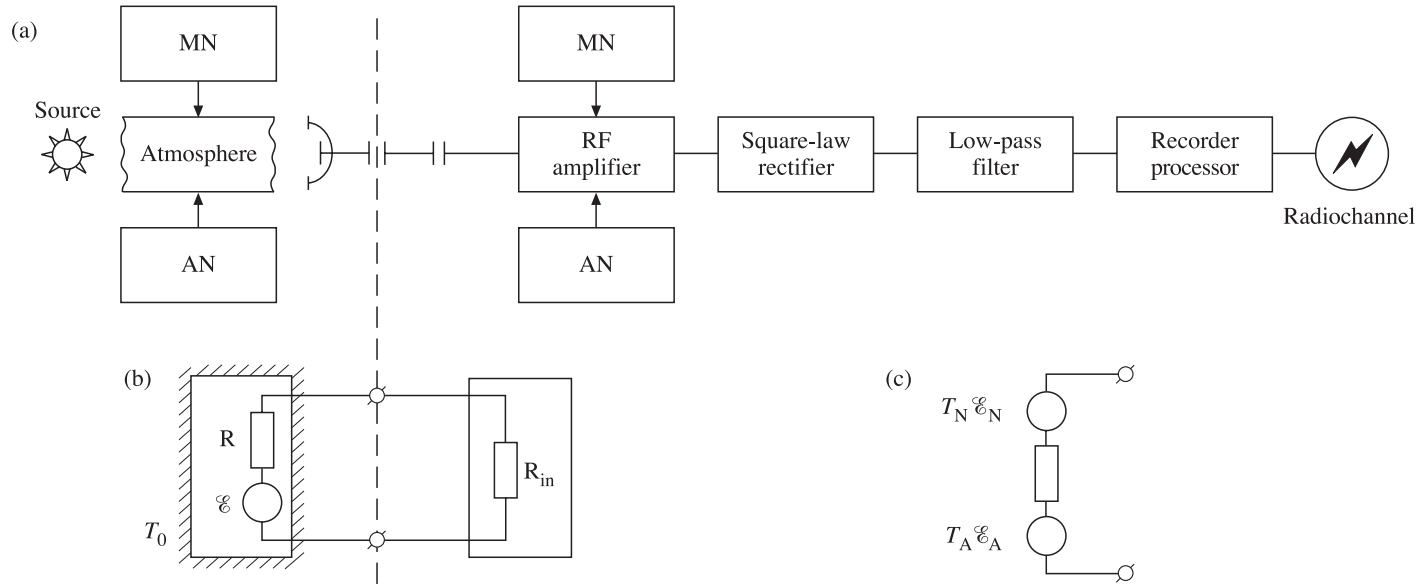


Figure 3.3. Schematic presentation of the transmission of information data from a natural object. (a) Physical scheme of the transmission of data: MN is a multiplicative noise; AN is an additive noise. (b) Equivalent scheme of the process of emission reception: E is equivalent noise source; R is equivalent active noise resistor; T_0 is equivalent temperature of the thermostat; R_{in} is the input resistance of the amplifier. (c) Equivalent scheme with due regard for the amplifier's noise. \mathcal{E}_A and \mathcal{E}_N are equivalent noise sources of the object under study and the amplifier; T_A is the antenna temperature; T_N is the noise temperature of the amplifier.

- possess a high sensitivity allowing it to reliably record variations in the thermal radiation of physical objects;
- provide the possibility of uniquely attributing a measured radiation signal to the spatial coordinates of corresponding emitting objects.

In this connection, the radiothermal complex designed for remote measurements should include at least four chief indispensable components:

- (1) an antenna system required for providing observation of the surface under investigation and for transforming the electromagnetic wave from free space into a measured signal;
- (2) a radiothermal receiver allowing it to record and measure the useful signal to the required accuracy;
- (3) a preprocessing device providing: antenna system control, data acquisition, preprocessing, calibration and recording into a memory device;
- (4) a device providing formation of the obtained information into the form required for transmission over communication links with subsequent thematic processing and mapping by means of a ground complex (the ground segment).

We will consider the functions of the first two components in more detail.

The antenna system is designed, primarily, for transforming electromagnetic waves, which propagate in free space, into the complicated modes of oscillations of electromagnetic waves propagating in guiding transmission lines (waveguides, coaxial cables). In free space the vector fields (see section 1.6) \mathbf{E} and \mathbf{H} are strictly transversal, i.e. both vectors are perpendicular to the propagation direction and, in addition, they are perpendicular to each other and form the right-hand orthogonal triple of vectors (of the TEM type). The ratio of amplitudes of electrical and magnetic fields in the planar wave (the wave resistance), propagating in free space, is strictly fixed and equals the value (in the SI system) of 376.6 ohms. However, in guiding systems the structure (or the mode) of propagating electromagnetic waves is different in principle: these waves can have both longitudinal and transversal components. The number of modes of oscillation can be infinite. The wave propagation characteristics (phase velocity, wavelength, wave resistance) in guiding systems depend on the ratio of the working wavelength and physical size of the guiding system. So, in coaxial cables the wave resistance usually equals fixed values of 50 or 75 ohms, whereas in waveguides the wave resistance can vary within wide limits – from 100 to 500 ohms depending on the type of a wave and geometrical size of a waveguide system. Thus, the antenna system should transform the oscillations of TEM type into the type of oscillation that propagates in the further antenna-feeder system and in the receiving complex directly. In this case, in accordance with the method of impedances, the antenna system should correlate the wave resistances of free space and of guiding systems (see below).

The second designation of antenna systems is the spatial-angular selection of a signal with the particular angular resolution required for solution of the stated problem, and for accomplishing spatial-angular scanning for the formation of the

observation band (or observation frame). In addition, in each resolution element the antenna system should receive a signal with a particular polarization, i.e. with a particular vector character of presentation of intensities of electrical and magnetic fields with respect to the geometry of the object under investigation (to the planar surface, for example).

In virtue of prominent dispersion properties, the antenna system should possess fairly homogeneous frequency properties of its basic characteristics throughout the working frequency band.

The radiometric receiving device consists of a high-frequency amplifier, a quadratic device and a low-frequency filter. The functions and properties of the two latter functional elements have been considered above (see sections 2.7 and 2.8). The function of a high-frequency amplifier consists in amplification of the signal, received by the antenna, in the frequency band strictly determined by the physical problem, for subsequent quadratic transformation.

Note that when the useful signal passes through the atmosphere and through the amplifying device, external interferences can be of two types: additive noise and multiplicative noise (Figure 3.3(a)). The physical significance of their separation is fairly transparent. The first type of interference (or noise) is an independent process with respect to a useful signal (for example, the thermal radiation of the atmosphere or amplifier), and, thus, their intensities are added (which gives rise to the name of this type of interference). The second type of interference is related to the useful signal distortion by the atmospheric medium (or amplifier) through the effect on the amplitude and phase of a signal, and usually it is represented as a product of the useful signal value by the distorting factor (which gives rise to the name of this type of interference).

This separation is, certainly, fairly conventional; but, nevertheless, it is quite convenient in practice. We shall demonstrate this below on practical examples and shall repeatedly use such an approach hereafter.

3.3 THE LANGUAGE OF EQUIVALENT CIRCUITS: THE ANTENNA, RADIOBRIGHTNESS AND NOISE TEMPERATURES

In virtue of the huge diversity of technological implementations of antenna systems and high-frequency amplifiers in the microwave range, and to introduce physical uniformity in the measurement process, it was recognized as expedient to use simplified equivalent circuits based on the impedance method (see section 1.6). We shall present the whole input portion in the measurement process as some noise source of emf (electromotive force). This source will have its internal resistance (which will correspond to the energy of a signal received by the antenna system), and the input resistance of an amplifier, on which, in its turn, the power of an external signal, transmitted from the antenna system, should be given off (Figure 3.3(b)). The character of a signal received by the antenna system represents the Gaussian random process with a value of variance corresponding to the intensity of an external signal to be measured (see section 2.2). In accordance with the Nyquist

theorem (see Chapter 4), the noise signal generated on the complex resistance $\dot{Z}(j2\pi f)$ has a similar statistical structure; this signal forms the spectral density (over positive frequencies) of the noise signal $G^+(f)$ as follows:

$$G^+(f) = 4kT_0 \operatorname{Re} \dot{Z}(j2\pi f), \quad (3.1)$$

where T_0 is the thermodynamic temperature of a thermostat, where the complex resistance is placed, and k is the Boltzmann constant (see Appendix A, Table A.4). If we represent the complex resistance as a purely active resistance (R) and take the investigated frequency band as a band-pass filter with band Δf , then the noise signal variance, or the mean square of noise emf, $\bar{\mathcal{E}}^2$, will be

$$\sigma^2 = \bar{\mathcal{E}}^2 = 4kT_0 R \Delta f. \quad (3.2)$$

Since the input resistance of the receiver represents a load resistance of the antenna, where the useful signal is directed, it is important to determine the conditions under which the maximum power from a source (the emf plays its part in this case) can be transmitted into the receiving device. This procedure is called the match (the conformity). Now we can easily obtain the conditions imposed on the values of resistances of the source (R) and of the input resistance of an amplifier (R_{in}), for obtaining the value of a maximum power given off on the input resistance. For this purpose we shall write the expression for power, P , given off on the input resistance, with allowance for the Joule–Lenz law, as follows:

$$P = I^2 R_{in} = \frac{\mathcal{E}^2}{(R + R_{in})^2} R_{in}. \quad (3.3)$$

By equating the derivative of this expression with respect to R to zero, we can get the important relationship, namely, $R = R_{in}$. In other words, for providing the maximum power transmission to the receiver input, it is necessary to fulfil the conditions (match conditions) of equality of the source resistance and the input resistance of the amplifier. In this case the time-averaged value of maximum power, P_{max} , given off on the input resistance, will be equal, with allowance for the Nyquist formula, to

$$P_{max} = \frac{\bar{\mathcal{E}}^2}{4R} = k T_0 \Delta f. \quad (3.4)$$

The expression obtained is very important methodologically, since it stipulates the expediency of the introduction of the temperature system of units for characterizing the spectral density of a noise power given off on a matched load of the antenna at reception of the external noise electromagnetic radiation. For this purpose the antenna temperature is introduced as the equivalent thermodynamic temperature of a noise resistance, which is equal to the input resistance of an amplifier and whose spectral power density is equal to the spectral power of the received external signal. Thus, by equating the intensity (the value of a variance) of the external noise signal to the intensity of the introduced artificial source, we obtain the antenna temperature value (in absolute degrees) expressed in terms of the

spectral density of the received external source $G(s)$ as

$$T_A(f) = \frac{G(f)}{k}. \quad (3.5)$$

If the antenna system operates in such a mode, where the spectral density of the received signal corresponds to the spectral density of the physical emitting object itself, then in such a case the temperature of an artificial source is called brightness (or radiobrightness) temperature. We shall postpone the analysis of the relationship between brightness and antenna temperatures in the general form till Chapter 5. And now we note the following important point. Any amplifying instrument, being a physical object at a particular thermodynamic temperature, possesses its natural (thermal) fluctuation electromagnetic radiation in exactly the same frequency band where the amplification of an external signal takes place. Since these two sources (external and internal) are statistically independent, their interaction in the power sense can be reduced to the sum of variances at the amplifier's output. However, in practical and experimental respects it is much more convenient to consider their relationship normalized to the amplifier's input, taking into account the linear gain of a system. Thus, we shall have at the amplifying system's input as it were two statistically independent sources of a noise signal – from the external object under study and from the internal noises of an amplifier. The temperature of the latter source is naturally called the noise temperature of an amplifying system. The total temperature at the amplifying system's input will be equal in this case to the sum of the antenna temperature, caused by the energy from the source under study, and the noise temperature of an amplifier (Figure 3.3(c)). Certainly, the values of these temperatures can differ considerably. So, for studying important wave effects on the sea surface, reliable recording of radiothermal signals in the range from 0.1 to 10–15 K is required, whereas the best amplifying systems have noise temperatures ranging from 300 to 1000 K. The amplifiers, used in everyday conditions (radio receivers, TV sets), have noise temperatures reaching some millions and hundred millions absolute degrees, and they are not used straightforwardly for studying thermal emissions.

In spite of the seemingly artificial character of the temperature ideology introduced in the measurement process, we shall uncover below a serious physical significance of such an approach (see Chapters 4 and 5). This is associated, first of all, with the peculiarities of black-body radiation in the microwave region of the electromagnetic spectrum.

3.4 COMPENSATORY SCHEME OF NOISE SIGNAL MEASUREMENT

As we have already noted, the perfect (and, we note, optimum) device for receiving noise-type signals of various physical natures, including electromagnetic emissions, is the system consisting of the ideal (noiseless) amplifier, a quadratic detector and an integrator (the low-pass filter), that forms signal accumulation. The present measuring scheme is accomplished in all electromagnetic spectrum bands,

beginning from the optical and up to the microwave and lower-frequency bands. Certainly, each band, in accordance with the working wavelength values, possesses its peculiarities, both in radiation receivers and in the general circuitry of an entire device.

However, the presence of unremovable thermal noise radiation in the amplifying device, as well as the fluctuation variations of the gain, essentially changes the basic measuring scheme presented above. This can be demonstrated by the following example taken from recent radio-astronomical practice. The radiothermal signal value, recorded by the RT-22 radio telescope (of the Crimean astrophysical observatory) from the Crab Nebula was equal to 2.5 K, whereas the noise temperature of the receiving device was 300 K with a passband of 1 MHz. Remembering relationships (2.96) and (2.97), we have the signal at the radiometer output in the following form: the constant component is proportional to the sum of the noise temperature of a receiving device and received signal, as well as the residual (after transformation) noise with the variance value equal to

$$\sigma_F^2 = (\bar{V})^2 \frac{1}{2\Delta f \tau}. \quad (3.6)$$

Here account is taken of the fact that the effective passband of a low-pass filter is $\Delta F = \frac{1}{4\tau}$ (see relation (2.72)), and by Δf is meant the total passband of a high-frequency channel. As we have mentioned above, it is convenient to reduce relation (3.6), by means of appropriate calibrations, to the input of the whole receiving system and to consider the relation between the signal determining the intensity of radiation under study and the residual noise component from the same radiation just at the receiving system input. In this case the root-mean-square variation of a noise component will be equal to

$$\sqrt{\sigma_F^2} = (T_N + T_S) \frac{1}{\sqrt{2\Delta f \tau}}, \quad (3.7)$$

and, accordingly, the noise ‘pick-to-pick’ of the Gaussian noise will be $6\sqrt{\sigma_F^2}$. By substituting the aforementioned values of the receiving system’s parameters (for $\tau = 1$ sec) into (3.7), we obtain the root-mean-square variation value as 0.2 K and the ‘pick-to-pick’ value as 1.2 K. Figure 3.4(a) shows the time recording of an output signal at an output of the receiving system of a radio telescope, when the source under investigation passes through the antenna pattern ($T_N + T_S$), and the recording without the presence of a source (T_N). The complexity of the measurement situation is fairly clear: against the background of a great signal (300 K) we must reliably record a useful signal, which is essentially (more than 100–200 times) lower in amplitude. Therefore, we must have an even more sensitive (by an order of magnitude at least) measurement system (in continuous signal). In order to record the small addition to an output signal caused by a useful signal, it was suggested that we compensate for the continuous voltage caused by intrinsic noises of a receiving device, by means of a special source of constant voltage placed at the receiving system’s output. Thus, we arrive at the so-called compensatory scheme of noise signal measurement shown in Figure 3.5(a). This is the simplest scheme for

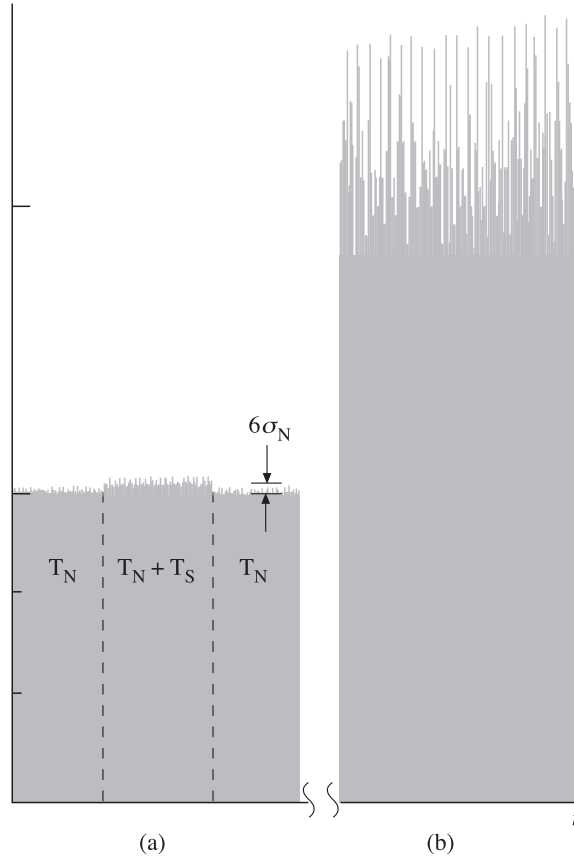


Figure 3.4. The output signal record of a radiometer (in arbitrary units). (a) Record with the square-law detector and the low-pass filter (the integrator); T_N and T_S are noise temperatures of the amplifier and the signal. (b) Record without the low-pass filter.

measuring the noise signal. However, its principal sensitivity is higher than in any other scheme. As an illustration, Figure 3.4(b) demonstrates the situation where the low-pass filter (the integrator) is absent from the system's output. Figure 3.4(b) visually indicates the advantages of using a low-pass filter that we have mentioned above many times (see section 2.8). The physical essentials of the compensatory scheme operation is as follows. As we have seen in (2.95) and (2.96) and in Figure 3.4(a), the output signal consists of a continuous component which is proportional to the intensity of a noise signal formed from the intrinsic noise of an amplifying system, and is equal to

$$\bar{V}_N = \beta\sigma_N^2 = \beta G_N(f) \Delta f = \beta T_N k \Delta f = k_1 G_A(f) T_N k \Delta f, \quad (3.8)$$

where $G_A(f)$ is the linear power gain of an amplifying system. Since this parameter determines the transition and amplification of the Wiener power spectrum of the

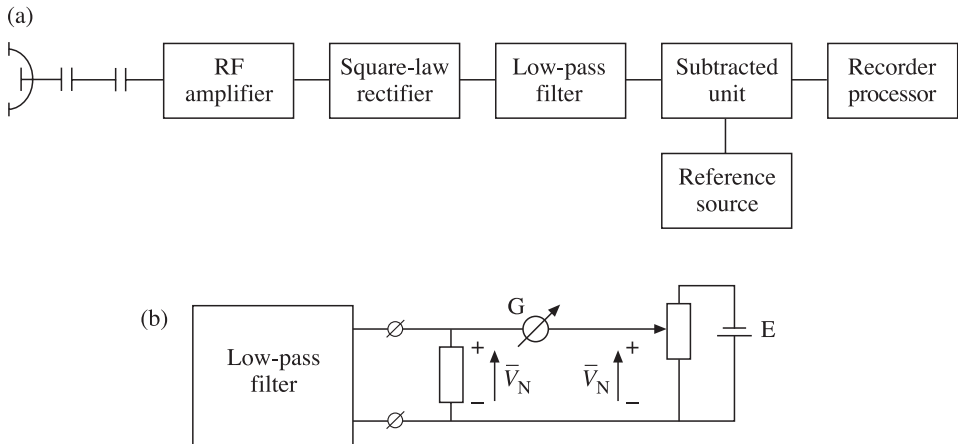


Figure 3.5. Functional scheme of a compensative radiometer. (a) Block diagram of a compensative radiometer. (b) Simplified variant of a subtracted circuit. G is a galvanometer; E is an electric potential source.

original signal, in experimental practice this function is called the frequency response of an amplifying system. It is equal to the square of the magnitude of the transmission coefficient of the high-frequency part of the receiver. Parameter k_1 is the linear transmission coefficient of the remaining components of an amplifying and recording system. The second constant (or slowly varying) component will be determined by the intensity of an external noise signal subject to measurement, and it is equal to

$$\bar{V}_S(t) = \beta\sigma_S^2 = k_1 G_A(f) T_S(t) k \Delta f. \quad (3.9)$$

The fluctuation component at the output will be mainly determined by an instrument's noise, and its RMS can be determined according to (3.7).

To compensate for the continuous component of an output signal caused by an amplifier's noise (3.8), the subtracting unit and the source of a compensatory (reference) constant signal are introduced into the circuit (see Figure 3.5(a)). The simplest version of such a device is presented in Figure 3.5(b); the compensation is accomplished by the voltage from the external electrical potential source. It is such compensatory devices which were the first instruments, historically, in producing the first compensatory radiometers. The compensatory voltage is set up for carrying out measurements of a particular type and does not change, usually, during the cycle of measurements. So, for example, such a scheme has been successfully used in radio-astronomical investigations of the Sun and other powerful radio-emission sources. It is important to note here that, in this case, not only the noises of a receiving device are compensated by relation (3.8), but also the signal caused by the mean value of the intensity of radio-emission of the source itself (for the Sun it equals 6000 K), is compensated by relation (3.9), and the radio-emission variations against the background of a powerful thermal emission of the source are investigated.

Under the conditions of onboard observations of highly spatially varying sources (Earth's radio-emission is an example of such a source), the compensatory techniques used above become rather inconvenient from the viewpoint of experimental implementation. However, the main factor limiting the use of compensatory devices is found to be the fluctuation mode of the system's gain variations (or, as we have said above, the multiplicative interferences). In many cases such interferences eliminate the advantages of compensatory devices. This situation will be described in more detail in the next section.

3.5 THE FLUCTUATION THRESHOLD SENSITIVITY OF RADIOMETRIC SYSTEMS

In this section we shall consider the most important characteristic of radiometric systems – their sensitivity. This characteristic has a lot of equivalent names: the power threshold of sensitivity, the threshold signal, the threshold sensitivity, the fluctuation threshold of sensitivity. A principal difficulty of introducing this characteristic lies in the fact that at the radiometric complex output we have quantities of different orders: a slowly varying signal from useful radiation subject to measurement and the fluctuation signal, being a ‘remainder’ of the noise component after quadratic transformation of both the main signal and the additive noise of an amplifier (see section 2.8 and equations (2.95), (2.96), (3.8) and (3.9)). On the basis of rich observational experience of the radio-astronomers and radio-physicists it was found worthwhile to introduce the following definition of the sensitivity of a radiometric receiver (Bunimovich, 1951; Troitskii, 1951; Esepkinsa *et al.*, 1973). By the threshold sensitivity of instruments for measuring the intensity of the fluctuation electromagnetic radiation is meant such a noise signal at the receiving system's input that is equal in magnitude, at the system's output, to the root-mean-square deviation of the fluctuation signal caused by the intrinsic noises of the amplifying channel.

To make the introduced definition clearer we consider the example of a signal recording at the output of a compensatory device (Figure 3.6). Since the mean value of a signal caused by instrument's noises is balanced, we shall have at the system's output only the fluctuation Gaussian random process caused by the residual transformed noises of an instrument with the root-mean-square deviation corresponding to relation (3.7). At time $t_0 - t_1$ the external noise signal of intensity $\Delta\delta$ arrives, which causes the deviation of a constant level at the system's output equal to one-sixth of the total noise ‘track’ and corresponding to the value of a root-mean-square deviation of the fluctuation component at the system's output. It is the signal of such intensity that represents the threshold sensitivity of a system. Now we shall turn to the quantitative side of the matter.

Let us remember the expression for the total intensity of a random signal at an output of the low-pass filter (see section 2.8 and equation (2.96)). However, it should be remembered that, in contrast to relation (2.96), the mean value of the signal (V_F) will be determined only by the external noise signal ΔT , and the variance of a fluctuation component (σ_F^2) will be determined both by the noises of an instrument

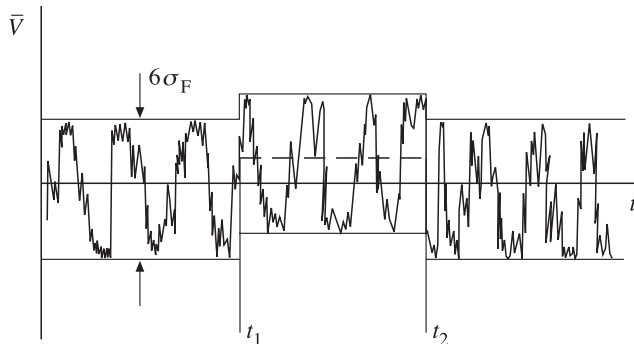


Figure 3.6. The output signal record (Gaussian random process) of a compensative radiometer. The input noise signal that is equal to the sensitivity threshold is given within $t_1 - t_2$. σ_F is RMS variation of noise signal after the low-pass filter (see equation (3.7)).

and by a signal (certainly, it is implied in this case, that the value $\Delta T \ll T_N$). Thus, equating $V_F = \sigma_F$, we have the following important relation for expressing the threshold sensitivity:

$$\Delta T = \sqrt{2} T_N \sqrt{\frac{\Delta F}{\Delta f}} = \frac{T_N}{\sqrt{2\Delta f \tau}}. \quad (3.10)$$

If the time constant of a system equals 1 sec, then the threshold sensitivity is called normalized.

Now we pay attention to the fact that the introduction of the threshold sensitivity definition has been based, primarily, upon the practical experience of the experimenters, radio-astronomers, of separating a weak signal from the background of Gaussian fluctuations by means of visual averaging the time records. Subsequent studies in the field of recognition of signals and patterns have shown that the human eye – brain system represents a quite perfect instrument for separating very weak signals from the fluctuating background.

Now we shall estimate the normalized threshold sensitivity of a radiometric system for studying the continuous spectrum with the following characteristics: $T_N = 300$ K and a total passband of 10^9 Hz. It can easily be seen that the threshold sensitivity will be equal to 7×10^{-3} K, which is quite a high value. In this case it should be recognized that the receiving system can separate the useful noise signal from the background of the noise signal of the instrument having the same statistical characteristics and 4×10^4 times(!) exceeding the useful signal.

Special investigations in the field of sensitive measuring technique have shown that the compensatory scheme of random signal measurement is optimum and has, in principle, a higher threshold sensitivity than any other types of radiometric receivers. However, the further use of such a type of receiving devices has fairly quickly revealed a serious disadvantage of such schemes, associated with the unremovable fluctuations of the receiving system's gain. The physical sense of the noise arising can easily be understood by considering expression (3.9), where the constant

component of a useful signal is proportional to the gain of a system. And, thus, it can be seen from this situation that fairly slow drifts of the gain value, i.e. $G_A(t)$ (or the multiplicative noises), will be non-separable from the variations of a useful signal $T_S(t)$. The occurrence of a fluctuating regime of multiplicative type in amplifying systems is a fully fundamental property and is associated with the physical properties of the instruments which comprise the amplifying system (electronic devices, solid-state instruments). This unremovable fluctuation regime, considered as a random process (or as an unremovable amplifier noise), possesses specific spectral density (the Wiener spectrum), namely, $G_{FN} \propto A/f^\alpha$ ($\alpha \approx 1$, and A is a constant depending on the type of amplifier) called the flicker-noise; and the physical effect itself is called the flicker-effect. A vast and scientific literature is devoted to radio-engineering and solid-state aspects of flicker-effect investigation, and so we shall not discuss this aspect here. Another issue is important for us: this type of fluctuation signal belongs to the so-called ‘colour’ noise (see section 2.5), and its contribution at very low frequencies can be very great because of the logarithmic divergence of the integral for calculating the noise variance (section 2.5). In other words, as the duration of the observation process increases (and, accordingly, the low-pass limit in the integral for calculating the variance decreases), the flicker-noise contribution will sharply grow and can essentially overlap the variations of a useful signal. The qualitative picture of the interrelation between frequency bands of flicker-noise, a low-pass filter, slow variations of a useful signal (V_S), and a low-pass limit of the variance integral (which is equal to the reverse value of the total experiment performing time) is presented in Figure 3.7. Depending on the type of amplifying device (constant A in the expression for the Wiener spectrum for flicker-noise), the detailed picture of the interrelation between the bands can greatly differ, of course. If the experiment performing time is limited, the flicker-noise variance σ_{FN}^2 is also limited, generally speaking, i.e.

$$\sigma_{FN}^2 = \int_F^{F_0} G_{FN}(f) df < M, \quad (3.11)$$

where $\Delta t = 1/F$ is the performing time, F is the low-pass limit of the variance integral and F_0 is the upper limit of the integral and the upper limit of a low-pass filter. Note, that the frequency range $[F_0, F]$ includes all frequency variations of the useful signal and flicker-noise which can be recorded by a radiometric instrument with the given characteristics. If the mentioned frequency range is sufficiently broad (the F_0/F ratio equals two or three orders of magnitude), then there exists some possibility of separating fairly rapid variations of the signal from the background of slow changes in the gain (for example, by additional frequency filtering). However, if the signal varies throughout the frequency range, then the separation of these components is virtually impossible.

For quantitative estimation of the effect of an amplifier’s flicker-noise on the value of a receiving system’s threshold sensitivity, we shall consider expression (3.9), where the relationship between the output signal after quadratic transformation and the system’s gain value is expressed linearly. For this purpose we shall make use of the procedure of finding the correlation function at linear transformation of the

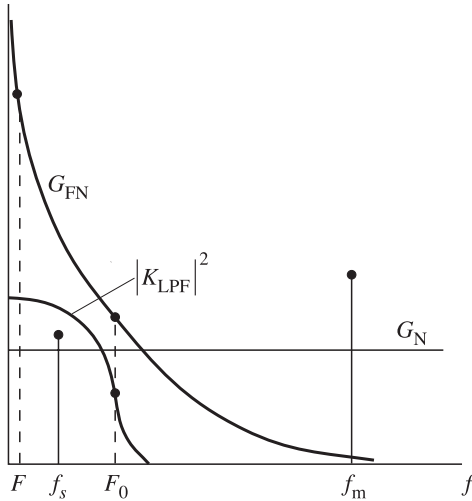


Figure 3.7. The correlation between output spectra of a compensative radiometer (in arbitrary units). G_{FN} is a flicker-noise spectrum; G_N is an amplifier noise spectrum as a result of square-law transformation for input noise signal; f_s is spectral signal component under study; $|K|^2$ is a frequency characteristic of the low-pass filter (the integrator); F and F_0 are frequencies of lower and upper bounds for the variance integral (equation (3.11)); f_m is the modulation frequency for a switched radiometer.

process (see section 2.6). So, for the value of signal variance after linear transformation (2.67) we have, with allowance for (3.8) and (3.11) and a subsequent low-pass filter,

$$B_{LF}^{FN}(0) = \sigma_{LF}^2 = \int_F^{F_0} G_{FN}(f)(k_1 T_N k \Delta f)^2 |\dot{K}(j2\pi f)|^2 df. \quad (3.12)$$

Assuming that in the filter band $|K(j2\pi f)|^2 = 1$, we obtain the estimate for a signal variance caused by the fluctuation regime of a gain (the flicker-noise):

$$\sigma_{LF}^2 \approx (k_1 k T_N \Delta f)^2 \sigma_{FN}^2. \quad (3.13)$$

Using the same methodical approach, as we applied above for determining the threshold sensitivity, we shall estimate the threshold sensitivity determined by the flicker-noise only. For this purpose we shall equate the value of the signal which is caused by the threshold signal at the system's input (3.9), to the value of root-mean-square deviation of a signal caused by the flicker-noise only (3.13). Thus, the threshold sensitivity value caused by the flicker-noise only, is equal to

$$\Delta T_{FN} = T_N \frac{\sqrt{\sigma_{FN}^2}}{G_A}. \quad (3.14)$$

Experiments have shown (Esepkina *et al.*, 1973), that in real amplifiers the flicker-noise RMS equals $\sigma_{FN} \approx (10^{-2} \div 10^{-3})G_A$. Since the output signal fluctuations

caused by intrinsic noises of an amplifier and the fluctuations caused by multiplicative variations of the gain can be considered as independent random processes, the expression for the sensitivity of a compensatory radiometer, with regard to amplification fluctuations, should be written as follows:

$$\Delta T = \sqrt{\Delta T_N^2 + \Delta T_{FN}^2} = T_N \sqrt{\frac{1}{2\Delta f \tau} + \left(\frac{\sigma_{FN}}{G_A}\right)^2}. \quad (3.15)$$

Substituting all the parameter values presented above, we can easily see that the threshold sensitivity equals ~ 3 K, which means that the sensitivity is nearly 400 times lower than the ideal version of an instrument. Such a considerable loss in the equipment sensitivity requires consideration of completely new designs of observational instruments that would eliminate the influence of gain instabilities. The idea arises of some stable pilot-signal which would pass throughout the amplification channel together with the basic signal and, by analysing the change of a pilot-signal, it would be possible to monitor the drifting of the gain and to compensate for them quite quickly. Such a type of instrument, and the technique, were proposed by Professor R. Dicke in 1946. The measuring technique was called the modulation method of noise signal measurement, and the instrument itself was called the modulation radiometer, or the Dicke-type (or switched) radiometer.

3.6 THE MODULATION METHOD OF NOISE SIGNAL MEASUREMENT

The idea of a stable pilot-signal, which, along with the main (working) signal, passed through all transformation stages in a receiving device and, naturally, ‘bore’ in itself all ‘parasitic’ features of the amplification process with their consequent compensation, appeared so attractive in the experimental respect that it is now used in the vast majority of devices intended for recognizing a weak signal and separating it from the background of various parasitic variations in a receiver. So, this methodology is widely used at reception and recording of electromagnetic radiation in a wide wavelength range, beginning at the optical and up to super-low-frequency wavelength. This technique is widely used for the reception of acoustic signals and in mechanical systems (the recording of small oscillations or vibrations). The particular technological implementation of an instrument constructed according to this principle can be quite peculiar in some cases (for example, of hybrid type – the optical-mechanical devices) in IR engineering and Michelson interferometers (Bell, 1972; Persky, 1995)). And with such a complicated technological implementation it is not always possible to isolate directly all principal components of this technique. A fairly rich technical literature is devoted to the applied usage of modulation methods (or their improved modifications). Here we are interested in using this method in radiometric microwave receivers of weak electromagnetic emissions.

3.6.1 Modulation radiometer block-diagram

To implement the basic idea of the modulation method we select the main signal and the stable pilot-signal in time, commuting corresponding sources in succession. For this purpose a new additional device – the modulator (or switch) – is installed before the radio-frequency amplifier. It provides alternate connection of an amplifier input to an antenna and to a special reference noise source (Figure 3.8). The reference source generates, throughout the reception band of an amplifying system, a stable noise signal that is identical in its statistical characteristics to the noise signal of the source under investigation. The most simple and reliable noise source is the radio-physical device called the matched load; this is a waveguide- or coaxial-type device, which absorbs the whole electromagnetic energy falling on it. It can easily be seen that this device is a full analogue of the black body in optics, and the intensity of its emission corresponds to the emission of an absolutely black body (Planck's function). With allowance for the Rayleigh–Jeans approximation in the microwave band, its brightness temperature is equal to the thermodynamic temperature. And, thus, the matched load placed in the thermostat represents an ideal reference noise source.

As a result of receiver input reconnections, the amplified emission is modulated with a special frequency called the modulation frequency. The correct choice of this frequency is of principal importance, of course, since it influences the efficiency of operation of the whole instrument. The reconnection frequency of a modulator is chosen to be fairly high, so that the gain cannot essentially change for one reconnection period (Figure 3.7). Apparatus studies have shown that the frequency of 1 kHz is optimum for the majority of types of amplifiers. The modulation depth depends on the difference between the received and the reference signals. This low-pass modulation of a signal conserves after quadratic detection as well. The special low-pass preamplifier selects the useful signal with a modulation frequency after detection and suppresses noise components caused by the flicker-noise and appearing after quadratic transformation (Figure 3.7). Then the signal at the modulation frequency is delivered to the special detector, which possesses phase properties (a synchronous detector) and is controlled by the reference voltage from the reference voltage generator which, in its turn, controls the operation of a modulator at the system's input. At the synchronous detector output a voltage is generated which is proportional to the difference between signals from the antenna and from a reference source, but without the presence of the flicker-noise of a high-frequency amplifier. The low-pass filter, determining the finite passband (or time constant), is used as a final integrator. In modulation radiometers the useful signal from the antenna comes to an amplifier input during the modulation half-period and, as a result, the effective sensitivity of the radiometer of such a type is twice as bad as the sensitivity of a compensatory radiometer (see below). However, the technological advantages gained in working with an instrument of this type compensates for a small loss in sensitivity.

The frequency and temporal transformations of signals in the given type of instruments are quite complicated. For this reason we shall use below both

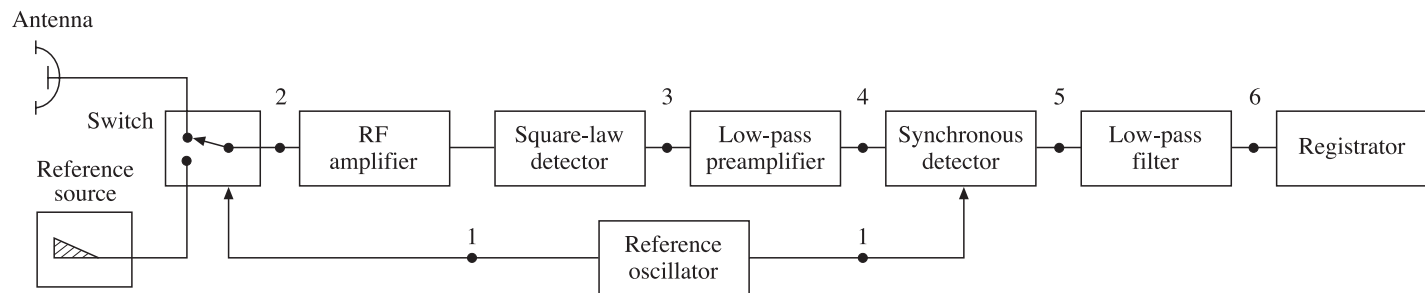


Figure 3.8. Functional scheme (block-diagram) of a switched radiometer. The places where temporal and spectral features of this scheme will be considered in detail are marked by figures.

temporal and spectral cyclograms of device operation when considering the principles of functioning of a modulation scheme.

3.6.2 Temporal and spectral cyclograms

In the block-diagram of Figure 3.8, six points are marked at which we shall consider temporal and frequency transformations of signals. Point 1 (Figure 3.9(a)) indicates the time sequence of a usually pulse signal with a frequency of 1 kHz used for controlling a modulator and a synchronous detector. The Fourier series expansion of this signal gives the following well-known expression (Gradshteyn and Ryzhik, 2000) for the amplitude-phase spectrum of a pulse signal:

$$S(\omega) = U \frac{4}{\pi} \left(\cos \Omega t - \frac{1}{3} \cos 3\Omega t + \frac{1}{5} \cos 5\Omega t - \dots \right), \quad (3.16)$$

where U is the pulse signal amplitude, $\Omega = 2\pi f_M$ and f_M is the modulation frequency. The magnitude of a power spectrum (modulo) of a signal is presented in Figure 3.9(b) (point 1). It can be seen from relation (3.16), that the amplitudes of a spectrum of symmetrical pulse sequence fall as $1/(2N+1)$ ($N = 0, 1, 2, \dots$), and the amplitudes of a power spectrum as $1/(2N+1)^2$. As a result of reconnection at the amplifier input, a high-frequency pulse signal with variable intensity is formed: in one half-period of the modulation frequency its intensity (rather than the amplitude) will be equal to the sum of the antenna temperature of a useful signal (under investigation) and the noise temperature of an amplifier ($T_1 = T_S + T_N$). In the other half-period this intensity will be equal to the sum of the reference temperature (T_0) and the noise temperature of an amplifier ($T_2 = T_0 + T_N$). The diagram in Figure 3.9(a) (point 2) presents the qualitative form of a fluctuating amplitude of emissions whose intensities are equal to T_1 and T_2 , respectively. The spectral form (we should bear in mind that Wiener spectra are being considered here) of this signal is presented in Figure 3.9(b) (point 2). The high-frequency amplifier does not change the qualitative picture (point 2) and only increases the amplitude (and, accordingly, the power) of a signal (as much as millions of times, usually). For clarity, we shall consider each modulation half-period after quadratic detection separately. Each temporal half-period will contain a constant component of a signal, which is proportional to the signal intensity in the given half-period, as well as the components of a transformed signal and flicker-noise, which are identical for each half-period (Figure 3.9(b), point 3). Considering both half-periods simultaneously, we can represent the signal obtained as a single noise signal, which will have the different mean value. Considering Figure 3.9(b) (point 3), we can easily see the important function, which should be executed by the intermediate low-pass preamplifier – (LPPA): it should suppress flicker-components, leaving untouched the components of a pulse signal whose amplitude equals the $T_1 - T_2$ (or, respectively, $T_S - T_0$) difference. Technically this is performed as follows: the LPPA cuts off in the narrow Δf_{LPPA} band the frequency components corresponding to the pulse spectrum, and strengthens them, while suppressing all remaining frequency components, including those from flicker-noise (Figure 3.9(a) and (b), point 4). Such a

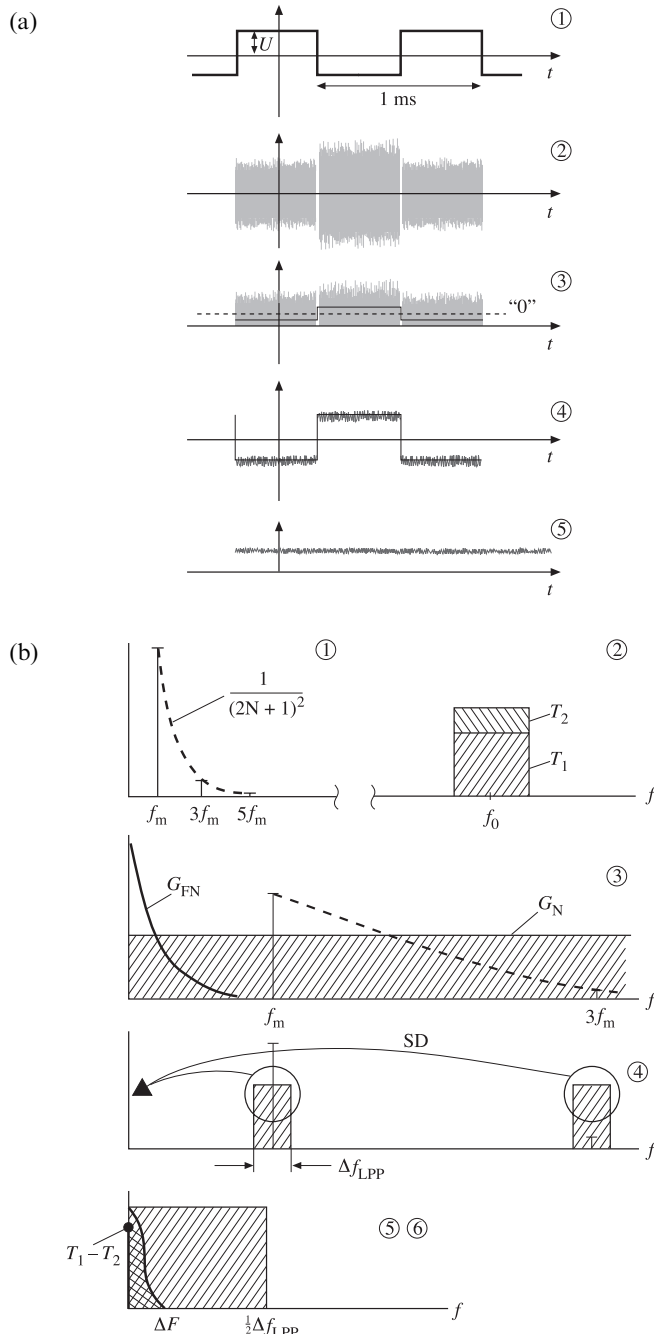


Figure 3.9. Temporal and spectral cyclograms of working for a switched radiometer. (a) Temporal cyclogram. (b) Spectral cyclogram. Figures by diagrams correspond to those places that are marked on Figure 3.8. Notation is explained in the text.

type of a filter-amplifier is called a comb filter. The next important component of a circuit is the synchronous detector. The functions of this component are very important for performing the whole signal processing procedure; therefore, we shall consider its properties in more detail below. Here we point out only the fact that the synchronous detector forms a direct current signal which is proportional to the pulse amplitude with small residual noises in its passband. This procedure is shown qualitatively in Figure 3.9(a) and (b) (point 4). Finally, the signal in the form of the $T_1 - T_2$ difference is formed by means of its passage through the low-pass filter (the integrator) (Figure 3.9(a) and (b), points 5 and 6). It can easily be seen from physical considerations that the LPPA passband has supplementary character during signal processing and should, obviously, vanish in the final result. The detailed calculations indicate that this indeed is the fact.

3.6.3 Synchronous detector

The synchronous detector is a rather critical component of the whole modulation instrument and, therefore, it is expedient to consider the basic principles of its operation. The synchronous detector is a device in which the active parameter oscillates at a frequency equal to the frequency of a delivered external signal, but with arbitrary phase, generally speaking. The simplified wiring scheme of an instrument is presented in Figure 3.10 in the form of a series connection of two active resistances R_1 and R_2 , one of which is variable and controlled by the reference signal. For simplicity, we shall consider the control with a harmonic signal:

$$R_2 = R_0[1 + A \cos(\Omega t + \varphi_2)], \quad (3.17)$$

and the input voltage will also be considered as harmonic:

$$u_1 = u_0 \cos(\Omega t + \varphi_1). \quad (3.18)$$

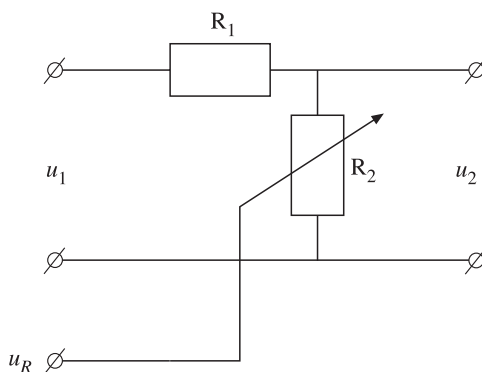


Figure 3.10. Physical presentation of the work of a synchronous detector.

Using Ohm's law and taking into account the simplifying inequality $R_1 \gg R_2$, we obtain the output voltage of the device in the form:

$$u_2 = B \frac{1}{2} \cos(\varphi_1 - \varphi_2) + \frac{B}{A} \cos(\Omega t + \varphi_1) + \frac{B}{2} \cos(2\Omega t + \varphi_1 + \varphi_2), \quad (3.19)$$

where $B = Au_0(R_0/R_1)$.

Of principal importance here is the appearance of the value of an initial signal at direct current (zero frequency) or, in other words, the performing of a strict linear detection procedure. However, the output signal will also depend on the phase difference of initial and controlling signals. In this case it can easily be seen from (3.19) that the signal maximum will be achieved at a zero phase difference, the negative signal will take place at the phase difference of π , and at the phase difference of $\pi/2$ the signal will be absent at the output of the device. Thus, the device is phase-sensitive. This property of a synchronous detector has been actively used in modulation devices both for adjustment work and for external calibration purposes (see section 3.7).

Now we shall consider the operation of this circuit at the rectangular synchronous pulsation of both an input signal itself and a controlling one. For this purpose we shall take advantage of the Fourier expansion of a rectangular pulse, presented above in (3.16), and perform a procedure similar to (3.19). In so doing the constant component of an output signal can be written as:

$$u_2 = B \frac{16}{\pi^2} \frac{1}{2} \left(1 + \frac{1}{9} + \frac{1}{25} + \dots \right). \quad (3.20)$$

The expression in brackets represents the well-known converging series, the sum of which is equal to $\pi^2/8$ (Gradshteyn and Ryzhik, 2000). Thus, the value of a numerical coefficient at constant component will be equal to unity, which is twice as great as for harmonic signals. If one of the signals is harmonic and the second is of pulse-type, then, using the same methodology, it can easily be shown that the numerical coefficient will be $2/\pi$, i.e. the intermediate value, as would be expected. For this reason, as well as according to a number of purely technological circumstances, the purely pulse regimes are used in modulation systems, both for modulation of the main input signal and for its processing at a synchronous detector.

3.6.4 Modulation reception peculiarities

The use of a reference source in modulation instruments for eliminating the parasite effect of the flicker-noise of modulated emission results, however, in some peculiarities in practical observational work. To consider these peculiarities we return to a more in-depth analysis of the signal at point 3 (Figure 3.11) on the temporal diagram. After the quadratic detector, each half-period contains a constant component proportional to T_1 and T_2 , as well as the noise components including

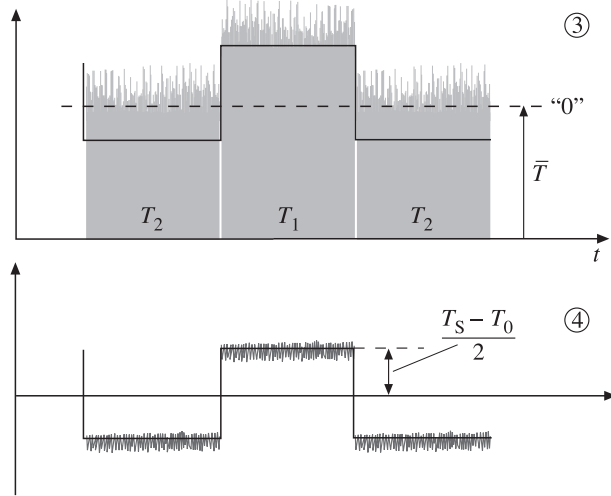


Figure 3.11. Detailed temporal cyclogram for outputs of a square-law detector (3) and a low-pass preamplifier (4).

that from flicker-noise. The constant value of a signal in each half-period can be written as follows:

$$\begin{aligned}\bar{V}_1 &= \beta(\overline{u_1^2}) = \beta k(T_N + T_S) \Delta f \\ \bar{V}_2 &= \beta(\overline{u_2^2}) = \beta k(T_N + T_0) \Delta f.\end{aligned}\quad (3.21)$$

The graphical construction in Figure 3.11 indicates, that the mean value of signal over the whole modulation period can be written as

$$\bar{T} = T_2 + \frac{T_1 - T_2}{2} = T_N + \frac{T_S + T_0}{2}. \quad (3.22)$$

As we have already noted, the most important function of the LPPA is the elimination of this constant component of a signal along with flicker-noise components which are adjacent to the constant component (see the frequency diagram in Figures 3.7 and 3.9(b)). At the LPPA output we have a symmetrical pulse signal with the amplitude proportional to $(T_1 - T_2)/2$ or $(T_S - T_0)/2$, and the fluctuation components passed through the LPPA passband. Expanding the pulse signal into the Fourier series, we shall obtain the analytical expression for a signal at the LPPA output:

$$V_{\text{LPPA}} = \beta k \frac{T_S - T_0}{2} \Delta f \frac{4}{\pi} \left(\cos 2\pi f_M t - \frac{1}{3} \cos 3 2\pi f_M t + \frac{1}{5} \cos 5 2\pi f_M t - \dots \right) \quad (3.23)$$

where by $A_1(t)$ are meant all fluctuation components passed through the LPPA passband. The further transformation occurs in a synchronous detector by

multiplying the signal of (3.23) by a pulse signal and separating the constant component (see above). Remembering relation (3.20), we obtain the signal at the low-pass filter output V_{LPF} in the following final form:

$$V_{\text{LPF}} = \frac{1}{2} \beta k (T_S - T_0) \Delta f + A_1(t), \quad (3.24)$$

where by $A_1(t)$ are meant all fluctuation components passed through the low-pass filter. The analysis of the final relation (3.24) for the modulation instrument gives rise to some important features of this type of measuring devices.

First, the signal in the form of the difference between the signal under investigation and reference signal is recorded at the system's output. If these signals are equal, a zero reading is recorded at the system's output, though the signal under investigation is present at the system's input. Such a 'relative zero' in the receiving system's readings is related to the modulation scheme construction methodology. In this connection, a special type of external calibration is required in receiving systems of such a kind.

Second, the output signal of radiometric receiving systems is calibrated and normalized in the form of a scale of absolute temperature in Kelvins, reduced to the receiving system's input.

Third, because of the presence of phase-sensitive components (modulator and synchronous detector) inside a system, the output signal is also phase-sensitive with respect to the phase of the control signal for a synchronous detector. If the signals for modulator and synchronous detector are phased, then the output signal is positive with respect to the 'relative zero'. If the phase difference equals π (i.e. the signals are in the antiphase), then the signal is negative with respect to the 'relative zero'. If, however, the phase difference equals $\pi/2$, then the useful signal at the system's output is absent (the 'absolute zero'). In the following section we shall demonstrate these features for the example of the calibration of a radiometer.

3.6.5 Threshold sensitivity

As we have noted above, the threshold sensitivity of a receiving system is determined by those noise components that have passed right through a system after quadratic transformation. The spectrum of noise components after quadratic transformation is fairly complicated: it includes both the components from the noise of an instrument and the flicker-noise components (Figure 3.9(b), point 3). The LPPA passes only the components from the amplifier noise linked to harmonic components of a modulation pulse. Since the system under consideration is linear, for calculating the intensity of output (with respect to LPPA) fluctuations we shall consider the signal correlation function at the LPPA output taking into account the fact that the amplitude-spectral characteristics of the LPPA (in power) represents a comb filter (Figure 3.9(b), point 4) in the form of:

$$B_{\text{LPPA}}(\tau) = \sum_{N=0}^{\infty} \int_{(2N+1)\omega_M - (\Delta\omega_M/2)}^{(2N+1)\omega_M + (\Delta\omega_M/2)} G_N(\omega) \cos(2N+1)\omega\tau d\omega, \quad (3.25)$$

where $G_N(\omega)$ is the low-frequency component of quadratic transformation (see section 2.8 and relation (2.92)), $\omega_M = 2\pi f_M$, $\Delta\omega_M = 2\pi\Delta f_M$. As we have already noted, the relationship between the modulation frequency and high-frequency band of an amplifier is such that $f_M \ll \Delta f$. Then we can let $G_N(\omega) = G_N(0)$ (see Figure 3.9(b), points 3 and 4). Besides, in order to almost completely reproduce the pulse signal, it is sufficient to pass, for example, N of its harmonics ($N = 5-7$). Thus, for N and f_M values that are not too high the condition of $Nf_M \ll \Delta f$ conserves for the highest harmonic, and in relation (3.25) the $G_N(\omega) = G_N(0)$ condition can be conserved. After performing integration, we can get

$$B_{LPPA}(\tau) = 2\beta^2 \frac{\sigma^4}{\Delta\omega} \frac{\sin \frac{\Delta\omega_M \tau}{2}}{\frac{\Delta\omega_M \tau}{2}} \sum_{N=0}^{\infty} \cos(2N+1)\omega_M \tau, \quad (3.26)$$

where

$$\sigma_{LPPA}^2 = \overline{V_{LPPA}^2} = 2\beta^2 \frac{\sigma^4}{\Delta\omega} \Delta\omega_M$$

is the variance (intensity) of the fluctuation signal $V_{LPPA}(t)$ at the LPPA output. The signal formed at the LPPA output comes to the input of a synchronous detector and is multiplied by the reference signal having symmetrically rectangular form:

$$V_{SD}(t) = V_{LPPA}(t) \frac{4}{\pi} \left(\cos \omega_M t - \frac{1}{3} \cos 3\omega_M t + \frac{1}{5} \cos 5\omega_M t - \dots \right). \quad (3.27)$$

Now we determine the correlation function of a signal at the synchronous detector output, making use of ergodic properties of the process under consideration (see section 2.2):

$$B_{DS}(\tau) = \overline{V_{SD}(t) V_{SD}(t+\tau)} = \overline{V_{LPPA}(t) V_{LPPA}(t+\tau)} \\ \times \frac{16}{\pi^2} \overline{\left(\cos \omega_M t - \frac{1}{3} \cos 3\omega_M t + \dots \right) \left(\cos \omega_M(t+\tau) - \frac{1}{3} \cos 3\omega_M(t+\tau) + \dots \right)}. \quad (3.28)$$

The mean value of two latter series multiplied by each other can be written as

$$\sum_{N=0}^{\infty} \frac{1}{(2N+1)^2} \cos(2N+1)\omega_M \tau. \quad (3.29)$$

The complete expression for the correlation function is fairly complicated. For our purposes it is sufficient to separate the largest-scale component, which is determined as a constant component in the time-averaging of a product of two series, namely,

$$\sum_{N=0}^{\infty} \cos(2N+1)\omega_M \tau \sum_{N=0}^{\infty} \frac{1}{(2N+1)^2} \cos(2N+1)\omega_M \tau. \quad (3.30)$$

Making the necessary trigonometric transformations, we shall obtain the expression for a constant component of the product of these series:

$$\frac{1}{4} \left(1 + \frac{1}{3^2} + \frac{1}{5^2} + \dots \right) = \frac{\pi^2}{32}. \quad (3.31)$$

Thus, the correlation function of a signal after synchronous detector will contain both a large-scale and a small-scale component, which will be designated by $B(\tau, \omega_M)$:

$$B_{SD}(\tau) = \frac{1}{2} \overline{V_{LPPA}^2} \frac{\sin \frac{\Delta\omega_M \tau}{2}}{\frac{\Delta\omega_M \tau}{2}} + B(\tau, \omega_M). \quad (3.32)$$

Of interest to us is the first item, which determines the part of the spectrum of a signal at the synchronous detector output directly adjacent to a zero frequency. For this purpose, remembering the relation for the spectral density for positive frequencies $G^+(f) = 2\pi G(2\pi f)$ and the relationship between the correlation function and spectral density (2.26), we obtain:

$$G^+(f) = 4 \frac{1}{2} \overline{V_{LPPA}^2} \int_0^\infty \frac{\sin \frac{\Delta\omega_M \tau}{2}}{\frac{\Delta\omega_M \tau}{2}} \cos 2\pi f \tau d\tau. \quad (3.33)$$

The integral can be taken (Gradshteyn and Ryzhik, 2000) under the condition of $0 < f < \Delta f_M / 2$, which is usually satisfied under particular conditions. Thus, taking into account (3.26), we have

$$G^+(f) = 2\beta^2 \frac{\sigma^4}{\Delta f}, \quad (3.34)$$

here Δf is the passband of the basic high-frequency amplifier. Then the variance of a fluctuation signal at low-pass filter's output will be equal to

$$\sigma_{LPF}^2 = \int_0^{\Delta F} G^+(f) df = 2\beta^2 \sigma^4 \frac{\Delta F}{\Delta f}. \quad (3.35)$$

From this relation it is possible to find, with regard to (3.26), the reference deviation (RMS) of the fluctuation signal at an output of the whole receiving system

$$\sigma_{LPF} = \sqrt{2} \beta k T_N \Delta f \sqrt{\frac{\Delta F}{\Delta f}}. \quad (3.36)$$

And, at last, using the conditions of determination of the threshold sensitivity of a receiving system (ΔT) and comparing (3.35) and (3.24), where we let $T_S - T_0 = \Delta T$, we obtain the value of the threshold sensitivity for the modulation receiver:

$$\Delta T = 2\sqrt{2} T_N \sqrt{\frac{\Delta F}{\Delta f}}. \quad (3.37)$$

As should be expected, the LPPA band value dropped out from the final result and the sensitivity of the modulation radiometer was found to be twice as bad as the radiometer of a compensatory scheme. This is explained physically by the fact that due to modulation at the system's input the signal under investigation is present at the instrument's input during half of the observation time only. This implies that the power of a useful signal is two times lower than in the case of a compensatory radiometer, under identical noise properties of a receiving system. However, as we have noted, in this case the modulation scheme possesses serious advantages as compared to the compensatory (ideal) scheme.

For other forms of modulation and demodulation (synchronous detection) the threshold sensitivity will be slightly worse, in virtue of the decrease in transformation coefficients we considered earlier. So, for sinusoidal modulation and demodulation the threshold sensitivity will worsen (with respect to the ideal scheme) – by as much as 2.82 times. By these reasons, rectangular modulation and demodulation is used in the majority of systems for the reception of weak noise radiation.

The detailed analysis of the operation of various schemes of fluctuation radiation reception, apart from those considered above – compensatory and modulation (Esepkinsa *et al.*, 1973) – has shown that, for identical noise and band parameters of a receiving system, the schemes of radiometric systems possess a threshold sensitivity value in the form of relation:

$$\Delta T = \alpha T_N \sqrt{\frac{\Delta F}{\Delta f}} = \frac{\alpha}{2} \frac{T_N}{\sqrt{\Delta f \tau}}, \quad (3.38)$$

where α is the coefficient determining the efficiency of operation of a particular scheme. The compensatory scheme (with $\alpha = \sqrt{2}$) has the best sensitivity. All the remaining schemes give the α value in the range from 2 to 4. The reader can consult the detailed analysis of various schemes in the specialized radio-astronomical and radiophysical literature (see, for example, Esepkinsa *et al.*, 1973).

3.6.6 Null-balancing type

The detailed examination of expressions (3.23) and (3.8) indicates that the essential part of an output signal of the modulation radiometer can be presented in the following form:

$$V_{LPF} = \frac{1}{2} k_1 G_A k (T_S - T_0) \Delta f. \quad (3.39)$$

It can be seen from this expression that flicker-noise can still influence the output signal of a modulation instrument, though in a highly suppressed form. Using the methodology of calculating the threshold sensitivity of a radiometric device with an allowance for flicker-noise, considered above, and taking into account (3.39),

we obtain the expression for the threshold sensitivity of a modulation radiometer with allowance for flicker-noise:

$$\Delta T = \sqrt{T_N^2 \frac{\Delta F}{\Delta f} + (T_S - T_0)^2 \left(\frac{\sigma_{FN}}{G_A} \right)^2}. \quad (3.40)$$

It can be seen from this expression that the flicker-noise effect will be determined by the relation: $(T_S - T_0)/T_N$. If in real observations this parameter is essentially smaller than unity, then we can hope for virtually full compensation and elimination of the flicker-noise effect on measurement results. However, in the regime of onboard measurements of the thermal radiation of the Earth's surface, where the natural background radiation can vary within considerable limits – from 150 K (water surfaces) up to 300 K (forest massifs) – the value of the considered parameter can be significant (from 0.1 to 0.5). And in this case a virtually uncontrollable flicker-noise contribution can already be very noticeable. To exclude this offensive effect, about thirty years ago (1972–1974) the null-balancing schemes of observations in modulation radiometers were proposed both for ground-based and for onboard observations (see Chapter 14). The physical essence of this method consists in the additional introduction of a noise signal into the signal channel. This signal does not differ in its statistical characteristics from signal characteristics and has such intensity that the sum of signals is precisely equal to the value of the reference temperature throughout the measurement cycle. Such a type of measurements is called the null-balancing scheme of measurements. It can easily be seen from (3.40) that such a technique provides a full pay-off in sensitivity for the modulation scheme of measurements. This type of measurements is illustrated schematically in Figure 3.12(a). Almost instantaneous balance between the reference temperature and the antenna temperature has been achieved with the help of an additional noise generator, whose intensity is controlled by the special feedback circuit, for producing the so-called ‘noisy regime’ in a signal circuit. The use of such a regime makes it possible to fairly reliably distinguish and record radiobrightness contrasts up to 0.1 K and lower against the brightness background of the water surface (150 K) (see Chapter 12). Other modifications of a null-balancing regime are also possible. As an example, Figure 3.12(b) shows the input part of a modulation radiometer with controlled noise reference temperature. The horn antenna of the reference channel is pointed to the zenith, thus ensuring the reception of stable radio-emission of the atmosphere at the level of tens of absolute degrees with subsequent addition of radiation (if necessary) from the controlled noise source to provide a null-balancing regime. Such an instrument scheme is used, as a rule, in studying low-noise physical objects, such as the Earth's atmosphere in the centimetre wavelength band, the relic background of the universe, water surfaces with strong water mineralization, and artificial metal surfaces and similar physical objects, which are very ‘cold’ in the radiothermal respect.

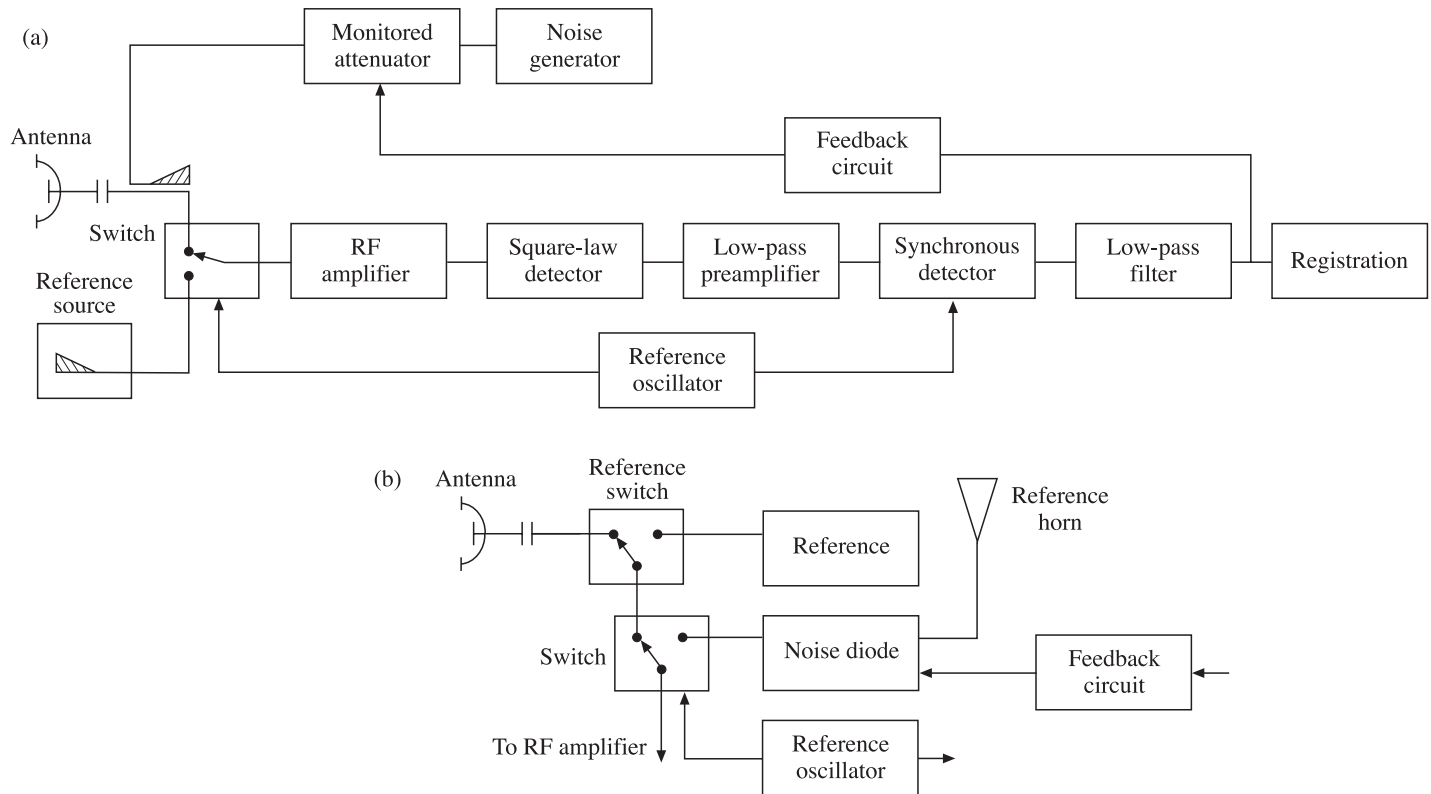


Figure 3.12. Block-diagram of a null-balancing radiometer. (a) The null-balancing scheme with noise balancing in the input circuit. (b) The scheme with noise balancing in the reference circuit.

3.7 EXPERIMENTAL METHODS OF THRESHOLD SENSITIVITY MEASUREMENT

The previous analysis suggests that the basic parameters of a radiometer, which determine its threshold sensitivity, are noise and frequency responses of the main radio-frequency amplifier and the time constant of an output integrator (the low-pass filter). Knowledge of these parameters makes it possible to calculate the expected threshold sensitivity from relation (3.38). In the process of development and adjustment of radiometric complexes a set of measurement procedures has to be performed. They include: the measurement of losses in the input channel and in its separate components; the contribution of separate cascades to the general noise temperature; and the frequency responses of separate cascades and the compatibility of their frequency properties. There is a rich special radio-engineering literature devoted to the theory and practice of such fine measurements. Here we shall propose some practical recommendations for the measurement and estimation of the basic parameters of a radiometric complex, the threshold sensitivity first of all. In observational practice technological circumstances frequently arise in which it becomes necessary to rapidly and reliably check the threshold sensitivity of a radiometric system. As we have noted above, the generally accepted criterion for determining the threshold sensitivity of a radiometric system is the equality of a minimum noise signal at the system's input to the reference deviation (RMS) of output fluctuations of the system (see relations (3.10) and (3.38)). Thus, for experimental determination of the threshold sensitivity it is necessary to record, with the help of a self-recorder or digital recorder, the output signal of a radiometric system with no signal at an input. The recording should be performed at a large enough scale in both axes – of signal and time – so that the fluctuation character (the Gaussian noise) of an output signal may be clearly seen, and then to deliver a calibrating noise signal of known magnitude to an input of the whole receiving system. As a result, we obtain on the self-recorder's tape the record, in the form of a peculiar 'noisy zigzag path', of the normal random process (see Chapter 2) with a calibrating stepwise signal. Thereby, the whole receiving system and its recording section will be calibrated and reduced to the receiving system's input. As an indicative example, Figure 3.13 presents the registration recording of an output fluctuation signal with calibration signals of an onboard high-sensitivity modulation radiometer of 8-millimetre wavelength band (Militskii *et al.*, 1975). All calibration procedures demonstrated below were performed under flight conditions aboard the Russian IL-18 airplane-laboratory in 1975 (see Chapter 14).

In accordance with statistical procedures (Bendat and Pirsol, 1966; Esepkina *et al.*, 1973; Cressie, 1993), the reference deviation can be determined from the experimental data as follows. The readings of output signal a_i are counted from some conventional zero in regular time intervals Δt . It is important that the intervals be (4–5 times) greater than the time constant of an output integrator (τ), since otherwise the neighbouring values of readings will not be independent, and this circumstance can essentially distort the sought result. It is also important to be sure that the 'pure' Gaussian random signal of a receiving system is present at the

system's output, because the application of analogue-to-digital converters, which is widespread now, seriously distorts the original statistics of a signal (Bendat and Pirsol, 1966). An experienced experimenter can usually determine the 'purity' of a signal as a Gaussian one from the form of a noise signal recording. Further on, the mean value, the squares of deviation from the mean value and, finally, the reference (unbiased) deviation are found from n readings (Bendat and Pirsol, 1966) as:

$$\sigma = \sqrt{\frac{\sum_{i=1}^n (\bar{a} - a_i)^2}{n - 1}}, \quad (3.41)$$

where \bar{a} is the mean value. Further, using the known calibration signal, we find the price of an output scale: $k = T_k/a_k$, and then we find the value of a reference deviation (the threshold sensitivity), in absolute degrees, reduced to the receiving system's input, $\Delta T = k\sigma$. The procedure is fairly lengthy, in general, since it requires the digitization of a great number of readings. If the system contains a digital processor in its design, then the aforementioned procedure can be performed automatically and regularly, in accordance with the programme of observations.

As we have noted above, the reference deviation magnitude, measured from a limited realization (the n value) can noticeably differ from the limiting (true) reference deviation value. Experimenters often (and rather successfully) use the other approach associated with the 'three sigma rule' for the normal distribution (see section 2.2). The total ('pick-to-pick') width of noise signal recording for a considerable time interval is determined, in essence, by the probability of the random signal escaping the prescribed interval. Thus, comparing the total pick-to-pick with the price of a scale of an output signal and calculating one-sixth of this magnitude, we obtain a value for the threshold sensitivity of a radiometric system that is sufficient (for practical purposes) and reliable (to a satisfactory accuracy of 15–20%). Figure 3.13(a) demonstrates this procedure for two time constants, 0.25 and 1 sec. The threshold sensitivity has changed (improved), as would be expected, by as much as twice. The next diagram, Figure 3.13(b), presents the registration of an output signal for the same instrument, but with a time constant of 4 sec and two velocities of motion of the self-recording instrument's tape: the left-hand part at a velocity of 1800 mm/hour, and the right-hand one at 240 mm/hour. This procedure is specially performed to demonstrate the characteristic form of the transition exponential process of an output integrator, the full time of which is, as known, of the order of 5τ , or, for the given version of a scheme, 20 sec (the left-hand half of Figure 3.13(b)). The characteristic correlation of signal fluctuations (the 'smooth' signal) is also revealed on the noise track (pick-to-pick) over time scales shorter than 5τ . As the tape motion velocity decreases (or the temporal signal accumulation increases), the character of the signal recording becomes close to the random Gaussian signal (the right-hand part of Figure 3.13(b)). The threshold sensitivity of an instrument lowers twice more. Figure 3.13(c) demonstrates, for the same instrument, the procedures of finding the 'relative zero' of the instrument's output scale and the change of phase (by π) of a controlling signal by a synchronous detector. For this purpose the calibrated source of a noise signal – the matched

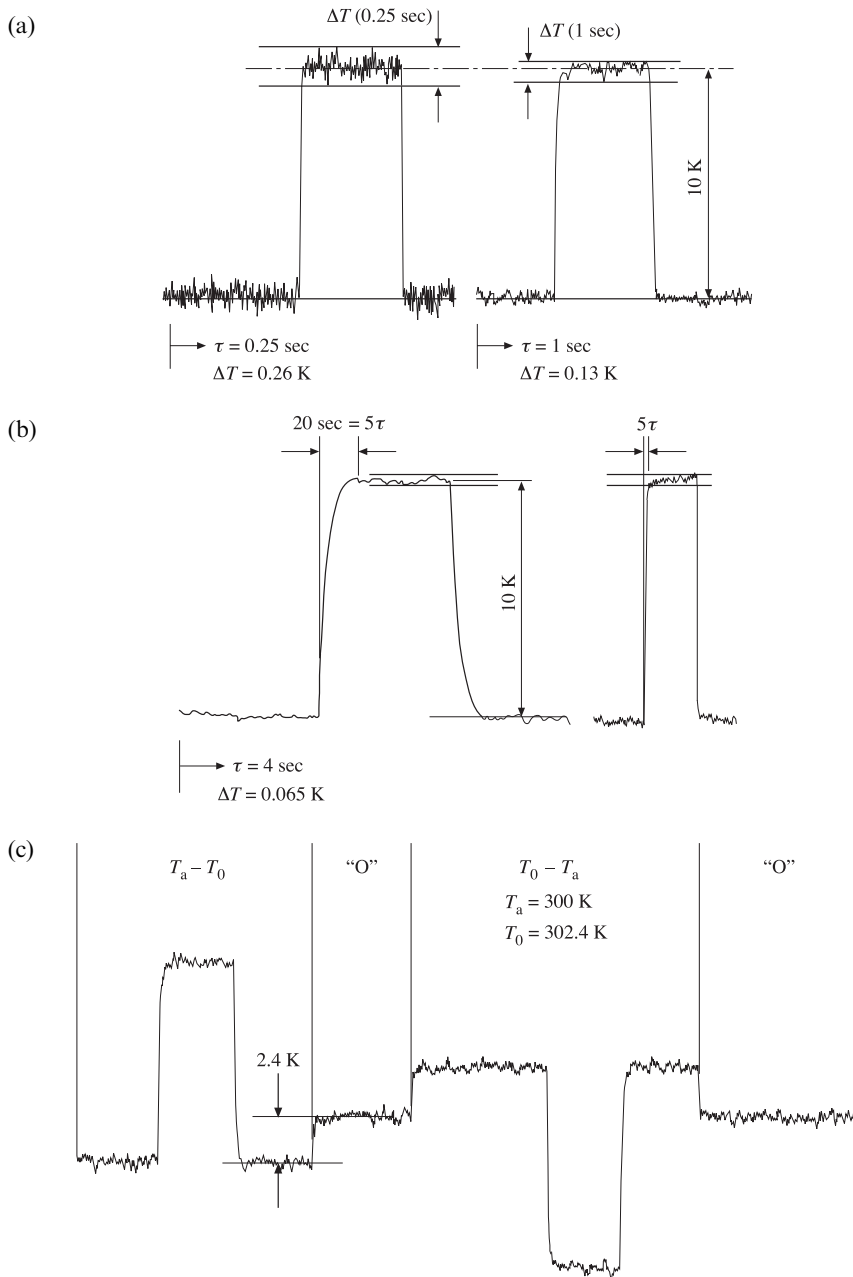


Figure 3.13. Experimental registrogam of an output fluctuation Gaussian signal for calculating the radiometer threshold sensitivity using a 'step input' signal equal to 10 K: (a) for two time constants – 0.25 s and 1 s; (b) for 4 s and for two recording velocities – 1800 mm/h (left) and 240 mm/h (right); (c) the records of a step input signal for two various phases of modulation signal to a synchronous detector. Notation is explained in the text.

load with a fixed thermodynamic temperature of 300 K – was connected to the basic signal channel, and the recording of a signal was performed with a calibrating impulse of 10 K (this part of registration is designated as $T_a - T_0$). To check the accuracy of the reference temperature value and the correctness of setting the ‘relative’ zero, the following procedure was performed. While the synchronous detector was operating, the modulator was set at the fixed position (to the signal channel), and the recording of the signal was accomplished. In this case the signal represented the difference of two identical quantities (T_0) and was, accordingly (conventionally speaking, of course), an ‘absolute’ zero for the output signal scale. This part of the registration is designated as ‘O’ in Figure 3.13(c). The analysis of the registration clearly shows that the merging of two ‘zero’ records took place at 2.4 K (from the calibration step data). Since the input signal (the matched load) was carefully calibrated in advance (300 ± 0.1 K), the mentioned effect is due to the fact that the value of a signal from the reference source was 302.4 K (rather than 300 K, as was supposed earlier). The next part of the recording, designated as $T_0 - T_a$, was performed by changing the phase (by π) of the control signal on the synchronous detector and at the previous phase of the controlling voltage on the modulator. It can easily be seen that, with respect to the ‘absolute’ zero, this recording is mirror-symmetrical to the $T_a - T_0$ recording, which is just as would be expected, strictly speaking. Thus, the example considered above has demonstrated the experimental (under onboard conditions) capabilities of determining: the threshold sensitivity of a radiometric instrument; its time constant; the calibration and setting of its output signal scales; and correcting the reference signal value.

3.8 MEASUREMENT OF THE FREQUENCY RESPONSES OF RADIOMETRIC SYSTEMS BY FOURIER SPECTROSCOPY METHODS

Measurement of the frequency responses of linear amplifying systems are carried out by well-known radiotechnological measurement procedures. However, unlike determinate signals, fluctuation electromagnetic radiation, while possessing a very broad thermal radiation spectrum, occupies the whole passband of a receiving system, including the far wings of the passband. The signal, formed by the whole of this band, is just subject to quadratic transformation. As a result, the effective signal at the quadratic converter output will be proportional to the integral of the square of the power frequency response of the amplification cascade. In order to show this for the frequency response of arbitrary form $G_A(\omega)$, we shall write the expression for the spectral density of a noise signal at an amplifier’s output $G_N(\omega)$, with regard to the matching condition at its input (see section 3.3 and equations (3.8) and (3.9)), as follows:

$$G_N(\omega) = kT_N G_A(\omega). \quad (3.42)$$

In accordance with (2.23) and (2.27), we shall obtain the expressions for the correlation function and the value of the signal variance at the amplifier's output in the form of:

$$B_N(\tau) = \frac{1}{2} k T_N \int_{-\infty}^{\infty} G_A(\omega) \exp(j\omega\tau) d\omega \quad (3.43)$$

$$\sigma_N^2 = B_N(0) = \frac{1}{2} k T_N \int_{-\infty}^{\infty} G_A(\omega) d\omega. \quad (3.44)$$

Based on these relations, we can obtain the expression for the coefficient of noise signal correlation at an output, presented using frequency response of an amplifier, as follows:

$$R_N(\tau) = \frac{B_N(\tau)}{\sigma_N^2} = \frac{\int_{-\infty}^{\infty} G_A(\omega) \exp(j\omega\tau) d\omega}{\int_{-\infty}^{\infty} G_A(\omega) d\omega}. \quad (3.45)$$

Certainly, all the relations obtained can also be written down using the positive frequencies and corresponding frequency response $G_A^+(f)$ only. So, the expression for the correlation coefficient will be:

$$R_N(\tau) = \frac{\int_0^{\infty} G_A^+(f) \cos 2\pi f \tau df}{\int_{-0}^{\infty} G_A^+(f) df}. \quad (3.46)$$

Now we shall write the correlation function of a signal after quadratic transformation (2.88) in the form more convenient for further analysis:

$$B_{SLD}(\tau) = \sigma_N^4 + 2B_N^2(\tau). \quad (3.47)$$

(For simplicity of expression we let the value $\beta = 1$.)

As we have noted, the spectral composition of a signal after quadratic transformation consists of two components: the information component disposed at direct current (a zero frequency), and the component responsible for noise components of a signal. The spectral density of the latter components $G_{SLD}(\omega)$ can be expressed via the correlation function of a signal at the amplifier's output as follows:

$$G_{SLD}(\omega) = \frac{2}{\pi} \int_{-\infty}^{\infty} B_N^2(\tau) \exp(-j\omega\tau) d\tau. \quad (3.48)$$

Making use of relations (2.23) and (2.24), we write down the integral in equation (3.49) as follows:

$$\begin{aligned} \int_{-\infty}^{\infty} B_N^2(\tau) \exp(-j\omega\tau) d\tau &= \frac{k T_M}{2} \int_{-\infty}^{\infty} G_A(\omega') d\omega' \int_{-\infty}^{\infty} B_N(\tau) \exp(-j\tau(\omega - \omega')) d\tau \\ &= \frac{(k T_N)^2 \pi}{2} \int_{-\infty}^{\infty} G_A(\omega') G_A(\omega - \omega') d\omega'. \end{aligned} \quad (3.49)$$

Substituting this relation into (3.48), we obtain the principal expression relating the spectral density of noise components of a signal at the quadratic detector's output with the integral of convolution of the amplitude-frequency characteristic of the amplifier of arbitrary form:

$$G_{\text{SLD}}(\omega) = (kT_N)^2 \int_{-\infty}^{\infty} G_A(\omega') G_A(\omega - \omega') d\omega'. \quad (3.50)$$

In this case the maximum value of spectral density, determining noise components of the detected signal, will be equal (for $\omega = 0$) to the following value:

$$G_{\text{SLD}}(0) = (kT_N)^2 \int_{-\infty}^{\infty} G_A^2(\omega) d\omega. \quad (3.51)$$

Note once again that the maximum value of the spectral density of a detected signal is proportional to the integral of the square of the amplitude-frequency characteristic of a power amplifier. Earlier we obtained the expression from the spectral density for the rectangular band characteristic (2.92) in another way, namely, using the Fourier transformation from a calculated correlation function. It should be noted that, since the rectangular band characteristic cannot be realized physically, the aforementioned results are usually considered as an important model-limiting case. However, in the case of real amplifying devices, expressions (3.50) and (3.51) can be rather complicated. For this reason it was decided, that it would be worthwhile to introduce (Bunimovich, 1951; Esepkins *et al.*, 1973) the notion of the equivalent low-pass band of detected noises (or the radiometric band of an instrument) (Δf_{RAD}) as the ratio of the total power of noise components (at the detector's output) to the maximum value of spectral density. Passing to positive frequencies and to the real amplitude-frequency characteristics of an instrument $G^+(f)$, we shall have:

$$\Delta f_{\text{RAD}} = \frac{2\sigma^4}{G^+(0)} = \frac{\left[\int_0^{\infty} G^+(f) df \right]^2}{\int_0^{\infty} [G^+(f)]^2 df}. \quad (3.52)$$

It can easily be seen from (3.52) that, for the rectangular band, the radiometric band value will be equal to the full absolute value of a band. In the case of other forms of amplitude-frequency characteristics, however, the situation can radically differ from such an idealized (and unfeasible) case (Bulatov *et al.*, 1980).

Remembering the threshold sensitivity determination procedure (see section 3.5), we equate the value of the square of a constant component at a detector's output, determined by the input signal equal to the threshold sensitivity, to the value of variance of a noise signal at the output of a low-pass filter with the effective band ΔF :

$$\sigma^4(\Delta T) = G^+(0) \Delta F. \quad (3.53)$$

After some transformations we shall have the value of the threshold sensitivity expressed via the radiometric band of a high-frequency amplifier and the effective

band of a low-pass filter:

$$\Delta T = \sqrt{2} T_N \sqrt{\frac{\Delta F}{\Delta f_{RAD}}}. \quad (3.54)$$

Since real amplifying devices sometimes have fairly complicated amplitude-frequency characteristics, the necessity arises for a comprehensive and quite simple (in respect of instrumentation) investigation technique. The material presented below is based on the results of experimental works performed at the Space Research Institute under the supervision of the author of this book in 1976–1978 (Bulatov *et al.*, 1980). The physical essence of these techniques is as follows. First, the artificial interference of broadband noise signals is generated at the input of a tested radiometric system; then, the interference signal (the Fourier spectrogram, in essence) is recorded at the output of a radiometric device; and, finally, the total appearance and form of the amplitude–frequency characteristic of the instrument are restored. The principal diagram of the experiment and radiometric instrument is presented in Figure 3.14. The broadband noise signal from the noise generator (conventionally, delta-correlated) is divided in half and delivered to the radiometer's input over circuits of various electrical length. At the radiometer's input, two noise signals, shifted in time relative to each other, are intermixed and enter the input of the amplifier itself with a complicated form of a restricted amplitude–frequency characteristic, which will just ‘impose’ correlation links on the input signal. It can easily be seen from comparison of Figures 3.2(d) and 3.14, that the experimental scheme used is, in essence, an analogue of Michelson's interferometer scheme and can be used for Fourier spectrometry purposes.

Slightly simplifying the situation, we shall consider the interference of noise signals in the so-called ‘quasi-monochromatic’ approximation. By changing the difference of circuit arms $l = l_1 - l_2$, the interference of harmonic signals E and $E \exp(-jkl)$ takes place at the radiometer's input, where $k = 2\pi/\lambda$. The sum of fields at an input is equal to $E_{in} = E(1 + \exp(-jkl))$, and the power in a narrow band of frequencies, df (in other words, the spectral density), is equal to

$$dP \approx E_{in} E_{in}^* df = 2E^2(1 + \cos kl) df \quad (3.55)$$

and, in accordance with (3.5), it is proportional to the input antenna temperature considered in the monochromatic approximation. In this case, the response of a radiometric device (T_Σ), considered throughout the band of an instrument and reduced to the radiometer's input, can be presented as:

$$T_\Sigma = \frac{\int_0^\infty T_N(f) G^+(f) df}{\int_0^\infty G^+(f) df}, \quad (3.56)$$

where

$$T_N(f) = \frac{a_0}{2} + a_1 \cos 2\pi f \tau; \tau = \frac{l}{c}.$$

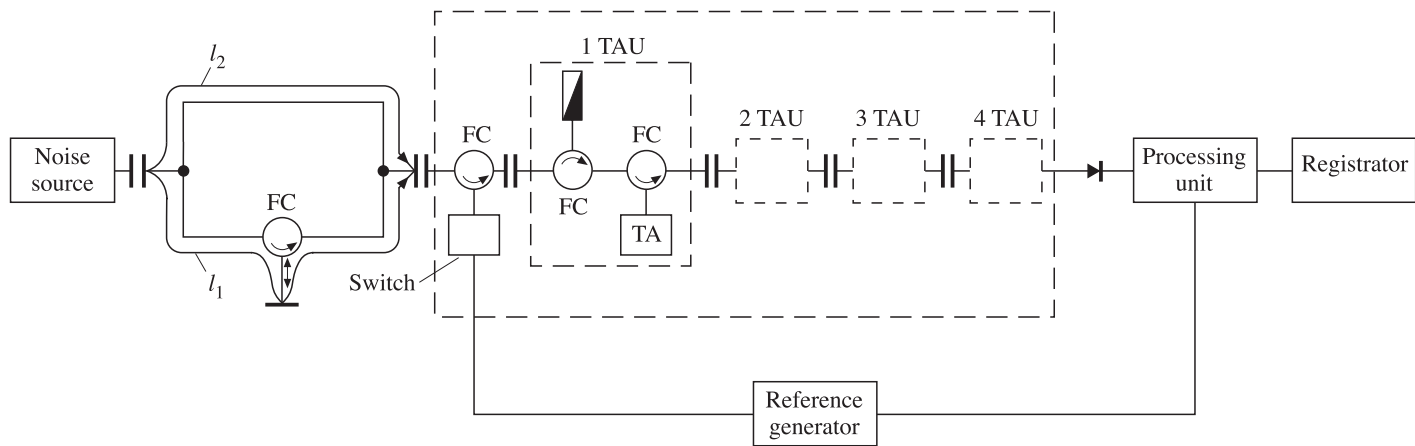


Figure 3.14. Block-diagram of the measurement scheme and the switched radiometer. TAU is a tunnelling amplifier unit; FC is a ferrite circulator (the single-acting device); TA is a tunnelling amplifier (Bulatov *et al.*, 1980).

Substituting this expression into (3.56), we obtain the expression for the system's response in the form of

$$T_{\Sigma}(\tau) = \frac{a_0}{2} + a_1 \frac{Q(\tau)}{\int_0^{\infty} G^+(f) df}, \quad (3.57)$$

where $Q(\tau)$ can be presented as

$$Q(\tau) = \int_0^{\infty} G^+(f) \cos(2\pi f \tau) df. \quad (3.58)$$

It can easily be concluded from this result that for continuous change of the delay between the signals we obtain the experimental registration of a correlation function of an amplitude-frequency characteristic (AFC) of the system's amplifier. Taking into account that the passband of a receiving device is fairly narrow, function $Q(\tau)$ can be presented as a slowly varying rounding (envelope shape), which determines the AFC form, and harmonic filling, which determines the central AFC frequency (see section 2.5):

$$Q(\tau) = q(\tau) \cos 2\pi f_0 \tau. \quad (3.59)$$

Such a separation of the experimental function $Q(\tau)$ into high-frequency filling and rounding (envelope shape) is a very convenient approach, which can be fairly easily performed under experimental conditions (see Figure 3.15(a)). It essentially makes it possible to facilitate further calculations. For symmetrical passbands the form of an amplitude-frequency characteristic in power can be restored (for positive frequencies) as follows:

$$G^+(F) = 4 \int_0^{\infty} q(\tau) \cos(2\pi F \tau) d\tau. \quad (3.60)$$

where $F = f - f_0 > 0$.

Now we consider these procedures for the aforementioned example of the interference pattern data for a direct amplification radiometer (Figure 3.15(a)). To restore the form of the AFC and determine its parameters, the experimental values of a rounding were smoothed by the least squares method and then approximated by the function of form

$$q(\tau) = K(1 + M\tau) \exp(-m\tau), \quad (3.61)$$

where M and m in the case under investigation were equal to $(7.5 \pm 0.3) \times 10^8 \text{ sec}^{-1}$ and $(12.3 \pm 0.4) \times 10^8 \text{ sec}^{-1}$, respectively. Using expression (3.60), we obtain, after some integral transformations, the analytical expression for the form of the AFC of the amplifying system under investigation:

$$G^+(f - f_0) = 4K \left\{ \frac{m}{m^2 + 4\pi^2(f - f_0)^2} + M \frac{m^2 - 4\pi^2(f - f_0)^2}{[m^2 + 4\pi^2(f - f_0)^2]^2} \right\}. \quad (3.62)$$

The form of the AFC obtained (positive frequencies) is presented in Figure 3.15(b), from which we can find the total passband from the level of $3 \text{ dB} - \Delta f_{1/2} = 272 \pm 8 \text{ MHz}$, which to an accuracy of measurement error coincides with the passband measured independently from a sweep-generator ($265 \pm 10 \text{ MHz}$). The form of the amplifying system's AFC differs in principle, of course, from the

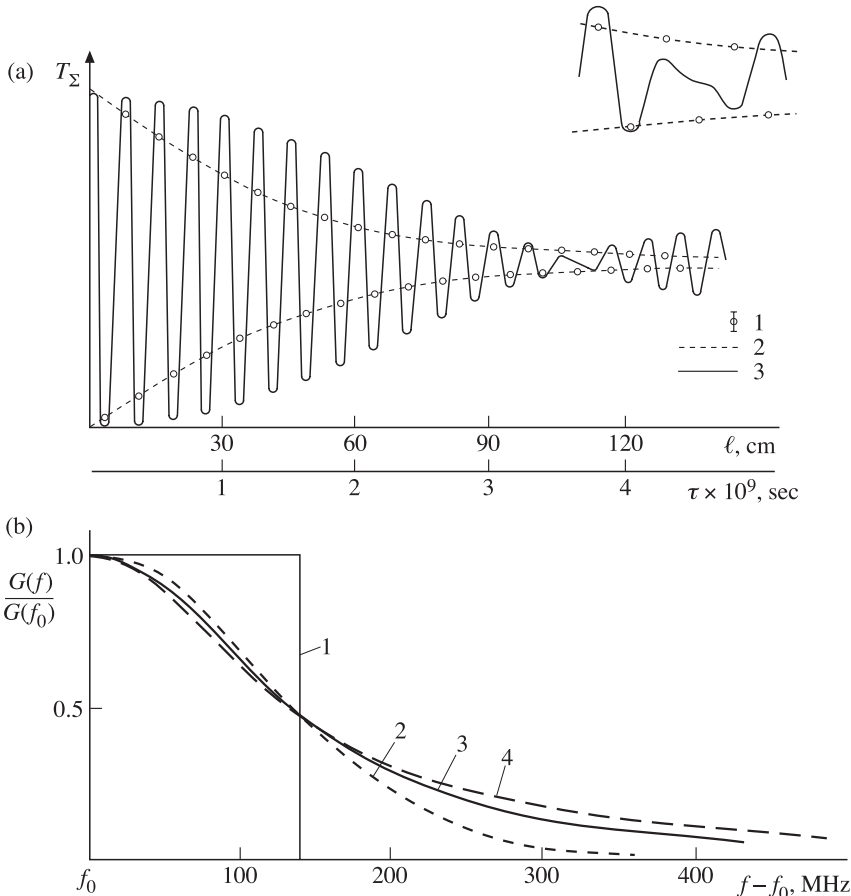


Figure 3.15. Experimental results by Fourier spectroscopy processing. (a) The experimental interferogram. 1: Experimental points (with mean-square errors). 2: The analytic envelope shape (see equation (3.61)). (3) The interferogram of a ‘rectangle’ passband with $\Delta f_{1/2} = 272 \text{ MHz}$. (b) The amplitude–frequency characteristics (AFC) of the same passband at 3 dB level. 1. The ‘rectangle’ passband. 2. The Gaussian shape of AFC. 3. The recovered AFC from experimental results. 4. The resonance (Lorentzian) shape of AFC.

rectangular passband and, accordingly, a rounding zero is absent in the experimental interferogram (see insert in Figure 3.15(a)). Its presence is the characteristic indicator of an idealized rectangular passband, which, as we have noted above, cannot be implemented in a physical experiment. The form of AFC studied is at the intermediate position between the Gaussian and Lorentzian forms of passbands (see section 2.5). The values of AFC parameters can be obtained using the relations we already know:

$$q(\tau) = \int_0^\infty G^+(F) \cos(2\pi F\tau) dF, \quad (3.63)$$

and, as a consequence of (3.49), we have

$$4 \int_0^\infty q^2(\tau) d\tau = \int_0^\infty [G^+(F)]^2 dF. \quad (3.64)$$

Thus, the estimate for the total power passband Δf_{PP} can be found as

$$\Delta f_{PP} = \frac{\int_0^\infty G^+(F) dF}{G^+(0)} = \frac{q(0)}{2 \int_0^\infty q(\tau) d\tau}, \quad (3.65)$$

and for the radiometric passband Δf_{RP} (under the definition given in works by Bunimovitch (1951) and Esepkinsa *et al.* (1973)) as

$$\Delta f_{RAD} = \frac{q^2(0)}{2 \int_0^\infty q^2(\tau) d\tau}. \quad (3.66)$$

Using the expression for $q(t)$ and the parameters found, we obtain the following values of passbands: $\Delta f_{PP} = 382 \pm 19$ MHz and $\Delta f_{RP} = 695 \pm 48$ MHz. The comparison of these quantities with the value of passband $\Delta f_{1/2}$, found from the AFC restoring data, indicates that the power and radiometric bands essentially differ from the $\Delta f_{1/2}$ value due to the power contribution of noise signal components passed through the ‘wings’ of an amplitude–frequency characteristic, i.e. through that part of the AFC which is not quite reliably determined from reference band measurements (for example, by using sweep-generators).

For more complicated frequency transformations in the amplifying system (for example, in the case of the so-called superheterodyne scheme, see section 3.9) the same form of the Fourier interferogram can have a rather intricate appearance, and the restoring of the total AFC form can represent quite a complicated problem.

Thus, the Fourier spectroscopy method enables us, in the case when a fairly simple and accessible experimental technique is available, to obtain reliable values of radiometric and power bands, as well as to reconstruct at full scale the analytical form of the complicated amplitude-frequency characteristics of amplifying microwave devices.

3.9 BASIC CONCEPTS OF AMPLIFYING DEVICES

Prior to considering radiometric systems with extreme sensitivities, we shall briefly outline the basic concepts of microwave amplifying receivers used in onboard radio-thermal and radio-astronomical measurements. Certainly, a vast radio-engineering literature is devoted to these problems. We will be interested here in the qualitative situation only. We make it clear that by a receiving device we mean a purely microwave amplifier (up to the quadratic device). The variety of amplifying devices used can be subdivided, in essence, into three large classes: detector receivers, direct amplification receivers and superheterodyne-type receivers.

3.9.1 Detector receivers

The simplest type of radiometric device is the detector receiver, in which the received microwave fluctuation electromagnetic radiation is immediately directed to the quadratic device, and the input passband of the device is determined by the frequency properties of the antenna system. Such receivers have been applied in radio-astronomy for studying intensive sources (the Sun, for instance), in early onboard radiothermal observations (the investigation of Venus on the *Mariner-II* spacecraft), as well as in receiving systems of the submillimetre band. In these types of receivers, despite high intrinsic noise characteristics, owing to their very broad frequency band (more than 25%), a threshold sensitivity can be achieved (of the order of 2–3 K) which is sufficient for some very important qualitative investigations, for example, for studying the presence of water vapour in the cloudy layer of Venus on the *Mariner-II* spacecraft by microwave techniques, or for searching the signals of extraterrestrial civilizations by microwave techniques in the frequency band of a ‘water hole’. Radiometric instruments of such a type relate to continuous spectrum radiometers and cannot be used for fine investigations of selective emissions.

3.9.2 Direct amplification receivers

Such a reception scheme implies considerable amplification of a signal under investigation in its intrinsic frequency band by means of low-noise receivers. In early radiometers, constructed according to this scheme in 1957–1965 for radioastronomical purposes, travelling-wave tubes, tunnel-type amplifiers and, later (in 1974–1977), low-noise parametric amplifiers have been utilized. The successes in solid-state electronics made it possible to produce quite low-noise (with a noise temperature of some hundreds of absolute degrees), small-sized and low-power-consuming solid-state amplifiers on the basis of field-effect transistors and tunnel-type amplifiers. The experience of designing and using radiometric onboard complexes has shown that such circuit solutions are worth using now up to frequencies of 50–60 GHz.

3.9.3 Superheterodyne-type receivers

The most widespread receivers of the microwave band are the superheterodyne type, since they are much more sensitive than detector receivers, and, at the same time, are fairly simple in technological implementation. The physical principle of the superheterodyne receiver operation was proposed at the dawn of the development of radio-engineering and has been actively applied in receiving devices of various electromagnetic wavelength bands. The essence of the operating principle is as follows. A fairly powerful electromagnetic harmonic radiation from the internal stable local oscillator is delivered to the nonlinear active element, called a mixer (or a frequency converter), at a frequency close to the working frequency of a signal. In relation to a weak input signal the mixer represents a linear element

with harmonically varying active parameters. It can easily be seen that, as a result of such an interaction, we shall have, at the device's output, signals of intermediate and summary frequencies. In this case the whole information load, concluded in the modulation of an input signal amplitude, will be 'transferred' to these frequencies without distortion. A further amplification process occurs at an intermediate frequency by means of intermediate frequency amplifiers (IFA). In this case the signal of summary frequency is suppressed. The value of the intermediate frequency is chosen in the frequency band where there exist low-noise stable amplifiers with the frequency band corresponding to the physical problem under consideration. So, for problems of studying selective emissions this relative (with respect to the input signal frequency) band could be 10^{-5} – 10^{-8} , and for problems of studying the continuous spectrum, 10^{-2} – 10^{-1} . The development of this scheme is the super-heterodyne receiver with a low-noise, high-frequency amplifier at the system's input. Such a scheme makes it possible to obtain in the onboard radiometric systems a record normalized sensitivity of the order of 0.05–0.1 K (see Chapter 14).

The advancement of investigations into the millimetre and submillimetre bands has led to the production of efficient waveguide mixers based on diodes with the Schottky barrier, as well as to using the quasi-optical schemes of mixers with the inclusion of both optical elements (lenses and mirror reflectors), and radiophysical elements (horns, amplifiers). In this case both single and repeated (cascade) frequency transformation is applied.

In concluding this section we notice that progress in designing and producing low-noise receiving systems proceeds with striking dynamics. In the very near future we shall, it seems, witness the production of onboard radiometric receiving systems that use hybrid optical-radiophysical schemes of construction, both for the receiving part directly, and for the information-computation system of onboard radiometric complexes.

3.10 LIMITING SENSITIVITIES OF RADIOMETRIC SYSTEMS

As we have noted above, the limiting sensitivity of radiometric systems is determined by three factors: (a) the sum of the noise temperature of the receiving device and the brightness temperature of the background against which the observations are carried out; (b) the frequency passband of a receiving system; (c) the time constant of the output integrator of a receiving system. Certainly, all these parameters are highly variable, depending on the type of physical problem being investigated and the instrumentation proposed for their performing. In fact, the procedure of optimizing all these parameters for a specific problem is the essence of the observational strategy of an experiment.

Not attempting an analysis of the whole variety of possible physical problems, we shall consider some quantitative evaluations of some of the more contrasting observational situations, which will be useful in the description of particular experiments.

Of course, some of the factors determining the sensitivity of a radiometric system are not completely in the experimenter's control. There is, first of all, the background thermal radiation against which the targeted observations are carried out, as well as the background cosmic radiation (the 'illumination' or 'noises of the firmament', conventionally) and the atmospheric emission. As we shall learn from further considerations, a virtually unremovable radiation comes through the so-called side lobes of antenna systems. If we imagine the possibility of using an ideal (noiseless) amplifier, then in this case the noise temperature in the formula for calculating the threshold sensitivity (3.38) will be determined by the noise temperature of background measurements only. In a real space experiment we have two (apart from the Sun) contrasting versions: the relic background of the universe with a brightness temperature of 2.7 K and 'hot' (certainly, in the sense of thermal radiation) surface covers on the Earth with a brightness temperature of about 300 K (tropical forests, deserts, glaciers). It can easily be understood that some striking results follow from (3.38): with other things (time constant and passband) being equal, the sensitivity thresholds of systems will differ by as much as 100 times (and in investigations of the Sun, 2000 times). Proceeding from this circumstance, the experts (Esepkina *et al.*, 1973; Strukov and Skulachev, 1984, 1986) usually consider reasonable the requirement that the noise of the receiving equipment be not greater than the background noise of the antenna in a particular experiment. Thus, in designing the noise characteristics of radiometric systems it is the radiation the properties of the potential physical objects under study that are taken into consideration in the first place.

The second important factor is the choice and setting of the time constant of an integrator (or the signal accumulation time). Contrast and indicative here may be the values used in the problems of studying the fine features of the radiothermal three-dimensional structure of the relic background of the universe and, for example, in the problems of studying three-dimensional fields of precipitation in the Earth's atmosphere. If in the first type of problems it is necessary to achieve a record sensitivity, of the order of millikelvins (0.001 K), which is caused by the requirements of the physical problem itself (Barreiro, 2000), then for achieving such characteristics the experimenters resort to signal accumulation for about a day ($\tau = 10^4\text{--}10^5$ sec) by using a fairly complicated procedure of signal processing (Strukov and Skulachev, 1986).

The other type of problem – the study of the three-dimensional field of precipitation – requires a maximum spatial resolution up to the 'instantaneous field of view', IFOV (one resolution pixel). In this case the surveying of a resolution pixel from a moving vehicle (airplane or satellite) can take insignificant time, of the order of 0.1 sec, for example. Thus, the sensitivity of a radiometric system, already normalized to pixel surveying time (i.e. the sensitivity in a pixel), will 3.3 times worsen as compared to that normalized for 1 sec. It is this value which is often given in the design instrumentation data (Colton and Poe, 1999). However, in studying the three-dimensional characteristics of Earth's surfaces, the necessity very often arises in comparing the radiation properties of quasi-homogeneous extended objects containing thousands and tens of thousands instantaneous pixels.

In this case the space-like brightness sensitivity is considered. This characteristic will be equivalent to signal accumulation in a number of pixels contained in the image. Of course, this characteristic can be much better than the sensitivity within the confines of the resolution pixel.

The third factor determining the threshold sensitivity of a radiometric system is the passband of a high-frequency amplifier. As we have already noted, this parameter is highly determined by the requirements of the statement of the physical problem. So, for studying the fine features of linear spectra (Chapter 11) a frequency resolution in radiometers/spectrometers is required that reaches 10^{-7} – 10^{-8} of the central carrier frequency. The values of bands are critical for such observations, since even a small expansion of this band for improving the threshold sensitivity can drastically affect the course of the experiment itself. For studying the radiation characteristics of Earth's surfaces (Chapters 8 and 12) the passband value is considerably less critical, and in continuous spectrum radiometers it can vary within considerable limits, virtually not influencing the final result. It can easily be seen that, other things being equal, the threshold sensitivity of spectroscopic instruments is much worse (almost 10^3 times) than in continuous spectrum radiometers. The problem of achieving sufficient sensitivity for spectroscopic instruments is quite topical now.

So, it is necessary to emphasize once again that the value of a normalized threshold sensitivity in itself, certainly characterizes the radiophysical properties of an instrument as a whole, but still does not determine, however, the efficiency of using a radiometric device in any remote sensing problem. From the observational practice viewpoint, of importance are also signal accumulation parameters and the passband (the amplitude–frequency characteristic) and the relationship between them. The ultimate efficiency of a remote sensing instrument can be determined only after detailed joint analysis of instrumentation parameters and spatial-temporal and radiation properties of the physical object under study. In the overwhelming majority of cases the onboard equipment developers have to search for compromise solutions in the construction of onboard radiometric complexes. We shall consider appropriate examples in analysing various types of microwave sensing problems in subsequent chapters (Chapters 8, 11, 12 and 14).

4

Thermal fluctuations and their fundamental laws

The subject of investigation in this chapter is the fundamental law of nature that relates the quantum fluctuation radiation of an object of any physical nature with its dissipative properties in macroscopic scales and is called the fluctuation–dissipation theorem – FDT. Attention is chiefly given to the physical aspect of the problem. Two approaches, which are important for remote sensing and instrumental applications, are analysed in this chapter. They are the quasi-stationary FDT approximation, called the Nyquist formula, and the geometric-optical approximation, the Kirchhoff law. In addition, methodological issues of the application of FDT results under real remote sensing conditions are considered.

4.1 THERMAL RADIATION AND THERMAL FLUCTUATIONS: A HISTORICAL REVIEW

One of the fundamental factors that explains the principal significance of thermal radiation (sometimes called thermal electric fluctuations) in remote sensing and astrophysical applications, is the fairly transparent physical relationship between the recorded radiation and the internal thermal structure of a physical object and its physical-chemical and physical-geometric features. In fact, all fundamental results of both remote sensing (of the Earth and planets) and astrophysics obtained up to the present, are largely based on using the results of remote observation of thermal radiation (thermal fluctuations), which is generated and reveals itself (certainly, in the observational respect) in different parts of the electromagnetic spectrum, depending on its temperature and physical properties. Of course, in addition to thermal radiation, many other electromagnetic emissions either fall from space to the Earth or are formed directly under Earth conditions. These emissions also have a fluctuation character, but are not pertinent to thermal radiation physics. The separation or extraction of various types of emissions from the experimental data

sometimes represents a complicated scientific problem in itself. In this book, as mentioned above, we shall consider thermal radiation issues only.

All physical objects having physical temperatures other than absolute zero are continuously emitting a fluctuating electromagnetic field arising from internal energy, which stipulates the possibility of spontaneous transitions between vibration–rotation levels of molecules in gases, oscillations of molecules in liquid and solid bodies and oscillations of a lattice in solid bodies, with subsequent de-excitation of electromagnetic quanta. The radiation has a typically quantum character and cannot be described within the framework of the classical Maxwellian theory of electromagnetism. The radiation energy covers a very broad range of wavelengths and has (as is usually stated in radiophysics and optics) a continuous spectrum of rather complicated form, the position of maximum of which depends on the thermal temperature of matter. As to terminological approaches, the literature offers a spectrum of names for this radiation: emission, emitted radiation, Planck's emission, black-body radiation, thermal emission, radiothermal emission, radio-emission, grey-body radiation, outgoing radiation.

The study of various parts of the electromagnetic spectrum of thermal radiation, and thermal fluctuations in general, has proceeded rather non-uniformly in the historical respect (Rytov, 1953, 1966; Levin and Rytov, 1967; Schopf, 1978). In studying thermal electrical fluctuations and thermal radiation there are two ranges of questions, the relation between which was elucidated long ago, but only in the early 1950s was it formulated mathematically as a unified theory called the fluctuation–dissipation theorem.

One of the areas we speak about arose considerably earlier in time; it concerns the issues of the thermal radiation of heated bodies considered in the optical wavelength band. Researchers have been interested in the relation between the emitting body and the environment from the beginning of the nineteenth century (P. Prevost, B. Stewart, A. J. Angstrom). But only G. R. Kirchhoff had sufficient insight into the subject to elucidate the primary ideas concerning ‘ray-radiation’ (emission) and absorption. Kirchhoff's work has rested upon a discovery made some months before that event by Kirchhoff and Bunsen: they found that Fraunhofer's absorption lines in the solar spectrum coincided with the lines of emission of known vapours and gases. Kirchhoff himself evaluated his discovery as the proof of the fact that matter outside the Earth consists of known chemical elements. Doubtless, this was one of the first outstanding discoveries in astrophysics (see Schopf (1978) for more details).

One of the fundamental results obtained by Kirchhoff, on the basis of application of thermodynamic laws to equilibrium thermal radiation, was the proof of the fact that the spectral density of this radiation is a universal function of frequency and temperature. The complete determination of the form of the universal function constituted the problem of the next stage of development in thermal radiation theory. The final solution of this problem, based on the quantum hypothesis and resulting in the expression for spectral density of the equilibrium (absolutely black-body) radiation, that is valid for any frequency, was given by M. Planck. The detailed and fascinating presentation of the (sometimes dramatic) history of this discovery was given in a book by H.-G. Schopf (1978).

Another, no less important, result which is very significant for the practice of remote sensing and astrophysical investigations was the theoretical proof, in the geometric-optical approximation, of the law called the Kirchhoff law. This law states that the ratio between ‘emissive’ ability (or radiation intensity) and absorbing ability is identical for all bodies (irrespective of their shape, chemical composition, aggregate state, surface properties, etc.) for a given temperature and for a given frequency. Subsequent investigations have shown that the universal constant in the Kirchhoff law is closely related to the spectral intensity of equilibrium radiation inside the enclosure of a thermostat. At present, several forms of the Kirchhoff law presentation are used in the theory and practice of remote sensing and astrophysical investigations, the physical sense of which is, certainly, identical. Some of these forms will be described in Chapter 6.

Another area where researchers have again (though much later) encountered thermal fluctuations is the so-called ‘noise’ in electrical circuits and, first of all, in amplifying devices, whose noise properties have already been mentioned many times in this book (see Chapter 3). The close relation between electrical noises and thermal radiation lies in the fact that this radiation represents a wave electromagnetic field generated by thermal electrical fluctuations in physical bodies of various natures. The physical explanation of the fact that a unified and rather general theoretical approach to such closely related physical phenomena has been absent for a long time lies in the great distinction between the frequencies of the electromagnetic oscillations of interest in each of the aforementioned areas. The questions related to thermal radiation arose and have been studied as optical problems using the methods of geometric optics (see section 1.6). On the other hand, electrical noise was found experimentally in the band of low radio frequencies, which made it possible to consider them within the framework of the theory of quasi-stationary currents only (see section 1.6).

However, in the 1940s the intensive development of radar engineering gave rise to considerable growth in the sensitivity of radio and radar receiving equipment (Skolnik, 1980; Brown, 1999). This made it possible to reliably record, in the decimetre and centimetre bands, thermal electromagnetic radiation coming from natural physical objects situated both on the Earth’s surface, and in space. It was this technological basis on which the new science – radio-astronomy – arose and continues to progress actively now (Esepkinsa *et al.*, 1973; Ruf, 1999; Barreiro, 2000; Kardashiov, 2000). A little later aerospace radio thermal location (microwave radiometry) and scatterometry of the Earth surface arrived and continue to be efficiently developed (Basharinov *et al.*, 1974; Sharkov and Etkin, 1976; Bass *et al.*, 1977; Raney, 1983; Kalmykov, 1996; Carver *et al.*, 1985; Shutko, 1986; Massonnet, 1996). Thus, the areas of thermal radiation and electrical noise ‘have touched each other’ closely in the microwave band.

Though the existence of electrical fluctuations of thermal origin in radio-engineering circuits and receivers has been obvious since the first steps in the development of Brownian motion theory in statistical physics at the beginning of the twentieth century, their experimental detection became possible as a result of the improvement of radio engineering devices and, first of all, amplifying systems at

the end of the 1920s. In 1927 J. B. Johnson found that at an output of the amplifier, to the input of which the active resistance is connected, additional noise – the chaotic voltage – was observed. As was found out later, this noise is of purely Gaussian type, and its intensity (the mean square – the variance) grows linearly with resistance R at an input and with increasing physical temperature. Almost simultaneously with these experiments H. Nyquist, using the existing physical concept of a random electromotive force (emf), localized in the active circuit, has showed that the spectral intensity (Wiener's spectrum), $G^+(f)$, of the fluctuation emf, localized in the arbitrary passive two-terminal circuit with impedance $\dot{Z}(j2\pi f)$, is

$$G^+(f) = 4kT \operatorname{Re} \dot{Z}(j2\pi f), \quad (4.1)$$

where k is the Boltzmann constant (see Appendix A), and T is the absolute temperature. In such a form, this formula, called the Nyquist formula (or the Nyquist theorem), gives the spectral intensity in the unit interval of positive frequencies and is valid in the non-quantum region of frequencies and temperatures, i.e. for $hf \ll kT$ (here h is Planck's constant, see Appendix A). The rigorous quantum-mechanical generalization of this formula, whose necessity was still pointed out by Nyquist himself, was performed much later, however, as a result of the quantum-mechanical derivation of the fluctuation-dissipation theorem (see, for instance, Levin and Rytov, 1967). The complete form of the spectral density, which is valid both for low temperatures, and for sufficiently high frequencies, $hf > kT$, is as follows:

$$G^+(f) = 2hf \coth \left(\frac{hf}{2kT} \right) \operatorname{Re} \dot{Z}(j2\pi f) \quad (4.2)$$

where $\coth x = (\exp(2x) + 1)(\exp(2x) - 1)$ is the hyperbolic cotangent. From quantum mechanics we know the expression for the mean energy of the so-called quantum oscillator:

$$\Theta(\omega, T) = \Theta(f, T) = \frac{hf}{2} + \frac{hf}{\exp(hf/kT) - 1} = \frac{hf}{2} \coth \left(\frac{hf}{2kT} \right), \quad (4.3)$$

in this case

$$hf = \hbar\omega = \frac{h}{2\pi}\omega.$$

In such a case the Nyquist formula can have the more compact quantum form:

$$G^+(f) = 4\Theta(f, T) \operatorname{Re} \dot{Z}(j2\pi f). \quad (4.4)$$

The further development of the theory of thermal fluctuations resulted in the appearance of a set of derivations of this formula and in far-reaching generalizations, from which it issues as a very simple special case. First of all, we should point out here the transition from concentrated fluctuation forces to detached random fields (both electrical and magnetic, in the general case) and the construction of spatial correlation functions for spectral amplitudes of detached fields in the frequency bands not limited by the quasi-static condition (see section 1.6) (Rytov, 1953). At that time, in the early fifties, H. B. Callen with co-workers proved the

fluctuation–dissipation theorem (FDT), which generalized Nyquist's result: first, to dissipative systems of an arbitrary physical nature; second, to the quantum region of frequencies and temperatures; and, third, to thermodynamic fluctuations described by any number of discrete functions of time. Thus, the possibility of regular application of FDT to distributed physical systems was opened up. This is just what was done a little later when it was applied to the Maxwell equations (Landau and Lifshitz, 1957), and the general FDT formulation was established for the case of distributed dissipative systems (Levin and Rytov, 1967).

Thus, as a result of the ‘merging’ of the two aforementioned directions, the theory of thermal fluctuations (thermal radiation) in electrodynamics represents one of the most important applications of the general theory of thermal fluctuations to arbitrary macroscopic systems. First of all, we shall indicate the principal importance of using this theory in the observational practice of microwave remote sensing, namely in those cases where the size of physical bodies is of the same order as the working wavelength (see section 1.6), and the diffraction phenomena in interaction problems make a noticeable and, sometimes (as in problems of emission and scattering from the wavy sea surface), overwhelming contribution.

Prior to considering the results of the application of the theory of thermal fluctuations to remote sensing, we shall discuss briefly, and mainly at the qualitative level, the physical essence of the fluctuation–dissipation theorem.

4.2 THE FLUCTUATION–DISSIPATION THEOREM: A QUALITATIVE APPROACH

The fluctuation–dissipation theorem is one of the fundamental laws of statistical physics. It establishes for an arbitrary dissipative physical system the relationship between the spectral density of spontaneous equilibrium fluctuations and its non-equilibrium properties, the energy dissipation in a system in particular. The detailed quantum-mechanical derivation of this theorem can be found both in original works by H. B. Callen with co-authors (Callen and Welton, 1951; Callen and Green, 1952), and in a series of textbooks and monographs on statistical physics (Landau and Lifshitz, 1957; Rytov, 1953, 1966; Levin and Rytov, 1967).

To elucidate the qualitative physical issues, it is sufficient to consider the special case where the fluctuations in a system are determined by a single random quantity. We designate it by ξ and assume that at the equilibrium state its mean value is zero. Suppose also, that the system is situated in a thermostat and, accordingly, obeys the canonical Gibbs (J. W. Gibbs) distribution. Further, the interaction with a thermostat is supposed to be weak, so the system's energy can be introduced, which is uniquely determined by the state of the system itself. Using quantum-mechanical approaches, it can be shown that the spectral density of equilibrium fluctuations of the quantity ξ is expressed in terms of the levels of energy E_n of the considered system and magnitudes of matrix elements $\xi_{n,m}$. However, the actual calculation of E_n and $\xi_{n,m}$ for a real macroscopic system requires consideration of the micromechanism of fluctuations, and, generally, for real physical bodies the problem seems to be

virtually hopeless. Note that the intensity of spontaneous internal thermal fluctuations is described by means of E_n and $\xi_{n,m}$. Certainly, the macroscopic dynamics of a system is not reflected at all in any way in the quantum-mechanical structure, since the macroscopic process in a system, by which we mean the average variation of system's parameters $\bar{\xi}$, may be caused in a dissipative system by the external effect of macroscopic forces only.

The theoretical and practical value of FDT consists, in particular, in the fact that for thermodynamic equilibrium systems it gets rid of the necessity to find directly E_n and $\xi_{n,m}$ for a real physical body by expressing the spectral density of fluctuations in terms of a particular macroscopic characteristic of a system – its general susceptibility.

Suppose the system under consideration is disturbed by the effect of the external force $f(t)$. Now let this force be sufficiently small that the macroscopic response can be found from the linearized equation of motion and, accordingly, the spectral amplitude $\bar{\xi}$ to be linearly related with the spectral amplitude of the disturbing force $f(\omega)$:

$$\overline{\dot{\xi}(\omega)} = \dot{\alpha}(j\omega)f(\omega). \quad (4.5)$$

Quantity $\dot{\alpha}(j\omega) = \alpha'(\omega) - j\alpha''(\omega)$, determined by relation (4.5) and called the general susceptibility, is introduced for weak effects allowing for linearization of the macroscopic equations of motion for the physical system under consideration. Since for real $f(t)$ quantity $\bar{\xi}(t)$ should also be real, we have $\dot{\alpha}(-j\omega) = \dot{\alpha}(j\omega)$, i.e. α' is an even function, and α'' an odd one.

Often in physical practice the basic equation for a system is used in the form of macroscopic response for the rate of time variation of the basic parameter of a system, and then the relation for spectral amplitudes of velocity $\dot{\bar{\xi}}(t)$ and external force $f(t)$ is presented as:

$$\overline{\dot{\xi}(\omega)} = \dot{Y}(j\omega)f(\omega), \quad (4.6)$$

where coefficient $\dot{Y}(j\omega)$ is called the admittance of a system. The general susceptibility $\dot{\alpha}(j\omega)$ is associated with the admittance of a system by relation $\dot{Y}(j\omega) = j\omega\dot{\alpha}(j\omega)$ (see Appendix B, equation (B.7)). The reciprocal quantity to the admittance is called the impedance of the system, $\dot{Z}(j\omega) = 1/\dot{Y}(j\omega)$. If we address the theory of electrical circuits (see sections 1.6 and 2.6), then we find that similar parameters are introduced for describing the processes in electrical circuits as well.

The quantum-mechanical consideration of energy dissipation in a system eventually results in the following important relation between the spectral density of fluctuations, $G_\xi(\omega)$, and the general susceptibility, which just expresses the physical essence of FDT:

$$G_\xi(\omega) = \frac{\Theta(\omega, T)}{\pi\omega} \alpha''(\omega). \quad (4.7)$$

Here $\Theta(\omega, T)$ is the mean energy of a quantum oscillator (4.3); in this case the frequencies are considered in the whole frequency band (both positive and negative).

The fundamental relation (4.7) indicates that the spectral intensity of equilibrium fluctuations is determined by the imaginary part of a system's susceptibility,

that is the quantity describing the dynamic behaviour of a linearized macroscopic system beyond any relation with the fluctuations. Note here the following important point: the dynamics of a system under strong external effects, where the macroscopic equations of motion can also be nonlinear, has no relation to thermodynamic fluctuations. So, the macroscopic non-linearity (the deviation from Ohm's law in electrical circuits) can be revealed only for essentially non-equilibrium distribution of current carriers in conductors, or, in other words, beyond the FDT action framework (Levin and Rytov, 1967).

According to (4.7), the total intensity (the variance) of fluctuations in a system is:

$$\overline{\xi^2} = \int_{-\infty}^{\infty} G_{\xi}(\omega) d\omega = \frac{1}{\pi} \int_{-\infty}^{\infty} \frac{\Theta(\omega, T)}{\omega} \alpha''(\omega) d\omega. \quad (4.8)$$

Let us consider now another form of FDT, which is fairly often utilized. It is based on the so-called Langevinian conception of fluctuation forces. (It was this conception that was utilized by Nyquist for deriving his formula (4.1).) These equivalent random forces are introduced into linearized macroscopic equations of motion of a system as a 'reason' for fluctuations, i.e. these forces are introduced along with true external forces. Thus, by quantity $f(\omega)$ in equation (4.5) can be meant the spectral amplitude of a random equivalent force, and equation (4.5) can be understood as the equation relating spectral amplitudes of macroscopic random processes $\xi(t)$ and $f(t)$. Recalling the relation between the spectra of linearly bound processes (2.65), we obtain from relations (4.5) and (4.7) the formula for the spectral intensity G' of the fluctuation force $f(t)$:

$$G'(\omega) = \frac{G_{\xi}(\omega)}{|\dot{\alpha}(j\omega)|^2} = \frac{\Theta(\omega, T)}{\pi\omega} \frac{\alpha''(\omega)}{|\dot{\alpha}(j\omega)|^2}. \quad (4.9)$$

As an example, we shall use this formula for deriving the Nyquist relation. As we noted above (section 1.6), in the general case for linear concentrated circuits the generalized coordinates are the charges q_j and the generalized velocities are the currents $\dot{q}_j = I_j$. The spectral amplitudes of currents I_j and electromotive forces \mathcal{E}_j are specified by Kirchhoff's generalized equations (Krug, 1936; Rytov, 1966)

$$T_j = \sum_k \dot{Y}_{jk}(j\omega) \mathcal{E}_k, \\ \mathcal{E}_j = \sum_k \dot{Z}_{jk}(j\omega) I_k, \quad (4.10)$$

here $\dot{Y}_{jk}(j\omega)$ and $\dot{Z}_{jk}(j\omega)$ are mutually reciprocal matrices of the admittance and impedance k of electrical circuits. If we deal with a single active resistance R , then its admittance is $1/R$ and, accordingly, the general susceptibility is $\dot{\alpha}(j\omega) = 1/j\omega R$, and its imaginary part is $\alpha''(\omega) = 1/\omega R$. Thus, the intensity of fluctuations according to relation (4.9) will be equal to:

$$\sigma^2 = \overline{\mathcal{E}^2} = \frac{2}{\pi} R \int_0^{\infty} \Theta(\omega, T) d\omega. \quad (4.11)$$

In the classical approximation, i.e. when $\hbar\omega \ll kT$ and, here, $\Theta(\omega, T) = kT$, and using the Langevinian conception (4.9), we (transferring to positive frequencies) obtain the well-known Nyquist relation we have already used many times before:

$$\sigma^2 = \overline{\mathcal{E}^2} = 4kTR\Delta f. \quad (4.12)$$

In studying the limiting sensitivity of mechanical systems, such as mechanical gravitational wave detectors (Yamamoto *et al.*, 2001), the same Nyquist formula is used in a slightly different form (certainly, without changing the physical essence of the phenomenon), namely, in the form of the relationship between the thermal noise spectrum and the mechanical response of a system:

$$G(\omega) = -\frac{4kT}{\omega} \operatorname{Im} \dot{H}(j\omega). \quad (4.13)$$

The transfer function, $\dot{H}(j\omega)$, is written as

$$\dot{H}(j\omega) = \frac{\dot{X}(j\omega)}{\dot{F}(j\omega)}, \quad (4.14)$$

where $\dot{F}(j\omega)$ and $\dot{X}(j\omega)$ are the Fourier components of the applied mechanical force and the displacement at the observation point, respectively. The imaginary part of the transfer function represents the phase lag between the force and the displacement, which is related to the dissipation of a system.

Below we shall summarize the basic qualitative components of FDT.

- (1) Any dissipative system of arbitrary physical nature possesses spontaneous equilibrium fluctuations whose intensity is determined by the macroscopic dissipative properties of a system. As examples of various FDT applications to concentrated and distributed systems, we point out the investigations of thermal fluctuations in liquids (Landau and Lifshitz, 1957), in mechanical systems, in plasma, in electronic gas, in hydrodynamics and, which is closest to our subject, the studies of thermal fluctuations of electromagnetic fields (Levin and Rytov, 1967).
- (2) The FDT action spreads to any relationship between frequencies and temperatures, beginning with the classical limit $hf \ll kT$, both for low temperatures and for high frequencies, $hf \gg kT$.
- (3) In applying FDT to the electrodynamics, its action spreads to any relationship between the geometrical size of a system and the working wavelengths of the fluctuation electromagnetic field of radiation. In the case of geometrical optics, $L \gg \lambda$, FDT asymptotically ‘transfers’ into the form of Kirchhoff’s law, and in the quasi-static case, $L \ll \lambda$, into the Nyquist formula (4.1). Surprising is the fact that in the intermediate, most complicated (diffraction) case, $L \sim \lambda$, it was possible to find in the most general case (Rytov, 1966; Levin and Rytov, 1967) a rather transparent relationship between the emissive and absorbing properties of media (Rytov’s formulae) (see section 4.3).

4.3 THERMAL FLUCTUATIONS IN THE ELECTRODYNAMICS

As we have already indicated, the most important application of the general theory of thermal fluctuations in arbitrary macroscopic systems is the theory of thermal fluctuations (radiation) in Maxwell's electrodynamics, as applied, first of all, to microwave sensing problems. There are two important aspects here.

The first aspect is associated with the fact, that the general conditions of the macroscopic electrodynamics applicability will be spread to the similar approach (Stratton, 1941; Landau and Lifshitz, 1957; Levin and Rytov, 1967). First, it is necessary that the inhomogeneities of macrofields (the working wavelength of the electromagnetic radiation) be much larger than the microinhomogeneities caused by the molecular structure of emitting bodies. This requirement is fulfilled for a broad range of electromagnetic radiation, including the band of optical frequencies. Besides, the phenomenological concept of matter as a dielectric continuum (dielectric formalism) (section 1.6) in Maxwellian theory implies the exclusion from the statistical electronics, i.e. from accounting for such parameters as the elementary charge, the number of elementary charges per unit volume, thermal velocities of microcharges, their free path length, etc. Nevertheless, since the electrodynamics part of a problem is solved in this case by means of the general Maxwell equations, the results obtained cover all diffraction phenomena occurring under the given physical and geometrical conditions, including, naturally, the extreme cases as well, for instance, the quasi-stationary approximation and the geometrical optics.

The second aspect concerns the following circumstance. As we have noted above, thermal radiation has a typically quantum character and cannot be straightforwardly described within the framework of the classical Maxwellian theory of electromagnetism. Within the phenomenological theory framework the fluctuation electromagnetic field is represented as the field generated by random 'detached' sources of Langevinian type, distributed in the volume of a medium under investigation (Landau and Lifshitz, 1957; Levin and Rytov, 1967). In spite of using a rather artificial approach – the introduction of detached fluctuation fields – such an approach allows us to formulate any problem on equilibrium thermal fluctuations of electromagnetic quantities as a usual boundary value problem of electrodynamics and, thereby, to use in thermal radiation problems the full power of diffraction electrodynamics. And most striking is the fact that the strict (diffraction) theory of fluctuation fields in electrodynamics can be reduced, in the most general form, to a simple and delicate form of relationship between fluctuation (radiative) and dissipative characteristics of physical media (Levin and Rytov, 1967). Following the aforementioned authors, we shall first consider the contents of the electrodynamic FDT as applied to the electromagnetic field and then the diffraction generalization of the Kirchhoff law.

So, as we have already noted, within the phenomenological theory framework the fluctuation electromagnetic field can be considered as the field generated by random detached currents spread in a medium. To calculate the energy characteristics of the fluctuation field, including spatial characteristics of the fluctuation

illuminated radiation, it is necessary to know the spatial correlation of the spectral amplitudes of these random currents, which, strictly speaking, constitutes the matter of the electrodynamic FDT. Both in distributed and discrete systems, the FDT allows us to associate the correlation functions of detached fields (currents) with the dissipative properties of a system, which are laid down in macroscopic (linearized) equations of the system. If these equations are Maxwellian (see section 1.6), then they just determine the spatial correlation of detached electrical and magnetic fields, and in this case the dissipative properties of a medium will be described by macroscopic constitutive equations of the medium (see section 1.6).

In applying the general theory of thermal fluctuations to the electromagnetic field the conventional form of field equations is utilized (see section 1.6 and equation (1.1)). In this case the conductivity current and free charges are not separated from the polarization current and polarization (i.e. in relations (1.1) quantities j and ρ are supposed to be zero). As far as the fluctuation ‘forces’ are concerned, they can be expressed in different ways, either as detached inductions, or as detached strengths, or as detached currents. If we make use of the last approach, then the macroscopic equations of the electromagnetic field, to which FDT should be applied, are represented by the Maxwell equations of the form (in the Gaussian system of units):

$$\begin{aligned} \text{rot } \mathbf{H} &= \frac{\partial \mathbf{D}}{\partial t} + \frac{4\pi}{c} \mathbf{j}_e \\ \text{rot } \mathbf{E} &= -\frac{\partial \mathbf{B}}{\partial t} - \frac{4\pi}{c} \mathbf{j}_m \end{aligned}, \quad (4.15)$$

where \mathbf{j}_e and \mathbf{j}_m are the detached fluctuation currents (electrical and magnetic), which ‘cause’ thermal fluctuations of all electrodynamic quantities. Many authors have utilized various physical approaches in applying FDT to the electromagnetic theory: the use of the discrete and continuous FDT forms, and the use of the detailed equilibrium principle, as well as a number of indirect physical considerations. The use of various physical approaches results in the following expression for spatial spectral amplitudes of random currents for the isotropic medium:

$$\overline{\mathbf{j}_{ej}(\mathbf{r}) \cdot \mathbf{j}_{ek}^*(\mathbf{r}')} = -\frac{j\omega\Theta(\omega, T)}{8\pi^2} [\dot{\varepsilon}^*(\mathbf{r}) - \dot{\varepsilon}(\mathbf{r}')] \delta_{jk} \delta(\mathbf{r} - \mathbf{r}'), \quad (4.16)$$

where subscripts j and k denote spatial components ($j = k = 1, 2, 3$). Recalling the expressions for the dielectric constant of a medium, this expression can be simplified and reduced to the form:

$$\overline{|\mathbf{j}_e(\mathbf{r})|^2} = \frac{\omega\Theta(\omega, T)}{4\pi^2} \varepsilon''(\mathbf{r}). \quad (4.17)$$

Expressions (4.16) and (4.17) just constitute the matter of the electrodynamic form of FDT, generalized to continuous dissipative systems, in application to the electromagnetic field. The physical essence of these expressions corresponds to the basic matter of FDT, namely: the intensity of electromagnetic fluctuations (electromagnetic radiation) in a medium is immediately directly associated with macroscopic

dissipation properties in a system, which are reflected by constitutive equations of a medium (see section 1.6). Of course, all spatial features of the medium under study, reflected in constitutive equations (the inhomogeneity, anisotropy), will directly stipulate the correlation properties of intensity of detached sources and, certainly, the properties of the field of thermal radiation of a studied physical object, which just will be recorded by an external observer. The developed approaches are valid for the homogeneous medium only under the condition of retaining the prerequisites for the phenomenological description of the medium in Maxwellian electromagnetism. In other words, in this case the medium can be partitioned into physically elementary volumes, which are small when compared with macroscopic inhomogeneities of a medium, but contain a great number of microparticles. Under these conditions the statistical approach to the description of the state of a medium in such elementary volumes is conserved. If the conditions of distribution of microparticles in these volumes are close to equilibrium (see section 4.4) with some local temperature, then formulas (4.16) and (4.17) can also be spread to a non-uniformly heated (nonequilibrium) medium, provided that the temperature in the coefficient $\Theta(\omega, T)$ is a function of a point.

However, from the viewpoint of observational remote sensing practice, the expressions obtained are not sufficient, since they determine the state inside the medium, whereas remote sensing instruments record the electromagnetic radiation escaped from the medium into free space, where the remote-sensing instruments are situated. Since the detached currents are distributed over the whole volume of an emitting body, the obvious method of calculating the external ('illuminated') electromagnetic field consists in using the regular methods of electrodynamics for the region determined by the emitting body's form. However, because we deal with the spatial distribution of detached currents in the medium volume, for the overwhelming number of real media (or physical bodies) the formulation of a complete electrodynamic problem can be very complicated. As we have noted above (section 4.1), the intensities of the field emitted by the medium (which are of interest for us from the remote sensing point of view) can be found by the more simple and physically transparent method developed by Levin and Rytov (1967).

The essence of the method is as follows. The two fields are compared: the radiation field, which is recorded by an instrument in the external (with respect to the medium studied) space, and the supplementary field of the planar wave coming in the direction in which the radiation intensity is of interest for ourselves. Those diffraction fields should be taken as supplementary, which are formed at irradiating the investigated medium by waves issuing from elementary dipoles situated at the outer space points we are interested in. The application of the electrodynamic theorem of reciprocity in combination with FDT results in the universal relations between the spatial correlation functions of spectral amplitudes of the radiation field of the given medium, on the one hand, and the thermal losses (in this field) of the diffraction supplementary field generated by the dipole situated at the observation point. The considered approach is no longer bound by any limitations between the characteristic body size, L , and the working wavelength, λ (as in the case of the

Kirchhoff law and the Nyquist formula), and allows us to find any spatial characteristics of the radiation field at any distance from a body.

If by $\mathbf{A}(\mathbf{r})$ and $\mathbf{B}(\mathbf{r})$ are meant any two of six components of strengths \mathbf{E} , \mathbf{H} of the thermal radiation field, considered at two different distances \mathbf{r}_1 and \mathbf{r}_2 from a body, then the mean value of bilinear combinations of components of strengths of the radiation field is related with thermal losses of the total diffraction field from point sources $Q_{AB}(\mathbf{r}_1, \mathbf{r}_2)$ as follows:

$$\mathbf{A}(\mathbf{r}_1) \cdot \mathbf{B}^*(\mathbf{r}_2) = \frac{2}{\pi} \Theta(\omega, T) Q_{AB}(\mathbf{r}_1, \mathbf{r}_2). \quad (4.18)$$

And if the question is the intensity of radiation of the whole body volume, considered at one point of the outer space and having specific polarization, then (4.18) can be transformed to the integral form:

$$\overline{|E_p(\mathbf{r})|^2} = \frac{2}{\pi} \int_V \Theta[\omega, T(\mathbf{r}_1)] d\mathbf{Q}_{EE}(\mathbf{r}, \mathbf{r}_1). \quad (4.19)$$

where the integral is taken over the whole volume, V , of the emitting body (a medium) with regard to the field of temperature $T(\mathbf{r}_1)$ non-uniformly distributed inside a body. Here $E_p(\mathbf{r})$ is the projection of the fluctuation electrical vector at the observation point P of the outer space with current radius-vector \mathbf{r} on the direction of the dipole moment, and \mathbf{r}_1 is the current radius-vector, determining the point of position of the detached current inside the emitting body. The solution contains both a wave (far) field, carrying the energy away from a body, and a quasi-stationary (near) thermal field, which is concentrated in a layer adjacent to the body surface, whose thickness is of the order of the working wavelength, and rapidly decreases with the distance from a body. The quasi-stationary fields do not participate in the energy transfer (see Chapter 5), but make their contribution to the volume density of energy of the fluctuation field, which sharply grows near the emitting body surface. The diffraction effects, recorded in the far field, as well as the detection and calculation of the quasi-stationary field, represent principally new advantages of the fluctuation electrodynamics as compared to the classical theory of thermal radiation (the Kirchhoff laws).

Formulae (4.18) and (4.19) are, in essence, basic equations to the whole theory of thermal electromagnetic fields. These formulae (sometimes called Rytov's formulae), which relate the second moments of spectral amplitudes of the fluctuation field with thermal losses of the diffraction field of point sources, can be considered as the generalization of the classical expression of the Kirchhoff law to the diffraction region (Rytov, 1966; Levin and Rytov, 1967).

Certainly, to find the diffraction field losses it is necessary, again, to solve the appropriate electrodynamic problems by regular methods. However, these problems are much simpler, than those considered above, where it was necessary to solve the problem on spatially distributed detached currents, i.e. the currents distributed in a complicated manner in the emitting body's volume. In some cases it is possible to use for this purpose either the existing solutions of diffraction problems or the approximate solutions, where some features of a specific problem are used (such as the local

application of geometric optics, the presence of a skin effect, the local scales of surface roughness, etc.).

As an example, we shall consider the results of the solution of the aforementioned problem for the situation, which is often encountered in remote sensing practice. We mean the case where it is necessary to measure the intensity of radiation of the absorbing half-space with a smooth boundary with a remote sensing device standing outside of this space. Such a model situation is a basic one in analysing any experimental data, obtained in sounding the Earth's surface, and for this reason we shall repeatedly return to these results throughout this book. Let the half-space $z < 0$ be filled with an isotropic conducting medium with a complex dielectric constant, and in the region $z > 0$ the medium is isotropic too, but it is transparent with the real index of refraction, n (see section 1.6). For the wave field, i.e. the radiation field, which can be recorded by the external (with respect to the emitting medium) instrument, the solution of the fluctuation electrodynamic problem should result immediately in the Kirchhoff law. In addition, the solution will also contain the quasi-stationary field components, which, however, very rapidly decrease with the distance from the surface and make no contribution to the energy flux. The experimental recording of such a field is a rather complicated and ambiguous problem. In accordance with the developed methodology (Levin and Rytov, 1967), the electrical and magnetic dipoles with corresponding dipole moments are placed at any point of the transparent half-space (over the planar boundary), and then it is necessary to find the diffraction field losses in the emitting half-space. This problem, called Sommerfeld's problem, is a classic one in the problem of radio wave propagation over the Earth's surface (Stratton, 1941; Alpert *et al.*, 1953).

The complete solution of this problem leads to the following result: the power characteristics of the fluctuation thermal field in the far region (the radiation zone), the Poynting vector in particular, do not depend on the distance from the medium and can be expressed, for a fixed direction and fixed body angle, as the radiation intensity (see Chapter 5 for more details) as follows:

$$I_\omega = I_{\omega 0} n^2 (1 - |R|^2), \quad (4.20)$$

where by $I_{\omega 0}$ is meant the equilibrium intensity formed inside the emitting body, R is the Fresnel coefficient of reflection of a planar electromagnetic wave from the smooth boundary of the emitting medium (with account taken of polarization and the angle of observation), and n is the index of refraction of a transparent external medium. The expression presented is, in essence, the Kirchhoff law for radiation of the absorbing half-space. The physical sense of this relation is fairly transparent: the formed equilibrium intensity of an infinite half-space undergoes reflection at the planar interface boundary. In this case the value of the energy, reflected inside the medium, will be equal to $I_{\omega 0} |R|^2$. Thus, the energy will be illuminated into the outer space and recorded by a remote instrument in accordance with relation (4.20).

4.4 LOCAL THERMAL EQUILIBRIUM

As we have already noted, FDT is valid for systems with thermodynamic equilibrium. In statistical physics by thermal equilibrium is meant the physical state, into which any closed macroscopic system comes after a fairly long time interval has elapsed. At thermodynamic equilibrium the detailed balance is established; that is, any elementary process in a system is balanced by the corresponding reverse process. The detailed balance takes place for the processes, which change the kinetic energy and the direction of motion of both the macroscopic particles of a system and the state of elementary particles, atoms, molecules and ions, and the state of their excitation for the processes of ionization and recombination, dissociation and formation of molecules, etc. At the thermal equilibrium state the parameters of a system do not change in time; however, they can undergo thermal fluctuations about their mean values. The thermal radiation arises under the detailed equilibrium conditions in a substance from all non-radiating processes, i.e. from various types of collisions of particles in gases and plasma, and from exchanging energies of electron and oscillatory motions in liquids and solid bodies. From the detailed balance of processes follows a spectrum of important physical consequences which are expressed as theorems and laws. They include, first of all, FDT, the Planck law of radiation, the Kirchhoff law of radiation, the Stefan–Boltzmann law of radiation, Boltzmann's distribution of particles over energies, Maxwellian distribution of particles over velocities, the law of energy equidistribution a system's degree of freedom, the ergodic hypothesis. In this case the temperatures, appearing in formulae describing these laws and distributions, are identical in all parts of the equilibrium system and for all sorts of particles, i.e. the temperature *of the whole system* is meant here.

In the real physical reality, however, for the majority of physical bodies the conditions of conservation of thermodynamic equilibrium are absent, generally speaking. This indicates that any physical body emits from its surface some specific portion of the electromagnetic energy which arises inside a body due to physical-chemical reactions, to internal heat sources, to mass transfer inside a body and to other causes. The outgoing energy flux, which exists in such cases, and, accordingly, the gradient (drop) of temperatures between internal and external parts of a system are directly incompatible with the notion of full thermal equilibrium.

The important supposition (hypothesis) on local thermal equilibrium (LTE) is used for similar physical objects. According to this hypothesis, the temperature is different in different elements of a studied medium; there exists the outgoing energy radiation flux (the radiation field is anisotropic), but in this case equilibrium is conserved in very small (elementary) volumes of a medium. But these volumes still contain such a great number of particles (macroscopic particles, molecules, atoms, ions, etc.), that their state can be characterized by the local temperature and other thermodynamic parameters. In their turn, these parameters in macroscopic scales are not constants, but depend on coordinates and time. But in each elementary volume a detailed balance is established, which is determined by the local value of

temperature, and in this local scale all physical corollaries of the detailed balance (such as FDT, Boltzmann's and Maxwell's distribution laws, the Kirchhoff law of radiation, etc.) are valid. At the local thermal equilibrium of a medium's elements the state of the medium is one of nonequilibrium, in general. So, under these conditions the thermal radiation is characterized by the value of the temperature at a given point (locally), but the thermal radiation is not in thermal equilibrium with the substance at the scale of the whole body (or medium) under study. In such a case the emission of radiation into the external space and the redistribution of the temperature regime inside a body (or medium) are possible. To maintain the stationary state, in which the gradient thermal field is conserved, the thermal energy losses must be replenished at the expense of extraneous (and, probably, internal) sources.

The reason for the application of the LTE hypothesis to physical objects both on the Earth, and in space lies in the circumstance that the radiation absorbed by an elementary volume of the medium is greatly reprocessed into different forms of energy before it leaves this volume (i.e. is illuminated). As is known from the thermodynamics, such a reprocessing at the scale of the elementary volume proceeds in the direction of establishing thermodynamic equilibrium. So, the whole absorbed portion of radiation energy falling on the opaque solid body is rapidly redistributed over internal energy states in accordance with the local equilibrium distribution inside the solid body. In gases the absorbed radiation energy is redistributed via various kinds of collisions between gas particles: atoms, molecules, electrons and ions. In the majority of cases such a redistribution proceeds fairly rapidly, and the energy levels of gas will be populated in accordance with the equilibrium distribution corresponding to local conditions (Sobolev, 1997).

The local thermal equilibrium is a good approximation to reality for many physical objects and their separate sections. Examples of such objects are: the Earth's atmosphere, surfaces of the Earth, various astrophysical objects. The LTE hypothesis greatly facilitates the calculation of radiation characteristics of such kinds of media (using the so-called LTE models). Certainly, there exists a spectrum of physical conditions in which the LTE assumption is invalid. Examples of such conditions are: (1) highly rarefied gases, in which the rate and efficiency of collisions of particles resulting in redistribution of absorbed energy are low; (2) very rapid non-stationary processes with high gradients of parameters, in the course of which the population density of energy levels has no time to come into correspondence with new conditions; (3) extreme radiation fluxes, in which the absorption of energy and the population density of the upper energy levels are so great, that, owing to collision processes, the equilibrium population density of lower levels will not be achieved. Giving the LTE hypothesis up (in the so-called NLTE models) it becomes necessary to investigate the relations between collision and radiation processes and their influence on the energy distribution between various levels, which represents a fairly complicated problem. Such investigations are carried out in studying shock waves (large gradients), nuclear explosions (non-stationary processes, large gradients, extreme fluxes), gas dynamics of flights at high altitudes and in outer space (very low densities). The greatest deviation from LTE conditions is observed in laser and maser sources, in which the substance with a metastable energy level is

excited by the external source. This is because the excited state is metastable and is chosen such that the population density reaches values that essentially differ from equilibrium values (the inverse population density), and is then illuminated into the external space in a coherent manner.

Such problems are of special interest and are not considered in this book. We shall suppose here that the local thermal equilibrium exists in the media we shall investigate later.

Applying the aforementioned radiation laws under local thermal equilibrium conditions to emission and absorption of thermal radiation in physical bodies, we can study radiation transfer processes both inside and outside the physical body, within the framework of the so-called phenomenological theory of radiative transfer (Chapter 9). The significance of this theory for remote sensing problems and astrophysical applications can scarcely be exaggerated. In fact, all fundamental results in remote sensing (and, largely, in the astrophysics) obtained so far are based to an overwhelming extent on the use of the methodology and interpretation of conclusions of the theory of radiation transfer under local thermal equilibrium conditions.

5

Emission fields and antenna systems

The purpose of this chapter is to consider the basic characteristics of the emission field of natural objects and the physical features of receiving the emission by microwave antenna complexes. Using the method of equivalent circuits, the basic notions of brightness and antenna temperatures are introduced, which have been widely used in the theory and practice of passive microwave remote sensing and in radio-astronomy. The basic data on radio-astronomical instruments and antenna complexes are presented. On the basis of spatial-spectral notions, the antenna smoothing equation is introduced and the procedures of restoring radiothermal images are analysed. On the basis of passive microwave remote sensing experience, the basic methods of measuring the parameters and calibrations of onboard antenna systems are introduced and analysed.

5.1 BASIC CHARACTERISTICS OF THE EMISSION FIELD

The analysis of radiative transfer in natural media essentially differs from the standard formulation of the problem of propagation of waves in electromagnetism as planar waves (see section 1.6). This is, first of all, due to the fact, that at each point of the medium (or of the medium's surface) the propagation of emission cannot be represented by a single vector. In order to characterize the emission falling on a given point, it is necessary to know the emission from all directions and, in addition, it is important to take into account the solid angles from which the external radiation falls on an elementary volume, and the solid angle from which the observation and recording of emission will be carried out. For this reason, to describe the amount of radiation energy transferred in the given direction per unit time and inside an infinitesimal solid angle, in remote sensing, astrophysics and heat exchange problems a fundamental physical quantity is introduced, which is called the spectral (monochromatic) radiation intensity. This quantity is introduced in a

strictly differential form, and then, on its basis, a spectrum of integral quantities is introduced which are widely used in the theory and practice of remote sensing, in astrophysics and radio-astronomy, as well as in heat exchange problems (Troitskii, 1954; Chandrasekhar, 1960; Sobolev, 1963; Siegel and Howell, 1972; Ozisik, 1973; Marchuk, 1976; Ulaby *et al.*, 1981, 1982, 1986; Kondratyev *et al.*, 1995; Apresyan and Kravtsov, 1996; Thomas and Stamnes, 1999).

5.1.1 Spectral intensity

For the determination of spectral intensity we shall consider the elementary area dA around the point of space with coordinate \mathbf{r} , which is characterized by unit vector \mathbf{n} in the direction to a normal (Figure 5.1). Let dE_ν be the quantity of the energy of radiation in the frequency band between ν and $\nu + d\nu$, which propagates inside an infinitesimal solid angle $d\Omega$ in the direction of vector $\mathbf{\Omega}$ and passes through the elementary area dA (here we have in mind the total radiation, i.e. the external radiation passing through the area and the thermal radiation of the object, as well as the radiation reflected by the area) for the time interval from t to $t + dt$. Designate by θ the polar angle between the unit vector \mathbf{n} and the radiation propagation direction $\mathbf{\Omega}$. The spectral radiation intensity $I_\nu(\mathbf{r}, \mathbf{\Omega}, t)$ is defined as the following limit:

$$I_\nu(\mathbf{r}, \mathbf{\Omega}, t) = \lim_{dA, d\Omega, d\nu, dt \rightarrow 0} \left[\frac{dE_\nu}{dA \cos \theta d\Omega d\nu dt} \right]. \quad (5.1)$$

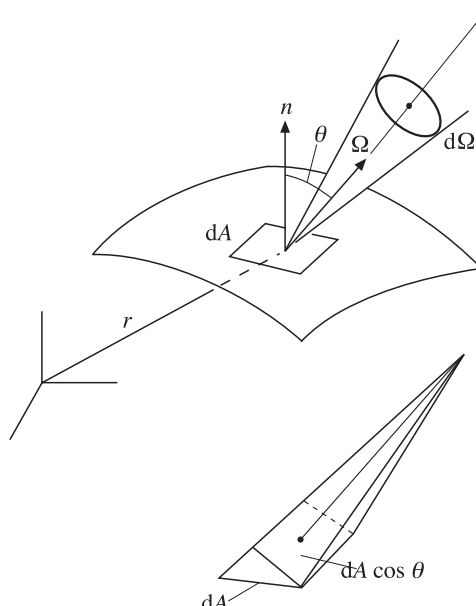


Figure 5.1. System of axes for the determination of spectral intensity. See explanations of designations in the text.

In this expression $dA \cos \theta$ is the projection of surface dA on the plane perpendicular to direction Ω . Note that in this definition the intensity is determined in terms of a surface projection on the observation direction Ω . The determination of radiation intensity with respect to the surface element area (as was done here) has an important physical advantage, namely, the equal intensity of emission of an ideal black body in all directions (see, for example, Siegel and Howell, 1972). Of course, the intensity of natural objects depends on the radiation propagation direction, and for this reason the functional dependence on the observation direction Ω is introduced into definition (5.1). Generally speaking, the angular dependencies of radiation intensity are, as we shall see soon, a very important information parameter for determining the physical properties of objects from remote measurement data.

According to expression (5.1), the spectral intensity is equal to the amount of radiation energy (in appropriate units, see Appendix A) passing through a unit area perpendicular to the propagation direction Ω , inside a unit solid angle whose axis coincides with direction Ω , in a unit frequency band which includes the working frequency ν , and per the unit of time.

The dimension of the quantity considered in the SI system is $\text{W m}^{-2} \text{Hz}^{-1} \text{sr}$.

If the radiation intensity emitted by the surface element or falling on it, is considered within the finite frequency band, lying between ν_1 and ν_2 and inside the solid angle concluded between $\Omega_1(\theta_1, \varphi_1)$ and $\Omega_2(\theta_2, \varphi_2)$, then the quantity

$$\int_{\nu_1}^{\nu_2} \int_{\varphi_1}^{\varphi_2} \int_{\theta_1}^{\theta_2} I_\nu(\mathbf{r}, \theta, \varphi, t) \cos \theta \sin \theta d\theta d\varphi d\nu \quad (5.2)$$

represents the amount of radiation energy, falling on a unit surface area or emitted by it per unit time, within the frequency band from ν_1 to ν_2 inside the solid angle from Ω_1 to Ω_2 . The elementary solid angle $d\Omega$ in polar coordinates equals

$$d\Omega = \sin \theta d\theta d\varphi, \quad (5.3)$$

where θ is the polar angle between the emission direction and the normal to the surface, and φ is the azimuthal angle around the normal. Then expression (5.2) can be presented in the following standard form:

$$\int_{\nu_1}^{\nu_2} \int_{\varphi_1}^{\varphi_2} \int_{\mu_1}^{\mu_2} I_\nu(r, \mu, \varphi, t) \mu d\mu d\varphi d\nu, \quad (5.4)$$

where $\mu = \cos \theta$.

In optics, astronomy and radio-astronomy the considered characteristic is called the brightness of a physical object (Prochorov, 1984).

If this characteristic is considered throughout the range of positive frequencies, then it is called the total radiation intensity.

5.1.2 Spectral radiation flux

In determining this quantity, of importance is the radiation flux vector (or power flux vector) $\mathbf{q}_\nu(\mathbf{r})$, which is obtained by integrating the quantity $\Omega I_\nu(\mathbf{r}, \Omega)$ over the

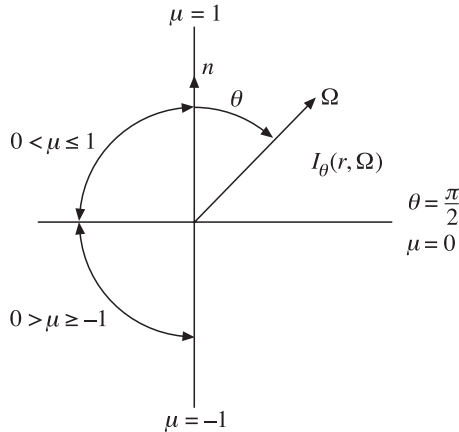


Figure 5.2. System of axes for resulting emission flow. See text for explanations of the designations.

spherical solid angle

$$\mathbf{q}_\nu(\mathbf{r}) = \int_{\Omega=4\pi} I_\nu(\mathbf{r}, \boldsymbol{\Omega}) \boldsymbol{\Omega} d\Omega. \quad (5.5)$$

In studying natural surfaces and making various types of antenna measurements, of importance is the knowledge of a component of this vector in the given particular direction \mathbf{n} . This quantity is called the net radiation flux in the given direction \mathbf{n} and is determined as a scalar product of vectors $\mathbf{q}_\nu(\mathbf{r})$ and \mathbf{n} :

$$q_{\nu n}(\mathbf{r}) = \mathbf{n} \cdot \mathbf{q}_\nu(\mathbf{r}) = \int_{\Omega=4\pi} I_\nu(\mathbf{r}, \boldsymbol{\Omega}) (\boldsymbol{\Omega} \cdot \mathbf{n}) d\Omega \quad (5.6)$$

Let θ be the polar angle between directions $\boldsymbol{\Omega}$ and \mathbf{n} (Figure 5.2). Then the scalar product of vectors is equal to the cosine of polar angle, and expression (5.6) will take the form:

$$q_{\nu n}(r) = \int_{\varphi=0}^{2\pi} \int_{\mu=-1}^{+1} I_\nu(\mathbf{r}, \mu, \varphi) \mu d\mu d\varphi. \quad (5.7)$$

Here $q_{\nu n}(\mathbf{r})$ is the density of the net radiation flux through the unit of area perpendicular to direction \mathbf{n} , per time unit, in a unit frequency band, formed by radiation falling from all directions within the limits of a spherical solid angle. Recalling the physical interpretation of Poynting's vector (Stratton, 1941; and see also section 1.6) as the density of the energy flux at any point of the field intersecting a unit area, whose normal is oriented in the direction of vector $[\mathbf{E} \mathbf{H}]$, the quantity $q_{\nu n}(\mathbf{r})$ can be interpreted as the magnitude of Poynting's vector of resulting radiation intersecting a unit area with the normal \mathbf{n} .

In studying the radiation of natural surfaces and various types of radio sources, the 'radiation flux' term is often used to characterize a unidirectional flux of electromagnetic energy. It corresponds to expression (5.7), in which the integral is taken

over the directions lying on the same side of an area (one-sided ozone-directional flux). In astronomy such a quantity is called the brightness in a unit frequency band, and the net flux through an area equals the difference of one-sided fluxes on both sides of an area.

The dimension of the considered quantity is $\text{Wm}^{-2} \text{Hz}^{-1}$. In radio-astronomy the quantity equal to $10^{-26} \text{Wm}^{-2} \text{Hz}^{-1}$ is called the flux unit, or jansky = Jy (see Appendix A).

In the equilibrium radiation field (for example, inside the thermostat) the net radiation flux through any surface area is zero. This result can easily be obtained from expression (5.7), if we substitute there the value of intensity which does not depend on the direction.

If the question is of the one-directional flux of the black-body radiation into free space from a unit surface, then in this case the expression for a flux will be written as

$$q_{\nu n}(\mathbf{r}) = \int_{\varphi=0}^{2\pi} \int_{\mu=0}^{+1} I_{\nu}(\mathbf{r}, \mu, \varphi) \mu d\mu d\varphi, \quad (5.8)$$

and in the case where the radiation does not depend on direction, i.e. $I_{\nu}(\mathbf{r}, \Omega, t) = I_{\nu 0}$, the expression for one-directional flux will be equal to

$$q_{\nu n}(\mathbf{r}) = \pi I_{\nu 0}(\mathbf{r}). \quad (5.9)$$

The relation obtained is called Lambert's cosine law. It has been widely applied both in theoretical works (the ideal light-scattering scheme and the ideal black-body radiation scheme), and in microwave remote sensing practice as the characteristic of an ideal black-body emitter in calibration operations.

We pay attention to one more important circumstance. On the basis of a reciprocity theorem, proved in Maxwellian electromagnetism (Stratton, 1941; Slater, 1942; Alpert *et al.*, 1953), it can be shown that the electromagnetic characteristics of emitting objects have the same form and quantitative values as if the same objects were to absorb the electromagnetic energy. Thus, the characteristics considered above can equally be related both to emitting objects (the terrestrial surfaces and radio sources) and to the objects absorbing the external electromagnetic energy (antenna systems, for instance).

If this characteristic is considered throughout the range of positive frequencies, then it is called the total intensity flux.

5.1.3 Spectral radiant energy density

The element of the medium's volume, in which the complicated radiation processes take place, contains at each time instant some particular amount of radiation energy, which falls on it from all directions within the limits of a spherical solid angle. The amount of electromagnetic radiation energy contained in a unit volume, in a unit frequency band, is called the spectral radiant energy density and is designated by symbol $u_{\nu}(\mathbf{r})$.

The relationship between the spectral radiant energy density of the electromagnetic field and Poynting's vector has already been established by ourselves for the

mode of planar waves in the form of (1.19). Using this relationship and taking into account the circumstance that the radiation of intensity $I(\mathbf{r}, \Omega)$ falls on the volume's element from all directions, the spectral radiant energy density is determined by the following expression:

$$u_\nu(\mathbf{r}) = \frac{1}{c} \int_{\varphi'=0}^{2\pi} \int_{\mu'=-1}^{+1} I_\nu(\mathbf{r}, \mu', \varphi') d\mu' d\varphi', \quad (5.10)$$

where c is the radiation propagation velocity in a medium. For dielectric transparent media with the index of refraction n the expression (5.10) takes the form:

$$u_\nu(\mathbf{r}) = \frac{n}{c_0} \int_{\varphi'=0}^{2\pi} \int_{\mu'=-1}^{+1} I_\nu(\mathbf{r}, \mu', \varphi') d\mu' d\varphi'. \quad (5.11)$$

In an equilibrium radiation field (for example, the radiation inside the thermostat) expression (5.11) is reduced to the well-known form:

$$u_\nu(\mathbf{r}) = \frac{4\pi n}{c_0} I_\nu(\mathbf{r}). \quad (5.12)$$

We shall repeatedly use this expression hereafter in considering the thermal radiation laws (Planck's formula and Kirchhoff's law) (Chapter 6).

The integral spectral radiant energy density $u(\mathbf{r})$ is obtained by integration of $u_\nu(\mathbf{r})$ over positive frequencies:

$$u(\mathbf{r}) = \int_0^\infty u_\nu(\mathbf{r}) d\nu. \quad (5.13)$$

In general, we note, that the processes of scattering, absorption and emission by the element of volume and by the element of surface of natural media are very complicated. Therefore, in the scientific and technical literature different approaches and definitions are used for describing the processes of the interaction of electromagnetic waves with volume and surface elements of the medium under study. The discussion of these concepts is beyond the framework of this book. We shall introduce and consider some additional definitions as they are required. An in-depth analysis of basic concepts can be found in a series of fundamental works (Chandrasekhar, 1960; Sobolev, 1963; Siegel and Howell, 1972; Ozisik, 1973).

5.2 MICROWAVE ANTENNAS AND THEIR CHARACTERISTICS

As we have noted, the most important function of the antenna system consists in forming the radiation with strictly defined and prespecified characteristics. According to the reciprocity theorem, in electrodynamics any antenna system can be used both for receiving the electromagnetic signal, and for emitting it with the same spatial-angular characteristics. We shall utilize this circumstance quite often hereafter, without additional explanation.

5.2.1 Emission of radiowaves

The emission of electromagnetic waves is associated with the process of emission by oscillating electrical charges, the simplest emitter being the electrical (or magnetic) dipole of length $l \ll \lambda$ and oscillation frequency ω .

At distances $r < \lambda$ the field can be considered to be quasi-static and rapidly decreasing with distance as r^{-2} and r^{-3} (the induction fields). The emission of energy cannot be associated with such fields. The energy flux, flowing through the unit area per unit time, is expressed by Poynting's vector component perpendicular to this area. In quasi-static fields \mathbf{E} and \mathbf{H} are shifted in phase by $\pi/2$, as it takes place in standing waves. As a result, Poynting's vector, while oscillating with a double frequency, time-averaged in the period is exactly equal to zero. As we have noted above (section 1.6), the distinction of Poynting's vector from zero can be caused only by fields \mathbf{E} and \mathbf{H} , which oscillate with equal phase (as in running waves) and decrease in proportion to $1/r$ (and, accordingly, the Poynting's vector magnitude decreases as $1/r^2$). It is interesting to note that the latter conclusion follows directly from the energy conservation law, since in the absence of losses in a medium the total energy flux in space (the source power) should not change with the distance. And since the area of closed surfaces, enveloping the source of electromagnetic radiation, grows as r^2 , it is necessary, that the magnitude of Poynting's vector be proportional to r^{-2} . Thus, the field of a source in the near zone is some kind of a preliminary phase under generation of running fields responsible for radiation and carrying remote information about a physical object.

One more important point is associated with the representation of the total power which is absorbed by the antenna element from incident radiation. Using the impedance method (section 1.6), the total power received by an antenna element can be presented as the power absorbed in some active resistance, which is called the radiation resistance. As we have already noted, the increase of antenna operation efficiency, and, accordingly, the maximum power received from ambient space, can be assured under the regime of 'match' between the wave resistance of space and the input resistance of a measuring device. It is just this procedure which is performed by the antenna system.

5.2.2 Antenna directional pattern (ADP)

The important function of the antenna system consists in forming the radiation with particular and prespecified characteristics and, first of all, with the specified directional pattern, i.e. with the angular distribution (in three-dimensional space) of the radiation field amplitude. Along with the amplitude pattern, the power gain pattern is often used. This is the angular distribution of the radiation energy flux density (the Poynting's vector magnitude or the intensity of emission in the given direction) of the antenna in the far zone (the emission zone). For antennas of complicated configuration both these directional patterns have a multi-lobed structure, which is caused by the interference of waves emitted and scattered by various antenna elements. If the fields of all elements are added in synchronous

phase, then the corresponding maximum is called the main lobe. The directional pattern is depicted in various forms – as a three-dimensional, relief picture; as a planimetric map with the lines of equal levels, or by means of separate planar cross-sections, or more often by two orthogonal cross-sections passing through the direction of a major maximum and \mathbf{E} and \mathbf{H} vectors. Since the main part of the power emitted or received by an antenna is localized within the main lobe, the antenna emission directivity is characterized by the antenna beamwidth at half-maximum points (the 3 dB width) at the half power level $\theta_{0.5}$ (or $\theta_{3\text{dB}}$) or at zero level θ_0 (at zero points). The majority of beam antennas are shown to satisfy the $\theta_0 \cong 2.5\theta_{0.5}$ relation, which is widely used in observational practice. The $\theta_{0.5}$ quantity determines the linear angular resolution of an antenna and can be approximately estimated by the following formula (in radians):

$$\theta_{3\text{dB}} \approx 1.22 \frac{\lambda}{D}, \quad (5.14)$$

where D is the geometric size (the aperture) of the antenna at the given cross-section of the directional pattern. This relation coincides with Rayleigh's criterion, which is used in optics for evaluating the resolution capability of optical systems (Born and Wolf, 1999; Mandel and Wolf, 1995). This criterion makes it possible to determine numerically the resolution capability of an instrument by using a sample double source: at the angular distance between components, lower than $\theta_{0.5}$, the diffraction images of components merge into a single maximum. The quantitative characteristic considered is purely geometrical and only testifies to the possibility of obtaining the appropriate detailed structure of an image. However, the possibility of restoring the true brightness distribution over a studied object from the smoothed images obtained by an antenna represents a separate specific problem, which is stipulated, first of all, by the relation between the useful signal and noise components. In the so-called super-beam antennas this limitation is overcome either by producing some specific, sharply oscillating background distribution in the aperture (unstable to the lowest fluctuations), or by introducing some additional model presentations of a studied object into the restoration procedure. As the D/λ ratio decreases, the antenna directional pattern broadens. However, even for an extremely small antenna (the elementary emitter) the directional pattern is not fully isotropic (unlike the elementary acoustic emitters). For example, the directional pattern of electrical and magnetic dipoles has the form of a toroid whose axis coincides with the dipole axis (Born and Wolf, 1999).

In order to quantitatively understand the situation with the angular resolution in a microwave band, we shall estimate the diameter of an antenna aperture (at the working wavelength of 1 cm) required for obtaining, with its help, a resolution capability equal to the resolution of the human eye (1 minute of arc). Substituting these values into formula (5.14), we obtain that the aperture diameter must be very great, namely, 42 m. The design and manufacture of antennas of such a size is a very complicated and costly procedure.

When it is necessary to obtain higher resolutions (than those determined by Rayleigh's criterion), investigators resort to a method which differs from the

mechanical increase of the aperture size. This method consists in producing a set of sparse-aperture antennas with a specialized system of processing. Such systems are called radio interferometers; they can be manufactured both in ground-based, and in onboard versions (Esepkinsa *et al.*, 1973; Matveenko *et al.*, 1983; Ruf, 1999; Kardashiov, 2000; Rosolen *et al.*, 1999). Under ground conditions another approach is also applied, namely, the arranging of a set of a great number of closely placed small antennas with a complex (and rigid) system of electrical linkage between them. Such systems are called cophased beam arrays, and they are, apparently, a major modern development in ground-based radio-astronomy (Feder, 2000; Parfitt *et al.*, 2000). There have also been some attempts at producing very large (up to 500 metres in diameter) mechanical mirrors situated in geological folds of the Earth's surface (the so-called Arecibo-style dish) (Peng and Nan, 2002). As far as onboard systems are concerned, then, taking into account the flying vehicle's motion over the surface being investigated, it is also possible to sharply increase the resolution capability by accumulating the thermal signal received; i.e. some kind of a synthetic aperture microwave radiometry is formed in this case (Milman, 1988; Ruf *et al.*, 1988; Camps *et al.*, 1998; Goutoule and de Boer, 2000; Dong *et al.*, 2000; Wu *et al.*, 2000).

The structure of the field of systems of emitters depends on their mutual position, on the general configuration of a system, on phase and amplitude relations between the currents in elementary emitters, on the availability and arrangement of non-emitting (passive, structural) components, etc. However, a common factor is the circumstance that, at a distance from the aperture plane equal to several wavelengths (in the wave zone), the rapidly decreasing fields of induction become insignificant, and the radiation field is determined by a superposition of fields excited by emitters. It is important to note that the presence of structural components in the radiation field of antenna systems greatly influences the side-lobe area, whereas the shape of a main lobe is not sensitive to the form of the basic aperture or to the presence of various structural components. Physically, this is associated with the fact that the formation of side lobes is the result of the interference of edge waves (in accordance with the Huygens–Fresnel principle) over the directions which represent the lines of constant value of the phase difference of edge waves (a hyperbola). It is important to note also that the formation of side lobes already takes place in the near field of antenna emission (the Fresnel zone), whereas the main lobe is formed in the far zone (the Fraunhofer zone) only. This pattern is demonstrated qualitatively in Figure 5.3.

The spatial evolution of the antenna emission field, generated by the broad synphase aperture, is shown conventionally in Figure 5.3 under an assumption of sufficient angular ‘narrowness’ of the directional pattern. At close distances (actually, within the limits of $\lambda < r \leq (D^2/n\lambda)$, where $n > 10–20$ is an integer) the synphase property of the front is not yet violated, and the wave behaves as if it were almost planar. This is the geometric optics zone, or the so-called searchlight ray zone, in which virtually the whole power emitted by an antenna is concentrated. Then, in the range of distances $r \cong D^2/n\lambda$ ($10 > n > 1$) the synphase property is essentially violated, which is accompanied by strong oscillations of the field amplitudes (and,

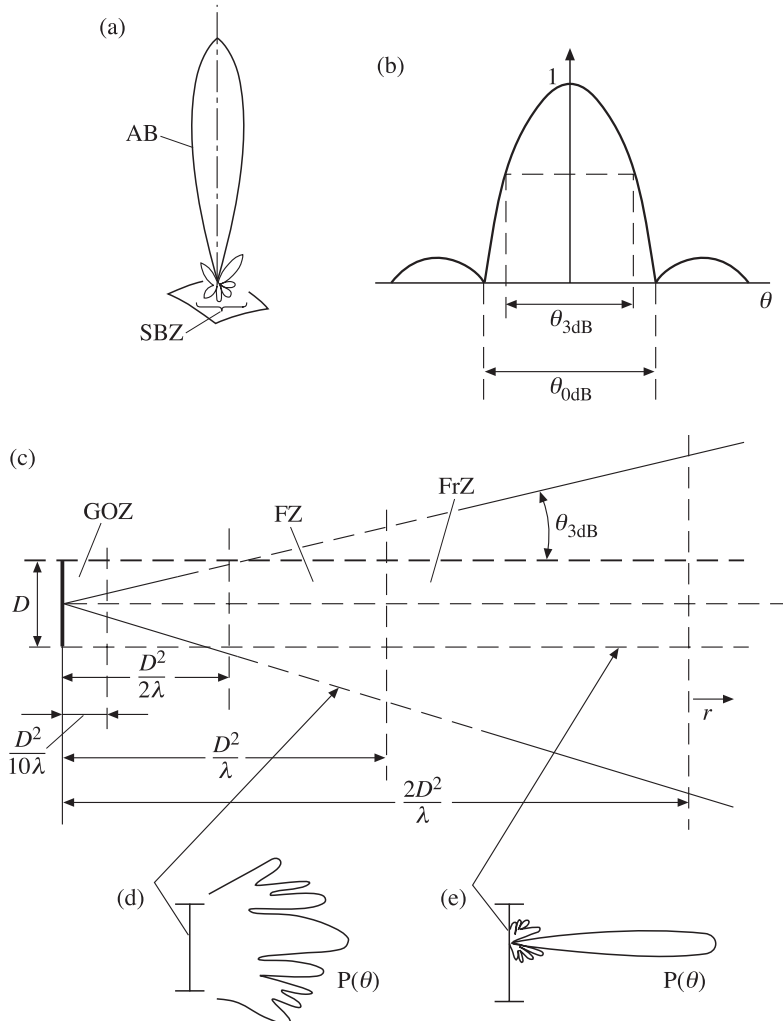


Figure 5.3. Schematic presentation of an antenna directional pattern (ADP) formation. (a) ADP is in plane polar coordinates. AB is an antenna (main) beam; SBZ is side beam zone. (b) ADP section is in Cartesian coordinates. (c) Special evolution of emergent wave beam. GOZ is geometrical optics zone; FZ is Fresnel zone (pulsed beam zone); FrZ is Fraunhofer zone (far zone). (d) ADP in Fresnel zone. (e) ADP in Fraunhofer zone.

accordingly, of Poynting's vector), in the direction of propagation as well. This is the Fresnel diffraction zone. And, finally, for $r \gg D^2/\lambda$ (or, as conventionally accepted, for $r > 2D^2/\lambda$) the wave front becomes spherical, the field decreases as $1/r$ (and, accordingly, the Poynting's vector magnitude as $1/r^2$), and the oscillations of amplitudes in the direction of propagation actually disappear. This is the far zone of an antenna (or the Fraunhofer zone), where it is already possible to operate with the

notion of directional pattern, i.e. with the dependence of the field amplitude on the angular coordinates only.

The question of the relation between the power of the signal received by the main and side lobes (or, in other words, the question of the antenna system efficiency) is so important for microwave systems (for a number of reasons) that we shall consider it in a separate section.

Note, once again, one of important corollaries of the reciprocity theorem, namely, the full coincidence of directional patterns of an antenna in its operation both in reception and in emission modes.

5.2.3 The effective surface

For receiving antennas, along with their angular characteristics, the parameters determining the total power of a received signal are of importance. According to the definition of antenna directional pattern (ADP) as a characteristic of the antenna which performs reception of a planar electromagnetic wave intensity from a given direction, and taking into account (5.2) and (5.8), we can write a power signal received by an antenna from the external source as

$$W_\nu d\nu = \frac{1}{2}A d\nu \iint_{4\pi} I_\nu(\theta, \varphi) P(\theta, \varphi) d\varphi \sin \theta d\theta, \quad (5.15)$$

where coefficient A characterizes the degree of efficiency of an antenna as an instrument designed for the reception of a received signal's power. This parameter is called the effective area (surface) of an antenna system (its dimension is m^2).

Thus, expression (5.15) represents the power of the monochromatic flux received by an antenna from the external radiation throughout its physical surface per unit frequency band. It should be noted here that the external radiation falls on the antenna system from all directions within the limits of a spherical solid angle.

If the whole power falling on the antenna aperture were to be absorbed by it, then the effective surface would be equal to the geometric area of its aperture. Since, however, some part of the power is scattered by structure elements, and another part is lost in Joule's (resistance) losses, the effective surface of a real antenna will always be lower than the geometrical surface of an aperture.

If we consider the planar surface, then, in accordance with (5.2), by the generalized response to a planar electromagnetic wave of such a simple structure (some kind of ADP) can be meant the quantity $P(\theta) = \cos \theta$. Of course, such a structure is not used as a real antenna.

If, for an incident external radiation, $I(\theta, \varphi) = \text{const}$, or, in other words, the question is about the wide-angle (relative to ADP) source, then in this case (5.15) is transformed to the following form:

$$W_\nu d\nu = \frac{1}{2}A d\nu I_\nu \Omega_A, \quad (5.16)$$

where by Ω_A is meant the quantity called the total antenna-pattern solid angle:

$$\Omega_A = \iint_{4\pi} P(\theta, \varphi) d\Omega. \quad (5.17)$$

It is not difficult now to find the relation of this characteristic to the plane angular characteristics. Suppose (for clarity), that the ADP represents a symmetric spherical cone with the plane angular aperture $\theta_{0.5}$ and $P(\theta, \varphi) = 1$. Using the well-known definition of a solid angle as the ratio of the area of a sphere, limited by this angle, to the square of the radius of a sphere, we have

$$\Omega = \frac{S(\theta)}{R^2} = 2\pi(1 - \cos \theta). \quad (5.18)$$

Considering the small plane angles only (the beam antennae), we shall have, after some transformations:

$$\Omega_A = \frac{\pi}{4} \theta_{3dB}^2. \quad (5.19)$$

This relation gives rise to the name of solid angles as square degrees, which is often used in observational practice. We should have in mind here, that one steradian contains 3282 square degrees (see Appendix A).

If, however, a very compact source (in relation to the ADP angular size) is observed, then it can easily be seen that relation (5.15) can be reduced to the following form (if the source is directed strictly to the main lobe):

$$W_\nu d\nu = \frac{1}{2} A d\nu I_S \Omega_S \quad (5.20)$$

Here I_S and Ω_S are the intensity and angular size (a solid angle) of a compact source.

5.2.4 Antenna directivity

This numerical (dimensionless) parameter (D) means the quantity, which indicates to what extent the directional properties of the given antenna differ from an ideal spherical emitter, i.e. an emitter whose directional pattern in power equals unity regardless of spherical coordinates. Thus, the antenna directivity is equal to:

$$D = \frac{4\pi}{\Omega_A}. \quad (5.21)$$

For beam antennas this quantity can be equal to tens or hundreds of thousands of units.

5.2.5 Antenna gain

This numerical parameter $G(\theta, \varphi)$ means the product of an antenna directivity and its normalized ADP in power, i.e.

$$G(\theta, \varphi) = DP(\theta, \varphi). \quad (5.22)$$

It is clear from physical considerations that the antenna parameters considered above (the effective area, solid angle and antenna directivity) are closely interrelated. So antenna theory (see, for example, Tseytin, 1966) rigorously indicates that the following relation takes place:

$$A\Omega_A = \lambda^2, \quad (5.23)$$

where λ is the working wavelength. It follows from this relation, that the antenna directivity is related to its effective area as:

$$D = \{4\pi/\lambda^2\}A. \quad (5.24)$$

We shall repeatedly use these relations hereafter.

The antenna systems characteristics listed above depend on the frequency, of course. The frequency range, in which the characteristics can be considered invariable, is called the antenna passband. In many cases, however, antenna systems can be built whose parameters insignificantly vary within a very wide frequency band, and, thus, the frequency limitations of the entire receiving system will be stipulated by input components of amplifying devices (see Chapter 3).

A huge band of wavelengths, emitted or received by antennas, and the diversity of fields of their application (communications, television, radar, remote sensing, radio-astronomy) gave rise to many types and configurations of antenna systems, described in a number of specialized publications.

The problems of designing antennas with specified characteristics for the appropriate field of application constitute the subject of special research and design work. And here for various fields of application (such as radio communication, radar, microwave sensing) quite specific requirements should be satisfied which may not be so significant for other applications. Below we shall consider the basic requirements of antenna systems designed for microwave sensing.

5.3 ANTENNAS AND BRIGHTNESS TEMPERATURES

Before formulating the basic requirements for antenna systems for microwave sensing we shall consider in more detail the important problem (we have already considered briefly before) of the determination of and relationship between antennas and brightness temperatures in microwave sensing.

One of the important parameters characterizing the power of a signal received by an antenna and transmitted directly to a receiving device is the antenna temperature. This definition is introduced proceeding from the following equivalent scheme of measurements (Figure 5.4). A portion of the electromagnetic energy of a source, released by the solid angle of ADP, passes through the antenna system, being transformed into the mode of the electromagnetic wave propagating in the transmission line. The conditions of transformation of received electromagnetic signal energy, which include also the transformation of modes of oscillations, are specially selected in such a manner that the maximum power of the signal, received by an antenna, be transmitted into a receiving device. The design features of this transformation in a particular antenna and in the antenna transmission line can be very complicated. For the purposes of the physical understanding of this process, investigators resort to the equivalent schemes (see section 3.3). The whole process of signal reception and transformation by an antenna system is represented in the form of the emf source and active resistance (R_A), which is some kind of equivalence of the antenna and is placed in the thermostat with physical temperature

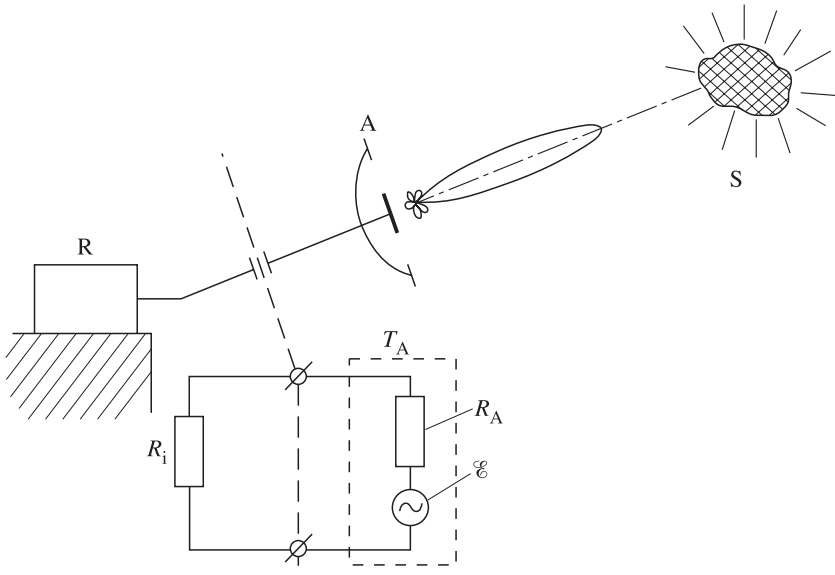


Figure 5.4. Schematic presentation of receiving procedure for the antenna temperature determination. S is a source; A is antenna; R is a radiometer. T_A is a thermostat temperature (antenna temperature); E is effective emf.

T_A . The amplifying device is presented in the form of input active resistance (R_i) (Figure 5.4). As we have already seen (see section 3.3), the maximum transmission of power from an antenna system into an amplifying device is possible only under the condition of coordination, i.e. with the equality $R_A = R_i$. Under this condition the whole of the power received by an antenna in the frequency band unit, $W_\nu \, d\nu$, hits directly into a receiving device and, in accordance with (3.4), we can write

$$W_\nu \, d\nu = kT_A \, d\nu. \quad (5.25)$$

By W_ν here, in essence, is meant the spectral density of a signal received by an antenna from an external source (see equation (3.5)).

Thus, the antenna temperature T_A (reduced to the frequency band unit) can be determined (and measured) as the physical temperature of the conventional thermostat with a coordinated resistance, in which, owing to thermal motion (the fluctuations), the fluctuation power is released, which is equal to the power of a fluctuation signal received by an antenna system. It is important to note that, according to the definition introduced above, the antenna temperature is reduced to the frequency band and, accordingly, it is proportional to the spectral density of a signal received by an antenna.

In order to find the relation between the antenna temperature and emission properties of a source, we shall write the expression for the power, transformed by an antenna, in another form, namely, from the viewpoint of the amount of

a signal's energy received by an antenna from free space. Recalling expression (5.15), we have:

$$W_\nu d\nu = \frac{1}{2} A d\nu \iint_{4\pi} I_\nu(\theta, \varphi, \nu) P(\theta, \varphi) d\Omega. \quad (5.26)$$

Further on, not considering the physical nature of an external source, we shall use (still in a formal manner) for the source intensity the expression that follows from the Rayleigh–Jeans law (see Chapter 6 for more details), namely:

$$I_\nu(\theta, \varphi, \nu) = \frac{2k}{\lambda^2} T_B(\theta, \varphi, \nu). \quad (5.27)$$

Here by $T_B(\theta, \varphi)$ we shall mean the brightness temperature of a source (or of the surface of an emitting medium). Note, that, according to the definition introduced above, the brightness temperature of a source itself (as well as the antenna temperature of the same source) is reduced to the frequency band unit and, accordingly, it is proportional to the spectral density of the fluctuation signal of a source (see equation (3.5)). Note once again that the introduced definition of brightness temperature is in no way related to radiation physics. It is equally used both for physical objects with thermal emission (such as the terrestrial surface) and for objects with a non-thermal character of emission (such as the artificial sources of pseudo-noise emission in radar, the radio-emission of the ionosphere and magnetosphere, and the astrophysical objects of maser radiation).

Substituting expressions (5.23), (5.25) and (5.27) into (5.26) and making some simple transformations, we obtain the following important relation for the antenna temperature expression:

$$T_A(\nu) = \frac{\iint_{4\pi} T_B(\theta, \varphi, \nu) P(\theta, \varphi) d\Omega}{\iint_{4\pi} P(\theta, \varphi) d\Omega}. \quad (5.28)$$

Since the antenna temperature is proportional to the spectral density of a signal, the total power of a signal (W), received by the antenna system and reduced to the amplifying system input, will be equal to:

$$W = k \frac{1}{\frac{1}{\Delta\nu} \int_{\Delta\nu} G(\nu) d\nu} \int_{\Delta\nu} G(\nu) T_A(\nu) d\nu, \quad (5.29)$$

where $G(\nu)$ is the amplitude-frequency characteristic (in power) of the receiving amplifier. If the antenna temperature does not change within the limits of the amplifier passband, then expression (5.29) is simplified up to the form, which is often used in practical estimation calculations:

$$W = k T_A \Delta\nu = k T_A \Delta f, \quad (5.30)$$

where $\Delta\nu = \Delta f$ is the power passband of the amplifier unit (see section 3.8).

Let us return to analysing the expression for the antenna temperature (5.28). It can easily be seen, that, depending on the relation between the effective angular size

of a source and antenna and on the source intensity value, the antenna temperature value can vary within wide limits. Consider now two extreme cases: the first, where the angular size of a source is essentially larger than the angular size of ADP (the so-called extended source), and the second, where the angular size of a source is essentially smaller than the angular characteristics of ADP (the so-called discrete source, or ‘hot spots’).

5.3.1 Extended source

The extended source includes, for example, emitting surfaces of Earth surface type (sea surface, land) as observed from low-orbit spacecraft and from aircraft, as well as the detailed investigations of emission of the surface of the Sun, Moon and planets by means of beam antenna systems. Since for this type of source its angular size $\Omega_S \gg \Omega_A$, T_B can be considered to be a constant value within the limits of the angular size of ADP and can be brought outside the integration sign. In this case (5.28) acquires the following form:

$$T_A(\theta, \varphi) = T_B(\theta, \varphi). \quad (5.31)$$

At first sight, the expression obtained for the antenna temperature is paradoxical, since the received power from a source does not depend on the distance to a source and on antenna system parameters. However, this paradox is only apparent since, as the distance r (the height over the studied surface) increases, under beam antenna conditions and within the limits of angular resolution of ADP the emitting area increases as r^2 , whereas the Poynting vector magnitude decreases as r^{-2} , and, thus, the total power, collected from the ADP-illuminated area (or instantaneous field of view), remains unchanged.

5.3.2 Discrete source

The discrete source includes such sharp and intensive inhomogeneities on the terrestrial surface as forest fires, erupting volcanoes, and breaking sea waves, as well as numerous remote radio-astronomical objects (quasars, pulsars, radio galaxies, maser sources).

Since for this type of source its angular size $\Omega_S \ll \Omega_A$, quantity $P(\theta, \varphi)$ can be considered to be constant and equal to unity within the limits of angular sizes of a source. This allows us to apply the theorem of the average to the upper integral. In this case the expression for antenna temperature is transformed as follows:

$$T_A = \frac{\iint_{4\pi} T_B d\Omega}{\iint_{4\pi} P d\Omega} = T_{BS} \frac{\iint_{4\pi} d\Omega}{\iint_{4\pi} P d\Omega} = T_{BS} \frac{\Omega_S}{\Omega_A}, \quad (5.32)$$

where T_{BS} and Ω_S are the averaged values of intensity of a source (within the limits of its solid size) and its angular size.

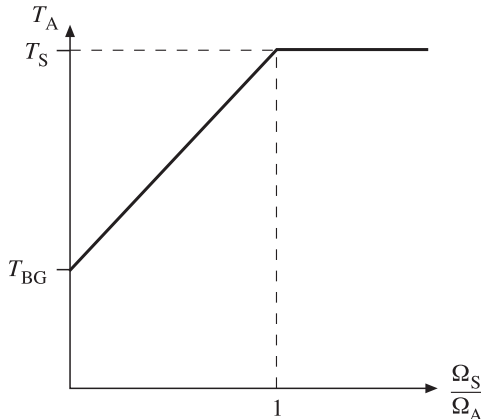


Figure 5.5. The relationship of antenna temperature value to a solid angular value of source. T_{BG} and T_S are brightness temperatures of thermal background and of a ‘warm’ source (see equation (5.33)).

It can easily be seen that the expression obtained critically differs from the expression for an extended source. The antenna temperature value depends both on the distance to a source (in terms of the value of its solid angle size), on its intensity, and on the antenna system parameters.

Using these two extreme cases, we can easily write the expression for antenna temperature of a bright discrete source with intensity T_S with solid angular size Ω_S against the extended thermal background T_{BG} :

$$T_A = T_S \frac{\Omega_S}{\Omega_A} + T_{BG} \left(1 - \frac{\Omega_S}{\Omega_A} \right). \quad (5.33)$$

Figure 5.5 presents the dependence of antenna temperature on the angular (in a solid angle measurement) size of a ‘hot’ source against the ‘cold’ background ($T_S > T_{BG}$). Note that, as the source area increases, its contribution to the total temperature (or, as is sometimes said, the radio contrast) increases linearly and, when reaching the size of the ADP field of view area, reaches a maximum. Certainly, the opposite situation is also possible, namely, the ‘cold’ source against the ‘warm’ background. A typical example of such a situation is the presence of an opening in ice – the so-called polynya (the ‘cold’ source) in a marine ice sheet (the ‘warm’ background) (see Chapter 8).

To describe the discrete sources which cannot be resolved in detail for some reason or other, the notion of the magnitude of energy flux from a source is introduced into radio-astronomy. In some cases this definition has started to be used in microwave sensing as well. The spectral source flux implies the following quantity:

$$F_\nu = \iint_{4\pi} I_\nu(\theta, \varphi, \nu) P(\theta, \varphi) d\Omega. \quad (5.34)$$

Table 5.1. The main characteristics of radiotelescopes (the Crimea, Pushchino)

Radiotelescope location	Antenna diameter, m	Antenna beamwidth, plane angular minute	Effective surface, m ²	Noise temperature, K	Flux sensitivity, Jy
Simeis (the Crimea)	22	2.5	150	80	0.4
Eupatoria (the Crimea)	70	0.7	1500	60	0.03
Pushchino (Moscow region)	22	2.5	110	120	0.8

Using the expression for the Rayleigh–Jeans law, the theorem of the average, and taking into account the small angular size of a source, we can rewrite (5.34) in the form:

$$F_\nu = \frac{2k}{\lambda^2} \iint_{4\pi} T_B d\Omega = \frac{2k}{\lambda^2} T_{BS} \Omega_S. \quad (5.35)$$

Thus, the antenna temperature from a discrete source can be presented in three equivalent forms:

$$T_A = T_{BS} \frac{\Omega_S}{\Omega_A} = \frac{1}{2k} A F_\nu = \frac{A}{\lambda^2} T_{BS} \Omega_S. \quad (5.36)$$

It follows from this condition, that the sensitivity of the radiothermal complex can be defined both as the sensitivity in antenna temperature, and as the sensitivity in minimally detectable fluxes from pointwise (discrete) objects of investigation. As we have already noted, in radio-astronomy the flux unit, or jansky (Jy), is accepted as the flux measurement unit and the 3C 273 quasar radio-emission source with a radiation flux of 30 Jy is often used for estimations in calibration work. As an example, we refer to the operational data and flux sensitivity data for a series of Russian radio telescopes (Table 5.1) (Matveenko *et al.*, 1983), the information on which is not widespread in Western literature.

5.4 THE SCATTERING COEFFICIENT OF ANTENNAS

The principal feature of radiothermal observations (unlike radio communication or reception of radio broadcasting and television programmes) consists in the fact that the statistical properties of a signal, received at the main lobe (the ‘useful’ signal, conventionally) and at side lobes (the ‘parasitic’ signal), are identical (Gaussian noise). Also of importance is the fact that the contribution of these components is

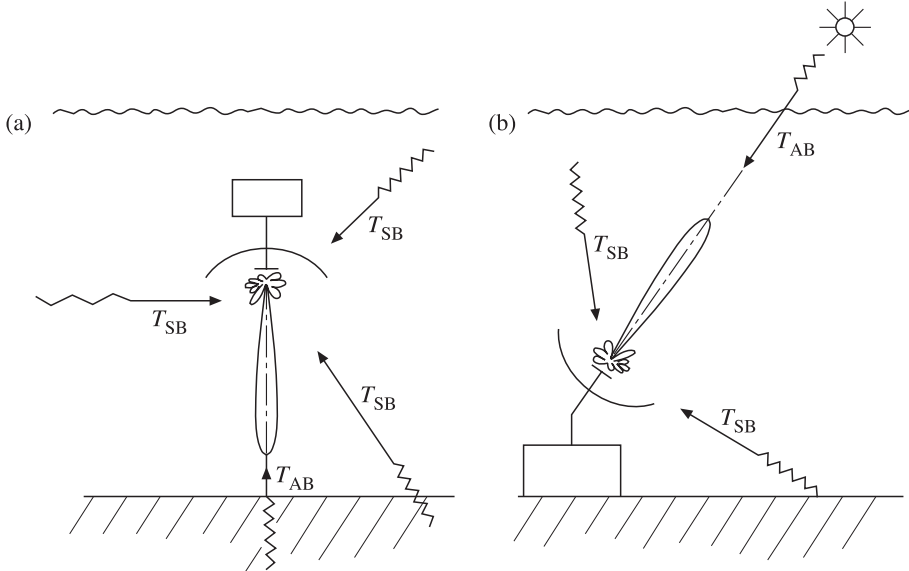


Figure 5.6. Schematic presentation of the antenna temperature components. (a). Airborne radiometric variant of observations. (b). Radio-astronomical variant of observations.

comparable in intensity. Thus, the recognition and detection of these components from purely statistical tests is impossible. Moreover, in a series of cases the useful signal (or its spatial-temporal variation) constitutes a value essentially lower than the noise radiation contribution into the side-lobe field of ADP. The problem of maximally reducing the contribution of side-lobe radiation to the total signal is of major importance, both for radio-astronomy (Esepkinsa *et al.*, 1973) and for microwave sensing.

Figure 5.6 shows the onboard radiothermal instruments installed on the flight vehicle in the Earth's atmosphere, and the main components of a received noise signal. The total noise signal can be separated into three groups: the noise signal received at the main lobe (antenna beam), and the noise signals received in the side-lobe (side-beam) zone. The latter signals will include the components received from the Earth's surface and from the atmosphere. Since all these components are statistically independent, their intensities (variances) are added (see section 2.2), and, thus, the expression for antenna temperature can be written as:

$$T_A = \frac{\iint_{4\pi} T_B P d\Omega}{\iint_{4\pi} P d\Omega} = \frac{\iint_{\Omega_{AB}} T_B P d\Omega}{\iint_{4\pi} P d\Omega} + \frac{\iint_{\Omega_{SB}} T_B P d\Omega}{\iint_{4\pi} P d\Omega}. \quad (5.37)$$

Now we introduce the following important definition: the coefficient, which characterizes the portion of energy, emitted (or absorbed) by an antenna into the

side-lobe zone, will be called a scattering coefficient and will be defined in accordance with the following relation:

$$\beta = \frac{1}{\iint_{4\pi} P d\Omega} \iint_{\Omega_{SB}} P d\Omega. \quad (5.38)$$

The averaged temperatures of radiation over solid angles of the main lobe and over the remaining space are written as:

$$T_{AB} = \frac{\iint_{\Omega_{AB}} TP d\Omega}{\iint_{\Omega_{AB}} P d\Omega}; T_{SB} = \frac{\iint_{\Omega_{SB}} TP d\Omega}{\iint_{\Omega_{SB}} P d\Omega}. \quad (5.39)$$

In such a case, expression (5.37) can easily be rewritten in the following form, which is often used in observational practice:

$$T_A = T_{AB}(1 - \beta) + T_{SB}\beta. \quad (5.40)$$

The total signal, received by an onboard radiothermal complex, will consist of the components received by an instrument in quite different directions (from various solid angles), but (we emphasize once again) completely indiscernible statistically. In the majority of cases it is expedient to separate the T_{SB} component into a component determined over the lower hemisphere and a component determined over the upper hemisphere. Whereas in the lower hemisphere the emission emanates from the Earth's surface, in the upper hemisphere the emission is determined by emission from the atmosphere and outer space (the 'relic' background and radio sources) (Figure 5.6).

As an instructive example, we shall consider the problem of a scattering coefficient of the model antenna composed of two cones: the main lobe (with ADP equal to unity) and the side-lobe zone with ADP equal to $P_1 = -40$ dB. This level of side emission is considered as quite good. To calculate the scattering coefficient value we perform the following transformations:

$$1 - \beta = \frac{\iint_{4\pi} P d\Omega - \iint_{\Omega_{SB}} P d\Omega}{\iint_{4\pi} P d\Omega} = \frac{\iint_{\Omega_{AB}} P d\Omega}{\iint_{\Omega_{AB}} P d\Omega + \iint_{\Omega_{SB}} P d\Omega} = \frac{1}{1 + P_1 \frac{\Omega_{SB}}{\Omega_{AB}}}. \quad (5.41)$$

Since the question is now about the antenna with high resolution, the solid angle of a side-lobe zone can be replaced, with good approximation, by the total solid angle of 4π . And then, recalling expression (5.21), we shall write the scattering coefficient in terms of the value of directivity as:

$$1 - \beta = \frac{1}{1 + P_1 G}. \quad (5.42)$$

Suppose the antenna directivity to be $G = 1000$. In this case the solid angle of an antenna will be 0.012 steradians and, accordingly, its value in square degrees will be equal to 39.3. In the linear dimension, however, the ADP will be 6.2 angular degrees. Antennas with such angular characteristics are often used in microwave practice (see Chapter 14). Substituting the values of antenna directivity and side-lobe level into (5.42), we obtain the value of the scattering coefficient of an antenna to be 0.09 (or 9%). We pay attention to the fact that, although the side emission level is very low, the energy escaping to side emission is significant. Certainly, this is a consequence of the large solid angle zone of side lobes.

We can easily see the reasons why the emission contribution to the side-lobe zone may be critical for carrying out an observational experiment. Suppose, that we use the aforementioned antenna (as the ‘ground-based’ radio telescope, Figure 5.6(b)) for studying the radio-emission of the Moon (the brightness temperature is 250 K and the angular size is 0.5°). Using formula (5.32), we obtain the value of antenna temperature at the main lobe as

$$T_{AB} = 250 \left(\frac{0.5}{6.2} \right)^2 = 1.6 \text{ K.} \quad (5.43)$$

The space surrounding an antenna (the Earth surface and atmosphere) has (on the average) a brightness temperature value of about 270 K. Thus, the total antenna temperature of an antenna will be:

$$T_A = 1.45 + 24.3 = 25.75 \text{ K.} \quad (5.44)$$

It follows from this fact, that 94% of a signal received by an antenna constitutes a ‘parasitic’ signal. Changing the position angle of the main lobe of an antenna (in the guidance or tracking mode) will also change this parasitic signal – in a virtually uncontrollable manner. This model example clearly demonstrates the major problem of ground radio telescopes: the necessity of maximally reducing the powerful parasitic signal from the ground objects and atmosphere (Esepkinsa *et al.*, 1973).

Referring to the study of extended and fairly homogeneous objects (such as the sea surface) (Figure 5.6(a)), the situation seems to be essentially simplified here, since the expression (5.40) can be rewritten as follows:

$$T_A = T_{AB} - (T_{AB} - T_{SB})\beta. \quad (5.45)$$

Detailed onboard experiments under full-scale conditions have shown (Veselov *et al.*, 1981) that the difference between the temperatures measured at the main lobe and at the side-lobe zone is quite small (of the order of 20–30 K). In such a case, using the aforementioned model example for the situation with an extended source (Figure 5.6(a)) (with the brightness temperature of 200 K), we have the value of the total antenna temperature in the form

$$T_A = 200 - 30 \times 0.09 = 197.3 \text{ K.} \quad (5.46)$$

It can be seen from this expression that the possible relative error is (at first sight) fairly insignificant (about 1.5%). However, those addressing the physical problems

of studying the World Ocean surface much higher requirements, namely, the measurement of brightness contrasts (at the main lobe) at the level of 0.1–5 K. Thus, in formulating such problems the possible radiothermal variations of the same order, which arise from radiothermal surface contrasts in the side-lobe zone (and which, accordingly, cannot be controlled on the solid angle zone of 2π), can already be considered inadmissible – the more so as at installation on a flight vehicle the side-lobe zone (but, we note, not the shape and angular size of the main lobe) can essentially be distorted because of design features of attaching the antenna system to the vehicle. The appropriate experimental methodology on detailed measurement of onboard antenna systems and on performing calibration procedures has now been developed (see section 5.8).

In concluding this section we note that similar problems do not arise with the reception of television and radio broadcasting programmes and in radio communications, though the scattering coefficient of television antennas can reach 50–70%. This is due to the fact that the useful signal, received at the main lobe, exceeds by a factor of 10^7 – 10^9 (on the average), the signal received by a receiver from an ambient medium in the side-lobe zone; and, thus, the ‘parasitic’ signal is not distinguishable against the useful signal. However, in the case of detailed radar and scatterometric measurements, where an output powerful signal is emitted, the problem of reducing the reception of ‘parasitic’ backscattering in the side-lobe zone is also topical. However, in virtue of the specificity of active measurements, the methodology used in this case differs from that used in passive radiothermal measurements.

5.5 ANTENNA TEMPERATURE OF ANTENNA WITH RESISTANCE LOSS

The above considerations have related to ideal (lossless) antenna systems, i.e. to receiving systems not possessing intrinsic resistance losses at reception and transmission of a signal. However, real antenna systems and antenna transmission lines (ATL), which connect the antenna itself and a receiving device, possess determinate (and unremovable) resistance losses and, accordingly, intrinsic fluctuation emission (see Chapter 4). In radiothermal observations (unlike radio communications or reception of broadcast radio and television programmes) the statistical properties of signals, received by an antenna and arising in the antenna and antenna transmission lines, are identical (the Gaussian noise), and, certainly, they cannot be distinguished by means of purely statistical procedures. Besides, if the radiothermal measurements are carried out by means of a receiving system that is conditional on strong (and not constant) temperature gradients (as, for example, in the case of an instrument installed onboard a spacecraft without a thermal control system), then the values of ‘parasitic’ signals can be comparable to, and even exceed, ‘useful’ values.

There exists, certainly, a fairly complete theory of calculating the losses in antenna systems and intrinsic radiation. Here, however, we shall make use of

physical considerations for estimating the contribution of resistance losses to the emission properties of antennas. Suppose that an antenna system with the power transmission coefficient η and the receiving device itself are immersed in thermostat conditions with temperature T_0 . The antenna temperature, received by a receiving device, will consist of two statistically independent components: the external signal ηT_{A0} , received directly by an antenna and partially decreased due to resistance losses, and signal T_{ATL} , which arises directly in the antenna transmission line. Since these signals are statistically independent, their intensities (variances) can be added. In this case the total signal at the receiver input will be as follows:

$$T_A = T_{A0}\eta + T_{ATL}. \quad (5.47)$$

Since the whole system is situated inside the thermostat, the full equilibrium conditions should be satisfied. In other words, the signal, which directly hits the antenna aperture, is equal to T_0 , and the total signal recorded by a receiver should also be equal to T_0 . Substituting the values mentioned into expression (5.47) and performing very simple manipulations, we obtain the value of brightness temperature of the fluctuation signal caused by resistance losses in a line:

$$T_{ATL} = T_0(1 - \eta). \quad (5.48)$$

This expression is widely used in the practice of microwave remote sensing and radio-astronomical observations. We shall also use this relation repeatedly below. From the viewpoint of thermal radiation physics, the relation obtained is nothing other than the Kirchhoff law in an unusual form.

Thus, the total signal, reaching the amplifier's input after passage through the antenna transmission line, can be written as:

$$T_A = T_{A0}\eta + T_0(1 - \eta). \quad (5.49)$$

We emphasize, that by T_0 here is meant the thermodynamic temperature of an antenna and antenna transmission line. This directly stipulates the importance of the problem of the thermal stabilization of an antenna transmission line. So, if for any physical reason it is necessary to perform radiothermal measurements to an accuracy of ΔT , then the thermal stabilization of an antenna transmission line should be better, than $\Delta T/1 - \eta$, throughout the course of the experiment. For example, for an antenna system with $\eta = 0.9$ and for a measurement accuracy of 0.1 K the thermal stabilization of an antenna and antenna transmission line should be better than 1 K. Such a design problem in itself and the temporal stability of these parameters can be quite complicated in the case of an antenna system installed on a space vehicle (Ruf, 2000a,b; Njoku *et al.*, 2000b; Keihm *et al.*, 2000; Colton and Poe, 1999).

The complete expression for the antenna temperature with regard to the contribution of a side emission (equation (5.40)) and intrinsic noises (equation (5.49)) can be written in the form

$$T_A = T_{AB}(1 - \beta)\eta + T_{SB}\beta\eta + T_0(1 - \eta). \quad (5.50)$$

Making use of the model examples from the previous paragraph, we shall estimate the contribution from side emission and from intrinsic noises into the total signal. For the example of radio-astronomical observations, taking account of the ‘true’ signal value as 1.6 K, the brightness temperature in the side-lobe zone as 270 K, the values $\eta = 0.9$ and $\beta = 0.09$ and thermodynamic temperature of an antenna as 300 K, we obtain the following value for a total signal:

$$T_A = 1.3 + 21.87 + 30 = 53.17 \text{ K.} \quad (5.51)$$

It follows from this result that more than 97% of signal intensity relates to the ‘parasitic’ signal. Thus, one of the most important design problems in the development of radio telescopes is to ensure minimum losses at signal transmission from an antenna to a receiving device (Tseytlin, 1966; Esepkinsa *et al.*, 1973; Wilson and Hutmeyer, 2000; Poperechenko, 2000; Peng and Nan, 2002).

In the case of onboard observations, taking into account the same values of the parameters, we shall have the value for a total signal as:

$$T_A = 197.3 \times 0.9 + 30 = 207.6 \text{ K.} \quad (5.52)$$

Unlike the previous case (equation (5.46)), we have now some kind of overcompensation (due to intrinsic noises) of a received signal, that is to say, the value of a received signal is greater than the value of a ‘true’ signal (200 K). As in the case of radio-astronomical observations, in designing radiothermal onboard complexes great attention is paid to minimization of losses in ATL. And so the designers try to manage, if at all possible, without including ATL components into the structure, by connecting the antenna directly to a receiving device (Amirkhanyn *et al.*, 1978; Strukov and Skulachev, 1984, 1986).

These model examples clearly indicate the importance of carefully accounting for the contribution of side lobes’ emission and intrinsic antenna emission into the total signal and for the further procedure of restoring the ‘true’ signal. In actual observational practice the situation can, of course, be even more complicated than the model examples considered above.

Problems like those considered above virtually do not arise with reception of broadcast television and radio programmes and with radio communications. This is explained by the fact that the useful signal exceeds the signal which arises in the antenna transmission line by an order of magnitude on the average. Thus, the ‘parasitic’ signal is not distinguishable against the useful signal background (like in the case of radiation reception at side lobes).

5.6 SPATIAL-TEMPORAL DYNAMICS IN PASSIVE REMOTE SENSING

The previous analysis has related to the time-independent regime of observation. Real radiothermal observations, however, include the time-dependent aspect; for example, the motion of a flight vehicle over the surface being studied and, accordingly, the finite time of observation of an object. As we have noted above (section 3.5), the peculiarity of passive remote sensing lies in the fact that the main system

parameters (threshold sensitivity, the observation time constant, the instantaneous field of view of an antenna) are rigidly interrelated. And, in this connection, the spatial-temporal dynamics of the measurement process itself imposes fairly strict limitations both on the time of observation of an object and on the possibility of its recognition against the background of the intrinsic noise of the instrument. Certainly, similar problems also arise in the other fields of application of radio-physical systems (radio communications, television); but in those areas the relationships between these parameters are, for a number of reasons, essentially less critical.

To understand these interrelations we shall consider the model example: a radio-thermal complex with an ideal antenna ($\eta = 1.0$ and $\beta = 0$) having a conical-shaped ADP, installed on a moving (at altitude H) carrier. If during the motion the vehicle encounters a contrast source with brightness temperature T_S and area S , then, in accordance with (5.33), we have the extreme value for antenna temperature in the form:

$$T_A = T_S \frac{S}{S_A} + T_{BG} \left(1 - \frac{S}{S_A} \right). \quad (5.53)$$

where $S_A = H^2 \Omega_A$ is the instantaneous field of view (IFOV) illuminated by an antenna on a studied surface.

As an example, we shall estimate the antenna temperature value for a water ice opening (a ‘cold’ object with $T_S = 150$ K), occurring in a sea ice sheet (a ‘warm’ background with $T_{BG} = 270$ K). If the ice opening area is equal to a half of the area of the instantaneous field of view of an antenna, then the minimum value of antenna temperature will be 210 K. In this case the contrast with the surrounding background will be negative and equal to 60 K. Note, that it is quite difficult to restore the emission characteristics of an object from the contrast value only, without resorting to additional information about the object geometry.

Let us consider now the same situation in dynamics, i.e. with allowance for the vehicle motion and finite sensitivity of the radiometer. If by quantity V we mean the velocity of motion of a carrier on which the instrument is installed, then the full time, t , of ‘scanning’ the contrast object in the antenna’s field of view will be

$$t = \frac{D_A}{V} = \frac{\theta H}{V}, \quad (5.54)$$

where $D_A = \theta H$ is the diameter of the field of view for beam antennas.

Here we should remember, that the radiometric complexes receive and process a signal not instantaneously, but with the delay function of exponential type (see Chapter 3) with time constant τ . Thus, the total signal at instrument’s exit is set up after $(4-5)\tau$. Therefore, to obtain at the instrument’s exit the ‘total’ signal from a contrast object, we must ensure the following inequality: $t > 10\tau$. It follows from this condition, that the orbital features of a vehicle and the antenna system characteristics impose strict limitations on the constant of an instrument, namely:

$$\tau < \frac{\theta H}{10V}. \quad (5.55)$$

Violation of this inequality will result in the situation where the contrast objects will not be completely (either in intensity or in their characteristic size) presented in the output signal of a radiometer.

On the other hand, the time constant appears in the expression for the fluctuation sensitivity of a radiometer (see section 3.5), i.e. in the expression for the sensitivity threshold. In this case, for reliable recognition against the background of intrinsic noise of the instrument the value of the signal from a contrast object should not be lower than $3\Delta T/\sqrt{\tau}$, where ΔT is the normalized fluctuation sensitivity threshold (see section 3.5). The value of signal ΔT_S from a contrast object in the form of a circle of diameter D_S will be equal to

$$\Delta T_S = (T_S - T_{GB}) \frac{\Omega_S}{\Omega_A} = (T_S - T_{GB}) \frac{\pi D_S^2}{16H^2\theta^2} \quad (5.56)$$

and, taking into account the above considerations on the recognition of a signal from an object, we shall have the second inequality the instrument's constant should satisfy:

$$\frac{\Delta T}{\sqrt{\tau}} < (T_S - T_{GB}) \frac{D_S^2}{16H^2\theta^2}. \quad (5.57)$$

It can easily be seen that, unlike inequality (5.55), inequality (5.57) has an opposite character, i.e. it limits the time constant value ‘from below’. Combining (5.55) and (5.57), we obtain a useful interval of time constant values, the fulfilment of which will allow us to completely record a signal against the background of noise components of an instrument:

$$\left(\frac{\Delta T}{T_S - T_{GB}} \right)^2 \left(\frac{4H\theta}{D_S} \right)^4 < \tau < \frac{\theta H}{10V}. \quad (5.58)$$

Consider now the numerical example: on the possibility of recognition of a ‘cold’ object – the ice opening – against the ‘warm’ background by means of a radiothermal instrument with a normalized sensitivity of 0.1 K and ADP equal to 2.8° (or $1/20$ radians). The radiothermal system parameters are close to those existing now (see Chapter 14). We shall suppose the satellite orbit’s altitude to be 600 km, and the diameter of the circular-shaped ice opening to be 1 km. Substituting these values into (5.58), we obtain the following result:

$$144 < \tau < 0.4. \quad (5.59)$$

It can easily be seen that the requirements presented in (5.59) are mutually exclusive, and, therefore, the total signal cannot be recorded under the conditions mentioned. If, however, the object has a diameter an order of magnitude greater, namely, 10 km, then the situation radically changes, and the inequality will have the following form:

$$0.014 < \tau < 0.4, \quad (5.60)$$

which can surely be satisfied with the time constant of 0.05 sec. Figure 5.7 schematically presents the record of an output signal of a radiometer in the case of its recording above the considered object at the instrument’s time constant of 0.05 sec

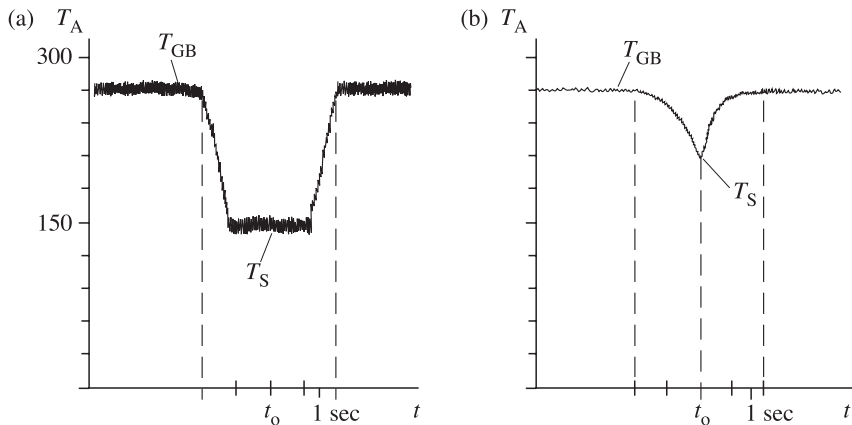


Figure 5.7. The signal registration at the moment (t_0) of the flight over a thermal ‘cold’ object. The integrator time parameter is (a) 0.05 s and (b) 1 s.

(Figure 5.7(a)) and at 1 sec. The principal distinctions between the two cases are clearly seen: in the first case the signal has completely recorded the object, whereas in the second case, in spite of the fact that the sensitivity of the system increased by nearly five times, the signal has obviously not been recorded completely. In this case the signal appears as though it consists of two ‘torn off’ exponents. This gives rise to the important and reliable experimental approach that would testify to complete signal recording: it is necessary to obtain, in the form of signal registration of such an object, either the ‘plane bottom’ (if the contrast is negative), or the ‘plane cover’ (if the contrast is positive).

5.7 THE EQUATION OF ANTENNA SMOOTHING

As we have already noted (see Chapter 1), the most important characteristic of an object is its spatial structure. However, in studying the spatial structure of objects in the microwave band investigators are in a much less favourable position (as compared to optics and the IR band) because of the greater length of the electromagnetic wave and, accordingly, the lower resolution capability. This circumstance has forced radio-astronomers to search for new methods of achieving high resolution that would allow them to ‘synthesize’ the image through the reception of a signal by several spaced radiotelescopes. And outstanding results have been obtained in this way, such as the fine structure of the region at the centre of our galaxy or the fine structure of distant quasars. In these works the resolution capability of synthesized radiotelescopes essentially exceeded the resolution capability which can be obtained by classical methods in optics. The theory and practice of image synthesis are based on the spatio-spectral methodology of generalization of properties of a radio-telescope as a filter of spatial frequencies.

The recently appearing spectrum of remote sensing problems requiring high spatial resolution in the microwave band put on the agenda the problem of synthesizing spatial fields by means of onboard radio interferometers taking into account the motion of a carrier (Milman, 1988; Ruf *et al.*, 1988; Camps *et al.*, 1997, 1998; Camps and Swift, 2000; Goutoule and de Boer, 2000; Dong *et al.*, 2000). In spite of the obvious necessity of actively introducing spatio-spectral methodology into the theory and practice of microwave remote sensing, such ideas are not generally accepted yet in the microwave sensing. Nevertheless, we shall try to consider in this section the basic ideas of such an approach, which are mainly based on the experience of radio-astronomical observations (Esepkinsa *et al.*, 1973).

The principal problem of onboard radiothermal satellite instruments is forming the radiobrightness field of an object under investigation. The radiobrightness distribution over the investigated surface, $T_B(x, y, t)$, can be generally considered as a three-dimensional random function of spatial coordinates (x, y) and time (t) with a virtually unlimited detailed structure. As with any optical instrument (Born and Wolf, 1999), in microwave remote sensing the radiothermal satellite instruments play the part of a linear operator which influences the functions describing the object under investigation. The principal point in performing this operation (which is clear intuitively) consists in the fact that, in virtue of the limited angular resolution of an antenna, we shall essentially lose the details of any radio image obtained. A matter of principle here is whether we can restore the ‘true’ radio image, and, if so, how close it will be to the original. This very complicated problem is sometimes called the problem of ‘superresolution’. But, before proceeding to analysis of the problem of restoring the true image, we shall consider the main principles of the spatio-spectral notions.

The fundamental formula, which will describe the procedure of the linear operator effect on spatio-energy characteristics of the investigated radiobrightness field can be obtained from the antenna temperature expression (5.28) with allowance for the vehicle motion over the investigated surface. In other words, the expression for ADP should be written in the moving Cartesian coordinate system $P(x - x'; y - y')$, where $x = V_x t$ and $y = V_y t$ (here V_x and V_y are the components of velocity of ADP motion along the corresponding coordinates). The integral that determines the value of the solid angle of an antenna (5.17) is in this case a constant quantity, and it is usually omitted in the basic formula. Transforming the antenna temperature expression from the polar coordinate system, fixed with the flight vehicle’s antenna, into the system of Cartesian coordinates, fixed with the surface investigated, we obtain the following important relation called the equation of antenna smoothing:

$$T_A(x, y) = \int_{-\infty}^{\infty} \int_{-\infty}^{\infty} T_B(x'; y') P(x - x'; y - y') dx' dy', \quad (5.61)$$

where by $T_B(x', y')$ is meant the ‘true’ radiobrightness field of an object. A thorough examination of relation (5.61) indicates, that it is none other than the

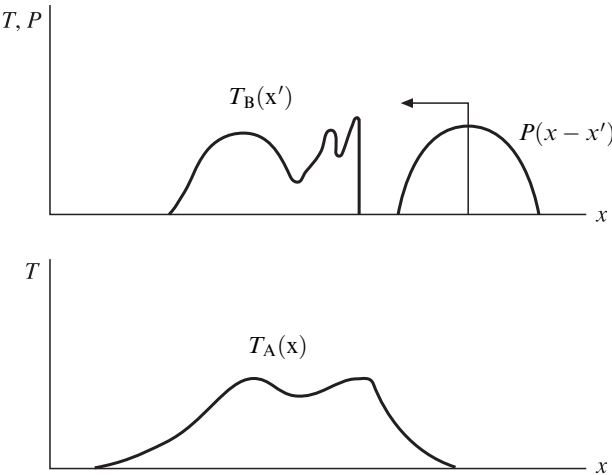


Figure 5.8. Schematic presentation of smoothing procedure for a complicated one-dimensional source $T_B(x')$ by antenna directional pattern (ADP) $P(x - x')$. $T_A(x)$ is the result of smoothing procedure.

convolution integral, which is usually written, with allowance for a commutative property, as:

$$T_A = T_B * P = P * T_B. \quad (5.62)$$

Generally speaking, the very fact that the observed field is a result of the convolution operation, testifies that the antenna system does not ensure obtaining the true result at observation, but yields some modified result. So, some kind of ‘smoothing’ of small details of the basic (or ‘true’) radio image takes place. For this reason the integral transformation of (5.61) was called the equation of antenna smoothing (Bracewell and Roberts, 1954). Figure 5.8 illustrates the sense of this transformation qualitatively. The instrument with the instantaneous field of view $P(x' - x)$ moves over the one-dimensional (for simplicity) radio object $T_B(x')$. As a result of smoothing, the instrument has recorded a signal which, generally speaking, essentially differs from the ‘true’ one, mainly by the absence of some fine (in scale, but not in physical significance) details. Certainly, if we imagine, that the ADP is infinitely narrow (as, for example, the delta-function), then in this case all details will be reproduced.

Let us show one more striking example of a smoothing procedure in the one-dimensional case for an object and ADP whose intensity and spatial form can be written as two plane sources (Figure 5.9). Substituting these values into (5.61), we obtain the result of convolution in the form:

$$T_A = \int_{-\infty}^{\infty} T_0(x') P_0(x - x') dx' = \frac{T_0 P_0}{\Delta x} \begin{cases} x_0 + \Delta x - x, & x > x_0 \\ -x_0 + \Delta x - x, & x < x_0. \end{cases} \quad (5.63)$$

The important circumstance here is the fact, that the obtained signal has a basically different (in relation to an object) form; that is to say, it represents a triangle (rather

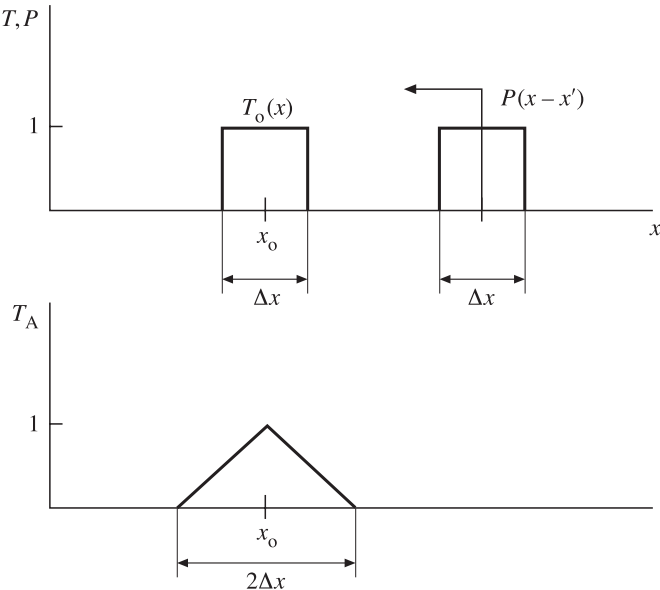


Figure 5.9. The smoothing procedure for two identical plane sources. $T_o(x)$ is a source $P(x - x')$ is ADP. $T_A(x)$ is the result of smoothing procedure.

than a rectangle). In this case its recorded size is twice as large as the original signal from the object. The analysis of the result of this simple model situation already demonstrates the difficulties the investigator can encounter in real observational practice.

As a contrasting example, take the study of brightness fields of a very narrow ADP, of delta-shaped type, for instance. In this case the basic relation can be rewritten as:

$$T_A = \int_{-\infty}^{\infty} P(x - x') T_B(x') dx' = \int_{-\infty}^{\infty} \delta(x - x') T_B(x') dx' = T_B(x). \quad (5.64)$$

It follows from this relation, that the instrument will precisely reproduce the brightness profile of an object. The opposite situation (frequently used in radio-astronomy) is also possible, where the bright point-like source is used as a supplementary one for determining the antenna characteristics, that is:

$$T_A(x) = \int_{-\infty}^{\infty} P(x') \delta(x - x') dx' = P(x). \quad (5.65)$$

Now we introduce some important spatio-spectral notions for describing the procedure of smoothing. For this purpose we shall introduce (still only formally) the Fourier transformation for functions determining the ADP and the field of a

source, in the following form:

$$\dot{S}_B(u, v) = \int_{-\infty}^{\infty} \int_{-\infty}^{\infty} T_B(x, y) \exp [2\pi j(xu + yv)] dx dy \quad (5.66)$$

$$\dot{S}_P(u, v) = \int_{-\infty}^{\infty} \int_{-\infty}^{\infty} P(x, y) \exp [2\pi j(xu + yv)] dx dy. \quad (5.67)$$

We shall determine the obtained functions by $S_B(u, v)$ as a two-dimensional spatial spectrum of distribution of the source brightness $T_B(x, y)$, and $S_P(u, v)$ as a two-dimensional spatial spectrum (or the spatial frequency characteristic) of an antenna. In this case u and v will be spatial frequencies in two orthogonal directions x and y . If the whole transformation procedure occurs on the investigated surface, then the dimension of spatial frequencies will be $1/m$. Quite frequently, however (for example, in radio-astronomy), the transformation procedure is performed in the so-called picture plane, while remaining in the solid space (using the polar and azimuthal angles). In this case the dimension of spatial frequencies will be $(\text{radian})^{-1}$ or $(\text{degree})^{-1}$. If the source possesses azimuthal isotropy, it is convenient to pass to the other coordinate system – the polar radius ρ and the wave number k . In this case the appearance of the Fourier transformation will be quite different (Rytov, 1966), namely:

$$\dot{S}(k) = \int_0^{\infty} T_B(\rho) J_0(k\rho) \rho d\rho, \quad (5.68)$$

where $J_0(k\rho)$ is the zero-order Bessel function.

Equation (5.61) can be easily transformed into an algebraic one. Applying the two-dimensional Fourier transformation to both its parts, we obtain (see Appendix B):

$$\dot{S}_A(u, v) = \dot{S}_B(u, v) \dot{S}_P(u, v), \quad (5.69)$$

where $S_A(u, v)$ is the spatial spectrum of a signal recorded by an instrument. It can easily be seen that the obtained relation exactly repeats the relations we have used in analysing the propagation of electrical signals through the linear systems (and through the filters, in particular) (see section 2.6). Observational practice indicates that the source will always have a richer spectrum, and the antenna, as a filter of spatial frequencies, will remove high-frequency components (or smaller details, in other words), i.e. it will operate as a low-pass filter. The analogy with filtering systems is very important, since it opens the way to using powerful spectral methods developed in communications theory and in optics, as applied to the generalization of properties of signal transformation by antenna systems, which can now be considered as filters of spatial frequencies. The object, in its turn, can be characterized by the spectrum of spatial frequencies. As Born and Wolf (1999) have shown, a more general characteristic of the electromagnetic radiation field can also be introduced, which determines all its properties accessible to study by means of an instrument which is sensitive to quadratic-in-the-field quantities. This is a mutual coherence function, which includes both a spatial (the spatial spectrum)

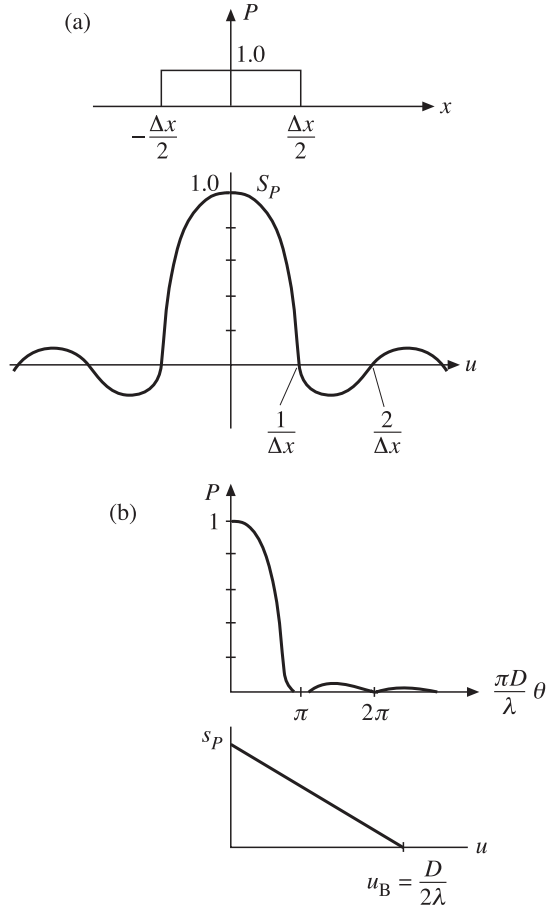


Figure 5.10. Examples of the relationship between antenna directional pattern (ADP) and special spectrum. (a) Ideal ADP (without side lobes zones). (b) Real ADP (with side lobes zone).

and a temporal characteristic of the radiation field of an object. The application of such a characteristic requires very serious theoretical training of the investigator; therefore, we shall refrain from the description and application of such an approach in this book.

As examples of spatial frequency characteristics of antenna systems, we shall consider two model situations. The first example is as follows. Suppose the antenna to have illuminated on an investigated surface the one-dimensional rectangular segment Δx (Figure 5.10). Using (5.67), we shall write the expression for the spatial one-dimensional spectrum of an illuminated area:

$$S_P = \int_{-\Delta x/2}^{+\Delta x/2} \exp(j2\pi ux) dx. \quad (5.70)$$

After some transformations we obtain the expression for the spatial spectrum of the area in the form of well-known function (Figure 5.10):

$$S_P = \Delta x \frac{\sin(u\pi\Delta x)}{u\pi\Delta x}. \quad (5.71)$$

Attention should be paid to the following circumstance: the presence of infinitely high frequencies (infinitely small details) in the spatial spectrum of an illuminated area, a situation, which is, certainly, inadmissible physically. This paradox is related to the selected model for ADP – the cutoff from a cone without the presence of side lobes. As we have noted above, such a model is unrealizable physically because of diffraction effects.

Consider now the realistic (with inclusion of a side-lobe radiation) ADP model, which is often used for estimation calculations. But now we shall consider it in the angular measure:

$$P(\theta) = \left(\frac{\sin \frac{\pi D}{\lambda} \theta}{\frac{\pi D}{\lambda} \theta} \right)^2, \quad (5.72)$$

where D is the diameter of a circular aperture and θ is the polar angle. From this expression we can easily obtain the total ADP value at zero points by equating the parameter to $\pm\pi$; then $\theta_0 = 2\lambda/D$. This problem can be solved also for finding the resolution from a half level, i.e. from the 3 dB level (by the graphical method, for example); then $\theta_{3\text{dB}} = 1.3\lambda/D$. The performed estimations relate to the ADP model of (5.72) type only, and for other realistic forms of ADP the estimates will, of course, be a little bit different numerically.

Using (5.67), we obtain the expression for a spatial one-dimensional spectrum of realistic ADP, by making use of well-known expression for definite integrals (Gradshteyn and Ryzhik, 2000):

$$S_P(u) = \begin{cases} \frac{\lambda}{D} \left(1 - \frac{u}{u_b} \right), & u \leq u_b, \\ 0, & u > u_b, \end{cases} \quad (5.73)$$

where $u_b = D/2\lambda$.

Here it is important to note that, unlike (5.71), the expressions for a spatial spectrum of the realistic ADP is different – the real antenna does not pass high-frequency components of a signal, i.e. it operates as a low-pass filter (Figure 5.10(b)). In this case the boundary frequency is equal to the reciprocal of the total ADP value, which is just what should be expected, generally speaking. The in-depth analysis of spatial frequency characteristics of various forms of antenna aperture is presented in the book by Esepkina *et al.* (1973).

In the theory of antennas the fundamental statement proved is that any realistic antenna is always limited in spatial frequencies and, therefore, we always lose the fine information on the spatial properties of a source. This does not mean, however, that it is impossible to restore some part of the spatial information. We shall discuss this issue below. If we consider the spatial smoothing procedure in the physical

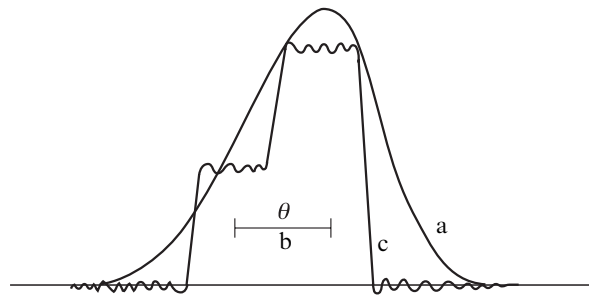


Figure 5.11. The restoration of a stepped signal model from the convolution of this model with the ideal ADP. (a) Result of the convolution. (b) Antenna beamwidth at 3 dB points. (c) Result of the recovery.

coordinate space, then, as we have seen, it can be described in an integral form (see equation (5.61)). This implies that it is impossible to achieve unambiguous restoration of the true (original) profile of a signal, since the regular procedure of deriving the integrand in the input signal from the expression for a prototype function for the convolution integral does not exist. If, however, we make use of the spectral-frequency presentation, then the result sought will directly follow from relation (5.69); that is to say, the spatial spectrum of the original signal will be equal to:

$$S_B(u, v) = \frac{S_A(u, v)}{S_P(u, v)}. \quad (5.74)$$

And, further, using the Fourier transformation, we can reconstruct (restore) a signal in physical space:

$$T_B(x, y) = \int_{-\infty}^{\infty} \int_{-\infty}^{\infty} \frac{S_A(u, v)}{S_P(u, v)} \exp(-j2\pi(ux + vy)) du dv. \quad (5.75)$$

The expression $[S_P(u, v)]^{-1}$ is naturally called the restoring filter.

Experimental investigations and modelling have shown that such a technique ‘works’ most efficiently at restoring the spatial structure of a source, where its spatial features subject to study are close in their values to the spatial characteristics of an antenna. Figure 5.11 presents the result of a model example of restoring the stepped and asymmetrical model of a source from its convolution from the ADP, whose characteristic size is comparable with the angular size of the resulting response (Kostenko, 1973). Analysis of the drawing reveals a striking peculiarity, consisting in the fact that the direct analysis of a spatial form of the convolution (the response of a system) which is only slightly asymmetric does not indicate in any way that the original source is double and sharply asymmetric. The presence of sinusoidal components in a restored signal is caused by cutting off high-frequency spatial harmonics in the response spectrum while performing the Fourier-transformation procedure (5.75). This procedure has been successfully used in laboratory radiothermal test investigations both in scalar and vector representations of the relationship between the antenna radiation characteristics and the radiation properties of the

investigated media (Holmes *et al.*, 1975; Truman *et al.*, 1977). In virtue of the great computational expense, the framework of use of such an approach in real onboard observations is essentially limited, and the aforementioned technique has not been widely used.

The restoration procedure considered above is, however, in its essence, a far-reaching idealization of the real experimental process. This is related to the fact that in the real experiment the uncontrollable signal (noise) is always present, whose origin is caused both by the intrinsic noise of the instrument and by so-called spatial noise. The statistical properties of these components are Gaussian and do not differ from the statistical properties of an original (useful) source (certainly, in the case of radiothermal observations only). We have already discussed in detail the intrinsic (thermal) noise of an instrument and its spectral characteristics in Chapter 3. The external spatial noise (this is the conventional name) is determined by signals of those physical objects which cannot be resolved by an antenna system of the given instrument unit and, therefore, can be presented as a combination of delta-function-type sources. Such a type of signal is sometimes called the ‘non-resolvable sources noise’. An excellent radio-astronomy example of such a type of signal is the radio image of the field of unresolved point-like sources presented on Plate 1. Of course, a similar situation can be found in radiothermal investigations of the Earth’s surfaces (the wavy sea surface, for example, see Chapter 12). Since the measured signal and the intrinsic noise are added in power as independent signals at the receiving system’s output, the intrinsic noise is sometimes transferred formally into the external spatial representation, whence the basic information is drawn, in essence (Plate 1).

Since both these components possess additivity properties with respect to the useful signal intensity, the total result can be written as:

$$T_A(x) = \int_{-\infty}^{\infty} T_B(x') P(x' - x) dx' + N(x). \quad (5.76)$$

The spectral density of intensity of intrinsic and external (spatial) noise of an instrument possesses broadband properties, because these components can be presented as a set of delta-function-type sources (see section 2.5). The application of a restoring filter $[S_P(u, v)]^{-1}$ leads in this case to the onset of (as the mathematicians say) singularities in the solution and to sharp amplification of high-frequency components (harmonics) caused by the predominating contribution of broadband noise. The situation described above is presented qualitatively in Figure 5.12. The resulting image is covered in this case by the background consisting of sharply flickering pixels of an image. Such a type of signal was called a speckle-type signal; it is well-known in television (‘snow’ on the TV screen in the absence of a basic signal) and in synthetizing the image in the scatterometry at reception of a backscattered signal. Certainly, the appearance of such a hindering (parasitic) signal sharply suppresses the possibilities of identification and recognition of a basic (useful) signal.

The problem considered thus relates to the class of so-called incorrectly formulated problems (Tichonov and Arsenin, 1979). A spectrum of methods is proposed for its solution. In the given case we shall indicate a fairly efficient approach, based

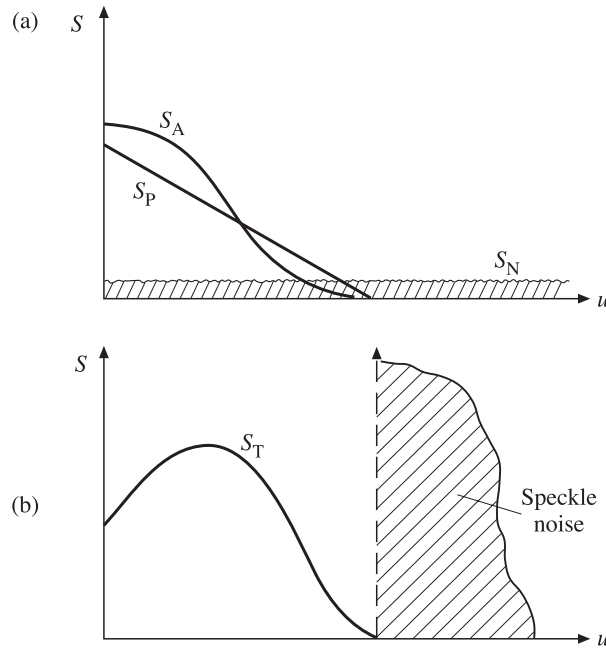


Figure 5.12. Qualitative picture of the restoration of a signal in the presence of noise components. (a) Spectra of antenna temperature (S_A), ADP (S_P) and noise (S_N). (b) The result of the recovery. See explanations in the text.

on the theory of minimizing root-mean-square prediction. In this case the best estimate (in the one-dimensional case) $\hat{T}_{B0}(x)$ of a true spatial signal $T_B(x)$ is

$$\hat{T}_{B0}(x) = \int_{-\infty}^{\infty} S_A(u) H_0(u) \exp(-2\pi j u x) du, \quad (5.77)$$

where the filter $H_0(u)$ is determined by the expression

$$H_0(u) = \frac{1}{S_P(u)} \frac{|S_P(u) S_B(u)|}{|S_P(u) S_B(u)|^2 + |S_N|^2}. \quad (5.78)$$

It can be shown that such a filter ensures the minimum of a root-mean-square error of prediction:

$$\varepsilon^2 = M[\hat{T}_{B0}(x) - T_B(x)]^2. \quad (5.79)$$

Thus, $H_0(u)$ describes the optimum characteristic of a restoring filter of spatial frequencies. It can be seen from expression (5.78), that the numerator and denominator of this relation include the power spectrum of a true signal, distorted by the linear instrument in the absence of noise, and the power spectrum of the noise itself. For each spatial harmonic of the signal spectrum obtained from the experiment, there exists a superposition of the corresponding noise power and the original signal

filtered by the instrumental function. Therefore, the filter (5.78) can be constructed, provided that it is possible to separate the aforementioned spectral components of the resulting signal observed. Therefore, the principal problem for the processing software lies in finding the estimates (of polynomial type usually) for $|S_N(u)|$ and $|S_P(u) S_B(u)|$ by approximating them in the spectral region by the least squares method using the *a priori* information on the original source structure. The success in restoring the radio-astronomical signals by the aforementioned method (and by ideologically close procedures) are quite impressive for today. There is no doubt, that this type of procedure will be widely applied in the very near future in the field of microwave remote sensing as well.

5.8 OUTDOOR CALIBRATION OF RADIOMETER INSTRUMENTS: THE METHOD OF CONTRASTING HALF-SPACES

As we have already noted, the procedure of reception and recording of radiothermal emission has some peculiarity (with respect to radio communications, television, radar), related to the physical features of the radiothermal emission of studied objects and of the receiving system itself.

For these reasons calibration procedures occupy a specific place in microwave sensing. They are subdivided, in essence, into two parts; the calibration of the receiving device itself (the determination of absolute scales, the sensitivity; see Chapter 3) (the indoor calibration, conventionally) and the calibration of the antenna system and antenna transmission line (the outdoor calibration). The indoor calibration is usually performed by means of two calibration (internal) sources, which are situated constructively just inside the receiving onboard satellite instruments and operate according to some particular, prespecified programme. The outdoor calibration is a considerably more complicated procedure, since the design philosophy of a flight vehicle (aircraft or satellite) and the features of antenna system mounting on a flight vehicle can essentially change the antenna field characteristics in the side-lobe zone. Thoroughly performed indoor and outdoor calibrations make possible the so-called absolute measurements, i.e. the antenna temperature transferring to the radiobrightness temperature of an investigated object (certainly, with regard to its geometrical properties). In some cases, however, there is no necessity to obtain the absolute values of a signal. In some measurements it is important to obtain the contrast in the values of a signal, taking into account that all remaining parameters of a system and ambient space remain virtually unchanged. Such a type of measurement was called relative measurement. In the process of real full-scale investigations, both the first and second type of measurement is used, depending on the particular situation. In some cases the combined approach to the solution of experimental problems is required.*

* Note here that there is no generally accepted treatment of notions of absolute and relative measurements, and some authors give different physical meanings to these notions.

Even at the first stage of radiothermal investigation of terrestrial surfaces (1967–1973) (see Chapter 14), when the normalized sensitivity of onboard radiometers was 1.5–2 K, the necessity for detailed analysis of the radiation field of an antenna system, with regard to the features of antenna mounting on a flight vehicle, was fully recognized (Rabinovich *et al.*, 1968, 1970). In the mid-1970s, the appearance of onboard highly sensitive radiothermal satellite instruments (with normalized sensitivity of up to 0.03–0.1 K) (Amirkhanyn *et al.*, 1975) put on the agenda the necessity of developing an efficient technique of absolute and relative radiothermal measurements in the regime of direct onboard observations. On the basis of many years of experience of processing the experimental data of onboard observations, the author of this book proposed in 1975, and then verified in the course of a series of onboard experimental works, the special technique of processing the radiobrightness registograms with the purpose of obtaining estimates of important antenna parameters (the scattering coefficient, the background radiation in the side-lobe zone, the main lobe width) in the regime of direct onboard measurements (Veselov *et al.*, 1981). The proposed technique is based on the transparent physical idea that, when the flight vehicle passes through two sharply contrasted (in the radiobrightness sense) semi-infinite surfaces (from sea to land, for instance), the radiothermal signal registogram gives a peculiar picture of the transition signal, which can reveal the integral features in the radiation field of an antenna system. This method, called the method of contrast half-spaces (MCH), has been actively used since in various modifications, for example, for restoring the main lobe of ADP of onboard satellite instruments (Savorskii *et al.*, 2000). Another interesting example of using this method is the calibration of active–passive satellite instruments of the interplanetary Cassini spacecraft (in the International Cassini mission) at a gravity-assist during its Earth swing-by on its further journey to Saturn. The ground track of the instrument's ADP passed over the surface of Pacific Ocean and over the abrupt transition at the ocean–land boundary (with South America). The radiometric and scatterometric parts of satellite instruments were calibrated from the radiothermal and backscattered ocean–land contrast (West *et al.*, 2000).

A fairly complicated signal (see relations (5.37) and (5.50)) arrives at the radio-metric receiver's input, the useful information being contained, in essence, in a single component (T_{AB}) only. Its value is determined by the signal energy reception at the main lobe of an antenna, since the position of the latter in space is quite well known. But the information, which comes into the side-lobe zone (T_{SB}) is, actually, difficult to use, since the characteristics of antenna radiation in these DP zones are virtually unknown to a sufficient accuracy (because the side-lobe radiation is sensitive to design features of a particular specimen of antenna and to the features of its mounting on a carrier). Besides, it is difficult to unambiguously interpret the signals coming to the side-lobe zone from their spatial position relative to the antenna carrier. An indicative illustration of this statement is the registogram of a radiothermal signal recorded in passing through the land–water transition (and back) over Lake Ladoga by means of high-sensitivity radiometric R-2 satellite instruments (at the working wavelength of 2 cm) installed on the Russian IL-18 aircraft-laboratory (Figure 5.13). The signal structure in the 2' zone of the ‘water–

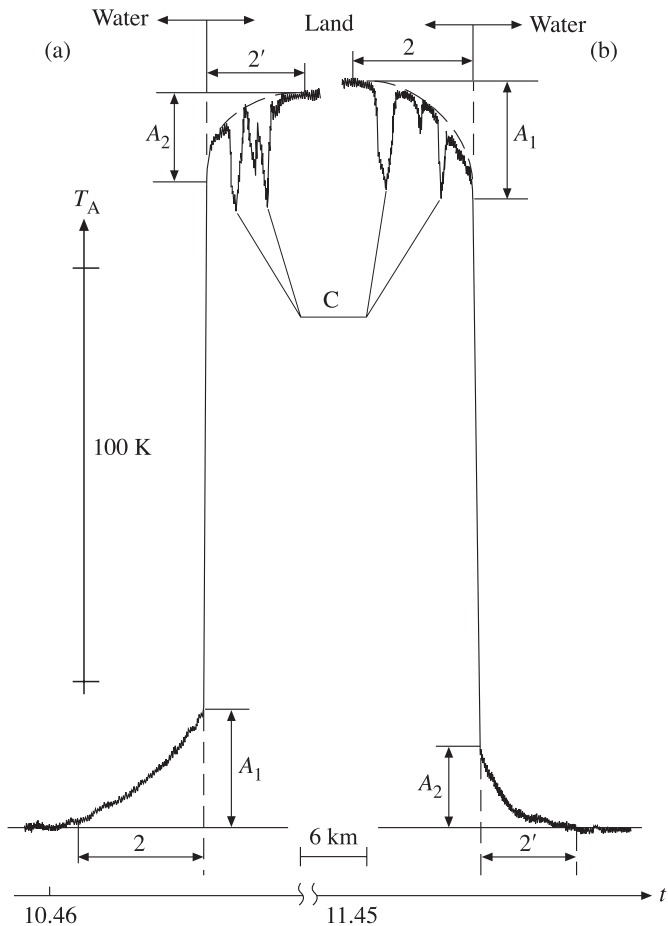


Figure 5.13. Fragments of the output radiometer signal of airborne (Russian IL-18) instruments (radiometer R-2) when crossing a water–land transition. The working area is Lake Ladoga (Russia). The working date was 9 September 1975. The flight height is 4000 m. Moscow time and spatial scale are shown on abscissa. Temperature scale is shown on ordinate. See notation A_1 , A_2 , C , 2 , $2'$ in the text. (a) Water–land transition. (b) Land–water transition.

land’ fragment (Figure 5.13(a)) and in the 2 zone of the ‘land–water’ fragment (Figure 5.13(b)) is determined by simultaneous reception (by an antenna) of radio-emission from highly separated (in the physical space) fragments of radiothermal background of the surface: a smoothly varying signal component (shown by the dashed line on the drawing) is caused by reception of emission from the land in the side-lobe zone, whereas the strong negative variations (defined by C) are caused by reception of emission from the land elements at the main lobe. The contribution to the total signal from emission reception at the side lobes in the forward half-space from the land–water contrast is designated by symbol A_1 , and the same contrast at

the side lobes in the backward half-space by symbol A_2 . At the return passage (Figure 5.13(b)) through the same geographical region the situation was, certainly, mirrored. It can easily be seen that the given antenna system of the satellite instruments possesses small integral asymmetry of forward and backward half-spaces of emission in the side-lobe zone.

Thus, the total (over the whole observational half-space 2π) Fourier restoration (as it can be performed for laboratory investigations) is not possible at all in the onboard version. The information parameter subject to measurement is the quantity T_{AB} and its variations, which should be discriminated against the background of variations of T_{SB} and noise signals of an antenna and transmission line (with losses), which are statistically indiscernible from the basic signal. For this reason there is no necessity, from the practical point of view, to perform the total (and very laborious) Fourier restoration of antenna parameters.

Thus, the absolute measurements of T_{AB} can be performed through knowledge of the indoor calibration of a radiometer (for example, the scale and radiobrightness temperature of an equivalent), the performance coefficient and temperature of the antenna transmission line (ATL), and the antenna scattering coefficient and radiobrightness temperature of the underlying surface, whose emission is accepted at side lobes, i.e. the T_{SB} value.

The difficulties, associated with accounting for the transmission line's performance coefficient and temperature profile, can either be taken into account in experimental practice, or eliminated by appropriate design solutions. The most radical way of doing this is by the total thermal stabilization of the ATL, the antenna and the high-frequency part of a radiometer, by the use of antennas with maximum performance coefficient and by the design matching of the radiometer's input unit with the antenna. Here the latter term is constant and can be taken into account at processing or at preliminary calibration. It can also be seen from these considerations, that, in performing absolute measurements, even under these most favourable conditions, the difficulty arises in determining the scattering coefficient – under onboard conditions – and the quantity T_{SB} , which is determined by the type of surface and ADP in the side-lobe zone.

In performing, however, the relative (within the limits of the given working mission and with the same type of homogeneous surface) measurements and under the condition of small variations of radiobrightness, knowledge of the ATL scattering coefficient and performance coefficient is required. In other words, the signal variation at the main lobe ΔT_{AB} is related to the measured variation of ΔT_A as follows:

$$\Delta T_{AB} = \frac{\Delta T_A}{(1 - \beta)\eta}. \quad (5.80)$$

Thus, for performing the correct absolute and relative onboard radiothermal experiments it is necessary to measure and verify, to an accuracy sufficient for practical purposes, the following parameters:

- (a) the ADP main lobe value;
- (b) the scattering coefficient value;

- (c) the value of T_{SB} of various surfaces for the given antenna specimen and its design features.

As we have noted above, the scattering coefficient is the antenna system characteristic, whose value depends both on a particular specimen of antenna, and on a series of design features of the antenna mounting on the flight vehicle (the method of fastening, the shape of the fairing, etc.). The ground or laboratory verification of such a parameter is fairly labour-consuming for natural reasons, though in some critical cases it is carried out on flight vehicle models (Rabinovich *et al.*, 1970). For this reason it is desirable to find the method of determination (or estimation to an acceptable accuracy) of the scattering coefficient under onboard conditions and its regular re-verification in the course of lengthy flight experiments. The data on the beam efficiency (i.e. the quantity $1 - \beta$) of radiometric space satellite instruments presented in the literature (see, for example, Njoku *et al.*, 1999; Mo, 1999), are the result of calculations from ground measurement data, but in no way the result of real observations. With the modern technology of antenna systems production, the extreme values of scattering coefficients for immovable antennas equal 3–10% (unique samples) and 10–15% (standard samples). For scanning systems with an immovable irradiator the scattering coefficients increase up to 10–15% (unique samples) and 15–20% (standard samples). In general, it should be mentioned, the methods of minimizing the scattering coefficient for various types of antennas are but weakly developed so far. The available data in the specialized radio-engineering literature give only rough classification of antennas in average values of a scattering coefficient. Detailed analysis has shown that it is horn and horn-parabolic antennas which best satisfy all the requirements formulated above. These antennas possess minimum scattering coefficient value and maximum performance coefficient (PC), up to 98–99%; they can also be well coordinated in the necessary band and constructively integrated with the microwave receiver set into a single thermally stabilized unit (Amirkhanyn *et al.*, 1975; Strukov and Skulachev, 1984, 1986; Cherny and Chernyavsky, 2001; Njoku *et al.*, 1999; Mo, 1999; Ruf, 2000a,b). It is interesting to note that the cophased array version, which was used for the microwave unit of Nimbus 5 and 6 satellites (Allison *et al.*, 1974), has now been completely rejected for potential satellite instruments because of the small performance coefficient of such antennas, the single-frequency mode of operation and the rather high value of the scattering coefficient. Preference is now for the horn and parabolic types of antennas with the mechanical mode of scanning with conical geometry (see Chapter 14).

As far as the brightness values of various surfaces are concerned, the situation is rather complicated. As the special ground experiments have shown, the averaged value of radiobrightness temperature, falling on side lobes, is approximately 10–30% lower than the value received by the main lobe. However, the question of measuring this quantity and its statistical characteristics still remains open in the case of onboard experiments, where the surface (with unknown radiobrightness characteristics, in the general case) is investigated by means of an antenna for which the ADP in the side-lobe zone is also known with high uncertainty. True, experimental practice is more hopeful. This is due to the fact that the reception in the side-lobe

zone is accomplished in a fairly wide solid angle (of the order of 2π), and for this reason the averaged value of temperature fluctuates quite insignificantly for the given type of surface. This allows us to use the averaged T_{SB} value for absolute measurements, and for relative measurements, within the limits of a straight flight over sufficiently homogeneous surfaces, T_{SB} can be considered to be constant. Thus, it seems apparently impossible to escape the limits of ± 10 K in the absolute onboard measurements without using the *a priori* information on radio-emission of the surface and special techniques for determining the emission received in the side-lobe zone, and also without checking the scattering coefficient value. In performing ground-based laboratory radiothermal experiments the technique of calibration of a measurement system by the ‘black-body’, ‘artificial zenith’ and a quiet water surface allows us to reasonably reliably determine the scattering coefficient of an antenna and the side-lobe emission T_{SB} (certainly, within the given conditions of performing the experiment). The accurate implementation of a similar technique allows us to achieve an accuracy of up to 0.2 K (or 0.3%) at laboratory absolute measurements of water surface emission,* as compared to the theoretical radiobrightness value calculated on the basis of modern data on dielectric characteristics of water (see Chapter 8).

The special technique of graphical processing the regisograms received from the surfaces, which highly differ in the radiothermal sense, is considered below. This processing allows us to evaluate the aforementioned parameters to an acceptable accuracy ($\approx 5\text{--}10\%$) and to verify them in a regular manner under onboard conditions without disassembling the antenna systems.

Figures 5.14 and 5.15 present fragments of regisograms of the channel of the R-18 radiometer installed on the Russian IL-18 aircraft-laboratory (see Chapter 14), at the working wavelength of 18 cm, at transition through two highly contrasted radiothermal zones of the earth’s surface: the fresh water Balkhash and Ladoga lakes and the land. The antenna represents a cutting-off from a parabolic cylinder with a vibrator power supply and with the main lobe width (on the 3 dB level) of 18° . The experiment was performed in such a manner, that the intersection of the water–land interface boundary took place in the same geographical region, but at various heights of the carrier (aircraft) – from 600 m to 4300 m. Here Figure 5.14 presents the fragments of a regisogram of a land–water transition (in one direction) (Lake Ladoga) and Figure 5.15 the fragments of a regisogram of a water–land transition and a return run over the same geographic region, a land–water transition (Lake Balkhash). The qualitative analysis of regisograms (Figures 5.13–5.16), obtained in different geographical zones and by various remote sensing instruments, shows, nevertheless, that the character of radiothermal signals at sharp transitions is quite similar. The presence of two zones are represented: a zone of slow signal variation and a zone of rapid signal variation. Depending on the experiment geometry, the clearness of these zones on the regisograms is certainly different: the higher the vehicle flight altitude, the clearer the zones. This feature is especially well seen

* Experiments were performed in 1976 under the direct guidance of the author of this book (Bordonskii *et al.*, 1978).

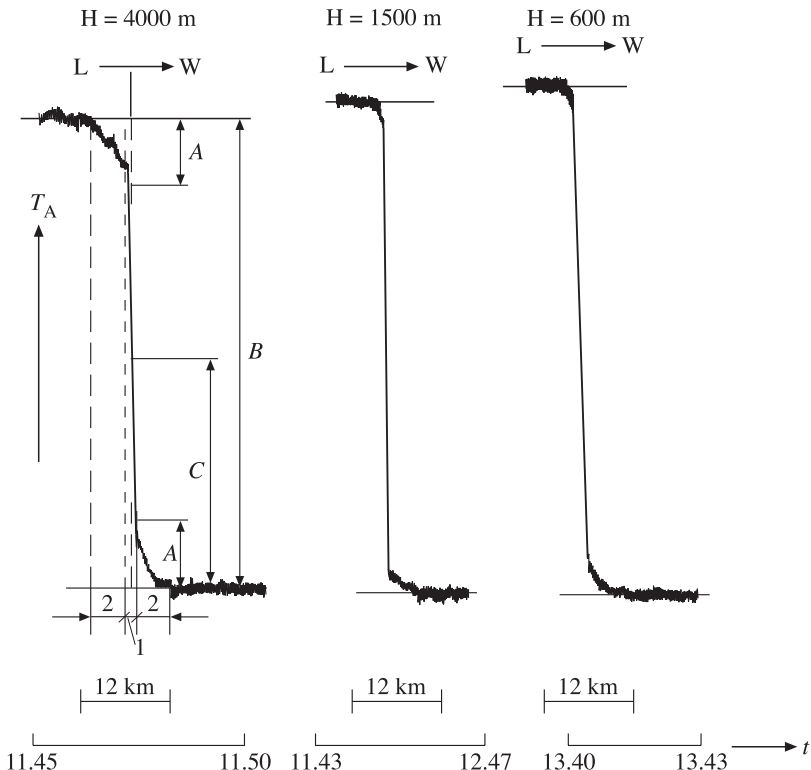


Figure 5.14. Fragments of the output signal of airborne (Russian aircraft-laboratory IL-18) radiometer R-18 ($\lambda = 18\text{ cm}$) when crossing a land–water transition at various heights ($H = 4000\text{ m}$, 1500 m and 600 m). The working area is Lake Ladoga (Russia). The working date was 9 September 1975. Moscow time and spatial scale are shown on abscissa. See notation A, B, C, 1, 2 in the text.

on the regisograms in Figure 5.16, where the results of flights at the land–water transition (in one direction) at different altitudes (Lake Ladoga, instrument R-2) are presented. To clear up the situation, we shall consider the simplified geometry of the experiment whose flight part is shown schematically in Figure 5.17(a), where Ω' and Ω'' are solid angles of the main and side lobes directed to the land. Figures 5.17(b) and (c) presents schematically the regisograms of the radiothermal signal of the land–water transition with separation of some characteristic zones. The analysis of radiothermal regisograms of highly sensitive radiometers, obtained in flight through the transition between two highly contrasting (in the radiothermal sense) surfaces (such as a quiet water surface and a homogeneous rocky coast), shows the presence of two prominent zones (in the corresponding time scale of recording): the prolonged zones with a smooth signal variation (zones 2 and 2') (Figures 5.17(b) and (c)) and the zone of rapid and virtually linear drop (zone 1). Zones 2 are formed when the radio-emission of a contrasting half-space is generated within the solid

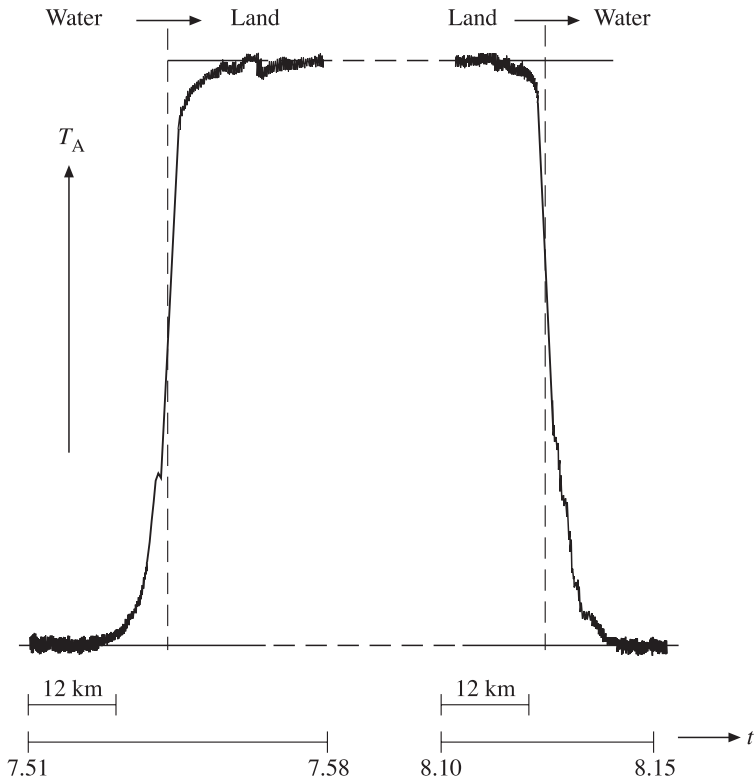


Figure 5.15. Fragments of the output signal of airborne radiometer R-18 when crossing a water–land and a land–water transition. The working area is Balkhash Lake. The flight height is 4300 m. The working date was 25 April 1975. Moscow time and spatial scale are shown on abscissa.

angle of the side antenna emission, and zone 1 when the same radio-emission is generated within the solid angle of the main lobe. Figure 5.17(c) presents schematically the case where the main lobe width is extremely small (the delta-function), and the side emission remains at the same level (as is observed in the real experiment; see Figure 5.16). As the experiments have shown, zones 2 are virtually symmetrical for many types of antenna used; and this indicates that the side-lobe radiation of antennas, averaged in solid angles into the forward and backward half-spaces, are generally equal.

With regard to expressions (5.37)–(5.40) and (5.50), obtained above, the antenna temperature of an onboard instrument at the time the flight vehicle intersects the water–land boundary by a flight vehicle can be written as:

$$T_A = [T_{ABL}\beta' + T_{ABW}(1 - \beta')](1 - \beta)\eta + T_{SBL}\beta''\eta + T_{SBW}(\beta - \beta'')\eta + T_0(1 - \eta), \quad (5.81)$$

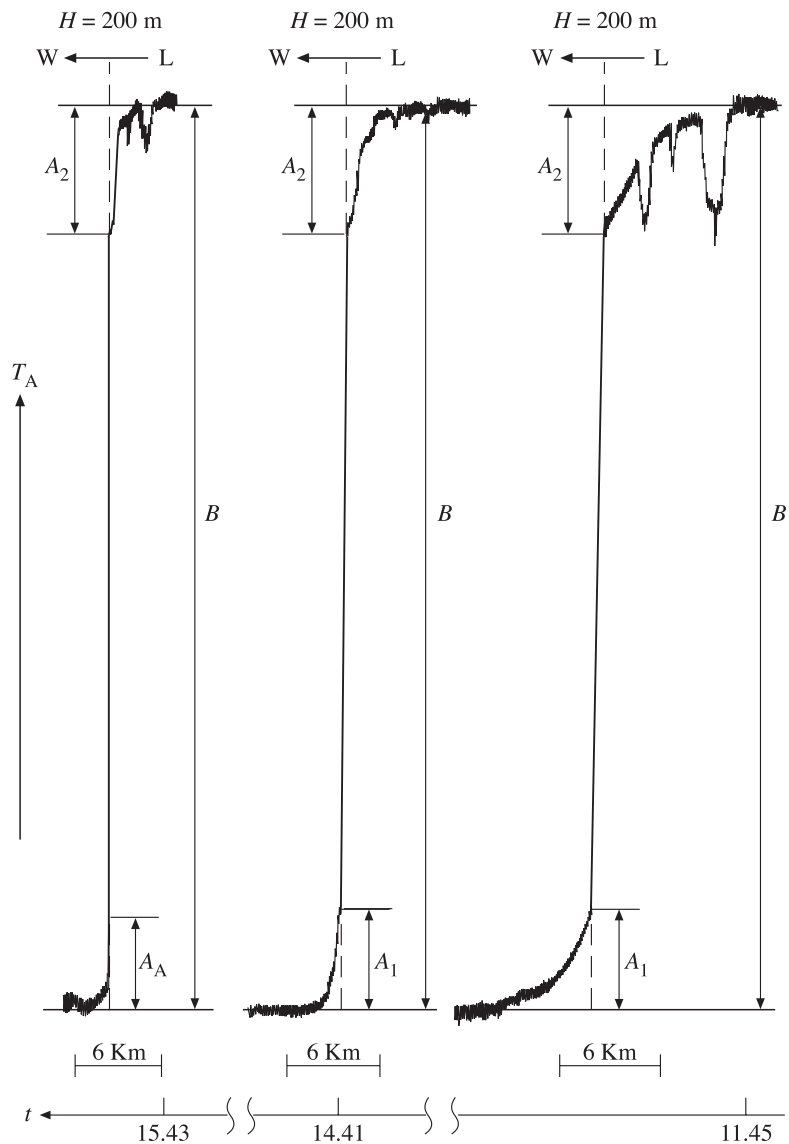


Figure 5.16. Fragment of the output signal of airborne radiometer R-2 when crossing a land–water (L–W) transition at various heights ($H = 4000 \text{ m}, 600 \text{ m}, 200 \text{ m}$). See notation A_1, A_2, B in the text. Legends as for Figure 5.13.

where T_{ABL} , T_{ABW} are the radiobrightness temperatures received at the main lobe from the surface of land and water, respectively; T_{SBL} and T_{SBW} are the radiobrightness temperatures received in the side-lobe zone from the surface of land and water, respectively. Quantities β' and β'' are the scattering coefficients of a

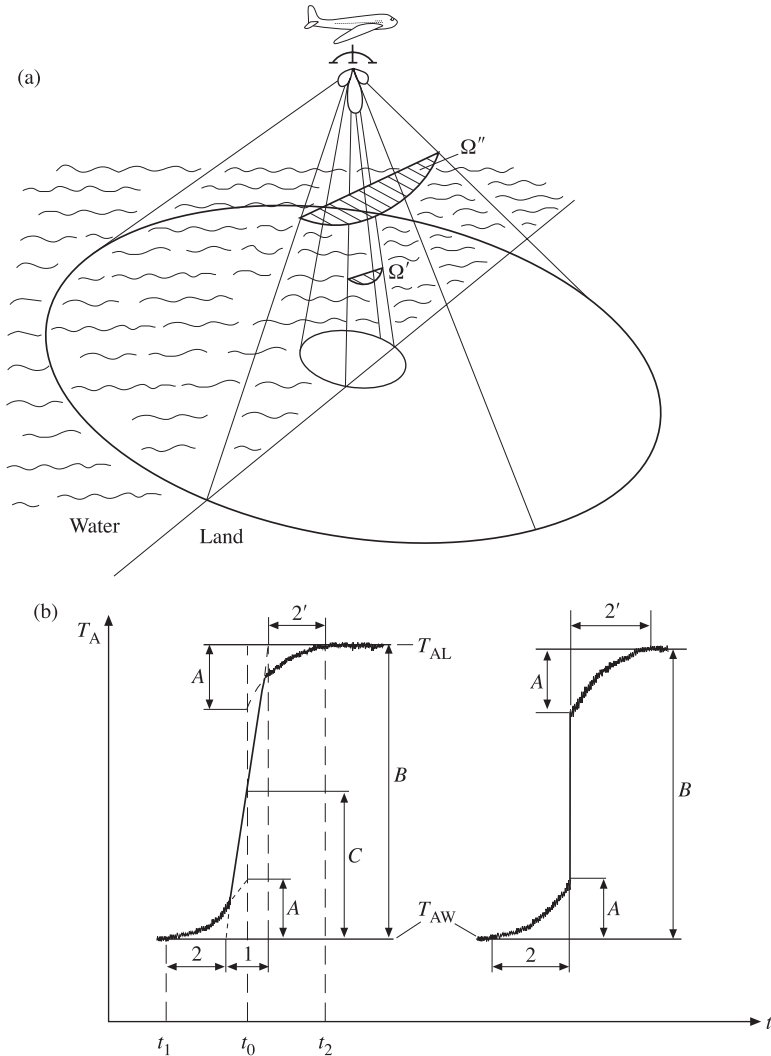


Figure 5.17. Schematic presentation of a water–land transition airborne experiment. (a) Simplified geometry of the experiment. (b) Qualitative picture of output radiometer signal (in arbitrary units). (c) Output signal when a main lobe zone is a delta-function. See notation in the text.

part of the main lobe and of the side-lobe zone, directed to the land surface, and they can be expressed as

$$\beta' = \frac{\iint_{\Omega'} P d\Omega}{\iint_{\Omega_{AB}} P d\Omega}; \beta'' = \frac{\iint_{\Omega''} P d\Omega}{\iint_{4\pi - \Omega_{AB}} P d\Omega}. \quad (5.82)$$

From the analysis of relation (5.81) it can easily be seen that, irrespective of absolute values of brightness temperatures of contrast half-spaces, the character of antenna temperature T_A of the transition will be symmetrical (if the side emission of an antenna is symmetrical integrally), in the linear part of a regstrogram (zone 1) the main contribution being made by the first term (5.81), and in zones 2 by the second one. The expression for the antenna temperature value for a middle of transition T_{AM} (at time instant t_0 in Figure 5.17(b)) is equal to:

$$T_{AM} = \frac{T_{ABL} - T_{ABW}}{2}(1 - \beta)\eta + \frac{T_{SBL} - T_{SBW}}{2}\beta\eta + T_0(1 - \eta). \quad (5.83)$$

In the case where the whole solid angle of an antenna is directed to one of contrast half-spaces (far from the transition), the expression for antenna temperature can be presented as (T_{AL} at a flight over the land and T_{AW} over the water):

$$\begin{aligned} T_{AL} &= T_{ABL}(1 - \beta)\eta + T_{SBL}\beta\eta + T_0(1 - \eta) \\ T_{AW} &= T_{ABW}(1 - \beta)\eta + T_{SBW}\beta\eta + T_0(1 - \eta). \end{aligned} \quad (5.84)$$

Now we shall consider the features of transition regstrograms. These features include (see Figures 5.13–5.14, 5.16 and 5.17) the value of the total antenna temperature drop between two contrasting surfaces B and the contribution A of a contrast between the surfaces to the forward and backward half-spaces of a side-lobe zone (these zones are shown schematically in Figure 5.17(a)). The total brightness contrast of the land–water transition, recorded at instrument's output, will be:

$$B = T_{AL} - T_{AW} = (T_{ABL} - T_{ABW})(1 - \beta)\eta + (T_{SBL} - T_{SBW})\beta\eta. \quad (5.85)$$

The brightness contrast contribution from surfaces into the side-lobe zone (into the forward and backward half-spaces separately) will be equal to:

$$A = (T_{SBL} - T_{SBW})\frac{\beta}{2}\eta. \quad (5.86)$$

The parameters directly measured at the instrument's output are the values of antenna temperatures T_A (relations (5.81) and (5.84)), which can be determined by using the indoor calibration of a radiometer. In their turn, T_0 and η can be obtained from the data of measurement of the antenna transmission line temperature and from the preliminary (pre-flight) measurements, for example, by the method of two loads (see Chapter 7). The principal unknown quantities remain the values of the antenna scattering coefficient (under specific conditions of its installation on the given flight vehicle) and the averaged values of brightness temperatures of contrast surfaces in the side-lobe zone for the given antenna (5.39). However, as detailed studies of this problem have shown (Veselov *et al.*, 1981), the situation is not desperate. The fact is, that the contrasts between brightness temperatures, measured at the main lobe and at the side-lobe zone, are very close:

$$T_{SBL} - T_{SBW} \approx T_{ABL} - T_{ABW}. \quad (5.87)$$

This equality is observed to an accuracy better than 5%. In this case β and its components into the forward β_F and backward β_B half-spaces can be estimated, in the first approximation, directly from the transition regisrogram geometry (Figures 5.16 and 5.17):

$$\beta = \frac{2A}{B}; \beta_F = \frac{A_1}{B}; \beta_B = \frac{A_2}{B}. \quad (5.88)$$

It is important to note that the given estimate does not depend either on the internal scale of an output instrument or on the value of losses in the antenna line.

5.8.1 MCH procedure

To construct the correct procedure for the method of contrasting half-spaces (MCH) and for further calculations of the receiving system's parameters it is necessary to specify, proceeding from theoretical estimates (see Chapter 8), the value of T_{ABW} and use the proposed iteration procedure ('a ring') to clear up the physical substantiation of the theoretic value. So, the following procedure is proposed:

- (1) First we perform the preliminary estimation of β from the transition regisrogram (expression (5.88)).
- (2) Then, specifying the theoretical value of T_{ABW} and the estimate of β , we obtain the T_{SBW} value by the following formula:

$$T_{SBW} = \frac{1}{\beta\eta} [T_{AW} - T_0(1 - \eta) - T_{ABW}(1 - \beta)\eta]. \quad (5.89)$$

- (3) Using the obtained T_{SBW} value, we find T_{SBL} according to the expression:

$$T_{SBL} = \frac{2A}{\eta\beta} + T_{SBW}, \quad (5.90)$$

where the value of A is taken on the indoor calibration scale.

- (4) Using the obtained value of the total drop (in the indoor scale) and the theoretical value of T_{ABW} , we obtain the estimate for T_{ABL} :

$$T_{ABL} = \frac{B - 2A}{\eta(1 - \beta)} + T_{ABW}. \quad (5.91)$$

- (5) Using the results of steps (1) and (2), we obtain the second (improved) estimate for the β' value:

$$\beta' = \frac{2A}{T_{SBL} - T_{SBW}} \frac{1}{\eta}. \quad (5.92)$$

- (6) Proceeding from the measured value of T_{AW} and obtained values of T_{SBW} and β' , we calculate the T'_{ABW} value by formula:

$$T'_{ABW} = \frac{1}{\eta(1 - \beta')} [T_{AW} - T_0(1 - \eta) - T_{SBW}\eta\beta'] \quad (5.93)$$

for further comparison with the theoretical value.

Table 5.2. Antenna characteristics of microwave instruments onboard airplane-laboratory IL-18 (1975–1976)

Radiometer design	Working wavelength, cm	Sensitivity, $\tau = 1$ sec	Antenna type; aperture dimension, cm	θ_{3dB} degree of circle (calculated)
R0.8	0.8	0.08	Parabolic antenna; 30	1.9
R2	2	0.04	Parabolic antenna, with displaced irradiator; 100	1.4
R8	8	0.05	Horn-parabolic antenna; 65	9.0
R18	18	0.4	Cage-parabolic antenna with dipole irradiators; 70 × 70	18

(7) Using the obtained value of β' , we obtain the restoring coefficient for relative measurements (see expression (5.81)):

$$k_R = \frac{1}{(1 - \beta')\eta}. \quad (5.94)$$

As an example, we shall perform the indicated procedure for the experimental data of the R18 (I, II) instrument (see Chapter 14 and Table 5.2).

(I). The flight took place on 25 April 1975, over Lake Balkhash and the steppe regions adjacent to it. The brightness temperatures of the water surface and land (on the indoor scale) were 164 K and 267 K, the performance coefficient of an antenna transmission line was estimated (from the ground measurements) as 0.66, $T_0 = 280$ K (the in-flight measurements) (Figure 5.15).

The execution of the indicated procedure gives the following results:

- (1) The estimation of a scattering coefficient gives the value of 0.27.
- (2) $T_{SBW} = 95$ K (with the theoretical value of $T_{ABW} = 108$ K).
- (3) $T_{SBL} = 251$ K.
- (4) $T_{ABL} = 264$ K.
- (5) $\beta' = 0.264$.
- (6) $T'_{ABW} = 107.5$ K.
- (7) $k_R = 2.04$.

(II). The flight took place on 9 September 1976, over Lake Ladoga and rocky regions adjacent to it. The brightness temperatures of the water surface and land (on the indoor scale) were 182 K and 272 K, the performance coefficient of the antenna transmission line was estimated (from the ground measurements) as 0.57 (the design

modifications in the antenna system installation took place in April 1975), $T_0 = 275$ K (the in-flight measurements) (Figure 5.14).

The execution of the indicated procedure gives the following results:

- (1) The estimation of a scattering coefficient gives the value of 0.31.
- (2) $T_{\text{SBW}} = 116$ K (with the theoretical value of $T_{\text{ABW}} = 110$ K).
- (3) $T_{\text{SBL}} = 274$ K.
- (4) $T_{\text{ABL}} = 267$ K.
- (5) $\beta' = 0.308$.
- (6) $T'_{\text{ABW}} = 111.9$ K.
- (7) $k_R = 2.54$.

The comparison of theoretical values of the brightness temperature of the water surface with the measured value proves the reliability of the procedure. In addition, it follows from the obtained data that the basic approximation (5.87) is satisfied to an accuracy better than 2%.

Attention should be paid to the fact that all iterative steps must be executed and mutually verified. And, in addition, analysis of the physical sense of results is necessary, since in some cases the peculiarity of the initial data can lead to ‘falling’ on a diverging branch of the iteration ring, which can give physically meaningless results (such as $\beta > 1$). The indicated procedures can easily be executed onboard the flight vehicle by means of special processing units.

5.8.2 Estimation of the main lobe width

From the graphical representation of a radiothermal signal we can obtain one more important characteristic: the estimation of the angular size of the main lobe under onboard conditions. It can easily be seen that zone 1 (Figure 5.17(b)) in the angular measure characterizes the total main lobe width, and from simple geometrical considerations it is possible to obtain a satisfactory estimate of the main lobe width (by the 0 dB level, i.e. the full lobe):

$$\theta_{0\text{dB}} = 2 \arctg \frac{V \Delta t}{2H}, \quad (5.95)$$

where Δt is the time of passage through zone 1 (Figure 5.17(b)) and V and H are the velocity and altitude of the carrier. And, since for the majority of beam antennas the $2.3\theta_{3\text{dB}} = \theta_{0\text{dB}}$ relation is valid to an acceptable accuracy, we obtain the following estimate for the main lobe value by the 3 dB level:

$$\theta_{3\text{dB}} = \frac{V \Delta t}{2.3H}. \quad (5.96)$$

The comparison of the estimates, found by the indicated method and calculated proceeding from the design data (Table 5.2 and 5.3), shows satisfactory correspondence. In conclusion, we consider briefly the typical errors. For example, Vinogradov (1976) completely arbitrarily takes for the spatial resolution on the surface a quantity equal to half of the total transition, i.e. $\frac{1}{2}\{(t_2 - t_1)V\}$ (see Figure 5.17(b)), which

Table 5.3. Measured antenna characteristics of microwave instruments by the MCH method

Time and location of experiments	Radiometer design	θ_{3dB} (calculated) degree of circle	θ_{3dB} (measured) and RMS, degree of circle	Scattering coefficient, (measured) and RMS
25 April 1975; Lake Balkhah	R18	18	18 ± 0.5	0.20 ± 0.03
9 September 1976; Lake Ladoga	R18 R2	18 1.4	18 ± 0.5	0.24 ± 0.03 0.26 ± 0.03
13 July 1976; the Barents Sea	R8 R2 R0.8	9 1.4 1.9	9.3 ± 0.3 2.2 ± 0.2 2.5 ± 0.2	0.25 ± 0.05 0.27 ± 0.05 0.21 ± 0.05

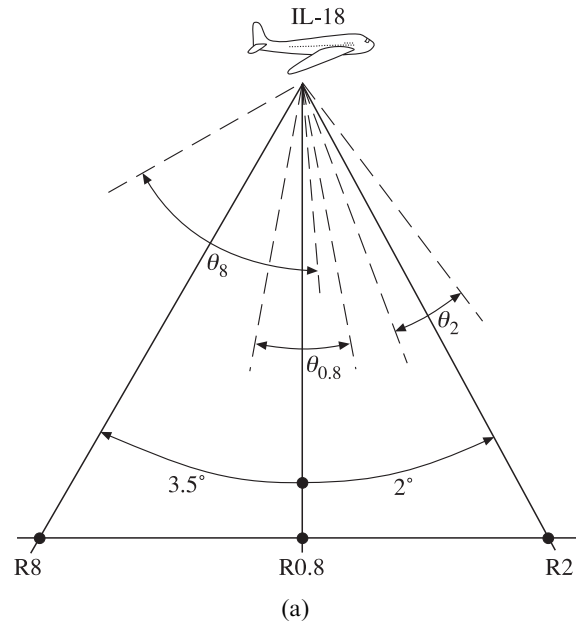
more than twice exceeds the design value of a spatial resolution (the half of zone 1). However, the estimation we have carried out by the proposed technique for the ‘Nimbus-5’ spacecraft from the land–water transition registrograms, contained in the paper mentioned, gives the value of 25–27 km. This estimate fully agrees with the design spatial resolution values found proceeding from the spacecraft antenna parameters measured on the Earth. Thus, Vinogradov’s (1976) concept of finding the spatial resolution as a half of the transition length should be recognized to be wrong and his strong criticism of ‘Nimbus-5’ spacecraft developers to be unsubstantiated. Similar errors, nevertheless, have been repeated in some publications, including Western literature.

5.8.3 Geometry of position of beams of multifrequency instruments

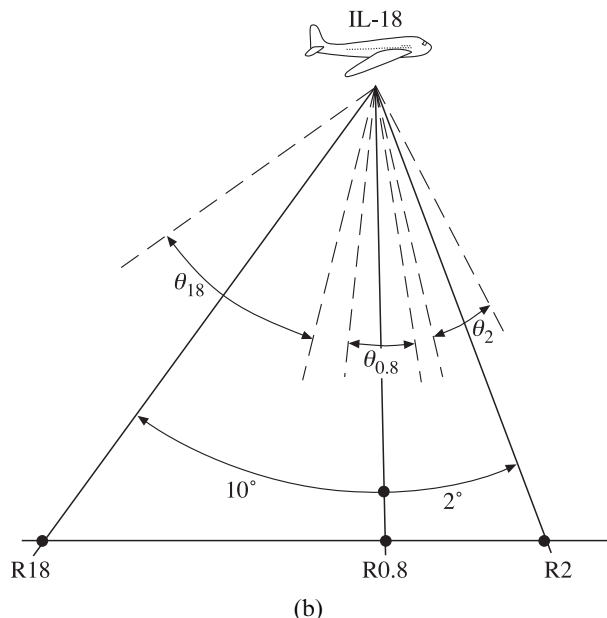
The accurate timing of centres of transition registrograms for multifrequency instruments allows us to solve one more important problem – of the mutual spatial-angular position of centres of antenna directional patterns for various transition lines (channels). For an example of the solution of such a problem we take the result of the following experiment on studying the mutual position of ADP centres of multifrequency radiothermal airborne instruments of the IL-18 aircraft-laboratory (Table 5.2) (Amirkhanyan *et al.*, 1975; Bespalova *et al.*, 1976a,b, 1979; Antonov *et al.*, 1995). The ADP axes for the channels of 0.8, 2, 8 and 18 cm are presented in Figures 5.18 and 5.19. Note that it is impossible to reveal these geometrical features by any other experimental method.

5.9 ANTENNA PARAMETERS OF AIRBORNE MICROWAVE INSTRUMENTS

As an example of using the proposed technique, we shall consider the estimation (by means of the MCH method) of antenna parameters of airborne, high-sensitivity



(a)



(b)

Figure 5.18. Schematic presentation (in no scale) of geometry for main axes and values of ADP main lobes of radiometric instruments onboard Russian aircraft-laboratory IL-18 (September 1975–July 1976): (a) for radiometers R2; R0.8; R8; (b) for radiometers R2; R0.8; R18.

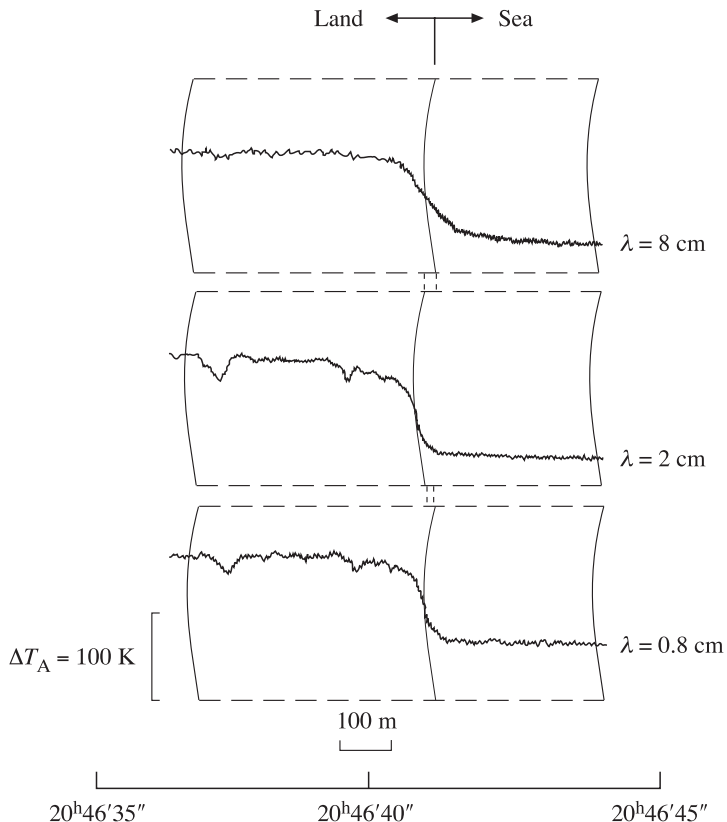


Figure 5.19. Fragments of synchronous output signals of airborne radiometers R8, R2 and R0.8 when crossing a land-sea transition. The working area is the Barents Sea, the Cape of Kanin Nose (13 July 1976; $H = 400$ m). Moscow time and indoor temperature calibration are shown on abscissa and on ordinate.

microwave instruments, produced at the Space Research Institute of the Russian Academy of Sciences, which underwent flight tests in 1975–1976 (see Chapter 14). The basic characteristics of radiothermal microwave airborne instruments of the Russian IL-18 aircraft-laboratory are presented in Table 5.2. Note that the table presents the data on the normalized fluctuation threshold sensitivity of instruments, measured directly under onboard conditions. The table also gives the numerical estimates of angular characteristics of the ADP main lobe, obtained in accordance with theoretical concepts (see expression (5.14)).

The antenna parameters of instruments have been estimated using a great volume of in-flight data obtained during 1975–1976 in various regions of Russia: Lake Balkhash (April 1975), Lake Ladoga (September 1975), and the Barents Sea (July 1976).

The examples of fragments of registrograms, obtained at the intersection of contrasting land–water surfaces, are given in Figures 5.13 and 5.16 (channel R-2,

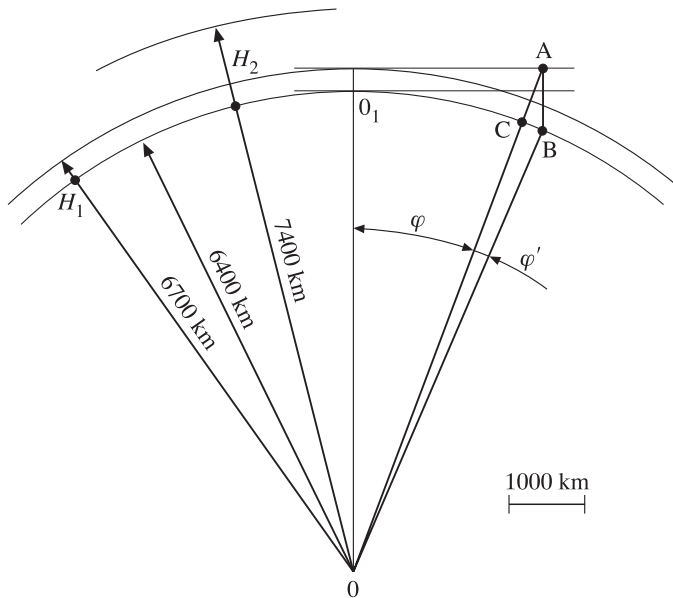


Figure 5.20. Scheme of satellite experiment geometry (longitudinal section in orbit plane). $H_1 = 300 \text{ km}$; $H_2 = 1000 \text{ km}$. O is the centre of the globe. See the rest of the notation in the text.

wavelength of 2 cm) and in Figures 5.14 and 5.15 (channel R-18, wavelength of 18 cm). Figure 5.20 shows the fragment of synchronous regisograms for channels R-8 (wavelength of 8 cm), R-2 and R-0.8 (wavelength of 0.8 cm). The analysis of regisograms indicates that, as the aircraft altitude increases (from 200 to 4000 m), the degree of discrimination in the regisogram details increases (for the given aircraft velocity and registrator recording rate). The altitudes of 2000–4000 m were found to be most favourable from the viewpoint of discriminating the regisogram details and their subsequent analysis for airborne instruments. The results of regisograms processing in accordance with the MCH method are presented in Table 5.3. The analysis of the table shows good correspondence between calculated and measured (by the proposed technique) ADP main lobe widths for channels R-8 and R-18. At the same time, considerable (1.5-fold) discrepancies between the measured main lobe widths for the R-2 channel are observed. This circumstance was related to design features of the antenna mounting onboard the aircraft, specifically, to the mechanical displacement of the irradiator from the centre of the parabola and, as a consequence, to incomplete use of the aperture area. It was impossible to reveal this circumstance before flight tests under ground conditions.

Using synchronous regisograms of several channels (Figure 5.20), the geometry of the position of the main lobes' axes was calculated (see Figures 5.18 and 5.19). Noticeable displacements of the main lobes' axes of various channels are

related to the features of the mechanical installation of antennas onboard the aircraft, and these features should be taken into account in performing fine spatial experiments.

Another processing problem consisted in the experimental estimation of a scattering coefficient for antennas of the spectral bands used. It follows from the analysis of Table 5.3 that the antenna systems did not have a high value of efficiency: the scattering coefficient values varied from 0.21 to 0.31 for various antennas. It should be emphasized that at this stage of experimental works no special measures were undertaken to decrease the side-lobe radiation of standard antenna systems. Some variations of the scattering coefficient value for the antenna of the R-18 channel, measured at different seasons of years 1975–1976, were caused by design modifications, which took place at antenna mounting.

The most interesting point here is the feature of side-lobe radiation by the antenna system for the R-2 channel. The onboard experiments revealed the obvious anisotropy (Figures 5.13 and 5.16) in the zones of this antenna radiation into the forward and backward hemispheres (with respect to the velocity vector of an aircraft). Using the considered technique (see expression (5.88)), we can obtain values of the scattering coefficient over the forward (β_F) and backward (β_B) half-space for the antenna of the R-2 channel:

$$\beta_F = 0.17 \pm 0.01; \beta_B = 0.095 \pm 0.005. \quad (5.97)$$

The physical reason for such a sharp anisotropy of side-lobe radiation is the aforementioned displacement of an irradiator from the focal point of a parabola for design reasons. Of course, it is obviously impossible to reveal such fine features of side-lobe radiation under ground-based tests.

5.10 ANTENNA PARAMETERS OF SATELLITE MICROWAVE INSTRUMENTS

The MCH method, developed in section 5.8 for the determination of antenna system parameters for microwave instruments, can be successfully used for measuring the indicated parameters of space systems as well. The only additional point in such applications is the problem of taking into account the sphericity of an experiment, which is schematically presented (in a reduced scale) in Figure 5.21 for spacecraft orbital altitudes of 300 km and 1000 km. It can be seen from this drawing, that the distinctions between plane-parallel and spherical geometries can be characterized by the ratio:

$$\frac{O_1B - O_1C}{O_1C} = \frac{(\varphi - \varphi')R - \varphi R}{\varphi R} = \frac{\varphi'}{\varphi} \quad (5.98)$$

It follows from trigonometric relations, that

$$\frac{\varphi'}{\varphi} = \frac{2}{\varphi} \operatorname{arctg} \frac{R + H}{2R} \operatorname{tg} \varphi - 1. \quad (5.99)$$

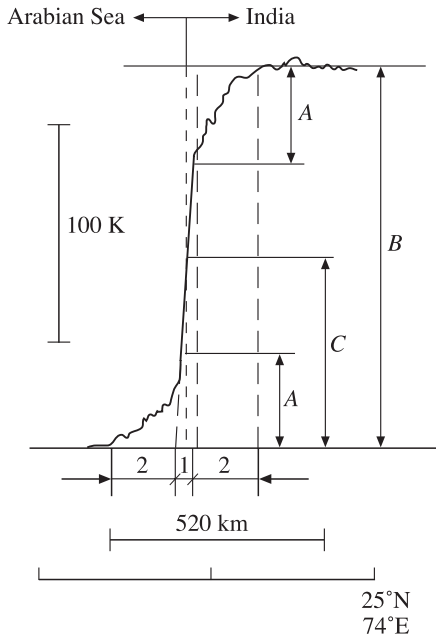


Figure 5.21. Fragment of radiometer ($\lambda = 3.4$ cm) output signal of satellite (Russian ‘Kosmos-243’) instruments when crossing India–Arabian Sea transition (24 September 1968). Spatial scale and indoor temperature calibration are shown in figure. See notation in Figure 5.17.

For small values of angle φ and, accordingly, for small distances on the Earth’s surface (the 10° variation of angle φ corresponds to 1000 km on the Earth’s surface) we obtain:

$$\frac{\varphi'}{\varphi} = \frac{CB}{O_1 C} \approx \frac{H}{R}. \quad (5.100)$$

Thus, it is clear from geometrical considerations, that the noticeable distinctions from planar geometry (for example, when CB will be equal to some resolution elements) can take place for the following spatial size of an investigated area on the Earth’s surface:

$$O_1 C = \frac{CB}{H/R} = \frac{200}{H/R}. \quad (5.101)$$

So, for $H = 300$ km (the ‘Cosmos-243’ satellite) $O_1 C$ will be 5000 km, and for $H = 1000$ km (the ‘Nimbus-5’ satellite) $O_1 C$ will be 1300 km.

Within the limits of 50–200 km, however, the sphericity of the problem can be neglected, since the distortions will be less than the instantaneous field of resolution of microwave satellite instruments ($CB < 8$ km for the ‘Cosmos-243’ satellite and less than 17 km for the ‘Nimbus-5’ satellite).

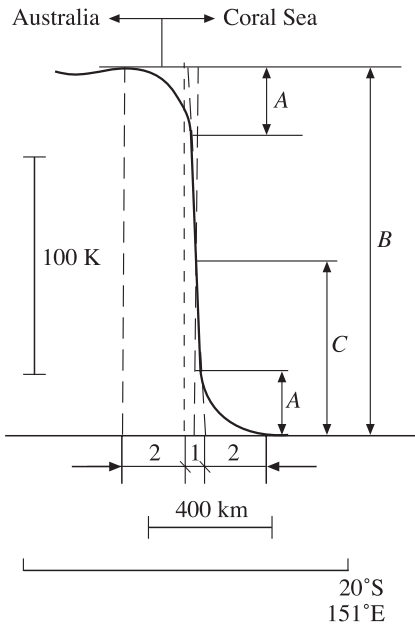


Figure 5.22. Fragment of radiometer ($\lambda = 8.5$ cm) output signal of satellite ‘Kosmos-243’ instruments when crossing Australia–Coral Sea transition (25 September 1968). See notation in Figure 5.21.

To determine the parameters of space antenna systems we have used the available (in the literature) regisrograms of land–ocean transitions for microwave instruments of the ‘Cosmos-243’ and ‘Cosmos-384’ satellites (Basharinov *et al.*, 1969, 1971, 1973, 1974) and of the ‘Nimbus-5’ satellite (Vinogradov, 1976). Some characteristics of radiothermal satellite instruments are presented in Table 5.4. Note that the scattering coefficient values for antennas were taken from the data of laboratory (ground and pre-flight) tests. The regisrograms of land–ocean transitions, with characteristic regions of brightness temperature variation drawn on them (as it was done in Figure 5.17), and the geographical coordinates are presented in Figures 5.22–5.24.

The analysis of Table 5.4 indicates that the accuracy of main lobe width determination is 10% better than the widths measured under Earth conditions, and for the ‘Nimbus-5’ antenna the data almost exactly coincide. The only exception is the result of the processing of the transition on 10 December 1970, in the region with coordinates of 80°N lat. and 13°E long. (6.0° as compared to 4.0°), which is explained by the ‘spread’ character of radiothermal background of the land–ocean transition, rather than by the main lobe width of ADP. As would be expected, the scattering coefficient values for antennas of the ‘Cosmos-243’ and ‘Cosmos-384’ satellites obtained from the results of the processing of the land–ocean transitions, are almost 2–2.5 times greater than the values obtained in the laboratory. At the

Table 5.4. Antenna parameters of satellite microwave instruments

Spacecraft (launch year)	Orbit height, km	Time experiments	Positions of land–ocean transition	Working wavelength, cm	Antenna type	ΔX , km	$\theta_{3\text{dB}}^*$, degree	$\theta_{3\text{dB}}$, degree	β^*	β (measured)
'Cosmos-243' (1968)	210–319	24 September 1968	20°	8.5	HP	30–50	8.5	6.5	0.2	0.28 ± 0.05
			151°							
			25°	3.4	HP	15–25	4.0	4.3	0.15	0.32 ± 0.05
			74°							
'Cosmos-384' (1970)	212–314	10 December 1970	35°	3.4	HP	15–25	4.0	4.5	0.15	0.30 ± 0.05
			5°							
			8°	3.4	HP	15–25	4.0	4.8	0.15	0.25 ± 0.05
			13°							
'Nimbus-5'	1008–1043	September 1973	—	1.55	CPA	25	1.6	1.57	—	0.15 ± 0.05

HP, horn parabolic antenna; CPA, cophased array with electronic scanning. β^* and θ^* are values of scattering coefficient and ADP main lobe, obtained by laboratory test; ΔX is special pixel on terrestrial surface.

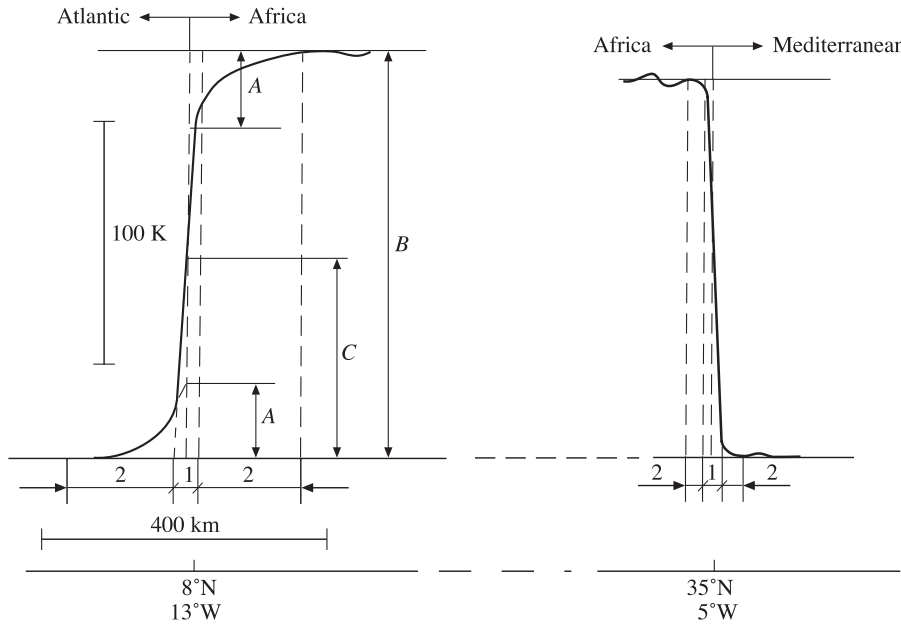


Figure 5.23. Fragment of radiometer ($\lambda = 3.4\text{ cm}$) output signal of satellite Russian 'Kosmos-384' instruments when crossing Africa (10 December 1970). See notation in Figure 5.17.

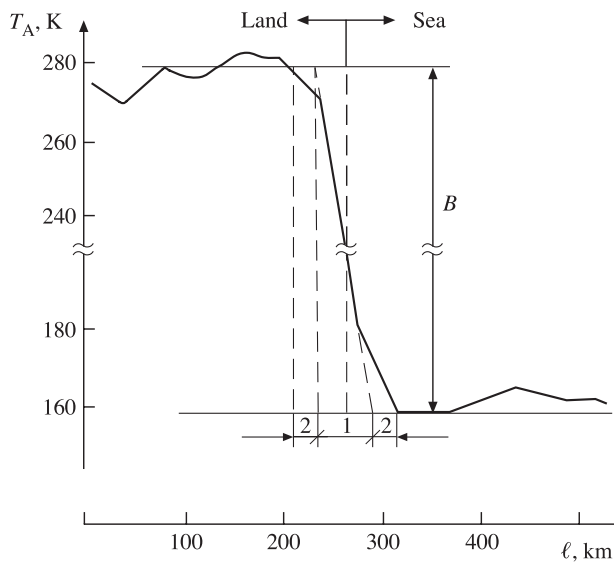


Figure 5.24. Fragment of radiometer ($\lambda = 1.55\text{ cm}$) output signal of satellite 'Nimbus-5' radiometric instruments when crossing land-sea transition (September 1973). See notation B, 1, 2 in the text.

same time, the phased array of the ‘Nimbus-5’ satellite demonstrates fairly high values of scattering coefficient. Thus, in general, the scattering coefficient values obtained from the laboratory data (for example, Mo (1999)) cannot reflect the real flight situation at all.

The indicated examples testify to the possibility of using the proposed technique for determining the antenna parameters of radiothermal satellite instruments in flight condition (under the condition of detailed signal recording at the transition of a sharp boundary of contrasting surfaces).

6

Black-body radiation

The subjects for consideration in this chapter are the black-body model, which is of primary importance in thermal radiation theory and practice, and the fundamental laws of radiation of such a system. Natural and artificial physical objects, which are close in their characteristics to black bodies, are considered here. The quantitative black-body radiation laws and their corollaries are analysed in detail. The notions of emissivity and absorptivity of physical bodies of grey-body radiation character are also introduced. The Kirchhoff law, its various forms and corollaries are analysed on this basis.

6.1 THE IDEAL BLACK-BODY MODEL: HISTORICAL ASPECTS

The ideal black-body notion (hereafter the black-body notion) is of primary importance in studying thermal radiation and electromagnetic radiation energy transfer in all wavelength bands. Being an ideal radiation absorber, the black body is used as a standard with which the absorption of real bodies is compared. As we shall see later, the black body also emits the maximum amount of radiation and, consequently, it is used as a standard for comparison with the radiation of real physical bodies. This notion, introduced by G. Kirchhoff in 1860, is so important that it is actively used in studying not only the intrinsic thermal radiation of natural media, but also the radiations caused by different physical nature. Moreover, this notion and its characteristics are sometimes used in describing and studying artificial, quasi-deterministic electromagnetic radiation (in radio- and TV-broadcasting and communications). The emissive properties of a black body are determined by means of quantum theory and are confirmed by experiment.

The black body is so called because those bodies that absorb incident visible light well seem black to the human eye. The term is, certainly, purely conventional and has, basically, historical roots. For example, we can hardly characterize our Sun,

which is, indeed, almost a black body within a very wide band of electromagnetic radiation wavelengths, as a black physical object in optics. Though, it is namely the bright-white sunlight, which represents the equilibrium black-body radiation. In this sense, we should treat the subjective human recognition of colours extremely cautiously. So, in the optical band a lot of surfaces really approach an ideal black body in their ability to absorb radiation (examples of such surfaces are: soot, silicon carbide, platinum and golden niellos). However, outside the visible light region, in the wavelength band of IR thermal radiation and in the radio-frequency bands, the situation is different. So, the majority of the Earth's surfaces (the water surface, ice, land) absorb infrared radiation well, and, for this reason, in the thermal IR band these physical objects are ideal black bodies. At the same time, in the radio-frequency band the absorptive properties of the same media differ both from a black body and from each other, which, generally speaking, just indicates the high information capacity of microwave remote measurements.

6.1.1 Definition of a black body

A black body is an ideal body which allows the whole of the incident radiation to pass into itself (without reflecting the energy) and absorbs within itself this whole incident radiation (without passing on the energy). This property is valid for radiation corresponding to all wavelengths and to all angles of incidence. Therefore, the black body is an ideal absorber of incident radiation. All other qualitative characteristics determining the behaviour of a black body follow from this definition (see, for example, Siegel and Howell, 1972; Ozisik, 1973).

6.1.2 Properties of a black body

A black body not only absorbs radiation ideally, but possesses other important properties which will be considered below.

Consider a black body at constant temperature, placed inside a fully insulated cavity of arbitrary shape, whose walls are also formed by ideal black bodies at constant temperature, which initially differs from the temperature of the body inside. After some time the black body and the closed cavity will have a common equilibrium temperature. Under equilibrium conditions the black body must emit exactly the same amount of radiation as it absorbs. To prove this, we shall consider what would happen if the incoming and outgoing radiation energies were not equal. In this case the temperature of a body placed inside a cavity would begin to increase or decrease, which would correspond to heat transfer from a cold to a heated body. But this situation contradicts the second law of thermodynamics (the question is, certainly, on the stationary state of an object and ambient radiation). Since, by definition, the black body absorbs a maximum possible amount of radiation that comes in any direction from a closed cavity at any wavelength, it should also emit a maximum possible amount of radiation (*as an ideal emitter*). This situation becomes clear if we consider any less perfectly absorbing body (a grey body), which should

emit a lower amount of radiation as compared to the black body, in order that equilibrium be maintained.

Let us now consider an isothermal closed cavity of arbitrary shape with black walls. We move the black body inside the cavity into another position and change its orientation. The black body should keep the same temperature, since the whole closed system remains isothermal. Therefore, the black body should emit the same amount of radiation as before. Being at equilibrium, it should receive the same amount of radiation from the cavity walls. Thus, the total radiation received by the black body does not depend on its orientation and position inside the cavity; therefore, the radiation passing through any point inside a cavity does not depend on its position or on the direction of emission. This implies that the equilibrium thermal radiation filling a cavity is isotropic (the property of isotropy of black-body radiation). And, thus, the net radiation flux (see equation (5.7)) through any plane, placed inside a cavity in any arbitrary manner, will be strictly zero.

Consider now an element of the surface of a black isothermal closed cavity and the elementary black body inside this cavity. Some part of the surface element's radiation falls on a black body at some angle to its surface. All this radiation is absorbed, by definition. In order that the thermal equilibrium and radiation isotropy be kept throughout the closed cavity, the radiation emitted by a body in the direction opposite to the incident beam direction should be equal to the absorbed radiation. Since the body absorbs maximum radiation from any direction, it should also emit maximum radiation in any direction. Moreover, since the equilibrium thermal radiation filling the cavity is isotropic, the radiation absorbed or emitted in any direction by the ideal black surface encased in the closed cavity, and related to the unit area of surface projection on a plane normal to the beam direction, should be equal.

Let us consider a system comprising a black body inside a closed cavity which is at thermal equilibrium. The wall of the cavity possesses a peculiar property: it can emit and absorb radiation within a narrow wavelength band only. The black body, being an ideal energy absorber, absorbs the whole incident radiation in this wavelength band. In order that the thermal equilibrium be kept in a closed cavity, the black body should emit radiation within the aforementioned wavelength band; and this radiation can then be absorbed by the cavity wall, which absorbs in the given wavelength band only. Since the black body absorbs maximum radiation in a certain wavelength band, it should emit maximum radiation in the same band. The black body should also emit maximum radiation at the given wavelength. Thus, the black body is an ideal emitter at any wavelength. However, this in no way implies uniformity in the intensity of black-body emission at different wavelengths (the 'white noise' property). The peculiar spectral (and, accordingly, correlation) properties of black-body radiation could only be revealed by means of quantum mechanics.

The peculiar properties of a closed cavity have no relation to the black body in the reasoning given, since the emission properties of a body depend on its nature only and do not depend on the properties of a cavity. The walls of a cavity can even be fully reflecting (mirroring).

If the temperature of a closed cavity changes, then, accordingly, the temperature of a black body enclosed inside it should also change and become equal to the new temperature of a cavity (i.e. a fully insulated system should tend to thermodynamic equilibrium). The system will again become isothermal, and the energy of radiation absorbed by a black body will again be equal to the energy of radiation emitted by it, but it will slightly differ in magnitude from the energy corresponding to the former temperature. Since, by definition, the body absorbs (and, hence, emits) the maximum radiation corresponding to the given temperature, the characteristics of an enclosing system have no influence on the emission properties of a black body. Therefore, the total radiation energy of a black body is a function of its temperature only.

In addition, according to the second law of thermodynamics, energy transfer from a cold surface to a hot one is impossible without doing some work at a system. If the energy of radiation emitted by a black body increased with decreasing temperature, then the reasoning could easily be constructed (see, for example, Siegel and Howell, 1972), which would lead us to a violation of this law. As an example, two infinite parallel ideal black plates are usually considered. The upper plate is maintained at temperature higher than the temperature of the lower plate. If the energy of emitted radiation decreased with increasing temperature, then the energy of radiation, emitted by the lower plate per unit time, would be greater than the energy of radiation emitted by the upper plate per unit time. Since both plates are black, each of them absorbs the whole radiation emitted by the other plate. For maintaining the temperatures of plates the energy should be rejected from the upper plate per unit time and added to the lower plate in the same amount. Thus, it happens, that the energy transfers from a less heated plate to more heated one without any external work being done. According to the second law of thermodynamics, this situation is impossible. Therefore, the energy of radiation emitted by a black body, should increase with temperature. On the basis of these considerations we come to the conclusion, that the total energy of radiation emitted by a black body is proportional to a monotonously increasing function of thermodynamic temperature only.

All the reasoning we set forth above proceeding from thermodynamic considerations represents quite important, but, nevertheless, only qualitative, laws of black-body radiation. As was ascertained, classical thermodynamics is not capable of formulating the quantitative laws of black-body radiation in principle.

6.1.3 Historical aspects

Until the middle of the nineteenth century a great volume of diverse experimental data on the radiation of heated bodies was accumulated. The time had come to comprehend the data theoretically. And it was Kirchhoff who took two important steps in this direction. At the first step Kirchhoff, together with Bunsen, established the fact that a quite specific spectrum (the set of wavelengths, or frequencies) of the light emitted and absorbed by a substance corresponds to that particular substance. This discovery served as a basis for the spectral analysis of substances. The second step consisted in finding the conditions, under which the radiation spectrum of

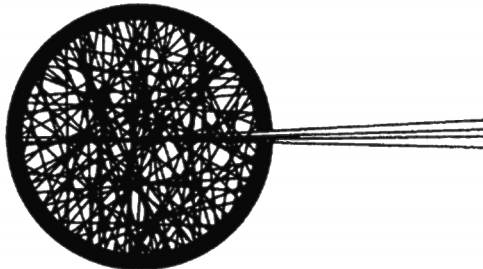


Figure 6.1. Classic experimental model of black-body source.

heated bodies depends only on their temperature and does not depend on the chemical composition of the emitting substance. Kirchhoff considered theoretically the radiation inside a closed cavity in a rigid body, whose walls possess some particular temperature. In such a cavity the walls emit as much energy as they absorb. It was found that under these conditions the energy distribution in the radiation spectrum does not depend on the material the walls are made of. Such a radiation was called ‘absolutely (or ideally) black’.

For a long time, however, black-body radiation was, so to speak, a ‘thing-in-itself’. Only 35 years later, in 1895, W. Wien and O. Lummer suggested the development of a test model of an ideal black body to verify Kirchhoff’s theory experimentally. This model was manufactured as a hollow sphere with internal reflecting walls and a narrow hole in the wall, the hole diameter being small as compared to the sphere diameter. The authors proposed to investigate the spectrum of radiation issuing through this hole (Figure 6.1). Any light beam undergoes multiple reflections inside a cavity and, actually, cannot exit through the hole. At the same time, if the walls are at a high temperature the hole will brightly shine (if the process occurs in the optical band) owing to the electromagnetic radiation issuing from inside the cavity. It was this particular test model of a black body on which the experimental investigations to verify thermal radiation laws were carried out, and, first of all, the fundamental spectral dependence of black-body radiation on frequency and temperature (the Planck formula) was established quantitatively. The success of these experimental (and, a little bit later, theoretical) quantum-approach-based investigations was so significant that for a long time, up until now, this famous reflecting cavity has been considered in general physics textbooks as a unique black-body example. And, thus, some illusion of black body exclusiveness with respect to natural objects arises. In reality, however (as we well know both from the radio-astronomical and remote sensing data, and from the data of physical (laboratory) experiments), the natural world around us, is virtually saturated with physical objects which are very close to black-body models in their characteristics.

First of all, we should mention here *the cosmic microwave background (CMB) of the universe* – the fluctuation electromagnetic radiation that fills the part of the universe known to us. The radiation possesses nearly isotropic spatial-angular field with an intensity that can be characterized by the radiobrightness temperature

of 2.73 K. The microwave background is, in essence, some kind of ‘absolute ether at rest’ that physicists intensively sought at the beginning of the twentieth century. A small dipole component in the spatial-angular field of the microwave background allowed the researchers to determine, to a surprising accuracy, the direction and velocity of motion of the solar system. The contribution of the microwave background as a re-reflected radiation should certainly be taken into account in performing fine investigations of the emissive characteristics of terrestrial surfaces from spacecraft.

The second (but not less important) source of black-body radiation is the star nearest to the Earth – *the Sun* (see section 1.4). The direct radar experiments, performed in the 1950s and 1960s, have indicated a complete absence of a radio-echo (within the limits of the receiving equipment capability) within the wide wavelength band – in centimetre, millimetre and decimetre ranges. Detailed spectral studies of solar radiation in the optical and IR bands have indicated the presence of thermal black-body radiation with a brightness temperature of 5800 K at the Sun. In other bands of the electromagnetic field the situation is essentially more complicated – along with black-body radiation there exist powerful, non-stationary quasi-noise radiations (flares, storms), which are described, nevertheless, in thermal radiation terms.

The third space object is our home planet, – *the Earth*, which possesses radiation close to black-body radiation with a thermodynamic temperature of 287 K. The basic radiation energy is concentrated in the 8–12 micrometre band, in which almost all terrestrial surfaces possess black-body radiation properties. Just that small portion of radiation energy which falls in the radio-frequency band is of interest for microwave sensing. The detailed characteristics of radiation from terrestrial surfaces in this band have shown serious distinctions of many terrestrial media from the black-body model.

In experimental measurements of the radiation properties of real physical bodies it is necessary to have an ideally black surface or a black emitter as a standard. Since ideal black sources do not exist, some special technological approaches are applied to develop a realistic black-body model. So, in optics these models represent hollow metal cylinders having a small orifice and cone at the end, which are immersed in a thermostat with fixed (or reconstructed) temperature (Siegel and Howell, 1972). In the radio-frequency band segments of waveguides or coaxial lines, filled with absorbing substance (such as carbon-containing fillers), are applied. Multilayer absorbing covers, which are widely used in the military-technological area (for instance, Stealth technology), are applied as standard black surfaces in this band. It is clear, that objects covered with such an absorbing coat are strong emitters of the fluctuation electromagnetic field. It is important also to note that in the radio-frequency band a closed space with well-absorbing walls (such as a concrete with various fillers) represents a black-body cavity to a good approximation. For these reasons the performance of fine radiothermal investigations in closed rooms (indoors) makes no sense. (Of interest is the fact that it was in a closed laboratory room that in 1888 Hertz managed to measure for the first time the wavelength of electromagnetic radiation.)

6.2 BLACK-BODY RADIATION LAWS

But now we return to the quantitative laws of black-body radiation. The general thermodynamic considerations allowed Kirchhoff, Boltzmann and Wien to derive rigorously a series of important laws controlling the emission of heated bodies. However, these general considerations were insufficient for deriving a particular law of energy distribution in the ideal black-body radiation spectrum. It was W. Wien who advanced in this direction more than the others. In 1893 he spread the notions of temperature and entropy to thermal radiation and showed, that the maximum radiation in the black-body spectrum displaces to the side of shorter wavelengths with increasing temperature (the Wien displacement law); and at a given frequency the radiation intensity can depend on temperature only, as the parameter appeared in the (ν/T) ratio. In other words, the spectral intensity should depend on some function $f(\nu/T)$. The particular form of this function has remained unknown.

In 1896, proceeding from classical concepts, Wien derived the law of energy distribution in the black-body spectrum (the Wien radiation law). However, as was soon made clear, the formula of Wien's radiation law was correct only in the case of short (in relation to the intensity maximum) waves. Nevertheless, these two laws of Wien have played a considerable part in the development of quantum theory (the Nobel Prize, 1911).

J. Rayleigh (1900) and J. Jeans (1905) derived the spectral distribution of thermal radiation on the basis of the assumption that the classical idea on the uniform distribution of energy is valid. However, the temperature and frequency dependencies obtained basically differed from Wien's relationships.

According to the results of fairly accurate measurements, carried out before that time, and to some theoretical investigations, Wien's expression for spectral energy distribution was invalid at high temperatures and long wavelengths. This circumstance forced Planck to turn to consideration of harmonic oscillators, which have been taken as the sources and absorbers of radiation energy. Using some further assumptions on the mean energy of oscillators, Planck derived Wien's and the Rayleigh–Jeans' laws of radiation. Finally, Planck obtained the empirical equation, which very soon was reliably confirmed experimentally on the basis, first of all, of the Wien–Lummer black-body model. Searching for the theory modifications which would allow this empirical equation to be derived, Planck arrived at the assumptions constituting the quantum theory basis (the Nobel Prize, 1918).

6.2.1 The Planck law (formula)

According to quantum statistics principles, the spectral volume density of radiation energy can be determined (see relation (5.10)) by calculating the equilibrium distribution of photons, for which the radiation field entropy is maximum, and taking into consideration that the photon energy with frequency ν is equal to $h\nu$, where h is the Planck constant (Table A.4). If the radiation field is considered to be a gas obeying the Einstein–Bose statistics, then we obtain the Planck formula for the

volume density of radiation (see, for example, Schilling, 1972; Amit and Verbin, 1999):

$$u_\nu(T) d\nu = \frac{8\pi h\nu^3}{c^3} \frac{1}{[\exp(h\nu/kT) - 1]} d\nu, \quad (6.1)$$

where k is the Boltzmann constant (Table A.4).

Apart from a rigorous quantum derivation of Planck's formula, there exists a spectrum of heuristic approaches (see, for example, Penner, 1959).

From the remote sensing point of view, of principal significance is the other radiation field characteristic, namely, the spectral radiation intensity, which is measured at once by remote sensing devices. With allowance for relation (5.12), the spectral intensity of black-body radiation into the transparent medium with refractive index n will be specified by the following expression:

$$I_\nu(T, \nu) = \frac{2h\nu^3 n^2}{c_0^2} \frac{1}{[\exp(h\nu/kT) - 1]}. \quad (6.2)$$

It can easily be seen from this relation that the black-body radiation into the transparent medium is n^2 times greater than when emitting into a vacuum (the Clausius law).

In many practical applications in determining the spectral intensity of radiation the wavelength is used instead of frequency. It is impossible to transfer from frequency to wavelength by simply replacing the frequency with the wavelength in expression (6.2), because this expression includes the differential quantity. However, this expression can be transformed taking into account that the energy of radiation, emitted within the frequency band $d\nu$, that includes frequency ν , is equal to the energy of radiation, emitted within the wavelength band $d\lambda$ that includes the working wavelength λ ,

$$I_\nu(T, \nu) |d\nu| = I_\lambda(T, \lambda) |d\lambda|. \quad (6.3)$$

The wavelength depends on the medium, in which the radiation propagates (see section 1.6). Subscript 0 denotes that the considered medium is the vacuum. At the same time, the electromagnetic radiation frequency does not depend on the medium. The frequency and wavelength in a transparent dielectric medium (λ) are related by the equation:

$$\nu = \frac{c_0}{n\lambda}. \quad (6.4)$$

Supposing the refractive index of a transparent medium to be independent of the frequency, we shall obtain, after appropriate differentiation, the expression of Planck's formula for the intensity of black-body radiation into the transparent medium, expressed in terms of the wavelength in a medium, as:

$$I_\lambda(T, \lambda) = \frac{2hc_0^2}{n^2 \lambda^5} \frac{1}{[\exp(hc_0/n\lambda kT) - 1]} \quad (6.5)$$

In the SI system the intensity, presented in such a form, is measured in $\text{W}/(\text{m}^3 \text{sr})$. Often, in the IR band especially, the wavelength is measured in micrometres; then the

dimension of radiation intensity will be $\text{W}/(\text{m}^2 \text{sr } \mu\text{m})$. However, it is convenient to use the frequency presentation of Planck's formula (6.2) in the cases where the radiation propagates from one medium into another, since in this case the frequency remains constant and the wavelength changes.

In many practical applications (remote sensing, heat transfer, radio-astronomy) of interest is the surface density (per unit of the surface) of a spectral flux of black-body radiation determined in the form of equation (5.5) and (5.9). Substituting the spectral density value from (6.5), we have

$$q_\lambda(T) = \frac{C_1}{n^2 \lambda^5} \frac{1}{[\exp(C_2/n\lambda T) - 1]}, \quad (6.6)$$

where the quantities

$$C_1 = 2\pi h c_0^2; C_2 = \frac{hc_0}{k} \quad (6.7)$$

were called the first and second radiation constants (see Table A.4).

Note that $q_\lambda(T)$ represents the amount of radiation energy emitted by the unit area of the black-body surface at temperature T per unit time, in the wavelength band unit, in all directions within the limits of the hemispherical solid angle. In the SI system this quantity is measured in W/m^3 , and if the wavelength is measured in micrometres then this quantity is measured in $\text{W}/(\text{m}^2 \mu\text{m})$.

Figure 6.2 presents the spectral distribution of the surface density of a monochromatic black-body radiation flux $q_\lambda(T)$, calculated by formula (6.6) for $n = 1$. In order to understand better the implication of this equation, Figure 6.2 gives the

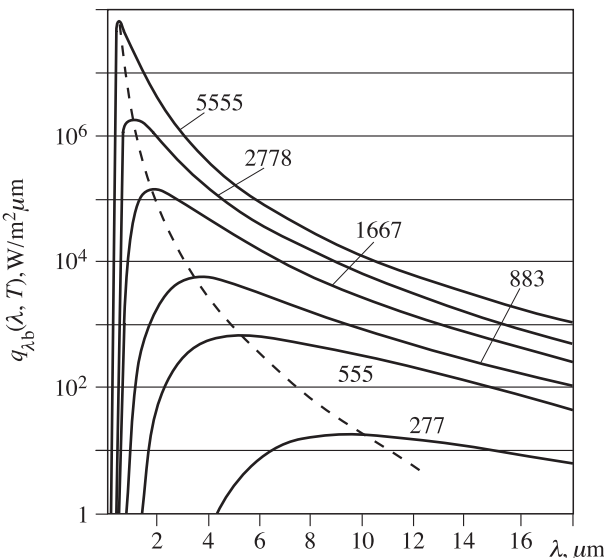


Figure 6.2. Hemispherical spectral radiation flux of black bodies for some values of temperatures versus wavelengths. Black-body temperatures are shown by figures next to the curves. Positions of spectral radiation flux maxima are shown by a dotted line.

wavelength dependencies of hemispherical spectral surface density of radiation flux for several values of absolute temperature. A peculiarity of Planck's curves is the increase of the energy of radiation, corresponding to all wavelengths, with increasing temperature. As was shown in section 6.1, qualitative thermodynamic considerations and everyday experience indicate that the energy of total radiation (including all wavelengths) should increase with temperature. It also follows from Figure 6.2 that this conclusion is also valid for the energy of radiation corresponding to each wavelength. Another peculiarity is the displacement of maxima of the spectral surface density of radiation flux to the side of shorter wavelengths with increasing temperature. The cross-sections of the plot in Figure 6.2 at fixed wavelengths, which determine the radiation energy as a function of temperature, allow us to state that the energy of radiation, emitted at the short-wave extremity of the spectrum, increases with temperature faster than the energy of radiation corresponding to greater wavelengths. Figure 6.2 indicates the position of the wavelength band in the visible spectrum region. For a body at temperature of 555 K only a very small fraction of energy falls on the visible spectrum range, which is virtually imperceptible by the human eye. Since the curves at lower temperatures are dropping from the red section toward the violet extremity of the spectrum, then, at first, the red light becomes visible with increasing temperature (the so-called Driper point, corresponding to 525°C). At sufficiently high temperature the emitted light becomes white and consists of a set of all wavelengths of the visible spectrum. The radiation spectrum of the Sun is similar to the radiation spectrum of a black body at a temperature of 5800 K, and a considerable portion of released energy falls on the visible spectrum range. (This type of radiation is sometimes called 'white' noise – as we see, quite wrongly.) More likely, owing to very long biological evolution, the human eye became most sensitive precisely in the spectrum region with maximum energy.

Equation (6.6) can be presented in a more convenient form that allows us to avoid constructing the curves for each value of temperature; for this purpose equation (6.6) is divided by temperature to the fifth power:

$$(q_\lambda(T, \lambda)/T^5) = \frac{\pi I_\nu(T, \lambda)}{T^5} = \frac{C_1}{(\lambda T)^5} \frac{1}{[\exp(C_2/\lambda T) - 1]}. \quad (6.8)$$

This equation determines quantity $q_\lambda(T, \lambda)/T^5$ as a function of single variable λT . The plot of such a dependence is presented in Figure 6.3; it substitutes a set of curves in Figure 6.2.

The Planck law for energy distribution in the black-body spectrum gives a maximum value of the intensity of radiation that can be emitted by any body at the given temperature and wavelength. This intensity plays a part of an optimum standard, with which the characteristics of real surfaces can be compared.

But, more simply, approximate forms of the Planck law are sometimes applied. However, it is necessary to bear in mind that they can be used only in that range, where they provide acceptable accuracy.

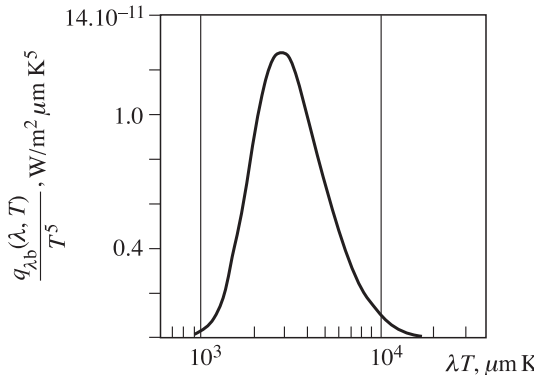


Figure 6.3. Hemispherical of black-body spectral radiation flux distribution versus generalized coordinates.

6.2.2 The Wien radiation law

If the term $\exp(C_2/\lambda T) > 1$, then equation (6.8) is reduced to the expression

$$\frac{I_\lambda(T, \lambda)}{T^5} = \frac{C_1}{\pi(\lambda T)^5 \exp(C_2/\lambda T)}, \quad (6.9)$$

which is known as the Wien radiation law. For the values of $\lambda T < 3000 \mu\text{m K}$ this formula gives an error within the limits of 1%.

6.2.3 The Rayleigh–Jeans radiation law

Another approximate expression can be obtained by expanding the denominator in equation (6.8) into the Taylor series. If λT is essentially greater than C_2 , then the series can be restricted by the second term of expansion, and equation (6.8) takes the form:

$$\frac{I_\lambda(T, \lambda)}{T^5} = \frac{C_1}{\pi C_2} \frac{1}{(\lambda T)^4}. \quad (6.10)$$

This equation is known as the Rayleigh–Jeans radiation law. This formula gives an error within the limits of 1% for the values of $\lambda T > 7.8 \times 10^5 \mu\text{m K}$. These values are outside the range usually considered in IR thermal radiation, but they are of principal importance for the radio-frequency band. The frequency presentation of the Planck formula is usually applied in this band, and then the Rayleigh–Jeans law takes the widely used form:

$$I_\nu(T, \nu) = \frac{2\nu^2}{c_0^2} nkT = \frac{2f^2}{c_0^2} nkT. \quad (6.11)$$

6.2.4 The Wien displacement law

Another quantity of interest, which relates to the black-body radiation spectrum, is the wavelength λ_m , to which corresponds the maximum of surface density of an emitted energy flux. As is shown by the dotted curve in Figure 6.2, this maximum displaces to the side of shorter wavelengths as the temperature increases. Quantity λ_m can be found by differentiating the Planck function from equation (2.12) and by equating the obtained expression to zero. As a result, the transcendental equation is obtained

$$\lambda_m T = \frac{C_2}{5} \frac{1}{1 - \exp(-C_2/\lambda_m T)}, \quad (6.12)$$

whose solution is as follows:

$$\lambda_m T = C_3 \quad (6.13)$$

and represents one of expressions of the Wien displacement law. The values of constant C_3 are given in Table A.4. According to equation (6.13), as the temperature increases, the maxima of surface density of the radiation flux and its intensity displace to the side of shorter wavelengths in inverse proportion to T . If we consider the black-body radiation into a transparent medium (with refractive index n), then the Wien law takes the form of

$$n\lambda_{m,n} T = C_3, \quad (6.14)$$

where $\lambda_{m,n}$ is the wavelength corresponding to the maximum of radiation in the transparent medium.

Of interest is the fact that the substitution of the wavelength from the Wien displacement law (6.13) into equation (6.8) results in the following expression:

$$I_\lambda(T, \lambda_m) = T^5 \frac{C_1}{\pi C_3^5 [\exp(C_2/C_3) - 1]}. \quad (6.15)$$

It follows from this relation, that the maximum value of radiation intensity increases in proportion to temperature to the fifth power. Generally speaking, it is this relation that was obtained by Wien in 1893.

It can easily be seen from the expression obtained that the maximum of spectral intensity of the microwave background of the universe at radiation temperature of 2.73 K will be approximately equal to 1 mm.

6.2.5 The Stefan–Boltzmann law

Integrating $q_\lambda(T)$ over all wavelengths from zero to infinity (or, accordingly, $q_\nu(T)$ in the frequency presentation), we obtain by means of expressions for determinate integrals (Gradshteyn and Ryzhik, 2000) the surface density of the total black-body radiation flux $q(T)$ as:

$$q(T) = \int_0^\infty q_\lambda(T, \lambda) d\lambda = \int_0^\infty q_\nu(T, \nu) d\nu = \pi \int_0^\infty I_\nu(T, \nu) d\nu = n^2 \sigma T^4, \quad (6.16)$$

where the Stefan–Boltzmann constant σ is equal (see Table A.4) to:

$$\sigma = \frac{2\pi^5 k^4}{15c_0^2 h^3}. \quad (6.17)$$

Similar expressions can also be obtained for the total radiation intensity:

$$I(T) = \int_0^\infty I_\nu(T, \nu) d\nu = n^2 \frac{\sigma}{\pi} T^4 \quad (6.18)$$

and for the total volume density of radiation (for vacuum):

$$u = \int_0^\infty u_\nu(T, \nu) d\nu = a T^4, \quad (6.19)$$

where a is called the radiation density constant (see Table A.4).

Let us consider now the instructive example, associated with the relation of the amount of energy, emitted from the unit of black body's surface into vacuum within the whole frequency band and in the radio-frequency band separately. Using relations (6.16), we obtain the total power, emitted by a black body from 1 square metre at room temperature (300 K), which is equal to 450 W. Now, using the Rayleigh–Jeans law (6.11), we obtain the expression for the Stefan–Boltzmann law in the long-wavelength approximation, as follows:

$$q(T) = \frac{2}{3} \frac{\pi k}{c_0^2} T \nu^3. \quad (6.20)$$

From this expression we can easily obtain the estimate for the total power emitted by a black body from 1 square metre at $T = 300$ K throughout the radio-frequency band from zero frequency up to 10^{11} Hz (the wavelength is 3 mm). It is equal to 10^{-4} W. Thus, the amount of energy falling on the whole radio-frequency band is 10^{-7} times lower than the total power of black-body radiation. In this case an even smaller part (10^{-9}) of the total power will fall on the whole, for example, centimetre band. And, in spite of such small values of radiation power in the radio-frequency band, modern microwave remote radio systems successfully record such low levels of a thermal signal (see Chapter 3).

6.2.6 Correlation properties of black-body radiation

From the viewpoint of the theory of random processes (Chapter 2), the spectral volume density of radiation energy $u_\nu(\nu)$ represents a spectral density of fluctuating strengths $E(t)$ and $H(t)$ of the thermal radiation field. This can easily be seen, taking into consideration relations (1.17), (2.27), (5.13). In each of the planar waves into which this field can be decomposed, the relation between the vectors of running planar waves is given by expression (1.11), all directions of strengths being equiprobable. As a result of small transformations in (1.17), it can be seen that the electric and magnetic energies are equal, and E and H components in any arbitrary direction have identical correlation functions but are not correlated among themselves. Thus,

the correlation properties can be considered with respect to any component of the electromagnetic field strength.

Let us find the correlation coefficient corresponding to the spectral density (6.1), i.e. the quantity

$$R_u(\tau) = \frac{B_u(\tau)}{B_u(0)}, \quad (6.21)$$

where

$$B_u(\tau) = \frac{2}{\pi} \int_0^\infty u_\nu(T, \nu) \cos 2\pi\nu d\nu \quad (6.22)$$

Substituting here expression (6.1) for the spectral density and calculating the integral, we obtain (Rytov, 1966):

$$R_u(\tau) = 15 \left[\frac{3}{\operatorname{sh}^4 \beta} - \frac{3}{\beta^3} + \frac{2}{\operatorname{sh}^2 \beta} \right] = \frac{15}{2} \frac{d^3}{d\beta^3} L(\beta), \quad (6.23)$$

where $L(\beta) = \operatorname{cth} \beta - (1/\beta)$ is the Langevin function, and $\beta = 2\pi^2 k T \tau / h$ ($\operatorname{sh} x$, $\operatorname{cth} x$ are hyperbolic sine and cotangent).

The form of the correlation coefficient from the temporary lag is shown in Figure 6.4 and, as should be expected, it certainly does not look like the delta-function. First of all, we note that for $\beta \cong 1.37$ (which corresponds to $\tau_0 = h/2\pi k T$) the positive correlation is changed to a negative one. This implies that for temporary shifts $\tau < \tau_0$ the values of component $E_p(t)$ in some fixed direction p will more frequently have at instants t and $t + \tau$ the same sign, and for $\tau > \tau_0$ the opposite sign. The temporary lag τ_0 can be put in correspondence to the spatial correlation radius $\lambda_0 = c\tau_0$, which to an accuracy of numerical coefficient coincides with the wavelength $\lambda_m = 0.2(hc/kT)$ in the Wien displacement law. From the comparison of these expressions we can obtain the following important relation:

$$\lambda_0 = 0.35\lambda_m. \quad (6.24)$$

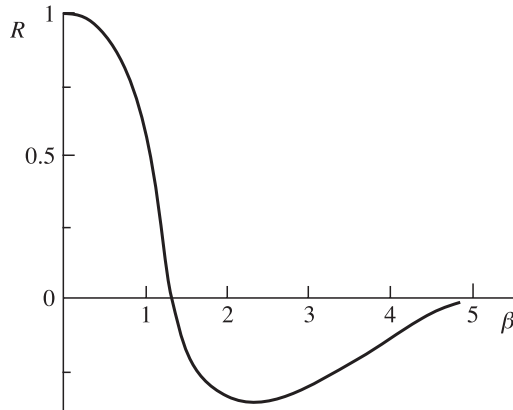


Figure 6.4. Correlation coefficient of spectral black-body radiant energy density versus generalized lag $\beta = 2\pi^2 \frac{k T \tau}{h}$.

It can easily be found from this relation that the spatial correlation radius of the microwave background of the universe equals a quite macroscopic value, namely, $\lambda_0 = 0.35$ mm. It is interesting to mention, that earlier (in 1971) it was proposed to measure the velocity of solar system motion relative to the microwave ('absolute ether at rest') background by recording the variable part of the interferogram (in other words, the correlation coefficient (6.24)) just at the place where it changes its sign (near λ_0) (Soglasnova and Sholomitskii, 1971).

At spatial distances greater than $(4\text{--}5)\lambda_0$ the correlation sharply drops, and the statistical process of emission at such scales can be represented as a non-correlated random (white) noise. Generally speaking, it is this circumstance which is often used in analysing thermal radiation.

6.3 THE KIRCHHOFF LAW

As we have noted above (Chapter 4), the fluctuation–dissipation theorem, which represents one of the fundamental laws of statistical physics, establishes for an arbitrary dissipative physical system the relationship between the spectral density of spontaneous equilibrium fluctuations and its nonequilibrium properties and, in particular, the energy dissipation in a system. For the wave field of an absorbing half-space, i.e. for the field of radiation which can be recorded by an external (relative to the emitting medium) instrument, the solution of the fluctuation electrodynamic problem directly results in the Kirchhoff law in the form of (4.20).

Before describing the properties of non-black physical bodies, it is useful to introduce the definitions of emissive ability and absorbing ability and also to consider the Kirchhoff law forms that are often used for analysing the emitting half-space (i.e. when there are two material media with a sharp boundary between them), as well as for analysing the radiation transfer processes in a transparent infinite medium (the atmosphere). In the first case (the planar version) the measuring instrument is inside one of media and measures the radiation of the other one. In the second case (the solid version) the instrument is directly inside the medium, whose radiation it just measures. Below we shall consider the first version in detail. As far as the solid (three-dimensional) version is concerned, we shall postpone the detailed study of radiation transfer processes for this version until Chapter 9.

6.3.1 Emissive ability

This characteristic, which is sometimes called the emissivity, indicates what portion of black-body radiation energy constitutes the radiation energy of a given body. The emissive ability of a real physical body depends on such factors as its temperature, its physical and chemical composition, its intrinsic geometrical structure, its degree of surface roughness, the wavelength to which the emitted radiation corresponds, and the angle at which the radiation is emitted. For remote microwave sensing problems it is necessary to know the emissive ability both in any required direction (the

angular characteristics) and at various wavelengths (the spectral characteristics). In this case the degree of remote information capacity of angular and spectral characteristics is strongly distinguished, generally speaking, depending on the type of a physical object under study. This radiation characteristic is called the directional emissive ability (or the directional emissivity).

In calculating a body's total energy losses through radiation (as in heat-and-power engineering problems) it is necessary to know the radiation energy in all directions and, for this reason, the emissivity, averaged over all directions and wavelengths, is used in such calculations. For calculating a complicated heat exchange through radiation between surfaces, the emissivities can be required, which are averaged only over the wavelengths and not over the directions. So, the researcher should possess the emissivity values, averaged in different ways, and they should be obtained, most frequently, from the available experimental data.

In this book we shall keep to the definition of directional spectral emissivity. If necessary, this emissivity can then be averaged over the wavelengths and the directions, and, finally, over wavelengths and directions simultaneously. Averaged over the wavelengths, they are called total (integral) quantities, and the quantities averaged over the directions are called hemispherical quantities (Siegel and Howell, 1972).

Recalling the definitions of spectral intensity of emission from the unit of a physical body's surface (see section 5.1), we shall define the directional emissivity as the ratio of the spectral intensity of a real surface $I_\nu(\mathbf{r}, \Omega, T, \dots)$, which depends on body's temperature, physical and chemical composition, intrinsic geometrical structure and degree of surface roughness, as well as on the observation angle and working wavelength (frequency), to the black-body intensity $I_{\nu B}(\nu, T)$ at the same temperature and at the same wavelength (frequency) (6.2):

$$\kappa_\nu(\mathbf{r}, T, \nu, \Omega, \dots) = \frac{I_\nu(\mathbf{r}, T, \nu, \Omega, \dots)}{I_{\nu B}(T, \nu)} \quad (6.25)$$

This expression for emissivity is most general, since it includes the dependencies on the wavelength, direction and temperature. The total and hemispherical characteristics can be obtained by appropriate integration (Siegel and Howell, 1972).

As far as the volumetric version is concerned, here we should note that the directional spectral emissivity of a unit homogeneous volume of the medium is equal to the ratio of intensity of radiation, emitted by this volume in the given direction, to the intensity of radiation emitted by a black body at the same temperature and wavelength.

6.3.2 Absorbing ability

The absorbing ability of a body is the ratio of the radiation flux absorbed by the body to the radiation flux falling (incident) on the body. The incident radiation possesses the properties inherent in a particular power source. The spectral distribution of the incident radiation energy does not depend on temperature or on the physical nature of an absorbing surface (so long as the radiation, emitted by the

surface, is not partially reflected back onto this surface). In this connection, in defining the absorbing ability (as compared to emissivity), additional difficulties arise, which are related to the necessity of taking into account the directional and spectral characteristics of incident radiation.

By the directional spectral absorptivity $\alpha(\mathbf{r}, \Omega, T, \dots)$ we shall mean the ratio of the spectral intensity of absorbed radiation $I_{\nu a}(\mathbf{r}, \Omega, \nu, T, \dots)$ to the spectral intensity of incident radiation at the given wavelength and from the given direction $I_{\nu 0}(\mathbf{r}, \Omega, \nu, T, \dots)$:

$$\alpha_\nu(\mathbf{r}, T, \nu, \Omega, \dots) = \frac{I_{\nu a}(\mathbf{r}, T, \nu, \Omega, \dots)}{I_{\nu 0}(\mathbf{r}, T, \nu, \Omega, \dots)}. \quad (6.26)$$

In addition to the incident radiation dependence on the wavelength and direction, the directional spectral absorptivity is also a function of temperature, physical and physico-chemical properties of an absorbing surface.

6.3.3 The Kirchhoff law forms

This law establishes the relation between the abilities of emitting and absorbing the electromagnetic energy by any physical body. This law can be presented, to an equal degree of certainty, in terms of spectral, integral, directional or hemispherical quantities. In the case of microwave sensing it is expedient for us to dwell on the directional properties. From equations (5.1) and (6.25), the energy of radiation, emitted by a surface element from dA in the frequency band $d\nu$, within the limits of solid angle $d\Omega$ and during time dt , is equal to

$$dE_\nu = \kappa_\nu(\mathbf{r}, T, \nu, \Omega, \dots) I_{\nu B}(T, \nu) dA \cos \theta d\Omega d\nu dt. \quad (6.27)$$

If we assume the element dA at temperature T to be inside the isothermal, ideally black, closed cavity, also at temperature T , then the intensity of radiation, falling on the element dA in the direction Ω , will be equal to $I_{\nu B}(T, \nu)$ (remember the property of isotropy of radiation intensity of an ideal black cavity) (section 6.1). For maintaining the isotropy of radiation inside an ideal black closed cavity, the fluxes of absorbed and emitted radiation, determined by equations (6.26) and (6.27), should be equal and, therefore, the following relation should be met:

$$\kappa_\nu(\mathbf{r}, T, \nu, \Omega, \dots) = \alpha_\nu(\mathbf{r}, T, \nu, \Omega, \dots). \quad (6.28)$$

Equality (6.28) sets the relationship between the fundamental properties of physical substances and is valid, without limitations, for all media in a state of thermodynamic equilibrium. It represents the most general form of the Kirchhoff law. It is just this form of the law that was presented by G. Kirchhoff in his famous work published in 1860 (see Schopf (1978) for more details).

The following important corollary follows from (6.28). Since in its physical sense quantity α is always less than unity, the emissive ability of any physical body is concluded between zero and unity, i.e. $0 < \kappa < 1$. This characteristic is used very widely in microwave sensing, since it allows us to estimate and compare the emission

properties of investigated substances without resorting to the measurement of radiation energy values.

Another formulation of Kirchhoff's law, also set forth by him, is also possible. The ratio of the radiation intensity of a physical body, heated up to temperature T , to its absorptivity is a universal function of temperature and frequency, which does not depend on the physical and geometrical properties of a body. Proceeding from (6.25), (6.26) and (6.28), we have:

$$\frac{I_\nu(\mathbf{r}, T, \nu, \Omega, \dots)}{\alpha_\nu(\mathbf{r}, T, \nu, \Omega, \dots)} = I_{\nu B}(T, \nu). \quad (6.29)$$

Kirchhoff himself considered the finding of an explicit form of this universal function to be 'the problem of fundamental importance' for physics (Schopf, 1978).

One further form of Kirchhoff's law is used in microwave sensing (and we shall use it later). It follows from the relations presented above:

$$I_\nu(\mathbf{r}, T, \nu, \Omega, \dots) = \kappa(\mathbf{r}, T, \nu, \Omega, \dots) I_{\nu B}(T, \nu). \quad (6.30)$$

As we have seen, in section 1.4, electromagnetic waves propagate in free space, where there exist two components of a wave, which oscillate at right angles with respect to each other and with respect to the wave propagation direction. In the particular case of equilibrium thermal radiation these two components of polarization are equal. Strictly speaking, relations (6.28)–(6.31) are fulfilled for each polarization component, and, in order that they be valid for the total incident radiation, the radiation should have equal polarization components. Thus, the original equilibrium radiation is non-polarized (which, however, is invalid for grey bodies) (see Chapter 7).

The Kirchhoff law was proved for the case of thermodynamic equilibrium in an isothermal closed cavity and, hence, it is strictly valid only in the absence of a resulting thermal flux directed towards the surface or away from it. Under real conditions, as a rule, there exists a resulting flux of electromagnetic radiation, so that relations (6.28) and (6.30) are approximate, strictly speaking. The validity of this approximation is confirmed by reliable experimental data, according to which in the majority of practical cases the ambient radiation field does not have any significant influence on the values of emissive and absorbing abilities. Another confirmation of this approximation is a substance's ability to be at the state of local thermodynamic equilibrium (section 4.4), in which the set of energy states during absorption and emission processes corresponds, to a very close approximation, to their equilibrium distributions (corresponding to the local temperature in this case). Thus, the spreading of Kirchhoff's law to natural nonequilibrium systems is not the result of simple thermodynamic considerations, but, most likely, it is a result of the physical nature of substances. Owing to this circumstance, in the majority of cases the substance is capable of independently maintaining a local thermodynamic equilibrium and, thus, to possesses 'independence' of its properties from the ambient radiation field.

In conclusion, we note that, as astrophysical investigations have shown, the Kirchhoff law can actually also be applied in cases where the radiation is not in

full equilibrium with the substance, and its distribution over frequencies essentially differs from Planck's one. However, the Kirchhoff law is not applicable in cases where thermodynamic equilibrium conditions are strongly violated (nuclear explosions, shock waves, the interplanetary medium). This law is not suitable for determining the emissivities of sources of non-thermal radiation (synchrotron, maser radiation, thunderstorm activity) and sources of quasi-deterministic radiation (radio- and TV-broadcasting, communications).

7

Grey-body radio-emission

The purpose of this chapter is to consider the basic characteristics of the radiation field of one of the most important and widely used physical models of natural objects, namely, the grey half-space with a smooth boundary. Definitions of the reflective and polarization properties of such media are introduced. The physical features of polarized radiation reception by microwave complexes are analysed. Using the impedance forms of boundary conditions of the Maxwellian equations, the model for calculating the plane-parallel layered media is formulated. This model is widely used in the theory and practice of passive microwave remote sensing. On the basis of the plane-parallel layered media method the electrodynamic problem of radio-emission of inhomogeneous non-isothermal media is analysed in detail. The results and limitations of the quasi-monochromatic approach to calculating the radiation characteristics of layered media are considered, in particular, the quasi-coherency properties of a noise signal with a limited spectrum as applied to the problem of emission of a two-layered medium.

7.1 SURFACE REFLECTIVITY

Before proceeding to the basic subject of this chapter, we note that by grey physical bodies we shall mean physical objects whose radiation properties differ from the radiation of ideal black bodies in the wavelength band under consideration. Or, in other words, physical objects, whose emissivity differs from unity (and whose wavelength (frequency) dependence can be rather intricate, generally speaking), can serve as a source of quite valuable remote information. The physical reasons for this can be quite diverse: the physical-chemical properties of a medium, the degree of a surface roughness, the temperature properties, the subsurface structures (inhomogeneities) and others. Note that in the other wavelength bands (for example, in the IR band) by the ‘grey’ term are meant, generally speaking, the other features of

radiation, for example, the independence of the spectral emissivity from the wavelength (Siegel and Howell, 1972).

It is much more complicated to determine the reflective properties of a surface element than the emissivity or absorbing ability (see section 6.3). This is explained by the fact that the reflectivity of a surface depends not only on its physical properties and on the physical body's temperature, but also on the directions of incident and reflected radiation. In general, the study of the reflective properties of surfaces is a very complex problem. Various definitions and approaches are used in the science and science-technological literature for the description and investigation of radiation reflection from a surface element. In the physics literature the whole of the class of these definitions is sometimes defined as scattering indicatrix (Prochorov, 1984). The discussion of various concepts accepted in optics and radiophysics can be found in books by Peake (1959); Siegel and Howell (1972); Ozisik (1973); Skolnik (1980); Ishimaru (1978, 1991). We have no scope to analyse in detail these concepts and the relationships between them within the framework of this book. Here we shall consider only those concepts that concern radiation reflection from surfaces and that we will need later.

7.1.1 Reflection distribution function

Consider a monochromatic radiation beam of intensity $I_\nu(\mathbf{r}, \Omega') d\Omega'$, which falls on the surface element dA . Let θ' be the angle between the incident beam and the normal to the surface (Figure 7.1). The quantity of energy of radiation, falling on a unit area of the surface element per unit of time in a unit range of frequencies, is equal to

$$I_\nu(\mathbf{r}, \Omega') \cos \theta' d\Omega'. \quad (7.1)$$

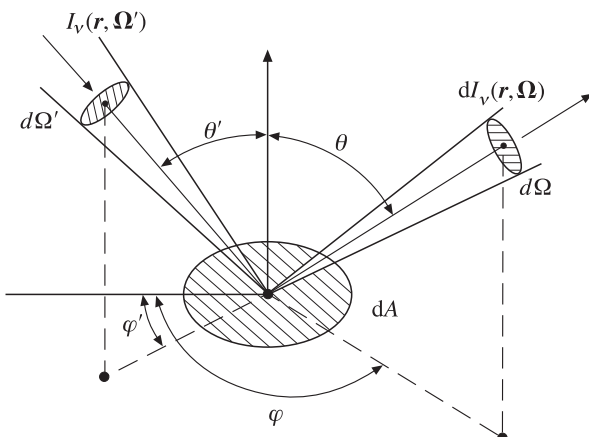


Figure 7.1. Schematic beam representation of the incident and reflected radiations for the determination of bidirectional reflectivity.

Some part of this radiation will be reflected by the surface in all directions within the limits of a hemispherical solid angle. Let $dI_\nu(\mathbf{r}, \Omega')$ be the intensity of radiation reflected in the direction of observation Ω . The reflected radiation intensity is related to the incident radiation energy by the spectral distribution function (or by the bidirectional reflectivity) of the reflected radiation (the reflection indicatrix) $f_\nu(\mathbf{r}, \Omega', \Omega)$ defined as follows:

$$f_\nu(r, \Omega', \Omega) = \frac{dI_\nu(\mathbf{r}, \Omega)}{I_\nu(\mathbf{r}, \Omega') \cos \theta' d\Omega'}. \quad (7.2)$$

The quantity so defined can be either greater or less than unity, depending on the surface structure. For example, for mirror-reflecting surfaces the total incident radiation comprised within the limits of solid angle $d\Omega'$, is reflected within the limits of solid angle $d\Omega = d\Omega'$, whose axis is the direction determined by angles $\theta = \theta'$ and $\varphi = \varphi' \pm \pi$.

Using the generalized reciprocity theorem, which was first formulated by Helmholtz, it can be shown (Siegel and Howell, 1972), that the reflection indicatrix is symmetric with respect to incidence and reflection directions:

$$f_\nu(\mathbf{r}, \Omega', \Omega) = f_\nu(\mathbf{r}, \Omega, \Omega'). \quad (7.3)$$

The reflective properties of the surface are completely defined, if the reflection indicatrix is known for all directions of a hemispherical space. However, it is extremely difficult to obtain such information experimentally; for this reason the total reflection indicatrix is not used, as a rule, in remote sensing practice. The integral (averaged over angles) reflective characteristics are widely used in IR sensing practice. In its turn, the integrally angular approach is seldom applied in microwave sensing.

7.1.2 Directional-hemispherical reflectivity

In the case where the surface is rather rough with respect to the electromagnetic field wavelength, the situation can arise in which the surface is irradiated by the radiation beam from a given direction, and the reflected radiation is scattered within the limits of a hemispherical solid angle (over the surface). A similar scattering regime is characteristic of terrestrial surfaces when they are irradiated by sunlight as well as by IR radiation sources. In this case the spectral directional-hemispherical reflectivity $\rho_\nu(\mathbf{r}, \Omega' \rightarrow 2\pi)$ is determined as follows:

$$\rho_\nu(\mathbf{r}, \Omega' \rightarrow 2\pi) = \frac{\int_{\Omega=2\pi} dI_\nu(\mathbf{r}, \Omega) \cos \theta d\Omega}{I_\nu(\mathbf{r}, \Omega') \cos \theta d\Omega'}. \quad (7.4)$$

Using the definition of the reflection indicatrix, we can relate $\rho_\nu(\mathbf{r}, \Omega' \rightarrow 2\pi)$ with $f_\nu(\mathbf{r}, \Omega', \Omega)$ as follows:

$$\rho_\nu(\mathbf{r}, \Omega' \rightarrow 2\pi) = \int_{\varphi=0}^{2\pi} \int_{\mu=0}^1 f_\nu(r; \mu', \varphi'; \mu, \varphi) \mu d\mu d\varphi. \quad (7.5)$$

The case is often considered, which is opposite to that described above, when the radiation falls on the surface element from all directions within the limits of a hemispherical solid angle (over the surface), and the reflected radiation intensity is measured only in the given direction Ω . In such a case the hemispherically directional reflectivity $\rho_\nu(\mathbf{r}, 2\pi \rightarrow \Omega)$ can be presented (provided that the incident radiation does not depend on the direction) in the form:

$$\rho_\nu(r, 2\pi \rightarrow \Omega) = \int_{\varphi'=0}^{2\pi} \int_{\mu'=0}^1 f_\nu(\mathbf{r}; \mu', \varphi'; \mu, \varphi) \mu' d\mu' d\varphi'. \quad (7.6)$$

Using the reciprocity theorem, it can easily be seen that in the case where $\varphi = \varphi'$ and $\theta = \theta'$, the following equality is met:

$$\rho_\nu(\mathbf{r}, \Omega' \rightarrow 2\pi) = \rho_\nu(\mathbf{r}, 2\pi \rightarrow \Omega). \quad (7.7)$$

7.1.3 Hemispherical reflectivity

Consider the situation where radiation falls on a surface from all directions within the limits of a hemisphere (above the surface) and is reflected in all directions as well. This situation is typical of the case where terrestrial surfaces are irradiated by solar radiation scattered by dense cloudiness (diffuse illumination). With allowance for the definition of a directional-hemispherical reflectivity (7.4) the spectral hemispherical reflectivity $\rho_\nu(\mathbf{r})$ is determined as follows:

$$\rho_\nu(\mathbf{r}) = \frac{\iint_{\Omega'=2\pi} \rho_\nu(\mathbf{r}, \Omega' \rightarrow 2\pi) I_\nu(\mathbf{r}, \Omega') \cos \theta' d\Omega'}{\iint_{\Omega'=2\pi} I_\nu(\mathbf{r}, \Omega') \cos \theta' d\Omega'}. \quad (7.8)$$

If the incident radiation does not depend on the direction, then, with allowance for (7.5), we obtain the relation between the reflection indicatrix and $\rho_\nu(\mathbf{r})$

$$\rho_\nu(\mathbf{r}) = \frac{1}{\pi} \int_{\Omega'=2\pi} \left[\int_{\Omega=2\pi} f_\nu(\mathbf{r}, \Omega', \Omega) \cos \theta d\Omega \right] \cos \theta' d\Omega'. \quad (7.9)$$

If $f_\nu(\mathbf{r}, \Omega', \Omega)$ does not depend on directions (or, in other words, has diffuse character of scattering), expression (7.9) is simplified and takes the form:

$$\rho_\nu(\mathbf{r}) = \pi f_\nu(\mathbf{r}). \quad (7.10)$$

7.1.4 Diffuse and specular reflection

The surface is called a diffuse reflector if the intensity of reflected radiation is the same over all angles of reflection within the limits of a hemisphere and does not depend on the angle of incidence. The surface is called a specular or mirror reflector if the incident and reflected beams are symmetrical with respect to the normal at the point of incidence, and the reflected beam is concluded inside the solid angle $d\Omega$ equal to a solid angle containing the incident beam $d\Omega'$ (i.e. $d\Omega = d\Omega'$). The

assumption on diffuse and specular reflections is often used in the theory and practice of remote sensing, of heat transfer, since it results in considerable simplifications; the real surfaces, however, are neither ideally diffuse, nor ideally specular. We should note here, that, depending on the wavelength used and on the degree of surface roughness, the contributions of specular and diffuse components in the process of full scattering by a studied medium can drastically differ. So, in the optical and IR bands the majority of solid terrestrial media (including vegetation) represent diffuse reflectors. At the same time, the disturbed sea surface represents the most complicated (and dynamical) combination of diffuse and quasi-specular reflectors (the field of patches of sunlight) (Figure 2.1). In the microwave band the specular component plays a noticeable part, both for electromagnetic waves scattering on the sea surface and for scattering on the land surface. In its turn, the vegetation can be presented, depending on the wavelength, either as a highly diffuse (scattering) object, or as an ideal black body (an ideal absorber), or as their complicated scattering-absorbing combination of fractal type (see, for example, Peake, 1959; Fung and Chen, 1981; Franceschetti *et al.*, 1999a,b; Chauhan, 2002; Wu and Liu, 2002; Miesch *et al.*, 2002). Generally speaking, it is the choice of the most adequate scattering model of a studied surface which represents, to a considerable degree, the modern problem of microwave radiation of rough terrestrial covers (such as the disturbed sea surface, vegetation, the processed surface of soils and grounds) (see Chapter 12 for more details).

7.2 EFFECTIVE RADIATION OF REFLECTING SURFACE

Let us consider a beam of monochromatic radiation of intensity $I_\nu(\mathbf{r}, \Omega') d\Omega'$, which falls on the surface element dA (Figure 7.1). The quantity of the energy of radiation, falling on the surface area unit per unit time, within a unit frequency band, is equal to $I_\nu(\mathbf{r}, \Omega') \cos \theta' d\Omega'$, where θ' is the angle between the incident beam direction and the normal to the surface. In accordance with the definition of spectral directional absorbing ability (see equation (6.26)), the quantity of radiation energy absorbed by the surface area unit per unit time, within a unit frequency band, can be presented as follows:

$$dE_\nu = \alpha_\nu(\mathbf{r}, \nu, T, \Omega', \dots) I_\nu(\mathbf{r}, \Omega') \cos \theta' d\Omega'. \quad (7.11)$$

If the surface is supposed to be opaque, i.e. it absorbs and reflects the radiation, then the energy of absorbed radiation will be equal to the difference between the incident radiation energy and reflected radiation energy

$$dE_\nu = I_\nu(\mathbf{r}, \Omega') \cos \theta' d\Omega' - \rho_\nu(\mathbf{r}, \Omega' \rightarrow 2\pi) I_\nu(\mathbf{r}, \Omega') \cos \theta' d\Omega'. \quad (7.12)$$

Substituting (7.11) into (7.12), we obtain the relation between the directional absorbing ability and the directional-hemispherical reflectivity as:

$$\alpha_\nu(\mathbf{r}, T, \nu, \Omega') = 1 - \rho_\nu(\mathbf{r}, \Omega' \rightarrow 2\pi). \quad (7.13)$$

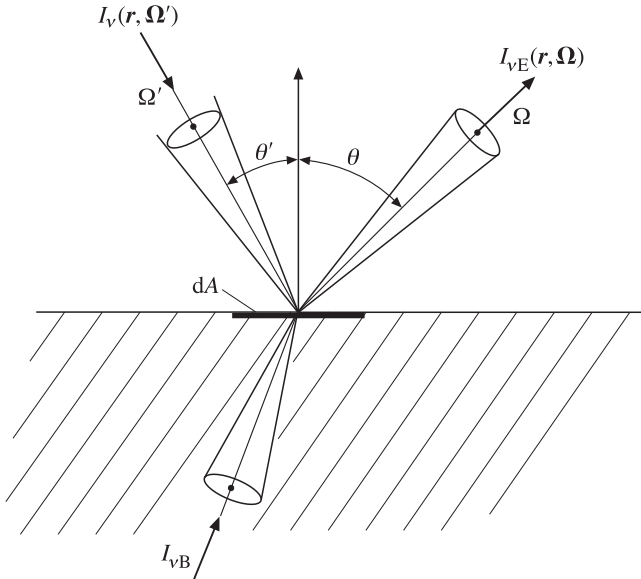


Figure 7.2. Schematic beam representation of the emitted, incident and reflected radiations for the determination of effective emission.

The latter characteristic is related, in its turn, in an integral manner with the reflectivity indicatrix (7.5).

If the investigated medium is at a state of local thermodynamic equilibrium (see section 4.4), and the Kirchhoff law (6.28) is satisfied, then the latter expression can be written in the following form:

$$\kappa_\nu(\mathbf{r}, T, \nu, \Omega) = 1 - \rho(\mathbf{r}, \Omega \rightarrow 2\pi). \quad (7.14)$$

Here it should be emphasized that the directional-hemispherical reflectivity should be considered from that direction where the observation with an instrument is carried out (in accordance with the Kirchhoff law).

The intensity of monochromatic effective radiation $I_{vE}(\mathbf{r}, \Omega)$ of an opaque surface element in the observation direction Ω will be equal to the sum of intensities of thermal and reflected radiation (Figure 7.2). This is due to the fact that stochastic processes are independent, and their intensities can be summed. If the surface is at temperature T and has spectral emissivity $\kappa(\mathbf{r}, \Omega)$, then the intensity of thermal radiation will be determined by expression (6.30). As to the external radiation, it should be noted generally that the surface element is irradiated from all directions within the limits of a hemisphere, and the intensity of radiation, reflected by this element in the observation direction Ω , can be obtained according to relation (7.2). Thus, the total effective radiation from the surface element can be written as follows:

$$I_{vE}(\mathbf{r}, \Omega) = \kappa_\nu(\mathbf{r}, \Omega) I_{vB}(T, \nu) + \int_{\Omega'=2\pi} f_\nu(\mathbf{r}, \Omega, \Omega') I_\nu(\mathbf{r}, \Omega') \cos \theta' d\Omega'. \quad (7.15)$$

The formula obtained is very widely used in remote microwave sensing practice, in quite different modifications, by the way. Here, as we have already noted, a serious problem is the adequate choice of a surface scattering model, i.e. the choice of function $f_\nu(\mathbf{r}, \Omega', \Omega)$.

Now we consider two important cases, which are often used in microwave sensing practice: a surface with specular reflection and a surface with diffuse reflection. For a mirror surface the reflection indicatrix can formally be presented as a product of delta-function $\delta(\Omega - \Omega')$, that expresses the mirroring property of a surface, and the spectral power reflectivity from the direction $\Omega' - R_{\nu P}(\Omega')$. The value of this reflectivity can be determined on the basis of the wave electromagnetic theory. Besides, we note, that the mirror surfaces possess the property of isotropy in the azimuthal direction. In this case the effective radiation of a unit surface can be written as a dependence on the polar angle (observation angle) θ only:

$$I_{\nu E}(\mathbf{r}, \theta) = \kappa_\nu(\mathbf{r}, \theta) I_{\nu B}(T, \nu) + R_{\nu P}(\theta) I_\nu(\theta'). \quad (7.16)$$

A similar procedure, performed for the relation between the emissivity and reflectivity (7.14), makes it possible to obtain the following important expression:

$$\kappa_\nu(\mathbf{r}, \theta) = 1 - R_{\nu P}(\mathbf{r}, \theta). \quad (7.17)$$

Comparing this expression with the electrodynamic solutions of the fluctuation-dissipation theorem (see section 4.3), we can easily see a complete analogy between expression (7.17), obtained from the energy conservation law, and the electrodynamic solution (4.20) for radiation of a semi-infinite space with a smooth boundary.

For diffusively emitting and reflecting surfaces quantities κ_ν and f_ν weakly depend on angles; as a result, the expression for effective radiation can be presented in a slightly different form (provided that the incident radiation does not depend on the direction):

$$I_{\nu E}(\mathbf{r}, \Omega) = \kappa_\nu I_{\nu B}(T, \nu) + I_\nu \rho_\nu(2\pi \rightarrow \Omega). \quad (7.18)$$

Here it is important to note that the external radiation will appear in a resulting radiation in a rather complicated manner. Whereas in the case of mirror surfaces, under conditions of real observations, there exist experimental techniques for separating out the information radiation component, which directly depends on the medium's properties, this procedure is much more difficult to perform for diffuse surfaces.

In the microwave band the relations presented above have usually been used in the terms of spectral brightness temperature of an investigated object $T_{\nu B}(\mathbf{r}, \Omega)$, which, with regard to the Kirchhoff law (equation (6.30)) and relation (5.27), can be presented as

$$T_{\nu B}(\mathbf{r}, \Omega) = \kappa_\nu(\mathbf{r}, \Omega) T_0, \quad (7.19)$$

where T_0 is the thermodynamic temperature of the investigated medium.

And, considering media with mirror boundaries possessing azimuthal isotropy properties, we can obtain the expression for effective spectral brightness temperature

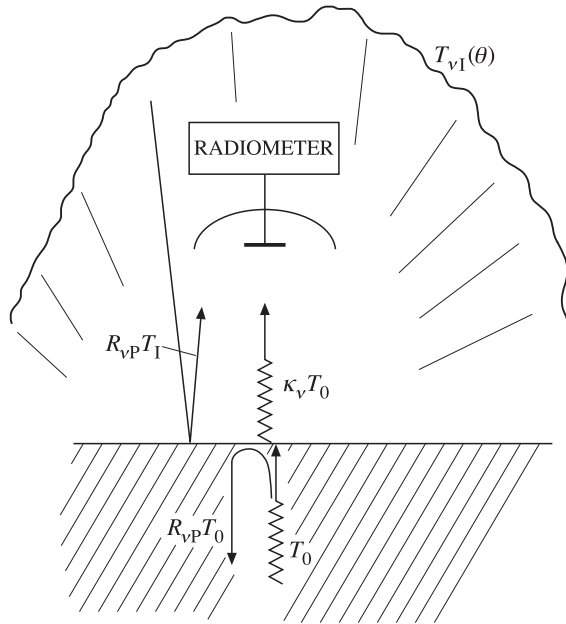


Figure 7.3. Schematic beam presentation of remote sensing measuring procedure. See explanations of notation in the text.

$T_{\nu BE}(\theta)$ with regard to the external brightness spectral integral illumination $T_{\nu I}(\theta)$ (sometimes called the firmament illumination)

$$T_{\nu BE}(\theta) = \kappa_\nu(\theta) T_0 + R_{\nu P}(\theta) T_{\nu T}(\theta). \quad (7.20)$$

The observational situation is illustrated schematically in Figure 7.3.

It should be noted that, unlike the IR band, in the microwave band the external brightness illumination varies in intensity within very wide limits – from 20–30 K up to 300 K – depending on the microwave working subrange and the state of cloudiness, and it also strongly varies depending on the observation angle (see Chapters 9 and 10).

In relation (7.20) the question is about spectral and differential (in angle) radiation characteristics of a medium. However, the total signal received by a radiometric system will depend both on the relationship between the angular characteristics of a studied object and the antenna system of a receiving device (see equation (5.28)), and on the amplitude-frequency characteristic of a receiving device (see equation (5.29)). We shall still be interested in the properties of physical media particularly; therefore, we shall further use relation (7.20), omitting for simplicity subscript ν . However, we shall always remember, that the question is about spectral characteristics.

Some important conclusions follow from relation (7.20). First, the brightness temperature of a physical medium, recorded by a remote instrument, is directly

related to the physical-chemical properties of a medium (via the emissive ability) and with its thermodynamic temperature. The spectral properties of a medium (for example, the dependence of its dielectric properties and, accordingly, of physical-chemical properties, on the working frequency) will also be displayed directly in spectral properties of the field of brightness temperature. Of importance here are the state and characteristics of the medium's boundary which, in their turn, have intrinsic and rather complicated spectral properties. The separation of volume and surface effects in a compound radiothermal signal is one of complicated problems of remote microwave sensing.

Second, since the emissivity of media, being under the conditions of local thermodynamic equilibrium, is less than unity (as a consequence of Kirchhoff's law), the brightness temperature of such media will always be lower, than the value of thermodynamic temperature of a medium (certainly, disregarding the firmament illumination). To restore the component, caused by physical-chemical properties, from the compound radiothermal signal, IR thermal remote measurements (along with radiothermal ones) of physical objects are usually applied. As a result, the information on a purely temperature field is obtained, and, then, the medium emissivity is restored. If it is indicated in such a manner that the medium emissivity exceeds unity, then, to a high probability, the radiation of a medium can be supposed to have a clearly non-thermal character (see section 4.4).

Third, to demonstrate the important role of brightness illumination, let us imagine mentally the following experiment. The investigated medium with an instrument are placed in a thermostat with emitting blackbody walls. In this case the brightness illumination temperature will not depend on the direction and will be equal to $T_I(\theta) = T_0$. Substituting this value into (7.20) and making some transformations, we obtain that the effective brightness temperature will be equal to T_0 and will not depend on the physical properties of the medium. In other words, remote measurements, carried out under thermostatic control conditions, will not bear any information substance.

This can easily be confirmed by some other relationships as well. If we investigate two media with different emissivities (but with equal physical temperatures), then it follows from (7.20), that in observing these two media the radiobrightness contrast ΔT_B will be:

$$\Delta T_B = (T_0 - T_1) \Delta \kappa. \quad (7.21)$$

It can be seen from this relation that, in spite of distinctions in physical properties of the media, determined as $\Delta \kappa = \kappa_1 - \kappa_2$, the measured radiobrightness contrast tends to zero as $T_I \rightarrow T_0$. Under terrestrial atmosphere conditions such a situation takes place, for example, in the wavelength band of about 5 mm. Similar thermostated situations take place also in closed laboratory rooms, which makes it difficult to perform fine radiothermal measurements in such rooms.

Even earlier detailed onboard radiothermal experiments (1975–1979) have shown that the mirror component plays an essential part in forming the microwave effective radiation, even if the surface is optically rough. As an example, Figure 7.4 shows the fragments of radiothermal signal reception

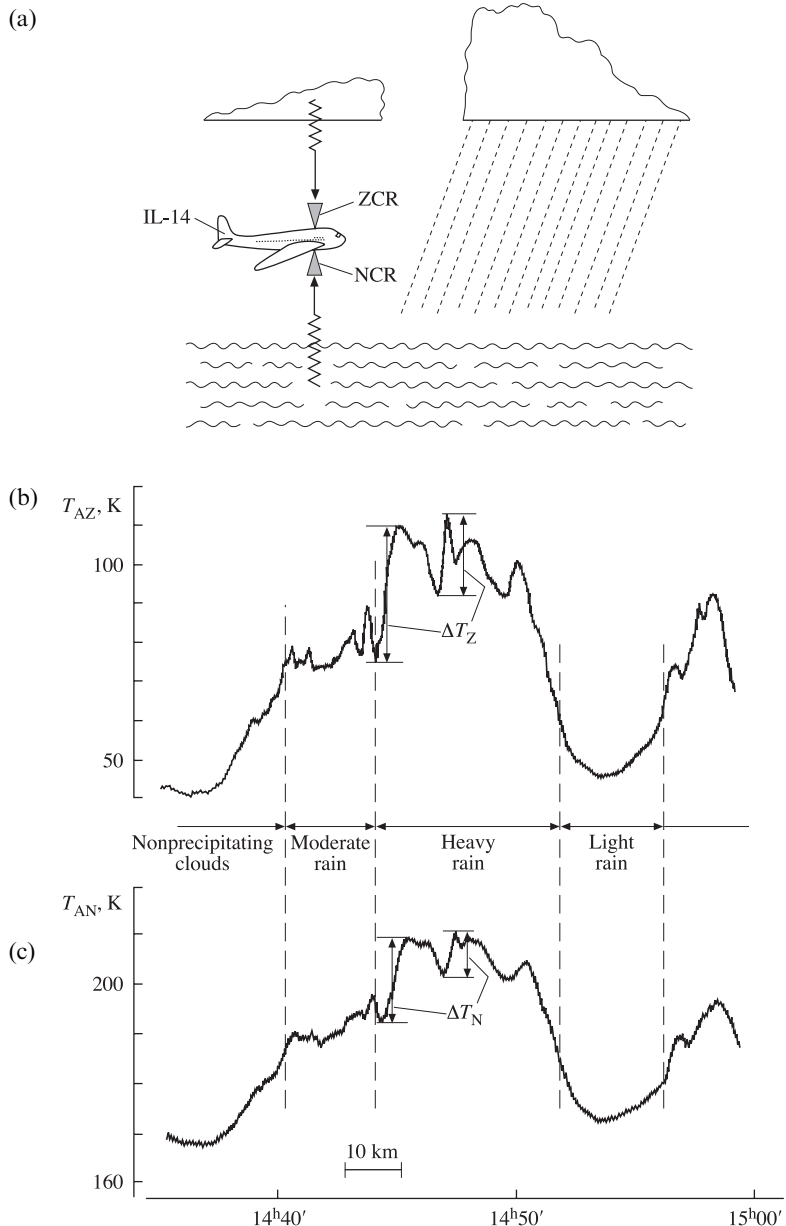


Figure 7.4. Remote microwave results of the specialized nadir-zenithal airborne (Russian IL-14) instruments (radiometer RZN 0.8). The working area is the north part of the Caspian Sea on 22 April 1979. (a) Schematic presentation of measuring procedure. ZCh and NCh are the zenithal and nadir channels respectively. (b) and (c) are fragments of the radiometer output signal for zenithal channel T_{AZ} and nadir channel T_{AN} . Moscow time, spatial scale and indoor temperature calibration are shown on abscissa and on ordinate.

registograms, obtained by means of a specialized onboard radiothermal device, which receives radiations simultaneously in the nadir mode (with respect to a flight vehicle) and in the zenith mode by two identical radiometers – zenithal instruments and nadir instruments. Specialized nadir-zenithal instruments of 8-mm band were manufactured and installed on the Russian IL-14 aircraft-laboratory by co-workers of the Space Research Institute of the Russian Academy of Sciences. The onboard experiments were carried out in the Caspian Sea area of water under complicated meteorological conditions, at strong sea surface disturbance and at low altitude of flight (200–400 m) (Figure 7.4(a)). The analysis of registograms of nadir and zenithal channels (Figure 7.4(b), (c)) showed their virtually full identity from the viewpoint of variations of radiothermal peculiarities. Depending on precipitation intensity, the external illumination varies within very wide limits – from 40–50 K for a cloudy atmosphere up to 70–80 K – for precipitation of average intensity, and up to 100–110 K for hail showers. Accordingly, in the nadir channel the signal intensity varies from 170 K to 200–210 K. It should be noted, that it is virtually impossible to obtain such a detailed spatial structure of precipitation of various intensity by other techniques.

Proceeding from relation (7.20) and using the data of nadir T_N and zenithal T_Z channels, the first (and rather rough) estimation of sea surface emissivity can be given as:

$$\kappa \cong \frac{T_N - T_Z}{T_0 - T_Z}. \quad (7.22)$$

Substituting the values for various illumination intensities, we obtain the emissivity value for the disturbed sea surface as 0.51–0.53. This can also be done in another way, by considering the contrasts in the nadir (ΔT_N) and zenithal (ΔT_Z) channels' intensity from the same spatial peculiarity. In this case we have:

$$1 - \kappa = \frac{\Delta T_N}{\Delta T_Z}. \quad (7.23)$$

Substituting corresponding values of contrasts from the two channels (they are marked in Figure 7.4(b), (c)) for the same radiothermal peculiarity, we obtain the emissivity value as 0.51–0.52. It can be seen from this result that the estimates obtained by two methods – from the ‘absolute’ values and from contrasts – are very close. Thus, we can conclude that the use of a mirror model in interpreting radiothermal observations is quite justified, in the first approximation at least.

7.3 REFLECTION AND TRANSMISSION OF PLANE WAVES AT THE PLANE INTERFACE BOUNDARY

In the overwhelming majority of cases remote sensing practice deals with inhomogeneous media having rough boundaries. The full solution of the problem of radiation of such media is rather complicated. We shall consider some of the

problems in this book. For constructing complex models it is very useful to know the solutions of some simple problems, which, nevertheless, play a fundamental part. The simplest problem on wave propagation in the inhomogeneous medium is the problem of a plane monochromatic wave falling on a plane interface boundary of two media with different dielectric properties (the specular model of reflection). As is known, refracted (transmitted) and reflected waves arise in this case. Of importance here are the boundary conditions of the Maxwellian equations, which are presented not in the form of relation between the amplitudes of fields at the boundary (see equation (1.6)), but in the form of complex field reflectivities and transmissivities and (real) power reflectivities and transmissivities (Brekhovskikh, 1957; Veremey *et al.*, 1978; Finkelstein and Mendelson, 1980; Wilheit, 1978).

Let the interface boundary between two semi-infinite homogeneous media coincide with the plane $z = 0$ of the Cartesian coordinate system. The media disposed above ($z > 0$) and below ($z < 0$) the boundary are characterized by parameters ϵ_1 and ϵ_2 , respectively ($\mu_1 = \mu_2 = 1$) (see section 1.6). To this boundary from the first medium falls a plane wave at angle θ_0 to axis z with circular frequency $\omega = 2\pi\nu$ and wave vector $\mathbf{k}_0 = k_1 \mathbf{m}_0$ ($k_1 = (\omega/c)\sqrt{\epsilon_1}$, where \mathbf{m}_0 is the unit vector of the normal to the incident wave front) (see section 1.6). Then we make the plane of incidence that contains vector \mathbf{k}_0 and axis z , coincident with the plane xz . We denote the wave vector of the reflected wave by $\mathbf{k}_1 = k_1 \mathbf{m}_1$ and the wave vector of the transmitted wave by $\mathbf{k}_2 = k_2 \mathbf{m}_2$; \mathbf{n}_0 is the unit vector of the normal to the interface boundary, directed from medium 2 to medium 1. According to (1.29) and (1.11), the electric and magnetic fields can be written as follows. For the incident wave:

$$\begin{aligned}\mathbf{E}_I &= \mathbf{E}_0 \exp [jk_1(\mathbf{m}_0 \mathbf{r}) - j\omega t] \\ \mathbf{H}_I &= \frac{[\mathbf{m}_0 \mathbf{E}_0]}{Z_1} \exp [jk_1(\mathbf{m}_0 \mathbf{r}) - j\omega t]\end{aligned}\quad (7.24)$$

for the reflected wave:

$$\begin{aligned}\mathbf{E}_R &= \mathbf{E}_1 \exp [jk_1(\mathbf{m}_1 \mathbf{r}) - j\omega t] \\ \mathbf{H}_R &= \frac{[\mathbf{m}_1 \mathbf{E}_1]}{Z_1} \exp [jk_1(\mathbf{m}_1 \mathbf{r}) - j\omega t]\end{aligned}\quad (7.25)$$

and for the transmitted wave:

$$\begin{aligned}\mathbf{E}_T &= \mathbf{E}_2 \exp [jk_2(\mathbf{m}_2 \mathbf{r}) - j\omega t] \\ \mathbf{H}_T &= \frac{[\mathbf{m}_2 \mathbf{E}_2]}{Z_2} \exp [jk_2(\mathbf{m}_2 \mathbf{r}) - j\omega t].\end{aligned}\quad (7.26)$$

Here Z_1 and Z_2 are the complex impedances of the first and second media (see equation (1.30)). To simplify the recording, we shall assume in this paragraph $\epsilon_0 = \mu_0 = 1$. This condition will in no way influence the final result. At $z = 0$ the boundary conditions should be satisfied, which are reduced to the requirement of continuity of tangential components of vectors \mathbf{E} and \mathbf{H} of the total wave field

(see equation (1.6)). Hence, at $z = 0$ the fields should satisfy the equations

$$\begin{aligned} [\mathbf{n}_0 \mathbf{E}_0] \exp[j(\mathbf{k}_0 \mathbf{r})] + [\mathbf{n}_0 \mathbf{E}_1] \exp[j(\mathbf{k}_1 \mathbf{r})] &= [\mathbf{n}_0 \mathbf{E}_2] \exp[j(\mathbf{k}_2 \mathbf{r})], \\ [\mathbf{n}_0 [\mathbf{m}_0 \mathbf{E}_0]] \exp[j(\mathbf{k}_0 \mathbf{r})] + [\mathbf{n}_0 [\mathbf{m}_1 \mathbf{E}_1]] \exp[j(\mathbf{k}_1 \mathbf{r})] &= \frac{Z_1}{Z_2} [\mathbf{n}_0 [\mathbf{m}_2 \mathbf{E}_2]] \exp[j(\mathbf{k}_2 \mathbf{r})]. \end{aligned} \quad (7.27)$$

Since relations (7.27) should be satisfied at all points of the plane $z = 0$ (the condition of homogeneity of the plane boundary), this gives rise to the requirement of identical dependence of the fields of all three waves on coordinates x and y at $z = 0$. Therefore, the phase multipliers in the exponents should be identical and, hence,

$$k_1 \sin \theta_0 = k_1 \sin \theta_1 = k_2 \sin \theta_2. \quad (7.28)$$

This results in the well-known law of reflection for specular boundaries:

$$\theta_0 = \theta_1, \quad (7.29)$$

and in Snell's law for angles of incidence and transmission:

$$k_1 \sin \theta_0 = k_2 \sin \theta_2. \quad (7.30)$$

Note that here the question is about the complex values of both angles and amplitudes of wave vectors.

To determine the amplitudes of reflected and transmitted waves and, accordingly, the complex reflectivities and transmissivities, we turn to the system of equations (7.27). In this case we shall consider the waves of two different linear polarizations: the horizontally polarized wave with vector \mathbf{E} perpendicular to the plane of incidence ($E_x = E_z = 0, E_y \neq 0$), and the vertically polarized wave with vector \mathbf{E} lying in the plane of incidence ($E_y = 0, E_x \neq 0, E_z \neq 0$). A wave with arbitrary elliptical polarization can be obtained as a linear combination of these two solutions. In the first case, for the wave with horizontal polarization, we obtain from (7.27) the equations for unknown amplitudes E_1 and E_2

$$\begin{aligned} E_0 + E_1 &= E_2, \\ \frac{1}{Z_1} (E_0 \cos \theta_0 - E_1 \cos \theta_0) &= \frac{1}{Z_2} \cos \theta_2. \end{aligned} \quad (7.31)$$

Solving (7.31), we find the complex Fresnel coefficients, which relate the amplitudes of reflected and transmitted waves to the amplitude of an incident wave, i.e. the reflectivity and transmissivity:

$$\dot{R}_{\text{H}12} = \frac{E_1}{E_0} = \frac{Z_2 \cos \theta_0 - Z_1 \cos \theta_2}{Z_2 \cos \theta_0 + Z_1 \cos \theta_2} = |\dot{R}_{\text{H}12}| \exp(j\varphi_{\text{RH}}), \quad (7.32)$$

$$\dot{i}_{\text{H}12} = \frac{E_2}{E_0} = \frac{2Z_2 \cos \theta_0}{Z_2 \cos \theta_0 + Z_1 \cos \theta_2} = |\dot{i}_{\text{H}12}| \exp(j\varphi_{\text{tH}}). \quad (7.33)$$

For the vertically polarized wave the calculation is more convenient to perform for vector \mathbf{H} , which is perpendicular to the plane of incidence in the given case. The

calculations, completely similar to those made above, lead to the expressions:

$$\dot{R}_{V12} = \frac{H_1}{H_0} = \frac{Z_1 \cos \theta_0 - Z_2 \cos \theta_2}{Z_1 \cos \theta_0 + Z_2 \cos \theta_2} = |\dot{R}_{V12}| \exp(j\varphi_{RV}), \quad (7.34)$$

$$\dot{i}_{V12} = \frac{H_2}{H_0} = \frac{2Z_2 \cos \theta_2}{Z_1 \cos \theta_1 + Z_2 \cos \theta_2} = |\dot{i}_{V12}| \exp(j\varphi_{iV}). \quad (7.35)$$

Some more important conclusions follow from relations (7.32)–(7.33) and (7.34)–(7.35), namely: by using the method of permutation of indices and summation, we obtain the relations between the reflectivities above R_{12} and below R_{21} the boundary and the reflectivities and transmissivities (for any polarization):

$$\dot{R}_{12} = -\dot{R}_{21}, \quad (7.36)$$

$$1 + \dot{R}_{12} = \dot{i}_{12}, \quad (7.37)$$

$$1 - \dot{R}_{21} = \dot{t}_{21}. \quad (7.38)$$

These relations are sometimes called the impedance form of boundary conditions.

In microwave sensing theory and practice the power reflectivities and transmissivities (or the coefficients in power) are often used. Their physical meaning is related to the active energy transfer by the electromagnetic field in media and between the media (through the boundary). The power reflectivities and transmissivities of the boundary of two media are defined as corresponding ratios of averaged values of the Poynting vector (see equation (1.20)):

$$R_{P12} = \frac{\bar{S}_1}{\bar{S}_0} = |\dot{R}_{12}|^2; t_{P12} = \frac{\bar{S}_2}{\bar{S}_0} = \frac{\text{Re} \sqrt{\dot{\varepsilon}_2}}{\text{Re} \sqrt{\dot{\varepsilon}_1}} |\dot{i}_{12}|^2. \quad (7.39)$$

The formulas are presented here for the condition of normal incidence of a plane wave on the interface boundary. The energy conservation law for the boundary of transparent (loss-free) media is usually formulated (Stratton, 1941) as a continuity of normal components of the total energy flux above the boundary and below the boundary:

$$\mathbf{n}_0(\bar{S}_0 + \bar{S}_1) = \mathbf{n}_0 \bar{S}_2 \quad (7.40)$$

and this directly results in the relation we have repeatedly used before, namely,

$$R_{P12} + t_{P12} = 1. \quad (7.41)$$

However, more detailed investigations, carried out more recently (Veremey *et al.*, 1978; Finkelstein and Mendelson, 1980), have shown that for absorbing media the total energy flux is not generally equal to the sum of energy fluxes of partial waves. So, in determination of the energy conservation law we should use the energy flux of the total field (above the boundary), rather than the sum of components of energy fluxes. In such a statement (for the horizontal polarization) the energy conservation

law (the continuity of normal components of the flux of energy of the total field) can be written as follows:

$$\operatorname{Re} [(\mathbf{E}_0 + \mathbf{E}_1)\{(\mathbf{H}_0 \cos \theta_0)^* + (\mathbf{H}_1 \cos \theta_1)^*\}] = \operatorname{Re} [\mathbf{E}_2(\mathbf{H}_2 \cos \theta_2)^*]. \quad (7.42)$$

Here the power transmissivity at oblique incidence is equal to

$$t_{P12} = \frac{(\mathbf{n}_0 \bar{\mathbf{S}}_2)}{(\mathbf{n}_0 \bar{\mathbf{S}}_0)} = \frac{\operatorname{Re} [\mathbf{E}_2(\mathbf{H}_2 \cos \theta_2)^*]}{\operatorname{Re} [\mathbf{E}_0(\mathbf{H}_0 \cos \theta_0)^*]} = \frac{\operatorname{Re} (\sqrt{\dot{\varepsilon}_2} \cos \theta_2)^*}{\operatorname{Re} (\sqrt{\dot{\varepsilon}_1} \cos \theta_0)^*} |t_{12}|^2. \quad (7.43)$$

After some transformations we obtain from (7.39) the relations between power coefficients in the following form:

$$R_{P12} + t_{P12} = 1 + 2|\dot{R}_{12}| \frac{\operatorname{Im} \sqrt{\dot{\varepsilon}_1}}{\operatorname{Re} \sqrt{\dot{\varepsilon}_1}} \sin \varphi_{12}, \quad (7.44)$$

where $\dot{R}_{12} = |R_{12}| \exp(-j\varphi_{12})$. Such a relation takes place for the vertical polarization as well.

The above relation does not contradict the energy conservation law, since the additional term in the right-hand side is the result of superposition of incident and reflected fluxes and arising from the directional interference flux (the normal incidence) in the absorbing medium (Veremey *et al.*, 1978). If the medium from which the observation is performed is transparent (i.e. $\operatorname{Im} \sqrt{\dot{\varepsilon}_1} = 0$), then we arrive at the former treatment of the energy conservation law (7.41), which shall be used hereafter.

7.4 POLARIZATION FEATURES OF RADIATION OF A GREY HALF-SPACE WITH A SMOOTH BOUNDARY

We shall use the results obtained above for considering the important problem of the radiation characteristics of a grey half-space with a smooth boundary. The simplified geometry of the problem is presented in Figure 7.5(a). The flight vehicle is in the medium 1 and observes the smooth surface at the polar angle of incidence θ . This angle is sometimes called a zenithal angle. In virtue of the properties of azimuthal isotropy of emission of smooth surfaces, all radiation characteristics do not depend on the observation azimuth. Since we consider an extended source (i.e. the solid angle of the antenna directivity pattern of an instrument is less than the solid angle of a radiation object), the value of a signal does not depend on the distance to an object (see equation (5.31), and, accordingly, the flight vehicle altitude over the studied surface has no significance).

Of principal importance here are the polarization characteristics of the emitting surface. The type of polarization of the received radiation will be determined by the polarization properties of the receiving instrument's antenna system. At present, there exists a great diversity of technological implementations of polarization measurements – from the reception of a purely linear polarization up to reception of polarizations rotating clockwise and counterclockwise. The appearance of complex types of polarizations is associated with the electromagnetic field interaction with

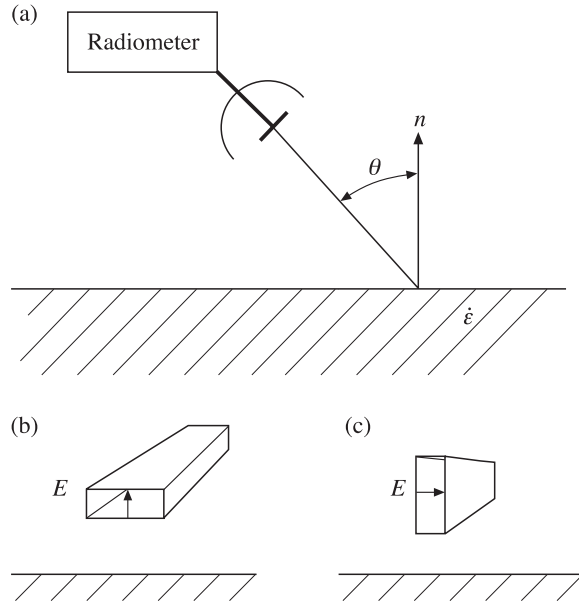


Figure 7.5. Schematic presentation of the remote sensing polarization procedure. (a) Cross-section in the plane of incident. (b) The reception of signal with vertical polarization by a waveguide horn-type antenna. (c) The reception of signal with horizontal polarization.

charged particles (the magnetosphere, the ionosphere). In our fairly simple case, of great significance is also the linear polarization of radiation, geometrically bound to the plane of interface. In this case the electromagnetic waves of two orthogonal polarizations can be distinguished: the horizontally polarized wave with vector \mathbf{E} perpendicular to the plane of incidence and the vertically polarized wave with vector \mathbf{E} lying in the plane of incidence.

With respect to the instruments this can be done rather simply – it is known that in the limited waveguides of transmission lines an infinite number of modes of oscillation can propagate, except the TEM mode which propagates in free space (see section 1.6). If, however, the relations between the values of geometric width (a) and height (b) of a waveguide (Figure 7.5(b), (c)) and the working wavelength are strictly fixed, the situation can be achieved where only one mode of oscillations propagates in the waveguide, this mode having the strictly defined direction of vector \mathbf{E} , perpendicular to the wide wall of a waveguide. In this case the waveguide device plays the part of some kind of polarization filter, thus ensuring the reception of an electromagnetic wave of only one polarization. It can easily be seen that, when the long wall of a waveguide is parallel to the studied surface (Figure 7.5(b)), the reception of a vertically polarized electromagnetic wave will be accomplished. If the waveguide is turned through 90 degrees, when its narrow wall will be parallel to the studied surface, the mode of reception of a horizontally

polarized wave will be accomplished (Figure 7.5(c)). Certainly, it is important to take into account all these features when an antenna system is being installed on a flight vehicle. It is also important to take this into account when interpreting the observational data in the case of flight vehicle manoeuvring; for example, airplane pitch and roll manoeuvres can lead to significantly different results.

If we hypothetically imagine that a vehicle with an instrument is inside a semi-infinite isothermal medium, then in this case the instrument can be considered to be under conditions of thermostatic equilibrium. Thus, its readings will correspond to the value of thermodynamic temperature of the medium regardless of the direction of observation and of the polarization type.

Let us return to the values of Fresnel's coefficients (in the field) for two polarizations (equations (7.32)–(7.34)) and write them down in a simpler and more accessible form, which is often used in microwave sensing practice:

for horizontal polarization

$$\dot{R}_H = \frac{\cos \theta - \sqrt{\dot{\varepsilon} - \sin^2 \theta}}{\cos \theta + \sqrt{\dot{\varepsilon} - \sin^2 \theta}} \quad (7.45)$$

and for vertical polarization

$$\dot{R}_V = \frac{\dot{\varepsilon} \cos \theta - \sqrt{\dot{\varepsilon} - \sin^2 \theta}}{\dot{\varepsilon} \cos \theta + \sqrt{\dot{\varepsilon} - \sin^2 \theta}}. \quad (7.46)$$

In these expressions θ is the angle of observation in the external medium, and $\dot{\varepsilon} = \varepsilon_1 + j\varepsilon_2 = \varepsilon_1(1 + tg\delta)$ is the complex dielectric permeability of the medium studied and δ is the dielectric loss angle.

Since the boundary between media is smooth, then, using the model of specular boundary (see equation (7.17)), we can obtain the values of the medium's emissivity for two polarizations:

$$\kappa_i(\mathbf{r}, \theta, \dot{\varepsilon}) = 1 - |\dot{R}_i(\mathbf{r}, \theta, \dot{\varepsilon})|^2, \quad (7.47)$$

where $i = h, v$.

Expressions (7.47) are very widely used in microwave sensing theory and practice, since they determine the fundamental basis in calculations and interpretation of more complicated models.

The full expressions for horizontal and vertical components of emissivity for a medium with arbitrary losses can be written as:

$$\kappa_H(\theta) = \frac{4\sqrt{\varepsilon_1} \cos \theta A \cos(\psi/2)}{\cos^2 \theta + \varepsilon_1 A^2 + 2\sqrt{\varepsilon_1} \cos \theta A \cos(\psi/2)}, \quad (7.48)$$

$$\kappa_V(\theta) = \frac{4\sqrt{\varepsilon_1} \cos \theta \sqrt{1 + \operatorname{tg}^2 \delta} A \cos(\delta - \psi/2)}{\varepsilon_1^2 \cos^2 \theta (1 + \operatorname{tg}^2 \delta) + A^2 + 2\sqrt{\varepsilon_1} \cos \theta \sqrt{1 + \operatorname{tg}^2 \delta} A \cos(\delta - \psi/2)}, \quad (7.49)$$

where $A = \sqrt{\left(1 - \frac{\sin^2 \theta}{\varepsilon_1}\right)^2 + \operatorname{tg}^2 \delta}$ and $\psi = \operatorname{arctg} \left[1 - \frac{\sin^2 \theta}{\varepsilon_1}\right]^{-1} \operatorname{tg} \delta$.

7.4.1 Nadir measurements

In measurements at observation angles equal to zero (nadir measurements) the distinction between the vertical and horizontal polarizations disappears. The medium emissivity (with arbitrary losses) can be rewritten in a more compact form:

$$\kappa(0) = \frac{4\sqrt{\varepsilon_1} \cos \delta \cos(\delta/2)}{\varepsilon_1 + 2\sqrt{\varepsilon_1} \cos \delta \cos(\delta/2) + \cos \delta}. \quad (7.50)$$

For media with small losses (transparent media), i.e. for which $\operatorname{tg}\delta \rightarrow 0$, expression (7.50) can be even more simplified:

$$\kappa(0) = \frac{4\sqrt{\varepsilon_1}}{(\sqrt{\varepsilon_1} + 1)^2}. \quad (7.51)$$

From this simple expression, nevertheless, follows a rather important conclusion: virtually all natural substances on the Earth possess emissivities whose values lie within some restricted region. So, it follows from consideration of Figure 7.6, which shows the dependences of emissivity on dielectric properties, that for transparent media the emissivity is limited to values ranging from 1, for media with $\varepsilon_1 \rightarrow 1$, to the value of 0.36, for media of fresh water type (for decimetre and metre wavelength bands; see Chapter 8). For transparent media with nonzero values of $\operatorname{tg}\delta$ expression

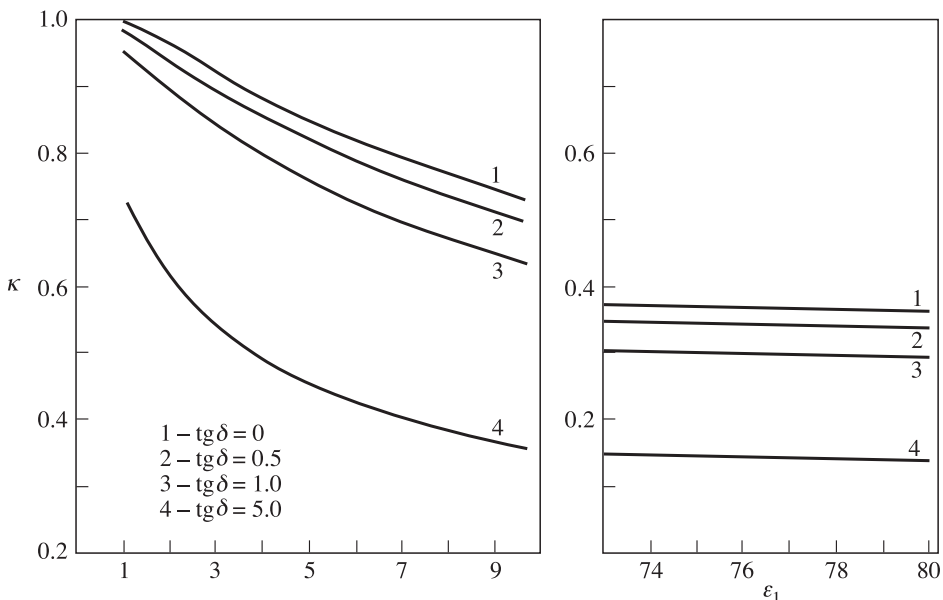


Figure 7.6. Emissivity of dielectric medium with smooth surface at nadir observation as a function of real relative dielectric constant (ε_1) at four values of loss angle tangent.

(7.50) can be expanded in a power series of δ , and we obtain the analytical form of dependence of emissivity on parameter δ :

$$\kappa = \kappa_0 [1 - \frac{3}{8} \delta^2]. \quad (7.52)$$

It is interesting to note here, that the increase of losses in a medium (the increase of parameter δ) results in decreasing the value of the medium's emissivity. This dependence is not so strong, generally speaking. So, it can be seen from relation (7.52) that, for the emissivity to change (decrease) by 5%, the angle of losses should increase considerably – from nearly zero up to values of 0.13–0.15. This implies that the change of losses in a medium influences the value of emissive properties much less than the variations of the real value of dielectric constant. Note that the above conclusions concern the physical models of solid and liquid media exclusively. For gases the situation is radically different (see Chapter 11).

The set of dielectric characteristics illustrated in Figure 7.6 is, of course, for demonstration only, since the real and imaginary parts of dielectric permeability of real substances are rigidly interrelated by fundamental Kronig–Kramers relations, and they should not be selected completely arbitrarily, of course.

The revealed decrease in the value of emissivity of a semi-infinite medium with increasing losses seems, at first sight, a paradoxical violation of Kirchhoff's law. This is not the case, however. As we have seen in section 4.3, the radiation emitted from the medium is caused by that part of the equilibrium thermal energy of a semi-infinite space which did not undergo reflection (see equation (4.20)). Its intensity is associated with the reflective properties of the medium, which increase (though insignificantly) with increasing losses in the medium and, thereby, lower the value of emissivity.

7.4.2 Angular measurements

Historically, the first microwave instruments were of purely nadir type (Basharinov *et al.*, 1969, 1974; Bespalova *et al.*, 1976a; Amirkhanyan *et al.*, 1975). However, it became clear fairly quickly, that the polarization properties (i.e. the properties which are revealed in observation at angles which differ from the nadir) of composite surfaces play an important part (see, for instance, Ulaby *et al.*, 1981, 1982, 1986; Fung and Chen, 1981; Paloscia and Pampaloni, 1988). They make it possible to determine the type of a surface and its state, to distinguish the signals from the surface and from vegetation, and to determine the properties of dynamic surfaces (such as the disturbed sea surface, for example). Virtually all modern radiothermal (both aircraft- and space-based) instruments operate under conditions which make it possible to record the radiation of a studied surface at fixed angles and at two polarizations (or at their combination) simultaneously (see Chapter 14).

For transparent media (at $\operatorname{tg}\delta \ll 1$) the emissivities for the modes of horizontal and vertical polarizations can be written in a fairly symmetrical form:

$$\kappa_H(\theta) = \frac{4\sqrt{\varepsilon_1} \cos \theta \sqrt{1 - \frac{\sin^2 \theta}{\varepsilon_1}}}{\cos^2 \theta + \varepsilon_1 \left(1 - \frac{\sin^2 \theta}{\varepsilon_1}\right) + 2\sqrt{\varepsilon_1} \cos \theta \sqrt{1 - \frac{\sin^2 \theta}{\varepsilon_1}}}, \quad (7.53)$$

$$\kappa_V(\theta) = \frac{4\sqrt{\varepsilon_1} \cos \theta \sqrt{1 - \frac{\sin^2 \theta}{\varepsilon_1}}}{\varepsilon_1 \cos^2 \theta + \left(1 - \frac{\sin^2 \theta}{\varepsilon_1}\right) + 2\sqrt{\varepsilon_1} \cos \theta \sqrt{1 - \frac{\sin^2 \theta}{\varepsilon_1}}}. \quad (7.54)$$

Figure 7.7 presents the calculated values of emissivities for water surface and dielectric media, which are used for modelling fertile soils with different moisture content.

Since our original model of a specular surface was based on the solutions of Maxwellian equations in the plane waves mode, all polarization features, known from Maxwellian theory, will be equally reflected in the solutions obtained for the emissive characteristics of media with smooth boundaries (Stratton, 1941; Alpert *et al.*, 1953). Here we note, first of all, the principal difference in the behaviour of an angular dependence for horizontal and vertical polarization. Whereas the behaviour of the horizontally polarized emissivity does not have any features, emission with vertical polarization has a prominent maximum. From the Maxwell electrodynamics viewpoint, its origin can be explained simply enough: this is a zero

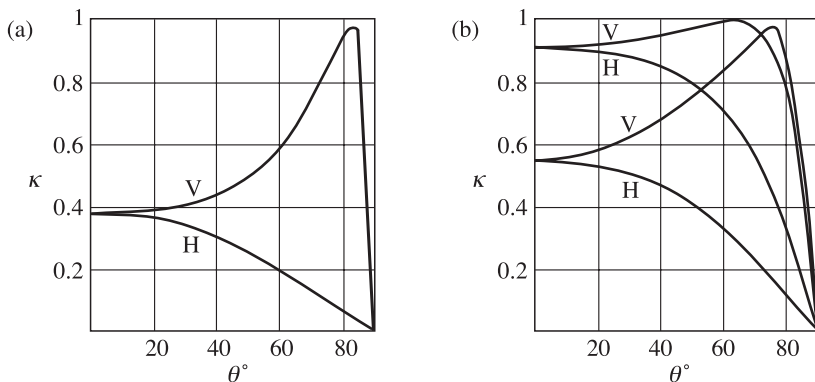


Figure 7.7. Polarization properties of emissivities of water surface and dielectric media. (a) Emissivity of water surface at 19°C as a function of the incident angle (zenith angle) for horizontal (H) and vertical (V) polarization at 10.5 GHz. (b) Emissivity of two dielectric media calculated with $\varepsilon = 3.5 + j0.1$ (upper curve) and $\varepsilon = 20 + j10$ (lower curve).

value of the Fresnel coefficient for vertical polarization at the Brewster angle (θ_{BR}). Equating the Fresnel coefficient value to zero (7.34), we obtain:

$$Z_1 \cos \theta_{\text{BR}} = Z_2 \cos \theta_2. \quad (7.55)$$

Taking the square of both parts of the equality and taking into account Snell's law for transparent media ($\text{tg} \delta = 0$), we shall have, after some transformations:

$$\text{tg} \theta_{\text{BR}} = \sqrt{\varepsilon_1}. \quad (7.56)$$

It is seen from this relation, that for pure dielectrics there exists the angle of incidence, called the Brewster angle, at which the incident wave passes to the second medium entirely (without reflections). From the thermal radiation viewpoint, the appearance of the Brewster angle can be interpreted as follows. When the Brewster angle appears, the wave resistance of an emitting medium becomes equal to the wave resistance of a vacuum, and the wave energy entirely escapes the medium where it was formed. In other words, at these angles and at vertical polarization the medium behaves as an ideal black body. It follows from (7.56) that for media with high values of dielectric properties ('cold' media in the radiothermal sense) the Brewster angle tends to 90° (for water, to $87\text{--}88^\circ$), whereas for media with a small dielectric constant value ('warm' media) the Brewster angle tends to 45° (Figure 7.7(b)).

Now we shall consider the variations of emissivity which can be related to a small deviation of angles at nadir investigations. These variations of angles are usually determined by features of a flight vehicle's manoeuvres. Expanding relations (7.53)–(7.54) into the Taylor series at $\theta = 0$ for small values of observation angles, we obtain:

$$\kappa_{\text{VH}}(\theta) = \kappa_0 \left[1 \pm \frac{\sqrt{\varepsilon_1} - 1}{\sqrt{\varepsilon_1} + 2} \frac{\theta^2}{2} \right], \quad (7.57)$$

where the plus sign relates to vertical polarization, and the minus sign to horizontal polarization. This fact suggests that the sensitive radiometric complex can behave as a device designed for detecting quite small inclines on a smooth surface. So, a surface incline of only 2° will result in quite a noticeable change of a radiothermal signal – by 2.5–3 K. The sign of the signal changing will be determined by the relation between the polarization plane of the instrument and the vector normal to the surface.

Now we shall consider the opposite situation: when the observation angle tends to 90° . For this purpose we introduce the complementary angle $\theta = 90^\circ - \alpha$. This angle is sometimes called the grazing angle. Expanding relations (7.53)–(7.54) into the Taylor series of α , we obtain

$$\kappa_V(\alpha) \cong 4\sqrt{\varepsilon_1} \alpha; \kappa_H(\alpha) \cong \frac{4}{\sqrt{\varepsilon_1}} \alpha. \quad (7.58)$$

It can be seen from this relation that for natural media the vertical polarization value will always exceed the horizontal polarization values.

To understand the situation more clearly, we shall consider the following qualitative example (Figure 7.8). A flight vehicle with a radiometric receiver that

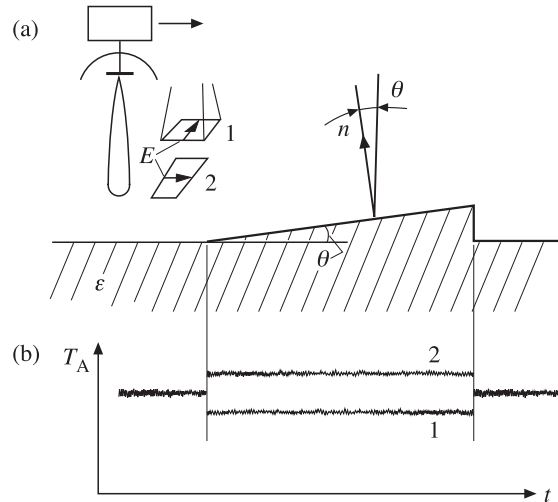


Figure 7.8. Schematic presentation of airborne remote sensing measuring procedure for the incline of a smooth surface with θ angle slope. 1, the reception of horizontal polarization; 2, vertical polarization. (a) Cross-section in the plane of incident. (b) Radiothermal signal registrations for horizontal (1) and vertical (2) polarizations.

measures two orthogonal polarizations approaches the incline of a smooth surface with slope θ (the cross-section is presented in Figure 7.8). When the vehicle is above the main surface, the observation is carried out in the nadir mode, and there is no distinction between two signals. When the vehicle reaches point x_1 , the polarization geometry of observation sharply changes, because there arises the finite observation angle between the normal to the surface incline and the line-of-sight of the instrument's antenna, and, therefore, the difference in the signals of the polarization channels appears. Channel 1 will receive the horizontal polarization of radiation of the surface incline, and channel 2 the vertical one. Since the surface incline's slope is small, the variations of signals will be equal in magnitude and will differ in sign (equation (7.57)). As the vehicle turns through 90° around its axis, it is as if the channels change their places: channel 1 will receive the vertical polarization and channel 2 the horizontal one. When the vehicle escapes the incline observation zone at point x_2 , the signals of the channels become equal again.

It can also easily be understood from the given geometry that in the case of flight vehicle manoeuvring (for example, when the aircraft engages in roll manoeuvres over a plane surface) the channels will give different results, i.e. channel 1 will receive the vertical polarization and channel 2 the horizontal one. When the aircraft performs pitching manoeuvres the channels will exchange places in their attribution to polarization measurements. Since the polarization sensitivity of a plane surface's emission to terrain the incline of which is quite high, this circumstance must be taken into account when interpreting observational data from flight vehicles performing various manoeuvres. So, a similar situation arises when observing the large-scale

surfaces of planets from spacecraft, which are in the permanent solar–stellar orientation mode (as, for example, the Russian automatic interplanetary station ‘Mars-3’ studying the large-scale surfaces of Mars). In such a case, during the orbital motion of the satellite the surface observation angle varies from 90° down to $10\text{--}15^\circ$. And, moreover, the roll angle γ between the plane of observation and the plane of vertical antenna polarization varies within the limit of 180° . It is clear that such mixed polarization regimes seriously hamper the interpretation of measurement results (Shapirovskaia, 1973).

Of interest is the fact that the first scanning radiothermal space instruments (for example, the ESMR instrument onboard ‘Nimbus-5’ (Allison *et al.*, 1974)) were designed in such a manner that the scanning mode be performed across the vehicle’s route. As a result, each pixel (IFOV) in the scanning line was at its own observation angle, and, moreover, the spatial resolution varied 3–5 times. Under such conditions various zones of obtained radiothermal image have appeared in different polarization situations, which seriously hampered the interpretation of observations. This fact was quite quickly understood, and it was found inexpedient to use such a (transversal) scanning mode. Virtually all modern onboard radiothermal instruments apply a conical scanning mode, where each IFOV of the image is considered at a constant (and fixed) observation angle and in the fixed polarization mode (Chapter 14).

7.5 FEATURES OF EMISSION OF A TWO-LAYER STRUCTURE IN THE MONOCHROMATIC APPROXIMATION

Important special cases of layered media in the ‘ocean–atmosphere’ system are inhomogeneous structures of the ‘film–water’ type. They include such inhomogeneities on the ocean surface as disperse foam structures, layers of oil products on the sea surface, water–ice complexes (ice–water and water–ice), etc.

Let us consider in more detail the features of emission of such a structure, which consists of the plane-layered medium 2 on the backing produced from the semi-infinite medium 3. The observation is carried out from a vacuum – medium 1 with dielectric permeability $\varepsilon_1 = 1$. The expression for the monochromatic (i.e. considered under the assumption of an infinitely narrow passband of the receiving device) emissivity of a two-layered structure κ_{123} can be presented, using Kirchhoff’s law, as follows:

$$\kappa_{123} = 1 - |\dot{R}_{123}|^2, \quad (7.59)$$

where \dot{R}_{123} is the complex Fresnel coefficient a the two-layered medium when observing it from medium 1.

The calculation of this monochromatic Fresnel coefficient for a two-layered medium will be carried out using the method of summation of coherent partial beams, in just the same manner as is done in optics (Born and Wolf, 1999). Certainly, the use of such a monochromatic approach to thermal radiation problems (or, in other words, to noise radiation) requires theoretical and

experimental confirmation, which will be given in section 7.6. It is interesting to mention that, when earlier (at the beginning of the 1960s) experimenters made use of such an approach for interpreting the results of radiothermal measurements of the ice–water system (Tuchkov, 1968), this brought a sharply negative response from theorists. Nevertheless, the interference patterns in the thermal emitted radiation are a well-substantiated experimental fact now and have been actively used for solving a series of practical problems (Blinn *et al.* 1972; Glotov *et al.*, 1975; Bespalova *et al.*, 1978, 1983).

The geometry of the method of summation of partial beams is as follows (Figure 7.9): the plane wave falls on a two-layer structure with smooth boundaries at angle θ_1 , is refracted in medium 2, passes through it and is reflected from the boundary with medium 3. Then this wave passes again through medium 2 and, being refracted at the upper boundary, escapes medium 2 at the same angle θ_1 . By virtue of coherence with the basic primary wave, the escaping wave does have an impact. Since a part of energy will reflect from the upper boundary downwards to the boundary with medium 3, the whole cycle will be repeated again. The total retarding phase ψ in a medium with complex refraction index \dot{n} is equal (see section 1.6) to:

$$\dot{\psi} = \dot{n}z/c_0 = \frac{2\pi}{\lambda_0}\dot{n}z. \quad (7.60)$$

Thus, the total retarding phase between the reflected primary beam and the beam that escaped medium 2, will be:

$$(AB + BC)\dot{n}_2 \frac{2\pi}{\lambda_0} - AD \frac{2\pi}{\lambda_0}. \quad (7.61)$$

The following relations can easily be obtained from trigonometric considerations:

$$(AB + BC) = \frac{2h}{\cos \theta_2}; AD = 2h \operatorname{tg} \theta_2 \sin \theta_1. \quad (7.62)$$

Taking account of Snell's law in the form of $\dot{n}_2 \sin \theta_2 = \sin \theta_1$ and after some transformations the total retarding complex phase ψ can be presented as

$$\dot{\psi} = \frac{4\pi h}{\lambda_0} \dot{n}_2 \cos \theta_2 = \frac{4\pi}{\lambda_0} \sqrt{\dot{\varepsilon}_2 - \sin^2 \theta_1} = \alpha - j\beta. \quad (7.63)$$

The total signal, obtained as a sum of interfered beams (this procedure is conventionally shown in Figure 7.9 as a collecting optical lens effect), represents an infinite series of relative complex amplitudes of partial beams:

$$\begin{aligned} \dot{R}_{123} &= \dot{R}_{12} + i_{12}\dot{R}_{23} \exp(j\dot{\psi}) + i_{12}i_{21}\dot{R}_{23}\dot{R}_{21}\dot{R}_{23} \exp(j2\dot{\psi}) + \dots = \\ &= \dot{R}_{12} + i_{12}i_{21}\dot{R}_{23} \exp(j\dot{\psi}) [1 + \dot{R}_{23}\dot{R}_{21} \exp(j\dot{\psi}) + \dots]. \end{aligned} \quad (7.64)$$

Since the magnitude of product $|\dot{R}_{23}\dot{R}_{21}|$ is less than unity, the expression in square brackets is none other than the geometrical progression. Using the well-known expression for the sum of geometrical progression, as well as the impedance

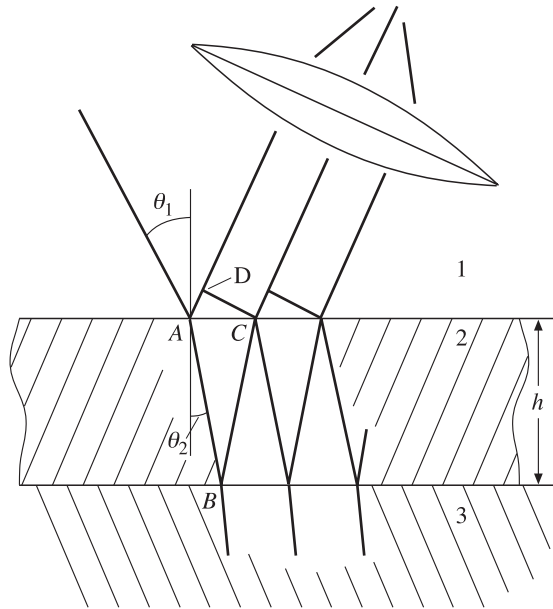


Figure 7.9. Reflections and transmissions of plane waves at the smooth boundaries of a two-layered structure. See the explanations of notation in text.

boundary conditions, we obtain the expression for the total coefficient of reflection from the two-layered medium:

$$\dot{R}_{23} = \frac{\dot{R}_{12} + \dot{R}_{23} \exp(j\psi)}{1 + \dot{R}_{23}\dot{R}_{12} \exp(j\psi)}. \quad (7.65)$$

Note that relation (7.65) can easily be generalized to the case of an isothermal multilayer structure, either by means of the impedance method (see section 7.7), or by means of the method of oriented graphs (Raev *et al.*, 1975). The study of prominently non-isothermal structures (i.e. structures with distinct gradients in the temperature field) was essentially more complicated for natural reasons (Klepikov and Sharkov, 1983, 1993; and see section 7.7).

Now we shall remain with the isothermal case and consider the situation where the film medium possesses small losses (the transparent medium with $\operatorname{tg}\delta \rightarrow 0$). This situation is fairly frequently encountered in sensing practice. In this case the emissivity of a two-layered medium can be written as:

$$\kappa = \frac{(1 - R_{12}^2)(1 - R_{23}^2)}{1 + R_{12}^2 R_{23}^2 + 2R_{12}R_{23} \cos(\psi + \varphi_{23})}, \quad (7.66)$$

where $\dot{R}_{23} = R_{23} \exp(j\varphi_{23})$.

A new feature in emission of two-layered media consists in the presence of interference effects, which are related to the multiple reflection of plane

electromagnetic waves from the boundaries of media. The monochromatic emissivity of the total structure oscillates depending on the film depth, the period of oscillations, H , in the case of transparent (lossless) dielectric film being determined from (7.66) at $\delta_2 = 0$:

$$H = \frac{\lambda}{2\sqrt{\varepsilon_2 - \sin^2 \theta}}. \quad (7.67)$$

The values of thicknesses for which the emission is maximum or minimum, are equal to:

$$h_{\max,\min} = \frac{\pi m - \varphi_{23}}{4\pi\sqrt{\varepsilon_2 - \sin^2 \theta}}. \quad (7.68)$$

Here $m = 1, 2, 3, \dots$ are integers, the emissivity maximum corresponding to odd m values and the emissivity minimum to even ones. It follows from (7.68) that for finite film thicknesses $h > 0$ the first extreme value of emissivity is a maximum $m = 1$, because, as can be shown for the oil–water system, the inequality $\pi > \varphi_{23}$ ($\varphi_{23} < 1$) takes place. In the case of other combinations of dielectric parameters (for example, the ice–ground structure) the first extremum of the $\kappa(h)$ dependence can be a minimum. This result is quantitatively confirmed by the $\kappa(h)$ dependences for ice–water and ice–ground structures (Figure 7.10). The electrophysical parameters of the media are indicated in Figure 7.10. Note that a thin film layer, some millimetres (3–5 mm) thick, can drastically change the emissive characteristics of a medium; so, the contrast of temperatures for water can exceed 100 K, and for ground 30 K. Note that the brightness temperatures of a structure are higher than the brightness temperature of a water surface (the structure is ‘warmer’ than the

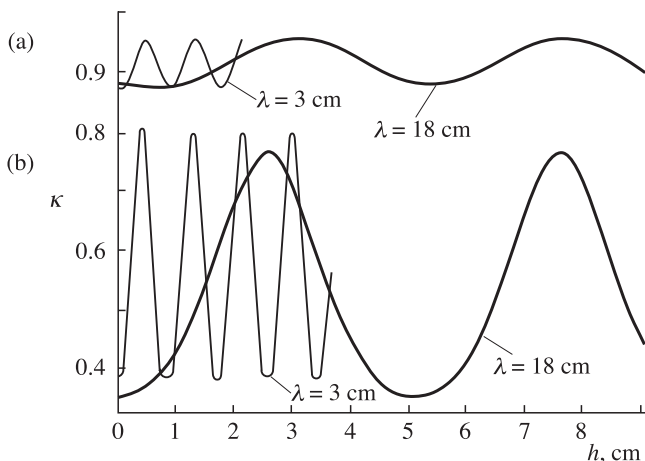


Figure 7.10. Relationships of emissivity of two-layered structures as a function of the ice depth. (a) Air–ice–soil structure; for ice $\varepsilon_1 = 3.2$; for soil $\varepsilon_1 = 12.5$ and $\operatorname{tg}\delta = 0.3$ (at 3 cm) and $\varepsilon_1 = 15$ and $\operatorname{tg}\delta = 0.07$ (at 18 cm). (b) Air–ice–water structure; see explanation of water data in Chapter 8.

backing). At the same time, for the ice–ground (or water–ice) structure the minimum temperature can be lower than the temperature of the ground (the structure is ‘colder’ than the backing).

The aforementioned effect with matching or mismatch influence of a film interlayer on the emission of a backing is similar, physically, to the antireflection effect or darkening effect in optics (Born and Wolf, 1999).

For small film thicknesses the contrast $\Delta T_B(h)$ can be approximated by the quadratic dependence on h :

$$\Delta T_B(h) = F(\lambda, \varepsilon_2)h^2, \quad (7.69)$$

where $F(\lambda, \varepsilon_2)$ essentially depend both on the wavelength, and on the dielectric properties of a film. The detailed calculations are presented in paper by Raizer *et al.* (1975b). The indicated dependence was experimentally confirmed in multi-frequency remote studies of fields of thermal radiation of catastrophic oil spills in the Caspian Sea (Bespalova *et al.*, 1978).

It follows from the analysis of Figure 7.10 that the dielectric properties of a backing have no effect, virtually, on the period of oscillations $\kappa(h)$ (except a small ‘phase’ shift), which is determined by electrical properties of the film layer and radiation wavelength (7.67).

As the film thickness increases with finite losses, the interference effects weaken, and the contribution of natural thermal radiation of a layer is added. As a result, the $\kappa(h)$ quantity asymptotically escapes the radiation level, which is determined by the film’s dielectric properties only. For a crude oil film with dielectric parameters $\varepsilon = 2.2 - j0.008$, quantity $\Delta T_B(h)$ will be constant only for $h > 1.4 \times 10^2 \lambda$. This results, for example, at the wavelength $\lambda = 0.8 \text{ cm}$, in the layer thickness of about one metre. For more considerable losses in the film material, of the order of $\operatorname{tg}\delta \approx 0.1\text{--}0.2$, the interference pattern ‘disappears’ just at $(h/\lambda) \approx 1\text{--}1.5$. At the same time, for natural media with the tangent of the dielectric loss angle $\operatorname{tg}\delta \approx 10^{-3}$ the influence of losses in a medium for the first 4–5 oscillations at $(h/\lambda) \approx 1.5$ is virtually imperceptible.

Let us estimate the thickness of a film, for which it is possible to neglect the influence of small losses of oil, $\operatorname{tg}\delta \ll 1$, in determination of the radiobrightness temperature of an emitting surface. Taking into consideration that for $\operatorname{tg}\delta < 1$ and emission into the nadir $\beta \approx (2\pi h/\lambda)\sqrt{\varepsilon_2} \operatorname{tg}\delta$, we obtain addition to unity in the expansion $\exp(\pm\beta) \approx 1 \pm \beta$, which equals the value less than 0.01 and does not cause more than a 1% change in the emissivity value $\kappa(h)$. It follows from this result that for crude oils with characteristic dielectric parameters $\varepsilon_2 = 2.2$ and $\operatorname{tg}\delta = 3.6 \times 10^{-3}$ the influence of such losses on the considered radio-emission can be neglected (to an accuracy of 1%), provided that $h/\lambda < 0.3$.

The analysis of Figures 7.11 and 7.12, where the polarization dependences of the film–water structure are presented, indicates that the presence of a film of substance with other electrical parameters on the emitting surface drastically changes the polarization properties of the system as a whole. First, we note that for $h/\lambda > 1$ both at the vertical and (which is interesting to note) at the horizontal polarization ‘pseudobrewster’ angles appear, whose values, as well as the emissivity value, are

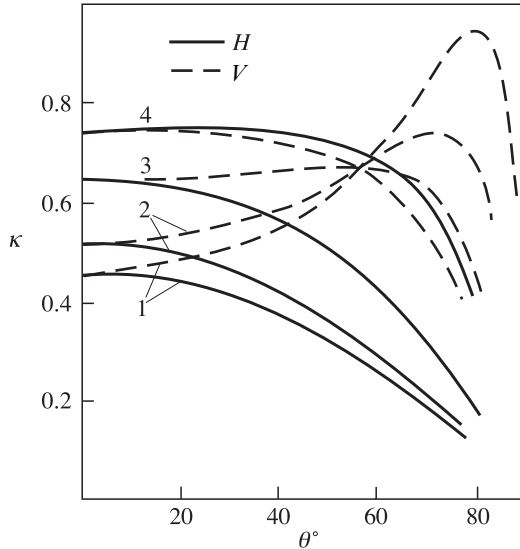


Figure 7.11. Polarization properties at 0.8 cm of oil sheet–water structure. For oil $\epsilon_1 = 2.2$; $\operatorname{tg}\delta = 0$. For curves 1–4 oil sheet thickness is 0, 0.04, 0.08, 0.12 cm respectively.

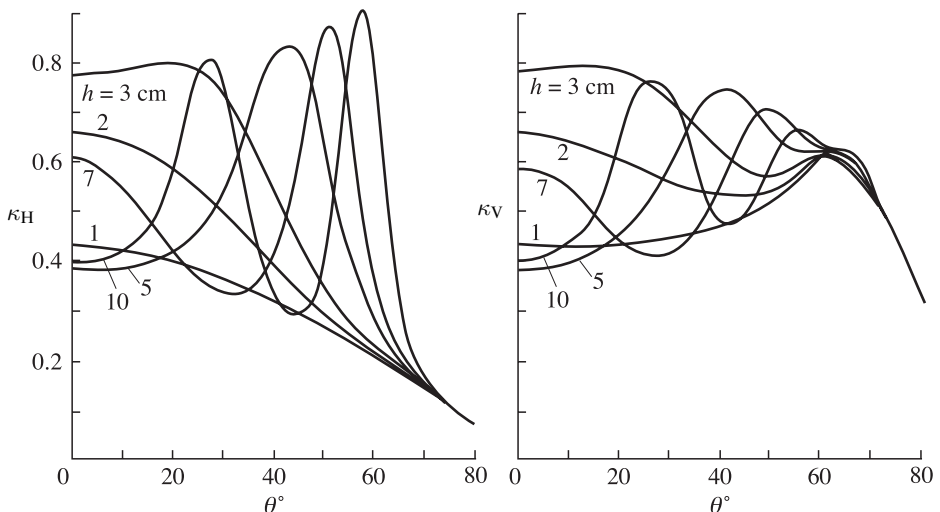


Figure 7.12. Polarization properties of air–ice–water structure. For ice $\epsilon_1 = 3.2$, $\operatorname{tg}\delta = 0$; for fresh water $\epsilon_1 = 44.78$, $\operatorname{tg}\delta = 0.95$. Ice sheet depths are shown by figures next to the curves.

rather sensitive to changes of the film thickness. So, when parameter h/λ changes by 20–30%, a qualitative rearrangement of the type of polarization characteristics can occur (Figure 7.12). The measurements of a horizontally polarized radio-emission component possess greatest sensitivity to film thicknesses up to 1 mm at observation

angles up to $40\text{--}50^\circ$. Second, in measurements of a vertically polarized radio-emission component at the Brewster angle for a film medium (under assumption of small losses, $\operatorname{tg}\delta \ll 1$) the emissivity does not depend on the film thickness and is determined by the emissivity of a clean surface of water.

Physically, this is related to a zero coefficient of reflection from the boundary of media 1–2 for a vertically polarized component of radiation at the Brewster angle $R_{V12}(\theta_{\text{BR}}) = 0$. Indeed, from (7.65) at $\operatorname{tg}\delta \ll 1$ and $\theta = \theta_{\text{BR}}$ we have (superscript ‘V’ is omitted hereafter):

$$\kappa_{123}(\theta = \theta_{\text{BR}}) = 1 - R_{23}^2(\theta_{\text{BR}}). \quad (7.70)$$

And, on the other hand, we can obtain the following relation between reflectivities for any components of polarization of a two-layered medium

$$\dot{R}_{23} = \frac{\dot{R}_{22} - \dot{R}_{13}}{\dot{R}_{12}\dot{R}_{13} - 1}. \quad (7.71)$$

From (7.71) for $R_{12}(\theta_{\text{BR}}) = 0$ we have $R_{23}(\theta_{\text{BR}}) = -R_{13}(\theta_{\text{BR}})$ and, further, with regard to (7.70), we have:

$$\kappa_{123}(\theta_{\text{BR}}) = \kappa_{13}(\theta_{\text{BR}}). \quad (7.72)$$

Thus, the vertically polarized radiation of the surface with a film is equal to the radiation of a clean surface at an angle which corresponds to the equality $R_{12}(\theta_{\text{BR}}) = 0$. This results in a curious experimental technique of determining the dielectric properties of a film coating. So, measuring the angular dependence of the brightness contrast between the clean surface and that covered with a film, $\Delta T_B(\theta)$, for a vertically polarized component of radio-emission, and determining angle θ_0 , for which $\Delta T_B(\theta) = 0$, we can estimate the dielectric permeability of contamination as $\operatorname{tg}^2\theta_0 = \varepsilon_2$ (the well-known Brewster relationship). It follows from this relationship that in the region of $\varepsilon_2 = 1.78\text{--}2.55$ (which corresponds to basic types of widely used liquid oil products) the corresponding angle will be $\theta_0 = 54\text{--}58^\circ$. It is obvious that the accuracy of determination of ε_2 by the proposed technique will be ± 0.15 units at an accuracy of the measured angle value of $\pm 1^\circ$.

The characteristic form of spectral dependences for the ‘matching’ (or the ‘antireflecting’ optics version) case (i.e. when $\varepsilon_2 < \varepsilon_3$) is presented in Figure 7.13, and that for the ‘mismatch’ case ($\varepsilon_2 < \varepsilon_3$) in Figure 7.14. The latter version is interesting physically owing to the fact that the water film possesses wave resistance, which ‘mismatches’ the system, and the part of thermal radiation energy of the backing (the ice in the given case) is reflected ‘backwards’, which just explains the abnormally low brightness temperature of the system as a whole (Figure 7.14). As it would be expected, the dielectric properties of water play a decisive part in the given case and change both the values of emissivities and the form of frequency dependences; this influence becoming stronger with increasing wavelength (Figure 7.14).

Let us consider briefly the question of the solution of a reverse problem: the determination of electrical parameters and thickness from the data of radio measurements of thermal radiation of the film-backing system. Owing to the periodicity in $\kappa(h)$ dependence it is impossible, strictly speaking, to measure the film thickness with a one-frequency instrument. However, the use of n radio-frequency channels and the

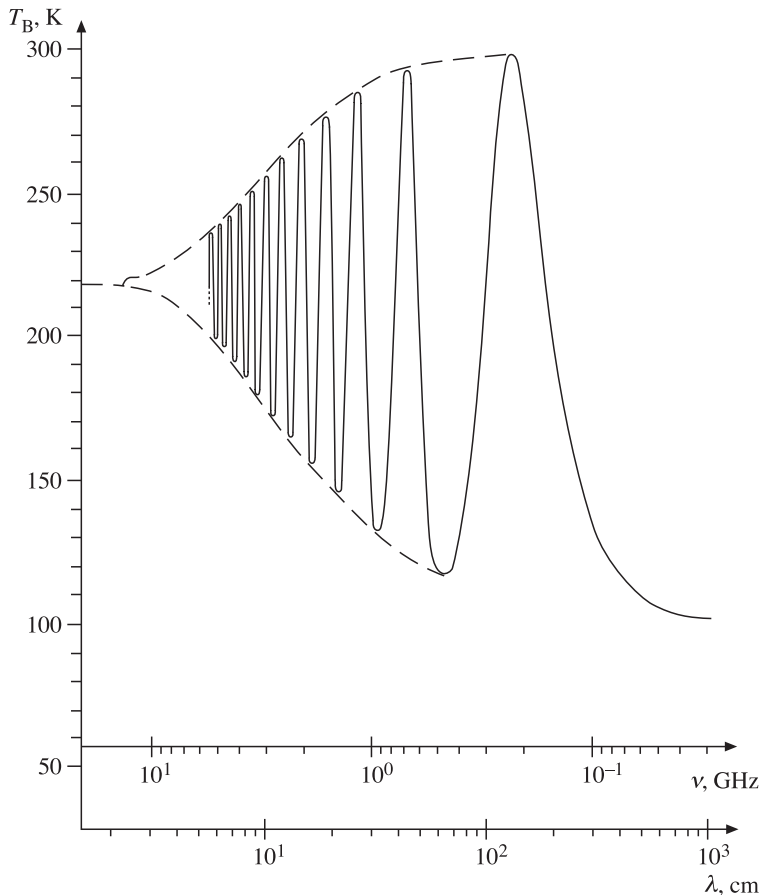


Figure 7.13. Spectral characteristics of the emission of an isothermal three-layered structure with nadir observation. For the second layer $\varepsilon_1 = 10$ and $\operatorname{tg}\delta = 0.04$; its depth is 10 cm. For the third layer $\varepsilon_1 = 100$ and $\operatorname{tg}\delta = 0.1$.

presentation of emissivity in the n dimensional space (at various wavelengths) makes it possible almost completely to avoid the uncertainty. Popov *et al.* (1976) have shown theoretically that the use of a three-dimensional image of emissivity for these purposes results, virtually, in a complete elimination of ambiguity. This has been experimentally confirmed for the first time in multifrequency remote studying of thermal emission fields of oil spreads in the Caspian Sea in 1976–1977 (Bespalova *et al.*, 1978). Detailed investigations (Raizer *et al.*, 1975b; Glotov *et al.*, 1975) of radiobrightness temperature gradients ΔT_B from parameters ε_2 and in the region of small thicknesses h have shown that in radiometric measurements of film thicknesses there exists an ambiguity of the order of 40–50%, caused by the absence of information on the true value of dielectric properties of a film. To estimate the latter value, polarization measurements (near the Brewster angle in a film) can be used.

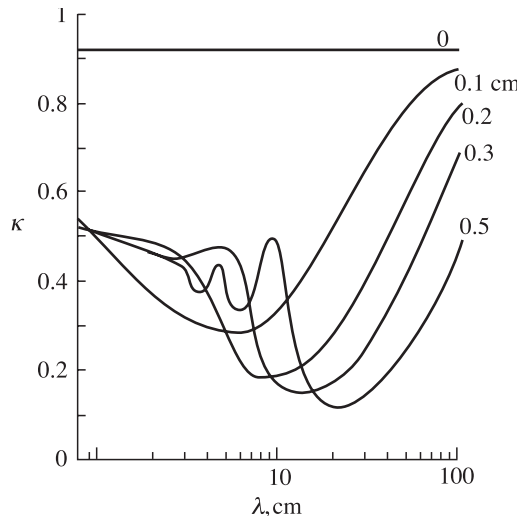


Figure 7.14. Spectral characteristics of the emission of air–water–ice structure with nadir observation. For ice $\varepsilon_1 = 3.2$; $\operatorname{tg}\delta = 0$. Spectral properties of water dielectric constants are specified by the Debye relaxation model (Chapter 8). Water sheet depths (cm) are shown by figures next to the curves.

7.6 PROPERTIES OF QUASI-COHERENCE IN THERMAL EMISSION AND THE LIMITS OF ITS APPLICABILITY

The interference patterns in thermal emission, revealed in previous sections, follow from the monochromatic approximation, i.e. they are obtained under assumption of an infinitely narrow passband of the receiving device. This feature of radiation represents, in essence, only an instrumental effect, since the interference as such arises ‘inside’ the receiving device because of the limited-in-frequency amplitude-frequency characteristic (AFC). This feature is not inherent in natural radiation as such. In addition, we note that the interference effects are most clearly revealed in the presence of pronounced dielectric boundaries in the natural structure (for example, a film of oil on the water surface). In the presence of smooth transition dielectric layers these effects are largely suppressed, however (section 7.7).

This effect – interference patterns in thermal emission – is considered in the present section, following Popov and Sharkov (1976), generally, for AFC of arbitrary form, and in more detail for the three most widespread special cases.

For greater physical clarity we shall consider the radio-emission of a very simple layered structure: the plane-parallel homogeneous layer 2, which covers a semi-infinite homogeneous medium 3. For simplifying derivations we shall assume the losses in media to be absent, that is, the dielectric permeabilities of considered media to be real. With allowance for these assumptions, the monochromatic (i.e. considered in the infinitely narrow frequency band) emissivity of a structure will take the form

(section 7.5):

$$\kappa(f) = \frac{(1 - R_{12}^2)(1 - R_{23}^2)}{1 + R_{12}^2 R_{23}^2 + 2R_{12} R_{23} \cos(2\pi f \tau)}, \quad (7.73)$$

where $\tau = (2h\sqrt{\epsilon_2})/c$ is the delay time of a wave, reflected from the upper and lower boundary of a layer, with respect to the wave passed into a layer; R_{21} and R_{32} are the Fresnel coefficients for corresponding interface surfaces of media; h is the thickness of layer 2; c is the speed of light in vacuum; and $f = \nu$ is the frequency. It follows from (7.73) that the dependence of κ on the frequency and on the layer thickness has an oscillating character. It is important to note that the amplitude of oscillations is constant in the absence of losses in a layer.

The thermal emission of heated bodies of arbitrary geometrical shape is a random process with a virtually uniform ‘white’ spectrum of brightness temperature in the radio-frequency band and delta-correlated values of intensity of electrical and magnetic fields (Chapter 6).

The high-frequency channel (ahead of a square-law detector) of a receiving radiometric system restricts the spectrum as a result of received noise radiation of an intrinsic (power) AFC $G(f)$, thus establishing correlation link between instantaneous values of a noise output signal with nonzero correlation time $\tau_0 = 1/\Delta f$, where

$$\Delta f = \frac{1}{G_{\max}} \int_{\Delta f} G(f) df$$

is the effective passband width of the microwave channel of the radiometer (Chapter 3).

The radiobrightness temperature of an isothermal two-layered structure, measured by a radiometer that is medium 1 (in the absence of external illumination of the atmosphere and firmament), is equal to

$$T_B = \kappa_{\Sigma} T_0, \quad (7.74)$$

where T_0 is the thermodynamic temperature of the total structure and κ_{Σ} is the emissivity averaged over the effective band of transmitted frequencies of a radiometer:

$$\kappa_{\Sigma}(\tau) = \frac{1}{G_{\max} \Delta f} \int_{\Delta f} \kappa(f) G(f) df. \quad (7.75)$$

It can be seen from this relation that the monochromatic approximation (7.73) quite well describes the measured emissivity of a layered structure only in the presence of a narrowband radiometric device. It is clear that the narrowband condition has the form of $\Delta f \ll 1/\tau$, where τ is the delay time between plane waves in a two-layered system (see section 7.5). Or, in other words, the delay time between plane waves is much less than the correlation time of a receiving system $\tau \ll \tau_0$. One of the methods for increasing the sensitivity of radiometric systems consists in extending the band of transmitted frequencies (Chapter 3). But, in this case, the greater the Δf the smaller the layer thicknesses for which the monochromatic approximation is valid. The violation of the band-narrowness condition results in decreasing the amplitude of

interference oscillations (which bear the useful information) down to their complete vanishing at $\tau \gg \tau_0$. Therefore, for high values of Δf and τ the calculation of the emissivity of a layered structure should be carried out by formula (7.75). However, the direct integration of (7.75) results in quite cumbersome expressions, even in the case of the simplest form of AFC functions. And for complicated AFC forms it even becomes impossible to derive accurate analytical expressions for emissivity κ_Σ . In this connection, it is of interest to derive simple approximate formulas for performing analytical consideration.

The mathematical approach described below, which was offered by Popov and Sharkov (1976), can be useful not just in considering thermal radio-emission of layered structures. This is because physically similar effects of interference of noise signals with a limited spectrum take place in optical systems and in transmission lines as well (Born and Wolf, 1999; Bulatov *et al.*, 1980).

The function of frequency $\kappa_\Sigma(f, t)$, appearing in expression (7.75), is an even, periodic and differentiable function of delay time τ and can be expanded in the Fourier series in cosines:

$$\kappa(f, \tau) = \frac{a_0}{2} + \sum_{n=1}^{\infty} a_n \cos(2\pi fn\tau). \quad (7.76)$$

Substituting expansion (7.76) into formula (7.75) and interchanging summation and integration, we obtain:

$$\kappa_\Sigma(\tau) = \frac{a_0}{2} + \frac{1}{\Delta f} \sum_{n=1}^{\infty} a_n \int_0^{\infty} G_0(f) \cos(2\pi fn\tau) df. \quad (7.77)$$

The integrals in the right-hand side of (7.77) present the Fourier transforms for AFC of a radiometer's $G_0(f)$; $G_0(f) = G(f)/G_{\max}$. Since the spectrum of received radiation is supposed to be 'white', function $G_0(f)$ is the spectrum of power of an output (after the high-frequency part of a radiometer) signal, and its Fourier transform, according to the Wiener–Khinchin theorem, is equal to the autocorrelation function of an output signal. That is, (7.77) can be written as:

$$\kappa_\Sigma(\tau) = \frac{a_0}{2} + \frac{1}{\Delta f} \sum_{n=1}^{\infty} a_n Q(n\tau), \quad (7.78)$$

where $Q(n\tau)$ are the values of the autocorrelation function of a noise output signal of a radiometer, corresponding to the shift in time by $n\tau$. Accordingly, the n th term of series (7.78), as well as of series (7.76), relates to the n th beam, which issues from the structure after n reflections from the lower boundary of layer 2. Therefore, the argument of the autocorrelation function in the n th term of series (7.78) is equal to $n\tau$, the delay time of the n th beam. As n grows, the Fourier coefficients a_n and the values of the autocorrelation function $Q(n\tau)$ tend to zero, owing to which series (7.78) rapidly converges for not too small τ values.

Let us estimate the behaviour of $\kappa_\Sigma(\tau)$ dependences for three AFCs of various form, which are most widespread in the practice of radiometric receiving systems

(see Chapter 3):

(a) rectangular type

$$G_0^R(f) = \begin{cases} 1 & f_1 < f < f_2 \\ 0 & f < f_1; f > f_2, \end{cases} \quad (7.79)$$

(b) of resonance circuit type (sometimes called Lorentz's; see Chapter 2)

$$G_0^L(f) = \frac{1}{1 + 4\left(\frac{f - f_0}{\Delta f}\right)^2}, \quad (7.80)$$

(c) Gaussian

$$G_0^G(f) = \exp \left\{ -2.773 \left(\frac{f - f_0}{\Delta f} \right)^2 \right\}, \quad (7.81)$$

where Δf is the bandwidth at the level of 3 dB and f_0 is the central frequency of the system's passband.

For the rectangular AFC, expression (7.78) is transformed to the form

$$\kappa_{\Sigma}^R(\tau) = \frac{a_0}{2} + \frac{1}{\pi \Delta f \tau} \sum_{n=1}^{\infty} \frac{a_n}{2} \cos(2\pi f_0 n \tau); \sin(\pi \Delta f n \tau), \quad (7.82)$$

for Lorentz's AFC, to the form

$$\kappa_{\Sigma}^L(\tau) = \frac{a_0}{2} + \sum_{n=1}^{\infty} a_n \exp(-\pi \Delta f n \tau) \cos(2\pi f_0 n \tau), \quad (7.83)$$

and for the Gaussian AFC, to the form

$$\kappa_{\Sigma}^G(\tau) = \frac{a_0}{2} + \sum_{n=1}^{\infty} a_n \exp \left\{ -\frac{\pi \Delta f^2}{2.773} n^2 \tau^2 \right\} \cos(2\pi f_0 n \tau). \quad (7.84)$$

And also, in all formulas:

$$\frac{a_0}{2} = \frac{(1 - R_{12}^2)(1 - R_{23}^2)}{1 - R_{12}^2 R_{23}^2}. \quad (7.85)$$

Owing to rapid convergence of the series (7.75) for not too small τ values in formulas (7.79)–(7.81), only the first two terms can be retained in a series. Then we obtain (after calculating coefficient a_1):

$$\begin{aligned} \kappa_{\Sigma}^R &= \frac{a_0}{2} \left[1 - 2R_{12}R_{23} \frac{\sin(\pi \Delta f \tau)}{\pi \Delta f \tau} \cos(2\pi f_0 \tau) \right], \\ \kappa_{\Sigma}^L &= \frac{a_0}{2} [1 - 2R_{12}R_{23} \exp(-\pi \Delta f \tau) \cos(2\pi f_0 \tau)], \\ \kappa_{\Sigma}^G &= \frac{a_0}{2} \left[1 - 2R_{12}R_{23} \exp \left\{ -\frac{\pi^2 \Delta f^2}{2.773} \tau^2 \right\} \cos(2\pi f_0 \tau) \right]. \end{aligned} \quad (7.86)$$

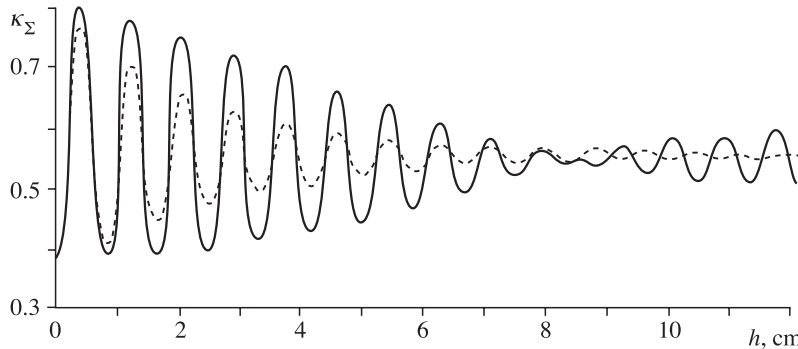


Figure 7.15. Relationships of two-layered medium (ice–water) emissivity averaged over the amplitude–frequency characteristic (AFC) versus ice depth with nadir observation at $T_0 = 273 \text{ K}$; $f_0 = 10 \text{ GHz}$, $\Delta f = 1 \text{ GHz}$; for ice $\varepsilon_1 = 3.2$ and $\operatorname{tg}\delta = 0$; for water $\varepsilon_1 = 44.8$ and $\operatorname{tg}\delta = 0.95$. Continuous curve corresponds to a rectangular AFC; and dotted curve corresponds to a Lorentz-type AFC.

The formulas obtained indicate that the emissivity $\kappa_{\Sigma}(\tau)$ of a layered structure, averaged over AFC, oscillates with increasing layer thickness at the same period as the monochromatic one. However, unlike the monochromatic approximation, the oscillations attenuate in the given case, the attenuation being the faster the wider the frequency band. The envelope of oscillations is determined by the AFC form and represents, for the rectangular AFC, the function of type $\sin x/x$, for Lorentz's, $\exp(-x)$ and for the Gaussian $\exp(-x^2)$. The limit, to which the $\kappa_0(t)$ dependence tends for $\tau \rightarrow \infty$, does not depend either on the width or on the form of AFC, and coincides with the average-over-a-period value of the monochromatic dependence (7.73).

To estimate the accuracy of the approximate formulas obtained, numerical integration was carried out by computer, using accurate relations for the ice–water structure. Figure 7.15 presents the calculated dependences for the rectangular and Lorentz's AFCs. A similar curve for the Gaussian AFC differs from Lorentz's in one respect only: the amplitude of oscillations decreases more rapidly in this case. Formulas (7.86) qualitatively well describe the behaviour of these dependences; the maximum error, corresponding to the layer thickness $h \approx 0$, is less than 5% and rapidly decreases as h grows.

Let us compare the emissivity values of a layered structure, calculated by numerical integration, with the results of experiments (Blinn *et al.*, 1972). Figure 7.16 shows the dependences of the $T_B(h)/T(\infty)$ on the thickness of a layer of sand on a metal backing. The form of AFC of the radiometric device used is not indicated in the authors' paper; however, the calculation shows that, among all AFC forms considered above, the rectangular one provides best agreement with the experiment. For comparison, Figure 7.16 gives the same dependence for the monochromatic approximation.

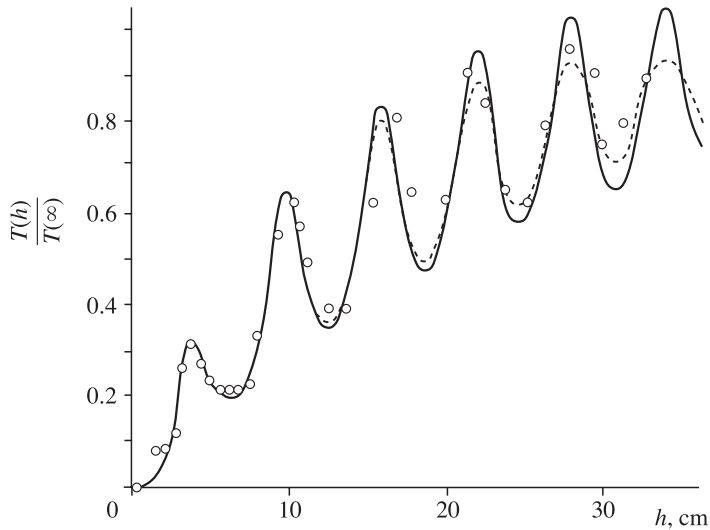


Figure 7.16. The ratio $T(h)/T(\infty)$ versus a layer depth for sand–metal plate structure with nadir observation, at $f_0 = 1.42$ GHz, $\Delta f = 0.15$ GHz; for sand $\varepsilon_1 = 2.95$ and $\operatorname{tg}\delta = 0.05$. Continuous curve corresponds to monochromatic approximation; dotted curve corresponds to signal averaged over a rectangular AFC; circles correspond to experimental data by Blinn *et al.* (1972).

Note that similar complicated interference patterns usually accompany laboratory measurements of electromagnetic wave transmission through plane-layered objects (see, for example, Kohn, 1997).

The special analysis of dissipation in a film medium has shown (Raizer *et al.*, 1975b), that the presence of losses in a layer makes attenuating of oscillations faster and slightly shifts them in phase, not involving any qualitative changes. Thus, the form and width of AFC of a radiometric system essentially influence the character of interference dependences at reception of thermal radio-emission of layered media and, therefore, the ultimate information capacity of microwave passive systems.

7.7 THERMAL EMISSION OF MULTI-LAYERED NON-ISOTHERMAL MEDIA

One major feature of radiothermal sensing methods is they may be used to obtain physical information about the internal structure of the medium studied. A whole class of boundaries between media (ice–water surface, dry and moist soil, soil–groundwater etc.) are classified, firstly by strong, non-uniform absorption (including in the vertical direction) and secondly by smooth variation of the physical characteristics in the media together with discontinuities and jumps in the

dielectric and thermal vertical profiles – in other words, situations where the scale of dielectric (or thermal) non-uniformity is comparable with the wavelength λ :

$$\left| \frac{\Delta \varepsilon}{\Delta z} \right| \geq \frac{\varepsilon}{\lambda}.$$

Problems of the electrodynamics of sharp non-uniform, strongly absorptive media are known to be very complicated, since they cannot be described adequately either in the framework of theory of radiative transfer or by classical approximations, for example, the WKB (Wentzel, Kramers, Brillouin) method (Levin and Rytov, 1967; Stogryn, 1970; Shulgina, 1975; Tsang *et al.*, 1975).

Over a prolonged period a large variety of modifications of the plane-parallel model of microwave emission has been utilized without detailed analysis of the ranges of their feasibility (see, for instance, Tuchkov, 1968; Basharinov *et al.*, 1968; Tsang and Kong, 1976; Wilheit, 1978; Bardati and Solimini, 1984).

In its fully completed form microwave emission theory was formulated by Klepikov and Sharkov in 1983 and developed in 1993 (Klepikov and Sharkov, 1983, 1993). The theory may be applied when describing emission in any irregular non-isothermal multi-layered media without restrictions, which are typical for previous modifications.

Klepikov and Sharkov performed a detailed theoretical study of the processes leading to the development of the natural radiation of highly non-uniform, non-isothermal, plane-stratified media with arbitrary variations of the dielectric and temperature-related parameters.

7.7.1 Physical substance of the problem

Kirchhoff's law, which relates the intensity of the radiation from a real medium to the radiation from an absolutely black body, may be used to determine the emissivity of a semi-infinite sphere using the energetic coefficient of reflection of an auxiliary plane wave from the interface between media (see Chapter 4 and section 7.4). This approach can only be applied correctly to isothermal media. On the other hand, use of the phenomenological radiation transfer equation (which describes the energy balance in a section of the medium) to calculate the thermal radiation of non-isothermal media is limited to cases of media with small losses and fairly smooth variations of the complex dielectric constant (see Chapter 9). In this case, all waves multiply-reflected in the medium, together with the corresponding interference effects, are neglected.

First attempts to consider thermal emission for the comparatively simple cases of two- and three-layered media with different temperatures were performed by Tuchkov (1968) and Basharinov *et al.* (1968). They used the method where direct and reflected energy fluxes are summed to obtain the expressions for brightness temperature that define the emission of a complete structure. Such a method did not take account of phase relationships for multiply-reflected waves and, hence, a number of important effects were neglected.

A rigorous solution to the problem of the thermal radiation of a non-uniform, non-isothermal medium may be obtained using electrodynamics fluctuation theory for thermal radiation, in which the relationship between the correlations of the external fluctuating fluxes and the thermodynamic temperature of the medium in equilibrium is determined by the fluctuation/dissipation theorem (FDT) (see Chapter 4). In the work of Stogryn (1970) the FDT and the solution of the wave equation for the propagation of waves in a non-uniform medium were used to obtain a second-order differential equation with two boundary conditions for the intensity of thermal radiation, and a quasi-classical approximation (WKB) was used to compute the brightness temperature for weakly non-uniform media. This solution actually takes account of the variation of the thermal radiation of individual areas of the medium with variations of the real part of their dielectric constant, but ignores interference effects. This process was developed in a paper by Shulgina (1975), where, in particular, it was shown that the solution obtained by the WKB method is a well-defined generalization of the phenomenological radiation transfer equation to the case of arbitrary absorption, since it takes account of the refraction of rays in an absorbing medium. The same paper also determined a condition for the applicability of the WKB method to non-uniform media in the form of an inequality

$$\left| \frac{d\varepsilon}{dz} \right| \ll \frac{2\pi}{\lambda} \varepsilon$$

(λ is the wavelength of radiation in free space, ε is the dielectric constant of the medium), which implies that the scale of the non-uniformity is large in comparison with the wavelength. For media with sharp variations of the dielectric parameters at distances comparable with the radiation wavelength, known solutions using the WKB method were not suitable.

An accurate closed-form solution of the problem of the thermal radiation from non-uniform, non-isothermal media has only been found for a number of smooth profiles of dielectric parameters and temperature. An example of such a solution for exponential profiles was given in work by Tsang *et al.* (1975). Because of the variety of possible types of vertical profiles of the parameters of media, including sharp changes of the latter, approximation methods are particularly important.

One such approach involves studying the radiation from a half-space with arbitrary vertical profiles of the complex dielectric constant and the temperature, in the framework of a model of a stratified medium. Based on the results of Stogryn (1970), the wave equation for waves in a stratified medium was solved in a paper by Tsang *et al.* (1975) using a Green function for a multilayered structure, and the intensity of the radiation for the whole medium was computed in the form of a sum of terms for each layer. The amplitudes of the direct and reflected waves from each layer were found, independently from the radiation problem, using a matrix method for the whole structure; this complicates physical interpretation and comparison with solutions obtained using other methods. An analogous problem in the work of Wilheit (1978) was solved by computing the energy functions for wave transmission from each layer to the surface, using an iterative method to satisfy the boundary conditions in each layer. However, here, interference

effects were calculated for the subcase in which the electric field vectors of the back waves are collinear, which only arises for radiation with a horizontal polarization.

In this section, we describe (following Klepikov and Sharkov, 1983, 1993) a method for analysing the thermal radiation from stratified, non-uniform, non-isothermal media for an arbitrary angle of observation and an arbitrary polarization type; this differs from previous work in that the expressions for the brightness temperature are derived in a sequence of stages, being deduced initially for a single layer bounded on both sides and then generalized to all the layers of the structure as a whole. In this approach, the closed-form nature of the final result provides for more complete identification of both the physical characteristics of the method used and the constraints on its applicability to the problem of the emission of non-uniform, non-isothermal media.

7.7.2 Thermal emission of non-isothermal media with arbitrary parameters

Let us consider a time-stationary, non-uniform, vertically non-isothermal, non-magnetic medium bounded by the plane xy and occupying the region $z < 0$. We shall assume that the medium is in local thermodynamic equilibrium, whence the scale of non-uniformities of the parameters of the medium is considerably greater than the radius of correlation of the fluctuating fluxes, and the radiation at each point of space is described by Planck's law. From physical considerations, it is clear that, for arbitrary constraints on the value of the profiles of the complex dielectric constant $\dot{\varepsilon}(z)$ and the temperature $T(z)$, for computation of the brightness temperature T_{br} with an arbitrary given accuracy, it is sufficient to consider a layer of finite thickness D , outside which the medium is assumed to be uniform and isothermal. In accordance with the model of a stratified medium, the layer D is divided into N planar layers of thickness d_j (not generally equal). In each layer, the dielectric constant $\dot{\varepsilon}_j$ and the temperature T_j are assumed to be constant and equal to the average values of $\dot{\varepsilon}(z)$ and $T(z)$ in the j th layer. Thus, the continuous profiles of the parameters of the medium are replaced by step functions. The legitimacy of this substitution and the consequent computational errors will be considered below (section 7.7.4).

Suppose that an auxiliary planar monochromatic wave $E = E_0 \exp(i\mathbf{k}_0 \mathbf{r})$ with wave vector \mathbf{k}_0 propagates from the upper half-space $\varepsilon = 1$ to the plane xy at an angle θ_0 to the normal to the medium interface, where λ is the wavelength in free space and

$$\mathbf{k}_0 = \frac{2\pi}{\lambda} \{ \sin \theta_0, 0, \cos \theta_0 \}. \quad (7.87)$$

The above assumption that the parameters of the medium are constant in each layer enables us, when computing the radiation intensity, to apply Kirchhoff's law to each layer individually. In this case, this reduces to determining the full absorption of the wave power by the planar layer, which is bounded on both sides, taking into account interference due to reflection from the boundaries.

Let us consider a wave propagating at an angle θ_j (in a medium with absorption, the angle of refraction is complex) in the layer of thickness d_j with given wave

reflection (Fresnel) coefficients (in terms of the amplitude of the electric field) R_j^+ and R_j^- within the layer from the upper and lower boundaries respectively, where E_{0j} is the amplitude of the electric field at the (internal) upper boundary of the layer and the wave vector \mathbf{k}_j is:

$$\mathbf{k}_j = \frac{2\pi}{\lambda} \{ \sin \theta_j, 0, \cos \theta_j \} \sqrt{\dot{\epsilon}_j}, \quad (7.88)$$

where $\dot{\epsilon}_j$ is the complex dielectric constant. In what follows, when we are considering an individual layer, we shall omit the index.

The full field of the wave layer, taking into account multiple reflection, consists of the sum of two infinite series of direct and multiply-reflected, non-uniform planar waves with amplitudes decaying in a geometrical progression; thus, this may be written in the form

$$E_{\Pi}(z) = E_0 \frac{\mathbf{h}^+ \exp(i k_z z) + \mathbf{h}^- \operatorname{Re} e^{-ik_z(z-d)}}{1 - R^+ R^- \exp(-2ik_z d)}, \quad (7.89)$$

where \mathbf{h}^+ and \mathbf{h}^- are unit vectors corresponding to the direction of the vector of the electric field of the wave in the layer (with horizontal and vertical polarizations).

The density of full losses of the wave in the layer in the direction normal to the boundary is equal to the integral of the imaginary part of the complex Poynting vector over the whole thickness (Stratton, 1941):

$$\Pi = \frac{2 \operatorname{Im} k_z}{E_0^2} \int_0^d |E_{\Pi}|^2 dz, k_z = k \cos \theta. \quad (7.90)$$

In accordance with the generalized law of Kirchhoff for the theory of radiation (with the condition $h\nu \ll kT$, where h and k are the Planck and Boltzmann constants (respectively) and ν is the radiation frequency, which is usually in the microwave band), the brightness temperature T'_{br} at boundary of the layer (on the internal side) has the form

$$T'_{\text{br}} = \Pi T, \quad (7.91)$$

where T is the temperature of the layer.

By virtue of the statistical independence of the radiation of different layers, the brightness temperature on the surface of the medium is the sum of the brightness temperature of all the layers with weight coefficients $M_j = |E_{0j}/E_0|^2$, which characterize the attenuation of the power of the wave as it propagates from the corresponding layer to the surface, taking into account multiple reflection in all overlying layers

$$T_{\text{br}} = \sum_{j=1}^N T_{\text{br}} M_j = \sum_{j=1}^N \Pi_j T_j M_j. \quad (7.92)$$

Thus, the problem of determining the thermal radiation reduces to determining the transmission and reflection coefficients for a plane wave in a stratified medium. The wave characteristics of a multi-layered medium may be successfully determined using the tried and tested method of impedance characteristics, whereby the main equations may be written in the compact form of iterative equations. A detailed

description of the method, as applied to a stratified medium, was given by Klepikov and Sharkov (1983).

For the calculation of the brightness temperature from formula (7.92), taking into account (7.90), for a horizontally polarized wave, we have

$$T_{\text{brh}} = \sum_{j=1}^N \frac{T_j |W_j|^2}{|1 - R_j^- R_j^+ \exp(2i\psi_j)|^2} \left[(1 - \exp(-2\text{Im}\varphi_j))(1 + |R_j^- \exp(i\psi_j)|^2) \right. \\ \left. + 4 \frac{\text{Im}\psi_j}{\text{Re}\psi_j} \text{Re}(R_j^- \exp(i\psi_j))(\text{Im}\exp(i\psi_j)) \right] \frac{\text{Re}Z_j}{\text{Re}Z_0} + T_{N+1} |W_{N+1}| \frac{\text{Re}Z_{N+1}}{\text{Re}Z_0}. \quad (7.93)$$

Similarly, for the vertical polarization, we have

$$T_{\text{brv}} = \sum_{j=1}^N \frac{T_j |W_j|^2}{|1 - R_j^- R_j^+ \exp(2i\psi_j)|^2} \left[(1 - \exp(-2\text{Im}\psi_j))(1 + |R_j^- \exp(i\psi_j)|^2) \right. \\ \left. + 4 \frac{\text{Im}\psi_j}{\text{Re}\psi_j} \text{Re}(R_j^- \exp(i\psi_j)) \text{Im}(\exp(i\psi_j)) \left(\frac{|k_zj| - k_x^2}{|k_j|^2} \right) \right] \frac{\text{Re}Z_j}{\text{Re}Z_0} \\ + T_{N+1} |W_{N+1}|^2 \frac{\text{Re}Z_{N+1}}{\text{Re}Z_0}. \quad (7.94)$$

Both formulas implicitly involve the wave parameters and Z_j , R_j^+ , R_j^- and W_j , depending on the polarization. The formulas are summed over all layers $j = 1, \dots, N$. The index $j = N + 1$ describes the parameters of the uniform isothermal medium outside the layer D . W_j denotes the transmission coefficient (in terms of amplitude) from the internal side of the upper boundary of the layer j to the boundary of the medium, expressed in terms of input impedances Z_{in} as follows:

$$W_j = \prod_{m=1}^j \frac{Z_{\text{in}m-1}^+ + Z_{m-1}}{Z_{\text{in}m-1}^+ + Z_m}. \quad (7.95)$$

Since the component of the power of the total field of the wave normal to the boundary is conserved (see section 7.3), it is possible to determine the relationship between W_j and the coefficients M_j namely the attenuation of the wave power on transmission from the upper boundary of layer j to the surface of the medium:

$$M_j = |W_j|^2 = \frac{\text{Re}Z_j}{\text{Re}Z_0}. \quad (7.96)$$

The index ‘0’ relates to the region observed, namely the free space. Since the conversion to the energy characteristics of the propagation of waves in stratified media only takes place after the amplitude of the field in free space has been found, the calculation is not complicated by effects such as interference from waves reflected by the boundary division of the absorbing media.

When analysing the expressions (7.93) and (7.94) it is easy to see that the first terms in the square brackets characterize the absorption and the natural radiation of direct and back waves in each layer individually, while the second terms denote the change in the absorption of waves due to their interaction (interference). This fact does not contradict the law of conservation of energy since it implies that spatial redistribution of the heat release takes place within the medium with the interaction of back waves, but the general energy balance (incident, reflected, transmitting and absorbing) is preserved, as shown for a single boundary between two absorbing media (Veremey *et al.*, 1978). Thus, in the presence of wave interference, neighbouring areas of the spectrum (even with equal parameters) may contribute different values to the resulting radiation. It is a basic fact that the value of the radiation of each layer is affected by the dielectric characteristics of the medium not only between the layer and the surface but also as a whole. Strictly speaking, it is impossible to determine the true contribution of an individual layer to the resulting radiation without knowing the full dielectric characteristics of all its surroundings.

We note that the method studied is a monochromatic approximation. It remains valid for a narrow spectral interval such that the phase difference between the harmonic components at the length of the scale of the non-uniformity is small (see section 7.6 and Popov and Sharkov, 1976).

7.7.3 Limiting cases of general theory

We would naturally expect the above general solution of the thermal radiation problem for a stratified non-uniform isothermal medium to include, in the limit, all known approximation methods for similar problems. It is not difficult to check this directly.

We assume that the medium is weakly non-uniform so that it is possible to neglect multiply-reflected waves except those at the boundary of the medium R_0 . In this case, $R_j^- = 0$.

$$(|W_j|^2 / \operatorname{Re} Z) = (1 - |R_0|^2) / \operatorname{Re} Z_1 \left| \prod_{m=1}^j \exp(i k_{zm} d_m) \right|^2. \quad (7.97)$$

We denote the impedance of the layer at the boundary of the medium by Z_1 . Under these conditions, equations (7.93) and (7.94) take the form

$$\begin{aligned} T_{\text{br}} = & \sum_{j=1}^N T_j (1 - |R_0|^2) (1 - \exp(-2 \operatorname{Im} k_{zj} d_j)) \left| \exp(i \sum_{m=1}^j k_{zm} d_m) \right|^2 \frac{\operatorname{Re} Z_j}{\operatorname{Re} Z_1} \\ & + T_{N+1} (1 - |R_0|^2) \left| \exp(i \sum_{m=1}^j k_{zm} d_m) \right|^2 \frac{\operatorname{Re} Z_{N+1}}{\operatorname{Re} Z_1}. \end{aligned} \quad (7.98)$$

Letting the value of d_j tend to zero and the area of the summation tend to infinity, and representing the exponent in the first factor as a series, we convert from

summation to integration

$$T_{\text{br}} = (1 - |R_0|^2) \int_0^\infty T(z) 2 \operatorname{Im} (k(z) \cos \theta(z)) \\ \times \exp \left[-2 \int_0^\infty \operatorname{Im} k(z') \cos \theta(z') dz' \right] \frac{\operatorname{Re} Z(z)}{\operatorname{Re} Z(0)} dz. \quad (7.99)$$

The last expression agrees, within the accuracy of the notation, with the solution by WKB-method (Shulgina, 1975), which is a subcase of the general solution for the given conditions. With the additional assumptions that the variations of the dielectric constant of the medium $\operatorname{Re} \varepsilon(z) \cong \text{const}$, $Z(z) \cong Z(0)$ are small and that the absorption by the medium $\operatorname{Re} \dot{\varepsilon}(z) > \operatorname{Im} \dot{\varepsilon}(z)$ is insignificant, and transferring to the real angle of refraction $\theta'(z) = \operatorname{Re} \theta(z)$, where $k(z) \cos \theta(z) \cong k(z) / \cos \theta'(z)$, we obtain the well-known solution of the phenomenological equation of radiation transfer (ERT) (see Chapter 9)

$$T_{\text{br}} = (1 - |R|^2) \int_0^\infty T(z) \frac{2 \operatorname{Im} k(z)}{\cos \theta'(z)} \exp \left(-2 \int_0^z \operatorname{Im} k(z') / \cos \theta'(z') dz' \right) dz. \quad (7.100)$$

The physical difference between (7.99) and the solution of the ERT is the calculation of the refraction-related perturbations of the outgoing thermal flux from the absorbing medium (imaginary term). Since $2 \operatorname{Im} k(z) = \gamma(z)$ is the absorption in the medium, expression (7.99) for a uniform absorbing medium may be written in the form obtained by Shulgina (1975):

$$T_{\text{br}} = \kappa(\theta, \lambda) \int_0^\infty \gamma(z) S(\theta) T(z) \exp(-\gamma(z') S(\theta) dz') dz, \quad (7.101)$$

where θ is the angle of observation outside the medium measured from the nadir, and $S(\theta)$ is the refraction coefficient

$$S(\theta) = \left(\frac{\varepsilon_1 - \sin^2 \theta}{\varepsilon_1 (\sqrt{1 + \operatorname{tg}^2 \delta} - 1)} \right)^{1/2} \left[\sqrt{1 + \frac{\varepsilon_1^2 \operatorname{tg}^2 \delta}{(\varepsilon_1 - \sin^2 \theta)}} - 1 \right]^{1/2}. \quad (7.102)$$

Here, $\dot{\varepsilon} = \varepsilon_1(1 + i \operatorname{tg} \delta)$ is the complex dielectric constant of the medium.

A special calculation of the refraction coefficient for a broad range of wavelengths (from 0.33 to 75 cm) and values of the angles of observation (from 0 to 89°) performed by Sharkov (1978), showed that the contribution of refraction to the polarization characteristics of the absorbing media (seawater and freshwater) is quite small: S differs from the value of this coefficient calculated for a medium with low losses by <4%, which amounts to a corresponding change in the brightness temperature of <0.004 K.

Whence, it follows that the results of the phenomenological theory of radiative transfer hold for weakly absorbing media ($\operatorname{tg} \delta \ll 1$) and are also applicable to media with strong absorption ($\operatorname{tg} \delta \geq 1$, for example, seawater) provided the real part of the complex dielectric constant ($\varepsilon_1 \gg 1$) is sufficiently high; thus, the difference between the refraction coefficient and the value determined by Snell's law is small. It is for this

physical reason that methods developed for the calculation of the radio-emission of pure transparent media in due course (Troitskii, 1954, 1967; Chandrasekhar, 1960) describe the absorbing media emission adequately.

The derivation of equations (7.93)–(7.94) was based on the computation of the full losses of waves (in terms of amplitude) in the whole multi-layered structure, which is equivalent to determination of the difference in power of the incident and reflected waves and corresponds to Kirchhoff's law for stratified isothermal media, where $T_j = \text{const}$,

$$T_{\text{br}} = (1 - |R_\Sigma|^2)T, \quad (7.103)$$

where R_Σ is the reflection coefficient of water on the free-space side, taking into account all multiple reflections in the multi-layered medium. We have already used this result in section 7.5.

The comparatively simple subcase of a three-layered medium with different temperature layers was considered in due course in work by Tuchkov (1968) and Basharinov *et al.* (1968), where the direct and multiply-reflected fluxes of thermal radiation from different layers were summed to obtain the expression for the average brightness temperature (Basharinov *et al.*, 1968):

$$T_{\text{br}321} = \frac{[T_3(1 - R_{32}^2) \exp(-\tau_2) + T_2(1 \exp(-\tau_2))(1 + R_{32}^2 \exp(-\tau_2))](1 - R_{12}^2)}{1 - R_{12}^2 R_{32}^2 \exp(-2\tau_2)}. \quad (7.104)$$

The value of the index 1 relates to the free space, the coefficients R_{ij} are the moduli of the Fresnel coefficients for the two media, and τ_2 is the optical depth of the intermediate layer 2.

Comparing with (7.93)–(7.94), we note that equation (7.104) involves a number of simplifications which limit its area of applicability. Firstly, it does not take account of phase relationships for multiply-reflected waves and interference effects are not considered. Instead of this, it describes their power characteristics, which is to some extent justified for a brightness temperature averaged over a sufficiently broad range of frequencies, where the term ‘sufficiently’ remains undetermined. For example, the sign in the denominator of (7.104) depends on the phase of the Fresnel coefficients at the two boundaries, which in turn depends on the equations for ε_2 and ε_3 .

Secondly, on passing the boundaries of absorbing medium, it is not the sum of the normal components of the fluxes of wave energy which is continuous, but the normal component of the energetic flux of the field as a whole (see section 7.3). Thus, strictly speaking, the power of the passing wave t_{p12} is not equal to the difference between the incident and the reflected waves $t_{p12} \neq 1 - |R_{12}|^2$. Thirdly, as previously shown for interfering waves in an absorbing medium, there occurs a redistribution of absorption of the wave energy in space, which was described in (7.93)–(7.94) by an interference term.

For the brightness temperature of temperature of a three-layered medium with equal temperatures in the layers, (7.93)–(7.94) provides an accurate expression

$$T_{\text{br}} = \frac{T_2[(1 - \exp(2\beta))|1 - R_{12}|^2(1 + |R_{32}|^2 \exp(-2\beta)) + 4\beta/\alpha \operatorname{Re}(R_{32} \exp(j\psi))] \operatorname{Re} Z_2}{\operatorname{Re} Z_1 |1 - R_{12} R_{32} \exp(2i\psi)|^2} \\ + T_3 |(1 - R_{12})(1 - R_{32})|^2 \exp(-2\beta) \operatorname{Re} Z_3, \quad (7.105)$$

where $\psi = \alpha + i\beta = k_z d$, τ_2 in (7.104) corresponds to 2β , Z_j are the impedances of the media and R_{ij} are the complex (unlike (7.104)) Fresnel reflection coefficients. In this expression, it is not difficult to observe all the differences from (7.104) listed above.

7.7.4 Conditions for the method's feasibility

The method described above for analysing thermal radiation is accurate for stratified non-uniform media; in other words, it assumes strictly constant parameters of the medium and equilibrium in each layer. Let us consider in more detail the restriction of the applicability of the method to the problem of thermal radiation from real media with arbitrary parameter profiles. Firstly, at each point of space, the conditions for the applicability of the FDT should be satisfied, which implies the equilibrium of the energy distribution (in terms of degrees of freedom) and small radii of correlation τ_k of the outside fluctuating fluxes in relation to the scales of the non-uniform and non-isothermal anomalies of the medium $d_j \gg \tau_k$. Secondly, the legitimacy of the representation of the continuous parameters of the medium in the form of a stratified structure must be verified. This is not difficult, assuming relatively small errors in the computation of the characteristics of the propagation (phase and amplitude) $|\Delta\psi_j/\psi_j| \ll 1$ and the radiation $\Delta T'_{\text{br}}/T'_{\text{br}} \ll 1$ in each layer due to the replacement of the real parameter profiles by average values (for simplicity, the values of the parameters in the centre of the layer):

$$d_j \ll \frac{4\sqrt{6}|\varepsilon_j|}{|\partial\varepsilon_j/\partial z|}, d_j \ll 2\sqrt{\frac{6N_j}{(\partial^2 T_j/\partial z^2)}}. \quad (7.106)$$

The second condition was based on the assumption that the attenuation of radiation in a layer is small. Here, d_j does not depend on the first derivative of the temperature profile.

The given estimates do not take into account wave interference within a layer, since this is impossible without using additional information about its surroundings. However, it is possible to estimate the maximum effect of interference, assuming the boundary layer is an absolute reflector. Here, condition (7.106) does not depend on the wavelength of the radiation:

$$d_j \ll \frac{|\varepsilon_j|^2}{|\partial\varepsilon_1/\partial z|} 8\sqrt{\frac{3 \operatorname{Im}(\sqrt{\varepsilon_j})}{|\sqrt{\varepsilon_j}|}}, d_j \ll 4\sqrt{\frac{3 T_j \operatorname{Im}(\sqrt{\varepsilon_j})}{(\partial^2 T_j/\partial z^2)|\sqrt{\varepsilon_j}|}}. \quad (7.107)$$

For a fixed thickness of the layers, in general, the number of layers is given by $N = D / \min(d_i)$.

Naturally, the radiation of layers far from the external boundary of the medium is attenuated and the contribution of their errors to the total brightness temperature is less than that of neighbouring layers. Thus, as the distance from the boundary of the medium increases, the stringency of the conditions on the thickness of the layers decreases. Consequently, in order to decrease the overall volume of the actual calculation, it is convenient to use (other conditions remaining the same) a variable step for the subdivision of the layer, which increases with the distance from the boundary of the medium.

The previous conditions were found independently for variations of the profiles of the dielectric constants and temperature of individual layers, since joint estimation of the computational error due to their variations is very complicated. Thus, finally, the number of sublayers into which it is sufficient to divide media with complicated parameter profiles may be simply determined as a function of the convergence of numerical computations of T_{br} for a sequentially increasing number of subdivisions.

7.7.5 Spectral characteristics of thermal emission for some stratified media

The goal of this subsection is to identify the main characteristics of the field of radiation of non-isothermal, non-uniform media. These may be identified most clearly by analysis of the spectral characteristics of the thermal radiation of a series of model media, obtained by numerical modelling (relevant algorithms were described in work by Klepikov and Sharkov (1983)). Let us compare the results of applying the method described in the second section (7.7.2) with other methods, based on the example of a three-layered, non-isothermal medium (observation of a medium with $\varepsilon_1 = 1$) and the model A:

$$\begin{aligned}\varepsilon_2 &= 10 + i1; & T_2 &= 200 \text{ K} & 0 < z < 10 \text{ cm} \\ \varepsilon_3 &= 100 + i10; & T_3 &= 300 \text{ K} & 10 \text{ cm} < z.\end{aligned}$$

Figure 7.17 shows graphs of the brightness temperature against wavelength for observations in the nadir. Curves 1–5 were calculated using the accurate formulae (7.105), the WKB method (7.99), the radiation transfer equation (7.100), Kirchhoff's method (7.103) with average temperature 300 K, and formula (7.104) for an average temperature of the three-layered medium (by summing the thermal fluxes), respectively.

In the short-wave area of the frequency band, where the wavelength of the radiation is far less than the characteristic size of the non-uniformities of the medium and the radiation is largely determined by the thin surface layer, approximation methods give a good approximation to the graph of T_{br} calculated using the accurate formula. The differences in the values of T_{br} for Kirchhoff's method (curve 4) are associated with chosen value $T = 300$ K, for which the emissivity of the medium $\kappa = 1 - |R|^2$ corresponds accurately to the value obtained by the accurate formula ($\kappa = 0.7272$).

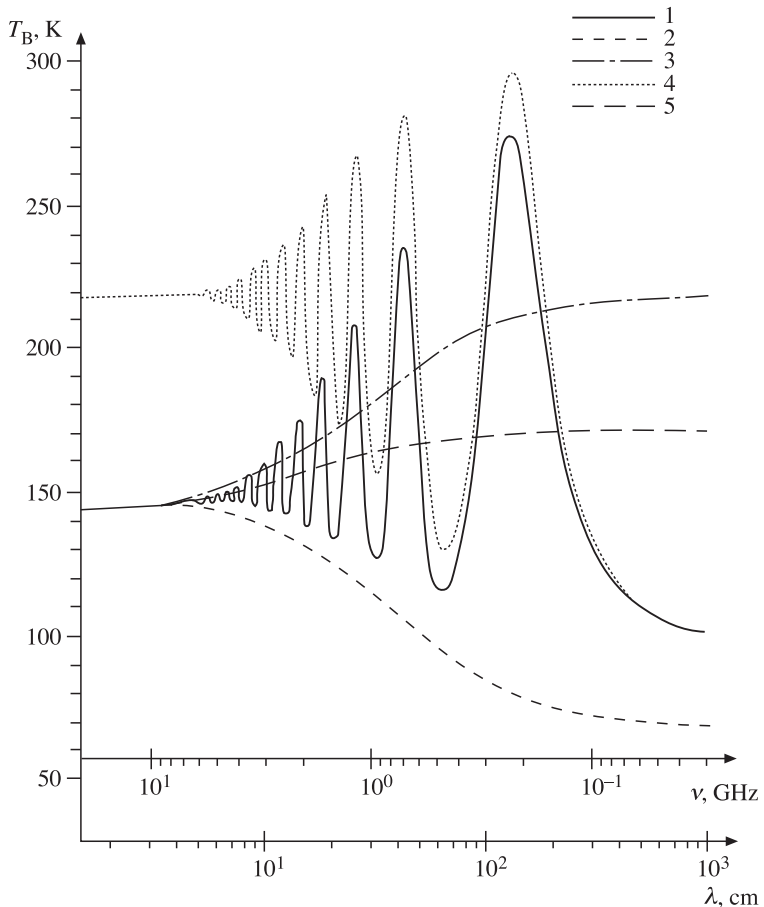


Figure 7.17. Spectral characteristics of the natural radiation of a three-layered non-isothermal medium (model A). 1–5, see explanation in text.

However, for the whole spectrum of frequencies, and particularly the long-wave area, the errors of each of the approximation methods are very significant (up to 100 K). For example, the method of summing the thermal fluxes (curve 5) gives ‘clearly average’ spectral variations of T_{br} without interference features. In other words, the spectral averaging built into the method is carried out over practically the full range of frequencies used. Most striking (numerical) differences are observed in the spectral variations of the curves 2 and 3 obtained by the WKB and ERT method, which are apparently very similar to each other (see formulas (7.99) and (7.100)).

Consideration of this model example shows that not one of the approximation methods provides correct calculation of the emissivity of highly non-uniform, non-isothermal media over a broad band of wavelengths.

Very large numerical differences between the spectral graphs of T_{rmbr} for the accurate method and for the approximation methods are found where relatively local temperature jumps occur in an area of interfering waves, reflected by the dielectrical non-uniformities of the medium. Figure 7.13 shows the spectral variation of the radiation ($\theta = 0$) from an isothermal three-layered medium (model B) with profiles

$$\begin{aligned}\varepsilon_2 &= 1 + i0.4, \quad 0 < z < 10 \text{ cm} \\ \varepsilon_3 &= 100 + i10, \quad 10 \text{ cm} < z\end{aligned}$$

calculated using Kirchhoff's law for isothermal media. The spectral variation for this medium, but with a sharp temperature anomaly $T = 900 \text{ K}$ for $7.5 < z < 7.75 \text{ cm}$ in the intermediate layer (model C), is shown in Figure 7.18. From a comparison of the two graphs it is easy to see the change in the nature of the modulation of the spectral

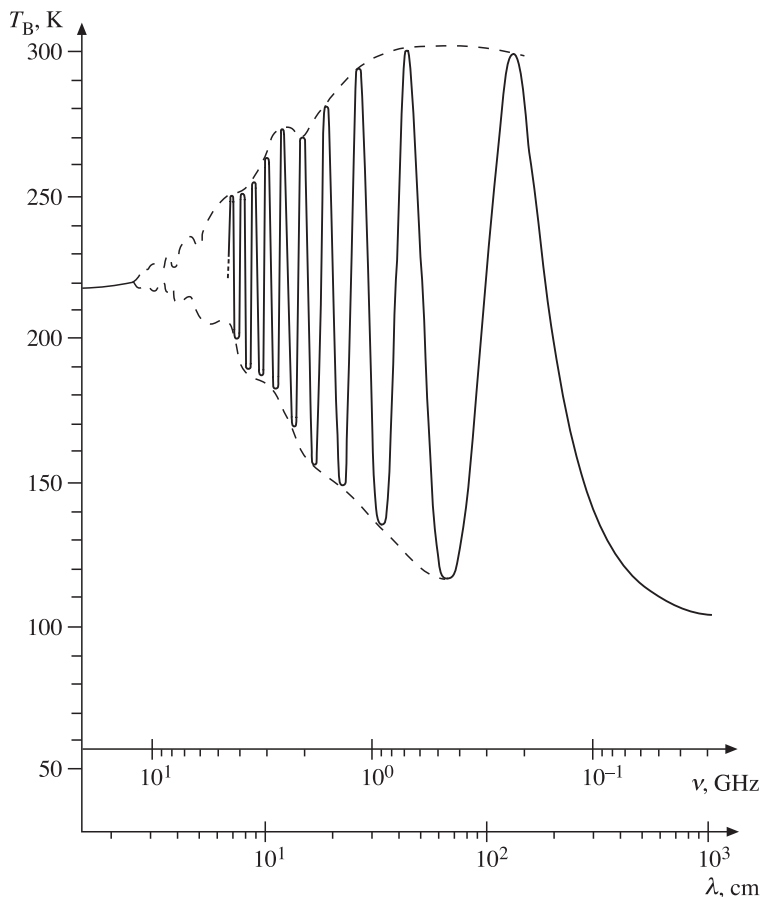


Figure 7.18. Spectral characteristics of the natural radiation of a three-layered medium (model B) with a sharp ‘pulse-like’ temperature anomaly.

curve of the radiation from the medium in the presence of the temperature anomaly. In fact, as a result of reflection, a mixed wave occurs in the intermediate layer; in other words, both travelling and standing waves occur. Thus, within the layer there is a special redistribution of the energy losses and consequently the different areas of the medium give different contributions to the resulting radiation. At frequencies corresponding to the position of the bulge of the standing waves at the point of a temperature jump, the contribution of the radiation of this layer to the total value T_{br} is a maximum. Conversely, when the position of the node of the standing waves and the thermal anomaly coincide, the contribution to T_{br} is a minimum. From these considerations it is clear that the maximum value of the modulation coefficient (all other conditions being equal) is attained for a temperature jump of much less than half the wavelength of the radiation. Consequently, the thinner the anomalous layer, the broader the band of frequencies in which modulation is observed. Its frequency is largely determined by the change in phase of waves from the anomalous layer to the neighbouring dielectric non-uniformity of the medium. This modulation effect is most clearly visible for a three-layered medium although it is also found in perturbed form for more complicated profiles of the dielectric parameters. A sufficient condition for modulation of the thermal radiation is the presence of a thin layer with an anomalous temperature in an area of the medium where there exist interfering waves.

Figure 7.19 and 7.20 illustrate the occurrence and relative positions of two types of modulation of the spectrum of thermal radiation from a three-layered medium, associated with the presence of a layer with anomalous values of the imaginary part of the dielectric constant and the temperature. The first effect takes the form of amplitude modulation and the second that of an additional sinusoidal component. If effects of approximately equal value are collocated, the resulting shape of the modulation will be almost one-sided (analogue of amplitude/phase modulation).

Thus, use of the accurate expressions (7.93)–(7.94) to calculate the thermal radiation from non-uniform, non-isothermal media with local anomalies and with arbitrary absorption leads to the occurrence of effects ignored by the calculations of the approximation methods (WKB method, theory of radiative transfer, Kirchhoff's law etc.).

It is certainly interesting to analyse the errors in the calculations of the spectral variations of the radiation from media with smoothly varying parameters as a function of the number of subdivisions N of the layer. Figures 7.21(a) and (b) show the results of numerical calculations of T_{br} for two typical profiles of the complex dielectric coefficients and the temperature, namely a linear and an exponential profile. In the calculations, we chose two ways of dividing the non-uniform area of the medium of thickness D into layers: a linear method, in which the thickness of all the layers was the same $d_j = D/N$, and an exponential method in which the thickness of the layers increased as the distance from the boundary of the medium

$$d_j = 2d_{j-1}, \sum_{j=1}^N d_j = D.$$

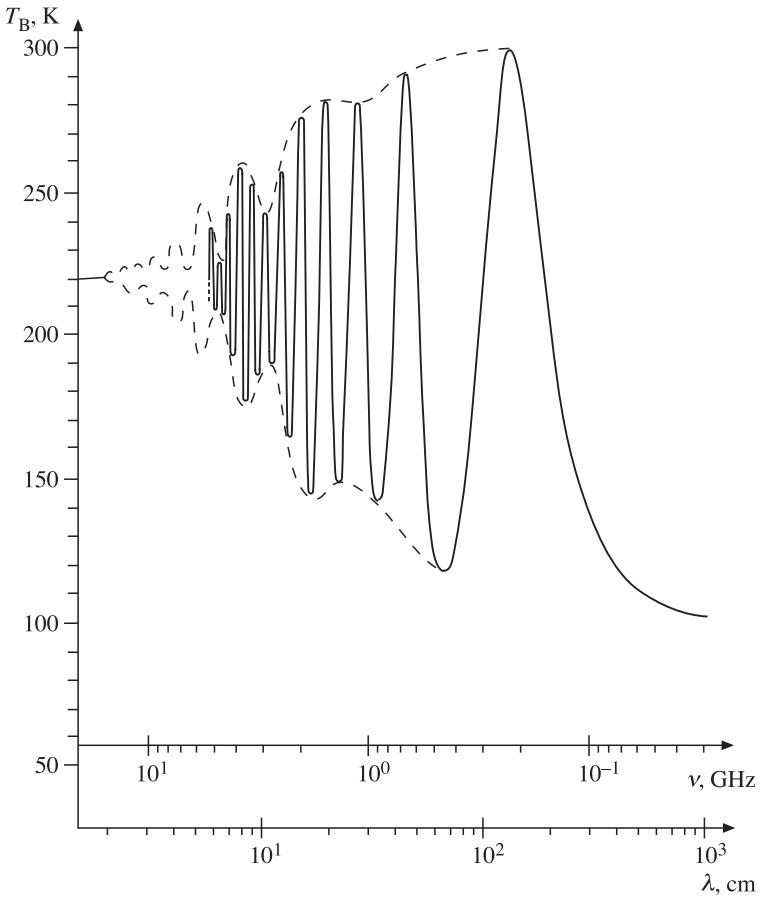


Figure 7.19. Spectral characteristics of the natural radiation of a three-layered medium with a ‘pulse-like’ anomaly of dielectric losses (model C).

From the figure, it is easy to see that in the band of wavelengths from ~ 0.1 to 100 cm there are considerable variations in the radiation spectra. For $N = 128$, for both types of profiles of the parameters, the radiation spectra exhibit a stationary form, and are practically unchanged for small variations of the number of subdivisions. Thus, they may be assumed to be ‘true’ (in the asymptotic sense) and compared with radiation spectra for other values of N . Maximum errors in the spectra as a function of N are given in Table 7.1.

It is clear from the table that the exponential subdivision into layers provides for faster and more uniform convergence of the results throughout the whole spectral interval, this being more noticeable for the exponential profiles of the parameters.

In this way, based on the application of a generalization of Kirchhoff’s law to a model of a stratified medium with a planar boundary, we have obtained a closed-form for thermal radiation in a monochromatic approximation, taking into account

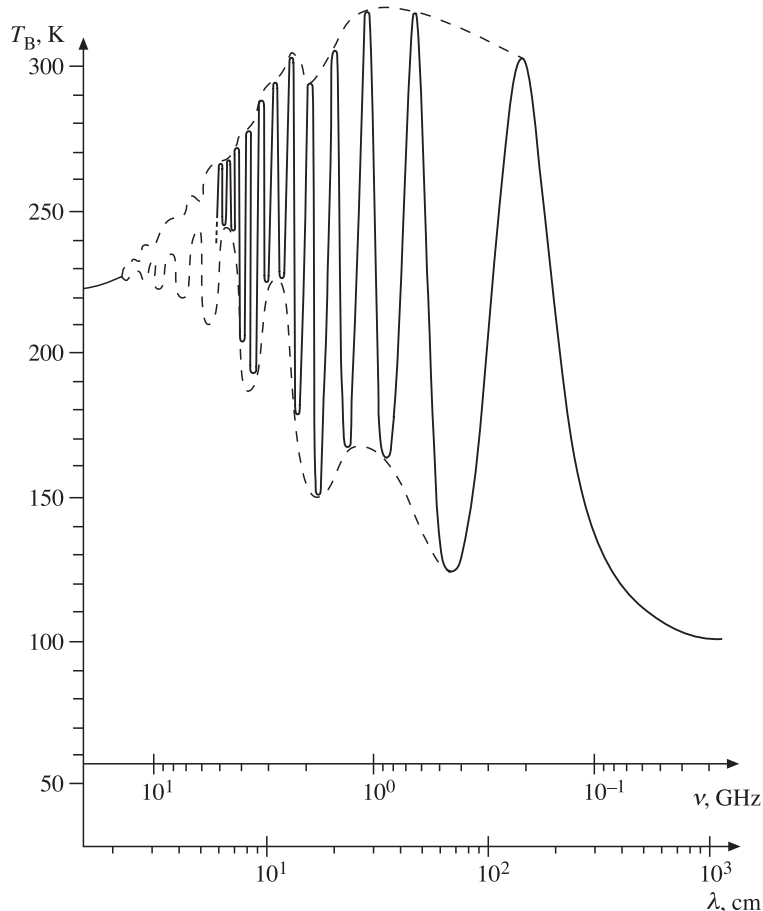


Figure 7.20. Spectral characteristics of the natural radiation of a three-layered medium with an anomalous value of the dielectric losses (model C) and with a sharp ‘pulse-like’ temperature anomaly.

Table 7.1. Maximum errors in T_{br} , K

Number of layers	Parameter profile			
	Linear		Exponential	
	Type of subdivision			
1	22	—	17	—
4	12	8	15	7
16	2	2	6	1

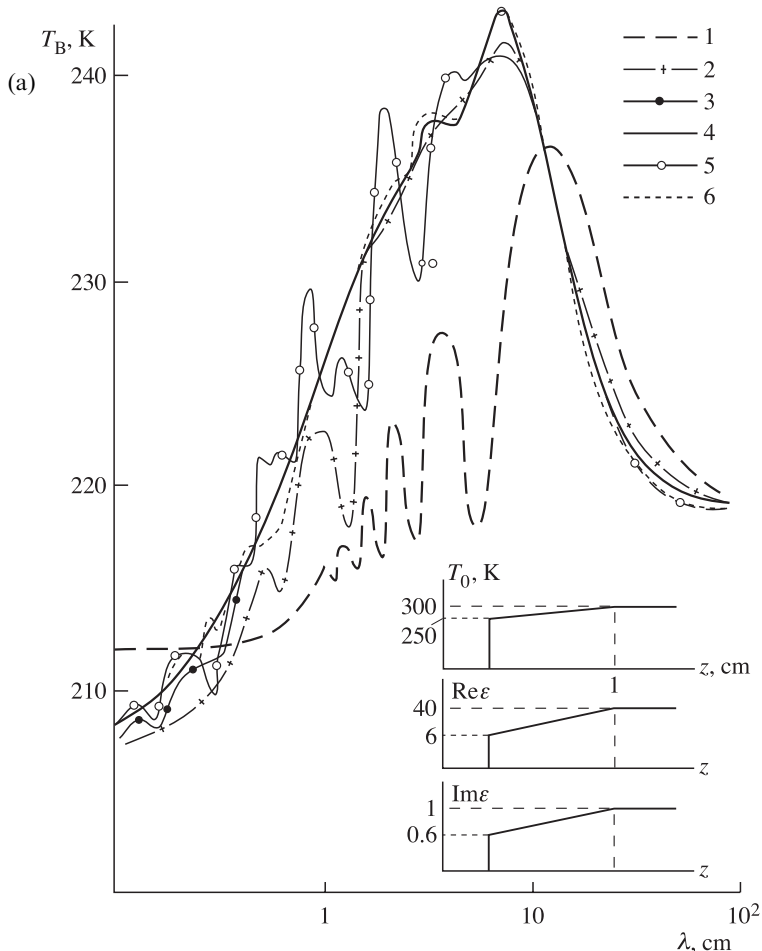


Figure 7.21. Spectral characteristics of natural radiation as a function of the number of subdivisions, N , of the layer in the medium, with linear (a) and exponential (b) stratifications of the dielectric and thermal parameters: 1, a single layer; 2, 4 layers; 3, 16; 4, 128 (linear subdivision); 5, 4; 6, 16 (exponential subdivision).

interference effects. The solution involves a dependence on the wavelength, the angle of observation and the type of polarization of the radiation. It is shown that, for specific conditions satisfied for most types of real media in the microwave and IR band, this solution enables us to determine the spectral characteristics of the thermal radiation from a vertically non-uniform, non-isothermal medium with arbitrary absorption, with reasonable accuracy. The solution also includes known methods of calculating the brightness temperature such as solution of the radiation transfer equation, Kirchhoff's law for isothermal media and solution by the WKB method, and is a generalization of these.

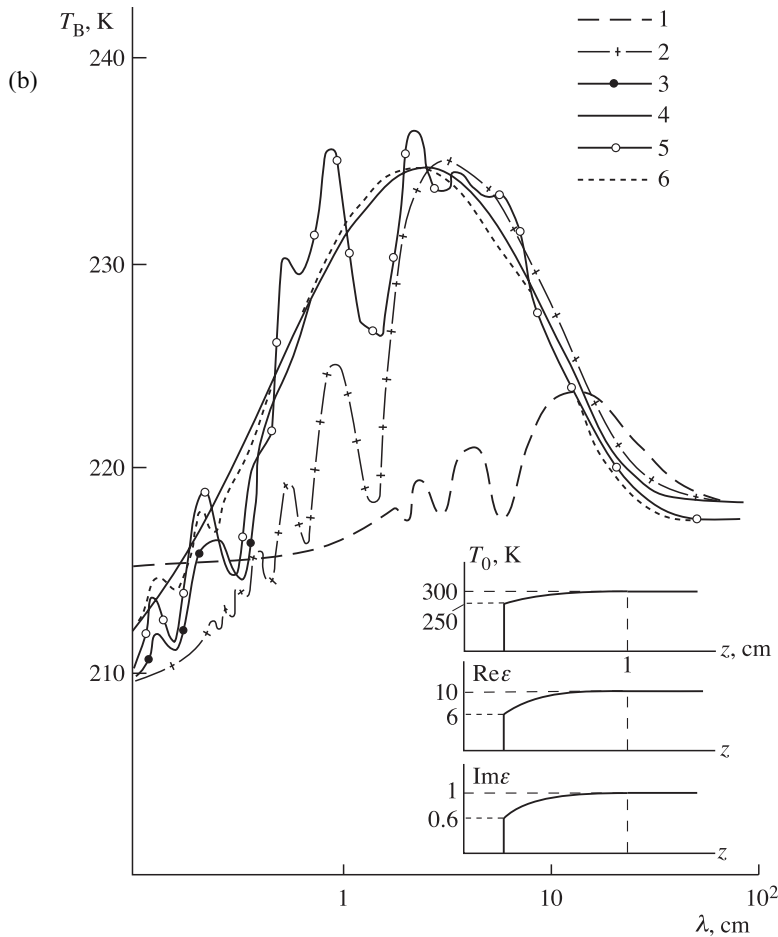


Figure 7.21 (b)

Using the method described we have developed a computer-based algorithm and carried out numerical analysis of the thermal radiation spectra for a number of characteristic cases of non-uniform, non-isothermal media. The greatest differences between the spectral variations of the radiation for this method and those for existing methods occur in the presence of relatively local temperature jumps of width less than the wavelength. Here, in addition to the usual modulation of the spectral characteristics of the radiation due to interfering waves reflected by the dielectric non-uniformities of the medium, there is additional modulation in the form of sinusoidal components which are damped as the wavelength of the radiation decreases.

The method described in this section and the computational algorithm may be used to solve more complicated problems of thermal radiation, for example, for media with three-layered temperature and dielectric anomalies with rough boundary divisions, and also for media with random parameter non-uniformities.

8

Dielectric and emissive properties of terrestrial surfaces

The purpose of this chapter is to consider the basic characteristics (the intensity and spectral dependencies) of the radiation field of physical substances most widespread on the surface and in the atmosphere of the Earth. The frequency properties of the characteristics of dielectrics are considered from the viewpoint of the phenomenological approach to studying the relaxation mechanisms (the Debye model and models with a multiplicity of relaxation times). The basic statements of dielectric spectroscopy theory and practice are presented. The main attention in the chapter is given to studying the dielectric and emissive properties of salt (seawater) and freshwater and to the relation of these properties to the physicochemical structure of these substances by determining the frequency dispersion of electromagnetic properties of dielectrics. The dielectric and emissive properties of natural objects, containing freshwater and aqueous electrolytic solutions at different phase states, are considered. These states include: freshwater ice, sea ice, glacial ice, moist fertile soil, salinas. The chapter presents a rich set of experimental findings on emissive characteristics and dielectric properties of substances distributed both on the Earth and on terrestrial planets.

8.1 FREQUENCY DISPERSION OF THE ELECTROMAGNETIC PROPERTIES OF DIELECTRICS

Virtually all known natural substances and physical objects on our planet belong (when considering their electromagnetic properties) to the class of dielectrics. This class includes all atmospheric (non-ionized) gases, virtually all liquids (including fresh and ocean water), solid bodies (soil, grounds, rocks), vegetation, artificial (manufactured) materials and buildings, and also the objects of animate nature. The basic mechanisms of interaction of such physical systems with the electromagnetic field are reduced to redistribution of the electronic density of internal

electric charges in a medium and to polarization features arising in the distribution of charges (see section 1.6).

8.1.1 Dispersive properties

The polarization of a dielectric when an electric field is applied takes place, not instantaneously, but over a certain time called the relaxation time. The temporary character of the relaxation process is rigidly bound to the physicochemical properties and structure of the substance and is clearly exhibited in studying frequency characteristics of electromagnetic properties – the so-called dispersive properties. The range of frequencies in which the expressed changes of dielectric properties of substances mostly take place is called the dispersion region. Investigation of the dispersive properties of substances can provide very important information on the structure of physical objects and on their physicochemical composition. Investigations can be carried out both directly, by laboratory study of the dielectric properties of substances, and remotely, by studying the spectral properties of thermal radiation. The microwave band of electromagnetic waves represents just that range of frequencies where dispersive phenomena become essential for the overwhelming majority of earth covers, and, on the other hand, where macroscopic description by means of classic Maxwellian electrodynamics is possible (see section 1.6). Thus, the electrical polarization of a dielectric can be described within the framework of Maxwellian electrodynamics, taking into account the principal circumstance that the unambiguous time-dependence of values of the electrical and magnetic induction fields with the instantaneous values of electric and magnetic fields is violated. In other words, the physical system will possess a certain inertia when the external electrical field is applied, or some kind of memory when the external field is removed and the system tends to the equilibrium state. Since in remote sensing tasks fairly weak values of electric fields are applied, the relationship between the induction and electrical field remains linear.

Under the physical limitations indicated the most general form of relation between the induction and electrical field at all previous time instants can be written in the form of the following integral relationship (Landau and Lifshitz, 1957):

$$\mathbf{D}(t) = \varepsilon_{\infty} \mathbf{E}(t) + \int_0^{\infty} f(\tau) \mathbf{E}(t - \tau) d\tau, \quad (8.1)$$

where $f(\tau)$ is the function of time which characterizes the process of relaxation of the electrical polarization at the application or removal of the external electrical field and depends on the physical and physicochemical properties of the medium, ε_{∞} is the dielectric permittivity of a medium at high frequencies, i.e. at frequencies lying outside the active relaxation region of the given relaxation mechanism.

Transferring to a set of monochromatic components (by using the Fourier expansion), in which the time-dependence is given by multiplier $\exp(-j\omega t)$, we obtain the relation between \mathbf{D} and \mathbf{E} (in the SI system) as follows:

$$\mathbf{D} = \varepsilon_0 \nu \mathbf{E} + \mathbf{P} = \varepsilon(\omega) \varepsilon_0 \nu \mathbf{E}, \quad (8.2)$$

where ε_{0V} is the permittivity constant of vacuum* (see section 1.6), \mathbf{P} is the polarization vector, and $\dot{\varepsilon}(\omega)$ is the relative complex permittivity unambiguously bound with the process of establishing the balance in a dielectric and defined as:

$$\dot{\varepsilon}(\omega) = \varepsilon_\infty + \int_0^\infty f(\tau) \exp(j\omega\tau) d\tau. \quad (8.3)$$

The frequency-dependence of $\dot{\varepsilon}(\omega)$ is said to be the law of its dispersion, or its dispersive properties.

Function $\dot{\varepsilon}(\omega)$ is complex, generally speaking. From the definition of (8.3) it directly follows, that

$$\dot{\varepsilon}(-\omega) = \dot{\varepsilon}^*(\omega). \quad (8.4)$$

Separating in this relation the real and imaginary parts, we obtain

$$\varepsilon_1(-\omega) = \varepsilon_1(\omega); \varepsilon_2(-\omega) = -\varepsilon_2(\omega). \quad (8.5)$$

Thus, $\varepsilon_1(\omega)$ is an even, and $\varepsilon_2(\omega)$ an odd function of frequency. For low frequencies (as compared to the active relaxation zone) the function $\varepsilon(\omega)$ can be expanded in a series in powers of ω . The expansion of the even function $\varepsilon_1(\omega)$ contains the terms of even powers only, and the expansion of the odd function $\varepsilon_2(\omega)$ the terms of odd powers. In the limit $\omega \rightarrow 0$ function $\dot{\varepsilon}(\omega)$ in dielectrics tends, certainly, to the relative permittivity, which is usually designated as ε_0 (this designation should not be confused with the permittivity of vacuum (see section 1.6)). Therefore, in dielectrics the expansion of $\dot{\varepsilon}(\omega)$ begins with the constant term ε_0 ; the expansion of $\varepsilon_2(\omega)$, however, begins, generally speaking, with a term proportional to ω . This is especially clearly seen in the analysis of the Maxwell equations for dielectrics in the presence of noticeable direct current conductivity (perfect conductors). Using equations (1.1a) and (1.3), we obtain the following limiting expression for $\varepsilon(\omega)$ for low frequencies (Landau and Lifshitz, 1957):

$$\dot{\varepsilon}(\omega) = j \frac{\sigma}{\omega \varepsilon_{0V}}. \quad (8.6)$$

Thus, in dielectrics with a noticeable direct current conductivity the expansion of function $\varepsilon(\omega)$ begins with the imaginary term proportional to $1/\omega$, which is expressed in terms of conventional direct current conductivity. As the frequency further increases, the value of this term sharply decreases, and the relaxation mechanisms come into effect. They are manifested as specific (and sometimes rather complicated) frequency dependencies, including electromagnetic energy dissipation. Thus, for dielectrics with internal relaxation mechanisms of external energy transformation and in the presence of finite direct current conductivity in them the complete expression for the complex dielectric constant $\dot{\varepsilon}_\sigma(\omega)$ can be written as:

$$\dot{\varepsilon}_\sigma(\omega) = \dot{\varepsilon}_R(\omega) + j \frac{\sigma}{\omega \varepsilon_{0V}}, \quad (8.7)$$

where $\dot{\varepsilon}_R(\omega)$ is the relaxation part of the permittivity.

* This quantity is redesignated in this chapter (with respect to section 1.6) to avoid confusion into designations.

Such dielectrics are called ‘poor’ conductors of electricity in physics (Landau and Lifshitz, 1957).

In practical applications this form of dielectric constant is written using the numerical expression for the permittivity constant of vacuum (see section 1.6 and Appendix A, Table A.4) in a somewhat different, but, certainly, fully equivalent form

$$\dot{\varepsilon}_\sigma(\lambda) = \dot{\varepsilon}_R(\lambda) + 60\sigma\lambda, \quad (8.8)$$

where the wavelength is taken in metres, and the dimension of electrical conductivity in $(\Omega m)^{-1}$ (see Appendix A, Table A.2).

In practical applications no distinction is usually made between these two parts of the expressions presented above, putting the term caused by the direct current conductivity directly into the expression for an imaginary part of the dielectric constant caused by a pure relaxation mechanism. In studying liquid electrolytes, the relaxation part of a dielectric constant $\dot{\varepsilon}_R(\omega)$ is called the ‘adjusted’ part, which means the value of $\dot{\varepsilon}(\omega)$ with subtraction of the correction for the ‘through’ (ionic in solutions) component of conductivity. Hereafter we shall use, for simplicity, the full expression for a dielectric constant, not using the subscript in (8.7) or (8.8).

The presence of full dielectric losses, as follows from (8.2), results in the appearance of a phase shift between instantaneous values of the induction and electric field vectors. Physically, this is equivalent to the appearance of the effects of time delay of polarization in a medium with respect to the external field. The spectral (wavelength) dependence of the tangent of the angle of losses can be written in this case as

$$\operatorname{tg} \delta(\lambda) = \frac{\varepsilon_2(\lambda) + 60\sigma\lambda}{\varepsilon_1(\lambda)}. \quad (8.9)$$

In the optical and IR wavelength bands the frequency properties of relaxation mechanisms of dielectrics are often presented and studied in the form of spectral (frequency or wavelength) dependencies of real and imaginary parts of the complex index of refraction. The transition to a complex dielectric constant can be accomplished according to well-known rules (see section 1.6, equations (1.26)–(1.28)).

In the limit $\omega \rightarrow \infty$ function $\dot{\varepsilon}(\omega)$ tends to unity. This is already clear from simple physical considerations: if the field changes rapidly enough, the polarization processes, resulting in establishing induction \mathbf{D} differing from \mathbf{E} , have no time to occur at all. So, it becomes possible to find (Landau and Lifshitz, 1957) the limiting form of function $\dot{\varepsilon}(\omega)$ at high frequencies, which is valid for any body – metal or dielectric – indifferently. That is to say, the frequency of a field must be high as compared to the frequencies of motion of all (or, at least, of the majority of) electrons in atoms of the given substance. If this condition is met, we can, in calculating the polarization of the substance, consider the electrons to be free, neglecting their interaction among themselves and with the nuclei of atoms (the so-called electronic polarization). Actually, the field of applicability of such an approach begins from the far ultraviolet (UV) band for the lightest elements, or from X-ray frequencies for heavier elements.

The majority of substances which are of interest for remote sensing activity (such as water vapour, water, ice and soil) possess a lot of relaxation mechanisms whose active zones (the dispersion regions) stretch from virtually zero frequencies (tens and hundreds of hertz) up to the optical and UV bands. Because of the drastic distinction in the values of frequencies, relaxation mechanisms in natural substances are usually analysed completely independently for various frequency bands of electromagnetic radiation. Therefore, to avoid confusion, one should have in mind that quantity ε_∞ in one relaxation mechanism can serve as ε_0 in another (the next on the frequency axis) mechanism. Moreover, cases of ‘superposition’ of various mechanisms are possible. It is just such a situation we shall soon encounter in studying relaxation mechanisms in water.

8.1.2 The Kronig–Kramers relations

Since function $\dot{\varepsilon}(\omega)$ was determined in a fairly general form (8.2), it has turned out that some quite general and important properties of this function can be established by considering ω as a complex variable ($\omega = \omega' + j\omega''$). Since function $f(\tau)$ in (8.3) is, by its physical sense, finite for all values of its argument, it follows from the definition of (8.3) that in the whole upper half plane of $\dot{\varepsilon}(\omega)$ there exists an unambiguous function which does not turn to infinity anywhere. In other words, it does not have any singular points. One should pay attention to the fact that the conclusion on the absence of singular points in the $\dot{\varepsilon}(\omega)$ function in the upper half plane is, from the physical point of view, a consequence of the causality principle. This principle consists in the fact that the integration in (8.3) is carried out only over the time preceding the given instant t , as a result of which the range of integration in formula (8.3) extends from 0 to ∞ (but not from $-\infty$ to $+\infty$). The use of well-known theorems from the theory of complex variable functions makes it possible to obtain the important relations between the imaginary and real parts of function $\dot{\varepsilon}(\omega)$. If we are dealing with a pure dielectric, the aforementioned relations state (Landau and Lifshitz, 1957), that:

$$\varepsilon_1(\omega) - 1 = \frac{1}{\pi} \int_{-\infty}^{\infty} \frac{\varepsilon_2(x)}{x - \omega} dx, \quad (8.10)$$

$$\varepsilon_2(\omega) = -\frac{1}{\pi} \int_{-\infty}^{\infty} \frac{\varepsilon_1(x) - 1}{x - \omega} dx, \quad (8.11)$$

where the crossed sign of integral implies that the integral is understood in the sense of its major value. Relations (8.10)–(8.11) are called the Kronig–Kramers relations. Remember that the only essential property of the $\dot{\varepsilon}(\omega)$ function used in deriving these formulas is the absence of singular points in the upper half-plane. Therefore, we can say that the Kronig–Kramers formulas are a direct consequence of the physical causality principle.

Making use of odd function $\dot{\varepsilon}(\omega)$, formula (8.10) can be reduced to the form

$$\varepsilon_1(\omega) - 1 = \frac{2}{\pi} \int_0^\infty \frac{x\varepsilon_2(x)}{x^2 - \omega^2} dx. \quad (8.12)$$

If the conductor is considered, then at point $\omega = 0$ function $\dot{\varepsilon}(\omega)$ has a pole, near which $\dot{\varepsilon}(\omega) = j(\sigma/\omega\varepsilon_{0V})$ (see (8.6)). This results in the appearance of the additional term in formula (8.12):

$$\varepsilon_2(x) = -\frac{1}{\pi} \int_{-\infty}^\infty \frac{\varepsilon_1(x)}{x - \omega} dx + \frac{\sigma}{\omega\varepsilon_{0V}}. \quad (8.13)$$

The principal physical significance of the Kronig–Kramers relations consists in the fact that they stipulate the strict and unambiguous analytical dependence between frequency properties of real and imaginary parts of the dielectric constant (or the complex index of refraction). The frequency dielectric properties of natural media cannot change in an arbitrary (not mutually interrelated) manner. They allow researchers to reconstruct the frequency characteristic of one of the parts of a dielectric constant if the other one is measured (or obtained empirically) well enough. For example, the measured frequency-dependence of dielectric losses in a medium unambiguously determines the frequency characteristic of the dielectric permittivity (and vice versa). The strict and unambiguous relationship (8.12) enables us to find the frequency characteristic of the dielectric permittivity, even from the approximately measured experimental function $\varepsilon_2(\omega)$. The considered relations are often also used for correlating the measurements of the frequency characteristic of dielectric parameters in the case of these measurements being carried out with serious errors (for whatever technical reason). The techniques of application of the Kronig–Kramers relations are diverse and many-faceted.

Since, as we have already noted, in the natural media we encounter, in a series of cases, the superposition of various relaxation mechanisms (see section 8.2), the direct use of the Kronig–Kramers relations for particular applications within limited frequency bands requires a thorough and detailed approach and analysis. In addition, for poor dielectrics there exist frequency bands where function $\dot{\varepsilon}(\omega)$ loses its physical sense in connection with the effects of spatial inhomogeneity of the field. In such cases the use of specific formal procedures is necessary.

8.2 PHYSICAL MECHANISMS OF THE POLARIZATION OF DIELECTRICS

The mechanisms of polarization of dielectrics are diverse and depend on the structure of the substance and on the character of the physicochemical bonds. For example, in ionic crystals (NaCl and others) the polarization is a result of shifting the ions relative to each other (ionic polarization) and of the deformation of electronic shells of individual ions (electronic polarization). In crystals with a covalent bond (the diamond, for instance) the polarization is mainly caused by displacement of electrons giving rise to chemical bonds. In so-called polar dielectrics the molecules

(or the radical groups) represent electric dipoles, which are chaotically oriented in space in the absence of the external electrical field and acquire a predominant orientation in the presence of the external field. Such an ‘orientational’ polarization is typical for many liquids (such as freshwater) and gases. A similar polarization mechanism is related to a ‘jump’ of individual ions from one equilibrium position into another under the electrical field effect. Such a mechanism is observed most frequently in electrolytes (salt water and seawater) and in substances with a hydrogen bond, for example in ice, where the hydrogen ions have several equilibrium positions.

In the electronic polarization mechanism the maximum of losses (the dispersion region) falls in the optical frequencies ($\approx 10^{15}$ Hz) and in the near-IR band. In the polarization caused by displacement of ions, the maximum of dielectric losses shifts to the IR band (10^{12} to 10^{13} Hz). The lower frequencies (in the radio-frequency band) correspond to the maximum of losses at orientational polarization of individual molecules (freshwater, water vapour) or of clusters of molecules (salt water).

In low-molecular organic compounds each molecule has a single dipole and its rotational dynamics is weakly associated with adjacent dipoles. Polar polymeric compounds consist of a great number of dipoles of polar links bound by chemical bonds. Their rotational dynamics depend on each other. The maxima of dielectric losses for such media lie within a wide range of frequencies (10^4 to 10^8 Hz). The forces of intermolecular dipole–dipole interaction between molecules and side groups of adjacent links preclude the turning of links (around simple bonds). As a result, the links undergo only rotational oscillatory motions, rather than full rotation. However, in the absence of freedom of rotation there are some sections in a polymeric chain, called segments, which are capable of changing their form independently of each other. The smaller the segment, the greater the flexibility of molecules and the higher the polymer’s capability to be oriented in the electrical field. Depending on the temperature range, the dipole-group and dipole-segmental polarizations are revealed in polar polymers, the dipole-group polarization being typical for polymers.

In some cases it becomes possible to obtain very rigid chemical bonds in polymers. Owing to the low mobility of the basic polymeric chain and limited capability of motion of individual groups and links, the dipole-group polarization is insignificant, and in the glassy state the dielectric permittivity of polymers is at a minimum. And also at a minimum are the dielectric losses and losses for pure conductivity. Such polymers are widely used in technological applications as polymeric and composite insulating materials (rubbers, plastics, glasses). A similar situation arises in some widely used building materials (such as asphalt, cement, concrete and some modern synthetic materials).

In electrically inhomogeneous media the intersurface polarization can take place, which is caused by the motion of free carriers of charges, which are accumulated near the interface boundaries of regions with heightened specific resistance (intercrystalline sheets, microcracks, fluctuations of physicochemical composition, etc.). The maxima of dielectric losses for such media lie within a wide range of

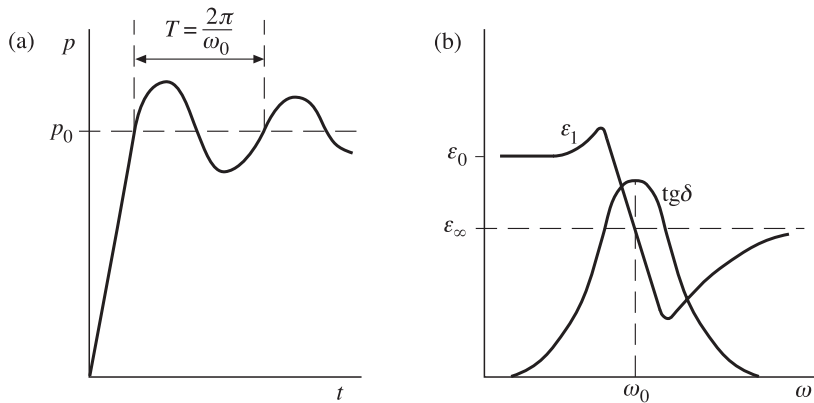


Figure 8.1. Schematic presentation of the effect on polarization properties in the case of the resonance mechanism. (a) Polarization variation in time in cases where the external electric field is switched on. (b) Frequency characteristics of $\epsilon_1(\omega)$ and $\text{tg}\delta(\omega)$.

frequencies (10^3 to 10^9 Hz). Bright natural examples of such media are various modifications of seawater and freshwater ice, wet soil with bound water electrolytes inside the soil, as well as the water–ice system and snow cover at the phase transition instant.

The frequency character of $\epsilon_1(\omega)$ and $\text{tg}\delta(\omega)$ dependencies in the dispersion region is determined by the polarization mechanism. In the case of ionic and electronic polarization on applying the external field \mathbf{E} the variation in time t has a character of attenuating oscillations (Figure 8.1(a)). Accordingly, the frequency dependencies of $\epsilon_1(\omega)$ and $\text{tg}\delta(\omega)$ are called resonance dependencies (Figure 8.1(b)). This is due to the fact that, since the polarization of a dielectric is mainly caused by small displacements of electrons and ions, the dielectric can be considered as a set of harmonic oscillators which experience forced oscillations with attenuation in the alternating field. This type of polarization is sometimes called the deformation polarizability of dielectrics.

In orientational (dipolar) polarization the latter one has a relaxation character (Figure 8.2(a)), and then the frequency dependencies of $\epsilon_1(\omega)$ and $\text{tg}\delta(\omega)$ are called relaxation dependencies (or Debye-type relaxations) (Figure 8.2(b)). The times of polarization establishment or disappearance depend in this case on the intensity of the thermal motion of atoms, molecules (or ions), i.e. on the physicochemical structure of the substance and on the physical temperature. In orientational polarization the characteristic relaxation time is determined by the time of orientation of individual molecules in the direction of the external field \mathbf{E} . It depends on the value of dipole moments of molecules, on the viscosity of a medium, on the dipole–dipole interaction energy and on the other physicochemical parameters. At room temperature the characteristic time varies within very wide limits, from 10^{-3} to 10^{-10} s, for gases and fluids, this time being, as a rule, lower than for solid bodies. In solid dielectrics the dipole polarization is often caused by weakly bound ions, which can have several equilibrium positions. Under the effect of an external field and thermal

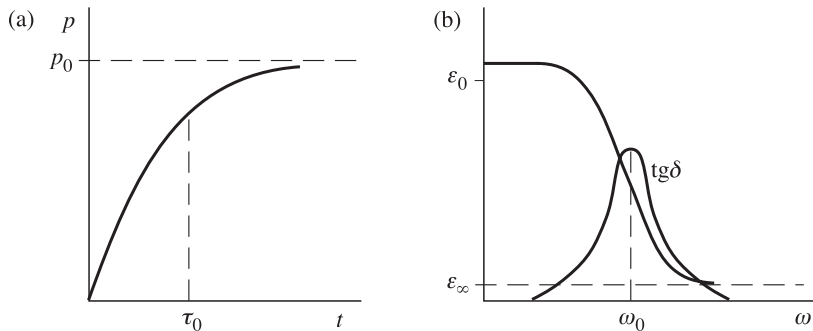


Figure 8.2. Schematic presentation of the effect on polarization properties in the case of the relaxation mechanism. (a) Polarization variation in time in cases where the electric field is switched on. (b) Frequency characteristics of $\epsilon_1(\omega)$ and $\text{tg}\delta(\omega)$.

motion the ions can transfer from one equilibrium position to another, while overcoming potential barriers. In this case the characteristic times vary within a wide range, occupying large time domains.

In electrically inhomogeneous media an intersurface polarization is observed that is caused by the motion of free carriers of charge accumulating near the boundaries of regions with sharply distinguished electrical properties. In these media processes of a complicated percolation type take place, as well as the processes of propagation of the charge-density wave state (Pinteric *et al.*, 2001; Bordonskii and Filipova, 2002). These effects are related to the multi-scale structural features and to the hierachic, fractal-type structure of current-conducting admixtures (Park, 2001). The issues of finding the characteristic time domains in such systems are fairly complicated and ambiguous. Studies in this direction are being efficiently developed now.

In real dielectrics several polarization mechanisms with different characteristic times can often take place simultaneously, which results in a more complicated character of frequency dependencies of $\epsilon_1(\omega)$ and $\text{tg}\delta(\omega)$. In this case in some frequency bands the mechanisms of pure Debye type and of resonance type can merge with relaxation systems that have a wide spectrum of dielectric relaxation times. For these reasons the separation and fixation of various mechanisms from the real experimental data represents a complicated experimental problem.

As an important example, we shall consider the frequency features of the complex index of refraction for liquid water in a very wide wavelength band – from 10^{-4} to 10^{+4} cm, i.e. ranging over eight orders of magnitude (see Figure 8.3). The analysis of an imaginary part of the index of refraction indicates that some kind of basic pattern (designated as KDC in Figure 8.3) of the frequency-dependence of $\chi(\lambda)$ is the characteristic form of the pure Debye-type relaxation mechanism. It has a maximum at a wavelength of about 1 cm and then the characteristic drops in the direction of increasing values of wavelengths as λ^{-1} and in the direction of decreasing values of wavelengths as λ^{+1} . The total band of frequencies included in this mechanism are called the Debye absorption band. The index of refraction (its real

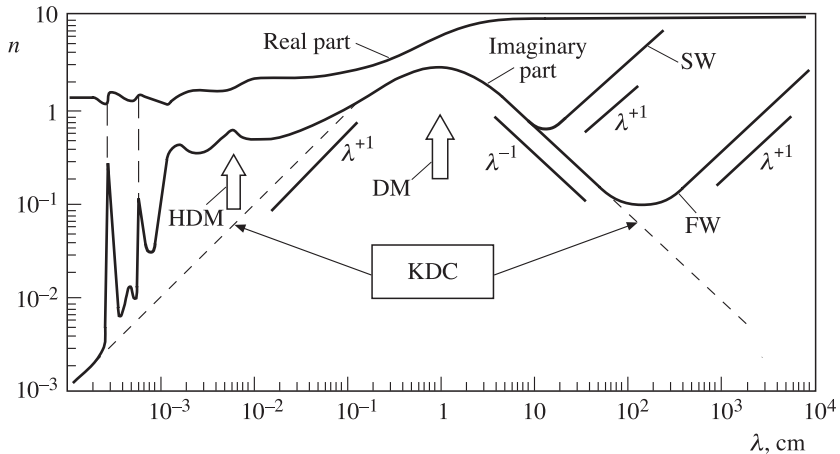


Figure 8.3. The semi-quantitative presentation of a complex index of refraction for liquid water. The temperature is 25°C. KDC is the key Debye contribution. DM is the maximum of the Debye absorption band. HDM is the maximum of the hyper-Debye absorption band. FW is freshwater. SW is salt (sea) water. Graphs are by E. Sharkov using data from work by Ray (1972); Afsar and Hasted, 1977; Sharkov (1983, 1984); Liebe *et al.* (1991).

part) is characterized by the rapid drop (decrease) of its value at the absorption maximum frequency (Figure 8.2(b)). Beginning with the wavelengths of about 1 mm another relaxation mechanism comes into effect. It is called the hyper-Debye-type mechanism, though it is, in general, very close to the pure Debye-type mechanism with an absorption maximum near 0.06 mm. This circumstance sharply distorts the characteristic Debye-type drop in absorption in the direction of short wavelengths (Figure 8.3). The next (in the direction of shorter wavelengths) absorption maximum, also of the Debye type, falls in the wavelength of about 0.02 mm. The next two absorption bands with maxima at wavelengths of 6×10^{-4} and 3×10^{-4} cm are already determined by resonance types of polarization, which have a typical frequency form both in absorption and in the real index of refraction (Figure 8.1(b)).

As far as salt water (electrolyte) is concerned, for a long time (more than 50 years) there had existed a naive knowledge about the pure Debye-type relaxation mechanism in the polarization properties of electrolytes, in which only one known component, caused by ionic conductivity, was taken into account (see equations (8.7)–(8.8)). Strictly speaking, this knowledge is reflected in Figure 8.3 in the frequency dependencies of the imaginary part of the index of refraction at long wavelengths for fresh water (with low conductivity) and for salt water (with high conductivity). However, the critical insight into the problem, undertaken by E. Sharkov (1984), has demonstrated the complete groundlessness of this point of view. The relaxation mechanism of electrolytes was found to significantly differ from the Debye-type, both in the type of absorption band, and in a sharp (and rather surprising) dependence of electrostatic permittivity on the salt concentration of a solution. We shall analyse this problem in more detail in section 8.

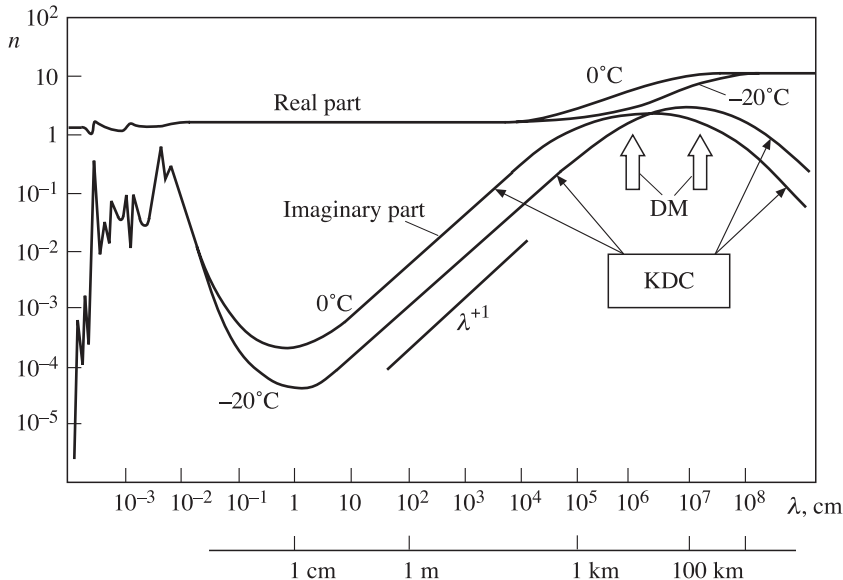


Figure 8.4. The semi-quantitative presentation of a complex index of reflection for ice samples. The temperature range is $0\text{--}20^\circ\text{C}$. Graphs are by E. Sharkov using an interpolation between microwave data and infrared data (Ray, 1972; Fujita *et al.*, 2000; Matsuoka *et al.*, 1996). See notation in Figure 8.3.

The phase transition of liquid water into the solid state is characterized by a basic change of its polarization properties. The frequency characteristics of the complex index of refraction for water in a solid state (ice) are presented in Figure 8.4 within a very wide wavelength band – from 10^{-4} to 10^{+9} cm (or thirteen orders of magnitude (!)). A key feature of the polarization properties of ice is the fantastic ‘jump’ in the numerical value of relaxation wavelength from 1 cm to $10\text{--}100\text{ km}$ (depending on the temperature), i.e. 6–7 orders of magnitude. Such a grand reconstruction in the polarization mode of the most widespread substance on our planet (water) nonplussed researchers for a long period of time. It was believed that for the solid phase of water (freshwater ice) the pure Debye relaxation model remained valid with changing the value of the time relaxation constant only.

Modern investigations have shown that for the microwave band ($1\text{--}100\text{ GHz}$) the real part of the relative dielectric permittivity of freshwater ice (for homogeneous samples) still remained a fairly definite and stable quantity that is almost independent of frequency $\varepsilon_1(\omega) = 3.15$ (Matzler, 2000; Fujita *et al.*, 2000). It was found that the imaginary part can be presented in this band as an articulation of two branches – the high-frequency tail of the Debye dispersion and the low-frequency tail of lattice vibration in the far-infrared region. In this connection, it emerges that the imaginary part depends critically on weak mineralization (which is always present in natural freshwaters), on the presence of organic substance and admixtures of gas bubble type, and to the thermodynamic temperature. But, in general, modern

authors adhere to the Debye relaxation spectrum $\varepsilon_2(\omega) \sim \omega^{-1}$ (Bordonskii, 1990; Fujita *et al.*, 2000; Bordonskii *et al.*, 2002). In the low-frequency (kilohertz and hertz) band the chief effect is the structural (possibly, of Debye-type) polarization of fractal and percolation type, as well as the presence of mineral admixtures (the chemical purity of a sample). Here we are dealing, apparently, with a complicated, complex mode of polarization. The researchers began to fix their attention on this wavelength band in connection with two issues: (1) studying the depth distribution of moisture in soils and grounds (Stoffregen *et al.*, 2002); and (2) the attempts of active electromagnetic sensing the surface covers of Mars with the purpose of detecting subsurface water, water-ice and rock–ice–water mixtures in them (Grimm, 2002).

The solid phase, formed from seawater, turned out to be so complicated (in the electrodynamic sense) and diverse that it is difficult now to compose a generalized picture of dielectric properties. This is because of the fact that they were found to be strongly dependent on the mineral composition of seawater in a particular area, on the temperature and on the meteorological history of the solid phase formation. This results, in its turn, in the formation of a variety of types of sea-ice with sharply distinctive dielectric properties. The strong spatial-temporal variability of sea-ice fields and their hierachic structure highly complicate the pattern-recognition procedures in remote microwave observations (Bespalova *et al.*, 1976b; Comiso and Kwok, 1996; Belchansky and Alpatksy, 2000; Comiso, 2000).

Because glacial ice (in the Antarctic, Greenland, mountain glaciers) is formed via the morphological ice formation from precipitated snow, rather than from a liquid phase, then, obviously, the internal geometrical structure in three-dimensional mesoscales has a strong effect on the dielectric and emissive properties of the glacial ice fields. This has been clearly exhibited even in the first radiothermal investigations of the Antarctic ice cover – the so-called ‘Antarctica puzzle’ (Basharinov *et al.*, 1971; Gurvich *et al.*, 1973; Gloersen *et al.*, 1974). In glacial ice samples, taken for laboratory investigation, the dielectric properties (in ‘micro-scales’) were found to be close to those of freshwater ice, but with strong temperature effects and dielectric anisotropy (Matsuoka *et al.*, 1996, 1997). However, the overall pattern (in the wide wavelength band) of glacial ice’s dielectric properties has not been developed yet.

The judgements have already repeatedly been stated that, in spite of having identical names, all these substances – freshwater ice, sea-ice and glacial ice, as well as freshwater and seawater – are significantly different in the electrodynamic sense, if they are qualified by class of dielectric and, accordingly, by emissive characteristics.

8.3 RELAXATION POLARIZATION MODELS

Many substances on our planet belong to the class of polar dielectrics whose overall polarization is made up from deformational and orientational polarizations. In this case, however, the prevailing type of polarization in these substances is

the orientational one. Therefore, below we shall consider in more detail the basic types of models of orientational (relaxation) polarization and, first of all, the Debye-type models (with a single relaxation time), as well as relaxation models with a wide spectrum of relaxation times (the concept of a multiplicity of relaxation times).

8.3.1 The Debye model

The formulas for the description of frequency dependencies of the simplest-type relaxation polarization and the simplest hydrodynamic model of such a relaxation were established by P. Debye (Debye, 1929). The processing methodology, developed in this work, was widely disseminated afterwards in processing the experimental results obtained from studying a vast class of dielectrics, as well as systems of a different physical nature. This circumstance is physically associated with the fact that here is considered the simplest and, as it turned out later, a completely fundamental model, where the polarization dependence $f(\tau)$ (see equations (8.1) and (8.3)) is exponential:

$$f(\tau) = \text{const} \exp(-\tau/\tau_0) = \frac{\varepsilon_0 - \varepsilon_\infty}{\tau_0} \exp(-\tau/\tau_0), \quad (8.14)$$

where τ_0 is some characteristic quantity having the dimension of time and indicating that during the time τ_0 the polarization will change (increase and decrease) e times.

The substitution of (8.14) into (8.3) and appropriate integration results in the expression:

$$\dot{\varepsilon}(\omega) - \varepsilon_\infty = \frac{\varepsilon_0 - \varepsilon_\infty}{1 + j\omega\tau_0}. \quad (8.15)$$

Separating the real and imaginary parts of the complex dielectric permittivity, we obtain the well-known Debye formulas:

$$\varepsilon_1(\omega) = \varepsilon_\infty + \frac{\varepsilon_0 - \varepsilon_\infty}{1 + \omega^2\tau_0^2}, \quad (8.16)$$

$$\varepsilon_2(\omega) = (\varepsilon_0 - \varepsilon_\infty) \frac{\omega\tau_0}{1 + \omega^2\tau_0^2}. \quad (8.17)$$

These formulas have been widely used in various areas of natural science (not only in dielectric relaxation theory), since the exponential system's response to the external (stepwise) effect is characteristic of a very wide class of physical systems – radio-engineering and radiophysical systems for instance (see Chapters 2 and 3).

The spectral behaviour of quantities $\varepsilon_1(\omega)$ and $\varepsilon_2(\omega)$ as a function of $\lg(\omega t)$ is presented in Figure 8.5 in the dimensionless form. As the figure shows, in the low-frequency $\lg(\omega t) < -3$ and high-frequency $\lg(\omega t) > 3$ ranges no variation of the complex permittivity with $\lg(\omega t)$ is observed. For intermediate values $-3 \leq \lg(\omega t) \leq 3$ the appearance of dispersion $\varepsilon(\omega)$ is typical. From Figure 8.5 it directly follows that the relaxation maximum frequency is related to the relaxation time as follows: $f_S = (2\pi\tau)^{-1}$. In some cases the notion of the relaxation maximum

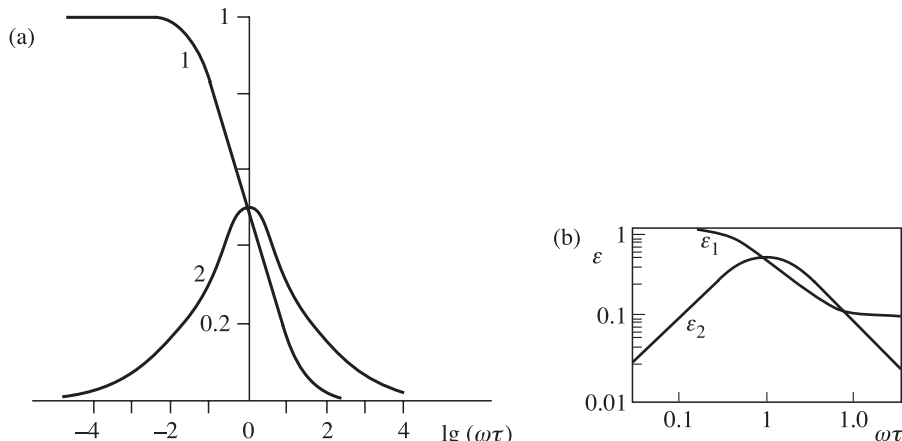


Figure 8.5. Frequency properties of $\varepsilon_1(\omega)$ and $\varepsilon_2(\omega)$ for Debye type dielectric media: (a) in semi-logarithmic coordinates in normalized dimensionless form, 1, $(\varepsilon_1(\omega) - \varepsilon_\infty)/(\varepsilon_0 - \varepsilon_\infty)$, 2, $\varepsilon_2(\omega)/(\varepsilon_0 - \varepsilon_\infty)$; (b) in bi-logarithmic coordinates for single Debye relaxation between $\varepsilon_0 = 1$ and $\varepsilon_\infty = 0.1$.

wavelength is used, whose value is equal to $\lambda_S = c(2\pi\tau)^{-1}$. The analysis of an imaginary part of the index of refraction of real media (water) indicates that in exactly this part of the frequency band the Debye mechanism forms some kind of pattern (designated as KDC in Figure 8.3) of the frequency dependence $\varepsilon_2(\lambda)$ (Figure 8.5(b)). This pattern represents the characteristic form of the pure Debye-type relaxation mechanism, which has a maximum at the wavelength λ_S and then the characteristic drops in the direction of long wavelengths as λ^{-1} and in the direction of shorter wavelengths as λ^{+1} (Figure 8.5(b)). This frequency peculiarity is quite typical for the pure Debye-type mechanism only, and we shall use it in analysing the experimental data and in revealing the Debye type of relaxation.

It follows from the equation, that for $\omega = 0$, $\varepsilon_1 = \varepsilon_0$, where ε_0 is (as we have already noted) the static dielectric constant. At very low frequencies the dipoles have time enough to synchronously follow the variation of the external electric field, and the polarization reveals itself completely. The value of the factor of losses $\varepsilon_2(\omega)$ is insignificant in this case. At very high frequencies the dipoles have no time to be oriented; they can be considered as motionless, and the orientational polarization is absent in this case. Therefore, for $\omega \rightarrow \infty$ $\varepsilon_2 = 0$ as well. Note that the frequency tending to infinity is certainly a purely formal procedure. Really, here we deal with the region lying outside the sphere of influence of the given relaxation mechanism. However, as we have already shown for the example of the dielectric properties of water, the merging of effects of various mechanisms is possible in some frequency bands (see Figure 8.3 and section 8.2). The prominent dispersion of quantity $\varepsilon(\omega)$ is characteristic for the intermediate range of frequencies.

The relaxation time τ was introduced for the first time as a parameter into the relaxation Debye theory (Debye, 1929). The substance response to the effect of the

external electromagnetic field, varying in time according to the harmonic law, is described by the phenomenological equation (8.3). The response function depends on the character of thermal motion of polar molecules. It is the dynamics of molecules which is usually associated with the relaxation time. The given parameter characterizes, in the general case, the process of spontaneous transition of a nonequilibrium macroscopic system into the state of thermodynamic equilibrium. The relaxation time depends on the temperature and on the intermolecular interaction potential. This quantity is determined directly from the experiment and corresponds, in the general case, to the frequency at which the maximum of dielectric losses is achieved. The reverse relaxation time $1/\tau_0$ characterizes the rate of dipoles' polarization establishment during the field action time. The use of the 'relaxation' term is most justified in describing the dynamics of molecular processes as the rate of equilibrium state establishment after removing the external effect. Exactly such a sense is given to the relaxation parameter that appeared in equations (8.15)–(8.17) in the Debye relaxation theory.

The simplest of existing ideas on the character of relaxation processes in polar liquids are based either on the hydrodynamic (and phenomenological) Debye model (Debye, 1929), or on the Frenkel model (Frenkel, 1975). In the Debye model the process of molecules reorientation in the liquid phase is considered to be the result of rotational diffusion of a solid sphere in the continuous viscous medium. According to Frenkel, on the other hand, the reorientation of molecules in the liquid phase is accomplished by jumps, by overcoming some potential barrier. Both models, in spite of their great difference, result in the simplest type of relaxation process, which can be characterized by a single relaxation time τ_0 . In other words, the spectrum $G(\tau)$ of relaxation times (if it does really exist) can be presented in the form of delta-function $G(\tau) = \delta(\tau - \tau_0)$.

It was shown in some papers that a single relaxation time will always be observed in a liquid, if the following conditions are satisfied:

- (1) the orienting interactions between molecules are absent;
- (2) the molecules' reorientation process (when applying or removing the external electric field) takes place as the rotation with friction or as the transition over the potential barrier; and
- (3) all dipoles are at equivalent positions.

If these conditions are met, the dielectric characteristics of a polar liquid as a function of the external field frequency will correspond to the Debye model (with a single relaxation time).

The following relation can easily be obtained from the Debye formulas (8.16) and (8.17):

$$\left[\varepsilon_1(\omega) - \frac{\varepsilon_0 - \varepsilon_\infty}{2} \right]^2 + \varepsilon_2^2 = \left(\frac{\varepsilon_0 - \varepsilon_\infty}{2} \right)^2. \quad (8.18)$$

Expression (8.18) represents the equation of a circle with radius $(\varepsilon_0 - \varepsilon_\infty)/2$.

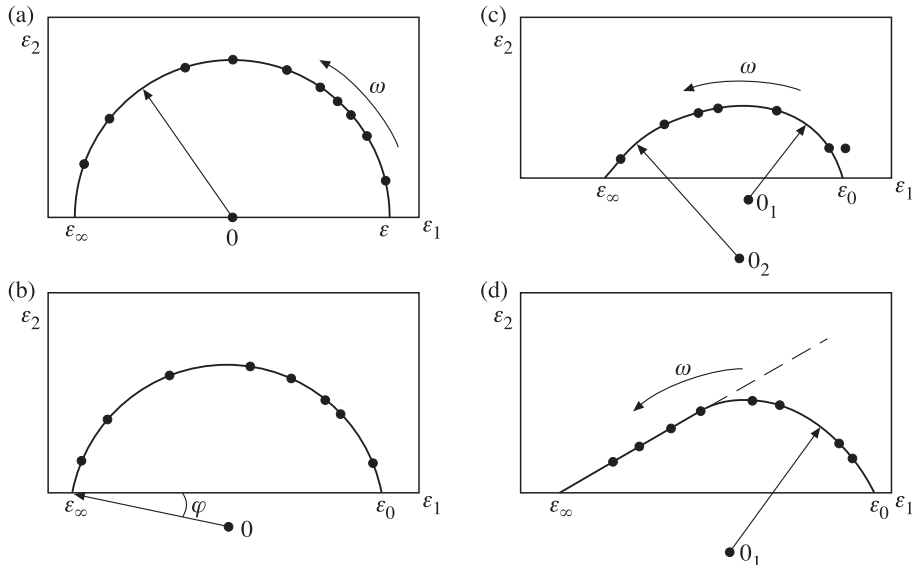


Figure 8.6. Relationship of the imaginary part of complex permittivity as a function of the real part (Cole–Cole diagram) for dielectric medium with various polarization mechanisms. (a) Debye model, (b) Cole–Cole model, (c) Davidson–Cole model, (d) Havriliak–Negami model. Experimental data are marked by black dots. The arrow points to an increase in frequency.

Therefore, for performing the diagram technique on the experimental data correspondence to the Debye model it is necessary to plot the values of ε_1 along the abscissa axis and the values of ε_2 , found at various frequencies, at $T = \text{const}$, along the ordinate axis. And if the Debye formulas are valid, we shall obtain a full semicircle, whose centre lies on the abscissa axis at point $(\varepsilon_0 - \varepsilon_\infty)/2$ (Figure 8.6(a)). The position of the experimental data in the Cartesian coordinate system $\varepsilon_1 - \varepsilon_2$ was called the Cole–Cole diagrams. The deviations in the experimental data position from a semicircle will testify to the obvious deviation of relaxation properties of a dielectric from the Debye model. Such a kind of presentation is used not only in analysing the relaxation properties of dielectrics, but in studying the other physical systems with the relaxation mechanism close to the Debye one.

The relaxation time value can be estimated by formulas which directly follow from the Debye relations (8.16)–(8.17):

$$\tau_0 = \frac{1}{\omega} \frac{\varepsilon_2(\omega)}{\varepsilon_1(\omega) - \varepsilon_\infty}, \quad (8.19)$$

where the real and imaginary parts of the dielectric permittivity are taken from the experimental data at the working (given) frequency of measurements.

The diagram technique is very convenient for estimating the values of ε_0 and ε_∞ , based on using strictly linear interpolation in the following relations being a

consequence of the Debye formulas:

$$\varepsilon_1(\lambda, t) = \varepsilon_0(t) - \lambda_S(t) \frac{\varepsilon_2(\lambda, t)}{\lambda}, \quad (8.20)$$

$$\varepsilon_1(\lambda, t) = \varepsilon_\infty(t) + \lambda \frac{\varepsilon_2(\lambda, t)}{\lambda_S(t)}. \quad (8.21)$$

The symmetry in the Debye formulas makes it possible to form one more series of graphical techniques for experimental data processing; they are summarized in the book by Akhakov (1977).

The deviations in using the Cole–Cole diagram and linear approximations are so noticeable and impressive that they can serve as clear evidence of the deviation of a dielectric's polarization properties from the Debye model. Some indicative examples of using these approaches in analysing the dielectric properties of fresh and salt water are presented in papers by Sharkov (1983, 1984, 1996c) and Liebe *et al.* (1991) (see also sections 8.4 and 8.5 below).

8.3.2 Models of multiplicity of relaxation times

The Debye model successfully describes the frequency dispersion of the complex dielectric permittivity for some dielectrics (such as freshwater or alcohols). However, many cases are known (and of importance for us is to mention, first of all, solutions of salts: electrolytes and seawater), where the Debye formulas do not describe the experimental frequency dependencies in principle. However, the success of the Debye model was so great, that the further development of non-Debye relaxation mechanisms has advanced mainly by way of using the concept of a multiplicity of Debye relaxation times for non-Debye-type dielectrics. Certainly, such an approach is only one of those possible; however, it dominates now in dielectric relaxation theory. Its essence is as follows.

In liquids and solid substances (of polymer type), consisting of composite clusters of molecules or of polyatomic molecules, a variety of dielectric Debye relaxation times is observed where each dipole has its own polarization establishment time. In other words, there exists some particular distribution of dielectric relaxation times around its most probable value. The character of the distribution and its parameters will be just those important physical characteristics that determine the structure of the substance. And it can be supposed that for polar high-molecular systems (including organic compounds) the existence of a variety of dielectric relaxation times should be observed all the more.

Thus, if the number of relaxation times is fairly high, their distribution can be presented as a continuous set of times. And in this case we can use the methodology of introducing the distribution density $F(\tau)$ (or, as is sometimes said, the ‘spectrum’) of Debye-type relaxation times in the field of their existence (see Chapter 2). In the general case the complex dielectric permittivity is written as

$$\frac{\dot{\varepsilon}(\omega) - \varepsilon_\infty}{\varepsilon_0 - \varepsilon_\infty} = \int_0^\infty \frac{F(\tau) d\tau}{1 + j\omega\tau}, \quad (8.22)$$

where $F(\tau) d\tau$ is the fraction of the Debye relaxation processes with the relaxation time falling in the range of $\tau + d\tau$. If we suppose the existence of a single relaxation time in a system (or, in other words, $F(\tau) = \delta(\tau - \tau_0)$), then expression (8.22) automatically transfers into the Debye relationship (8.15). As usual, natural normalization is introduced for function $F(\tau)$, namely,

$$\int_0^\infty F(\tau) d\tau = 1. \quad (8.23)$$

Separating the real and imaginary parts of expression (8.22), we obtain:

$$\frac{\varepsilon_1(\omega) - \varepsilon_\infty}{\varepsilon_0 - \varepsilon_\infty} = \int_0^\infty \frac{F(\tau) d\tau}{1 + \omega^2 \tau^2}, \quad (8.24)$$

$$\frac{\varepsilon_2(\omega)}{\varepsilon_0 - \varepsilon_\infty} = \int_0^\infty \frac{\omega \tau F(\tau) d\tau}{1 + \omega^2 \tau^2}. \quad (8.25)$$

In view of the fact that the relaxation spectra, as experiments have shown, overlap considerable spans of time, the distributions of dielectric relaxation times are considered in the logarithmic coordinates. That is, with the replacement of variables $s = \ln(\tau_0/\tau)$ the new function $Z(s)$ of relaxation times distribution is introduced, which follows from the normalization condition:

$$\int_0^\infty F(\tau) d\tau = \int_{-\infty}^\infty Z(s) ds = 1. \quad (8.26)$$

Then expressions (8.24) and (8.25) will take the form, respectively,

$$\frac{\varepsilon_1(\omega) - \varepsilon_\infty}{\varepsilon_0 - \varepsilon_\infty} = \int_{-\infty}^\infty \frac{Z(s) ds}{1 + \exp[2(x - s)]}, \quad (8.27)$$

$$\frac{\varepsilon_2(\omega)}{\varepsilon_0 - \varepsilon_\infty} = \int_{-\infty}^\infty \frac{\exp(x - s) Z(s) ds}{1 + \exp[2(x - s)]}, \quad (8.28)$$

where $x = \ln(\omega \tau_0)$.

Thus, the procedure of the experimental data analysis is reduced to searching for function $Z(s)$, since it is just an instantaneous frequency characteristic of molecular mobility in a studied object and is determined by physicochemical properties of the latter.

Strictly speaking, finding a true distribution function $Z(s)$ is reduced to the solution of so-called reverse problems of the dielectric spectrometry (Usmanov, 1996), namely, to the relations:

$$\int_{-\infty}^\infty \frac{Z(s) ds}{1 + \exp[2(x - s)]} = U(x), \quad (8.29)$$

$$\int_{-\infty}^\infty \frac{\exp(x - s) Z(s) ds}{1 + \exp[2(x - s)]} = V(x), \quad (8.30)$$

where $U(x)$ and $V(x)$ designate quantities $(\varepsilon - \varepsilon_0)/(\varepsilon_0 - \varepsilon_\infty)$ and $\varepsilon_2/(\varepsilon_0 - \varepsilon_\infty)$,

which were obtained experimentally with some measurement errors. The latter, in their turn, represent an additive type of noise having a fluctuation character, with the normal distribution law (see Chapter 2).

Indeed, the solution of integral equations (8.29) and (8.30) results in the well-known reverse problem of restoring $Z(s)$ from the approximate values of $U(x)$ and $V(x)$, which is just an indicator of incorrectly stated problem (Tichonov and Arsenin, 1979). The sought distribution function $Z(s)$ is determined by solving the first-order Fredholm equation of convolution type. Really, the integral equations (8.29) and (8.30) can easily be rewritten in the form of the first-order Fredholm equation of convolution type. For example, equation (8.30) can be written as

$$\int_{-\infty}^{\infty} K(x-s)Z(s) \, ds = V(x), \quad (8.31)$$

where

$$K(x-s) = \frac{\exp(x-s)}{1 + \exp[2(x-s)]} = \frac{1}{2} \operatorname{ch}(x-s) \quad (8.32)$$

($\operatorname{ch}(x-s)$ is the hyperbolic cosine) is called the core of the integral equation. For solution of the integral equations of convolution type some rather complicated techniques of statistical regularization are applied, including Tichonov's method of regularization (Tichonov and Arsenin, 1979), which require serious mathematical training and appropriate computer means (Usmanov, 1996).

Historically, however, the first graphical constructions applied in polarization investigations of dielectrics were those of the Cole–Cole diagram type. Such approaches were called the ‘traditional’ methods, applying the ‘matching’ empirical functions of distribution of dielectric relaxation times, offered by Cole and Cole (1941), Davidson and Cole (1950), Havriliak and Negami (1967) as well as the series of other functions. Such a graphical ‘traditional’ approach was found to be, nevertheless, in many cases a rapid and rather reliable method for studying the dielectrics. And for these reasons such an experimental technique is actively applied now (we shall demonstrate this below in the analysis of dielectric properties of freshwater and electrolytes). It should be emphasized that similar graphical approaches are used not only in studying dielectrics, but also in studying physical systems of a quite different nature which possess relaxation properties at the same time.

Now we consider briefly the technique of graphical determination of limiting values of dielectric permittivity for a given (single) relaxation mechanism. The values of parameters ε_0 and ε_∞ in the case of applying any of considered empirical distribution functions $Z(s)$ are determined similarly. If $\omega\tau \rightarrow \infty$, then in all cases $\varepsilon_1(\omega) \rightarrow \varepsilon_\infty$ and $\varepsilon_2(\omega) \rightarrow 0$; therefore, $\varepsilon(\omega) \rightarrow \varepsilon_\infty$. When $\omega\tau \rightarrow 0$, $\varepsilon_1(\omega) \rightarrow \varepsilon_0$ and $\varepsilon_2(\omega) \rightarrow 0$; then $\varepsilon(\omega) \rightarrow \varepsilon_0$. For these reasons the dielectric parameters ε_0 and ε_∞ can be found as the points of intersection of experimental dependencies $\varepsilon_2 = f(\varepsilon_1)$ with the axis of real numbers at high and low frequencies for any polarization mechanism. In the given context we mean, certainly, the frequency bands in which the given (single) relaxation mechanism is actively manifested. The most probable

dielectric relaxation time τ_0 (under the action of any mechanism) is determined from the condition of maximum of the frequency dependence of the factor of losses:

$$2\pi f_0 \tau_0 = 1, \quad (8.33)$$

where f_0 is the frequency of a maximum of the factor of losses. As a rule, in the region of active manifestation of polarization properties the experimental dependence $\varepsilon_2 = f(\omega)$ has a prominent extremum (see examples in Figures 8.3 and 8.4), and f_0 is determined fairly reliably for the given mechanism. If, however, the interrelation between various mechanisms is complicated, the problem of determination of the frequency of a maximum of losses and limiting values of dielectric permittivity represents a fairly complicated problem (Sharkov, 1983, 1984, 1996c; Liebe *et al.*, 1991). In this case it is necessary to use *a priori* data about possible relaxation mechanisms.

8.3.3 The Cole–Cole model

As we have noted above, many experimental results are known where the Debye formulas do not describe the frequency behaviour of dielectric properties of a dielectric. In this case the experimental curve $\varepsilon_2 = f(\varepsilon_1)$ is not a full arc of semicircle with the centre lying on the abscissa axis. It represents either a non-full arc segment of a circle, or ‘bevelled arcs’, composed as though of two semicircles with spaced centres and with various values of radii. More complicated constructions are also possible, such as the line segment transferring into the arc segment of a circle. It is important to note that each of these geometrical constructions corresponds to some particular feature of the relaxation mechanism.

If the experimental curve $\varepsilon_2 = f(\varepsilon_1)$ represents an arc of a semicircle with the centre lying below the abscissa axis (Figure 8.6(b)), then in this case, as the special investigations have shown (Cole and Cole, 1941), the dielectric permittivity can be described by the following empirical equation called the Cole–Cole equation:

$$\frac{\dot{\varepsilon}(\omega) - \varepsilon_\infty}{\varepsilon_0 - \varepsilon_\infty} = [1 + (j\omega\tau_0)^{1-\alpha}]^{-1}, \quad (8.34)$$

where τ_0 is some average (or effective) value of the relaxation time of the dielectric polarization process, and α is some parameter describing the character of distribution of relaxation times. All these considerations are valid, of course, provided that the concept of multiplicity of relaxation times is accepted.

As the solution of integral equations (8.29)–(8.30) has shown, the Cole–Cole equation corresponds to the symmetrical distribution of relaxation times, which is close to the Gaussian distribution and is determined by the function:

$$Z(s) = \frac{1}{2\pi} \frac{\sin(\pi\alpha)}{\operatorname{ch}[(1-\alpha)s] + \cos(\pi\alpha)}. \quad (8.35)$$

Investigation of the molecular mobility of dipoles of some polar substances has shown that the use of a purely normal (Gaussian) distribution of relaxation times is expedient. However, the direct use of the techniques of reverse spectrometry

problems (8.29)–(8.30) is rather cumbersome in this case, which requires the development of a series of approximate methods (Usmanov, 1996).

8.3.4 The Davidson–Cole model

Suppose the molecular structure of a dielectric is such that the distribution of relaxation times has a sharply asymmetric form. So, for example, the dielectric does not have any relaxators with a relaxation time lower than the specified one. In this case the aforementioned circumstance is clearly exhibited on the graphical presentation $\varepsilon_2 = f(\varepsilon_1)$ as well – it becomes sharply asymmetric also. If the function of distribution of relaxation times $Z(s)$ is written in a sharply asymmetric form:

$$Z(s) = \begin{cases} \frac{\sin(\beta\pi)}{\pi} (1 - \exp(-s))^{-\beta} & \tau > \tau_0, \\ 0 & \tau \leq \tau_0 \end{cases} \quad (8.36)$$

then, as Davidson and Cole (1950) have shown, the complex dielectric permittivity can be presented by the following semi-empirical Davidson–Cole equation:

$$\frac{\dot{\varepsilon}(\omega) - \varepsilon_\infty}{\varepsilon_0 - \varepsilon_\infty} = (1 - j\omega\tau_0)^{-\beta}. \quad (8.37)$$

In the graphical form of the Cole–Cole diagram this model represents a ‘bevelled arc’ composed as though of two non-full arcs with spaced centres and with various values of radii (Figure 8.6(c)). Special graphical techniques were developed for the determination of distribution parameters (Akhadov, 1977; Usmanov, 1996).

8.3.5 The Havriliak–Negami model

Two various empirical expressions for the function of distribution of relaxation times, used earlier for description of the ‘arc segment’ (8.34) and ‘bevelled arc’ (8.37), can be generalized in the form of the Havriliak–Negami distribution (Havriliak and Negami, 1967):

$$\frac{\dot{\varepsilon}(\omega) - \varepsilon_\infty}{\varepsilon_0 - \varepsilon_\infty} = [1 + (j\omega\tau_0)^{1-\alpha}]^{-\beta}. \quad (8.38)$$

If we assume that in equation (8.38) $\beta = 1$, we shall obtain the expression for the Cole–Cole distribution function in the form of (8.34). For $\alpha = 0$ we obtain the expression for the Davidson–Cole distribution function in the form of (8.37), and at simultaneous equalities $\alpha = 0$ and $\beta = 1$ formula (8.38) represents the Debye function (8.15). Figure 8.6(d) represents the asymmetric arc function $\varepsilon_2 = f(\varepsilon_1)$, which corresponds to the Havriliak–Negami distribution function. As seen from the figure, this theoretical curve $\varepsilon_2 = f(\varepsilon_1)$ is linear in the high-frequency band and represents an arc segment in the low-frequency band. To check the possibility of quantitative description of the experimental data of dielectric measurements by the empirical Havriliak–Negami distribution function (8.38), it is necessary to determine graphically the values of five dispersion parameters $(\varepsilon_0, \varepsilon_\infty, \alpha, \beta, \tau_0)$.

Parameter ε_0 is obtained by extrapolation up to intersection of dielectric permittivity $\varepsilon_1(\omega)$ with the abscissa axis in the low-frequency band, and parameter ε_∞ is found by linear extrapolation of experimental data points $\varepsilon_2 = f(\varepsilon_1)$ up to intersection with the same axis in the high-frequency band (Figure 8.6(d)). The other parameters are determined by the special graphical procedure (Usmanov, 1996).

Detailed dielectric investigations of complex polar dielectrics (of natural and artificial origin) have indicated that in many natural substances there takes place the superposition of both relaxation dipole processes and the phenomena of resonance character, and this occurs in rather complicated combinations (the simplest versions are demonstrated in Figures 8.3 and 8.4). For analysing such complicated dipole-cluster dielectric processes, researchers have used, along with the models listed above, some more complicated empirical functions of distribution of relaxation times and, accordingly, more complicated graphical data processing techniques.

As a whole, we note that the recognition of various polarization mechanisms from the experimental data represents a quite specific problem, and its detailed discussion is beyond the scope of this book. The appropriate useful information can be drawn up from the original sources and the specialized literature (Cole and Cole, 1941; Davidson and Cole, 1950; Havriliak and Negami, 1967; Akhadov, 1977; Usmanov, 1996).

8.4 DIELECTRIC PROPERTIES OF FRESHWATER

The development and manufacturing of high-sensitivity microwave remote sensing and scatterometric onboard systems in recent years (see Chapter 14) makes it possible to investigate fine features of radiobrightness fields (of the order of 0.5–0.1 K and lower) and backscattering fields (0.5 dB) of the Earth surfaces. This circumstance necessitates, in its turn, the development and formation of a high-precision relaxation model of the dielectric characteristics of liquid water, since in the majority of problems of remote sensing the terrestrial surfaces and dispersive atmospheric formations the relaxation model represents a fundamental basis for theoretical and practical calculations (see Chapters 7, 11 and 12). Using known microwave remote sensing and radiolocation relations, it can easily be shown (Sharkov, 1983) that the relative dielectric constant variations of $\pm 5\%$ may cause radiobrightness contrasts of $\pm(1.5\text{--}2)$ K (in the centimetre and millimetre bands) and scattering cross-section variations of $\pm(0.05\text{--}0.15)$ dB (for grazing angles in the millimetre and centimetre bands). Therefore, the problem of developing such a numerical relaxation model should be stated now. Such a model would allow us to describe the experimental results to an accuracy not worse than $\pm 1\%$ in a wide range of temperatures and wavelengths (from 1 km to the submillimetre band). In spite of the fact that the indicated problem was first formulated rather long ago (Sharkov, 1983), recent investigations (Lipton *et al.*, 1999) have shown, that its final solution should not be expected soon. This is, first of all, due to the situation in

studying the structural properties of liquid (fresh) water and the physicochemical properties of supercooled water.

8.4.1 The structure of water

The structure of liquid water is the subject of intensive investigations and discussions at present (see, for example, Sinyukov, 1976; Horne, 1969). The polar nature of a water molecule and its ability to generate strong intermolecular hydrogen bonds result in associating water molecules into the multi-molecular complex containing a multitude of molecules. Liquid water represents a mixture of such sets, or ‘clusters’, with more or less ‘free’, or monomeric, water molecules. As the temperature grows, the clusters are ‘melted’, and, since their specific volume is greater than that of non-associated water, the hydrostatic pressure results in the destruction of structured sections existing in a liquid.

Our ideas on the shape of a water molecule are mainly based on studying its gaseous state. However, there is no reason to believe that in water, or in any fluid, the structure of a molecule is quite different.

According to modern notions, the electron cloud of a water molecule has the shape of truncated four-bladed propeller, which can be placed in an irregular cube. In this case the oxygen atom is at the centre, and the two hydrogen atoms are at opposite corners of one of the cube’s faces (Figures 8.7(a) and (b)). The H–O–H angle constitutes $104^\circ 31'$. Two of the eight electrons of an oxygen atom are situated near its nucleon, another two electrons are associated with hydrogen atoms, and two non-separated pairs of electrons form the branches, which extend up to opposite corners of that cube’s face which is opposite to the face occupied by the hydrogen atoms. These branches of an electron cloud are of special interest for us, because, being the areas of concentration of negative charges, they attract positively charged hydrogen atoms of adjacent molecules and provide the bond between water molecules (the so-called hydrogen bond) (Figure 8.7(c)). The O–H distance for a water molecule in the gaseous phase equals 0.9568 Å and slightly increases in the solid (ice) phase, reaching 0.99 Å.

Although the problem of the precise distribution of a molecule charge has yet to be finally solved, it is in any case of importance that the charge distribution causes a large electrical dipole moment of a water molecule and a strong hydrogen bond between the molecules. These quantum-mechanical characteristics are of principal importance, because, if the water molecules did not have negatively charged electron cloud branches and dipole moments, they would not be able to interact between each other, and no liquid water would exist on the Earth’s surface. The World Ocean would be gaseous and, accordingly, no evolved biological life would exist on the Earth.

Water vapour does not have any structure. It consists of monomeric water molecules, rarely encountered dimers of water. The first models of liquid water structure are subdivided into two types: some theories consider the water structure as a homogeneous continuum; in other models the existence of a mixture of various structures is supposed. But in both cases the structure of a solid state (ice) is used as a

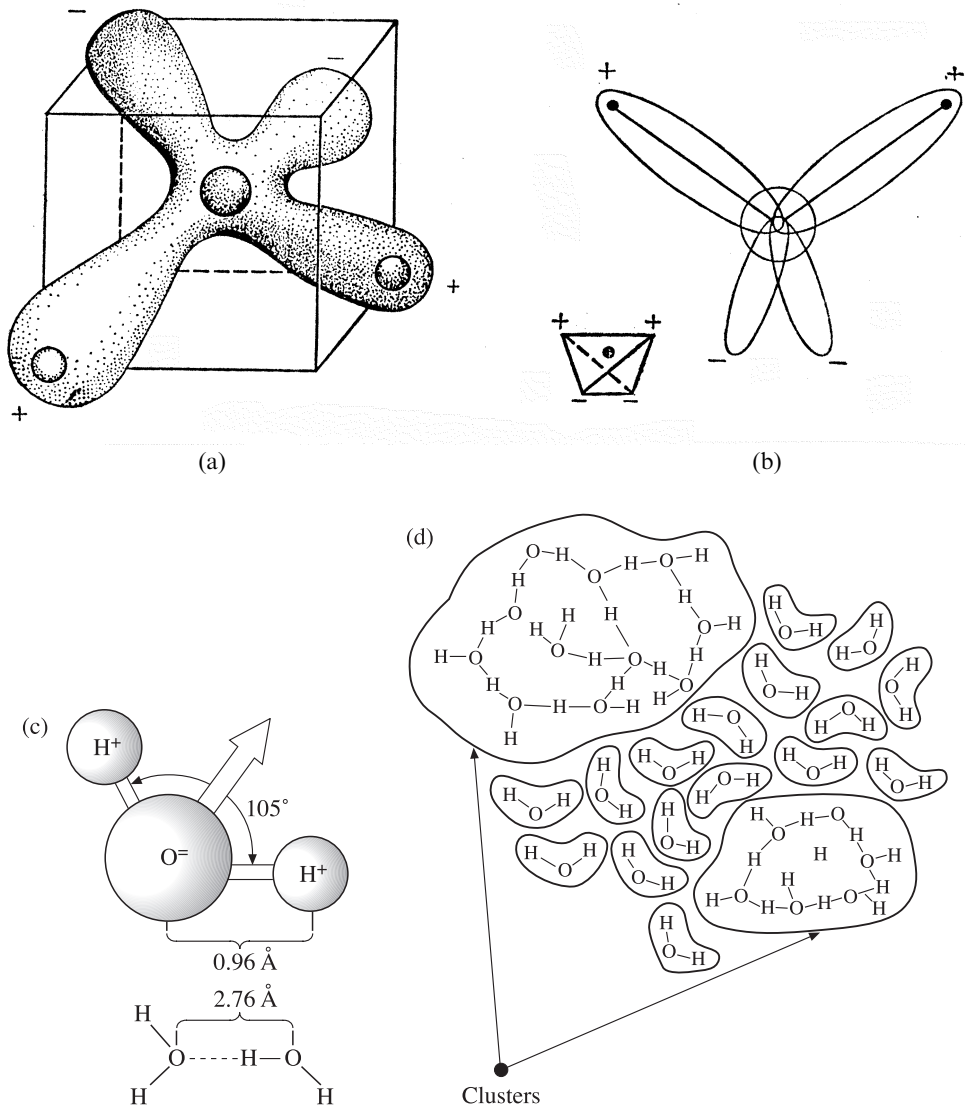


Figure 8.7. Electronic and structural peculiarities of the water molecule. (a) Electronic ‘clouds’ of water molecule. (b) Molecular orbitals of water molecule. (c) Schematic presentation of structural properties of water molecule and hydrogen bond. The direction of the dipole moment is marked by a white arrow. (d) The structure of liquid water in the Frank–Wen model of ‘flickered’ clusters (Horne, 1969).

starting point. Further development has led to the cluster Frank–Wen model. Its essence consists in the fact that liquid water is supposed to represent a conglomerate of ‘flickered’ clusters composed of molecules associated by hydrogen bonds and ‘floating’ in a more or less ‘free’ water (Figure 8.7(d)). The theory does not

postulate the existence of remainders of a crystal lattice of ice and does not explain in detail either exactly how the water molecules are combined in clusters or whether the quasi-crystalline structure exists inside the clusters at all. Of principal significance here is the idea of the ‘flickering’ nature of clusters, which are constantly forming and dissolving. Outside the clustered zones the hydrogen bonds are broken up, and the water behaves as a ‘monomeric non-bonded water’ (Horne, 1969).

In the case of both quasi-crystalline and cluster models the presence of monomeric water molecules in parcel of water is postulated and, accordingly, there should exist a certain contribution of monomers to the relaxation properties. Such ideas are very close to the original hydrodynamic Debye model (Debye, 1929), namely, the idea of a solitary dipole in a viscous homogeneous medium. This model leads to the well-known Debye relaxation mechanism (with a single relaxation time) (section 8.3). It can easily be seen here that the presence of both quasi-crystalline structures and flickering clusters should generate a variety of relaxators with various relaxation times and, thereby, it should sharply transform the purely Debye model of liquid water into one of versions of models with a multiplicity of relaxation times. However surprising this idea may seem, the study of dielectric relaxation (see below) indicates that in fresh water (unlike in electrolytes, e.g. salt water) there exists only one type of rotating particle (relaxator), which is presumably supposed to be a dipole-monomer with a single relaxation time.

Another complicated problem in this area is the structure of highly supercooled (well below freezing point) water, whose presence is experimentally recorded in convective cloudy systems (Rosenfeld and Woodley, 2000). The question is: does the supercooled water keep the structure of so-called ‘warm’ water (with temperature higher than 0°C), or is it significantly rearranged (Angell, 1982)? No unambiguous answer to this question has yet been given.

However, in spite of certain successes in studying the physicochemical properties of liquid water, no-one has managed to develop a strictly quantum (without phenomenological enclosures in the form of structural models) theory of the electrodynamic properties of liquid water that allows one to obtain design values of the dielectric parameters of water to a high degree of accuracy (~1%). Researchers have for a long time been forced to follow the path of developing and modernizing semi-empirical dependencies of appropriate parameters in the Debye (D) relaxation model (equation (8.15)) or in the Cole–Cole (C-C) model (equation (8.34)), as new and new experimental data have appeared (Saxton, 1952; Hasted, 1961, 1972; Ray, 1972; Rozenberg, 1972; Mason *et al.*, 1974; Mitnik, 1978; Kaatze and Giese, 1980; Zaghloul and Buckmaster, 1985; Sharkov, 1983, 1996c; Liebe *et al.*, 1991).

Whereas all these models are fairly close in respect of the qualitative character of frequency dependencies of dielectric properties of water, they are quite contradictory in their detail. This concerns, first of all, the values of the distribution parameter α (i.e. the definition of the type of model, in essence) and of the ‘optical constant’, and the dependencies of these parameters on temperature. So, in the generalized paper by Mason *et al.* (1974) the proposed two versions of relaxation models for liquid fresh water – the D model and the C-C model – were compared with the experimental data available in 1974. This comparison has not shown any essential advantages in using

the C-C model as compared to the Debye model. Both models, in general (for some particular applications), to a low but satisfactory degree of accuracy (of 4–7%), are supported by the experimental data on the complex permittivity (CP) in the metre, decimetre and centimetre bands. Further advance into the millimetre and submillimetre bands is characterized, however, by sharp distinctions between the initial experimental data, reaching 25% or more, even within the narrow temperature range of 19–22°C (Sharkov, 1983). Data for a wider temperature range are absent. This situation was also noticed later by Liebe *et al.* (1991). It can easily be seen (Sharkov, 1983) that, in re-calculating for emissive characteristics (Chapter 7), the uncertainty in values of radiobrightness temperature for the water surface reaches 15–20 K. And such an accuracy is already inadmissible when studying a variety of modern remote sensing tasks (see Chapters 7 and 12).

Sharkov (1983) has shown that the main physical reason for discrepancy between empirical models (in parameter ε_∞ , first of all) is the illegitimate use of experimental data obtained in the millimetre and submillimetre bands (i.e. outside the sphere of influence of the purely Debye absorption band) for forming the simplest empirical models, for example, the D model. However, the question of determining the high-frequency boundary of the Debye absorption band could not be considered in detail because of the absence of experimental data within a wide temperature range at that time. Liebe *et al.* (1991) have since shown that in this range the formation of the double Debye model with a double relaxation time value was possible. In other words, the question can be raised here about using the Davidson–Cole model (equation (8.34)) in this wavelength band. Strictly speaking, exactly this possibility is demonstrated by the qualitative pattern of frequency characteristics of the dielectric properties of water presented in Figure 8.3.

The purpose of this section is: (1) to compare, to a high degree of accuracy ($\sim 1\%$), the parameters of existing empirical design models both among themselves and with the D model parameters obtained by Sharkov (1983, 1996c) and Liebe *et al.* (1991) from CP experimental data processing in 1975–1991; and (2) to form the high-precision numerical relaxation model of the dielectric properties of liquid water and to consider the possibilities of its being applied to the solution of remote sensing tasks.

In so doing, special attention is given to determining the type of relaxation model that would adequately describe the dielectric parameters of liquid water in the millimetre band, as well as for supercooled water (in the temperature range from 0° to –40°C).

8.4.2 The experimental data processing technique

The values for the parameters of model D were obtained by Sharkov (1983, 1996c) by means of the diagram technique, which is based on constructing the linear approximation dependencies from the experimental data presented in the rectangular coordinate system (8.20)–(8.21). It follows from these relations that the sought values of the $\varepsilon_0(t)$ and $\varepsilon_\infty(t)$ parameters are determined at the point of intersection of linear approximations of data points on the ordinate axis. And the $\lambda_S(t)$ values are

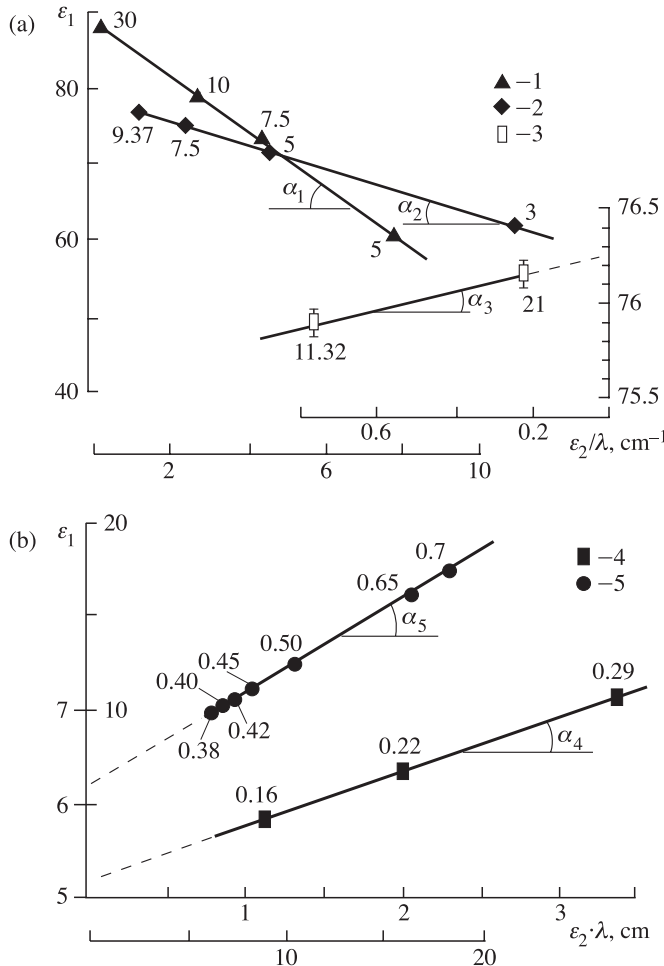


Figure 8.8. Experimental diagrams for $\varepsilon_1(\lambda)$ as function $\varepsilon_2(\lambda)/\lambda$ (a) and for $\varepsilon_1(\lambda)$ as function $\varepsilon_2(\lambda) \cdot \lambda$: (1) evidence of work (Kaatze and Giese, 1980) at $t = -4.1^\circ\text{C}$; (2) evidence of work (Burdette *et al.*, 1980) at $t = 23^\circ\text{C}$; (3) evidence of work (Ho and Hall, 1973) at $t = 30^\circ\text{C}$; (4) evidence of work (Blue, 1980) at $t = 20^\circ\text{C}$; and (5) evidence of work (Demyanov *et al.*, 1974). The solid lines show linear interpolations for equations (8.20) and (8.21). Experimental points are marked with wavelengths (in centimetres), at which they are obtained. Values for tangents of angles α_1 , α_2 , α_3 , and cotangents of angles α_4 , α_5 are given in corresponding columns in Table 8.1.

determined, accordingly, from the gradient of slope (the tangent or cotangent of the angle of slope, respectively) of the indicated dependencies. Examples of such constructions are presented in Figure 8.8(a) for centimetre and decimetre bands, and in Figure 8.8(b) for the millimetre band. The experimental data processing results are presented in Table 8.1 and in Figures 8.9–8.11. The discussion of the values of the

Table 8.1. Parameters of the D relaxation model for freshwater from experimental evidence

No. (1)	$t, ^\circ\text{C}$ (2)	ε_0 (3)	ε_∞ (4)	λ_s, cm (5)	λ, cm (6)	Reference (7)
1	-4.1	89.1 ± 0.3		3.76 ± 0.1	2.3; 3.0; 3.4; 4.1; 5; 7.5; 10; 16.7; 30	Kaatze and Giese, 1980
2	0	87.8 ± 0.2		3.30 ± 0.05	3.9; 4.57; 5.66	Pottel and Lossen, 1967
3	0		5.9 ± 0.1	3.28 ± 0.05	0.82; 1.72; 1.18; 1.98	Pottel and Lossen, 1967
4	5	88.0 ± 0.5	5.0 ± 0.3	2.95 ± 0.03	3.19; 2.14	Lyaschenko <i>et al.</i> , 1976
5	20		5.2 ± 0.05	1.76 ± 0.05	0.163; 0.22; 0.29	Blue, 1980
6	20		5.9 ± 0.1	1.68 ± 0.05	0.38; 0.4; 0.42; 0.45; 0.5; 0.65; 0.70; 0.818	Demyanov <i>et al.</i> , 1974
7	23	79.0 ± 0.3		1.60 ± 0.03	3; 5; 7.5; 9.4; 14.3	Burdette <i>et al.</i> , 1980
8	25	78.2 ± 0.1		1.61 ± 0.02	5.66; 11.49	Pottel and Lossen, 1967
9	25	76.5 ± 0.5	5.0 ± 0.3	1.44 ± 0.02	3.19; 2.14	Lyaschenko <i>et al.</i> , 1976
10	25	78.9 ± 0.3	5.2 ± 0.3	1.60 ± 0.05	0.88; 1.55; 3.12	Van Loon and Finsy, 1957
11	30	76.27 ± 0.08			11.32; 20.98	Ho and Hall, 1973
12	35	75.2 ± 0.3		1.27 ± 0.05	0.82; 1.12; 1.72; 2.41; 3.9	Pottel and Lossen, 1967
13	50	70.9 ± 0.4		0.92 ± 0.03	0.82; 1.12; 1.72; 2.41; 3.9	Pottel and Lossen, 1967
14	50	69.5 ± 0.5	5.0 ± 0.3	0.77 ± 0.02	3.19; 2.14	Lyaschenko <i>et al.</i> , 1976
15	60	66.8 ± 0.1			17.24; 52.00	Pottel and Lossen, 1967
16	60	65 ± 1			0.84; 0.63; 3.15	Asheko <i>et al.</i> , 1989
17	80	60 ± 1			0.63; 0.84; 3.15	Asheko <i>et al.</i> , 1989

Note. Original experimental evidence for processing performed by Sharkov (1983) was carried over from literature references. λ are operating wavelengths. Errors indicated on parameters are determined from graphical processing.

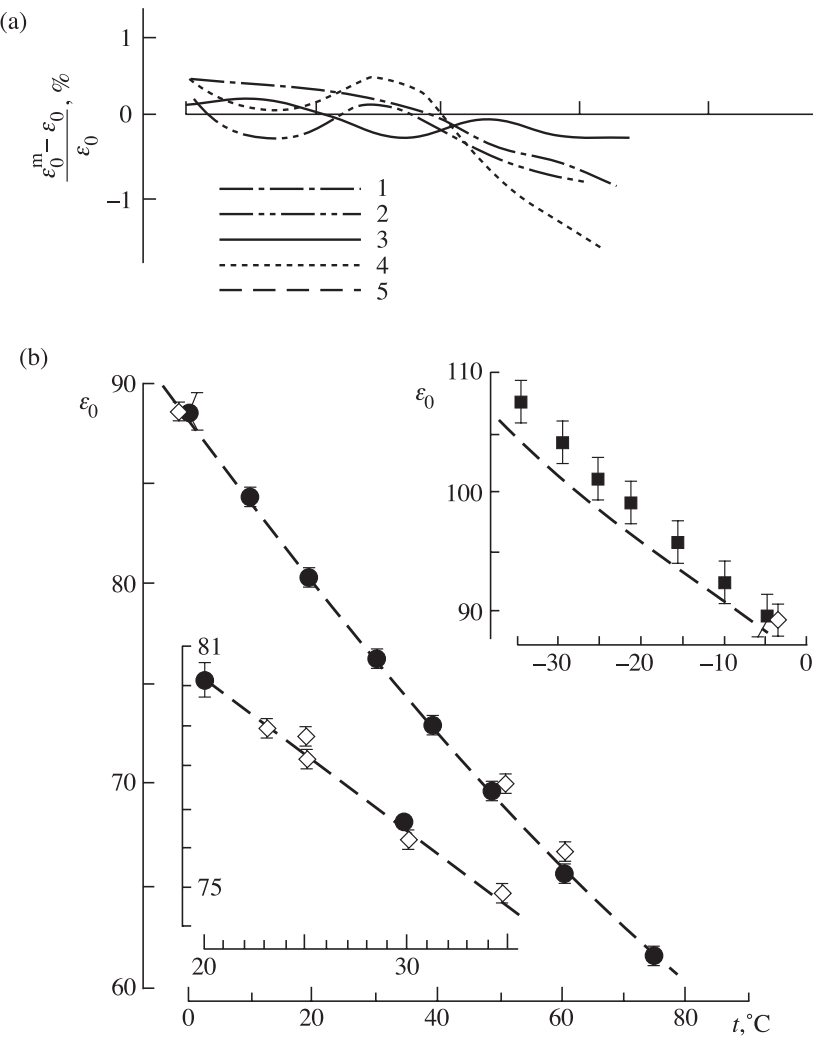


Figure 8.9. Temperature-dependence of static constant of liquid water. (a) Values ε_0 of models I–IV relative to model VI ε_0 (Mason *et al.*, 1974). (1 is model I; 2 is model II; 3 is model III; and 4 is model IV). (b) Absolute values of $\varepsilon_0(t)$. Dots present data of model IV with 90% confidence intervals. Squares present experimental evidence of work (Hasted and Shahidi, 1976). Diamonds present results obtained by Sharkov (1983) with processing experimental evidence available in literature (numerical values are given in Table 8.1). (5) Data of model VII, interpolating with equation (8.44).

parameters of model D thus obtained is given below. The efficiency of the considered technique (Sharkov, 1983, 1996c) is demonstrated by the inset in Figure 8.8. It can be seen here that the construction (8.20) enables us to obtain the value of parameter $\varepsilon_0(t)$ (with regard to errors of both geometrical constructions and experiment

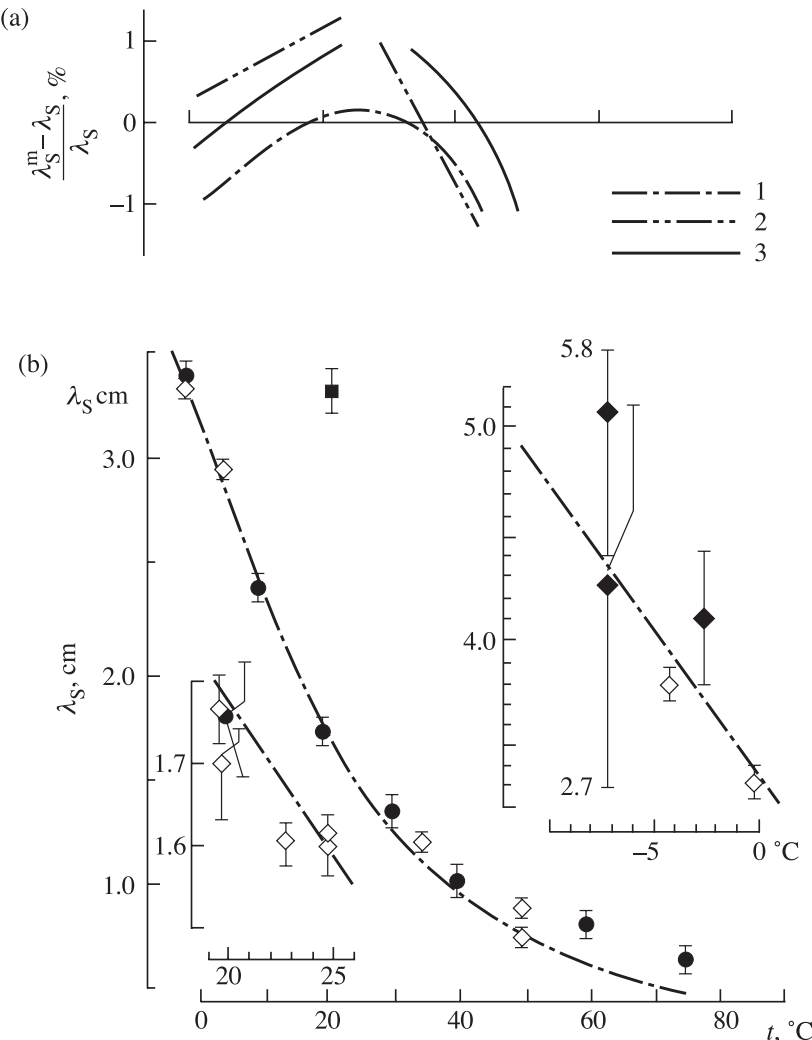


Figure 8.10. Temperature-dependence of relaxation wavelength. (a) Values λ_S of models I–III relative to model VI λ_S (Mason *et al.*, 1974) (1 is model I; 2 is model II; 3 is model III). (b) Absolute values of $\lambda_S(t)$. Solid dots present data of model VI with 90% confidence intervals. Solid diamonds present result obtained by Sharkov (1983) with processing remote sensing data of Akvilanova and Kutuza (1978). Open diamonds present results obtained by Sharkov (1983) with processing laboratory evidence on dielectric properties of liquid water (numerical values are given in Table 8.1).

(Ho and Hall, 1973)) to a record accuracy – better than 0.1%, in fact, $\varepsilon_0 = 76.27 \pm 0.08$ ($t = 30^\circ\text{C}$). This result is virtually inaccessible using the other graphical techniques, in particular, in constructing the standard C-C diagram (using equation (8.18) and Figure 8.6(a)).

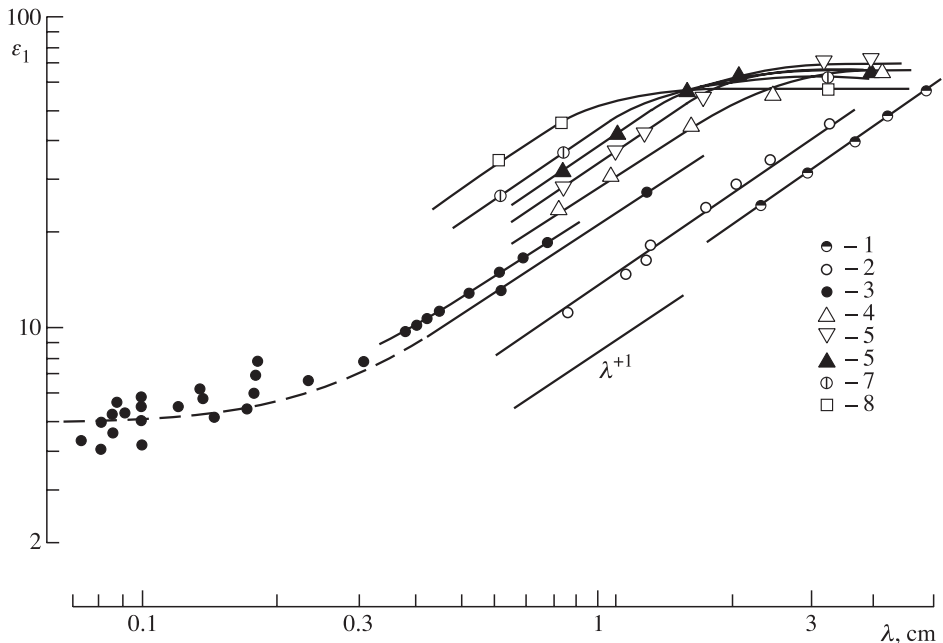


Figure 8.11. Frequency dependence of the real part for the complex permittivity at temperatures from -4.1°C to 80°C . 1 is at temperature -4.1°C (Kaatze and Giese, 1980). 2 is at temperature 0°C (Hasted, 1972; Pottel and Lossen, 1967). 3 is at temperature $19\text{--}21^\circ\text{C}$ (Blue, 1980; Demyanov *et al.*, 1974; Apletalin *et al.*, 1970; Meriakri *et al.*, 1980; Volkov *et al.*, 1980). 4, 5, 6 are at temperature 25°C , 35°C and 50°C (Pottel and Lossen, 1967). 7 and 8 are at temperatures 60°C and 80°C (Asheko *et al.*, 1989).

8.4.3 Empirical models

Consider the values of parameters $\varepsilon_0(t)$, $\varepsilon_\infty(t)$ and $\lambda_S(t)$ for some relaxation models used now in practical calculations (in all formulas the temperature is expressed in Celsius degrees and $\lambda_S(t)$ in centimetres).

The Saxton–Hasted–Stogryn model, formed from the data obtained by Saxton (1952), Hasted (1961) and Stogryn (1971) and called here model I conventionally, is as follows:

$$\begin{aligned}\varepsilon_0(t) &= 87.74 - 0.4008t + 9.398 \times 10^{-4}t^2 + 1.4 \times 10^{-6}t^3, \\ \lambda_S(t) &= 3.0[1.11 - 3.82 \times 10^{-2}t + 6.938 \times 10^{-4}t^2 - 5.096 \times 10^{-6}t^3], \\ \varepsilon_\infty(t) &= 4.9 \pm 0.98, \\ \alpha &= 0.\end{aligned}\tag{8.39}$$

The working range of temperatures, over which, in this author's opinion, this approximation model is valid, is as follows: $0 \leq t \leq 40^\circ\text{C}$.

The Ray model (Ray, 1972), called here model II conventionally, is as follows:

$$\begin{aligned}\varepsilon_0(t) &= 78.54[1.0 - 4.579 \times 10^{-3}(t - 25.0) + 1.19 \\ &\quad \times 10^{-5}(t - 25.0)^2 - 2.8 \times 10^{-8}(t - 25.0)], \\ \lambda_S(t) &= 3.383 \times 10^{-4} \exp\left\{\frac{2513.18}{t + 273}\right\}, \\ \varepsilon_\infty(t) &= 5.27 + 2.164 \times 10^{-2}t - 1.313 \times 10^{-3}t^2, \\ \alpha(t) &= 6.0926 \times 10^{-2} - \frac{16.81}{t + 293}.\end{aligned}\tag{8.40}$$

The working range of temperatures, over which, in this author's opinion, this approximation model is valid, is as follows: $-20^\circ\text{C} \leq t \leq 50^\circ\text{C}$.

The Rozenberg model (Rozenberg, 1972), called here model III conventionally, is as follows:

$$\begin{aligned}\varepsilon_0(t) &= 88.2 - 0.4088t + 0.00081t^2, \\ \lambda_S(t) &= 1.466 \exp\{-0.0634t\} + 1.36 \times 10^{-4}t^2 - 2.729 \times 10^{-2}t + 1.873, \\ \varepsilon_\infty(t) &= 5.5, \\ \alpha &= 0.\end{aligned}\tag{8.41}$$

The working range of temperatures, over which, in this author's opinion, this approximation model is valid, is as follows: $-40^\circ\text{C} \leq t \leq 75^\circ\text{C}$.

The other designed empirical models are to some extent a consequence of the abovementioned models, but with some changes in the temperature dependencies of parameters. For example, the models used by Rabinovich and Melentev (1970) (called here model IV conventionally), differ from model I in the $\varepsilon_\infty(t)$ dependence, in accordance with the data of Hasted and ElSabeh (1953), namely,

$$\varepsilon_\infty(t) = 5.0 + 0.0225t\tag{8.42}$$

and model V, in a paper by Klein and Swift (1977), in the $\varepsilon_\infty(t)$ dependencies, namely,

$$\varepsilon_0(t) = 88.045 - 0.4147t + 6.295 \times 10^{-4}t^2 + 1.075 \times 10^{-5}t^3.\tag{8.43}$$

Note that the authors, as a rule, have not studied in detail the validity of approximation models in the indicated temperature ranges.

Statistical processing of the experimental data obtained before 1974 has allowed Mason *et al.* (1974) to formulate the model VI, which was presented in the original paper in the form of tables of mean values and 90% confidence intervals ($0 < t < 75^\circ\text{C}$) and reproduced in Figures 8.9, 8.10 and 8.12. This model, having been most justified experimentally for the year 1979, consists of two versions: the purely Debye model and the C-C model, the distinctions between these versions in their mean $\varepsilon_\infty(t)$ values not exceeding 0.05% and in their $\lambda_S(t)$ values, 1.5%. The confidence intervals are for $\varepsilon_\infty(t)$ less than 0.5%, and for $\lambda_S(t)$ about 3.5%. In other

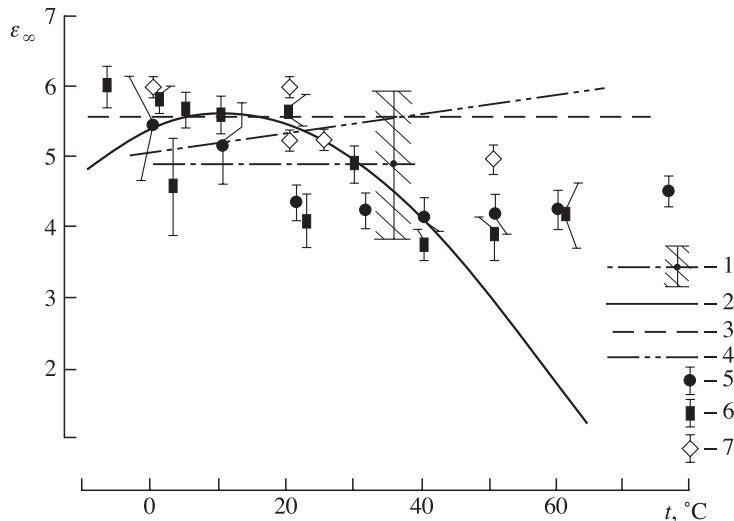


Figure 8.12. Temperature-dependent ‘optic’ constant in the Debye model. 1: model I with its uncertainty range. 2: model II. 3: model III. 4: model IV. 5: model V with 90% confidence intervals. 6: model VI with the standard confidence intervals. 7: Results obtained by E. Sharkov (1983) with processing evidence of various authors (see Table 8.1).

words, according to the data of Mason *et al.* (1974), one can state that the distinctions in $\varepsilon_\infty(t)$ and $\lambda_S(t)$ parameters in both the models mentioned are essentially lower than the 90% confidence intervals of each parameter value for a separately taken model. Therefore, the introduction of the C-C model (which is more complicated than the D model) for describing the dielectric properties of water (at least from the viewpoint of the $\varepsilon_\infty(t)$ and $\lambda_S(t)$ parameters) is completely unjustified (see Sharkov (1983) for more details). This circumstance is a major point, since it unambiguously indicates the prevalence of relaxators with a single (and strictly defined) relaxation time in the structure of freshwater.

A similar processing, performed in 1981 by Kaatze and Uhlendorf (1981) on the same basis material, but taking in some additional experimental data, allowed these authors to formulate the numerical Debye relaxation model (called here model VII conventionally), which is close to model VI with respect to $\varepsilon_\infty(t)$ and $\lambda_S(t)$ parameters. The distinctions between these models in the mean $\varepsilon_\infty(t)$ values are less than 0.2% ($t = 0\text{--}60^\circ\text{C}$) and 1–0.2% for $\lambda_S(t)$ values. In the same paper, Kaatze and Uhlendorf proposed the following compact formula for $\varepsilon_\infty(t)$:

$$\lg \varepsilon_0(t) = 1.94404 - 0.00199t. \quad (8.44)$$

The working range of temperatures, over which, in this author’s opinion, this approximation is valid, is as follows: $-4.1^\circ\text{C} \leq t \leq 60^\circ\text{C}$.

It is important to note that Kaatze and Uhlendorf (1981) (as well as, by the way, the authors of model VI (Mason *et al.*, 1974)) have neither found a regular

dependence for the optical constant $\varepsilon_\infty(t)$, nor presented it in analytical form. The reasons for this (strange at first sight) circumstance will be discussed below.

8.4.4 The analysis of the $\varepsilon_o(t)$ and $\lambda_S(t)$ parameters

Proceeding from the above considerations, our further study (following Sharkov, 1983) will be as follows: (1) to analyse thoroughly the temperature dependencies of $\varepsilon_o(t)$ and $\lambda_S(t)$ in the numerical models I–V as compared to model VI (in the relative ratio); (2) to compare the numerical calculations by models VI and the approximation (8.44) of model VII with the magnitudes of the $\varepsilon_\infty(t)$ and $\lambda_S(t)$ parameters obtained by Sharkov (1983) from experimental data processing (Table 8.1) under the assumption that the model D for fresh water is valid. The numerical values of parameters are given in the table along with the values of working wavelengths, the CP data of which were used in the graphical techniques of (8.20)–(8.21). The analysis of Figure 8.9 indicates that the approximating formulas for the static constant $\varepsilon_\infty(t)$ of models I–IV correspond well to each other and to models VI and VII: the distinctions in the approximation expressions do not exceed 0.5%.

The numerical values obtained by Sharkov (1983) from the CP experimental data processing by the technique of (8.20)–(8.21) (see Table 8.1), confirm to a fairly high accuracy (better than 0.4%) the validity of numerical approximation models (see Figure 8.9 (inset)). The analysis of the $\varepsilon_\infty(t)$ dependence indicates the predominantly linear decrease of static constant values with temperature with gradient $(\Delta\varepsilon_0/\Delta t) = -0.37$ per degree Celsius. Thus, in numerical calculations in the temperature range of 0–60°C any of the aforementioned approximations can be used to a degree of accuracy of the order of 0.5%.

It is of interest to note that attempts to find, by means of fine experiments (Szwareński, 1982), any features in the frequency characteristic of the complex dielectric constant in the decimetre and metre wavelength bands, which would differ from the Debye model, have failed. This fact testifies once again to the undoubtedly prevalence of solitary relaxators in the polarization properties of water, as well as to a vanishing contribution of water clusters, which seems rather strange by itself. As we shall show below, the real situation is significantly different even for weak electrolytes.

Of special interest (see Sharkov, 1983, 1996c; Liebe *et al.*, 1991; Lipton *et al.*, 1999) is the study of the dielectric properties of supercooled water (below 0°C) in connection with suppositions on the rearrangement of an like-ice structure of ‘warm’ water at a temperature lower than 0°C into some kind of ferroelectric structure (Angell, 1982), as well as in connection with the problems of remote sensing of convective cloudy systems. However, because of natural difficulties, detailed experimental data on measuring the CP of finite volumes of supercooled water are still absent. So, in 1976, Hasted and Shahidi (1976) presented the results of some fine laboratory experiments (at a frequency of 1652 Hz) on measuring the CP for supercooled water in the form of microdrop emulsion dispersed in an organic solution. The results of these experiments on measuring, in essence, the static constant ($-35 \leq t \leq -5.0^\circ\text{C}$) are shown in the inset in Figure 8.9 along with the fitting

formula (8.44). From comparison of these data it can be concluded, that the dielectric properties of supercooled water (at least from the viewpoint of parameter $\varepsilon_\infty(t)$) can be satisfactorily described within the framework of the relaxation model of ‘warm’ water (model VII). And, apparently, no sharp transformation of the relaxation mechanism in liquid water at negative temperatures does occur.

As far as the fitting dependencies of the relaxation wavelength are concerned, Figure 8.10 illustrates particular quantitative conformities in the approximations of various models in the range of $t = 0\text{--}40^\circ\text{C}$. The best conformity is observed between models I and VI, namely, the differences in λ_S values do not exceed 1% ($t = 0\text{--}50^\circ\text{C}$). For models III and VI the differences are of the order of 2–3%; the worst situation occurs for model II, where the distinctions exceed 5–10%. The numerical values of λ_S , obtained by Sharkov (1983) in experimental data processing (see Table 8.1), show that for the range of $20\text{--}25^\circ\text{C}$ the approximation of model I (inset in Figure 8.10) is most suitable. Thus, for numerical calculations in the temperature range of 0 to -40°C the $\lambda_S(t)$ approximation of model I should be recommended. With increasing $t > 40^\circ\text{C}$ all three models (I–III) sharply worsen in their conformity with model VI. The reasons for this are discussed below. Reliable experimental data on the temperature dependence of $\lambda_S(t)$ for supercooled water are absent. And we can only suppose that, if the exponential character of the $\lambda_S(t)$ dependence conserves also for $t = -40^\circ\text{C}$, then the relaxation wavelength can reach values of the order of 10 cm. Such a conclusion is substantiated by the results of our CP data processing for water at $t = -4.1^\circ\text{C}$ (see the inset in Figure 8.10), as well as by the estimates of $\lambda_S(t)$ for supercooled water obtained earlier by the original technique using the experimental data from the double-frequency radio-thermal system in sensing the supercooled drop clouds (Akvilonova and Kutuza, 1978). However, the analysis of the inset in Figure 8.10(b), where these results are reproduced (with appropriate re-calculation to fit them into the scale of the plots), indicates that final conclusions about the numerical approximation model can hardly be drawn because of considerable measurement errors.

8.4.5 Analysis of parameter $\varepsilon_\infty(t)$

Before proceeding to the analysis of optical constant values in the existing relaxation models, we shall consider the general contemporary situation concerning the availability of experimental data on frequency CP dependencies in the band ranging from short centimetre to submillimetre waves. It can easily be seen from the analysis of relations (8.16)–(8.17), that it is just this wavelength band where the features of spectral CP dependencies of water should make the main contribution to the formation of the values of parameter $\varepsilon_\infty(t)$. And their analysis will allow us to reveal the reasons for discrepancies in the empirical models in relation to the mentioned parameter.

Figure 8.11 presents the experimental (1970–1991) data on measuring the spectral dependence of a real part of CP in the wavelength band of $3\text{--}0.07\text{ cm}$ and in the temperature range of -4.1 to 80°C , as well as the fitting curves corresponding to these data. The analysis of the spectral dependencies presented indicates two

important circumstances. First, in the millimetre and submillimetre bands, experimental data are extremely limited over the temperature range. So, in the 0.07–0.5 cm band the data are available only in the range of 19–21°C. Second, even in this rather limited temperature range the conformity of compared experimental data over spectral dependencies is quite weak: approaching the submillimetre band the divergence between the ε_1 values exceeds 30–40%. The reasons for such serious nonconformities are related, most likely, to systematic errors in the experimental techniques used. So, Demyanov *et al.* (1974) have used the balance absorption method; Blue (1980) has measured the reflection coefficient; and Apletalin *et al.* (1970), Meriakri *et al.* (1980) and Volkov *et al.* (1980) have applied quasi-optical techniques. The experimental nonconformities mentioned should serve as a basis for in-depth study of the source of measurement errors, because the existing situation with the experimental CP data in the millimetre and submillimetre bands cannot be regarded as satisfactory. Similar conclusions were drawn later by Liebe *et al.* (1991) and Lipton *et al.* (1999). The experimental data in this region of electromagnetic waves are quite important for correct formation of the ‘optical constant’, since this band is some kind of transition between the modes of purely Debye and super-Debye absorptions in the submillimetre band (see Figure 8.3). It is still impossible to form a reasonable picture of spectral CP dependence in the millimetre and submillimetre bands within the temperature range required for remote sensing applications (from –40 to +90°C) (Sharkov, 1983, 1996c; Lipton *et al.*, 1999). However, taking into consideration the available data (Figure 8.11) and the character of spectral dependence of the Debye ‘branch’ in $\varepsilon_1(\lambda)$ as λ^{+1} (see relation (8.16)), we can state quite confidently that at $t \approx 0^\circ\text{C}$ the boundary wavelength λ_B between the purely Debye and super-Debye bands tends to 0.3–0.4 cm; for ‘supercooled’ water ($t \leq -10^\circ\text{C}$) $\lambda_B \approx 1\text{--}2\text{ cm}$, whereas for ‘hot’ water ($t > 60^\circ\text{C}$) λ_B sharply ‘runs’ into the submillimetre region ($\lambda_B \approx 0.08\text{--}0.06\text{ cm}$, or in the frequency band of $12\text{--}17\text{ cm}^{-1}$). The estimations of parameter $\varepsilon_\infty(t)$ carried out by different techniques bear a burden of the experimental nonconformities mentioned and of a limited (over the temperature range) volume of experimental data.

Figure 8.12, in which the plots of $\varepsilon_\infty(t)$ are constructed for existing models (the D model), illustrates their rather weak conformity with various models, not only in the quantitative, but even in the qualitative respect. So, the early (1952–1961) relaxation models (Saxton, 1952; Hasted, 1961; Van Loon and Finsy, 1957) were based on the idea that the optical constant does not depend (to a low degree of accuracy, of about 20%) on the temperature (model I), or on the data (Hasted and El Sabeh, 1953), which were interpreted later as a weak temperature growth (model IV). This attitude of the authors was justified, because they did not have at their disposal any reliable experimental data in the millimetre wavelength band at that time.

However, the subsequent (1961–1981) acquisition of experimental data on the CP of water (including those in the millimetre band) did not elucidate the situation in any way. So, in accordance with Ray’s (1972) data, model II supposes a strong decrease of $\varepsilon_\infty(t)$ (Figure 8.12) down to 1 and below (at a temperature of 65°C), which is a doubtful physical result. Subsequent science publications did not confirm this fact either.

Rozenberg (1972), the author of model III, kept to the early models, supposing the optical constant $\varepsilon_{\infty} = 5.5$ to be constant within a wide temperature range, from -40 to $+75^{\circ}\text{C}$, without estimating the accuracy of this parameter. The author of model III, however, did not have at his disposal any appropriate experimental base to formulate such conclusions.

The digital models, formed by Mason *et al.* (1974) (model VI) and Kaatze and Uhlendorf (1981) (model VII), were constructed on the same experimental facts. Their analysis (Sharkov, 1983, 1996c) enables us to reveal a peculiarity which is traced as a considerable decrease of ε_{∞} – from 6.0 down to 4.0 – with increasing temperature. On the other hand, in model VII the values of the parameter ε_{∞} change drastically (up to 20%) as the temperature varies by 1°C only (see Figure 8.12: for $t = 20^{\circ}\text{C}$ $\varepsilon_{\infty} = 5.5$, and for $t = 21^{\circ}\text{C}$ $\varepsilon_{\infty} = 4.0$). Such ‘kicks’ in the optical constant values did not allow the authors of model VII to formulate the analytical form of the temperature dependence of $\varepsilon_{\infty}(t)$. One more interesting point follows from the analysis of Figure 8.12: the earliest relaxation model (model I by Saxton (1952)) includes, in essence, all modern approximation approaches for $\varepsilon_{\infty}(t)$ values.

Sharkov (1983) has shown that such an (‘unstable’) situation is due to the fact that the procedure of calculating the ε_{∞} values has illegitimately included the experimental data obtained at wavelengths lying beyond the field of influence of the purely Debye absorption band. For example, for $t = 20^{\circ}\text{C}$ the use of data at wavelengths shorter than 0.2 cm is incorrect. In this case, as mentioned above, the boundary wavelength between a purely Debye and super-Debye absorption bands very heavily depends on temperature. The analysis of processing of the experimental data obtained in 1980–1991, undertaken by Sharkov (1983) with account taken of the circumstance mentioned above, has shown (Figure 8.12) that the $\varepsilon_{\infty}(t)$ values, formed from relation (8.21) and from the data of various authors, lie within the limits of 5.0–5.9 in the wide range of temperatures ($t = 0$ – 50°C).

To finally solve the question of the temperature dependence of $\varepsilon_{\infty}(t)$, as well as of $\lambda_S(t)$ of the relaxation D model for freshwater, it is necessary to carry out successive experiments (by the unified technique) on measuring CP with regard to some kind of a ‘choice rule’ (Sharkov, 1983), namely: for ‘cold water’ ($t = 0$ – 20°C) in the wavelength band of 1–3 cm, for ‘warm’ water ($t = 20$ – 40°C) in the wavelength band of 0.6–1.5 cm and for ‘hot’ water ($t = 40$ – 90°C) in the wavelength band of 0.1–0.5 cm. Ignorance of the ‘choice rule’ formulated above, and the illegitimate inclusion into the processing procedure of the experimental data at wavelengths lying beyond the range of the purely Debye relaxation band for the temperature range under study (as was just done in constructing the models I and VI), will result in the aforementioned nonconformities in the $\varepsilon_{\infty}(t)$ parameter in the models. Sharkov (1983) has presented a demonstration example of the illegitimate construction of $\varepsilon_{\infty}(t)$ with a special ‘capture’ of the frequency region of super-Debye absorption. As a result, the range of ‘kicks’ in $\varepsilon_{\infty}(t)$ values was from 3.8 to 4.6 as the temperature varied by one degree only (from 21 to 22°C), which is a physically contradictory result.

The attempts to introduce the double-Debye model, undertaken by Liebe *et al.* (1991), slightly improved the situation, but, nevertheless, full clarity in the

relaxation model for the band of short millimetre and submillimetre waves was not achieved.

Thus, for the majority of remote sensing applications satisfactory approximation formulas for the static constant ($t = -40$ to $+90^\circ\text{C}$) and relaxation wavelength ($t = 0\text{--}40^\circ\text{C}$) can be used from models I and VII. For supercooled and ‘hot’ water, however, additional purposeful investigations should be carried out, since a satisfactory temperature approximation of the relaxation wavelength value is absent. The approximation formulas for the ‘optical’ constant can be used only if account is taken of the essential ($\sim 20\%$) uncertainties in the parameter values. To finally solve the question of the temperature dependence of the ‘optical’ constant, a set of experiments should be carried out with allowance for the revealed ‘rule of choice’ of the temperature ranges and working wavelengths studied.

8.5 DIELECTRIC PROPERTIES OF SALT WATER

A cosmic feature of our planet lies in its riches of salt water. The World Ocean contains about 1413×10^{18} kg of aqueous solution of electrolyte of medium concentration. Salt water occupies about 71% of planet Earth’s surface. The substances contained in such a huge amount of water can be subdivided into two categories. The first category includes dissolved substances such as salts, organic compounds and dissolved gases; the second category includes substances forming an independent phase, such as bubbles of gas and solid particles of both inorganic and organic origin. In addition, electrolytes and non-electrolytes are sometimes distinguished among dissolved substances. When dissolved in water, electrolytes form the particles which are able to transfer the electric charge (the ions) and, thereby, to decrease the electric resistance of a system. This phenomenon is not characteristic of non-electrolytes.

The substances dissolved in seawater are represented primarily by salts. The chemical composition of seawater is rather complicated in detail. Here it is sufficient to mention that a ‘typical’ specimen of seawater weighting 1 kg contains about 19 g of chlorine in the form of chloride ions, 11 g of sodium ions, 1.3 g of magnesium ions and 0.9 g of sulfur (mainly in the form of sulfate-ions). In other words, seawater represents an aqueous 0.5 M solution of NaCl and 0.05 M solution of MgSO₄. In addition, sea water contains small admixtures or traces of almost all the elements of Mendeleev’s table.

The well-known physical fact that the water possesses a considerable heat capacity suggests that the oceans represent an excellent thermostat for the entire climatic system of the Earth. This simple and, at the same time, fundamental fact involves some unusual consequences – it provides one of the necessary conditions (the ‘greenhouse’ effect) for the origin and development of biological life on Earth. In addition, the existence of moderate (and, moreover, comfortable for a human being) climatic conditions where there is a moderating influence from neighbouring seas has played an important part in the history and development of human civilization.

The oceans of the Earth represent an actively functioning system, which is regulated, first of all, by thermohaline processes. Therefore, the knowledge and monitoring of spatial-temporal fields of the ocean's surface salinity and of the surface field of temperature are most important problems of remote sensing (Miller, 2000; Miller and Payne, 2000; Miller *et al.*, 1998; Schmitt and Montgomery, 2000).

8.5.1 Electrolyte structure

The presence of electrolyte drastically changes the structure of water (Sinyukov, 1976; Horne, 1969; Dzens-Litovskii, 1967). The local violation of the water structure near an ion or, more correctly, the region of this violation, is called the hydrated atmosphere of an ion. It has a complicated composition and consists of an inner zone with an ordered structure and an outer zone with the reordered structure of water. Hydration can be quantitatively described by means of hydration numbers of ions or on the basis of the notion of the time a water molecule remains in an equilibrium state near an ion and in the pure water structure. The experimental investigation of hydration is fairly laborious; however, generally speaking, the greater the density of the charge of a cation, the stronger it is hydrated; cations are usually hydrated stronger than the corresponding anions.

Water structure theories based on the assumption of the existence of the destroyed structure of ice or ice-like crystalline structure in a liquid explain the strengthening or splitting effect of ions by the fact, how easily they can be disposed at emptinesses of a structure or at the place of a water molecule in the frame.

In accordance with the Frank–Wen model of liquid water, based on the idea of flickering clusters, the ion in the solution is supposed to be surrounded by two structured layers of water molecules – the two-zone model (Figure 8.13). The inner layer (A), which, apparently, can be identified with what is called a ‘primary’ hydration sphere, is more dense owing to electrostriction. And the water molecules inside this layer are less mobile and form strong bonds with an ion in its Coulomb field. By electrostriction is meant the appearance of mechanical spatial deformations in the dielectric structure under the effect of the electric field of an ion. Since in such a type of interaction the polarization of dielectrics in the electric field is proportional to the square of the electric field strength, the quadratic effects can appear in the ultimate polarization properties of a dielectric (see Prochorov, (1984) and also Chapter 2).

At a greater distance from an ion (region C in Figure 8.13(a)) the water molecules remain ‘normal’, though they can be very weakly polarized by the electric field being present everywhere. Of special interest is the intervening layer (B). In this space the Coulomb field of an ion is still strong enough to be capable of violating the ‘normal’ structure of liquid water. But, nevertheless it is still insufficiently great to be capable of causing rearrangement of water molecules and generating any new structure (as, for example, in the layer A). Therefore, layer B represents a region of comparative reordering. In any case, the ordering or

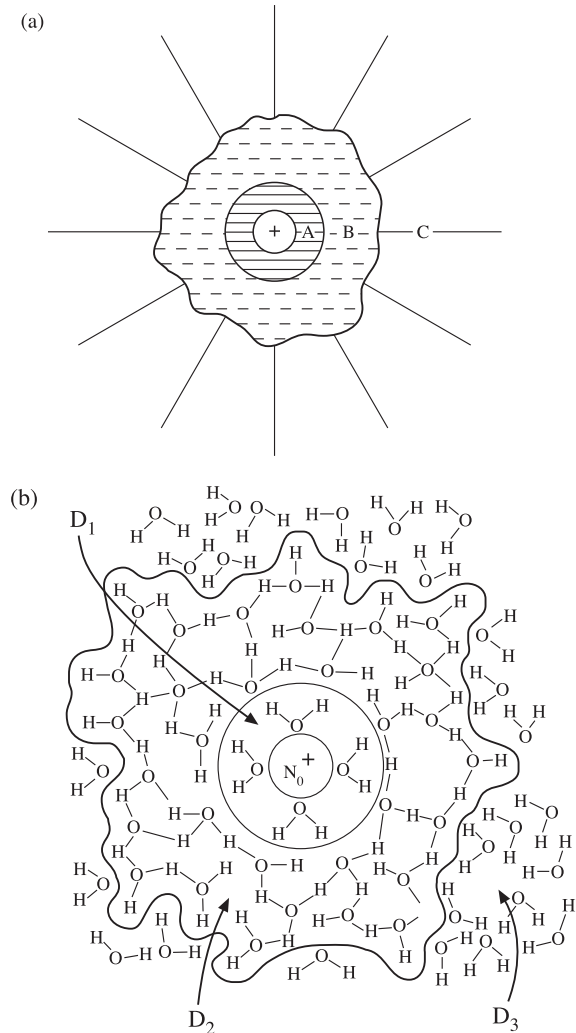


Figure 8.13. Schematic presentation of a hydro-rotation atmosphere of an ion in water solution. (a) Two-zone model. A: the ‘inner’ layer; B: the intervening layer (space); C: ‘normal’ water or the ‘outer’ layer (space). (b): Two-dimensional pattern of structure-ordered hydro-rotation atmosphere for ion Na^+ . D₁: Electrostriction zone. D₂: Frank–Wen cluster zone. D₃: the intervening space (‘free’ water).

reordering effect of an ion depends on which one of indicated layers predominates. A very orderly zone is supposed (Sinyukov, 1976; Horne, 1969) to exist in the unchangeable state for all ions, whereas the specific properties of various types of ions are caused by changing a very disorderly zone B. Investigations of viscosity variation with the electrolyte concentration allow us to quantitatively evaluate the influence of various ions on water structure. The ions strengthening the water

structure, such as Na^+ and Mg^{2+} , increase the water viscosity (positive hydration), whereas the ions destroying the water structure, such as, for example, Cl^{-1} , K^+ and Cs^+ , increase its fluidity (negative hydration). One should keep in mind that, depending on the temperature of solution, the degree of an ion's influence on the water structure can drastically change – so, at 27°C the hydration process for a sodium ion changes from positive to negative. Similar features exist for other ions and cations as well. Subsequent investigations have shown that these features are most likely to be associated with the structure features of an ordered zone owing to the fact that the inner, very orderly zone is, in its turn, separated into two subzones (Figure 8.13(b)). The zone closest to an ion consists of a very orderly pattern of water molecules which experience strong electrostriction; and adjacent to it is the zone that is determined by the size of the Frank–Wen cluster zone with weaker electrostriction effects. The inner electrostriction zone can be identified with the so-called primary hydration shell. This is apparently confirmed by the fact that in the case of the Na^+ ion it contains four water rigidly structured molecules, whereas in the general very orderly zone (zone A) of the hydration atmosphere of a sodium ion the number of water molecules varies (depending on temperature) from 52 to 21 (Figure 8.13(b)) (Horne, 1969).

As the concentration of salts increases up to 1.5–2 mol/l, the boundaries of zone B come into contact, and the free water zones in the electrolyte virtually disappear (the full solvation regime). As the concentration further increases, the solution assumes a structure resembling a composition of a melt of salts with conservation of the crystalline structure elements (Sinyukov, 1976).

As we have noted above, the water molecule as a whole can experience two types of motion – translational and rotational. The water molecule is characterized by the high value of electric dipole moment; therefore, in the external electric field this molecule tends to be turned and to assume the position corresponding to the external field direction. The time of relaxation of a rotational process can be determined by measuring the frequency dependence of the full dielectric constant in the alternate electric field, and such results (see section 8.4) are quite indicative. At a particular temperature only one value of relaxation time is observed, and this indicates, that the reorientation of particles of only one type takes place. Experiments on water viscosity, as well as dielectric investigations have shown that the only reoriented particles in a liquid water are the monomers, rather than any polymeric forms $(\text{H}_2\text{O})_n$. Apparently, the polymeric (cluster) water complexes do not possess pronounced electric dipole moments and cannot essentially distort the general Debye polarization pattern of liquid (fresh) water (Figure 8.3). This result is, without doubt, of momentous significance. However, its psychological effect was so great that for more than 40 years the validity of the purely Debye model for electrolytes has been stated with variations (with a negative sign) of only numerical values for the static constant and relaxation wavelength. Such a rather ‘naive’ point of view has been put forward, without any proof being adduced, for a long time, not only by specialists in the physico-chemistry of water solutions (Hasted *et al.*, 1948; Lane and Saxton, 1952; Horne, 1969), but by radio-engineers and radio-physicists as well (Krasik and Rosenberg, 1970; Akindinov *et al.*, 1976). And only in 1984 has Sharkov

(1984) critically analysed in detail the previous experimental data and his own data and shown the necessity of this point of view being largely reconsidered.

So, in spite of the progress made in the study of the thermodynamic and the physicochemical properties of solutions of strong electrolytes, there is no quantitative theory of electrodynamic properties of such water systems which would allow us to determine the dielectric parameters by calculation. In papers by Hasted *et al.* (1948) and Lane and Saxton (1952), on the basis of experiments carried out within a rather limited frequency band, it was stated that the dielectric characteristics of strong solutions of electrolytes (and the aqueous solution of NaCl in particular) are described by the purely Debye relaxation model only. And the first estimations of parameters of this model were given (in tabular form) in the same papers as a function of temperature and salinity of a solution. This presentation has been widely publicized and was reflected in its final form in Stogryn's (1971) empirical model. And, furthermore, this presentation has been actively propagandized by the authors of a series of subsequent papers (Hasted and El Sabeh, 1953; Hasted and Roderick, 1958; Yastremskii, 1961; Ermakov *et al.*, 1975; Klugman, 1980). But these authors' own experimental data obviously contradicted the statement that the dielectric properties of strong electrolytes are described by the purely Debye relaxation model. Detailed comparison of the experimental data on the dielectric parameters of electrolyte solutions obtained in the centimetre and millimetre bands, with corresponding calculations by Stogryn's model, allowed Sharkov (1984) to state that the viewpoint on attributing strong electrolyte solutions to the purely Debye type should be accepted as being invalid. Because this circumstance is important for microwave sensing applications, the next section will be devoted to a more attentive study of this problem (following Sharkov (1984)).

8.5.2 The experimental data processing technique

The Debye type of a polar liquid is known to be a particular case of the more general relaxation model, the so-called Cole–Cole (C-C) model. According to this model (equation (8.34)), the complex dielectric permittivity (CP) is described by the following empirical relation:

$$\dot{\varepsilon}(\lambda, S, t) = \varepsilon_{\infty}(S, t) + \frac{\varepsilon_0(S, t) - \varepsilon_{\infty}(S, t)}{1 + \left[j \frac{\lambda_S(S, t)}{\lambda}\right]^{1-\alpha(S, t)}}, \quad (8.45)$$

where $\varepsilon(\lambda, S, t) = \varepsilon_1(\lambda, S, t) + j\varepsilon_{2C}(\lambda, S, t)$; ε_0 and ε_{∞} are the static and ‘optical’ constants of a model, $\alpha(S, t)$ is the parameter of distribution of relaxation times, $\lambda_S(t)$ is the relaxation wavelength, λ is the working wavelength, S is the salinity (in parts ‰), t is the temperature; $\varepsilon_{2C}(\lambda, S, t)$ is the corrected value of the imaginary part of CP (in accordance with (8.8)):

$$\varepsilon_{2C}(\lambda, S, t) = \varepsilon_2(\lambda, S, t) - 60\sigma(S, t)\lambda, \quad (8.46)$$

i.e. $\varepsilon_2(\lambda, S, t)$ minus the correction for the ionic conductivity component. In the

limiting case $\alpha(S, t) \rightarrow 0$ the C-C model transfers into the purely Debye relaxation model. The assigning of an investigated electrolyte (the aqueous solution of NaCl) to the corresponding relaxation type and the estimation of the model's parameters (in the general case, α , λ_S , ε_0 and ε_∞) were accomplished by constructing the C-C diagrams from the experimental data. These diagrams represent a set of curves which approximate the experimental data points in the Cartesian coordinate system (Figure 8.6(b)). Quantities ε_0 and ε_∞ were found as the abscissa values when fitting curves intersect the abscissa axis, and quantities α and λ_S were estimated by relations

$$\lambda_S = \lambda \left[\frac{V(\lambda, S)}{U(\lambda, S)} \right]^{1/(1-\alpha(S))}, \quad (8.47)$$

$$\alpha = \frac{2}{\pi} \Psi, \quad (8.48)$$

where V and U are the distances from the experimental point of a fitting semicircle up to points ε_0 and ε_∞ , respectively, Ψ is the angle (in radians), formed by the abscissa axis and the line connecting the centre of a circle with point ε_∞ . To determine unambiguously the relaxation model type by the technique considered, the accuracy of the initial experimental data on ε_0 and ε_{2C} should be not worse than 5–7%.

8.5.3 Spectral dependences of strong electrolytes

The measurements of the dielectric parameters of highly absorbing strong solutions of electrolytes to the indicated accuracy represent a fairly complicated experimental problem. At present, a limited amount of successive experimental data on measuring the CP of a solution of NaCl is available. These data are predominantly concentrated within a narrow wavelength band of 3.5–2.5 cm and are obtained at temperature of 25°C. And only separate data points are available in the other frequency and temperature ranges (see the reference book by Akhakov (1977)).

For this reason, to obtain the general picture it seems expedient to thoroughly and critically analyse the available experimental data in the centimetre and millimetre bands (Sharkov, 1984). As far as the decimetre and metre bands are concerned, the uncertainty in the experimental data on dielectric parameters is very great (up to qualitative distinctions in the same dependencies). For example, according to the data by Smirnov and Sharkov (1979), the value of $\varepsilon_1(\lambda, S, t)$ in the decimetre band decreases with increasing concentration of aqueous solution of NaCl. According to other data (Klugman, 1980), this value increases; and according to the data of Christensen *et al.* (1966) and by Smirnov and Sharkov (1979), $\varepsilon_{2C}(\lambda, S, t)$ assumes even negative values in the decimetre band for $S \geq 100\%$. It is still impossible to obtain a rather unambiguous picture in the decimetre and metre bands. In this connection, we shall limit further consideration to the analysis of the experimental data (on electrolytes) obtained in the range 3.6–0.4 cm.

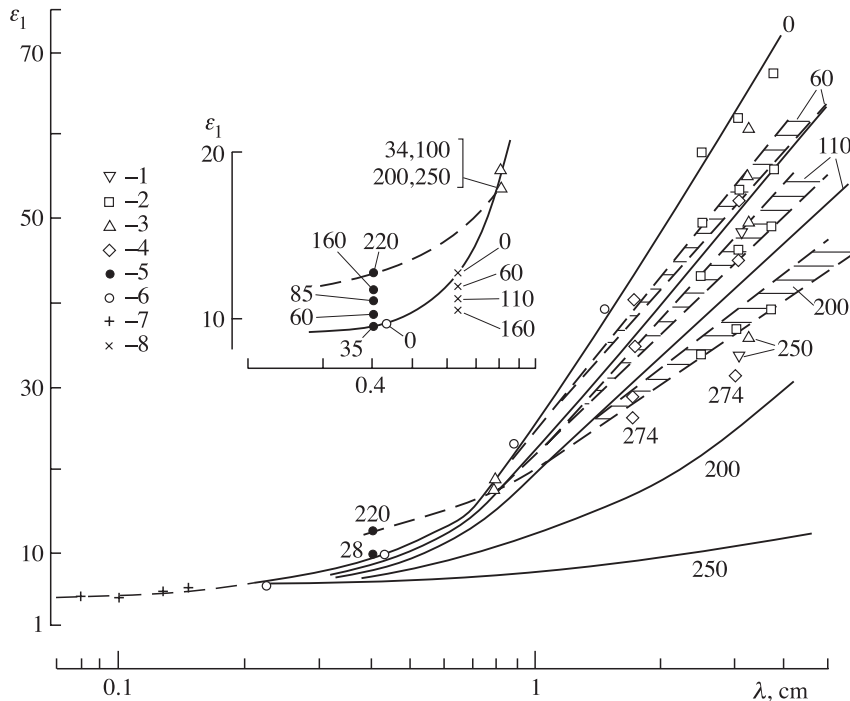


Figure 8.14. Spectra of the real part of the permittivity of water solution NaCl in the range 0.4–3.5 cm at 25°C. Symbols and dotted lines display experimental data. Shaded areas present spread of data. Solid lines are calculations of spectra of $\epsilon_1(\lambda)$ for water solution NaCl in accord with the Stogryn model. Figures next to experimental data and curves present values of salinity (in parts ‰). Open triangles (at 0.8 cm) are data by Onishenko and Sharkov (1982). 1, data by Harris and O'Konski (1957). 2, Barthel *et al.* (1970). 3, Yastremskii (1961). 4, Christensen *et al.* (1966). 5, Ermakov *et al.* (1975) (at 20°C). 6, Van Loon and Finsy (1975). 7, Apletalin *et al.* (1970). 8, points calculated by E. Sharkov using empirical Lane and Saxton model (1952) at 25°C.

The joint analysis of the data, obtained by Onishenko and Sharkov (1982), and of the results in the 4-mm band (Ermakov *et al.*, 1975), points to the necessity of essential correction of the widespread point of view, that the CP (and, hence, the emissive characteristics) are not sensitive to salinity variations in the millimetre band (see, for example, Wilheit, 1979; Wilheit and Chang, 1980; Ulaby *et al.*, 1981, 1982, 1986; Miller, 2000). The results, obtained by Onishenko and Sharkov (1982), are presented in Figures 8.14 and 8.15. Together with the data from papers by Ermakov *et al.* (1975), Harris and O'Konski (1957), Barthel *et al.* (1970), Yastremskii (1961) and Christensen *et al.* (1966), these results form a set of frequency dependencies, in the band 0.4–3.5 cm, of the real and imaginary parts of the CP of aqueous solutions of NaCl for various degrees of concentrations (the salinity was determined in parts ‰). On the same figures are plotted the frequency dependencies, in the band 0.08–3.5 cm, of distilled water's CP according to the data

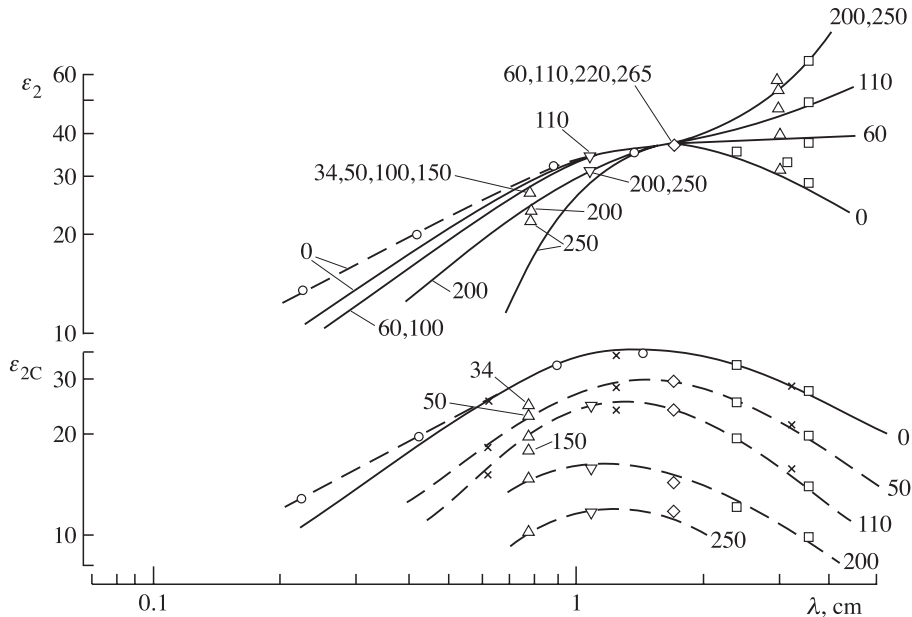


Figure 8.15. Experimental and calculated spectra of imaginary full ε_2 and corrected ε_{2C} parts of the permittivity of water solution NaCl. Dotted lines are curve-fitting of experimental data. Legends as for Figure 8.14.

taken from papers by Grant and Shack (1967), Apletalin *et al.* (1970) and Van Loon and Finsy (1975).

The analysis of frequency dependencies of $\varepsilon_1(\lambda)$, presented in Figure 8.14, gives rise to the following important conclusion. In the band of 0.8 cm there exists the critical wavelength λ_{CR} , at which the converging (from the long-wave extremity) branches of a set of frequency dependencies are ‘retracted’ and then diverge as the wavelength decreases (see Figure 8.14 (inset)). Thus, the analysis of these data indicates the existence of two characteristic regions in the frequency dependence of $\varepsilon_1(\lambda)$: for $\lambda > \lambda_{CR}$ the concentration dependence gradient $k_1 = (1/\varepsilon_1)(\partial\varepsilon_1/\partial S)$ is negative and equals $k_1 = -0.25\%$ per 1‰ of change of salinity (with increasing salinity up to 200‰). At the same time, for $\lambda < \lambda_{CR}$ coefficient k_1 changes its sign – it becomes positive and equals about 0.15% (per 1‰) at the wavelength of 0.4 cm.

Figure 8.15 presents the sets of frequency dependencies of an imaginary part of CP according to the data by Onishenko and Sharkov (1982) and bringing in the data of papers by Ermakov *et al.* (1975), Harris and O’Konski (1957), Barthel *et al.* (1970), Yastremskii (1961), Christensen *et al.* (1966) and Van Loon and Finsy (1975), as well as the so-called ‘corrected’ $\varepsilon_{2C}(\lambda, S, t)$, i.e. with subtraction of the correction for the ‘through’ (ionic) component of conductivity.

Here it is interesting to note, that in the $\varepsilon_2(\lambda)$ dependencies some critical wavelength ($\lambda_{CR} \sim 1.7$ cm) is also observed, at which the sensitivity of $\varepsilon_2(\lambda)$ to salinity is absent, i.e. $k_2 = (1/\varepsilon_2)(\partial\varepsilon_2/\partial S) \approx 0$. In this case, unlike the dependence

of a real part of CP, the opposite situation arises: for $\lambda > \lambda_{\text{CR}}$ and $k_2 < 0$ for $\lambda < \lambda_{\text{CR}}$. In considering the $\varepsilon_{2C}(\lambda, S, t)$ dependence attention should be given to the following important circumstance. As seen from Figure 8.15, in general, the character of the frequency dependence of $\varepsilon_{2C}(\lambda, S, t)$ remains similar to $\varepsilon_2(\lambda)$ for the freshwater (i.e. to the form of the Debye relaxation maximum). However, the maximum value of $\varepsilon_{2C}(S)$ sharply drops with increasing mineralization: it decreases almost three times as S increases up to 250%. In this case the relaxation wavelength shifts to the side of shorter wavelengths: whereas for freshwater $\lambda_S \approx 1.75$ cm, for salinity of 250% the value of λ_S equals 1.2 cm. A sharp decrease of relaxation losses can be, apparently, explained by formation of a quasi-crystalline structure in the electrolyte and by orientational stabilization of a considerable part of polar molecules of water.

Let us now compare the experimental data obtained with calculations of CP values carried out using the empirical Stogryn model (shown by solid curves in Figures 8.14 and 8.15). Analysis of the figures indicates that, whereas in mineralizations of solutions up to 60% (in the band of 1.5–3.5 cm) the indicated model can describe the frequency dependencies accurately enough (to $\sim 10\text{--}15\%$), for $S > 100\%$ and $\lambda < 1$ cm this model fails to give even a qualitatively correct description of the modern experimental data. Note that the earlier (1951–1952) experiments (Lane and Saxton, 1952), on the results of which Stogryn based his empirical model of CP of electrolytes, contained an obvious systematic error in measuring ε_1 in the 6-mm band. So, according to the data of the paper by Lane and Saxton (1952), ε_1 decreases with increasing mineralization of a solution, whereas the real situation is just the opposite (see Figure 8.14 (inset)). It was this circumstance which gave Lane and Saxton reason to suppose, that the dielectric characteristics of strong electrolytes were described by the relaxation Debye model, and to present the first estimates of the model's parameters (in tabular form) depending on the temperature and salinity of the solution. This presentation has been widely publicized (as we have already mentioned above) and was formulated in a completed form in Stogryn's empirical model (Stogryn, 1971). However, the comparison of the data, calculated by the model of Lane and Saxton (1952) (for $t = 25^\circ\text{C}$ and $\lambda = 0.62$ cm), with the results of modern experiments (Figure 8.14 (inset)) reveals the systematic error indicated (Onishenko and Sharkov, 1982). Furthermore, we note that Stogryn has compared the calculations by his model with the experiments, in which the mineralization values were limited to 28% only. Though at the time, when he had formed his model, there were already publications (Harris and O'Konski, 1957; Barthel *et al.*, 1970; Yastremskii, 1961; Christensen *et al.*, 1966) on investigations of electrolytes with salinity of up to 275%.

Thus, the critical analysis of available experimental data and those obtained by Onishenko and Sharkov (1982) revealed a fairly complicated character of frequency dependencies of CP of strong electrolytes in the centimetre and millimetre bands. The widespread empirical model of Stogryn does not describe satisfactorily the mentioned dependencies either from the quantitative or from the qualitative side. A new empirical model must be constructed which would more adequately describe the experimental frequency and concentration dependencies of CP.

8.5.4 The C-C diagrams for strong electrolytes

The C-C diagrams presented in Figure 8.16 are constructed (Sharkov, 1984) for 10, 20 and 25°C using the experimental data, obtained in the wavelength band from 3.6 to 0.8 cm, and for freshwater in the band of 17.2–0.4 cm. It is impossible to construct the C-C diagrams for a wider temperature range (i.e. for $t < 10^\circ\text{C}$ and $t > 25^\circ\text{C}$) because of the absence of successive experimental data at several frequencies in the millimetre and centimetre bands.

The analysis of constructed C-C diagrams for the investigated electrolyte indicates that, in spite of the fact that the used experiments have been performed in different years and by different techniques, nevertheless, the general picture is revealed unambiguously enough: the C-C diagrams of the strong NaCl solution represent not full semicircles (as for polar Debye-type liquids), but only partial arcs, whose centre is essentially displaced from the abscissa axis, this effect being most strongly prominent in cooling the electrolyte (in our case for $t < 10^\circ\text{C}$) (Figure 8.16(a)–(c)).

This circumstance enables us to draw a major conclusion, that the dielectric parameters of strong electrolytes are described by the relaxation Cole–Cole model ($a \neq 0$), rather than by the purely Debye relaxation model ($a = 0$), as had long been thought. This circumstance entails a series of consequences and, in particular, quite different (as compared to purely Debye ones) dependencies of the C-C model parameters of electrolyte solutions on temperature and concentration (see below). And this circumstance, in its turn, drastically changes the physicochemical concepts of the structure of electrolytes (Sinyukov, 1976; Horne, 1969).

Now we shall analyse the validity of the experimental data of papers by Hasted *et al.* (1948), Hasted and ElSabeh (1953) and Lane and Saxton (1952), because it was the results of these papers, which underlay the Debye model concept for electrolytes and have been used till now in constructing and modifying the physicochemical models of electrolyte solutions. The validity of the experimental data from papers by Hasted *et al.* (1948), Hasted and ElSabeh (1953) is questionable because of certain circumstances. First, the value $\varepsilon_1(S)$ of the real part of CP, obtained (in the centimetre wavelength band) for $S = 60\%$, is greater than for $S = 28\%$, which obviously contradicts both the accepted general picture of concentration dependencies $\varepsilon_1(S)$, and the other experiments presented later in the same wavelength band. Besides, if we analyse the data by Hasted *et al.* (1948), Hasted and ElSabeh (1953) by the considered technique for obtaining the C-C model parameters, then the ε_∞ value becomes either negative (for 10°C and $S = 34$ and 60%) or zero (for 20°C and $S = 60\%$). In this case the value of parameter ε_0 for the NaCl solution numerically corresponds to the ε_0 value for freshwater. Similar data processing results clearly indicate serious systematic errors in the original measurements carried out by Hasted *et al.* (1948) and Hasted and ElSabeh (1953).

As far as the paper by Lane and Saxton (1952) is concerned, then, as was shown in paper by Onishchenko and Sharkov (1982) (see above), the experimental data on the dielectric properties of a strong electrolyte, obtained in that paper in the millimetre wavelength band, also contain serious systematic errors which have resulted in

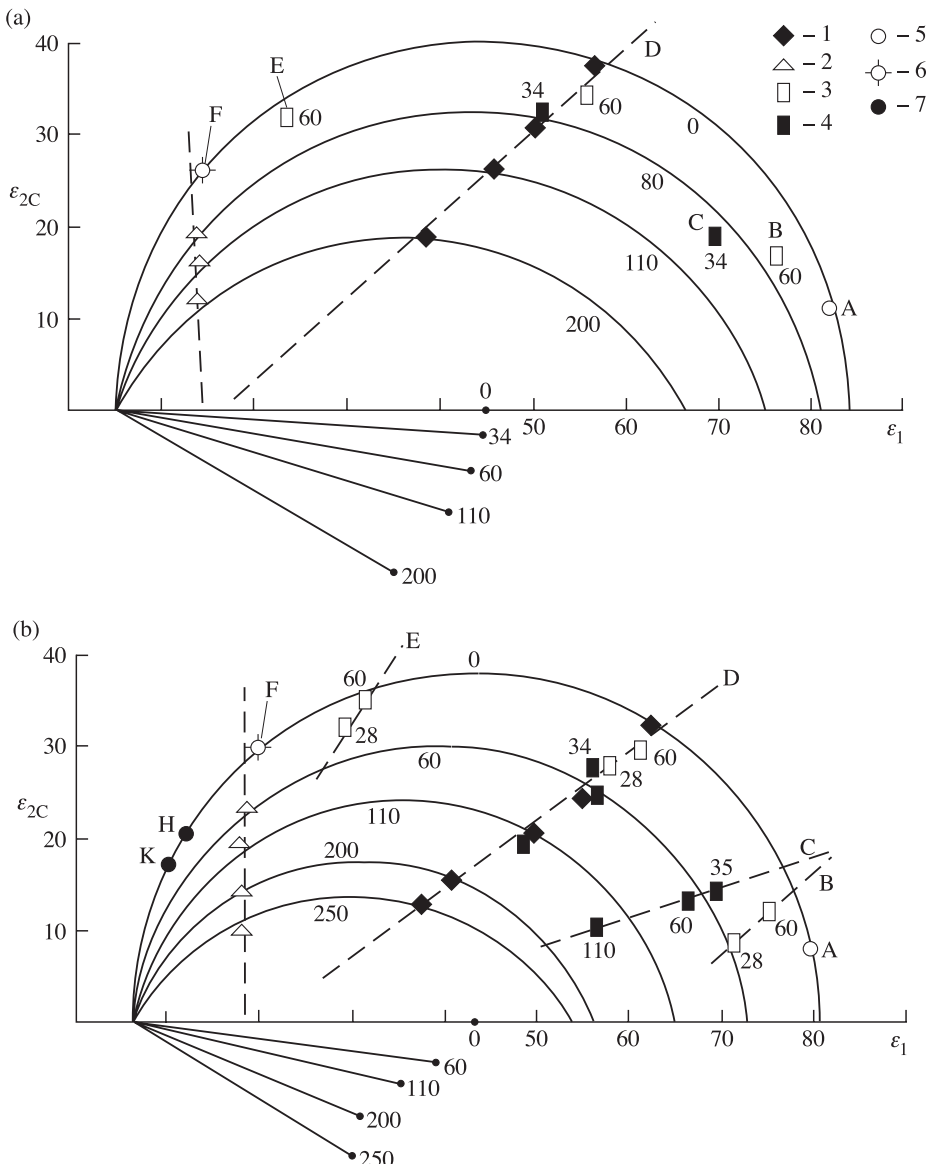


Figure 8.16. Cole-Cole diagrams for the water solution NaCl at 10°C (a), 20°C (b) and 30°C (c). Diagrams by E. Sharkov (1984) using the following data: 1, Yastremskii (1961); 2, Onishchenko and Sharkov (1982); 3, Hasted and ElSabeh (1953); 4, Hasted *et al.* (1948); 5, Grant *et al.* (1957); 6, Grant and Shack (1967); 7, Demyanov *et al.* (1974); 8, Barthel *et al.* (1970); 9, Christensen *et al.* (1966); 10, Hasted and Roderick (1958); 11, Pottel and Lossen (1967). Figures next to experimental data and curves show values of salinity (in parts ‰). Letters display operating wavelengths for (a) and (b) diagrams: A = 17.24 cm; B = 9.22; C = 10; D = 3.2; E = 1.26; F = 0.8; H = 0.5; K = 0.4. For (c) diagram: A = 11.49 cm; B = 10; C = 5.66; D = 3.6; E = 3; F = 2.5; G = 1.76; H = 0.8.

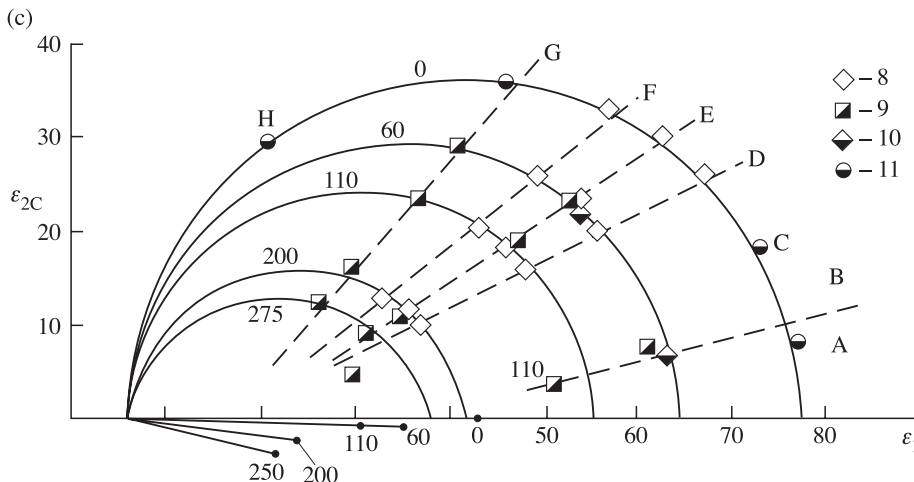


Figure 8.16 (c)

qualitative contradictions with the modern data. That is to say, according to the data of Lane and Saxton (1952), the $\varepsilon_1(S)$ value at the wavelength of 0.62 cm decreases with increasing electrolyte concentration, whereas in reality the $\varepsilon_1(S)$ value should rise. We can easily be convinced of the latter conclusion by considering the corresponding C-C diagrams (see Figure 8.16(a) and (b)). For the indicated reasons the data of these papers have not been used in the analysis presented below, though they have been plotted on C-C diagrams for illustration (see Figure 8.16(a) and (b)).

8.5.5 The C-C model parameters for strong electrolytes

The concentration dependencies of the relaxation times distribution parameter are virtually linear (Figure 8.17(a)) – the lower the solution temperature, the greater the deviation in dielectric properties of electrolyte from the Debye model. A more thorough study indicates an important feature of the dependencies considered; namely, at any values of solution salinity a pretty sharp (virtually jump-wise) decrease of the $\alpha(S)$ value is observed in the narrow temperature range (22–25°C). At 25°C the deviation of the considered model from the Debye one is insignificant (especially for low salinities of solution). This fact is enough to just explain why the results of processing performed by Sharkov (1984) almost fully correspond to the results of the processing of the early data (Barthel *et al.*, 1970) by the Debye model, undertaken in the paper by Ermakov *et al.* (1975) (see Figure 8.17(b) and (c)). Generally speaking, this circumstance just explains why many researchers adhere to the purely Debye model of electrolytes, since the main scope of experiments was accomplished in the range of ‘room’ temperatures.

The analysis of obtained concentration $\varepsilon_0(S)$ dependencies (Figure 8.17(b)) indicates that, though the qualitative character of these curves in relation to similar dependencies of the Debye model was conserved (i.e. $\varepsilon_0(S)$ decreases with

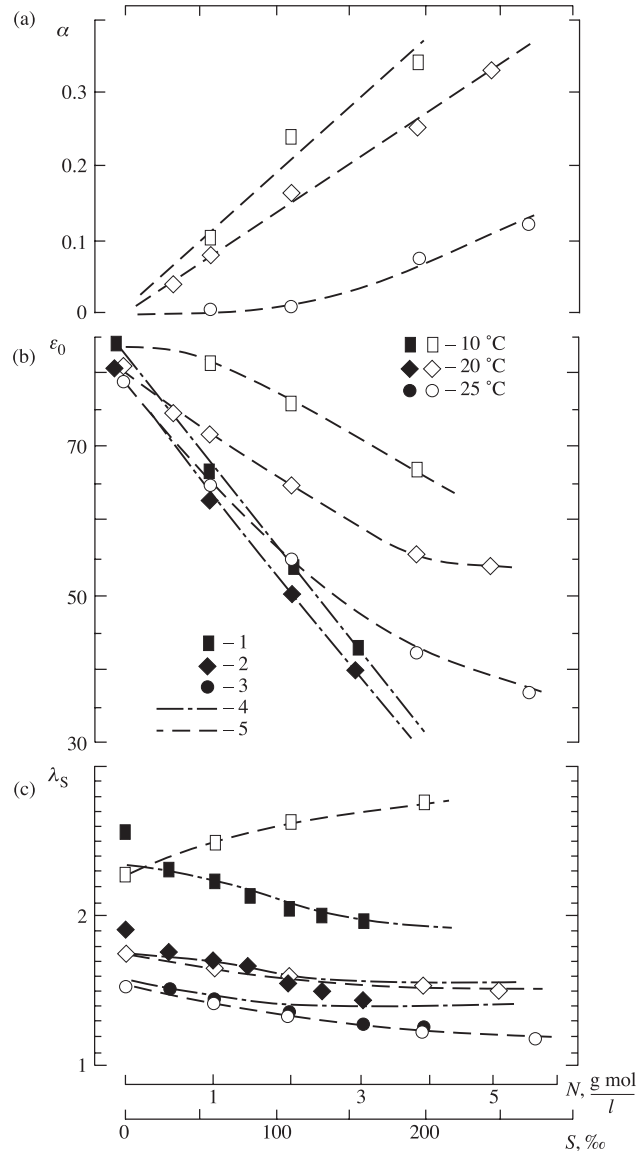


Figure 8.17. Relation of C-C and D model parameters to salinity of water solution NaCl. (a) distribution parameter; (b) static constant; (c) relaxation wavelength. S is salinity (in parts per thousand). N is molar concentration (in g mol/l). Open symbols display processing results obtained by Sharkov (1984) using data by Yastremskii (1961), Ermakov *et al.* (1975), Onishenko and Sharkov (1982), Harris and O'Konski (1957), Barthel *et al.* (1970), Christensen *et al.* (1966), Demyanov *et al.* (1974), Grant *et al.* (1957), Grant and Shack (1967); Pottel and Lossen (1967). Solid symbols: 1, 2 and 3, results obtained by Ermakov *et al.* (1975) using D model; 4 and 5, calculations using Stogryn (1971) model and Sharkov (1984) model.

increasing concentration of a solution), nevertheless the $k_0 = (1/\varepsilon_0)(\partial\varepsilon_0/\partial S)$ gradient considerably decreased. Note that this gradient is one of the basic parameters featuring in physicochemical models of electrolyte solutions. Whereas in the Debye model the value of this gradient was 0.23–0.3 (per one %) and virtually did not depend on temperature (see Figure 8.17(b)) in Stogryn's approximation model, processing with regard to features of the C-C model revealed a strong temperature dependence – from 0.1 (at 10°C) up to 0.18–0.2 (at 25°C), the main drop being a fall, as in the case of $\alpha(S, t)$, to the temperature range of 22–25°C.

The magnitudes of $\varepsilon_0(S)$ also underwent considerable variations – their values were found to be essentially higher than the purely Debye $\varepsilon_0(S)$ values – by 30–40% for $S = 60 \geq 100\%$. Note also a certain physical incorrectness of Stogryn's approximation of $\varepsilon_0(S)$ (or $\varepsilon_0(N)$), obtained in accordance with the Debye model concept: at solution salinity greater than 250‰ ($N \geq 5.1$) the ε_0 values become negative (at 20°C), which is invalid physically. If, however, we proceed from the C-C model, then, as can easily be seen from the analysis of Figure 8.17(b), the essentially nonlinear character of the concentration dependence of $\varepsilon_0(N)$ is observed (even at $t = 25^\circ\text{C}$), and the static constant does not assume values lower than 35 (for solution salinity up to 250‰). For cooled water ($t = 10^\circ\text{C}$) the $\varepsilon_0(S)$ dependence is much weaker, and for weak and medium electrolytes ($S \leq 50\%$) the values of static constant virtually do not differ from ε_0 of fresh water. At the same time, the distribution parameter reaches the value of 0.1, which noticeably differs from the Debye model data.

The results of diagram processing by the C-C model technique, presented in Figure 8.17 for determining the character of the relaxation wavelength variation with solution salinity, reveal the qualitative distinction from the data known in the literature (the Debye model) (Stogryn, 1971; Yastremskii, 1961). Here we should mention, first of all, that at 10°C the λ_S value increases (in the Debye model it decreases) with increasing electrolyte solution concentration, whereas at 20°C the qualitative character of dependencies coincides with the Debye model, though some quantitative distinctions take place (see the curves for 20 and 25°C). A virtual coincidence of Sharkov's (1984) results with those calculated by Ermakov *et al.* (1975) in accordance with the Debye model concept is not surprising (Figure 8.17(c)), because the relaxation process in electrolyte solutions at these temperatures (according to Sharkov's (1984) results) approaches the purely Debye type with $a \rightarrow 0$. (This is very noticeable on the C-C diagrams in Figure 8.16(c) as well.) A pretty sharp variation of model parameters near 25°C can be associated most likely with the change in character of the hydration processes (from negative to positive) for chlorine ions at 27°C (Sinyukov, 1976).

The analysis of presented data indicates that the dependencies of the optical constant on temperature and salinity are weakly prominent for the studied variations of temperature (10–25°C) and salinity (0–250‰) and are expressed by the relation

$$\varepsilon_\infty = 5.8 \pm 0.2, \quad (8.49)$$

not revealing any quantitative regularities inside these boundaries. The indicated relation has more likely a qualitative character, since there are no systematic data

Table 8.2. Calculated values of A_i and B_i coefficients in approximations $\varepsilon_0(S, t)$; $\lambda_S(S, t)$ and $\alpha(S, t)$

	$t = 10^\circ\text{C}$		$t = 20^\circ\text{C}$		$t = 25^\circ\text{C}$	
	A	B	A	B	A	B
ε_0	-3.15×10^{-6}	-3.92×10^{-4}	1.60×10^{-6}	-1.79×10^{-3}	3.11×10^{-6}	-2.99×10^{-3}
λ_S	-2.26×10^{-6}	1.54×10^{-3}	1.52×10^{-6}	-1.02×10^{-3}	6.21×10^{-7}	-1.02×10^{-3}
α	0	1.82×10^{-3}	0	1.22×10^{-3}	1.62×10^{-6}	0

on the dielectric properties of strong electrolytes in the short-millimetre wavelength band at the boundary of transition into the super-Debye absorption band.

In virtue of the practical importance of semi-empirical models of the dielectric parameters of electrolytes (for example, for the theory and practice of microwave remote sensing), we shall present below the results of least-squares approximation (Sharkov, 1984) of the Cole–Cole model parameters $\varepsilon_0(S, t)$, $\alpha(S, t)$ and $\lambda_S(S, t)$, obtained after processing the corresponding diagrams, as the following quadratic forms:

$$\begin{aligned}\varepsilon_0(S, t) &= \varepsilon_0(0, t)[1 + F_1(S, t)], \\ \lambda_S(S, t) &= \lambda_S(0, t)[1 + F_2(S, t)], \\ \alpha(S, t) &= F_3(S, t), \\ F_i(S, t) &= B_i(t)S + A_i(t)S^2,\end{aligned}\tag{8.50}$$

where $i = 1, 2, 3$, and $\varepsilon_0(0, t)$ and $\lambda_S(0, t)$ correspond almost precisely (to an error lower than 1%) to the Debye model approximations for the freshwater (Stogryn, 1971). Because the number of temperature points was limited (10, 20 and 25°C), in determination of the parameters the corresponding analytical approximations $A_i(t)$ and $B_i(t)$ have not been found, but are presented in the form of Table 8.2.

In conclusion to this section we note that the results of analysis (Sharkov, 1984) gave rise to the new semi-empirical relaxation model for the dielectric properties of a strong monoelectrolyte of aqueous solution of NaCl. However, at present it is not possible to give a full answer to the question on concentration dependencies of the Cole–Cole model parameters for a monoelectrolyte within a wide range of temperatures. This requires the reliable and, mainly, sequential experiments to be performed by a unified technique in the wavelength band from 0.2 to 5–6 cm and in the wide range of temperatures – from 80 – 90°C to negative ones (a supercooled electrolyte solution).

8.5.6 Dielectric properties of polyelectrolytes

As we have already noted, the thorough study of the dielectric properties of mixed electrolytes is rather complicated because of the diversity of the physicochemical

features of components of natural electrolytes. Nevertheless, the existing (and, of course, not complete) data indicate that the main contribution to the polarization properties of solutions is made by the strong NaCl electrolyte, which is virtually fully dissociated in an aqueous solution. Below are presented the experimental data on measuring the dielectric parameters of a mixed solution of salts which is close in composition to seawater (Smirnov and Sharkov, 1979).

Table 8.3 presents the results of an investigation of the dielectric characteristics in the microwave bands ($\lambda = 10, 18, 75$ and 150 cm) of composite solutions of sodium chloride, magnesium chloride and magnesium sulfate (the partial concentrations of components are indicated in Table 8.3). The same table gives the possible radiothermal contrasts of radio-emission of corresponding media (see equation (7.47)). It follows from the analysis of the data of Table 8.3 that the admixtures of magnesium salts very weakly influence, in general, the real part of the dielectric constant of a mixture (it remains constant within the limits of the experimental error) and essentially increase the attenuation in an electrolyte. Owing to this fact, the basically negative contrast in radiothermal characteristics of composite solutions with respect to a monosolution is possible (from $+0.2$ to -4.0 K).

The highly sensitive radiothermal complexes, now existing in experimental practice, will probably, make it possible to remotely determine the physicochemical features of composite natural salt solutions from the spectral characteristics of their radio-emission.

8.6 SPECTRAL AND TEMPERATURE CHARACTERISTICS OF THE EMISSIVE PROPERTIES OF WATER BASINS

Using the models of dielectric properties of water and electrolytes developed above, we shall analyse theoretically the emissive properties of smooth surfaces of the aforementioned media with allowance for atmosphere illumination based on relation (7.20):

$$T_B(\lambda, S, \theta, t) = \kappa(\lambda, S, \theta, t)T_0 + [1 - \kappa(\lambda, S, \theta, t)]T_I(\lambda, \theta), \quad (8.51)$$

where $\kappa(\lambda, S, \theta, t)$ is the emissivity of a smooth water surface, determined by Fresnel's coefficients $R(\lambda, S, \theta, t)$ from relation (7.17), which is a direct consequence of Kirchhoff's law. Here T_0 is the thermodynamic temperature of the studied surface and $T_I(\lambda, \theta)$ is the brightness temperature of the sky and atmosphere.

The analysis of Figure 8.18, where the frequency dependencies $\kappa(\lambda)$ are presented within a wide wavelength band, indicates that the studied dependence contains two wavelength bands which essentially differ in temperature and salinity effect on $\kappa(\lambda)$. The frequency boundary lies (conventionally) in the $5\text{--}7\text{ cm}$ band. Below this wavelength value the emissivity very weakly depends on salinity, in contrast to the thermodynamic temperature dependence, where a strong negative gradient is observed. In the decimetre and metre bands the salinity has a strong effect on $\kappa(\lambda)$ (mainly through increasing the losses in the aqueous medium), the salinity effect being increased with the working wavelength. Besides, the temperature

Table 8.3. Dielectric characteristics of mixed electrolyte solutions

Type of solution mixture and component concentrations (%)	$\lambda = 10 \text{ cm}, t = 18^\circ\text{C}$			$\lambda = 18 \text{ cm}, t = 10^\circ\text{C}$			$\lambda = 75 \text{ cm}, t = 18^\circ\text{C}$			$\lambda = 150 \text{ cm}, t = 18^\circ\text{C}$		
	ε_1	ε_2	$\Delta T_B, \text{K}$	ε_1	ε_2	$\Delta T_B, \text{K}$	ε_1	ε_2	$\Delta T_B, \text{K}$	ε_1	ε_2	$\Delta T_B, \text{K}$
NaCl(20)	77.7	39.8	0	81.1	44.8	0	80.3	80.4	0	80.5	168	0
NaCl(20)+MgCl ₂ (5,4)	76.4	40.6	+0.26	80.7	48.3	-0.95	80.1	86.2	-1.58	80.3	172	-0.45
NaCl(20)+MgCl ₂ (7,8) +MgSO ₄ (5)	76.1	44.7	-1.0	80.2	51.6	-1.85	79.7	94.5	-3.92	80.6	187	-2.47

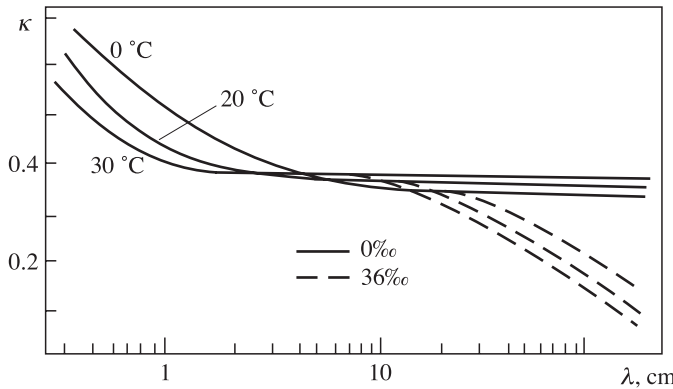


Figure 8.18. Spectra of smooth water surface emissivity at temperatures 0, 20 and 30°C for fresh and saltwater.

dependence has a positive gradient for freshwater and a negative gradient for salt (sea) water. The detailed numerical data on temperature and salinity dependencies of emissivity for the wavelengths ranging from 1 mm to 1 m are presented in papers by Hyatt (1970), Rabinovich and Melentev (1970), Lepley and Adams (1971) and Raizer *et al.* (1974). These tabulated values should be used with caution, because all these calculations were based, in essence, on the early models (Saxton and Lane, 1952) of dielectric properties of water and aqueous solutions of electrolytes (see sections 8.5 and 8.6).

The presence of sky illumination $T_I(\lambda, \theta)$ qualitatively changes the observational situation (Raizer *et al.*, 1975a): strong (up to 1000 K) metre-band cosmic radiation (of the Sun and the galaxy) essentially narrows down the information region of salinity and temperature dependence $T_B(\lambda, \theta, S, t)$ from the side of metre-band waves (Figure 8.19) and, in general, strongly transforms the spectral dependencies of brightness temperature with respect to the spectral dependencies of emissivity (Figure 8.18).

The temperature and salinity effect on the radio-emission of a water surface is most prominent in the 50–70 cm band, the temperature gradient ($\Delta T_B / \Delta t$) (i.e. the quantity, which just determines the remote sensing efficiency) being qualitatively different for salt and freshwater. Figure 8.20 shows the thermodynamic temperature dependencies of $T_B(S, t)$ for fresh and seawater (for salinity of 20‰ and 37‰) at the wavelengths of 18 and 75 cm. All brightness temperature variations are nearly linear – for freshwater the value of the $\Delta T_B / \Delta t$ gradient equals about 0.5 K at 1°C for centimetre and decimetre bands. For seawater the positive gradient decreases and assumes negative values in the metre band (−0.3 K/1°C for the wavelength of 75 cm). Figure 8.21 presents the salinity dependencies of brightness temperature at the same wavelengths with account taken of illumination. Variation (increase) of a solution's salinity results in a lowering the radiobrightness temperature at these wavelengths. However, at higher temperatures ($t = 40^\circ\text{C}$) a prominent nonlinearity of the salinity dependence of T_B is noticeable, which is related physically to a sharp growth of

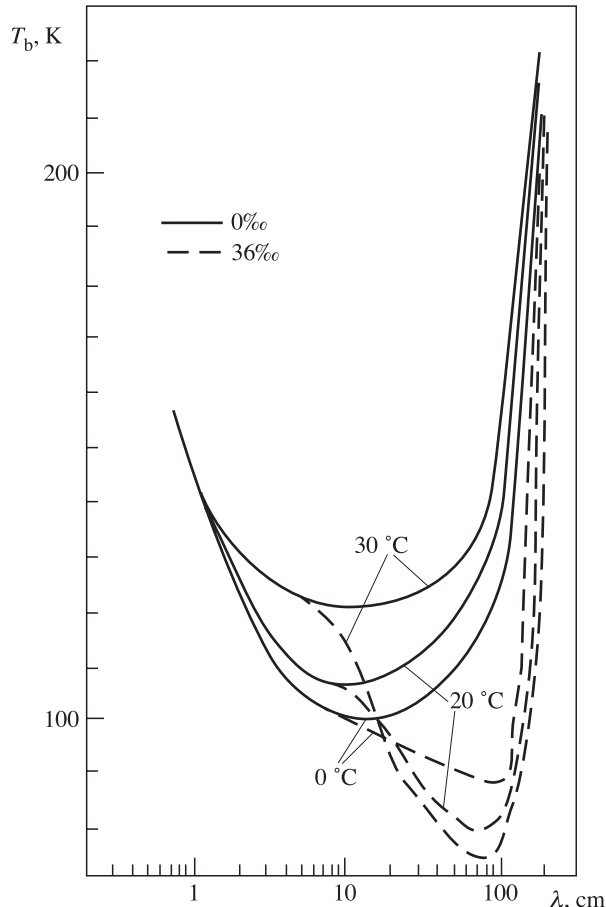


Figure 8.19. Spectra of radiobrightness temperature of a smooth water surface at temperatures 0, 20 and 30°C for fresh and salt water.

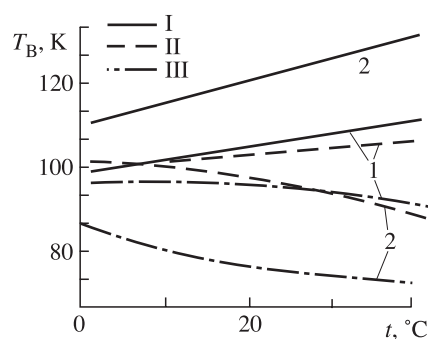


Figure 8.20. Temperature-dependent radiobrightness of a smooth water surface at wavelengths 18 cm (1) and 75 cm (2). I: fresh water. II: salinity is 20‰. III: 36‰.

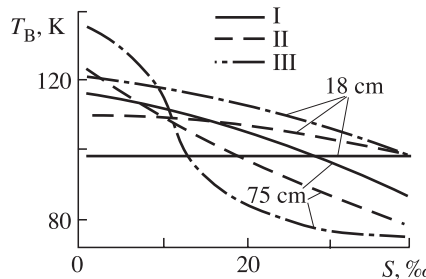


Figure 8.21. Salinity-dependent radiobrightness of a smooth water surface at wavelengths 18 and 75 cm. I: at temperature 0°C . II: 20°C . III: 30°C .

dielectric losses at low concentrations of salts (5–15%). As the temperature decreases, the nonlinearity of the $T_B(S)$ dependence noticeably becomes smoother. So, whereas for the wavelength of 75 cm and at 30°C the gradient for weak salinities can reach 4–5 K (at 1‰), for 18 cm it decreases down to 0.5. At $t = 0^\circ\text{C}$ the salinity dependence of brightness temperature in the decimetre band completely disappears (Figure 8.21). Thus, investigations of salinity in the polar regions of the ocean using this wavelength band (18–21 cm) are rather problematic. Brightness contrast calculations were performed (Smirnov and Sharkov, 1979) on evidence derived from experimental dielectric data (see Table 8.4).

It is of interest to note that, according to the data of Smirnov and Sharkov (1979), the influence of the other (apart from sodium chloride) salts in mixed solutions provide a negative contrast (in relation to a monosolution), but of rather small magnitudes (from 0.2 to 3.9 K) (see Table 8.3).

The experimental data, obtained in the course of aircraft work on studying surface salinity fields (Droppleman *et al.*, 1970; Chukhrai and Shutko, 1978; Blume and Kendall, 1982; Blume *et al.*, 1977), are, generally, in satisfactory agreement with the developed model.

As an effective example, we shall consider the results of aircraft investigations of the sea surface salinity (SSS) field of the coastal zone of the Atlantic Ocean near Chesapeake Bay (Miller, 2000). These investigations have been carried out by means of the microwave passive instrument at the wavelength of 21.4 cm. The fluctuation sensitivity threshold of the instrument, normalized with respect to the salinity value by using the contrast value calculated from the aforementioned model, was found to be some tenths of a part ‰ for the three-dimensional pixel of 1 × 1 km (see section 5.6). Plate 2 (see the colour section) shows the spatial fields of sea surface salinity of the coastal zone of the Atlantic Ocean before (Plate 2(a)) and after (Plate 2(b)) tropical cyclone ‘Fran’ passed through the southern states of the USA (on September 8–10, 1996). This powerful cyclone caused strong rainfall in the basin of rivers feeding the Chesapeake Bay. A strong freshwater pulse through the river drainage basins into the coastal zone of the Atlantic Ocean was formed, and it was recorded on the radiothermal microwave maps (Plate 2). It would not be possible to obtain a similar result using contact means (from on board a ship) in the spatial-temporal scales investigated.

Table 8.4. Dielectric characteristics of strong electrolyte NaCl

Normality, mol/l	Salinity, ‰	$\lambda = 10 \text{ cm}, t = 18^\circ\text{C}$			$\lambda = 18 \text{ cm}, t = 10^\circ\text{C}$			$\lambda = 75 \text{ cm}, t = 18^\circ\text{C}$			$\lambda = 150 \text{ cm}, t = 18^\circ\text{C}$		
		ε_1	ε_2	$\Delta T_B, \text{K}$	ε_1	ε_2	$\Delta T_B, \text{K}$	ε_1	ε_2	$\Delta T_B, \text{K}$	ε_1	ε_2	$\Delta T_B, \text{K}$
0	0	79.4 (78.33)	10.2 (13.52)	0	81.7 (82.48)	6.8 (10.21)	0	82.3 (80.79)	4.1 (1.86)	0	82.1 (80.82)	3.7 (0.93)	0
0.20	12	78.4	27.3	3.1	82.3	34.7	5.3	80.4	56.3	9.4	82.3	116	23.2
0.31	17.9	76.2	34.9	4.2	82.9	42.2	5.3	79.7	73.7	14.4	80.4	160	30.9
0.63	36.0	76.4	47.2	8.0	83.1	57.8	11.4	80.2	108	23.3	79.9	203	36.5
1.83	100.1	72.0	65.8	13.6	77.6	79.2	17.1	79.4	139	30.2	77.8	231	39.2
3.92	200.7	68.1	78.6	18.3	71.8	97.6	22.1	72.7	165	35.4	74.1	258	41.9
5.08	250	64.9	82.3	19.0	72.2	104	23.5	70.2	178	37.5	70.9	267	42.8

Note. Figures in brackets are theoretical values of water dielectric constant on the D model basis.

8.6.1 Requirements for SSS observations

Salinity is a significant variable for upper ocean dynamics at very high latitudes (near-freezing temperatures and ice formation lead to a salinity-dominated stratification), in the western Pacific warm pool (very high precipitation and evaporation), and in subtropical high-salinity regions. The warm pool also represents a region, where the surface freshwater flux induces a shallow salt stratification and a ‘barrier layer’, that isolates the surface from the main thermocline, with important consequences for surface layer heating. Salinity also has a strong influence (the halosteric effect) on the calculation of surface layer heat storage from the observed sea level. The application of remotely sensed SSS to the study of these different ocean dynamics phenomena implies different requirements for space, time and even salinity resolution, due to the different scales involved and the contrast in surface water characteristics. Typical values required to resolve some of the specific phenomena are (Kerr *et al.*, 2000c,d):

- Barrier layer effects on the tropical Pacific heat flux: 0.2 practical salinity unit ($1 \text{ psu} = 1\%$), $100 \times 100 \text{ km}$, 30 days.
- Halosteric adjustment of heat storage from the sea level: 0.2 psu, $200 \times 200 \text{ km}$, 7 days.
- N. Atlantic thermohaline circulation: 0.1 psu, $100 \times 100 \text{ km}$, 30 days.
- Surface freshwater flux balance: 0.1 psu, $300 \times 300 \text{ km}$, 30 days.

The North Atlantic thermohaline circulation and convection in the subpolar seas has the most demanding requirements, and it is the most technically challenging, because of the lower brightness/SSS ratio at low water temperatures. A compromise for all these different requirements would be met by considering the optimized requirements as a general goal for the SMOS mission (Schmitt and Montgomery, 2000; Kerr *et al.*, 2000c,d; Martin-Niera *et al.*, 2000) (see also Chapter 14).

Here we note that the first successful remote aircraft experiments, performed in Russia and USA at the end of 1970s and at beginning of the 1980s (Chukhrai and Shutko, 1978; Blume and Kendall, 1982; Blume *et al.*, 1977), gave rise to unjustifiable hopes for the rapid implementation of space experiments to study salinity fields by means of antenna systems having huge apertures (Blume *et al.*, 1978) for ensuring the necessary spatial resolution. Though these projects have failed, expert oceanologists nevertheless believe that the study of the spatial-temporal variability of the surface salinity field of the World Ocean with the spatial resolutions available soon will be one of the problems given priority in the future development of remote sensing (Lagerloef *et al.*, 1995; Miller *et al.*, 1998; Schmitt and Montgomery, 2000; Miller, 2000; Miller and Payne, 2000).

At present, great efforts are being directed towards scientific-technological development of radio-interferometric technology, which is sometimes called passive aperture synthesis, for ensuring acceptable spatial resolution (Milman, 1988; Camps *et al.*, 1997, 1998; Camps and Swift, 2000; Kerr *et al.*, 2000b, 2000c, 2000d; Wigneron *et al.*, 2000; Martin-Neiza and Goutoule, 1997). Parallel to this approach, designers are working on versions of antennas with large-scale apertures,

but with a lightweight structure (inflatable antennas), as well as deployable mesh surfaces and other structural versions of antennas (Njoku *et al.*, 1999, 2000b; Wilson *et al.*, 2000).

8.7 EMISSIVE PROPERTIES OF ICE SURFACES

The ice surfaces of congealing seas at middle and high latitudes, as well as glacial ice surfaces (Antarctica, Greenland, glaciers in mountains) are quite important objects, which essentially influence the hydrological and meteorological characteristics of the Earth's surface–atmosphere system. In this case the phase transitions of water and ice are accompanied by releasing and absorbing huge masses of heat, by changes in the optical regime and salinity, by the generation of strong electrical fields. The ice surface of seas, oceans and land is a fine regulator in the thermal and dynamical interaction of the ocean and atmosphere. Its inhomogeneities in width and huge spatial size mean that high-speed and reliable means are required to determine and diagnose age gradations, cohesion, the size of ice fields and their thickness. As durable investigations of Earth's ice surfaces by various remote sensing techniques have shown, microwave methods provide significantly different information on the structure and physicochemical composition of ice systems as compared to the data provided by the methods in the optical and IR wavelength bands. This is due to the fact that the phase transition of liquid water into the solid state is characterized by radical changes in dielectric properties (see section 8.2).

If, however, the ice surface is qualified with regard to its place in the system of dielectrics (and, accordingly, with regard to emissive characteristics), one can distinguish at least three types of ice systems – glacial ice, freshwater ice and sea ice. All these types of ice surfaces are substances which significantly differ in the electrodynamical respect. In addition, we note that their role in thermal and dynamical interaction in the ocean–atmosphere system is significantly different as well.

Since **glacial ice** (Antarctica, Greenland, glaciers in mountains) is generated through a very complicated morphological formation from precipitated snow, rather than from a liquid phase, the strong influence of the internal geometrical structure on dielectric and emissive properties of glacial ice fields over great spatial scales is obvious. As we have noted above (section 8.2), the dielectric properties of glacial ice specimens are very close to freshwater ice characteristics – the real part of the dielectric constant is virtually constant in the microwave band with very small variations in temperature and structure. In other words, the so-called dielectric anisotropy takes place here (Matsuoka *et al.*, 1996, 1997). The imaginary part, however, was found to be strongly influenced by weak mineralization, by the presence of organic substance and admixtures of gas bubble type, and by thermodynamic temperature. However, since the magnitude of this part is small, its value and variations have virtually no effect on emissive characteristics. Using equation (7.47) one can easily obtain the emissivity value for glacial ice – it will be equal to 0.93. And, thus, the radiothermal contrast between the ice surface and water surface

can constitute considerable values namely, 100–150 K. Note that the indicated radio-thermal contrast is greatest among the natural surfaces of the Earth.

However, the first investigations of the thermal radiation of glacial ice in Antarctica, carried out by Russian researchers from the ‘Kosmos-243’ satellite in 1968, brought about an unexpected surprise. A serious decrease of emissive properties of resonance type was recorded in the centimetre band in the inner regions of Antarctica (Basharinov *et al.*, 1971) and then in Greenland. This result was confirmed later by the American investigations from the ‘Nimbus-5’ satellite in 1972 (see Plate 3). The effect was so unexpected and obscure, that it was called ‘Antarctica’s puzzle’. The essence of the problem lies in the fact that in formally restoring the dielectric properties of Antarctica’s inner regions by the known formulas (7.47) a physically contradictory result is obtained – the continental regions of Antarctica would represent the lakes of freshwater in this case.

This ‘puzzle’ was soon (in 1973) resolved by the efforts of Russian scientists (Gurvich *et al.*, 1973). The frequency-selective variation of thermal radiation of Antarctica’s inner regions was found to be caused by the effect of volume dissipation of a substance’s thermal radiation on mesoscale geometrical features of the structure of a glacier in its formation from the snow mass. Certainly, the use of the homogeneous dielectric model to interpret emissive characteristics is not admissible in the given case.

The microwave investigations have clearly indicated a complicated internal structure of the glacial ice surfaces of Antarctica and Greenland in mesoscales. Neither contact measurements, nor optical observations could reveal these features at all.

A more interesting point is that the exchange between the atmosphere and the Antarctic ice sheet takes place largely through sublimation processes, i.e. through the direct transition from the solid state to a gaseous one (avoiding the melting process). Thereby, some peculiar areas in the Antarctic ice sheet are formed, which can serve in many respects as the Earthly analogues of the northern ice cap of Mars (Siegert and Fisher, 2002).

Drifting sea ice is a rather peculiar physical body. Unlike glacial ice, it represents, first of all, a multicomponent system, which includes solid, liquid and gaseous phases. The solid phase represents an ice-crystalline consolidated skeleton, the liquid phase is a ‘pickle’ formed from the seawater, and the gaseous phase represents air bubbles of a quite diversified, dispersed structure. Under natural conditions sea ice almost always represents a three-phase system. This essential fact determines its physico-mechanical properties: the ice as a solid body always exhibits viscoelastic properties, and as a dielectric it shows essential electrical spatial-temporal inhomogeneity; and, accordingly, it includes a spectrum of relaxation mechanisms (see section 8.2). The above considerations and the severity of the hydrometeorological conditions of formation and existence of ice make the direct (contact) investigation of electrophysical properties of sea ice a really complicated experimental and technological problem. Nevertheless, even the first microwave radiothermal investigations with highly sensitive instruments (Bespalova *et al.*, 1976b) have demonstrated a

highly efficient recognition of various types of sea ice and its spatial and temporal characteristics.

As we have already noted, it is difficult to form a detailed picture of the dielectric properties of sea ices, since they strongly depend on the mineral composition of sea water in a particular basin, as well as on the temperature and meteorological history of solid phase formation. For this reason, contemporary researchers follow an opposite path in a certain sense – they carry out remote microwave investigations of various types of sea ice and then restore the electrophysical characteristics of drifting sea ice in accordance with some particular model (see, for instance, Hewison and English (1999)). On the basis of the results of these authors, we shall consider some types of sea ice and the spectral features of their emissive properties.

Grease ice is a matt, brownish ice undulating as surface waves, but it also includes flat, shiny ice rind. This category is thinner than 10 mm, and the emissivities show a strong dependence on thickness, ranging from those of open water to thick new ice (Figure 8.22 and Table 8.5).

Nilas includes light, dark, and rafted nilas, which could not be resolved radiometrically. This is a flat, new ice with no air or brine pockets and, hence, it exhibits no significant surface or volume scattering. The emissivity is dependent on the ice thickness, saturating when it is greater than about 30 mm. The upper line (Figure 8.22 for the nilas diagram) represents a best fit calculated for only the thicker samples of Baltic nilas. This shows high emissivity across the spectrum, as expected. The limited amount of Arctic nilas observed generally has a lower emissivity than that found in the Baltic owing to the difference in salinity. The lower curve in this diagram is a fit to only the Arctic samples, which may be thinner than the ice used to calculate the Baltic nilas line.

Bare new ice is a thicker, homogeneous, flat, dark ice formed within the last few days, undisturbed by pressure ridging or snowfall. It is characterized by flat emissivity spectra. This ice excludes Arctic samples.

Snow-covered new ice is as above, but includes a thin surface (a few centimetres) of fresh, dry snow. This category also includes a **pancake** ice (close-packed, regular, circular floes of less than 10 m diameter) and **icecakes** (similar, with larger diameter). Lower frequencies see a higher effective emissivity, as they penetrate the snow to the slightly warmer underlying surface. **Compact consolidated ice**, when the snow surface was wetter, is included in this category because of its spectral characteristics.

Broken ice covers a variety of forms, from pure slush found in fine-grained **Shuga, brash ice** to larger, crushed ice floes making up close and very close pack ice. This grouping shows a large range of spectra owing to the irregularity of the samples' ice fields.

Compact consolidated ice comprises large ice floes that have frozen together, often with ridging and variable amounts of dry snow surface. This is the most extensive ice type observed in the Baltic, and is typically 30–50 cm thick. The spectrum (Figure 8.22) shows lower emissivity at higher frequencies, characteristic of the volume-scattering mechanism of small brine and air pockets within the thicker, older ice pack and its snow cover.

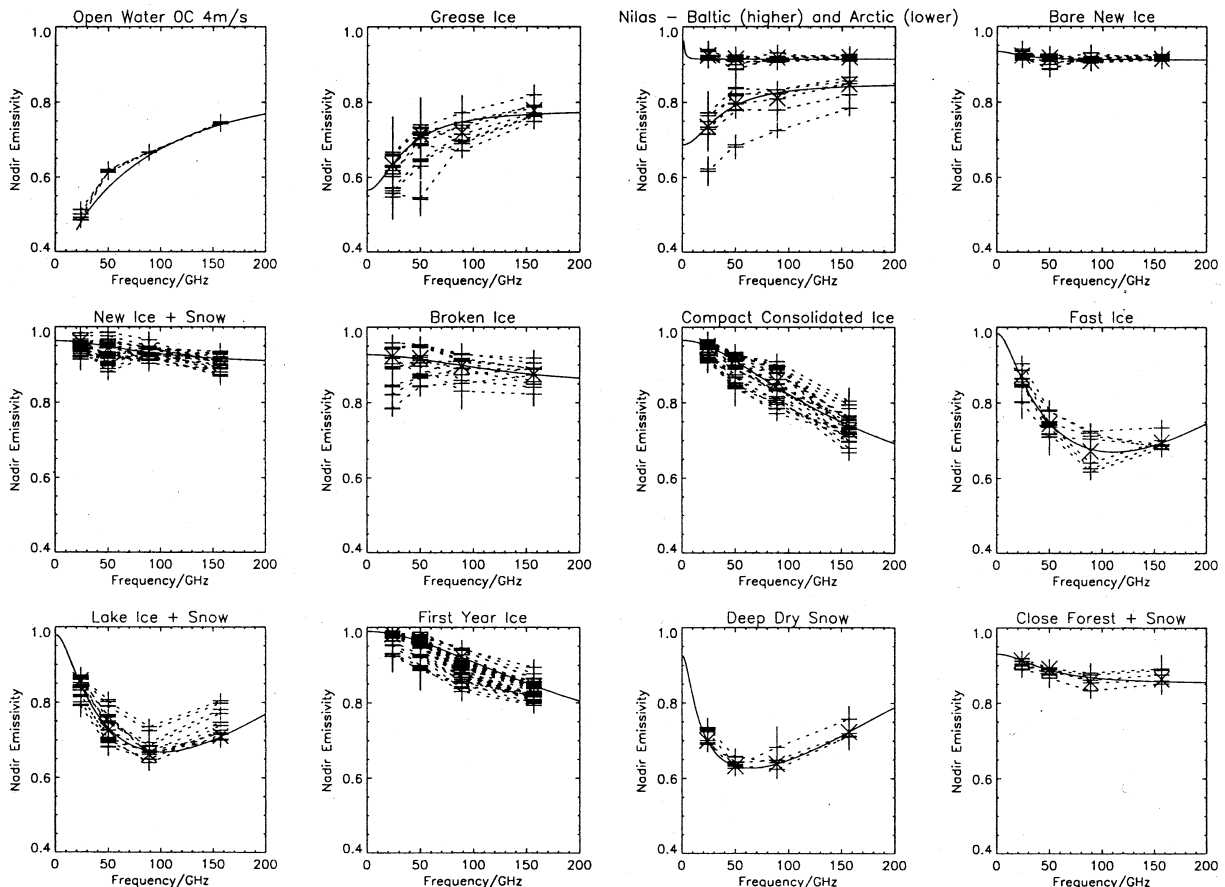


Figure 8.22. Nadir emissivity spectra of natural media. All samples within each surface category are shown, linked with dashed lines, and error bars represent the standard error of mean. The average dependences are shown as continuous lines (Hewison and English, 1999).

Table 8.5. Average emissivity of surface categories

Category	Nadir emissivity			
	(24)	(50)	(89)	(157)
Water, 0°C	0.504	0.617	0.660	0.743
Grease ice	0.632	0.714	0.720	0.779
Baltic nilas	0.924	0.916	0.918	0.919
Bare new ice	0.923	0.918	0.910	0.915
New ice + snow	0.961	0.944	0.937	0.915
Broken ice	0.923	0.918	0.897	0.875
Compact pack ice	0.950	0.913	0.857	0.726
Fast ice	0.872	0.744	0.672	0.969
Lake ice + snow	0.858	0.726	0.662	0.711
First year ice	0.981	0.964	0.922	0.844
Deep dry snow	0.700	0.633	0.640	0.724
Close forest + snow	0.923	0.891	0.857	0.864
Fresh wet snow	0.957	0.962	0.964	0.955

Note. Figures in brackets are working frequencies in GHz.

Fast ice is the landlocked ice found along the northern shore of the Baltic. It is typically 60 cm thick, and has a flat surface as it cannot be affected by pressure ridging, and occasionally has a thin (a few centimetres) surface of snow. This is the oldest of the Baltic ice types (although still ‘first year’), and the volume scattering is evident – even at 24 GHz. Some samples did show spectra intermediate between that of fast ice and other types. A trend is evident for an increase in emissivity above 100 GHz, which suggests increasing absorption, although scattering is still a dominant mechanism.

Despite the snow cover, **lake ice** areas showed very similar emissivity spectra to fast ice, which has a similar structure. This provides evidence that the brine pockets do not dominate the volume-scattering process.

Attention should be paid to the considerable scattering (or, as authors Hewison and English (1999) say, the errors) in separate realizations of spectral characteristics. This is associated with a strong spatial–temporal variability of sea ice fields and with their complicated hierarchical structure. This phenomenon was noticed long ago, beginning with the first works on the remote study of sea ices (Bespalova *et al.*, 1976b). But until now these hierarchical spatial features of sea ice fields have not been investigated fully enough, which greatly complicates the procedures of image recognition of remote microwave observations from spacecraft (Comiso and Kwok, 1996; Parkinson *et al.*, 1999; Belchansky and Alpatzky, 2000; Comiso, 2000).

The analysis of emissive properties of sea ices, however, results in the conclusion that the identification (within a limited band) of various types of ice from microwave spectra is not satisfactory. It is necessary both to essentially extend the range of working frequencies (up to decimetres), and to use the polarization properties, as

well as the features of spatial patterns of objects both in the radiothermal and in the scatterometric mode of observation (Matzler and Wiesmann, 1999; Pulliainen *et al.*, 1993, 1999; Pulliainen and Hallikainen, 2001; Wiesmann and Matzler, 1999; Wiesmann *et al.*, 2000).

We shall pay attention also to the fact that the use of simple relaxation models (of the Debye model type) for interpreting complex electrophysical systems, such as various types of sea ice, can lead to paradoxical conclusions. So, Hewison and English (1999), when interpreting the frequency properties of lake ice covered with snow, obtained the value of a static constant of dielectric permittivity (for the Debye model, section 8.3) for such a system, which is essentially lower (1.78) than the optical constant value (67.1). This indicates that the range of use of the models of homogeneous dielectrics with simple relaxation mechanisms for real natural media is fairly limited, and in many cases the application of simple relaxation models (of the Debye type) is not productive.

8.8 RADIATION PROPERTIES OF THE TERRESTRIAL SURFACES

Apart from the huge water and ice areas, a considerable part of the Earth's surface are the continents, which, in their turn, have a great type of diverse surfaces. In this section we shall consider the dielectric and radiation properties of the terrestrial surfaces in the homogeneous, isothermal, half-space approximation (the primitive models) as a fundamental model for forming more complicated electrodynamic models, which are better suited to the real terrestrial surfaces.

8.8.1 Primitive models

Under indicated conditions (homogeneous and isothermal) the radiation characteristics of the emitting half-space are determined by the dielectric properties of a medium and by the physical temperature (see equations (7.20), (7.44)). In order to imagine more clearly the qualitative distinctions in radiation properties of the terrestrial media, we shall consider the dependence of the emissivity of some terrestrial media on dielectric properties and, accordingly, the microwave contrasts received by remote sensing devices.

Figure 8.23 presents the diagram of dielectric properties of some (natural and artificial) media and their emissivity. The 'coldest', in the microwave sense, of the earth media is the water surface and, especially, the sea surface in the decimetre and metre bands. From the artificial media the 'coldest' are the metal surfaces, since the real and imaginary parts of the dielectric constant tend (formally) to infinity. As usual, the coefficient of reflection (in power) in the centimetre band equals less than 0.05–0.01.

Rock and sandy surfaces, in contrast to aqueous media, are 'hot' media with emissivity values of about 0.9–0.95 in a very wide wavelength band – from a few millimetres up to kilometres. Glacial ice, as well as the surface media on the Moon,

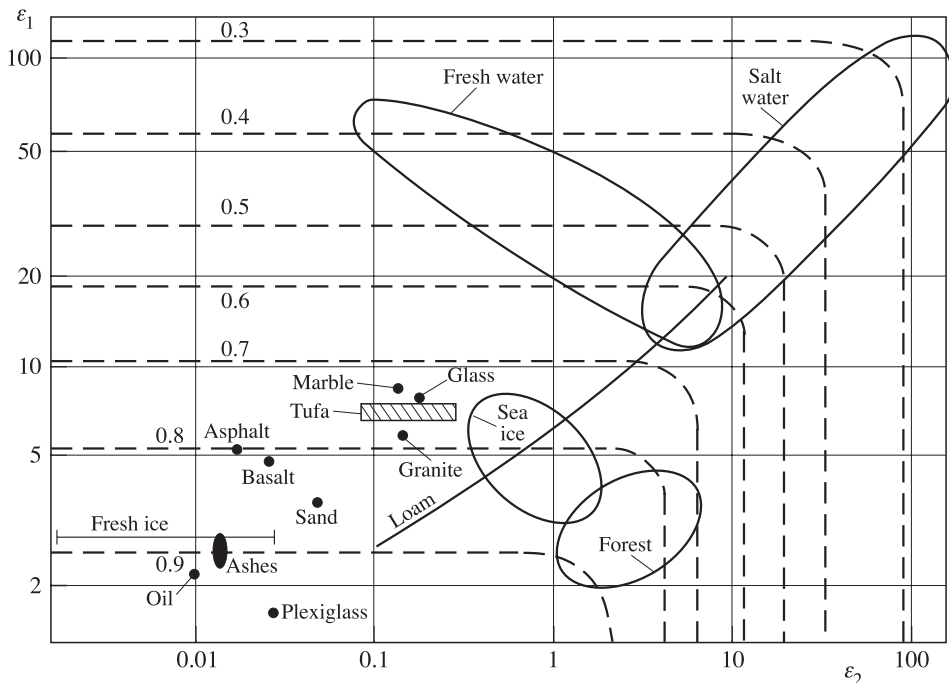


Figure 8.23. Emissivity curves for vertical incidence and for different permittivities of various terrestrial media. Dashed lines show levels of constant emissivity.

Mars, Venus and Mercury can also be attributed to the same group of ‘hot’ natural media.

As we have already noted (section 8.2), in some cases very rigid chemical bonds can be obtained in artificial polymeric systems by means of special processing. The consequence of this is a low mobility of the basic polymer chain and a limited possibility for motion of separate groups and links. Thus, the dipole-group polarization is insignificant and the dielectric permittivity of polymers is minimal; also minimal are the dielectric losses and losses for pure conductivity. A similar situation arises in some widely used building materials (such as glass, asphalt, cement, concrete and modern synthetic building materials). The emissivity of such materials, as well as of rocks, reaches the values of 0.95–0.99 (Figure 8.23) in a very wide wavelength band.

The intermediate (‘warm’) class of emitting terrestrial surfaces represents substances which contain water (both fresh and salt) in various physicochemical forms. First of all, one should mention here the soils of both naturally occurring type, and of the agricultural landscape. Among these surfaces can also be included vegetation, which contains in its basis a great amount of saline aqueous solutions. However, one should bear in mind in this regard, that the radiation properties of vegetation *in vivo* are largely determined by its geometrical characteristics, rather than by dielectric

properties as such. This circumstance is clearly seen for large tracts of forest and for a grassland (Figure 8.23), whose emissivity is close to black-body radiation.

Let us now consider these basic classes of Earth more closely.

8.8.2 Rocks

The detailed studies of the dielectric properties of the terrestrial rocks in the microwave band, carried out at the end of the 1950s and in the 1970s, were based on the need to solve radio-astronomical problems in studying the surface layers of the Moon, and later of Mars, based on the belief that there is a certain identity of rocks constituting the upper surfaces of the Moon, Mars and Earth (Troitskii, 1954, 1967; Krotikov, 1962; Parkhomenko, 1965; Alekseev *et al.*, 1967; Tikhonova and Troitskii, 1970; Krupenio, 1974).

Since prominent electronic polarization is observed in rocks (see section 8.2), the absence of frequency dependence of dielectric properties within a wide range of frequencies, from the submillimetre up to the kilometre band, is obvious. This has been confirmed by direct experiments, generally speaking (Krotikov, 1962; Parkhomenko, 1965). In these investigations the dependencies on the chemical composition and density of the terrestrial rocks studied (such as quartz, granite, pumice, tuff, volcanic ashes, basalt) were found. Beginning with wavelengths of about several kilometres ($\sim 10^4$ Hz), the low-frequency polarization mechanisms and, in particular, intersurface polarization come into effect. Because these wavelengths are not used directly in remote sensing, we shall return to discussing the microwave band. Detailed study in this band has shown that some invariant can be formed between the real part of a dielectric constant, the tangent of dielectric loss angle ($\operatorname{tg}\delta$) and the density of the substance investigated. Such invariants from the density were found experimentally for the terrestrial rocks in 1962 (Krotikov, 1962) and were called Krotikov's relations:

$$\frac{\sqrt{\varepsilon_1} - 1}{\rho} = a = \text{const}; \frac{\operatorname{tg}\delta}{\rho} = b = \text{const}. \quad (8.52)$$

Subsequent laboratory experiments (Tikhonova and Troitskii, 1970) made it possible to reveal the values of constants in Krotikov's relations depending on the rock structure (holocrystalline and decrystallized) and on the content of silicon oxide, SiO_2 , that determines the history of the given rock formation. It was shown to an acceptable accuracy that Krotikov's constants depend on the SiO_2 percentage (x) as follows:

$$\frac{\sqrt{\varepsilon_1} - 1}{\rho} = a = \frac{40}{x}; \frac{\operatorname{tg}\delta}{\rho} = b = \frac{A}{x^3}. \quad (8.53)$$

Thus, having obtained from microwave observations the a and b values, it is possible to restore the SiO_2 content from the a value and then the type of crystalline structure from the b value. Then, from the type of rock and SiO_2 content, one can restore the relationship between the other oxides as well. Using this particular remote technique, the basic parameters of lunar soil were determined before the landing of the Apollo mission spacecraft. These parameters included, in particular, the dielectric constant

($\epsilon_1 = 2-2.5$), the density ($0.75-1 \text{ g/cm}^3$), the type of rocks (the SiO_2 content is 57%), the homogeneity of rocks over the lunar surface (lands and seas) and the absence of considerable dust cover. The indicated relationships are used now in microwave studies of radiation of regolith covers of Mercury (Shchuko and Kartashov, 1999).

8.8.3 Soils

Soil moisture represents one of the basic components of the power budget at the land-atmosphere boundary mainly through its influence on the latent energy exchange. From the point of view of scientific and agricultural-technological problems, it is important to obtain the data on soil moisture stored at various soil horizons. They include: the surface soil moisture, which is determined by the water content in the liquid state in the upper 5 cm of soil and the stored water at horizons up to 20 cm and at horizons up to 1 m. The stored water can be present both in vegetation, in the root system of plants and in the form of unbound and bound water, snow and ice in the soil bulk. For apparent hydrological and meteorological reasons the surface soil moisture rather poorly correlates with the stored water. Therefore, one of the basic problems of agricultural technology and the hydrogeology of land consists in detecting the moisture profile and in clear separation of these types of soil moisture. The cost of direct observation of soil moisture is very high and its performance is very labour-consuming; therefore, remote aerospace monitoring of soil moisture fields is the only reasonable alternative (Schultz, 1988; Vinnikov *et al.*, 1999; Schultz and Engman, 2000).

A series of techniques for remote sensing of soil moisture have recently been proposed (Schultz and Engman, 2000). They can be implemented under the strict constraint of the absence of cloud cover, and also preliminary data on the observed territory (such as the soil character, the type of surfaces) should be available. These techniques include the method of moisture determination from the data of measurements of reflected solar radiation in the near-infrared band ($1.0-1.5 \mu\text{m}$), which is based on that fact that the reflectivity greatly decreases with increasing moisture. Much more sensitive to moisture variation is the degree of polarization of light reflected by soil in the visible range – which has stimulated the development of the polarization method. An increase in the heat capacity of soil with growing moisture produces the contrast of surface temperatures and, hence, of thermal radiation from wet and dry areas of soil – which serves as a physical basis for the method of moisture determination from the data of measurements of infrared thermal radiation. A principal feature of these methods is the very insignificant depth of the skin-layer ($1-10 \mu\text{m}$), from which the information is obtained (see section 1.6), and, as a result, difficulties arise in the interpretation of results. The principal disadvantages of the methods considered are the non-feasibility of the method in the presence of cloudiness and the necessity of taking account of the influence of the thickness of the atmosphere.

Most promising, for the purposes of global monitoring of soil moisture, are passive and active microwave methods (Sharkov and Etkin, 1976; Njoku and

Kong, 1977; Schmugge and O'Neill, 1986; Ulaby *et al.*, 1981, 1982, 1986; Reutov and Shutko, 1990a,b; Promes *et al.*, 1988; Njoku and Li, 1999; Shutko, 1982, 1986; Singh *et al.*, 2000; Rao *et al.*, 1999; Schultz and Engman, 2000; Kerr *et al.*, 2000a; Paloscia *et al.*, 1999, 2000a; Paape *et al.*, 2000; Stoffregen *et al.*, 2002; Yechiel and Wood, 2002). The physical basis for the possibility of soil moisture determination by means of passive techniques is the fact that, as the moisture increases, the dielectric permittivity of soil grows, and, therefore, its emissivity and radiobrightness temperature decrease. Note here that the reflectivity recorded by microwave active instruments (scatterometers and ground-penetrating radars), is not bound up with the influence of the thermodynamic temperature and thermophysical properties of a medium (unlike passive microwave techniques). Therefore, active and passive microwave techniques can provide various scientific information of measurements.

The fact of radiobrightness temperature decreasing with increasing ground moisture was clearly traced for the first time when the data of the measurements of microwave radiation, obtained from the ‘Kosmos-243’ satellite (1968) at wavelengths of 0.8–8.5 cm, was processed. In papers by Basharinov *et al.* (1969, 1971) it was noted that a lowering of the radiobrightness at the areas of continents in the latitude belt of 30–50° was observed at the places of moistening of terrestrial surfaces, where the emissivity of soils was equal to 0.7–0.8. The vast amount of statistical material obtained as a result of processing the data of microwave radiation measurements from the ‘Kosmos-243’ satellite, revealed the virtually linear character of radiobrightness temperature decreasing with growing moisture at the wavelengths of 3.4 and 8.5 cm in measurements over agricultural landscape. The subsequent series of ground and aircraft measurements confirmed the fact that the radiation properties of various types of surfaces depend on moisture. Since then complicated models have been developed, which take into account temperature and moisture profiles, the type of soil and the contribution of moist and rough vegetation (Kondratyev *et al.*, 1970, 1973; Popov *et al.*, 1974; Shulgina, 1975; Schmugge and O'Neill, 1986; Liou *et al.*, 1999; Burke and Simmonds, 2001). Let us now discuss in more detail the possibilities of soil moisture determination by means of the passive microwave sensing technique.

The radiobrightness temperature of soil, measured in the direction of the normal, is determined as follows ($S(\theta) = 1$ in equations (7.101)–(7.102)):

$$T_B = \kappa(m) \int_0^\infty \gamma(z, m) T(z) \exp \left\{ - \int_0^z \gamma(z', m) dz' \right\} dz, \quad (8.54)$$

where $\kappa(z, m)$ is the soil emissivity, $\gamma(z, m)$ is the absorption coefficient, $T(z)$ is the temperature profile in soil and m, z are the moisture and the vertical coordinate, respectively. The integral expression in (8.54) is sometimes called the effective temperature. Note that this expression is valid for smooth (with respect to used wavelength) profiles of thermal and electrical parameters of a medium (see section 7.7 for more details).

The emissivity of soil depends both on its properties (its physicochemical structure, electrical parameters, the features of its distribution in depth), and on the interface surface characteristics (smoothness or roughness, the presence of vegetation). For bare soil or for a surface whose radius of roughness is much greater than the wavelength the emissivity factor $\kappa(z, m)$ can be determined in terms of Fresnel's mirror reflection coefficient, if the emitting layer of soil is homogeneous in depth:

$$\kappa(m) = 1 - |R(m)|^2. \quad (8.55)$$

Special investigations of the reflection coefficients of soil, which is linearly inhomogeneous in depth, have shown (Shulgina, 1975) that for real soils the influence of inhomogeneity on the reflection coefficient is insignificant and that these coefficients can be calculated, to a first approximation, by Fresnel's formulas. (Only at great wavelengths, of the order of 60 cm, and for soils having a dry surface is the influence of inhomogeneity essential.) However, even in the case of a smooth surface, the radiobrightness temperature of soil represents a fairly complex functional of temperature and moisture (8.54). Since in the general case the remote sensing task should consist in studying both the moisture content characteristics and the temperature regime of the soil, it is worth considering the influence of soil moisture (as a function of emissivity) and the influence of the temperature profile separately.

Suppose we have an isothermal medium (i.e. $T(z) = T_0$) with a constant (in depth) value of moisture. From (8.54) it can easily be seen that the radiobrightness temperature of a medium will be equal to

$$T_B = \kappa(m)T_0. \quad (8.56)$$

On the basis of detailed experimental data from studying two different types of ground (sandy and clayey) in a wide band of wavelengths (from 0.8 to 226 cm), Popov *et al.* (1974) have calculated the emissivity of these types of ground in the mentioned band of waves, which virtually covered the whole band now used in remote sensing practice. Figure 8.24 presents the dependencies of emissivities of clay (a) and sand (b) on the volume moisture for several wavelengths calculated by formula (8.55). The contribution of an imaginary part of the dielectric constant of a medium to the medium's emissivity equals the relative value of up to 30% for moisture of about 20%. Therefore, this contribution cannot be neglected (as it has been in some papers). It can be seen from the analysis of the plots in Figure 8.24, that both for low ($m < 5\%$) and high ($m < 15\%$) moistures the $\kappa(m)$ dependence essentially deviates from the linear. It should be noted that the linear model is also often (and worthlessly) used in the empirical models. The linearity of these dependencies (and, in the case of the isothermal model, the linearity of moisture dependencies of the radiobrightness temperature) can take place only within a limited range of moistures (from 5% up to 15% approximately), this interval being essentially dependent on the working wavelength range and on the type of ground. For high moisture variations the plots of Figure 8.24 should be used as calibration curves. A sharp nonlinearity for low moisture values is associated, physically, with a complicated mechanism of water interaction with soil's skeleton

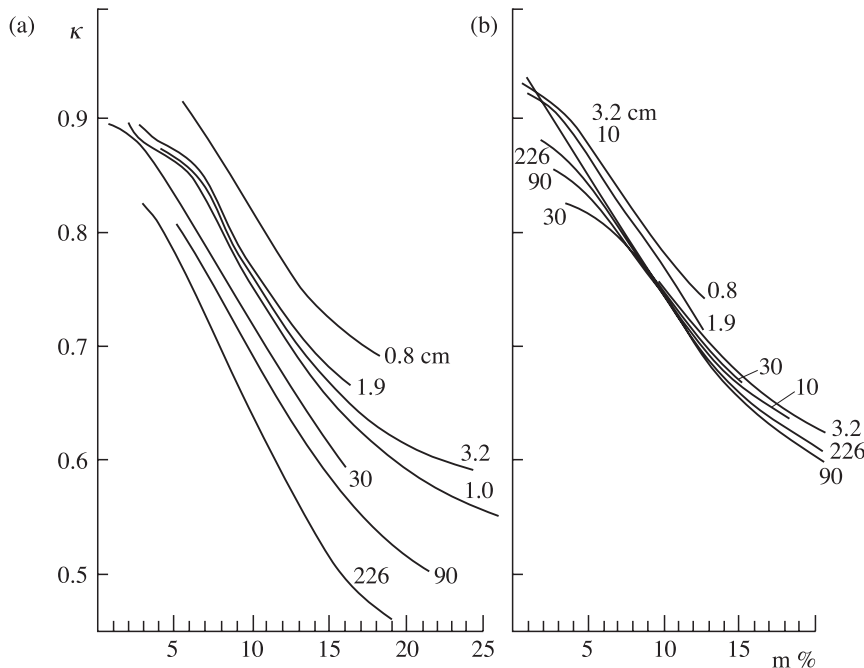


Figure 8.24. Nadir field moisture-dependent emissivity of bare soils: clay (a) and sand (b) surfaces at various wavelengths (cm) (figures next to curves).

and pores, which results in changing the dielectric properties of water and in giving rise to the so-called strongly bound water (Boyarskii *et al.*, 2001; Xu and Sun, 2002; Park, 2001).

From the practical point of view, it is important to know the ‘sensitivity’ of the radiobrightness temperature to moisture variations ($\Delta T_B/\Delta m$). The estimates of this value disregarding the sky illumination at the rectilinear section of the plot (at $T_0 = 300$ K) give for a clayey ground at the wavelength of 226 cm the value of 8.6 K/%; at the wavelength of 90 cm, 7.5 K/%; at 30 cm, 7.2 K/%; at 3 cm, 7 K/%. For sandy ground the $\Delta T_B/\Delta m$ value is virtually constant throughout the considered wavelength band and equals about 6.1 K/%. For moisture higher than 15% at all wavelengths a sharply nonlinear saturation section begins, where the aqueous solution makes, physically begins, the main contribution to the microwave emission.

Now we shall analyse the sky illumination effect on the radiobrightness temperature of moist ground (see equation (7.20)). The noise temperature of the sky at zenith does not exceed 10 K in the range from 3 up to 30 cm, and as the wavelength further increases, it sharply grows up to 500 K for $\lambda = 300$ cm (Esepkins *et al.*, 1973). With increasing the observation angle θ (as you approach the horizon) the noise temperature of sky grows according to the law $T_I = T_{IZ}/\cos \theta$, where T_{IZ} is the noise temperature at zenith.

From formulas (7.20) it can easily be seen that the presence of sky illumination decreases quantity $\Delta T_B / \Delta m$. This effect, which is not so essential at wavelengths of 3 to 30 cm at the wavelength $\lambda = 226$ cm at the thermodynamic temperature of ground $T_0 = 300$ K, leads to virtually full independence of the radiobrightness temperature on the moisture and on the type of ground, since in this case expressions (7.20) give $T_B = T_0$. Radiobrightness temperature variation, corresponding to 1% moisture variation, will be equal, taking account of sky illumination, for clay (sand) at the wavelength of 90 cm to 6.4 (4.2) K/% and at the wavelength of 30 cm to 7.1 (6.0) K/%, at the wavelength of 3 cm to 6.7 (6.0) K/%. As would be expected, the radiobrightness temperature sensitivity to moisture variation is at a maximum in the wavelength band from 3 up to 30 cm, in which the noise temperature of sky is minimum.

It is interesting to note that the presence of moisture has an essential effect on polarization characteristics of radiation of a medium (section 7.4). The basic characteristic in this case is the polarization factor determined by the relation

$$p(\theta) = \frac{T_{BV}(\theta) - T_{BH}(\theta)}{T_{BV}(\theta) + T_{BH}(\theta)}, \quad (8.57)$$

where T_{BV} and T_{BH} are radiobrightness temperatures of vertically and horizontally polarized components of radiation. Since the effective temperature does not depend on the type of polarization, the expression for the polarization factor is simplified:

$$p(\theta) = \frac{\kappa_V(\theta) - \kappa_H(\theta)}{\kappa_V(\theta) + \kappa_H(\theta)}. \quad (8.58)$$

The calculations by formula (8.58) indicate that the moisture dependence of polarization factor (Figure 8.25) is nearly linear with the slope of about 1% per 1% of moisture for clay, and 0.6–1.0% per 1% of moisture for sand up to moisture values of 15–20%, after which the tendency to saturation begins to reveal itself. If the radiometric system makes it possible to distinguish the 1% variation of the polarization factor (here by the per cent is meant the unit of measurement of polarization factor, rather than the relative per cents), then for $\theta = 45^\circ$ about 10 gradations of moisture from 0 to 20% can be distinguished confidently.

Let us estimate now the sky illumination effect on polarization measurements. Substituting expression (7.20) with corresponding indices into (8.57) and taking into account (8.55), we obtain

$$p(\theta) = \frac{\kappa_V(\theta) - \kappa_H(\theta)}{\kappa_V(\theta) + \kappa_H(\theta) + \frac{2T_I(\theta)}{T_0 - T_I(\theta)}}. \quad (8.59)$$

The solid line in Figure 8.26 presents the dependencies of polarization factor p on the observation angle (a) and on the wavelength (b) for clay of 10% moisture ($T_0 = 300$ K) calculated by formula (8.59). The dashed line indicates the same dependencies disregarding the sky illumination. As can be seen from Figure 8.26(a), the

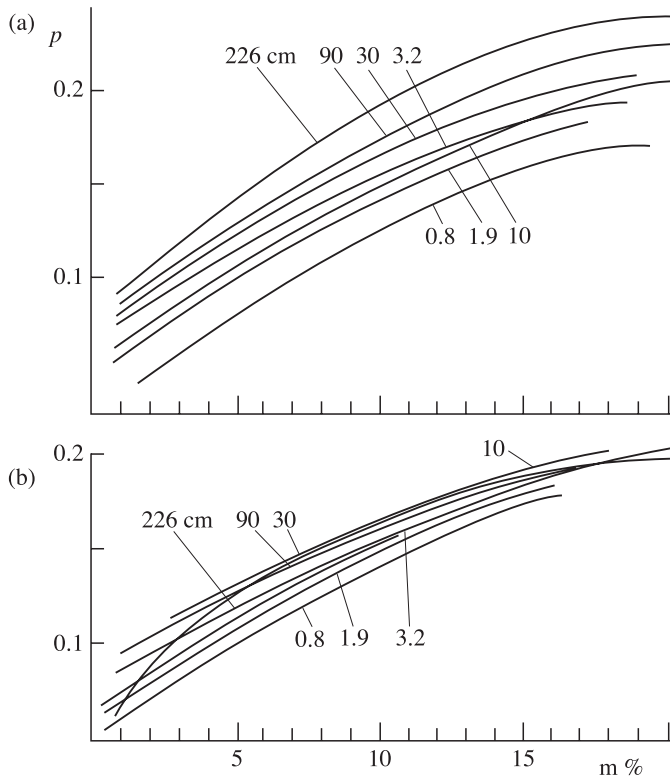


Figure 8.25. Field moisture-dependent polarization coefficient of bare clay (a) and sand (b) soils at various wavelengths (cm) (figures next to curves). The observation angle is 45° .

difference between polarization factor values with allowance for sky illumination and the same values disregarding sky illumination reaches a considerable value (more than 30% for $\lambda = 0.8 \text{ cm}$, $\theta = 80^\circ$). At great observation angles ($\theta = 80^\circ$) the maximum appears in the dependence, and then a sharp drop takes place. For each observation angle (Figure 8.26(b)) there exists some critical wavelength, at which the polarization factor drops to zero.

It is clear from the physical considerations that the main contribution to the microwave emission of a semi-infinite medium is made by the layer of some particular depth, because the radiation of all underlying layers decays in overlying ones. This estimation can be performed quite easily, assuming a variable upper limit in the integral expression for the effective temperature (8.54). Then the expression for the effective temperature will be as follows:

$$T_B = T_0(1 - \exp(-\gamma z)). \quad (8.60)$$

It can easily be seen from this expression, that the main contribution (about 90%) to the thermal radiation of a semi-infinite medium is made by the layer of finite depth

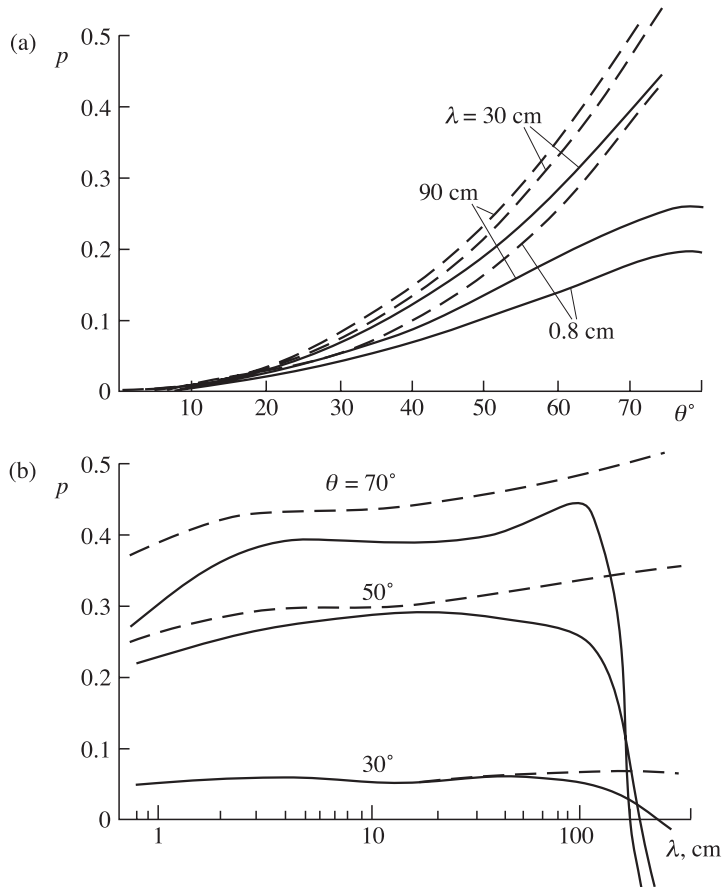


Figure 8.26. Polarization features of radio-emission for clay soil surface with moisture 10% ($T_0 = 300$ K) taking into consideration 'sky' radio-emission (continuous lines) and not taking it into consideration (dashed lines): (a) the relationship of polarization coefficient versus observation angle; (b) the relationship of polarization coefficient versus work wavelengths.

l_{ef} , which is equal to

$$l_{\text{ef}} = \frac{2.3}{\gamma} (\text{m}). \quad (8.61)$$

The calculated values of quantity l_{ef}/λ for moisture of 10% for sand (clay) in the band of 20 cm were 4.5 (1) and in the band of 75 cm were 5.3 (0.53).

Now we shall consider the effect of the temperature regime of soil on its emissive properties. The analysis of the data on the temperature regime of soil, carried out by Kondratyev *et al.* (1970), has shown that the temperature profiles are well approximated by the relation:

$$T(z) = \{[T'(0) + \alpha(T_0 - T_2)z]z + T_0 - T_2\} \exp(-\alpha z) + T_2, \quad (8.62)$$

where T_0 is the temperature at $z = 0$; $T'(0)$ is the temperature gradient near the surface; T_2 is the asymptotic value of temperature for $z \rightarrow \infty$; and α is the empirical parameter. According to the data of some investigations, in summer at any time of day $T = T_2$ even at the depth of about 40 cm (Liou *et al.*, 1999).

Generally speaking, temperature profile approximation by expression (8.62) is possible for any profile characterized by monotonous transition to T_2 or possessing a maximum or minimum (i.e. where the diurnal or seasonal ‘wave’ of the thermal regime in the soil bulk is investigated).

As a first approximation, we shall consider the case of $\gamma = \text{const}$. This case is accomplished in the region of wavelengths, for which the absorption coefficient is sufficiently high that, at the distance of effective depth of radiation penetration into soil ($0 < z < l_{\text{ef}}$), the moisture and, along with it, the absorption coefficient has no time to be changed noticeably.

Making integration (8.54) with allowance for (8.62), we obtain

$$T_B = \kappa(m) \left[\frac{T'(\theta)}{\gamma(1 + \alpha/\gamma)^2} + \frac{\alpha}{\gamma} \frac{T_0 - T_2}{(1 + \alpha/\gamma)^2} + T_2 \right]. \quad (8.63)$$

Let us now show how, by measuring the radiobrightness temperature at several wavelengths (in other words, implementing microwave spectroscopy), one can determine the moisture and the temperature profile parameters. Consider the range of wavelengths, for which $(\alpha/\gamma) < 1$. In this case equation (8.63) takes a more simple form

$$T_{Bj} = \kappa_j(m) \left[T_0 + \frac{T'(0)}{\gamma_j(m)} \left(1 - 2 \frac{\alpha}{\gamma_j(m)} \right) \right]. \quad (8.64)$$

Thus, in the wavelength range under consideration, the radiobrightness temperature is determined by the values of temperature and its gradient at the surface, but does not depend on the asymptotic value of temperature. Since the emissivity is a complicated function of moisture, for determining it, as well as for finding three other unknown quantities – m , α and $T'(0)$ (T_0 can be considered to be specified) – it is necessary to have the measurement data for radiobrightness temperature at four wavelengths ($j = 1, 2, 3, 4$), at which the absorption coefficients satisfy the inequality $(\alpha/\gamma) < 1$. Though this system of equations is nonlinear, nevertheless it can be resolved, for example, by the method proposed by Kondratyev *et al.* (1970). That is to say, from the four measured values of radiobrightness temperature in the range of wavelengths for which $(\alpha/\gamma) < 1$, provided that T_0 is specified (quantity T_0 can be obtained from the data of measurements in the thermal infrared band) and from the moisture dependence of absorption coefficients at these wavelengths, it is possible to determine the soil moisture and the temperature gradient near the surface, the surface emissivity and the exponential factor of the temperature profile which characterizes the thermal ground regime.

The case of $(\alpha/\gamma) < 1$, considered above, occurs at strong absorption of electromagnetic waves in a medium. The second extreme case of great wavelengths, for which $(\alpha/\gamma) \gg 1$, enables one to determine the asymptotic value of the temperature

profile T_2 from the equality

$$T_B = \kappa(m) T_2. \quad (8.65)$$

This is the case of weak absorption, and, naturally, the main contribution to the radiobrightness temperature is made by the layers at temperature T_2 . The inequality $(\alpha/\gamma) \gg 1$ is met for decimetre-band wavelengths. For example, for the wavelength of 60 cm, as the moisture changes from 3% to 12%, the (α/γ) ratio changes from 60 to 15, approximately.

The further development of this approach has lead Kondratyev and Shulgina (1971) to the idea of using the periodic scanning at a fixed observation angle in order to eliminate the given surface temperature in measurements (see equation (8.63)) and to limit the study by quantities depending on temperature profile parameters we are interested in. So, in the range of wavelengths for which $(\alpha/\gamma) < 1$, equation (8.64) for fixed observation angle θ takes the form

$$T_{Bj} = \kappa_j(m, \theta) \left[T_0 + \frac{T'(0) \cos \theta}{\gamma_j(m)} \left(1 - 2 \frac{\alpha \cos \theta}{\gamma_j(m)} \right) \right]. \quad (8.66)$$

As a result of periodic scanning over the observation angle $\theta = \theta_0 + \theta_1 + \theta_1 \cos \Omega t$, the received signal (8.66) also is a periodic function of time, but in this case the amplitude of the first Fourier harmonic no longer depends on T_0 . This makes it possible to use, as a method of measuring the useful signal, its separation at frequency Ω (for example, by the synchronous detection method; see Chapter 3) and the determination of temperature profile parameters and characteristics of soils from the amplitude of the first harmonic. If we make use of the circumstance that within a rather wide range of observation angles ($0 < \theta \leq \pi/4$) the emissivity only weakly depends on the observation angle (see, for instance, Hewison and English, 1999), then we can perform integration and obtain the following expression for the amplitude of the first harmonic of a received signal

$$T_{Bj}^{(1)} = -2\kappa_j(m) \frac{T'(0)}{\gamma_j(m)} \left[\sin \theta_0 J_1(\theta_1) - \frac{\alpha}{\gamma_j(m)} \sin 2\theta_0 J_1(2\theta_1) \right], \quad (8.67)$$

where $J_1(x)$ is the Bessel function (Gradshteyn and Ryzhik, 2000). In this case the constant component can be presented in the form

$$T_{Bj}^{(0)} = \kappa_j(m) T_0, \quad (8.68)$$

because the corrections, caused by the fixed observation angle and scanning amplitude, will be small (2–3%). The proposed differential technique is reduced to measuring the ratio of the first harmonics (8.67) at various wavelengths and to subsequent determination of moisture and thermal profile characteristics. The advantage of such an approach consists in the fact that the ratios of harmonics can be measured to a greater accuracy than harmonics themselves.

Thus, the proposed method makes it possible, in the homogeneous half-space approximation, to determine by means of the microwave spectroscopy method (at

observation to the nadir or in the mode of periodic scanning over the observation angle) the basic characteristics of the state of a surface layer of soil: the moisture and temperature profile parameters.

However, in many practical cases the one-frequency modes of measurement in the decimetre band (the channel of the 21 cm wavelength) have been successfully used. In these cases fairly simple semi-empirical two-layer models were applied at data interpretation for remote determination of soil water content (in the layer of 0–2 cm) and effective temperature (at the depth of 11 cm) (Burke and Simmonds, 2001; Liou *et al.*, 1999; Ruf and Zhang, 2001).

Even the first microwave investigations of mesoscale and macroscale fields of moisture have indicated a very important feature of constructing these fields, namely, a complicated multiscale hierachic structure. The detailed analysis of these problems is beyond the scope of this book, and we recommend the reader to address the specialized literature on this subject (Schugge *et al.*, 1988; Sadeghi *et al.*, 1988; Engman, 1997; Vinnikov *et al.*, 1999; Crow and Wood, 1999).

8.8.4 Tilled soil

Humus, one of the most important components of tilled soil, has a basic effect on the structure and physical properties of soil. The presence of humus in soils, even in small quantities, can drastically change their structural-functional hydrophysical and mechanical properties, the changes being due both to aggregation of the mineral part of elementary soil particles (called the skeleton), and to modification of its surface. Humus is a very complicated set of various compounds, the most basic of which are humic and fulvic acids. The molecules of humic acids have a loose, spongy structure with a great number of inner pores and, owing to this circumstance, they noticeably change the water-retaining ability of soils.

From the optical sensing viewpoint, humic substances colour the soil in darkish tones, and this circumstance makes it possible to distinguish soils with varying humus contents in the optical band. The spectral reflectivity of soil depends not only on the quantity of humus in it, but also on the spectral reflective properties of the soil-forming rock. For this reason the relative error of determination of humus content can be quite high. Furthermore, in the optical band the information is obtained from a very thin surface film (see section 1.6), which is subject to various external effects. Especially high error occurs in cases where the humus content is low (1–2%): it reaches 200–300% (Bobrov and Galeyev, 2001). The remote measurements of microwave properties of soils with considerable humus content are of undoubtedly practical interest. Detailed investigations of the dielectric and emissive properties of humus-containing soils have not been carried out yet; therefore, it is important to evaluate the first in-the-field experiments in this field. Bobrov and Galeyev (2001) have shown that radiothermal contrasts exhibit themselves not in the static state, but in the dynamic action mode (of intensive irrigation) and subsequent drying of soil. Experimental investigations of the dynamics of the radiobrightness temperature of soils with various humus contents were carried out at frequencies of 6.25 and 8.0 GHz. And it was shown here, after

fairly intensive irrigation of the surface of test sites because of the various changes of soil structure and differences that arise in the drying rate, that a radiobrightness contrast (up to 60 K) appears, which is retained for 2–3 days. In this case the ratio of diurnal variations of emissivity for two sites with various humus contents depends on the initial moistening. Noticeable structure-changing effects, which influence the brightness contrast value, have been noticed after short-term freezing of the soil surface. All this testifies to the fact that the entire system is fairly complicated and, apparently, it is sharply nonlinear from the viewpoint of both temporal dynamics and spectral emissive characteristics.

8.8.5 Vegetation

Vegetation on the Earth's surface represents a complicated and diverse system from the viewpoint of its electrodynamic properties. This is, first of all, due to a complicated hierarchic geometrical construction – a root system, a trunk, a system of branches and then a system of leaves and fruits. The dielectric properties of each of these subsystems, in their turn, depend in a complicated manner on the dielectric properties of electrolytes which supply a plant with nutrients from a soil and then with photosynthetic products (see, for instance, McDonald *et al.* (1999)). From the remote sensing point of view, the observational strategy and electromagnetic models will depend, first of all, on the required generalization of an image. If the question is about macroscales and mesoscales (as, for example, in the case of investigations of the Amazon rainforest area, the Sahel zone in Africa or a vast prairie grassland (Birrer *et al.*, 1982; Calvet *et al.*, 1995, 1996; Sharkov, 1998; Liou *et al.*, 1999; Prigent *et al.*, 1997, 2000, 2001), then in such a case it is possible to use the electromagnetic models of continuous homogeneous medium (of the film-on-the-substrate type) (see section 7.5) or the cloud model over the smooth boundary within the radiative transfer theory framework (see Chapter 9). Since vegetation possesses a certain attenuation frequency response, it represents some kind of frequency filter which 'blocks' remote investigations of the soil beneath vegetation. For example, Liou *et al.* (1999) have shown that, whereas in the decimetre band (21 cm) it is possible to obtain information under the dense grass cover of the US prairie, then the microwave devices of the SSM/I complex set (see Chapter 14) at frequencies of 9, 37 and 85 GHz are no longer sensitive to the soil moisture (under the grass cover), though these channels are sensitive to moisture in bare soil. Here one should have in mind that between the state (the degree of ripeness and the vegetation growth stage) of vegetation (which is determined from the optical sensing data by means of the NDVI technique), soil moisture state and thermal regime there are no direct correlation links (Chen *et al.*, 1997; Sharkov, 1998). This is due to the fact that the soil–plant system represents a sharply nonlinear system in the spatial-temporal dimension, and the vegetation growth stages and the degree of ripeness (the colour NDVI index) reflect the state of moisture with a considerable time delay, however, at quite certain spatial-temporal averaging. So, Choudhury (1987) has shown that the polarization difference (i.e. the difference of vertically and horizontally polarized brightness temperature, observed at 37 GHz frequency of SMMR on

board the ‘Nimbus-7’), in monthly averaging correlates, to a high degree of confidence, with the NDVI index fields for arid and semi-arid regions of India, Africa and Australia. In other words, the polarization difference in the microwave sensing can serve as a fine indicator of the primary surface productivity in arid zones.

If we consider the scales of several (groups) or a single plant, then the electrodynamic model should take into account the hierarchic (fractal) construction of separate subsystems of plants, each of which has both its intrinsic hierarchic system of construction and its intrinsic dielectric properties (Ramson *et al.*, 1997; Ferrazzoli and Guerriero, 1996; Ferrazzoli *et al.*, 2000; McDonald *et al.*, 1999).

Of importance also are investigations of the biological evolution of a vegetation system’s elements. A rather unusual and, at the same time, quite indicative example in this respect can serve for the comparison of optical and microwave brightness images of vegetation objects – a leaf each from an oak and a birch tree (Plate 4). The microwave images of the leaves were obtained at the 600 GHz frequency and are presented in ‘false’ colours (Rehm and Brand, 1999). Whereas the optical image gives a picture of surface distribution of the chlorophyll components of a leaf, the microwave image provides information on the temperature regime and spatial distribution of electrolyte solutions inside the leaf bulk. Obtaining such complex information by the other methods is rather problematic.

9

Foundations of radiative transfer theory

This chapter presents the phenomenological basis and principal energy considerations underlying radiative transfer theory (RTT). The analysis of basic equations and fundamental concepts, required for studying radiative transfer in absorbing, emitting and scattering media, are given in this chapter. The formal and approximate solutions of the equation of radiative transfer, given in this chapter, are widely used in subsequent chapters when considering radiative transfer in dispersed media (hydrometeors and aerosols in the atmosphere). Attention is chiefly given to the analysis of solutions of the transfer theory intended for studying thermal radiation processes in the microwave band.

9.1 RADIATIVE TRANSFER THEORY PHENOMENOLOGY

Although the principal solution of thermal radiation problems is possible using the fluctuation–dissipation theorem (see Chapter 4), the practical solution of many problems is rather complicated and requires the application of other physical approaches. First of all, one should mention here the energy approach associated with particular phenomenological concepts developed in studying electromagnetic radiative transfer in absorbing, emitting and scattering media. The phenomena of energy transfer by radiation in media, which can absorb, emit and scatter radiation, have been of interest for a long time. This interest was aroused by the study of complicated and interesting phenomena related to astrophysical problems, remote sensing, nuclear explosions, flows in hypersonic compressed layers, rocket engines and plasma generators designed for nuclear fusion. Although some of these applications appeared quite recently, the absorption and emission processes in gases have aroused interest for more than a hundred years. One of the first investigations was devoted to electromagnetic radiation absorption by the terrestrial atmosphere. This problem has always stirred the optical astronomers, who have

observed the light from the Sun and more distant stars. The distorted spectra of black-body radiation of the Sun in the near-IR band, obtained for a number of years beginning with 1880 (see Siegel and Howell, (1972) for more details), have testified to essential wavelength dependence of emissive properties of gases in the terrestrial atmosphere. Solar radiation absorption by the cloudless atmosphere was caused, as was found later, primarily by water vapour and carbon dioxide existing in the atmosphere. As a matter of fact, these investigations were the first systematic remote studies of the Earth's atmosphere using the 'regular transmission' technique.

The emission of gases (and, later, of plasma systems) has also been of interest for astrophysicists in connection with studies of the structure of stars. Models of stellar atmospheres and of the Sun were proposed describing the energy transfer processes in these objects, after which the emission spectra, calculated on the basis of these models, have been compared with those obtained experimentally. It was these investigations, on the basis of which the phenomenological foundations were developed and radiative transfer theory was constructed and advanced both for astronomy and for remote sensing applications (Troitskii, 1954; Chandrasekhar, 1960; Sobolev, 1963; Staelin, 1969; Kondratyev and Timofeev, 1970; Malkevich, 1973; Marchuk, 1976; Marchuk *et al.*, 1986; Sabins, 1987; Apresyan and Kravtsov, 1996; Thomas and Stamnes, 1999; Matzler, 2000). An overwhelming majority of the physical results obtained in astronomy, radio-astronomy and remote sensing was based, one way or another, on using the methodology of radiative transfer theory.

In industry the problem of emission of gases became topical in the 1920s in connection with studying heat exchange in furnaces (smelting of steel and glass), in combustion chambers of engines and later, in the 1950s and 1960s, in rocket engines (Ozisik, 1973; Siegel and Howell, 1972). At the same time, it was found that similar physical approaches and, accordingly, the equations can govern the processes of the propagation of neutrons in nuclear reactors (Murray, 1957). This undoubtedly gave a new impetus to the detailed investigation of transfer processes.

In studying radiative transfer in absorbing, emitting and scattering media, two very important features arise. First, in such media the absorption and emission of radiation occur not only at the boundaries of a system, but also at every point inside a medium. The same is true for scattering. For complete solution of the energy transfer problem it is necessary to know the volume field of temperature and physical properties of a medium at each point of a system. By a point of a system here is meant a physically infinitesimal (unit) volume of a medium, which contains a fairly large number of particles, the interaction between which can provide the local thermal equilibrium conditions (see Chapter 4). By particles here is meant either a set of macroscopic particles (aerosols, water drops, snow and ice particles, volcanic ashes or particles of another nature), or a set of quantum particles (atoms and molecules of gases).

In the first version transfer theory is considered at the macroscopic level bringing in the results of Maxwell's theory of scattering on macroscopic particles (Mie scattering theory). The properties of a physical medium, in which the process takes place,

are taken into account by a set of some (phenomenological in a certain sense) coefficients determined either experimentally or by calculations.

In the second version the electromagnetic field is considered as a combination of particles (the ‘photon gas’), and the radiative transfer process of interest is considered as the interaction of these particles with the particles of substance on the basis of quantum-mechanical concepts (see Chapter 11 for more details).

To find the local values of radiation intensity in a medium the ‘astrophysical’ approach is applied (Siegel and Howell, 1972), where the complete equation of radiative transfer is solved. As it will be shown later, the radiation intensity is related to energy transferred along some selected direction. Having determined the variation of the intensity of radiation along the path of its propagation, we can get an idea of how absorption, emission and scattering processes influence radiative transfer. Such an approach is most efficient in considering the problems related to absorption and emission of the terrestrial atmosphere and to the structure of stars, and in other problems where the quantity sought is the spectral intensity of radiation at a point of the medium. The solution of a complete problem, as we shall see later, encounters considerable mathematical difficulties.

Second, the spectral characteristics of rarefied systems (gases) have much sharper changes (usually narrow lines of various types), than the spectral characteristics of solid or liquid bodies. Such a kind of noise emission is called selective radiation (see Chapter 11). The physical nature of this circumstance is well known now: it lies in the features and distinctions of the quantum-mechanical structure of gases and solid bodies. Therefore, for studying the radiation of gaseous media it is necessary, as a rule, to consider in detail the spectral characteristics (i.e. the so-called radio spectroscopy methods should be applied). In using approximations, based on the properties averaged over the spectrum, special caution is required. The majority of simplifications, which are introduced in solving the radiation problems of physical media, are made with the purpose of avoiding these difficulties. So the ‘astrophysical’ approach often undergoes serious simplification to facilitate its use in engineering calculations carried out mainly with the purpose of determining the integral (over frequencies or solid angles) of energy fluxes, rather than the differential radiation intensity (Ozisik, 1973; Siegel and Howell, 1972). However, in solving remote sensing problems such simplifications are inadmissible, since in the majority of cases very important information on polarization and the spectral characteristics of investigated objects is lost.

9.1.1 RTT applicability conditions

The use of RTT in relation to real media is based on some physical simplifications which allow us, generally speaking, to advance in studying radiative transfer in composite (for example, multiphase) media, where the direct use of the Maxwell theory is troublesome. It should be mentioned here that, in the majority of works on the presentation of the RTT fundamentals and application of the theory, the physical suppositions underlying this theoretical presentation are as a rule neither discussed nor analysed.

- (1) The use of the geometric optics approximation, where the electromagnetic radiation wavelength is essentially lower than the scale of variation of a macro-system's parameters. This approximation, as known, uses the beam conceptions for electromagnetic wave propagation in a medium (see section 1.6).
- (2) The use of the approximation of electromagnetic rarefaction of a medium, where the distance between particles, constituting an elementary volume of a medium, essentially exceeds the working wavelength. The original flux, falling on an elementary volume, reaches each particle. The particles do not 'shade' each other, and there is no mutual interference between the particles. Thus, the total effect of electromagnetic field interaction with a group of particles is achieved by summing the interaction effects on each particle.
- (3) The relationship between the size of individual particles and the working wavelength is arbitrary, i.e. all diffraction effects at the electromagnetic field interaction with an individual particle should be taken into account.
- (4) All processes of the external electromagnetic field interaction with a unit volume of a medium are reduced to three acts only – the absorption act, the emission act and the scattering act (see section 9.2 for more details).

These conditions will be referred to and analysed at the appropriate places in the presentation of the foundations of RTT.

9.2 ENERGY TRANSFORMATION BY A VOLUME ELEMENT

Consider a beam of radiation with intensity $I_\nu(\mathbf{r}, \Omega)$ propagating in the absorbing, emitting and scattering medium in a given direction. The energy of radiation will decrease owing to its absorption by substance and owing to the deviation of a part of the radiation from the initial trajectory as a result of scattering in all directions. But, at the same time, the energy will increase because of thermal radiation emission by the substance volume. The absorption, scattering and emission of radiation by a substance have effect on the energy of a radiation beam that propagates in it. In this case the total balance of change of the initial intensity can be, certainly, both positive and negative. Besides, a strong inhomogeneity of the energy balance, both over the substance volume and over the observation direction, is possible. These properties have been analysed in detail in books by Chandrasekhar (1960), Sobolev (1963), Ozisik (1973), Siegel and Howell (1972). In this section we briefly consider radiation interaction with a volume element using the phenomenological concepts of three acts of radiation interaction with the substance volume element – the act of absorption, the act of emission and the act of scattering.

9.2.1 The act of absorption

Consider a beam of monochromatic radiation with intensity $I_\nu(\mathbf{r}, \Omega')$ restricted by the elementary solid angle $d\Omega'$ and falling along the normal to the element of surface dA of the layer of width dS (Figure 9.1). As the incident radiation propagates in the

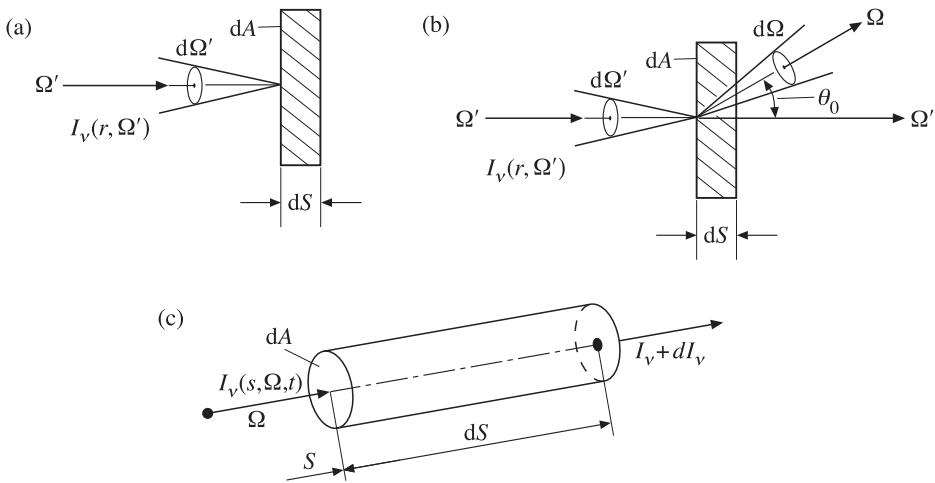


Figure 9.1. Schematic presentation of the geometry of the radiative transfer procedure by a volume element: (a) the act of absorption; (b) the act of scattering; (c) the total energy transformation.

substance, the part of radiation is absorbed by this substance. Designate by $\gamma_\nu(r)$ the spectral absorption coefficient, which is equal to the fraction of incident radiation, absorbed by substance over the unit of the radiation propagation path length, and has the dimension of $(\text{length})^{-1}$. Then the quantity

$$\gamma_\nu(\mathbf{r}) I_\nu(\mathbf{r}, \Omega') d\Omega' \quad (9.1)$$

characterizes the absorption of the incident radiation $I_\nu(\mathbf{r}, \Omega')$ by substance from the direction Ω' per unit of time, in a unit of volume $dA dS$ and in a unit frequency band.

If the radiation falls on a volume element from all directions within the limits of a total solid angle, then expression (9.1) should be integrated over all solid angles (see section 5.1):

$$\gamma_\nu(\mathbf{r}) \int_0^{2\pi} \int_{\mu'=-1}^{+1} I_\nu(\mathbf{r}, \mu', \varphi') d\mu' d\varphi'. \quad (9.2)$$

This expression characterizes the absorption, by substance, of radiation falling on a separated volume element from all directions within the limits of a spherical space, per unit of time, in a unit of volume and in a unit frequency band (with the dimension of $\text{W/m}^3 \text{Hz}$).

9.2.2 The act of emission

In the problems of radiative transfer in absorbing, emitting and scattering media the supposition of a local thermal equilibrium (LTE) is used almost always with the purpose of deriving the expression for the intensity of thermal radiation of a volume element (see section 4.4). In essence, the question here is about the volumetric form

of Kirchhoff's law (see section 6.3). The LTE conditions imply that any small volume element of a medium is at the local thermodynamic equilibrium, owing to which the state of any point can be characterized by local temperature $T(\mathbf{r})$. This supposition is lawful in the case where the collisions of particles in a substance occur so frequently that they result in a local thermodynamic equilibrium at each point \mathbf{r} of a medium. In this case the emission of radiation by a volume element can be described by means of the volumetric form of Kirchhoff's law. If we designate by $J_\nu(\mathbf{r})$ the radiation emitted by a unit volume of substance per unit of time, within the limits of a unit solid angle and in a unit frequency band (with dimension of $\text{W}/(\text{m}^3 \text{Hz St})$), then the emission of radiation by substance can be expressed in terms of the Planck function for the intensity of radiation of an ideal black body:

$$J_\nu(\mathbf{r}) = \gamma_\nu(\mathbf{r}) I_{\nu B}[\nu, T(\mathbf{r})], \quad (9.3)$$

where $I_{\nu B}(T)$ is determined by formula (6.2).

If the supposition of a local thermodynamic equilibrium is inapplicable for the studied system (this requires some special investigation), then the emission of radiation by a substance becomes a function of energetic states in the system, and the problem of radiative transfer in such media is essentially complicated.

9.2.3 The act of scattering

If the medium includes inhomogeneities in the form of small particles, then the radiation beam, while passing through this medium, will be scattered in all directions. For example, particles of dust or drops of water in the atmosphere scatter electromagnetic waves passing through such a medium, as well as the thermal radiation formed in other spatial parts of a medium. Thus, the general picture of thermal radiation of the whole medium may be rather complicated.

Absolutely homogeneous media do not exist in nature, except in an absolute vacuum. However, in many cases the medium can be considered to be optically (or electromagnetically) homogeneous, if the linear size of inhomogeneities is known to be considerably smaller than the radiation wavelength. For example, a cloudless atmosphere in the microwave band satisfies these conditions. One should also distinguish coherent from incoherent scattering. The scattering is called coherent if the scattered radiation has the same frequency as the incident radiation, and incoherent if the frequency of scattered radiation differs from that of the incident radiation – owing to turbulent motion of macroscopic particles in air, for instance. As a whole, the scattering problem is very complicated. A considerable literature is devoted to studying these problems (see, for instance, Ishimaru, (1978, 1991)). In this chapter we shall consider only the simplest version of coherent single scattering. Nevertheless, the scattering of microwave radiation in numerous real media is well described within the framework of this approximation.

Consider a beam of monochromatic radiation with intensity $I_\nu(\mathbf{r}, \Omega')$, which propagates in the direction Ω' within the limits of elementary solid angle $d\Omega'$, whose axis coincides with the chosen direction, and falling along the normal to the surface dA of the elementary layer dS (Figure 9.1(b)). While the incident

radiation passes through the medium, part of it is scattered by substance. Designate by $\sigma_\nu(\mathbf{r})$ the spectral scattering coefficient, which is equal to the fraction of incident radiation scattered by substance in all directions over the unit of length of the propagation path of radiation and having the dimension of $(\text{length})^{-1}$. Then the quantity

$$\sigma_\nu(\mathbf{r}) I_\nu(\mathbf{r}, \Omega') d\Omega' \quad (9.4)$$

characterizes the scattering, by substance, of the incident radiation $I_\nu(\mathbf{r}, \Omega') d\Omega'$ in all directions per unit of time, in a unit of volume and in a unit frequency band. In other words, this is the part of the energy which will be completely extracted from the external radiation beam falling on a unit volume in the direction Ω' . However, expression (9.4) does not provide complete information on the distribution of scattered radiation over the directions. The distribution over the directions can be described by means of the phase function (or scattering indicatrix) $p_\nu(\Omega' \rightarrow \Omega)$, normalized in such a manner, that

$$\frac{1}{4\pi} \iint_{\Omega=4\pi} p_\nu(\Omega' \rightarrow \Omega) d\Omega = 1. \quad (9.5)$$

Note that the quantity

$$\frac{1}{4\pi} p_\nu(\Omega' \rightarrow \Omega) d\Omega \quad (9.6)$$

has an important physical sense: it determines the probability of the fact, that the radiation, falling in the direction Ω' , will be scattered within the limits of the elementary solid angle $d\Omega$ in the direction Ω , i.e. in the direction of observation. Then the quantity

$$[\sigma_\nu(\mathbf{r}) I_\nu(\mathbf{r}, \Omega') d\Omega'] \frac{1}{4\pi} p_\nu(\Omega' \rightarrow \Omega) d\Omega \quad (9.7)$$

characterizes the scattering, by substance, of the incident radiation per unit of time, in a unit of volume, in a unit frequency band within the limits of elementary solid angle $d\Omega$ with axis Ω . In other words, we have the case, where the radiation, falling on the volume from the direction Ω' , is re-scattered by a studied unit volume of substance in the direction of observation Ω . When the radiation falls on a volume element from all directions within the limits of a spherical solid angle, the integration of (9.7) over all incident solid angles gives the expression

$$\frac{1}{4\pi} \sigma_\nu(\mathbf{r}) d\Omega \iint_{\Omega'=4\pi} I_\nu(\mathbf{r}, \Omega') p_\nu(\Omega' \rightarrow \Omega) d\Omega', \quad (9.8)$$

which characterizes the scattering of radiation, which falls on a volume element from all directions within the limits of a spherical solid angle and scattered within the limits of elementary solid angle $d\Omega$ with the observation axis Ω per unit of time, in a unit of volume and in a unit frequency band. From the viewpoint of an external observer, this part of the radiation has the character of an extra source of radiation, which is seen from observer's direction. As we shall see soon, it is this integral which

presents basic mathematical difficulties in solving the problems of radiative transfer in scattering media.

In the case, where the scattering particles of a medium are homogeneous and isotropic, and possess spherical symmetry, and there is no preferential direction of scattering in a medium, the scattering indicatrix depends only on the angle θ_0 between the directions Ω' and Ω . It follows from the geometrical considerations (Gradshteyn and Ryzhik, 2000), that the angle θ_0 between the incident and scattered beams is determined by the expression

$$\cos \theta_0 = \cos \theta \cos \theta' + \sin \theta \sin \theta' \cos(\varphi - \varphi') \quad (9.9)$$

or

$$\mu_0 = \mu \mu' + \sqrt{1 - \mu^2} \sqrt{1 - (\mu')^2} \cos(\varphi - \varphi'), \quad (9.10)$$

where θ, φ and θ', φ' are polar coordinates determining the directions Ω' and Ω , and μ, μ' and μ_0 are equal to $\cos \theta, \cos \theta'$ and $\cos \theta_0$, respectively.

When the scattering indicatrix depends only on the angle θ_0 , expression (9.8) takes the form of

$$\frac{1}{4\pi} \sigma_\nu(\mathbf{r}) d\Omega \int_0^{2\pi} \int_{-1}^{+1} I_\nu(\mathbf{r}, \mu', \varphi') p_\nu(\mu_0) d\mu' d\varphi', \quad (9.11)$$

where μ_0 is determined by formula (9.10).

The simplest scattering indicatrix for the case of isotropic (ideal) scattering is as follows:

$$p_\nu(\mu_0) = 1. \quad (9.12)$$

Thus, the total radiation emitted by the volume element per unit of time, recalculated for a unit of volume, in a unit frequency band and within a unit solid angle, whose axis represents the given direction Ω , consists of thermal radiation and scattered radiation and can be presented as

$$J_\nu(\bar{r}) + \frac{1}{4\pi} \sigma_\nu \iint_{\Omega'=4\pi} I_\nu(\mathbf{r}, \Omega') p_\nu(\Omega' \rightarrow \Omega) d\Omega'. \quad (9.13)$$

If Kirchhoff's law is valid and the medium does not have preferential direction of scattering, this expression takes the following form:

$$\gamma_\nu(\mathbf{r}) I_{\nu B}[T(\mathbf{r})] + \frac{1}{4\pi} \sigma_\nu(\mathbf{r}) \int_0^{2\pi} \int_{-1}^{+1} I_\nu(\mathbf{r}, \mu', \varphi') p_\nu(\mu_0) d\mu' d\varphi'. \quad (9.14)$$

Here the first term describes thermal radiation emitted by heated substance of a unit volume, and the second term describes the radiation falling on the same volume element from all directions within the limits of a spherical solid angle and scattered in the observation direction Ω .

Thus, as a result of the main radiation beam interaction with a unit volume of substance, two (conventionally, positive) radiation components will exist, which put the energy into the main flux recorded by an observer, and two components (conventionally, negative), which extract the energy from the main flux. As we have already noted, the total balance of change of the initial intensity can be, certainly,

both positive and negative, depending on the relationship between the processes of emission, scattering and absorption in a unit volume.

The scattering concept described above is called a single scattering regime. There exist, of course, other approaches to the description of scattering process, for example, taking into account multiple scattering. The study of such approaches is a subject for separate consideration, however; so we refer the interested reader to the specialized literature (Ishimaru, 1978, 1991).

The introduction of definitions for spectral absorption and scattering coefficients and scattering indicatrix in this paragraph was done in a purely phenomenological manner. The next important stage is the problem of attributing the values of the introduced coefficients to the structure of substance (for example, formed as a cloud of water particles). This procedure will be performed in Chapter 10. Now we shall proceed to deriving the basic equation of radiative transfer theory.

9.3 THE RADIATIVE TRANSFER EQUATION

The spatial-angular distribution of radiation intensity $I_\nu(\mathbf{r}, \Omega)$ in a studied medium satisfies the so-called radiative transfer equation. Quite various approaches can be used for deriving this equation. It can be obtained using rigorous methods of statistical physics, by using the Boltzmann equation for radiative transfer as a transfer of photon gas. On the other hand, it is possible to use energy considerations, writing the energy balance equation for some elementary volume on the beam propagation path (Chandrasekhar, 1960; Sobolev, 1963; Ozisik, 1973). An equivalent equation was obtained in the theory of transfer of neutrons (Murray, 1957). We shall make use of the energy approach as most instinctive physically.

Consider the emitting, absorbing and scattering medium characterized by the spectral absorption coefficient $\gamma_\nu(\mathbf{r})$ and spectral scattering coefficient $\sigma_\nu(\mathbf{r})$. The beam of monochromatic radiation with intensity $I_\nu(\mathbf{r}, \Omega)$ propagates in this medium in the observation direction Ω along the path s . We choose the elementary volume in the form of a cylinder with cross section dA , length ds , disposed in the vicinity of coordinate s , the axis of a cylinder coinciding with the direction of s (Figure 9.1(c)). (As subsequent investigations have shown, the form of a unit volume does not play any part in deriving the basic equation.) Let $I_\nu(s, \Omega)$ be the radiation intensity at point s , and $I_\nu(s, \Omega) + dI_\nu(s, \Omega)$ be the radiation intensity at point $s + ds$, and dI_ν be the variation (positive or negative) of the intensity flux when it passes the path ds .

The quantity

$$dI_\nu(s, \Omega) dA d\Omega d\nu dt \quad (9.15)$$

represents the difference of energies of radiation, which intersects the surface dA at points $s + ds$ and s for the time interval dt in the vicinity of t , in the frequency band $d\nu$ in the vicinity of ν , and propagates within the limits of a unit solid angle $d\Omega$ with respect to the direction Ω .

Designate by W the increase of the beam radiation energy in this volume, related to a unit of volume, time (in the vicinity of t), frequency (in the vicinity of ν) and solid angle (with respect to the direction of observation Ω). Then the quantity

$$W_\nu dA ds d\Omega d\nu dt \quad (9.16)$$

represents the increase of the energy of radiation of a beam concluded in the elementary cylindrical volume $dA ds$ and propagating within the limits of solid angle $d\Omega$ with respect to the direction Ω for the time interval dt within the frequency band $d\nu$.

Equating (9.15) and (9.16), we obtain

$$\frac{dI_\nu(s, \Omega)}{ds} = W_\nu. \quad (9.17)$$

Now we can obtain the expression in the explicit form with respect to W_ν using the results obtained in section 9.2. For an absorbing, emitting and scattering medium, quantity W_ν is formed by the components caused by increments and losses of radiation energy:

$$W_\nu = W_E - W_A + W_{IS} - W_{AS}. \quad (9.18)$$

The first term on the right-hand side represents the radiation energy increment caused by thermal radiation of a medium and related to the unit of time, volume, solid angle and frequency. If the local thermodynamic equilibrium is established in a medium, then W_E will be related to the Planck function and spectral absorption coefficient by relationship (9.3), i.e. $W_E = J_\nu(\mathbf{r})$. The second term represents the radiation energy losses caused by radiation absorption by a medium and related to the unit of time, volume, solid angle and frequency. They can be written as follows:

$$W_A = \gamma_\nu(s) I_\nu(s, \Omega). \quad (9.19)$$

The third term corresponds to the radiation energy increment caused by radiation falling on a medium from all directions of a spherical space and scattered by a medium in the observation direction. This quantity, like the two previous ones, is related to the unit of time, volume, solid angle and frequency. For purely coherent scattering in the isotropic medium the third term can be presented as

$$W_{IS} = \frac{1}{4\pi} \sigma_\nu(s) \iint_{4\pi} I_\nu(s, \Omega') p_\nu(\Omega') \rightarrow \Omega d\Omega'. \quad (9.20)$$

The last term corresponds to beam energy losses due to radiation scattering by a medium, as a result of which the beams are deflected from the direction Ω . These losses are also related to the unit of time, volume, solid angle and frequency. They can be written as follows:

$$W_{AS} = \sigma_\nu(s) I_\nu(s, \Omega). \quad (9.21)$$

The substitution of the expressions obtained into (9.17) gives the radiative transfer equation in the form of

$$\begin{aligned} \frac{dI_\nu(s, \Omega)}{ds} + [\gamma_\nu(s) + \sigma_\nu(s)]I_\nu(s, \Omega) &= \gamma_\nu(s)I_{\nu B}[T(s)] \\ &+ \frac{1}{4\pi}\sigma_\nu(s)\iint_{\Omega'=4\pi} T_\nu(s, \Omega')p(\Omega' \rightarrow \Omega)d\Omega'. \end{aligned} \quad (9.22)$$

Most frequently this equation is presented in a more compact form:

$$\frac{1}{\beta_\nu(s)} \frac{dI_\nu(s, \Omega)}{ds} + I_\nu(s, \Omega) = S_\nu(s), \quad (9.23)$$

where the following designations are used:

$$S_\nu(s) = (1 - \omega_\nu)I_{\nu B}[T(s)] + \frac{1}{4\pi}\omega\iint_{\Omega'=4\pi} I_\nu(s, \Omega')p_\nu(\Omega' \rightarrow \Omega)d\Omega', \quad (9.24)$$

$$\beta_\nu(s) = \gamma_\nu(s) + \sigma_\nu(s), \quad (9.25)$$

$$\omega_\nu = \frac{\sigma_\nu(s)}{\gamma_\nu(s) + \sigma_\nu(s)}. \quad (9.26)$$

In these relations $S_\nu(s)$ is called the source function, $\beta_\nu(s)$ the spectral extinction coefficient, $\omega_\nu(s)$ the spectral albedo, which represents the ratio of a scattering coefficient to the extinction coefficient. In studying the transfer processes in gaseous media the spectral albedo is often called the probability of survival of a quantum and is designated as $\Lambda_\nu(s)$. Note once again, that all definitions of medium's parameters presented above are related to the unit volume of substance, rather than to its individual components (for example, the drops of water in a cloud).

Equation (9.22) is the integro-differential partial derivative equation, since the full derivative d/ds contains partial derivatives with respect to spatial coordinates, if it is written in the explicit form for the given coordinate system, and the sought-for intensity $I_\nu(s, \Omega)$ is under the sign of integral in the source function. For this reason the solution of equation (9.22) represents a very complicated problem even for the one-dimensional case. Below we shall consider some important special cases of RTT.

9.4 SPECIAL CASES OF THE RADIATIVE TRANSFER EQUATION

Since obtaining complete solutions of the transfer theory equation for the arbitrary case is rather troublesome, we shall consider some important special cases of RTT, whose solutions are often used in experimental and observational practice (remote sensing, radio-astronomy).

9.4.1 A purely scattering medium

By a purely scattering medium we mean a medium that neither absorbs nor emits thermal radiation, but only scatters electromagnetic radiation, i.e. where $\omega_\nu(s) = 1$, and, hence, $\beta_\nu(s) = \sigma_\nu(s)$. Certainly, in such a case the scattering of the external (with respect to the medium studied) radiation takes place. Natural analogues of such media in the optical band are cloud systems in the terrestrial atmosphere, which consist of small crystals of snow and ice or of volcanic dust particles. The diffuse regime of illumination in such systems has the colloquial designation ‘milk’. Important examples of such media can serve for the cloudy atmosphere of Venus and the Martian atmosphere (in the presence of dust-storms). For such media the basic equation (9.23) is simplified:

$$\frac{1}{\beta_\nu(s)} \frac{dI_\nu(s, \Omega)}{ds} + I_\nu(s, \Omega) = \frac{1}{4\pi} \iint_{4\pi} I_\nu(s, \Omega') p_\nu(\Omega' \rightarrow \Omega) d\Omega'. \quad (9.27)$$

It can easily be seen, however, that the equation for scattering media is still integro-differential and does not have any direct solution. To solve it, one resorts to special methods of solution or to simplifications (Chandrasekhar, 1960; Sobolev, 1963; Ozisik, 1973).

9.4.2 The absorbing and emitting medium

Absorbing and emitting media are characterized by the fact, that they absorb the external radiation passing through them, and emit thermal radiation (the emitted radiation), but do not scatter it, virtually, i.e. $\omega_\nu(s) = 0$ ($\sigma_\nu(s) = 0$). Analogues of such a type of media (for the microwave band) are wide spread in nature. They include: cloud systems (small drops of water, snowflakes and hailstones), clouds of dust, sandy storms, a drop-spray phase on the sea surface, precipitation of various sorts.

For such media the basic equation (9.22) takes the form:

$$\frac{1}{\beta_\nu} \frac{dI_\nu(s, \Omega)}{ds} + I_\nu(s, \Omega) = I_{\nu B}[T(s)]. \quad (9.28)$$

Unlike the basic equation (9.22) and preceding equation (9.27), the latter equation is purely differential, and its solution can be obtained in the closed form:

$$I_\nu(s, \Omega) = I_0 \exp(-\beta s) + \int_0^s I_{\nu B}[T(s')] \exp(-\beta s') ds', \quad (9.29)$$

where I_0 is the boundary condition, or, otherwise, the intensity of the external (with respect to the medium) radiation at the medium’s boundary. For better visualization, we present here the one-dimensional version of the solution of equation (9.29) for a homogeneous medium with respect to the electromagnetic parameters ($\beta_\nu(s) = \gamma_\nu(s) = \text{const}$), but with inhomogeneous heating of the medium ($I_{\nu B}[T(s)]$). The first term of the solution reflects, how much the external radiation will be absorbed by the medium as the observation point advances in the medium. As

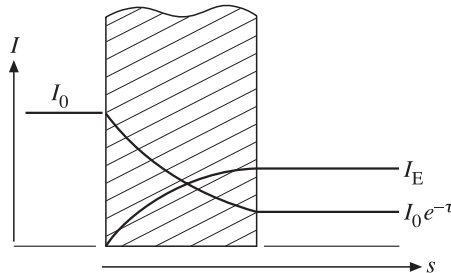


Figure 9.2. Schematic presentation of the radiative transfer passing through the absorbing and emitting one-dimensional layer. I_0 is the external radiation; I_E is the emitted radiation.

should be expected, the external radiation decreases according to the exponential law. The intensity of thermal radiation of the medium is reflected in the second term value and is related to the thermal profile $T(s)$ in a complicated manner (via the Planck function). If the medium is supposed to be not only homogeneous but also isothermal, i.e. $T(s) = T_0 = \text{const}$, then in this case the solution of (9.29) can be reduced to the form:

$$I_\nu(\nu, s) = I_0 \exp(-\beta s) + I_{\nu B}(\nu, T_0)(1 - \exp(-\beta s)). \quad (9.30)$$

Note that the second term in this expression is none other than the Kirchhoff law. Figure 9.2 shows schematically the relationship between two components formed after external radiation passage through the layer of homogeneous and isothermal medium. The relation obtained is important, since it is often used in experimental practice for various preliminary estimations.

9.4.3 Transparent medium

The non-absorbing, non-emitting and non-scattering medium is called transparent (or diathermal). For such a medium the absorption and scattering coefficients are zero. Substituting $\sigma_\nu(s) = \gamma_\nu(s) = 0$ into equation (9.22), we obtain:

$$\frac{dI_\nu(s, \Omega)}{ds} = 0; I_\nu(s, \Omega) = \text{const.} \quad (9.31)$$

This implies that the radiation intensity in a transparent medium remains constant everywhere in any direction.

9.4.4 The ‘cold’ layer approximation

The ‘cold’ layer approximation characterizes the situation, where the external radiation falling on a medium essentially exceeds, in its intensity, the thermal radiation of the medium, which possesses both nonzero absorption coefficient and nonzero scattering coefficient. In other words, the $I_0 \gg I_{\nu B}[T(s)]$ condition is satisfied. A similar situation is met frequently enough under the natural conditions

as well. So, solar radiation in the optical band (under terrestrial conditions) essentially exceeds the thermal radiation of terrestrial media. The power of artificial sources (radio broadcasting, television, communications, radar sources) essentially exceeds thermal radiation of terrestrial media in the microwave band (see Chapter 1). Using this approximation for relation (9.29), we have:

$$I_\nu(s) = I_{\nu_0} \exp \left[- \int_0^s \beta_\nu(z) dz \right]. \quad (9.32)$$

The exponential factor in this expression is often written in another form by introducing the dimensionless quantity

$$\tau(s) = \int_0^s \beta(z) dz. \quad (9.33)$$

The dimensionless quantity τ is called the optical thickness (opacity) of a layer of scattering and absorbing medium having thickness s , and is a function of all values of absorption and scattering coefficients over the spatial scales from 0 to s .

It can easily be seen, that the given relation is none other than the well-known and widely used ‘in optics’ Bouguer law for absorbing and scattering media (Born and Wolf, 1999; Siegel and Howell, 1972). As far as the microwave sounding problems are concerned, the frameworks of application of the Bouguer law are rather limited, since in this band natural radiations have a compatible order in intensity and, therefore, various constituents should be taken into account when performing measurements under the natural conditions (see Chapters 5 and 12).

9.5 EQUATION OF RADIATIVE TRANSFER FOR THE PLANE-LAYER CASE

As we have noted, the basic equation of radiative transfer is the integro-differential equation, and obtaining its complete solution for the general three-dimensional case is a very complicated problem. However, it is quite useful to trace the formal integration of equation (9.22), so that in some important practical cases it will be possible to obtain results that satisfactorily agree with experimental and observational data. Here we should mention, first of all, the one-dimensional, plane-parallel case. This geometry is widely used in studying the terrestrial atmosphere and terrestrial surfaces over spatial scales where the Earth’s curvature does not play a noticeable part.

We shall consider a medium composed of planar layers perpendicular to axis oy , the electromagnetic properties of the medium being constant in each layer. Let s be the length measured in the arbitrary direction Ω and θ be the polar angle between the direction Ω and positive direction of axis oy (Figure 9.3). The derivative with respect to direction d/ds can be expressed in terms of derivatives with respect to the spatial

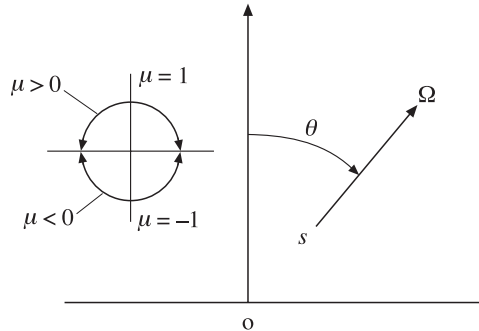


Figure 9.3. The coordinate system for the plane-parallel case. Notation is explained in the text.

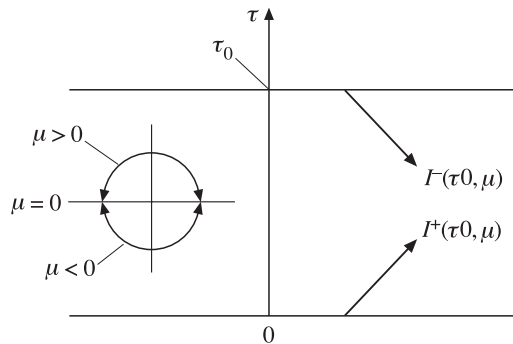


Figure 9.4. The coordinate system for the formal solution of the radiative transfer equation for the plane-parallel case. $I^+(0, \mu)$ and $I^-(\tau_0, \mu)$ are outgoing and incident components of the sought-for radiation. τ_0 is the value of opacity for the upper boundary of a layer.

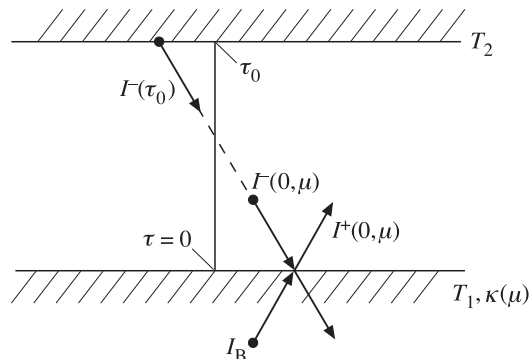


Figure 9.5. The mirror-reflecting, emissive and black boundary conditions for the radiative transfer equation solution. T_2 is the temperature of the upper black-body boundary. T_1 and $\kappa(\mu)$ are the temperature and the emissivity and the lower reflecting boundary. Notation is explained in Figure 9.4.

coordinate y in the form

$$\frac{d}{ds} = \frac{\partial}{\partial y} \frac{dy}{ds} = \mu \frac{\partial}{\partial y}, \quad (9.34)$$

where μ is the cosine of angle θ between the radiation transmission direction Ω and axis oy , i.e.

$$\mu = \cos \theta, \quad (9.35)$$

and the partial derivatives with respect to x and z for the plane-parallel case are equal to zero. Then the equation of radiative transfer (9.21) takes the following form:

$$\frac{\mu}{\beta_\nu} \frac{\partial I_\nu(y, \mu, \varphi)}{\partial y} + I_\nu(y, \mu, \varphi) = S(y, \mu, \varphi), \quad (9.36)$$

where the source function will be written as

$$S_\nu(y, \mu, \varphi) = (1 - \omega_\nu) I_{\nu B}[T(y)] + \frac{\omega_\nu}{4\pi} \int_{\varphi'=0}^{2\pi} \int_{\mu'=0}^{+1} p(\mu_0) I_\nu(y, \mu, \varphi) d\mu' d\varphi' \quad (9.37)$$

and μ_0 is the cosine of angle between the directions of incident radiation and radiation scattered by a volume element (see equation (9.10)).

Further on, when equation (9.36) is solved mathematically, it is convenient to reduce it to the so-called dimensionless form, making use of the concept of the optical thickness of a layer (9.33). Then equation (9.36) will take the form

$$\mu \frac{\partial I_\nu(\tau, \mu, \varphi)}{\partial \tau} + I_\nu(\tau, \mu, \varphi) = S_\nu(\tau, \mu, \varphi), \quad (9.38)$$

where

$$S_\nu(\tau, \mu, \varphi) = (1 - \omega_\nu) I_{\nu B}[T(\tau)] + \frac{\omega_\nu}{4\pi} \int_{\varphi'=0}^{2\pi} \int_{\mu'=-1}^{+1} p(\mu_0) I_\nu(\tau, \mu, \varphi) d\mu' d\varphi'. \quad (9.39)$$

If the boundary conditions for the equation of radiative transfer are characterized by axial symmetry, then the intensity of radiation in the medium studied does not depend on the azimuthal angle, and equation (9.38) is simplified:

$$\mu \frac{\partial I_\nu(\tau, \mu)}{\partial \tau} + I_\nu(\tau, \mu) - (1 - \omega_\nu) I_{\nu B}[T(\tau)] + \frac{\omega_\nu}{4\pi} \int_{\mu'=1}^{+1} I_\nu(\tau, \mu') \int_{\varphi'=0}^{2\pi} p(\mu_0) d\varphi' d\mu'. \quad (9.40)$$

To fulfil the integration over φ' in this relation and, thus, to essentially simplify the right-hand side of equation (9.40), one resorts to the following approach. The scattering indicatrix $p(\mu_0)$ is expanded over the orthogonal Legendre polynomials (Gradshteyn and Ryzhik, 2000):

$$p(\mu_0) = \sum_{n=0}^N a_n P_n(\mu_0); a_0 = 1, \quad (9.41)$$

where $P(\mu_0)$ is the Legendre polynomial of the n th order from the argument μ . The physical prerequisites for choosing just such a type of orthogonal expansion are related, first of all, with the fact that the scalar wave equation for systems of

particles allows, in the Maxwell theory, the following separation of angular and spatial variables and has particular solutions of the following form (Stratton, 1941):

$$\Psi \sim \frac{\cos l\varphi}{\sin l\varphi} \{P_n(\cos \theta)\} Z_{n+1/2}(r). \quad (9.42)$$

In this case the spherical Bessel function $Z_{n+1/2}(r)$ can be presented in the far radiation zone as

$$Z_{n+1/2}(r) \sim [\exp(-jkr)(kr)^{-1}], \quad (9.43)$$

where k is the wave number.

Thus, using the features of the orthogonal expansion over the Legendre polynomials, the internal integral in the right-hand side of relation (9.40) can be integrated, and the following expression is obtained (see Ozisik (1973) for more details):

$$\int_0^{2\pi} p(\mu_0) d\varphi' = 2\pi \sum_{n=0}^N a_n P_n(\mu) P_n(\mu'). \quad (9.44)$$

The substitution of (9.44) into (9.40) represents the equation of radiative transfer in the case of axial symmetry as

$$\mu \frac{\partial I_\nu(\tau, \mu)}{\partial \tau} + I_\nu(\tau, \mu) = (1 - \omega) I_{\nu B}[T(\tau)] + \frac{\omega_\nu}{2} \int_{-1}^{+1} p(\mu, \mu') I_\nu(\tau, \mu') d\mu', \quad (9.45)$$

where

$$p(\mu, \mu') = \sum_{n=0}^N a_n P_n(\mu) P_n(\mu'). \quad (9.46)$$

In this case the scattering indicatrix $p(\mu, \mu')$ of a unit volume does not depend on the azimuthal angle. Relation (9.46) has a number of important special cases, which are widely used in observational practice. So, the case of $N = 0$ corresponds to the so-called isotropic scattering, $N = 1$ to the indicatrix of linearly anisotropic scattering, i.e.

$$p(\mu, \mu') = 1 + a_1 \mu \mu', \quad (9.47)$$

and $N = 2$ to the indicatrix of anisotropic scattering of the second order:

$$p(\mu, \mu') = 1 + a_1 \mu \mu' + \frac{1}{4} a_2 (3\mu^2 - 1)[3(\mu')^2 - 1]. \quad (9.48)$$

The indicatrix of the important case of so-called Rayleigh scattering can be obtained from (9.48) for $a_1 = 0$ and $a_2 = 1/2$, i.e.

$$p(\mu, \mu') = \frac{3}{8}[3 - \mu^2 + (3\mu^2 - 1)(\mu')^2]. \quad (9.49)$$

Below we shall transfer to the formal solution of the equation of radiative transfer in the planar case in the presence of axial symmetry (9.45). To solve this equation, one establishes, first of all, the so-called double-flux approximation. For this purpose the unknown intensity $I_\nu(\tau, \mu)$ is separated into two components: the direct (or outgoing) one $I_\nu^+(\tau, \mu)$, $\mu > 0$, and the reverse (or incident) one $I_\nu^- - (\tau, \mu)$, $\mu < 0$ (Figure 9.4). From the viewpoint of experimental practice such a separation is

quite lawful and justified since, when a receiving device is at the upper boundary of a layer, we receive radiation formed by the volume of a medium and the escaping (outgoing) from this medium. And when we are at the lower boundary of a medium, we receive radiation falling (incident) from the medium's volume on a receiving device. The separation of the intensity into two components in performing particular measurements is clear enough and, therefore, no special explanations are usually made in describing the experiments. In this approach the equations for outgoing and incident components of the sought-for radiation and the corresponding boundary conditions will be as follows:

$$\mu \frac{\partial I_\nu^+(\tau, \mu)}{\partial \tau} + I_\nu^\pm(\tau, \mu) = S(\tau, \mu), \quad (9.50)$$

$$I_\nu^+(\tau, \mu)|_{\tau=0} = I_\nu^+(0, \mu); 0 < \mu \leq 1, \quad (9.51)$$

$$I_\nu^-(\tau, \mu)|_{\tau=\tau_0} = I_\nu^-(\tau_0, \mu); -1 \leq \mu < 0. \quad (9.52)$$

These equations are not independent, however, but represent an interdependent system, since they contain the source function, which can be written in this representation as:

$$\begin{aligned} S_\nu(\tau, \mu) = & (1 - \omega_\nu) I_{\nu B}[T(\tau)] \\ & + \frac{\omega_\nu}{2} \left[\int_0^1 p(\mu, \mu') I_\nu^+(\tau, \mu') d\mu' + \int_{-1}^0 p(\mu, \mu') I_\nu^-(\tau, \mu') d\mu' \right]. \end{aligned} \quad (9.53)$$

The formal solution of equations (9.50) can be obtained by means of the well-known integrating multiplier method. For an outgoing flux we have:

$$I_\nu^+(\tau, \mu) = I_\nu^+(0, \mu) \exp(-(\tau/\mu)) + \frac{1}{\mu} \int_0^\tau S(\tau', \mu) \exp(-(\tau - \tau')/\mu) d\tau' \quad (9.54)$$

for $\mu > 0$.

For an incident flux after traditional replacement of μ by $-\mu$ the solution has the form:

$$I_\nu^-(\tau, -\mu) = I_\nu^-(\tau_0, \mu) \exp(-(\tau_0 - \tau)/\mu) + \frac{1}{\mu} \int_\tau^{\tau_0} S_\nu(\tau, -\mu) \exp(-(\tau' - \tau)/\mu) d\tau'. \quad (9.55)$$

In these relations, for example (9.54), the first term in the right-hand side represents, in the explicit form, the contribution of radiation from the boundary surface with $\tau = 0$, which has attenuated on passage through a medium to depth τ without scattering. The second term represents the contribution of the source function within the range of values from $\tau = 0$ to τ into the intensity of radiation at depth τ . The terms of relation (9.55) have similar physical sense (with correction for geometry). The formal expressions (9.54) and (9.55) are not solutions in the true sense, since in the general case the source function and the intensities at the boundaries depend on the unknown intensity of radiation emitted by the medium. And, therefore, they cannot be directly used as initial expressions in solving the problem

under consideration. Below we shall demonstrate how the problem can be solved up to the final result for a series of important practical cases.

9.6 BOUNDARY CONDITIONS

In section 9.5 the formal values of functions $I_\tau^+(\tau, \mu), \mu > 0$ and $I_\tau^-(\tau, \mu), \mu < 0$ have been used as boundary conditions at the boundaries of $\tau = 0$ and $\tau = \tau_0$, respectively. In this section we shall present explicit expressions for these boundary conditions in the case of transparent and non-transparent boundary surfaces being diffuse and mirroring reflectors.

9.6.1 The transparent boundaries

If the boundary surfaces $\tau = 0$ and $\tau = \tau_0$ are transparent, and the adjacent surrounding space is a vacuum (i.e. it does not interact with radiation), then the boundary conditions for the incident (from outside) radiation in the case of axial symmetry can be written as

$$I_\nu^+(0, \mu) = f_{1\nu}(\mu); \mu > 0, \quad (9.56)$$

$$I_\nu^+(\tau_0, \mu) = f_{2\nu}(\mu); \mu < 0, \quad (9.57)$$

where $f_{1\nu}(\mu)$ and $f_{2\nu}(\mu)$ are specified functions of parameter μ . If the incident radiation, falling on a studied layer from outside, is constant, formulas (9.56) and (9.57) are simplified to the form

$$I_\nu^+(0) = f_{1\nu}; \mu > 0, \quad (9.58)$$

$$I_\nu^-(\tau_0) = f_{2\nu}; \mu < 0, \quad (9.59)$$

where $f_{1\nu}$ and $f_{2\nu}$ are constants.

Typical examples of such kinds of boundary conditions are solar radiation falling on the upper boundary of the terrestrial atmosphere and other extra-terrestrial sources of radio-emission of galactic and extra-galactic origin.

9.6.2 The black boundaries

If both boundary surfaces $\tau = 0$ and $\tau = \tau_0$ are black (i.e. fully absorbing the incident radiation) and are maintained at constant temperatures T_1 and T_2 , respectively, then the spectral intensity of radiation emitted by these surfaces is described by the Planck function at the surface temperature (see Chapter 6). Then the boundary conditions can be written as:

$$I_\nu^+(0) = I_{\nu B}(T_1), \quad (9.60)$$

$$I_\nu^-(\tau_0) = I_{\nu B}(T_2), \quad (9.61)$$

where $I_{\nu B}(T)$ is the Planck function, whose value does not depend on the direction.

A typical natural example of such a type of boundary (for the microwave band) is the upper boundary (conventional, in a certain sense) of the terrestrial atmosphere, on which falls the black-body radiation of the relic background of the universe with brightness temperature of $T_2 = 2.7$ K.

9.6.3 Mirror-reflecting and black boundaries

In the microwave band, as we have already argued (see Chapter 7), some part of terrestrial surfaces can be considered in the approximation of mirror-reflecting media with a power reflection coefficient distinct from unity. Thus, such a type of boundary on the one hand will be the source of thermal radiation, and, on the other hand, will reflect the incident radiation falling on it from the studied medium.

Now we consider the situation with the boundary conditions, which is quite close to real situations in experimental practice when studying the terrestrial atmosphere. In such a case, the upper boundary represents a black body with a brightness temperature of 2.7 K (see relation (9.61)). The radiation at the lower boundary will be formed from the thermal radiation of the surface with emissivity $\kappa_1(\mu)$ and temperature T_1 and from re-reflected radiation with the Fresnel power coefficient $|R(\mu)|^2$, which was formed at the lower boundary of a studied layer. In virtue of the fact that the emissive and reflective properties of the surface depend on the polarization of radiation received by a receiving system, the outgoing flux under these conditions will also possess polarization properties, though distinct from the polarization properties of the surface itself. Corresponding examples will be considered below.

So, for the conditions at the upper black-body boundary and at the lower reflecting boundary (Figure 9.5) the unknown boundary conditions can be presented in the form:

$$I^-(\tau_0) = I_{\nu B}(T_2), \quad (9.62)$$

$$I_\nu^+(0, \mu) = \kappa(\mu)I_{\nu B}(T_1) + |R_\nu(\mu)|^2 I_\nu^-(0, \mu). \quad (9.63)$$

We shall repeatedly use the boundary conditions of type (9.62) and (9.63) hereafter.

9.7 RADIATIVE TRANSFER IN THE EMITTING AND ABSORBING MEDIUM

One of the most important particular cases in the radiative transfer theory is the approximation of emitting and absorbing medium (without scattering, i.e. $\omega = 0$). This approximation is especially widely used in the microwave band. For the conditions of purely gaseous terrestrial atmosphere, without the presence of hydro-meteors, the relation $\omega = 0$ is met accurately. But even in the presence of hydro-meteors at wavelengths greater than 1 cm this condition is met to a good accuracy (see Chapter 10). For this reason, we shall present in this section the explicit expressions of radiation intensity for some particular observational schemes.

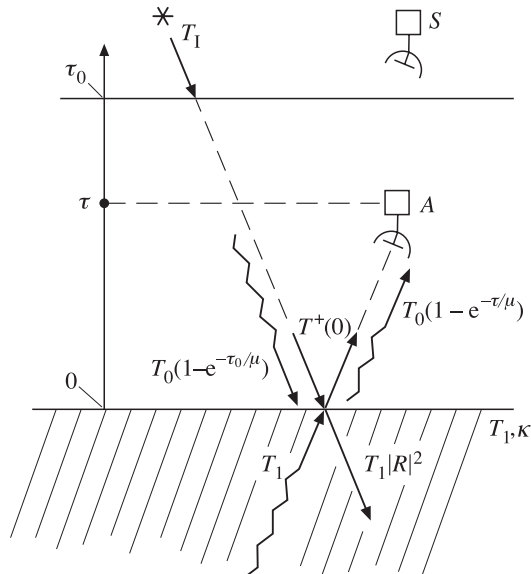


Figure 9.6. The measurement scheme for recording the outgoing radiation by the aircarrier (A) (aircraft) inside the atmosphere and by a satellite (S) outside the atmosphere. Notation is explained in the text.

Figure 9.6 presents the measurement scheme for recording the outgoing radiation in the conventional electrodynamically homogeneous, non-isothermal atmosphere over the solid (or liquid) surface. The recording microwave device is installed either on an aircraft inside the atmosphere at the given altitude (the dimensionless coordinate τ), or on a satellite outside the atmosphere. We shall suppose that outside the conventional atmosphere the attenuation in a medium is absent; therefore, for a satellite version the altitude coordinate can be $\tau = \tau_0$.

As we have already noted, the Rayleigh–Jeans approximation is valid in the microwave band, and, hence, we can proceed to presentation of the solution of (9.54) and (9.55) in the form of brightness temperatures. Then the source function will be equal to $S(\tau) = T_0(\tau)$ and, thereby, it reflects the non-isothermal character of the atmosphere.

Thus, the complete solution for outgoing radiation, which is recorded at the dimensionless altitude $\tau(h)$, will be equal to:

$$T_B^+(\tau, \mu) = T_B^+(0, \mu) \exp(-(\tau/\mu)) + \frac{1}{\mu} \int_0^{\tau(h)} T_0(\tau') \exp(-(\tau - \tau')/\mu) d\tau'; \mu > 0. \quad (9.64)$$

The boundary condition at the lower boundary will be formed from two components – the thermal radiation of the surface and the incident radiation from the

atmosphere, re-reflected by this surface:

$$T_B^+(0, \mu) = \kappa(\mu) T_2 + |R(\mu)|^2 T_B^-(0, -\mu). \quad (9.65)$$

In its turn, the incident radiation, falling from the atmosphere to the lower boundary, will also consist of two components – the external radiation (the radiation of illumination) T_I fallen on the upper atmosphere's boundary and attenuated in the atmosphere medium, and the thermal radiation of the atmosphere formed inside the atmosphere. The complete solution for incident radiation at the lower boundary will take the form:

$$T_B^-(0, -\mu) = T_I \exp(-(\tau_0/\mu)) + \frac{1}{\mu} \int_0^{\tau_0} T_0(\tau') \exp(-(\tau'/\mu)) d\tau'; \mu > 0. \quad (9.66)$$

For greater physical clarity we assume the atmosphere to be isothermal, i.e. $T_0(\tau) = T_0$. Note that the isothermal approximation for atmospheric problems should be used with great caution, since it is known from the thermohydrodynamics that such atmospheres are dynamically unstable under gravity conditions.

So, the expressions for the isothermal atmosphere will be as follows:

$$T_B^+(\tau, \mu) = T_B^+(0, \mu) \exp(-(\tau/\mu)) + T_0[1 - \exp(-(\tau/\mu))], \quad (9.67)$$

$$T_B^+(0, \mu) = \kappa(\mu) T_2 + |R(\mu)|^2 [T_I \exp(-(\tau_0/\mu)) + T_0(1 - \exp(-(\tau_0/\mu)))]. \quad (9.68)$$

Note that the outgoing recorded radiation consists of two components – the contribution of the atmosphere itself and the contribution from the surface and external radiation. As we have already noted, all these components possess identical statistical properties and cannot be distinguished by this criterion. So, it is necessary to use the polarization features of total radiation to separate various components. Note that the last term in these expressions is none other than the numerical expression of Kirchhoff's law.

The obtained expressions for outgoing radiation (9.64) and (9.67) are widely used in various modifications in experimental microwave remote sensing practice.

9.8 FEATURES OF RADIATION OF A HALF-SPACE WITH THE SEMI-TRANSPARENT ATMOSPHERE

In this section we shall consider in more detail the features of radiation of the surface–atmosphere system and also will present the observational techniques that are used in studying the electromagnetic properties of the atmosphere.

For physical clarity we shall consider the simplest isothermal version, where both the atmosphere and the surface are at the same thermodynamic temperature T_0 , and external radiation is absent, i.e. $T_I = 0$. Using relation (9.67), we obtain in this case the expression for the outgoing flux intensity at the upper boundary for observation into the nadir ($\mu = 1$) in the following form:

$$T_B(\tau_0, 0) = T_0[1 - |R(0)|^2 \exp(-2\tau_0)]. \quad (9.69)$$

It follows from this relation that the emissivity of the surface–atmosphere system κ_{SA} will be equal to:

$$\kappa_{\text{SA}}(\tau_0, 0) = 1 - |R(0)|^2 \exp(-2\tau_0). \quad (9.70)$$

Recall that in the absence of the atmosphere the surface emissivity κ_{S} will be

$$\kappa_{\text{S}}(\tau_0, 0) = 1 - |R(0)|^2. \quad (9.71)$$

Note that the doubled value of the optical thickness (path) in the exponent is physically related to the fact that three types of radiation make contribution to the total radiation in a statistically independent manner, namely: (1) the thermal outgoing radiation of the atmosphere, (2) the re-reflected incident radiation of the same atmosphere, and (3) the thermal radiation of the surface.

9.8.1 Brightness contrast

Note that in experimental practice are brightness contrast is important in studying complex geophysical objects. Suppose we are interested in the brightness contrast at observation of the surface–atmosphere system and surface only. In this case the expression for the brightness contrast can be presented as:

$$\Delta T_{\text{B}}(\tau_0, 0) = T_{\text{BSA}}(\tau_0, 0) - T_{\text{BS}}(\tau_0, 0) = T_0 |R(0)|^2 (1 - \exp(-2\tau_0)), \quad (9.72)$$

and the emissivity contrast can be written as:

$$\Delta \kappa = \kappa_{\text{SA}} - \kappa_{\text{S}} = |R(0)|^2 (1 - \exp(-2\tau_0)). \quad (9.73)$$

If the homogeneous atmosphere possesses semi-transparent properties, i.e. $t < 1$, then in this case, expanding the exponential function into a series and retaining the first two terms, we shall have

$$\Delta T_{\text{B}}(\tau_0, 0) \cong T_0 |R(0)|^2 2\gamma h, \quad (9.74)$$

$$\Delta \kappa(\tau_0, 0) \cong |R(0)|^2 2\gamma h. \quad (9.75)$$

The relations obtained give rise to some important consequences, which are widely used in experimental practice. First, the brightness contrast is always positive in the presence of absorbing and emitting atmosphere. However, as we shall see below, the situation can drastically change when scattering is present in the atmospheric formations. Second, the value of contrast for a semi-transparent atmosphere is proportional to the electrodynamic properties of the atmosphere medium, and, knowing the values of temperature and atmosphere's height from accompanying measurements, we can obtain the value of attenuation in the atmosphere substance. Third, as the value of the optical path of the atmosphere increases (via increasing the height or attenuation in the atmosphere), the emissive properties of a system will tend to the properties of black-body radiation (Figure 9.7). In this situation the information on the surface and the electrodynamic properties of the atmosphere will be completely ‘blocked’ (see Chapter 6).

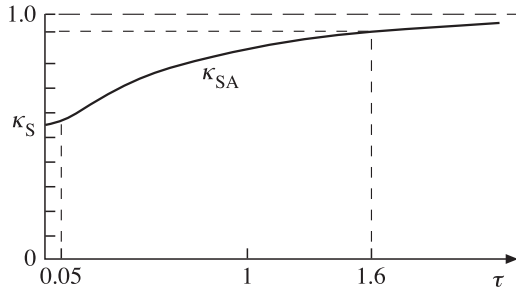


Figure 9.7. Emissivity of the atmosphere–surface system as a function of the atmospheric optical thickness. The symbol κ_S presents the surface emissivity; κ_{SA} is the atmosphere–surface system emissivity.

By virtue of this circumstance, in experimental practice the atmosphere is subdivided (fairly conventionally, of course) into three types: the transparent atmosphere with $\tau < 0.05$ (and, accordingly, with the emissivity contrast $\Delta\kappa < 0.1$); the non-transparent atmosphere with system emissivity $\kappa_{SA} > 0.95$ and accordingly, $\tau \geq 1.6$, and the semi-transparent atmosphere with optical path values in the range of $0.05 < \tau < 1.6$ (Figure 9.7). It can easily be seen that the measurements in the semi-transparent atmosphere will be most informative for remote sensing, as we shall see below.

9.8.2 Angular measurements

By virtue of the fact, that the emitting half-space possesses polarization properties (see Chapter 7), these properties will reveal themselves (in a rather peculiar manner, however, as we shall see later) in measurements of the surface–atmosphere system as well.

So, for the isothermal, planar surface–atmosphere system under observation at angle θ we obtain from relations (9.67) and (9.68) the following value for the outgoing radiation intensity:

$$\kappa_{SA_i}(\mu) = 1 - |R_i(\mu)|^2 \exp(-2\tau_0/\mu). \quad (9.76)$$

where $i = H, V$ are the horizontal and vertical components of an outgoing flux, respectively, and $\mu = \cos \theta$.

As we already know, the emissivity of the planar half-space (both components) tends to zero as the observation angle tends to 90° , and, accordingly, the Fresnel coefficient tends to unity. However, it can easily be seen from (9.73), that for $\theta \rightarrow 90^\circ$ and, passing to the other complementary angle $\alpha = 90^\circ - \theta$, the limiting value of κ_{SA} can be written as:

$$\kappa_{SA_i}(\alpha) \cong 1 - \exp(-2\tau_0/\alpha) \rightarrow 1 \quad (9.77)$$

for any values of the optical path of the atmosphere. In other words, the radiation of the surface–atmosphere system represents black-body radiation at grazing observation angles (Figure 9.8). In such a case measurement of the surface's properties and

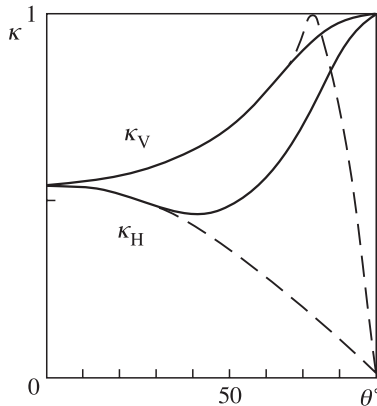


Figure 9.8. Polarization dependences of the atmosphere–surface system (solid lines) and of the surface (dashed lines).

of the electrodynamic properties of the atmosphere is impossible. The physical sense of such a paradoxical (at first sight) situation is related to the initial specifying of a plane-layered model of the atmosphere. In real atmosphere investigation practice it is necessary, of course, to take into account the sphericity of the atmosphere, which eliminates the paradoxical effect mentioned. It is important to note that such an observation mode, which is called the limb method of studying the atmosphere, has been widely disseminated recently, since it makes it possible to record and study in detail very fine features of radiation both of the terrestrial atmosphere (Hartmann *et al.*, 1996; Masuko *et al.*, 2000), and of the atmospheres of planets (Mars, in particular) as well.

9.8.3 The oblique section method

The features of thermal signal transmission on oblique tracks allow us to use some measurement techniques, very useful in observations, which are generically called the oblique section method. This method was proposed and developed in radio-astronomical practice. Now it is used, with various modifications, in remote observation as well.

The observational scheme of the oblique section method is as follows. The instrument is situated at the lower boundary of the atmosphere layer and records the intensity of an incident flux (9.66). If there is a strong thermal source with brightness temperature T_{BS} outside the atmosphere, then the total intensity of an incident flux can be written as

$$T_{\text{B}}^-(\mu) = T_{\text{BS}} \exp(-\tau_0/\mu) + T_0(1 - \exp(-\tau_0/\mu)), \quad (9.78)$$

(for the sake of convenience we have replaced μ with $-\mu$).

Here the first term describes the received radiation from the extraneous (external) source, and the second term corresponds to the contribution of the

thermal radiation of the atmosphere. This makes it possible to follow one of two experimental techniques: either to study source intensity variations as the source passes across the sky (for ‘regular transmission’), or to use forced scanning over the observation angle at reception of thermal radiation of the atmosphere. Each of these techniques possesses both positive and negative features in their direct use in observational practice (Haroules and Brown, 1968; Gorelik *et al.*, 1975).

A principal feature of the oblique section method is the circumstance that the variation of the angular dependence of a received signal in various modifications is identical, namely, as a secant of the observation angle. This makes it possible to essentially simplify the measurements, that is, to avoid absolute radiothermal measurements and pass to the mode of relative measurements. The latter approach is, of course, much easier and more reliable both methodologically and in respect of the technological implementation.

To better understand the essence of the oblique section method we rewrite the expression for an incident flux in the following form:

$$\frac{T_B^- - T_0}{T_{BS} - T_0} = \exp(-\tau_0 \sec \theta). \quad (9.79)$$

Differentiating over the parameter $\sec \theta$, we obtain from (9.76) the following expression:

$$-\frac{1}{T_B - T_0} \frac{d[T_B(\theta) - T_0]}{d(\sec \theta)} = \tau_0 \exp(-\tau_0 \sec \theta), \quad (9.80)$$

and, substituting here the expression for an exponential function from (9.79), we find the relation sought:

$$\tau_0 = -\left(\frac{1}{T_B - T_0}\right) \frac{d(T_B - T_0)}{d(\sec \theta)}. \quad (9.81)$$

And, passing to finite differences, we shall have

$$\frac{\Delta[T_B(\theta) - T_0]}{T_B(\theta) - T_0} = -\tau_0 \Delta(\sec \theta). \quad (9.82)$$

Thus, quantity τ_0 can be determined from the relative measurements of variations of the external signal intensity as a function of $\sec \theta$.

A similar approach can also be used in measuring the thermal radiation of the atmosphere (the second term in expression (9.78)). Performing a similar operation, we shall obtain the expression for the optical path in the form:

$$\tau_0 = \frac{1}{T_B - T_0} \frac{d(T_B - T_0)}{d(\sec \theta)}. \quad (9.83)$$

In other words, the optical path value can be obtained as a tangent of the angle of a slope of the plot of relative variations of thermal radiation versus $\sec \theta$. As an indicative example, we shall present the data of measurements of thermal radiation of a cloudless atmosphere (for clear weather conditions), carried out simultaneously at two frequencies: 19 GHz and 35 GHz (Figure 9.9) (Haroules and Brown, 1968). It follows from the measurement data, that under the meteorological

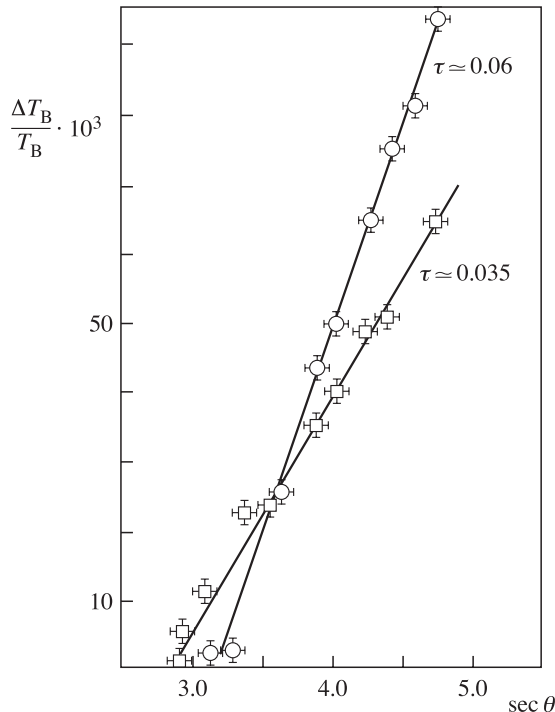


Figure 9.9. Measured atmospheric opacity at 19 (squares) and 35 GHz (circles) under clear weather conditions (temperature, 4°C ; pressure 1000.9 mbar ; water vapour 2.4 g/m^3) (Haroules and Brown, 1968).

conditions studied the opacity of the terrestrial atmosphere at the frequency of 19 GHz was found to be 0.035, and at the frequency of 35 GHz, 0.06. It follows from this result that under the meteorological conditions studied the state of the atmosphere can be characterized as a transparent atmosphere.

A final objective of this kind of experiment is obtaining spectral characteristics of absorption of the atmosphere within a wide wavelength range, which, in its turn, determines the physicochemical and aggregate composition of the atmosphere (see Chapters 10 and 11).

9.9 RADIATIVE TRANSFER IN THE EMITTING, ABSORBING AND SCATTERING MEDIUM

To evaluate the contribution of scattering to radiative transfer, we consider a model situation where we shall take into account the full scattering losses, but disregard the contribution of rescattering (see section 9.2). In other words, the source function will be taken into account as it is written in relation (9.53); however, we shall still disregard the contribution of the integral, i.e. we let $p(\mu_0) = 0$. This model

approach makes it possible to evaluate the upper boundary of possible losses during radiative transfer in a scattering medium.

The values of scattering albedo for particles in the terrestrial atmosphere for the millimetre and centimetre bands vary within very wide limits, from 0.1 to 0.7. In the optical band, however, the albedo in cloudy systems can reach the values of 0.99 and greater.

Taking into account the model approach conditions, we obtain from relations (9.54) and boundary conditions (9.63) the expression for an outgoing flux at the upper boundary of the atmosphere in the form of

$$T_B^+(\tau_0, \mu) = \kappa T_2 \exp(-\tau_0/\mu) + (1 + |R(\mu)|^2 \exp(-\tau_0/\mu))(1 - \omega) T_0(1 - \exp -\tau_0/\mu). \quad (9.84)$$

It follows from the expression obtained that, as $(\tau_0/\mu) \rightarrow \infty$, the limiting value of intensity tends to $(1 - \omega)T_0$. In other words, under such conditions the surface-atmosphere system emits as a black-body emitter, but with essentially lower effective thermodynamic temperature. In this case one sometimes says, that the ‘cooling’ of a medium occurs because of ‘the inner radiative scattering losses’. The incident radiation, falling on a volume element and scattered by it, will be subjected to further multiple scattering on other medium’s elements and, eventually, will dissipate in a medium. The processes of multiple scattering in scattering media are, certainly, very complicated and represent a subject of independent investigation (Marchuk, 1976; Ishimaru, 1978, 1991).

As we have already noted, of importance in the observational practice are background contrasts – the difference between radiation of the surface-atmosphere system and radiation of the surface only. Making easy transformations using (9.84), we obtain the expression the radiothermal contrast at observation of the nadir:

$$\Delta T_B(\mu = 1) = T_0 |R|^2 (1 - \exp(-2\tau_0)) \left[1 - \frac{\omega}{|R|^2} \frac{1 + |R|^2 \exp(-\tau_0)}{1 + \exp(-\tau_0)} \right]. \quad (9.85)$$

And, assuming the atmosphere to be transparent ($\tau \ll 1$), we simplify expression (9.85) to the form:

$$\Delta T_B \cong T_0 |R|^2 2\tau_0 \left[1 - \frac{\omega}{2} \frac{1 + |R|^2}{|R|^2} \right]. \quad (9.86)$$

Let us analyse the relations obtained. First, it should be noted at once that the contrast in the presence of scattering atmosphere (unlike non-scattering atmosphere) can have both positive and negative sign. Second, the contrast depends, in a rather complicated manner, not only on the properties of the atmosphere itself, but on the emissive properties of the surface. If the surface is rather ‘cold’ in the radiothermal sense, i.e. $\kappa \rightarrow 0$, then the value of contrast is positive and can be presented as

$$\Delta T_B = T_0 (1 - \exp(-2\tau_0)) (1 - \omega) \cong T_0 2\tau_0 (1 - \omega). \quad (9.87)$$

In the opposite case, for ‘warm’ ‘black-body’ surfaces ($\kappa \rightarrow 1$), the situation is reversed: the contrast is negative, and its value can be written as:

$$\Delta T_B = -T_0\omega(1 - \exp(-2\tau_0)) \cong -2T_0\omega\tau_0. \quad (9.88)$$

From relation (9.86) it can also easily be seen that at a certain value of surface emissivity the value of contrast will be zero. This value of κ can be estimated as

$$\kappa \cong \frac{2(1 - \omega)}{2 - \omega}. \quad (9.89)$$

It can be seen from this relation that, for example, for a cloud with albedo $\omega = 0.7$ the surface emissivity, for which the effect of presence of a cloud is absent, will be equal to $\kappa = 0.5$.

The physical meaning of the obtained results is rather transparent. In the case of ‘warm’ surfaces, the scattering cloud does not compensate in a full measure for those scattering losses of radiation, outgoing from the surface, which are introduced by the cloud itself. In the case of ‘cold’ surfaces the situation is the reverse – the cloud not only fully compensates scattering losses, but, in addition, makes its own contribution into the total radiation, thus providing a positive contrast.

The importance of the model situation, considered above, lies in the fact that this simple example clearly demonstrates the important fact that the scattering can drastically change the whole radiation energetics in an emitting and scattering system.

9.10 RADIATION OF THE INHOMOGENEOUS AND NON-ISOTHERMAL HALF-SPACE

Making use of the formal solution of the basic transfer equation (9.54) and (9.55), we obtain the explicit expression for radiation intensity in another important case – for a medium with stratified electromagnetic and thermal parameters. We mean the non-isothermal half-space with inhomogeneous electromagnetic properties. The natural analogues of such media are widespread: they include both inhomogeneous soils and grounds with complicated moisture and temperature profiles, inhomogeneous vegetation with a complicated internal thermal regime, the non-isothermal surface microscopic layer of the ocean, inhomogeneous rocks, and surface layers of the Moon, Mars and other planets.

So, we shall consider the absorbing and emitting medium (without scattering, $\omega = 0$) with arbitrary profiles of electromagnetic properties $\gamma(z)$ and temperature $T_0(z)$ (here z denotes the layer depth from the surface). We shall consider, for convenience, the solution of (9.52) for an incident flux at the lower boundary of a layer:

$$I_\nu^-(0, \mu) = I^-(\tau_0, \mu) \exp(-\tau_0/\mu) + \frac{1}{\mu} \int_0^{\tau_0} S(\tau', \mu) \exp(-\tau'/\mu) d\tau'. \quad (9.90)$$

Since we consider the half-space, we shall tend $\tau_0 \rightarrow \infty$ and pass from the dimensionless optical path to the dimensional layer depth z . Then we use the presentation of intensity in terms of the brightness temperature. And, finally, after some transformations we shall have the expression for the so-called effective temperature T_{ef} of the non-isothermal and inhomogeneous half-space, measured from the internal side of a layer, in the form:

$$T_{\text{ef}}(\theta) = \int_0^{\infty} T(z)\gamma(z) \frac{1}{\cos \theta} \exp \left\{ -\frac{1}{\cos \theta} \int_0^z \gamma(z') dz' \right\} dz. \quad (9.91)$$

Since in considering half-spaces the coordinate z in the positive direction is usually pointed to the depth of a layer, we change the coordinate system from what was accepted earlier in studying the atmospheres to the opposite one. Note also that angle θ in expression (9.91) represents an internal angle in a medium (rather than the external observation angle θ_0 related to θ by Snell's law). A fairly complicated functional dependence of the electrodynamic properties of a medium under the sign of integral is explained by the following circumstance. Any unit layer in a medium absorbs that radiation which passes through it from underlying layers and, at the same time, it emits thermal energy that will be partially absorbed by overlying layers. The intensity expressed in (9.91) is formed directly under the half-space boundary; and, finally, that energy will escape into free space, which is proportional to the following value:

$$T_{Bi}(\theta_0) = [1 - |R_i(\theta_0)|^2] T_{\text{ef}}(\theta), \quad (9.92)$$

where $i = H, V$ (horizontal and vertical polarizations).

It is important to note that the internal radiation of a medium, described in terms of effective temperature, does not possess polarization properties. The radiation acquires these properties only after intersecting the planar boundary.

By virtue of the aforementioned specificity of thermal radiation formation, it can easily be concluded from expression (9.91) that the depth of the layer at which the basic part of emitted energy can be formed has a quite finite value. We have already made this estimation for moist soils in section 8.8. For this purpose we shall consider the isothermal medium with homogeneous parameters and variable lower limit (the depth). Then at observation into the nadir we obtain the expression for the brightness temperature in the form:

$$T_B(z) = [1 - |R(0)|^2] T_0 (1 - \exp(-\gamma z)). \quad (9.93)$$

It directly follows from this result, that the effective depth z_{ef} of homogeneous space, which forms 90% of radiation intensity (the so-called skin layer of radiation), equals the following value:

$$z_{\text{ef}} = \frac{2.3}{\gamma} = 0.18 \frac{\lambda}{\sqrt{\frac{\varepsilon_1}{2} \left(\sqrt{1 + \tan^2 \delta} - 1 \right)}}, \quad (9.94)$$

where ε_1 and $\tan \delta$ are electrical parameters of an emitting medium.

If the medium is transparent, i.e. $\operatorname{tg}\delta \ll 1$, then the above expression is simplified:

$$z_{\text{ef}} \cong 0.36 \frac{\lambda}{\sqrt{\varepsilon_1} \operatorname{tg}\delta}. \quad (9.95)$$

It can easily be seen from this relation, that for terrestrial media the values of effective depths vary within very wide limits. So, for the glacial ice, whose electrical parameters are $\varepsilon_1 = 3$ and $\operatorname{tg}\delta \approx 0.001$, for the decimetre wavelength band (30 cm for instance) the effective depth will be 63 m. In the same wavelength band for fresh water ($t = 0^\circ\text{C}$) ($\varepsilon_1 = 80$ and $\operatorname{tg}\delta \approx 0.04$) the effective depth will be about 30 cm, whereas for salt water, under the same conditions, $z_{\text{ef}} \approx 1.3$ cm. In the millimetre band (8 mm) the skin layer of radiation for an aqueous medium will be 1 mm only.

If the emitting medium is highly inhomogeneous in electrical and temperature parameters, then the direct estimation of a skin layer from relations (9.94) and (9.95) is unacceptable, strictly speaking, since the picture of internal radiation can be very complicated (see section 7.7.2).

It is interesting to note that if we transfer to the isothermal case ($T_0(z) = T_0$), then the complex integral (9.91) for effective temperature transforms to the value T_0 regardless of the profile of electrodynamic properties of a medium. In other words, the semi-infinite isothermal medium represents a black-body emitter for any values of electrodynamic properties and profiles.

Comparing the expression obtained with relation (7.100), we can easily see their full identity. However, at the same time, both the limits of applicability of radiative transfer theory and clear limitations in using this theory become obvious (see section 7.7.3). This is due to the fact that in the presence of electrical losses in the studied medium ($\operatorname{tg}\delta \neq 0$) Snell's law should be used, strictly speaking, in the complex form and, hence, the value of angle θ inside the medium will also be complex. Thereby expression (9.91) loses its physical sense as radiation intensity. Thus, strictly speaking, the results of radiative transfer theory are applicable for transparent media only. However, some special investigations, carried out beyond the radiative transfer theory framework (Shulgina, 1975; Sharkov, 1978; Klepikov and Sharkov, 1983), have shown, in fact, that the situation is not so dramatic. The contribution of absorbing properties of a medium to refractive characteristics of a medium is quite small (see section 7.7.3). And, therefore, the transfer theory results can be successfully used for media with considerable absorption (such as sea water) as well.

The aforementioned formulas (9.91) and (9.92) are widely used in analysing the emissive properties of inhomogeneous and non-isothermal media, both for remote sensing applications and in radio-astronomy. So, it was from radio-astronomical (remote) observations, using the transfer theory results, that the features of the thermal regime of the subsurface layers of the Moon were revealed and, it was by means of Krotikov's relations (8.52) that the physicochemical properties of surface and subsurface layers of the Moon were first determined (Troitskii, 1954, 1967; Tikhonova and Troitskii, 1970). These results served as a basis for

developing the modules designed for landing on the lunar surface. Similar investigations have been subsequently carried out for the Martian surface as well.

9.11 APPROXIMATE METHODS FOR SOLUTION OF THE COMPLETE TRANSFER EQUATION

The mathematical difficulties that arise in solving the complete integro-differential equation of the transfer theory (9.23) have resulted in the appearance of a series of approximate approaches and methods for solution of the radiative transfer equation. At present, the approximate methods of solution of the radiative transfer equation form an independent mathematical discipline. Here it should be noted that quite different (initially) physical prerequisites are laid down in various approaches, and, therefore, the spheres of applicability of these methods are very different from each other. As a result, the matching of solutions of various approximate methods among themselves, sometimes represents, a very complicated problem in itself. So, in the approximations of thin-optical and thick-optical layers (the latter is also called the diffusive approximation, or the Rosseland approximation) simplifications are used that follow from the corresponding limiting value of the medium's thickness. In Eddington's and Schuster-Schwarzchild's approximations the simplifications are related to the introduction of some special assumptions on the angular distribution of radiation intensity. In the method of exponential approximation of a core the integro-exponential functions in the formal solution are replaced by the exponents. The spherical harmonics method and the Gaussian quadratures method are the most well-developed techniques allowing us to obtain high-order approximations using fairly simple procedures.

In this paragraph we shall describe two of the aforementioned approximate methods for solution of the radiative transfer equation in the schematic form. For more detailed study of the approximate methods we can recommend the reader the following papers on the same subject: Chandrasekhar, 1960; Sobolev, 1963; Malkevich, 1973; Ozisik, 1973; Marchuk, 1976; Marchuk *et al.*, 1986; Sabins, 1987; Thomas and Stamnes, 1999; Barichello *et al.*, 1998. The approximate methods are necessary from two points of view. First, they provide various simple methods for the solution of fairly complicated radiative transfer problems. In this case, however, their application is limited by the circumstance that the accuracy of the approximate method cannot be estimated without comparing it to the accurate solution or to the results obtained from accurate solutions of the Maxwell electromagnetic theory. Therefore, in using the approximate methods for studying particular natural media, some caution should be exercised, since the accuracy of any approximate method is not always clear enough. Second, in solving the reverse remote sensing problems, of principal significance is the possibility of describing the radiation of a studied natural medium by means of fairly simple analytical formulas. The use of numerical models (such as the Monte Carlo method) (Marchuk, 1976) does not allow to form the algorithms for reverse problems.

9.11.1 The spherical harmonics method

The spherical harmonics method enables one to obtain the approximate solution of the radiative transfer equation by using the initial assumption on a special form of an unknown solution. The physical basis for such a choice is the feature of electromagnetic energy scattering on particles, which allows for separating the angular and spatial variables in the Maxwell theory (Stratton, 1941). This method was first proposed by J. H. Jeans in 1917 in connection with the problem of radiative transfer in stellar atmospheres. The detailed description of the method of spherical harmonics as related to radiative transfer can be found in a series of papers (Chandrasekhar, 1960; Sobolev, 1963; Ozisik, 1973; Marchuk, 1976; Thomas and Stammes, 1999; Barichello *et al.*, 1998).

Consider the radiative transfer equation for a planar layer of a grey medium under axial symmetry conditions:

$$\mu \frac{\partial I_\nu(\tau, \mu)}{\partial \tau} + I_\nu(\tau, \mu) = (1 - \omega)I_B[T(\tau)] + \frac{\omega}{2} \int_{-1}^{+1} p(\mu, \mu') I(\tau, \mu') d\mu', \quad (9.96)$$

where it is supposed that the volume element scattering indicatrix can be presented in the form of expansion over the Legendre polynomials, but, unlike (9.46), with the other coefficients:

$$p(\mu, \mu') = \sum_{n=0}^{\infty} (2n+1) f_n P_n(\mu) P_n(\mu'). \quad (9.97)$$

Suppose that the unknown radiation intensity $I_\nu(\tau, \mu)$ can also be expanded in a series over the Legendre polynomials in the following special form, separating spatial and angular coordinates:

$$I(\tau, \mu) = \sum_{m=0}^{\infty} \frac{2m+1}{4\pi} P_m(\mu) \Psi_m(\tau). \quad (9.98)$$

If function $\Psi_m(\tau)$ is known, then the radiation intensity can be found from (9.98). For this reason we shall analyse in more detail the determination of function $\Psi_m(\tau)$. The substitution of expansions (9.97) and (9.98) into the basic equation (9.96) after some simplifications, determined by the orthogonality properties of the Legendre polynomials and by their recurrent formula (Ozisik, 1973), we obtain the system of ordinary differential equations with respect to function $\Psi_m(\tau)$ ($m = 0, 1, 2, \dots$):

$$(m+1)\Psi'_{m+1} + m\Psi'_{m-1} + (2m+1)(1 - \omega f_m)\Psi_m = 4\pi(1 - \omega)I_B[T(\tau)]\delta_{0m}, \quad (9.99)$$

where $f_0 = 1$ and prime denotes the differentiation with respect to τ .

For example, for the simplest isotropic scattering it is necessary to let in equation (9.96) all functions f_m equal to zero, except f_0 , which is equal to unity.

Equations (9.96) form an infinite system of ordinary differential equations with an infinite number of unknown functions $\Psi_m(\tau)$. In practice, however, systems with a finite number of equations $m = N$ are considered, where the term $\Psi'_{m+1}(\tau)$ is neglected. The aforementioned procedure is certainly very important for the final solution and, hence, it should be substantiated from the physical point of view.

As a result, the following system of equations is obtained:

$$\begin{aligned}\Psi'_1 + (1 - \omega)\Psi_0 &= 4\pi(1 - \omega)I_B[T(\tau)] \\ 2\Psi'_2 + \Psi'_0 + 3(1 - \omega f_1)\Psi_1 &= 0 \\ &\dots \\ N\Psi'_{N-1} + (2N + 1)(1 - \omega f_N)\Psi_N &= 0\end{aligned}\tag{9.100}$$

which represents the system of $N + 1$ linear ordinary differential equations with $N + 1$ unknown functions $\Psi_0, \Psi_1, \dots, \Psi_N$ and is called the P_N approximation.

The solution of system (9.100), as known, can be written as a sum of the solution of the corresponding system of homogeneous equations and a particular solution. The latter, however, cannot be accurately determined until the function of black-body radiation intensity (i.e. the thermal regime inside the medium) is known. Let us find the solution of the system of homogeneous equations in the form of

$$\Psi_m^H(\tau) = g_m \exp(k\tau); m = 0, 1, \dots, N,\tag{9.101}$$

where g_m are arbitrary constants, and k are unknown exponent indices. The substitution of (9.101) into the system of homogeneous equations, obtained from (9.100), gives the following system of $N + 1$ homogeneous algebraic equations with respect to coefficients g_m :

$$k[(m+1)g_{m+1} + mg_{m-1}] + (2m+1)(1 - \omega f_m)g_m = 0,\tag{9.102}$$

where $m = 0, 1, 2, \dots, N, f_0 = 1$ and $g_{N+1} = 0$.

In the case of isotropic scattering, we let $f_0 = 1$, and $f_m = 0 (m \neq 0)$.

Then (9.102) is simplified and takes the form of

$$k[(m+1)g_{m+1} + mg_{m-1}] + (2m+1)(1 - \omega \delta_{0m})g_m = 0.\tag{9.103}$$

For the system of homogeneous algebraic equations (9.103) to possess a nontrivial solution, the determinant, composed of coefficients of the equations, should be equal to zero. Thus, as a result of performing the procedure mentioned, we obtain the allowable values of k_i for each value of ω . Then for each of k_i the set of $g_m(k_i)$ values ($m = 0, 1, 2, \dots, N$) is determined from equation (9.102), after which the solution of the system of homogeneous equations for isotropic scattering, obtained from (9.100), can be written in the form of

$$\Psi_m^H(\tau) = \sum_{i=0}^N A_i g_m(k_i) \exp(k_i \tau); m = 0, 1, 2, \dots, N.\tag{9.104}$$

The complete solution for function $Y_m(t)$ can be presented as

$$\Psi_m(\tau) = \Psi_m^H(\tau) + \Psi_m^P,\tag{9.105}$$

where the particular solution $\Psi_m^P(\tau)$ depends on the spatial distribution of radiation intensity of an ideal black body, i.e. on the internal thermal regime in the medium. The unknown coefficients A appearing in (9.104) are found from the boundary conditions of a problem. Once functions $\Psi_m^P(\tau)$ are determined, the unknown

distribution of radiation intensity is found by formula (9.98). Here we note that there are also many other presentations of the solution of (9.104) related specifically to particular physical problems (Chandrasekhar, 1960; Sobolev, 1963; Ozisik, 1973; Barichello *et al.*, 1998).

As a particular case, we shall consider below the P_1 -approximation for isotropic scattering. This approximation is obtained from (9.100), if we accept $N = 1, f_m = \delta_{0m}$ and neglect the term $d\Psi_2(\tau)/d\tau$, i.e.

$$\left. \begin{aligned} \Psi'_1(\tau) + (1 - \omega)\psi_0(\tau) &= 4\pi(1 - \omega)I_B(T) \\ \Psi'_0(\tau) + 3\Psi_1(\tau) &= 0. \end{aligned} \right\} \quad (9.106)$$

Rearranging the equations of system (9.106), we shall have the expressions for Ψ_0 and Ψ_1 separately:

$$\left. \begin{aligned} \frac{d^2\Psi_0}{d\tau^2} &= 3(1 - \omega)[\Psi_0 - 4\pi I_B(T)] \\ \frac{d^2\Psi_1}{d\tau^2} &= (1 - \omega)\left[3\Psi_1 + 4\pi \frac{d}{d\tau}I_B(T)\right]. \end{aligned} \right\} \quad (9.107)$$

After determining function Ψ_0 from the solution of equation (9.107) and taking into account (9.106), we obtain the expression for the unknown intensity

$$T(\tau, \mu) = \frac{1}{4\pi} \left[\Psi_0(\tau) - \mu \frac{d\Psi_0(\tau)}{d\tau} \right] \quad (9.108)$$

The expressions for Ψ_0 will include both the boundary conditions and the thermal regime features. In the theory of stellar atmospheres (Sobolev, 1963) this approximation of a complete solution of the spherical harmonics method is called the Eddington approximation.

In remote sensing the spherical harmonics method (in the $P_2 - P_4$ approximation format) has been widely used in studying the thermal radiation of both small dispersed systems (non-precipitation clouds, aerosols) and medium dispersed systems (drizzle-type precipitation clouds), where the scattering still does not make a noticeable contribution to the total radiation balance of a system (see Chapter 10).

9.11.2 The Gaussian quadratures method

The Gaussian quadratures method makes it possible to obtain the approximate solution of the radiative transfer equation via the approximate presentation of integrals in the basic equation by the so-called Gaussian quadratures and subsequent transformation of the initial integro-differential equation into the system of ordinary differential equations.

We separate the unknown intensity into the direct (outgoing) component $I(\tau, \mu)$, $\mu \in (0, 1)$, and the reverse component $I(\tau, \mu)$, $\mu \in (-1, 0)$, as we have already done it

in section 9.5, and we shall write the basic integro-differential equation in a slightly different (as compared to (9.50)–(9.53)) form:

$$\begin{aligned} \mu \frac{\partial I(\tau, \mu)}{\partial \tau} + I(\tau, \mu) &= (1 - \omega) I_B[T(\tau)] \\ &+ \frac{\omega}{2} \left[\int_0^1 p(\mu, \mu') I(\tau, \mu') d\mu' + \int_0^1 p(\mu, -\mu') I(\tau, -\mu') d\mu' \right] \end{aligned} \quad (9.109)$$

for $0 < \tau < \tau_0$, $\mu > 0$ and

$$\begin{aligned} \mu \frac{\partial I(\tau, -\mu)}{\partial \tau} + I(\tau, -\mu) &= (1 - \omega) I_B[T(\tau)] \\ &+ \frac{\omega}{2} \left[\int_0^1 p(\mu, -\mu') I(\tau, \mu') d\mu' + \int_0^1 p(\mu, \mu') I(\tau, -\mu') d\mu' \right] \end{aligned} \quad (9.110)$$

for $0 < \tau < \tau_0$, $\mu > 0$.

Note that equations (9.109)–(9.110) are valid for positive values, i.e. $\mu \in (0, 1)$, and two intensity components are distinguished by means of designations $I(\tau, \mu)$ and $I(\tau, -\mu)$.

The integral terms in above equations can be approximately presented by the sums with using the formula for the double Gaussian quadrature:

$$\int_0^1 f(\tau, \mu') d\mu' \cong \sum_{j=1}^N a_j f(\tau, \mu_j); \mu > 0, \quad (9.111)$$

where a_j are weighting multipliers (Christoffel's coefficients), which are determined by the Gaussian quadrature formula, and μ_j are the discrete values of μ , which are determined by the Gaussian quadrature formula (Gradshteyn and Ryzhik, 2000).

The integro-differential equations (9.109) and (9.110) are transformed, by means of the N -point formula for the Gaussian quadrature, into the system of $2N$ ordinary differential equations with respect to intensities $I(\tau, \mu_i)$ and $I(\tau, -\mu_i)$ ($i = 1, 2, \dots, N$). After some transformations equations (9.109) and (9.110) can be reduced to the form (Ozisik, 1973):

$$\frac{dI(\tau, \mu_i)}{d\tau} - \sum_{j=1}^N \alpha_{ij} I(\tau, \mu_j) - \sum_{j=1}^N \beta_{ij} I(\tau, -\mu_j) = \frac{1}{\mu_i} (1 - \omega) I_B[T(\tau)], \quad (9.112)$$

$$\frac{dI(\tau, -\mu_i)}{d\tau} + \sum_{j=1}^N \beta_{ij} I(\tau, \mu_j) + \sum_{j=1}^N \alpha_{ij} I(\tau, -\mu_j) = -\frac{1}{\mu_i} (1 - \omega) I_B[T(\tau)], \quad (9.113)$$

where $\mu_i \in (0, 1)$, $i = 1, 2, \dots, N$ and

$$\alpha_{ij} = \frac{1}{\mu_i} \frac{\omega}{2} a_j p(\mu_i, \mu_j) - \frac{\delta_{ij}}{\mu_j}, \quad (9.114)$$

$$\beta_{ij} = \frac{1}{\mu_i} \frac{\omega}{2} a_j p(\mu_i, -\mu_j). \quad (9.115)$$

Equations (9.112) and (9.113) represent the system of $2N$ linear ordinary differential equations with $2N$ unknown values $I(\tau, \mu_i)$ and $I(\tau, -\mu_i)$, ($i = 1, 2, \dots, N$), which should be solved simultaneously with $2N$ corresponding boundary conditions.

Suppose that the solution of a homogeneous system of equations, corresponding to the system of (9.112) and (9.113), can be written in the form of

$$I(\tau, \mu_i) = g_i(k) \exp(k\tau); I(\tau, -\mu_i) = g_i^*(k) \exp(-k\tau), \quad (9.116)$$

where $i = 1, 2, \dots, N$.

After substitution of these solutions into homogeneous parts of equations (9.112) and (9.113) we shall obtain the system of $2N$ linear homogeneous algebraic equations with respect to $g_i(k)$ and $g_i^*(k)$ with k as a parameter. The allowable values of k are found from the condition, that the determinant composed of coefficients $g_i(k)$ and $g_i^*(k)$ becomes zero, if the resulting system of algebraic homogeneous equations has a nontrivial solution. Once the values of k_j are found, the algebraic equations are solved for each value of k_j ($j = 1, 2, \dots, 2N$) and the corresponding values of $g_i(k)$ and $g_i^*(k)$ ($i = 1, 2, \dots, N$) are determined. The general solution of the system of equations (9.112) and (9.113) is written as a linear sum of general solutions of homogeneous equations and a particular solution:

$$I(\tau, \mu_i) = \sum_{j=1}^N c_j g_i(k_j) \exp(k_j \tau) + I^p, \quad (9.117)$$

$$I(\tau, -\mu_i) = \sum_{j=1}^N c_j g_i^*(k_j) \exp(-k_j \tau) + I^p, \quad (9.118)$$

where c_j denotes $2N$ constants of integration, which should be found from $2N$ boundary conditions. For an isothermal medium the particular solution is found quite easily, and for a non-isothermal medium some special techniques can be used.

In microwave remote sensing the Gaussian quadratures method (true, in a slightly transformed form) has been applied in studying thermal radiation of almost all transparent media with inclusion of small dispersed scatterers (England, 1974, 1975). The internal scattering results in the effect of ‘darkening’ (or ‘cooling’) thermal radiation of the whole medium. In this case the ‘cooling’ effect will increase as the scattering albedo grows and medium’s dielectric constant decreases. These effects should be expected from physical considerations (see section 9.9).

Natural media where these effects are possible include the glacial ice sheets of Antarctica and Greenland. As we have noted above (section 8.7), the negative

frequency-selective spatial variation of thermal radiation of internal regions of Antarctica is caused by the effect of volume scattering of a glacial medium. Similar effects are quite possible for ground structures of the Moon and Mars as well.

9.11.3 Approximate formulas

In the cases where fairly simple algorithms for reverse microwave remote sensing problems can be formed (see Chapter 13), the necessity arises of using approximate formulas which will take into account the main scattering effects. However, the pure absorption approximation, which is often used in practice (see section 9.4), where the scattering effects are fully ignored, unsatisfactorily describes the radiation of a scattering layer (of the atmosphere) for optical thickness values greater than 1.5.

Earlier Basharinov *et al.* (1967) suggested a method for the description of the radiothermal emission of a planar isothermal layer by means of effective coefficients of transmission, q , and reflection, r , in the following simple form:

$$T_B = T_0(1 - q - r), \quad (9.119)$$

where T is the temperature of a medium,

$$q = \frac{(1 - r_0^2) \exp(-k\tau_0)}{1 - r_0^2 \exp(-2k\tau_0)}; r = r_0 \frac{1 - \exp(-2k\tau_0)}{1 - r_0 \exp(-2k\tau_0)}. \quad (9.120)$$

Here τ_0 is the total weakening in a scattering medium (for example, in a rain), and coefficients k and r_0 for a symmetrical scattering indicatrix are equal to

$$k = \sqrt{1 - \omega}; r_0 = \frac{1 - k}{1 + k}. \quad (9.121)$$

The expressions for q and r were obtained by Ambartsumyan (Sobolev, 1963) on the basis of one-dimensional model of the scattering of stellar atmospheres. In deriving (9.119) the Kirchhoff law was used, where it was supposed that, owing to scattering, the fraction of radiation equal to rT was reflected backwards and was as though ‘extracted’ from the basic energy balance. The comparison of results of a complete solution of the transfer equation and calculations by formula (9.119), carried out on paper by Basharinov *et al.* (1967), has shown that expression (9.119) gives overestimated values of radiobrightness temperatures, the distinctions not exceeding 15%.

Smirnov (1984) believes the following form of expression for the brightness temperature to be more correct:

$$T_B = T_0[1 - q - r(1 - q)]. \quad (9.122)$$

Here it was supposed that the part of radiation that was not dissipated in the medium possessed effective reflection. In this case the radiobrightness temperatures of outgoing T^+ and incident T^- radiation of the ‘atmosphere – underlying surface’

system can be written in the following form:

$$T^- = (1 - r)T_0(1 - q \exp(-\tau_0)) + r\kappa T_S, \quad (9.123)$$

$$\begin{aligned} T^+ &= (1 - r)[\kappa T_S q \exp(-\tau_0) + T_0(1 - q \exp(-\tau_0))] \\ &\quad + (1 - \kappa)T^- q \exp(-\tau_0), \end{aligned} \quad (9.124)$$

where T_0 is the average temperature of a medium with scattering (the atmosphere with precipitation), τ_0 is the total absorption in a medium (in the atmosphere), κ is the underlying surface emissivity and T_S is the underlying surface temperature. The second term in (9.123) describes the part of the underlying surface radiation that is reflected from the precipitation layer owing to scattering.

The special modelling of radiation of a medium with scattering (the atmosphere with precipitation) by the Monte Carlo method (Smirnov, 1984) has demonstrated a good agreement between calculations by formulas (9.123) and (9.124) and modelling results. It was also shown in that paper, that the radiation intensity value only weakly depends on the form of a scattering indicatrix and can be approximately described by the single scattering model.

In conclusion, it should be mentioned that, depending on the physical and geometrical features of a specific problem, many of approximate formulas can be obtained for forming the algorithms of reverse problems.

10

Electromagnetic properties of disperse media

The purpose of this chapter consists in considering basic electromagnetic characteristics of disperse media, which are widespread in the terrestrial atmosphere. The basic notions are introduced for quantitative absorption and scattering characteristics of both secluded particles and disperse media having the form of clouds of independent, randomly located scatterers. The principal concepts of Mie scattering theory and approximations used in practice, such as Rayleigh scattering, resonance scattering, and geometric optics approximation, are presented in the chapter. The basic characteristics describing the mechanical disperse properties of heterogeneous mixtures are introduced. The absorbing and scattering properties of natural polydisperse media, containing water drops and water particles in various phase states, are considered. The chapter presents a rich set of experimental findings on the absorption and scattering characteristics of disperse media spread in the terrestrial atmosphere. The main attention is given to the analysis of electromagnetic characteristics intended for studying the scattering and absorption processes in disperse media, in the microwave band predominantly. The basic results are presented of investigation of highly concentrated disperse media included absorbing scatterers in the microwave band.

10.1 ELECTROMAGNETIC PROPERTIES OF SECLUDED PARTICLES

From the viewpoint of radiative transfer theory, of principal interest for us are the transmission and scattering characteristics of an electromagnetic wave in the presence of a cloud of randomly located, electromagnetically independent scatterers. We shall analyse this problem in this chapter in two stages. First, we shall consider a secluded particle and study its scattering and absorption characteristics. At the second stage we shall take into account the contributions of a great number of non-correlated particles and derive the general relations for a wave propagating in

a cloud of randomly distributed particles. The first of these stages – the analysis of characteristics of a secluded particle – is described in this section. This issue has been exhaustively elucidated in a series of publications (Stratton, 1941; Shifrin, 1951, 1968, 1971; Hulst, 1981; Born and Wolf, 1999; Deirmendjian, 1969; Ishimaru, 1978; Bohren and Hoffman, 1983; Ivazyn, 1991). For this reason, we shall consider here only the basic physical approaches to this complicated problem as applied to microwave sensing tasks.

10.1.1 The scattering cross-section and the scattering amplitude

When a secluded and solitary particle is irradiated by the electromagnetic wave, some part of the incident power is scattered and leaves a particle irrevocably, and the other part is absorbed and transforms into heat eventually. These two basic phenomena – scattering and absorption – can be described most conveniently by supposing the particle to be illuminated by a planar incident wave.

Consider a linearly polarized planar electromagnetic wave propagating in a medium with relative dielectric and magnetic permittivities equal to unity. The electric field of such a wave has a form (see section 1.6):

$$\mathbf{E}_i(\mathbf{r}, \Omega') = E_0 \mathbf{e}_i \exp[jk(\Omega' \cdot \mathbf{r})] \quad (10.1)$$

Here E_0 is the field amplitude; $k = 2\pi/\lambda$ is the wave number, λ is the wavelength in a medium (external with respect to a particle), Ω' is the unit vector in the direction of propagation of an external field, and \mathbf{e}_i is the unit vector specifying the direction of the external field polarization.

This wave falls on a particle (Figure 10.1) with relative dielectric permittivity ε_p , which is complex, generally speaking, and depends on the coordinates, since the particle can be absorbing and inhomogeneous. The field at distant R , measured from some point inside a particle in the direction of unit vector Ω , is equal to the sum of field \mathbf{E}_i of an incident wave and a field \mathbf{E}_s of a wave scattered on a particle. At distances $R > D^2/\lambda$ (D is the characteristic size of a particle, for example, its diameter) owing to the interference of waves coming from various points of a particle, the amplitude and phase of field \mathbf{E}_s vary in a very complicated manner (the so-called near field mode) (see section 5.2). In this case the observation point \mathbf{r} is said to be in the near zone of a particle. For $R > D^2/\lambda$ the scattered field \mathbf{E}_s behaves as a spherical wave and can be presented in the form

$$\mathbf{E}_s(R) = \dot{\mathbf{f}}(\bar{\Omega}', \Omega) \frac{\exp(jkR)}{R}; R > \frac{D^2}{\lambda}, \quad (10.2)$$

where the scattering amplitude $\dot{\mathbf{f}}(\Omega, \Omega')$ describes the amplitude, phase and polarization of a scattered wave in the far zone in the observation direction Ω provided that the planar wave, propagating in the irradiation direction Ω' , falls on a particle. It should be noted that even in the case of linear polarization of an incident wave the scattered wave of a particle of complicated shape would possess elliptical polarization, generally speaking. The scattering amplitude is very important, because its

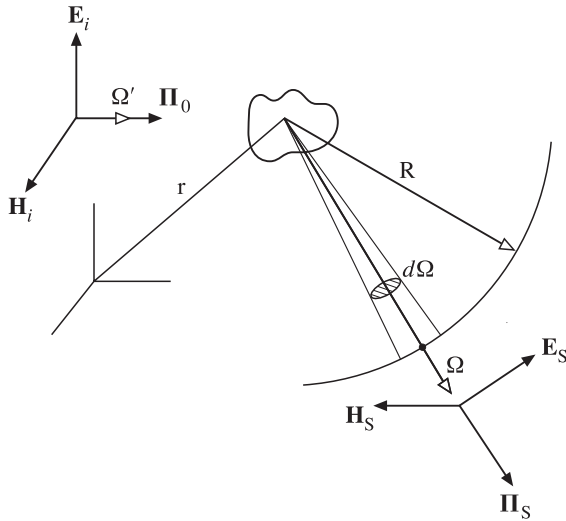


Figure 10.1. Schematic presentation of the geometry in scattering studies in particles. Notation is explained in the text.

value contains information on internal dielectric properties, geometrical shape and size of a particle.

Consider now the density Π_s of a flux of power (see section 1.6), scattered in the directions of wave Ω at distance R from a particle, when the wave with power flux density Π_0 falls on a particle from the direction Ω' . Here Π_0 and Π_s are the vectors of a power flux density of incident and scattered waves in the corresponding directions:

$$\Pi_0 = \frac{|\mathbf{E}_i|^2}{2Z_0} \Omega'; \quad \Pi_s = \frac{|\mathbf{E}_s|^2}{2Z_0} \Omega, \quad (10.3)$$

where Z_0 is the characteristic impedance of a medium (see section 1.6). The total power P (measured in watts), which will be scattered by a particle into the ambient space, can be determined as

$$P_s(\Omega') = \iint_{4\pi} |\Pi_s(\Omega', \Omega)| d\Omega \quad (10.4)$$

and then the ratio

$$\sigma_s(\Omega') = \frac{P_s(\Omega')}{|\Pi_0|} \quad (10.5)$$

is called the integral scattering cross-section of a particle. It can easily be seen that this value has the dimension of m^2 . The physical sense of the introduced quantity consists in the fact that it indicates the difference in losses for power scattering by a particle with respect to its geometrical cross-section (or its geometrical shadow). If the particle has a complicated shape, then the total scattering cross-section depends on the direction from which the external radiation falls on a particle.

Now we introduce another important definition characterizing the power and spatial-angular scattering of incident external radiation, falling on a solitary particle, by this particle. The differential scattering cross-section of a particle is determined as follows:

$$\sigma_d(\Omega', \Omega) = \lim_{R \rightarrow \infty} \left[R^2 \frac{|\Pi_s|}{|\Pi_0|} \right] = |\dot{f}(\Omega', \Omega)|^2. \quad (10.6)$$

It follows from expression (10.6) that $\sigma_d(\Omega', \Omega)$ has the dimension of area divided by a solid angle. Note that the differential scattering cross-section has unambiguous physical sense only when the considered distances from a particle exceed the size of a far zone. In the opposite case (or in the presence of some other particle near the investigated one) the physical unambiguity of the introduced definition is lost.

In radar and scatterometric applications the bistatic radar scattering cross-section σ_B and backscattering cross-section σ_{BS} are often used. They are related to $\sigma_d(\Omega', \Omega)$ by equations

$$\sigma_B(\Omega', \Omega) = 4\pi\sigma_d(\Omega', \Omega); \sigma_{BS} = 4\pi\sigma_d(\Omega', -\Omega'). \quad (10.7)$$

Quantity σ_{BS} is also called the radar scattering cross-section. The physical sense of these definitions can be elucidated as follows. Suppose that within the limits of the total solid angle of 4π the power flux density is constant and equals the value of the density for the direction Ω . Then the cross-section of a plate, from which such a power is scattered, is equal to the value of σ_d for the direction Ω multiplied by 4π . Note that the other definitions of backscattering cross-section are sometimes used as well (Skolnik, 1980).

10.1.2 The absorption cross-section

Now we shall consider that part of an incident flux energy, falling on a particle, which will be completely absorbed by a particle and then will transfer into heat. Certainly, if a particle is inhomogeneous in its electromagnetic properties, then all diffraction phenomena arising inside a particle should be taken into account in calculating the absorption. For some unification of the description of scattering and absorption processes the following definition is introduced. By the absorption cross-section $\sigma_A(\Omega')$ is meant the ratio of the total power P_A , which was absorbed in particle's volume, to the density of the flux power, which falls on a particle from the direction Ω' ,

$$\sigma_A(\Omega') = \frac{P_A}{|\Pi_0(\Omega')|} \quad (10.8)$$

The dimension of the absorption cross-section is expressed in m^2 . If a particle is inhomogeneous in its composition, then the absorption cross-section will depend on the direction of incident external radiation. Since the question is about the absorption of electromagnetic energy, this quantity can have no direct relation to the geometry of a particle.

10.1.3 The extinction cross-section

Now we shall consider the following important point. Since we have noted that the energy scattered by a particle is considered in the far zone of a particle, this part of energy ‘leaves’ a particle irrevocably. Thus, no statistical bond exists between the power absorbed by a particle and the power scattered by the same particle. Only under this condition can one introduce the definition describing the total losses (or extinction) of a particle in the form of a sum of losses for scattering and absorption:

$$\sigma_E(\Omega') = \sigma_S(\Omega') + \sigma_A(\Omega'). \quad (10.9)$$

Quantity $\sigma_E(\Omega')$ is called the extinction cross-section (or the total cross-section).

10.1.4 The single scattering albedo

The relation between absorption and scattering processes, which occur when a particle is irradiated by a flux of electromagnetic radiation, is undoubtedly, a very important factor in studying the total energy balance in transforming (or extracting) the energy of a basic external flux by a particle. The ratio of the extinction scattering cross-section to the total cross-section is called the single scattering albedo of a solitary particle:

$$\omega(\Omega') = \frac{\sigma_S(\Omega')}{\sigma_S(\Omega') + \sigma_A(\Omega')} . \quad (10.10)$$

For natural media the value of albedo varies within very wide limits. So, for optically transparent media in the terrestrial atmosphere (drops of water), the value of albedo is close to unity (0.95–0.99). In the microwave band the albedo of water particles lies within the limits of 0.01–0.8 (Oguchi, 1983), whereas for particles, close in their electromagnetic properties to the black body (such as the hollow water spheres), the albedo is virtually zero (Raizer and Sharkov, 1981).

Note that the albedo of a unit of medium’s volume introduced earlier (see section 9.2–9.3) can essentially differ from the albedo of a solitary particle, since the first of these definitions depends on the polydisperse composition of a medium or, in other words, on the relationship between the working wavelength and the range of particles’ sizes.

10.1.5 The scattering indicatrix

It is obvious from physical considerations, that any particle of complicated shape will scatter incident radiation in space in an inhomogeneous manner. To describe the character of a spatial-angular scattering on a particle the special dimensionless function $p(\Omega', \Omega)$ is introduced, which is the called the scattering indicatrix, in the following form:

$$p(\Omega', \Omega) = 4\pi \frac{\sigma_d(\Omega', \Omega)}{\sigma_E(\Omega')} . \quad (10.11)$$

The dimensionless quantity $p(\Omega', \Omega)$ is sometimes called the phase function and is widely used in radiative transfer theory (in the optical band especially). Note that this name has purely historical roots. Physically, the phase function describes the scattered power and has no relation to the phase of an incident wave (see equation (10.2)). The term ‘phase function’ arose in astronomy and is related to the phases of the Moon (Ishimaru, 1978).

Using relations (10.6), (10.10) and (10.11), we obtain the equations which associate all the electromagnetic parameters of a particle introduced above:

$$\begin{aligned}\sigma_S(\Omega') &= \iint_{4\pi} \sigma_d(\Omega', \Omega) d\Omega = \iint_{4\pi} |\dot{f}(\Omega', \Omega)|^2 d\Omega \\ &= \frac{\sigma_E(\Omega')}{4\pi} \iint_{4\pi} p(\Omega', \Omega) d\Omega,\end{aligned}\quad (10.12)$$

$$\omega(\Omega') = \frac{\sigma_S}{\sigma_E} = \frac{1}{\sigma_E} \iint_{4\pi} |\dot{f}(\Omega', \Omega)|^2 d\Omega = \frac{1}{4\pi} \iint_{4\pi} p(\Omega', \Omega) d\Omega.\quad (10.13)$$

These relations clear up the physical sense of the introduced parameter – the scattering indicatrix. Suppose that the particle will scatter uniformly within the total solid angle 4π surrounding it, i.e. $p(\Omega', \Omega) = 1$. Then particle’s albedo will be equal to unity, and the total cross-section of the particle will be determined by its scattering cross-section only. In such a case the particle is called purely scattering.

Note that the aforementioned approach to forming the scattering indicatrix of a particle is not unique. There are, however, other approaches to the definition of a scattering indicatrix (Skolnik, 1980). Then relations (10.12) and (10.13) will have other numerical coefficients.

10.1.6 The optical theorem

The extinction cross-section describes total power losses in an incident wave caused by wave scattering and absorption in a particle. It is important to note that a close relationship has been found to exist between the behaviour of a wave, scattered in the forward direction, and the extinction cross-section. The appropriate general relation forms the content of the so-called optical theorem, or the forwards scattering theorem. The optical theorem states that the extinction cross-section is related to an imaginary part of the forwards scattering amplitude $\dot{f}(\Omega', \Omega)$, and this relation has a form (Born and Wolf, 1999):

$$\sigma_E = \frac{4\pi}{k} \operatorname{Im} \dot{f}(\Omega', \Omega) \mathbf{e}_i,\quad (10.14)$$

where Im implies ‘the imaginary part’, and \mathbf{e}_i is the unit vector characterizing the direction of polarization of an incident wave.

This theorem is often used for theoretical calculations of the extinction cross-section when the scattering amplitude is known. The application of this theorem is rather difficult in the experimental respect, since it requires separating an incident

external flux from the radiation scattered by a particle ‘forwards’. Note that in quantum theory there exists a full analogue of the theorem mentioned, which associates the imaginary part of the amplitude of elastic forwards scattering with the total cross-section of a particle at scattering on the other particle (Prochorov, 1984).

10.1.7 Integral presentations of scattering amplitude and absorption cross-section

The mathematical description of a scattering amplitude and scattering and absorption cross-sections can be accomplished in one of two ways. For simple-shaped bodies, such as a sphere or an infinite cylinder, the accurate expressions for the mentioned quantities can be found. The accurate solution for a homogeneous dielectric sphere, which is called the Mie solution (or the Mie theory), will be considered in section 10.2. However, in the majority of practically important cases the shape of particles is not simple. For this reason, a number of techniques have been developed, allowing us to obtain the values of unknown cross-sections proceeding from integral presentations of a scattering amplitude (Ishimaru, 1978).

Considering the field in the far zone, scattered by a particle, and knowing the field inside a particle $\mathbf{E}(\mathbf{r})$, one can obtain from the solutions of Maxwell’s equations the following integral expression for the scattering amplitude of an inhomogeneous particle:

$$\mathbf{f}(\Omega', \Omega) = \frac{k^2}{4\pi} \int_V \{-\Omega \times [\Omega \times \mathbf{E}(\mathbf{r})]\} \{\dot{\varepsilon}(\mathbf{r}) - 1\} \exp(-jk\mathbf{r}\Omega) dV. \quad (10.15)$$

This is the accurate expression for a scattering amplitude $f(\Omega', \Omega)$ in terms of the total electric field $\mathbf{E}(\mathbf{r})$ inside a particle. Note that the double vector product inside the integral represents a component of the scattered field perpendicular to Ω for any direction of a vector of the total electric field $\mathbf{E}(\mathbf{r})$ inside a particle (Figure 10.2). The main difficulty of the procedure considered consists in the fact that, strictly speaking, the total electric field $\mathbf{E}(\mathbf{r})$ inside a particle is unknown; as a result, expression (10.15) does not provide a closed description of a scattering amplitude in terms of known

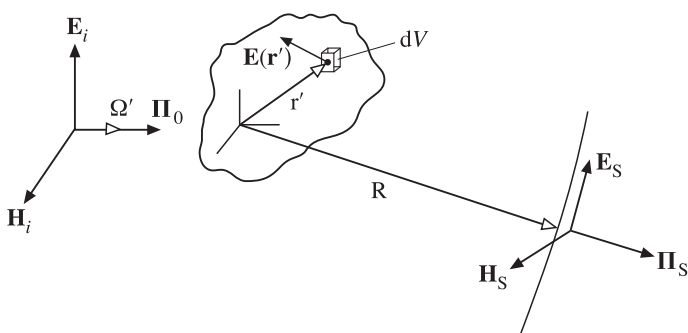


Figure 10.2. The geometrical positions of the point within the particle (r') and the observation point (R) studies of scattering amplitude. Notation is explained in the text.

quantities. However, in many practically important cases the field $\mathbf{E}(\mathbf{r})$ can approximately be replaced by some known function and, thus, one can obtain the useful approximate expression for the scattering amplitude of complicated particles, such as spheroids or multi-layered spheres (Bhandari, 1985; Rysakov and Ston, 2001).

In its turn, the absorption cross-section of any dielectric body represents a volume integral of losses inside a particle:

$$\sigma_A = k \int_V \varepsilon_2(\mathbf{r}) |\mathbf{E}(\mathbf{r})|^2 dV. \quad (10.16)$$

In this expression the incident wave amplitude is chosen to be equal to unity.

Expressions (10.15) and (10.16) are the accurate integral expressions for the scattering amplitude and for the absorption cross-section in terms of unknown total field $\mathbf{E}(\mathbf{r})$ inside a particle.

10.2 BASIC CONCEPTS OF MIE THEORY

The important problem in electromagnetic radiation scattering by material particles consists in finding the relationship between the properties (i.e. the size, shape, dielectric characteristics) of particles to the angular distribution of scattered radiation and to the external radiation absorption by particles. Such a problem arises in many fields of science and technology (such as astrophysics, biochemistry, radiophysics, optical oceanography). For this reason, numerous theoretical and experimental investigations have been carried out to study electromagnetic wave scattering. Historically, such investigations were first been carried out in the optical band and then were spread to the IR and radio wavelength bands.

One of first researchers, J. Rayleigh, proceeding from purely dimensional considerations, obtained the famous asymptotic approximate solution for radiation scattering by spherical particles whose size is small as compared to the wavelength of incident radiation falling on the particle. This work was followed by the general theory of radiation absorption and scattering by homogeneous particles having simple geometrical shape, such as a sphere or a circular cylinder. This theory was formulated by G. Mie in 1908. In the Mie theory, based on the solution of fundamental Maxwell's equations, the idealized situation was considered, namely, a simple spherical particle made of a homogeneous, isotropic material and placed in a homogeneous, isotropic, dielectric, boundless medium and irradiated by planar waves propagating in a particular direction. A purely dielectric spherical particle does not absorb radiation, whereas an electrically conducting spherical particle partially absorbs, partially scatters and partially transmits the incident radiation. The derivation of Mie's solution, as well as the mathematical and physical aspects of his theory, including the features of numerical calculation algorithms, are contained in a series of books (Stratton, 1941; Shifrin, 1951, 1968, 1971; Hulst, 1981; Born and Wolf, 1999; Deirmendjian, 1969; Ozisik, 1973; Ishimaru, 1978; Ivazyn, 1991). The solutions for the amplitude of a scattered wave for a sphere have a form of complicated series containing the Riccati–Bessel functions and the

Riccati–Hankel functions of increasing order. The results of Mie's solution are most useful for determining absorption and scattering coefficients, as well as the scattering indicatrix for spherical particles suspended in a dielectric medium, provided that the particles are spaced at a rather great distance from each other. Some special experiments were carried out for determining the minimum distance between spherical particles ensuring their independent scattering. It was found that for some optical scatterers the mutual interference can be neglected if the distance between the centres of spherical particles is greater than three diameters. In the majority of applied problems (the studies of cloudy systems, snowfalls, aerosols) the particles are separated by much greater distances from each other. Note, however, that in the Mie theory the idealized case is considered, namely, a secluded spherical particle, which acts as an independent point-like scatterer in a boundless medium, whereas the scatterers met with in the majority of practical applications have an arbitrary geometrical shape. At present, great efforts are being made to study electromagnetic radiation scattering by particles of arbitrary shape and orientation and complicated structure (such as multilayer particles, spheroids) (Bhandari, 1985; Rysakov and Ston, 2001). Nevertheless, we shall consider below the results of Mie's theory, since this is a unique fundamental theory now available, and its results are useful in many idealized cases.

10.2.1 Parameters of the Mie theory

A series of dimensionless parameters are introduced in the theory, which are widely used in practice.

The ratio of cross-section values, introduced above, to the geometrical cross-section is called the efficiency factor and designated by Q_i , where i is equal to A, S or E (which means absorption, scattering or extinction, respectively). Thus, one can write

$$Q_i = \frac{\sigma_i}{\pi a^2}, \quad (10.17)$$

where a is the radius of a sphere. As follows from (10.9), the efficiency factors satisfy the relation

$$Q_E = Q_S + Q_A. \quad (10.18)$$

By the size parameter is meant the ratio of the length of circumference of a studied sphere to the working wavelength x ($0 < x < \infty$)

$$x = \frac{2\pi a}{\lambda} = \frac{\pi D}{\lambda}, \quad (10.19)$$

where D is the diameter of a sphere.

The complex parameter m of refraction of sphere's substance relative to dielectric properties of an ambient boundless space is

$$\dot{m} = \frac{\dot{n}_{SP}}{\dot{n}_S} = n + j\chi. \quad (10.20)$$

Here n_{SP} is the index of refraction of sphere's substance, and n_S is a similar characteristic of the ambient space. If the ambient space is not a vacuum, but a medium with a high value of n_S , then parameter $|m|$ can be less than unity. For example, such a situation takes place in studying the propagation and scattering of electromagnetic waves of the optical band in a marine medium in the presence of air bubbles.

Since the sphere is a symmetrical particle, the scattering does not depend on an azimuthal angle, but is a function of scattering angle θ_0 concluded between the directions of incident and scattered beams. Thus, we introduced one more parameter – the scattering angle. Here it is necessary to keep in mind, that if the incident flux possesses strictly linear polarization, then the (secondary) radiation, scattered by a sphere, acquires the character of elliptically polarized radiation (Stratton, 1941), and its description requires bringing in the azimuthal angle. If, however, the primary field is non-polarized (the case of natural thermal radiation), then the secondary radiation is weakly polarized. This makes it possible to present the scattering indicatrix in the form of series over the Legendre polynomials

$$p(\cos \theta_0) = 1 + \sum_{j=1}^{\infty} A_j P_j(\cos \theta_0), \quad (10.21)$$

where θ_0 is the scattering angle, $P_j(\cos \theta_0)$ are the Legendre polynomials, A_j are expansion coefficients, which are functions of parameter x and parameter of refraction only.

To get an idea about the results of the Mie theory, we shall write the expressions for the efficiency factors of extinction and of scattering, which can be presented in the form of infinite series:

$$Q_E = \frac{2}{x^2} \sum_{n=1}^{\infty} (2n+1) \{ \operatorname{Re} (\dot{a}_n + \dot{b}_n) \}, \quad (10.22)$$

$$Q_S = \frac{2}{x^2} \sum_{n=1}^{\infty} (2n+1) \{ |\dot{a}_n|^2 + |\dot{b}_n|^2 \}, \quad (10.23)$$

where Re is the real part of a sum. If the particle does not absorb the incident radiation (i.e. the index of refraction is a real number and the particle is a pure scatterer), then expressions (10.22) and (10.23) lead to identical results. If the particle absorbs the incident radiation, then the index of refraction is complex, and the efficiency factor of absorption Q_A is obtained from the definition of Q_E (10.18) in the form of

$$Q_A = Q_E - Q_S. \quad (10.24)$$

The efficiency factor for the backscattering cross-section Q_{BS} can be presented as follows:

$$Q_{BS} = \frac{\sigma_{BS}}{\pi a^2} = \frac{1}{x^2} \left| \sum_{n=1}^{\infty} (2n+1)(-1)^n (\dot{a}_n - \dot{b}_n) \right|. \quad (10.25)$$

In radar technology this parameter was called the effective scattering area (ESA) of a target (Skolnik, 1980). In this case the diagram showing the dependence of ESA on the angle of wave incidence on a scatterer is called the ESA diagram (this is just the scattering indicatrix, in its essence).

The complex \dot{a}_n and \dot{b}_n coefficients in formulas (10.22), (10.23) and (10.25) are called the Mie coefficients. They represent complicated functions, expressed in terms of the Riccati–Bessel functions, and are written in the form:

$$\dot{a}_n = \frac{\Psi_n(x)[\Psi'_n(y)/\Psi_n(y)] - \dot{m}\Psi'_n(x)}{\xi_n(x)[\Psi'_n(y)/\Psi_n(y)] - \dot{m}\xi'_n(x)}, \quad (10.26)$$

$$\dot{b}_n = \frac{\dot{m}\Psi_n(x)[\Psi'_n(y)/\Psi_n(y)] - \Psi'_n(x)}{\dot{m}\xi_n(x)[\Psi'_n(y)/\Psi_n(y)] - \xi'_n(x)}, \quad (10.27)$$

where the prime denotes differentiation with respect to the argument under consideration. The Riccati–Bessel functions $\Psi_n(z)$ and $\xi_n(z)$ are associated with the Bessel function of non-integer order by the relations:

$$\Psi_n(z) = \left(\frac{\pi z}{2}\right)^{1/2} J_{n+1/2}(z), \quad (10.28)$$

$$\xi_n(z) = \left(\frac{\pi z}{2}\right)^{1/2} J_{n+1/2}(z) + (-1)^n j J_{-n-1/2}(z), \quad (10.29)$$

where $z = x$ or y , and the complex argument y is determined as follows $y = \dot{m}x$.

The physical sense of the Mie coefficients is as follows. The primary (external) electromagnetic wave excites some particular forced oscillations inside the substance of a sphere and on its surface. These forced oscillations can be subdivided into the electric and magnetic modes of oscillations on the basis of the existence of a corresponding radial component in a scattered (forced) field. So, if the electric vector of a scattered field has a radial component, which is caused by electric charges distributed over the surface, then such a mode of oscillations is called the oscillations of electrical type. The amplitudes of oscillations of such a type are expressed in terms of b_n coefficients. If the scattered field is excited by means of a_n coefficients only, then the structure of the field will be as if it was produced by variable magnetic charges disposed on the surface of a sphere. And such a field is called a field of magnetic type. Thus, it can be considered (Stratton, 1941), that a_n coefficients represent the amplitudes of oscillations of magnetic type, and b_n coefficients those of electrical type. If the frequency of an impressed (external) field approaches any characteristic frequency of the natural electromagnetic oscillations of a system, then the resonance phenomenon arises. This is just the condition where the denominators in expressions (10.26) and (10.27) tend to zero. But since in a system (inside the sphere) the absorption is always present, the denominators of the Mie coefficients can be reduced to their minimum values, but they cannot be made equal to zero. Thus, the mathematical catastrophe – the arising of infinite amplitudes – does not occur.

Though the Mie solution is strictly applicable to the whole range of $m - x$ values, it was found fairly quickly, that the numerical calculations of a scattering indicatrix and efficiency factors for arbitrary m and x values are rather laborious. For example, the convergence of series determining the Mie coefficients becomes very slow when the relative size of a sphere increases as compared to the incident radiation wavelength. Another difficulty consists in the irregularity of the values of a_n and b_n coefficients. On one hand, this makes the interpolation procedures rather unreliable (Shifrin, 1951, 1968), and, on the other hand, in performing detailed numerical calculations, a lot of resonance modes arise, some of which can be ‘false’ (Conwell *et al.*, 1984). Fortunately, for many practically important tasks (including remote sensing) there is no necessity to perform calculations by the Mie theory throughout the range of $m - x$ values. One can restrict calculations to the limiting values of the Mie solution, which, in their turn, can be determined by simplified techniques. So, for example, for high values of parameter x (i.e. for a large spherical particle as compared to the wavelength) the convergence of the accurate Mie solution becomes very poor. However, in such cases the geometric optics laws are applicable for determining the scattering indicatrix and efficiency factors, and the final expressions become quite simple. For very small x values the accurate Mie formula is essentially simplified, if one applies the power series expansions of spherical Bessel functions with respect to Mie’s a_n and b_n coefficients. However, the procedure of expansion of efficiency factors in power series with respect to small x values and the physical interpretation of expansion terms turns out to be rather complicated.

Detailed investigations of mathematical features of the expressions for efficiency factors, undertaken for a wide frequency band of electromagnetic waves and for dielectric properties of substances encountered in natural media, have shown that three regions can be found in which the scattering on particles possesses some peculiarity.

The first region, or the Rayleigh scattering region, is characterized by the following conditions: first, the size of particles is small as compared to the wavelength of an external field, i.e. $a \ll \lambda (x \ll 1)$; and, second, $|m|x \ll 1$. The first condition implies that we are in the quasi-static approximation (see section 1.6) and can make use of the laws of electrostatics. The second condition requires the absence of electromagnetic resonances inside a particle. As usual, the traditional value of $a = 0.05\lambda (x < 0.3)$ is accepted as an upper limit of a particle’s radius for this approximation. But in this case the second condition should, certainly, be satisfied as well.

The second region, or the resonance (the Mie) scattering region, is characterized by the presence of a great number of resonance features and very complicated scattering indicatrix. For these reasons this region has proved to be most complicated for investigations. The values of x are usually concluded within the limits of 0.25–0.5 to 50.

The third region (the high-frequency region, or the geometrical optics region) is characterized by the presence of a geometrical shadow behind the particle. This results in the situation where the extinction cross-section will tend to the doubled geometrical cross-section of a particle (of arbitrary shape, it should be added). This

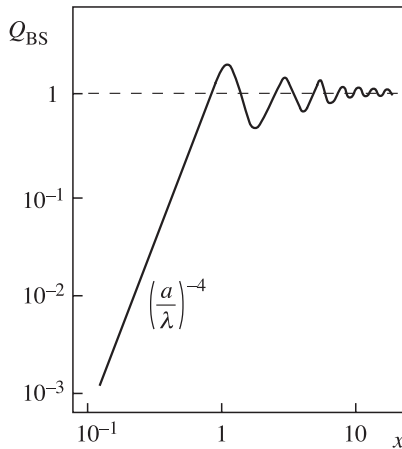


Figure 10.3. The backscattering efficiency factor of a metal sphere as a function of the size parameter (at microwave bands).

phenomenon is called the extinction paradox, and it has several (and different) physical explanations.

As an indicative example, we shall consider the dependence of the efficiency factor of backscattering for a metal sphere (Figure 10.3). This object is often used as an experimental standard for calibrating microwave antenna systems and complicated receiving radio-engineering complexes (early-detection radar stations, for instance).

From the analysis of the plot, presented in the logarithmic scale, it can easily be seen that the whole region of the size parameter values can really be subdivided into three characteristic sub-regions: the Rayleigh scattering region, where Q_{BS} decreases as $1/\lambda^4$; the resonance Mie region, where the resonance dependencies are explicitly exhibited; and the geometrical optics region, where the Q_{BS} value is equal to the geometrical cross-section value of a large particle. Of interest is the fact that for the dimension parameter value equal to unity takes place the first and most strong Mie resonance, at which the backscattering cross-section exceeds by nearly three times the size of the geometrical shadow. Physically, this is due to the fact that the sphere intensively scatters ‘backwards’ as a resonance half-wave vibrator, i.e. $\pi a = \lambda/2$.

10.3 RAYLEIGH SCATTERING FEATURES

Because the features of electromagnetic field scattering by small particles are of great importance for practical applications (and for remote sensing primarily), we shall consider in more detail the features of Rayleigh scattering.

For small particles ($x \ll 1$), provided that the internal resonances are absent $|m|x \ll 1$, the exact Mie formulas are simplified, if we use the power series expansion of spherical Bessel functions with respect to the Mie coefficients. The expansion of

the Mie solution in power series with respect to small x values can be presented as follows (Shifrin, 1951; Hulst, 1981):

$$\begin{aligned} Q_E = & -\text{Im} \left\{ 4x \frac{m^2 - 1}{m^2 + 2} + \frac{4}{15} x^2 \left(\frac{m^2 - 1}{m^2 + 2} \right)^2 \frac{m^4 + 27m^2 + 38}{2m^2 + 3} + \dots \right\} \\ & + \text{Re} \left\{ \frac{8}{3} x^4 \left(\frac{m^2 - 1}{m^2 + 2} \right)^2 + \dots \right\}. \end{aligned} \quad (10.30)$$

Separate investigations have shown that the first term (in braces) characterizes the efficiency factor of absorption, and the second term characterizes the efficiency factor of scattering. The result is valid for $x \ll 1$ and $|m|x \ll 1$.

It is quite useful to obtain similar results proceeding from physical approaches. We shall make use of two approaches: we consider the scattering on a small particle in the quasi-static approximation and the scattering on a solitary dipole emitter.

It is known from electrostatics that the field inside a dielectric sphere, placed in the permanent external electric field \mathbf{E}_i with linear polarization, is homogeneous and equals (Stratton, 1941):

$$\mathbf{E} = \frac{3}{\varepsilon + 2} \mathbf{E}_i; \mathbf{E}_i = E_0 \mathbf{e}_i, \quad (10.31)$$

where \mathbf{e}_i is the unit vector in the direction of incident wave polarization.

Substituting this relation into (10.15), we obtain the expression for a scattering amplitude for the external field with linear polarization in the form:

$$f(\Omega', \Omega) = \frac{k^2}{4\pi} \left[\frac{3(\varepsilon - 1)}{\varepsilon + 2} \right] V [-\Omega \times [\Omega \times \mathbf{e}_i]]. \quad (10.32)$$

Note that the double vector product is here the sine of angle θ_0 between the polarization vector and the direction of observation, and V is the geometrical volume of a particle. The differential scattering cross-section of a particle will be equal, in accordance with (10.6), to

$$\sigma_d(\theta_0) = \frac{\pi^2}{\lambda^4} \left[\frac{3(\varepsilon - 1)}{\varepsilon + 2} \right]^2 V^2 \sin^2 \theta_0. \quad (10.33)$$

Note that the scattering cross-section is inversely proportional to the fourth power of wavelength and directly proportional to the square of the volume scatterer's. It was these two properties of small scatterers which were obtained by Rayleigh by bringing in the theory of dimensions.

It is of interest is to compare the relation obtained with the backscattering cross-section. Substituting the value of angle $\theta_0 = (3/2)\pi$ into (10.33) and remembering formula (10.7), we have:

$$\sigma_{BS} = \frac{4\pi^3}{\lambda^4} \left[\frac{3(\varepsilon - 1)}{\varepsilon + 2} \right]^2 V^2. \quad (10.34)$$

As would be expected, all basic features of scattering in the Rayleigh region (the wavelength and volume dependencies) have conserved for backscattering as well.

Using relation (10.12), we shall consider now the scattering cross-section for a small dielectric particle:

$$\sigma_s = \iint_{4\pi} \sigma_d d\Omega = \frac{\pi^2}{\lambda^4} \left[\frac{3(\varepsilon - 1)}{\varepsilon + 2} \right]^2 \int_0^\pi \sin^3 \theta d\theta \int_0^{2\pi} d\varphi = \frac{128\pi^5 a^6}{3\lambda^4} \left(\frac{\varepsilon - 1}{\varepsilon + 2} \right)^2. \quad (10.35)$$

Separating this expression with the real geometrical cross-section, we obtain the well-known Rayleigh equation (or relation) for the efficiency factor of scattering (with allowance for the size parameter of a particle):

$$Q_s = \frac{8}{3} x^4 \left(\frac{\varepsilon - 1}{\varepsilon + 2} \right)^2. \quad (10.36)$$

Comparing the obtained expression with the expansion of the accurate Mie solution (10.30), we see that the Rayleigh approximation is a direct consequence of the Mie solution (the first term in the real part of the expansion) for purely dielectric spheres. The absorption cross-section is zero in this case (see relation (10.16)). Using the obtained expressions (10.33) and (10.35), we shall obtain the expression for the indicatrix of scattering of linearly polarized radiation by a small particle:

$$p(\theta_0) = 4\pi \frac{\sigma_d}{\sigma_s} = \frac{3}{2} \sin^2 \theta_0. \quad (10.37)$$

It follows from this expression that for small particles there takes place a very strong and peculiar feature in the angular characteristics of scattering – the scattering indicatrix has the form of a torus; in this case the maximum of scattering is observed in the direction of reverse and direct scattering ($p = 3/2$). In the directions with $\theta_0 = 0$ and 180° the scattering is completely absent. This feature of Rayleigh scattering is often used for interpreting physical and observational experiments with coherent sources.

Another physical approach is related to using the features of the radiation (i.e. considered in the far zone) field of an elementary emitter in electrodynamics: the dipole – which can be excited by the external electromagnetic field. The radiation field of a dipole is known (Born and Wolf, 1999) to consist of one electric component E_θ and one magnetic component H_φ , the vectors being in phase. The electric component is related with its polarization vector \mathbf{P} as follows:

$$E_\theta = k^2 |\dot{P}| \frac{\exp(jkR)}{R} \sin \theta, \quad (10.38)$$

where θ is the polar angle measured from the direction of the polarization vector. In its turn, the polarization vector is related with the complex polarizability α and the external field as $\dot{P} = \alpha E_i$. By the polarizability of particles is meant their capability to acquire the dipole moment in the external electric field. For relatively simple physical systems the relationship between the polarizability α and macroscopic dielectric properties of substance can be established by means of the Lorentz – Lorenz

formulas (Prochorov, 1984):

$$\dot{\alpha} = \frac{\dot{\varepsilon} - 1}{\dot{\varepsilon} + 2} \frac{3}{4\pi} V. \quad (10.39)$$

Substituting expression (10.38) into (10.6), we obtain the value of the scattering amplitude for the dipole:

$$\dot{f}(\theta) = k^2 \dot{\alpha} \sin \theta. \quad (10.40)$$

Making computational procedures similar to those presented above, we shall obtain for the efficiency factor exactly the same expression as (10.36). For these reasons Rayleigh scattering is sometimes called dipole-type scattering.

The absorption cross-section can be obtained from expression (10.16), if we substitute into it relation (10.31), in the form of

$$\sigma_A = k \varepsilon_2 \left| \frac{3}{\dot{\varepsilon} + 2} \right|^2 V. \quad (10.41)$$

And then for the efficiency factor of absorption we shall have:

$$Q_A = \frac{4}{3} x \varepsilon_2 \left| \frac{3}{\dot{\varepsilon} + 2} \right|^2 = 12x \frac{\varepsilon_2}{|\dot{\varepsilon} + 2|^2}. \quad (10.42)$$

The expression obtained exactly corresponds to the first term in the imaginary part of the expansion of the accurate Mie solution (10.30).

It is important to consider some special cases, which are often met with in observational practice.

10.3.1 Metal particles

The dielectric properties in the microwave band of such substances are characterized by high values of real and imaginary parts of the dielectric constant. It follows from this circumstance, that $Q_S \approx (8/3)x^4$, and $Q_A \rightarrow 0$. In other words, small metal particles intensively scatter electromagnetic radiation and, virtually, do not absorb it.

10.3.2 Soft particles

By such kind of particles are meant the particles, whose substance possesses very weak absorbing properties ($\varepsilon_2 \ll 1$) (transparent particles) and whose index of refraction is close to unity ($\varepsilon_1 - 1 \ll 1$). Such particles include water particles in the optical band, aerosol particles in the atmosphere in the microwave band and many other types of particles. It follows from this fact that $Q_S \approx (8/3)x^4(\varepsilon_1 - 1)^2$, and $Q_A \approx (4/3)x\varepsilon_2$. Unlike with metal particles, the general picture of scattering of soft particles will radically change depending on the relationship between the size and properties of the particles' substance. For very small particles ($x < 0.05$) the albedo can be approximated as follows: $\omega \sim 10^3 x^3$, and, thus, as the size of particles decreases, their absorbing properties will essentially prevail over scattering ones, in spite of a very weak absorption of the particles' substance itself. Figure 10.4 presents

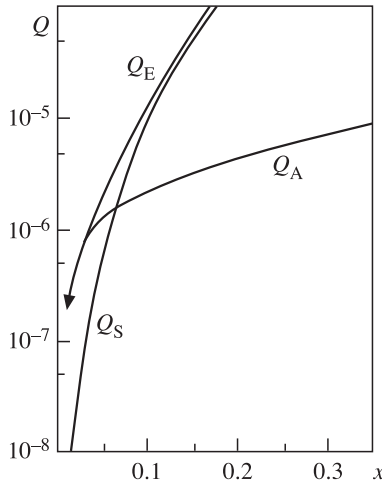


Figure 10.4. The efficiency factors of scattering (Q_S), absorption (Q_A) and extinction (Q_E) for small spheres (in the case of light loss, $m = 1.32 - j10^{-5}$) as a function of the size parameter (Deirmendjian, 1969).

the calculated values of the factors of efficiency of extinction, scattering and absorption for small, but finite-in-size dielectric spheres ($0.025 < x < 0.35$) with weak absorption. The analysis of this figure indicates that for such particles the critical size, in a certain sense, will be of the order of 0.05–0.1. When this size is exceeded, the particles become purely scattering ($\omega \rightarrow 1$), as a matter of fact.

10.3.3 Water particles

As we have noted (Chapter 8), the dielectric characteristics of water possess prominent frequency properties in the microwave band. For these reasons the general picture of the scattering of water particles will essentially change depending on the relationship between the physical size of particles and the working wavelength band. Nevertheless, some estimations of the behaviour of scattering and absorption factors can be made now. So, for centimetre and decimetre bands for fresh water (see Chapter 8) $\varepsilon_1 \gg 1$ and $\varepsilon_2 < 1$, and, thus, $Q_S \approx (8/3)x^4$ and $Q_A \approx 12x \operatorname{tg}\delta(1/\varepsilon_1)$. For small particles ($x < 0.05$) the albedo can be approximated as follows: $\omega \sim 3 \times 10^3 x^3$, and, thus, as the particle size decreases, the absorbing properties of water drops will essentially prevail over scattering ones, as in the case of soft particles.

In conclusion to this section, we summarize the Rayleigh scattering features as follows:

- the scattering cross-section (and backscattering cross-section) is inversely proportional to the fourth power of the wavelength and directly proportional to the square of the scatterer's volume;

- the absorption cross-section is inversely proportional to the first power of the wavelength and directly proportional to the value of the scatterer's volume;
- the scattering has dipole character and does not depend on the shape of particles;
- the scattering indicatrix for the wave of linear polarization has toroidal shape of the surface; in this case the scattering maximum is observed in the direction of reverse and direct scattering ($p = 3/2$). In the directions with $\theta_0 = 0$ and 180° the scattering is absent altogether. For non-polarized radiation the indicatrix can be presented in the form of

$$p(\theta_0) = \frac{3}{4}(1 + \cos^2 \theta_0). \quad (10.43)$$

The indicated features of scattering are rather peculiar and are not met in the other scattering regions (the Mie region and the geometrical optics region). For this reason they are often used in observational practice as characteristic signs for the detection of Rayleigh-type scattering.

10.4 FEATURES OF SCATTERING PROPERTIES OF AQUEOUS PARTICLES

The most important class of scatterers in the terrestrial atmosphere are aqueous drops, which are present in various physical media, such as cloudy systems of various classes, fogs, precipitations of various types, and spray sheet on a stormy sea surface.

As we noted earlier (Chapter 8), the dielectric characteristics of water possess prominent frequency features in the microwave band. For these reasons the general picture of scattering of aqueous particles will essentially change depending on the relationship between the physical size of particles and the working wavelength band, and in each particular case of experimental investigations the detailed calculation of scattering parameters is required. It is necessary to make use of the available calculation tables for the microwave band with subsequent interpolation procedures (Krasik and Rosenberg, 1970; Skolnik, 1980; Oguchi, 1983; Lhermitte, 1988; Bohren and Hoffman, 1983; Ivazyn, 1991). Nevertheless, we shall demonstrate, for a series of examples, some general properties of electromagnetic waves scattering by aqueous spheres.

Figure 10.5 presents calculated values of efficiency factors of extinction, scattering and backscattering for aqueous spheres at wavelengths of 0.8 and 0.2 cm depending on the size parameter in the range of its values up to 15. Considering the plots of the region of values for $x < 1$, it can easily be seen that the behaviour of efficiency factors corresponds to the features of the Rayleigh region (see section 10.3). The prominent maximum is observed in the Mie region for all efficiency factors at $x = 1$. However, as the size parameter increases, the extinction and scattering decrease very slowly to the values equal to two and unity, respectively, not exhibiting any prominent resonance properties in this case. Unlike extinction and

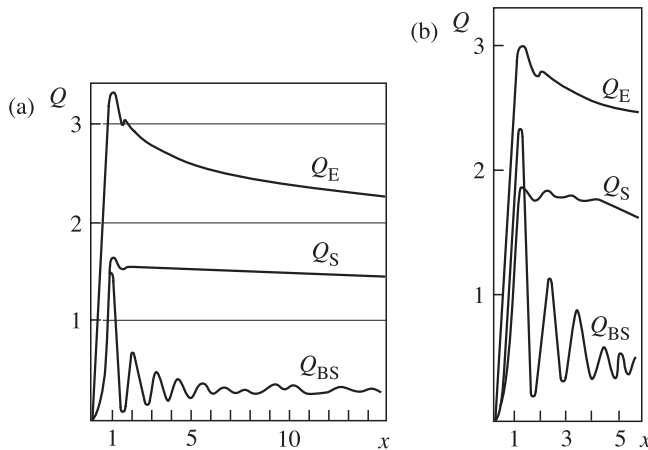


Figure 10.5. The efficiency factors of scattering (Q_S), backscattering (Q_{BS}) and extinction (Q_E) for aqueous spheres: (a) $\lambda = 0.2 \text{ cm}$ and $t = 20^\circ\text{C}$; (b) at $\lambda = 0.8 \text{ cm}$ and $t = 20^\circ\text{C}$.

total scattering, the backscattering possesses sharp and strong resonance properties up to the values of $x = 10$. In the geometrical approximation the efficiency factor of extinction becomes equal to two, i.e. it twice exceeds the geometrical diameter of a sphere ('the extinction paradox'). In this case the rate of tending to their limiting values is essentially different for extinction and for scattering; as a result, for large drops the losses for scattering exceed the losses for absorption. This circumstance is well illustrated by the calculated plot (in the bilogarithmic scale) of a single scattering albedo that depends on the size parameter of spheres (Figure 10.6). The data were calculated in a wide range of frequencies – from 4 GHz (the wavelength of 7.5 cm) up to 100 GHz (the wavelength of 3 mm) – and of drops' radii (0.5–3.0 mm). Virtually irrespective of the wavelength band, for $x < 0.5$ the albedo is lower than 0.1, and the scattering contribution to the total losses is very small. Note that in this case the decrease of albedo for small drops has a prominent character of exponential dependence as x^3 , as it should be expected for the Rayleigh region (see section 10.3). For $x > 1$ the contribution of scattering into the total losses of large drops sharply increases, reaching 60–70% of the total losses (in other words, of the extinction).

Figure 10.7 presents the frequency dependencies (in the bilogarithmic scale) of the efficiency factor of extinction for aqueous spheres with fixed radii in a wide frequency band – from 5 GHz (6 cm) to 300 GHz (1 mm). The analysis of this figure shows all the aforementioned characteristic regions of scattering – for large wavelengths the exponential drop as λ^{-n} is observed for the sphere of fixed radius. This dependence characterizes the beginning of the Rayleigh scattering region. For short wavelengths the efficiency factor of extinction tends to the value of 2. At intermediate wavelengths the resonance Mie maximum is observed (it is rather smeared in this coordinate system). It is interesting to note that the plot clearly demonstrates only the transition region from the first Mie maximum to the Rayleigh region and the very beginning of the Rayleigh region. So, as the fixed

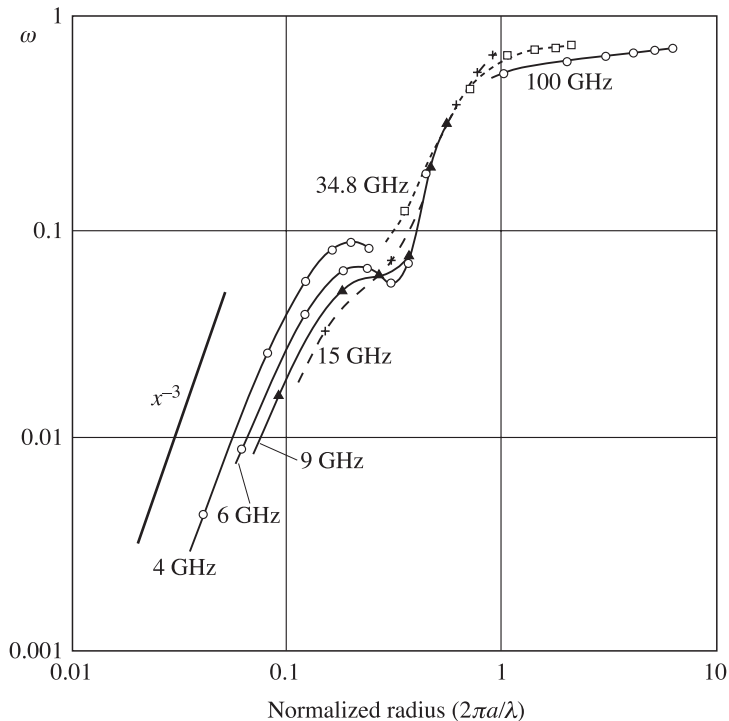


Figure 10.6. Single-scattering albedo of aqueous spheres as a function of size parameter (normalized radius) at 4, 6, 9, 15, 34.8 and 100 GHz. The points on each curve correspond from the left, to drop radii 0.5, 1.0, 1.5, 2.0, 2.5 and 3.0 mm respectively (Oguchi, 1983).

radius decreases, the exponent of the power-law drop also decreases and finally reaches a value equal to two, but already in the purely Rayleigh region (see (10.30)).

10.5 ELECTROMAGNETIC PROPERTIES OF POLYDISPERSE MEDIA

As we have already noted (section 1.6), the structure of a substance in the Maxwell theory is specified by introducing the phenomenological dielectric and magnetic parameters for continua. In radiative transfer theory (the macroscopic version) the structure of a substance is presented in a different manner – in the form of a cloud of randomly distributed particles in a continuum (for example, in the terrestrial atmosphere or in the sea) with the parameters of attenuation and scattering in a medium (calculated per unit of a beam path in a medium). A lot of quite various physical structures in the terrestrial atmosphere and in the ocean can be attributed to such kinds of media. Virtually all of them have the character of polydisperse media, i.e. media with particles of different sizes. Physically, this is related with the circumstance that, because all polydisperse media are open physical systems, a certain dynamical

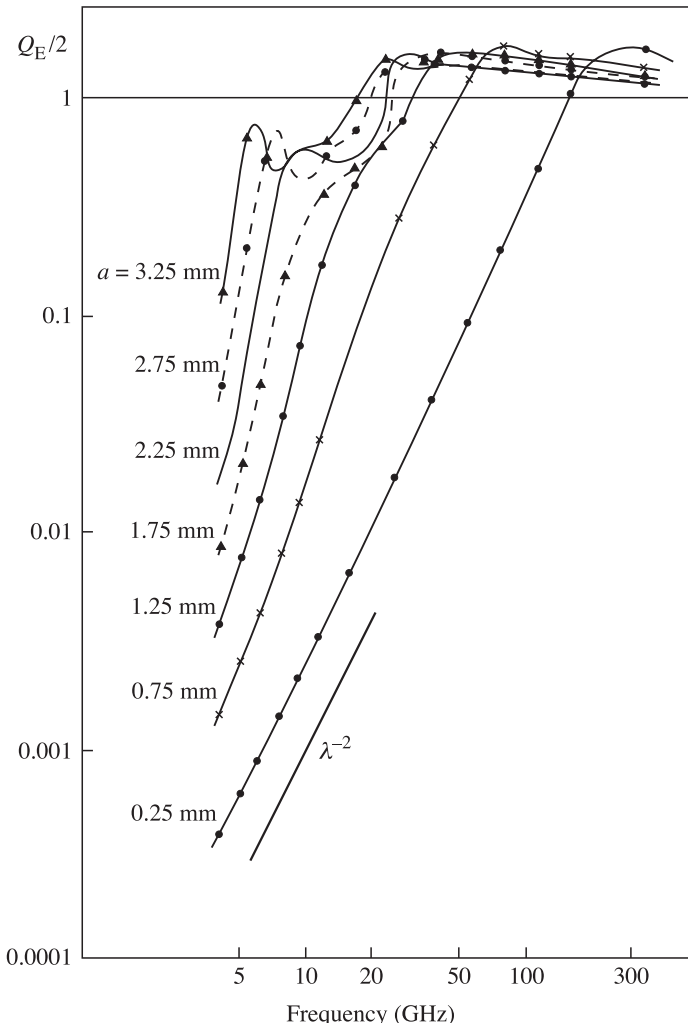


Figure 10.7. The extinction factor of spherical raindrops as a function of frequency ($t = 20^\circ\text{C}$) (Oguchi, 1983).

equilibrium can be established in the dynamical process of particles' birth and death only. The latter circumstance stipulates the principal presence of polydisperse-composed particles in media. In this section we shall consider the basic mechanical characteristics which are used in describing the disperse mixtures, and the procedure of transition from the characteristics of scattering of individual particles to the electromagnetic parameters of a unit volume.

Physical systems consisting of some combination of substances (which are, by themselves, in different phase states) are usually subdivided into two large classes: heterogeneous mixtures and homogeneous mixtures (Nigmatulin, 1978).

By heterogeneous mixtures here are meant systems which contain macroscopic (with respect to molecular scales) and chemically non-interacting inhomogeneities (or admixtures). From a huge number of possible heterogeneous mixtures existing in nature, some comparatively regular structures can be distinguished which are called disperse mixtures. Such systems, which usually consist of two phases, include, for example, aqueous drops in air or air bubbles in sea water (the so-called aerated layer) and the hexagonal structure in sea foam. In this case the particles are called a disperse phase, and their carrier medium the disperse phase. By *homogeneous mixtures* are meant systems in which the substance is intermixed at the molecular level. The so-called *colloidal mixtures* occupy an intermediate position.

Below we shall consider some mechanical characteristics determining the dispersity of disperse systems.

10.5.1 The density function

The most important characteristic of the microstructure (dispersity) of disperse systems is the differential density function of particles in size, designated by $n(r, x, y, z, t)$, where r is the radius of particles (instead of the radius, sometimes the diameter, surface, volume or mass of particles are used); x, y, z are spatial coordinates; t is time. Proceeding from the definition, quantity $n(r, x, y, z, t) \, dr \, dx \, dy \, dz$ is the number of particles having radius from r to $r + dr$ in the volume of $dx \, dy \, dz$ in the vicinity of point (x, y, z) at time instant t . Naturally, in the practice it is impossible to determine the value of $n(r, x, y, z, t)$ at all points of the studied space simultaneously. For this reason the microstructure of a disperse system is often characterized by *size spectra* of particles $n(r)$, averaged over time and space, or by related integral distribution parameters, which are proportional to distribution moments of any order. For example, the important characteristics of a disperse medium's microstructure are the density of particles, the total mass of water (or water content) and the radar reflectivity.

In the theoretical respect the density function plays a fundamental part, since it determines the physical features of a system and its possible evolution.

It follows from physical considerations that for $r \rightarrow 0$ and for $r \rightarrow \infty$ the density of a number of particles must tend to zero (within the framework of the given physical system). The dimension of this parameter, as can easily be seen from its definition, is cm^{-4} .

10.5.2 The volume density of particles

An important integral parameter is the volume density of particles (or the number density) N (cm^{-3}), defined by the following integral transformation from the spectrum of particles:

$$N(\text{cm}^{-3}) = \int_0^\infty n(r) \, dr = \int_0^\infty n(D) \, dD, \quad (10.44)$$

where D is the diameter of particles. This characteristic determines the absolute number of particles in a unit volume. It follows from this relation, that $n(r) = 2n(D)$.

10.5.3 The integral distribution function

In experimental practice it is often convenient to present the observational results in the form of volume density of particles with the lower variable limit $N(r)(\text{cm}^{-3})$, i.e. in the form:

$$N(r) = \int_r^{\infty} n(r) \, dr. \quad (10.45)$$

This characteristic determines the absolute number of particles in a unit volume beginning with some particular (fixed) value of size. A lot of measuring devices, which record the size of particles, operate using this particular characteristic, and in order to transfer to the density function it is necessary to perform numerical (or graphical) differentiation of obtained results.

10.5.4 The relative density function

In theoretical analysis, as well as in processing and comparing the experimental results of various types, it is expedient to use the relative density distribution function in the form:

$$f(r) = \frac{n(r)}{N}; \int_0^{\infty} f(r) \, dr = 1. \quad (10.46)$$

As can be seen from the definition, the dimension of this parameter is cm^{-1} .

10.5.5 The density sampling probability

In the experimental respect, the dispersity characteristics of a system are usually found by detecting and estimating the density sampling probability, or, in other words, by forming and constructing experimental histograms. This procedure is rather complicated, in general, and requires from a researcher both experience and skills in solving such tasks, and a clear understanding of the basic physical problem. We shall briefly describe this procedure, predominantly in the qualitative respect.

Let the experimental data on particles obtained range in radius from a to b . The total number of recorded particles is N . We divide the range of radii by j , the number of bunching intervals. In each of these intervals N_j particles will be recorded. The size of a bunching interval equals Δr_j . Then by

$$P_j = \frac{N_j}{N}; j = 1, \dots, k \quad (10.47)$$

will be meant a sampling probability of the presence of particles in the given bunching interval. Here k is the total number of bunching intervals. Here

$$N = \sum_{j=1}^k N_j. \quad (10.48)$$

The sampling probability $P_j(r_j)$, presented in graphical form, represents the experimental histogram.

By the density function of sampling probability is understood the following quantity:

$$f_j(r_j) = \frac{N_j}{N\left(\frac{b-a}{k}\right)}. \quad (10.49)$$

From the normalization conditions it follows that

$$\sum_{j=1}^k f_j(r_j) \Delta r_j = 1. \quad (10.50)$$

If the sizes of bunching intervals are the same (Δr), then the relationship between the density function of the sampling probability and the sampling probability (the experimental histogram data) can be presented as follows:

$$f_j(r_j) = \frac{P_j}{\Delta r} (\text{cm}^{-1}). \quad (10.51)$$

It can easily be concluded from the relation obtained, that $f(r_j)$ is the finite-difference analogue of the relative distribution function (10.46).

10.5.6 The total mass and the relative volume concentration of water

In some meteorological problems, as well as in the tasks of microwave sensing of the terrestrial atmosphere, it is necessary to know the total mass of a substance (the water, for example) in a unit of volume of the disperse medium (the cloud, for example). If the disperse medium consists of regular spheres of various diametre, then, by definition, the total mass of substance in a unit volume (or the water weight content, conventionally) W (g/cm^3) can be obtained from the following relation:

$$W = \frac{4}{3}\pi\rho \int_0^\infty r^3 n(r) dr = \frac{4}{3}\pi\rho N \int_0^\infty f(r)r^3 dr, \quad (10.52)$$

where r is the density of substance of spheres.

In many application problems it is necessary to know the relative volume concentration of substance (or volume concentration), C (the dimensionless quantity), which can be obtained from the following relation:

$$C = \frac{W}{\rho} = \frac{4}{3}\pi \int_0^\infty r^3 n(r) dr. \quad (10.53)$$

The characteristics considered are proportional to the third moment of the size distribution of particles. However, some remote investigations, such as radar studies of the structure of cloudy systems, require knowledge of the moments of much higher order.

10.5.7 Radar reflectivity

By this characteristic $Z(\text{cm}^3)$ is meant the following quantity:

$$Z = \int_0^\infty n(r)r^6 \, dr. \quad (10.54)$$

The physical sense of this characteristic can easily be understood using the expression for backscattering of an individual particle (10.34) in the Rayleigh approximation in calculating the backscattering of a unit volume σ_0 with the density function of reflective spheres $n(r)$:

$$\sigma_0 = \int_0^\infty \sigma_{\text{BS}} n(r) \, dr = \frac{64}{\lambda^4} \pi^5 \left| \frac{\dot{\varepsilon} - 1}{\dot{\varepsilon} + 2} \right|^2 \int_0^\infty n(r)r^6 \, dr \quad (10.55)$$

This relation indicates that the signal, scattered back from a cloudy structure, is proportional to the sixth moment of the density function of drops in a cloudy mass. It can easily be seen from this result that drops of large and super-large size (having $r > 100$ micrometre) play a very essential part in the process of backscattering electromagnetic radiation from cloudy systems. Moreover, these drops are main carriers of radar remote information in the cloudy systems (Doviak and Zrnić, 1984; Doviak and Lee, 1985). However, in radiothermal investigations the situation is essentially different – the thermal radiation depends on the total mass of water in a drop cloud and, thus, the signal is proportional to the third moment of the density function of drops in a cloudy mass. All these features are important in the interpretation of observational data.

10.5.8 Rainfall rates

If disperse systems possess prominent dynamical properties (for example, precipitations of various phase types), then in their remote analysis the parameter characterizing the quantity of a substance precipitated on a unit area per unit time is of importance. Such a characteristic, which is widely used in meteorological and remote investigations, is called the rainfall rate, R (cm/s). It is determined by the following expression:

$$R = \int_0^\infty n(r) V(r) \frac{4}{3} \pi r^3 \, dr, \quad (10.56)$$

where $V(r)$ is the velocity of motion of drops of corresponding radius. For the conditions of rainfall drops in the terrestrial atmosphere a series of empirical relations was established between the precipitation rate and the radius of a drop. They include, in particular, the linear relation $V (\text{m/s}) = 75r (\text{cm})$ for sufficiently small-sized rainfall drops, and for larger drops the precipitation rate becomes constant and does not depend on their size (Kollias *et al.*, 1999). This indicates that the rainfall rates will be proportional to the fourth moment (or to the third moment, depending on the diameter of drops) of the density function of drops in a

cloudy mass of precipitating drops. In meteorological practice the dimension of R is usually reduced to millimetres per hour.

10.5.9 Natural polydisperse media

In order to present a generalized qualitative picture of density functions for natural polydisperse systems (for terrestrial atmosphere conditions), we shall consider the data of Figure 10.8. It follows from the analysis of these data that the most finely disperse and, at the same time, most intensive (in density function value) are various types of fogs, i.e. the media which are formed immediately after the phase transition of water vapour into the liquid state. The greatest range in dispersity is occupied by various types of aerosols in the terrestrial atmosphere. In spite of the fact that the aerosol mass constitutes only 10^{-9} of the total mass of the atmosphere, it essentially influences the atmospheric radiation processes and, therefore, the weather and climate as well. Depending on their physicochemical origin, the aerosols are subdivided into five model types: maritime, continental, urban-industrial, volcanic and

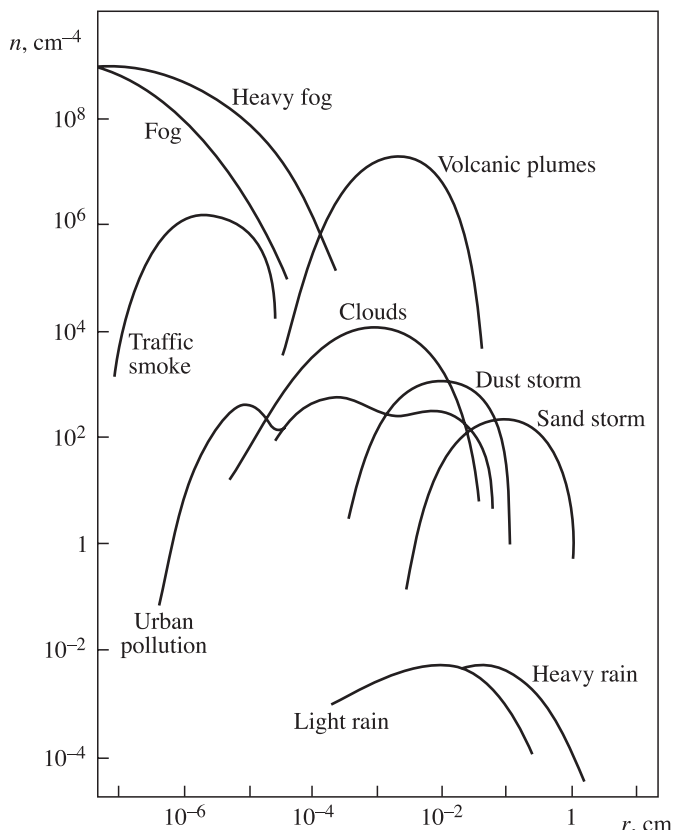


Figure 10.8. Particle-size distributions (the density functions) for natural disperse media.

stratospheric. All these types strongly differ both in the characteristic range of particle size, and in their intensity. The distributions can also have a multimodal form, as in the case of urban aerosol, for instance (Figure 10.8).

The drop-cloudy systems of the terrestrial atmosphere represent an extremely inhomogeneous medium permanently varying in space and in time. This is due, first of all, to the great diversity of particular physical causes and mechanisms of initiating the phase transition of water vapour into the liquid state. Therefore, depending on the spatial-temporal scale of a particular investigation, the distribution parameters can have very wide ranges of variation of their numerical parameters (Deirmendjian, 1969; Ivazyn, 1991; Krasiuk and Rosenberg, 1970; Marchuk *et al.*, 1986; Rozenberg, 1972; Houze, 1993; Marshak *et al.*, 1994; Jameson *et al.*, 1998).

The most grossly disperse systems in the terrestrial atmosphere are meteorological systems with precipitation. As in the case of cloudy systems, precipitations possess strong spatial-temporal variations (the so-called multi-fractal structure) (see Chapter 2). This greatly complicates the interpretation and comparison of remotely sensed and in situ results by the researchers (Rodgers and Adler, 1981; Atlas *et al.*, 1981; Velden and Smith, 1983; Jameson, 1991; Niemczynowicz and Bengtsson, 1996; Olsson, 1996; Kostinski and Jameson, 1997; Taylor and English, 1995; Marshak *et al.*, 1997; Smith *et al.*, 1998; Skofronick-Jackson and Wang, 2000; Simpson *et al.*, 1988, 2000; Deeter and Evans, 2000; Liu and Curry, 2000; Bennartz and Petty, 2001; Lohnert and Crewell, 2003).

10.5.10 Analytical forms of the density function

In the last 50 years a great amount of experimental work has been carried out devoted to searching for the most acceptable analytical form of a density function for disperse systems of various physical natures. From the theoretical side the efforts were directed towards the solution of complicated problems of kinetics of physicochemical media using, for example, the solution of a system of the Fokker–Planck–Smolukhovsky equations. The following analytical expression for the density function, known as the gamma distribution, is considered the most theoretically substantiated one:

$$n(r) = ar^\mu \exp(-br^\gamma), \quad (10.57)$$

where a, b, μ, γ are the parameters determining all the characteristic features of the distribution. Almost all empirical distributions, formed earlier from the experimental data, can be obtained from the given distribution.

Using expressions (10.44), (10.53) and (10.57), we obtain the following formulas for the relative density:

$$C = \frac{4\pi}{3} \int n(r)r^3 dr = \frac{4}{3}\pi a\gamma^{-1} b^{-(\mu+4)/\gamma} \Gamma\left(\frac{\mu+4}{\gamma}\right). \quad (10.58)$$

Letting $\gamma = 1$, we obtain the expression for the volume density:

$$N = \int_0^\infty n(r) dr = ab^{1-\mu} \Gamma(\mu + 1). \quad (10.59)$$

Here, as in (10.58), $\Gamma(x)$ denotes the gamma function (Gradshteyn and Ryzhik, 2000), from which this distribution assumed its name.

Using (10.57) and (10.59), we can obtain the expression for the relative density function:

$$f(r) = b^{\mu-1} \frac{r^\mu}{\Gamma(\mu+1)} \exp(-br). \quad (10.60)$$

This distribution is now characterized by two parameters only b and μ . This expression is often written down in a slightly different (but equivalent) form:

$$f(r) = \frac{1}{\Gamma(\mu+1)} \mu^{\mu+1} \frac{r^\mu}{r_m^{\mu+1}} \exp\left\{-\mu \frac{r}{r_m}\right\}. \quad (10.61)$$

Here parameter μ characterizes the distribution halfwidth, and parameter r_m determines the so-called modal (most probable) distribution radius. Serious efforts are now undertaken to determine these parameters for natural disperse media from the experiment. So, for fogs and clouds the values of parameter μ are concluded within the limits of 1–10, and those of the modal radius within the limits of 0.1–10 micrometres.

It is interesting to mention that in 1948 J. Marshall and W. Palmer suggested a simple empirical relation for the density function of rainfalls in the form:

$$n(r) = N_0 \exp(-\Lambda r), \quad (10.62)$$

where

$$N_0 = 1.6 \times 10^4 (\text{m}^{-3} \times \text{mm}^{-1}); \quad \Lambda = 8.2 R^{-0.21} (\text{mm}^{-1}). \quad (10.63)$$

Here radius is expressed in millimetres and R in millimetres per hour.

Such a distribution was found to successfully describe the averaged experimental data both for drizzling rains, for widespread rains, and for convection and thunder-storm rains (true, with significant modification of the numerical values of N_0 and Λ). The Marshall–Palmer drop-size distribution, as well as the distributions close to it (such as the Laws–Parsons relation), are widely used now as well (Oguchi, 1983). One has also managed to obtain a fairly simple empirical relation between precipitation intensity and water content (the mass of substance in a unit volume) in a medium, namely:

$$W = 0.06 R^{0.88}, \quad (10.64)$$

where the water content has dimension of grams per cubic metre, and the precipitation intensity millimetres per hour. There exist also other numerical versions of the given formula.

Theoretical and numerical investigations of the physicochemical kinetics problems, including the processes of condensation of water vapour, the coalescence between drops and drop break-up, have shown that, generally, the theoretical spectra of drops are qualitatively close to the exponential Marshall–Palmer distribution, though there are some features, which are not described by a rule of thumb of the given distribution. This relates, first of all, to the multimodal character of theoretical distributions and to considerably greater density in the small drop-size range ($r < 0.1 \text{ mm}$), than in the case of exponential approximation. All these features result

in noticeable variations in the electromagnetic properties of a medium (Jameson, 1991; List, 1988).

10.5.11 Parameters of attenuation and scattering of a polydisperse medium

In accordance with the basic concept of the radiative transfer theory, namely, the electromagnetic rarefaction of a medium, the incident radiation, falling on an investigated volume from outside, completely ‘illuminates’ all particles present in a unit volume (see Chapter 9). Therefore, when the medium contains a cloud of spherical particles of the same composition, but of different size, the spectral coefficients of attenuation (extinction) and of scattering can be calculated by formulas

$$\gamma(\text{cm}^{-1}) = \int_0^\infty Q_E \pi r^2 n(r) \, dr, \quad (10.65)$$

$$\sigma(\text{cm}^{-1}) = \int_0^\infty Q_S \pi r^2 n(r) \, dr. \quad (10.66)$$

When the radiation beam propagates in a medium, which contains N spherical particles of the same composition and the same size (each having radius R) in the unit volume, the cross-sections of absorption and scattering (or the efficiency factors of extinction Q_E and of scattering Q_S) can be related to spectral coefficients of total attenuation (extinction) and scattering by simpler relations:

$$\gamma(\text{cm}^{-1}) = Q_E \pi r^2 N \quad (10.67)$$

and

$$\sigma(\text{cm}^{-1}) = Q_S \pi r^2 N. \quad (10.68)$$

If the particles are grouped together in size into the intervals with radius r_j ($j = 1, 2, \dots, M$), then the integrals presented above can be replaced by the sums. If in expressions (10.65)–(10.66) the integrals cannot be obtained analytically, then numerical integration is carried out and the tables are compiled (Krasik and Rosenberg, 1970; Skolnik, 1980; Oguchi, 1983; Lhermitte, 1988; Ivazyn, 1991). It should be emphasized once again that all these expressions are obtained under important physical limitations: the electromagnetic rarefaction of a medium and the absence of interactions between particles.

Consider at first the Rayleigh approximation. Since the absorbing properties of particles prevail in this approximation, the spectral absorption coefficient can be presented as:

$$\gamma = k_1(\lambda) \int_0^\infty r^3 n(r) \, dr, \quad (10.69)$$

where $k_1(\lambda)$ is the numerical coefficient. On the other hand, the total mass of medium’s substance W (in a unit volume) will be equal to

$$W = \frac{4}{3} \pi \rho \int_0^\infty r^3 n(r) \, dr. \quad (10.70)$$

The comparison of these expressions indicates that the spectral extinction coefficient for a medium with particles in the Rayleigh approximation is proportional to the total mass of substance in a unit volume:

$$\gamma = k_2(\lambda)W \quad (10.71)$$

and, what is very important, it does not depend on the form of the density function. Thus, in remote investigations in the Rayleigh region, information on the form of a density function of the disperse medium cannot be obtained, at least directly.

Since water possesses prominent spectral properties in the centimetre and millimetre bands, for the band of 0.5–10 cm and for liquid-drop clouds ($t = 180^\circ\text{C}$) the following simple approximation can be established:

$$\frac{\gamma}{W} = \frac{0,43}{\lambda^2}. \quad (10.72)$$

Here W is expressed in grams per cubic metre and absorption in decibels per kilometre. Physically this is related to the fact that the parameter in expression (10.42), which depends on the dielectric properties of water, has an approximation of type $1/\lambda$ on the long-wavelength branch of the Debye relaxation maximum (see Chapter 8). However, in the case of crystalline clouds (hailstones, snowflakes) the extinction decreases by two to three orders of magnitude (other things being equal). And the wavelength dependence can be accepted to be $1/\lambda$ (because the explicit wavelength dependence of the real part of the dielectric constant is absent for ice). There also exist some further experimental data approximations in the Rayleigh region. However, all of them have a frequency character close to (10.72).

Consideration of a wider range of particle size and wavelength requires numerical operations with (10.65) and (10.66). Special calculations of the coefficient of extinction per unit of path (the specific attenuation – attenuation for a 1-km propagation path), carried out in the 1–1000 GHz range for various drop-size distributions and precipitation intensities (Figure 10.9), have shown that the frequency dependencies have a characteristic form – a rapidly growing rise from the side of large wavelengths, a weak maximum in the frequency range of about 100 GHz and a slow drop to the side of higher frequencies. As would be expected, these dependencies do not reveal any sharp maxima which are specific for the Mie region of an individual particle. Besides, the growing regions can be characterized as transition regions from the ‘smeared’ Mie maximum to the Rayleigh region. In this case the frequency approximation of extinction for high-intensity precipitation, which has large-sized drops and, accordingly, a great scattering, is closer to the $1/\lambda^4$ dependence. Whereas for weak precipitation (with a small dispersity of drops and, accordingly, with very weak scattering and strong absorption, this approximation is closer to that of the Rayleigh region – $1/\lambda^2$ (see relation (10.72) and Figure 10.9). It should also be noted that the distinctions in extinction values for various distributions are the greater, the higher the working frequency and the lower the precipitation intensity. We have already said that the Rayleigh region is not sensitive to the form of distribution of drops (see expression (10.71)). As to the strong precipitations, in this case the intensive scattering of large-sized drops in some sense ‘blocks’ the

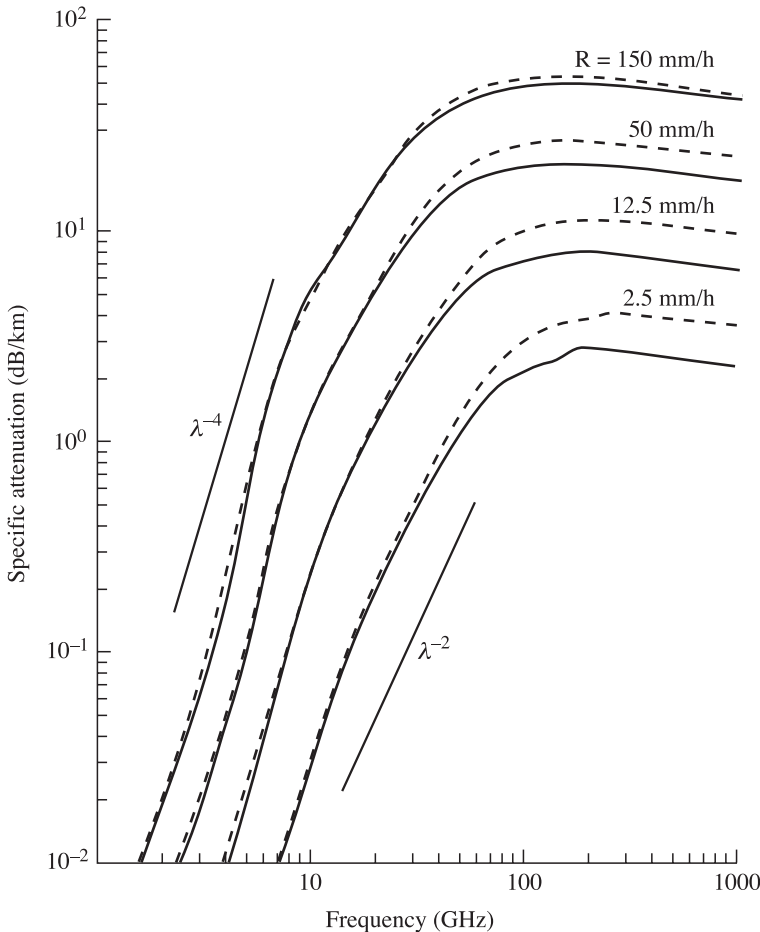


Figure 10.9. Frequency characteristics of rain attenuation at 20°C , for Laws-Parsons (solid curves) and Marshall-Palmer (dashed curves) drop-size distributions. Parameters are rain rates (mm/h) (Oguchi, 1983).

contribution from the absorption of small-sized drops into the total extinction of a disperse medium. Special experiments (Oguchi, 1983; Wolf and Zwiesler, 1996) have really shown that in the millimetre frequency band for rainfalls in the terrestrial atmosphere the sensitivity of the degree of extinction in a medium to the type of distribution is very high, and, therefore, this band is fairly efficient for the remote investigation of fine features of disperse media.

It is rather indicative and instructive to compare the frequency properties of the value of extinction (per unit of path) of various disperse media, which are typical for the terrestrial atmosphere (Figure 10.10). Certainly, in this case the question is about the qualitative picture of the phenomenon, and the data presented are not intended

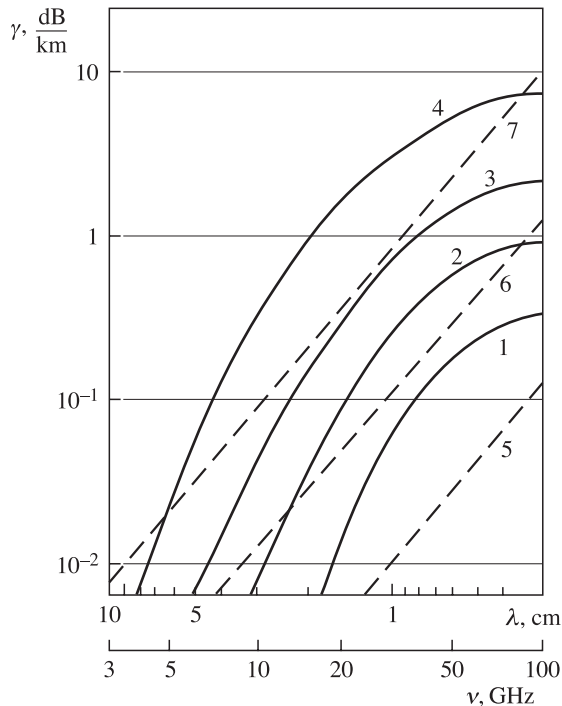


Figure 10.10. Frequency characteristics of attenuation for natural disperse media: rain (solid curves) and fog (dashed curves). Notation is explained in the text.

for quantitative interpretation of particular experiments. The solid lines in Figure 10.10 give the wavelength dependencies of the extinction coefficient for rainfalls with intensities of 0.25 (curve 1), 1.0 (curve 2), 4 (curve 3) and 16 mm/hour (curve 4). According to the existing meteorological classification, these intensities correspond to drizzle, light, moderate and heavy rainfalls. The dashed curves in the figure show the extinction in clouds and fogs, calculated by formula (10.72) for the water content of 0.032 (curve 5), 0.32 (curve 6) and 2.3 g/m^3 (curve 7). These fogs correspond to the visual ranges (in the optical band) of about 600, 120 and 30 m. As follows from the analysis of these data, the picture is rather ambiguous, in general. So, the extinction in a thick sea fog (curve 7) exceeds the extinction in a moderate rainfall (curve 3) in the millimetre and centimetre wavelength bands. And in the long-wave centimetre band the extinction in a thick fog even exceeds the extinction in heavy precipitation. This seems paradoxical, at first sight. However, physically this is associated with a different relationship between contributions to extinction from large-sized (scattering) and small-sized (absorption) drops in various disperse media. So, for the intensive rainfall the frequency dependence of extinction is proportional to $1/\lambda^4$ in the centimetre band, and for the fog to $1/\lambda^2$, which results in an apparent paradox at long centimetre waves.

10.6 FEATURES OF RADIATIVE TRANSFER IN DENSE MEDIA

In connection with the intensive development of microwave diagnostics of composite natural media in the ocean–atmosphere system, it is of interest to study the features of the transmission and scattering of electromagnetic waves in randomly inhomogeneous media with densely disturbed, discrete, highly absorbing scatterers, where the size of particles, the distance between particles, d , and the electromagnetic radiation wavelength, λ , are quantities of the same order. Such important microwave remote sensing tasks include the study of electromagnetic waves scattering and radiation in the cloudy atmosphere with considerable volume densities (more than 0.1%) of hydrometeors (Oguchi, 1983; Nemarich *et al.*, 1988; Lhermitte, 1988), in the drop-spray phase of gravitation waves breaking (Cherny and Sharkov, 1988), in snow–water disperse media (Wen *et al.*, 1990; Boyarskii *et al.*, 1994), in foam-type disperse systems (Raizer and Sharkov, 1981) and in other similar natural media.

With the indicated parameters of a disperse medium the physical conditions of applicability of the radiative transfer theory are obviously violated (see Chapter 9). However, the desirability of using the numerous results of radiative transfer theory doubtless requires, solution of the question on the limits of effectiveness of the theory itself. Certainly, this complicated problem cannot be solved within the framework of radiative transfer theory itself. Its solution is possible either within the multiple scattering framework, or in the experimental way. The theoretical analysis of this problem is far beyond the scope of the present book. Here we shall only describe the results of fine laboratory experiments, which are closest to the subject of the present book, namely, the microwave sensing of dense disperse media. The experiments were carried out during 1976–1986 under the scientific guidance of the author of the present book (Bordonskii *et al.*, 1978; Miliitskii *et al.*, 1976, 1977, 1978; Raizer and Sharkov, 1981; Cherny and Sharkov, 1988, 1991a,b).

Though there are many experiments studying the electromagnetic properties of tenuous discrete systems with $d \sim (10-10^4)\lambda$ and volume density $C \sim (10^{-2} - 10^{-4})\%$ (see the review by Oguchi (1983)), no results from studies of electromagnetic properties in the radio-frequency band of dense dynamical media with absorbing scatterers are to be found in the literature. The principal methodological problem in the statement of such experiments lies in the experimental difficulties of producing dynamical dense drop structures with strictly controlled parameters. However, the statement of such experiments is extremely topical, both from general theoretic and from practical points of view. And, first of all, these experiments are necessary for finding the limiting values of densities at which the mechanisms of electromagnetic interaction of solitary absorbing scatterers are ‘switched on’. The experiments, carried out in the optical band for transparent media and for semi-transparent particles (‘soft particles’) have shown (Varadan *et al.*, 1983; Wen *et al.*, 1990), that the essential contribution of multiple scattering falls on the range of densities exceeding 1%, this value of boundary being strongly dependent on the particle size parameter. These numbers cannot, certainly, be directly applied to discrete media with highly absorbing scatterers and can serve

as a quantitative landmark only. The papers by Cherny and Sharkov (1991a,b) contain the results of experimental investigations of characteristics of transmission, backscattering and thermal radiation of millimetre-band electromagnetic waves in a disperse discrete medium with the volume density of spherical scatterers ranging from 0.05% to 4.5%. In this case the average distance, d , between the centers of particles varied within the limits from 2.3 to 0.9λ .

10.6.1 Disperse medium and its characteristics

As we have already noted, the fulfilment of the necessary radiophysical experiments meets with the difficulties of producing, in a free-fall mode, aqueous particles of quasi-monochromatic (in the size spectrum and in the magnitude of velocities) flow with a high density of spherical-shaped particles. On the one hand it is necessary to avoid dynamical deformation and decay of particles of fairly large diameters (of the order of 2–3 mm) and having high velocities of motion (5–10 m/s). On the other hand, the gravitational and turbulent coalescence between drops should not be allowed. The cascade processes mentioned result in a very wide spectrum of particles under natural conditions (in cloudy systems and precipitations, for instance) (see section 10.5). This circumstance, in its turn, essentially hampers the interpretation of the radiophysical experiments. The processes of deformation and decay of drops in a flow are controlled by two dimensionless numbers: the Rayleigh number (for a sphere) $Ra = 2aV\rho\mu^{-1}$ and the Weber number $W = a^2V\rho(2\sigma)^{-1}$. Here V is the steady velocity of a drop; a is the drop radius; ρ and μ are density and viscosity of air; and σ is the surface tension of water. The laminar regime of air flow around drops (the Stokes regime) is kept up to $Ra \approx 300$, and the critical value of W for ensuring the dynamical stability of drops equals 10. The analysis of various methods of forming dense media has led the authors to the conclusion that it is necessary to use a forced regime with a particular flow velocity, rather than a free flow regime. The highly dense disperse medium was produced by averages of a spray system made as a special injector with a removable grid. The grid represents a plate of a particular profile with orifices. The number and diameter of orifices determine the density and size of the drops, whereas the profile determines the value of flow divergence, which also influences the density. The sphericity of drops was specially controlled – the eccentricity of drop ellipses did not exceed 0.3 (for high densities) and 0.1 (for low densities). For the conditions of the described experiment the Ra number was 200 to 300 (for various flow velocities) and $W = 0.03$. Thus, under the experimental conditions both the laminar regime of air flow around a drop (the Stokes condition) was ensured, and the processes of decay and the rise of a wide (decay) spectrum of scatterers was not allowed. If the injector is directed downwards, then the drops, being accelerated under the force of gravity, produce uniform density variation down the flow. Thus, for a single grid it is possible to obtain a wide range of variation of density with the same dispersity (Figure 10.11(a),(b),(c)). The control and measurement of the particle density were carried out by the stereoscopic photography method using two synchronized mirror cameras with telescopic lenses and with a special light flash system (with a flash duration of 10^{-6} s). In addition, the

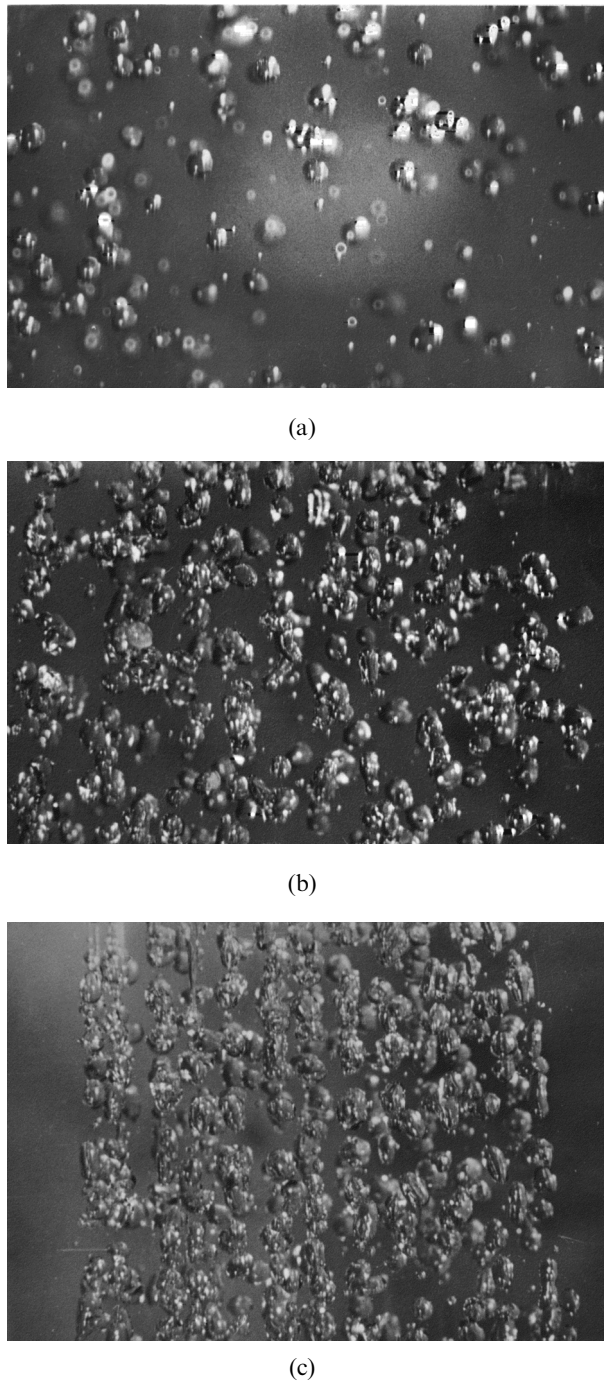


Figure 10.11. Photographs of disperse water drop medium with relative volume concentrations: (a) 0.28%; (b) 1.5%; (c) 4.50%.

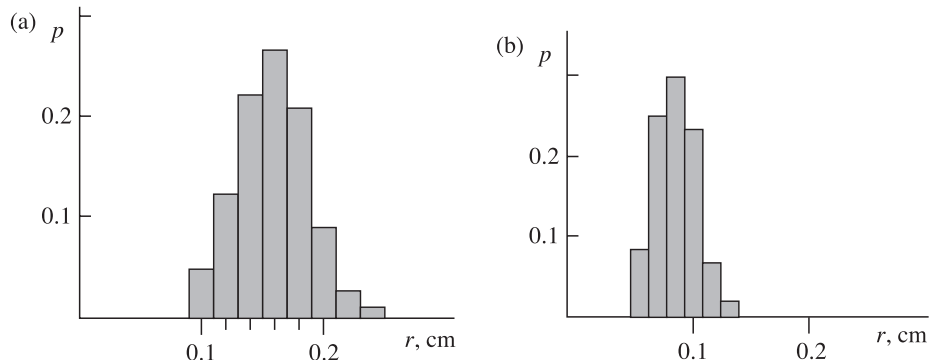


Figure 10.12. The experimental histograms of droplet radii for medium N_1 (a) and for medium N_2 (b).

velocity of drops was measured by the method of tracks (the reflecting blinks on the photo images, Figure 10.11(a)). The operator has analysed the stereo pairs obtained with a stereoscope and, when comparing them with a test-object, determined the number of drops and their disperse properties (at a fixed time instant). The radiophysical measurements were carried out for two types of disperse media whose histograms are presented in Figure 10.12. The form of particle distribution functions $n(r)$ ($\text{dm}^{-3} \text{ mm}^{-1}$) was approximated by the gamma distribution:

$$\begin{aligned} n_1(r) &= 0.38N_1r^9 \exp(-0.73r^3) \\ n_2(r) &= 73.5N_2r^8 \exp(-3.66r^3) \end{aligned} \quad (10.73)$$

The values of N_1 and N_2 are proportional to the volume density of particles. The average value of radius for medium 1 equals 0.15 cm (and, accordingly, the size parameter $x_1 = 1.18$), and for medium 2 it equals 0.09 cm ($x_2 = 0.7$). The special statistical estimation of fluctuations of the countable particle flux density has shown that the root-mean-square deviation of density was less than 2% (of the average value of N). In this case the samplings, spaced in time from 1 hour to 3 hours, relate to the same general set. It is clearly seen from the analysis of histograms that in forming the dense flux one managed to avoid decay and coalescence processes, and the spectrum of particles could be considered to be close to monochromatic. For these types of media the authors have calculated the extinction, scattering and absorption coefficients in accordance with (10.13), (10.65) and (10.66). In addition, the single-scattering albedo was calculated for the unit volume of a polydisperse medium, using the function of size distribution of particles obtained from the experiment. The calculations were carried out for the working radiation wavelength $\lambda = 8 \text{ mm}$ and the complex index of refraction of water $m = 5.39 - j2.81$, which corresponds to the water temperature $t = 22^\circ\text{C}$ and salinity $S = 0\%$. By virtue of the fact that the tenuous medium approximation with a near-monochromatic spectrum is used here (see relations (10.67) and (10.68)), the scattering albedo for

the unit volume of a medium will correspond to the value of albedo of a solitary particle (so, for medium $N_1 \omega = 0.63$, and for medium $N_2 \omega = 0.43$) and will not depend on the medium density.

10.6.2 Experimental technique

The purpose of the experiment was to measure the radiophysical characteristics of a disperse dynamical medium with strict control of the disperse medium parameters. The measurements were carried out in three modes: bistatic (radiation transmission through the medium within the line-of-sight limits), scatterometric (backscattering investigation) and radiometric. The extinction of the medium was measured in the first version, the backscattering cross-section in the second one and thermal radiation of a disperse medium in the third version. The fluctuations of scattered radiation intensity were measured along with its average values. The extinction, absorption and scattering coefficients, the scattering and backscattering albedo (in the ‘cold’ layer approximation) and the thermal radiation of a disperse medium with a spherical scattering indicatrix were calculated using the analytical solution of the equation for a plane-parallel layer (in the ‘pure’ absorption approximation).

10.6.3 Average values of electrodynamical characteristics

Comparing the experimental and theoretical values of extinction and thermal radiation for the disperse medium 1 (the average diametre of particles was 0.3 cm), we can see the distinction, which is noticeably revealed with increasing density of particles (Figure 10.13). One can distinguish the region of low deviation of experimental from theoretical data and the region of greater deviation. The boundary that separates these regions corresponds to a value of particle volume density approximately equal to 0.8%, this boundary being the same both for extinction and for thermal radiation. Considering the results of investigation of the extinction value for disperse medium 2 (where the average diametre of particles was 0.2 cm), we can see that the aforementioned boundary lies in the region of particle volume density values of 0.15%. Now we shall analyse the dependence of extinction values for a disperse medium on the number N of particles in a unit volume (the countable density), rather than on the particle volume density C . It can be seen from Figure 10.13 that in this case the boundaries mentioned lie in the range of $N_0 = 500\text{--}550 \text{ dm}^{-3}$ for both types of disperse medium. That is, they virtually coincide. In its turn, quantity N_0 determines the average distance between particles as $d \sim N^{1/3}$. Therefore, now we can characterize the aforementioned boundary by the distance between particles, i.e. by $d \sim 1.5\lambda$.

Thus, from the analysis of experimental data and from theoretical calculations it follows, that the radiative transfer theory in the tenuous medium approximation satisfactorily describes electromagnetic properties (the average values) of a discrete disperse medium with absorbing scatterers, provided that the distance between particles $d > 1.5\lambda$. In the case where $d < 1.5\lambda$, the experimental data principally differ from calculated data. For example, for the particle volume density

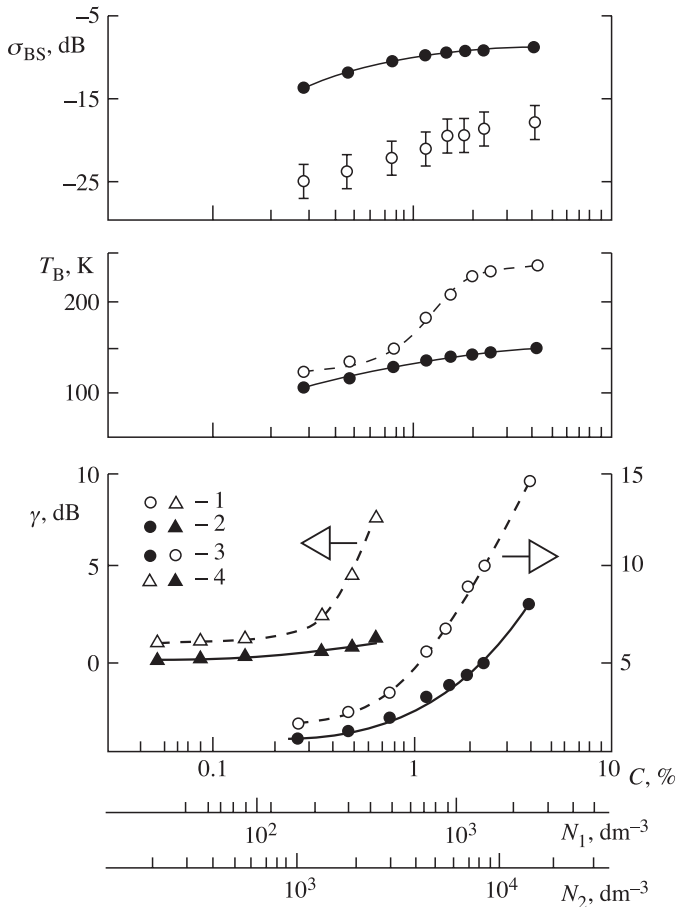


Figure 10.13. The extinction coefficient (γ), radiobrightness temperature (T_B) and backscattering cross-section (σ_{BS}) of disperse water drop media as functions of the volume concentration (C) and the number density (N): (1) experimental data; (2) theoretical results; (3) data for medium N_1 ; (4) data for medium N_2 .

$C = 4.5\%$ ($d = 0.9\lambda$) the distinction for the radiobrightness temperature equals 86 K, and for the extinction value -6.5 dB. As far as the backscattering is concerned, here the experimental and theoretical data (in the cold layer approximation) essentially (by about 10 dB) differ throughout the range of particle densities. Now, using the experimental data, we shall estimate the disperse medium parameters for the particle volume density value $C = 4.5\%$ ($d = 0.9\lambda$).

The electrodynamical parameters have been estimated by means of a specially developed technique of complex combining the data of active and passive measurements for the same investigated medium (Cherny and Sharkov, 1991a). In this case the expressions for radiobrightness temperature were obtained in the ‘pure’ absorption approximation (see Chapter 9). It is important to note that the

inclusion of the integral term into the transfer equation that describes the ‘internal re-scattering’ in a layer does not essentially change the spectral characteristics of a medium in the case of absorbing scatterers considered. This follows from the comparison of calculations with the results of solving a similar problem by the double spherical harmonics method and by the Monte Carlo method. Of importance is the fact that, for indicated values of density of particles in a medium, the electro-dynamical parameters of a disperse medium have essentially changed as compared to calculated values (for a tenuous medium) obtained in the single-scattering approximation. So, the scattering albedo of a unit volume of disperse medium N_1 decreased three times (from the value of 0.63 down to 0.22). The extinction and absorption coefficients, on the contrary, increased about 1.5 times (from the value of 0.63 up to 0.94 cm^{-1}) and three times (from the value of 0.23 up to 0.73 cm^{-1}), respectively. And the scattering coefficient value decreased twice in this case (from the value of 0.40 down to 0.21 cm^{-1}). The result considered indicates that for the disperse dense medium with absorbing scatterers the interaction of particles results, primarily, in growing absorption in a medium and, therefore, in increasing its thermal radiation and, in addition, in decreasing scattering properties of a medium.

10.6.4 Fluctuation mode of extinction

It is important to note that in the same paper Cherny and Sharkov (1991a) have demonstrated experimentally the principal change of the character of the fluctuation mode of extinction in a dense medium. This effect is visually illustrated in Figure 10.14, which presents the registograms of an external harmonic signal transmitted through the medium, this signal being considered at an intermediate frequency. The fluctuations of intensity of transmitted radiation are observed in the form of mirror-symmetrical amplitude modulation of the signal. The measurements were carried out with extinction recording by exposure to microwave radiation. It can easily be seen that the statistical characteristics of a signal sharply change in the case of two distinguishing densities. One of the possible physical causes, explaining fluctuations of radiation transmitted through a medium, could be associated with changing the countable number of particles in the volume under study. We shall indicate, however, that this is not the case.

So, we shall consider, for example, in accordance with the Bouguer law, the ratio of intensities of external radiation, weakened by a medium, for different time instants

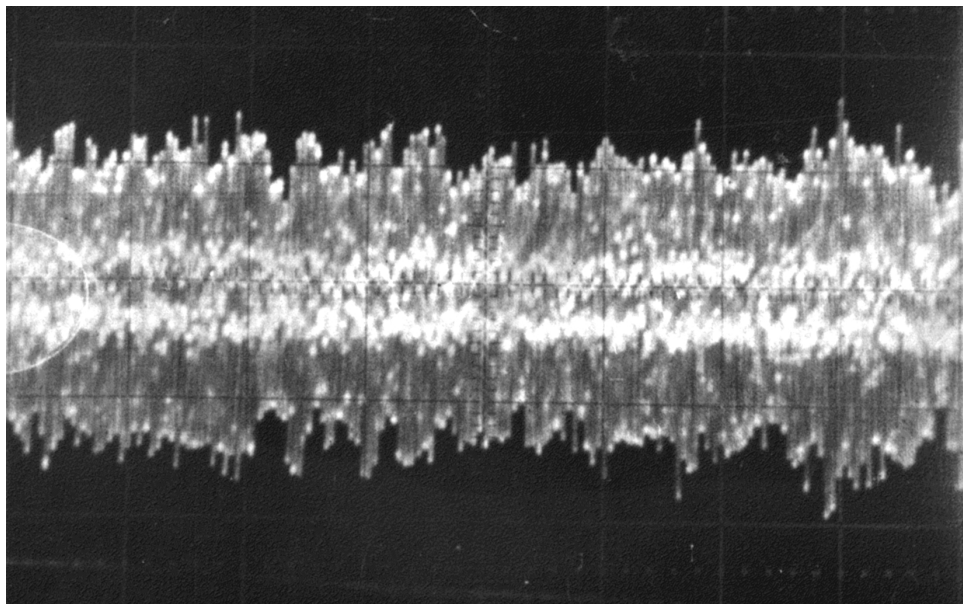
$$(I_1/I_2) = \exp(\tau_2 - \tau_1) \quad (10.74)$$

or

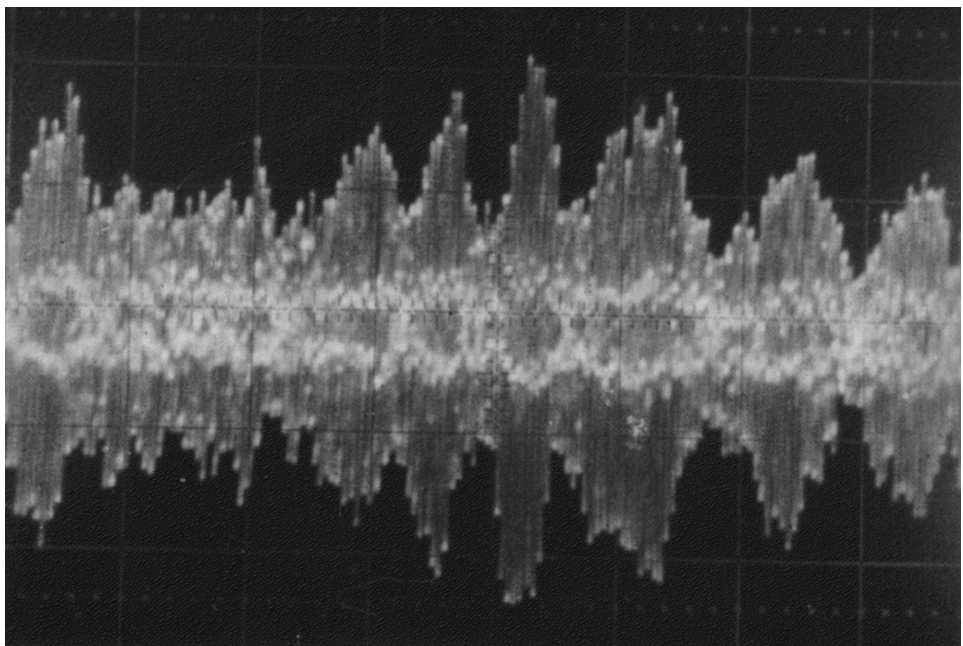
$$\tau_2 - \tau_1 = \ln(I_1/I_2), \quad (10.75)$$

where τ_1 and τ_2 are opacities of an investigated disperse medium at different time instants. Since in the single-scattering approximation for a medium with a monochromatic spectrum of particles we have $\tau = Q_E \pi r^2 N s$ (here s is the linear size of a medium), one can write the following finite-difference relation:

$$(\Delta N/N) = (\Delta \tau/\tau) = (1/\tau) \ln(I_1/I_2). \quad (10.76)$$



(a)



(b)

Figure 10.14. The photographic regisograms of a signal (at intermediate frequency) transmitted through a water drop medium with volume concentrations 0.28% (a) and 4.5% (b).

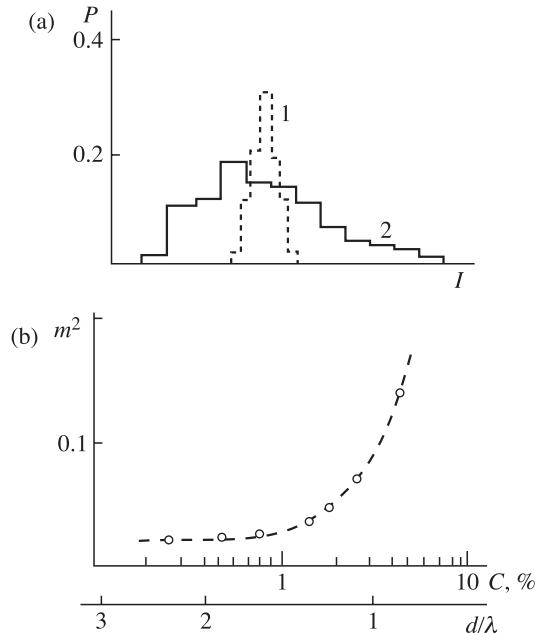


Figure 10.15. The statistical characteristics of radiation intensity of a signal transmitted through a water drop medium: (a) the density function (experimental histograms) with two volume concentrations: (1) 0.28%; (2) 4.5%; (b) the scintillation index m^2 as a function of the volume concentration and of the distance between particles.

Proceeding from this relation, we shall estimate the maximum value of $(\Delta N/N)$ for the volume density of particles of a disperse medium $C = 4.5\%$, at which $(I_{\max}/I_{\min} = 6.1$, and the quantity $\tau = \gamma/4.34 = 3.34$ represents the average value of opacity. Substituting this value into (10.76), we find $(\Delta N/N) = 54\%$, but this is impossible, since the particle density fluctuations in a disperse flow do not exceed 2% with the probability of 0.95. Thus, a sharp growth of the variance of fluctuations of a medium's extinction are not determined by fluctuations of the number of particles in the flow, but has another physical nature.

We pay attention to the principal point that, as the density of particles increases, the character of fluctuations also changes. So, the probabilistic distribution of intensity of a signal, transmitted through the investigated medium at $C = 0.28\%$, has a prominent normal character, whereas at $C = 4.5\%$ the intensity fluctuations are distributed according to the normal logarithmic law (Figure 10.15). This circumstance is clearly exhibited on registograms in visual observation as well (Figure 10.14). For the mentioned volume density values and, accordingly, for $(d/\lambda) \sim 1.5$ the so-called scintillation index sharply increases (Figure 10.15(b)). The latter characteristic is often used in optical observations, which gave rise to the term. However, the mentioned characteristics do not provide a detailed picture of the distribution of fluctuations over the scales of interactions (see Chapter 2). Let

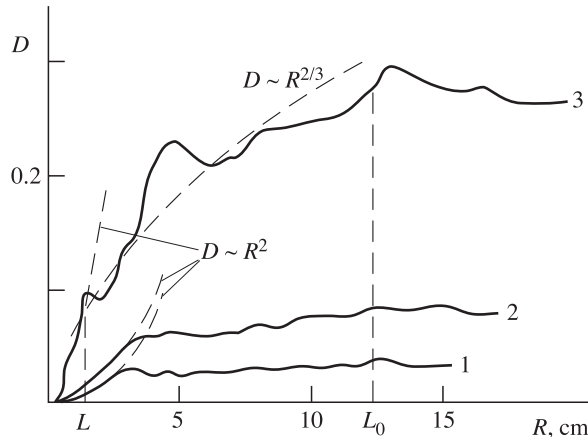


Figure 10.16. The structure function of intensity fluctuations for a signal transmitted through a water drop medium with three volume concentrations: (1) 0.28%; (2) 1.5%; (3) 4.5%.

us consider the behaviour of a structural function expressed in terms of spatial coordinates. The transition from spectral-temporal coordinates t and f to a spatial-frequency presentation of R and k (the spatial-wave number) (see Chapter 5) can be accomplished based on the hypothesis of ‘freezing’ inhomogeneities in a moving flow:

$$R = Vt, k = \frac{2\pi f}{V}, \quad (10.77)$$

where V is the particle flux velocity in the direction perpendicular to radiation transmission. Figure 10.16 presents the structural function of intensity fluctuations for three values of volume density of a disperse medium. Now we shall analyse the behaviour of a structural function, which represents the mean square of the magnitude of an increment of the fluctuation component $I(R)$ of intensity $I(R)$ (Rytov *et al.*, 1978):

$$D(R_1, R_2) = \langle |I(R_1) - I(R_2)|^2 \rangle. \quad (10.78)$$

If the studied spatial field has the character of locally homogeneous one, i.e. depending only on the difference of scales of interactions $R = R_1 - R_2$, then the form of a structural function can be essentially simplified:

$$D(R) = 2[B(0) - B(R)], \quad (10.79)$$

where $B(R)$ is the spatial correlation function (see Chapter 2 and 5). The important property of a structural function consists in the fact that it excludes from consideration the large-scale inhomogeneities L_0 . In our case the latter represent the characteristic size of a particle flux. The correlation function takes into account fluctuations of any scale in equal measure. For this reason the use of a structural function is physically justified in those cases where we are interested in the fluctuations on scales much smaller than L_0 .

For $C = 0.28\%$ and $C = 1.5\%$ the rapid saturation of a structural function takes place on scales of the order of $R = 3\text{ cm}$. For $C = 4.5\%$ the form of a structural function essentially differs from previous cases. Here both the internal ($l_0 = 1.5\text{ cm}$) and the external ($L_0 = 12\text{ cm}$) scale of inhomogeneities is clearly exhibited, and in the interval of $l_0 < R < L_0$ the structural function grows as $D \sim R^{2/3}$. The limiting value of a structural function (in the saturation region) is equal to a double value of the variance of fluctuations.

Thus, the analysis shows that for the volume density of particles $C = 4.5\%$ ($d = 0.9\lambda$) the scattering of electromagnetic radiation in a medium occurs on spatial inhomogeneities whose scale lies in the interval between $l_0 = 1.5\text{ cm}$ and $L_0 = 12\text{ cm}$, which is much greater than the size of particles (the diametre is 0.3 cm) and the distance between them ($d = 0.7\text{ cm}$). This fact, in its turn, confirms the existence of collective effects in scattering. The circumstance that the intensity fluctuations are distributed according to the normal logarithmic law and the spectrum of fluctuations and a structural function can be described by well-known exponential laws of ' $-5/3$ ' and ' $2/3$ ', respectively, indicates to the turbulent-vortex character of fluctuations with quasi-vortex inhomogeneities. Therefore, the discrete disperse medium for $d < \lambda$ can be considered to acquire the properties of a continuous randomly inhomogeneous medium, in which the spatial fluctuations of dielectric permittivity take place (Rytov *et al.*, 1978).

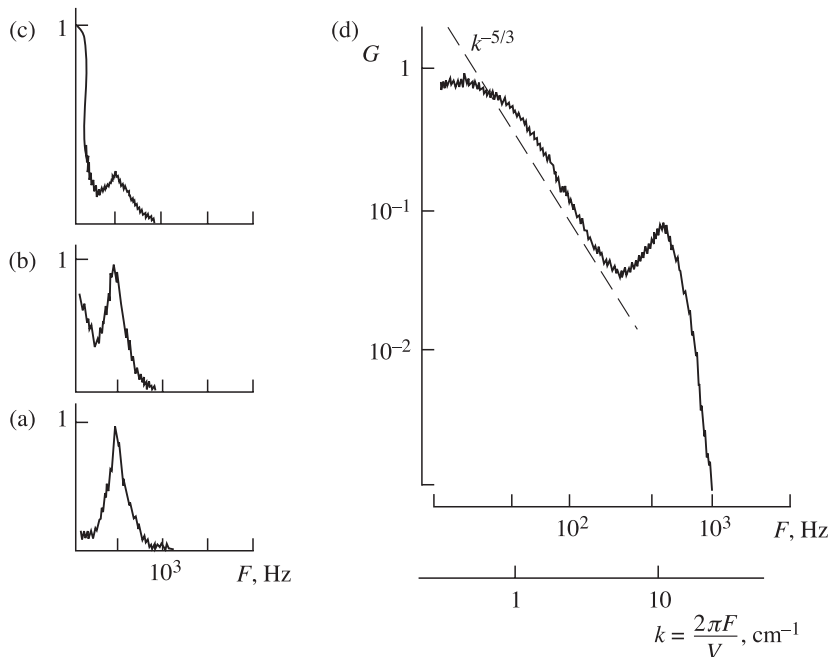


Figure 10.17. Normalized Doppler spectra of backscattering signal from a disperse medium with three volume concentrations: (a) 0.28% ; (b) 1.5% ; (c) 4.5% ; (d) 4.5% in bi-logarithmic coordinates. $V_D = 1.7\text{ m/s}$; $V = 2\text{ m/s}$.

Consider now the results, obtained by means of the Doppler scatterometre, in the mode of observation of microwave radiation backscattering by the same disperse medium (Cherny and Sharkov, 1991b). Figure 10.17 presents the Doppler spectra of a scatterometric signal backscattered by a disperse medium. The measurements were carried out in such a manner that the moving flux of particles had a velocity component in the direction of the instrument. As a result, the power of radiation scattered by particles lies in the spectrum of a scattered signal at the Doppler frequency f_D determined by the velocity component in the direction of instrument $f_D = 2v_D/\lambda$, which is clearly seen for the particle volume density $C = 0.28\%$. However, as the particle density grows (Figure 10.17(b),(c)), the form of a spectrum essentially changes and, along with the Doppler components, the additional component appears in the spectrum, which is concentrated near ‘zero’ frequencies (for $C = 4.5\%$). The appearance of ‘zero’ frequencies in a spectrum in the case of moving scatterers can be physically related to the loss of temporal coherence of the scattered signal. This makes impossible the phase detection of a signal with the purpose of obtaining information on the object velocity based on the Doppler effect.

The presentation of results in the bilogarithmic coordinate system (Figure 10.17(c)) reveals an interesting point – the spectrum of an ‘incoherent’ component obeys the exponential law of ‘ $-5/3$ ’ in the frequency band of 20–200 Hz. Moreover, the range of spatial frequencies k , where the spectrum obeys the ‘ $-5/3$ ’ law in the backscattering mode, is exactly the same as in the case of radiation transmission within the line-of-sight limits (by exposure to microwave radiation) (see Figure 10.16). It can be supposed that, both in the bistatic and in the scatterometric mode of measurements, the fluctuations of intensity have an identical nature. The exponential law in the spectrum of scattering, as well as the gamma distribution of intensity amplitudes, can be treated as the result of scattering from the fractal, geometrically bound structure (or from a turbulent-vortex space) in a volume body of discrete flow (Lakhtakia *et al.*, 1987; Varadan *et al.*, 1983).

The analysis of calculated and experimental data indicates that there exists a quite specific (critical) value of the distance between absorbing scatterers ($d/\lambda \leq 1.5$), which makes a basic rearrangement of both average values of electro-dynamical parameters, and the fluctuation mode.

It is of interest to compare the experimental results with the electrostatically closely dense medium condition, obtained theoretically in the book by Rytov *et al.* (1978):

$$n\alpha \geq 1, \quad (10.80)$$

where n is the average density of scatterers and α is the polarizability of particles, which in the Rayleigh approximation is equal to

$$\alpha = r^3 |(\dot{\epsilon} - 1)/(\dot{\epsilon} + 2)|, \quad (10.81)$$

where ϵ is the complex dielectric constant of the scatterer’s material. Condition (10.80) describes physically the contribution of induced dipoles, closest to an

original particle, to the effective field. So, taking into account, for a critical value of $d = 1.5\lambda$, $n \approx 2.6 \text{ cm}^3$, we have

$$n|\alpha| = 1.2 \times 10^3 \ll 1.$$

Thus, long before satisfying the condition (10.80) the dense discrete medium basic changes its properties and becomes similar, in a certain sense, to a continuous medium with fluctuating parameters.

It is interesting to note that seemingly similar physical structures (a set of hollow aqueous spheres) manifest themselves, however, in a quite opposite manner: even a compact, dense packing of scatterers of such a type does not make any noticeable contribution to the electrodynamics of a system, owing to a very weak effect of interaction between single structures. Each of hollow aqueous spheres represents an almost black-body emitter, which does not possess any noticeable scattering properties and does not interact with surrounding components of a system (Raizer and Sharkov, 1981).

11

Selective radiation

This chapter considers the basic energy concepts, including the detailed equilibrium principle, and the basic mechanisms of selective radiations underlying the quantum model of radiative transfer theory (RTT). The chapter presents the analysis of basic equations and fundamental concepts required for studying radiative transfer in gas media. The total solution of the equation of radiative transfer, given in the present chapter, has been widely used in considering radiative transfer in the terrestrial atmosphere. The main attention is given to the analysis of solutions of radiative transfer theory intended for studying radiative transfer processes in the microwave band.

11.1 MECHANISMS OF SELECTIVE RADIATION

The direct use of results of a macroscopic version of radiative transfer theory, investigated in Chapters 9 and 10 for quantum systems, cannot apparently give satisfactory results by virtue of the physical character of the methodological approach itself. Whereas researchers understood this circumstance for the optical and IR bands at the beginning of the twentieth century, for the microwave band the features of transmission in gas media became topical only at the end of the 1940. This has been associated with intensive exploration of the short-centimetre and millimetre bands for the tasks of meteorology, radar, radio-astronomy and, a bit later, for remote sensing of the terrestrial atmosphere (Zhevakin and Naumov, 1967; Kislyakov and Stankevich, 1967; Tseitlin, 1966; Staelin, 1969; Kondratyev and Timofeev, 1970; Malkevich, 1973; Rosenkranz, 1975; Skolnik, 1980; Brown, 1999). A significant step in this direction was made in 1945 by R. Dicke, who discovered the microwave (in the centimetre band) radiation of the properly terrestrial atmosphere using the modulation method of noise radiation reception proposed by himself (see Chapter 2).

Unlike in the macroscopic systems, radiation processes in quantum systems should be investigated from a different viewpoint, namely, using the photon model of radiative transfer, as well as quantum notions on some atomic and molecular processes. The emission of radiation is a process of emitting the photons, and the absorption of radiation is the capture of photons by a quantum particle. Selective radiation arises in atoms and molecules at energy transitions from the upper levels downward, and selective absorption is the reverse process. According to quantum mechanics, the energy transition in transferring between energy levels ($E_2 > E_1$) is related to the frequency of emitted or absorbed radiation as follows: $E_2 - E_1 = h\nu = \hbar\omega$, where h is the Planck constant and $\hbar = h/2\pi$. In other words, a strictly fixed frequency corresponds to the transition between particular energy levels. Therefore, in the absence of any external phenomena the emission (and, accordingly, the absorption) spectrum of a quantum system will have the form of a delta-shaped line, which cannot be recorded by spectroscopic instruments. In reality, however, under real physical conditions the spectral lines of gases have a quite finite width and shape in the form of narrow lines and frequency bands. These types of radiation, caused by features of the internal structure and the internal dynamics of a quantum system, can be reliably recorded by spectroscopic instruments. We shall note here that it is the shape of radiation lines (or bands) that bears the basic information load on the physical state of gases.

Such a process, in which the atom or molecule absorbs or emits a photon, but neither ionization nor recombination of ions and electrons takes place, is called the bound-bound absorption or emission. The atom or molecule transfers from one quantified energy state to another. This can be rotational, vibrational or electronic states in molecules and electronic states in atoms. Since the bound-bound transitions correspond to particular discrete energy levels, the absorption and emission coefficients will have sharp peaks in frequency dependence in the form of a series of spectral lines. Usually, the molecule has a ‘grid’ of electronic levels (and, accordingly, frequency peaks), which are spaced both far from each other and close to each other. These levels represent, basically, rotation-vibration levels of energies. Since these selective lines have a finite width owing to various broadening factors, in some cases (as, for example, for oxygen emission lines in the terrestrial atmosphere) separate lines ‘merge’ into the frequency bands and sometimes have a very complicated shape.

If the atom (or molecule) absorbs an external photon, whose energy is sufficient to cause ionization, a generated ion and free electron can have arbitrary kinetic energy. Therefore, the coefficient of bound-free absorption represents a continuous function of frequency, until the energy of an external photon is sufficient for atom ionization. The reverse process is called free-bound emission (recombination). In this case the ion and free electron recombine, releasing a photon, and the energy of the generated atom corresponds to that of discrete bound states. The free emission forms a continuous spectrum, since the recombining particles can have arbitrary kinetic energy. The recombination of quantum systems into electronic levels with high values of the principal quantum number and subsequent cascade processes to underlying levels result in the formation of lines, which are called recombination lines. This type of microwave line plays a major part in radio-astronomy when

studying the interstellar medium structure (Sunyaev, 1986). It is virtually impossible to realize the conditions for generating recombination radio lines under terrestrial conditions directly.

The full picture of radiation (and, accordingly, absorption) spectra of quantum systems can be very complicated – it can either include separate lines, or form bands, or possess a continuous spectrum. So, the electronic spectra, caused by changing electronic motion, cover the ultraviolet and visible regions, the vibration spectra – near- and medium-infrared regions, and the rotational spectra – the far infrared and the microwave parts of spectrum. Some part of these lines can be ‘immersed’ in a continuous spectrum. The theory of molecular and atomic spectra and the experimental spectroscopic results are outlined in a series of monographs (see, for instance, Penner, 1959; Chandrasekhar, 1960; Sobolev, 1963; Basharinov *et al.*, 1968; Siegel and Howell, 1972).

The selective radiations of elementary quantum oscillators (atoms and molecules) in the microwave band are related to the presence of discrete energy levels having rather small differences of levels, of the order of some hundredth or thousandth fractions of an electronvolt. So, the quantum with frequency of 2.4×10^{14} Hz will correspond to an energy drop of 1 eV (see Appendix A, Table A.6). And, accordingly, the quantum of centimetre-band radiation with frequency of 24 GHz (a wavelength of 1.25 cm) will possess energy of 10^{-4} eV. It is important to note also that the energy of a quantum can also be presented in the temperature scale; that is to say, when quantity kT is expressed in eV, then the temperature $T = 11\,600$ K corresponds to the value of $kT = 1$ eV. And then the absolute temperature of ~ 1.2 K can be put in correspondence with the quantum of centimetre-band radiation with a frequency of 24 GHz.

Responsible for radiation in the microwave band are quite specific energy transitions, namely:

- electronic atomic transitions between close levels with high quantum numbers;
- transitions between molecular rotational levels and rotation–vibration levels;
- transitions between atomic and molecular levels of fine and superfine structure.

The intensity of spontaneous radiation of a set of oscillators is determined by the intensity of transition (the force of an oscillator) and the population of emitting levels. The form of radiation lines depends on the temperature of oscillators and on their interaction with an ambient medium. Under equilibrium conditions the population of energy levels is determined by the Boltzmann distribution, and only under this condition, according to the Kirchhoff law (recall that this is a direct consequence of the fluctuation–dissipation theory, FDT), there exists an unambiguous relation between the emissivity and absorptivity of a quantum system. For a set of quantum particles at the equilibrium state, the detailed equilibrium principle proposed in 1916 by A. Einstein is valid. Using these backgrounds and supplementing them with a photon model, we can proceed now to the microscopic formulation of the equation of radiative transfer for quantum systems.

11.2 THE DETAILED EQUILIBRIUM PRINCIPLE

Consider the bound–bound transitions in an absorbing medium subjected to the effect of incident radiation with spectral intensity $I(\Omega)$. For the sake of simplicity we shall consider the medium to consist of atoms not interacting between each other and having two energy levels ($E_j > E_i$). Assume also the medium to be enclosed inside a black envelope at constant temperature – this is the equilibrium radiation condition (see section 4.4). The atom in a medium can absorb the energy of incident radiation and, as a consequence of this, it can execute transition from energy state i to state j . Therefore, the state j will possess a greater energy than the state i , or, in other words, the state j is ‘excited’ with respect to i . The number of transitions per time unit from the level i to j depends on the incident radiation intensity and on the population of the state i . Let n_i be the number of atoms in a unit volume at state i . We introduce now the Einstein coefficient B_{ij} , which is determined as the probability of transition per unit of time in a unit volume from state i into state j under an effect of the incident radiation flux in a unit of solid angle, and is a function of the considered set of atoms only. Thus, with regard to the radiation flux, falling from all directions, the number of transitions per unit of time will be equal to

$$\left(\frac{dn_i}{dt} \right)_{i \rightarrow j} = B_{ij} n_i \int_{\Omega=4\pi} I(\Omega) d\Omega \quad (11.1)$$

Since the Einstein coefficients depend only on states i and j of a particular set of atoms, they can be taken out of the sign of the integral over a solid angle.

The number of transitions from the excited state j to the initial state i depends on two factors. These factors are: spontaneous radiation, which depends on population n_j at the excited state, and induced (stimulated) radiation, which depends on population n_j and on the radiation field strength. So, we introduce A_{ji} as the probability of transitions by spontaneous radiation in a unit of solid angle, and we shall consider B_{ji} to be the probability of transitions at induced radiation. Then the number of transitions from state j to state i will be equal to

$$\left(\frac{dn_j}{dt} \right)_{j \rightarrow i} = 4\pi n_j A_{ji} + n_j B_{ji} \int_{\Omega=4\pi} I(\Omega) d\Omega \quad (11.2)$$

Since for a set of randomly oriented, emitting atoms, at the equilibrium state, the spontaneous radiation is isotropic on the average, then $4\pi A_{ji}$ is the probability of transition from state j to state i by spontaneous radiation of energy over all directions.

For a set of atoms, at the equilibrium state, the detailed equilibrium principle proposed by A. Einstein is valid. The essence of this principle consists in the fact that at the equilibrium state the rates of direct and reverse transitions between any two states should be equal, if all transition processes are taken into account. Therefore, quantities dn/dt in equations (11.1) and (11.2) are equal, i.e.

$$B_{ij} n_i \int_{\Omega=4\pi} I(\Omega) d\Omega = 4\pi n_j A_{ji} + n_j B_{ji} \int_{\Omega=4\pi} I(\Omega) d\Omega \quad (11.3)$$

and in this case, under equilibrium conditions, in a supposed isothermal ideally black envelope, the radiation intensity is equal to the radiation intensity of an ideally black body $I_B(\nu, T)$ (see Chapter 6). For the equilibrium black-body radiation the intensity of an incident flux is also isotropic; therefore,

$$\int_{\Omega=4\pi} I_B(\nu, T) d\Omega = 4\pi I_B(\nu, T) \quad (11.4)$$

Solving equation (11.3) with respect to $I_B(\nu, T)$, we obtain

$$I_B(\nu, T) = \frac{A_{ji}}{(n_i/n_j)B_{ij} - B_{ji}} \quad (11.5)$$

Under thermal equilibrium conditions the populations of energy levels are related to each other according to the Boltzmann distribution law. If E_i and E_j are the energy states, then, according to the Boltzmann distribution law,

$$\frac{n_i}{n_j} = \exp \left[-\frac{E_i - E_j}{kT} \right], \quad (11.6)$$

where k is the Boltzmann constant. Since the difference of energies $E_j - E_i$ is equal to the photon energy, which is either absorbed or emitted, and, in accordance with this phenomenon, the transition from E_i to E_j or backwards takes place. Then, with regard to this circumstance, expression (11.5) can be rewritten as:

$$I_B(\nu, T) = \frac{A_{ji}}{B_{ij} \left(\exp(h\nu/kT) - \frac{B_{ji}}{B_{ij}} \right)}. \quad (11.7)$$

Comparing this expression with the expression for Planck's spectral black-body radiation intensity (6.2), we obtain the following relations between the Einstein coefficients:

$$B_{ij} = B_{ji}, \quad (11.8)$$

$$\frac{A_{ji}}{B_{ij}} = \frac{h\nu}{2\pi^2 c_0^2} = I_B(\nu, T) (\exp(h\nu/kT) - 1). \quad (11.9)$$

Although up to the time of the derivation of these relations induced radiation has not been found experimentally, the analysis based on equations (11.2) and (11.3) convincingly indicates that it does really exist. If we discard the term that takes into account the induced radiation in equation (11.3), and then carry out the analysis in the same order, then, according to Einstein's derivation, the final equation will be as follows:

$$I_\nu(\nu, T) = \frac{2h\nu}{c_0^2 \exp(h\nu/kT)}. \quad (11.10)$$

It can be shown by simple comparison, that the relation obtained is none other than the Wien radiation law (see relation (6.9)). Thus, it is the comparison of Einstein's derivation with Planck's formula that was a decisive theoretical factor for the

assertion of the existence of induced radiation. But only in 1954 did the special experiments on the amplification and generation of microwave electromagnetic radiation at the wavelength of 1.24 cm, using beams of ammonia (NH_3) molecules and a specially produced population inversion, make it possible to finally prove the existence of induced radiation (Prochorov, 1984).

11.3 THE PHOTON MODEL AND THE TRANSFER EQUATION FOR QUANTUM SYSTEMS

The radiation field and radiative transfer for quantum systems can be sequentially described by means of the photon model. It is useful both in studying the physics of radiative transfer in quantum systems, and in using numerical calculation schemes, for example, the Monte Carlo method (Marchuk, 1976).

11.3.1 Photon model

In considering radiation as a set of photons, the conditions at any point of a medium are specified by means of the function f of the distribution of photons.

Let

$$f(\nu, \mathbf{r}, S) d\nu dV d\Omega \quad (11.11)$$

be the number of photons moving in the direction S in the volume dV with coordinate \mathbf{r} in the frequency range $d\nu$, that includes frequency ν , inside the solid angle $d\Omega$, whose axis coincides with the direction S . Each photon possesses energy $h\nu$. Then the radiation energy in a unit volume and in a unit of frequency range is equal to the integral from quantity $h\nu f(\nu, \mathbf{r}, S) d\Omega$ over all solid angles. It is called the volume density of monochromatic radiation energy and is written in the form:

$$U_\nu(\nu, \mathbf{r}) = h\nu \int_{4\pi} f(\nu, \mathbf{r}, S) d\Omega \quad (11.12)$$

To determine the radiation intensity it is necessary to know the radiation flux in the direction S that intersects the site dA perpendicular to the direction S . The velocity of photons is equal to c , and the density of a flux of photons that intersects the site dA in the direction normal to it, equals $f d\nu d\Omega$. Then the number of photons, intersecting the site dA in the direction S per unit time, is equal to $cf d\nu d\Omega dA$. The energy, transferred by these photons, will be equal to $h\nu cf d\nu d\Omega dA$. By the spectral intensity of radiation we mean the energy of radiation, transferred in the given direction per unit of time through the unit site perpendicular this direction, in a unit of a solid angle and in a unit of frequency range. Then the radiation intensity at point r in the direction S is written in the form:

$$I_\nu(\nu, \mathbf{r}, S) = h\nu cf(\nu, \mathbf{r}, S) d\Omega. \quad (11.13)$$

Excluding f from (11.12) by means of (11.13), we shall find the relation between

the volume density of radiation energy and radiation intensity:

$$U_\nu(\nu, \mathbf{r}) = \frac{1}{c} \int I_\nu(\nu, \mathbf{r}, S) d\Omega \quad (11.14)$$

This integral is often used in studying the density of the integral radiation flux.

11.3.2 Transfer equation

The transfer equation for macroscopic systems was derived in section 9.3. Now we shall consider it from the microscopic point of view, using the physical concepts on a detailed equilibrium and a photon model. The pencil of beams with intensity $I_\nu(\nu, \mathbf{r}, S)$ passes through a gas along the path S . Let the atoms (or molecules) of gas be at one of two energy states i or j , where j is the excited state with respect to i , so that $E_j > E_i$. The volume densities of atoms at these states are equal to n_i and n_j , respectively. On the section dS of the path the losses or increments of energy determine the change of intensity on this section. If we neglect the scattering, then, in accordance with the Einstein model, the variations of intensity of the external flux will be conditioned by spontaneous radiation, absorption and induced radiation. In this case it can easily be thought that spontaneous and induced radiation will make a positive contribution to the change of a current intensity of the electromagnetic radiation flux. And, in its turn, the induced absorption will provide a negative contribution, or, in other words, the extraction of energy from the external flux. Applying the photon model and taking into consideration only transitions between two energy levels, we obtain the increment (per unit of path) of the beam intensity owing to spontaneous radiation, as a product of three quantities: a number of transitions per unit of time (or the probability of spontaneous transition A_{ji}), a number of particles n_i in a unit volume and the transition energy $h\nu$. Thus, we can write:

$$\frac{dI_\nu(\nu, \mathbf{r}, S)}{ds} = A_{ji}n_j h\nu. \quad (11.15)$$

Similar relations can be derived for induced radiation and absorption taking into account the circumstance that the flux is recorded in one direction only. Then the transfer equation will be as follows:

$$\frac{dI_\nu(\nu, \mathbf{r}, S)}{ds} = A_{ji}n_j h\nu + B_{ji}n_j I_\nu h\nu - B_{ij}n_i I_\nu h\nu. \quad (11.16)$$

Though, strictly speaking, the radiation of a considered system is not fully equilibrium, nevertheless, the Einstein coefficients obtained above can still be used, since they depend only on the energy states and on the considered set of atoms (rather than on the external radiation). Using relations (11.8) and (11.9), we obtain the final expression for the equation of radiative transfer in quantum systems:

$$\frac{1}{a_\nu} \frac{dI_\nu(\nu, \mathbf{r}, S)}{ds} = I_{\nu B}(\nu, T) - I_\nu(\nu, \mathbf{r}, S), \quad (11.17)$$

where

$$a_\nu = B_{ij}n_i h\nu (1 - \exp(-h\nu/kT)). \quad (11.18)$$

From comparison of the obtained equation with the equation for a macroscopic version of the transfer theory (9.22) it follows that the quantum version of the transfer equation fully corresponds to the transfer equation for absorbing and emitting macroscopic media (see relation (9.28)), and coefficient a_j is similar to the absorption coefficient in the macroscopic equation. If we discard the induced radiation in the Einstein approach (as was done in deriving relation (11.10)), then coefficient a_ν will contain only the terms in front of the brackets, and in this case it is called the true absorption coefficient a_ν^+ . It can be seen from (11.18) that the true absorption coefficient is directly proportional to two quantities, namely, the population of initial states of absorbing components n_i and coefficient B_{ji} , which determines the probability of transitions per unit of time from state i to state j . The calculation of population n_i , at least in the case of local thermodynamic equilibrium, is a problem of statistical mechanics.

The Einstein coefficients for many electronic transitions can be calculated by means of quantum mechanics, and, therefore, coefficient a_ν can be found on the basis of the microscopic approach. In determining the spectral absorption coefficient by the methods of statistical and quantum mechanics it is necessary to know the transition processes which can take place. As we have noted, in atoms and molecules of complicated structure such a great number of transitions is possible that researchers either restrict themselves to calculation of the most important transitions only, or try to apply the statistical or simplified model (Penner, 1959; Zhevakin and Naumov, 1967; Loudon, 1973).

11.4 MECHANISMS OF BROADENING OF SPECTRAL LINES

If a gas is non-dissociated and non-ionized, the internal energy of the gas (disregarding the energy of translational motion) is presented by discrete vibration, rotational and electronic energy states of atoms or molecules. The absorption of a photon can cause transition from one energy state of an atom or molecule into a state with higher energy. Since only discrete energy states participate in these transitions, only those photons with a strictly definite amount of energy can be absorbed. Therefore, the discrete transitions result in the absorption of the photons of strictly definite frequency, causing the appearance of dark lines in the transmission spectrum, i.e. the radiation transmitted through a layer of the investigated gas. For this reason such a process is called absorption in lines. According to the Kirchhoff law, the radiation of the same system will represent a linear radiation in the form of spectral lines. From the spectral approach viewpoint, such a type of absorption and emission can be presented in the form of a delta-shaped function (see Chapter 2). However, many physical conditions in which gases exist result in broadening the lines, which therefore have a finite frequency range with the centre at the

frequency of basic transition. The value of this range and the change of absorptivity (emissivity) within its limits (in other words, the shape of a line) depend on the physical process that causes spectral line broadening. For these reasons, the parameters of lines (or bands) of radiation contain valuable information on the physical state of gases. This information includes, for example, the physicochemical structure of a gas; the temperature and pressure in a gas medium; the relative velocity of motion of an object; the degree of deviation of gas medium conditions from the equilibrium (the degree of nonequilibrium); the possible actuation of other physical mechanisms; the inhomogeneity of distribution of parameters in a gas medium; and other features. Therefore, the shape of a line is the chief factor of interest for radioastronomy and remote sensing tasks. Some of the important broadening mechanisms are called natural broadening, Doppler broadening and collisional broadening (the broadening due to collisions).

11.4.1 The line shape

The variation of the absorption (emission) coefficient depending on frequency within the limits of a broadened single spectral line is called the line shape. The shape of a typical spectral line is presented in Figure 11.1. The central part of a line is sometimes called the line nosing, and the descending branches of a curve, which are far from the central frequency, are called the line wings. Because of the great physical importance of the line shape it was accepted as being expedient to introduce the integrated absorption coefficient S_{ij} for a single line, which presents the integral over the total frequency band (here the integration is possible both over the circular frequency $\omega = 2\pi\nu$ and over the frequency ν):

$$S_{ij} = \int_0^{\infty} a_{\omega}(\omega) d\omega = \int_0^{\infty} a_{\nu}(\nu) d\nu \quad (11.19)$$

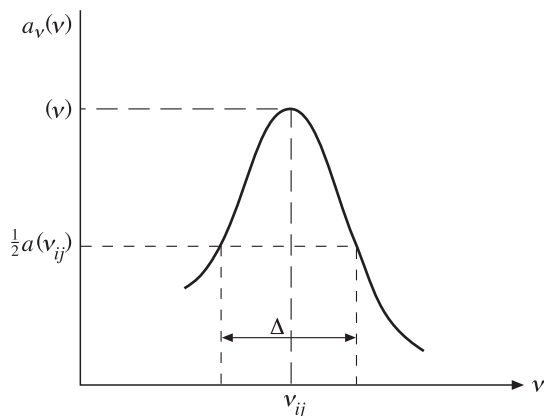


Figure 11.1. Schematic sketch of single spectral line shape. Notation is explained in the text.

and the line-shape parameter with a natural normalization:

$$b_{ij}(\omega) = \frac{a_\omega(\omega)}{S_{ij}}; \int_0^\infty b_{ij}(\omega) d\omega = 1. \quad (11.20)$$

Often for the line-shape parameter the normalization is carried out for the value of $b_{ij}(\omega_{ij})$ at the central transition frequency.

Note that these definitions result in the simple relation:

$$\frac{b_{ij}(\omega)}{b_{ij}(\omega_{ij})} = \frac{a_\omega(\omega)}{a_\omega(\omega_{ij})}, \quad (11.21)$$

which means saving the line shape at its normalization.

One of the important quantitative characteristics of the line shape is the ‘full’ half-width of the line, designated by Δ . This parameter represents the line width (in the units of frequency in the given consideration) at the middle of a maximum height of the line (Figure 11.1). Such an approach ensures the unambiguous choice of a definite line width required for describing its properties. Since quantity $a_\omega(\omega)$ asymptotically tends to zero with increasing difference $|\omega - \omega_{ij}|$, it is rather difficult (and sometimes impossible) to define the line width in terms of frequencies, at which quantity $a_\omega(\omega)$ becomes close to zero. Since different terminology can be used in various literature sources, particular care should be exercised in applying the line width notion. So, the line-shape parameter is sometimes defined in the system of ‘true’ (noncircular) frequencies, and by the line width is meant the ‘full’ half-width of the line with the numerical factor of one half (Zhevakin and Naumov, 1967). From the normalization condition (11.20) it follows that $b_\nu(\nu) = 2\pi b_\omega(2\pi\nu)$, and also $a_\nu(\nu) = 2\pi a_\omega(2\pi\nu)$.

Generally speaking, the contours of spectral lines are determined by many perturbation influences, which have an effect on the magnitudes of the energy levels of an emitting quantum system (atom or molecule). Below we shall consider three basic and most physically clear broadening mechanisms, as well as the line shapes stipulated by them.

11.4.2 Natural broadening

The natural broadening of a line is closely associated with Heisenberg’s uncertainty principle, according to which:

$$\Delta E_j \Delta t_j \sim \frac{\hbar}{2\pi}, \quad (11.22)$$

where ΔE_j and Δt_j imply, respectively, the indeterminacy in energy of the upper level, from which the transition occurs, and the indeterminacy in time, during which the quantum system exists at this (excited) level. In the absence of the external field of radiation Δt_j can be identified with the variations of an emissive (fluorescent) lifetime of the considered transition. The physical sense of this parameter is as follows: if the external flux saturating a quantum system is ‘switched off’, then

excited atoms (molecules) will return into the basic state, and the stored energy will be scintillated in the form of a flux of quanta. The number of atoms at excited state N_j and, therefore, the intensity of an emitted flux, will decrease as

$$N_j = N_j^0 \exp(-A_{ji}t) \quad (11.23)$$

In this case $\tau_R = (1/A_{ji})$ and is called the emissive (fluorescent) lifetime. The observation of this fluorescent radiation is just the experimental method of measuring the Einstein coefficient A_{ji} .

The relationship, similar to (11.22), takes place for the lower energy state as well. Therefore, the indeterminacy in the transition frequency will be equal to

$$\Delta\nu = \frac{1}{h}(\Delta E_j + \Delta E_i) = \frac{1}{2\pi}(\gamma_j + \gamma_i), \quad (11.24)$$

where γ_j and γ_i designate the reverse lifetimes of levels. It follows from this relation that the indeterminacies in an emitted frequency and, accordingly, the width of a spectral line, will be related to indeterminacies of energy levels, and also they will be inversely proportional to lifetimes at two energy states. As follows from the quantum mechanics (Penner, 1959), the density function (the probability) of the fact that the energy of a system at any ‘blurred’ m-state lies between E and $E + \Delta E$, is equal to:

$$W(E) dE = \frac{\gamma_m}{h} \frac{dE}{\left(\frac{2\pi}{h}\right)^2 (E - E_m)^2 + \left(\frac{\gamma_m}{2}\right)^2}. \quad (11.25)$$

If we designate by $J(\nu)$ the probability of observation of the radiation frequency lying between ν and $\nu + d\nu$, and integrate (11.25) over all possible values of E , then we obtain the following expression for $J(\nu)$:

$$I(\nu) d\nu = \frac{\gamma_i + \gamma_j}{4\pi^2(\nu - \nu_{ij})^2 + \frac{1}{4}(\gamma_i + \gamma_j)^2}. \quad (11.26)$$

The physical sense of the obtained expression consists in the fact, that it describes the shape of a line of emission (absorption) for the transition under the natural broadening conditions. From this expression it is possible to obtain the line-shape parameter (11.20) in the form of the so-called Lorentz shape (or resonance) line (in circular frequencies):

$$b_{ij}(\omega) = \frac{\Delta_n/(2\pi)}{\Delta_n^2/4 + (\omega - \omega_{ij})^2}. \quad (11.27)$$

It can easily be seen from this expression, that the line shape is symmetrical with respect to ω_{ij} in the units of frequency and depends on the line half-width Δ_n and on the transition frequency ω_{ij} . The maximum value of the line shape at the transition frequency will be

$$b_{ij}(\omega_{ij}) = \frac{2}{\pi} \Delta_n, \quad (11.28)$$

and the integral is

$$2 \int_{\omega_{ij}}^{\infty} \frac{\Delta_n/2\pi}{\Delta_n^2/4 + (\omega - \omega_{ij})^2} d\omega = 1, \quad (11.29)$$

which corresponds to the normalization condition for the line shape (see expression (11.20)).

The physical sense of a half-width of the line under natural broadening can be understood by comparing expressions (11.27) and (11.26). The value of the half-width of a line (in circular frequency units) is determined by the finite lifetime of an excited state: $\Delta_n = \gamma_j = 1/\tau_R$. The numerical values of lifetimes of atoms and molecules lie in a very wide band – for electronic transitions they lie between 10^{-9} and 10^{-6} s, and in vibrational transitions they have the order from 10^{-3} to 10^{-1} s. And, accordingly, for lifetimes of the order of 10^{-8} s the half-width of a line (in frequency units) will be lower than 10 MHz.

11.4.3 Doppler broadening

The atoms or molecules of absorbing or emitting gas are not at the stationary state, but have some definite distribution of velocities related to the energy of their thermal motion. If for a motionless atom or molecule the frequency of light, emitted or absorbed in the given transition, is equal to ω_{ij} , then the frequency of electromagnetic radiation, absorbed or emitted by a molecule moving at velocity v_x in the direction of a line of sight, is equal, according to the Doppler principle, to

$$\omega = \omega_{ij} \left(1 - \frac{v_x}{c}\right). \quad (11.30)$$

It is known from statistical mechanics that at the thermal equilibrium state and in the absence of an external field of force the distribution of velocities of a homogeneous ideal gas obeys the Maxwell distribution law. The latter can be written both for velocity vector magnitudes (in three-dimensional space), and for projections of a vector of velocities on selected directions (on the one-dimensional axis x , for example). Note also that the Maxwellian distribution of molecules over velocities can also be established as a result of mutual collisions between molecules in their chaotic thermal motion. Various forms of this distribution are used in various physical investigations. So, in the case of remote sensing we have a situation where the observer perceives radiation propagating along a single coordinate axis. In this case the velocities of interest are directed along this axis, either towards the observer, or away from him (i.e. along the velocity vector projection on the observation axis).

According to the classical Maxwell model, the number of particles dn , having velocity magnitude in the range from v up to $v + dv$, is determined by the expression:

$$\frac{dn}{n} = \left(\frac{m}{2\pi k T}\right)^{3/2} \exp(-mv^2/2kT) 4\pi v^2 dv. \quad (11.31)$$

Here v is the magnitude of a particle's velocity, m is the particle mass, k is the

Boltzmann constant, T is the absolute temperature of a thermostat where the particles in the total quantity of n are enclosed. It can easily be seen that the distribution is valid for $v \geq 0$ and belongs to the gamma distribution type. However, the distribution for the velocity vector projection on the chosen direction has an essentially different character and can be obtained using the well-known transformation in probability theory (Feller, 1971) that forms an analytical relationship between the density function p_v of the length of a random vector in three-dimensional space and the density p_x of the length of its projection in a fixed direction:

$$p_x(t) = \int_t^\infty p_v(y) \frac{dy}{y}. \quad (11.32)$$

The reverse transformation can also be obtained:

$$p_v(t) = -tp'_x(t), t > 0. \quad (11.33)$$

Applying the first transformation for distribution (11.31), it can be shown that the projections of random vectors in space on any axis of any Cartesian system have a normal density with zero expectation. Thus, at the thermal equilibrium state the fraction dn/n of molecules whose velocity projections in the given direction (the observation direction is axis x) lie between v_x and $v_x + dv_x$, is equal to

$$\frac{dn}{n} = \left(\frac{m}{2\pi kT} \right)^{1/2} \exp \left(-\frac{mv_x^2}{2kT} \right) dv_x, \quad (11.34)$$

which corresponds to the normal distribution with zero expectation. It is interesting to note that in his study of the velocity distribution of molecules in three-dimensional space Maxwell has proceeded from the opposite approach. That is to say, he supposed that in any Cartesian coordinate system three velocity components represent independent random variables with zero expectation. And this circumstance entails the Maxwell distribution over velocities (11.31) by means of transformation (11.33).

Using (11.30) and (11.31), we eliminate v_x and determine the numerical value of a fraction of molecules emitting in each elementary increment of the frequency range owing to the Doppler broadening. As a result, we obtain the formula of a spectral line corresponding to the Gaussian shape of distribution, i.e.

$$b_{ij}(\omega) = \frac{2\sqrt{\ln 2}}{\sqrt{\pi}\Delta_D} \exp \left[-4(\omega - \omega_{ij})^2 \frac{\ln 2}{\Delta_D^2} \right], \quad (11.35)$$

where Δ_D is the ‘full’ half-width of the line at the Doppler broadening. The shape parameter $b_{ij}(\omega)$ depends only on Δ_D and the transition frequency ω_{ij} , where

$$\Delta_D = \frac{2\omega_{ij}}{c} \left(\frac{2kT}{m} \ln 2 \right)^{1/2} \quad (11.36)$$

that is, Δ_D depends on ω_{ij} , T and m . The dependence of Δ_D on $T^{1/2}$ indicates that the Doppler broadening is essential at high temperatures.

The relations obtained above have been derived under the assumption of the absence of relative velocities between the observer's coordinate system and the emitting gas medium. If, however, such velocities do take place (as, for example, for space objects observed from the Earth), then the Doppler shift will be observed as the change of the basic transition frequency and, therefore, of the frequency shift of the whole line.

11.4.4 Collisional broadening

The classical theory of collisional broadening rises from electronic theory, developed by H. Lorentz in 1905–1906. This theory, in describing an absorbing system, uses the notion of attenuating oscillations of a linear oscillator with a finite attenuation coefficient.

Collisions between the atoms (or molecules) in a gas medium can be an important source of broadening of the line of emission (absorption). A comprehensive analysis of collisional broadening is fairly complicated (Penner, 1959; Loudon, 1973). Here we shall consider only those details of the physical process of collisional broadening which are necessary for illustrating the nature of this mechanism. The main attention will be given to the same pair of energy states, which has been used previously. In the present case, however, we shall disregard the Doppler and natural (emissive) contributions to the line width; therefore, the quantum particles emit the wave at a fixed frequency. Disregarding an emissive line width is equivalent to the supposition that the emissive lifetime is high as compared to the mean time between collisions of quantum particles. Let us consider a single excited atom that emits light at frequency ν_{ij} . One can imagine that the wave train of electromagnetic radiation is continuously emitted by the atom so long as it undergoes collision. During collision the energy levels of an emitting atom are shifted by the effect of forces of interaction between two colliding atoms. Therefore, during collision the emitted wave train is interrupted. When the wave with frequency ν_{ij} is restored after collision, all its characteristics coincide with the characteristics of this wave before collision, except the phase, which is not bound to the wave phase before collision. If the duration of collision is fairly short, then any radiation emitted during collision can be neglected, whereas the frequency of light is shifted relative to ν_{ij} . In this case the collisional broadening effect can be adequately described on the basis of a model in which each excited atom always emits at frequency ν_{ij} . However, during each collision the phase of an emitted wave randomly changes. The observed scattering of emitted frequencies is stipulated by the fact that the wave breaks into finite trains, whose Fourier components contain, among others, the frequencies which differ from the true value of ν_{ij} . The wave train, emitted by a single atom, is depicted schematically in Figure 11.2, which shows the time dependence of the electric field amplitude $E(t)$ at a fixed observation point. The collision time is designated by the vertical line, which is followed by the random change of the wave phase. According to the kinetic theory of gases (see Loudon, 1973; Prochorov, 1984), the probability $p(\tau) d\tau$ of the fact that the time of free path of an atom (molecule) lies in the interval from τ to

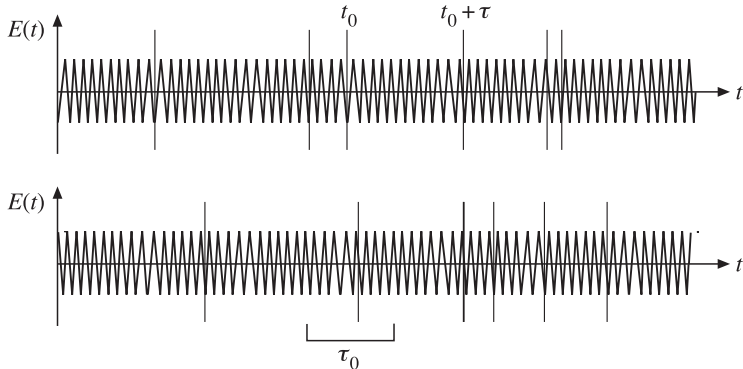


Figure 11.2. Schematic presentation of an electrical field amplitude in the form of oscillation intervals, emitted by a single atom. Vertical lines denote collisions, separated by free run times, the average time of which is shown as τ_0 .

$t + dt$, is determined by the expression

$$p(\tau) d\tau = \left(\frac{1}{\tau_0} \right) \exp\left(-\frac{\tau}{\tau_0}\right) d\tau, \quad (11.37)$$

where the mean free path time τ_0 (s) can be written as

$$\tau_0 = 3 \times 10^{-10} \frac{P_0}{P}. \quad (11.38)$$

Here P and P_0 are the values of pressure at the studied altitude and on the ground, respectively. Free path times in Figure 11.2 are chosen in accordance with the probability distribution presented in (11.37). Let us consider a period of the free path time of an atom beginning at time t_0 and with duration τ . From the Maxwellian electrodynamics point of view, the complex amplitude of the radiation field can be written as follows:

$$E(t) = E_0 \exp[-j\omega_{ij}t + \varphi], \quad t_0 < t < t_0 + \tau, \quad (11.39)$$

where φ is the wave phase for the given free path, and E_0 and ω_{ij} are the same for any free path. The field $E(t)$ in (11.39) can be presented in the form of spectral presentation as the Fourier integral (see Chapter 2). Then the amplitude of a complex spectrum at arbitrary frequency ω is determined as:

$$\dot{S}(\omega) = \frac{1}{2\pi} \int_{t_0}^{t_0 + \tau} E(t) \exp(j\omega t) dt = \frac{E_0}{2\pi} \exp[j(\omega - \omega_{ij})t_0 + \varphi] \frac{\exp[j(\omega - \omega_{ij})\tau]}{j(\omega - \omega_{ij})}. \quad (11.40)$$

It follows from this relation, that the Wiener spectrum (the spectral intensity) of

radiation of a train of oscillations can be written as

$$G_\tau(\omega) \cong |\dot{S}(\omega)|^2 = \left(\frac{E_0}{\pi}\right)^2 \frac{\sin^2[(\omega - \omega_{ij})\tau]}{(\omega - \omega_{ij})^2}. \quad (11.41)$$

The frequency dependence of a train of oscillations with the limited generation time is proportional to the well-known dependence $(\sin x/x)^2$. However, at any time the total intensity of radiation of a gas medium consists of the contributions from a great number of excited atoms (molecules). The free path times of different atoms are distributed according to the expression for the probability (11.37). As a consequence, for finding the total intensity of radiation of a medium the value of intensity of radiation of a train of oscillations should be multiplied by the probability (11.37) and integrate the result over all values of τ :

$$G(\omega) = \int_0^\infty G_\tau(\omega)p(\tau) d\tau \cong \frac{1}{2} \frac{1}{(\omega - \omega_{ij})^2 + (1/\tau_0)^2}. \quad (11.42)$$

Therefore, the frequency distribution of the emission line with collisional broadening has the Lorentz shape characterized by the width of $2/\tau_0$. Now we estimate the length of a train of oscillations for microwave radiation under terrestrial atmospheric conditions. So, for the gas density, corresponding to the pressure of 10^5 Pa (the sea surface level) at a temperature of 20°C the mean value of time of collisions is 3×10^{-10} s. For radiation with the wavelength of 1 cm (30 GHz) the wave period will be 3×10^{-11} s, and, thus, the train of oscillations for a collisional mechanism will be generated by ten oscillations of the electromagnetic wave only. At the same time, for natural broadening the train of oscillations will be equal to 1000 and more wave periods and, accordingly, the line stipulated by this type of broadening will be at least 100 times narrower than the line of collisional broadening.

A more detailed study results in the following expression for the line shape parameter:

$$b_{ij}(\omega) = \frac{\Delta_C/2\pi}{\Delta_C^2/4 + (\omega - \omega_{ij})^2}, \quad (11.43)$$

i.e. it has the same shape as at natural broadening.

The ‘full’ half-width Δ_C is determined by the frequency of collisions (or by the mean free path time), and its approximate value can be found from the kinetic theory of gases

$$\Delta_C = 8\sqrt{\pi}D^2 P(MkT)^{-1/2}, \quad (11.44)$$

where D is the diameter of atoms or molecules, P is the pressure of one gas component. Note that the half-width value for the collisional mechanism (unlike the Doppler one) is proportional to the gas pressure and inversely proportional to $T^{1/2}$. Thus, the broadening due to collisions becomes a key mechanism at high pressures and low temperatures.

It is of interest to note that the subsequent detailed quantum-mechanical analysis of the collisional broadening mechanism has resulted in comparatively small variations (and only on the wings) of the line shape, which was obtained as

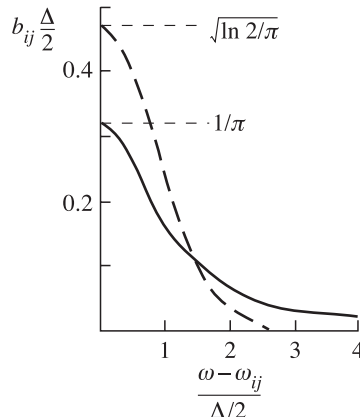


Figure 11.3. A line shape for Doppler (broken line) and Lorentzian (solid line) broadenings. Areas, bordered by each curve and coordinates axes, are equal.

early as at the beginning of the twentieth century by H. Lorentz proceeding from the classical concepts of the kinetic theory of gases (Penner, 1959; Zhevakin and Naumov, 1967).

The collisional broadening often represents a key mechanism in application problems of microwave radiation transmission through the terrestrial atmosphere; so, the other broadening mechanisms can be neglected in these cases. Figure 11.3 gives the comparison of the Doppler and Lorentz line shapes for the same values of their half-widths and the area restricted by the curves. As compared to the Doppler shape, the Lorentz shape has a smaller height at the line centre, but a greater height near the line wings. Even if the Doppler broadening is determining near the line centre, the collisional broadening is often an important mechanism in forming the line far from the line centre (on the line wings).

11.4.5 Compound shape of the line

The expressions for the widths of lines, excited by various mechanisms, indicate that, depending on the physical conditions in a gas medium (temperature, pressure), the widths of lines can vary within very wide limits. So, for example, under terrestrial atmospheric conditions up to the altitudes of the order of 50 km the mean value of the interval of Doppler broadening is essentially smaller than the lifetime at an excited state – on one hand. But, on the other hand, the relationship between the temperature and pressure are such that the collisions become a key factor in forming the width and shape of lines of emitting gases. At altitudes higher than 50 km the situation is just the opposite: the line shape is almost completely determined by the Doppler broadening mechanism. A similar situation takes place in the open space as well.

However, when the contributions of the Doppler, collisional and, probably, emissive broadening are comparable in magnitude, it is necessary to determine

the compound shape of a line, stipulated by these three simultaneously acting processes. Let us consider, first, the combination of mechanisms resulting in a line broadening which separately determine the line shape described by functions $F_1(\omega)$ and $F_2(\omega)$. The corresponding compound shape of a line is described by the function

$$F(\omega) = \int_{-\infty}^{\infty} F_1(x)F_2(\omega + \omega_0 - x) dx \quad (11.45)$$

Here ω_0 is the common central frequency for two distributions. The integral relation, presented above is none other than the convolution integral. Proceeding from physical considerations, one can say that the integration in (11.45) relates each frequency component of distribution F_1 with the broadened distribution that corresponds to the mechanism resulting in distribution F_2 . Obviously, by repeated applications of equation (11.45) it is possible to associate any number of mechanisms resulting in line broadening. Note also, that the final shape of a line does not depend on the order of associating the contributions, so that the value of the integral in (11.45) is invariant with respect to exchanging the places of functions F_1 and F_2 .

Now we carry out two curious examples. If two sources of broadening (for example, collisions between the molecules of various components of a gas medium) result in the Lorentz shapes of a line with widths Δ_{L_1} and Δ_{L_2} , then it can easily be seen, that the total line is also Lorentz one and has the width

$$\Delta_L = \Delta_{L_1} + \Delta_{L_2}. \quad (11.46)$$

However, if the broadening mechanisms result in the Gaussian shapes of lines with differing widths, Δ_{D_1} and Δ_{D_2} (for example, two identical gas components with different temperatures), then the compound line will also be Gaussian with the width determined, however, by the absolutely different relation:

$$\Delta_D^2 = \Delta_{D_1}^2 + \Delta_{D_2}^2. \quad (11.47)$$

11.4.6 Voigt line

Let us consider the important type of a symmetrical line contour, which arises as a result of simultaneous action of the Doppler and collisional mechanisms with the same central frequency. The analysis of a compound line indicates, that it is impossible to obtain the analytical expression for the line shape in this case. As usual, the form of this line is kept in the normalized integrated shape with a precision of constant coefficients (Penner, 1959):

$$F(\xi, a) = \int_{-\infty}^{\infty} \frac{\exp(-y)^2}{a^2 + (\xi - y)^2} dy, \quad (11.48)$$

where

$$a = \frac{\Delta_C}{\Delta_D} (\ln 2)^{1/2}; \xi = \frac{\omega - \omega_{ij}}{\Delta_D} (\ln 2)^{1/2}. \quad (11.49)$$

For the purposes of the practical use of this type of line detailed numerical tables were compiled. The corresponding line shape was called the Voigt line. It has a shape intermediate shape between the Lorentz and the Gaussian.

11.4.7 Model of bands

The gases usually dealt with in remote sensing tasks are either diatomic or polyatomic and, consequently, possess vibrational and rotational energy states, which are not peculiar to monoatomic gases. At moderate temperatures the transitions between vibrational and rotational states usually make the main contribution to the absorption coefficient in the most important regions of the thermal radiation spectrum.

With increasing temperature of gaseous systems (at burning of gases) the processes of dissociation, ionization and electronic transitions become more noticeable. So, the contribution of these processes into the absorption coefficient should also be taken into account. If the gas absorption coefficient is determined experimentally, the contributions from radiation in the lines and continuous radiation are summed. In calculating these coefficients it is necessary to analyse each absorption process separately and then to calculate the total coefficient by summing up the contributions from various processes as independent processes. As a rule, the rotational-vibrational bands of spectral absorption consist of a group of closely situated spectral lines appearing owing to transitions between vibrational and rotational energy states. The absorption lines in some parts of the spectrum are situated so close together, that in the majority of cases the single lines cannot be isolated by spectroscopic instruments. Owing to broadening, the lines either seem to be overlapping (because of the finite value of instrument's spectral resolution), or are overlapping in reality – the lines, while merging, generate the so-called absorption bands. The great number of possible energy transitions, which can result in the appearance of a set of spectral lines, is explained by the presence of a set of energy levels and transitions whose radiation frequencies can fall in quite different spectral intervals. The transitions between rotational levels of the same vibrational state correspond to small values of the difference in energies. Therefore, these transitions correspond to the lines within the limits of bands situated in the far-infrared and microwave regions. A principal feature of the microwave band is the presence of single absorption lines of major components of the terrestrial atmosphere – water vapour and oxygen. If the transitions from the rotational level in one electronic and vibrational state to the rotational level in the other electronic and vibrational state take place, then high values of the difference in energies are obtained, and the system of bands is formed in the high-frequency visible and ultraviolet regions of spectrum. The radiation bands are usually separated by the sections of the spectrum of relatively weak absorption. These sections of the spectrum are called the transparency windows.

A possible approach to the description of gas properties consists in studying the absorptivity of bands and lines separately and in deriving empirical relations describing the characteristic of each band. So, two models are widely used which represent

two extreme cases of the disposition of single lines and the intensity of emission in them.

In the Elsasser model all lines have identical Lorentz shape (equation (11.43)), as well as identical height and distance between the lines (and, therefore, an identical value of integrated absorption coefficient S_C for all lines). In this case quantity a_ω becomes a periodic function of frequency. This function depends on parameters determining the contour of the Lorentz lines, as well as on the distance, δ , between them. The absorption coefficient for any particular value of frequency is determined by summing the contributions from all adjacent lines. Summing all contributions with allowance for relation (11.43) that describes the Lorentz contour of a line, we obtain

$$a_\omega(\omega) = \frac{S_C}{2\pi} \sum_{n=-\infty}^{\infty} \frac{\Delta_C}{\Delta_C/4 + (\omega - n\delta)^2}. \quad (11.50)$$

According to the other model (the Mayer–Goody model), the vibrational–rotational band consists of a great number of non-uniformly (randomly) disposed lines having arbitrary distribution of intensity. According to this model, the position of lines and their intensity do not depend on each other.

Many additional difficulties arise in considering gaseous mixtures. For example, the partial pressure, p , of absorbing gas in a multi-component mixture varies depending on T and P ; the population of energy levels depends on temperature T , and the overlapping of spectral lines varies depending on pressure P . It is fairly difficult to formulate the analytical dependence of the line shape on T, p and P for the mixture of real gases. The getting of practically useful results largely depends on experimental investigations, and the theory is used as an indicator in this respect.

11.5 RADIATION TRANSMISSION THROUGH A GAS LAYER

We shall consider the problem of electromagnetic radiation transmission through a layer of gas having selective frequency properties. Earlier we obtained the basic equation of transfer theory for quantum systems (11.17). Here we shall present this equation for consideration (for the sake of simplicity and clarity) in the one-dimensional case, where the external radiation, possessing its specific (arbitrary, generally speaking) spectral characteristics $I_{\nu O}(\nu)$, passes through a layer of absorbing and emitting gas. This equation is as follows:

$$\frac{dI_\nu(\nu, s)}{ds} = a_\nu(\nu, s)I_{\nu B}[\nu, T(s)] - a_\nu(\nu, s)I_\nu(\nu, s). \quad (11.51)$$

The boundary condition in this case can be written as $I_\nu(\nu, 0) = I_{\nu O}(\nu)$. Dependencies $a_\nu(\nu, s)$ and $I_{\nu B}[\nu, T(s)]$ characterize the electrodynamic and thermal spatial features of the medium studied. Solving equation (11.51), for example, by the

well-known integrating multiplier method, for the given boundary condition, we obtain the following solution:

$$I_\nu(\nu, s) = I_{\nu O} \exp \left[- \int_0^s a_\nu(\nu, s') ds' \right] + \int_0^s a_\nu(\nu, s') I_{\nu B}[\nu, T(s')] \exp \left[- \int_{s'}^s a_\nu(\nu, s'') ds'' \right] ds'. \quad (11.52)$$

If we suppose that the pressure, temperature and structure of gas are constant in a medium, then $a_\nu(\nu)$ and $I_{\nu B}[\nu, T]$ do not depend on the coordinate, and equation (11.52) can be presented in the following, widely used, form:

$$I_\nu(\nu, s) = I_{\nu O} \exp(-a_\nu(\nu)s) + I_{\nu B}(\nu, T)(1 - \exp(-a_\nu(\nu)s)). \quad (11.53)$$

The multipliers of the values of intensities play an important part in remote sensing practice. For this reason they received their characteristic names. So, the spectral transmissivity factor $\Gamma(\nu)$ of homogeneous absorbing gas of thickness s , measured in the radiation transmission direction, is determined in the form of

$$\Gamma_\nu(\nu) = \exp(-a_\nu(\nu)s), \quad (11.54)$$

and the spectral absorptivity α_ν in the form of

$$\alpha_\nu(\nu) = 1 - \exp(-a_\nu(\nu)s) = 1 - \Gamma(\nu). \quad (11.55)$$

If we use the Kirchhoff law (Chapter 4) in the form of equality of the spectral absorptivity and spectral emissivity, then formula (11.55) will also characterize the spectral emissivity of a gas layer of thickness s .

In a number of cases (in the infrared and optical bands especially) the spectral properties of instruments are insufficient for separating the spectral absorption lines of gases. In this case it becomes necessary to consider the integral characteristics of intensity I in the finite band $\Delta\nu$ of an instrument:

$$I = \int_{\Delta\nu} I_\nu(\nu) d\nu = \int_{\Delta\nu} I_{\nu O} \exp(-a_\nu s) d\nu + \int_{\Delta\nu} I_{\nu B}(\nu, T)(1 - \exp(-a_\nu s)) d\nu. \quad (11.56)$$

If the frequency band $\Delta\nu$ contains a sufficient number of narrow lines and, at the same time, it is sufficiently small, so that it is possible to replace $I_{\nu O}(\nu)$ and $I_{\nu B}[\nu, T]$ in this frequency band by their average values $I_{\nu O}$ and $I_{\nu B}(T)$, respectively, then $I_{\nu O}(\nu)$ and $I_{\nu B}(T)$ can be taken out of the sign of integral, and equation (11.56) will take the form of

$$I = \overline{I_{\nu O}} \int_{\Delta\nu} \Gamma_\nu(\nu) d\nu + \overline{I_{\nu B}(T)} \int_{\Delta\nu} \alpha_\nu(\nu) d\nu. \quad (11.57)$$

The strict calculation of integrals in expression (11.57) is rather difficult even for simple types of lines, as, for example, for the Lorentz-type line. Special methods of calculating these integrals have been developed and improved, both for single lines and for Elsasser's, Mayer–Goody's and other types of models.

The analysis of expression (11.53) indicates that there exist two radically different forms of exhibiting spectral lines – in the form of so-called ‘absorption’ lines and ‘straight’ lines, depending on the type and conditions of the experiment.

11.5.1 The ‘cold’ layer approximation

This approximation is characterized (see section 9.3) by the fact that the external (with respect to the gas layer) radiation essentially exceeds the thermal radiation of a gas layer. In this case the radiation intensity at the gas layer exit can be presented as

$$I_\nu = I_{\nu O} \exp[-a_\nu(\nu)s]. \quad (11.58)$$

If the layer has small optical thickness $\tau_\nu = a_\nu(\nu)s \ll 1$, then the expression obtained is simplified

$$I_\nu = I_{\nu O}(1 - a_\nu(\nu)s). \quad (11.59)$$

It directly follows from this relation that, if the input electromagnetic signal possesses a broadband (and planar) spectrum, then the output signal will appear as an ‘inverted’ line (or absorption line) (Figure 11.4(a)). The ‘dark’ Fraunhofer lines in the optical bright spectrum of the Sun are an example of such lines.

If the layer is not semi-transparent and the optical path value exceeds the value of unity, then the form of the absorption line will be essentially distorted (Figure 11.4(a)). And, in its turn, the informative saturation of such a type of measurement will sharply decrease.

11.5.2 Thermal radiation approximation

In its turn, in the aforementioned approximation, only that component in expression (11.53) is considered, which is bound to thermal radiation. And, thus, we have the following expression for thermal radiation of a gas layer:

$$I_\nu = I_{\nu B}(\nu, T)[1 - \exp(-a_\nu(\nu)s)]. \quad (11.60)$$

In the case of a semi-transparent gas layer with a small optical thickness value the expression is simplified:

$$I_\nu = I_{\nu B}(\nu, T)a_\nu(\nu)s. \quad (11.61)$$

It follows from this expression that for a semi-transparent gas layer its spectral properties will be determined by multiplying the straight radiation line and the spectral form of an ideal black body (see Chapter 6). If the line is narrowband enough, then the $I_{\nu B}(\nu, T)$ value in the spectral range of the line can be presented by the average (constant) value, and then the radiation spectrum of gas will exactly correspond to the radiation line.

If the gas layer is not semi-transparent and the optical path value exceeds the value of unity, then the form of the straight line will be distorted, but in a

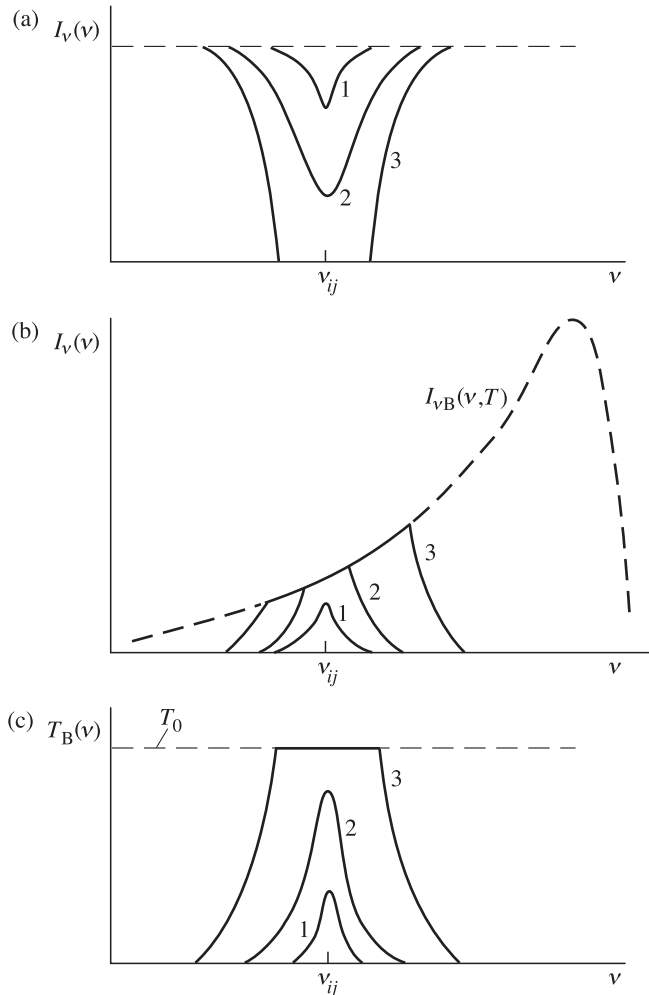


Figure 11.4. Schematic sketches of spectral intensity transfer by way of a gas layer: (a) intensity transmission through a gas layer (in cold layer approximation); (b) the spectral emission of a gas layer (in the form of an intensity); (c) the spectral radiobrightness temperature of a gas layer. Figures show gas layers with increased values of optical paths ($\tau_1 < \tau_2 < \tau_3$). $I_{\nu B}(\nu, T)$ is the Planck function.

completely different manner than in the case of absorption line distortion. That is to say, the straight line of gas radiation will seem to gradually fill in the spectral form of an ideal black body (Planck's function), until it is completely filled for $\tau \rightarrow \infty$ (Figure 11.4(b)). Thus, the radiation of any gas at very high optical thickness values corresponds to the black-body radiation, and the measurements carried out under such conditions will not yield any information on the physicochemical properties of the gas.

11.5.3 The Rayleigh–Jeans approximation

As we have already noted, in the microwave band the Rayleigh–Jeans approximation for spectral black-body radiation (Chapter 6) can be applied, and the brightness temperature notion can be used. Using these approaches for expression (11.53), we obtain the solution of the basic equation (11.51) in terms of brightness temperatures:

$$T_B(\nu) = T_{BS}(\nu) \exp[-a_\nu(\nu)s] + T_0[1 - \exp[-a_\nu(\nu)s]], \quad (11.62)$$

where by T_0 is meant the thermodynamic temperature of a gas layer and by $T_{BS}(\nu)$ the brightness temperature of external radiation. Note that the introduction of this term for external radiation is rather formal, because the physical nature of radiation from this source can be arbitrary and should not obligatorily have the character of thermal radiation.

As in the case of a gas layer with a small optical path value in terms of thermal intensity, the radiation of a gas layer in the ‘brightness temperature – frequency’ coordinate system will represent a straight line. However, as the optical path value grows, the shape of the line will be distorted, but in a completely different manner as in the case of intensity – the line will form a kind of small house with a flat top to the roof (Figure 11.4(c)). A representative example of this situation can be, as we shall see below, the radiation of a set of lines of emission of oxygen in the terrestrial atmosphere close to the wavelength of 5 mm.

11.5.4 Two-layer approximation

In the cases where the spatial density of the gas or its composition varies the shape of the line of absorption and emission will essentially differ from the shape of the profile of a homogeneous layer line. And it will also depend on the distribution of a spatial density of quantum oscillators (atoms and molecules) and admixtures causing collisions, as well as on the thermodynamic properties of a system. Total absorption in a medium with a variable density is presented in the form of an integral along the direction of sighting

$$\tau_\nu(\nu) = \int_0^L a_\nu(\nu, s) ds. \quad (11.63)$$

Consider now the simplified hypothetical model: the two-layer homogeneous gas ($L = L_1 + L_2$), but with different broadening mechanisms related to the same frequency of central transition ν_{ij} . So, we suppose that in the first layer collisional broadening predominates, and in the second layer the broadening is determined by Doppler thermal scattering. Then the full optical path of a system will be equal to the sum of the optical paths in layers:

$$\tau(\nu) = \tau_1 + \tau_2 = S_C b_{ijC} L_1 + S_D b_{ijD} L_2. \quad (11.64)$$

Depending on the position of observation frequency with respect to the central transition frequency, the contribution of various mechanisms will be different and,

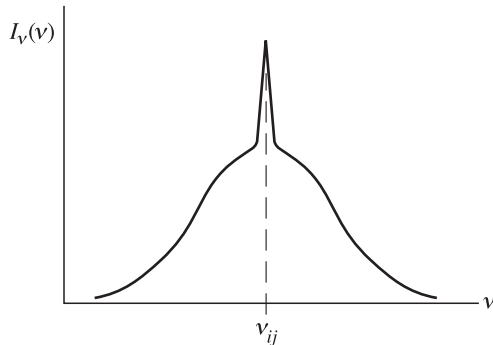


Figure 11.5. Schematic presentation of a total profile for the compound emission line of a non-homogeneous structure.

therefore, the total profile of a line will have a fairly complicated shape. So, for $|\nu - \nu_{ij}| \gg \Delta_D$, i.e. on the far line wings, the collisional mechanism $\tau_1 > \tau_2$ will predominate:

$$\tau \cong \tau_1 = S_C \frac{\Delta_C}{4\pi^2(\nu - \nu_{ij})^2} L_1. \quad (11.65)$$

In the resonance region of a line for $|\nu - \nu_{ij}| \ll \Delta_C$ the Doppler broadening mechanism will predominate, i.e. $\tau_1 > \tau_2$:

$$\tau \cong \tau_2 = S_D \frac{2\sqrt{\ln 2}}{\sqrt{\pi}\Delta_D} \exp\left[-16\pi^2(\nu - \nu_{ij})^2 \frac{\ln 2}{\Delta_D^2}\right] L_2. \quad (11.66)$$

The schematic shape of the total profile of the integral absorption (emission) line of a two-layer system is shown in Figure 11.5. If in the gas medium the additional complicated thermal picture is present, then the total profile shape will be even more complicated. Even in this simplifying example there is the necessity for careful analysis of the shape of the line, both in the resonance region (near the central transition) and in the peripheral region or line wings.

11.6 MICROWAVE RADIATIVE TRANSFER IN THE TERRESTRIAL ATMOSPHERE

Microwave radiative transfer in the free terrestrial atmosphere is determined, first of all, by the molecular oxygen and atmospheric water vapour content, as well as by the altitude distribution of basic meteorological elements (including altitude dependences of pressure, temperature, humidity and other parameters). The contribution of other gaseous components (such as hydroxyl, ozone, nitrogen oxide) to microwave transfer is essentially lower, so the contribution of minor gaseous components will not be considered in the present book. Certainly, this does not deny at all the

importance of their contribution to the total energy balance of the terrestrial atmosphere.

11.6.1 Atmospheric models

A variety of atmospheric models are used to study in detail the microwave radiation of the atmosphere, chosen according to the physical problem addressed. Since in the given formulation we need the qualitative formulation of the problem, we shall make use of the so-called exponential model. In this atmospheric model the altitude profiles of temperature $T(H)$ are described by a linear function, and the pressure and humidity profiles are approximated by exponential functions, that is,

$$\left. \begin{aligned} T(H) &= T_0 - kH, & H < 11 \text{ km} \\ T(H) &= T_{11}, & H > 11 \text{ km} \end{aligned} \right\}, \quad (11.67)$$

$$p = p_0 \exp(-\alpha_p H), \quad (11.68)$$

$$\rho = \rho_0 \exp(-H/H_V), \quad (11.69)$$

where $k = 6.5^\circ\text{C}/\text{km}$ is the altitude gradient of temperature, H_V is the characteristic height of water vapours, ρ is the absolute humidity (g/m^3) that determines the quantity of water vapour (g) contained in 1 m^3 of humid air (g/m^3). The altitude profile of specific humidity, q , that determines the quantity of water vapour (g) contained in 1 m^3 of humid air (g/kg), can be described under normal conditions by the exponential function up to altitudes of the order of 16 km, that is,

$$q(H) = \begin{cases} q_0 \exp(-\alpha_0 H), & 0 \leq H \leq 16 \text{ km}, \\ q_1, & 16 < H < 75 \text{ km}, \end{cases} \quad (11.70)$$

where $\alpha_0 = 0.48 \text{ km}^{-1}$; $q_1 = 0.46197 \times 10^{-3}$.

Under anomalous humidity distributions it can occur that layers arise which contain either greater or lower moisture content as compared to (11.69).

The special atmospheric models take into account both seasonal and latitudinal characteristics and determine the altitude profiles of temperature, air density and humidity for latitudinal belts of the terrestrial globe, as well as for separate regions of dry land and sea water areas under typical seasonal conditions (Kondratyev and Timofeev, 1970; Sakerin and Kabanov, 1997; Zuev and Komarov, 1987; Randel *et al.*, 1996; Trenberth, 1997; Pokrovskaya and Sharkov, 1997; Sharkov, 1998).

11.6.2 Stratified atmosphere radiation

The radiobrightness temperature of thermal radiation of a stratified atmosphere under the local thermodynamic equilibrium conditions can be written, according to (11.52), in the conventional form as

$$T_B(\nu) = \int_0^\infty \gamma(H) T(H) \exp\left[-\int_0^H \gamma(z) dz\right] dH, \quad (11.71)$$

where $\gamma(\nu, H) = a_\nu(H)$ is the spectral absorptivity of all gaseous components of the atmosphere, which depends both on frequency and on the height over the earth's surface. Note that in the given formula the dimension of this quantity is neper/m, and in measurement practice the dimension of dB/m is used (see relations (1.33) and (1.34) of Chapter 1). This relation does not include the contribution from the boundary surface medium.

To make clearer physical aspects of the contribution into radiation of gaseous components, the notion of the mean temperature $T_{AV}(\nu)$ is usually introduced. This quantity is equal to the isothermal atmosphere temperature with the radiobrightness equivalent to (11.71). Thus, relation (11.71) can be presented in the form:

$$T_B(\nu) = T_{AV}(\nu) \int_0^\infty \gamma(H) \exp\left[-\int_0^H \gamma(z) dz\right] dH = T_{AV}(\nu)[1 - \exp(-\tau(\nu))], \quad (11.72)$$

where $\tau(\nu)$ is the total absorption of all gaseous components of the atmosphere at the given frequency in the beam propagation direction. With account taken of the vertical profile of temperature distribution in the troposphere, the mean temperature of the atmosphere can be written in the form:

$$T_{AV}(\nu) = \frac{\int_0^\infty \gamma(H) T(H) \exp\left[-\int_0^H \gamma(z) dz\right] dH}{\int_0^\infty \gamma(H) \exp\left[-\int_0^H \gamma(z) dz\right] dH} = T_0 - \Delta T(\nu), \quad (11.73)$$

where $T_0(0)$ is the temperature near the Earth surface, $\Delta T(\nu) = 10\text{--}30\text{ K}$, depending on the state of the atmosphere and absorption intensity.

Since in the free atmosphere for wavelengths greater than 8 mm and for observation angles lower than 80° the total absorption value $\tau \ll 1$, then relation (11.71) is approximated by the linear dependence with respect to the total absorption and cosecant of observation angle θ :

$$T_B(\nu) \cong [T_0 - \Delta T(\nu)]\tau(\nu) \operatorname{cosec} \theta. \quad (11.74)$$

It can easily be seen from this relation that the emissive characteristics of the atmosphere will be presented in the form of radiation straight lines.

Absorption in the free atmosphere is mainly determined by selective absorptions in oxygen and water vapour. The character of processes responsible for radiation and the line shape essentially depend on the emitting layer height. At altitudes lower than 70 km the average interval between collisions of molecules constitutes only a small part of the lifetime of excited states. This corresponds to fulfilment of local thermodynamic equilibrium conditions and allows collisions to be considered as a factor determining the spectral line shape. At these altitudes the pressure exceeds units of millibars; the broadening of the absorption line of water vapour due to collisions, evaluated by the relation $\Delta\nu(\text{Hz}) \sim 3 \times 10^9 p/p_0$, equals units of megahertz (and greater) and considerably exceeds the values of Doppler broadening, which equals fractions of megahertz. Relaxation times, having the order of fractions

of a microsecond, under these conditions exceed the values of an interval between collisions estimated by the relation

$$t(s) \sim 3 \times 10^{-10} p/p_0. \quad (11.75)$$

At altitudes exceeding 50 km the radiation equilibrium takes place, and the line shape assumes the character of a mixed Voigt line and then, as the altitude increases, it is conditioned by purely Doppler broadening.

11.6.3 Molecular oxygen

This gas is of undoubtedly interest for remote investigations, since its abundance in the Earth's atmosphere up to altitudes of the order of 100 km (the so-called homosphere) represents a nearly constant quantity which does not depend on seasonal conditions. In addition, the oxygen absorption bands in the microwave region possess some certain and universal specificity, which makes it possible to use them for studying temperature profiles, both in the surface layer of the atmosphere (at altitudes up to 0.5 km), in the troposphere (at altitudes of 0.5–7 km), and in the stratosphere and lower mesosphere (35–55 km) (Zhevakin and Naumov, 1967; Rosenkranz, 1975; Naumov *et al.*, 1999).

The microwave spectrum of the oxygen molecule O has some specific features. The oxygen molecule does not have any electrical dipole moment, but, owing to the presence of an unpaired electron, it has a considerable magnetic moment. At ground level the structure of terms of an oxygen molecule is triplet one. The microwave spectrum arises from transitions between triplet levels of a fine structure formed by the coupling of a rotational angular momentum (the quantum number N) and electronic spin (the quantum number s). The quantum number of the total angular momentum will be $J = N + s$. The selection rules ($\Delta J = \pm 1, \Delta N = 0$) allow for two types of transition of a magnetic dipole – the transitions arise between the state $J = N$ and the state $J = N \pm 1$ in the form of two series of transition lines of various intensity, grouped in a rather narrow range of the order of 15 GHz near the frequency 60 GHz, and contain a single and prominent line at the frequency of 118.74 GHz (the wavelength of 2.53 mm). The line broadening is determined by the mechanism of collisions of oxygen molecules between each other and with the molecules of nitrogen.

The spectra of absorption in atmospheric oxygen have been first calculated by J. Van-Vleck, then updated by Zhevakin and Naumov (1967) and then considered by Rosenkranz (1975) as applied to microwave sensing.

The coefficient of absorption in atmospheric oxygen $\gamma_0(\nu)$ can be presented as

$$\gamma_0(\nu) = CP \left(\frac{\nu}{T} \right)^2 F(\nu), \quad (11.76)$$

where T is expressed in K, pressure P in millibars, frequency in GHz, and C is 1.434 for $\gamma_0(\nu)$ in dB/km. For the expression of F the first order of approximation of the theory of overlapping lines results in the following expression (Rosenkranz, 1975):

$$F = P \left\{ \sum_N \Phi_N [f_N^+(\nu) + f_N^+(-\nu) + f_N^-(\nu) + f_N^-(-\nu)] \right\} + \frac{0.70 w_b}{\nu^2 + (Pw_b)^2}, \quad (11.77)$$

where

$$f_N^\pm = \frac{w_N(d_N^\pm)^2 + (\nu - \nu_N^\pm)y_N^\pm}{(\nu - \nu_N^\pm)^2 + (Pw_N)^2} \quad (11.78)$$

and d_k is the amplitude of the k th line, ν_k are their frequencies, Φ_k is the population of a primary level bound with this transition, y_N^\pm is the interference factor (mbar); the resonance half-width w_N (GHz/mbar) equals

$$w_N = 1.16 \times 10^{-3} \left(\frac{300}{T} \right)^{0.85} \quad (11.79)$$

and the half-width of a non-resonant component w_b (GHz/mbar) is equal to

$$w_b = 0.48 \times 10^{-3} \left(\frac{300}{T} \right)^{0.89}. \quad (11.80)$$

The detailed values of diagonal matrix elements, populations of levels, interference factors can be obtained from the paper by Rosenkranz (1975).

For a single and very strong line at the wavelength of 2.53 mm the expression for $\gamma_0(\nu)$ can be presented in the simpler form (Kotlyar and Novak, 1987):

$$\gamma(H, \nu) = 1.2305 \frac{P(H)\nu^2}{[T(H)]^3} \exp \left\{ -\frac{4.14}{T(H)} \right\} \frac{4\nu^2 \Delta\nu(H)}{(\nu_0^2 - \nu^2)^2 + 4\mu^2[\Delta\nu(H)]^2}, \quad (11.81)$$

where $\nu_0 = 118.750\,343$ GHz, $P(H)$ and $T(H)$ are pressure and temperature profiles, $\Delta\nu$ is the half-width of this line:

$$\Delta\nu(H) = [(\Delta\nu_C(H))^2 + (\Delta\nu_D(H))^2]^{1/2}. \quad (11.82)$$

Here $\Delta\nu_C$ and $\Delta\nu_D$ correspond to impact and Doppler mechanisms:

$$\Delta\nu_D = 7.52 \times 10^{-6} \sqrt{T(H)}; \Delta\nu_C(H) = \alpha P(H)(0.21 + 0.78\beta) \left[\frac{300}{T(H)} \right]^n, \quad (11.83)$$

where $\beta = 0.75$, $n = 0.9$, $\alpha = 2.131 \times 10^{-3}$ GHz/mbar.

Of great scientific and practical interest is the oxygen absorption band centred with respect to the wavelength of 5 mm and composed of 49 fairly intensive spin-rotational lines with the azimuthal quantum number $K < 49$ (Staelin, 1969; Rosenkranz, 1975; Troitsky *et al.*, 1993; Naumov *et al.*, 1999). The widths of these spectral lines near the earth's surface are ~ 1 GHz, whereas the mean distance between the centres of lines is ~ 0.5 GHz. The consequence of this circumstance is the overlapping of spectral lines in low layers of the atmosphere. It is these overlapped lines which form the absorption band considered. The oxygen lines are distinguished at altitudes $h > 20$ km, where the atmospheric pressure decreases down to values of ~ 40 mbar. The majority of lines (about 20) are concentrated in the range of frequencies of 55–65 GHz, and 14–15 spectral lines fall on each of the

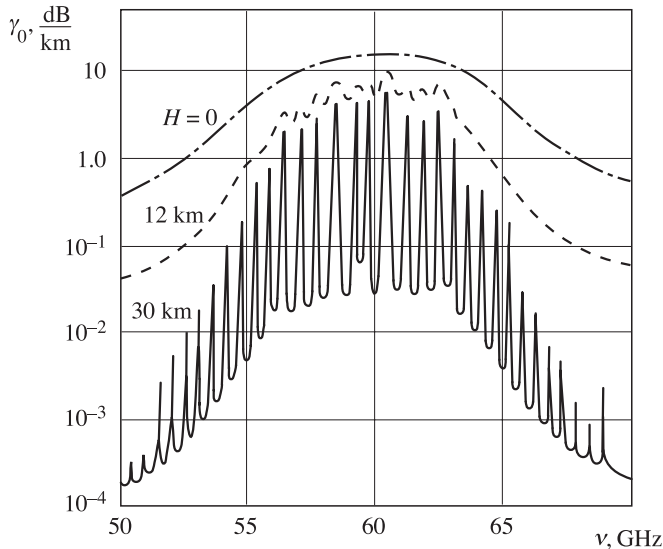


Figure 11.6. Frequency characteristics of the one-way attenuation in terrestrial oxygen in the 5-millimetre range at various altitudes (H , km) above the ground.

ranges 45–55 GHz and 65–75 GHz. The optical thickness of the atmosphere increases in the long-wavelength section of the band – from values of ~ 0.3 at the frequency of 50 GHz up to values of ~ 3 at the frequency of 55 GHz. At the centre of the 5-mm band the values essentially exceed unity: $\tau \approx 10\text{--}45$. At the short-wavelength wing of the band the optical thickness decreases from the indicated values and becomes of the order of 0.3. The qualitative picture of the absorption spectrum in atmospheric oxygen for various altitudes over the earth's surface is demonstrated in Figure 11.6. It can easily be seen that the electromagnetic signal transmission at wavelengths close to 5 mm at the earth's surface level is virtually impossible, since even at the distance of 10 km the attenuation of a signal can exceed 10^{20} times. Note that all these events take place under conditions of an optically transparent atmosphere.

The monotonous character of optical thickness variation on the band wings is violated by its increasing at the centres of some lines located here. The character of spectral dependence of the optical thickness in the 5-mm band determines also the spectral dependence of radiobrightness temperature in this band at zenithal observation from the earth's surface (see relation (11.71) and Figure 11.7). At the centre of the 5-mm band of the contribution of separate lines to radiobrightness temperature of the atmosphere is screened by their high absorption in lower layers of the atmosphere, and distinguishing resonances in radio-emission are revealed only on wings of the 5-mm band. It can easily be seen from relation (11.71), that the maximum value of a spectral curve will just be equal to the value of the weighted mean temperature of the atmosphere (which equals 285 K in the given case).

The altitude dependence of the oxygen absorption coefficient has a fairly complicated character, strictly speaking (see relations (11.76), (11.81) and (11.83)).

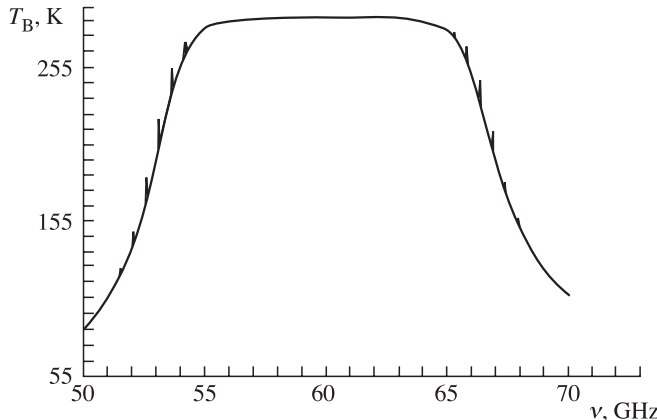


Figure 11.7. Frequency characteristics of the brightness temperature with zenithal observation in the 5-millimetre range at sea level condition.

However, observational experiments have shown that exponential (or linearly exponential) dependence can be quite satisfactory for remote sensing purposes. It has the form:

$$\gamma_0(\nu, H) = \gamma_0(\nu, O) \exp\left(-\frac{H}{H_0}\right), \quad (11.84)$$

where quantity H_0 characterizes the effective height of the oxygen layer that absorbs microwave radiation. This quantity strongly depends on the region where the sensing frequency is selected. So, for regions lying outside the resonance frequencies, quantity H_0 equals about 5.1–5.3 km. At the same time, near the resonance transition points the effective path length can increase 2–5 times owing to absorption in the high layers of the atmosphere and equals, for example, $H_0 = 21$ km for $\nu = 63$ GHz.

According to (11.84), the total absorption of oxygen at zenithal observation will be

$$\tau_0(\nu) = \int_0^{\infty} \gamma_0(\nu, H) dH \cong \gamma_0(\nu, O) H_0. \quad (11.85)$$

When the outgoing radiation flux is observed in the frequency range where the molecular oxygen transition lines (the 5-mm band and the 2.53-mm line) are situated, the shape of the radiobrightness temperature spectrum of the atmosphere depends on the vertical temperature distribution and on the altitude profile of the absorption coefficient (11.70). The stability of the altitude distribution of oxygen and the features of absorption lines allow one to use the information on the shape of the outgoing radiation spectrum across a wide range of microwave remote sensing problems. They include the detailed investigations of temperature profiles in the boundary layer of the atmosphere (Troitsky *et al.*, 1993; Naumov *et al.*, 1999), in the troposphere (Rosenkranz *et al.*, 1972; Kapitza, 1983; Kotlyar and Novak, 1987; Kotlyar and Khapin, 1990; Gasiewski and Johnson, 1993), as well as in the stratosphere and mesosphere (Kondratyev, 1997; Naumov *et al.*, 1999).

11.6.4 Atmospheric water vapour

The remote investigation of the spatial distribution of water vapour on various spatial and temporal scales is of principal significance in studying the thermal and hydrodynamic state of the troposphere and stratosphere (Kondratyev and Timofeev, 1970; Mitnik, 1972; Kramer, 1996; ESA, 1996b; English *et al.*, 1999; Hartmann *et al.*, 1996; Holton *et al.*, 1995; WMO, 1990a,b; Randel *et al.*, 1996). This is, first of all, due to the huge stores of heat hidden in spatial fields of water vapour. Note here that in the optical band water vapour represents a transparent medium and cannot be recorded by optical instruments directly.

Unlike the oxygen molecules, the physical nature of absorption spectra of water vapour is caused by completely different factors, namely, by the volume structure of a vapour molecule. So, the rotational spectra of molecules of a volume structure of symmetrical and asymmetrical top type are directly related either to the molecule structure symmetry or, on the contrary, with its asymmetry. The rotational spectrum of molecules of symmetrical top type can be presented (similarly to the rotational spectrum of linear molecules) in the form of a set of equispaced lines (the so-called equidistant spectrum). The energy levels of molecules having asymmetrical top structure (as, for example, the molecules of water vapour or triatomic oxygen (ozone)) do not have any simple analytical presentation. Even in the presence of slight asymmetry the absorption spectrum of a molecule drastically differs from a set of equispaced lines, thus forming a sharply non-equidistant spectrum. The detailed calculation of energy transitions, beginning with the long-wavelength extremity, gives the following values of wavelengths of most intensive microwave lines in the band of $\lambda > 300$ micrometres: 1.35 cm; 0.164; 0.093; 0.079; 0.054; 0.04 and 0.034.

The calculations of microwave absorption spectra of monomeric molecules of water vapour in the terrestrial atmosphere, carried out by Van-Fleck, have been essentially updated later by S. A. Zhevakin and L. P. Naumov. They have described the absorption line shape by solving the kinetic equation and by taking into account the contribution of absorption from ‘wings’ over all rotational transitions of the microwave band (Zhevakin and Naumov, 1967). The features of microwave lines are under detailed study at present (Bhattacharya *et al.*, 1983; Bauer *et al.*, 1986).

The absorption coefficient of water vapour $\gamma_{\text{WV}}(\nu, H)$ for the first and most informative line of 1.35 cm can be presented in the following semi-empirical form:

$$\gamma_{\text{WV}}(\nu, H) = \gamma_{\text{WVR}}(\nu, H) + \gamma_{\text{WVNR}}(\nu, H), \quad (11.86)$$

where the ‘resonance’ term $\gamma_{\text{WVR}}(\nu, H)$ is described by the relation

$$\begin{aligned} \gamma_{\text{WVR}}(\nu, H) &= \frac{343\nu^2 \Delta\nu a(H)}{[T(H)]^{5/2}} \exp\left(-\frac{644}{T(H)}\right) \\ &\times \left[\frac{1}{(\nu - \nu_0)^2 + [\Delta\nu(H)]^2} + \frac{1}{(\nu + \nu_0)^2 + [\Delta\nu(H)]^2} \right]. \end{aligned} \quad (11.87)$$

Here $\nu_0 = 22.235$ GHz. The ‘non-resonance’ term is

$$\gamma_{\text{WVNR}}(\nu, H) = 2.55 \times 10^{-3} \frac{\nu^2 a(H) \Delta\nu(H)}{[T(H)]^{3/2}}. \quad (11.88)$$

In this case the line half-width is determined as

$$\Delta\nu(H) = \frac{0.126 P(H) \left[1 + 0.11 \frac{a(H) T(H)}{P(H)} \right]}{[T(H)]^{0.626}}, \quad (11.89)$$

where $P(H)$ there is the pressure profile.

The width of spectral lines at altitudes of up to 50 km is determined by collisions of water vapour molecules with nitrogen molecules.

The altitude dependence of the absorption coefficient is determined by the altitude distribution of meteorological elements. Because of the high sensitivity of water vapour content to thermohydrodynamical processes in the atmosphere (and, especially, in the troposphere), the altitude dependence of water vapour can be very complicated and represents, in itself, a subject of special investigations (Rosenkranz *et al.*, 1982; Zuev and Komarov, 1987; Sakerin and Kabanov, 1997; Pokrovskaya and Sharkov, 1997). Since the altitude dependencies of humidity and pressure at the ground state have predominantly exponential character, the exponential (or linearly exponential) altitude dependence of absorption can be assumed to be quite satisfactory for sensing purposes. It has the following form:

$$\gamma_{\text{WV}}(\nu, H) = \gamma_{\text{WV}}(\nu, O) \exp\left[-\frac{H}{H_W}\right], \quad (11.90)$$

where H_W characterizes the effective height of a water vapour layer.

It follows from this relation, that the total absorption of the atmosphere will be

$$\tau_{\text{WV}}(\nu) = \int_0^\infty \gamma_{\text{WV}}(\nu, H) dH \cong \gamma_{\text{WV}}(\nu, O) H_W. \quad (11.91)$$

For the non-resonance region the effective height of a layer equals 2.1 km. For the resonance region (near the absorption maximum) the effective height two to three times exceeds the H_W value in the non-resonance region. Thus, the variation of the total absorption and, accordingly, the spectral variations of brightness temperature are sensitive to variations of water vapour distribution at low values of pressure, i.e. in the region of fairly high altitudes. Figure 11.8 presents the spectrum of brightness temperature at zenithal observation of the atmosphere in the 1.35-cm absorption line under the condition of exponential profile of humidity and for a profile with anomalous distribution in the high-altitude layers of the atmosphere. This indicates that in sufficiently selective microwave observations the anomalous distributions of water vapour in the atmosphere can be estimated by means of radiospectrometers.

Of special interest are microwave investigations of the water vapour content in the stratosphere and mesosphere, which are being carried out at present. Water

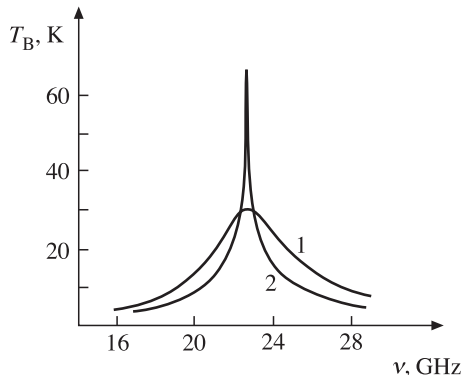


Figure 11.8. The effect of vertical humidity profile on water vapour emission line shape at 22.2 GHz frequency: (1) for exponential profile; (2) for the profile with irregular distribution.

vapour (along with ozone) plays an important part in physicochemical processes in the middle atmosphere (Rosenlof *et al.*, 1997; Holton *et al.*, 1995). Since the amount of water vapour in the middle atmosphere is very low, the investigations are carried out using the strong absorption lines of 183 and 325 GHz. And these investigations are carried out using the special limb observation technique in order to maximally increase the optical path in the sighting direction (Weinstock *et al.*, 1995; Abbas *et al.*, 1996; Hartmann *et al.*, 1996; Bevilacqua *et al.*, 1996).

11.6.5 Absorption of microwaves in the terrestrial atmosphere

Let us consider the general character of spectral absorption in the terrestrial atmosphere, taking into account two basic gases and making allowance for disperse media (primarily, rain precipitation). As we have already noted, from the viewpoint of electromagnetic interactions, the gaseous and disperse media of the terrestrial atmosphere are independent processes. Therefore, their energy contributions (the absorption of electromagnetic waves) can be summed up. It is just this basis on which complex semi-empirical models are usually constructed for calculating the characteristics of electromagnetic wave propagation in the atmosphere with different meteorological states. So, in particular, H. J. Liebe (1989) constructed the atmospheric millimetre-wavelength propagation model, which is specially intended for practical calculations in observational remote sensing problems.

The millimetre-wavelength absorption spectrum of the terrestrial atmosphere with allowance for two basic gases (water vapour and oxygen) and in the presence of rain precipitation of various intensities is shown in Figure 11.9. Under clear atmosphere conditions, except for a fairly weak line of water vapour absorption at the frequency of 22.2 GHz, four basic absorption bands dominate in the spectrum, namely: (a) a complex of rotational lines of oxygen at the frequency of 60 GHz; (b) a single strong oxygen absorption line at the frequency of 118 GHz; (c) two strong water vapour absorption lines at the frequencies of 183 and 325 GHz. Along with the

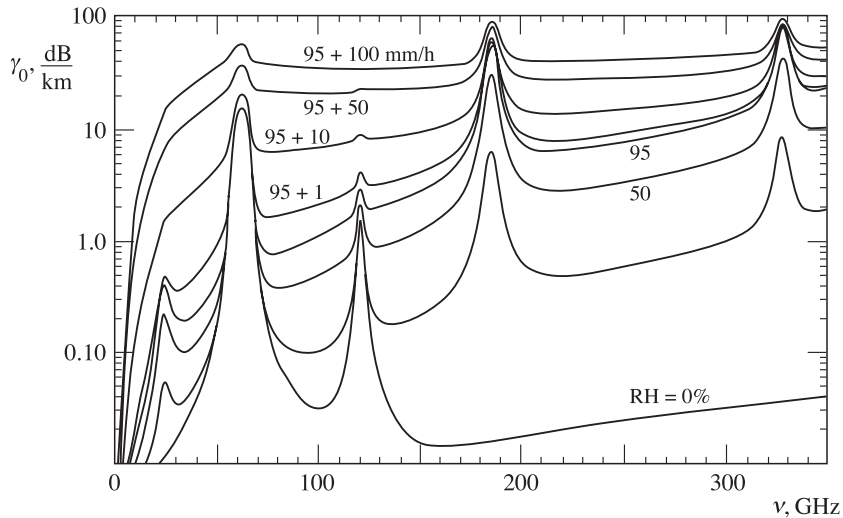


Figure 11.9. One-way attenuation in the terrestrial atmosphere over the frequency range from 0 to 350 GHz for four rain cases ($R = 1, 10, 50, 100 \text{ mm/h}$) added to a sea level condition ($P, T, \text{RH} = 95\%$). Also shown are dry ($\text{RH} = 0\%$) and moist ($\text{RH} = 10\%, 50\%$). RH is relative humidity. RH magnitudes 10, 50, 95 and 100% correspond to 2, 10, 17 and 20 g/m^3 for absolute humidity (Liebe, 1989).

strong absorption lines mentioned, there exist some very weak absorption lines in the oxygen and water vapour spectra (Liebe, 1989) which cannot be represented in the scale of Figure 11.9. By virtue of their ‘weakness’, they are not usually utilized in remote sensing applications. The contribution of other atmospheric gases (such as ozone) to the total absorption is also rather weak. The spectral windows, where the local minimum of atmospheric absorption is achieved (the transparency windows), are centred on frequencies of 36, 90–100, 150 and 210–300 GHz. The values of absorption in transparency windows are mainly determined by the presence of water vapour and systematically increase as the frequency grows. It is important to note that, whereas in oxygen absorption bands (of 60 and 118 GHz) the presence of water vapour has virtually no effect, in all other frequency bands the influence of water vapour dominates.

The presence of disperse structures (such as fogs, precipitation of various types) in the atmosphere drastically changes the spectral picture of absorption in the millimetre wavelength band. So, a quite weak rain precipitation with intensity of 10 mm/hour virtually completely ‘blocks’ not only transparency windows but even oxygen absorption bands themselves (Figure 11.9). Such a high sensitivity of short-centimetre and millimetre wavelength bands to the state of gaseous and disperse media of the atmosphere made it possible to produce, even at the earliest stage of development of microwave remote sensing methods (in the 1960s), effectively operating radiothermal ground-, space- and aircraft-based complexes (Haroules and Brown, 1968; Rabinovich *et al.*, 1968, 1970; Basharinov *et al.*, 1968, 1969,

1971, 1974; Staelin, 1969, 1981; Akvilonova *et al.*, 1971, 1973; Kondratyev *et al.*, 1975; Amirkhanyn *et al.*, 1975; Kakar and Lambrigtsen, 1984). Multifrequency radiothermal techniques for investigating gaseous components and disperse structures in the terrestrial atmosphere and appropriate microwave instrumentation are being actively developed now as well (English, 1995; Bruzzi, 1995; Ferraro *et al.*, 1996; Weinstock *et al.*, 1995; Wang *et al.*, 1997a,b,c; Kondratyev, 1997; Wang *et al.*, 1998a,b; English, 1999; Matzler, 2000; Konig *et al.*, 2000; Bizzari and Spera, 2000; Bizzari *et al.*, 2000; IPCC, 2001).

12

Radiative properties of the terrestrial 'surface-atmosphere' system

The purpose of the present chapter is to consider and analyse some directions of microwave remote sensing being actively developed at present by the researchers in various science teams. The solutions of the equation of the transfer theory for a homogeneous layer of a gaseous-disperse medium are considered as a methodological basis for detailed study of the hydrometeorological parameters of the terrestrial atmosphere. The results of ground-, aircraft- and space-based observations and monitoring of integral parameters of the water vapour content of the atmosphere and thermodynamic temperature profiles are presented. The results of analysing the contribution of microwave measurements into classification schemes of recognizing various types of cloudy systems are given. The chapter also presents the basic results of observation of the wavy sea surface by microwave radiothermal aircraft- and space-based complexes, including situations with breakings of sea waves and vast oil spillage.

12.1 RADIATION OF THE HOMOGENEOUS OCEAN-ATMOSPHERE SYSTEM

Numerical integrations of the radiative transfer equation for the atmosphere-ocean system in the microwave frequency band on the basis of equations (9.64)–(9.66) were performed by a variety of authors (Wilheit and Fowler, 1977; Tsang *et al.*, 1977; Wilheit and Chang, 1980; Mitnik, 1986; Sasaki *et al.*, 1987; Liebe, 1989; Kotlyar and Khapin, 1990; Matzler, 1992, 2000).

12.1.1 The basis model

This spatio-homogeneous model, which was described in detail by Mitnik (1986), enables one to estimate the influence of hydrometeorological parameters and viewing

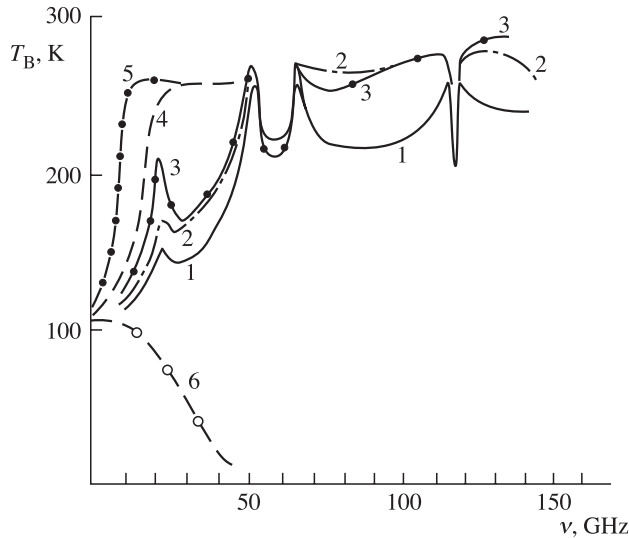


Figure 12.1. Qualitative microwave spectra of the brightness temperature for the ocean–atmosphere system in sensing at the nadir with a satellite: (1) standard cloudless atmosphere; (2) clouded atmosphere: $Q = 0.38 \text{ kg m}^{-2}$; (3) tropical atmosphere; (4) rain cloud at 5 mm h^{-1} ; (5) rain cloud at 25 mm h^{-1} ; (6) contribution of surface emission.

angle θ variations on the brightness temperatures $T_B(\nu, \theta)$ for horizontal (H) and vertical (V) polarizations in the frequency range of 0.5–300 GHz.

The examples of calculated $T_B(\nu, \theta)$ spectra for microwave emission of the atmosphere–ocean system with a smooth sea surface (at 35‰ salinity) using equations (9.64)–(9.66) under standard gaseous cloudless atmosphere (curve 1), standard cloudy atmosphere (total cloud water content $Q = 0.39 \text{ kg/m}^2$ at $t = -10^\circ\text{C}$) (curve 2), tropical atmosphere (curve 3) and rain cloud conditions (curves 4 and 5) are presented in Figure 12.1.

Initially it should be pointed out, that, first, the distinctive properties of emission spectra are observed for the standard and tropical atmosphere in the ranges of 20–40 and 80–110 GHz, and, second, the brightness temperature sharply decreases in the ranges of strong gaseous oxygen absorption (the band of 55–65 GHz and the strong line at 118 GHz). These features are determined from the temperature profile properties and from the peculiarities of the oxygen weighting function. So, Figures 12.2 and 12.3 show the detailed spectra of brightness temperature of the atmosphere – ocean system for the strong oxygen line of 118 GHz and the normalized weighting functions (see equation (9.64)) for various working frequencies in the frequency range of 115–118.7 GHz (Kotlyar and Khapin, 1990). The odd-shaped spectra of the 118 GHz line have attracted our attention with respect to the standard temperature profile (curve 1), the summer arctic temperature profile (curve 2) and the tropical profile (curve 3). Figure 12.3 shows that radio-emission in the frequency band of 115–117 GHz is formed at altitudes of 0–8 km (curves 1 and 2).

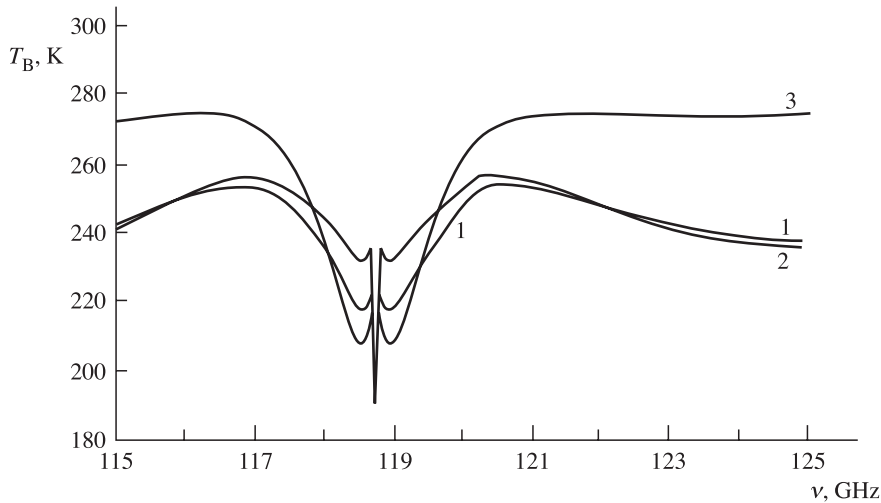


Figure 12.2. Spectra of the brightness temperature for the ocean-atmosphere system in sensing at the nadir with a satellite at frequency range 115–125 GHz (Kotlyar and Khapin, 1990).

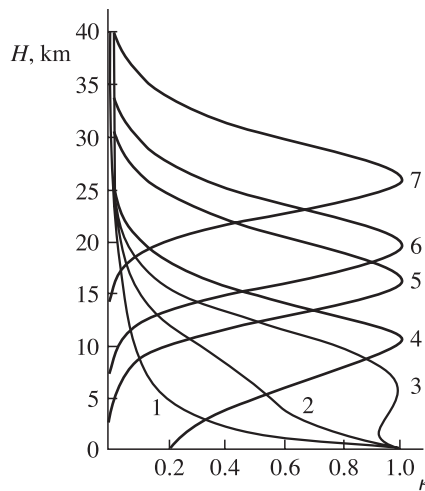


Figure 12.3. Normalized weighting functions $\kappa(H)$ in sensing at the nadir with a satellite at frequency range 115–118.5 GHz (Kotlyar and Khapin, 1990).

The weighting functions for the band of 117–118.5 GHz are characterized by a sharp decrease of emissivity and possess maximum values at altitudes of 5–16 km (curves 3–5). The minimum brightness temperature values at about 118.5 GHz are derived from the fact that the emission at these frequencies is formed in the tropopause (12–25 km) area, where very low temperatures prevail. Radio-emission in the frequency range of 118.5–118.7 GHz is formed in the terrestrial stratosphere

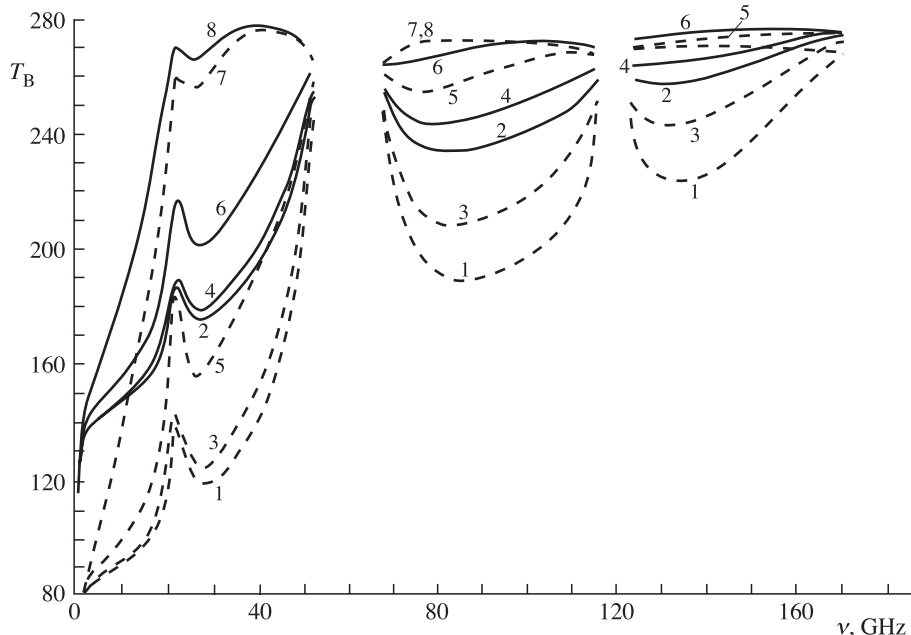


Figure 12.4. Theoretical spectra of the brightness temperature for the ocean–atmosphere system at microwave frequency range. Dashed and solid lines represent respectively the horizontal and vertical polarization signals. See notation in the text (Mitnik, 1986).

where the temperature increases with altitude (curves 6 and 7). So, the radio-emission received by radioset channels at frequencies in the band of 115–118.5 GHz carries useful information about the thermodynamic temperature profile in the altitude layer from 0 to 30 km.

The model examples of calculated spectra for horizontal and vertical polarization ($\theta = 45^\circ$) with $\nu = 1\text{--}170\text{ GHz}$ are presented in Figure 12.4 (Mitnik, 1986). In the standard cloudless atmosphere (curves 1 and 2) the total water vapour content is $V = 1.3\text{ g/cm}^2$. The cloudiness of stratified forms (St., Sc., curves 3 and 4) are characterized by the following parameters: $Q = 0.1\text{ kg/m}^2$, $t = +10^\circ\text{C}$, $V = 1.3\text{ g/cm}^2$. In the case of cumuli of medium vertical development (Cu med., curves 5 and 6) $Q = 0.5\text{ kg/m}^2$, $t_C = +10^\circ\text{C}$, $V = 5.1\text{ g/cm}^2$. For heavy cumuli at $\nu > 40\text{ GHz}$ the distinctions in polarization are very small due to the increase in optical thickness in the sensing direction.

First of all, we shall consider cloudiness with small and mean values of the total liquid water content ($Q < 0.5\text{ kg/m}^2$). From the analysis of numerical experimental data it follows that maximum variations of the brightness temperatures, stipulated by alterations in cloudiness parameters, are noticed over the ranges of $\sim 25\text{--}50$, $\sim 70\text{--}113$ and $\sim 125\text{--}170\text{ GHz}$. At $Q = 0.1\text{--}0.3\text{ kg/m}^2$ and $t_C = -10$ to $+10^\circ\text{C}$ (which is natural for the clouds of St., Sc., Ac, As Cu hum) the brightness contrast of cloudy areas against the cloudless background

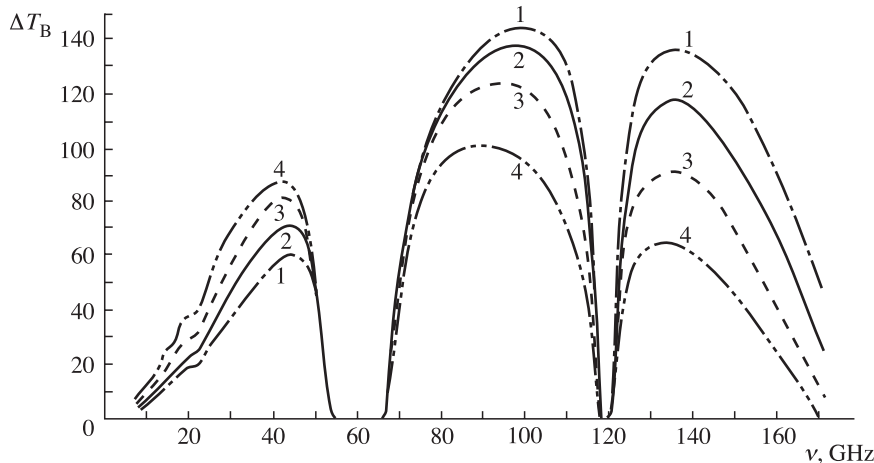


Figure 12.5. Theoretical spectra of partial derivatives of the brightness temperature of a clouded atmosphere with total cloud liquid water content at low Q values: (1) $t_C = +10^\circ\text{C}$; (2) $t_C = 0^\circ\text{C}$; (3) $t_C = -10^\circ\text{C}$; (4) $t_C = -20^\circ\text{C}$ (Mitnik, 1986).

$\Delta T_B(\nu, t) = T_{BC}(\nu, t) - T_B(\nu)$ is observed in the nadir direction: 3–25 K at $\nu = 25$ –50 GHz, ~10–40 K at $\nu = 75$ –110 GHz and ~5–35 K at $\nu = 125$ –155 GHz. For sensing at the angle of 45° for horizontal polarization the corresponding contrast will grow up to ~6–40, ~15–55 and ~7–45 K.

The sensitivity of the brightness temperature of the atmosphere–ocean system to the cloudiness parameters variation can be characterized by partial derivatives spectra $\alpha(\nu) = T_B(\nu)/Q$ and $\beta(\nu) = T_B(\nu, t)/t_C$.

In the range of $\nu < 53$ GHz the $\alpha(\nu)$ derivative grows monotonously with frequency up to the maximum at $\nu = 43$ –45 GHz; then it is followed by decreasing owing to the oxygen absorption increase (Figure 12.5). The temperature drop from $+10$ to 20°C is accompanied by its increasing by a factor of about 1.6–2.2 depending on the frequency. At $\nu = 43$ GHz the $\alpha(\nu)$ values are equal to $60 \text{ K}/(\text{kg/m}^2)$ at $t_C = +10^\circ\text{C}$ and $87 \text{ K}/(\text{kg/m}^2)$ at $t_C = -20^\circ\text{C}$.

At measurements with $\theta = 45^\circ$ the values of α for vertical polarization are roughly the same as with $\theta = 0^\circ$ (nadir), and for horizontal polarization they are about 1.5–1.6 times greater.

In the transparency window of 70–115 GHz the brightness contrasts and the values of the $\alpha(\nu)$ derivative are weaker as compared to lower frequencies, at positive temperatures particularly. The change of the derivative sign from negative to positive is an important distinctive feature. The maximum values of $\alpha(\nu)$ at $\theta = 0^\circ$ may be as great as 100 – $140 \text{ K}/(\text{kg/m}^2)$ in accordance with t_C and fall within the spectral range of 87 to 100 GHz. At $\theta = 45^\circ$ the $\alpha(\nu)$ values increase by a factor of 1.4–1.6 for horizontal polarization and decrease by about 25% for vertical polarization.

In the frequency band of 125–170 GHz the maximum values of derivatives are lower than those at $\nu = 70$ – 115 GHz, the difference increasing as the temperature

drops. This results from the cumulative effect of cloud and water vapour absorption spectra and from increasing sea surface emissivity.

12.1.2 Integral parameters

The analysis of spectral dependencies of the gaseous-disperse medium of the atmosphere shows that the use of the data of measurements of microwave radiation in the centimetre and millimetre bands has many significant advantages as compared to using the data of measurements in the infrared and optical bands for similar purposes. The basic feature of microwave radiation in the 3 cm – 1 mm band is its high informative capacity, which is caused by a strong dependence of radiation intensity on hydrometeorological parameters of the atmosphere and on its gaseous components in the semi-transparent medium regime (Chapters 10 and 11). And in this case for a number of physical characteristics of the studied medium (the water vapour content of the atmosphere, the liquid water content of clouds, the rates of liquid and solid precipitation, the content of minor gaseous components) the variations of microwave radiation are about linearly related with the values of integral parameters of the gaseous-disperse atmosphere. This allows one to essentially simplify the procedures of restoring physical parameters from the data of remote microwave measurements. It is for just these reasons that this band has attracted the close attention of researchers from the very beginning of the active phase of purposeful remote investigations of thermal radiation of the ocean–atmosphere system in 1968–1972 (Basharinov *et al.*, 1969, 1971, 1973; Staelin, 1969; Akvilanova *et al.*, 1971; Mitnik, 1972; Rosenkranz *et al.*, 1972) up to the most recent time (Gasiewski and Johnson, 1993; Abbas *et al.*, 1996; Hartmann *et al.*, 1996; Bartsch *et al.*, 1996; Wang *et al.*, 1997a, b, c; Mitnik and Mitnik, 2003; Raffalski *et al.*, 1998; Karmalkar *et al.*, 2002; Lohnert and Crewell, 2003). Apparently this tendency will be maintained in the future as well.

Now we shall demonstrate the advantages of this band proceeding from the results we have obtained earlier (Chapters 10 and 11). So, the radiobrightness temperature of downward radiation of the semi-transparent gaseous-disperse atmosphere at upward-looking measurements can be presented as

$$T_B(\nu) = [T_0 - \Delta T(\nu)][\tau_G(\nu) + \tau_D(\nu)] \operatorname{cosec} \theta, \quad (12.1)$$

where $t_G(\nu)$ and $t_D(\nu)$ are optical paths of gaseous and disperse components of the atmosphere, respectively (see relations (11.74)). Similar relations can also be obtained for upward radiation with allowance for re-emission of a studied layer from the surface (see relations (9.69) and (9.74)). Since the optical path value is an integral characteristic both for gaseous components (see relation (11.85)), and for disperse components (see relation (10.71)), the brightness temperature $T_B(\nu)$, measured at different frequencies ν_i , can be presented by a fairly simple regression relation

$$T_B(\nu_i) = a_0(\nu_i) + \sum a_j(\nu_i)P_j, \quad (12.2)$$

where P_j are unknown integral parameters of gaseous and disperse media of the

atmosphere and, first of all, the water vapour content of the atmosphere V (kg/m^2) the liquid water content of clouds Q (kg/m^2), the liquid and solid precipitation rates, and the content of minor gaseous components (ozone, chlorine oxide and other gases). The electromagnetic properties of disperse systems are considered in the Rayleigh approximation in this case. The $a_j(\nu_i)$ coefficients are usually found by the least-squares method under monitored conditions when remote observations of seasonal, latitudinal and geographical features are performed. To solve a very important problem of separating the components bound with water vapour and cloud liquid-water content, the two-channel ($i = 2$) technique was proposed earlier for determining the total vapour content and total cloud liquid-water content. This technique has used the measurements at the frequency close to the frequency of the first strong water vapour transition (22.235 GHz) and at the frequency chosen in the transparency window, but with a strong dependence on a disperse-drop phase (the band of 28–32 GHz). Using (12.2), we obtain in this case:

$$V = A_{0V} + A_{1V}T_B(\nu_1) + A_{2V}T_B(\nu_2), \quad (12.3)$$

$$Q = A_{0Q} + A_{1Q}T_B(\nu_1) + A_{2Q}T_B(\nu_2). \quad (12.4)$$

Theoretically, the optimal choice of frequencies for the two-frequency algorithm is considered to be as follows: the central transition frequency is $\nu_1 = 22.235$ GHz and frequency $\nu_2 = 31.4$ GHz. This choice of frequencies, which ensures the maximum signal-to-noise ratio at measurements, suggests a constancy of pressure and temperature profile. In practical observations, where the pressure and temperature are variable quantities, this choice is not optimal. Depending on the local position latitude (the arctic region, middle latitudes, tropics), on the observation time and on hydrometeorological features of the region, the choice of observation frequencies can vary (Wang *et al.*, 1992; Karmalkar *et al.*, 2002). A principal step in the further development of this algorithm is the introduction of additional channels in the transparency window of 90 GHz and in the line of 183 GHz, which allows one to essentially improve the retrieval accuracy of the total cloud liquid-water content (Matzler, 1992; Wang *et al.*, 1992; Lohnert and Crewell, 2003; Weng *et al.*, 2003).

At present, there exists a variety of both ground complexes in various latitudinal belts, and aircraft multifrequency systems for observation and monitoring of the total liquid-water content (of vapour and drops) in the atmosphere (Rosenkranz *et al.*, 1972, 1982; Rassadovsky and Troitsky, 1981; Amirkhanyn *et al.*, 1975; Wang *et al.*, 1994; English, 1995; Taylor and English, 1995; Antonov *et al.*, 1995; Wang *et al.*, 1997a; Skofronick-Jackson and Wang, 2000).

For space observations a similar algorithm was first utilized in processing the data from measuring the upward radiation of the ocean-atmosphere system by means of radiothermal multifrequency instruments installed on the ‘Cosmos-243’ satellite (1968). This complex included the channels of 0.8, 1.35, 3.2 and 8.5 cm. The measurements, carried out with this complex, made it possible to obtain for the first time statistically significant estimates of the content of water vapour (in the 1.35-cm channel), small-drop water (in the 0.8-cm channel) and liquid precipitation (in the 3.2-cm channel) over the oceans. The mean latitudinal distribution of total

humidity over the Pacific, Atlantic and Indian oceans was found to be similar. The measurements, carried out from September 23 till September 27 1968, have shown that about 0.7% of water in the terrestrial atmosphere is in the liquid-drop state (Basharinov *et al.*, 1969, 1974; Akvilanova *et al.*, 1971, 1973).

The next step was the launching of the ‘Nimbus-6’ satellite (1975) with radio-thermal instruments working in frequency channels of 22.235 and 31.65 GHz for implementing the two-channel algorithm. This complex also included oxygen channels (at 52.85, 53.85 and 55.45 GHz) and polarization observations in the transparency window at the 37 GHz frequency.

The modern multifrequency space-based two-polarization microwave complexes (the Advanced Microwave Scanning Radiometre (AMSR) onboard the ADEOS-2 satellite and the Advanced Microwave Sensing Unit (AMSU) onboard the NOAA 15 and NOAA 16 satellites essentially expand the possibilities of microwave systems while keeping the two-channel algorithm as an integral part of the general measurement ideology. In addition, these systems allow one to retrieve not only the integral parameters of liquid-water content (in vapour and liquid phase), but also the sea surface temperature and the surface wind speed, and also to separate the total liquid-water content of a solid phase (ice) and the surface precipitation rates (Kidder *et al.*, 2000; Shibata, 2000; Weng *et al.*, 2003; Mitnik and Mitnik, 2003).

12.1.3 Temperature profiles

One of the most important problems in meteorology is the retrieval of temperature profiles of the atmosphere in the extended altitude interval from remote sensing data of measurements of downward (observations at the earth’s surface) and upward (observations on flight vehicles) radiation fluxes. The investigations carried out over a long period of time have shown that the optimal procedure for solving this problem is remote sensing in the millimetre-wavelength band in spin-rotational lines of oxygen (see Chapter 11). The possibilities of using radiation of this particular atmospheric gas are related, on the one hand, with a high stability of the content of molecular oxygen in the atmosphere (as opposed to water vapour content), whose radiation intensity essentially depends on the thermodynamic temperature. And, on the other hand, in this band high-sensitivity radiospectrometres are implemented with spectral resolution ranging from thousands to units of megahertz, i.e. with $(\Delta\nu/\nu) \sim 10^{-4}\text{--}10^{-5}$. Such high resolutions in the passband of receiving systems of radiospectrometres (see Chapter 3) are necessary for selecting the radio-emission coming from various layers of a studied gas medium. To better understand the physical basis of such kinds of measurements we shall make use of the solutions of the gas medium transfer equation for the microwave range given by equations (9.64) and (9.66). We shall rewrite these relations in a more general form

$$T_B(\nu) = \int_0^{H_0} T(s)K(\nu, s) ds, \quad (12.5)$$

where $K(\nu, s)$ is called the kernel of the equation, or a weighting function. Since

each elementary gas layer possesses absorption of the radiation of the preceding layers and, at the same time, emits its own energy, the general altitude form of a weighting function can be rather complicated and, depending on the chosen observation frequency, can possess an altitude maximum. In other words, there will exist a layer altitude at which the emission will be determining for the emission of the total column of gas. Thus, the radiospectrometric reception of radiation with high resolution makes it possible to select and retrieve the temperature profile. Various geometries of the experiment (as, for example, observations from the earth's surface or from flight vehicles) results, generally speaking, in various forms and values of weighting functions. One of examples of a set of weighting functions for the line of 118 GHz in observation from a spacecraft is presented in Figure 12.3. In observation from the earth's surface the boundary layer of the atmosphere is sensed at the frequency of 60 GHz up to altitudes of 0.5 km. Sensing at 53.5, 54.5 and 55 GHz frequencies provides information on the temperature regime of the troposphere. When sensing at frequencies of 53.0633 and 53.0668 GHz by means of high-resolution instruments ($\Delta\nu/\nu \sim 10^{-5}$) one can obtain data on temperature distribution at altitudes of the order of 35–55 km (Naumov *et al.*, 1999). If the receiving device possesses a broad passband, of the order of ($\Delta\nu/\nu \sim 0.05\text{--}0.1$), then the received signal will contain the integral-over-altitude information on weighted-mean temperature without discriminating the altitude profile.

From the mathematical point of view equation (12.5) represents the integral Fredholm equation of the first kind for determining the altitude profile of temperature. This problem relates to a scope ill-defined, in the classical sense, problems and requires special methods of solution (Tichonov and Arsenin, 1979; Naumov *et al.*, 1999).

Thus, radiothermal instruments for thermal sensing of various atmospheric altitudes are subdivided into three classes, in accordance with the physical conditions of forming radiation in oxygen spectral lines, namely:

- high-resolution spectral instruments (6–8 channels), $\Delta\nu \sim 1\text{--}3$ MHz, for remote sensing of the stratosphere and mesosphere in distinguishing resonances of the 5-mm band;
- medium-resolution spectral instruments (4 or 5 channels), $\Delta\nu \sim 200\text{--}300$ MHz, for troposphere sensing at the wing of the 5-mm absorption band in the range of 53–58 GHz;
- broadband single-channel radiometers, $\Delta\nu \sim 2\text{--}4$ GHz, for sensing the boundary layer of the atmosphere at the absorption band centre in the range of 58–62 GHz.

The radiothermal complexes for thermal sensing produced until now are situated both at stationary observation stations and on transportable platforms, and in a ship version (Ciotti *et al.*, 1987; Troitsky *et al.*, 1993; Antonov *et al.*, 1995; Raffalski *et al.*, 1998; Cimini *et al.*, 2003; Kadygov *et al.*, 2003).

12.2 MICROWAVE REMOTE SENSING OF CLOUD FIELDS

Clouds play a crucial role in the earth’s climate by having an influence on key parameters, such as the radiation budget, the heating of the earth’s surface, and the diabatic heating of the atmosphere. They play a dual role on the top of the atmosphere radiation budget. In the short-wave region, clouds reflect the incoming radiation back to space, thereby decreasing the amount of solar energy available for absorption in the atmospheric column and at the surface. On the other hand, in the long-wave region they absorb the radiation emitted by the earth’s surface and the lower atmosphere and re-radiate it to space at a lower temperature, thereby causing the greenhouse effect. The net effect of clouds is the sum of these two processes, and it depends on the type and amount of clouds present at any particular geographic region of interest. Therefore, in a broad sense the distribution of cloud type and amount determines the distribution of energy sources and sinks in the terrestrial atmosphere, and, hence, is important to the general circulation of the atmosphere (Palmen and Newton, 1969; Webster, 1994).

The importance of clouds in the tropical parts of the World Ocean to global climate arises from the impact of clouds on radiative fluxes, atmospheric latent heating, and the fresh water flux into the ocean. The impact of clouds on the earth’s radiation balance and the distributions of cloud types and amounts have been a subject of many investigations (e.g., Marchuk *et al.*, 1986; Akilonova *et al.*, 1973; Akvilanova and Kutuza, 1978; Kutuza and Smirnov, 1980; Matveev *et al.*, 1986; Doviak and Zrnic, 1984; Cahalan, 1989; Houze, 1993; Davis *et al.*, 1996; Chang and Chiu, 1997; Kondratyev *et al.*, 1995; Liu *et al.*, 1995; JSTC, 1995; Arrault *et al.*, 1997; Meneghini *et al.*, 1997; Liu and Curry, 1998, 1999, 2000; Sharkov, 1998; Lin *et al.*, 1998a, b; Jameson *et al.*, 1998; Stephens *et al.*, 1998; IPCC, 2001; and references therein).

The results of a microscale cloud case study were presented by Intrieri *et al.* (1995) to illustrate the advantages of multi-wavelength observations. The combination of measurements from ground-based lidar (optic), radar (microwaves), interferometres and radiometers (microwaves) yield two-spatial geometrical, microphysical and radiative information not attainable by any one of these instruments alone.

There is no question that the potential satellite systems for investigations of fine cloud structures will carry multi-wavelength instruments. The role of microwave radiometry in the clouds project will be fundamental (Bizzari and Spera, 2000; Bizzari *et al.*, 2000).

12.2.1 Cloud classification schemes – the contribution of microwave radiometry

Different cloud types play different roles in the climate, with convective clouds providing the dominant contribution to precipitation and the layer clouds with their larger horizontal extent having a greater influence on radiative fluxes. Furthermore, the type of cloud associated with precipitation determines the impact of the precipitation on the tropical sea surface temperature and ocean mixed layer

characteristics. Deep convective precipitation is typically associated with strong surface winds, and the ensuing fresh water is easily mixed into the ocean below. By contrast, precipitation associated with shallow, isolated convection is generally accompanied by low wind speeds, resulting in the formation of a fresh water lens on the ocean surface that acts to stabilize the upper ocean and allows the sea surface temperature to warm (Webster, 1994; Webster and Lukas, 1992).

Therefore, the classification of cloud and precipitation regimes is very important to understanding the cloud effects on the earth's environment, particularly in the tropical oceans. Nevertheless, there is a lack of a universally accepted classification scheme of cloud systems. The most traditional approaches (schemes) consist in discrimination of the cloud fields via cloud-top height variations from infrared and visible cloud images by GMS, NOAA and Meteosat systems. Fuller data, based on visible and infrared radiances, are collected for the International Satellite Cloud Climatology Project (ISCCP) (see, for example Rossow and Schiffer, 1991; ISTC, 1995; IPCC, 2001) and by the Meteorological Satellite Center of Japan from GMS-IR data.

The classification of cloud types using combined infrared and visible satellite data typically uses the visible channel to provide information on cloud thickness and the infrared channel to provide information on the cloud-top height (Rossow and Schiffer, 1991). However, this approach does not allow one to infer the properties of deep clouds because of the saturation of both infrared and visible radiation. The large pixel-size and the lack of information regarding cloud height hamper cloud retrieval schemes that solely use satellite microwave data. To overcome the drawbacks associated individually with visible/infrared and microwave cloud retrieval schemes from satellite, a combined classification scheme was proposed by Liu *et al.* (1995) that uses combined infrared and microwave data. Using satellite microwave data also provides information on precipitation which cannot be obtained from the traditional infrared/visible classification schemes.

The proposed cloud classification scheme utilizes the cloud-top temperature obtained from infrared measurements (GMS-4) and a microwave index that is formed from special sensor microwave/imager (SSM/I) data of F-10 and F-11 DMSP satellites (see Chapter 14). The infrared data are used to determine the cloud-top temperature, and the microwave data are used to determine an index that includes both microwave scattering and emission. GMS infrared data are employed to separate cloudy from clear-sky pixels and to derive cloud-top temperature. A simple histogram-threshold method is used to determine cloudy pixels (Rossow and Schiffer, 1991).

The difference between cloud-top temperature and its brightness temperature should be smaller because of the thinner absorption layer above the cloud top than above the sea surface. The higher the cloud-top height, the smaller the difference. Accordingly, the cloud-top temperature, T_C , is calculated from the brightness temperature, T_{IR} , by the following equation:

$$T_C = T_{IR} + 8 \left(\frac{T_{IR}}{150} - 1 \right) \quad (12.6)$$

That is, the difference between T_C and T_{IR} is about 8 K near the sea surface (300 K) and decreases linearly as the cloud-top height increases.

A ‘semi-empirical’ ‘microwave index’ f is defined as follows to represent the strength of the microwave signal from a cloudy pixel:

$$f = \left(1 - \frac{D}{D_0}\right) + 2\left(1 - \frac{PCT}{PCT_0}\right), \quad (12.7)$$

where D represents the polarization at 19 GHz given by $D = T_{B19V} - T_{B19H}$, and T_{B19V} and T_{B19H} are, respectively, vertically and horizontally polarized brightness temperatures at 19 GHz; D_0 is D at the threshold for precipitation; PCT is the 85 GHz polarization-corrected temperature defined as $PCT = 1.818T_{B85V} - 0.818T_{B85H}$, and T_{B85V} and T_{B85H} are, respectively, vertically and horizontally polarized brightness temperatures at 85 GHz; and PCT_0 is PCT at the threshold for the onset of precipitation. The precipitation threshold is determined according to the rainfall algorithm, whereby the threshold is derived from the SSM/I data themselves for every $5 \times 5^\circ$ which includes climatological information. The first term on the right-hand side of (12.7) represents the microwave emission signal and the second term the scattering signal, so that index f accounts for both emission and scattering. Because the PCT rarely drops below 150 K, the maximum value of $(1 - PCT/PCT_0)$ is almost a half of the maximum value of $(1 - D/D_0)$. A factor of 2 is therefore given to the scattering term, so that the emission and the scattering terms have equal contributions to the microwave index function.

The rainfall algorithm includes the following features: (1) different formulas are used for non-precipitating and precipitating clouds; (2) a scheme for calculating clear-sky brightness temperature is included, which can easily be turned by observed SSM/I data, and the contribution of the components other than liquid water (i.e. the sea surface and atmosphere) can be remote without being biased; (3) the cloud mean temperature, to which the liquid water path retrieval is very sensitive, is derived from the SSM/I brightness temperature and cloud-top temperature determined from the infrared satellite data (GMS data in this case); and (4) the effects of precipitating-size water drops and ice particles and of the inhomogeneity of the rain field in a satellite footprint are accounted by combining 19 and 37 GHz measurements.

As shown by Liu *et al.* (1995), the microwave index f is a good indicator for rainfall rate and ‘dense ice’. In addition, the cloud-top temperature is also used for cloud classification. Clouds are classified into eight classes based on the microwave index f and the GMS cloud-top temperature (Figure 12.6), namely: (1) a warm non-precipitating cloud, (2) a warm precipitating cloud, (3) a mid-top non-precipitating cloud, (4) a mid-top precipitating cloud, (5) a thin high-top non-precipitating cloud, (6) a deep high-top non-precipitating cloud, (7) an anvil with stratiform precipitating cloud, and (8) a deep convective precipitating cloud.

The classes defined are based primarily upon cloud physical considerations. The warm clouds have cloud-top temperatures warmer than 0°C. No ice-phase particles would be expected in these clouds. The mid-top clouds have cloud-top temperatures from 0 to –40°C, and the clouds in these categories could be of mixed phase (or

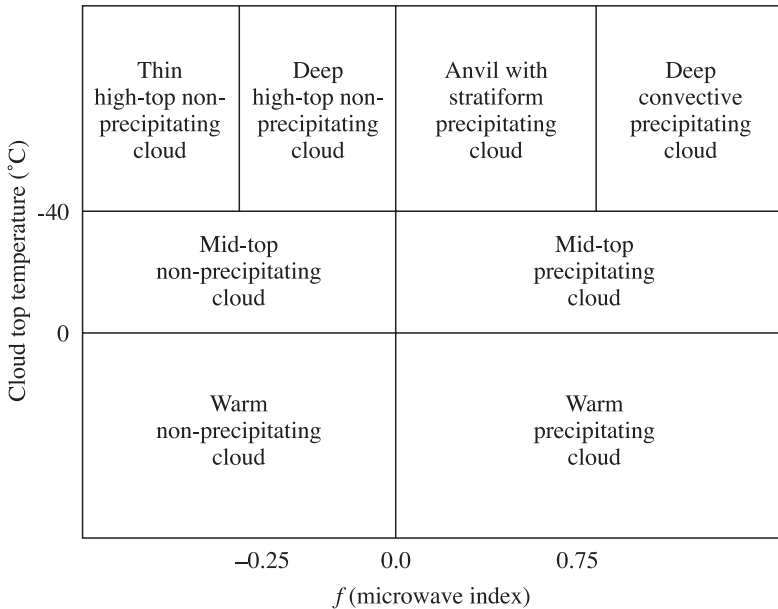


Figure 12.6. Schematic diagram of the microwave index f versus cloud top temperature for cloud classification (Liu *et al.*, 1995).

either phase). The cloud-top temperatures for the last four cloud types are colder than -40°C . Ice-phase particles can be easily observed in these clouds.

Precipitating and non-precipitating clouds are separated based on the value of the microwave index greater or less than zero. For clouds with tops colder than -40°C , four different cloud types are further defined. The thin, high-top, non-precipitating cloud, $f < 0.25$, has almost no liquid water. The deep, high-top, non-precipitating cloud has a liquid water path as large as about 150 g/m^2 , on the average, when $f = 0$. It could consist of several layers, perhaps, a liquid-water cloud layer underlying a cirrus deck, and rainfall is not detected.

Anvil with a stratiform precipitating cloud has a greater liquid water content and is precipitating. Besides, having a greater liquid water content and heavy rainfall rate, the most striking feature of deep convective precipitating cloud compared to anvil with stratiform precipitating cloud is that it contains a significant amount of ‘dense ice’. As mentioned earlier, the ice water path from SSM/I only reflects the ‘dense ice’ particles with large size and densities, such as graupel. A strong updraft is required to produce and maintain the ‘dense ice’ in the cloud, which may only occur in deep convective clouds. Therefore, although the separation between anvil with stratiform precipitating cloud and deep convective cloud is based on cloud physical consideration, i.e. whether or not there is a significant amount of ‘dense ice’, it also reflects the difference in cloud dynamics for the two cloud types. It can be seen that the dense ice index is about 200 g/m^2 at $f = 0.75$ (the boundary between anvil with stratiform precipitating cloud and deep convective cloud). The choice of $f = 0.75$

instead of $f = 0.5$ (where the ice index is equal to 0) is based on the significance of dense ice amount. Because some soft ice (such as snow) and raindrops may slightly reduce the 85 GHz brightness temperature, they may also be interpreted as dense ice by the retrieval algorithm (although the magnitude should be very small). Also, the algorithm itself may produce error in dense ice amount. Therefore, to safeguard the significance of dense ice amount the authors have chosen $f = 0.75$.

The classification scheme was validated by aircraft radar data obtained from the TOGA experiment in the tropics (Liu *et al.*, 1995). In summary, the classification scheme generally works well for most of the clouds in this region, showing good agreement with radar observation for large cloud systems and being able to distinguish reasonably well between precipitating and non-precipitating clouds. However, the classification scheme has difficulties in resolving the small, isolated clouds that are sometimes associated with locally heavy rainfall.

The results obtained by Wang *et al.* (1998b) lead to the conclusion that thick cirrus clouds with large ice particles may be sensed with millimetre-wave radiometry (the 150 and 220 GHz ranges). Over the land, cirrus clouds may give spurious millimetre-wave brightness temperature signatures, caused by skin temperature reductions due to cloud shadowing. According to the Millimetre-wave Imaging Radiometre (MIR) data, the skin temperature effect may be corrected using the 89 GHz channel, resulting in the T_B at 150 and 220 GHz due to ice particle scattering. The thick cirrus, for which the millimetre-wave measurements are useful, has saturated infrared temperatures and attenuated lidar backscattering. Thus, these results illustrate the potential utility of millimetre- and sub-millimetre-wave radiometry for complementing the visible and infrared measurements of cirrus cloud microphysics.

A radically new classification method is developed based on investigation of geometrical multi-fractal features (but not radiance discrimination) of various cloud types (Lovejoy and Mandelbrot, 1985; Lovejoy and Schertzer, 1985; Baryshnikova *et al.*, 1989a, b; Davis *et al.*, 1994, 1996). The geometrical approach is still at a primitive stage of development. But there is no question that the potential integral discrimination schemes using both radiance infrared and microwave variations and fractal geometrical features of cloud systems can give encouraging results.

12.2.2 Microwave remote sensing of rainfalls

A key link in the hydrological cycle is rain that falls from cloud systems in the tropics, which amounts to two-thirds of total global precipitation. Precipitation, by means of its associated latent heat release, is a major energy source driving the hydrological cycle and the large-scale circulation of the atmosphere. The vertical profile of latent heat release greatly influences the structure and speeds of the important wave patterns by which events in the tropics affect the global weather and climate (Simpson, 1988; WMO, 1990a,b; Simpson *et al.*, 1988, 2000; Theon *et al.*, 1992; Webster, 1994; Raschke and Jacob, 1993; Trenberth, 1997; Sharkov, 1998; Stockade *et al.*, 1998; Sorooshian *et al.*, 2000).

One of the most crucial and least-known components of the global hydrological cycle is the precipitation over the tropical oceans, which has never been measured before; the indirect estimates can disagree by as much as 100% or more (Theon *et al.*, 1992). Conventional rainfall measurements are scarce in the tropics. Satellite observation is thus the only effective way to provide continuous monitoring of precipitation events. The need to improve satellite retrieval of rainfall rate/amount has motivated the Tropical Rainfall Measuring Mission (TRMM) (Simpson *et al.*, 1988, 2000; Kummerow *et al.*, 1998, 2000; Takanashi *et al.*, 2000), the Global Precipitation Climatology Project (GPCP) (Arkin and Xie, 1994) and Precipitation Mission (ESA, 1996c). While the monthly time scale has been the focus of most satellite retrieval efforts, it is becoming increasingly apparent that higher space and time resolution rainfall products are needed for diagnostic studies of air/sea interactions and to provide forcing for ocean models.

The current satellite rainfall observations and retrieval algorithms can be categorized into infrared (IR), visible and infrared combined (VIS/IR), passive microwave, and a combination of IR, passive microwave and radar microwave.

Visible/infrared radiation upwelling from clouds, and eventually measured by space-borne radiometers, is reflected/emitted by the top layers of the clouds, and it is (at most) weakly correlated to the microphysical structure of the underlying cloud and precipitation layers. Thus, the VIS/IR precipitation retrieval algorithms cannot be based on information directly associated with precipitation, but are based on the fact that high and thick – i.e. highly reflective and radiometrically cold (for VIS/IR radiation, respectively) – clouds are associated with precipitation, particularly in convective systems.

Two limitations of the VIS/IR optimization method should be emphasized. First, it can be only provide an indication of rain/no-rain, and not a quantitative rainfall rate. Second, it will fail if the region outside the radar coverage has a different type of rainfall from that within the radar coverage. In addition, all that can be said about the adjacent region is the fractional area containing rain. A method of conveying this into the average rainfall rate is needed. Probably, VIS/IR from a geostationary imager would be sufficient.

Passive and active microwave measurements from air/space-based instruments have, in principle, a great potential for estimating precipitation because the upwelling radiation over the precipitating cloud is directly responsive, in a frequency-dependent fashion, to precipitation microphysics. Since the passive microwave precipitation retrieval techniques are linked in a more direct way to the physical characteristics of the rainfall itself than the infrared techniques, more accurate instantaneous rainfall rates can, in principle, be determined using the microwave techniques.

In comparison with visible/infrared observations, passive microwave observations provide better physical information for estimating surface rainfall because microwaves can penetrate clouds and interact directly with hydrometeors at lower levels. The upwelling passive microwave brightness temperatures are determined from the surface emissivity and vertical distributions of the ice and liquid content of clouds. At low microwave frequencies (<37 GHz) the brightness temperature

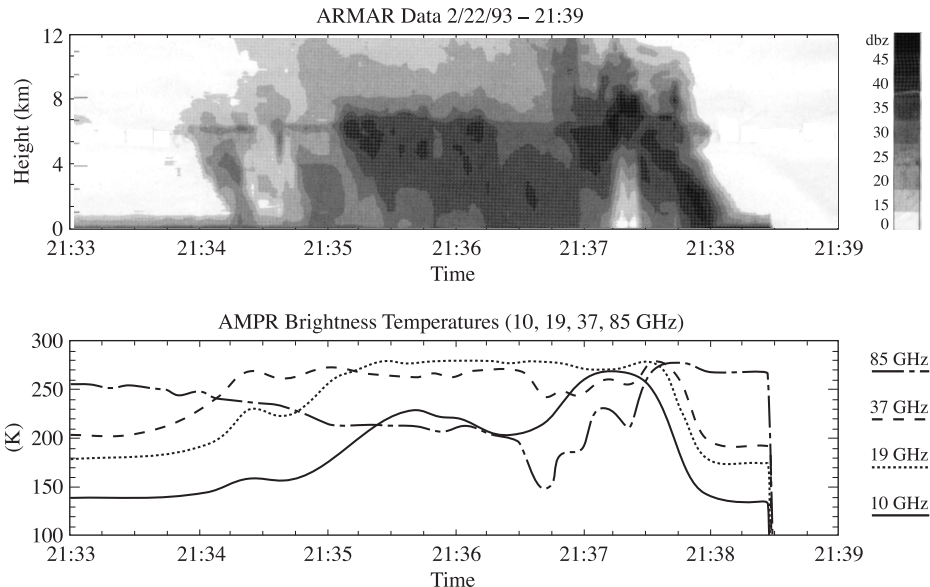


Figure 12.7. Backscattering and thermal radiation signals of a tropical convective cloud system observed by the Airborne Rain-Mapping Radar (ARMAR) and the Advanced Microwave Precipitation Radiometer (AMPR) during TOGA COARE (22 February 1993): (a) radar reflectivity altitude profile of the convective cloud from ARMAR; (b) the spatial profile of brightness temperatures from AMPR for 10, 19, 37 and 85 GHz (Hong *et al.*, 2000).

responds mostly to emission from rain and cloud liquid, and thus the observed brightness temperature increases over the radiometrically cold ocean. In contrast, at high frequencies ($>37\text{ GHz}$), the brightness temperature responds mainly to scattering from cloud ice, and the observed brightness temperature decreases over both ocean and land backgrounds. Figure 12.7 depicts one instructive experimental case that was observed by the Airborne Rain-Mapping Radar (ARMAR), which measured backscattering fields, and the Advanced Microwave Precipitation Radiometer (AMPR), which measured thermal radiation fields, during the Tropical Ocean and Global Atmosphere Coupled Ocean – Atmosphere Response Experiment (TOGA COARE) (Hong *et al.*, 2000).

Rainfall retrieval from satellite and aircraft passive microwave brightness temperatures has been investigated by many researchers using various approaches, from a linear regression (Allison *et al.*, 1974; Wilheit and Chang, 1980) to complicated model-retrieval brightness temperature procedures (Tsang *et al.*, 1977; Viltard *et al.*, 1998; Marzano *et al.*, 1999; Hong *et al.*, 2000).

However, the estimates of precipitation derived from modern satellite microwave observations currently suffer from a serious drawback. Owing to the complexity of the problem and to difficulties related to the characteristics of the radiometers which have been used so far, the quantification of precipitation from satellite passive microwave radiance data still remains, to a large extent, unresolved.

Several algorithms for the retrieval of precipitation have been proposed in the last decade or so, but a consensus algorithm has yet to be developed by the scientific community – for a brief description of several passive microwave algorithms, mostly based on the DMSP-SSM/I (Defence Meteorological Satellite Program – Special Sensor Microwave Imager) image data, and one based on the NOAA-MSU (Microwave Sounding Unit) vertical profile data (see ESA (1996c) and Sharkov (1998)).

The data furnished by SSM/I have been used to provide estimates of precipitation, but suffer from problems, which are due not only to deficiencies of the retrieval techniques themselves, but also to the characteristics of the instrument such as the SSM/Ts space and temporal sampling, which is not adequate for correct observation of precipitation, as well as its frequency selection and scan geometry. The Special Sensor Microwave/Imager (SSM/I) aboard the Defense Meteorological Satellite Program (DMSP) spacecraft provides infrequent sampling, especially in the tropics. Even with the two separate DMSP spacecraft at present in operation, the average local coverage is only about twice a day. The inadequate temporal coverage of SSM/I seriously limits its application in climatic studies. It has been reported that precipitation in the tropics undergoes a preferred diurnal cycle depending on location. Therefore, even with accurate instantaneous precipitation retrieval, the SSM/I observations are not suitable for estimating daily rainfall accumulations because two samples are far from sufficient to capture the daily averaged precipitation.

The detailed analysis of requirements for satellite missions for rainfall measurements and for verification of satellite rainfall algorithms is contained in books (Atlas *et al.*, 1984; Ferraro *et al.*, 1996; Gairola, 1999; Olsson, 1996; Rodgers *et al.*, 1994; Ruf *et al.*, 2000; ESA, 1996c; Sharkov, 1998).

12.3 MICROWAVE REMOTE SENSING OF SURFACE OCEANIC HEAT FLUX FIELDS

The ocean interacts with the atmosphere through exchanges of momentum, heat and moisture. The differential heating of the atmosphere by the ocean fuels atmospheric circulation, which, in its turn, drives ocean currents and redistributes the fuel. Short-term climate changes are believed to be strongly influenced by such exchanges. Locally, the ocean absorbs heat in the summer and releases it in the winter; globally, heat accumulated in the tropics is transported poleward by ocean currents. The redistribution of heat reduces the extreme temperature contrasts that otherwise would exist. The heat and moisture fluxes change both the horizontal and the vertical density gradients of the atmosphere and the ocean. They, in their turn, modify the wind and current shears. The moisture flux associates the energy cycle to the hydrological cycle. In the atmosphere, condensation provides not only the means for precipitation, but much of the diabatic heating as well. In the ocean, evaporation cools the upper layer and increases the salinity. The ocean exchanges heat with

the atmosphere through radiative and turbulence processes. Both the sensible heat and moisture fluxes are largely transported by turbulence in the atmosphere. The moisture flux carries latent heat, which is much greater than the sensible heat, both in the mean and the variability over much of the ocean. In the past, large-scale fluxes were computed using meteorological reports from ships of opportunity. In the tropical and southern oceans, ship observations are sparse, so the temporal and spatial variabilities of fluxes cannot be determined accurately using the ship data alone. Space-borne sensors can provide repeated global coverage of meteorological parameters. So, observations of the sea surface using infrared or microwave radiometers provide important information for studying the dynamical and thermodynamical processes in the upper ocean layer and in the atmospheric layer. Both infrared and microwave radiometers measure the water temperature in a thin layer near the water surface, the so-called skin layer. Its thickness is of the order of a few hundredths of a millimetre for infrared measurements and a few millimetres or smaller for microwave radiation. The processes of heat, moisture, and momentum exchange between the ocean and atmosphere result in water-temperature profiles with very large gradients near the sea surface. For this reason the water temperature, determined with standard *in situ* measurements (at a depth of 1 or 2 m) and with microwave and IR instruments, can be substantially different. The understanding of physical processes that control the temperature profiles near the sea surface is one of the critical points for satellite oceanography (Robinson, 1985; Blume *et al.*, 1977; Liu, 1990). The heat flux in water is dominated by turbulent and molecular transport. However, very close to the surface, in a layer of about 0.5 mm, the turbulent heat transfer at the surface is zero and, hence, at some depth in the range of 0.02–0.5 mm the main contribution to the total heat flux is made by the molecular conductivity of water. If the temperature profile, or at least the temperature gradient, is measured within this layer, it is possible to recover the total heat flux between the ocean surface and atmosphere.

The idea to use the microwave multiwave sensing instruments (passive radio-spectroscopy) with different skin depths in the non-isothermal sea surface skin-layer for measuring the water temperature gradient was proposed for the first time by Sharkov (1978). However, in the microwave range the problem of these measurements is complicated, since the surface emission essentially depends on sea-wave conditions, so the wave intensity and wave-breaking can vary in wide ranges. Nevertheless, such or similar approaches can be used well in laboratory practice (Gaikovich *et al.*, 1987), as well as on moving ships (Trokhimovski *et al.*, 1998; Cimini *et al.*, 2003) and on low-altitude airborne platforms.

The modern methods for diagnosis of large-scale thermal interaction between the ocean and the atmosphere from satellite microwave measurements follow the approach based on the semi-empirical equations of a global aerodynamic method (the so-called meteorological bulk parameterization) used as a connecting link between the radiative and heat-exchange characteristics of these environments. A physical foundation of this approach is the fact that the main parameters in the bulk formulas (the ocean surface temperature, air temperature and humidity, wind speed in the near-surface atmosphere) are directly involved in the formation and

transformation of the natural microwave radiance of the ocean–atmosphere system (Liu, 1990).

Another strategy for using the satellite microwave radiometric measurement data is associated with the assimilation of these data in the form of direct indicators of the intensity and the dynamics of heat and moisture exchange (Olson *et al.*, 1999; Grankov *et al.*, 2000). This approach corresponds to the idea of using remote microwave measurement data not only to convert them into parameters accepted in geophysics (temperature, moisture content of the medium, wind speed, etc.), but also to characterize the generalized (essentially thermal energy) indicators, such as the radiation index of the ground surface dryness, the intensity of heat and moisture exchange between the atmosphere and the ground surface, the latent heating distribution and other elements of the energy budget.

As inferred from Chapter 10, the measurements of upwelling microwave brightness temperatures provided by microwave instruments are sensitive to observed distributions of precipitating liquid and ice-phase hydrometeors. Since precipitation is the end-product of hydrometeor phase-change processes in clouds, and since the latent heat is released and consumed by these processes, the passive microwave measurements yield an indirect measurement of latent heating processes. A method for remote sensing of three-dimensional latent heating distributions in precipitating tropical weather systems from the satellite passive microwave observations was developed by Olson *et al.* (1999). In this approach, the cloud model that simulated hydrometeor latent heating vertical profiles, which have radiative characteristics consistent with the given set of multispectral microwave radiometric observations, was composed to create the best estimate of the observed profile by the special retrieval ‘Bayesian’ technique. An estimate of the areal coverage of convective precipitation within the radiometer footprint is used as an additional constraint on the contributing model profiles. This constraint leads to more definitive retrieved profiles of precipitation and latent heating in synthetic data tests. The remote sensing method is applied to Special Sensor Microwave/Imager (SSM/I) observations of tropical systems, which occurred during the TOGA COARE, and to Hurricane Andrew observations (1992). Although the instantaneous estimates of rain rates are high-biased with respect to coincident radar rain estimates, the precipitation patterns are reasonably correlated with radar patterns, and the composite rain rate and latent heating profiles show respectable agreement with estimates obtained from forecasting models and from heat/moisture budget calculations (Rodgers and Adler, 1981; McMurdie and Katsaros, 1985; Rodgers *et al.*, 1994; Sharkov, 1998; Nerushev *et al.*, 2001).

Another approach was developed by Grankov *et al.* (2000). Based on the results obtained in the Atlanteks-90 experiment and simulations, it has been shown that the brightness temperature of the ocean–atmosphere system’s microwave emission can serve as a direct numerical characterization of synoptic variations in the intensity of heat and moisture exchange at its interface. The parameters interlinking heat fluxes and the ocean–atmosphere system brightness temperature are the emission of molecular oxygen in the resonance band at 5 mm, and the total atmospheric moisture content in the 1.35-cm resonance line. The interrelation, for example,

between the mean daily variations of fluxes of total (latent and explicit) heat and the ocean–atmosphere system’s brightness temperature, is very close; the value of the correlation coefficient between these quantities varies from 0.83 to 0.92 as a function of the radiation wavelength; the brightness temperature reacts particularly clearly to the sharp changes in heat fluxes observed in the Atlanteks-90 experiment in the period of cyclonic reconstruction of the atmosphere. The results of this analysis confirm the role of the total atmospheric moisture content in the processes of heat and moisture exchange at the ocean – atmosphere system’s boundary, divide on synoptic time scales and, at the same time, attest to the importance of this parameter as a remote characteristic of the thermal state of the system.

Below we shall consider in more detail the radiothermal methodology of studying the transition skin-layer of the ocean–atmosphere system.

12.3.1 Radiothermal spectroscopy of the ocean–atmosphere transition layer

As we have noted, an important example of non-isothermal structure in the ocean – atmosphere system is the transition microlayer on the ocean surface through which the mass- and heat-transfer between the ocean and atmosphere occurs. The problem of studying the heat exchange between the ocean surface and the atmosphere within the framework of the small-scale interaction model is reduced (under weak sea wave conditions) to the problem of experimental determination of characteristics of temperature profile characteristics in the thin stable surface layer of the sea.

The use of unique contact instruments made it possible to find, that the temperature profile in the surface layer of the sea, which exists both at night and in the day, is highly non-isothermal and has an exponential character (Khundzhia *et al.*, 1977; Robinson, 1985):

$$T(z) = T_2 + (T_1 - T_2) \exp(-\beta z). \quad (12.8)$$

where $T(z)$, T_1 and T_2 are temperatures, respectively, at depth z , at the depth of isothermal layer bedding and on the surface. Such a ‘cold’ surface layer 2–5 mm to 10–20 cm deep was recorded, for example, in the Black Sea (in summer and autumn) with sea waves up to wind force 3 (Khundzhia *et al.*, 1977). In the same paper it was shown that the value of the total heat energy flux (q) from the sea to the atmosphere, which is composed of molecular heat exchange on the ocean–atmosphere boundary, and of latent heat for water evaporation from the sea surface, is determined by the following expression:

$$|q| = \Lambda \beta (T_1 - T_2), \quad (12.9)$$

where Λ is the molecular heat conduction coefficient of ocean water. Thus, from experimentally found characteristics of the temperature profile (the difference between T_2 and T_1 and quantity β) one can determine the total heat flux returned by the sea into the atmosphere during thermal interaction. The determination of features of the spatial structure of the temperature field of the sea’s subsurface layer by the remote sensing method can have a defining significance in heat- and mass-exchange processes in the open sea. However, the use of IR thermal systems for

solving the mentioned problem is inconvenient, since the effective emitting layer in this band of electromagnetic waves represents a very thin surface film having a thickness of the order of 5–10 micrometre, and for this reason the contribution of the considered non-isothermal character of temperature to the IR thermal radiation is low.

A more optimal remote sensing technique, which allows one to approach the experimental solution of the problem of determining small-scale heat exchange characteristics at the ocean–atmosphere boundary, is the use of radiothermal microwave instruments (Sharkov, 1978), because the effective emitting layer in this band extends up to a thickness compared with the ‘cooled’ transition layer, and the contribution of the non-isothermal character of temperature to the radio-emission of such a surface will be considerable.

In this problem it is possible to use the approximation of radiation of non-uniformly heated absorbing medium with allowance for refractive distortion of a flux (see relations (7.101) and (7.102)). Using these relations, after some transformations we shall obtain the following expression for the contrast of radiobrightness temperature ΔT_B of a quiet water surface with temperature T_2 , caused by the non-isothermal character of the subsurface layer:

$$\Delta T_B = \kappa(\lambda, \theta, T) \frac{T_1 - T_2}{1 + \frac{\beta}{\gamma(\lambda)S(\theta, \lambda)}}, \quad (12.10)$$

where $\gamma(\lambda)$ is the coefficient of attenuation in the sea medium, λ is the working wavelength. Figure 12.8 presents the spectral dependencies of the $\Delta T_B/\Delta T_0$ ratio, where $\Delta T_0 = T_1 - T_2$ at nadir-looking observation for a fresh (salinity of 0‰) and

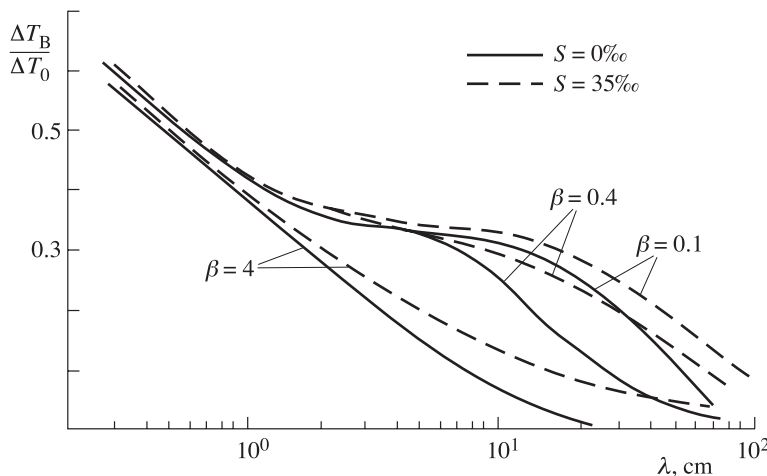


Figure 12.8. Theoretical microwave spectra of relative variations of the brightness temperature for water surfaces with a non-isothermal skin-layer in a nadir sensing of fresh ($S = 0\text{‰}$) and sea ($S = 35\text{‰}$) water and for the following profile parameters: $\beta = 0.1, 0.4, 4.0$.

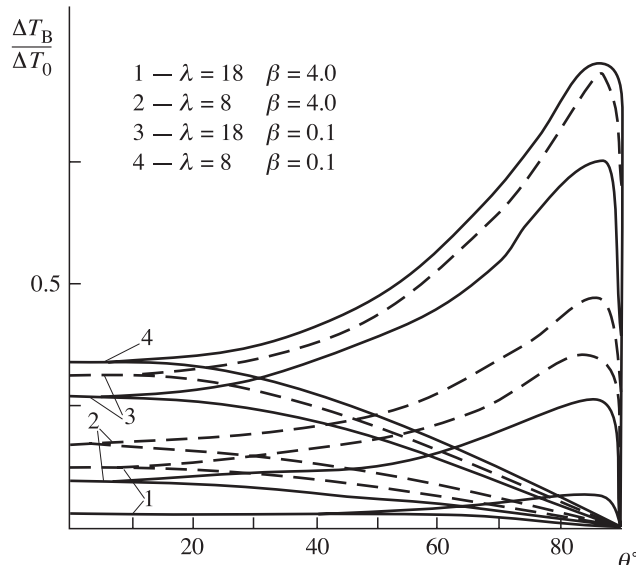


Figure 12.9. Polarization characteristics of relative variations of the brightness temperature for water surfaces with a non-isothermal skin-layer in a nadir sensing of fresh (solid curves) and sea (dashed curves) water and for the following profile parameters: $\beta = 0.1$ and 4.0 , and at wavelengths 8 and 18 cm.

ocean water (salinity of 35‰), as well as for three temperature profiles (β values of $0.1, 0.4, 4.0 \text{ cm}^{-1}$). The former values of β correspond to shallower sections of water areas; the last value corresponds to deeper ones. The analysis of Figure 12.8 indicates that the most informative, from the viewpoint of recognition of the profile gradient (quantity β) for fresh and for sea water is the long-wavelength portion of the centimetre and the short-wavelength portion of the decimetre wavelength band. Radio-emission in the band of wavelengths shorter than 1cm is formed by a thin water interlayer, and, by virtue of this fact, the addition to radiobrightness temperature is mainly caused by the surface temperature variation. In the long-wavelength portion of the decimetre wavelength band (longer than 50cm) the effective layer of radio-emission both for sea and for fresh water essentially exceeds the non-isothermal region, and the contribution of this temperature profile feature into radio-emission decreases. The analysis of polarization characteristics of the relative addition to radiobrightness temperature, caused by the non-isothermal character of the temperature profile (Figure 12.9) indicates, that the $\Delta T_B / \Delta T_0$ dependence is qualitatively similar to the polarization characteristics of a smooth water surface – there is a prominent Brewster angle for the vertically polarized radiation component.

To solve the reverse problem, that is, to derive the $\Delta T_0 = T_1 - T_2$ difference and parameter β from the results of radio-emission measurements at several wavelengths, it is possible to make use of the construction of nomograms, which have the form of a set of intersecting straight lines in the problem under consideration. Figure 12.10

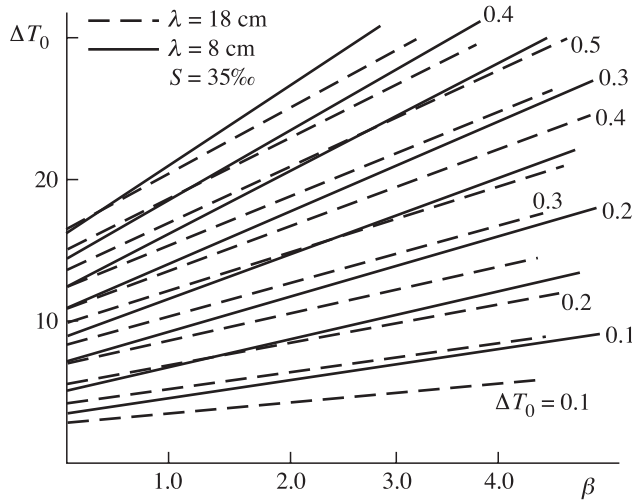


Figure 12.10. Diagram for recovering profile parameters ΔT_0 and β for sea water surface using measurements at two wavelengths, 8 and 18 cm. The measured parameter ΔT_B varies from 0.1 K in intervals.

presents the nomograms in ΔT_0 - β coordinates, calculated by (12.10) for two wavelengths, 18 and 8 cm, and for sea water of salinity 35‰. The parameter of sets is presented by the values of contrasts of radiobrightness temperatures obtained at observation of regions with various degrees of the non-isothermal property. The use of a component with an observation angle near the Brewster angle for reception of radio-emission of a vertically polarized component can increase by a factor of 2–2.5 the absolute measured values of contrasts of radiobrightness temperatures.

Since in actual observed cases ΔT_0 varied from 0.1 to 3°C, then, as follows from Figure 12.8, the contrast to radiobrightness temperature will constitute rather small values – degrees and fractions of a degree. The techniques close to this procedure have been successfully applied under laboratory conditions (Gaikovich *et al.*, 1987) and on board the research ship (Trokhimovski *et al.*, 1998). The now available high-sensitive multi-frequency radiothermal onboard complexes allow one to hope for a successful experimental solution of the important problem of ocean – atmosphere heat exchange under consideration.

12.4 MICROWAVE REMOTE SENSING OF THE OCEANIC SURFACE

As we have already noted, the inclusion of methods and means of microwave diagnostics into space observations in the period 1968–1979 (on the ‘Cosmos-243’, ‘Cosmos-384’, Seasat, and Nimbus-7 satellites) was undoubtedly a principal stage in the development of remote sensing of the World Ocean. The study and understanding of microwave patterns of the ocean surface have provided a significantly different

(as compared to the case of using the optical and infrared bands only) physical information capacity of microwave sensing in studying such dynamical objects as disturbance of the sea surface. This relates, first of all, to spatial–temporal statistical features of the sea state and the surface wind field. The electrodynamic properties of the sea surface disturbance and, first of all, the intensity of microwave radiation, is determined by the two areas of physical phenomena. The first one is related to the degree of roughness of the ruffled (but continuous) surface, or, in other words, with spatial features of the sea disturbance spectrum considered as a spatial–temporal statistical object (see Chapter 2). The second area is related to disturbance of the sea medium continuity, which reveals itself as breaking sea waves and the appearance of the intensive drop-spray phase and the bubble disperse phase of sea foam. Here, again, the consideration is performed within the framework of studying the electrodynamic properties of disperse media (see Chapter 10). The mentioned subdivision, certainly, is rather conventional, since the spatial-phase transformations belong to the same physical object. Nevertheless, from the viewpoint of electrodynamic models research, as detailed investigations have shown, such a subdivision is, undoubtedly valid. Each of these approaches has till now taken an individual direction of investigations, both in the experimental and the theoretical respect. Below we shall briefly consider some historical aspects and the modern state of investigations in these areas.

12.4.1 Rough sea surface

The results of theoretical investigations (Stogryn, 1967; Shulgina, 1972; Martsinkevich and Melentyev, 1975; Wentz, 1975; Wu and Fung, 1972) of the thermal radiation of a rough surface within the framework of geometrical optics approximation and using the statistical data on sea surface slope distribution of gravitational waves (Cox and Munk, 1954; Martsinkevich, 1970) gave rise to the statement of detailed experimental investigations, which were carried out in 1969–1970 from the special platform of the Argus Island tower near Bermuda at rough sea conditions (Hollinger, 1971). The experiment has demonstrated a fairly high sensitivity of brightness temperature variations on the horizontal polarization at 40–70° incidence angles to the wind speed under variable disturbance conditions and made it possible to obtain for the first time numerical values of gradients in the dependence of radiation intensity on the surface wind speed. Note that the wind speed magnitude only is meant here.

It was the results of these experiments that later underlay the measurement ideology and data processing algorithms for the Scanning Multichannel Microwave Radiometre (SMMR) installed on board the Seasat spacecraft (July–October 1978) and the Nimbus-7 satellite (launched in 1978). Using linear regression models, the global map of speeds (the speed magnitude) of the surface wind in the World Ocean area was first reconstructed for a period of one month (Prabhakara *et al.*, 1983). A series of interesting experiments (for example, by Kondratyev *et al.*, 1975; Martsinkevich, 1981; Guissard and Sobieski, 1987; Wentz *et al.*, 1986; Wilheit *et al.*, 1984; Wilheit and Chang, 1980; Sasaki *et al.*, 1987) were performed later;

however, the question on azimuthal properties of microwave radiation, i.e. on the relationship between the wind speed vector (or the wave vector of an energy-carrying wave) and the vector of linear polarization of the antenna system was not stated.

The experimental detection of stable azimuthal properties of thermal radiation of the disturbed sea surface under full-scale conditions in 1976 marked a radically new stage in the remote sensing of a rough dynamic surface (Bespalova *et al.*, 1979, 1982). This is related, first, to the fact that the obvious azimuthal properties indicate the diffraction character of electromagnetic field interaction with the surface roughness. This fact should be expected, strictly speaking, from general physical considerations, i.e. from the relation between the electromagnetic radiation wavelength and the gravitation-capillary wavelength of sea surface waves. But, because any reliable full-scale data on spatial spectra of gravitation-capillary waves were absent to the time of performing flight experiments, the strong and stable azimuthal effect in the field of thermal radiation of a wave-driven water surface in quite various areas (the open ocean, large lakes) and under various acceleration conditions (developed disturbance, non-developed fetch) was completely unexpected for the researchers. Secondly, the presence of a stable azimuth effect, recorded by remote sensing, makes it possible to restore not only the magnitude, but also the vector of the surface wind, which is an important parameter in the dynamical interaction of a wind flux with the dynamical surface.

The first cycle of airborne measurements of the azimuthal dependence of sea surface thermal emission at different polarizations under various weather conditions were performed by the specialists of the Space Research Institute (Moscow) using airborne microwave instruments with linear polarization during circular flights in 1976–1997 in the high-latitude sea areas of the Barents Sea and the White Sea (Bespalova *et al.*, 1979). The next cycles of these flight experiments were conducted in the Sea of Okhotsk, the Caspian Sea, the Black Sea, the Sea of Japan and Lake Ladoga in 1977–1979 (Bespalova *et al.*, 1982) and then near the Kamchatka peninsula in the north-west Pacific in 1981–1982. The measurements were carried out both far from the shore, where the ocean depth was about 1–5 km, and in the near-shore areas. The wind speed (sea state) and the energy wave fronts were estimated during the first cycle both, visually – by skilled aircraft operators using the Beaufort sea notation – and by processing the aerial photographs. Then the wind speed for these studies was estimated at typical flight altitudes of 200–1000 m using Doppler-based wind drift estimates. From these data the wind speed at the standard altitude of 10 m was calculated using the logarithmic dependence for the wind profile.

While the research aircraft performed circle patterns over wave-driven seas, the microwave radiometers aboard recorded cosine-like variations in brightness. Typical brightness temperature variations, measured during circular flights over the Caspian Sea and the Sea of Japan, are shown in Figures 12.11 and 12.12. The first cycle of measurements were carried out using nadir-looking microwave instruments at wavelengths from 0.8 to 18 cm and the SC-3 scatterometre at the wavelength of 3 cm. Owing to aircraft roll of 5–10° all radiometers were pointed during the circling at the same incidence angle, so that the linear polarizations oriented along the aircraft axis

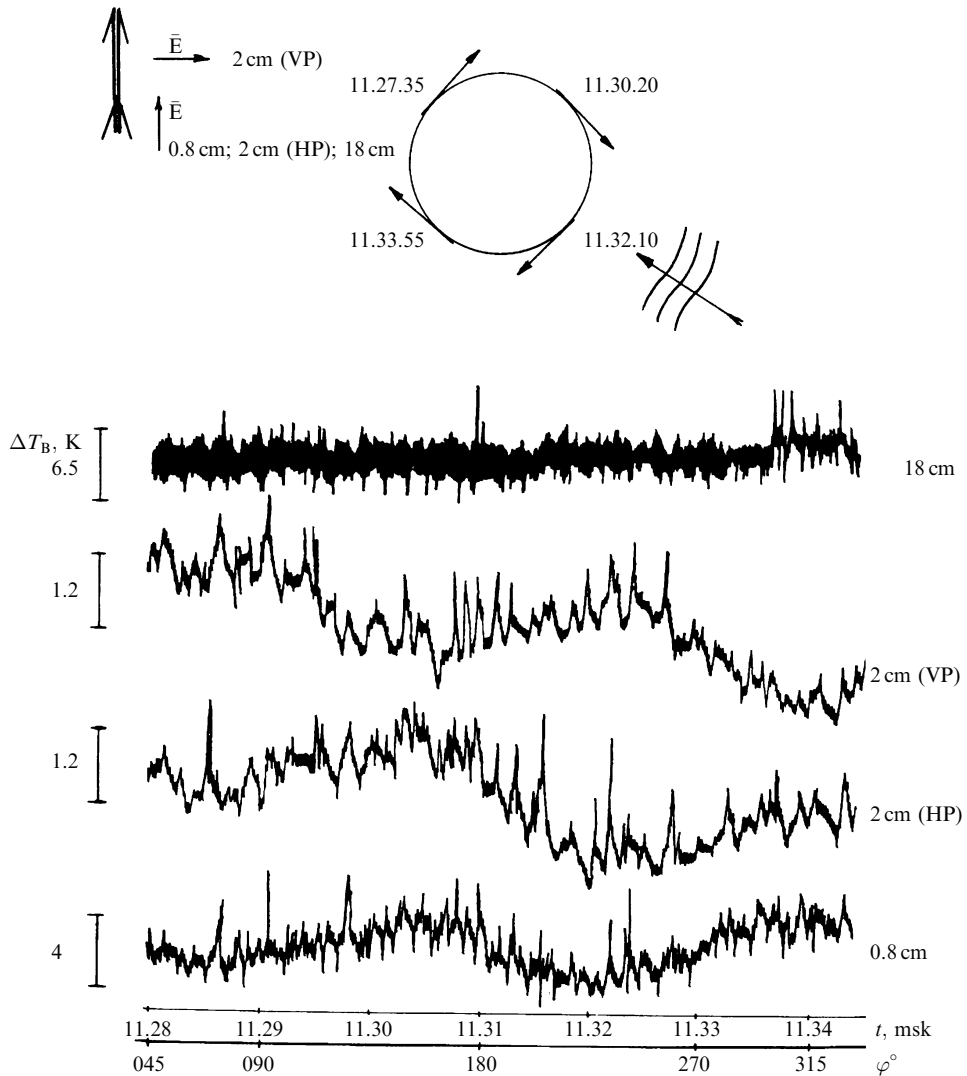


Figure 12.11. The experimental results of flight investigations that made possible the detection of the azimuthal anisotropy effect in sea surface microwave emission. The scheme of circular flights and the positions of the antennas' linear polarization vectors and of surface gravity wavefronts are presented at the top of the figure. The double arrow points along the longitudinal centreline of the research aircraft. The fragments of the output signals of airborne (Russian airplane-laboratory IL-18) radiometer R-18 (wavelength 18 cm), radiometer R2 (wavelength 2 cm, two polarizations: HP, the horizontal polarization; VP, the vertical polarization), and radiometer R0.8 (wavelength 0.8 cm) when circular flights were performed at a height of 300 m and microwave observations were performed with the nadir view angle. The working area is the North Caspian Sea (Russia). The date was 28 November 1977. Moscow time and the brightness temperature intensity scale are shown on the abscissa and on the ordinate.

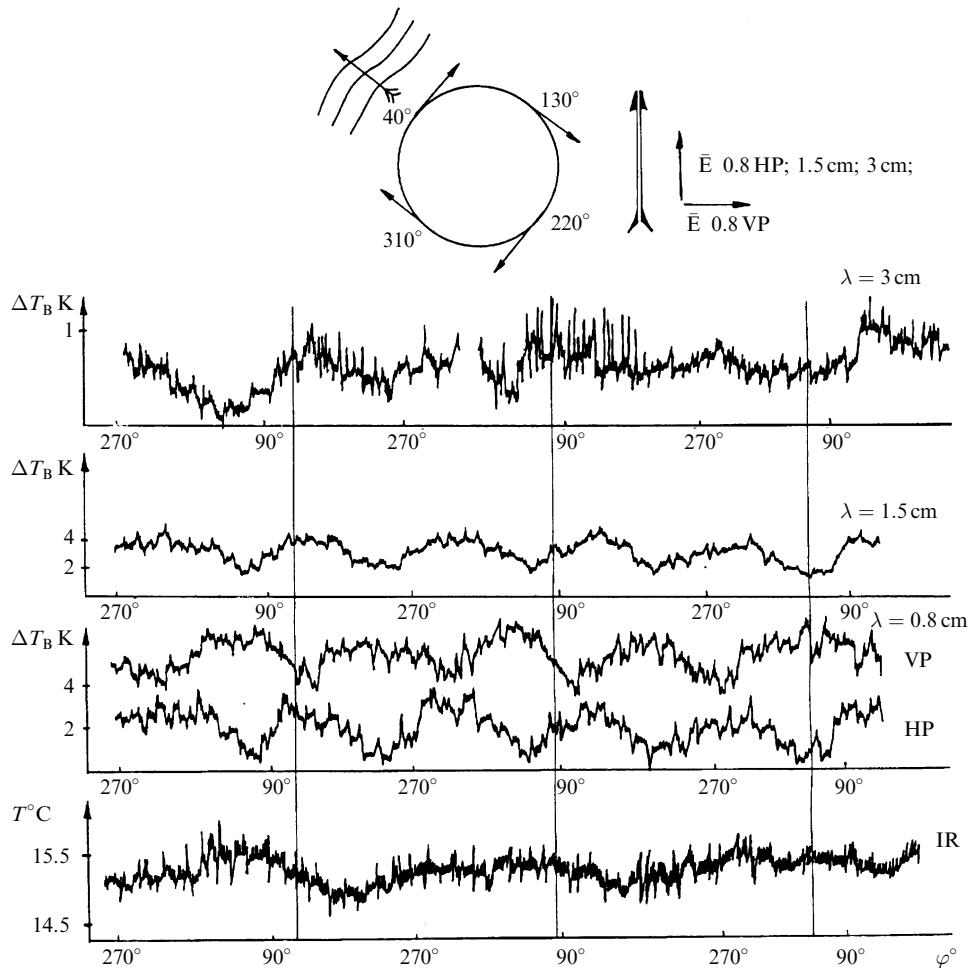


Figure 12.12. The experimental results of flight investigations (10 October 1978, the Sea of Japan) in the azimuthal anisotropy study of sea surface microwave emission. The scheme of circular flights and the position of the antennas' linear polarization vectors and of surface gravity wavefronts are presented at the top of the figure. The double arrow points along the longitudinal centreline of the research aircraft. The fragments of the output signals of airborne (Russian airplane-laboratory IL-14-I) radiometer R-3 (wavelength 3 cm), radiometer R0.8 (wavelength 0.8 cm, two polarizations: HP, the horizontal polarization; VP, the vertical polarization), radiometer R1.5 (wavelength 1.5 cm) and IR radiometer when circular flights were performed at a height of 300 m and microwave observations were performed with the nadir view angle. Sea state was 4 on the Beaufort scale. Moscow time and the brightness temperature intensity scale are shown on the abscissa and on the ordinate.

corresponded to horizontal polarization, and the perpendicular polarizations corresponded to vertical one. It is evident that the vertically polarized brightness temperature reaches a maximum in the upwind direction, whereas the orthogonal (horizontal) polarization exhibits a minimum in this same direction. In Figure 12.13 the backscattered signal measured at a view angle of 10° and wavelength of 3 cm is plotted. The azimuthal variations of emitted and backscattered microwave signals were observed to be very similar, thus confirming the hypothesis of a wind-driven wave origin.

The surprising results from the processing of the data of the first stage (1976–1977) of flight experiments, which were obtained under the guidance of the author of this book, have served as a powerful stimulus to the statement of laboratory and theoretical investigations, which were soon performed (Etkin *et al.*, 1978; Kravtsov *et al.*, 1978). The results of these works served as a basis of a new phase of detailed radiospectroscopic investigations of the emission fields of a wave-driven sea surface (Irisov *et al.*, 1987; Yueh *et al.*, 1995, 1999; Kuzmin and Pospelov, 1999; Kuzmin *et al.*, 2000; Trokhimovskii *et al.*, 2000; Kunkee and Gasiewski, 1997; Reising and Camps, 2000; Laursen *et al.*, 2000; Stogryn *et al.*, 1994; Connor and Chang, 2000; Goodberlet *et al.*, 1989).

As frequently happens in the history of the development of science, the effect of azimuthal anisotropy in the field of thermal radiation of the sea surface was, essentially, rediscovered much later (Yueh *et al.*, 1995, 1999). Now much attention is given to the detailed study of the features of the field of radiation from the side of both the experimenters and the theorists (Irisov, 1997; Cherny and Raizer, 1998). So, Trokhimovskii *et al.* (2000) by rather fine experiments have demonstrated a high sensitivity of the azimuthal anisotropy of thermal radiation of the sea surface to the parameters of the gravitation-capillary part of the sea disturbance spectrum. Trokhimovskii (1997) has demonstrated the possibility of restoring the gravitation-capillary part of the sea disturbance spectrum from the data of the measurement of polarization characteristics of thermal radiation of a wave-driven sea surface.

12.4.2 Sea wave breaking fields

The second complex of physical reasons stipulating a serious contribution to the thermal radiation of a wave-driven sea surface are the processes of the breaking of sea waves and the appearance of an intensive drop-spray phase and a bubble disperse phase of sea foam with their subsequent rapid and complicated spatial–temporal evolution. It should be mentioned that the experimental detection of intensive (of black-body type, virtually) thermal radiation of foam systems by Williams (1969) under very complicated (and, we might add hazardous) hydrometeorological conditions (such as the flight of a sporting-type airplane through the ‘wall’ of a tropical cyclone) was also rather unexpected for the researchers. This was associated with a supposition on the absence of noticeable absorption and scattering of electromagnetic waves of the microwave band on a set of quite small hollow air spheres and hollow hexagonal structures with very thin films of water that represented the foam system alone (Raizer *et al.*, 1976; Weaire and Hutzler, 2000).

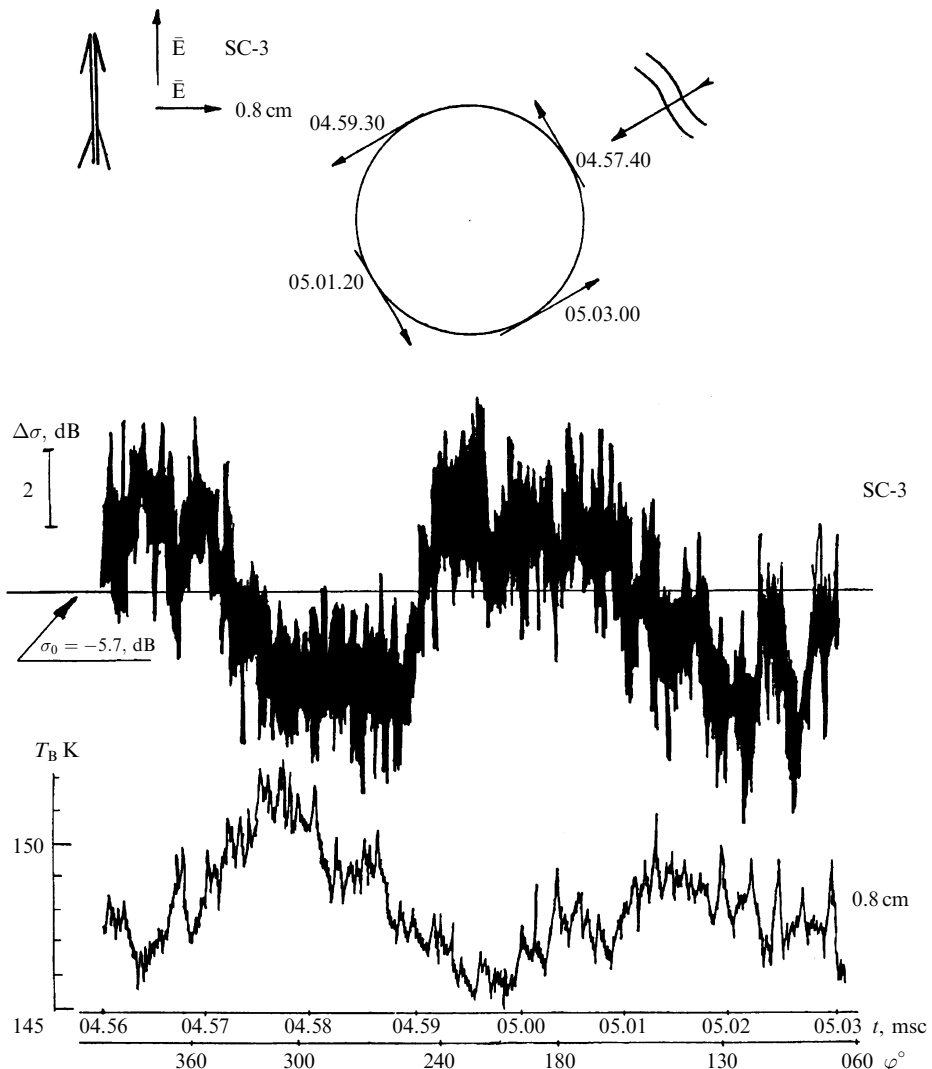


Figure 12.13. The experimental results of flight investigations (20 October 1978, the Sea of Japan) for the azimuthal anisotropy study in sea surface microwave emission and backscattering. The scheme of circular flights and the positions of the antennas' linear polarization vectors and of surface gravity wavefronts are presented at the top of the figure. The fragments of the output signals of airborne (Russian airplane-laboratory IL-14-II) radiometer R0.8 (wavelength 0.8 cm) and of scatterometer SC-3 (wavelength 3 cm) when circular flights were performed at a height of 300 m with the angle of 5° slope and microwave observations were performed with the nadir view angle relative to the aircraft. Sea state was 6 on the Beaufort scale. Moscow time and the brightness temperature and backscattering intensity scales are shown on the abscissa and on the ordinate.

Nevertheless, these results gave rise to the first (and rather naive, as it was found later) ideas and determinate models, according to which the basic elements, which determine the thermal radiation of the wave-driven sea surface, will be the foam systems of various classes and, accordingly, with increasing wind speed (from 5–6 m/s to typhoon velocities of 33–35 m/s) according to the power law (linear or quadratic) the radiation intensity will also increase up to values corresponding to black-body radiation (Dropelman, 1970; Williams, 1971; Matveev, 1971). Further detailed investigations of the radiophysical properties of foam systems and spatial-temporal disperse characteristics of foam systems under full-scale conditions, carried out under the guidance of the author of this book (Militskii *et al.*, 1976, 1977, 1978; Bordonskii *et al.*, 1978; Raizer and Sharkov, 1980, 1981; Vorsin *et al.*, 1984; Bondur and Sharkov, 1982, 1990; Pokrovskaya and Sharkov, 1986, 1987a, b; 1994; Zaslavskii and Sharkov, 1987; Sharkov, 1993a,b, 1994, 1995), have clarified the situation in many respects and indicated the imperfection of primary models and ideas. Below we shall present a brief review of works in this field.

The problem of detecting the effects of radio-emission of a drop-spray zone in sensing the sea surface from a low-flight carrier – an aircraft – has some principal features. In essence, the question is about solitary (in antenna’s field of view) and quite non-stationary physical objects possessing high emissivity. This imposes certain requirements on the parameters of onboard instruments, as well as on the choice for conditions for the experiment. So, the value of a radiothermal signal, recorded by a microwave complex installed on a moving carrier, can be presented as follows (see Chapter 5):

$$T_B(t) = \int_0^\infty d\left(\frac{x}{V}\right) h\left(t - \frac{x}{V}\right) \left[\iint G_0(x - x'; y - y') T_{BF}(x', y', t) dx' dy' \right], \quad (12.11)$$

where $h(t)$ is the impulse response of a receiving device (with the time constant t_0); $G(x, y)$ is the instantaneous field of view of the antenna directional pattern (ADP) on the surface; $(4/\pi)G^{1/2} = 2H \operatorname{tg}(\theta/2)$; H, V are the flight altitude and carrier velocity; θ is the angular resolution of ADP; $T_{BF}(x, y)$ is the radiothermal image of a foam structure (with the geometric size Δx and area S). This relation implies a great diversity of types of radiothermal signal recorded from a non-stationary, but ‘bright’ (in the radiothermal sense) object. So, it can easily be seen that for $\tau_0 \ll (\Delta x/V)$ and $G \simeq S_0$ the form of a recorded signal will represent an isosceles triangle with the base $2\Delta x/V$ and height $T_{BF} - T_{BS}$, where T_{BS} is the brightness temperature of thermal ‘background’ of the sea surface (see Chapter 5). As τ_0 increases up to values of $\Delta x/V$, the signal amplitude decreases, though ‘the appearance’ of a signal does not change qualitatively. If, however, $\tau_0 < (\Delta x/V)$, but $G < S$, then the signal shape represents a ‘little house with a cap’, and the brightness contrast ΔT_B will be the same quantity ($T_{BF} - T_{BS}$). If the object has a form of a point source, i.e. $G \gg S$, then the brightness contrast will have the other value $\Delta T_B = (S_0/G)(T_{BF} - T_{BS})$, and the signal shape ‘appearance’ will describe the shape of a main lobe of the antenna directional pattern (see the characteristic example in Chapter 5).

The representative implementation of a radiothermal signal from the wave-

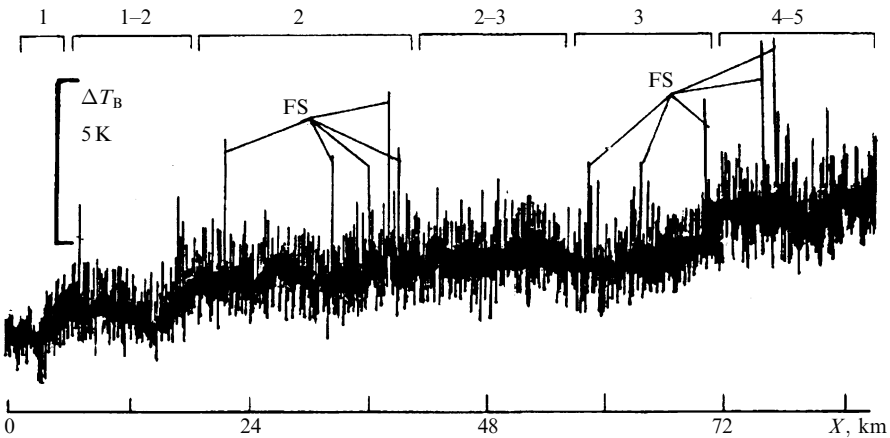


Figure 12.14. Fragment of the output signal of airborne (Russian airplane-laboratory IL-18) high-performance radiometer R2 (wavelength 2 cm) versus the flight distance X (km). The linear flight was performed at a height of 1000 m with the nadir view angle relative to the aircraft as the sea state increased from 1 ball to 5 balls in Beaufort notation. The working area is the north Caspian Sea (Russia). The date was 27 November 1977. FS are the emission signals from foam structures. Figures show the Beaufort numbers for the sea state.

driven sea surface (Figure 12.14) was obtained under the following conditions: the Caspian sea water area, a direct track extending 80 km along the section with seaway variation from 1 to 4 points of the Beaufort notation (according to visual estimates of a skilled on-board meteorologist); flight altitude $H = 1000$ m, carrier velocity $V = 350$ km/hour. The instruments consisted of a high-sensitivity radiometric system of the 2-cm band, with a sensitivity threshold of about $\Delta T = 0.03$ K with time constant $\tau_0 = 1$ s, and was installed aboard the Il-18 laboratory aircraft with a mirror-reflecting parabolic antenna with the directivity pattern width $\theta = 1.5^\circ$. The resolution spot on the surface for nadir-looking observation was $G = 25$ m. The analysis of Figure 12.14 indicates that, along with general increase of brightness temperature with seaway amplification caused by small-scale seaway components (including the azimuthal anisotropy effect), the presence of acute spikes – the signals from the foam-disperse zone – is characteristic. The synchronous air photography gave an idea of the sea surface structure under 4-point seaway conditions: the size of foam formations, generated at wind wave breaking, were of the order of 3–10 m. By virtue of a small time constant of integration $\tau_0 = 0.05$ s (in the flight mode), the amplitudes of ejecta were recorded virtually completely, the radio-thermal contrasts being equal to 3–4 K. The experimental situation corresponds to the condition of $G > S_0$, and, thus, $(T_{BF} - T_{BS})$ will be 80–100 K, which fully corresponds to theoretical estimations (Raizer and Sharkov, 1981). The second interesting example represents synchronous registograms of a scatterometre (3 cm) and radiometers (2 cm and 8 mm) obtained under 5- and 6-point seaway conditions

in performing circular flights (at an altitude of 300–600 m). They are presented in Figures 12.11 and 12.13. The histograms of microwave instruments clearly exhibit the signals from foam structures having the form of ‘triangles’ with contrast amplitude of the order of $T = 2\text{--}4\text{ K}$. Since the experimental situation is such, that $G > S_0$, but in this case $\tau_0 > \Delta x/V$, the low values of radiothermal contrasts are clear. Of importance is the fact that the scatterometer channel does not indicate the presence of foam structures because of their small reflectivity (Militskii *et al.*, 1976, 1977). However, subsequent full-scale investigations have shown (Cherny and Sharkov, 1988) that, in general, the situation is more complicated, and the relationship between the values of radiation and backscattered signals depends on the temporal stage of wave-breaking and on the appearance of a drop-spray phase against the background of foam structures, the drop-spray phase making a noticeable contribution to the backscattered signal. As the seaway amplifies (the sea surface state (SSS) is more than 6 points in the Beaufort notation), the regular azimuthal dependence (Figures 12.11 and 12.13) of polarization anisotropy is violated: the radiothermal field acquires more isotropic character, since a noticeable contribution to radio-emission is made by the drop-spray phase and foam formations, the obtaining of which does not have any azimuthal features regarding the wind direction.

Thus, in aircraft sensing the contribution of foam structures to the sea surface radiation can give signals of a diverse character, and the thermal radiation of individual foam structures can be revealed only by using synchronous air photography at high spatial resolution (10–20 cm), which is, obviously, not always possible. On the other hand, the use of a less high-speed and more manoeuvrable carrier – a helicopter – will allow for essentially increasing the observation time that considerably facilitates the experimental problem. In this case it is possible to perform detailed air photography of the studied surface for further identification of the data (Bondur and Sharkov, 1982, 1990).

In observation from space carriers, where the linear size of the field of view of the radiothermal instruments’ antenna equals 10–50 km, the recorded signal quantity can be written as:

$$T_B = T_{BS} \left(1 - \sum_{i=1}^{N(t)} S_{Fi} \right) + \sum_{i=1}^{N(t)} T_{BFI_i} S_{Fi}, \quad (12.12)$$

where $N(t)$ is the number of foam structures in a frame corresponding to a displayed ‘spot’ of the antenna directional pattern (ADP) on the surface. In this case it is necessary to know the detailed statistics of spatial fluctuations $N(t)$ in the appropriate spatial frame, as well as of geometric and emissive characteristics of foam systems of various types and the time of their ‘life’. These issues have been thoroughly studied in a cycle of works (Pokrovskaya and Sharkov, 1986, 1987a,b, 1994; Srokosz 1986; Zaslavskii and Sharkov, 1987; Bondur and Sharkov, 1982, 1990; Sharkov, 1993a,b, 1994, 1995). So detailed experimental results have shown (Pokrovskaya and Sharkov, 1987a,b, 1994; Sharkov, 1993a,b) that the stochastic model of large-scale breaking wave fields may be presented as a stochastic spatial whole-

numbers field of Markov type (the Poisson process) with independent discrete sources (events). The mean value of the specific density of foam structures (the centres of wave energy scattering) has a clear, strong (cubic) tendency to increasing with the wind speed and has a ‘threshold’ nature (the stepwise approximation) at a wind speed of 5 m/s (Bondur and Sharkov, 1982). It is interesting to note that later this relationship has also been found theoretically by Phillips (Phillips, 1988).

Detailed experimental investigations of the process of breaking and subsequent decaying of foam systems (Sharkov, 1994, 1995; Sharkov, 1996d) have shown that the process of gravity wave ‘preparation’ to breaking fall and the breaking itself takes some fraction (about 1/3) of the wave period. In other words, the nonlinear stage of the breaking process and the formation of a wave crest foam grows at fabulous rates. However, the process of decay of patch foam structures of a foam mass is characterized by exponential decay with considerable half-decay time (0.5–10 s), which depends on the physicochemical properties of sea water in the area.

Some new specific group of wave breakings, called microbreakings (MB), was detected by Sharkov (1994, 1995). MB have some particular properties: a short lifetime of the foam mass (~ 1 s); a small characteristic size (~ 0.4 m); the absence of accompanying patch foam; the faint optical contrast; wave–wind conditions being independent of average size. The instantaneous value of the surface foam covering (per unit space) for MB amounts to 0.6%. MB may be thought of as ‘noise’ fields in which the microbreakings exist.

As to radiothermal models of foam systems, detailed laboratory and theoretical investigations, carried out under the guidance of the author of this book during the period of 1974–1981, have shown that there exist two contrasting classes of foam systems – the emulsion monolayer and the layer of foam of polyhedral structure (Militskii *et al.*, 1978). In this case it was strictly demonstrated (Raizer and Sharkov, 1981), that the electrodynamical models of a homogeneous or inhomogeneous dielectric layer, with parameters corresponding to a heterogeneous mixture of water and air (Matveev, 1971), do not exhibit a quantitative agreement with the experiment. The same is true for the models of a discrete stratified medium (Williams, 1971; Stogryn, 1972; Rozenkranz and Staelin, 1972; Tang, 1974; Bordonskii *et al.*, 1978; Smith, 1988) and for the models of a smoothly varying transition dielectric layer (Bordonskii *et al.*, 1978). The electromagnetic properties of coarse-disperse media in the microwave band are most completely reproduced by continuous stratified-inhomogeneous models with strict allowance for diffraction properties of hollow spheres and hexagonal structures, with allowance for a blurred interface boundary between the disperse structure and the water surface and with allowance for the depth inhomogeneity of a dielectric layer (Raizer and Sharkov, 1981). Slightly simplifying the situation, one can say that the matter is as follows. For the electromagnetic range under consideration the hollow water spheres (or the hexagonal structures) represent some kind of small black bodies, which intensively absorb the electromagnetic energy owing to inter-bubble diffraction. The complete consideration of these issues is beyond the framework of the present book, and so, we can recommend the reader to consult the original literature (Raizer and Sharkov, 1981).

12.5 MICROWAVE REMOTE SENSING OF CATASTROPHIC OIL SPILLS ON THE SEA SURFACE

As a quite instructive example of the efficient use of microwave radiothermal instruments, along with active microwave means, we shall briefly describe the results of remote study of the evolution of catastrophical oil spills on the sea surface in regions of intensive oil output on the continental shelf. These investigations were carried out by the specialists of the Space Research Institute (Moscow) in 1976–1977 (Bespalova *et al.*, 1978, 1983).

The problem of the interaction of oil pollutions with a sea medium is significant in ecological and physical investigations of the ocean (Scott, 1978, 1999; Scott and Thomas, 1999). The main tasks in studying this problem are: the determination of sources and scales of pollutions, the estimation of thickness and volume of the oil layer as well as of spatial and temporal variability of oil slicks; the monitoring of further evolution of oil–water conglomerates and of the procedure of self-purifying of a sea medium.

The means of perspective remote sensing that allow one to approach the solution of these problems include side-looking radar (SLR) (Kalmykov, 1996), synthetic aperture radars (SAR) (Johannessen *et al.*, 1994) and radiothermal systems (Bartsch *et al.*, 1987). Using such instruments installed onboard flight vehicles, it is possible to measure, for a comparatively short time, the distribution of a specific cross-section of backscattering and radiobrightness fields over a considerable sea surface area. However, one should bear in mind that the physical reasons causing the appearance of contrasts in radiobrightness and backscattering fields can be quite different, and, therefore, the informative capability of these remote sensing data will also be mutually complementary. This section presents the experimental results of studying the spatial–temporal variability of wave-driven sea surface pollution by oil products in the region of Neftyanye Kamni (Oil Rocks) shoal (the Caspian Sea area), resulted from catastrophic oil spill under various hydrometeorological conditions. These studies were carried out from November 26 till December 1 1976, and from November till December, 1977. Unlike earlier works, these remote sensing experiments were performed using passive and active sensing means disposed on various carriers simultaneously. The latter means included the two-polarization centimetre-band 'Toros' SLR installed on the Russian An-24 aircraft, which was used earlier in geological and glaciological investigations. The passive remote sensing system included the multifrequency radiothermal radar instruments installed on board the Russian Il-18 aircraft laboratory (Amirkhanyn *et al.*, 1975).

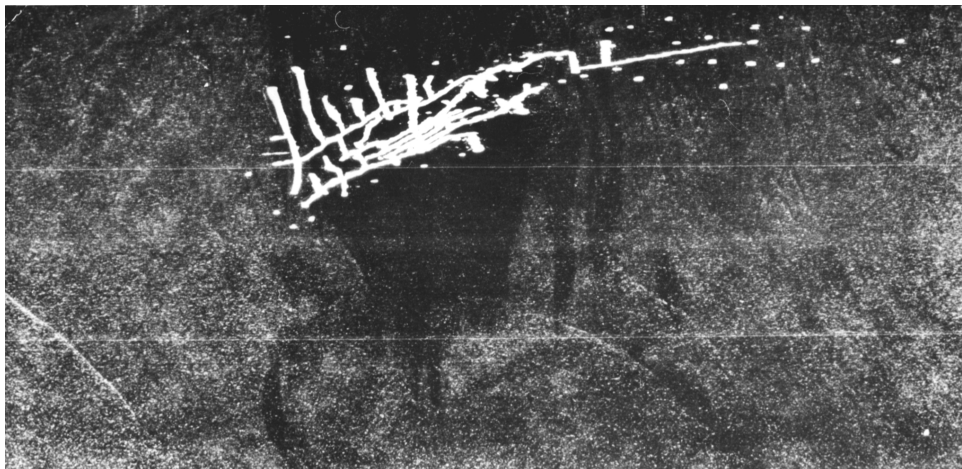
12.5.1 Investigation techniques and processing of the results

The techniques of performing and processing the results of a complex radiophysical experiment were as follows. The radar investigations were carried out simultaneously in two separate vertical–vertical (VV) and horizontal–horizontal (HH) channels. The flights were accomplished at the altitude of 1500 m by flying around the investigated sea area in the 'rectangular approach traffic pattern'. Since the radar image in the

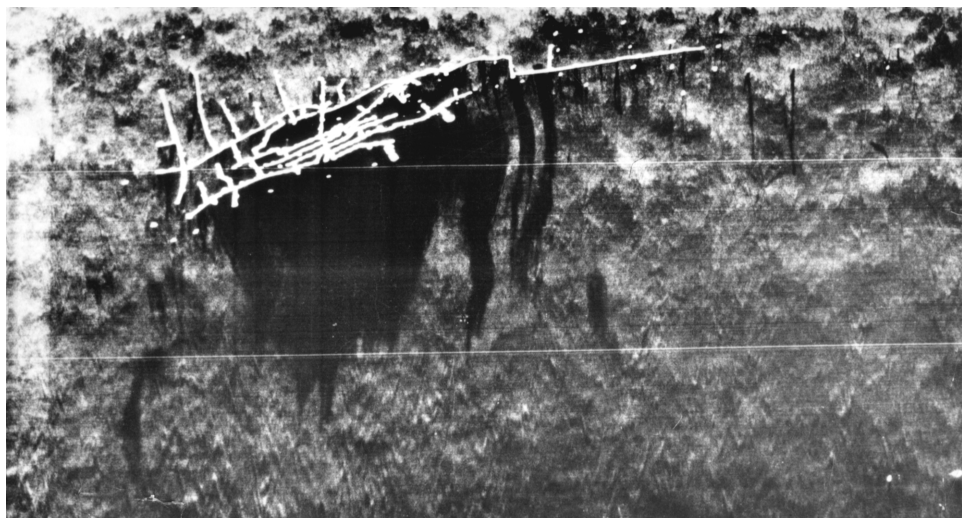
pollution zone was virtually homogeneous and did not contain any clearly discernible details (see Figure 12.15), the further analysis of the radar data was performed from planimetric representations of radar images (the planimetric map-schemes, Figure 12.16). The procedure of aircraft radiothermal experiments was as follows. The flights were accomplished at an altitude of 200 m with a velocity of 360 km/hour directly above the investigated water area with tacks intersecting at a particular, preselected point over a stable geographical landmark (a 'sprocket'). The results of radiothermal experiments are presented in the form of radiothermal map-schemes (Figure 12.17), where solid lines represent the levels of equal radiobrightness temperature (radio-isotherms). The technique of plotting radio-isotherms corresponds to the well-known rules of constructing synoptic maps in meteorology. The time of committing the flights over a full 'sprocket' or over of part one (from 1.5–2 hours to 0.5 hours) was accepted as a period of averaging the picture of hydrometeorological phenomena of corresponding scale.

12.5.2 Analysis of radar mapping data

The basic mechanism of radar signal backscattering by the sea surface is resonance Bragg scattering. For horizontal polarization at low view angles the scattered signal is mainly also formed, except for the Bragg mechanism, by signal reflection from the ridges of large waves before their breaking. The analysis of radar images obtained indicates that the signal splashes, caused by such reflections, are clearly seen over the whole swath width, that is, at incidence angles of 4–20° (Figure 12.15). The appearance of oil on the sea surface causes changes in radiowave backscattering for several reasons, the most essential of which is the suppression of high-frequency components of the spectrum of gravitation-capillary waves owing to sharp changing of attenuation with the appearance of the oil film on the sea surface. Figure 12.16 presents the contour map-schemes obtained from the positives of the VP (vertical polarization) channel, on which the evolution of considerable oil pollutions during 7 hours on November 26, 27 and 28, 1976 was recorded. The hydrometeorological situation on the night and morning of November 26 1976, was characterized by a steady north-east wind disturbance (3 points) against the background of swell from the north and north-east wind (5 m/s) at the sea surface state (SSS) of 2 points (Beaufort notation). The character of pollutions in the morning of November 26 1976, represents a vast uniform field of irregular shape with broad 'sleeves' elongated in the south-west direction. In general, the shape of the field was formed, apparently, under the effect of the north-east wind and seaway, which had existed during the hours of the night and morning. From about midday on the area of a spot began sharply to contract and divide into separate fields and bands, and by about 17 h 30 m the spot had virtually disappeared. This process was promoted by a drastic change of meteorological conditions – the north wind strengthening up to 12 m/s and wind disturbance increasing up to 4 points (the SSS was evaluated as 4 points). Thus, the total 'lifetime' of a vast oil slick amounted to 5 hours, and, supposing the exponential law of decay under natural conditions, the spot 'half-life' period, recorded by a radar, equals 1–1.5 hours under the given hydrometeorological conditions,



(a)



(b)

Figure 12.15. Backscattering images of a rougt sea surface obtained by side-looking radar ‘Toros’ (Russian research airplane AN-24) for the horizontal–horizontal (a) and vertical–vertical (b) polarization regimes in the presence of oil pollution near the ‘Oil Rocks’ oil installation (the Caspian Sea). Date of flight experiment was 26 November 1976. Black fields correspond to oil spills. The bright line system standing out sharply against the sea backscattering signal corresponds to the backscattering signal from the scaffold bridges of the oil installation.

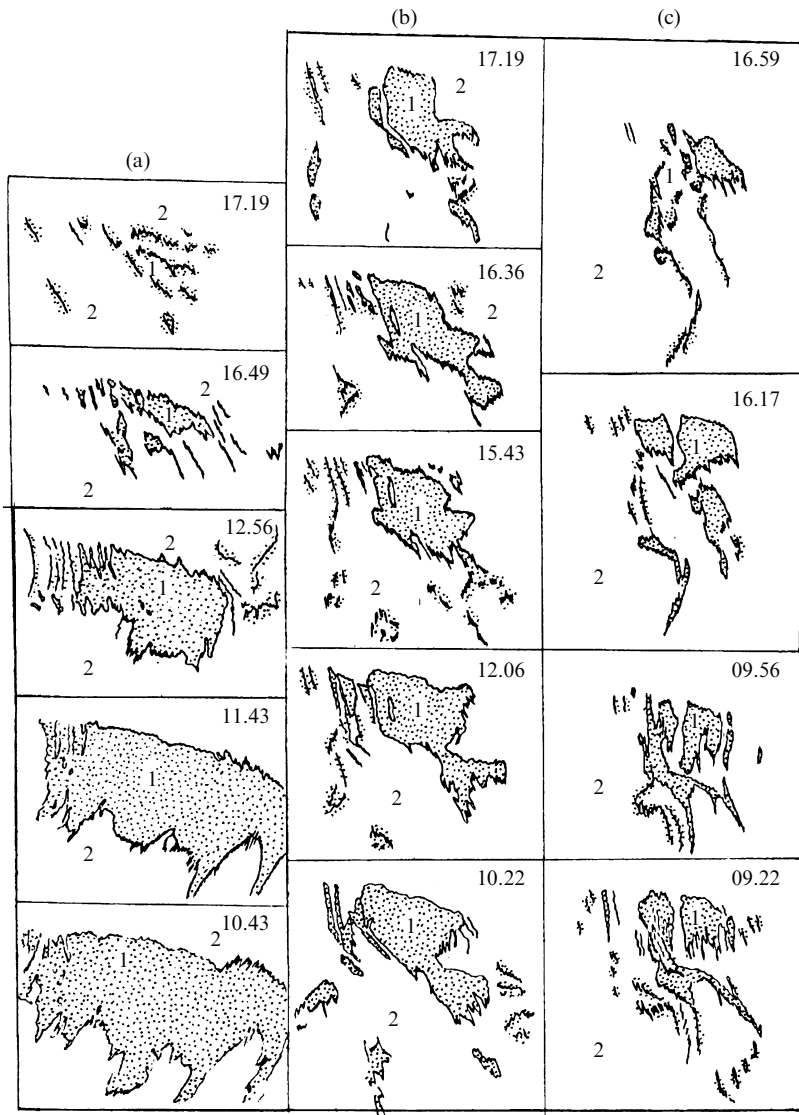


Figure 12.16. The spatial–temporal evolution of catastrophic oil spills presented by a temporal series of schematic maps of the backscattering images. (1) Oil spill fields; (2) rough sea surface without oil pollution. (a) Date of the experiment was 26 November 1976 from 10.43 (Moscow time) till 17.19. The surface wind speed and direction was 12 m/s and 360°. Sea state was 4 on the Beaufort scale. (b) Date of the experiment was 27 November 1976 from 10.22 (Moscow time) till 17.19. The surface wind speed and direction was 9 m/s and 360°. Sea state was 4 on the Beaufort scale. (c) Date of the experiment was 28 November 1976 from 09.22 (Moscow time) till 16.59. The surface wind speed and direction was 12 m/s and 360°. Sea state was 4 on the Beaufort scale. Figures in each scheme present the Moscow time of experimental image.

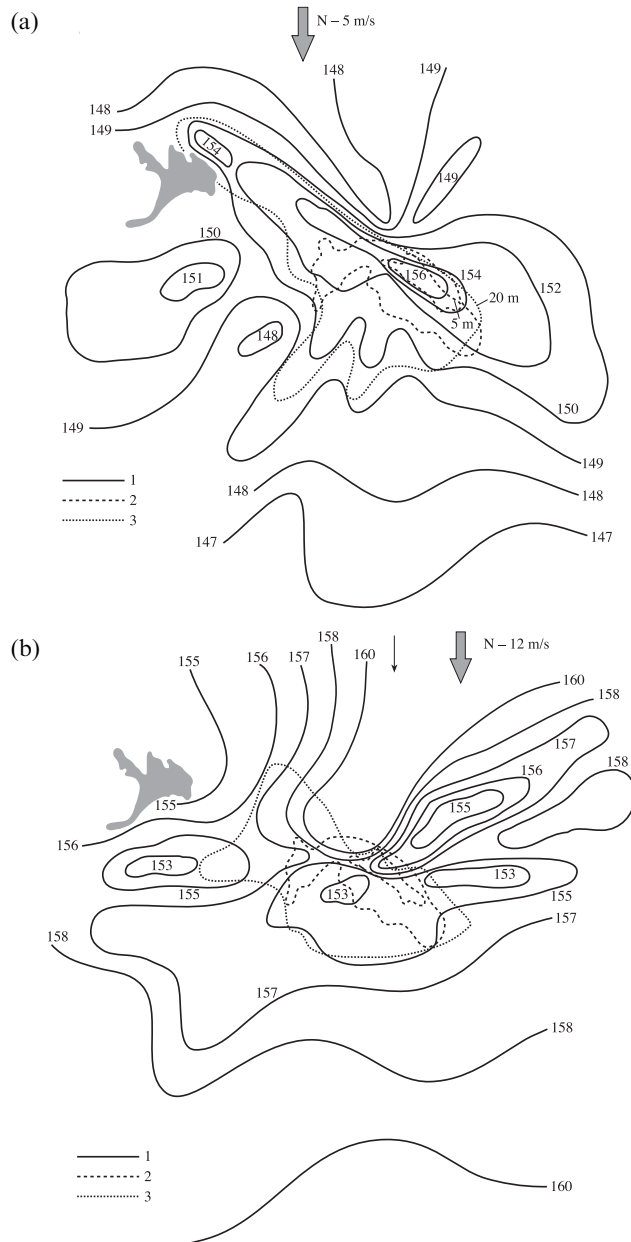


Figure 12.17. Radio-emission isothermal maps of the sea surface studied at wavelength 8 mm (26 November 1976): (a) radio map was performed during time from 09.35 till 11.30 (Moscow time); (b) radio map was performed during time from 13.35 till 15.55 (Moscow time). 1, radio isotherms (figures present absolute values of brightness temperature); 2, bathymetry data (m); 3, areas where an aircraft operator observed oil pollution. The heavy black arrows show the direction of the surface wind speed vector.

whereas in the laboratory conditions this value varies from 6 to 100 hours for an oil film.

The oil pollution on the morning of November 27 1976, appeared as a patchy formation of considerable area (and some small-size slicks) stretching in a south-east direction and formed by the north wind and a fairly strong undersea flow, which prevailed during the night, morning and day of November 27. Of interest is the fact that, despite a fairly heavy sea (4–5 points) and wind (8–9 m/s), the oil slick area has only slightly varied throughout the day of November 27. And only small areas of slick were carried away 15–20 km south-eastward. This is, apparently, explained by the fact, that oil had continued to leak from the source all this time.

The oil pollution of November 28 consisted of separate bands and spots stretching in a south-east direction; the extension of this area was 15–18 km. As a whole, the system of slicks only slightly varied up to 16 h 17 m and then began quite sharply to decrease.

12.5.3 Radiothermal measurement data analysis

The radiothermal investigation of oil pollution, carried out within a wide band of frequencies directly in the region of carrying out the experiments, made it possible to clearly reveal two effects arising at the interaction of the developed seaway with the film of oil products. One of the effects (the positive variations from 2 K at wavelength of 3 cm to 10 K at wavelength of 0.8 cm for a seaway of 1–2 points) is physically associated with the phenomenon of coordinating the wave resistances of two half-spaces – air and water – by the oil film (Figure 12.18). The second effect, observed at a seaway of 4–5 points (the negative variations relative to the radiobrightness of a non-disturbed background from –1 K at wavelength of 3 cm to –5.5 K at wavelength of 0.8 cm), is determined by suppressing the gravitation-capillary components (a ripple) of the seaway spectrum, drop-spray clouds and foam activity by the oil film (Figure 12.19). Both in the first and in the second case the spectral dependencies within the limits of wavelengths of 0.8–3.2 cm had the monotonous, nearly hyperbolic character of variation magnitude decreasing when the working wavelength increases (Figure 12.20).

Thus, radiothermal multifrequency measurements allow one to determine, under the indicated hydrometeorological conditions, the thickness of oil films (with corresponding spatial averaging). The radar mapping of the mentioned water area region (50×50 km), carried out over the days of the described experiments, made it possible to reveal the complicated spatial structure of the radiothermal field in this region. This structure included the zones of both heightened ('warm') and lowered ('cold') radiobrightness values (with respect to the background brightness), caused by the presence of visually detected pollution, as well some peculiar zones of negative 'radio shadow' and the 'warm' zones of a lobe-type structure. The characteristic radiomap-schemes are presented in Figure 12.17. For example, the radiomap of November 26 1976, for the time window of 9 h 35 m Msk to 11 h 30 m Msk had a 'warm' region (in the 0.8-cm channel), stretched from the south-east towards the north-west and corresponded, in general, to a visually observed pollution area. One

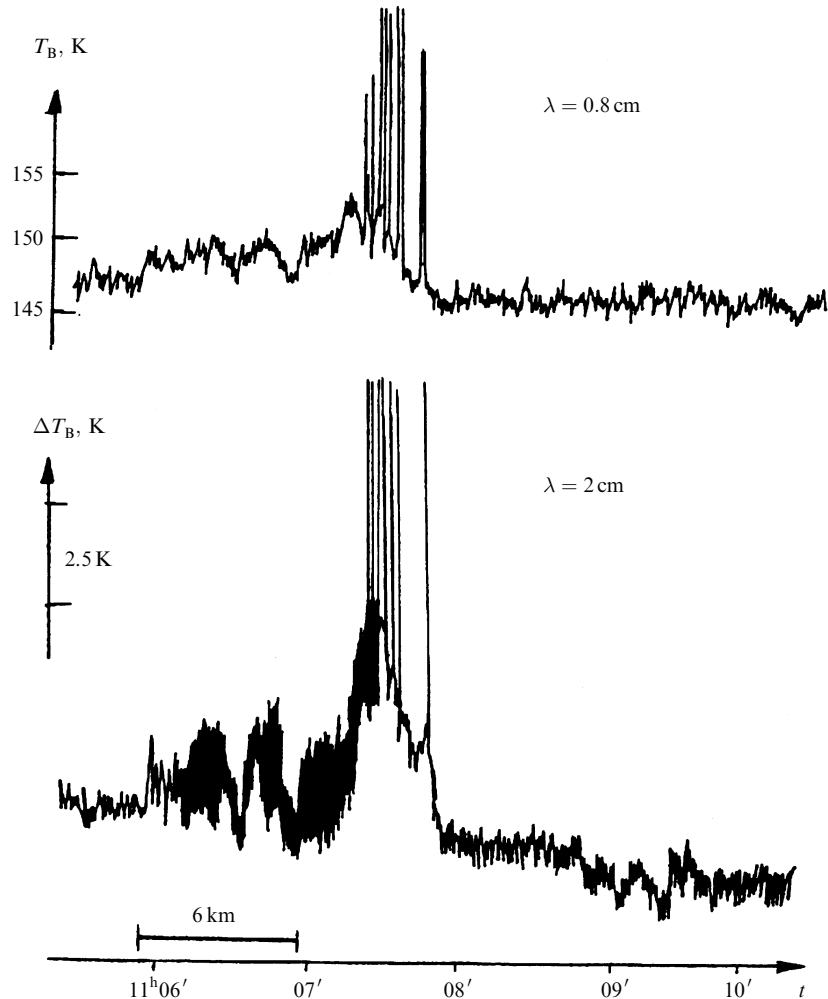


Figure 12.18. Fragments of synchronous output signals of airborne radiometers R2 and R0.8 when crossing an area under study. The working area is near the 'Oil Rocks' oil installation (the Caspian Sea). Date of flight experiment was 26 November 1976. ($H = 400$ m.) The surface wind speed and direction was 5 m/s and 45° . Sea state was 2 on the Beaufort scale. Temperatures of water and air were 12.2°C and 9.1°C . Moscow time, spatial scale and indoor temperature calibration are shown on the abscissa and on the ordinate. The strong linear variations standing out sharply against the sea emission signal correspond to the emission signal from the scaffold bridges of the oil installation.

should also pay attention to the presence of heightened (by 3–4 K as compared to the background) radiobrightness zones stretching out 10–15 km in the east and west directions and looking like lobes. The oil pollution on the sea surface is not visually observed in these regions, and the mentioned changes of radiobrightness

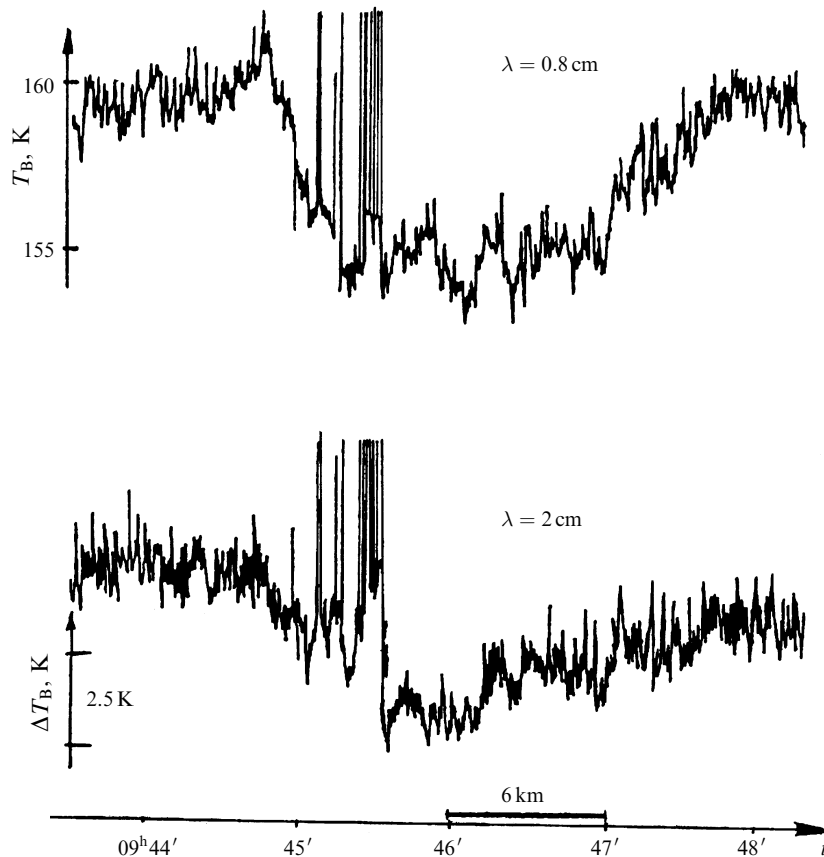


Figure 12.19. Fragments of synchronous output signals of airborne radiometers R2 and R0.8 when crossing an area under study. The working area is near the ‘Oil Rocks’ oil installation (the Caspian Sea). Date of flight experiment was 27 November 1976. ($H = 400$ m.) The surface wind speed and direction was 10 m/s and 360°. Sea state was 4 on the Beaufort scale. Temperatures of water and air were 10.2° and 8.2°C. Moscow time, spatial scale and indoor temperature calibration are shown on the abscissa and on the ordinate.

should be attributed to the increase of energy of gravitation-capillary components in the seaway spectrum. The analysis has shown that the radio image in the 2-cm channel corresponds, in general to the features of the radiomap obtained in the 0.8-cm channel. During the experiment the meteorological conditions sharply changed at the middle of the day: the wind strengthened up to 10–12 m/s, the northerly wind disturbance achieved 4 points, the SSS was estimated by 4 points. The flight took place from 13 h 55 m to 15 h 55 m. The aforementioned regime should be considered unsteady, since the time of the wind disturbance ‘tuning’ exceeds 3–4 hours. The radiopattern in the 0.8-cm channel (Figure 12.17(b)) underwent considerable changes: the radiobrightness of the sea background far from the region under

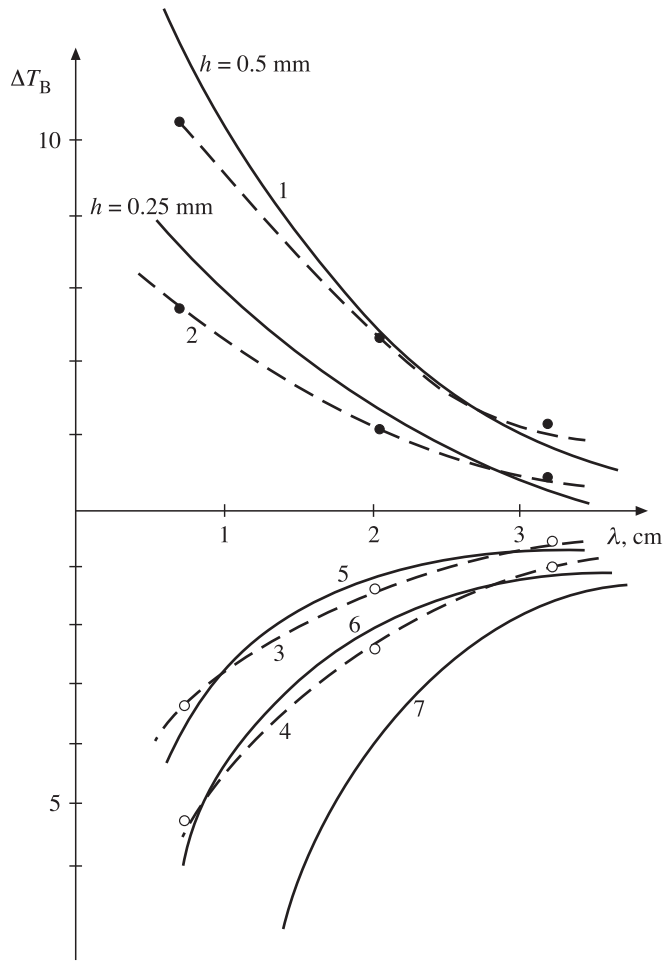


Figure 12.20. Experimental spectra of radiobrightness temperature variations against the pure (non-pollution) sea emission signal at three frequency channels (wavelengths 0.8, 2 and 3 cm) obtained at the same place on the sea surface: (a) positive variations (black points and broken curves) for weather conditions of 26 November 1976; (b) negative variations (circles and broken curves) for weather conditions of 27 November 1976. See figures and solid curve notation in the text.

study was now 159–160 K; that is, it increased by 10–11 K. An interesting feature of the considered radio images is the presence of a peculiar negative ‘radio shadow’ area to the south of the centre of the investigated area. The dimensions of the ‘shadow’ area were: 14–16 km in the southerly direction and 30–35 km in the east–west direction; the negative deviation from the sea background radiobrightness value (159–160 K) was quite small (2–4 K). This area is most clearly displayed in the 0.8-cm channel.

Considerable wind and seaway strengthening during the night from November 26 to 27 1976 (wind of 14 m/s and seaway of 5 points) distorted the picture of the oil pollution – the oil film was broken into local sections, which were carried away 15–20 km southward from the investigated region. In spite of this circumstance, the features of the radiopattern of November 27 corresponded, in general, to those obtained on the previous day. An important feature of the results considered is the experimentally detected rapid variability of radiothermal fields of the non-stationary seaways (the ‘radio shadow’ area). Here it should be noted that the velocity of evolution of such fine features of the radiothermal field (with variations of 0.5–2 K) is considerable, and the order of its magnitude corresponds to the order of the wind speed (in the case under consideration the rate of evolution of radio image details can be estimated as 3–7 m/s). This implies that to produce an ‘instantaneous’ radiopattern separating fine features of the radio fields of sea water areas of the order of 50×50 km the observation time should be less than 3–5 minutes, which is only made possible by using an airborne or spaceborne radiothermal surveying system.

12.5.4 Joint analysis of radar and radiothermal images

Combined radiothermal and radar map-schemes in the same scale and with approximately the same resolution element of 50–100 m are shown in Figure 12.21. Analysis of these maps (of November 26 1976) in the 0.8-cm channel and from radar observations, as well as of the dependencies of the averaged (in the resolution element) of the oil film thickness at the AOA, BOB cross-sections (Figure 12.21) allows one to conclude that there is a rather complicated internal structure to the oil slick. A characteristic feature of the pollution area is the existence of at least three zones. The first one represents a fairly stable ‘hot’ core with an area of about 4% of the total area of the slick, where 10% of the total oil mass is concentrated, and where, apparently, the source of pollution itself is localized. (According to the radar data, this source has continued to leak oil until 12 h 00 m, as seen from the beginning of analysis.) With increasing distance from the core southward, that is, in the direction of action of the wind and seaway, the second zone is observed – the rapid drop of film thickness (the spreading process). And then the third zone appears – the long ‘plateau’ occupying 70% of the total slick, with a slow change of film thickness from 0.1 mm and below, where, apparently, the process of evaporation occurs. More than 52% of the total oil mass is concentrated in the ‘plateau’ zone. Figure 12.22 gives a visual idea of the distribution of averaged thickness, h , over the AOA cross-section (curve 1) and over the BOB cross-section (curve 2). The same figure shows the oil slick boundaries, which are seen on the radar image (the radar for cross-section AOA and the radar for cross-section BOB). The comparison of radar and radiothermal data gives an estimate of the oil film thickness near the spot boundary, seen on radar images, as 20–40 micrometre. Figure 12.23 presents the results of superposition of schemes of four types of observations on December 1 1977: radar, radiothermal-radar, aerial photography and visual (the onboard observer), as well as the fragments of registograms in the 0.8-cm channel. The analysis of such a

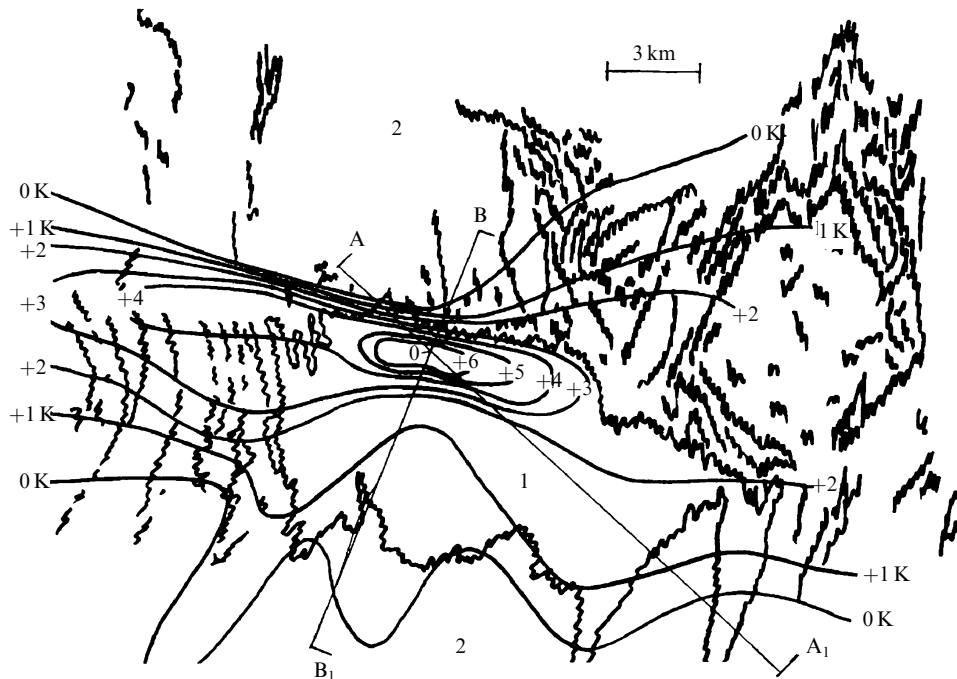


Figure 12.21. SLR schematic map (26 November 1976, 11.43 Moscow time) combined with fragments of the radio-emission isothermal map (9.30–11.30 Moscow time) of sea surface under study at wavelength 8 mm: 1, sea area polluted by oil spill with SLR data; 2, pure sea surface. Solid lines are radio isotherms. Figures are relative variations of radiobrightness temperatures. AOA₁ and BOB₁ are cross-sections under study.

superposition indicates that the results of radar, visual and aerial photography observations, in general, coincide well in detecting the oil spot boundaries. At the same time, the radiothermal-radar observations reveal the 'radio-shadow' features, which cannot be recorded by radar and other observation techniques.

12.5.5 Radiospectroscopic observations

To reveal in more detail the physical features observed in wave-driven sea surface pollution by oil, in Figure 12.20 the spectrum of radiobrightness temperature variations is constructed from the synchronous data of three frequency channels (0.8, 2 and 3 cm), recorded virtually at the same IFOV (with an accuracy of spacing the axes of the antenna directional patterns of about 15–20 m). The upper part of the figure shows the experimental frequency dependencies (the dotted line) of positive variations in the intensive pollution regions (on November 26 1976), just by the oil production ramps (curve 1) and 4 km southward from the ramps (curve 2). On the same figure are plotted the spectral curves (solid lines) of radiobrightness variations (relative to the quiet water surface), calculated within the planar-stratified

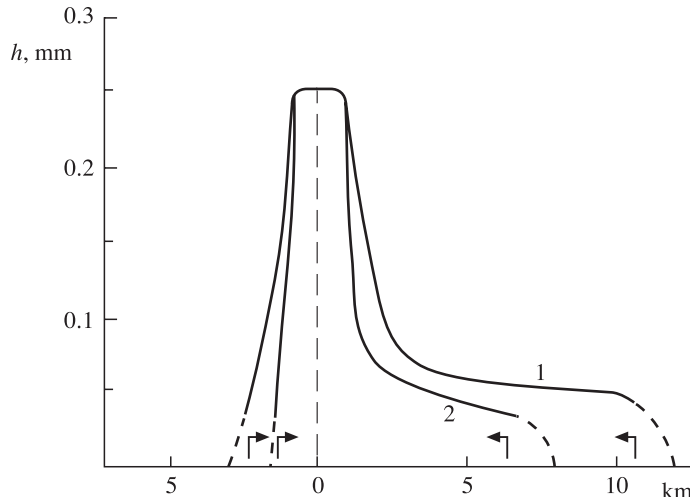


Figure 12.22. The spatial distribution of averaged oil film thickness over AOA_1 (curve 1) and over BOB_1 (curve 2) cross-sections. Arrows show the boundaries of backscattering images over AOA_1 and BOB_1 cross-sections.

model framework (Chapter 7) for two values of thickness of oil film on the water surface: 0.25 and 0.5 mm. As to the considered region of positive variations, the comparison of calculated and experimental spectra of radiobrightness variations indicates that, under the given hydrometeorological conditions and at the given level of generalization (a spatial resolution of 10–15 m) the planar-stratified model rather well explains, in general, the experimental data obtained. This makes it possible to estimate the thickness of a surface film of oil products and the total volume (or tonnage) of oil spreading after radio-mapping. The lower part of Figure 12.20 presents the experimental frequency dependencies (the dotted line) of negative variations in the Neftyanye Kamni (Oil Rocks) region (on November 27 1976) just by the oil production ramps (curve 3) and 1 km southward of the ramps (curve 4). The frequency dependencies have a monotonous, nearly hyperbolic character of decreasing value of negative variations with increasing working wavelength. The characteristic wavelength dependence of the radiobrightness spectrum variations gives an idea of its considerable contribution to the effect of suppressing drop-spray clouds by the oil film (see Chapter 10). Figure 12.20 presents the calculated dependencies of drop-spray clouds radiation (curves 3 and 4), which are plotted in such a manner that they coincide with the experimental dependencies at the wavelength of 2 cm. By the same formula it is possible to estimate, using the experimental data, the values of densities for the spray layer heights of 10 and 100 cm. These densities were found to be $C = 2 \times 10^{-3}$ for the first case and $C = 2 \times 10^{-4}$ for the second one. In other words, these values were quite close to those experimentally observed under similar seaway conditions. It is of interest to evaluate the frequency dependence of radiobrightness variations, caused by the appearance of a small transition layer 1 mm thick with dielectric parameters variation according to the

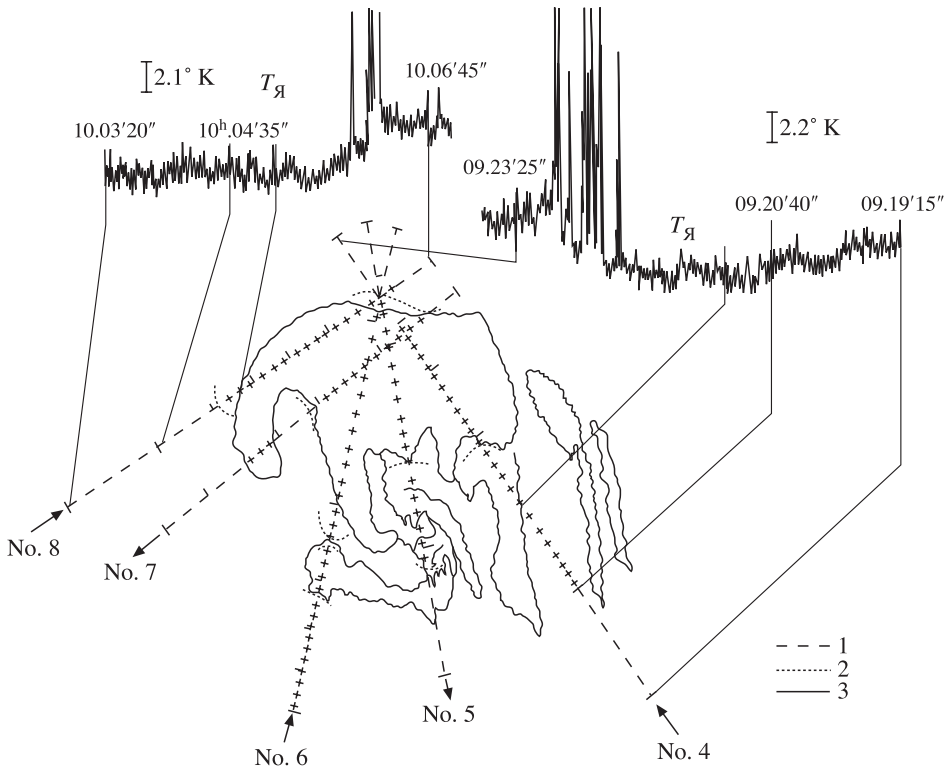


Figure 12.23. Schematic superposition of observing data from four types of sensing of oil pollution area (1 December 1977): by aerial photography (1), visual observation (2), radar (3) and radiometer (wavelength 0.8 cm). Radiothermal data was represented as temporal recordings. Figures and arrows near flight paths present their numbers and directions.

hyperbolic tangent law, and, thus, to simulate, in a certain sense, the radio-emission of a ripple on a large-size wave. The corresponding computer calculations on multi-layer software (Chapter 7) are reflected by curve 7. It can be seen that the wavelength dependence is essentially stronger, than λ^{-1} . Therefore, it is less reliable to explain the indicated effects by suppression of the fine-structural dielectric transition by the oil film than by suppression of drop-spray clouds.

To finally reveal the physical reasons for the origin of negative variations of radiobrightness of the wave-driven sea surface in the presence of oil pollution, it is necessary to expand the set of frequencies in remote sensing measurements.

13

Inversion problems for passive microwave measurements

The problems of restoring the values of the physical parameters of a natural medium from the data of remote sensing instruments are most important and complicated throughout the remote sensing information circuit. The features of interaction of electromagnetic waves of the microwave band have essentially extended the limits of traditional optical and IR observations and introduced completely new aspects into the issues of so-called inversion problems. The purpose of this chapter is to consider and analyse some basic elements of the problem of inversion of the physical parameters of a natural medium for microwave remote sensing which are now being actively developed by the researchers of various science teams.

13.1 FEATURES OF MICROWAVE MEASUREMENTS

As we have noted above (Chapters 1, 7 and 9), microwave measurements have a number of distinctive properties. First, the relationship between the intensity measured by remote sensing instruments and the thermodynamic characteristics of media under study is linear (the Rayleigh–Jeans approximation). Hence, it follows that microwave measurements can be used to obtain simple direct estimates of meteoparameters (such as the precipitable-water and liquid-water content of clouds). The earliest semi-empirical regression models for satellite and airborne observations with a monoconfiguration sensor (i.e., one polarization/frequency channel and the nadir view angle) were very simple. However, they made it possible to obtain fundamental results (as an example) on the global spatial distribution of water vapour and cloud liquid-water in the terrestrial atmosphere (Akvilonova *et al.*, 1971; Basharinov *et al.*, 1974; Veltlov and Veltishev, 1982).

Second, the fundamental distinctions of microwave bands from IR and visible bands consist in penetration and diffraction of interacting microwaves with media

under study. This provides support for a wide spectrum of complicated (forward) models including thermal states of volumes and surfaces of media under observation (Wilheit and Chang, 1980; Sasaki *et al.*, 1987; Novak *et al.*, 1983; Mitnik, 1986). The latest forward models involve diffraction effects under the interaction of electromagnetic microwaves with the elements of the surface and in volumes, such as gravity waves, various types of vegetation crops, forests (Shin and Kong, 1982; Ulaby *et al.*, 1986; Irisov *et al.*, 1987; Ferrazzoli and Guerriero, 1996; Wigneron *et al.*, 2003; Trokhimovski *et al.*, 2000). On the basis of integrated (including diffraction effects) forward models, advanced integrated inversion procedures are now being actively developed. The physical parameters that may be recovered with microwave measurements are as follows: moisture (underground); the soil temperature fields (under vegetation); the elements of a sea wave spectrum; the structure of vegetation; the physical-chemical composition of soil; sea foam structures; oil pollution; precipitation parameters; surface wind speed fields (Novak *et al.*, 1983; Calvet *et al.*, 1995, 1996; Ferrazzoli and Guerriero, 1996; ESA, 1996a,b,c; Trokhimovski, 1997).

13.2 BASIC CATEGORIES OF INVERSION PROCEDURES FOR MICROWAVE SENSING

The variety of scientific and economic problems facing remote sensing investigations generates a spectrum of diverse procedures for specific problems of recovering necessary physical parameters of the atmosphere and land surface. By virtue of the rather lengthy historical period of development of remote sensing in the optical band of electromagnetic waves, cadasters and the methodology of inversion problems have their own quite particular and completed systematization (Kondratyev and Timofeev, 1970; Malkevich, 1973; Stone, 1979; Avduevskii *et al.*, 1983; Asrar and Dokken, 1993; Attema, 1993; Kramer, 1996; Thomas and Stamnes, 1999; Schultz, 1988; Sharkov, 1998; Schultz and Engman, 2000).

The active development of microwave methods and means in the last 20–25 years has, in its turn, put on the agenda the possibility of the solution of significantly new classes of problems, both in scientific and in economic respects. First of all, we should mention here hydrological and soil problems (subsurface moisture and temperature regime of soils), agricultural problems (the degree of maturation of crops), oceanological problems (the state of the surface of ocean, the surface wind, the energy exchange, the evolution of the fields of salinity), glaciological problems (the state of glaciers, the state and evolution of drifting ice) and many other problems (Bespalova *et al.*, 1983; Schultz and Engman, 2000; Wigneron *et al.*, 2003; Paloscia and Pampaloni, 1988; Sharkov, 1998; Vinnikov *et al.*, 1999; Comiso and Stock, 2000; Boyarskii *et al.*, 1993; Belchansky and Alpatksy, 2000; Matzler, 2000; Derksen *et al.*, 2000a,b). A great diversity of new problems has generated, naturally, many new techniques for the solution of inversion problems, since this circumstance has given rise to some new problems, such as, for example, the relation between the spatial resolution, required for the given problem, and the existing spatial resolution

of microwave systems. Nevertheless, a particular systematization (categories) in the approach to the solution of inversion problems for microwave remote sensing is formed (Ingmann, 1991; Matzler, 2000; Wigneron *et al.*, 2003) we shall just briefly outline below.

The different approaches used to account for the effects, caused by microwave interactions with terrestrial surfaces, may be subdivided into three main categories: statistical techniques, forward model inversion, and explicit inversion. Other techniques, such as data assimilation (Kalman filter optimal estimation and variational data assimilation), have also been used.

13.2.1 Statistical techniques

In general, these techniques are based on regression analysis. For each pattern on images or on a group of pixels for airborne and spaceborne observations, linear relationships between the measured brightness temperature and physical parameters are established. The slope and intercept of the regression line are then analysed in terms of physical parameters and variables which can be estimated from ancillary data.

A large number of algorithms are used to retrieve information on land surfaces and terrestrial atmosphere from remote sensing data by direct manipulation of the measured signals through empirical relationships of the type:

$$x_j = F_j(T_{B1}, T_{B2}, \dots, T_{Bn}), \quad (13.1)$$

where T_{Bn} corresponds to measurements made for various configurations of the sensor, in terms of incidence angle θ , polarization, or frequency; and x_j is a relevant physical parameter. For example, for passive microwave measurements over land, two different statistical approaches may be distinguished (Wigneron *et al.*, 2003), namely:

- classification based on dual- or multi-configuration observations. For instance, based on observations of the Special Sensor Microwave/Imager (SSM/I) data and of brightness temperature thresholds, various classification rules have been developed to distinguish among dense vegetation, forest, standing water, agricultural fields, dry and moist bare soil, etc. However, until now no study is known to have directly addressed the problem of classifying soils with different water contents, although many studies have reported spatial relationships between brightness temperature or emissivity and surface moisture;
- surface soil moisture is statistically related to a combination of microwave emissivities and vegetation microwave indices, which are used to correct for soil roughness and vegetation effects.

13.2.2 Forward model inversion

In this approach, a model is used to simulate remotely sensed signatures (output) on the basis of land surface parameters (input). The inversion methods are developed to

produce an ‘inverse model’, in which the outputs are represented by the relevant land surface variables. The inversion methods are usually based on an iterative minimization routine of the root-mean-square error (RMSE) between the forward model simulations and observations.

The problem of forward model inversion to retrieve land surface variables can be defined as follows: the radiative transfer model Φ is used to simulate the microwave radiometric measurements $(T_B)_i$ ($i = 1, \dots, q$) corresponding to measurements made for various sensor configurations in terms of incidence angle, polarization, or frequency), as a function of the physical parameters x_j ($j = 1, \dots, p$) (the so-called ‘state variables’):

$$(T_B)_i = \Phi_i(x_1, x_2, \dots, x_p; s_{1i}, s_{2i}, \dots, s_{ri}) + \varepsilon_i \quad (13.2)$$

for $i = 1, \dots, q$ and where s_{ki} ($k = 1, \dots, r$; $i = 1, \dots, q$) stands for the configuration parameters which determine the observation conditions, and ε_i is the residual error between the simulated and measured brightness temperature values. Inverting the model consists of finding the set of variables under study x_j ($j = 1, \dots, p$) that provides the minimum value of the residual errors ε_i . Therefore, the retrieval methodology based on forward model inversion requires two main steps: (1) the selection of a forward model (Φ), and (2) the selection of a method for inversion by minimizing the residual error ε_i .

Both steps are specific for any particular retrieval problem and have been analysed in several publications (Ulaby *et al.*, 1981, 1982, 1986; Ingmann, 1991; Wigneron *et al.*, 2003).

Forward models may be classified into three main categories: (1) nonparametric data-driven models; (2) parametric data-driven models, where the model parameters are adjusted by comparison with observations; and (3) physical models, which include a physical description of the radiative transfer processes and where the model parameters can be directly related to the land surface and atmosphere characteristics. The majority of studies, which use nonparametric data-driven models (approach (1)), are based on the statistical regression analysis or on the neural network models. The models used in approach (2) require *a priori* knowledge of the functional form of the process that is being modelled. The model parameters are generally the ‘best-fit’ parameters computed by minimizing the squared error between the observations and the outputs of the model. The physical complex models (approach (3)) account for the multiple scattering effects that become important when the frequency exceeds a few gigahertz. In these approaches, a number of surface surfaces can be modelled as a continuous medium (Chapter 7) and the atmospheric systems as a discrete medium containing randomly distributed discrete scatterers characterized in terms of size, shape, density, and distribution of orientation (Chapter 10). However, these models require many input parameters and cannot be used easily to implement the retrievals of surface and atmospheric characteristics.

Once the forward modelling approach has been selected, the method for ‘inverting’ the model should be defined. A very common algorithm to invert a forward model is the statistical inversion approach. Its principle is to search for

input parameters (x_1, x_2, \dots, x_p) , consisting of the relevant geophysical parameters that minimize the squared error between the brightness temperature as measured from space $(T_B)_i$, and the actual outputs of the model $\Phi_i(x_1, x_2, \dots, x_p)$. Thus, the inversion problem is

$$\begin{aligned} \text{Min } G(x_1, x_2, \dots, x_p) = & \sum_{i=1}^q \frac{1}{2\sigma_i^2} [\Phi_i(x_1, x_2, \dots, x_p; s_{1i}, s_{2i}, \dots, s_{ri}) - (T_B)_i]^2 \\ & + \sum_{j=1}^p \frac{1}{2\lambda_j^2} (x_j - x'_j)^2, \end{aligned} \quad (13.3)$$

where $G(x_1, x_2, \dots, x_p)$ is the cost function; and (the *a priori* information) x'_j is the average value of the j th model parameter; λ_j is the standard deviation of the j th model parameter value; and σ_i is the standard deviation of measurement noise of the i th channel.

Many different iterative minimization algorithms (such as Tichonov's method, quasi-Newton, Simplex, etc.) are available to minimize the cost function $G(x_1, x_2, \dots, x_p)$ (Tichonov and Arsenin, 1979; Press *et al.*, 1986).

13.2.3 Explicit inverse

The explicit inverse of the physical process can be built by transferring the input (remote sensing measurements) into the output (the land surface parameters). In the majority of studies, neural networks (NN) are used to produce this explicit inverse function. First, the appropriate set of input–output data is generated using the forward model Φ_i . Then a copy of the forward model (Φ_i) is made by training the NN on the set of data. Hence, the NN is able to capture very complex and nonlinear relationships within its self-organizing connections. The advantage of the NN technique is that, once the NN has been trained, the parameter inversion can be accomplished quickly. In the field of microwave radiometry, the NN has been applied to estimate snow characteristics (Davis *et al.*, 1993; Derksen and LeDrew, 2000; Derksen *et al.*, 2000a,b), surface wind speed over the ocean (Stogryn *et al.*, 1994), clouds and precipitation (Li *et al.*, 1997), and soil and forest parameters (Gopal and Woodcock, 1996; Paloscia *et al.*, 2000b; Chang and Islam, 2000; Kothari and Islam, 1999; Wigneron *et al.*, 2003). Another simple way to invert a forward model using NN is to train an inverse model by reversing the roles of the inputs and outputs: the measured brightness temperature becomes the input nodes of the NN, and the land surface parameters become the output nodes. This method, known as explicit inversion, is widely used in remote sensing (Li *et al.*, 1997; Jimenez *et al.*, 2000). However, the forward model is characterized by ‘many-to-one mapping’ (i.e. the set of measurements cannot be uniquely related to environment variables). Several studies expressed concerns about the fact that the explicit inversion approach may lead to wrong results when the inverse image of the forward model is not convex (Davis *et al.*, 1993; Li *et al.*, 1997), and that the iterative constrained inversion

technique was found to be more appropriate, than the explicit inversion to deal with the many-to-one mapping.

13.2.4 Other techniques

Assimilation approaches (the Kalman filter optimal estimation and variational data assimilation) have been applied to the problem of retrieving the near-surface soil moisture and temperature profile from a time series of radiobrightness observations. Several studies have shown that the modelling of the heat and mass flow inside the sea surface-atmosphere and the soil can be used to derive information about the soil water content profile from the time series of microwave brightness temperatures. For instance, the feasibility of using the brightness temperature measurements (in the microwave and infrared channels) to solve the inverse problem, associated with soil moisture and heat profile, was proposed by Kondratyev and Shulgina (1971) (Chapter 8) and demonstrated by Liu and Minnis (2000) over bare soils. Burke and Simmonds (2001) have retrieved soil hydraulic properties from the time series of measured brightness temperatures over agricultural fields. Sequential and variational data assimilation approaches have been tested on experimental bare soil and vegetation (Calvet *et al.*, 1995, 1996; Macelloni *et al.*, 2001; Njoku and Li, 1999; Wigneron *et al.*, 1995, 2003) data sets and on a series of synthetic experiments based on the Southern Great Plains (SGP) 1997 Hydrology Experiment (Drusch *et al.*, 1999a,b; Liu and Minnis, 2000; Paloscia *et al.*, 1999). These studies have required continuous series of measurements, which were based on the coupling between soil-vegetation-atmosphere transfer models and radiative transfer models.

The detailed analysis of inversion problems for thermal atmospheric stratification and water vapour and cloud water stratification and spatial distributions with microwave measurements have been considered by Sharkov (1998).

14

Passive microwave space missions

The rapid introduction of microwave sensing methods and means into airspace observations in the last 10–15 years was a consequence, as we have shown above, of the significantly new (in relation to optical and infrared bands) physical information content of microwave sensing in studying terrestrial objects (the surface and the atmosphere). The development and evolution of instruments and research missions of microwave sensing has occurred, certainly, in a quite inhomogeneous and irregular manner. Nevertheless, at the present time none of potential large-scale satellite missions on earth investigation fails to employ passive and active radio-physical instruments in some configuration. The present chapter analyses some historical elements of the development of microwave missions (including the issues of instrument development), the state of the art and some prospects for the future.

14.1 ELEMENTS OF MICROWAVE RADIOMETRY HISTORY

The study and understanding of microwave patterns of the terrestrial surface–atmosphere system has cardinally changed both the configuration of existing satellite systems designed for sensing the Earth, and the character and informative saturation of the whole remote sensing area. However, microwave radiometry was initially born in the entrails of radio-astronomy as some kind of an auxiliary direction invoked to satisfy the needs of ground-based radio-astronomy, which had passed through stages of build-up and vigorous development in the 1940s and 1950s of the past century. This required, first of all, eliminating the influence of a disperse component (and, then, also of a gaseous component) of atmosphere radiation in the microwave band on high-precision radio-astronomical measurements carried out from the earth's surface. Some special techniques of performing radio-astronomical experiments (such as the diagram modulation method) (Esepkina *et al.*, 1973) have been directed to solving this problem. For these reasons the earliest

microwave investigations were entirely based on an instrumental foundation and on the methodological basis of radio-astronomy.

The first microwave investigations of radio-emission of the atmosphere at the wavelength of 1.5 cm were carried out by Professor Dicke in 1946 by means of the modulation method of measuring the noise signal proposed by himself. This technique, as well as the method of designing the instruments, underwent efficient development and improvement by radio-astronomers in quite various bands of the electromagnetic spectrum (Troitskii, 1951, 1954).

However, the further development and exploration of the short-centimetre and millimetre wavelength bands has put on the agenda the problems of the detailed spectral study of the characteristics of radiowave propagation in the atmosphere and in plasma-like media and of thermal radiation of geophysical media in these bands (Zhevakin and Naumov, 1967; Basharinov *et al.*, 1968). Both the instrumental base of radio-astronomy, and the measurement techniques began to undergo serious reconstruction. This was associated, first of all, with the brevity of the time for observing an object under study (a small accumulation time) and with the prominent polarization properties of geophysical objects. The problem also arose of manufacturing the small-sized instruments and antenna systems that have to be installed on moving platforms and flight vehicles. The existing stationary radio-astronomical instruments and the techniques of stationary (ground-based) measurements would obviously not have satisfied the necessary requirements. It may seem surprising, but historically the first extra-vehicular operation of microwave instruments was the launching of the Mariner-2 spacecraft in 1962 (Table 14.1), designed to study the structure and physicochemical content of the cloudy layers of Venus. It was, in fact, searching for water vapour by means of a two-frequency technique, which subsequently became a fully standard and conventional method in the system of space sounders of the terrestrial atmosphere (see Chapter 12 and below). The natural (as we know now) negative scientific result of this mission has been, nevertheless, an important step in the planetary research; and it confirmed the scientific significance of microwave sensing in onboard implementation.

A difficult stage of the establishment of microwave sensing as an independent discipline began in the middle of the 1960s: a series of air-based radiometric instruments was produced for meteorological investigations and military-technological applications (see the review by Khodyrev *et al.*, 1972). An important step at this stage was the development, for the first time in the USSR, of multifrequency onboard radiothermal instruments and their installation on the ‘Cosmos-243’ satellite that was launched in 1968 (Table 14.1). The significance of this space-based experiment can hardly be exaggerated. In essence, the principal possibility was demonstrated of receiving physical and geophysical information from outer space by means of radiothermal systems. In addition, some serious scientific results were obtained concerning the relation between the global integrated content of water vapour and liquid-drop water in the atmosphere, as well as some other results (see Chapter 12). This space-based experiment was repeated in 1970 on the ‘Cosmos-384’ satellite. However, these experiments have also revealed some limitations of the measurement methodology used – namely, a purely track mode

of measurements employing nadir-viewing antennas. Under such an observation mode it was impossible to obtain a spatial map of the distribution of the radiation field of geophysical objects and to find their polarization characteristics.

An important step in this direction was the development and launching of panoramic scanning radiothermal instruments ESMR on the Nimbus-5 satellite in 1972. Its characteristics were as follows: the frequency, 19.35 GHz; the swath-width of scan, 3000 km; and the instantaneous spatial resolution, 29 km. The scanning was performed in the cross-track mode by means of an electronically scanned phase array. The second item of instrumentation was the first version of the radiothermal probe (Table 14.1), which included three channels in the 5-mm line of oxygen and two channels for sensing according to the two-frequency technique (Chapter 12). This set has operated in the track mode. At this stage, in essence, there took place the formation and separation of microwave observation systems into three types: track-type systems, systems of panoramic (or scanner) type (the imagers), and measurement systems (or atmospheric sounders). This tendency has strengthened subsequently. However, each of these channels, in its turn, has continued operating in the mode of mono-configuration type, that is, one frequency/one polarization/one angle. Apart from using the centimetre band, in 1973 an attempt was undertaken to build an onboard radiometre of decimetre band (at the wavelength of 21 cm) with an angular resolution of 15°, and to operate this system onboard the Skylab spacecraft. Radiothermal instruments of centimetre band with a parabolic-type antenna system, having a considerable aperture (the diametre of 117 cm) and mechanical scanning, were installed on the same station.

The next step in microwave sensing was the inclusion of polarization measurements on the Meteor satellite (1974) in a track mode, and panoramic-type ESMR instruments (37 GHz) of have operated on the Nimbus-6 satellite in the two-polarization mode. The SCAMS sounder has also already operated in the scanner mode. It is important to note that in the microwave ESMR system the phase array was used for the last time as a scanning antenna system. The reason for this was, first of all, the high electromagnetic losses in the beam control system and, accordingly, the great noise contribution to the measured signal. Besides, the specialists had some doubts concerning the chosen cross-track type of scanning. This is associated with the fact that the elements of the surface under investigation are considered in a single frame at various angles, and, since the earth's surface and the sea surface have prominent polarization properties in the microwave band, a serious uncertainty arises in interpreting the microwave images. This problem was solved by developing and introducing a new type of scanning, namely, conical-type scanning, where all elements of the surface under investigation are observed at a strictly fixed viewing angle. Then the multifrequency (five frequencies), two-polarization (vertical and horizontal) panoramic SMMR instruments set was developed and launched in 1978 on two spacecraft simultaneously – Nimbus-7 and Seasat (Njoku *et al.*, 1980). Whereas the Seasat spacecraft has operated for three months only, Nimbus-7 has successfully functioned for nine years (up to 1988). According to the radiothermal SMMR system data, a set of interesting results was obtained on studying the state of the World Ocean surface, on the state of snow and glacial

Table 14.1. History of microwave radiometry in space.

Year of launch	Spacecraft	Instrument acronym	Frequencies (GHz)	Sensitivity (response time, s)	Swath width of scan (km)	Antenna type	Angle and spatial resolution	Principal parameters measured or inferred
1962	Mariner-2 (Venus fly by)	—	15.8 22.2	2 (1 s)	Planetary	Mechanically scanned parabola; diameter 50 cm	1300 km	Limb darkening; temperature; H ₂ O vapour
1968 1970	Cosmos-243 Cosmos-384	—	3.5 8.7 22.2 37	0.7 (1 s) 0.7 (1 s) 2.0 (1 s) 2.0 (1 s)	Nadir viewing	Parabolic horn Lens-loaded horn	8.6° 3.5° 3.5° 3.5° (15–50 km)	H ₂ O vapour and liquid; sea ice concentration; sea temperature
1972	Nimbus-5	ESMR NEMS	19.35 22.35 31.40 53.65 54.90 58.80	1.5 (0.05 s) 0.3 (2 s) 0.4 (2 s) 1.2 (2 s) 0.6 (2 s) 0.7 (2 s)	3000 Nadir viewing	Electronically scanned phase array; ±50° scan Five lens-loaded horns	1.4° (29 km) 185 km	Rain and H ₂ O vapour maps; firn and ice concentration and classification Temperature profile; H ₂ O vapour and liquid; firn and ice classification and snow cover
1973	Skylab	S-193 S-194	13.9 1.41	— 0.5 (1 s)	180 Nadir viewing	Mechanically scanned parabola; diametre 117 cm Phase array	2.8° (16 km) 15° (115 km)	Soil moisture Soil moisture
1974	Meteor	—	37	—	Dual polarization 35° from nadir	—	40 × 60 km	H ₂ O precipitation and vapour

1975	Nimbus-6	ESMR	37	1.0 (1 s)	1300	Dial polarization electronically scanned array	$0.7 \times 0.95^\circ$ (20×43 km)	Same as Nimbus-5 ESMR
		SCAMS	22.2 31.6 52.8 53.8 55.4		2700	Three rotating hyperbolic mirrors	150 km	Same as Nimbus-5 NEMS
1978 1979	TirosN, NOAA-5 NOAA-6	MSU	50.3		2300	Dual rotating mirrors	110 km	Temperature profile maps
			53.7 55.0 57.9					
1978 (1988)	Nimbus-7	SMMR	6.6 10.69 18.0 21.0 37.0	0.7 (0.1 s) 0.8 (0.06 s) 0.9 (0.06 s) 1.0 (0.06 s) 1.4 (0.06 s)	800 Incidence angle 50.3°	Conical scan single oscillating mirror; dial polarization; diameter 0.79 m	95 × 148 km 70 × 109 km 43 × 68 km 36 × 56 km 18 × 27 km	Same as ESMR; sea state (wind speed), sea temperature, snow cover; soil moisture
1978	Seasat	SMMR	6.6 10.7 18.0 21.0 37.0	0.9 (0.1 s) 0.9 (0.06 s) 1.2 (0.06 s) 1.5 (0.06 s) 1.5 (0.03 s)	600 Incidence angle 48.8°	Conical scan single oscillating mirror; dial polarization; diameter 0.79 m	4.2° 2.6° 1.6° 1.4° 0.8°	Same as SMMR Nimbus-7
1979	Salyut-6	KRT-10	2.5 (12 cm) 0.42 (72 cm)			Single parabolic mirror; diameter 10 m		Thermal maps of soil and sea surface

covers, on humidity conditions among others. Doubtless, the successful operation of the radiothermal SMMR instruments has marked by itself the termination of the primary stage (1968–1978) and the beginning of the contemporary stage of microwave space-based sensing in the centimetre and millimetre bands.

However, attempts to advance into the decimetre (and even into the metre) band with acceptable spatial resolution are continuing. So, the deployable KRT-10 space radiotelescope with an antenna mirror diametre of 10 m was successfully launched and operated at wavelengths of 72 and 12 cm on the Russian ‘Salyut-6’ manned space station in 1979 (Danilov *et al.*, 1979). This achievement gave, at the end of the 1970s, Russian and Western specialists a reason to hope for a rapid realization of ambitious projects on building giant radio-antennas with a mirror diametre of 100 m to 10 km (!) (Bujakos *et al.*, 1978; Card *et al.*, 1978; Blume *et al.*, 1978). These instruments should be designed for radio astronomy and microwave radio sensing applications. These hopes could not be realized, however. And only in the most recent times have similar projects became the subject of active discussion in the literature (Wilson *et al.*, 2000); and the ‘Radioastron’ project (Kardashiov, 2000) is at the stage of industrial implementation now.

14.2 ONGOING MISSIONS AND TENDENCIES OF THEIR DEVELOPMENT

Below we shall briefly outline a series of ongoing space missions studying and monitoring geophysical and meteorological systems of the earth. A key element of each mission is the inclusion of passive microwave instruments as a major integral part of the space observational system.

14.2.1 DMSP mission

The Defense Meteorological Satellite Program (DMSP) is a Department of Defense (DoD) program (Asrar and Dokken, 1993). The DMSP program was developed in an effort to study oceanographic, and solar–terrestrial physics environments. DMSP satellites are in a near-polar orbiting, Sun-synchronous orbit at an altitude of approximately 830 km above the earth. Each satellite crosses any point on the earth twice a day and has an orbital period of about 101 minutes thus providing complete global coverage of clouds every six hours. Earth DMSP satellite monitors the atmospheric, oceanographic and solar–geophysical environment of the earth. Visible and infrared sensors collect images of global cloud distribution across a 3,000 km swath during both daytime and night-time conditions. The coverage of the microwave imagery and sounders are one-half the visible and infrared sensors coverage; thus they cover the polar regions above 60° on a twice-daily basis but the equatorial region on a daily basis. The space environmental sensors record along track plasma densities, velocities, composition and drifts. Visible and infrared imagery from DMSP Operational Linescan System (OLS) instruments are used to monitor the global distribution of clouds and resolution, global coverage, and high

resolution, regional coverage, imagery recorded along a 3,000 km scan, satellite ephemeris and solar and lunar data. IR pixel values vary from 190 to 310 kelvins in 256 equally spaced steps. Onboard calibration is performed during each scan. Visible pixels are currently relative values ranging from 0 to 63 rather than absolute values in watts per square metre. Instrumental gain levels are adjusted to maintain constant cloud reference values under varying conditions of solar and lunar illumination. Telescope pixel values are replaced by photomultiplier tube (PMT) values at night. A telescope pixel is 0.55 km at high resolution and 2.7 km at low resolution. Low-resolution values are the mean of the appropriate 25 high-resolution values. A PMT pixel is 2.7 km at nadir. In addition to cloud images, ground-based sources, such as fires, and upper atmospheric sources, like the Northern Lights, night-time imagery records the aurora, city lights, manmade and natural fires and natural gas flaring. The TC images are the most prominent examples of the efficiency of the optical and IR OLS system.

The main element of the DMSP observing system is passive microwave instrumentation. The Special Sensor Microwave/Imager (SSM/I) aboard the Defense Meteorological Satellite Program (DMSP) spacecraft is a seven-channel, four-frequency, linearly polarized, passive microwave radiometric system which measures atmospheric, ocean and terrain microwave brightness temperatures at 19.35, 22.235, 37.0 and 85.5 GHz (Table 14.2). The data are used to obtain synoptic maps of critical atmospheric, oceanographic and selected land parameters on a global scale. SSM/I data are used to derive geophysical parameters; notably,

Table 14.2. SSM/I characteristics (DMSP mission).

Observation frequency (GHz)	19.35	22.235	37.0	85.5
Polarization (V/H)	V, H	V	V, H	V, H
Sensitivity (K)	0.5	0.7	0.4	0.8
Bandwidth (MHz)	250	250	1000	1500
Antenna beam width (degrees)	1.87	1.65	1.1	0.45
Spatial resolution along and across scan (km)	69 × 43	60 × 40	37 × 29	15 × 13
Scan period (s)		1.9		
Antenna offset angle (degrees)		51.2		
Earth-inclination angle (degrees)		53		
Swath width (km)		1400		
Mass (kg)		48.5		
Power (W)		45		

ocean surface wind speed, area covered by ice, age of ice, ice edge, precipitation over land, cloud liquid water, integrated water vapour, precipitation over water, soil moisture, land surface temperature, and snow cover.

The Special Sensor Microwave/Temperature (SSM/T-2) sensor is a five-channel, total power microwave radiometre, three channels situated symmetrically about the 183.31 GHz water vapour resonance line and window channels. This instrument was flown on all DMSP Block 5D-2 satellites starting with F11 launched in 1991. SSM/T-2 is designed to provide global monitoring of the concentration of water vapour in the atmosphere under all sky conditions by taking advantage of the reduced sensitivity of the microwave region to cloud attenuation.

This exciting and developing technology appears to be the logical synergistic consolidation of the imager and sounder type of instrument as SSMIS instruments onboard the DMSP F16 satellite and instruments being developed – the Conical Scanning Microwave/Sounder (CMIS) (Flaming, 2000).

14.2.2 TRMM

The Tropical Rainfall Measuring Mission (TRMM) (Simpson *et al.*, 1988; Kummerow *et al.*, 1998, 2000) is a joint space mission between Japan and the United States, with the cooperation of several other nations (TRMM Office, 1990). As originally planned, TRMM is a synergistic complement of three instruments – active and passive microwave and optics sensors. A key feature is the first rain radar to be flown in space. The other instruments are a multichannel, dual polarized, passive microwave radiometre and a high-resolution visible/infrared radiometre.

TRMM can be regarded as a ‘flying rain gauge’ because the improved measurement capability of the microwave instruments can be used to calibrate techniques based on infrared brightness temperatures. The calibrations are likely to be different in different climate regimes. After calibration, the improved IR techniques can be applied to fill in between TRMM swaths using geosynchronous data, and to upgrade many of the past rain estimations which used the proxy variable approach. A basic TRMM data product will be mean monthly rainfalls over areas 50 by 50 km for climate studies. The orbit has been selected to optimize the effectiveness of the instruments. The low 350-km altitude obtains good resolution for the instruments (the 19-GHz channel of the passive microwave instrument will have a resolution of about 10 km). The orbit inclination of 35° ensures overflights at different local times every day, covering the entire 24 hours in a month, permitting documentation of the diurnal variability of tropical rain. More extensive discussion of the TRMM motivation, design and scientific results are provided in the Report of the Science Steering Group (Simpson, 1988), and in annual publications of the TRMM Office (TRMM Office, 1994) and in publications (Simpson *et al.*, 2000).

The Precipitation Radar (PR) onboard TRMM is the first spaceborne rain radar. Major objectives of PR are: (1) to provide three-dimensional rainfall structure, (2) to achieve quantitative rainfall measurement over land as well as the

Table 14.3. TMI characteristics (TRMM).

Observation frequency	10.7, 19.4, 21.3, 37 and 85.5 GHz
Polarization	vertical/horizontal (21.3 GHz channel: horizontal only)
Horizontal resolution	6–50 km
Swath width	about 760 km
Scan mode	conical scan (49 degrees)
Data rate	8.8 kbps
Weight	65 kg
Power consumption	50 W

ocean; and (3) to improve the accuracy of TMI measurements by providing rain structure information.

The TRMM Microwave Imager (TMI) is a multi-channel/dual-polarized microwave radiometer which provides data related to rainfall rates over the ocean (Table 14.3). The TMI data together with PR data is the primary data set of precipitation measurements.

The Visible Infrared Scanner (VIRS) is a passive cross-track scanning radiometer which measures scene radiance in five spectral bands operating in the visible through the infrared spectral regions. The VIRS data provide information about convective cloud fields (cloud type, convective conditions).

The Cloud and the Earth's Radiant Energy System (CERES) is a passive broadband scanning radiometer which has three spectral bands in the visible through the infrared spectral regions and measures the earth's radiation budget and atmospheric radiation from the top of the atmosphere to the surface of the earth.

The Light Imaging Sensor (LIS) is an optical telescope and filter imaging system which will acquire and investigate the distribution and variability of both intracloud and cloud-to-ground lightning over the earth. The LIS data will also be used with PR, TMI and VIRS data to investigate the correlation of the global incidence of electrical activity with rainfall and other storm properties (including tropical cyclones).

14.2.3 Aqua mission

Earth Observing System PM1 (Aqua) was developed by NASA to investigate the mechanism of the earth's environment systems, such as atmosphere, cloud, snow ice, water and vegetation. The development and operation of Aqua are conducted as an international project. Aqua satellite was launched into orbit on May 4 2002. Orbit

Table 14.4. AMSR-E characteristics (Aqua mission).

Frequency (GHz)	6.9	10.7	18.7	23.8	36.5	89.0
Bandwidth (MHz)	350	100	200	400	1000	3000
Sensitivity (K)	0.3	0.6	0.6	0.6	0.6	1.1
IFOV (km)	75×43	48×27	27×16	31×18	17×8	6×4
Sample spacing (km)	10	10	10	10	10	5
Integration time (ms)	2.6	2.6	2.6	2.6	2.6	1.3
Beam efficiency (%)	95.3	95.0	96.3	96.4	95.3	96.0
Antenna diametre (m)	1.6					
Scan period (s)	1.5					
Antenna offset angle (degrees)	47.4					
Earth-inclination angle (degrees)	54.8					
Orbit type	Sun-synch., 98.2° incl., 705 km alt., 1:30 pm equator crossing					
Swath width (km)	1445					

parameters are the following: Sun-synchronous orbit at an altitude of 705 km; inclination is 98.2°; and period is 100 minutes.

Aqua carries five sensors: Advanced Microwave Scanning Radiometre (AMSR-E) developed by NASDA; atmospheric microwave sounder Humidity Sounder for Brazil (HSB) developed by INPE, Brazil, as well as NASA's Atmospheric Infrared Sounder (AIRS); Advanced Microwave Sounding Unit (AMSU); Clouds and the Earth's Radiant Energy System (CERES); and Moderate Resolution Imaging Spectroradiometre (MODIS).

AMSR-E instruments (Table 14.4) were modified for Aqua from the design used for AMSR, which was onboard ADEOS-2 at a later time. AMSR-E and AMSR are microwave sensors capable of accurately acquiring weak radiation from land surface and atmosphere with its wide frequency bands and obtaining the necessary data for the study of earth hydrologic circulation. Microwave sensors, unlike optical sensors, can continuously observe night and day, regardless of weather. Allocating AMSR on a morning orbit and AMSR-E on an afternoon orbit allows observation of everyday changes of the earth's environment, and it is expected to contribute to the study of the earth's environmental system (Shibata, 2000; Njoku *et al.*, 2000a; Koike *et al.*, 2000).

The EOS Aqua AMSR will measure geophysical parameters supporting several global change science and monitoring efforts. Of particular importance to its success

is an external calibration design, which has proved suitable in other satellite microwave instrumentation for long-term monitoring of subtle changes in temperature and other variables.

The science objectives of AMSR-E are the following:

- Precipitation: Precipitation has extremely important roles, through provision of water to the biosphere and as an air-conditioning agent that removes excess heat from the surface (through evaporation) and makes earth habitable. The AMSR will measure rain rates over both land and ocean. Over the ocean, the AMSR microwave frequencies can probe through smaller cloud particles to measure the microwave emission from the larger raindrops. The AMSR will provide sensitivity to oceanic rain rates as high as 50 mm/hour. Over land, the AMSR can measure the scattering effects of large ice particles which later melt to form raindrops. These measurements, though less direct as a measure of rainfall intensity, are converted to a rain rate with the help of cloud models.
- Sea surface temperature: Over the ocean, AMSR will provide sea surface temperatures (SST) through most types of cloud cover, supplementing infrared-based measurements of SST that are restricted to cloud-free areas. SST fluctuations are known to have a profound impact on weather patterns across the globe, and the AMSR's all-weather capability could provide a significant improvement in our ability to monitor SSTs and the processes controlling them.
- Total integrated water vapour: The total integrated water vapour of the atmosphere will be measured over the ocean, which is important for the understanding of how water is cycled through the atmosphere. Since water vapour is the Earth's primary greenhouse gas, and it contributes the most to future projections of global warming, it is critical to understand how it varies naturally in the earth's system.
- Wind speed: Ocean surface roughness is also measured by AMSR, which will be converted into a near-surface wind speed. These winds are one important component of how much water is evaporated from the surface of the ocean. The winds help to maintain the water vapour content of the atmosphere while precipitation continually removes it.
- Cloud liquid water: AMSR cloud water estimates over the ocean will help studies of whether clouds, and their ability to reflect sunlight, increase or decrease under various conditions. This could be an important feedback mechanism that either enhances or mitigates global warming, depending on whether clouds increase or decrease with warming.
- Sea ice: Monitoring of sea ice parameters, such as ice type and extent, is necessary to understand how this frozen blanket over the ocean acts to change climate through its ability to insulate the water against heat loss to the frigid atmosphere above it, and through its ability to reflect sunlight that would otherwise warm the ocean.
- Snow cover: In much the same way as the AMSR can see large ice particles in the upper reaches of rain systems, it also measures the scattering effects of snow cover. These measurements are empirically related to snow cover depth and

water content based upon field measurements. Like sea ice, snow cover has a large influence on how much sunlight is reflected from the earth. It also acts as a blanket, keeping heat from escaping from the underlying soil, and allowing deep cold air masses to develop during the winter. It further provides an important storage mechanism for water during the winter months, which then affects how much surface wetness is available for vegetation and crops in the spring. AMSR monitoring of snow cover will allow studies and monitoring of how snow cover variations interplay with other climate fluctuations.

- Soil moisture: Wet soil can be identified in the AMSR observations if not too much vegetation is present. The AMSR will provide the most useful satellite data yet for determination of how well low-frequency (6.9 GHz) microwave observations can be used to monitor surface wetness. Surface wetness is important for maintaining crop and vegetation health, and its monitoring on a global basis will allow drought-prone areas to be monitored for signs of drought.

The Advanced Microwave Sounding Unit (AMSU-A) is a 15-channel microwave sounder designed primarily to obtain temperature profiles in the upper atmosphere (especially the stratosphere) and to provide a cloud-filtering capability for tropospheric temperature observations. The first AMSU was launched in May 1998 on board the National Oceanic and Atmospheric Administration's (NOAA's) NOAA-15 satellite. The EOS AMSU-A will be part of a closely coupled triplet of instruments that include the AIRS and HSB. A passive multichannel microwave radiometer obtained 15-channel microwave sounder with a frequency range of 15–90 GHz provides atmospheric temperature measurements from the surface up to 40 km. AMSU instrument characteristics are the following: instrument instantaneous field of view is 3.3° ; linear scan field of view is $\pm 49.5^\circ$; swath width is 1650 km; spatial resolution at nadir is 40 km. The AMSU instrument measures air temperatures at five levels in the atmosphere.

14.2.4 ADEOS-II mission

Advanced Earth Observing Satellite-II (ADEOS-II), also known as Midori-2, is a Japanese (NASDA) remote sensing spacecraft launched December 14 2002 ($H = 805$ km, $\theta = 98, 69^\circ$, $T = 100.99$ min). The 3.7-tonne (with fuel), 5-kW spacecraft carries five instruments to monitor global climate trends (Kondratyev and Tanaka, 1997; Shibata, 2000). One, the Advanced Microwave Scanning Radiometre (AMSR) monitors water vapour, precipitation, sea surface temperature, wind and ice by means of the microwave emission emanating from the earth's surface and atmosphere (see above). It is a radiometre that operates in eight frequency bands covering 6.9 to 69 GHz and monitors the horizontal and vertical polarizations separately. With a dish of 2-m aperture, the spatial resolution is 5 km in the 89 GHz band degrading to 60 km at 6.9 GHz (Table 14.5) (Shibata, 2000). The Global Imager (GLI) is an optical sensor to observe solar radiation reflected from the earth's surface and to map vegetation, clouds, etc. The data are acquired in 23 visible/

Table 14.5. AMSR Characteristics (ADEOS-II mission).

Frequency (GHz)	6.9	10.65	18.7	23.8	36.5	89.0	50.3	52.8		
Spatial resolution (km)	50		25		15	5	10			
Bandwidth (MHz)	350	100	200	400	1000	3000	200	400		
Polarization	horizontal and vertical						vertical			
Incident angle (degrees)	about 55									
Cross polarization (dB)	under -20									
Swath width (km)	1600									
Dynamic range(K)	2.7–340									
Absolute accuracy (K)	1 (1σ)									
ΔT (K)	0.3–1.0 (1σ)						2 (1σ)			
Quantization (bit)	12	10								

near-infrared and 13 far-infrared channels. Scanning is accomplished by a rotating mirror covering 12 km along track and 1600 km a cross track at a resolution of 1.0 km. SeaWinds is a scatterometre that provides wind speed and direction by observing the microwave backscattering from ocean surfaces. With its 1.0-m dish, it scans the surface along conical surfaces at 18 rpm. It provides speed at an accuracy of 2 m/s, wind direction at an accuracy of 20°, both with a spatial resolution of 5 km. ILAS-2 (Improved Limb Atmospheric Spectrometre 2) maps the vertical distribution of O₃, NO₂, HNO₃, H₂O, CFC-11, CFC-12, CH₄, N₂O and ClONO₂, as well as the distribution of temperature and pressure, all in the stratosphere. It observes the absorption spectrum in the earth's atmospheric limb in the 3–13 μm wavelength band, and in the 753–784 nm band of the occulting Sun. The altitude resolution is 100 m. POLDER (POLarization and Directionality of Earth's Reflectances) measures the polarization, and spectral characteristics of the solar light reflected by aerosols, clouds, oceans and land surfaces. Eight narrowband wavelengths (443, 490, 564, 670, 763, 765, 865 and 910 nm) are covered by the instrument which facilitates identification of the physical and optical properties of the aerosols and their role in radiation budget.

NASDA will use Global Change Observation Mission (GCOM) to contribute process study and prediction of global change phenomena and preservation of global environments for 15 years with ADEOS-II (Sobue *et al.*, 2000; Shimoda, 2000). There are three main goals of GCOM: (1) understanding the material energy cycle, and documenting and predicting global warming, (2) understanding atmosphere–ocean interaction, radiative forcing and documenting and predicting

medium-to long-term climate changes, and (3) understanding ozone and the GHG circulation mechanism, and documenting and predicting ozone layer and atmospheric composition variabilities. The GCOM will consist of the GCOM-A satellite series, the GCOM-B satellite series and ground infrastructures. The GCOM-AI satellites will measure the ozone layer and greenhouse gases while the GCOM-BI satellites will observe the material and energy cycles. The main GCOM-BI instrument will be AMSR Follow On.

14.3 FUTURE PASSIVE MICROWAVE SPACE MISSIONS

In this section we shall briefly outline a series of potential space missions on studying and monitoring geophysical and meteorological systems of the earth. Each of them is at a completely different preparation stage – from a flight model ready for launching up to the engineering design stage. Each of these missions is directed at the solution of various geophysical and hydrometeorological problems; but, here, a key element of each mission is the inclusion of passive microwave instruments as a major integral part of a space observational system.

14.3.1 MTVZA-OK mission

The present mission is the combined optical–microwave imager/sounder MTVZA-OK (Russia) of spacecraft ‘Sich-1M’ (Russia/Ukraine), which will be launched in 2003 on Sun-synchronous orbit at an altitude of 650 km (Cherny and Chernyavsky, 2001).

MTVZA-OK will be used as the meteorological imaging/sounding system for the remote sensing of the ocean and the land surface, as well as for measuring global atmospheric temperature and water vapour profiles. The instrument is the next version of the microwave imager/sounder MTVZA deployed on spacecraft ‘Meteor-3M’ (Cherny and Raizer, 1998).

MTVZA-OK combines both optical and microwave systems deployed on a single scanning platform. Field of view (FOV) is common for optical and microwave imaging and sounding channels. MTVZA-OK microwave performance characteristics are given in Table 14.6. The microwave radiometre MTVZA-OK is based on the technology of combining in space and time multifrequency and polarization measurements. MTVZA-OK operating frequencies are located both in the transparent windows of atmosphere, 6.9, 10.6, 18.7, 23.8, 31, 36.5, 42, 48, 89 GHz, and in absorbing lines of oxygen 52–57 GHz and water vapour 183.31 GHz. In addition, the MTVZA-OK includes some complementary non-typical operating frequencies especially for oceanographic research. The instrument will provide measurements of atmosphere temperature profile to approximately 42 km and water vapour profile to 6 km.

All microwave radiometre channels are switched to single feed-horn antenna. The antenna system consists of an offset parabolic reflector of dimension 60 cm, illuminated by broadband feed-horn antenna. To retain the invariant viewing

Table 14.6. MTVZA-OK microwave frequency channel characteristics.

Channel no.	Centre frequency (GHz)	No. of pass-bands	Band-width (MHz)	Effective FOV (km × km)	Imagery pixel (km × km)	Sensitivity (K/pixel)	Approximate peak sensitivity altitude (km)
1	6.9	1	350	112 × 260	24 × 24	0.3	—
2	10.6	1	100	76 × 177	24 × 24	0.5	—
3	18.7	1	200	45 × 104	24 × 24	0.4	—
4	23.8	1	400	36 × 86	24 × 24	0.3	—
5	31	1	1000	30 × 69	24 × 24	0.3	—
6	36.5	1	1000	26 × 60	24 × 24	0.3	—
7	42	1	1000	22 × 53	24 × 24	0.4	—
8	48	1	1000	21 × 47	24 × 24	0.4	—
9	52.28	1	400	18 × 43	36 × 36	0.4	2
10	52.85	1	400	18 × 43	36 × 36	0.4	4
11	53.33	1	400	18 × 43	36 × 36	0.4	6
12	54.40	1	400	18 × 43	36 × 36	0.4	10
13	55.45	1	400	18 × 43	36 × 36	0.4	14
14	57.290344 ± 0.3222	4	50	18 × 43	48 × 48	0.4	20
15	57.290344 ± 0.3222	4	20	18 × 43	48 × 48	0.7	25
16	57.290344 ± 0.3222	4	10	18 × 43	48 × 48	0.9	29
17	57.290344 ± 0.3222	4	5	18 × 43	48 × 48	1.3	35
18	57.290344 ± 0.3222	4	3	18 × 43	48 × 48	1.7	42
19	89	1	4000	12 × 28	12 × 12	0.6	surface
20	183.31 ± 7.0	2	1500	7 × 16	24 × 24	0.5	1.5
21	183.31 ± 3.0	2	1000	7 × 16	24 × 24	0.6	2.9
22	183.31 ± 1.0	2	500	7 × 16	24 × 24	0.8	5.3

Channels 1–8, and 19 operate on both vertical and horizontal polarization, while other remaining channels operate on vertical polarization only.

angle and polarization in the scanning sector, the reflector and feed-horn antenna are mounted on a scanning platform containing the radiometers, digital data subsystem, power and signal transfer assembly, which rotates continuously about an axis parallel to the local spacecraft vertical.

The MTVZA-OK scanning platform rotates continuously about an axis parallel to the local spacecraft vertical with a period of 1.8 s during which the subsatellite point travels 12 km. The scan direction is from the right to the left when looking in the forward direction of the spacecraft, with an active scanning sector of 120°, resulting in a swath width of 2000 km. The viewing angle is 55.4° and the incidence angle with respect to the earth's surface is 65°. The sampling rate is 12 × 12 km for all microwave channels.

Russian specialists hope (Cherny and Chernyavsky, 2001; Grankov *et al.*, 2000) that MTVZA-OK will provide some very interesting and powerful capabilities for complementary studies of the ocean–atmosphere system. By combining optical and microwave observations in the same instrument, some mutually beneficial advantages for determining geophysical parameters are obtained. Both atmospheric temperature profile and atmospheric humidity profile, sea surface temperature and near-surface wind speed, ocean colour and processes of the active ocean layer will be observed concurrently, enabling flow visualization and upwelling area to be better observed as well as estimates of the ocean–atmosphere interaction.

14.3.2 CLOUDS mission

The cloud and radiation monitoring satellite (CLOUDS) is a project co-funded by the EC, conducted by 12 European partners (7 scientific institutes and 5 industrial companies), also cooperating with NOAA/ETL (Bruzzi, 1995; Bizzari and Spera, 2000; Bizzari *et al.*, 2000). It is the mission study of a monitoring satellite to perform measurements necessary to describe cloud–radiation interaction in operational models for climate and long-term weather prediction (Arkin and Xie, 1994; Asrar and Dokken, 1993; Houze, 1993; IPCC, 2001). Complementary to missions for process study, CLOUDS addresses the monitoring aspect. Therefore it has to comply with requirements of sufficiently frequent observing cycle, and operational sustainability. This prevents using active systems (radar and lidar) and leads to considering passive radiometry only, but exploiting as much as possible of the electromagnetic spectrum, with more polarizations and more viewing geometries. The objective of the CLOUDS project was to study the mission of a new satellite to provide accurate, comprehensive, consistent and frequent information on cloud structures and on the associated radiative parameters. The information would be used by meteorological services and research centres to improve weather forecasting and climate modelling.

CLOUDS is proposed as a monitoring mission. Its strategic objective is to extend the overall European service of climate monitoring from space, beyond what is achievable by the instrumentation at present foreseen for MSG and METOP/EPS, whose mission definition has been driven by nowcasting and short–medium-term weather prediction.

User requirements were established, specifying a list of geophysical parameters to be measured in the areas of:

- the ‘classical’ cloud parameters, mostly referring to the top surface, with emphasis on ice/liquid discrimination and size;

- the cloud interior, specifically water phase (ice or liquid) and whether drop-size is likely to produce precipitation;
- the outgoing radiation from the top of atmosphere to space;
- the main parameter impacting with both clouds and radiation in the 3-D atmosphere, i.e. aerosols;
- the primary source of clouds, i.e. water vapour, also primary factor of radiative processes in the 3-D atmosphere;
- the indicator of final removal of water from the atmosphere, i.e. precipitation.

The mission requirements established for CLOUDS were strongly conditioned by the monitoring objective, which implies compliance with long-term sustainability requirements, and the requirement for an observing cycle consistent with routine use.

The key aspect of the CLOUDS mission is the exploitation of the widest range of the electromagnetic field to collect as many ‘signatures’ as possible of the different parameters to be measured. The spectral range utilized spans from 340 nm to 4.3 cm, i.e. over five orders of magnitude. Six instruments are described, operating, respectively, in narrow channels of the UV/VIS/NIR/SWIR, the TIR/FIR, the sub-millimetre waves and the MW, in broadband channels from UV to FIR, and in a relatively large-band channel of VIS/NIR. Several channels have three or four polarizations, all take images fore and aft (conical scanning), one has multi-angle-viewing capability. The overall system size is estimated as 900 kg mass, 1600 W power, 1.1 Mbps data rate for real-time S-band transmission, and 30 Mbps data rate for global data recovery in X-band.

An important instrument requirement to note is that all channels in CLOUDS must have consistent scanning mechanism, so as to ensure compatible viewing geometry and make possible accurate co-registration, for a true multi-spectral approach, as necessary when dealing with fractal fields. Since most channels require differential polarization, conical scanning is most suitable.

The CLOUDS mission is implemented by six instruments:

- the CLOUDS Integrated Optical Payload (CIOP), composed of four instruments:
 - the Clouds and Aerosol Short-wave Imaging Radiometre (CASIR);
 - the CLOUDS Infra Red Imaging Radiometre (CIRIR);
 - the Broad-band Earth Radiation Imaging Radiometre (BERIR);
 - the Multi-Angle VIS Imaging Radiometre (MAVIR);
- the MW/sub-millimetre instruments:
 - the Cloud Ice and Water-vapour Sub-mm Imaging Radiometre (CIWSIR);
 - the Cloud Liquid-water And Precipitation Microwave Imaging Radiometre (CLAPMIR).

The two instruments covering the MW/sub-millimetre range perform conical scanning with the same speed of 1 scan per 2 s. The viewing geometry is the same as for the optical payload (45° off-nadir observing the scene under the zenith angle 53.2° , with two arcs of over $\pm 45^\circ$ fore and aft for a swath of nearly 1400 km).

The CIWSIR instrument includes channels in the sub-millimetre and very-high frequency MW range. Their main purposes are:

- to observe cloud ice with higher penetration in the cloud interior as compared with what is possible in the shortwave and in IR;
- to discriminate water phase in the cloud interior;
- to infer convective penetration in the troposphere through differential water vapour optical depth.

CIWSIR is a 6-frequency, 13-channel microwave radiometre—7 channels in the millimetre- (water vapour) and 6 channels in the sub-millimetre-range (ice clouds).

To be synergistic with the optical package and with CLAPMIR, the same viewing geometry is adopted. The main instrument features of CIWSIR, and its expected performances compared with requirements, are reported in Table 14.7.

The CLAPMIR instrument includes microwave channels in window and absorption bands. The main purposes are:

- to observe cloud liquid water, precipitating and non-precipitating, with inference of drop size;
- to discriminate water phase in the cloud interior and total-column water vapour;
- to infer a gross vertical profile of liquid/precipitating water cores as linked to air temperature.

Additional observations, outside the CLOUDS objectives, are: earth surface parameters such as sea-surface wind, sea-surface temperature, sea-ice cover and type, ice/snow cover and melting conditions, and soil moisture.

The CLAPMIR instrument will consist of an offset parabolic reflector of $1.6 \times 1.4\text{ m}$ dimensions, illuminated by a cluster of feeds. The reflector and feed horn antennas are mounted on a ‘drum’ which contains the receivers, a digital data unit, mechanical balancing subsystem and power supply. The entire drum assembly is rotated about the axis of the instrument by a coaxially mounted bearing and brushless DC motor. The polarimetric channels are designed to provide the third Stokes parameter by means of adding analogue correlators. To be synergistic with the optical package and with CIWSIR, the same viewing geometry is adopted. The main instrument features of CLAPMIR, and its expected performances compared with requirements, are reported in Table 14.8.

14.3.3 MEGHA-TROPIQUES mission

Supported by the French and Indian scientific communities, the MEGHA-TROPIQUES mission aims at studying the water cycle and energy exchanges in the tropical belt (Desbois, 1995, 1999; Aguttes *et al.*, 2000; Eymard, 1999; Narayanan, 1999). It will be jointly developed by the Indian Space Research Organization (ISRO) and the French Space Agency (CNES). The small satellite ($<600\text{ kg}$) could be launched as early as 2005 by an Indian launcher in a low inclination (22°) orbit. Longwave and shortwave outgoing fluxes from the top of

Table 14.7. Instrument features and expected performances of CIWSIR (CLOUDS mission).

IFOV	0.35° corresponding to ellipse of 13×7.8 km, equivalent to 10 km circular
Scanning	Conical, $\alpha = 45^\circ$, $\zeta = 53.2^\circ$, fore- and aft-views by $>\pm 45^\circ$ in azimuth, swath ~ 1400 km
Sampling	1 scan/2 s, 1 feed/channel, readings at 1.25 ms intervals
Antenna	$L = 40$ cm for channels 150 to 220 GHz, $L = 16$ cm for channels 463 to 874 GHz
Detection	Subharmonic Schottky-mixers for millimetre-channels, fundamentally pumped mixers for sub-millimetre channels
Resources	Mass: 79 kg, volume (cylindrical): diameter = 110 cm, $h = 43$ cm; power: 110 W; data rate 83.2 kbps

Channel centre (GHz)	Bandwidth (GHz)	Polarization	ΔT (required) (K)	ΔT (estimated) (K)
874.38 ± 6.0	3.0	two	1.0 @ 240	2.0 @ 240
682.95 ± 6.0	3.0	two	1.0 @ 240	1.2 @ 240
462.64 ± 3.0	2.0	two	1.0 @ 240	0.9 @ 240
220.50 ± 3.0	2.0	two	1.0 @ 240	0.9 @ 240
183.31 ± 1.0	1.0	one	1.0 @ 240	1.2 @ 240
183.31 ± 3.0	2.0	one	1.0 @ 260	0.9 @ 260
183.31 ± 7.0	4.0	one	1.0 @ 280	0.6 @ 280
150	4.0	two	1.0 @ 300	0.6 @ 300

the atmosphere will be derived from the ScaRaB radiometre, already developed in France (Desbois, 1999). Measurement of the atmospheric water vapour vertical distribution will be given by SAPHIR, a new microwave sounder around strong water line 183 GHz and MADRAS, the main and biggest instrument, will scrutinize cloud and precipitation properties. It is a conical scanning radiometre with six channels (10, 18, 23, 36, 89, and 157 GHz) and a resolution ranging from 60 km (10 GHz) to 6 km (157 GHz).

The main objective of the MEGHA-TROPIQUES mission is to study the convective systems that influence the tropical weather and climate. The tropical region is the domain of monsoons, squall lines and tropical cyclones. It is also characterized by large intra-seasonal, inter-seasonal and inter-annual variations, which may lead to catastrophic events such as droughts or floods. Any change in the energy and

Table 14.8. Instrument features and expected performances of CLAPMIR (CLOUDS mission).

IFOV	At 89 GHz: 0.175° corresponding to ellipse of 6.5×3.9 km, equivalent to 5 km circular. Bands 118 and 55 GHz: 0.35° corresponding to ellipse of 13×7.8 km, equivalent to 10 km circular. At other channels: changing with frequency according to the diffraction limits
Scanning	Conical, $\alpha = 45^\circ$, $\zeta = 53.2^\circ$, fore- and aft-views by $>\pm 45^\circ$ in azimuth, swath ~ 1400 km
Sampling	1 scan / 2 s
Antenna	$L = 160$ cm
Resources	Mass: 160 kg, volume (stowed): cylindrical diameter = 90 cm, $h = 180$ cm; power: 170 W; data rate 208 kbps

Channel centre (GHz)	Band-width (GHz)	Along-track IOFV (km)	Along-scan IOFV (km)	Average IFOV (km)	Samples/scan	Integration time (ms)	Polarization	ΔT (required) (K)	ΔT (estimated) (K)
118.75 ± 1.0	1.0	13.0	7.8	10	800	2.5	one	0.5 @ 230	1.0 @ 230
118.75 ± 1.5	1.0	13.0	7.8	10	800	2.5	one	0.5 @ 250	1.0 @ 250
118.75 ± 2.0	1.0	13.0	7.8	10	800	2.5	one	0.5 @ 270	1.0 @ 270
118.75 ± 4.0	1.0	13.0	7.8	10	800	2.5	one	0.5 @ 290	1.2 @ 290
89.0	3.0	6.5	3.9	5	1600	1.25	four	1.0 @ 300	1.0 @ 300
55	0.5	13.0	7.8	10	800	2.5	one	0.5 @ 230	1.0 @ 230
54	0.5	13.0	7.8	10	800	2.5	one	0.5 @ 250	1.0 @ 250
53	0.5	13.0	7.8	10	800	2.5	one	0.5 @ 270	1.0 @ 270
50	0.5	13.0	7.8	10	800	2.5	one	0.5 @ 290	1.0 @ 290
36.5	1.0	15.8	9.5	12	800	2.5	four	0.7 @ 300	0.6 @ 300
23.8	0.4	24.3	14.6	19	400	5	two	0.6 @ 250	0.6 @ 250
18.7	0.2	30.1	18.6	24	400	5	four	0.5 @ 300	0.6 @ 300
10.6	0.1	54.6	32.7	42	200	10	four	0.4 @ 300	0.4 @ 300
6.9	0.3	83.8	50.3	65	200	10	two	0.3 @ 300	0.3 @ 300

water budget of the land–ocean–atmosphere system in the tropics has an influence on global climate. The exchanges of energy in the intertropical zone influence the climate of the rest of the planet. These systems interact with the general circulation of the atmosphere in ways which are not fully understood, thus precluding reliable prediction of the events. Interactions with oceanic and continental surfaces have also

to be accounted for, as for example the consequences in various regions of the El Niño – La Niña events (Philander, 1990; Raschke and Jacob, 1993; Sadourny *et al.*, 1999; Sharkov, 1998).

Knowledge of the life cycle of tropical convective systems is limited by the lack of information from over the tropical oceans and many areas of tropical continents. Geostationary satellites provide a good space–time sampling of the cloud cover, but no information about water vapour profiles, deep cloud water content, or precipitation. Instruments to retrieve these quantities, based on microwave techniques, exist on polar orbiters, but they do not provide adequate sampling in the tropics (ESA, 1996b; Desbois, 1995, 1999; Gairola, 1999; Roca, 1999). TRMM, which was launched in 1997, is concerned mainly with estimation of tropical rainfall. The instruments used in TRMM are very well adapted to the study of tropical systems, but the low level of the orbit, and its inclination at 35°, do not allow a sampling of the equatorial region. Therefore the follow-up of this experiment calls for better sampling of the whole planet with passive instruments, using a constellation of satellites.

The principle of MEGHA-TROPIQUES is to get a satisfactory sampling of the intertropical band, and specially the latitudes between 10° and 20°, with instruments relevant for the water and energy budget of the tropical convective systems. This implies a low inclination orbit. The instruments have to be complementary to those that exist on geostationary satellites (VIS-IR imagers). Microwave instruments are, then, the right choice.

The basic principles of the MEGHA-TROPIQUES mission are therefore as follows:

- to provide simultaneous measurements of several elements of the atmospheric water cycle: water vapour, clouds, condensed water in clouds, precipitation and evaporation;
- to measure the corresponding radiative budget at the top of the atmosphere;
- to ensure high-temporal sampling in order to characterize the life cycle of the convective systems and to obtain significant statistics.

Given the general objectives and the principle of improved time sampling of the MEGHA-TROPIQUES experiment, the parameters that are specifically required by MEGHA-TROPIQUES are listed below. Different types of quantities are considered, according to the time scale (instantaneous, cumulated or time-averaged) and to the possibility of getting quantitative or qualitative information:

Instantaneous data:

- integrated water vapour: ~5% to 10% ~2 kg/m² (outside clouds);
- water vapour by layer (5 to 7 layers): 10% to 20%, (outside clouds);
- temperature, altitude of cloud top: 1 to 2 K, <500 m;
- precipitation: ~50% depending on rain, size of precipitating areas, convective/stratiform precipitation, range 0.5 to 50 mm/hour;
- latent heat release: indication on some classes, convective stratiform separation;
- liquid water content: 0.05 to 0.1 kg/m²;

- cloud ice content: absence/presence, size of anvil clouds, indication on particle size;
- radiation budget terms: $\sim 10 \text{ W/m}^2$;
- sea surface wind: 2 to 5 m s^{-1} ;
- vertical structure of systems: an indication of the vertical distribution of liquid water and precipitation in several layers (around 5).

SAPHIR is a continuous cross-track scanning. The mission specifications calls for determination with an accuracy of 10% to 20% of the humidity in six layers of the troposphere, over 10 km pixels, from 2 km up to 12 km height. To realize that performance, it is necessary to choose channels for which the atmospheric contribution to the radiance comes from different levels of the troposphere. This can be obtained by sampling an absorption line of water vapour by channels more or less close to the centre of the line. The selected line, already chosen for other instruments, is the strong line at 183.3 GHz. The sensitivity requirement is around 1.5 K.

MADRAS (Microwave Analysis and Detection of Rain And Atmosphere) is a canonical scanning radiometer; the microwave radiation from a scene is collected by antenna beams and then focused via a single dish to different horns. The requirement of two polarizations for most channels, classical in microwave radiometry, implies that the scenes have to be observed over a constant incidence angle. This incidence angle is between 50° and 55° (upper limit for each channel), in order to get the widest swath while keeping a manageable incidence angle.

The requirements for the channels and their respective mission is the following (frequency/resolutions):

- 10.6 GHz ($50 \times 80 \text{ km}$);
- 18.7 GHz ($50 \times 80 \text{ km}$);
- 23.8 GHz ($40 \times 65 \text{ km}$);
- 36.5 GHz ($40 \times 65 \text{ km}$);
- 89 GHz ($10 \times 16 \text{ km}$);
- 157 GHz ($6 \times 9 \text{ km}$).

The polarization is H + V, except for 23.8 GHz which is H or V. Sensitivity requirement is around 1 K for the highest channels (89 GHz and 157 GHz) and 0.5 K for the others. The dish effective (along the beam axis) diametre is 76 cm. The ratio focal/diametre is 0.8. The beam efficiency is 0.95. A single horn will be used for the three channels: 18, 23 and 36 GHz.

MEGHA-TROPIQUES satellite launch is foreseen for late-2005.

14.3.4 NPOESS program

The National Polar-orbiting Operational Environmental Satellite System (NPOESS) is a program currently in development for the purpose of providing global environmental measurements for use by the National Weather Service and other civil agencies, the Department of Defense (DoD), and the scientific research community (Flaming, 2000). NPOESS will replace the Polar-orbiting Operational

Environmental Satellite (POES) constellation currently operated by the National Oceanic and Atmospheric Administration (NOAA) and the DoD's Defense Meteorological Satellite Support Program (DMSP), a constellation of satellites which are also in polar orbit performing operational environmental measurements. International agreements are also pending with the European Organization for the Exploitation of Meteorological Satellites (EUMETSAT) to incorporate and consolidate portions of that program with NPOESS.

The first NPOESS satellite is projected to be launched in 2008. The program will include replenishment satellites, and will provide measurements for at least a 10-year period.

Five of the NPOESS critical sensors are currently in development. These five are the Ozone Mapping and Profiler Suite (OMPS), the Cross-track Infrared Sounder (CrIS), the Global Positioning System Occultation Sensor (GPSOS), the Visible/Infrared Imager Radiometre Suite (VIIRS) and the Conical Microwave Imager Sounder (CMIS).

The environmental data records (EDRs) measured by CMIS are extensive, and include the following:

- atmospheric vertical moisture profile;
- atmospheric vertical temperature profile;
- sea surface temperature;
- sea surface winds (speed and direction);
- soil moisture;
- precipitable water;
- precipitation (type/rate);
- pressure profile;
- total water content;
- cloud base height;
- cloud ice water path;
- cloud liquid water;
- snow cover/depth;
- fresh water ice;
- ice surface temperature;
- tea ice age and sea ice edge motion;
- surface wind stress;
- land surface temperature;
- vegetation/surface type.

These EDRs will be collected on a global basis approximately every 6 hours when the complete constellation of satellites is in place. These satellites will have nodal crossing times of 0530, 0930, and 1330, and will have CMIS on a satellite in each orbit.

It should be noted that CMIS will incorporate into a conical scan system both a surface measurement and atmospheric sounding capability; earlier instrumentation frequently performed surface measurements with a conical scan system, and employed a cross-track scan system for atmospheric soundings. CMIS represents a

Table 14.9. Microwave sensor comparison.

Mission	SSM/I	TMI	SSMIS	AMSR-E	CMIS
Antenna diametre (m)	0.6	0.6	0.7	1.6	2.5
Number of measurement channels	7	9	24	12	77
Mass (kg)	56	62	96	324	250
Power (W)	45	50	135	350	225
Operational design life (years)	3	3	5	6	7

continuation in the trend of microwave instruments that are more capable, but also more complex. In Table 14.9 some of the physical characteristics of the conical scan sensors mentioned above are compared with CMIS. The analysis of the table has distinctly guided the development of future microwave sensing instruments.

The approaches used by other instruments for satisfying measurement requirements suggest similar design characteristics may be used by CMIS. Soil moisture and sea surface temperature are measured by AMSR with a 6.9-GHz channel; atmospheric vertical temperature profiles are measured by AMSU-A using a series of channels in the 50–60 GHz range. The SSMIS (DMSP F16 satellite) is a instrument in terms of its development, and measures atmospheric water vapour using 150 GHz and 183 GHz channels; similar channels are also being used by AMSU-B to make the same measurements. Although not used in operational instruments constructed to date, the phenomenology suggests that frequencies greater than 183 GHz may have an application, if the appropriate technology can be developed. Thus, the measurements that CMIS must perform may span the frequency range from 6 to 183 GHz, or more, and may employ 77 channels and polarimetry methods for the measurement of vector winds. The physical size of the instrument, the large number of measurement channels required for the 20 EDRs, the sensitivity required for the measurement channels, and the very long operating life (7 years), all suggest the development of an extremely complex instrument.

14.3.5 OSIRIS concept

A concept Ocean-salinity Soil-moisture Integrated Radiometre-radar Imaging System (OSIRIS) has been deeply studied for remote sensing of sea surface salinity from space using a large deployable mesh antenna system (Wilson *et al.*, 2000). The antenna has a 6-m diametre offset-fed parabolic reflector with multi-channel feedhorns and radiometres and a radar, operating at L and S bands. The entire system rotates about the nadir axis, providing a conical scan across a 900-km wide swath at a spatial resolution of about 40 km from a 600-km orbit altitude. The study includes evaluation of deployable mesh antennas and preferred antenna, spacecraft, and launch vehicle configurations. The key system characteristics are

Table 14.10. Key baseline system characteristics of OSIRIS concept.

Radiometre frequencies (GHz)	1.41 and 2.69
Radiometre polarization	H, V; (1.41 GHz polarimetric)
Radar frequency (GHz)	1.26
Radar polarization	VV, HH, VH, HV
Antenna type	Offset-fed, parabolic, deployable mesh reflector
Aperture diametre (m)	6
Ocean incidence angle (degrees)	40
Number of feedhorns	2 (each L/S-band, V/H-polarization)
Beam widths (degrees)	2.6° (approx. equal all channels)
Antenna gain (dB)	35
Beam efficiency (%)	>90
Orbit type	Polar, Sun-synchronous, 6 a.m./6 p.m.
Altitude (km)	600
Spatial resolution (km)	35 × 45
Swath width (km)	900
Rotation rate (rpm)	6
Global coverage (days)	2–3
Radiometre ΔT per footprint (K)	0.2
Radiometre absolute accuracy and stability (K)	1 and 0.2
Radar precision/stability (dB)	0.2
Power (W)	350
Data rate (kbit/s)	25
Mass (kg)	530
Mission duration (years)	3

summarized in Table 14.10. The antenna conical scan system is a rotating, offset-fed, parabolic-mesh reflector, with two identical multichannel feedhorns, which feed the L- and S-band radiometres and the L-band radar. The two feedhorns provide separate beams that give overlapping contiguous footprints at the surface, and

allow the antenna system to rotate at 6 rpm which is half as fast as would be necessary with a single beam. The combined antenna and feed system rotates about the vertical axis, with antenna beams at an incidence angle of 40°. As the spacecraft moves, the 3-dB antenna footprints provide overlap along and across track in a helical coverage pattern. At an orbit altitude of 600 km, the 6-m antenna provides ~40-km spatial resolution, and a swath width of 900 km.

Another possible concept consists in using an inflatable antenna. Such an inflatable structure could enable the deployment of a large-aperture, low-mass, and low-cost antenna system in space, suitable for operation in the 1–3 GHz band needed for soil and salinity sensing (Njoku *et al.*, 1999).

Conclusion

The rapid introduction of microwave sensing methods and means into airspace observations in the last 10–15 years was a consequence, as we have shown above, of the significantly new (in relation to optical and infrared bands) physical information content of microwave sensing in studying terrestrial objects (the surface and the atmosphere). The development and evolution of instruments and research missions of microwave sensing has occurred, certainly, in a quite inhomogeneous and irregular manner. Nevertheless, at the present time, none of potential large-scale satellite missions on earth investigation fails to employ passive and active radio-physical instruments in some configuration. This tendency will doubtless be kept under close observation. And, moreover, the relative weight of microwave observation systems in the total remote sensing program will even, most likely, be augmented.

The author believes that his mission will be completed, if the physical fundamentals of microwave remote sensing, set forth in this book, will help the specialists in various geophysical disciplines – meteorologists, geophysicists, oceanologists, geologists, soil scientists, geographers – to understand those new information advantages that are embedded in microwave sensing, and will impel them to be actively engaged in a (fairly difficult) process of assimilation of remote microwave information. On the other hand, the author hopes that the specialists of other disciplines – radiophysicists, radio-engineers, electronics specialists – on acquaintance with the present book will discover for themselves new areas for the application of their abilities. The joint efforts of the specialists in various geophysical directions will, doubtless, be rewarded, and we shall become witnesses of new (and surprising) discoveries in various geophysical disciplines directed at studying the earth, as, for example, has taken place in oceanology.

References and bibliography

- Abbas M. M., Michelsen H.A., Gunson M. R., Abrams M. C., Newchurch M. J., Salawitch R. J., Chang A. Y., Goldman A., Irion F. W., Manney G. L., Moyer E. J., Nagaraju R., Risland C. P., Stiller G. P., and Zander R. (1996). Seasonal variations of water vapour in the lower stratosphere inferred from ATMOS/ATLAS-3 measurements of H_2O and CH_4 . Geophysical Research Lett. , Vol. 23, N 17, p. 2401-2404.
- Afsar M. N. , and Hasted J. B. (1977). Measurement of the optical constants of liquid H_2O and D_2O between 6 and 450 cm^{-1} . J. Opt. Soc. Amer., Vol. 67, N 7, p. 902-904.
- Aguttes J. P. , Schrige J., Goldstein C., Rouze M., and Raju G. (2000). MEGHA-TROPIQUES, a satellite for studying the water cycle and energy exchanges in the tropics. IEEE IGARSS 2000 Proceedings, Vol. VII, IEEE, New York, p. 3042-3044.
- Akhadov Ja. Yu. (1977) . Dielectric properties of binary solutions. Nauka Publ. House, Moscow, 420p. (in Russian).
- Akindinov V. V., Naryshkin V. I. , and Piazantsev A. M. (1976) . Electromagnetic fields in sea water . Radiotekhnika i elektronika (J. Communic. Techn. Electronics - Engl. transl.), Vol. 21, N 5, p. 913-944.
- Akvilanova A. B., and Kutuza B. G. (1978). Radiothermal emission of clouds. Radiotekhnika i elektronika (J. Communic. Techn. Electronics - Engl. transl.), Vol. 23, N 9, p. 1792-1806.
- Akvilanova A. B. , Mitnik L. M. , and Kutuza B. G. (1971). Global latitude distribution of cloud liquid water with "Cosmos-243" satellite data. Izvestya AN . Fizika atmosphery i okeana. (Izvestiya, Atmospheric and Oceanic Physics –English transl.), Vol. 7, N2, p. 139- 141.
- Akvilanova A. B., Basharinov A. E., Gorodezkii A. K., Gurvich A. S., Krylova M. S., Kutuza B. G., Matveev D. T., and Orlov A. P. (1973). Investigation of cloud parameters with "Cosmos-384" satellite data. Izvestya AN . Fizika atmosphery i okeana. (Izvestiya, Atmospheric and Oceanic Physics – English Transl.), Vol. 9, N2, p. 187-189 .
- Alekseev V. A. , Aleshina T. N., Krotikov V. D. , and Troitsky V. S. (1967). The influence of the roughness of the upper lunar cover on the emission capacity and the radiobrightness distribution. Astronomichesky jurnal (Astronomical journal), Vol. 44, N 5, p. 1070-1075 (in Russian).
- Allen P. M. (1997). Cities and regions as self-organizing systems. Models of complexity. Gordon and Breach, 267p.
- Allison L.J., Rodgers E.B., Wilheit T.T., Fett R.W. (1974). Tropical cyclone rainfall as measured by the Nimbus-5 electrically scanning microwave radiometer. Bull. Amer. Meteor. Soc., Vol.55, N9, p.1074-1089.
- Alpert I. L., Ginzburg V. L. , and Feinberg E.L. (1953). Radio-wave propagation. State technik-theoretic literature Publ. House, Moscow, 883 p. (in Russian).
- Amirkhanyan V. R., Bespalova E. A., Bulatov M. G., Veselov V. M., Vorsin N. N., Militskii Yu. A., Mirovskii V. G., Nemlicher Yu. A., Nikitin V. V., Raev M. D., Rabinovich Yu. I., Skulachev D. P., Strukov I.A., Shiraeva T. A., and Etkin V.S. (1975). Airborne microwave radiometric high-sensitive instruments for remote sensing of the Earth's surface. Preprint N Pr-244, Moscow, Space Research Institute, 16p. (in Russian)
- Amit D. J. , and Verbin Y. (1999). Statistical physics. An introductory course. World Scientific, Singapore, New Jersey etc., 580p.
- Andrade R. F. S., Schellnhuber H. J., and Claussen M. (1998) . Analysis of rainfall records: possible relation to self-organized criticality. Physica A, Vol. 254, N 3-4, p. 557-568.
- Anselmet F., Antonia R. A. , and Danaila L. (2001). Turbulent flows and intermittency in laboratory experiments. Planetary and Space Science, Vol. 49, N 12, p. 1177-1191.
- Angell C. A. (1982). Super cooled water. In "Water. A comprehensive treatise.", Vol. 7, Plenum Press, N.Y., London, p. 1-81.

- Antonov V.V., Armand N.A., Bobylev L.P., Bunkin F.V. et al. (1995). Russian spacecrafts for the Earth's study as a common ecological system. Preprint N Pr-1916. Moscow, Space Research Institute, 73p. (in Russian).
- Aoki I. (1988). Entropy flows and entropy productions in the Earth's surface and in the Earth's atmosphere. J. of the Physical Soc. Japan, Vol. 57 , N 9, p. 3262-3269.
- Apel J. R. (1994). An improved model of the ocean surface wave vector spectrum and its effects on radar backscatter . J. Geophysical Research, Vol. 99, N C8, p. 16269-16291.
- Apletalin V. N., Meriakri V. V., and Chigryai E. E. (1970). Measurements of absorbability and refractivity of the water at the band from 2 to 0,8 mm. Radiotekhnika i elektronika (J. Communic. Techn. Electronics - Engl. transl.), Vol. 15, N 7, p. 1502-1503.
- Apresyan L. A. and Kravtsov Yu. A. (1996). Radiation transfer: statistical and wave aspects. Gordon and Breach Publ., Amsterdam, 456 p.
- Arkin P. A.,and Xie P. (1994). The Global Precipitation Climatology Project: first Algorithm Intercomparison Project. Bull. Am. Meteorol. Soc., Vol. 75, p. 401-419.
- Armand N. A. , Ed. (1993). International Project PRIRODA. Instruments. Reference handbook. Institute of Radioengineering and Electronics RAS, Moscow,9 p.
- Armand N. A. , Savorsky V. P. , Smirnov M. T. , and Tischenko Yu. G. (2001). Earth nature resources research and ecological monitoring on the Russian segment of International Space Station (ISS). Earth Research from Space (Earth Obs. Remote Sensing - Engl. transl.). N 2. p. 55-60.
- Arrault J., Arneodo A., Davis A. and Marshak A. (1997). Wavelet based multifractal analysis of rough surfaces: application to cloud models and satellite data. Physical Review Letters, Vol. 79, N 1, p. 75-78.
- Asheko A. A. , Moroz V. I. , and Sharkov E. A. (1989). Dielectric and radiothermal properties of electrolyte water systems at 9,5 GHz . Preprint N Pr-1578 . Moscow, Space Research Institute, 41p. (in Russian)
- Asrar Gh. and Dokken D. J., Eds. (1993). EOS reference handbook. NASA, Washington, 145 p.
- Astafyeva N. M. (1996). Wavelet analysis : basic theory and some applications. Physics- Uspekhi , Vol. 39, N 11, p. 1085-1108.
- Astafyeva N. M. (1997). Nonlinear shear flow in rotating spherical layers and global atmosphere motion modeling. Izvestiya VUZ. Applied Nonlinear Dynamics. Vol. 5, N5, p. 3-29 (in Russian) .
- Astafyeva N.M., Pokrovskaya I.V., Sharkov E.A. (1994a). Scaling features of global tropical cyclogenesis. Doklady Acad. Nauk (Trans. of Russian Academy of Sciences / Earth Science Section- Eng. Transl.) , Vol.337, N4, p.517-520 .
- Astafyeva N.M., Pokrovskaya I.V., Sharkov E.A. (1994b). Hierarchical structure of global tropical cyclogenesis. Earth Research from Space. N2, p.14-23 (in Russian).
- Astafyeva N. M. and Sharkov E. A.(1998) Hierarchical structure of railway traffic popular service . Matematicheskoe modelirovanie (Mathematical Modeling). Vol. 10. N 7. P. 37- 47. (in Russian).
- Atlas D. , Ulbrich C.W. , Meneghini R. (1984). The multiparameter remote measurement of rainfall. Radio Sci., Vol. 19, N 1, p. 3- 22.
- Attema E. (1993). The geophysical validation of ERS-1 data products. Earth Observ. Quarterly, N40, p.5-7.
- Avduevskii V.S., Grishin S.D., Uspenskii V.K., Astashkin A.A., Saulskii V.K. (1983). On the problem of effectiveness and principal parameters of satellites for continuos observations of spontaneous natural phenomena. Earth Research from Space (Earth Obs. Remote Sensing- Engl. Transl.) , N2, p.117-124 (in Russian).
- Bak P., Tang C., and Wiesenfeld K. (1987). Self-organized criticality: an explanation of 1/f noise. Phys. Rev. Lett., Vol. 59, N 4 , p. 381-384.
- Bardati F., and Solimini D. (1984). On the emissivity of layered materials. IEEE Trans. Geosci. Remote Sensing, Vol. 22, N 4, p. 374-376.

- Barichello L. B. , Garcia R. D. M. , and Siewert C. E. (1998). A spherical-harmonics solution for radiative-transfer problems with reflecting boundaries and internal sources. *J. Quant. Spectrosc. Radiat. Transfer*, Vol. 60, N 2, p. 247-260.
- Barreiro R. B. (2000). The cosmic microwave background state of the art. *New Astronomy Review* , Vol. 44, N 3, p. 179-204.
- Barthel J. , Schmithals F., and Behret H. (1970). Untersuchen zur Dispersion der komplexen Dielektrizitäts-Konstante waßriger und nichtwaßriger Electrolylosungen. *Zeitschrift fur Physic. Chemie*. Vol. 71. N 1-3, p. 115-131.
- Bartsch N., Gruner K., Keydel W., and Witte F. (1987). Contributions to oil-spill detection and analysis with radar and microwave radiometry : results of the Archimedes II campaign. *IEEE Transc. Geoscience Remote Sensing* , Vol. 25, N 6, p. 677-690.
- Bartsch B., Bakan S., Fischer J. (1996). Passive remote sensing of the atmospheric water vapour content above land surface. *Adv. Space Res.*, Vol. 18, N 7, p. 25-28.
- Baryshnikova Yu.S., Zaslavskii G.M., Lupian E.A., Moiseev S.S., Sharkov E.A. (1989a). Fractal dimensionality of cloudiness IR images and turbulent atmosphere properties. *Earth Research from Space*, N1, p.17-26 (in Russian).
- Baryshnikova Yu.S., Zaslavsky G.M., Lupian E.A., Moiseev S.S., Sharkov E.A. (1989b).Fractal analysis of the pre-hurricane atmosphere from satellite data. *Adv. Space Res.*, Vol.9, N7, p.405-408.
- Basharinov A. E., Gushina I. Ya., and Zatitskii V. A. (1967). Effect of form of particles' albedo on the emissivity of scattering layer. *Radiotecnika I electronica*. (*J. Communic. Techn. Electronics – English transl.*), Vol. 12, N 2, p. 179-183.
- Basharinov A. E., Tuchkov L. T., Polyakov V. M., and Ananov N. I. (1968). Measurement of radiothermal and plasma radiation in the microwave band. Moscow, Sovetskoe radio Publ. House, 320p. (in Russian).
- Basharinov A. E. , Gurvich A. S. , Egorov S. T. (1969). The retrieval of geophysical parameters with thermal emission data by "Cosmos-243" satellite. *Doklady Acad. Nauk USSR* (Trans. of Russian Academy of Sciences / Earth Science Section- Eng. Transl.) , Vol.188 , N6, p.1273-1275.
- Basharinov A. E. , Gurvich A. S. , Egorov S. T. , Zhukov V. I., Kurskay A. A. , Malafeev D. T., Matveev D. T., Michailov A. S., and Shutko A. M. (1971). Results of observations for the thermal radioemission of the Earth's surface with data of the experiment by "Cosmos-243" satellite . *Kosmicheskie issledovaniya* (Cosmic Research – English Transl.), Vol. 9, N 2, p. 268-279.
- Basharinov A. E., Gorodezki A. K., Gurvich A. S., Egorov S. T., Kurskay A. A. , Matveev D. T., Orlov A. P. , and Shutko A. M. (1973). Brightness temperatures of Earth's surfaces at microwave and infrared bands with data of the experiment by "Cosmos-384" satellite. *Izvestya Acad. Nauk USSR. Fizika atmosphery i okeana.(Izvestiya, Atmospheric and Oceanic Physics –English Transl.)*, Vol. 9, N 2, p. 183-186.
- Basharinov A. E., Gurvich A. S., Egorov S. T. (1974). Radioemission of the Earth as a planet. Moscow, Nauka Publ., 188 pp. (in Russian).
- Basu S. and Levy B. , Eds . (1997) . Multidimensional filter banks and wavelets . Kluwer Academic Publishers, Dordrecht , 244 p.
- Bauer A. , Duterge B., and Godon M. (1986). Temperature dependence of water-vapor absorption in the wing of the 183 GHz line. *J. Quant. Spectrosc. Radiat. Transfer*, Vol. 36, N 4, p. 307-318.
- Belchansky G. I. and Alpatksy I. V. (2000) . Comparative analysis of the sea ice classification algorithms using "Okean-01" satellite data, mixture models and MLP neural networks. *Earth Research from Space* (*Earth Observ. Rem. Sens. - Engl. Transl.*). N4, p. 40-54.
- Bell R. J. (1972). Introductory Fourier transform spectroscopy. Academic Press, New York, London, 350p.
- Bendat J. S. and Piersol A. G. (1966). Random data: analysis and measurement procedures. Wiley-Interscience, N.Y., 450p.

- Beniston M. (1998) . From Turbulence to Climate. Numerical Investigations of the Atmosphere with a Hierarchy of Models. Springer, Berlin, 328p.
- Bennartz R., and Petty G. W. (2001). The sensitivity of microwave remote sensing observations of precipitation to ice particle size distributions. J. Applied Meteorology, Vol. 40, N 3, p. 345-364.
- Bespalova E. A., Melentiev V. V. , Rabinovich Y. I., Raizer V. Y., Popov A. E., , Sharkov E. A. , Shiryeva T. A., Etkin V. S. (1976a). Some results of measurements of the radioemission of soils and grounds with airborne high-sensitive radiometer at 3 cm band. Trudy GGI (Trans. of State Hydrological Institute), Issue 237, Leningrad, Hydrometeoizdat, p. 172-176 (in Russian).
- Bespalova E. A., Rabinovich Yu. I., Sharkov E. A. , Shiryeva T. A., and Etkin V. S. (1976b). Investigations of ice-forming processes with the radioemission data by air-borne instruments. Meteorologija i hidrologij (Russian Meteorology and Hydrology – English Transl.), N 2, p. 68-72.
- Bespalova E. A., Miltskii Y. A., Mirovskii V. G., Pokrovskaya I. V., Raev M. D., Sharkov E.A., Etkin V. S.(1978). Spectral characteristics of the radiothermal emission of the sea surface with oil pollution. Meteorologija i hidrologij (Russian Meteorology and Hydrology – English Transl.), N 10, p. 71-77.
- Bespalova E. A., Veselov V. M.,Glotov A. A. , Miltskii Y. A., Mirovskii V. G., Pokrovskaya I. V., Popov A. E. , Raev M. D., Sharkov E.A., Etkin V. S. (1979). Investigations of wind sea roughness's anisotropy with variability of thermal radioemission. Doklady Acad. Nauk (Trans. of Russian Academy of Sciences / Earth Science Section- Eng. Transl.) , Vol.246, N6, p.1482-1485.
- Bespalova E. A., Veselov V. M.,Gershenson V. E., Miltskii Y. A., Mirovskii V. G., Pokrovskaya I. V., Raev M. D., Trochimovskii J. G., Semin A. G., Smirnov N. K., Skachkov V. A., Khapin J. B., Chistjkov V. N., Sharkov E.A., Etkin V. S. (1982). On determination of wind speed with polarization anisotropy measurements of thermal and backscattering microwaves .Earth Research from Space. N1, p. 87-94.
- Bespalova E. A., Veselov V. M., Volyak K. I., Militskii Y. A., Mirovskii V. G., Popov A.E., Raev M. D., Sharkov E. A., Etkin V. S. (1983). Experimental detection of oil pollution on sea surface with passive-active methods of microwave remote sensing. Wodnye resursy (Water Resources - Engl. Transl.), N 1, p. 154-162.
- Beste D.C. (1978). Design of satellite constellations for optimal continuous coverage. IEEE Trans. Aerospace Electronic Systems, Vol.14, N 3, p.466-473.
- Bevilacqua R. M., Kriebel D. L., Pails T.A., Aelling C. P., Siskind D. E., Daehler M., Olivero J.J., Puliafito S. E., Hartmann G. K., Kampfer N., Berg A., and Croskey C. L. (1996). MAS measurements of the latitudinal distribution of water vapor and ozone in the mesosphere and lower thermosphere . Geophysical Research Lett., Vol. 23, N 17, p. 2317-2320.
- Bhandari R. (1985). Scattering coefficients for a multilayered sphere: analytic expressions and algorithms. Applied Optics, Vol. 24, N 13, p. 1960-1967.
- Bhattacharya C. K. , Uppal G. S. , Raina M. K. , and Dubey V. (1983). Determination of excessive absorption by atmospheric water vapour at 22,235 GHz. J. Atmospheric Terrestrial Physics, Vol. 45, N 8/9, p. 617-620.
- Bizzari B., and Spera P. (2000). The role of microwave radiometry in the CLOUDS project. In “Microwave Radiometry and Remote Sensing of the Earth’s Surface and Atmosphere”. Eds.: Pampaloni P. and Paloscia S. VSP BV , Utrecht, Boston, Koln, Tokyo , p. 493-502.
- Bizzari B., Bordi I., Bordi R., Coppo P., Desbois M., Gasiewski A., Grant N., Harries J., Kunzi K., Liberti G. L., Miao J., Mungnai A. Murray J., Rizzi R., Rose T., Slingo A., Spera P., Sutera A., Tibaldi S., Vial L. and Zimmermann P. (2000). CLOUDS – a cloud and radiation monitoring satellite. IEEE IGARSS 2000 Proceedings, Vol. II, IEEE, New York, p. 515-517.
- Blanchard D. C. , and Woodcock A. H. (1957). Bubble formation and modification in the sea and its meteorological significance. Tellus, Vol. 9, N 2, p. 145-158.

- Blanter E. M. and Shnirman M. G. (1997). Simple hierarchical systems: stability, self-organized criticality and catastrophic behavior. *Physical Review E*, Vol. 55, , N 6, p. 6397-6411.
- Blinn J. C. , Conel J. E. , and Quade J. G. Microwave emission from geological materials: observation of interference effects. *J. Geophys. Research*, Vol. 77, N23, p. 4366-4378.
- Blue M. D. (1980). Permittivity of ice and water at millimeter wavelengths. *J. Geophysical Research*, Vol. 85, N2, p. 1101-1106.
- Blume H. J. C. , Love A. W. , Van Melle M. J., and Ho W. W. (1977). Radiometric observation of sea temperature at 2,65 GHz over the Chesapeake bay. *IEEE Trans. Antennas Propagation*, Vol. 25, N 1, p. 121-128.
- Blume H. J., and Kendall B. (1982) Passive microwave measurements of temperature and salinity in coastal zones. *IEEE Trans. Geophys. Remote Sensing*, Vol. 20, N3, p. 394-404.
- Blume H., Kendall B. , and Swift C. (1978). Advanced systems requirements for ocean observations via microwave radiometers. *AIAA Paper*, N 1737, 6p.
- Bobrov P.P., and Galeev O. V. (2001). Changes of radiobrightness temperature of soils with the various humus content. *Earth Research from Space*. N 4, p. 74-80.
- Bohren C.F. and Hoffman D. R. (1983). Absorption and scattering of light by small particles. New York, Wiley , 530p.
- Boncyk W. C., Wilson W. J. , and Lambrightsen B.H. (2000). The enabling technologies of the geostationary synthetic aperture microwave sounder (GEO/SAMS). *IEEE IGARSS 2000 Proceedings*, Vol. VII, IEEE, New York, p. 3169-3171.
- Bondur V. G. and Sharkov E. A. (1982) Statistical properties of whitecaps on a rough sea. *Oceanology* , Vol. 22, N 3, p. 274-279.
- Bondur V. G. and Sharkov E. A. (1990) Statistical characteristics of linear geometric elements of foam structures on the sea surface for optical sensor data. *Sov. J. Remote Sensing*, Vol.6, N 4, p. 534-550.
- Bordonskii G. S. (1990). Thermal emission of ice cover over the fresh reservoirs. *Nauka Publ. House-Siberian Branch*, Novosibirsk, 104p. (in Russian).
- Bordonskii G. S. , Vasilkova I. B., Veselov V. M., Vorsin N.N., Militskii Y. A., Mirovskii V. G., Nikitin V. V. , Raizer V. Y., Khapin Y. B., Sharkov E. A. , and Etkin V.S. (1978). Spectral characteristics of the emissivity of foam formations. *Izvestia Acad. Nauk. Fizika atmosphery i okeana* (Izvestiya, Atmospheric and Oceanic Physics - Engl. Transl.), Vol.14, N 6, p.656-663.
- Bordonskii G. S. , Krylov S. D. , and Gurulev A. A. (2002). Estimation of fresh-water lake mineralization using thermal microwave emission of ice cover. *Earth Research from Space*. N4, p. 91-96.
- Bordonskii G. S., and Filipova T. G. (2002). The influence of the percolation on dielectric properties of frozen dispersion media. *Kondensirovannye sredy i mezhfaznye granizy* (Condensed media and inter-phasic boundaries) . Vol.4, N 1, p. 21-26 (in Russian).
- Borges A., Solana A., Plaza M. A., Sanz J. A., and Garcia Q. (2000). The MIRAS demonstrator pilot project. *IEEE IGARSS 2000 Proceedings*, Vol. VI, IEEE, New York, p. 2972-2974.
- Born M. and Wolf E. (1999). Principles of optics: electromagnetic theory of propagation, interference and diffraction of light. Seventh Edition. Cambridge U. P. , New York, 952p.
- Bouman C. and Newell A. C. (1998) . Natural patterns and wavelets. *Review of Modern Physica*, Vol. 70, N 1, p. 289-301.
- Boyarskii D. A. (1995). Passive microwave observation of snow and frozen soil at 3,95 GHz. *IEEE IGARSS 1995 Proceedings*, Vol. I, IEEE, New York, p. 383-385.
- Boyarskii D. A., Dmitriev V. V., Kleoorin N. I., Mirovskij V. G. and Etkin V. S. (1993). Theoretical and experimental studies of snow covers microwave emissivity. *J. Electromagnetic Waves and Applications*, Vol. 7, N 7, p. 959-970.

- Boyarskii D. A., Tikhonov V. V. , Kleorin N. I., Mirovskij V. G. (1994). Inclusion of scattering losses in the models of the effective permittivity of dielectric mixtures and applications to wet snow. *J. Electromagnetic Waves and Applications*, Vol. 8, N 11, p.1395-1410.
- Boyarskii D. A., and Tikhonov V. V. (2000). The influence of stratigraphy on microwave radiation from natural snow cover . *J. Electromagnetic Waves and Applications*, Vol. 14, p.1395-1410.
- Boyarskii D. A., Tikhonov V. V., and Komarova N. Yu. (2001). Model of dielectric constant of bound water for applications of microwave remote sensing . *Progress in Electromagnetics Research*, Vol. 35, p. 251-270.
- Bracewell R. N. and Roberts J. A. (1954) . Aerial smoothing in radioastronomy. *Aust. J. Phys.*, Vol. 7, N12, p. 615-640.
- Bradshow A. L. , and Schleicher K. E. (1980). Electrical conductivity of seawater. *IEEE J. Ocean. Eng.* , Vol. 5, N1, p. 50-61.
- Brekhovskikh L. M. (1957). Waves in layer mediums. Moscow, Publ. USSR Acad. Sciences, 502 p.
- Broglie L. de (1941). Problemes de propagations guidees des ondes electromagnetiques. Paris, Gauthier-Villars, 114p.
- Brown L. (1999). A radar history of World War II: technical and military imperatives. IOP, Philadelphie, 563p.
- Bruzzi S. (1995). The Envisat mission in the context of present and future Earth observation programs of the European Space Agency. *EARSeL Newsletter*, N 24, p.2-12
- Brindly J., Kapitaniak T., Barcilon A. (1992). Chaos and noisy periodicity in forced ocean-atmosphere models. *Physics Lett. A.*, Vol.167, N2, p.179-184.
- Bryant E. (1993). Natural Hazards. Cambridge University Press , Cambridge. 294 pp.
- Bujakos V. I. , Gvamichava A. S., Gorshkov L. A. et al. (1978). Space-borne radiotelescope increased without bounds. *Kosmicheskie issledovania* (Space Researches – English Transl.) , Vol. 16, N 6, p. 924-936.
- Bulatov M. G. , Sharkov E. A. , and Cherny I.V. (1980). On the interference of noisy signals with the arbitrary form of spectra. *Radiotekhnika i elektronika* (J. of Communic. Techn. Electronics - Engl. Transl.), Vol. 25, N 3, p. 552-559.
- Bunimovich V. I. (1951). Fluctuational processes in radioreceivers. "Sovetskoe radio" Publ. House, Moskow, 361p. (in Russian).
- Burdette E., Coin F., and Seols J. (1980). Invivo probe measurement technique for determining dielectric properties at VHE through microwave frequence. *IEEE Trans. MTT*, Vol. 28, N4, p. 414-427.
- Burgel van J.L., Le Marshall J., Lynch M.J. Upper temperature anomalies near Australian tropical cyclones using satellite microwave data. «Proceedings of the PORSEC'94. Melbourne, Australia. March 1-4, 1994.» Ed. by J. Le Marschall and J.D. Lasper. Melbourne, p.219-225.
- Burke E. J. and Simmonds L. P. (2001). Passive microwave emission from smooth bare soils: developing a simple model to predict near surface water content. *Intern. J. Remote Sensing*, Vol. 22, N 18, p. 3747-3761.
- Burroughs S. M. , and Tebbens S. F. (2001). Upper-truncated power laws in natural systems. *Pure Applied Geophysics*, Vol. 158, N 4, p. 741-757.
- Cahalan R. F. (1989). Overview of fractal clouds. In "Advances in remote sensing retrival methods", Ed. by Deepak A., Fleming H. E. , and Theon J. S. A. Deepak , Hampton, Va., p. 371-389.
- Callen H. B. and Welton T.A. (1951). Irreversibility and generalized noise. *Phys. Rev.*, Vol. 83, N 1, p. 34-41.
- Callen H. B. and Green R. F. (1952). On a theorem of irreversible thermodynamics, I. *Phys. Rev.*, Vol. 86, N 5, p. 704-710.
- Calvet J. C., Wigneron J. P., Chanzy A., Haboudane D. (1995). Retrieval of surface parameters from microwave radiometry over open canopies at high frequencies . *Remote Sensing Environ.*, Vol. 53, N 1, p. 46-60.

- Calvet J.C., Chanzy A., Wigneron J.P. (1996). Surface temperature and soil moisture retrieval in the Sahel from airborne multifrequency microwave radiometry. IEEE Trans. Geoscience Remote Sensing , Vol. 34, N 2, p. 588-600.
- Campbell B. A. , and Shepard M. K. (1996). Lava flow surface roughness and depolarized radar scattering. J. Geophysical Research, Vol. 101, N E8, p. 18,941-18,951.
- Card M., Kruszewskii E., and Guanstaferro A. (1978). Technology assessment and outlook. Astronautics and Aeronautics, Vol. 16, N 10, p. 48-54.
- Carvalho L. M. T. , Fonseca L. M. G., Murtagh F., and Clevers J. G. P. W. (2001). Digital change detection with the aid of multiresolution wavelet analysis. Int. J. Remote Sensing, Vol. 22, N 18, p. 3871-3876.
- Carver K. R., Elachi C.,and Ulaby F. T (1985). Microwave remote sensing from space. Proc. IEEE, Vol. 73, N 6, p. 970-996.
- Chandrasekhar S. (1960). Radiative transfer . Dover Publications, New York, 393 p.
- Chang A. T. C. and Chiu L. S. (1997) . Uncertainty in satellite rainfall estimates : time series comparison. Adv. Space Res., Vol. 19, N 3, p. 469-472.
- Chang D.-H., and Islam S. (2000). Estimation of soil physical properties using remote sensing and artificial neural network. Remote Sensing Environment, Vol. 74, p. 534-544.
- Chauhan N. S. (2002). Soil moisture inversion at L-band using a dual-polarization technique: a model-based sensitivity analysis. Int. J. Remote Sensing, Vol. 23, N 16, p. 3209-3227.
- Chen D., Engman E. T. , and W. Brutsaert (1997). Spatial distribution and pattern persistence of surface soil moisture and temperature over prairie from remote sensing . Remote Sens. Environment, Vol. 61, N 5, p. 347-360.
- Chen G., and Dong X. (1996). From chaos to order. Perspectives and methodologies. World Scientific, Singapore etc., 300 p.
- Cherny I. V. and Sharkov E. A. (1988). Remote radiometry of the sea wave breaking cycle. Earth Research from Space (Earth Obs. Remote Sensing - Engl. Transl.), N2, p. 17-28.
- Cherny I. V. and Sharkov E. A. (1991 a). Electrodynamics of discrete dispersive concentrated media with absorbing scattering particles . Preprint N Pr-1753, Space Research Institute, Moscow, 40 p. (in Russian).
- Cherny I. V. and Sharkov E. A. (1991 b). Characteristics of backscattering of electromagnetic waves by concentrated aerodispersive media . Pisma v Zhurnal Tech. Fiziki. (Technical Physics Letters - Eng. transl.) , Vol. 17, N 3, p. 73-77 .
- Cherny I. V. and Raizer V. Yu. (1998) . Passive microwave remote sensing of oceans. John Wiley and Sons/ PRAXIS , Chichester , New York etc. - 195 p.
- Cherny I. V. and Chernyavsky G. M. (2001). Combined optical-microwave imager/sounder MTVZA-OK . IEEE IGARSS 2001 Proceedings, Vol. V , IEEE, New York, p. 2016-2018.
- Chew W. C., Friedrich J. A. , and Geiger R. (1990). A multiple scattering solution for the effective permittivity of a sphere mixture. IEEE Trans Geosci. Remote Sensing, Vol. 28, p. 207-214.
- Choudhury J. R. (1987). Estimate of primary productivity over the thar Desert based upon Nimbus-7 37 GHz data: 1979-1985. Int. J. Remote Sensing, Vol. 8, N 12, p. 1885-1890.
- Christensen J. H., Smith A., Reed R., and Elmore K. (1966). Dielectric properties of phosphoric acid solutions at 25°C. J. Chemical Engineering Data ,Vol. 11, N 4, p. 60-63.
- Chuah H. T., Tan H. S. (1989) . A Monte Carlo method for radar backscatter from a half-space random medium. IEEE Trans. Geosci. Remote Sensing, Vol. 27, N 1, p. 86-93.
- Chui Ch. K. (1992). An introduction to wavelets. Academic Press, New York, 266pp.
- Chukhrai G. I. and Shutko A. M. (1978). Experimental evidences of the microwave emission-salinity relations . Doklady Acad. Nauk (Trans. of Russian Academy of Sciences / Earth Science Section- Eng. Transl.) , Vol.239, N6, p.1313-1315.

- Cimini D., Shaw J. A., Westwater E. R., Han Y., Irisov V., Leuski V. and Churnside J. H. (2003). Air temperature profile and air/sea temperature difference measurements by infrared and microwave scanning radiometers. *Radio Science*, Vol. 38, N3, 8045, doi:10.1029/2002RS002632.
- Ciotti P., Westwater E. R. , Decker M. T., Bedard A. J. , and Stankov B. B. (1987). Ground-based microwave radiometric observations of the temporal variation of atmospheric geopotential height and thickness. *IEEE Trans. Geosci. Remote Sensing*, Vol. 25, N 5, p. 600-615.
- Cole K.S. and Cole R. H. (1941). Dispersion and absorption in dielectric. I. Alternating currents characteristics. *J. Chem. Phys.*, Vol. 9, N 4, p. 341-351.
- Colton M. C. , and Poe G.A. (1999). Intersensor calibration of DMSP SSM/I's: F-8 to F-14, 1987-1997. *IEEE Trans. Geoscience Remote Sensing*, Vol. 37, N 1, p. 418-439.
- Comiso J. C. (2000). Variability and trends in Antarctic surface temperatures from in situ and satellite infrared measurements. *J. Climate*, Vol. 13, N 10, p. 1674-1696.
- Comiso J. C. , and Kwok R. (1996). Surface and radiative characteristics of the summer Arctic sea ice from multisensor satellite observations. *J. Geophysical Research*, vol. 101, N C12, p. 28,397-28,416.
- Comiso J. C., and Stock L. V. (2000). Interannual variability of Arctic summer characteristics using satellite observations. *IEEE IGARSS 2000 Proceedings*, Vol. III, IEEE, New York, p. 1329-1333.
- Connor L. N. , and Chang P. S. (2000). Determination of ocean surface wind speeds from the TRMM microwave imager. In "Microwave Radiometry and Remote Sensing of the Earth's Surface and Atmosphere". Eds.: Pampaloni P. and Paloscia S., VSP BV, Utrecht, Boston, Koln, Tokyo , p. 21-27.
- Conwell P.R., Barber P. W. , and Rushforth C. K. (1984). Resonant spectra of dielectric spheres. *J. Opt. Soc. Am. A*, Vol. 1, N1. p. 62-67.
- Cox C. and Munk W. (1954). Measurement of the roughness of the sea surface from photographs of the Sun's glitter. *Journal of the Optical Society of America*. Vol. 44, N 11, p. 838-850.
- Cressie N. A. C. (1993). Statistics for spatial data. John Wiley and Sons, New York, 900 p.
- Danilov Yu. , Kuleshov Yu. , and Rudakov V. (1979). The first space-borne radioteleskop . Nauka i zhizn' (Science and life), N11, p. 2-6 (in Russian).
- Danson F. M. and Plummer S. E. , Eds. (1995). Advances in environmental remote sensing. Chichester : John Wiley and Sons, 184 p.
- Davenport W. B. , and Root W. L. (1958). Random signals and noise. McGraw-Hill, N. Y., 460p.
- Davidson D. W. and Cole R. H. (1950). Dielectric relaxation in glicirine. *J. Chem. Phys.*, Vol. 18, N 10, p. 1417-1418.
- Davis A., Marshak A., Wiscombe W., and Cahalan R.(1994). Multifractal characterizations of nonstationary and intermittency in geophysical fields: observed, retrieved, or simulated. *J. Geophysical Research*, Vol. 99, N D4, p. 8055-8072.
- Davis A., Marshak A., Wiscombe W., and Cahalan R.(1996). Multifractal characterizations of intermittency in nonstationary geophysical signals and fields. A model-based perspective on ergodicity issues illustrated with cloud data. In "Current topics in nonstationary analysis", Ed. by Trevino G., Hardin J., Douglas B., and Andreas E. World-Scientific , Singapore, p. 97-158.
- Davis D. T., Chaen Z., Tsang L., Hwang J. N., and Cang A. T. C. (1993). Retrieval of snow parameters by iterative inversion of a neural network. *IEEE Trans. Geoscience Remote Sensing* , Vol. 31, N 4, p. 842-851.
- Debye P. (1929). Polar molecules. New York, The Chemical Catalog Company,Inc., 172pp.
- Deeter M. N. , and Evans K. F. (2000). A novel ice-cloud retrieval algorithm based on the millimeter-wave imaging radiometer (MIR) 150- and 250-GHz channels. *J Applied Meteorology*, Vol. 39, N 5 , p. 623-633.
- Deirmendjian D. (1969). Electromagnetic scattering on spherical polydispersions. American Elsevier Publishing Company, New York, 290pp.

- Demyanov A. A. , Semenov M. G. , and Tatarin V. A. (1974). Measurements of the complex dielectric properties of strong-absorptive fluids. *Pribory i technika experimenta* (Instruments and Experimental Techniques- English transl.), N 3, p. 132-133.
- Derksen C. and LeDrew E. (2000). Assessing the impact of melt and refreeze on SSM/I derived North American prairie snow water equivalent. *IEEE IGARSS 2000 Proceedings*, Vol. II, IEEE, New York, p. 454-456.
- Derksen C., LeDrew E., and Goodison B. (2000a). Temporal and spatial variability of North American prairie snow cover (1988 to 1995) inferred from passive microwave- derived snow water equivalent imagery. *Water Resources Res.*, Vol. 36, N 1, p. 255-266.
- Derksen C., LeDrew E., Walker A. and Goodison B. (2000b). The influence of sensor overpass time on passive microwave-derived snow cover parameters. *Rem. Sens. Env.*, Vol. 71, N 3 ,p. 297-308.
- Desbois M. (1995). TROPIQUES, a small satellite for studying water and energy cycles in the intertropical band, and atmosphere-ocean interactions. COSPAR Colloquium «Space Remote Sensing of Subtropical Oceans». Taipei, Taiwan, p.1-15A4-1-15A4-5.
- Desbois M. (1999). Megha-tropiques: Scientific objectives and general mission requirements. In *Megha-Tropiques*. First Science Workshop Proceedings, 19-22 May, 1999, ISRO H.Q., Bangalore, INDIA. Eds. Narayanan M. S., Manikam B., Gairola R. M. ISRO, CNES, p. 1.1-1.7.
- Diaz H. F. and Margraf V. ,Eds. (1993). El Nino : historical and paleoclimatic aspects of the Southern Oscillation. Cambridge Univ. Press, Cambridge, 490 p.
- Dobson M. C. and Ulaby F. T. (1986) Active microwave soil moisture research. *IEEE Trans. Geoscience Remote Sensing*. Vol. 24, N 1, p. 23-26.
- Dong X., Wu J., Zhu Y., Sun B., and Jiang J. (2000a). The design and implementation of CAS C-band interferometric synthetic radiometer. *IEEE IGARSS 2000 Proceedings*, Vol. II, IEEE, New York, p. 866-868.
- Doviak R. J. and Zrnic' D. S. (1984). Doppler radar and weather observation. Academic Press, Inc., Orlando, FL, 458 p.
- Doviak R. J. and Lee J. T. (1985). Radar for storm forecasting and weather hazard warning. *J. Aircraft* , Vol. 22, N12, p. 1059-1064.
- Droppleman J. D. (1970). Apparent microwave emissivity of sea foam. *J. Geophysical Research*, Vol. 75, N 3, p. 696-698.
- Droppleman J. D. , Mennella R. A., and Evans D. E. (1970) . An airborne measurement of the salinity variations of the Mississippi river outflow. *J. Geophysical Research*, Vol. 75, N 30, p. 5909-5913.
- Drusch M., Wood E. F., and Simmer C. (1999a). Up-scaling effects in passive microwave remote sensing : ESTAR 1.4 GHz measurements during SGP'97. *Geophysical Res. Letters*, Vol. 26, N 7, p. 879-882.
- Drusch M., Wood E. F. , and Lindau R. (1999b). The impact of the SSM/I antenna gain function on land surface parameter retrieval. *Geophysical Research Letters*, Vol. 26, 26, N 23, p. 3481-3484.
- Dubois J. (1998) Non-linear dynamics in geophysics. John Wiley and Sons/PRAXIS. Chichester, New York, etc., 261 p.
- Dubrovin B. A., Novikov S. P. , Fomenko A. T. (1986). Modern geometry. Methods and applications. Moscow, "Nauka" Publishing House, 758p. (in Russian).
- Dzens-Litovskii A. I. (1967) . Kara - Bogaz- Gol bay. "Nedra" Publ. House, Leningrad, 95p. (in Russian).
- Ellison W. , Balana A., Delbos G., Lamkaouchi K., Eymard L., Guillou C. , and Prigent C. (1998). New permittivity measurements of seawater. *Radio Science* , Vol. 33, N3, p. 639-648.
- England A. W. (1974). Thermal microwave emission from a halfspace containing scatterers . *Radio Science*, Vol.9, N 4, p. 447-454.
- England A. W. (1975). Thermal microwave emission from a scattering layer. *J. Geophysical Research*, Vol.80, N 12, p. 4484-4496.

- English S. J. (1995). Airborne radiometric observations of cloud liquid-water emission at 89 and 157 GHz : application to retrieval of liquid-water path. Quart. J. Roy. Meteor. Soc., Vol. 121, N 527, p. 1501-1524.
- English S. J. (1999). Estimation of temperature and humidity profile information from microwave radiances over different surface types. J. Applied Meteorology, Vol. 38, N10, p. 1526-1541.
- English S. J. , Eyre J. R. , and Smith J. A. (1999). A cloud-detection scheme for use with satellite sounding radiances in the context of data assimilation for numerical weather prediction. Quart. J. Roy. Meteor. Soc., Vol. 125, N 559, p. 2359-2378.
- Engman E. T. (1997). Soil moisture, the hydrologic interface between surface and ground waters. Remote Sensing and Geographic Information Systems for Design and Operation of Water Resources Systems. IAHS Publ. N 242, p. 129-140.
- Ermakov V. I., Levin V.V., Sherbakov V. V. , and Khubezov S. B. (1975). On the problem of the nature of the dielectric permittivity for electrolyte solutions. Zhurnal Fizicheskoi Khimii (Journal of Phys. Chemistry-English transl.), Vol. 49, N 7, p. 1749-1752 .
- Ermakov D. M. , and Smirnov M. T. (2001). Problems of superposition of satellite optical and microwave sensors data for their complex analysis. Earth Research from Space (Earth Obs. Remote Sensing - Engl. transl.). N 2, p. 45-54.
- ESA (1996a). Atmospheric Dynamic Mission. ESA SP-1196(4), ESA, Noordwijk, 70 p.
- ESA (1996 b).Atmospheric Profiling Mission. ESA SP-1196(7), ESA, Noordwijk, 58 p.
- ESA (1996c). Precipitation Mission. ESA SP-1196(8), ESA, Noordwijk, 82p.
- ESA (1997) . METESAT collection. The Weather Machine .N 4. ESA SR-1213, ESA, Noordwijk , CD ROM.
- Esepkina N. A. , Korolkov D. V. , and Pariiskii Yu. N. (1973). Radiotelescopes and radiometers . "Nauka" Publ. House, Moscow , 250 p. (in Russian).
- Esepkina N. A., Kruglov S. K., Masyrev M. M. , Molodyakov S. A., and Saenko I. I. (1997). Acousto-optic spectrum polarimeter for investigations of solar radio emission. Preprint N 122 SPb, Special Astrophysical Observatory, St Peterburg, 14p. (in Russian).
- Esepkina N. A., Zinchenko I. I., Saenko I. I. , Antyufeev A. V. , Vdovin V. F. , Eliseev A. I. , Kruglov S. K. , Lapkin I. V. , Myshenko V. V. , Nesterov N. S., Pirogov L. E., Shanin V. N., Shtanyuk A. M., and Shul'ga V. M. (2000). Spectroscopic observations in the 3-mm wavelength range at RT-22 CRAO using acousto-optical spectrum analyzer. Izvestia VUZ. Radiofizika. (Izvestiya , Radiophysics and Quantum Electronics - Engl. Transl.), Vol. 43, N 11, p. 935-941.
- Etkin V. S. , Vorsin N. N. , Kravtsov Yu. A. , Mirovskii V. G. , Nikitin V. V. , Popov A.E., and Troizkii I. A. (1978). The discovery of critical effects in the thermal radiation of a periodically uneven water surface. Izvestia VUZ. Radiofizika. (Izvestiya , Radiophysics and Quantum Electronics - Engl. Transl.), Vol. 21, N 3, p. 454-456.
- Evans D. D. (1973). Mathematical models for the reflection coefficients of dielectric half-spaces. Radio Science, Vol. 8, N 12, p. 1083-1092.
- Eymard L. (1999). Atmosphere and sea surface properties from microwave radiometry. Megha-Tropiques. First Science Workshop Proceedings,19-22 May, 1999, ISRO H.Q., Bangalore, INDIA. Eds. Narayanan M. S., Manikam B., Gairola R. M. ISRO, CNES, p. 19.1-19.16.
- Feder T. (2000). Radio astronomers plan mammoth telescope. Physics Today. Vol. 53, N 10, p. 70-71.
- Feller W. (1971). An introduction to probability theory and its applications. Vol. II. John Wiley and Sons, N. Y. , 478p.
- Ferraro R. R., Weng F., Grody N. C., Basist A. (1996). An eight-year (1987-1994) time series of rainfall, clouds, water vapour, snow and sea ice derived from SSM/I measurements. Bull. Amer. Meteor. Soc., Vol. 77, p. 891-905.

- Ferrazzoli P. and Guerrier L. (1996) . Passive microwave remote sensing of forests: a model investigation. IEEE Trans. Geosci. Remote Sensing. Vol. 34, N 2, p. 433-443.
- Ferrazzoli P., Wigneron J.-P., Guerrier L., and Chanzy A. (2000). Multifrequency emission of wheat: modeling and applications. IEEE Trans. Geosci. Remote Sensing. Vol. 38, N 6, p. 2598-2607.
- Finkelstein M. I., and Mendelson V. L. (1980). Correlation between energetic coefficients of the reflection and transmission of the electromagnetic waves on the boundary of two absorptive media . Radiotekhnika i elektronika (J. of Communic. Techn. Electronics - Engl. Transl.), Vol. 25, N 7, p. 1524-1526.
- Flaming M. (2000). The conical microwave imager sounder. The Earth Observer, Vol. 132, N3, p. 18-21.
- Foster J. L. , Hall D. K. , Chang A. T. C. , Rango A., Wergin W., and Erbe E. (1999). Effects of snow crystal shape on the scattering of passive microwave radiation. IEEE Trans. Geoscience Remote Sensing, Vol. 37, N 2, p. 1165-1168.
- Foster J. L., Barton J. S., Chang A. T. C., and Hall D. K. (2000).Snow crystal orientation effects on the scattering of passive microwave radiation. IEEE Trans. Geosci. Remote Sensing. Vol. 38, N 5, Part 2, p. 2430-2434.
- Franceschetti G., Migliaccio M., and Riccio D. (1996). An electromagnetic fractal-based model for the study of fading. Radio Science, Vol. 31, N 6, p. 1749-1759.
- Franceschetti G., Iodice A., Migliaccio M., and Riccio D. (1999a). Fractals and the small perturbation scattering model. Radio Science, Vol. 34, N 5, p. 1043-1054.
- Franceschetti G., Iodice A., Migliaccio M., and Riccio D. (1999b). Scattering from natural rough surfaces modeled by fractional Brownian motion two-dimensional processes. IEEE Trans. Antennas Propag. , Vol. 47, N 9, p. 1405-1415.
- Frenkel Ya. I. (1975). Kinetic theory of liquids. Leningrad, Nauka Publ. House , 592p.
- Frick P., Beck R., Berkhuijsen E., Patrikeyev I. (2001).Scaling and correlation analysis of galactic images. Monthly Notices Royal Astron. Soc., Vol.327, N4, p.1145-1157.
- Frisch U. (1995) . Turbulence: the legacy of A. N. Kolmogorov . Cambridge University Press, Cambridge , 350 p.
- Fujita S., Matsuoka T., Ishida T., Matsuoka K. , and Mae S. (2000). A summary of the complex dielectric permittivity of ice in the mehahertz range and its applications for radar sounding of polar ice sheets. In “Physics of ice core records”. Ed. by T. Hondoh. Hokkaido University Press, Sopro, pp. 185-212.
- Fung A. K. , and Chen M. F (1981). Emission from an inhomogeneous layer irregular interfaces. Radio Science, Vol. 16, N 3, p. 289-298.
- Fung A. K. , and Eom H. J. (1981). Note on the Kirchhoff rough surface solution in backscattering. Radio Science , Vol. 16, N 3, p. 299-302.
- Fung A. K., and Eom H. J. (1985). A study of backscattering and emission from closely packed inhomogeneous media. IEEE Trans. Geosci. Remote Sensing, Vol. 23, N 5, p. 761-767.
- Gaikovich K. P. , Reznik A. N., Sumin M. I., and Troizkii R. V. (1987) Determination of the temperature profile of water surface layer with its emission at microwave range. Izvestya AN . Fizika atmosphery i okeana. (Izvestiya, Atmospheric and Oceanic Physics –English Transl.), Vol. 23, N 7, p. 761-768.
- Gairola R. M. (1999). Rainfall and other ocean parameters from SSM/I, TRMM and TOPEX/Poseidon. Megha-Tropiques. First Science Workshop Proceedings,19-22 May, 1999, ISRO H.Q., Bangalore, INDIA. Eds. Narayanan M. S., Manikam B., Gairola R. M. ISRO, CNES, p. 16.1-16.21.
- Gasiewski A. J. , and Johnson J. T. (1993). Statistical temperature profile retrievals in clear-air using passive 118-GHz observations. IEEE Trans. Geoscience Remote Sensing , Vol. 31, N 1, p. 106-115.
- Gaspard P. (1997) . Chaos and hydrodynamics . Physica A, Vol. 240, N 1-2, p. 54-67.
- Ghanem R. , and Romeo F. (2001). A wavelet-based approach for model and parameter identification of non-linear systems. Int. J. Non-Linear Mechanics, Vol. 36, N 5, p. 835-859.

- Ghil M., Bensi R., Parisi G., Eds (1985). Turbulence and predictability in geophysical fluids dynamics and climate dynamics. North-Holland, Amsterdam, 205 p.
- Glantz M. , Katz R. and Nicholls N., Eds. (1991). Teleconnections linking worldwide climate anomalies. Cambridge Univ. Press, Cambridge , 545 p.
- Glass L. and Mackey M. C. (1988). From clocks to chaos. The rhythms of life. Princeton University Press. Princeton, 248 p.
- Glazman R. E.(1991). Statistical problems of wind-generated gravity waves arising in microwave remote sensing of surface winds. IEEE Trans. Geosci. Rem. Sens. ,Vol. 29, N 1, p. 135-142.
- Glazman R. E. and Weichman P. B. (1989). Statistical geometry of a small surface patch in a developed sea. J. Geophysical Research, Vol. 94, N C4, p. 4998-5010.
- Glazman R. E. and Weichman P. B. (1990). Reply. J. Geophysical Research, Vol. 95, N C2, p. 1771-1773.
- Gloersen P., Wilheit T.T., Chang T. C., Nordberg W. and Campbell W. J. (1974). Microwave maps of the polar ice of the Earth. Bull. Amer. Meteor. Soc., Vol. 55, N 12, p. 1442-1448.
- Gopal S. , Woodcock C. (1996). Remote sensing of forest change using artificial neural networks . IEEE Trans. Geosci. Remote Sensing. Vol. 34, N 2, p. 398-404.
- Gorelik A. G. , Raikova L. S. , and Frolov Y. A. (1975). Microwave radiometric methods for water vapour measurements in the lower troposphere. Meteorologia i hydrologia (Russian Meteorology and Hydrology- English transl.), N 5, p. 106-112.
- Gloersen P. (1984). Sea surface temperatures from Nimbus 7 SMMR radiances. J. Climate Applied Meteorology, Vol. 23, N 2,p. 336-340.
- Glotov A. A. , Matveev D. G., Mirovskij B. G., Raev M. d. , Raizer V. Y. ,Troitzkij I. A., Sharkov E. A. , and Etkin V. S. (1975). On the investigation of the thermal emission of the water surface with oil film. Meteorologia i hydrologia (Russian Meteorology and Hydrology – Engl. transl.), N 6, p. 90-93.
- Goodberlet M. A. , Swift C. T. , and Wilkerson J. C. (1989). Remote sensing of ocean surface winds with the special sensor microwave/imager. J. Geophysical Research, Vol. 94, N C10, p. 14,547-14,555.
- Goutoule J. M., and de Boer F. (2000). Large interferometer antenna synthesized by satellites in formation for Earth remote sensing. IEEE IGARSS 2000 Proceedings, Vol. II, IEEE, New York, p. 869-870.
- Gradshteyn I. S. and Ryzhik I. M. (2000). Tables of Integrals , Series, and Products. Sixth Edition. Edited by A. Jeffrey and D. Zwillinger. Academic Press, Orlando, Florida. 1163 p.
- Grankov A. G. , Mil'shin A. A. and Cherny I. V. (2000). Results of simulation of measurements from the Meteor-3M radiometer MTVZA and their validation with the data of DMSP SSM/I measurements in the North Atlantic . Earth Research from Space (Earth Obs. Remote Sensing - Engl. Transl.). N 4. ,p. 20-27.
- Grant E. , Buchman T. , and Cook H. (1957).Dielectric behavior of water at microwave frequencies. J. Chem. Phys. , Vol. 26, N1., p. 156-161.
- Grant E. , and Shack R. (1967). Complex permittivity measurement at 8,6 mm wavelength over temperature range 1-60° C. J. Appl. Phys., Vol. 18, N 12, p. 1807-1814.
- Greving M. , Ed. (2000). Annual report. Institut de Radio Astronomie Millimetrique, Domaine Universitaire de Grenoble, France. 76p.
- Grimm R. E. (2002). Low-frequency electromagnetic exploration for groundwater on Mars. J. Geophysical Research, Vol. 107, N E2, p.1-1 – 1-29.
- Grody N. C. (1988). Surface identification using satellite microwave radiometers. IEEE Trans. Geosci. Remote Sensing., Vol. 26, N 6, p. 850-859.
- Grody N. C. , and Pellegrino P. P. (1977). Synoptic-scale studies using the Nimbus 6 scanning microwave spectrometer. J. Applied Meteorology, Vol. 16, 8, p. 816-826.
- Guillou C., English S. J., Prigent C. and Jones D. C. (1996). Passive microwave airborne measurements of the sea surface response at 89 and 157 GHz. J. Geophysical Research, Vol. 101, N C2, p. 3775-3788.

- Guissard A. , and Sobieski P. (1987). An approximate model for the microwave brightness temperature of the sea. *Int. J. Remote Sensing*, Vol. 8, N 11, p. 1607-1627.
- Gurvich A. S. and Yurefiev V. N. (1970). Using ocean's thermal emission for the correction of the spaceboard microwave radiometer's sensibility. *Izvestya Acad. Nauk USSR . Fizika atmosphery i okeana*. (*Izvestiya, Atmospheric and Oceanic Physics –English Transl.*), Vol. 6, N 6, p. 523-527.
- Gurvich A. S., Kalinin V. I. and Matveev D. H. (1973). Influence of the internal structure of glaciers on their thermal radioemission. *Izvestya Acad. Nauk USSR . Fizika atmosphery i okeana*. (*Izvestiya, Atmospheric and Oceanic Physics –English Transl.*), Vol. 9, N 12, p. 713- 718 .
- Haken H. (1978). Synergetics, an introduction, 2nd ed., Vol. 1, Springer, Berlin-Heideberg-New York, 420.
- Hallikainen M. T., Ulaby F. T., and Abdelrazik M. (1986). Dielectric properties of snow in the 3 to 37 GHz range. *IEEE Trans. Antennas Propagation*, Vol. 34, N 11, p. 1329-1339.
- Haroules G. G. and Brown W. E. (1968). Radiometric measurement of attenuation and emission by the Earth's atmosphere at wavelengths from 4cm to 8mm. *IEEE Trans. Microwave Theory Techniques*, N9, p. 611- 621.
- Harris F. E. , and O'Konski C. T. (1957). Dielectric properties of aqueous ionic solution at microwave frequencies. *J. Phys. Chem.*, Vol. 61, N 3, p. 310-319.
- Hartmann G. K., Bevilacqua R. M., Schwartz P. R., Kampfer N., Kunzi K. F., Aellig C. P., Rerg A., Boogaerts W., Connor B. J., Crosskey C. L., Daehler M., Degenhardt W., Dicken H. D., Goldiezen D., Kriebel D., Langen J., Loidl A., Olivero J.J., Pauls T. A., Puliafito S. E., Richards M. L., Rudin C., Tsou J.J., Waltman W. B., Umluft G., and Zwick R. (1996). Measurements of O₃, H₂O and ClO in the middle atmosphere using the millimeter-wave atmospheric sounder (MAS). *Geophysical Research Lett.*, Vol. 23, N 17, p. 2313-2316.
- Harvey B. (1995). The new Russian Space Program. Chichester etc. : Wiley/PRAxis, 400p.
- Harujama Y. (1994). Progress of Japan's earth observation satellites. *Adv. Space Research*, Vol.14, N 1, p. 21-24.
- Hasted J. B. (1961). The dielectric properties of water. *Progress in dielectrics*. Vol. 3, p. 101-149.
- Hasted J. B. (1972). Liquid water: dielectric properties. In "Water. A comprehensive treatise.", Ed. by F. Franks . New York, Vol. 1, p. 255-309.
- Hasted J., Ritson D., and Collie C. (1948). Dielectric properties of aqueous ionic solutions. *J. Chem. Phys.* , Vol. 16, N 1, p. 1-11.
- Hasted J. B. and ElSabeh S. (1953). The dielectric properties of water in solution. *Trans. Faraday Soc.*, Vol. 49, Pt. 9, p. 1003-1011.
- Hasted J. B., and Roderick G. (1958). Dielectric properties of aqueous and alcohol electrolyte solutions. *J. Chem. Phys.*, Vol. 29, N 1, p. 17-26.
- Hasted J. B. , and Shahidi M. (1976). The low frequency dielectric constant of supercooled water. *Nature*. Vol.262. N 5571. P. 777-778.
- Havlin S. (1999). Scaling in nature: from DNA through heartbeats to weather. *Physica A*, Vol. 273, N 1-2, p. 46-69.
- Havriliak S. and Negami S. (1967) A complex plane representation of dielectric and mechanical relaxation process in some polymers. *Polimer*, Vol. 8, N 4, p. 161-310.
- Henley C. L. (1993). Statistics of a "self-organized" percolation model . *Physical Review Letters*, Vol. 71, N 17, p. 2741-2744.
- Hergarten S., and Neugebauer H. J. (1998). Self-organized criticality in a landslide model. *Geophys. Research Letters*, Vol. 25, N 6, p. 801-804.
- Ho W. and Hall W. F. (1973). Measurement of the dielectric properties of seawater and NaCl solution at 2,65 GHz. *J. Geophys. Research*, Vol. 78, N 27, p. 6301-6315.
- Holdom B. (1998). From turbulence to financial time series . *Physica A*, Vol. 254, N 3-4, p. 569-576.
- Holliger J. P. (1971). Passive microwave measurements of sea surface roughness. *IEEE Trans. Geoscience Electronics*, Vol. 9, N 3, p. 165-169.

- Holmes J. J., Balanis C. A., and Truman W. M. (1975). Application of Fourier transformations for microwave radiometric inversion.IEEE Trans. Antennas Propagation, Vol. 23, N 6, p. 797-806.
- Holton J. R., Haynes P. H., McIntyre M. E., Douglass A. R. , Rood R. B., Pfister L. (1995).Stratosphere-troposphere exchange. Rev. Geophys., Vol. 33, p. 403-439.
- Hong Y., Kummerow C. D., and Olson W. S. (1999). Separation of convective and stratiform precipitation using microwave brightness temperature. J. Applied Meteorology, Vol. 38, N8, p. 1195-1213.
- Hong Y. , Haferman J. L. , Olson W. S. , and Kummerow C. D. (2000). Microwave brightness temperatures from tilted convective systems.J. Applied Meteorology, Vol. 39, N 7, p. 983-998.
- Horn R. A. (1969) . Marine chemistry.The structure of water and tha chemistry of the hydrosphere. New York, London, Sydney, Toronto, Wiley-Interscience, 398p.
- Hoskins B. and Pearce R. , Eds. (1983). Large-scale dynamical processes in the atmosphere . Academic Press, London etc., 421 p.
- Houze R. A. (1993). Cloud dynamics. Intern. Geophys. Series, Vol. 53, Academic Press , 570 p.
- Hulst C. H. van de . (1981). Light scattering by small particles. New York, Dover Publications, 470 p.
- Huneycutt B. and Zuzek J. (2000) . Frequency use and needs of spaceborne active sensors. IEEE IGARSS 2000 Proceedings, Vol. VI, IEEE, p. 2457-2463.
- Hussain A. K. M. F. (1986). Coherent structures and turbulence. J. Fluid Mech., Vol. 173, p. 303-356.
- Hyatt H. A. (1970). Emission, reflection, and absorbtion of microwaves at a smooth air-water interface. J. Quant.Spectrosc. Radiat. Trasfer, Vol. 10, N 3, p. 217-247.
- Ingmann P. (1991). The physics and instrumentation of passive atmospheric sounding . ESA STR-231. Paris, ESA, p. 56.
- Intrieri J. M., Eberhard W. L., Uttal T., Shaw J. A., Snider J. B., Han Y. Orr B. W., Matrosov S. Y. (1995). Multiwavelength observations of a developing cloud system: the FIRE II 26 November 1991 case study. J. Atm. Sci., Vol. 52, N 23, p. 4079-4093.
- IPCC (Intergovernmental Panel of Climate Change) , (2001).Climate change 2001: the scientific basis. Eds.: Houghton J. T., Ding Y., Griggs D. J., Noguer M., van der Linden P. J., Dai X., Maskell K., and Johnson C. A. Cambridge Univ. Press, Cambridge, U. K. and New York. N. Y., USA , 881p.
- Irisov V. G. (1997). Small-slope expansion for thermal and reflected radiation from a rough surface. Waves in Random Media, Vol. 7, N1, p. 1-10.
- Irisov V. G. , Trochimovskii Yu. A., Etkin V. S. (1987). Radiothermal spectroscopy of sea surface. Doklady Acad. Nauk SSSR (Trans. of USSR Academy of Sciences - Engl. transl.), Vol. 297, N 3, p. 587-589.
- Ishimaru A. (1978) . Wave propagation and scattering in random media. Vol.I and II, Academic Press, New York, 540 pp.
- Ishimaru A. (1991). Wave propagation and scattering in random media and rough surfaces. Proc. IEEE, Vol. 79, N 10, p. 1359-1366.
- Ivanitskii G. R. , Medvinskii A. B., Deev A. A. and Tsyganov M. A. (1998). From Maxwell's demon to the self-organization of mass transfer processes in living systems. Physics-Uspekhi, Vol. 41, N 11, p. 115-1126.
- Ivanov P. Ch., Nunes Amaral L. A., Goldberger A. L. , Havlin S., Rosenblum M. G., Struzik Z. R. , and Stanley H. E. (1999). Multifractality in human heartbeat dynamics. Nature, Vol. 399, N 6735, p. 461-465.
- Ivazyn G.M. (1991). Propagation of millimeter and submillimeter wavelengths in clouds. Leningrad, Gidrometeoizdat, 478 p. (in Russian).
- Jameson A. R. (1991). The effect of drop-size distribution variability on radiometric estimates of rainfall rates for frequencies from 3 to 10 GHz. J. Applied Meteorology, vol. 30, N 7, p. 1025-1033.
- Jameson A. R., Kostinski A. B. , and Black R. A. (1998). The texture of clouds. J. Geophysical Research, Vol. 103, N D6, p. 6211-6219.
- Jimenez C., Eriksson P., and Askne J. (2000). Non-linear inversion of Odin sub-mm observations in the lower stratosphere by neural networks. In "Microwave Radiometry and Remote Sensing of the Earth-

- 's Surface and Atmosphere". Eds.: Pampaloni P. and Paloscia S. VSP BV , Utrecht, Boston, Koln, Tokyo , p. 503-511.
- Johannessen J. A., Digranes G., Espedal H., Johannessen O. M., Samuel P., Browne D., Vachon P. (1994). SAR ocean feature catalogue. ESA SP-1174. ESA, Noordwijk, The Netherlands, 106 p.
- Jones W.L., Black P., Delnore V., Swift C. (1981). Airborne microwave remote-sensing measurements of hurricane Allen. *Science*, Vol.214, N4518, p.274-280.
- Jones W. L. , Mehershahi R., Zec J., and Long D. G. (2000a). SeaWinds on QuikScat radiometric measurements and calibration. *IEEE IGARSS 2000 Proceedings*, Vol. III, IEEE, New York, p. 1027-1029.
- Jones W. L. , Susanj M., Zec J., and Park J.-D. (2000b). Validation of QuikScat radiometric estimates of rain rate. *IEEE IGARSS 2000 Proceedings*, Vol. III, IEEE, New York, p. 1229-1232.
- JSTC (Joint Scientific and Technical Committee) (1995). Plan for the Global Climate Observing System (GCOS).Version 1.0.May 1995,GCOS-14, WMO/TD-N 681, 60 p.
- Kaatze U., and Giese K. (1980). Dielectric relaxation spectroscopy of liquids: frequency domain and time domain experimental method. *J. Phys. E*, Vol. 18, N 2, p. 133-141.
- Kaatze U. and Uhendorf V. (1981). The dielectric properties of water at microwave frequencies. *Zeitschrift fur physikalische Chemie . Neue Folge*. Vol. 126, N 2, p. 151-165.
- Kadanov L. P. (1993). From order to chaos. Essays: critical, chaotic and otherwise. World Scientific, Singapore etc., 576 p.
- Kadygrov E. N., Shur G. N., and Viazankin A. S. (2003). Investigation of atmospheric boundary layer temperature , turbulence and wind parameters on the basis of passive microwave remote sensing. *Radio Science*, Vol. 38, N 3, 8048, doi:10.1029/2002RS002647.
- Kakar R. K. , and Lambrightsen B. H. (1984). A statistical correlation method for the retrieval of atmospheric moisture profiles by microwave radiometry. *J. Climate Applied Meteorology*, Vol.23, N 7, p. 11110-1114.
- Kalmykov A. I. (1996) Real-aperture radar (RAR) imaging from space. *Radio Science Bulletin*, N 276,p. 13-22.
- Kapitza H. (1983). The influence of clouds and rain on the determination profiles from microwave radiation at 54,4 GHz and 58,0 GHz. *Contributions to Atmospheric Physics*, Vol. 56, N 4, p. 452-463.
- Kardashiov N. S. (2000). Radiotelescope larger than Earth ("Radioastron"). *Zemlya i Vselennaya* (Earth and Universe), N 4, p. 3-10.
- Karkkainen K., Sihvola A. , and Nikoskinen K. (2000). Effective permittivity of mixtures: numerical validation by the FDTD method. *IEEE Trans. Geoscience Remote Sensing* , Vol. 38, N 3, p. 1303-1309.
- Karmakar P. K. , Maiti M., Chattopadhyay S., and Rahaman M. (2002). Effects of water vapor and liquid water on microwave absorption, and their application. *Radio Science Bulletin*, N 303, p. 32-36.
- Kaspersen J. H., and Krogstad P.A. (2001). Wavelet-based method for burst detection. *Fluid Dynamics Research*, Vol. 28, N 3, P. 223-236.
- Keihm S., Zlotnicki V., and Ruf C. S. (2000). TOPEX microwave radiometer performance evaluation, 1992-1998. *IEEE Trans. Geosc. Remote Sensing*, Vol. 38, N 3, p. 1379-1386.
- Kerr Y. H., Wigneron J.P., Ferrazzoli P., and Waldteufel P. (2000a). Soil moisture and vegetation biomass retrievals using L band , dual polarized and multi angular radiometric data in preparation of the SMOS mission. *IEEE IGARSS 2000 Proceedings*, Vol. III, IEEE, New York, p. 1244-1246.
- Kerr Y. H., Waldteufel P., Wigneron J. P., and Font J. (2000b). The soil moisture and ocean salinity mission : the science objectives of an L band 2-D interferometer. *IEEE IGARSS 2000 Proceedings*, Vol. VII, IEEE, New York, p. 2969-2971.
- Kerr Y. H., Font J., Waldteufel P., and Berger M..(2000c). The soil moisture and ocean salinity mission – SMOS. *Earth Obsev. Quarterly*, N 66, p. 18-26.
- Kerr Y. H., Waldteufel P., Wigneron J.-P., Martinuzzi J.-M., Lazard B., Goutoule J.-M., Tabard C., and Lannes A. (2000d). The soil moisture and ocean salinity mission : an overview. In "Microwave Ra-

- diometry and Remote Sensing of the Earth's Surface and Atmosphere". Eds.: Pampaloni P. and Paloscia S. VSP BV , Utrecht, Boston, Koln, Tokyo , p. 467-475.
- Kharkevich A. A. (1962). Spectra and analysis. Physic-mathematical Publishing House, Moscow, 235p.
- Khodyrev Yu. K. , Bespalova E. A. , Pashin Yu. N., Polaynina G. D., Serebrekayn A. L., Strukov I. A. , Shakhno O. F. , Sharkov E. A. , and Etkin V. S. (1972) . Issues of applications of radiophysical methods in the exploration of the atmosphere and the terrestrial surfaces with spacecrafts. Preprint N Pr-112, Space Research Institute, Moscow , 50p. (in Russian).
- Khundzhia G. G. , Gusev A. M. , Andreyev E. G. , Gurov V. V. , and Skorokhvatov N. A. (1977). On the structure of the ocean surface cold film and on the heat exchange of ocean with atmosphere. Izvestya AN . Fizika atmosphery i okeana. (Izvestiya, Atmospheric and Oceanic Physics -English Transl.), Vol. 13, N 7, p. 753-758.
- Kidder S. Q. , GolbergM.D. , Zehr R. M., DeMaria M., Purdom J. F. W. , Velden C. S., Grody N. C. and Kusselson S.J. (2000). Satellite analysis of tropical cyclones using the Advanced Microwave Sound- ing Unit (AMSU). Bulletin Amer. Meteor. Soc., Vol. 81, N 6, p. 1241-1260.
- Kirchner J. W. , and Weil A.(1998). No fractals in fossil extinction statistics. Nature, Vol. 395, N 6700, p. 337-338 .
- Kislyakov A. G. and Stankevich K. S. (1967) . Investigation of troposphere absorption of radio waves by radio astronomical methods. Izvestia VUZ. Radiofizika. (Izvestiya , Radiophysics and Quantum Elec- tronics - Engl. Transl.), Vol. 10, N 9-10, p. 1244-1265.
- Klein L. A. and Swift C. T. (1977). An improved model for the dielectric constant of sea water at mi- crowave frequencies. IEEE Trans. Antennas Propagation, Vol. 25, N 1, p. 104-111.
- Klepikov I. N. and Sharkov E. A. (1983). Thermal emission of stratified nonuniform nonisothermal me- dia . Preprint N Pr-801 , Space Research Institute, Moscow ,30p. (in Russian).
- Klepikov I. N. and Sharkov E. A. (1993) . Theoretical study of the natural emission of highly nonuniform nonisothermal media. Sov. J. Remote Sensing, Vol. 10, N6, p. 969-989.
- Klugman I. Yu. (1980). The dielectric permittivity of electrolytes. Zhurnal Fizicheskoi Khimii (Journal of Phys. Chemistry-English transl.), Vol. 54, N 8, p. 2045-2049.
- Kramer, H.J., Ed. (1996). Observation of the Earth and its Environment: survey of missions and sensors. 3rd Enlarged Edition. Berlin, Springer- Verlag, 960p.
- Koh G. (1997). Dielectric properties of ice at millimeter wavelengths. Geophysical Research Letters, Vol. 24, N 18, p. 2311-2313.
- Kohonen T. (1989). Self-organization and associative memory. Springer, New York, 320p.
- Kohlhase C. and Peterson C. E (1997). The Cassini mission to Saturn and Titan. ESA Bulletin, N 92, p. 55-68.
- Koike T., Njoku E., Jackson T. J., and Paloscia S.(2000). Soil moisture algorithm development and valida- tion for the ADEOS-II/AMSR. IEEE IGARSS 2000 Proceedings, Vol. III, IEEE, New York, p. 1558-1560.
- Kollias P., Lhermitte R. , and Albrecht B. A. (1999). Vertical air motion and raindrop size distributions in convective systems using a 94 GHz radar. Geophysical Research Letters, Vol. 26, N 20, p. 3109- 3112.
- Kondratyev K. Ya. (1997) The remote sensing of middle atmosphere from satellites: the new stage. Earth Research from Space (Earth Observ. Rem Sens. - Engl. Transl.) N2, p. 117-134.
- Kondratyev K. Ya. (2000). Global change at the turn of the Millenium. Herald Russian Academy Sci- ences, Vol. 70, N 9, p. 788-796.
- Kondratyev K. Ya., Timofeev Y. M. (1970). Thermal sensing of the atmosphere with satellites. Gidrome- teoizdat Publ. House, Leningrad, 410p. (in Russian).

- Kondratyev K. Ya., and Shulgina E. M. (1971). The determination of characteristics for soil with thermal radioemission measurements. Doklady Acad. Nauk USSR (Trans. of Russian Academy of Sciences / Earth Science Section- Eng. Transl.) , Vol.200, N1, p.88-90.
- Kondratyev K. Ya., Timofeev Y. M. , and Shulgina E. M. (1970). On possibility of determination of characteristics for surface layer soil with its thermal radioemission. Doklady Acad. Nauk USSR (Trans. of Russian Academy of Sciences / Earth Science Section- Eng. Transl.) , Vol.194, N6, p.1313-1315.
- Kondratyev K. Ya., Melentyev V. V. , Rabinovich Yu. I., and Shulgina E. M. (1973). The determination of some physical characteristics for surface soil layer using thermal radioemission. Doklady Acad. Nauk USSR (Trans. of Russian Academy of Sciences / Earth Science Section- Eng. Transl.) , Vol.208, N2, p.342-345.
- Kondratyev K. Ya., Rabinovich Yu. I., and Nordberg W., Eds. (1975). USSR/USA Bering sea experiment proceedings on the final symposium on the joint results of the joint Soviet-American expedition, Leningrad, May 12-17, 1974. Gidrometeoizdat Publ. House, Leningrad, 254p.
- Kondratyev K. Ya., Buznikov A., Pokrovsky O. (1995). Global Change and Remote Sensing. Chichester etc.: Wiley/PRAXIS, 300 pp.
- Kondratyev K. Ya., Johannessen O. M., Melentyev V. V. (1996) . High latitude climate and remote sensing. Chichester etc. : Wiley/PRAXIS, 200 pp.
- Kondratyev K. Ya. and Tanaka T. (1997).Advanced Earth observing satellite-II (ADEOS-II): new perspectives of global environmental monitoring .Earth Research from Space(Earth Observ. Rem. Sens. - Engl. Transl.) , N1, p. 105-121.
- Konig M. von, Bremer H. , Euring V., Goede A. , Hetzheim H., Kleipool Q., Kullmann H., and Kunzi K. (2000). An airborne submm radiometer for the observation of stratospheric trace gases. In "Microwave Radiometry and Remote Sensing of the Earth's Surface and Atmosphere". Eds.: Pampaloni P. and Paloscia S. VSP BV , Utrecht, Boston, Koln, Tokyo , p. 409-415.
- Kostenko V. I. (1973). Digital realization of the algorithm for radioimages recover as a example of Crab nebula brightness distribution. Izvestia VUZ. Radiofizika. (Izvestiya , Radiophysics and Quantum Electronics - Engl. Transl.), Vol. 16, N 5, p. 680-684.
- Kostinski A. B. , and Jameson A. R. (1997). Fluctuation properties of precipitation. Part I: on deviations of single-size drop counts from the Poisson disirubtion. J. Atmospheric Sciences, Vol. 54, 9, p. 2174-2186.
- Kothari R., and Islam S. (1999). Spatial characterization of remotely sensed soil moisture data using self organizing feature maps. IEEE Trans. Geoscience Remote Sensing, Vol. 37, N 2, p. 1162-1165.
- Kotlyar I. B. and Novak B. L. (1987). Estimating the accuracy of atmosphere temperature profiles from remote microwaves sensing (117 - 118,5 GHz) . Earth Research from Space (Earth Observ. Rem. Sens. - Engl. Transl.), N 6, p. 57-62.
- Kotlyar I. B. and Khapin Yu. B. (1990). Atmospheric radio brightness characteristics in the 2,53 mm line. Sov. J. Remote Sensing, Vol. 7, N 1, p. 61-71.
- Krasiuk N. P. and Rosenberg V. I. (1970). Ship-borne radiolocation and meteorology. "Sudostroenie " Publ. House, Leningrad, 324p. (in Russian).
- Kravtsov Yu. A. , Ed.(1997). Limits of forecasting. TzentrKom Publishing House, Moscow , 247 p. (in Russian).
- Kravtsov Yu. A., Mirovskaya Ye. A., Popov A. E., Troitskiy I. A. and Etkin V. S.(1978). Critical effects in the thermal radiation of a periodically uneven water surface. Izvestiya, Atmospheric and Oceanic Physics, Vol. 14, N7, p. 522-526.
- Krotikov V. D. (1962). Some electrical characteristics of terrestrial soils and their comparisons with characteristics of Moon's surface layers. Izvestia VUZ. Radiofizika. (Izvestiya , Radiophysics and Quantum Electronics - Engl. Transl.), Vol. 5, N 6, p. 1057-1061.
- Krug K.A. (1936). Foundations of the electrical engineering. Joint Scientific-Technical Publishing House, Moscow-Leningrad, 887p. (in Russian).
- Krupenio N. N. (1974). Density of Mars upper soil using data of radiophysical measurements at 3 cm band. Preprint N Pr-185. Space Research Institute , Moscow, 28p. (in Russian).

- Kummerow C. , Barnes W., Kozu T., Shuie J., and Simpson J. (1998). The Tropical Rainfall Measuring Mission (TRMM) sensor package. *J. Atmos. Oceanic Tech.*, Vol. 15, p. 809-817.
- Kummerow C. , Simpson J., Thiele O., Barnes W., Chang A.T.C., Stocker, Adler R. F., Hou A., Kakar R., Wentz F., Ashcroft P., Kozu T., Hong Y., Okamoto, Iguchi T., Kuroiwa H., Im E., Haddad Z., Huffman G., Ferrier B., Olson W. S., Zipser E., Smith E. A., Wilheit T. T., North G., Krishnamurti T., and Nakamura K. (2000). The status of the Tropical Rainfall Measuring Mission (TRMM) after two years in orbit. *J. Applied Meteorology*, Vol. 39, N12, p. 1965-1982.
- Kunkee D. B. , and Gasiewski A. J. (1997). Simulation of passive microwave wind direction signatures over the ocean using an asymmetric-wave geometrical optics model. *Radio Science*, Vol. 32, N 1, p. 59-78.
- Kutuza B. G. , and Smirnov M. T. (1980). The influence of clouds on radio-thermal radiance of “atmosphere-ocean surface” system. *Earth Research from Space (Earth Observ. Rem. Sens. - Engl. Transl.)*, N3, p. 76-83.
- Kuzmin A. V. and Pospelov M. N. (1999) . Measurements of sea temperature and wind vector by nadir airborne microwave instruments in Joint United States/Russia internal waves remote sensing experiment JUSREX'92. *IEEE Trans. Geoscience Remote Sensing*, Vol. 37, N4, p. 1907-1915.
- Kuzmin A., Pospelov M. , and Trokhimovski Yu. (2000). Sea surface parameters retrieval by passive microwave polarimetry. In “Microwave Radiometry and Remote Sensing of the Earth’s Surface and Atmosphere”. Eds.: Pampaloni P. and Paloscia S., VSP BV, Utrecht, Boston, Koln, Tokyo , p. 3-11.
- Lagerloef G. S. E., Swift C. T., and LeVine D. M. (1995). Sea surface salinity: the next remote sensing challenge. *Oceanography*, Vol. 8, N 2, p. 44-50.
- Lakhtakia A., Messier R., Varadan V. V., Varadan V. K. (1987) Fractal dimension from the back-scattering cross section. *J. Phys. A : Math. Gen.*, Vol. 20, p. 1615-1619.
- Lam L. (1998). Nonlinear physics for beginners : fractals, chaos, solitons, pattern formations, cellular automata, complex system. World Scientific Pub., Singapore, 348p.
- Lambrigtsen B. H. (2000). GEO/SAMS – the geostationary synthetic aperture microwave sounder . IEEE IGARSS 2000 Proceedings, Vol. VII, IEEE, New York, p. 2984-2987.
- Lane J., and Saxton J. (1952). Dielectric dispersion in pure polar liquids at very high frequencies. *Proc. Roy. Soc.*, Vol. 214A, N 1119, p. 531-545.
- Landau L.D. and Lifshitz E. M. (1957). Electrodynamics of continuous media. Gostechizdat Pub. House, Moscow, 340 p (in Russian) (Engl. Transl. – Pergamon, Oxford, 1960 , 350 p.).
- Larraza A., Putterman S. , and Roberts P. H. (1985). A universal 1/f power spectrum as the accumulation point of wave turbulence. *Physical Review Letters*, Vol. 55, N 9, p. 897-900.
- Laursen B. , Sobjerg S. , and Skou N. (2000). Ocean wind measured by an imaging, polarimetric radiometer. In “Microwave Radiometry and Remote Sensing of the Earth’s Surface and Atmosphere”. Eds.: Pampaloni P. and Paloscia S., VSP BV , Utrecht, Boston, Koln, Tokyo , p. 29-37.
- LeBlond P. H. and Mysak L. A. (1978). Waves in the Ocean. Elsevier Sci. Publ., Amsterdam , 602 p.
- Lepley L. K. and Adams W. M. (1971). Electromagnetic dispresion curves for natural waters. *Water Resources Research*, Vol. 7, N6, p. 1538-1547.
- Lessner G. (1982). The electrical conductivity of stationary and homogeneous electrolytes up to concentrations $c \approx 1$ mol/l. *Physica A*, Vol. 116, N 1-2, p. 272-288.
- Leung K. , Andersen J. V., and Sornette D. (1998). Self-organized criticality in an isotropically driven model approaching equilibrium. *Physica A*, Vol. 254, N 1-2, p. 85-96.
- Levin M. L. and Rytov S. M. (1967). Theory of equilibrium thermal fluctuations in electrodynamics. Nauka Publ. House, Moscow, 308 p.(in Russian).
- Lhermitte R. M. (1988). Cloud and precipitation remote sensing at 94 GHz. *IEEE Trans. Geosci. Remote Sensing*, Vol. 26, N 3, p. 207-216.
- Li S., Akyel C. , and Bosisio R. (1981). Precise calculation and measurements on the complex dielectric constant for lossy material using TM_{010} cavity perturbation techniques. *IEEE Trans. MTT*, Vol. 29, N 10, p. 1041-1047.

- Li L., Vivekanandan J., Chan C. H., and Tsang L. (1997). Microwave radiometric technique to retrieval vapor, liquid and ice: Part I. Development of a neural networ-basaed inversion method. IEEE Trans. Geoscience Remote Sensing, Vol. 35, N2, p. 224-236.
- Liebe H. J. (1989). MPM- an atmospheric millimeter wave propagating model. Int. J. Infrared and Millimeter Waves, Vol. 10, N 6, p. 631-650.
- Liebe H. J., Hufford G. A. , and Manabe T. (1991). A model for the complex permittivity of water at frequencies below 1 THz. Int. J. Infrared and Millimeter Waves, Vol. 12, N 6, p. 659-675.
- Lin B. , Wielicki B., Minnis P., and Rossow W.(1998a). Estimation of water cloud properties from satellite microwave, infrared and visible measurements in oceanic environments.1. Microwave brightness temperature simulations.J. Geophysical Research, Vol. 103, N D4, p. 3873-3886.
- Lin B. , Minnis P., Wielicki B., Dopelling D. R. , Palikonda R., Young D. F. , and Uttal T. (1998b). Estimation of water cloud properties from satellite microwave, infrared and visible measurements in oceanic environments.2. Results. J. Geophysical Research, Vol. 103, N D4, p. 3887-3905.
- Lin B. and Minnis P. (2000). Temporal variations of land surface microwave emissivities over the atmospheric radiation measurement program Southern Great Plains site. J. Applied Meteorology, Vol. 39, N 7, p. 1103-1116.
- Liou Y.-A. , Galantowicz J. F., and England A. W. (1999) . A land surface process/radiobrightness model with coupled heat and moisture transport for prairie grassland. IEEE Trans. Geoscience Remote Sensing, Vol. 37, N4, p. 1848-1859.
- Liou Y.-A., Teng Y.-T., Hove T.V., and Liljegren J. C. (2001). Comparison of precipitable water observations in the near tropics by GPS, microwave radiometer, and radiosondes. J. Applied Meteorology, Vol. 40, N 1, p. 5-15.
- Lipton A. E. , Griffin M. K. , and Ling A. G. (1999). Microwave transfer model diffrences in remote sensing of cloud liquid water at low temperatures. IEEE Trans. Geoscience Remote Sensing, Vol. 37, N1, p. 620-623.
- List R. (1988). A linear radar reflectivity-rainrate relationship for steady tropical rain. J. Atmos. Sci., Vol.45, N23, p.3564-3572.
- Liu G. (1998). A fast and accurate model for microwave radiance calculations. J. Meteor. Soc. Japan, Vol. 76, N 2, p. 335-343.
- Liu G., Curry J. A. , and Shen R. S. (1995). Classification of clouds over the western equatorial Pacific Ocean using combined infrared and microwave satellite data. J. Geophysical research, Vol. 100, N D7, p. 13811-13826.
- Liu G. , and Curry J. A. (1998). Remote sensing of ice water characteristics in tropical clouds using aircraft microwave measurements. J. Applied Meteorology, Vol. 37, N 4, p. 337-355.
- Liu G. , and Curry J. A. (1999). Tropical ice water amount and its relations to other atmospheric hydrological parameters as inferred from satellite data. J. Applied Meteorology, Vol. 38, N 8, p. 1182-1194.
- Liu G., and Curry J. A. (2000). Determination of ice water path and mass median particle size using multi-channel microwave measurements. J. Applied Meteorology ,Vol. 39, N 8, p. 1318-1329.
- Liu W. T. (1990) . Remote sensing of surface turbulence heat flux. In “ Surface waves and fluxes” , Vol. II, Eds. By Geernaert G. L. and Plant W. J. . Kluwer Academic Publ., p. 293-309.
- Lodders K. and Fegley B. (1998). The planetary scientist’s companion. Oxford University Press, New York, Oxford, 371p.
- Lohnert U. , and Crewell S. (2003). Accuracy of cloud liquid water path form groundbased microwave radiometry.1. Dependency on cloud model statistics. Radio Science, Vol. 38, N3, 8041, doi: 10.1029/2002RS002654.
- Long D. G. and Skouson G. B. (1996).Calibration of spaceborne scatterometers using tropical rain forests. IEEE Trans. Geosci. Remote Sensing, Vol. 34, N 2, p. 4134-424.
- Loudon R.(1973). The quantum theory of light. Oxford, Clarendon Press, 480p.

- Lovejoy S. and Schertzer D. (1985). Generalized scale invariance in the atmosphere and fractal models of rain. *Water Resources Research*, Vol.21, N8, p.1233-1250.
- Lovejoy S. and Mandelbrot B. B. (1985). Fractal properties of rain and a fractal model. *Tellus*, Vol. 37A, p. 205-232.
- Lovejoy S., Schertzer D., and Ladoy P. (1986). Fractal characterization of inhomogeneous geophysical measuring networks. *Nature*, Vol. 319, N 6048, p. 43-44.
- Lucero O. A. (1998). Invariance of the design storm in a region under a rainfall climate change at mid-latitudes. *Atmospheric Research*, Vol. 49, N 1, p. 11-20.
- Ludeke K. M. , and Kohler J. (1983). Microwave radiometric system for biomedical “true temperature” and emissivity measurements. *J. Microwave Power*, Vol. 18, N 3, p. 277-283.
- Lyaschenko A. K. , Goncharov V. S. , and Yastremskii P.S. (1976). Dielectric properties and structure of water solutions of the boric acid. *Zhurnal Structur. Khimii (J. Structural Chemie)* , Vol. 17, N 3, p. 462-465.
- Macelloni G., Paloscia S., Pampoloni P ., Ruisi R., Susini C. and Wigneron J. P. (2000a). Airborne passive microwave measurements on agricultural fields. In “Microwave radiometry and remote sensing of the Earth’s surface.”- Pampaloni P. and Paloscia S. Eds., VSP Press, Utrecht, The Netherlands , p. 59-70.
- Macelloni G., Paloscia S., Pampoloni P., Ruisi R., Tedesco M., Cagnati A., and Valt M. (2000b). Microwave emission of snow in Alpine regions and the detection of surface hoar. *IEEE IGARSS 2000 Proceedings*, Vol. IV, IEEE, New York, p. 1760-1762.
- Maeda K., Iida Y., and Manabe T. (2000) . Protection of spaceborne and terrestrial passive sensors to observe trace gasses from 200 to 700. GHz. *IEEE IGARSS 2000 Proceedings*, Vol. VI, IEEE, New York, p. 2467-2470 .
- Maier D., Kampfer N., Amacher W., Wuthrich M., Noe J. De La, Ricaud P. Baron P. Beadin G. Viguerie C., Pardo J.-R., Gallego J.-D., Barcia A., Cernicharo J., Ellison B., Siddans R., Matheson D., Kunzi K., Klein U., Barry B., Louhi J., Mallat J., Gustafsson M., Raisanen A., and Karpov A. (2000). EMCOR: a new radiometer for the measurement of minor constituents in the frequency range of 201 to 210 GHz. In “Microwave Radiometry and Remote Sensing of the Earth’s Surface and Atmosphere”. Eds.: Pampaloni P. and Paloscia S. VSP BV , Utrecht, Boston, Koln, Tokyo , p. 417-425.
- Malkevich M. S. (1973). Optical studies of the atmosphere from satellites. Moscow, “Nauka” Publ. House, 303 p. (in Russian).
- Mandel L. and Wolf E. (1995). Optical coherence and quantum optics. Cambridge University Press, Cambridge, 850p.
- Mandelbrot B. (1977). Fractals: forms, chance and dimension. W. H. Freeman and Co., San Francisco, Calif., 250 p.
- Mandelbrot B. (1982). The fractal geometry of nature. W. H. Freeman and Co., San Francisco, Calif., 461 pp.
- Mandelbrot B. B. (1989). Fractal geometry: what is it , and what does it do? *Proc. Royal Soc. London A*, Vol. 423, p. 3-16.
- Mandelbrot B. (1998). Is nature fractal? *Science*, Vol. 279, N 5352, p. 783-784.
- Marchuk G. I., Ed. (1976). Monte Carlo method in atmospheric optics. “Nauka” Publ. House, Novosibirsk, 280 p.
- Marchuk G. I., Kondratyev K. Ya., Kozodyerov V. V., Khvorostynov V. I. (1986). Clouds and climate. Gidrometeoizdat, Leningrad, 512 p. (in Russian).

- Marshak A., Davis A., Cahalan R., and Wiscombe W. (1994). Bounded cascade models as nonstationary multifractals. *Physical Review E*, Vol. 49, N1, p. 55-69.
- Marshak A., Davis A., Wiscombe W., and Cahalan R. (1997) . Scale invariance in liquid water distributions in marine Stratocumulus. Part II: multifractal properties and intermittency issues. *J. Atm. Sciences* , Vol. 54, N 11, p. 1423- 1444.
- Martin-Neira M. and Goutoule J. M. (1997). MIRAS- a two-dimensional aperture-synthesis radiometer for soil-moisture and ocean-salinity observations. *ESA Bulletin*. N 92, p. 95-104.
- Martin-Neira M., Font J., Skorosz M., Corbella I., and Camps A.(2000). Ocean salinity observations with SMOS mission. *IEEE IGARSS 2000 Proceedings*, Vol. VI, IEEE, New York, p. 2452-2454.
- Martsinkevich L. M. (1970). The distribution of sea surface slopes. *Meteorologia i hydrologia* (Russian Meteorology and Hydrology),N 10, p. 41-55.
- Martsinkevich L. M. (1981). A two-frequency microwave radiometric method for determination of wind velocity with the aid of a satellite. *Meteorologia i hydrologia* (Russian Meteorology and Hydrology) ,N 3, p. 59-67.
- Martsinkevich L. M. and Melentyev W. W. (1975). Model calculations of sea surface thermal emission for steady sea state. *Trudy GGO* (Trans. Main Geophys. Observatory), N 331, p. 73-85 (in Russian) .
- Marzano F. S., Mugnai A., Panegrossi G., Pierdicca N., Smith E. A., and Turk J. (1999). Bayesian estimation of precipitation cloud parameters from combined measurements of spaceborne microwave radiometer and radar. *IEEE Trans. Geoscience Remote Sensing*, Vol. 37, N 1, p. 596-613.
- Mason P. R. , Hasted J. B. , and Moore L.(1974). The use of statistical theory in fitting equations to dielectric dispersion data. *Advan. Molec. Relax. Processes.*,Vol.6,N3, p. 217-232.
- Masuko H., Manabe T., Seta M., Kasai., Ochiai S., Irimajiri Y. , Inatani J., Ikeda N., Nishibori T., Oze-ki H., Sato R., Fujii Y., Nakajima T., Watanabe H., Kikuchi K., and Koyama M. (2000). Superconducting submillimeter-wave limb emission sounder (SMILES) onboard Japanese experimental module (JEM) of International Space Station (ISS). *IEEE IGARSS 2000 Proceedings*, Vol. I, IEEE, New York, p. 71-73.
- Matsuoka T., Fujita S., and Mae S. (1996). Effect of temperature on dielectric properties of ice in the range 5-39 GHz. *J. Applied Physics*, Vol. 80, N 10, p. 5884-5890.
- Matsuoka T., Fujita S., Morishima S. and Mae S. (1997). Precise measurement of dielectric anisotropy in ice Ih at 39 GHz. *J. Applied Physics*, Vol. 81, N 5, p. 2344-2348.
- Matveenko L.I., Sagdeev R. Z., Kostenko V. I., Kogan L. R., Molotov E. P., Ignatov S. P., Severnyi A. B., Moiseev I. G., Efanov V. A., Sorochenko R. L., Martirosyan R. M., and Aslanyan A. M. (1983). Three-element very-long baseline radiointerferometer . *Pis'ma v AJ* (Astronomical Journal Letters – English transl.) , Vol. 9, N7, p. 415-420.
- Matveev D. T. (1971). On the spectrum of microwave emission of ruffled sea surface. *Izvestia Acad. Nauk. Fizika atmosphery i okeana* (Izvestiya, Atmospheric and Oceanic Physics - Engl. Transl.) , Vol.7, N 10, p.1070-10983.
- Matveev Yu. L., Matveev L. T., Soldatenko S. A. (1986) Global Cloudiness. *Gidrometeoizdat*, Leningrad, 288 p. (in Russian).
- Matzler Ch. (1992). Ground-based observations of atmospheric radiation at 5, 10, 21, 35 and 94 GHz. *Radio Science*, Vol. 27, N 3, p. 403-415.
- Matzler Ch. (1994a). Passive microwave signatures of landscapes in winter. *Meteorol. Atmos. Physics*, Vol. 54, p. 241-260.
- Matzler Ch. (1994b). Microwave (1-100 GHz) dielectric model of leaves. *IEEE Trans. Geoscience Remote Sensing* , Vol. 32, N5, p. 947-949.
- Matzler Ch. (1996). Microwave permittivity of dry snow. *IEEE Trans. Geoscience Remote Sensing* , Vol. 34, N2, p. 573-581.
- Matzler Ch. (1998). Microwave permittivity of dry sand. *IEEE Trans. Geoscience Remote Sensing* , Vol. 36, N1, p. 317-319.

- Matzler Ch., Ed. (2000). EUR 19543 - COST Action 712 - Radiative transfer models for microwave radiometry. Office for Official Publications of the European Communities, Luxembourg, 174 p.
- Matzler Ch., and Wiesmann A. (1999). Extention of the microwave emission model of layered snowpacks to coarse-grained snow. *Remote Sens. Environment*, Vol. 70, N 3, p. 317-325.
- McAvoy J. , and Buckmaster H. (1983). The 9GHz complex permittivity of water at 293 and 298 K. *J. Phys. D : appl. Phys.* Vol. 16, N 12, p. 2519-2523.
- McDonald K. C., Zimmermann R., Way J. B., and Chun W. (1999). Automated instrumentation for continuous monitoring of the dielectric properties of woody vegetation: system design, implementation, and selected in situ measurements. *IEEE Trans. Geoscience Remote Sensing*, Vol. 37, N 4, p. 1880-1894.
- McMurdie L. A. , and Katsaros K. B. (1985). Atmospheric water distribution in a midlatitude cyclone observed by the Seasat Scanning Multichannel Microwave Radiometer. *Monthly Weather Review* , Vol. 113, N 4, p. 584-598.
- Megie G., and Readings C. J. (2000). The Earth Explorer missions – current status. *Earth Observ. Quarterly*, N 66, p. 1-5.
- Meisch C., Briottet X., and Kerr Y. (2002). Bidirectional reflectance of a rough anisotropic surface. *Int. J. Remote Sensing*, Vol. 23, N 15, p. 3107-3114.
- Meneghini R. , Kumagai H., Wang J. R., Iguchi T., and Kozu T. (1997). Microphysical retrieval over stratiform rain using measurements from an airborne dual-wavelength radar-radiometer. *IEEE Trans. Geoscience Remote Sensing*, Vol. 35, N 3, p. 487-506.f
- Meriakri V. V. , Apletalin V. N. , Kopnin A. N., Kraftmacher G. A. , Semenov M. G. , Ushatkin E. F. , and Chigryai E. E. (1980). Submillimeter and directed ray spectroscopy and its applications. In “Problems of modern radiotechnics and Electronics”. Moscow, Nauka Publ. House, p. 164-180. (in Russian).
- Michielsen K. and De Raedt H. (2001). Integral-geometry morphological image analysis . *Physics Reports*, Vol. 347, N6, p. 461-538.
- Militskii Y. A., Strukov I. A. , and Etkin V. S. (1975). High-sensitive radiometer at 8-mm band with the broadband parametric amplifier. *Izvestia VUZ. Radiofizika*. (Izvestiya, Radiophysics and Quantum Electronics - Engl. Transl.), Vol. 18, N 5, p. 773-774.
- Militskii Y. A., Raizer V. Y., Sharkov E. A. , and Etkin V. S. (1976). On scattering microwave emission by foamy structures. *Pisma v JTF* (Journal Technical Physics Letters – English Transl.). Vol. 2, N 18, p. 851-855.
- Militskii Y. A., Raizer V. Y., Sharkov E. A. , and Etkin V. S. (1977). Scattering microwave radiation by foamy structures. *Radiotekhnika i elektronika* (J. of Communic. Techn. Electronics - Engl. Transl.), Vol. 22, N 11, p. 2299-2304.
- Militskii Y. A., Raizer V. Y., Sharkov E. A. , and Etkin V. S. (1978). On thermal emission of foamy structures. *Jour. Technicheskoi Fiziki* (Journal Technical Physics – English Transl.). Vol. 48, N 5, p. 1031-1033.
- Milne B. T. (1988). Measuring the fractal geometry of landscapes. *Appl. Mathem. Computation*. Vol. 27, p. 67-79.
- Miller J. L. (2000). Airborne remote sensing of salinity. *Backscatter*, Vol. 11, N 3, p. 24-27.
- Miller J. L. and Payne S. (2000). Remote sensing of coastal salinity: naval needs and developing capability. *IEEE IGARSS 2000 Proceedings*, Vol. VI, IEEE, New York, p. 2534-2536.
- Miller J. L. , Goodberlet M. A., and Zaitzeff J. B. (1998). Airborne salinity mapper makes debut in coastal zone. *EOS, Trans. Amer. Geophys. Union*, Vol. 79, N 14, p. 173-177.

- Milman A. S. (1988). Sparse-aperture microwave radiometers for Earth remote sensing. Radio Science, Vol. 23, N 2, p. 2193-205.
- Mishev D., Petrova V., Ivanov G. , Krumov A. , and Nazarsky T. (1985).Complex study of the atmospheric and ocean state, using data from the scientific equipment installed on “Meteor-Priroda” satellite. Acta Astronautica, Vol. 12, N 7/8, p. 469-474.
- Mitnik L. M. (1972). Measurements of water vapour over oceanic basins using microwave radiometrs, based on “Cosmos-243” satellite. Trudy ZAO (Trans. Central Aerological Observatory), Issue 103, p. 64-72 (in Russian).
- Mitnik L. M. (1978) . Emissive characteristics of water surface. Information Center, VNIIGMI-MCD, Obninsk, 65p. (in Russian).
- Mitnik L. M. (1986). Microwave radiometric investigation of cloud characteristics from satellites. Acta Astronautica. Vol. 13, N 4, p. 175-183.
- Mitnik L. M., and Mitnik M. L. (2003). Retrieval of atmospheric and ocean surface parameters from ADEOS-II Advanced Microwave Scanning Radiometer (AMSR) data; coprparison of errors of global and regional algorithms. Radio Scince, Vol. 38, N 4, 8065, doi:10.1029/2002RS002659.
- Moiseev S.S., Sagdeev R.Z., Tur A.V., Khomenko G.A., Shukurov A.M. (1983). Physical mechanism of developing vortex disturbances in atmosphere. Doklady USSR Acad. Sci., Vol.273, N3, p.549-553 (in Russian).
- Monin A. S. , and Shishkov Yu. A. (2000). Climate as a problem of physics. Physics-Uspekhi, Vol. 43, N 4, p. 381-406.
- MSC (Meteorological Satellite Center) (1986). Monthly report of the Meteorological Satellite Center , June-September, 1985, Tokyo, 250 p.
- Murray R. L. (1957). Nuclear reactor physics. Prentice-Hall, Englewood Cliffs, N. Y., 324p.
- Myers N. (1984). The primary source. Tropical forests and our future. W. W. Norton and Company, New York, London, 320 p.
- Nakajima T. Y. and Nakajima T. (1995). Wide-area determination of cloud microphysical properties from NOAA AVHRR measurements for FIRE and ASTEX regions. J. Atm. Sci., Vol. 52, N 23, p. 4043-4059.
- Narayanan M.S. (1999). Indian space programme in meteorology and oceanography. Megha-Tropiques. First Science Workshop Proceedings,19-22 May, 1999, ISRO H.Q., Bangalore, INDIA. Eds. Narayanan M. S., Manikiam B., Gairola R. M. ISRO, CNES, p. 2.1-2.8.
- Naumov A. P. , Osharina N. N. , and Troitsky A. V. (1999). Ground-based microwave thermal sounding of the atmosphere. Izvestia VUZ. Radiofizika. (Izvestiya , Radiophysics and Quantum Electronics - Engl. Transl.), Vol. 42, N 1, p. 45 -59 .
- Navarra A. , Ed. (1998) Beyond El Nino. Decadal Variability in the Climate Systems. Springer , London, Berlin etc, 374 p.
- Nemarich J. , Wellman R. J. , and Lacombe J. (1988). Backscattering and attenuation by falling snow and rain at 96, 140, and 225 GHz. IEEE Trans. Geosci. Remote Sensing, Vol. 26, N 3, p. 319-329.
- Nerushev A. F. , Petrenko B. Z. , and Kramchaninova E. K. (2001). Determination of tropical cyclone parameters derived from the VHF radiometer SSM/I. Earth Research from Space (Earth Obs. Remote Sensing - Engl. transl.). N 2, p. 61-68.
- Nesterov S. V. , Shamaev A. S. and Shamaev S. I., Eds. (1996). Methods, algorithms and facilities of aerospace computer radar tomography of Earth surface regions. Moscow, Scientific World , p. 272. (in Russian) .

- Newton P. (1998). Outlook- probably wet in parts. *Nature*. Vol. 329. N 6674.p. ?
- Nicolis G. and Prigogine I. (1977). Self-organization in nonequilibrium systems. Wiley- Interscience, New-York, 300 pp.
- Niemczynowicz J. and Bengtsson L. (1996). What practitioners need from theoreticians? *Atmospheric Research*, Vol. 42, N 1-4, p. 5-17.
- Nigmatulin R. I. (1978). Foundations of mechanics of heterogeneous mixtures . “Nauka” Publishing House, Moscow, 250p. (in Russian).
- Nihoul J. C. J. and Jamart B. M. , Eds. (1989). Mesoscale/synoptic coherent structure in geophysical turbulence. Elsevier Sci. Publ., Amsterdam, 842 p.
- Njoku E. G. and Kong J.A. (1977). Theory for passive microwave remote sensing of near-surface soil moisture. *J. Geophysical Research*, Vol. 82, N 20, p. 3108-3118.
- Njoku E. G. , Stacey J. M. , and Barath F. T. (1980). The Seasat scanning multichannel microwave radiometer (SMMR) : instrument description and performance. *IEEE J. Ocean. Eng.*, Vol. 5, N 2, p. 100-115.
- Njoku E. G. , and Li L. (1999). Retrieval of land surface parameters using passive microwave measurements at 6-18 GHz. *IEEE Trans. Geosci. Remote Sensing*, Vol. 37, N 1, p. 79-93.
- Njoku E. G., Rahmat-Samii Y., Sercel J., Wilson W. J., and Moghaddam M. (1999). Evaluation of an inflatable antenna concept for microwave sensing of soil moisture and ocean salinity. *IEEE Trans. Geosci. Remote Sensing*, Vol. 37, N 1, p. 63-78.
- Njoku E. G. , Li L. and Chan T. K. (2000a). Retrieving soil moisture from spaceborne passive microwave data. *IEEE IGARSS 2000 Proceedings*, Vol. III, IEEE, New York, p. 1247-1249.
- Njoku E. G., Wilson W. J., Yueh S. H., and Rahmat-Samii Y. (2000b). A large-antenna microwave radiometer-scatterometer concept for ocean salinity and soil moisture sensing. *IEEE Trans. Geosci. Remote Sensing*, Vol. 38, N 6, p. 2645-2655.
- Novak B. L., Trokhimovskii Yu. G., Etkin V. S. (1983). The optimization of working wavelengths in determining parameters of ocean-atmosphere system using thermal microwave measurements. *Izvestiy. Fizika Atmosf. Okeana*. (*Izvestyi - Physics, Atmosphere and Ocean - Engl. Transl.*). Vol. 19, N 9, p. 944-849.
- Oguchi T. (1983). Electromagnetic wave propagation and scattering in rain and other hydrometeors. *Proc. IEEE* , Vol. 71, N 9, p. 1029-1078.
- Ohring G. (1994). The current status of operational satellite products for climate studies. *Adv. Space Res.*, Vol. 14, N 1, p. 55-59.
- Olson W. S. , Kummerow C. D. , Hong Y., and Tao W.-K. (1999). Atmospheric latent heating distributions in the tropics derived from satellite passive microwave radiometric measurements. *J. Applied Meteorology*, Vol. 38, N6, p. 633-664.
- Olsson J. (1996). Validity and applicability of a scale-independent , multifractal relationship for rainfall. *Atmospheric Research*, Vol. 42, N 1- 4, p. 53-65.
- Onishenko S. G. and Sharkov E. A. (1982). On features of spectral characteristics for the dielectric parameters of concentrated electrolytes. *Radioitehnika i elektronika* (*J. Communications Technology and Electronics – English Transl.*), Vol. 27, N 10, p. 2050-2053.
- Ozisik M. N. (1973). Radiative transfer and interactions with conduction and convection. John Wiley and Sons, Inc . , New York , 450 pp.
- Paape K., Bennartz R. , and Fischer J. (2000). A combined two-scale model for microwave emissivities of land surfaces. In “Microwave Radiometry and Remote Sensing of the Earth’s Surface and Atmosphere”. Eds.: Pampaloni P. and Paloscia S., VSP BV, Utrecht, Boston, Koln, Tokyo , p. 71-80.

- Palmen E. and Newton C.W. (1969). Atmospheric circulation systems: their structure and physical interpretation. Intern. Geophys. Series 13. New York, Academic Press,603 p.
- Paloscia S. and Pampoloni P. (1988). Microwave polarization index for monitoring vegetation growth . IEEE Trans. Geosc. Remote Sensing, Vol. 26, N 5, p. 617-621.
- Paloscia S., Pampoloni P., Macelloni G. and Sigismondi S. (1999). Microwave remote sensing of hydrological parameters on the NOPEX area. Agricultural and Forest Meteorology, Vol. 98-99, p. 375-387.
- Paloscia S., Macelloni G., Pampoloni P. Santi E., and Koike T. (2000a). Soil moisture measuremants at global scale using active and passive microwave sensors. IEEE IGARSS 2000 Proceedings, Vol. III, IEEE, New York, p. 1241-1243.
- Paloscia S., Macelloni G., Pampoloni P., Ruisi R., and Susini C. (2000b). Airborne multi-frequency L- and Ka- band radiometric measurements over forests. IEEE IGARSS 2000 Proceedings, Vol. IV, IEEE, New York, p. 1402-1404.
- Parfitt A., Graeme J. , Kot J. , and Hall P. (2000). A case for the Luneburg lens as the antenna element for the square kilometre array radio teleskope. The Radio Science Bulletin, N 293, p. 32-37.
- Park Y. (2001). Effect of random fractals on the dielectric relaxation of a heterogeneous medium. Fractals, Vol. 9, N 3, p. 263-271.
- Parkinson C. L., Cavalieri, Gloersen P. , Zwally H. J. , and Comiso J.C. (1999). Arctic sea ice extents, areas and trends, 1978-1996. J. Geophysical Research, Vol. 104, N C9, p. 20837-20856.
- Parkhomenko E. I. (1965). Electrical properties of rocks. "Nauka" Publ. House, Moscow, 315p. (in Russian).
- Peake W. H. (1959). Interaction of electromagnetic waves with some natural surfaces. IRE Trans. on Antennas and Propagation (Special supplement).Vol. 7, N 12, p. S324-S329.
- Pease C. B. (1991) .Satellite Imaging Instruments. Chichester etc.: Wiley/ PRAXIS, 336 pp.
- Peng B. and Nan R. (2002). Modeling FAST, the world's largest single dish. Radio Science Bulletin, N300, p. 12-21.
- Penner S. S. (1959). Quantitative molecular specrtroscopy and gas emissivities. Addison-Wesley Publ. Company, Readings, London, 480p.
- Persky M. J. (1995). A review of spaceborne infrared Fourier transform spectrometers for remote sensing. Rev. Sci. Instrum., Vol. 66, N 10, p. 4763-4797.
- Petrenko B. Z. (1997). Robust two-channel correction of passive aerospace images. Earth Research from Space (Earth Observ. Rem. Sens. - Engl. Transl.). N 4, p. 42-49.
- Philander G.(1990). El-Nino, La Nino and the Southern Oscillation . Academic Press, San Diego, 350 p.
- Phillips O. M. (1988). Radar returns from the sea surface - Bragg scattering and breaking waves. J. Phys. Ocean., Vol. 18, N 8, p. 1065-1074.
- Pinteric M., Vuletic T., Tomic S., and Schutz J. U. von (2001). Complex low-frequency dielectric relaxation of the charge-density wave state in the $(2,5(\text{OCH}_3)_2\text{DCNQI})_2\text{Li}$. The European Physical J. B, Vol. 22, N3, p. 335-341.
- Pokrovskaya I. V. and Sharkov E. A. (1986). Spacial-statistical properties of whitecap fields on sea surface with optical remote sensing . Earth Research from Space (Sov. J. Remote Sensing – English Transl.), N 5, p. 18-25.
- Pokrovskaya I. V. and Sharkov E. A. (1987a). Foam activity on the sea surface as Markov random process. Doklady Acad. Nauk SSSR (Trans. of USSR Acad. of Sciences/ Earth Science Section - Engl. transl.), Vol. 293, N 5, p. 1108-1111.

- Pokrovskaya I. V. and Sharkov E. A. (1987 b). Optical remote sensing study of breaking gravity wave activity with developing sea roughness. Earth Research from Space (Sov. J. Remote Sensing – English Transl.), N 3, p. 11-22.
- Pokrovskaya I. V. and Sharkov E. A. (1994). Optical remote studies of the azimuthal characteristics of the breaking of sea gravity waves. Sov. J. Remote Sensing, Vol. 11, N 2, p. 311-318.

- Pokrovskaya I. V. and Sharkov E. A. (1997). Remote study of spatial fields of moisture content in the tropical atmosphere in the process of cyclogenesis. Earth Obs. Rem. Sens. Vol. 14, N6, p. 865-874.
- Poperechenko B. A. (2000). Highly efficient antenna systems for space communications and radio astronomy. Physics-Uspekhi, Vol. 43, N 9, p. 921-923.

- Popov A. E. and Sharkov E. A. (1976). Influence of form of amplitude-frequency characteristic of radiometer set on the reception of layer medium emission . Radiotekhnika i elektronika (J. of Communic. Techn. Electronics - Engl. transl.), Vol. 21, N 2, p. 405-408.

- Popov A. E. , Sharkov E. A. , and Etkin V. S. (1974). The emissive characteristics of wet soils at microwave bands. Meteorologia i hydrologia (Russian Meteorology and Hydrology – Engl. Trans.), N 10, p. 49-57.

- Popov A. E., Sharkov E. A. , Shiraeva T. A., Etkin V. S. (1976). Radioemission characteristics of wet soil layer structures at microwave band. Trudy GGI (Trans. of State Hydrological Institute), Issue 237, Leningrad, Hydrometeoizdat, p. 143-147 (in Russian).

- Pottel R. , and Lossen O. (1967). Die Komplexe Dielectrizitätskonstante waBriger Losungen einiger 1-1-wertiger Electrolyte in frequenzbereich 0,5 bis 38 GHz. Ber. Buusenges Phys. Chem., Vol. 71, N2, p. 135-146.

- Prabhakara C., Wang I., Chang A. T. C. , and Gloersen P. (1983). A statistical examination of Nimbus-7 SMMR data and remote sensing of sea surface temperature , liquid water content in the atmosphere and surface wind speed. J. Climate and Applied Meteorology, Vol. 22, N 12, p. 2023-2037.

- Press W. H., Flannery B. P., Teukolsky S. A., and Vetterling W. T. (1986). Numerical recipes- the art of science computing. Cambridge, Cambridge University Press , 320p.

- Prigent C., Wigneron J.-P. , Rossow W. B., and Padro-Carrion J. R. (2000). Frequency and angular variations of land surface microwave emissivities: can we estimate SSM/T and AMSU emissivities from SSM/I emissivities? IEEE Trans. Geosci. Remote Sensing, Vol. 38, N 5, Part 2, p. 2373-2386.

- Prigent C., Aires F., Rossow W., Matthews E.(2001). Joint characterization of vegetation by satellite observations from visible to microwave wavelengths: A sensitivity analysis. J. Geophys. Res., Vol. 106 , No. D18 , p. 20,665-20,675.

- Prochorov A. M., Ed. (1984). Physical encyclopaedia. Moscow, “Sovetskay encyclopaedia” Publ. House, 944p. (in Russian).

- Promes P. M., Jackson T. J., and O’Neill P. E. (1988). Significance of agricultural row structure on the microwave emissivity of soils. IEEE Trans. Geosci. Remore Sensing, Vol. 26, N 5, p. 580-589.

- Pulliainen J. , Karna J.-P., and Hallikainen M . (1993). Development of geophysical retrieval algorithms for the MIMR. IEEE Trans. Geoscience Remote Sensing , Vol. 31, N 1, p. 268-277.

- Pulliainen J., Grandell J., and Hallikainen M. T. (1999). HUT snow emission model and its applicability to snow water equivalent retrieval . IEEE Trans. Geoscience Remote Sensing , Vol. 37, N 3, p. 1378-1390.

- Pulliainen J., and Hallikainen M. (2001). Retrieval of regional snow water equivalent from space-borne passive microwave observations. Remote Sensing of the Environment, Vol. 75, N 1, p. 76-85 .

- Purcell E. M. (1965). Electricity and magnetism. McGraw-Hill , New York, 459p.

- Quattrochi D. A. and Goodchild M.F. (1997). Scale in remote sensing and GIS. Berlin, Springer, 406 p.
- Rabinovich Yu. I., Schukin G. G. , and Volkov V. G. (1968). On possible errors of absolute radioemission measurements. Trudy GGO (Trans. Main Geophysical Observatory) , N 222, p. 138-148. (in Russian).
- Rabinovich Yu. I., Schukin G. G. , Volkov V. G., and Krupenio N.N.(1970). Polarization measurements of surface emission at centimeter band. Trudy GGO (Trans. Main Geophysical Observatory) , N 235, p. 72-77. (in Russian).
- Rabinovich Yu. I. , and Melentev V. V. (1970). The effect of the temperature and salinity on the emission of a smooth water surface at centimeter band. Trudy GGO (Trans. Main Geophysical Observatory) , N 235, p. 78-123. (in Russian).
- Raev M. D., Sharkov E. A. , Shiraeva T. A. , and Etkin V. S. (1975). On the calculation of the thermal radioemission for the multi-layer structures with the method of oriented graphs by computer. Radiotekhnika i elektronica (J. of Communic. Techn. Electronics - Engl. Transl.), Vol. 20, N 3, p. 632-635.
- Raffalski U., Klein U., Franke B., Langer J., Sinnhuber B. M. , Trentmann J., Kunzi K. F., and Schrems O. (1998). Ground based millimeter-wave observations of Arctic chlorine activation during winter and spring 1996/97. Geophys. Research Letters, Vol. 25, N17, p. 3331-3334.
- Raizer V. Yu. and Sharkov E. A. (1981). On electromagnetic description of closely packed dispersed media. Izvestia VUZ. Radiofizika. (Izvestiya , Radiophysics and Quantum Electronics - Engl. Transl.), Vol. 24, N 7, p. 809-818.
- Raizer V. Yu. , Sharkov E. A. and Etkin V. S. (1974) . Electrical and emissive characteristics of water at decimeter and meter wave bands. Preprint N Pr-164, Space Research Institute , Moscow, 15p. (in Russian).
- Raizer V. Yu. , Sharkov E. A. and Etkin V. S. (1975a). Influence of temperature and salinity on the radioemission of a smooth ocean surface at decimeter and meter bands. Izvestiya Akad. Nauk USSR, Fizika Atm. Okeana (Izvestya. Atmospheric and Oceanic Physics- English trans.), Vol. 11, N 6, p. 652-655.
- Raizer V. Y., Sharkov E. A. , and Etkin V. S. (1975b). On the thermal radioemission of sea surface with oil pollution. Preprint N Pr-237. Space Research Institute , Moscow, 15p. (in Russian).
- Raizer V. Y., Sharkov E. A. , and Etkin V. S. (1976). Sea foam. Physico-chemical properties. Emissive and reflective characteristics. Preprint N Pr-306. Space Research Institute , Moscow, p. 25. (in Russian).
- Raizer V. Y. , and Sharkov E. A. (1980). On dispersal structure of sea foam. Izvestia Acad. Nauk SSSR. Fizika atmosphery i okeana (Izvestiya, Atmospheric and Oceanic Physics - Engl. Transl.) , Vol.16, N 7, p.772-776.
- Raju G. and Rana S.S. (1999). OCEANSAT-1 (IRS-P4) satellite and payloads. Megha-Tropiques. First Science Workshop Proceedings,19-22 May, 1999, ISRO H.Q., Bangalore, INDIA. Eds. Narayanan M. S., Manikiam B., Gairola R. M. ISRO, CNES, p. 3.1-3.4.
- Randel D. L., Vonder Haar T. H., Ringerud M. A., Stephens G. L., Greenwald and Combs C. L. (1996) . A new global water vapour data set . Bull. Amer. Meteor. Soc., Vol. 77, N 6, p. 1233-1246.
- Raney R. K. (1983). Synthetic aperture radar observations of ocean and land. Phil. Trans. Roy. Soc. London, Vol. A309, N 1508, p. 315-323.
- Ranson K. J., Sun G., Weishampel J. F., Knox R. G. (1997). Forest biomass from combined ecosystem and radar backscatter modeling. Remote Sensing of Environment, Vol. 59, N 1, p. 118-133.
- Rao B. M. , Thapliyal P. K., Pal P. K., Manikiam B., and Dwivedi A. (1999). Large scale soil moisture estimation using microwave radiometer data. Megha-Tropiques. First Science Workshop Proceed-

- ings, 19-22 May, 1999, ISRO H.Q., Bangalore, INDIA. Eds. Narayanan M. S., Manikiam B., Gairola R. M. ISRO, CNES, p. 23.1-23.22.
- Raschke E. and Jacob D. , Eds. (1993). Energy and water cycles in the climate system. Springer -Verlag, Berlin ,ets , 467 p.
- Rassadovsky V. A. , and Troitsky A. V. (1981). Remote radiometric atmospheric studies in the zone of tropical cyclone origin. Izvestya AN . Fizika atmosphery i okeana. (Izvestiya, Atmospheric and Oceanic Physics –English Transl.), Vol. 17, N 7, p. 698-705.
- Ray P. (1972). Broad band complex refractive indiced of ice and water. Applied Optics, Vol. 11, N 8, p. 1836-1844.
- Rehm G., and Brand H. (1999). Imaging of plants using radiometry at 600 GHz. IEEE IGARSS 1999 Proceedings, Vol. V , IEEE, New York, p. 2637-2639.
- Reid G. C. and Gage K. S. (1996). The tropical tropopause over the western Pacific : wave driving, convection and the annual cycle. J. Geophysical Research, Vol. 101, N D16, p. 21233-21241.
- Reising S. C. , and Camps A. J. (2000). A model of the wind direction signature in the Stokes emission vector from the ocean surface at microwave frequencies. IEEE IGARSS 2000 Proceedings, Vol. VI, IEEE, New York, p. 2745-2747.
- Reutov E. A. ,. and Shutko A. M. (1990a). Theoretical studies of the microwave emission of unified wet salty soils. Earth Research from Space (Earth Obs. Remote Sensing - Engl. Transl.). N 3. P. 73-81.
- Reutov E. A. ,. and Shutko A. M. (1990b). Experimental studies of the microwave emission of unified wet salty soils. Earth Research from Space (Earth Obs. Remote Sensing - Engl. Transl.). N 4. P. 78-84.
- Robinson I.S. (1985). Satellite Oceanography. Chichester ets.: Wiley/PRAXIS, 456 p.
- Roca R. (1999). Deep convection and water vapor in the tropical climate. Megha-Tropiques. First Science Workshop Proceedings, 19-22 May, 1999, ISRO H.Q., Bangalore, INDIA. Eds. Narayanan M. S., Manikiam B., Gairola R. M. ISRO, CNES, p. 10.1-10.10.
- Roca R. , and Ramanathan V. (2000). Scale dependence of monsoonal convective systems over the Indian Ocean. J. Climate, Vol. 13, N4, p. 1286-1298.
- Rochard G. (2000). “Do or Die” frequency list for passive remote sensing of the Earth. IEEE IGARSS 2000 Proceedings, Vol. VI, IEEE, New York, p. 2455-2456.
- Rodgers E.B. and Adler R.F. (1981). Tropical cyclone rainfall characteristics as determined from a satellite passive microwave radiometer. Mon. Weather Rev., Vol.109, p.506-521.
- Rodgers E.B., Chang S.W., Pierce H.F. (1994). A satellite observational and numerical study of precipitation characteristics in western North Atlantic tropical cyclones. J. Appl. Meteor., Vol.33, p.573-593.
- Rodrigues-Iturbe I. and Rinaldo A. (1997). Fractal river basins: chance and self-organization. Cambridge: Cambridge University Press, 547p.
- Rosenfeld D. and Woodley W. L. (2000). Deep convective clouds with sustained supercooled liquid water down to $-37,5^{\circ}$ C. Nature, Vol. 405, N 6785, p. 440-442.
- Rosenkranz P. W. (1975). Shape of the 5 mm oxygen band in the atmosphere. IEEE Trans. Antennas Propag., Vol. 23, N 4, p. 498-506.
- Rosenkranz P. W., and Staelin D. H. (1972). Microwave emissivity of ocean foam and its effect on nadir radiometric measurements. J. Geophysical Research, Vol.77, N 33, p. 6528-6538.

- Rosenkranz P. W., Barath F. T., Blinn J. C., Johnston E. J., Lenoir W. B., Staelin D. H., and Waters J. W. (1972). Microwave radiometric measurements of atmospheric temperature and water from aircraft. *J. Geophysical Research*, Vol. 77, N30, p. 5833-5844.
- Rosenkranz P. W., Komichak M. J. , and Staelin D. H. (1982). A method for estimation of atmospheric water vapor profiles by microwave radiometry. *J. Applied Meteorology*, Vol. 21, N 9, p. 1364-1370.
- Rosenlof K. H., Tuck A. F., Kelly K. K., Russell J. M., and McCormick M. P. (1997).Hemispheric asymmetries in water vapor and inferences about transport in the lower stratosphere. *J. Geophysical Research*, Vol. 102, N D11, p. 13213-13234.
- Rosolen C., Clerc V. , and Lecacheux SA. (1999). High dynamic range, interferences tolerant, digital receivers for radio astronomy. *Radio Science Bulletin*, N 291, p. 6-12.
- Rossow W. B. and Schiffer R. A. (1991). ISCCP cloud data product. *Bull. Amer. Meteorol. Soc.*, Vol. 72, N 1, p. 2-20.
- Rozenberg V. I. (1972). Electromagnetic scattering and attenuation in atmospheric particles. Leningrad, Gidrometeoizdat , 348p. (in Russian).
- Prigent C. , Phalippou L., and English S. (1997). Variation inversion of the SSM/I observations during the ASTEX campaign. *J. Applied Meteorology*, Vol. 36, N 5, p. 493-508.
- Ruf K. (1999). Technical and engineering challenges for the future of radio astronomy. *Radio Science Bulletin* , N 291, p. 13-18.
- Ruf C. S. (2000a). Detection of calibration drift in spaceborne microwave radiometers using a vicarious cold reference. *IEEE Trans. Geosci. Remote Sens.*, Vol. 38, N 1, P.44-52.
- Ruf C. S. (2000b). Statistical analysis of a lower bound on microwave radiometer brightness temperatures from space. *IEEE IGARSS 2000 Proceedings*, Vol. VII, IEEE, New York, p. 2824-2826.
- Ruf C. S., and Zhang H. (2001). Performance evaluation of single and multichannel microwave radiometers for soil moisture retrieval. *Remote Sensing Envir.* , Vol. 75, N 1, p. 86-99.
- Ruf C. S. , Swift C. T. , Tannerr A. B., and LeVine D. M. (1988). Interferometric synthetic aperture microwave radiometry for the remote sensing of the Earth. *IEEE Trans. Geoscience Remote Sensing*, Vol. 26, N 5, p. 597-611.
- Ruf C. S. , Principe C. M., and Neeck S. P. (2000) . Enabling technologies to map precipitation with near-global coverage and hour-scale revisit times. *IEEE IGARSS 2000 Proceedings*, Vol. VII, IEEE, New York, p. 2988-2990.
- Rysakov W., and Ston M. (2001). Light scattering by spheroids. *J. Quant. Spectr. Radiative Transfer*, Vol. 69, N 5, p. 651-665.
- Rytov S. M. (1953). The theory of electrical fluctuations and thermal emission. Moscow, USSR Academy Sciences Publ. House, 230p. (in Russian).
- Rytov S. M. (1966) . Introduction in statistical radiophysics. Moscow, "Nauka" Publ. House, 404 p. (in Russian).
- Rytov S. M. , Kravtsov Yu. A. , and Tatarskii V. I. (1978). Introduction in statistical radiophysics.Part II. Random fields. Moscow, "Nauka" Publ. House, 462 p. (in Russian).
- Sabins F.F. (1987) . Remote sensing. Principles and interpretation. N. Y. : W. H. Friman and Company, 368 p.
- Sadeghi A. M., Scott H.D., Waite W. P., Asrar G. (1988).Estimating soil water evaporation using radar measurements. *IEEE Trans. Geoscience Remote Sensing*. Vol. 26, N 4, p. 490-493.
- Sadourny R., Cordon F. and Bonazzola M.(1999). Tropical convection , water vapour transport and the general circulation of the atmosphere. *Megha-Tropiques*. First Science Workshop Proceedings,19-22 May, 1999, ISRO H.Q., Bangalore, INDIA. Eds. Narayanan M. S., Manikam B., Gairola R. M. ISRO, CNES, p. 11.1-11.10.
- Sakerin S. M. and Kabanov D. M. (1997). Using local and integral humidity characteristics for estimating vertical profiles. *Optics Atm. Ocean* , Vol. 10, N 1, p. 87-96 (in Russian).

- Sasaki Ya., Asanuma I., Muneyama K., Naito G., Suzuki T. (1987). The dependence of sea-surface microwave emission on wind speed, frequency, incidence angle, and polarization over frequency range from 1 to 40 GHz. IEEE Trans. Geoscience Remote Sensing., Vol. 25, N 11, p. 138-146.
- Savorskii V.P. , Armand N. A. and Milshin A.A. (2000). Experimental method for recover of antenna directional pattern of satellite borne instrumentation with local regularization method. Radiotekhnika i electronika (J. of Communic. Techn. Electronics - Engl. transl.), Vol. 45, N 10, p. 1210-1213.
- Saxton J. A. (1952). Dielectric dispersion in pure polar liquids of very high frequencies . Proc. Roy. Soc., Vol. 213A, N 115, p. 473-492.
- Schilling H. (1972). Statistische physik in beispielen . VEB Fachbuchverlag, Leipzig, 420p.
- Schmetz J. , Tjemkes S. A., Gube M., van de Berg L. (1997). Monitoring deep convection and convective overshooting with Meteosat . Adv. Space Res., Vol. 19, N3, p. 433-441.
- Schmitt R. , and Montgomery E. (2000). Salinity- a missing piece in the climate puzzle. Backscatter, Vol. 11, N 3, p. 10-16.
- Schmugge T. and O'Neill P. (1986). Passive microwave soil moisture research. IEEE Trans. Geoscience Remote Sensing. Vol. 24, N 1, p. 12-22.
- Schugge T. J. , Wang J. R. , and Asrar G. (1988). Results from the push broom microwave radiometer flights over the Konza Prairie in 1985. IEEE Trans. Geosc. Remote Sensing, Vol. 26, n 5, p. 590-596.
- Schuster H. G. (1984). Deterministic Chaos. An Introduction. Physik -Verlag GmbH, Weinheim, 240 p.
- Schultz G. A. (1988) .Remote sensing in hydrology. J. Hydrology. Vol. 100, p. 239-265.
- Schultz G. A., and Engman E. T. , Eds. (2000). Remote sensing in hydrology and water management. Springer-Verlag, Berlin , Heidelberg, 483 p.
- Schweitzer F. , Ed. (1997). Self-organization of complex structures. Gordon and Breach, Amsterdam, 622 p.
- Scofronick-Jackson G. M., and Wang J. R. (2000). The estimation of hydrometeor profiles from wide-band microwave observations. J. Applied Meteorology, Vol. 39, N 10, p. 1645-1657.
- Scott J. C. (1978). The historical development of theories of wave-calming using oil. History of Technology, Vol. 3, p. 163-186.
- Scott J. C. (1999). Ocean surface slicks- pollution, productivity, climate and life-saving. IEEE IGARSS 1999 Proceedings, Vol. III, IEEE, New York, p. 1463-1468.
- Scott J. C. , and Thomas N. H. (1999). Sea surface slicks-surface chemistry and hydrodynamics in radar remote sensing. Proceedings, Conference on wind-over-wave couplings, Salford University, 1997. Taylor & Francis, p. 221-229.
- Sethna J. P. , Dahmen K. A. , and Myers C. R. (2001). Crackling noise. Nature, Vol. 410, N 6825, p. 242-250.

- Shapirovskaia N. Ya. (1973) . On polarization radiothermal investigations of surfaces with spacecrafts. Kosmicheskie issledovania (Space Research- English Transl.) , Vol. 11, N 6, p. 907-912.
- Sharkov E. A. (1978). On using microwave radiometers for study of thermal interaction in atmosphere-ocean system. Radiotekhnika i electronika. (J. of Communic. Techn. Electronics - Engl. Transl.) Vol. 23, N 3, p. 655-658.
- Sharkov E. A. (1983) . On estimation of relaxation models for dielectric properties of water for remote sensing problems. Preprint N Pr-800. Space Research Institute , Moscow, p. 15. (in Russian).
- Sharkov E. A. (1984). Relaxation model for dielectric properties of concentrated electrolytes.Zhurnal Fizicheskoi Khimii (Journal of Phys. Chemistry-English transl.), Vol. 58, N 7, p. 1705-1710 .
- Sharkov E. A. (1993 a). Spatial features of sea wave breaking fields. « Symposium on the Air-Sea Interface. Marseilles. France. June 24-30.1993» . Book of Abstracts, p. 21.

- Sharkov E. A. (1993 b). Scaling properties of sea wave breaking fields. *Annales Geophysicae*. Part II, Suppl. II to Vol. 11, p. C310.
- Sharkov E. A. and Bondur V. G. (1993).Statistical characteristics of linear and area geometry of foam structures on the disturbed sea surface. «A Symposium on the Air-Sea Interface . Marseille. France. June 24-30.1993.» Book of Abstracts, p. 177.
- Sharkov E.A.(1994). Experimental investigations of lifetimes for breaking wave disperse zone. *Izvestia Acad. Nauk. Fizika atmosphery i okeana* (Izvestiya, Atmospheric and Oceanic Physics - Engl. Transl.), Vol.30, N 6, p.844-847.
- Sharkov E. A. (1995). Optical investigations of temporal evolution of foam structures on sea surface. *Earth Obs. Rem. Sens.*, Vol. 12, N 1, p. 88-101.
- Sharkov E.A. (1996a). The global tropical cyclogenesis as relaxation oscillator of the kinetic-diffusional type. *Annales Geophysicae*, Supplement II to Vol.14, Part II, p.C654.
- Sharkov E.A. (1996b). The global tropical cyclogenesis model for climate applications. «31 st Sci. Assembly of COSPAR, 14-21 July 1996». Abstracts. The University of Birmingham. England, p.8.
- Sharkov E. A. (1996 c). Precision relaxation model of dielectric properties of water for remote sensing problems. *Earth Obs. Rem. Sens.*, Vol. 13, N 6, p. 887-902.
- Sharkov E. A. (1996 d) . The nonlinear evolution of breaking sea gravity waves. *Annales Geophysicae*, Suppl. II to Vol. 14, Part II, p. C542.
- Sharkov E. A. (1997 a). Airspace observations of tropical cyclones. *Earth Research from Space (Earth Obs. Remote Sensing - Engl. Transl.)*. 1997. N 6. P. 78-111.
- Sharkov E.A. (1997 b). The global tropical cyclogenesis as a geophysical system slightly out of equilibrium. *Earth Obs. Remote Sensing* . 1997. Vol. 14. N6. P. 865-874.
- Sharkov E. A. (1998). Remote sensing of tropical regions. Chichester, N. Y., Weinheim, Brisbane, Singapore, Toronto. John Wiley and Sons / PRAXIS . 320 p.
- Sharkov E. A. (2000). Global Tropical Cyclogenesis .London, Berlin,Heidelberg, New York, etc. Springer/PRAXIS. 375 p.
- Sharkov E. A., and Etkin V. S. (1976). Possibilities of remote sensing of Earth surface with radio-physical instruments. In “ Space investigations of Earth’s resources “, Moscow, “Nauka” Publ. House, p. 99-109 (in Russian).
- Shchuko O. B. and Kartashov D. W. (1999) . Dependence of the Mercury radio emission from the upper cover structure and composition. *Izvestia VUZ. Radiofizika*. (Izvestiya , Radiophysics and Quantum Electronics - Engl. Transl.), Vol. 42, N 3, p. 203-214.
- Shepard M. K. , Brackett R. A. , and Arvidson R. E. (1995). Self-affine (fractal) topography: surface parameterization and radar scattering. *J. Geophysical Research*, Vol. 100, N E6, p. 11,709-11,718 .
- Shepard M. K. , and Campbell B. A. (1999). Radar scattering from a self-affine fractal surface: near-nadir regime. *Icarus*, Vol. 141, N 1, p. 156-171.
- Shibata A. (2000). AMSR/AMSR-E algorithm development and data distribution. *IEEE IGARSS 2000 Proceedings*, Vol. I, IEEE, New York, p. 59-61.
- Shifrin K. S. (1951). Scattering of light by a turbid medium. Moscow, Gostechizdat, 288p. (in Russian)
- Shifrin K. S. , Ed. (1968). Tables for light scattering. Vol. III. Coefficients of extinction, scattering and beam pressure. Leningrad, Hydrometeorological Publishing House, 350p. (in Russian).
- Shifrin K. S. (1971). Investigation of substance’s properties by single-scattering. In “Theoretical and applied problems of light’s scattering “. Minsk, “Nauka i technika” Publ. House , p. 228-244.
- Shimoda H. (2000). Global change observation mission (GCOM). *IEEE IGARSS 2000 Proceedings*, Vol. I, IEEE, New York, p. 53-55.
- Shin R. T. and Kong J. A. (1982). Theory for thermal microwave emission from a homogeneous layer with rough surfaces containing spherical scatterers. *J. Geophys. Research*, Vol. 87, N 7, p. 5566-5576.

- Shulgina E. M. (1975). Radioemission of a vertically nonuniform medium. Trudy GGO (Trans. Main Geophysical Observatory), N 331, p. 64-72 (in Russian).
- Shulgina E. M. (1972). Calculation of emissivity of disturbed sea surface at microwave band. Izvestia AN. Fizika atmosphery i okeana . (Izvestiya. Atmospheric and Oceanic Physics- Engl. Transl.) Vol. 8, N 7, p. 773-776.
- Shutko A. M. (1982). Microwave radiometry of lands under natural and artificial moistening. IEEE Trans. Geosci. Remote Sensing. Vol. 20, N 1, p. 18-26.
- Shutko A. M. (1986). Microwave radiometry of water surface and soils. "Nauka" Publ. House, Moscow, 189p. (in Russian).
- Siegel R. and Howell J. R. (1972). Thermal radiation heat transfer. New York, McGraw-Hill Book Company, 910p.
- Sihvola A.H. and Kong J. A. (1988). Effective permittivity of dielectric mixtures. IEEE Trans. Geosci. Remote Sensing, Vol. 26, N4, p. 420-429.
- Siegel R. and Howell J. R. (1972) . Thermal radiation heat transfer . McGraw-Hill Book Company, New York, 420 pp.
- Singh R. P., Mishra N. C. , and Sahoo P.K. (2000). Seasonal variations of brightness temperature at 85 GHz over India. Adv. Space Res., Vol. 26, N 7, p. 1081-1084.
- Simpson J., Ed. (1988). Report of the science steering group for a Tropical Rainfall Measuring Mission (TRMM). GSFC, Maryland, 94 p.
- Simpson J., Adler R.F., North G.R. (1988). A Proposed Tropical Rainfall Measuring Missions (TRMM) Satellite. Bull. Americ. Meteor. Soc. Vol.69, N 3, p. 278-295.
- Simpson J., Kummerow C. D. , Meneghini R. , Hou A., Adler R. F., Huffman G., Barkstrom B., Wielicki B., Goodman S.J., Christian H., Krishnamurti T. N., Yang S., and Ferrier B. (2000). The tropical rainfall measuring mission (TRMM). Earth Research from Space (Earth Obs. Remote Sensing - Engl. Transl.). N4. P. 71-90.
- Sinyukov V. V. (1976). Structure of the single-atom fluids, water and water solutions of electrolytes. Moscow, Nauka Publ. House, 256p. (in Russian).
- Skofronick-Jackson G. M. , and Wang J. R. (2000). The estimation of hydrometeor profiles from wide-band microwave observations. J. Applied Meteorology, Vol. 39, N10, p. 1645-1656.
- Skolnik M. I. (1980). Introduction to radar systems. McGraw-Hill Book Company, New York, 450 pp.
- Slater J. C. (1942). Microwave transmission. McGraw-Hill Book Company, New York, London. 308 pp.
- Smirnov M. T. (1984). Modeling of rain radioemission by Monte-Carlo method. Izvestia AN. Fizika atmosphery i okeana . (Izvestiya. Atmospheric and Oceanic Physics- Engl. Transl.) Vol. 12, N 9, p. 820- 826.
- Smirnov A. I. and Sharkov E. A. (1979). On dielectric and emissive properties of the strong salt water. Izvestya VUZ, Radiofizika (Radiophysics and Quantum Electronics- English Transl.), Vol. 22, N 10, p. 1285-1287.
- Smith P. M. (1988). The emissivity of sea foam at 19 and 37 GHz. IEEE Trans. Geosci. Remote Sensing, Vol. 26, N 5, p. 541-547.
- Smith D. M. , Kniveton D.R. , and Barrett E. C. (1998). A statistical modeling approach to passive microwave rainfall retrieval. J. Applied Meteorology, Vol. 37, N 2, p. 135-154.
- Sobolev V. V. (1963). A treatise on radiative transfer. Van Norstrand, Princeton , N. J. , 319p.
- Sobolev S. L. (1997). Local non-equilibrium transport models. Physics-Uspekhi, Vol. 40, N10, p. 1043- 1053.
- Sobti A. , and Moore R. K. (1976). Correlation between microwave scattering and emission from land and sea at 13,9 GHz. IEEE Trans. Geoscince Electronics, Vol. 14, N 4, p. 93-96.

- Sobue S., Tomii N., Moriyama T., Ishida C., Kohji T., and Kamijo S. (2000). NASDA's future Earth observation satellite plan. IEEE IGARSS 2000 Proceedings, Vol. VI, IEEE, New York, p. 2596-2598.
- Soglasnova V. A. and Sholomitskii G.B. (1971) On bolometric measurements of cosmic microwave background radiation. Preprint N Pr-90, Space Research Institute, Moscow, p. 8 (in Russian).
- Sorai K., Nishiyama K., Nasegawa T., Miyaji T., and Ukita N. (1998). A 500-MHz acousto-optical spectrometer for the Nobeyama 45-m radio telescope. Technical report N 60, Nobeyama Radio Observatory, Nagano, 10p.
- Sornette D. (2000). Critical phenomena in natural sciences. Springer. Berlin, Heidelberg, New York, etc., 434 p.
- Sorooshian S., Hsu K.-L., Gao X., Gupta H. V., Imama B., and Braithwaite D. (2000). Evaluation of PERSIANN system satellite-based estimates of tropical rainfall. Bull. Amerc. Meteor. Soc., Vol. 81, N 9, p. 2035-2046.
- Srokosz M. A. (1986). On the probability of wave breaking in deep water. J. Physical Oceanography, Vol. 16, N 2, p. 3832-385.
- Staelin D. H. (1969). Passive remote sensing at microwave wavelengths. Proc. IEEE, Vol. 57, N 4, p. 427-439.
- Staelin D. H. (1981). Passive microwave techniques for geophysical sensing of the Earth from satellites. IEEE Trans. Antennas Propagation , Vol. 29, N 4, p. 683-687.
- Steel M., Sheppard R. , and Grant E. (1984). A precision method for measuring the complex permittivity of solid tissue in the frequency domain between 2 and 18 GHz. J. Phys. E: Sci. Instr. , Vol. 17, N 1, p. 30-34.
- Stephens G. L., Jakob C., and Miller M. (1998). Atmospheric ice - a major gap in understanding the effects of clouds on climate. GEWEX News, Vol. 8, N 1 , p. 1, 4-8.
- Steranka L., Rodgers E. B., Gentry R. (1986). The relationship between satellite measured convective bursts and tropical cyclone intensification. Mon. Weather Rev., Vol.114, N8, p.1539-1546.
- Stockade T. N., Anderson D. L. T., Alves J. O. S., and Balmaseda M. A. (1998) . Global seasonal rainfall forecasting using a coupled ocean-atmosphere model. Nature. Vol. 392. N 6674.p. 370-373.
- Stoffregen H., Zenker T., and Wessolek G. (2002). Accuracy of soil water content measurements using ground penetrating radar: comparision of ground penetrating radar and lysimeter data. J. Hydrology, Vol. 267, N 3-4, p. 201-206.
- Stogryn A. (1967). The apparent temperature of the sea at microwave frequencies. IEEE Trans. Antennas Propagat., Vol. AP-15, N 3, p. 278-286.
- Stogryn A. (1970). The brightness temperature of a vertically structured medium. Radio Science , Vol. 12, N 12, p. 1397-1406.
- Stogryn A. (1971). Equations for calculating the dielectric constant for saline water. IEEE Trans. Microwave Theory Technology, vol. 19, N 8, p. 733-736.
- Stogryn A. (1972). The emissivity of sea foam at microwave frequencies. J. Geophysical Research , Vol. 77, N 9, p. 1658-1666.
- Stogryn A. (1986). Study of the microwave brightness temperature of snow from the point of view of strong fluctuation theory. IEEE Trans. Geosci. Remote Sensing, Vol. 24, N2, p. 220-231.
- Stogrin A. P. , Buttler C. T. , and Bartolac T. J. (1994) Ocean surface wind retrievals from special sensor microwave imager data with neural networs. J. Geophysical Research, Vol. 99, p. 981-984.
- Stone K. (1979). Ocean science. J. Wiley and Sons, N. Y., Chichester , 609 p.
- Stratton J. A. (1941). Electromagnetic theory. New York, London, McGraw-Hill Book Company, Inc., 615p.
- Strukov I. A. , and Skulachev D. P. (1984). "Relict" experiment. The first results. Pisma v astronomicheskii journal (Astronomy Letters- English transl.), Vol. 10, N1, p. 3-13.

- Strukov I. A. , and Skulachev D. P. (1986). Investigations of the anisotropy of cosmic microwave background. "Relict" experiment. In "Results of sciences and technique . Astronomy." Vol. 31. Astrophysics and space physics. Ed. by Sunyev R. A. Moscow, VINITI Publ. House, p. 37-73.
- Sunyaev R. A. , Ed.(1986). Space Physics. Small encyclopaedia. Moscow, "Soviet encyclopaedia" Publ. House. 783p. (in Russian).
- Szwarnowski R. (1982). A transmission line cell measuring the permittivity of liquids over the frequency range 90 MHz to 2 GHz. J. Phys. E : Sci. Instrum., Vol.15, N 10, p. 1068-1072.
- Tack R. E. (1994). Commercial distribution of data from RADARSAT, Canada's Earth observation satellite. Earth Research from Space, N 2, p. 118-124.
- Takanashi N., Kawanishi T., Kojima K., Oikawa K., Kuroiwa H., Okamoto K., Kozu T., Okumura M., Nakatsuka H. and Nishikawa K (2000). Two year operation of the Precipitation Radar (PR) on-board TRMM satellite. IEEE IGARSS 2000 Proceedings, Vol. III, IEEE, New York. P 1343-1345.
- Takayasu H. (1984). Stable distribution and Levy process in fractal turbulence. Progress of Theoretical Physics, Vol. 72, N 3, p. 471-479.
- Takayasu H. (1988). Fractal clusters and stable distribution. J. Physical Society Japan, Vol. 57, N 8, p. 2585-2587.
- Tang C. C. H. (1974). The effect of droplets in the air-sea transition zone on the sea brightness temperature. J. Physical Oceanography, Vol. 4, N 10, p. 579-593.
- Taylor J. P. and English S. J. (1995). The retrieval of cloud radiative and microphysical properties using combined near-infrared and microwave radiometry. Q. J. R. Meteorol. Soc., Vol. 121, p. 1083-1112.
- Taylor R. P. , Micolich A. P. , and Jonas D. (1999). Fractal analysis of Pollock's drip paintings. Nature, Vol. 399, N 6735, p. 422.
- Terradellas E., Morales G., Cuxart J., and Yague C. (2001). Wavelet method: application to the study of the stable atmospheric boundary layer under non-stationary conditions. Dynamics of Atmospheres and Oceans, Vol. 34, N 3-4, p. 225-244.
- Theon J.S., Matsuno T., Sakato T., Fuguno N., Eds. (1992). The global role of tropical rainfall. A. Deepak Publishing , Hampton, Va., 350 p.
- Thomas G. E. and K. Stamnes (1999). Radiative transfer in the atmosphere and ocean. Cambridge U. P. , New York, 517 p.
- Tichonov A. N. , and Arsenin V. Y. (1979). Methods of solution for non-correct problems. Moscow, "Nauka" Publ. House, 288p.
- Tikhonova T.V. , and Troitskii V. S. (1970). The thermal emission of the Moon and physical properties of its surface layer. Izvestia VUZ. Radiofizika. (Izvestiya , Radiophysics and Quantum Electronics - Engl. Transl.), Vol. 13, N 9, p. 1273-1311.
- Tilford S.G., Asrar G., Backlund P.W.(1994). Mission to planet Earth. Adv. Space Res., Vol.14, N1, p.5-9.
- Trenberth K. E. (1997) . Atmospheric moisture residence times and cycling: implications for how precipitation may change as climate changes. GEWEX News, Vol. 7, N 3, p. 1, 4-6.
- Trier S. B., Skamarock W. C., LeMone M. A. (1997). Structure and evolution of the 22 February 1993 TOGA COARE squall line: organization mechanism inferred from numerical simulation . J. Atmospheric Science , Vol. 54, N 3, p. 386-407.
- TRMM Office (1994). Meeting of the Tropical Rainfall Measuring Mission (TRMM) Joint Science Team (JTST). NASA/GSFC pub., Greenbelt, Maryland, Sept. 13-15, 1994, 266 pp.
- Troitskii V. S. (1951). On the theory of the measurement of weak signals with continuous spectrum. Jurnal technicheskoi phisiki (Journal of technical physics) . Vol. 21, N3,p. 994-1003 (in Russian).

- Troitskii V. S. (1954). On the theory of Moon's radioemission. Astronomicheskii jurnal (Astronomical Journal) , Vol. 31, N 6, p. 511-528 (in Russian).
- Troitskii V. S. (1967). Results of the Moon's investigation by its self-radiation. Izvestia VUZ. Radiofizika. (Izvestiya , Radiophysics and Quantum Electronics - Engl. Transl.), Vol. 10, N 9-10 , p. 1266-1282.
- Troitsky A. V. (1983). On possibility of atmospheric pressure remote determination by radiometric method from the Earth artificial satellite. Earth Research from Space (Earth Obs. Remote Sensing - Engl. transl.), N 4, p.33-38.
- Troitsky A. V. , Gajkovich K. P. , Gromov V. D., Kadygov E. N., and Kosov A. S. (1993). Thermal sounding of the atmospheric boundary layer in the oxygen absorption band center at 60 GHz. IEEE Trans. Geoscience Remote Sensing , Vol. 31, N 1, p. 116-120.
- Trokhimovskii Yu. G. (1997). The model for microwave thermal emission of sea surface with waves. Earth Research from Space (Earth Obs. Remote Sensing - Engl. transl.), N1, p. 39-49.
- Trokhimovski Yu.G., Westwater E. R. , Han Y., and Leuski V. E. (1998) . Air and sea surface temperature measurements using a 60-GHz microwave rotating radiometer. IEEE Trans. Geoscience Remote Sensing , Vol. 36, N 1, p. 3-15.
- Trokhimovski Yu.G., Irisov V. G., Westwater E. R. , Fedor L. S. , and Leuski V. E. (2000). Comparison of the sea surface brightness temperature measured during the Coastal Ocean Probing Experiment (COPE'95) from a blimp with model calculations. In "Microwave Radiometry and Remote Sensing of the Earth's Surface and Atmosphere". Eds.: Pampaloni P. and Paloscia S., VSP BV , Utrecht, Boston, Koln, Tokyo , p. 13-20.
- Truman W. M., Balanis C. A. , and Holmes J. I. (1977). Three-dimensional vector modeling and restoration of flat finite wave tank radiometric measurements. IEEE Trans. Antennas Propag., Vol. 25, N 1 , p. 95-104.
- Tsang L., Njoku E. , and Kong J.A. (1975). Microwave thermal emisson from a stratified medium with nonuniform temperature distribution.J. Applied Physics, Vol. 47, N 12, p. 5127-5133.
- Tsang L., and Kong J.A. (1976). Microwave remote sensing of a two-layer random medium. IEEE Trans. Antennas Propagation, Vol. 24, N 3, p. 283-288.
- Tsang L., and Kong J.A. (1977). Theory for thermal microwave emission from a bounded medium containing spherical scatterers. J. Applied Physics, Vol. 48, N 8, p. 3593-3599.
- Tsang L., Kong J. A., Njoku E., Staelin D. H., Waters J. W. (1977). Theory for microwave thermal emission from a layer of cloud or rain. IEEE Trans. Antennas Propag., Vol. 25, N 5 , p. 650-657.
- Tseytlin N. M. (1966). Application of radioastronomical methods in antennas technique. Moscow, "Sov. Radio" Publ. House, 213p. (in Russian).
- Tuchkov L. T. (1968) . Natural noise emissions at radiofrequencies. Moscow, "Sov. Radio" Publ., 161 p. (in Russian).
- Ulaby F. T., Moore R. K., Fung A.K. (1981, 1982, 1986). Microwave remote sensing- active and passive. Vol. I, II, III. Addison-Wesley Pub. Co., Reading, Mass., 2162 p.
- Ulaby F. T., Haddock T. F., Austin R . T. (1988). Fluctuation statistics of millimeter-wave scattering from distributed targets. IEEE Trans. Geoscience Remote Sensing,. Vol.26, N 3, p. 268-281.
- Vasil'ev L. N., Tyuflin A. S. (1992). The fractal nature of the spatial structure of geosystems. Sov. J. Remote Sensing, Vol. 9, N4, p. 630-642.
- Van Loon R. , and Finsy R. (1975). The precise microwave permittivity measurement of liquids using a multipoint technique and curve-fitting procedure. J. Phys. D : Appl. Phys. , Vol. 8, N 10, p. 1232-1243.
- Varadan V. K. , Bringi V. N., Varadan V. V. , and Ishimaru A. (1983). Multiple scattering theory for waves in discrete random media and comparision with experiments. Radio Science, Vol. 18, N 3, p. 321-327.

- Velden C. S. and Smith W.L. (1983). Monitoring tropical cyclone evolution with NOAA satellite microwave observations. *J. Climate and Applied Meteor.*, Vol.22, N5, p.714-724.
- Venslavskii V. B., Vorsin N. N. , Gaidanskii S. I., Gershenson V. E. , Glotov A. A. , Gromov V. K. , Lazarenko Y. P. , Mirovskii V. G., Stepanov K. G., Shamba A. S., and Etkin V. S. (1987). Shipborne gyrostabilized set for the microwave remote sensing of sea surface. Preprint N Pr-1246, Space Research Institute, Moscow, 34p.(in Russian).
- Veremey V. V. , Gorbunova T. A. , and Pugovkin L. V. (1978) . Energy balance with a light reflection from isotropic media boundary. *Optika i spectroscopia (Optics and spectroscopy)* , Vol. 44, N2, p. 345- 350 (in Russian) .
- Veselov V.M., Miltskii Yu.A., Mirovskii V.G., Sharkov E. A. and Etkin V.S.(1981) Experimental techniques for on-board radiometric antenna parameter determination . *Sov. J. Remote Sensing*, N2, p. 247-262.
- Vetlov I.P. and Veltishev N.F., Eds. (1982). Guide on using of satellite data for weather analysis and forecasting. Leningrad, Gidrometeoizdat, 292 pp (in Russian).
- Vicsek T. (1992). Fractal growth phenomena. World Scientific , Singapore etc., 528p.**
- Viltard N., Obligis E., Marecal V. , and Klapisz C. (1998). Retrieval of precipitation from microwave airborne sensors during TOGA COARE. *J. Applied Meteorology*, Vol. 37, N 7, p. 701-717.
- Vinnikov K. Y., Robock A., Qiu S., Entin J. K., Owe M., Choudhury B. J., Hollinger S. E. and Njoku E. G. (1999) . Satellite remote sensing of soil moisture in Illinois, United States. *J. Geophysical Research*, Vol. 104, N D4, p. 4145-4168.
- Vinogradov B. V. (1976). Spacio-temporal characteristics of radiothermal emission in the tropics on ESMR data from “Nimbus-5”. *Doklady Acad. Nauk* (Trans. of Russian Academy of Sciences / Earth Science Section- Eng. Transl.) , Vol.228, N5, p.1057-1060.
- Vinogradova M. B., Rudenko O. V., and Suchorukov A. P. (1979). Waves theory. Moscow, “ Nauka” Publishing House, 383 p. (in Russian).
- Volkov A. A. , Irisova N. A. , Lebedev S. N. , and Maltsev V. I. (1980). Measurements of ϵ' and ϵ'' of fluids at submillimeter band using the method of LRW-spectroscopy. Abstracts of III all-union Symp. on mm and submm waves. Gorkii , Vol.I, p. 215-216. (in Russian).
- Vorsin N. N. ,Glotov A. A., Mirovskii V. G., Raizer V. Y., Troizkii I. A., Sharkov E.A., and Etkin V. S. (1984). Natural radioemissive measurements of sea foam structures. *Sov. J. Remote Sensing* , Vol. 2, N3, p. 520-525.
- Voss R. (1989). Random fractals: self-affinity in noise, music, mountains and clouds. *Physica D* , Vol. 38, p. 362- 371.
- Wang J. R. , Boncyk W. C., Dod L. R. , and Sharma A. K. (1992). Retrieval of total precipitable water over high-latitude regions using radiometric measurements near 90 and 183 GHz. *J. Applied Meteorology*, Vol. 31, N 1`2, p. 1368-1378.
- Wang J. R. , Meneghini R., Kumagai H., Wilheit T. T., Boncyk W. C., Racette P., Tesmer J. R. , and Maves B. (1994). Airborne active and passive microwave observations of super typhoon Flo. *IEEE Trans. Geoscience Remote Sensing*, Vol. 32, N 2, p. 231-242.
- Wang J. R. , Racette P. , and Chang L. A. (1997a). MIR measurements of atmospheric water vapor profiles. *IEEE Trans. Geoscience Remote Sensing*, Vol. 35, N 2, p. 212-223.
- Wang J. R., Spinhirne J. D. , Racette P., Chang L. A. , and Hart W. (1997b). The effect of clouds on water vapor profiling from the millimeter-wave radiometric measurements. *J. Applied Meteorology*, Vol. 36, N 9, p. 1232-1244.
- Wang J. R. , Zhang J. , and Racette P. (1997c). Storm-associated microwave signatures in the frequency range of 90-220 GHz. *J. Atmospheric Oceanic Technology*, Vol. 14, N 1, p. 13-31.

- Wang J. R. , Zhang J. , and Racette P. (1998a) . Multiple aircraft microwave observations of storms over the western Pacific Ocean. *Radio Science*, Vol. 33, N 2, p. 531-368.
- Wang J. R. , Racette P. , Spinhirne J. D. , Evans K. F. , and Hart W. D. (1998b). Observations of cirrus clouds with airborne MIR, CLS, and MAS during SUCCESS . *Geophysical Research Letters*, Vol. 25, N 8, p. 1145-1148.
- Weaire D., and Hutzler S. (2000). *The physics of foams* . Oxford University Press, Oxford, 224p.
- Webster P. J. (1994). The role of hydrological processes in ocean-atmosphere interactions. *Reviews of Geophysics*, vol. 32, N 4, p. 427-476.
- Weinstock E. M., Hintsa E. J., Dessler A. E., and Anderson J. G. (1995). Measurement of water vapour in the tropical lower stratosphere during the CEPEX campaign: results and interpretation. *Geophys. Research Lett.*, Vol. 22, N 23 p., 3231-3234.
- Wen B., Tsang L. , Winebrenner D. P., and Ishimaru A. (1990). Dense medium radiative transfer theory: comparison with experiment and application to microwave remote sensing and polarimetry. *IEEE Trans. Geoscience Remote Sensing*, Vol. 28, N 1, p. 46-59.
- Wende C. D. (2000). NASA remote sensing mission and frequency issues. *IEEE IGARSS 2000 Proceedings*, Vol. VI, IEEE, New York, p. 2447-2451.
- Weng F., Zhao L., Ferraro R. R., Poe G., Li X. and Grody N. C. (2003). Advanced microwave sounding unit cloud and precipitation algorithms. *Radio Science*, Vol. 38, N4, 8068, doi:10.1029/2002RS002679.
- Wentz F. J. (1975). A two-scale scattering model for foam-free sea microwave brightness temperatures. *J. Geophysical Research*, Vol. 80, N 24, p. 3441-3446.
- Wentz F. J. , Mattox L. A. , and Peteherych S. (1986). New algorithms for microwave measurements of ocean winds : applications to Seasat and the special sensors microwave imager. *J. Geophysical Research*, Vol. 91, N C2, p. 2289-2307.
- West R. D., Moghaddam M., Johnson W. T. K. , Janssen M.A., Hamilton G. A., Liepack O. G., Bunker A., Berkun A. C., and Roth L. E. (2000). Cassini observes the Earth with Ku-band radar and radiometry. *IEEE IGARSS 2000 Proceedings*, Vol.I, IEEE, New York, p. 298-300.
- Wiesmann A. and Matzler Ch. (1999). Microwave emission model of layered snowpacks. *Remote Sens. Environment*, Vol. 70, N3, p. 307-316.
- Wiesmann A., Fierz C., and Matzler Ch. (2000). Simulation of microwave emission from physically modeled snowpacks. *Annals of Glaciology*, Vol. 31, p. 397-405.
- Wigneron J. P., Calvet J. C., Chanzy A., Grosjean O., Laguerre L. (1995). A composite discrete-continuous approach to model the microwave emission of vegetation. *IEEE Trans. Geosci. Remote Sensing*, Vol. 33, N 1, p. 201-211.
- Wigneron J.-P. , Waldteufel P., Chanzy A., Calvet J.-C., Marloie O., Hanocq F., and Kerr Y. (2000). Retrieval capabilities of L-band 2-D interferometric radiometry over land surfaces (SMOS mission). In "Microwave Radiometry and Remote Sensing of the Earth's Surface and Atmosphere". Eds.: Pampanoni P. and Paloscia S. VSP BV , Utrecht, Boston, Koln, Tokyo , p. 485-492.
- Wigneron J.-P. , Calvet J.-C. , Pellarin T., Van de Griend A. A., Berger M., and Ferrazzoli P. (2003). Retrieving near-surface soil moisture from microwave radiometric observations: current status and future plans. *Remote Sensing of Environment* , Vol. 85, N 4, p. 489-506.
- Wilheit T. T. (1978). Radiative transfer in a plane stratified dielectric. *IEEE Trans. Geosci. Electronics*, Vol. 16, N 2, p. 138-143.
- Wilheit T. T. (1979). A model for the microwave emissivity of the ocean's surface as function of wind speed. *IEEE Trans. Geosci. Electronics* , Vol. 17, N 4, p. 960-972.
- Wilheit T. T. and Fowler M. G. (1977). Microwave radiometric determinations of wind speed at the surface of the ocean during BESEX . *IEEE Trans. Antennas Propagation*, Vol. 25, N 1, p. 111-120.

- Wilheit T.T. and Chang A.T.C. (1980) . An algorithm for retrieval of ocean and atmospheric parameters from the observations of the scanning multichannel microwave radiometer. *Radio Science*. Vol. 15, N 3, p. 525-544.
- Wilheit T. T. , Gleaves J. R., Gatlin J. A., Han D., Krupp B.M., Milman A. S., and Chang E. S. (1984). Retrieval of ocean surface parameters from the Scanning Multifrequency Microwave Radiometer (SMMR) on the Nimbus-7 satellite. *IEEE Trans. Geosci. Remote Sensing*, Vol. 22, N2, p. 133-143.
- Williams G. F. (1969). Microwave radiometry of the ocean and the possibility of marine wind velocity determination from satellite observations. *J. Geophysical Research*, Vol. 74, N 18, p. 4591-4594.
- Williams G. F. (1971). Microwave emissivity measurements of bubbles and foam. *IEEE Trans. Geoscience Electronics*, Vol. 9, N 4 ,p. 221-224
- Wilson T. L. and Hutmeyer S. (2000). Tools of radio astronomy: problems and solutions. Springer-Verlag, New York, 162p.
- Wilson W. J. , Njoku E. G. and Yueh S. H. (2000). Active/passive microwave system with deployable mesh antenna for spaceborne ocean salinity measurements. *IEEE IGARSS 2000 Proceedings*, Vol. VI, IEEE, New York, p. 2549-2551.
- WMO, (1990 a). WCRP, Global Precipitation Climatology Project - implementation and data management plan. WMO/TD-N 367, Geneva, 47 p.
- WMO , (1990 b). Scientific plan for the TOGA coupled ocean-atmosphere response experiment. WCRP Publ. Series N 3 Addendum, WMO/TD-N 64 Addendum, WMO, Geneva, p. 75.
- Wolf D. A. de , and Zwiesler A. J. (1996). Rayleigh-Mie approximation for line-of-sight propagation through rain at 5-90 GHz. *IEEE Trans. Antennas Propagation*, Vol. 44, N3, p. 273-279.
- Wu J. (1981). Bubble population and spectra in near-surface ocean : summary and review of field measurements. *J. Geophysical Research*, Vol. 86, N C1, p. 457-463.
- Wu J., Dong X., Huang Y., and Jiang J. (2000). Some basic considerations of synthetic aperture radiometer. *IEEE IGARSS 2000 Proceedings*, Vol. VII, IEEE, New York, p. 3157-3159.
- Wu S. T. , and Fung A. K. (1972). A noncoherent model for microwave emissions and backscattering from the sea surface. *J. Geophysical Research*, Vol. 77, N 30, p. 5917-5929.
- Wu S. C., Chen M. F., Fung A. K. (1988). Scattering from non-gaussian randomly rough surfaces- cylindrical case. *IEEE Trans. Geosci. Remote Sensing*. Vol. 26,N 6,p. 790-798.
- Wu Z. and Liu A. (2002). Scattering of solar and atmospheric background radiation from a target. *Int. J. Infrared and Millimeter Waves*, Vol. 23, N6, p. 907-917.
- Xu Yong Fu , and Sun De An (2002). A fractal model for soil pores and its application to determination of water permeability. *Physica A*, Vol. 316, N 1-4, p. 56-64.
- Yamamoto K., Otsuka S., Ando M., Kawabe K. and Tsubono K. (2001). Experimental study of thermal noise caused by an inhomogeneously distributed loss. *Physics Letters*, Vol. 280, N 5-6, p. 289-296.
- Yang B. T. (1995). The first ocean remote sensing payload of the ROC: an introduction . COSPAR Colloquium . Space Remote Sensing of Subtropical Oceans. Taipei, Taiwan, p. 13A2-1 - 13A2-3.
- Yano J.-I., Moncrieff M. W. , Wu X., and Yamada. (2001a). Wavelet analysis of simulated tropical convective cloud systems. Part I: basic analysis. *J. Atmospheric Sciences*, Vol. 58, N 8, p. 850-867.
- Yastremskii P.S. .(1961). Dielectric permittivity and structure of water solutions of electrolytes. *Zhurnal Structurnoi Khimii (J. Structural Chemistry)* , Vol. 2, N 3, p. 268-278 (in Russian).
- Yechieli Y., and Wood W. W. (2002). Hydrogeological processes in saline systems: playas, sabkhas, and saline lakes. *Earth-Science Reviews*, Vol. 58, N 3-4, p. 343-365.

- Yueh S. H., Wilson W. J., Li F. K., Nghiem S. V., and Ricketts W. B. (1995). Polarimetric measurements of sea surface brightness temperatures using an aircraft K-band radiometer. IEEE Trans. Geosci. Remote Sensing, Vol. 33, N1, p. 85-92.
- Yueh S. H. , Wilson W. J. , Dinardo S. J. and Li F. K. (1999). Polarimetric microwave brightness signatures of ocean wind directions. IEEE Trans. Geoscience Remote Sensing , Vol. 37, N2, p. 949-959.
- Zaghoul H., and Buckmaster H. A. (1985). The complex permittivity of water at 9,356 GHz from 10 to 40°C. J. Phys. D : Appl. Phys., Vol. 18, N10, p. 2109-2118.
- Zapevalov A. S. and Smolov V. E. (1996). Modeling of spectral characteristics of sea wind waves in the remote sensing problems. Earth Research from Space (Earth Observ. Rem. Sens.- Engl. Transl.), N6 , p. 71-77.
- Zaslavskii G. M. and Sharkov E. A. (1987). Fractal features in breaking wave areas on sea surface. Doklady Acad. Nauk SSSR (Trans. of USSR Academy of Sciences - Engl. Trans.), Vol. 294, N6, p. 1362-1366 .
- Zeldovich Yu. B. , and Sokolov D.D. (1985). Fractals, similarity, intermediate asymptotics. Uspechi Fizicheskich Nauk (Physics-Uspekhi – English Transl.) , Vol. 146 , N 3, p. 493-506.
- Zhevakin S. A. and Naumov A. P. (1967). Propagation of centimeter, millimeter and submillimeter radiowaves in the Earth's atmosphere . Izvestia VUZ. Radiofizika. (Izvestiya , Radiophysics and Quantum Electronics - Engl. Transl.), Vol. 10, N 9-10, p. 1213-1243 .
- Zolotarev V. M. (1983). One-dimensional tolerance distributions. Nauka Publ. House, Moscow, 210pp. (in Russian).
- Zuev V. E. and Komarov V. S.(1987).Statistical models of the temperature and gaseous component of the atmosphere . D. Reidel Publ. Comp., Dordrechts -Boston-Lancaster-Tokio, 306 p.
- Zuzek J. E. (2000). Sensor frequency allocation issues for WRC-2000. IEEE IGARSS 2000 Proceedings, Vol. VI, IEEE, p. 2444-2446.
- Zuzek J. E. , Stevens G. and Marelli E. (2000). Protection of passive sensing use in the 18,6-18,8 GHz band. IEEE IGARSS 2000 Proceedings, Vol. VI, IEEE, New York, p. 2464-2466.